

A Reliability Study of Renewable Energy Resources and their Integration with Utility Grids

Samy M. Ghania
University of Jeddah
Saudi Arabia, Jeddah
sghania@uj.edu.sa

Khaled Mahmoud
University of Jeddah
Saudi Arabia, Jeddah
mrmahmoud@uj.edu.sa

Anas M. Hashmi
University of Jeddah
Saudi Arabia, Jeddah
ahashmi@uj.edu.sa

Received: 18 May 2022 | Revised: 9 June 2022 and 5 July 2022 | Accepted: 12 July 2022

Abstract-Reliability analysis is considered an impressive approach for investigating the planning and design processes of industrial and commercial electrical power distribution systems. Reliability analysis is mainly concerned with the analysis of devices and systems whose individual components are prone to failure risk. The demand for renewable energy resources that work in parallel or replace traditional energy resources is significantly increasing. The current research presents the reliability analysis of the IEEE 40-bus system integrated with large-scale PV and wind systems. Reliability parameters evaluation of power distribution systems will be performed using the zone branch methodology to divide the power system layout into several sections (protected zones). The compensating capacitors will be addressed to clarify their impacts on the system reliability indices. The 40-bus system, known as the IEEE Standard 493-1997, integrated with large-scale PV and wind is simulated using ETAP software. The simulation results reveal that the integration of renewable energy resources with the utility grids can improve the reliability indices. These simulation results are consistent with similar works found in literature and some standards in the field of reliability analysis. The integration of power distribution systems with renewable energy resources improves the reliability indices of the distribution grids.

Keywords-reliability analysis; zone branch methodology; renewable energy resources; high penetration level; impact of compensating capacitors

I. INTRODUCTION

The depletion of fossil fuels, their replacement by renewable energy resources, and the global impact on the environment are the main reasons to implement reliable energy resources. The reliability analysis of the power distribution systems integrated with large-scale renewable energy resources is a critical issue. For the last two decades, the PV/solar and wind energy resources have become the main solution to the rapidly increasing energy demand [1]. Therefore, the reliability analysis of renewable energy resources is receiving more

concern from utility engineers and researchers. Reliability analysis approach is used to determine the impact of distribution network components based on their types (overhead lines, cable, transformers, substation, renewable energy resources, etc.) on the system reliability [2, 3]. Many researches can be found about the reliability of energy generation systems connected with renewable energy resources [4, 5]. Several approaches have been attempted to enhance the renewable energy integration process. Distributed Generation (DG) and its integration have been investigated to dispatch bidirectional flows [6, 7]. The reliability of any system can be simply defined as the probability that a system can perform its intended function for a specified interval under specified conditions [8-10]. The reliability analysis of electrical power distribution systems integrated with renewable energy resources is performed using mathematical model approaches [11, 12]. These approaches aim to control the consequence of failures and to identify the frequency and their causes. Reliability computation mathematical models of the electrical power distribution systems should be developed to include the relationships between different sub systems [13, 14]. There are many approaches that can be implemented to study the reliability of the power distribution systems integrated with renewable energy resources [15, 16]. Various approaches such as the optimal location of protective and switching equipment, proper monitoring and maintenance, the use of distributed generation units, electrical energy storage, network automation and smart grid concepts, and preventive and reliability-based maintenance and repairs have been reported [17, 18]. One of the simplest and most practical approaches of reliability studies is sensitivity analysis by which the critical component of the system can be identified [15, 19]. The demand of increased reliability and optimum economic performance of utility grids integrated with renewable energy resources has become very important. Recently, concern have been given to the substantial growth in utilizing distributed energy resources. The more the electrical power distribution systems become larger and

interconnected with renewable energy resources, the more complex computational approaches are needed [20, 21]. These approaches should be able to assess the impacts of unreliable protective equipment and protection-coordination schemes on individual load point reliability indices within a given system configuration. One of these approaches is the zone branch methodology that overcomes many limitations and can be applied to a large electrical power distribution system [22, 23]. The main advantage of the zone branch methodology is that it can readily identify faulty protection schemes involving all the components of large electrical power distribution systems and can evaluate load point reliability indices.

The current research presents a full simulation of the 40-bus system known as the IEEE Std. 399-1997 system integrated with large-scale PV and wind systems with capacity up to 3GW. Simulations were performed to introduce the reliability concepts and indices of electrical distribution systems integrated with renewable energy resources for the two modes (ON and OFF of the grid) of the system. The reliability evaluation of power distribution systems was performed using the zone branch methodology in which the distribution system is divided into several sections (protected zones). The obtained results will be compared with similar works found in literature and some standards in the field of reliability analysis [24, 25].

The current research could be used by utility engineers that want to estimate the impact of the integrating renewable energy resources on system reliability. Moreover, it could be a very powerful planning tool for load scheduling and forecasting in order to meet the increasing demand of electrical energy.

II. RELIABILITY INDICES AND ZONE BRANCH METHODOLOGY

A. Reliability Main Concepts and Indices

Electrical power distribution systems are made up of components or subsystems. Each component has its own expected failure rate which is defined as the number of expected failures per unit in a given time interval [26, 27]. The failure rate is evaluated as $\lambda \left(\frac{f}{yr} \right)$:

$$\lambda = \frac{\text{Number of failures}}{\text{Total operating time of the unit}} \quad (1)$$

As the reliability function is actually a failure density function, the average time for a failure to occur and is known as the Mean Time To Failure (MTTF) which is given as [28]:

$$MTTF = \int_0^{\infty} e^{-\lambda t} dt = \frac{1}{\lambda} \quad (2)$$

The repair time is the time taken to change the unit state from the off state to the on state and it is denoted as MTTR. The failure rate is reciprocal of MTTF and similarly, the repair rate (r) is equal to the reciprocal of repair time. The percentage of time that the system is functioning is called availability (A), meanwhile its outage of services is the unavailability (\bar{A}) of the system:

$$A = \frac{\text{total hours of on time in 1 year}}{8760} = \frac{MTTF}{MTTF+MTTR} \quad (3)$$

$$\bar{A} = \frac{\text{total hours of off time in 1 year}}{8760} = \frac{MTTR}{MTTF+MTTR} \quad (4)$$

For systems that can be treated as a single component with a constant failure rate λ and repair rate μ the availability is:

$$A = \frac{MTTF}{MTTF+MTTR} = \frac{\frac{1}{\lambda}}{\frac{1}{\lambda} + \frac{1}{\mu}} = \frac{\mu}{\lambda + \mu} \quad (5)$$

Based on the functionality sequence point of view, the electrical power distribution systems are connected in series, in parallel, or in combinations. Each component in a series system has its own failure rate and reliability. The probability of all the components functioning is simply the product of the probabilities of individual components functioning. Consequently, if the components have exponential failure probabilities with corresponding failure rates, $\lambda_1, \lambda_2, \dots, \lambda_n$, then the system reliability and the MTTF can be presented as:

$$R_{system}(t) = R_1(t) X R_2(t) X \dots X R_n(t) \quad (6)$$

$$R_{system} = e^{-\lambda_1 t} X e^{-\lambda_2 t} X \dots X e^{-\lambda_n t} = e^{-\lambda t} \quad (7)$$

$$MTTF_{system} = \frac{1}{\lambda} \quad (8)$$

For the parallel systems, if the $Q(t)$ is the probability of failure in a given period, which is considered as the unreliability, then:

$$Q(t)_{system} = Q_1(t) X Q_2(t) X \dots X Q_n(t) \quad (9)$$

If all the components have the same $Q(t)$, then the system reliability $R(t)$ can be presented as:

$$Q(t)_{system} = Q^n(t) \quad (10)$$

$$R(t)_{system} = 1 - Q(t)_{system} \quad (11)$$

$$R(t)_{system} = 1 - [(1 - e^{-\lambda_1 t}) X (1 - e^{-\lambda_2 t}) X \dots (1 - e^{-\lambda_n t})] \quad (12)$$

If all the components have the same λ , then the system reliability and MTTF can be expressed as:

$$R(t)_{system} = 1 - [1 - e^{-\lambda t}]^n \quad (13)$$

$$MTTF = \frac{1}{\lambda} + \frac{1}{2\lambda} + \frac{1}{3\lambda} + \dots + \frac{1}{n\lambda} \quad (14)$$

Reliability evaluation of the electric power distribution systems depends on two basic parameters: load point indices and system reliability indices. The load point indices include the load point failure rate, the average outage time, and the average annual unavailability or outage. Load point indices are very important from the customer's viewpoint. System reliability indices are important for system performance. The system reliability indices can be divided into two categories: interruption indices and energy-oriented indices [29, 31]. Interruption indices are used to evaluate the average number of sustained interruptions noticed by a customer for long-term sustained interruptions. Based on the IEEE Standard 1366-2012, the four main interruption indices used are:

- System Average Interruption Frequency Index (SAIFI)
- System Average Interruption Duration Index (SAIDI)
- Customer Average Interruption Duration Index (CAIDI)
- Customer Total Average Interruption Duration Index (CTAIDI)

SAIFI indicates the average number of interruptions happened to a customer within one year. It is given by:

$$SAIFI = \frac{\sum N_i}{N_T} \quad (15)$$

where N_i is the total number of customers interrupted and N_T is the total number of customers served.

SAIDI is the most used index to evaluate the system performance through calculating the sustained interruption of each customer in service area during a determined period (minutes or hours) per year and it can be obtained by the following expression [21, 23]:

$$SAIDI = \frac{\sum r_i * N_i}{N_T} \quad (16)$$

where r_i is the restoration time for each interruption event.

CAIDI gives the average outage duration that any customer may have exposed. It can be calculated as:

$$CAIDI = \frac{\sum r_i * N_i}{N_i} \quad (17)$$

CTAIDI represents the average time the customer spends during interruptions. The value of this index is calculated as:

$$CTAIDI = \frac{\sum r_i * N_i}{C_N} \quad (18)$$

where C_N is the number of customers interrupted.

The Average Service Availability Index (ASAI) is the ratio of the total hours that the service is available during a determined period (usually monthly or yearly) to the total hours of customer demand [24, 26].

$$ASAI = 1 - \left(\frac{\sum r_i * N_i}{T * N_T} \right) \quad (20)$$

where T is the time under study.

Energy-oriented indices are very important in evaluating the load in distribution networks. The most important indices are the average load, the Expected Energy Not Supplied (EENS) index, and the Average Energy Not Supplied (AENS) index. EENS index is used to calculate the total energy generated but not supplied by the system and is calculated by:

$$EENS = \sum L_{a(i)} * U_i \quad (21)$$

where $L_{a(i)}$ is the average connected load at point i and U_i represents the average annual outage time at the load point i . AENS index represents the average value of the energy not supplied by the system corresponding to the total number of customers that are served.

$$AENS = \sum_i^n \frac{L_{a(i)} * U_i}{N_i} \quad (22)$$

LOEE is used to determine the total expected energy losses (KWh) when the load demand is not satisfied from the generation system [27].

$$LOEE = \sum_{i=1}^n e_i (EP_i < LED_i) \quad (23)$$

where EP_i is the generated total energy, LED_i is the total load demand, and e_i is the unsupported load demand.

B. Zone Branch Methodology

To evaluate the protection-coordination and reliability characteristics of the electrical power distribution systems, it is essential to divide the electrical power distribution system into protective zones. Any protective zone is a part of the power system and can isolate or detach itself automatically or manually from the remaining power system if a fault occurs in any of its links. These protective zones are connected in series or in parallel and each zone is formed by a group of branches. The symbol $\lambda(i,j)$ represents the failure rate of zone i within the branch j . Each zone branch has an isolating device labeled $S(i,j)$ and these isolating devices can be manual or automatic switches, fuses, reclosers, or a relay breaker combination. Each isolating device has a probability $q(i,j)$ it will not recognize and isolate any permanent faults of the equipment within its zone. The failure rate $\lambda(i,j)$ of any zone i and branch j is the sum of all the equipment failure rates whose failure will result in the operation of the isolating device of zone i and branch j only. The total failure rate $\lambda_T(i,j)$ (f/yr) and the annual downtime $\lambda_r(i,j)$ for any zone i and branch j can be calculated as:

$$\lambda_T(i,j) = \lambda_s + \sum RIA(z,k) \times FZB(k)^T \quad (24)$$

$$\lambda_r(i,j) = \lambda_s \times rs \sum RIA(z,k) \times FZB(k)^T \times R(z,k) \quad (25)$$

where λ_s is the failure rate of utility supply or plant supply, rs is the restoration duration of utility supply, z the zone branch number, k the total number of zone branches in system, $R(z,k)$ the repair or switching time of each zone branch, $FZB(k)$ is the failed zone branch array that contains the failure rate of each zone branch k , and $RIA(z,k)$ is the recognition and isolation array coefficients. Figure 1 presents a simple schematic of the zone branch and the main indices used in the sectionalization process.

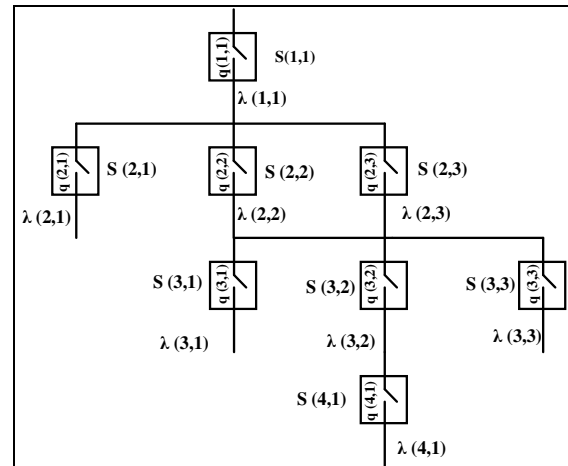


Fig. 1. Simple schematic of a branch zone with main parameters.

III. SIMULATED SYSTEM CONFIGURATION

In this section, the grid system, along with two large-scale renewable energy sources (PV and wind), is simulated using the ETAP software package. ETAP is an analytical engineering software package for simulation, design, monitoring, control, operator training, optimizing, and automating power systems. ETAP can be used to design, analyze, and exchange the system

data into many different simulating software packages like PSCAD to perform electromagnetic transient analysis, such as switching transients, insulation coordination, lightning surges, resonance, etc. The ETAP interface is a powerful tool needed to be more user-friendly rather than other simulating software packages. ETAP has impressive capabilities to simulate unlimited number of buses. The selected grid is the 40-bus system, also known as the IEEE Standard 493-1997 [25], which consists of loads, capacitor banks, transmission lines, and generators. This grid is a 13.8KV (RMS line-line) transmission system. Zone branch methodology can be applied in many different scenarios by sectionalizing the electrical power system single line diagram. These scenarios are based on the system configurations. Table I shows the main reliability data of the grid and the simulated solar and wind farms. The Table is truncated to fit and comply with the restrictions and limitations of the paper size and more data can be obtained from the Standard. The reliability values given in Table I are the design reliability parameters for each piece of equipment and instrument. These values are implemented as the base values for each element in the utility grid.

TABLE I. MAIN RELIABILITY DATA OF THE SIMULATED SYSTEM

Main characteristics of the transformers			
Trans. No.	Rating (MVA)	λ (Failure/year)	Replace time (h/year)
T1	15	0.0153	192
T2	15	0.0153	192
.....
T13	3.5	0.0059	79.3
T14	1.5	0.0059	79.3
Main characteristics of the motors/generators			
Motor. No.	Rating (MVA)	λ (Failure/year)	Replace time (h/year)
M1	0.7	0.0824	42.5
M2	0.5	0.0109	18.3
.....
M20	1.5	0.0714	75.1
M21	1.75	0.0404	76.0
G	10	0.00536	478.0
Main characteristics of the switchgear bus and bus ducts			
Bus bar. No.	Rating (MVA)	λ (Failure/year)	Replace time (h/year)
1	-	0.0034	26.8
2	-	0.0034	26.8
...	-
39	-	0.001048	11.5
40	-	0.003601	109.8
Main characteristics of each PV and Wind system			
Equip.	Rating (MVA)	λ (Failure/year)	Replace time (h/year)
PV systems	1500	1.254	5
Wind turbine	1500	0.02	50

In the current research, 5 different case studies will be implemented, as shown in Figure 2. The simplified schematic diagram of the simulated systems connected with the PV and wind systems can be seen in [26]. The PV system consists of 5 sub-farms, 300MW each. Meanwhile, the wind system consists of 5 sub-farms, also 300MW each. Each PV and wind farm will be connected to the main utility bus labelled by bus number 40 as shown in Figure 3. The PV/wind systems are connected to the main supply bus No.40 because of the large scale of the PV

and wind systems. The bus No. 40 is the utility bus and the proposed PV and wind system will phase out completely the utility supply. Also, based on the limitations of the IEEE 40 bus configuration for power capacity and total load flow, the renewable energy systems are connected to bus No. 40. The connected PV and wind farms with different capacities of 300, 600, 900, 1200, and 1500MW respectively are based on the proposed scale by the Electric holding company of Egypt for two different projects [30, 31]. As the bus No. 40 is the main utility bus, the renewable energy resources will be connected to this bus to work in parallel with the utility grid or phasing out the grid supply. Different scenarios for patching of the renewable sources will be simulated to calculate the impacts of connecting different renewable energy resources on the reliability indices.

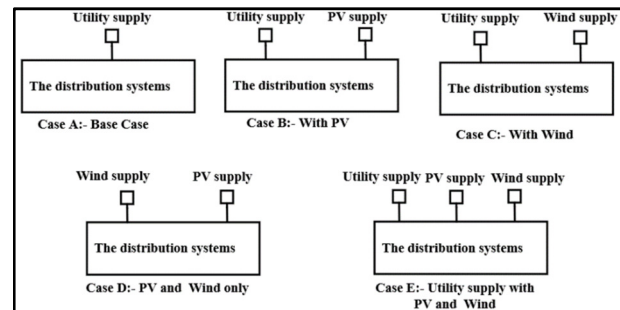


Fig. 2. Simple schematic of the different case studies.

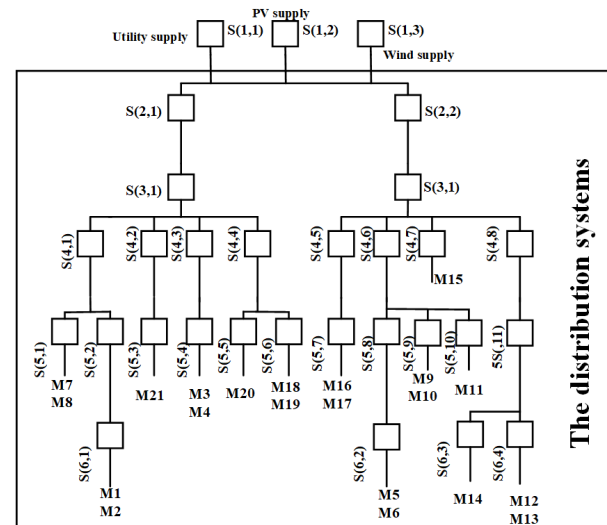


Fig. 3. The main zones for the grid model connecting PV and wind systems.

Figure 3 presents the main zones of the simulated model with connections with PV and wind systems. Different scenarios for patching of the renewable sources will be tackled. The main target is to investigate the different impacts on the reliability indices over the different cases of connecting PV and wind systems to the grid. Figure 4 presents a simple flowchart for the proposed simulated systems. Figure 5 presents a screenshot of the simulated IEEE 40 bus system with PV /Wind farms using the ETAP software.

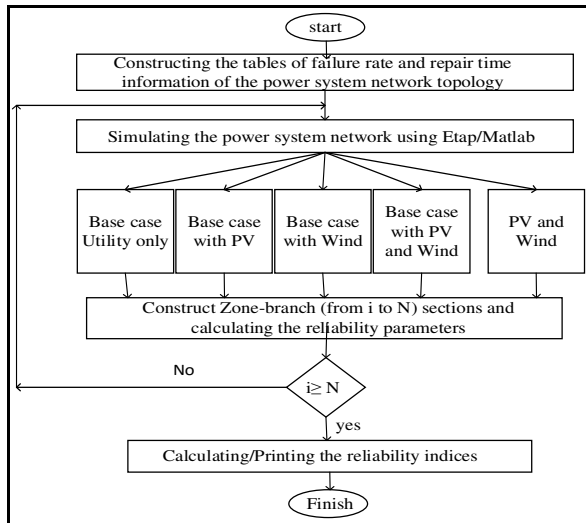


Fig. 4. Flowchart of the proposed approach.

IV. SIMULATION RESULTS

The IEEE 40 bus power distribution system was simulated to investigate the reliability indices for different case studies. Therefore, each case study was performed to show the impact of connecting PV and wind renewable energy resources to the utility grid on the different reliability indices. The zone branch methodology was used to sectionalize the different protective zones in the simulated system. These protective zones are used to calculate the reliability parameters for all the pieces of equipment included in the zone. The main target is to calculate the failure rate of each zone. For the new added zones of PV and wind systems, the zone failure/repair rates can be calculated by (24) and (25). Considering all the components inside the PV system and the circuit breaker, transformer, and busbar systems, the failure rate is: $\lambda_T(1,2) = \lambda(PV + Trans. + 2C.B + busbar) = 1.254 + 0.0153 + 2 * 0.012 + 0.03 = 1.3233\text{f/yr}$ and the replace time is 76.56h/f. Similarly, while considering all the components inside the wind system and the circuit breaker, transformer, and busbar systems $\lambda_T(1,3) = 0.09\text{f/yr}$ and the replace time is 18.91h/f. Based on the different zones shown in Figure 3, Table II tabulates the main reliability data of the different zones for the base-case and the different case studies. The renewable energy resources are added as Zone (1,2) and Zone (1,3) for PV and wind respectively. The failure rates of these two added zones are calculated and added with double-cell borders in Table II. Table III tabulates the different reliability indices for the different case studies while connecting the PV and wind systems with maximum capacity of 1500MW. It can be observed from Table III that when connecting PV and wind systems, the reliability indices are improved, and consequently, the performance of the electrical power distribution systems is improved. This improvement will be reflected to the energy continuity at the customer's side. Moreover, focus will be given to the 3 most important indices (EENS, AENS and LOEE) while demonstrating the impacts of the compensating capacitors connected as shown in Figure 5. The main configuration of the network topology is mentioned in [25].

The main voltage stability indices (reactive and active power, Voltage, and power factor) are used to pre-identify the location/size of the capacitor. Initially the optimal location depends on the network topology, configurations, loading, etc. In order to overcome this issue, the load flow study is performed using ETAP to determine the main voltage stability indices at each bus. Bus No. 3 is considered the main loading bus and based on the results of the load flow, it is found to have the worst voltage stability indices. So, this bus is connected to the compensating capacitors. The values of 4MVar and 8MVar of the compensating capacitors are proposed after trials to maintain the main targeted voltage stability indices (voltage not less than 98% and power factor not less than 0.9).

TABLE II. FAILURE RATE AND DURATION OF DIFFERENT ZONE BRANCHES

Case A: Base case (utility only)			
Zone	λ (failure/year)	Interruption (h/year)	Replace time (h/failure)
(1,1)	1.0583	2.16133	2.04226
(2,1)	0.0223	3.32788	149.232
---	-----	-----	-----
(6,3)	0.1032	8.120	75.339
(6,4)	0.1032	4.2711	41.3869
Case B (utility with PV)			
Zone	λ (failure/year)	Interruption (h/year)	Replace time (h/failure)
(1,1)	1.0583	2.16133	2.04226
(1,2)	1.3233	2.752	76.56
(2,1)	0.0223	3.32788	149.232
---	-----	-----	-----
(6,3)	0.1032	8.120	75.339
(6,4)	0.1032	4.2711	41.3869
Case C (utility with Wind)			
Zone	λ (failure/year)	Interruption (h/year)	Replace time (h/failure)
(1,1)	1.0583	2.16133	2.04226
(1,3)	0.09	2.3	18.91
(2,1)	0.0223	3.32788	149.232
---	-----	-----	-----
(6,3)	0.1032	8.120	75.339
(6,4)	0.1032	4.2711	41.3869
Case D (utility with PV and Wind)			
Zone	λ (failure/year)	Interruption (h/year)	Replace time (h/failure)
(1,1)	1.0583	2.16133	2.04226
(1,2)	1.3233	2.752	76.56
(1,3)	0.09	2.3	18.91
(2,1)	0.0223	3.32788	149.232
---	-----	-----	-----
(6,3)	0.1032	8.120	75.339
(6,4)	0.1032	4.2711	41.3869
Case E (PV and Wind without the utility)			
Zone	λ (failure/year)	Interruption (h/year)	Replace time (h/failure)
(1,2)	1.3233	2.752	76.56
(1,3)	0.09	2.3	18.91
(2,1)	0.0223	3.32788	149.232
---	-----	-----	-----
(6,3)	0.1032	8.120	75.339
(6,4)	0.1032	4.2711	41.3869

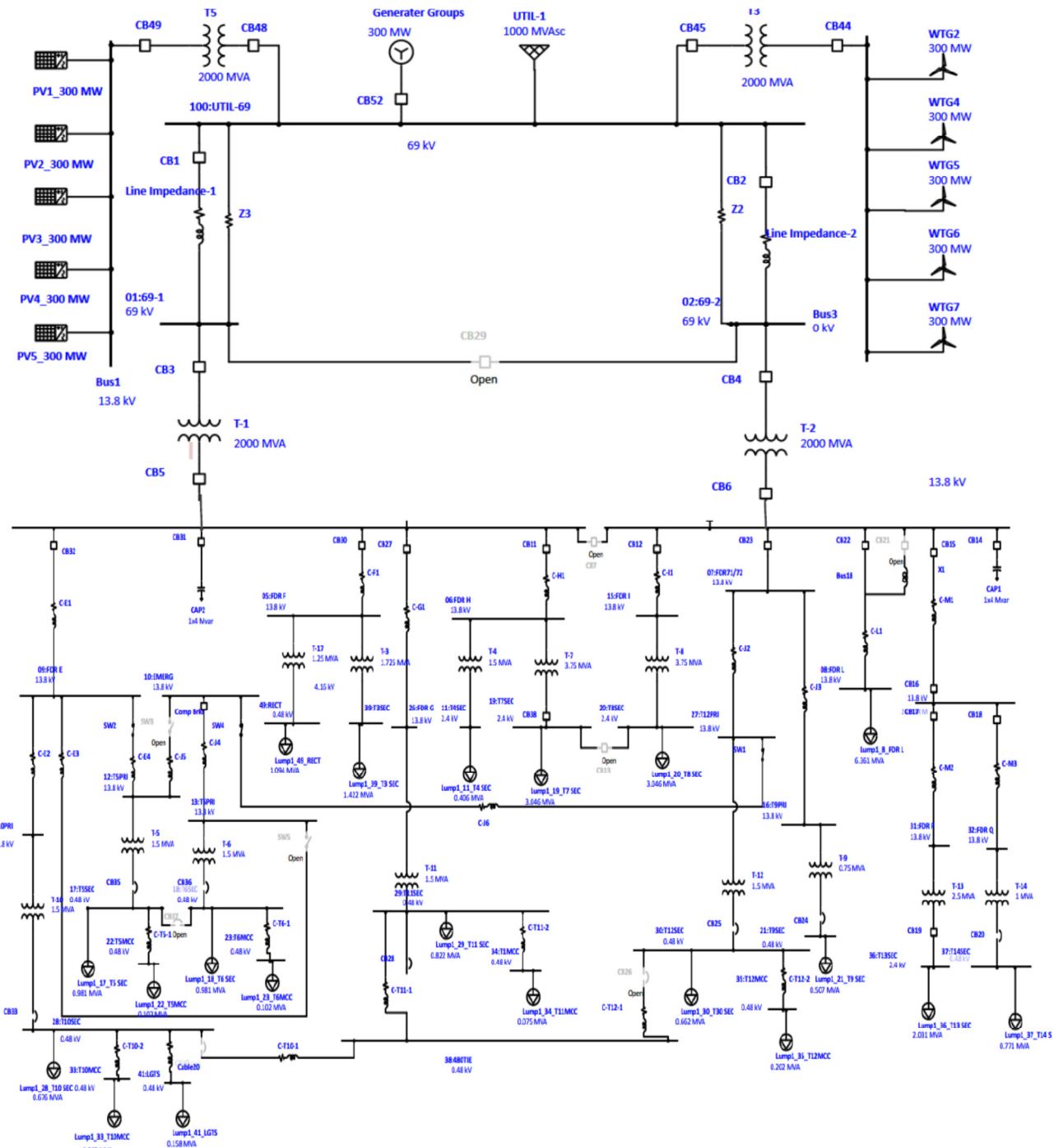


Fig. 5. Screenshot of the simulated IEEE 40 bus system with PV and wind farms.

TABLE III. SYSTEM PERFORMANCE RELIABILITY INDICES

Indices	Case A	Case B	Case C	Case E	Case D
SAIFI	0.1335	0.1348	0.1348	0.1361	0.1373
SAIDI	9.9537	9.9923	9.9923	10.0309	10.069
CAIDI	74.569	74.144	74.144	73.727	73.317
ASAI	0.9989	0.9989	0.9989	0.9989	0.9989
ASUI	0.00114	0.0011	0.0011	0.00115	0.0011
EENS	176.322	177.54	177.54	178.753	179.96
AENS	8.3963	8.4542	8.4542	8.512	8.5699
LOEE	294.21	296.15	296.52	297.13	300.75

The two capacitor banks of 4MVar are considered for the different case studies to show the improvement for reliability indices. Figure 6 presents the impact of using 8MVar capacitors on the total energy generated but not supplied by the system (EENS) for the different case studies. It can be noted that the EENS is improved by about 3%.

Table III shows that some reliability indices increase and others decrease with more penetration of PV and wind. The increasing/decreasing level depends on the system

configuration and the index definition. For example, the CAIDI is decreased and this decrease is considered as an improvement based on its meaning and the system's performance is consistent with [35]. Figure 7 presents the impact of using 8MVar capacitors on the AENS for the different case studies. It can be noted that the AENS improved when using the PV and Wind systems by about 7%. Figure 8 presents the impact of using 8MVar capacitors on LOEE for the different case studies. It can be noted that, LOEE is improved by using the PV and Wind systems by about 8%.

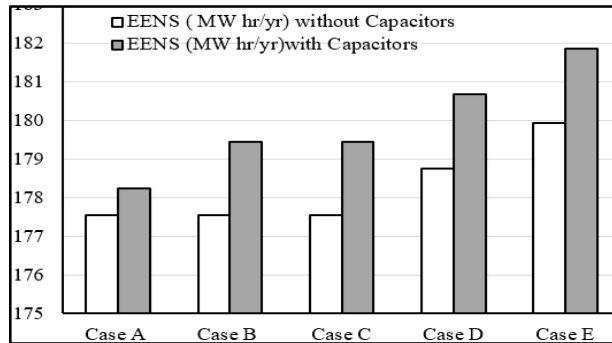


Fig. 6. Impact of the compensating capacitor on the EENS for different case studies.

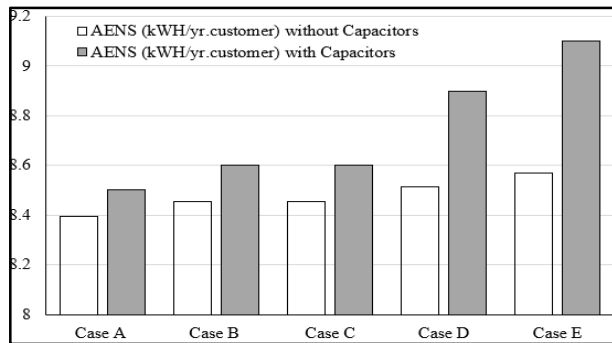


Fig. 7. Impact of the compensating capacitor on AENS for different case studies.

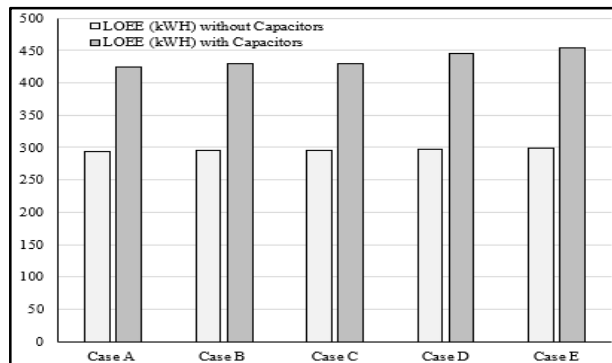


Fig. 8. Impact of the compensating capacitor on the LOEE for different case studies.

To verify and validate the obtained simulated results of the proposed model, they will be compared with the results of similar models found in literature. The reliability and its indices sensitivity analysis has been conducted for IEEE 94 – bus and

IEEE 69– bus with two different techniques [32, 34]. The Fault Index Matrix (FIM) technique was implemented in [33], and Gaussian distribution and fuzzy technique was used in [34]. EENS and SAIDI reliability indices are shown in Table IV for the proposed model and the two studied cases of the literature [33, 34]. The simulated results of the proposed method show reasonable consistency with the two other techniques with minor differences. The differences are less than 10% and mainly come due to the differences in the configuration and the loading conditions.

TABLE IV. SYSTEM PERFORMANCE RELIABILITY INDICES

Reliability indices	Proposed model	FIM [33]	FUZZY [34]
SAIDI	10.0309	11.2	11.5
EENS	178.753	181.1	187.8

V. CONCLUSIONS

The different reliability indices of the electric power distribution system of IEEE 40 bus integrated with large-scale PV and wind renewable energy source systems are elaborated with the use of the ETAP software. The integration process is simulated for the IEEE 40 bus grid with two renewable energy sources consisting of 5 sub-farms of 300MW each. The total capacities of PV and wind systems are 1500MW each. The power distribution system of IEEE 40 bus is sectionalized using the zone branch methodology that divides the power system network into several sections (protected zones) in order to calculate the different reliability parameters for the different zones including the new connected PV and wind systems. The reliability indices were evaluated for different case study scenarios.

The impact of penetrating PV and wind systems on the reliability indices is demonstrated in this study. Furthermore, the impact of connecting the compensating capacitor banks of 2x4Mvar on the most important reliability indices (EENS, AENS, and LOEE) has been investigated. The reliability indices can be improved by about 8% for integrating PV and wind systems. According to the obtained results, the integration of PV and wind systems into the electric power distribution systems improves their reliability indices. The obtained results have very good consistency and compliance with other research studies and with the standards related to the renewable energy sources. This research can be a pre-design powerful tool for system designers and utility engineers to avoid any maloperation or power discontinuity problems.

ACKNOWLEDGEMENT

This work was funded by the University of Jeddah, Jeddah, Saudi Arabia, under grant No. (UJ-21-DR-72). The authors, thank the University of Jeddah for the technical and financial support.

REFERENCES

- [1] O. US EPA, "Energy Resources for State, Local, and Tribal Governments," Jun. 19, 2017. <https://www.epa.gov/statelocalenergy>.
- [2] S. S. Refaat, H. Abu-Rub, M. Trabelsi, and A. Mohamed, "Reliability evaluation of smart grid system with large penetration of distributed energy resources," in *International Conference on Industrial*

- Technology, Lyon, France, Feb. 2018, pp. 1279–1284, <https://doi.org/10.1109/ICIT.2018.8352362>.
- [3] V. Vivek and C. P. Das, "Reliability Analysis using Renewable Energy Sources," *International Journal of Mechanical and Industrial Engineering*, vol. 1, no. 1, pp. 47–50, Jul. 2011, <https://doi.org/10.47893/IJME.2011.1011>.
 - [4] A. M. Huseynov and O. B. Azadkhanov, "Development of intellectual information-measuring system for Azerbaijan power system regime reliability control," in *Modern Electric Power Systems*, Wroclaw, Poland, Sep. 2019, pp. 1–3, <https://doi.org/10.1109/MEPS46793.2019.9394977>.
 - [5] L. Anan, "Application of MATLAB Software in Reliability Verification Test of Success or Failure Product," in *International Conference on Computer Systems, Electronics and Control*, Dalian, China, Dec. 2017, pp. 1191–1193, <https://doi.org/10.1109/ICCSEC.2017.8447042>.
 - [6] Y.-W. Chen and J. M. Chang, "EMaaS: Cloud-Based Energy Management Service for Distributed Renewable Energy Integration," *IEEE Transactions on Smart Grid*, vol. 6, no. 6, pp. 2816–2824, Aug. 2015, <https://doi.org/10.1109/TSG.2015.2446980>.
 - [7] R. A. Walling, R. Saint, R. C. Dugan, J. Burke, and L. A. Kojovic, "Summary of Distributed Resources Impact on Power Delivery Systems," *IEEE Transactions on Power Delivery*, vol. 23, no. 3, pp. 1636–1644, Jul. 2008, <https://doi.org/10.1109/TPWRD.2007.909115>.
 - [8] P.-C. Chen *et al.*, "Analysis of Voltage Profile Problems Due to the Penetration of Distributed Generation in Low-Voltage Secondary Distribution Networks," *IEEE Transactions on Power Delivery*, vol. 27, no. 4, pp. 2020–2028, Jul. 2012, <https://doi.org/10.1109/TPWRD.2012.2209684>.
 - [9] A. K. Verma, S. Ajit, and D. R. Karanki, *Reliability and Safety Engineering*. New York, NY, USA: Springer International Publishing, 2010.
 - [10] M. Rausand and A. Hoyland, *System Reliability Theory: Models, Statistical Methods, and Applications*, 2nd edition. Hoboken, NJ, USA: John Wiley & Sons, 2003.
 - [11] M. Xie, Y.-S. Dai, and K.-L. Poh, *Computing System Reliability: Models and Analysis*. New York, NY, USA: Kluwer Academic Publishers, 2004.
 - [12] E. A. Elsayed, *Reliability Engineering*, 2nd edition. Hoboken, NJ, USA: Wiley, 2012.
 - [13] J. Sun, V. Palade, X.-J. Wu, W. Fang, and Z. Wang, "Solving the Power Economic Dispatch Problem With Generator Constraints by Random Drift Particle Swarm Optimization," *IEEE Transactions on Industrial Informatics*, vol. 10, no. 1, pp. 222–232, Oct. 2014, <https://doi.org/10.1109/TII.2013.2267392>.
 - [14] A. Golshanfard and H. Hashemi-Dezaki, "Sensitivity Analysis of Distribution System Reliability for Identifying the Critical Elements," in *27th Iranian Conference on Electrical Engineering*, Yazd, Iran, Dec. 2019, pp. 522–526, <https://doi.org/10.1109/IranianCEE.2019.8786589>.
 - [15] M. Lwin, J. Guo, N. Dimitrov, and S. Santoso, "Protective Device and Switch Allocation for Reliability Optimization With Distributed Generators," *IEEE Transactions on Sustainable Energy*, vol. 10, no. 1, pp. 449–458, Jan. 2019, <https://doi.org/10.1109/TSTE.2018.2850805>.
 - [16] H. Hashemi-Dezaki, H. Askarian-Abyaneh, A. Shams-Ansari, M. DehghaniSaniji, and M. A. Hejazi, "Direct cyber-power interdependencies-based reliability evaluation of smart grids including wind/solar/diesel distributed generations and plug-in hybrid electrical vehicles," *International Journal of Electrical Power & Energy Systems*, vol. 93, pp. 1–14, Dec. 2017, <https://doi.org/10.1016/j.ijepes.2017.05.018>.
 - [17] M. Abdelghany and S. Tahar, "Cause-Consequence Diagram Reliability Analysis Using Formal Techniques With Application to Electrical Power Networks," *IEEE Access*, vol. 9, pp. 23929–23943, 2021, <https://doi.org/10.1109/ACCESS.2021.3051968>.
 - [18] H. H. Dezaki, H. A. Abyaneh, Y. Kabiri, H. Nafisi, K. Mazlumi, and H. A. Fakhrabadi, "Optimized protective devices allocation in electric power distribution systems based on the current conditions of the devices," in *International Conference on Power and Energy*, Kuala Lumpur, Malaysia, Nov. 2010, pp. 577–582, <https://doi.org/10.1109/PECON.2010.5697648>.
 - [19] K. Pereira, B. R. Pereira, J. Contreras, and J. R. S. Mantovani, "A Multiobjective Optimization Technique to Develop Protection Systems of Distribution Networks With Distributed Generation," *IEEE Transactions on Power Systems*, vol. 33, no. 6, pp. 7064–7075, Aug. 2018, <https://doi.org/10.1109/TPWRS.2018.2842648>.
 - [20] Z. Guo, H. Wang, Y. Wang, G. Liu, and Y. Li, "An improved algorithm for power system reliability sensitivity analysis," in *5th International Conference on Electric Utility Deregulation and Restructuring and Power Technologies*, Changsha, China, Nov. 2015, pp. 6–11, <https://doi.org/10.1109/DRPT.2015.7432200>.
 - [21] D. J. Smith, *Reliability, Maintainability and Risk: Practical Methods for Engineers including Reliability Centred Maintenance and Safety-Related Systems*, 8th ed. Butterworth-Heinemann, 2011.
 - [22] R. N. Allan and R. Billinton, *Reliability Evaluation of Power Systems*, 2nd ed. New York, NY, USA: Springer, 2013.
 - [23] G. Bhatt and S. Affljulla, "Analysis of large scale PV penetration impact on IEEE 39-Bus power system," in *58th International Scientific Conference on Power and Electrical Engineering of Riga Technical University*, Riga, Latvia, Oct. 2017, pp. 1–6, <https://doi.org/10.1109/RTUCON.2017.8124840>.
 - [24] Y. Xu and C. Singh, "Power System Reliability Impact of Energy Storage Integration With Intelligent Operation Strategy," *IEEE Transactions on Smart Grid*, vol. 5, no. 2, pp. 1129–1137, Mar. 2014, <https://doi.org/10.1109/TSG.2013.2278482>.
 - [25] "IEEE SA - IEEE 493-1997," *IEEE Standards Association*. <https://standards.ieee.org/ieee/493/726>.
 - [26] A. Chowdhury and D. Koval, *Power Distribution System Reliability: Practical Methods and Applications*. Hoboken, NJ, USA: John Wiley & Sons, 2011.
 - [27] B. Kekezoglu, O. Arikian, A. Erduman, E. Isen, A. Durusu, and A. Bozkurt, "Reliability analysis of hybrid energy systems: Case study of Davutpasa Campus," in *Eurocon*, Zagreb, Croatia, Jul. 2013, pp. 1141–1144, <https://doi.org/10.1109/EUROCON.2013.6625124>.
 - [28] S. S. Kar and L. B. Roy, "Probabilistic Based Reliability Slope Stability Analysis Using FOSM, FORM, and MCS," *Engineering, Technology & Applied Science Research*, vol. 12, no. 2, pp. 8236–8240, Apr. 2022, <https://doi.org/10.48084/etasr.4689>.
 - [29] B. M. Alshammari, "Probabilistic Evaluation of a Power System's Reliability and Quality Measures," *Engineering, Technology & Applied Science Research*, vol. 10, no. 2, pp. 5570–5575, Apr. 2020, <https://doi.org/10.48084/etasr.3441>.
 - [30] S. M. Ghanian and A. M. Hashmi, "Transient Overvoltages Simulation Due to the Integration Process of Large Wind and Photovoltaic Farms With Utility Grids," *IEEE Access*, vol. 9, pp. 43262–43270, 2021, <https://doi.org/10.1109/ACCESS.2021.3065874>.
 - [31] *Egypt Energy Policy Laws and Regulations Handbook: Volume 1 Strategic Information and Developments*. Washington DC, USA-Egypt: International Business Publications, 2015.
 - [32] M. Boukhalfa, A. Benaissa, M. R. Bengourina, A. Khoudiri, and M. Boudiaf, "Performance Enhancement of the DPC Control Based on a VGPI Controller Applied to a Grid Connected PV System," *Engineering, Technology & Applied Science Research*, vol. 12, no. 2, pp. 8253–8258, Apr. 2022, <https://doi.org/10.48084/etasr.4697>.
 - [33] T. Zhang, C. Wang, F. Luo, P. Li, and L. Yao, "Analytical Calculation Method of Reliability Sensitivity Indexes for Distribution Systems Based on Fault Incidence Matrix," *Journal of Modern Power Systems and Clean Energy*, vol. 8, no. 2, pp. 325–333, Mar. 2020, <https://doi.org/10.35833/MPCE.2018.000750>.
 - [34] I. Akhtar, M. Jameel, A. Altamimi, and S. Kirmani, "An Innovative Reliability Oriented Approach for Restructured Power System Considering the Impact of Integrating Electric Vehicles and Renewable Energy Resources," *IEEE Access*, vol. 10, pp. 52358–52376, 2022, <https://doi.org/10.1109/ACCESS.2022.3174365>.
 - [35] M. Z. Kamaruzaman, N. I. A. Wahab, and M. N. M. Nasir, "Reliability Assessment of Power System with Renewable Source using ETAP," in *International Conference on System Modeling & Advancement in Research Trends*, Moradabad, India, Nov. 2018, pp. 236–242, <https://doi.org/10.1109/SYSMART.2018.8746980>.

AUTHOR PROFILES



Samy M. Ghania was born in Egypt, in 1971. He received the B.Sc., M.Sc., and Ph.D. degrees in electrical engineering from the Faculty of Engineering, Benha University, Cairo, Egypt, in 1995, 2001, and 2005 respectively. In July 2006, he joined the University of Waterloo, Waterloo, ON, Canada, as a Postdoctoral Fellow. He is currently working as a Professor of electrical engineering at the University of Jeddah, Saudi Arabia. He has published several papers in international

journals and conferences in electrical machines, drives, interference, and electromagnetic simulation, and effects on the human body. He has carried several projects on electrical machine control using micro-controllers, DSP, programmable logic control, and renewable energy resources. His areas of interest include modeling and simulation of electrical machines, drives for electrical vehicles, and its control systems.



Khaled R. M. Mahmoud, is a Professor in the Mechanical and Materials Engineering Department, College of Engineering, University of Jeddah, Saudi Arabia. He received his Ph.D. degree from the Heinz Nixdorf Institute, University of Paderborn, Paderborn, Germany in 2005. He has pioneered research in vehicle dynamics and vehicle braking systems and has

published more than 35 research articles. He has reviewed several research papers in ISI journals, in fields such as Energy Conversion and Management and Vehicle dynamics. His current research is on the dynamics of hybrid vehicle systems and internal combustion engines fueled by alternative fuels.



Anas M. Hashmi was born in Saudi Arabia. He received the B.Eng. degree in electrical and electronic engineering with mathematics, the M.Sc. degree in electronic and ultrasonic instrumentation, and the Ph.D. degree in electrical and electronics engineering from the University of Nottingham, U.K. in 2011, 2012, and 2017 respectively. He was with the Optics and Photonics Group, University of Nottingham. Since

2014, he has been working with the University of Jeddah, Saudi Arabia and he is promoted as the Head of Electrical and Electronic Engineering Department. He is currently an Assistant Professor at the University of Jeddah. He has published 8 scientific articles. His research interests include the development of inexpensive differential ultrasonic calorimeter for accurate measurement of heat loss in machinery. He received the Best Paper Award at the 2016 IEEE International Conference for Students on Applied Engineering (ICSAE'2016).

Application of the Grey System Theory in Construction Management

A Case Study of Construction Paint Supplier Evaluation and Selection Criteria

Cuong Phu Pham

Faculty of Transport and Economics, Campus in Ho Chi Minh City, University of Transport and Communications, Vietnam
cuonggpp_ph@utc.edu.vn

Phong Thanh Nguyen

Department of Project Management
Ho Chi Minh City Open University
Ho Chi Minh City, Vietnam
phong.nt@ou.edu.vn

Phuong Thanh Phan

Department of Project Management
Ho Chi Minh City Open University
Ho Chi Minh City, Vietnam
phuong.pthanh@ou.edu.vn

Received: 18 June 2022 | Revised: 6 July 2022 | Accepted: 20 July 2022

Abstract-Material management is an important task in building construction. They account for a substantial proportion of investment capital and construction volume. However, as material prices are often affected by the market, choosing the right construction supplier is not an easy decision for contractors, especially for those materials required during the finishing phase of the construction. As one of these finishing materials is paint, identifying core criteria for evaluating and selecting the best construction paint supplier is a crucial economic choice for construction contractors. Assessing the importance of these criteria is a complex multi-criteria decision-making problem. To reflect the risks and uncertainties in this problem, the current paper presents a grey system theory approach to prioritize important criteria for selecting paint material suppliers in construction projects.

Keywords-construction management; project management; evaluation and selection criteria; material management; paint supplier; grey theory

I. INTRODUCTION

Material management is an essential task in the construction management of any civil engineering project because construction materials account for a high proportion of the total construction cost [1, 2]. In this regard, evaluating and selecting an efficient supplier of construction materials is a very important economic decision and helps the contractor manage materials effectively [3]. One definition of an efficient supplier is a company that specializes in distributing high-quality products in the proper quantity, at the proper time, for a fair price [4]. In a construction project, one commonly required and evaluated material is construction paint. Determining the critical criteria in selecting the construction paint supplier is essential to choosing the material supplier. However,

traditional assessment methods (e.g. scoring methods) are often based on the subjective opinions of construction experts, which often do not consider uncertainty in their expert judgments or opinions. This results in a final decision that is often irrational and sometimes inconsistent with reality. To improve this issue, this paper proposes a new quantitative model for prioritizing paint supplier evaluation and selection criteria based on the grey system theory.

II. RESEARCH BACKGROUND

Construction paint in civil engineering projects is available in liquid, paste, or powder form. The effect of construction paint is to create a solid film that adheres firmly to the building surface for building structure protection and esthetics. Choosing an efficient construction paint supplier is crucial for construction managers. In addition to helping the construction project attain the highest quality, it also helps reduce project cost and shorten the project implementation time. This study identifies the eight most important factors to consider when selecting the construction paint supplier in civil engineering projects based on a literature review of research papers and in-depth interviews with experts [5-21]. These criteria are: (F1) the reputation of the paint supplier, (F2) the quality management system certification of the paint supplier, (F3) the quality of construction paint materials, (F4) the number of paint categories and products, (F5) delivery time, (F6) terms and conditions of payment, (F7) price of the paint product, and (F8) the warranty period.

III. RESEARCH METHODOLOGY

One approach in studying uncertainty is the grey theory, introduced by Deng in [22-24]. It excels at analyzing mathematical systems with uncertain knowledge. When

working with discrete data and insufficient knowledge, grey system theory can be utilized to handle uncertainty or indeterminate problems. A grey system is defined as a system that includes grey variables and a grey number to provide ambiguous information [25]. Figure 1 illustrates the grey system theory.

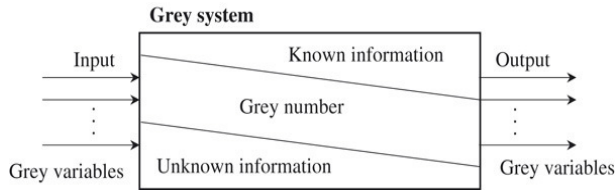


Fig. 1. Grey system theory.

The degree of information and connections between black and white systems are also explained by grey systems, in which grey numbers represent numbers with unknown precise values. Information that is partial, incomplete, or missing can take many different forms. This study uses grey numbers to reflect subjective judgments and reduce evaluation variance among construction experts. Table I [26] compares black, grey, and white systems.

TABLE I. COMPARISON OF BLACK, GREY, AND WHITE SYSTEMS

Parameter	Black system	Grey system	White system
Information	Unknown	Incomplete	Completely known
Appearance	Dark	Blurred	Clear
Processes	New	Changing	Old
Properties	Chaotic	Multivariate	Order
Methods	Negation	Change for better	Confirmation
Attitude	Letting go	Tolerant	Rigorous
Outcomes	No solution	Multi-solutions	Unique solution

TABLE II. LINGUISTIC SCALES WITH GREY NUMBERS

Level of importance	Linguistics scale	Grey numbers
1	EI = Equivalent Importance	[1, 2]
3	MI = Medium Importance	[2, 4]
5	SI = Strong Importance	[4, 6]
7	VSI = Very Strong Importance	[6, 8]
9	EMI = Extreme Importance	[8, 10]

Let x denote a closed and bounded set of real numbers. A grey number, denoted as $\otimes x$, is a number with an unknown exact value but within a known range. These grey numbers represent uncertain and ambiguous data. In this study, we propose a combination of grey system theory and the Analytical Hierarchy Process (AHP) decision-making method to reduce subjective judgments in prioritizing weights of important criteria in evaluating and selecting paint suppliers for a construction project. In the grey AHP approach, grey numbers are used instead of crisp sets and crisp numbers. The grey AHP method uses pairwise comparisons with linguistic scales and gray scales. The main computational steps to use grey AHP in this study are [27-47]:

Step 1. Define the research problem using traditional AHP. In this step, we identify the research problem, create the hierarchical structure, and construct the pairwise comparison matrix using construction experts' evaluations with linguistic

scales containing grey numbers in Table II. The grey comparison matrix using the geometrical mean formulation is constructed as follows:

$$D = \begin{bmatrix} \otimes x_{11} & \otimes x_{12} & \cdots & \otimes x_{1n} \\ \otimes x_{21} & \otimes x_{22} & \cdots & \otimes x_{2n} \\ \vdots & \vdots & \ddots & \vdots \\ \otimes x_{m1} & \otimes x_{m2} & \cdots & \otimes x_{mn} \end{bmatrix} \quad (1)$$

where $\otimes x_{ij}$ is the pairwise comparison concerning the i^{th} criterion over the j^{th} criterion.

Step 2. Calculate the normalized grey comparison matrix. The normalization for the grey numbers is given in (2)-(4).

$$D^* = \begin{bmatrix} [\underline{x}_{11}^*, \bar{x}_{11}^*] & [\underline{x}_{12}^*, \bar{x}_{12}^*] & \cdots & [\underline{x}_{1n}^*, \bar{x}_{1n}^*] \\ [\underline{x}_{21}^*, \bar{x}_{21}^*] & [\underline{x}_{22}^*, \bar{x}_{22}^*] & \cdots & [\underline{x}_{2n}^*, \bar{x}_{2n}^*] \\ \vdots & \vdots & \ddots & \vdots \\ [\underline{x}_{m1}^*, \bar{x}_{m1}^*] & [\underline{x}_{m2}^*, \bar{x}_{m2}^*] & \cdots & [\underline{x}_{mn}^*, \bar{x}_{mn}^*] \end{bmatrix} \quad (2)$$

$$\underline{x}_{ij}^* = \frac{\underline{x}_{ij}}{\frac{1}{2} \left(\sum_{i=1}^m \underline{x}_{ij} + \sum_{i=1}^m \bar{x}_{ij} \right)} = \frac{2\underline{x}_{ij}}{\sum_{i=1}^m \underline{x}_{ij} + \sum_{i=1}^m \bar{x}_{ij}} \quad (3)$$

$$\bar{x}_{ij}^* = \frac{\bar{x}_{ij}}{\frac{1}{2} \left(\sum_{i=1}^m \underline{x}_{ij} + \sum_{i=1}^m \bar{x}_{ij} \right)} = \frac{2\bar{x}_{ij}}{\sum_{i=1}^m \underline{x}_{ij} + \sum_{i=1}^m \bar{x}_{ij}} \quad (4)$$

Step 3. Calculate the grey weight of each criterion by determining the averages of the rows using (5):

$$\otimes w_i = \frac{\sum_{j=1}^n \otimes x_{ij}}{n} = \frac{\sum_{j=1}^n [\underline{x}_{ij}^*, \bar{x}_{ij}^*]}{n} \quad (5)$$

where $n = \{1, 2, \dots, N\}$ is the criterion set.

Step 4. Calculate the whitenization of the grey weights. The whited value of an interval grey weight is a crisp number with a potential value between the interval grey weight's upper and lower bounds, as follows:

$$M_i = (1 - \lambda) \underline{w}_i + \lambda \bar{w}_i \quad (6)$$

where λ is the whitening coefficient and $\lambda \in [0, 1]$.

Step 5. Calculate the Consistency Ratio (CR): To determine whether the decision-comparison preparers were consistent, this step involves examining the CR of the pairwise comparison matrix. The calculation of the CR from construction experts is [48-52]:

$$CR = \frac{CI}{RI} = \frac{\lambda_{\max} - n}{n - 1} \times \frac{1}{RI} \quad (7)$$

where CI is the consistency index, RI is the random index, and λ_{\max} is the largest eigenvalue.

IV. RESULTS AND DISCUSSION

For calculation simplicity, Table III presents the integrated grey comparison matrix, developed based on the synthesis of construction expert opinions using the geometrical mean formulation for grey numbers given in Table II. Next, we calculated the normalized grey comparison matrix using (2)-(4), as shown in Table IV. After obtaining the normalized grey comparison matrix, we calculate the grey weight of each criterion for evaluating and selecting the construction paint supplier by determining the row averages using (5). The whitenization of the grey weights, obtained by applying (6), is shown in Table V. We choose the value of λ to be 0.5 [52, 53]. Finally, we applied (7). The CR of this pairwise comparison matrix is $CR = 2.02\% < 10\%$, so the evaluation result is reliable because the pairwise comparison matrix is consistent. The top 5 most important criteria for evaluating and selecting the paint supplier in construction projects were determined to be F7, F1, F3, F2, and F6. Currently, the price of fuel (F7), especially gasoline, is quite high due to scarcity resulting from the conflict between Russia and Ukraine. This causes the paint prices on the market to increase. Therefore, construction contractors are more interested in the price than other criteria. Related to the second most important criterion, the reputation and branding of a paint supplier (F1): some large suppliers spend much money promoting their brands and products on all kinds of media, gaining notoriety in the business world, industry associations, and business partners. In contrast, some suppliers do not choose aggressive advertising methods but rely on their positive reputation to help them promote their branding. Terms and conditions of payment (F6) are usually provided in the purchase contract. Contracts are documents that

detail agreements between transaction objects created to achieve the needs of all parties. There are many forms of payment, including one-time payments or partial payments. The ability of the supplier to permit customers to owe money with attractive conditions will make the method of partial payment very popular because the contractor's cash flow is rarely consistent. In addition, to assist customers, the payment process needs to include whether the currency of the transaction is local (VND) or foreign (USD). The variety of options and convenience in financial transactions by the supplier will provide the contractor with more payment options. Because each contractor has its own form of currency storage and its own trading methods, some businesses pay in cash. Others pay through bank transfers, and foreign-owned companies use USD in their projects.

V. CONCLUSION

Applying a grey AHP, a new quantitative method, by integrating grey system theory with the AHP, we prioritize the critical criteria in the evaluation and selection process of building paint suppliers in construction projects. This new method has an advantage over traditional methods because it supports group decision-making. In addition, it also accounts for uncertainty in the judgments of construction professionals and data incompleteness. The 5 most important criteria for evaluating and selecting the paint supplier in construction projects are (F7) the price of the paint product, (F1) the reputation of the paint supplier, (F3) the quality of construction paint materials, (F2) the quality management system certification of the paint supplier, and (F6) the terms and conditions of payment.

TABLE III. INTEGRATED GREY COMPARISON MATRIX

[1.0000, 1.0000]	[1.5874, 3.1748]	[1.2599, 2.5198]	[4.5789, 6.6039]	[3.1748, 5.2415]	[2.5198, 4.5789]	[0.6300, 1.2599]	[5.2415, 7.2685]
[0.3150, 0.6300]	[1.0000, 1.0000]	[0.7937, 1.5874]	[2.0000, 3.6342]	[1.2599, 2.5198]	[1.2599, 2.5198]	[0.1733, 0.2752]	[5.2415, 7.2685]
[0.3969, 0.7937]	[0.6300, 1.2599]	[1.0000, 1.0000]	[3.1748, 5.2415]	[2.0000, 3.6342]	[1.5874, 3.1748]	[0.3969, 0.7937]	[3.6342, 5.7690]
[0.1514, 0.2184]	[0.2752, 0.5000]	[0.1908, 0.3150]	[1.0000, 1.0000]	[0.7937, 1.5874]	[0.3467, 0.6300]	[0.1376, 0.1908]	[0.7937, 1.5874]
[0.1908, 0.3150]	[0.3969, 0.7937]	[0.2752, 0.5000]	[0.6300, 1.2599]	[1.0000, 1.0000]	[0.6300, 1.2599]	[0.1733, 0.2752]	[0.7937, 1.5874]
[0.2184, 0.3969]	[0.3969, 0.7937]	[0.3150, 0.6300]	[1.5874, 2.8845]	[0.7937, 1.5874]	[1.0000, 1.0000]	[0.1733, 0.2752]	[2.0000, 3.6342]
[0.7937, 1.5874]	[3.6342, 5.7690]	[1.2599, 2.5198]	[5.2415, 7.2685]	[3.6342, 5.7690]	[3.6342, 5.7690]	[1.0000, 1.0000]	[6.6039, 8.6177]
[0.1376, 0.1908]	[0.1376, 0.1908]	[0.1733, 0.2752]	[0.6300, 1.2599]	[0.6300, 1.2599]	[0.2752, 0.5000]	[0.1160, 0.1514]	[1.0000, 1.0000]

TABLE IV. INTEGRATED GREY COMPARISON MATRIX

[0.2399, 0.2399]	[0.1474, 0.2948]	[0.1724, 0.3448]	[0.1908, 0.2752]	[0.1769, 0.2921]	[0.1642, 0.2984]	[0.1794, 0.3589]	[0.1690, 0.2343]
[0.0756, 0.1511]	[0.0929, 0.0929]	[0.1086, 0.2172]	[0.0833, 0.1514]	[0.0702, 0.1404]	[0.0821, 0.1642]	[0.0494, 0.0784]	[0.1690, 0.2343]
[0.0952, 0.1904]	[0.0585, 0.1170]	[0.1368, 0.1368]	[0.1323, 0.2184]	[0.1115, 0.2025]	[0.1035, 0.2069]	[0.1130, 0.2261]	[0.1172, 0.1860]
[0.0363, 0.0524]	[0.0255, 0.0464]	[0.0261, 0.0431]	[0.0417, 0.0417]	[0.0442, 0.0885]	[0.0226, 0.0411]	[0.0392, 0.0543]	[0.0256, 0.0512]
[0.0458, 0.0756]	[0.0368, 0.0737]	[0.0377, 0.0684]	[0.0260, 0.0530]	[0.0557, 0.0557]	[0.0411, 0.0821]	[0.0494, 0.0784]	[0.0256, 0.0512]
[0.0524, 0.0952]	[0.0368, 0.0737]	[0.0431, 0.0862]	[0.0660, 0.1200]	[0.0440, 0.0880]	[0.0652, 0.0652]	[0.0494, 0.0784]	[0.0645, 0.1172]
[0.1904, 0.3809]	[0.3374, 0.5357]	[0.1724, 0.3448]	[0.2184, 0.3029]	[0.2025, 0.3215]	[0.2369, 0.3760]	[0.2848, 0.2848]	[0.2129, 0.2778]
[0.0330, 0.0458]	[0.0128, 0.0177]	[0.0237, 0.0377]	[0.0263, 0.0525]	[0.0351, 0.0702]	[0.0179, 0.0326]	[0.0331, 0.0431]	[0.0322, 0.0322]

TABLE V. WHITENIZATION OF THE GREY WEIGHTS

(F1) The reputation of the paint supplier	0.2362
(F2) The quality management system certification of the paint supplier	0.1226
(F3) Quality of construction paint materials	0.1470
(F4) Number of paint categories and products	0.0425
(F5) Delivery time	0.0535
(F6) Terms and conditions of payment	0.0716
(F7) Price of the paint product	0.2925
(F8) Warranty period.	0.0341

ACKNOWLEDGMENT

The authors would like to thank the Professional Knowledge & Project Management Research Team (K2P), Ho Chi Minh City Open University, Vietnam for supporting this research.

REFERENCES

- [1] B. Abdzadeh, S. Noori, and S. F. Ghannadpour, "Simultaneous scheduling of multiple construction projects considering supplier selection and material transportation routing," *Automation in Construction*, vol. 140, Aug. 2022, Art. no. 104336, <https://doi.org/10.1016/j.autcon.2022.104336>.
- [2] S. Kar and K. N. Jha, "Exploring the Critical Barriers to and Enablers of Sustainable Material Management Practices in the Construction Industry," *Journal of Construction Engineering and Management*, vol. 147, no. 9, Sep. 2021, Art. no. 04021102, [https://doi.org/10.1061/\(ASCE\)CO.1943-7862.000125](https://doi.org/10.1061/(ASCE)CO.1943-7862.000125).
- [3] N. T. Phong, V. N. Phuc, and T. T. H. L. N. Quyen, "Application of Fuzzy Analytic Network Process and TOPSIS Method for Material Supplier Selection," *Key Engineering Materials*, vol. 728, pp. 411–415, 2017, <https://doi.org/10.4028/www.scientific.net/KEM.728.411>.
- [4] W. L. Ng, "An efficient and simple model for multiple criteria supplier selection problem," *European Journal of Operational Research*, vol. 186, no. 3, pp. 1059–1067, May 2008, <https://doi.org/10.1016/j.ejor.2007.01.018>.
- [5] P. T. Nguyen, "Determination of construction supplier evaluation criteria using word tags," *International Journal of Advanced and Applied Sciences*, vol. 5, no. 11, pp. 75–79, Nov. 2018, <https://doi.org/10.21833/ijaa.2018.11.010>.
- [6] M. K. Ghorabae, M. Amiri, E. K. Zavadskas, and J. Antucheviciene, "Supplier evaluation and selection in fuzzy environments: A review of MADM approaches," *Economic research-Ekonomska istrazivanja*, vol. 30, no. 1, pp. 1073–1118, 2017, <https://doi.org/10.1080/1331677X.2017.1314828>.
- [7] E. Plebankiewicz and D. Kubek, "Multicriteria Selection of the Building Material Supplier Using AHP and Fuzzy AHP," *Journal of Construction Engineering and Management*, vol. 142, no. 1, Jan. 2016, Art. no. 04015057, [https://doi.org/10.1061/\(ASCE\)CO.1943-7862.0001033](https://doi.org/10.1061/(ASCE)CO.1943-7862.0001033).
- [8] R. M. Monczka, R. B. Handfield, L. C. Giunipero, and J. L. Patterson, *Purchasing and Supply Chain Management*. Boston, MA, USA: Cengage Learning, 2015.
- [9] M. Safa, A. Shahi, C. T. Haas, and K. W. Hipel, "Supplier selection process in an integrated construction materials management model," *Automation in Construction*, vol. 48, pp. 64–73, Dec. 2014, <https://doi.org/10.1016/j.autcon.2014.08.008>.
- [10] E. Eshtehardian, P. Ghodousi, and A. Bejanpour, "Using ANP and AHP for the supplier selection in the construction and civil engineering companies; Case study of Iranian company," *KSCE Journal of Civil Engineering*, vol. 17, no. 2, pp. 262–270, Mar. 2013, <https://doi.org/10.1007/s12205-013-1141-z>.
- [11] J. Chai, J. N. K. Liu, and E. W. T. Ngai, "Application of decision-making techniques in supplier selection: A systematic review of literature," *Expert Systems with Applications*, vol. 40, no. 10, pp. 3872–3885, Aug. 2013, <https://doi.org/10.1016/j.eswa.2012.12.040>.
- [12] K. Shaw, R. Shankar, S. S. Yadav, and L. S. Thakur, "Supplier selection using fuzzy AHP and fuzzy multi-objective linear programming for developing low carbon supply chain," *Expert Systems with Applications*, vol. 39, no. 9, pp. 8182–8192, Jul. 2012, <https://doi.org/10.1016/j.eswa.2012.01.149>.
- [13] W. Xia and Z. Wu, "Supplier selection with multiple criteria in volume discount environments," *Omega*, vol. 35, no. 5, pp. 494–504, Oct. 2007, <https://doi.org/10.1016/j.omega.2005.09.002>.
- [14] M. Sevkli, S. C. Lenny Koh, S. Zaim, M. Demirbag, and E. Tatoglu, "An application of data envelopment analytic hierarchy process for supplier selection: a case study of BEKO in Turkey," *International Journal of Production Research*, vol. 45, no. 9, pp. 1973–2003, May 2007, <https://doi.org/10.1080/00207540600957399>.
- [15] C. Gencer and D. Gurpınar, "Analytic network process in supplier selection: A case study in an electronic firm," *Applied Mathematical Modelling*, vol. 31, no. 11, pp. 2475–2486, Nov. 2007, <https://doi.org/10.1016/j.apm.2006.10.002>.
- [16] C. Ho, P.-M. Nguyen, and M.-H. Shu, "Supplier Evaluation and Selection Criteria in the Construction Industry of Taiwan and Vietnam," *Information and Management Sciences*, vol. 18, no. 4, pp. 403–426, 2007.
- [17] C.-T. Chen, C.-T. Lin, and S.-F. Huang, "A fuzzy approach for supplier evaluation and selection in supply chain management," *International Journal of Production Economics*, vol. 102, no. 2, pp. 289–301, Aug. 2006, <https://doi.org/10.1016/j.ijpe.2005.03.009>.
- [18] C. Kahraman, U. Cebeci, and Z. Ulukan, "Multi-criteria supplier selection using fuzzy AHP," *Logistics Information Management*, vol. 16, no. 6, pp. 382–394, Jan. 2003, <https://doi.org/10.1108/09576050310503367>.
- [19] V. R. Kannan and K. C. Tan, "Supplier Selection and Assessment: Their Impact on Business Performance," *Journal of Supply Chain Management*, vol. 38, no. 3, pp. 11–21, 2002, <https://doi.org/10.1111/j.1745-493X.2002.tb00139.x>.
- [20] S. H. Ghodyspour and C. O'Brien, "A decision support system for supplier selection using an integrated analytic hierarchy process and linear programming," *International Journal of Production Economics*, vol. 56–57, pp. 199–212, Sep. 1998, [https://doi.org/10.1016/S0925-5273\(97\)00009-1](https://doi.org/10.1016/S0925-5273(97)00009-1).
- [21] D. S. Jarallah and A. M. R. Mahjoob, "Supply Chain Management of Infrastructure Projects in Iraq," *Engineering, Technology & Applied Science Research*, vol. 12, no. 3, pp. 8611–8616, Jun. 2022, <https://doi.org/10.48084/etasr.4904>.
- [22] S. Liu, Z. Fang, Y. Yang, and J. Forrest, "General grey numbers and their operations," *Grey Systems: Theory and Application*, 2012.
- [23] G.-D. Li, D. Yamaguchi, and M. Nagai, "A grey-based decision-making approach to the supplier selection problem," *Mathematical and Computer Modelling*, vol. 46, no. 3, pp. 573–581, Aug. 2007, <https://doi.org/10.1016/j.mcm.2006.11.021>.
- [24] D. Julong, "Introduction to grey system theory," *The Journal of Grey System*, vol. 1, no. 1, pp. 1–24, 1989.
- [25] G. Comert, N. Begashaw, and N. Huynh, "Improved grey system models for predicting traffic parameters," *Expert Systems with Applications*, vol. 177, Sep. 2021, Art. no. 114972, <https://doi.org/10.1016/j.eswa.2021.114972>.
- [26] S. Liu and J. Y. L. Forrest, *Grey Systems: Theory and Applications*. New York, NY, USA: Springer, 2010.
- [27] Y. Celikbilek, "A grey analytic hierarchy process approach to project manager selection," *Journal of Organizational Change Management*, vol. 31, no. 3, pp. 749–765, Jan. 2018, <https://doi.org/10.1108/JOCM-04-2017-0102>.
- [28] V. Thakur, "Locating temporary waste treatment facilities in the cities to handle the explosive growth of HCWs during pandemics: A novel Grey-AHP-OCRA hybrid approach," *Sustainable Cities and Society*, vol. 82, Jul. 2022, Art. no. 103907, <https://doi.org/10.1016/j.scs.2022.103907>.
- [29] S. Duleba, Y. Celikbilek, S. Moslem, and D. Esztergar-Kiss, "Application of grey analytic hierarchy process to estimate mode choice alternatives: A case study from Budapest," *Transportation Research Interdisciplinary Perspectives*, vol. 13, Mar. 2022, Art. no. 100560, <https://doi.org/10.1016/j.trip.2022.100560>.
- [30] A. Vafadarnikjoo and M. Scherz, "A Hybrid Neutrosophic-Grey Analytic Hierarchy Process Method: Decision-Making Modelling in Uncertain Environments," *Mathematical Problems in Engineering*, vol. 2021, Jun. 2021, Art. no. e1239505, <https://doi.org/10.1155/2021/1239505>.
- [31] J. Lin, W. Zhou, and S.-S. Yuan, "Research on User Experience Optimization of Tutorial Design for Battle Royale Games Based on Grey AHP Theory," in *International Conference on Human-Computer Interaction*, Jul. 2021, pp. 75–88, https://doi.org/10.1007/978-3-030-77277-2_6.

- [32] L. Li, Z. Liu, and X. Du, "Improvement of Analytic Hierarchy Process Based on Grey Correlation Model and Its Engineering Application," *ASCE-ASME Journal of Risk and Uncertainty in Engineering Systems, Part A: Civil Engineering*, vol. 7, no. 2, Jun. 2021, Art. no. 04021007, <https://doi.org/10.1061/AJRUA6.0001126>.
- [33] P. Golfam, P.-S. Ashofteh, and H. A. Loaiciga, "Integration of Gray System Theory with AHP Decision-Making for Wastewater Reuse Decision-Making," *Journal of Hazardous, Toxic, and Radioactive Waste*, vol. 25, no. 3, Jul. 2021, Art. no. 04021019, [https://doi.org/10.1061/\(ASCE\)JHZ.2153-5515.0000619](https://doi.org/10.1061/(ASCE)JHZ.2153-5515.0000619).
- [34] S. Ghosh, "Application of a New Hybrid MCDM Technique Combining Grey Relational Analysis with AHP-TOPSIS in Ranking of Stocks in the Indian IT Sector," in *Computational Intelligence in Communications and Business Analytics*, Santiniketan, India, Jan. 2021, pp. 133–149, https://doi.org/10.1007/978-3-030-75529-4_11.
- [35] G. Canbulut, E. Kose, and O. A. Arik, "Public transportation vehicle selection by the grey relational analysis method," *Public Transport*, Jun. 2021, <https://doi.org/10.1007/s12469-021-00271-3>.
- [36] A. Alkharabsheh, S. Moslem, L. Oubahman, and S. Duleba, "An Integrated Approach of Multi-Criteria Decision-Making and Grey Theory for Evaluating Urban Public Transportation Systems," *Sustainability*, vol. 13, no. 5, Jan. 2021, Art. no. 2740, <https://doi.org/10.3390/su13052740>.
- [37] F. Zhu, "Evaluating the Coupling Coordination Degree of Green Finance and Marine Eco-environment Based on AHP and Grey System Theory," *Journal of Coastal Research*, vol. 110, no. SI, pp. 277–281, Oct. 2020, <https://doi.org/10.2112/JCR-SI110-065.1>.
- [38] J. Sun, "Research on faculty and staff for constructing the 'double first-class' universities based on Grey-AHP comprehensive evaluation model," *Grey Systems: Theory and Application*, vol. 10, no. 4, pp. 467–478, Jan. 2020, <https://doi.org/10.1108/GS-12-2019-0059>.
- [39] Y. Qingchuan, N. Hai, S. Yuan, and Z. Jiaping, "Effectiveness Evaluation of Ship Communication System Based on Grey Analytic Hierarchy Process," in *International Conference on Aviation Safety and Information Technology*, New York, NY, USA, Oct. 2020, pp. 163–168, <https://doi.org/10.1145/3434581.3434610>.
- [40] S. Moslem and Y. Celikbilek, "An integrated grey AHP-MOORA model for ameliorating public transport service quality," *European Transport Research Review*, vol. 12, no. 1, Dec. 2020, Art. no. 68, <https://doi.org/10.1186/s12544-020-00455-1>.
- [41] J.-W. Liu, "Developing GAHP concepts for measurement of travel agency organizational performance," *Soft Computing*, vol. 24, no. 11, pp. 8051–8059, Jun. 2020, <https://doi.org/10.1007/s00500-019-04115-y>.
- [42] F. Shengxin and W. Aimin, "Measurement of corporate social responsibility of automobile enterprises based on AHP-GRA model," *Journal of Intelligent & Fuzzy Systems*, vol. 38, no. 6, pp. 6947–6956, Jan. 2020, <https://doi.org/10.3233/JIFS-179773>.
- [43] K. Zhou, G. Huang, and T. Xue, "Evaluation of Dangerous Chemical Transportation Scheme Based on Grey Analytic Hierarchy Process (GAHP)," in *6th International Conference on Frontiers of Industrial Engineering*, London, UK, Sep. 2019, pp. 62–66, <https://doi.org/10.1109/ICFIE.2019.8907778>.
- [44] M. Younas *et al.*, "Multi-objective optimization for sustainable turning Ti6Al4V alloy using grey relational analysis (GRA) based on analytic hierarchy process (AHP)," *The International Journal of Advanced Manufacturing Technology*, vol. 105, no. 1, pp. 1175–1188, Nov. 2019, <https://doi.org/10.1007/s00170-019-04299-5>.
- [45] Z. Meier, W.-T. Pan, S. Zhuohong, Z. Yingying, and Z. Zuchang, "Application of Data Mining Technology in Evaluating Real Estate Investment Plan Based on GRA-AHP," *Journal of Physics: Conference Series*, vol. 1284, no. 1, Dec. 2019, Art. no. 012037, <https://doi.org/10.1088/1742-6596/1284/1/012037>.
- [46] K. Chen, P. Chen, L. Yang, and L. Jin, "Grey clustering evaluation based on AHP and interval grey number," *International Journal of Intelligent Computing and Cybernetics*, vol. 12, no. 1, pp. 127–137, Jan. 2019, <https://doi.org/10.1108/IJICC-04-2018-0045>.
- [47] G. Huang, S. Sun, and D. Zhang, "Safety Evaluation of Construction Based on the Improved AHP-Grey Model," *Wireless Personal Communications*, vol. 103, no. 1, pp. 209–219, Nov. 2018, <https://doi.org/10.1007/s11277-018-5436-8>.
- [48] P. V. Nguyen, P. T. Nguyen, Q. L. H. T. T. Nguyen, and V. D. B. Huynh, "Calculating Weights of Social Capital Index Using Analytic Hierarchy Process," *International Journal of Economics and Financial Issues*, vol. 6, no. 3, pp. 1189–1193, May 2016.
- [49] L. T. H. Nhung, T. T. Phung, H. M. V. Nguyen, T. N. Le, T. A. Nguyen, and T. D. Vo, "Load Shedding in Microgrids with Dual Neural Networks and AHP Algorithm," *Engineering, Technology & Applied Science Research*, vol. 12, no. 1, pp. 8090–8095, Feb. 2022, <https://doi.org/10.48084/etasr.4652>.
- [50] H. I. Mohammed, Z. Majid, Y. B. Yamusa, M. F. M. Ariff, K. M. Idris, and N. Darwin, "Sanitary Landfill Siting Using GIS and AHP: A Case Study in Johor Bahru, Malaysia," *Engineering, Technology & Applied Science Research*, vol. 9, no. 3, pp. 4100–4104, Jun. 2019, <https://doi.org/10.48084/etasr.2633>.
- [51] T. N. Le, H. M. V. Nguyen, T. A. Nguyen, T. T. Phung, and B. D. Phan, "Optimization of Load Ranking and Load Shedding in a Power System Using the Improved AHP Algorithm," *Engineering, Technology & Applied Science Research*, vol. 12, no. 3, pp. 8512–8519, Jun. 2022, <https://doi.org/10.48084/etasr.4862>.
- [52] S. Pant, A. Kumar, M. Ram, Y. Klochkov, and H. K. Sharma, "Consistency Indices in Analytic Hierarchy Process: A Review," *Mathematics*, vol. 10, no. 8, Jan. 2022, Art. no. 1206, <https://doi.org/10.3390/math10081206>.
- [53] N.-A.-T. Nguyen, C.-N. Wang, L.-T.-H. Dang, L.-T.-T. Dang, and T.-T. Dang, "Selection of Cold Chain Logistics Service Providers Based on a Grey AHP and Grey COPRAS Framework: A Case Study in Vietnam," *Axioms*, vol. 11, no. 4, Apr. 2022, Art. no. 154, <https://doi.org/10.3390/axioms11040154>.

The Influence of Near- and Far-field Earthquakes on the Seismic Performance of Base-Isolated Nuclear Power Plant Structures

Van-Binh Tran

Faculty of Engineering and Technology
Ha Tinh University
Ha Tinh, Vietnam
binh.tranvan@htu.edu.vn

Sy-Minh Nguyen

Faculty of Engineering and Technology
Ha Tinh University
Ha Tinh, Vietnam
minh.nguyensy@htu.edu.vn

Tien-Hong Nguyen

Department of Civil Engineering
Vinh University
Vinh, Vietnam
tienhongkxd@vinhuni.edu.vn

Van-Hoa Nguyen

Department of Civil Engineering
Vinh University
Vinh, Vietnam
vanhoakxd@vinhuni.edu.vn

Thi Thuy-Huong Doan

Department of Civil Engineering
Vinh University
Vinh, Vietnam
doanhuongdhv@gmail.com

Duy-Duan Nguyen

Department of Civil Engineering
Vinh University
Vinh, Vietnam
duyduankxd@vinhuni.edu.vn

Received: 25 June 2022 | Revised: 14 July 2022 | Accepted: 16 July 2022

Abstract-This study aims to investigate the influence of near- and far-field earthquakes on the seismic performance of base-isolated Nuclear Power Plant (NPP) structures. Two earthquake motion groups of near-field and far-field characteristics are selected for fragility evaluation analysis. A base-isolated advanced reactor power 1400 (APR-1400) is employed for numerical analysis. A set of fragility curves are derived for various limit states based on the maximum likelihood estimation. The limit states are defined in terms of Lead Rubber Bearing (LRB) deformation capacity. The numerical results reveal that the median maximum deformations of LRBs were smaller for far-field ground motions than for near-field motions. Also, the comparison of fragility curves demonstrates that the probability of failure of base-isolated NPP structures is higher for near-field ground motions than far-field motions. It is crucial to select earthquake ground motions with both near- and far-field motions for the seismic evaluation of NPP structures.

Keywords-near-field earthquake; far-field earthquake; LRB; fragility analysis; nuclear power plant structure; lumped mass stick model

I. INTRODUCTION

The near-field strong ground motion consists of complex characteristics, mainly affected by the fault rupture velocity, the length of fault rupture, sliding direction, and other factors. Those characteristics can cause significant damage to structures during an earthquake. The influence of near-field earthquakes on the response of civil engineering structures has been numerously investigated in [1-7]. Some of the Nuclear Power Plants (NPPs) in Korea are located near fault ruptures. After the 2016 Gyeongju and 2017 Pohang earthquakes, the seismic safety of NPP structures is getting more and more attention.

Seismic analyses and fragility evaluations of NPP structures were implemented in [8-16]. Among that, remarkably, authors in [9-10] developed the seismic fragility curves of a non-isolated CANDU type NPP containment building for near-field ground motions based on the displacements obtained from the nonlinear time history analyses. Authors in [17] assessed the safety implication of near-field earthquakes on NPP structures designed according to the North American codes. They concluded that the near-field motion effects were not so damaging to the containment which is a relatively stiff structure. However, the effects of near-field forward-directivity, fling-step, and far-field motions on seismic fragility curves of base-isolated NPP structure were not evaluated.

The purpose of this study is to develop seismic fragility curves of a base-isolated APR-1400 NPP structure considering the influence of near- and far-field ground motions. For near-field earthquakes, two typical characteristics, forward-directivity and fling-step are accounted for in fragility analyses. The limit states are defined based on the shear strain capacity of Lead Rubber Bearings (LRBs). A set of fragility curves for limit states are generated using the maximum likelihood estimation. The influence of earthquake groups on fragility curves is also examined.

II. INPUT GROUND MOTIONS

Near-field earthquakes contain a large portion of fault energy in the form of pulses [2]. Pulses can normally be recognized through acceleration, velocity, and displacement time histories. Two typical effects in near-field ground motions are forward-directivity and fling-step phenomena. Forward directivity occurs where the fault rupture propagates with a velocity close to the shear-wave velocity. This is accompanied

Corresponding author: Duy-Duan Nguyen

by generating long-period, short-duration, and large-amplitude pulses in the velocity time histories. Displacement associated with such a shear-wave velocity is largest in the fault-normal direction for strike-slip faults [1, 3]. On the other hand, fling step effect produces the evolution of residual ground displacement due to the tectonic deformation associated with the rupture mechanism. This is generally characterized by a unidirectional high amplitude velocity pulse and a monotonic step in the displacement time history [2]. Figure 1 illustrates the time-history traces of near- and far-field earthquakes. A high-velocity pulse can be seen in the 1979 Imperial Valley earthquake. For the 1971 San Fernando earthquake, i.e. a far-field motion, no high pulses existed in the time histories. It should be noted that if a motion record has an epicentral distance less than 12km, it is considered as a near-field earthquake, otherwise it is considered a far-field motion [18].

In this study, two different groups of ground motions classified into near-field and ordinary far-field types were considered. For each group, 20 motion records were involved for fragility analysis. All used records were adopted from the PEER center database. Figure 2 shows the response spectra of ground motions in three groups. The thick curve indicates the mean spectrum.

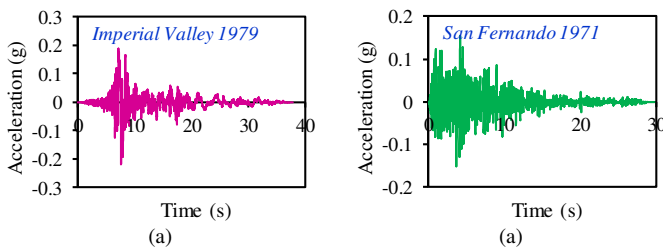


Fig. 1. Example of time-history traces of (a) near- and (b) far-field earthquakes.

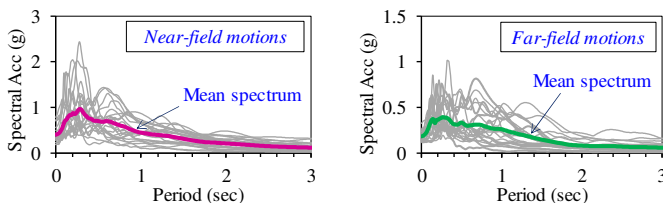


Fig. 2. Spectral accelerations of input ground motions.

III. STRUCTURAL MODELING

In this study, the advanced power reactor 1400 (APR-1400) developed by Korea Electric Power Corporation, was employed for numerical analysis. We focused our modeling on the Reactor Containment Building (RCB), the Internal Structure (IS), and the Auxiliary Building (AB). The Finite Element Model (FEM) of the base-isolated NPP structure was developed using the Lumped-Mass Stick Model (LMSM) in SAP2000 [19]. The masses and equivalent section properties were calculated based on the designed cross sections of the structures. The structures were modeled in terms of elastic beam elements. Furthermore, elastic shell elements were applied for the base-mat. The lumped masses were assigned to the associated element nodes. Figure 3(a) shows the FEM of

the base-isolated NPP structures and the mechanical properties of LRBs. For the base isolation system, 486 LRBs were installed under the base-mat to enhance the seismic performance of the NPP structures. Figure 3(b) illustrates the bilinear shear force-deformation model of LRBs due to shear forces. The bilinear model of LRB was assumed to be a parallelogram. Therefore, the values of Q_d , F_y , K_u and K_d in the negative direction are equal to those in the positive. The mechanical properties of LRBs are also described in Figure 3(b). The results of eigenvalue analysis are presented in Figure 4. The result is consistent with the findings in [20-21].

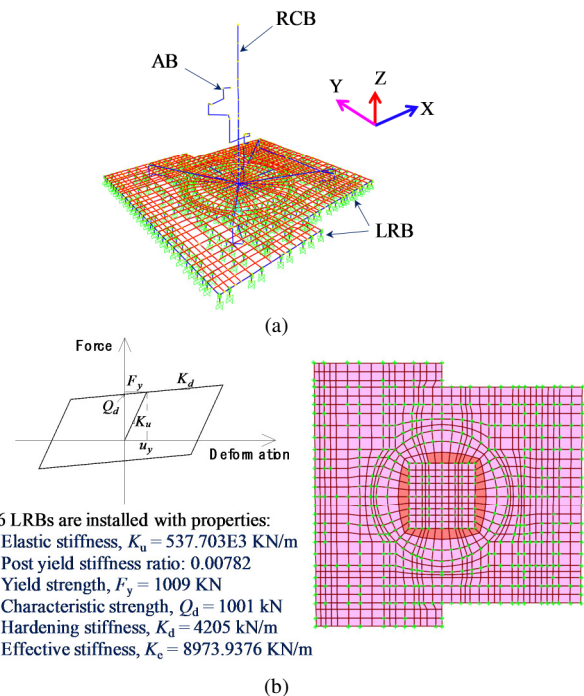


Fig. 3. FEM of base-isolated NPP structures and bilinear model of LRBs: (a) LMSM of base-isolated NPP structures, (b) arrangement and properties of LRBs.

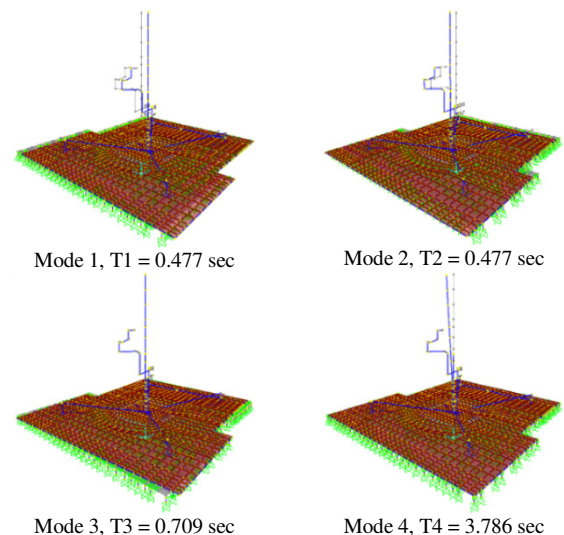


Fig. 4. Vibration mode shapes of base-isolated NPP structures.

IV. RESPONSE OF NPP STRUCTURES AND FRAGILITY ANALYSIS

A series of time-history analyses were performed. All ground motions were imposed on the NPP models in the horizontal direction. To evaluate the fragility of the base-isolated NPP structure, the hypothesis that LRB is the critical element was made. The superstructures are expected to vibrate within an elastic range during earthquakes. It is common to quantify the lateral displacement or/and acceleration responses of structures subjected to earthquakes [22-24]. Therefore, the seismic response of the base-isolated model is obtained in terms of the shear deformation behavior of LRBs. Figure 5 shows an example of the behavior of LRB during different types of earthquakes (i.e. near- and far-field motions) with a specified level $PGA = 0.4g$. It can be found that the deformation responses of LRBs due to near-field earthquakes are significantly larger than that under the far-field motion. Figure 6 shows the maximum lateral deformation of LRBs in various levels of PGA under different earthquake groups. The thick lines represent the mean results. Because of the pulse characteristic, the mean values of deformation of LRBs under near-field earthquakes are higher than those due to ordinary far-field earthquakes.

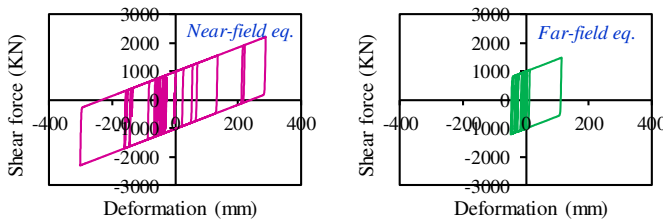


Fig. 5. Hysteretic behavior of LRB under earthquakes with $PGA = 0.4g$.

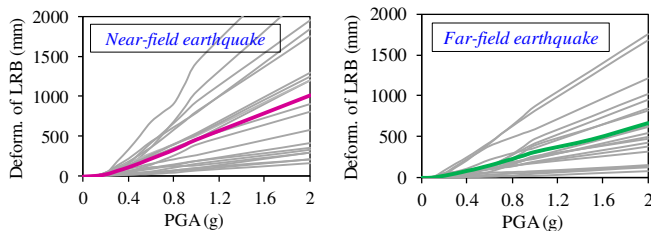


Fig. 6. Incremental displacements of LRB with PGA under near- and far-field earthquakes.

For developing fragility curves, a set of limit states should be pre-defined according to the damage levels of the components. This study used three defined limit states, namely slight, moderate, and extensive. These limit states were determined based on the shear strain of LRB. The shear strain (γ) is expressed by the ratio of the maximum lateral deformation (Δ) and the height of LRB (H). According to recent experimental studies [29-34], the LRB can reach an ultimate capacity of beyond 400% shear strain. We adopted these results to define three limit states, if the shear strain exceeds 100% (i.e. $\Delta \geq 40cm$) the slight limit state (LS1) is specified. If the shear strain goes beyond 200% (i.e. $\Delta \geq 80cm$) and 300% (i.e. $\Delta \geq 120cm$) the moderate (LS2) and extensive (LS3) limit states are respectively established.

Among several methods to develop seismic fragility curves, the Maximum Likelihood Estimation (MLE) approach [25] was used in this study. In this approach, the fragility function is assumed as a log-normal Cumulative Distribution Function (CDF) expressed by:

$$F_k(a) = \Phi \left[\frac{\ln(a/c_k)}{\zeta_k} \right] \quad (1)$$

where a is the earthquake intensity, namely PGA in this study, c_k and ζ_k are the median and the log-standard deviations of the log-normal CDF, and $\Phi(-)$ is the standard normal CDF. In (1), the subscript k indicates the k -th limit state when more than one limit state is considered. In the MLE, c_k and ζ_k are determined by maximizing the likelihood function. This function is defined by:

$$L = \prod_{i=1}^N [F_k(a_i)]^{x_i} [1 - F_k(a_i)]^{(1-x_i)} \quad (2)$$

where $F_k(a)$ increases when damage occurs and $1 - F_k(a)$, the probability of not experiencing a damage, increases when damage does not occur for an earthquake intensity a_i . N is the number of ground motions considered and x_i is a Bernoulli random variable that indicates whether the structure is damaged or not where 0 indicates no damage and 1 indicates damage. c_k and ζ_k are determined so that (2) is maximized with respect to c_k and ζ_k as follows:

$$\frac{\partial L}{\partial c_k} = \frac{\partial L}{\partial \zeta_k} = 0, \quad k = 1, \dots, N_{state} \quad (3)$$

where N_{state} is the number of limit states.

Fragility curves of base-isolated NPP structures were developed for the 3 limit states considering the three groups of ground motions. Figure 7 shows the fragility curves for the 3 limit states with different earthquake groups. It can be observed that the base-isolated NPP structure might behave as without damage if the level of PGA less than $0.6g$, which is significantly higher than the operational basis earthquake design level of APR-1400 NPP structures. Additionally, the isolated structure suffered no damage within $PGA 0.8g$ of far-field earthquakes.

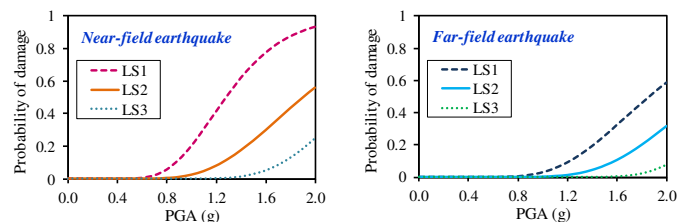


Fig. 7. Seismic fragility curves of base-isolated NPP structures subjected to near- and far-field earthquakes

Figure 8 shows the comparison of fragility curves for the three groups of earthquakes. It can be observed that the structural model under near-field motions is more vulnerable than that due to far-field earthquakes. This can be attributed to the obvious reason that the deformation of LRBs produced by near-field motions is higher than that under far-field motions.

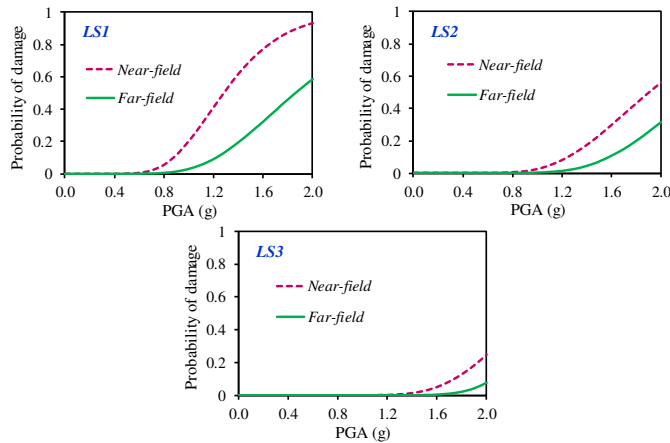


Fig. 8. Comparison of fragility curves of base-isolated NPP structures in different defined limit states.

V. CONCLUSIONS

In this study, seismic fragility curves of the base-isolated APR1400 NPP structures were derived for different limit states based on the maximum likelihood estimation. The influence of near-field and far-field ground motions was considered. Based on the numerical results, the following conclusions are drawn.

- The maximum deformations of LRBs were shown to be smaller for far-field earthquakes than for near-field ground motions. This is due to the high-amplitude pulse effect of near-field motions.
- The probability of failure of base-isolated NPP structures is significantly higher for near-field ground motions compared to that for far-field earthquakes.
- The NPP model has not suffered any damage within PGA 0.6g, which is higher than the safe shutdown earthquake design level of APR-1400 NPP structures.
- It is crucial to select earthquake ground motions with both near- and far-field motions for the seismic evaluation of NPP structures.

REFERENCES

- [1] E. Kalkan and S. K. Kunnath, "Effects of Fling Step and Forward Directivity on Seismic Response of Buildings," *Earthquake Spectra*, vol. 22, no. 2, pp. 367–390, May 2006, <https://doi.org/10.1193/1.2192560>.
- [2] M. Bhandari, S. D. Bharti, M. K. Shirmali, and T. K. Datta, "The Numerical Study of Base-Isolated Buildings Under Near-Field and Far-Field Earthquakes," *Journal of Earthquake Engineering*, vol. 22, no. 6, pp. 989–1007, Jul. 2018, <https://doi.org/10.1080/13632469.2016.1269698>.
- [3] R. Eskandari and D. Vafaei, "Effects of near-fault records characteristics on seismic performance of eccentrically braced frames," *Structural Engineering and Mechanics*, vol. 56, no. 5, pp. 855–870, 2015, <https://doi.org/10.12989/sem.2015.56.5.855>.
- [4] A. Karbassi, H. Hamidi, and P. Lestuzzi, "Fling-step effect on the seismic behavior of high-rise RC buildings during the Christchurch earthquake," Wellington, New Zealand, Feb. 2013.
- [5] M. Zhang, G. Parke, and Z. Chang, "The dynamic response and seismic damage of single-layer reticulated shells subjected to near-fault ground motions," *Earthquakes and Structures*, vol. 14, no. 5, pp. 399–409, 2018, <https://doi.org/10.12989/eas.2018.14.5.399>.
- [6] W.-I. Liao, C.-H. Loh, and B.-H. Lee, "Comparison of dynamic response of isolated and non-isolated continuous girder bridges subjected to near-fault ground motions," *Engineering Structures*, vol. 26, no. 14, pp. 2173–2183, Dec. 2004, <https://doi.org/10.1016/j.engstruct.2004.07.016>.
- [7] S. Zhang and G. Wang, "Effects of near-fault and far-fault ground motions on nonlinear dynamic response and seismic damage of concrete gravity dams," *Soil Dynamics and Earthquake Engineering*, vol. 53, pp. 217–229, Oct. 2013, <https://doi.org/10.1016/j.soildyn.2013.07.014>.
- [8] Y. Pan, C. E. Ventura, and W. D. Liam Finn, "Effects of Ground Motion Duration on the Seismic Performance and Collapse Rate of Light-Frame Wood Houses," *Journal of Structural Engineering*, vol. 144, no. 8, Aug. 2018, Art. no. 04018112, [https://doi.org/10.1061/\(ASCE\)ST.1943-541X.0002104](https://doi.org/10.1061/(ASCE)ST.1943-541X.0002104).
- [9] S. H. Eem, H. J. Jung, M. K. Kim, and I. K. Choi, "Seismic Fragility Evaluation of Isolated NPP Containment Structure Considering Soil-Structure Interaction Effect," *Journal of the Earthquake Engineering Society of Korea*, vol. 17, no. 2, pp. 53–59, 2013, <https://doi.org/10.5000/EESK.2013.17.2.053>.
- [10] I.-K. Choi, Y.-S. Choun, S.-M. Ahn, and J.-M. Seo, "Seismic fragility analysis of a CANDU type NPP containment building for near-fault ground motions," *KSCE Journal of Civil Engineering*, vol. 10, no. 2, pp. 105–112, Mar. 2006, <https://doi.org/10.1007/BF02823928>.
- [11] I.-K. Choi, Y.-S. Choun, S.-M. Ahn, and J.-M. Seo, "Probabilistic seismic risk analysis of CANDU containment structure for near-fault earthquakes," *Nuclear Engineering and Design*, vol. 238, no. 6, pp. 1382–1391, Jun. 2008, <https://doi.org/10.1016/j.nucengdes.2007.11.001>.
- [12] Q. He, X. Li, Y. Li, A. Liu, and J. Zhang, "Dynamic Nonlinear Time-History Analysis of Nuclear Power Plant under Near-Fault Ground Motion with Velocity Pulse," in *Seventh China-Japan-US Trilateral Symposium on Lifeline Earthquake Engineering*, Aug. 2017, pp. 242–249, <https://doi.org/10.1061/9780784480342.033>.
- [13] E. Lee, J. Kim, K. Joo, and H. Kim, "Evaluation of the Soil-structure Interaction Effect on Seismically Isolated Nuclear Power Plant Structures," *Journal of the Earthquake Engineering Society of Korea*, vol. 20, no. 6, pp. 379–389, 2016, <https://doi.org/10.5000/EESK.2016.20.6.379>.
- [14] G.-J. Kim, K.-K. Yang, B.-S. Kim, H.-J. Kim, S.-J. Yun, and J.-K. Song, "Seismic Response Evaluation of Seismically Isolated Nuclear Power Plant Structure Subjected to Gyeong-Ju Earthquake," *Journal of the Earthquake Engineering Society of Korea*, vol. 20, no. 7, pp. 453–460, 2016, <https://doi.org/10.5000/EESK.2016.20.7.453>.
- [15] J.-H. Lee and J.-K. Song, "Seismic Fragility Analysis of Seismically Isolated Nuclear Power Plant Structures using Equivalent Linear- and Bilinear-Lead Rubber Bearing Model," *Journal of the Earthquake Engineering Society of Korea*, vol. 19, no. 5, pp. 207–217, 2015, <https://doi.org/10.5000/EESK.2015.19.5.207>.
- [16] D. Van Nguyen, D. Kim, and D. Duy Nguyen, "Nonlinear seismic soil-structure interaction analysis of nuclear reactor building considering the effect of earthquake frequency content," *Structures*, vol. 26, pp. 901–914, Aug. 2020, <https://doi.org/10.1016/j.istruc.2020.05.013>.
- [17] K. Galal and A. Ghobarah, "Effect of near-fault earthquakes on North American nuclear design spectra," *Nuclear Engineering and Design*, vol. 236, no. 18, pp. 1928–1936, Sep. 2006, <https://doi.org/10.1016/j.nucengdes.2006.02.002>.
- [18] A. K. Chopra and C. Chintanapakdee, "Comparing response of SDF systems to near-fault and far-fault earthquake motions in the context of spectral regions," *Earthquake Engineering & Structural Dynamics*, vol. 30, no. 12, pp. 1769–1789, 2001, <https://doi.org/10.1002/eqe.92>.
- [19] "SAP2000." Computers and structures Inc, Berkeley, CA, USA, 2013.
- [20] D. D. Nguyen and C. N. Nguyen, "Seismic Responses of NPP Structures Considering the Effects of Lead Rubber Bearing," *Engineering, Technology & Applied Science Research*, vol. 10, no. 6, pp. 6500–6503, Dec. 2020, <https://doi.org/10.48084/etasr.3926>.
- [21] D.-D. Nguyen, B. Thusa, and T.-H. Lee, "Effects of Significant Duration of Ground Motions on Seismic Responses of Base-Isolated Nuclear Power Plants," *Journal of the Earthquake Engineering Society of Korea*, vol. 23, no. 3, pp. 149–157, 2019, <https://doi.org/10.5000/EESK.2019.23.3.149>.

- [22] J. A. Alomari, "Effect of the Presence of Basements on the Vibration Period and Other Seismic Responses of R.C. Frames," *Engineering, Technology & Applied Science Research*, vol. 9, no. 5, pp. 4712–4717, Oct. 2019, <https://doi.org/10.48084/etasr.3005>.
- [23] T. Nagao, "An Experimental Study on the Way Bottom Widening of Pier Foundations Affects Seismic Resistance," *Engineering, Technology & Applied Science Research*, vol. 10, no. 3, pp. 5713–5718, Jun. 2020, <https://doi.org/10.48084/etasr.3590>.
- [24] P. C. Nguyen, B. Le-Van, and S. D. T. V. Thanh, "Nonlinear Inelastic Analysis of 2D Steel Frames: An Improvement of the Plastic Hinge Method," *Engineering, Technology & Applied Science Research*, vol. 10, no. 4, pp. 5974–5978, Aug. 2020, <https://doi.org/10.48084/etasr.3600>.
- [25] M. Shinozuka, M. Q. Feng, J. Lee, and T. Naganuma, "Statistical Analysis of Fragility Curves," *Journal of Engineering Mechanics*, vol. 126, no. 12, pp. 1224–1231, Dec. 2000, [https://doi.org/10.1061/\(ASCE\)0733-9399\(2000\)126:12\(1224\)](https://doi.org/10.1061/(ASCE)0733-9399(2000)126:12(1224)).

Non-Profit Organization Project Selection Process Using the Hygiene Method of Multi-Criteria Decision Making

Ahmed Reyadh Radhi

College of Engineering
Al Musaib University of Babylon and
College of Engineering, University of Baghdad
Iraq
ahmedrr989@gmail.com

Abbas M. Burhan

Civil Engineering Department
College of Engineering
University of Baghdad
Baghdad, Iraq
abbasm.burhan@coeng.uobaghdad.edu.iq

Received: 4 July 2022 | Revised: 14 July 2022 | Accepted: 16 July 2022

Abstract-With the fast increase in technological development and society's needs, using Multi-Criteria Decision Making (MCDM) as a solution to tackle problems faced during a project's life cycle in different engineering fields gains interest. The use of artificial intelligence gave new opportunities to deal with problems faced during the optimization of unknown or known solutions and methods. Even more, the application of optimized solutions can be developed or modified by using different optimization approaches and methods. This paper proposes a model for the project selection process for non-profit organizations that have a limited budget and social factors strictly related to the selection process. This method is based on MCDM and takes into consideration criterion weights and experts' evaluation of projects according to the selection criteria using the hygiene method consisting of two stages, fuzzy logic, and TOPSIS.

Keywords-multi criteria decision making; TOPSIS; fuzzy logic; project selection; decision making; optimization

I. INTRODUCTION

MCDM can be considered as an applicable solution to overcome the constraints raised and need to be optimized in different engineering fields. Some optimization methods discussed in published papers are: Analytical Network Process (ANP), Visekriterijumska Optimizacija I Kompromisno Resenje (VIKOR), Artificial Neural Networks (ANNs), Analytical Hierarchy Process (AHP), Preference Ranking Organization Method for Enrichment of Evaluations (PROMETHEE), and the Technique of Order Preference by Similarity to Ideal Solution (TOPSIS). This paper introduces a hygiene method for the project selection process of non-profit organizations. Most papers related to project selection depend mainly on economic measures (numerical) neglecting the social factors that affect the selection process.

II. MULTI CRITERIA DECISION MAKING APPLICATION

A. Civil Engineering

PROMETHEE and AHP ranking proposals were used at the project construction sector and 7 critical paths of project were

examined with triangular fuzzy numbers to evaluate path selection criteria in [1]. VIKOR approach was also used to detect the critical path. In addition, fuzzy analytical network process was adopted in [2] in order to find activities' priority and correlation. A methodology named Construction Method Selection Model (CMSM) was introduced in [3], which consists of two main stages to assess and select the prefabrication construction method for projects. At first, the strategic stage, using Simple Multi-Attribute Rating Technique (SMART) resulted to 4 main attributes (project characteristics, market attribute, site conditions, and local regulations) and 12 sub – attributes with higher relative weights to project characteristics sub – attributes. The main objective of this stage was to assess the feasibility of the prefabrication process through the mentioned attributes. The second stage is the tactical stage, in which Multi-Attribute Utility Theory (MAUT) is used to evaluate the uncertainty associated with the project prefabrication ability taking sustainability performance into consideration.

A guidance method was proposed in [4] for engineering designers to select sustainable building materials depending on two main issues: evaluation criteria and stakeholder's requirements. The evaluation criteria were recognized using the sustainable Triple Bottom Line (TBL) method and the impact of each factor was determined by experts before applying the data to the Fuzzy Extended AHP (FEAHP) to get the final results. The sustainable assessment depends on 3 major categories: environmental, social-economic, and technical. More than 20 sub categories were directly responsible for the material evaluation process. The researchers used varimax rotation to reveal the correlation between the observed and latent criteria [4].

Ambiguities associated with project selection were studied using Fuzzy TOPSIS (FTOPSIS) in [5] to support contractors to choose the best project for bidding according to their abilities and the project requirements. This method is considered one of the multi attribute decision making methods

that give an acceptable representation to real world problems. The research uses triangular fuzzy number to represent verbal factors. The best alternative selection process was examined in [6] by project evaluation and selecting the best projects using Additive Ratio Assessment (ARAS) and AHP. AHP was used to build and assess the selection process structure and assign weights to the selection criteria while ARAS performed project ranking. This method cannot deal with qualitative criteria unless they are evaluated on a numerical scale.

Authors in [7] discuss the assessment of infrastructure design methods by embracing the Monte Carlo optimization multi attribute selection model. One of the main ruling factors of the process is the epistemic uncertainty risk that differs from each method to another. Authors in [8] described MCDM methods in relevance to their usage fields and their contribution in maintenance management. AHP was adopted in [9] to design a dynamic decision model for inspecting and maintaining reinforced concrete structures. The model aims to select the best alternative by pair-wise comparison between the criteria with global priority vector instead of depending on experts' opinions.

B. Environmental Engineering

Environmental engineering has its share of using artificial intelligence. TOPSIS and ANP were used in [10] to analyze the construction methods in accordance to the productivity aspect. The main analyzing factors are management, materials, costs, time, human force, environmental sustainability, planning, and architectural design with overall 24 sub-factors. The impact of factors is examined by the Decision Making Trial and Evaluation Laboratory Method (DEMATEL). Construction and demolition waste were optimized using a proposed methodology to support decision makers in [11]. The methodology consists of 3 main stages: At first, an index system is established depending on technical, financial, environmental, and social attributes. The second stage is the evaluation framework with experts' opinions through a multi criteria decision framework using the Trapezoidal Fuzzy Numbers (TrFN), interval numbers, and Triangular Fuzzy Numbers (TFN). The next stage is examining the correlation between the criteria using the ANP to detect the main and sub criteria in order to use the fuzzy Multi-Attributive Border Approximation area Comparison (MABAC) method as a final ranking tool. Fuzzy ANP (FANP) was exploited in [12] to build a methodology for sustainable project selection depending on criteria defined by experts' opinions. A multi criteria optimization procedure was introduced in [18] to develop and evaluate 5 renewable energy scenarios. PROMETHEE method was used taking into consideration the evaluation criteria and their weights. The Simos method was used for weight determination.

C. Transportation Engineering

Authors in [13] considered the problems related to the transportation sector problem solution optimization. They introduced an assessment for technologies used in 6 public transportation fare collection methods. The authors used were AGREPREF as an MCDM method to evaluate the methods according to 6 criteria (operation costs, safety, speed, demand of applications, multipurpose, simplicity and comfort). The

public transportation project selection problem in Istanbul city brought in the spotlight the use of optimization solutions [14]. A mathematical model was built in [14] by integer linear programming with IBM ILOG CPLEX 12.6.2 program. The selection process depended on selection constraints which are budget, travel time, station number accessed, and travel distance. The model's objective function looked to maximize the benefits from project proposals. The review in [15] worked with more than 50 papers from 1982 to 2019 and summarized the alternative multi criteria transport project evaluation methods instead of cost effective analysis.

D. Geotechnical Engineering

Geotechnical engineering tends to use the Particle Swarm Optimization (PSO) method due to the nonlinear behavior of the considered variables. Authors in [16] wrote a review paper on the use of PSO in various geotechnical engineering aspects. PSO was used in [17] to solve geotechnical difficulties related to slope stability, retaining wall, and shallow footings.

III. THE PROPOSED MODEL

Project selection is a very complex process. One of the most common goals is optimizing resource utilization. This process may be easier for private and marketing companies which use economic measures to evaluate the proposed project in addition to risk management taking into consideration organization resources. For government organizations, the social aspect enters as an active factor. Social goals and similar criteria are judged by experts or decision makers. For better understanding of the project selection process, some abbreviations need to be defined:

P_i : The proposed project (P_1, P_2, \dots, P_i)

Cr_j : Selection criteria (Cr_1, Cr_2, \dots, Cr_j)

X_{ij} : Project evaluation according to the criteria

E : no. of experts (1, 2, ..., e)

The proposed model uses trapezoidal fuzzy number to evaluate the qualitative criterion shown in Figure 1. The fuzzy number is calculated according to (1). The values of verbal evaluations responding to each trapezoidal fuzzy number are stated in Table I.

$$X_{ij} = (F_{ije}, G_{ije}, L_{ije}, M_{ije})$$

$$\mu(x) = \begin{cases} 0 & X < T_1 \\ \frac{X - T_1}{T_2 - T_1} & T_1 \leq X \leq T_2 \\ 1 & T_2 \leq X \leq T_3 \\ \frac{T_4 - X}{T_4 - T_3} & T_3 \leq X \leq T_4 \\ 0 & X > T_4 \end{cases} \quad (1)$$

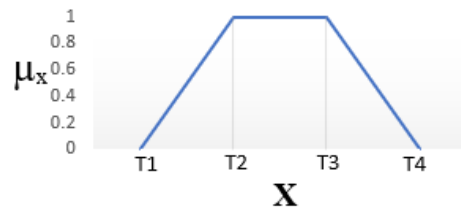


Fig. 1. Trapezoidal fuzzy numbers.

TABLE I. LINGUISTIC EVALUATION

Qualitative evaluation	Fuzzy number value
Very Low (VL)	(1, 1, 1.2, 2.8)
Low (L)	(1.2, 2.8, 3.2, 4.8)
Medium (M)	(3.2, 4.8, 5.2, 6.8)
High (H)	(5.2, 6.8, 7.2, 8.8)
Very High (VH)	(7.2, 8.8, 9, 9)

Each project evaluation provided by individual experts is multiplied by its own criteria weights. In order to aggregate experts' opinion regarding the proposed projects with respect to the selection process, criterion aggregating of fuzzy numbers needs to be performed according to the following equations:

$$\tilde{x}_{ije} = (F_{ije}, G_{ije}, L_{ije}, M_{ije})$$

$$F_{ij} = \text{Min} (F_{ije}) \quad (3)$$

$$G_{ij} = \frac{1}{e} \sum_{e=1}^e G_{ije} \quad (4)$$

$$L_{ij} = \frac{1}{e} \sum_{e=1}^e L_{ije} \quad (5)$$

$$M_{ij} = \text{Max} (M_{ije}) \quad (6)$$

The selection criteria can be categorized into benefit criteria (maximum value is preferred) or cost criteria (minimum value is preferred) according to the criteria category normalization equations. If the criterion is a benefit criterion we have:

$$\tilde{x}_{ij} = \left(\frac{F_{ij}}{\text{Max.M}_{ij}}, \frac{G_{ij}}{\text{Max.M}_{ij}}, \frac{L_{ij}}{\text{Max.M}_{ij}}, \frac{M_{ij}}{\text{Max.M}_{ij}} \right) \quad (7)$$

If it is a cost criterion:

$$\tilde{x}_{ij} = \left(\frac{\text{Min.F}_{ij}}{M_{ij}}, \frac{\text{Min.F}_{ij}}{L_{ij}}, \frac{\text{Min.F}_{ij}}{G_{ij}}, \frac{\text{Min.F}_{ij}}{F_{ij}} \right) \quad (8)$$

The next step is performing defuzzification for the input values using the middle of maxima that will be used at the second stage of optimization process matrix according to (9):

$$\mu_{x_{ij}} = \frac{(M_{ij}-F_{ij})(L_{ij}-G_{ij})}{2} \quad (9)$$

The vector normalization deals with the input criteria according to (10).

$$\bar{x}_{ij} = \frac{x_{ij}}{\sqrt{\sum_{i=1}^i (x_{ij})^2}} \quad (10)$$

The resulting matrix will be the Normalized Decision Matrix (NDM). NDM will be multiplied by criteria weights to determine the Weighted NDM (WNDM) as shown in (11).

$$\text{NDM} = \begin{bmatrix} \bar{x}_{11} & \bar{x}_{12} & \dots & \bar{x}_{1j} \\ \bar{x}_{21} & \bar{x}_{22} & \dots & \bar{x}_{2j} \\ \vdots & \vdots & \dots & \vdots \\ \bar{x}_{i1} & \bar{x}_{i2} & \dots & \bar{x}_{ij} \end{bmatrix}$$

$$\bar{x}_{wij} = \bar{x}_{ij} \times W_m \quad (11)$$

$$\text{WNDM} = \begin{bmatrix} w_1 \bar{x}_{11} & w_2 \bar{x}_{12} & \dots & w_j \bar{x}_{1j} \\ w_1 \bar{x}_{21} & w_2 \bar{x}_{22} & \dots & w_j \bar{x}_{2j} \\ \vdots & \vdots & \dots & \vdots \\ w_1 \bar{x}_{i1} & w_2 \bar{x}_{i2} & \dots & w_j \bar{x}_{ij} \end{bmatrix}$$

The next step is detecting the best and worst ideal values for each criterion according to its behavior, either it is a cost criterion, where minimum value is preferred or a benefit criterion where maximum value is preferred, in order to find the Euclidean distance from the proposed solution to the best and worst ideal solutions using (12) and (13) respectively.

$$D_i^+ = \sqrt{\sum_{i=1}^i (\bar{x}_{wij} - X_{ij}^+)^2} \quad (12)$$

$$D_i^- = \sqrt{\sum_{i=1}^i (\bar{x}_{wij} - X_{ij}^-)^2} \quad (13)$$

The distance between the proposed solution and the ideal best and worst solutions will be calculated by (14):

$$D_i = \sqrt{(X_2 - X_1)^2 + (Y_2 - Y_1)^2 + (Z_2 - Z_1)^2} \quad (14)$$

The performance score function that will rank the proposed projects is shown in (15)

$$P_i = \frac{D_i^-}{D_i^+ + D_i^-} \quad (15)$$

IV. AN ILLUSTRATIVE EXAMPLE

In this example, we consider a group of 6 projects with an expert committee consisting of 3 experts. Projects will be evaluated regarding 5 criteria which are the quantitative criteria Cr₁ (project cost) and Cr₂ (number of beneficiaries) and the qualitative criteria Cr₃ (organization staff expert), Cr₄ (project legal constraints), and Cr₅ (project meets end-user requirements). The owner organization has the expert weights and the weights regarding the quantitative criteria as shown in Tables II and III. The expert evaluations according to the qualitative criteria are shown in Table IV.

TABLE II. EXPERT WEIGHTS

Expert	Weight
E1	High
E2	Very High
E3	High

TABLE III. QUANTITATIVE CRITERIA

Projects	Cr ₁	Cr ₂
	Cost	Benefit
P1	1,125,000,000	2000000
P2	4,300,000,000	265000
P3	1,050,000,000	140000
P4	4,400,000,000	1170000
P5	4,700,000,000	180000
P6	450,000,000	1200000

TABLE IV. EXPERTS EVALUATIONS ON QUALITATIVE CRITERIA

	Expert 1			Expert2			Expert3		
	Cr ₃	Cr ₄	Cr ₅	Cr ₃	Cr ₄	Cr ₅	Cr ₃	Cr ₄	Cr ₅
P1	M	L	H	VH	H	M	L	M	H
P2	H	H	VL	VL	H	H	H	VL	L
P3	VL	VH	M	L	VH	L	H	H	VL
P4	VL	H	VL	VL	VH	H	VL	H	VL
P5	L	VH	H	H	L	VH	M	M	M
P6	VL	L	M	VH	M	VL	H	VH	L

The experts' evaluations for criteria weights are aggregated and normalized using trapezoidal fuzzy numbers in order to be transformed to crisp value taking into consideration the relative importance of expert weights shown in Table V. All the outputs will be used as input to TOPSIS. The calculation steps and their results are shown in Tables VI-X.

TABLE V. CRITERIA EVALUATION

Criterion	E ₁	E ₂	E ₃	Crisp %
Cr ₁	VH	VH	H	24%
Cr ₂	H	VH	H	22%
Cr ₃	M	H	M	17%
Cr ₄	H	H	M	19%
Cr ₅	H	M	H	18%

TABLE VI. QUALITATIVE CRITERIA FUZZY OUTPUT

Project	Cr ₃	Cr ₄	Cr ₅
	Benefit	Cost	Benefit
P1	0.4869	0.4698	0.3852
P2	0.4819	0.4740	0.4899
P3	0.4914	0.3489	0.4866
P4	0.4344	0.3522	0.4854
P5	0.4896	0.4572	0.4260
P6	0.4905	0.4684	0.4779

TABLE VII. NORMALIZED MATRIX

	Cr ₁	Cr ₂	Cr ₃	Cr ₄	Cr ₅
P1	0.1423	0.7597	0.4145	0.4440	0.3417
P2	0.5439	0.1007	0.4103	0.4480	0.4346
P3	0.1328	0.0532	0.4183	0.3297	0.4317
P4	0.5565	0.4444	0.3698	0.3328	0.4306
P5	0.5945	0.0684	0.4168	0.4321	0.3779
P6	0.0569	0.4558	0.4176	0.4427	0.4240

TABLE VIII. WEIGHTED NORMALIZED MATRIX

	Cr ₁	Cr ₂	Cr ₃	Cr ₄	Cr ₅
P1	0.0341	0.1698	0.0698	0.0827	0.0623
P2	0.1303	0.0225	0.0691	0.0834	0.0792
P3	0.0318	0.0119	0.0705	0.0614	0.0787
P4	0.1334	0.0993	0.0623	0.0620	0.0785
P5	0.1425	0.0153	0.0702	0.0804	0.0689
P6	0.0136	0.1019	0.0703	0.0824	0.0773

TABLE IX. IDEAL BEST AND WORST SOLUTIONS

	Cr ₁	Cr ₂	Cr ₃	Cr ₄	Cr ₅
V-	0.1425	0.0119	0.0623	0.0834	0.0623
V+	0.0136	0.1698	0.0705	0.0614	0.0792

TABLE X. PERFORMANCE AND PROJECT RANKING

	S -	S +	Pi	Ranking
P1	0.1917	0.0340	0.8492	1
P2	0.0243	0.1892	0.1140	5
P3	0.1143	0.1589	0.4183	3
P4	0.0919	0.1392	0.3978	4
P5	0.0112	0.2023	0.0527	6
P6	0.1581	0.0711	0.6897	2

V. CONCLUSION

MCDM methods have the advance of a methodology that tackles problems characterized by multi variable conditions,

factors, and constraints. Even more, the high level of work and research continuously develops many algorithms, and optimization methods. The of fuzzy logic, genetic algorithms, and real life phenomena simulations like Ant Colony Optimization, Grey Wolf Optimization, Particle Swarm Optimization, etc. enriched the optimization approach. These methods lead to deep learning and machine learning aspects. These technologies make a solid base for the exploitation of future opportunities and new challenges that will be tackled.

REFERENCES

- [1] S. Cristobal and J. Ramon, "Critical Path Definition Using Multicriteria Decision Making: PROMETHEE Method," *Journal of Management in Engineering*, vol. 29, no. 2, pp. 158–163, Apr. 2013, [https://doi.org/10.1061/\(ASCE\)ME.1943-5479.0000135](https://doi.org/10.1061/(ASCE)ME.1943-5479.0000135).
- [2] A. Ali-Mohammad, B. Mahdi, and A. Zahra, "The critical path definition with fuzzy multi criteria decision making," in *2010 The 2nd International Conference on Computer and Automation Engineering (ICCAE)*, Singapore, Oct. 2010, vol. 5, pp. 206–210, <https://doi.org/10.1109/ICCAE.2010.5451469>.
- [3] Y. Chen, G. E. Okudan, and D. R. Riley, "Decision support for construction method selection in concrete buildings: Prefabrication adoption and optimization," *Automation in Construction*, vol. 19, no. 6, pp. 665–675, Oct. 2010, <https://doi.org/10.1016/j.autcon.2010.02.011>.
- [4] P. O. Akadiri, P. O. Olomolaiye, and E. A. Chinyio, "Multi-criteria evaluation model for the selection of sustainable materials for building projects," *Automation in Construction*, vol. 30, pp. 113–125, Mar. 2013, <https://doi.org/10.1016/j.autcon.2012.10.004>.
- [5] Y. Tan, L. Shen, C. Langston, and Y. Liu, "Construction project selection using fuzzy TOPSIS approach," *Journal of Modelling in Management*, vol. 5, no. 3, pp. 302–315, Jan. 2010, <https://doi.org/10.1108/17465661011092669>.
- [6] T. Bakshi and B. Sarkar, "MCA Based Performance Evaluation of Project Selection," *International Journal of Software Engineering & Applications*, vol. 2, no. 2, pp. 14–22, Apr. 2011, <https://doi.org/10.5121/ijsea.2011.2202>.
- [7] M. Shahpari, F. M. Saradj, M. S. Pishvae, and S. Piri, "Assessing the productivity of prefabricated and in-situ construction systems using hybrid multi-criteria decision making method," *Journal of Building Engineering*, vol. 27, Jan. 2020, Art. no. 100979, <https://doi.org/10.1016/j.job.2019.100979>.
- [8] F. Zhang, Y. Ju, E. D. R. Santibanez Gonzalez, A. Wang, P. Dong, and M. Giannakis, "Evaluation of construction and demolition waste utilization schemes under uncertain environment: A fuzzy heterogeneous multi-criteria decision-making approach," *Journal of Cleaner Production*, vol. 313, Sep. 2021, Art. no. 127907, <https://doi.org/10.1016/j.jclepro.2021.127907>.
- [9] R. Alyamani and S. Long, "The Application of Fuzzy Analytic Hierarchy Process in Sustainable Project Selection," *Sustainability*, vol. 12, no. 20, Jan. 2020, Art. no. 8314, <https://doi.org/10.3390/su12208314>.
- [10] I. Olivková, "Comparison and Evaluation of Fare Collection Technologies in the Public Transport," *Procedia Engineering*, vol. 178, pp. 515–525, Jan. 2017, <https://doi.org/10.1016/j.proeng.2017.01.099>.
- [11] E. Özcan, M. Hamurcu, H. Alakaş, and T. Eren, "Project Selection by Using Constraint Programming," *Journal of Trends in the Development of Machinery and Associated Technology*, vol. 21, no. 1, pp. 89–92, Oct. 2018.
- [12] G. Yannis, A. Kopsacheili, A. Dragomanovits, and V. Petraki, "State-of-the-art review on multi-criteria decision-making in the transport sector," *Journal of Traffic and Transportation Engineering (English Edition)*, vol. 7, no. 4, pp. 413–431, Aug. 2020, <https://doi.org/10.1016/j.jtte.2020.05.005>.
- [13] M. Hajihassani, D. Jahed Armaghani, and R. Kalatehjari, "Applications of Particle Swarm Optimization in Geotechnical Engineering: A Comprehensive Review," *Geotechnical and Geological Engineering*, vol. 36, no. 2, pp. 705–722, Apr. 2018, <https://doi.org/10.1007/s10706-017-0356-z>.

- [14] A. R. Kashani, R. Chiong, S. Mirjalili, and A. H. Gandomi, "Particle Swarm Optimization Variants for Solving Geotechnical Problems: Review and Comparative Analysis," *Archives of Computational Methods in Engineering*, vol. 28, no. 3, pp. 1871–1927, May 2021, <https://doi.org/10.1007/s11831-020-09442-0>.
- [15] D. Mazzeo, C. Baglivo, N. Matera, P. M. Congedo, and G. Oliveti, "A novel energy-economic-environmental multi-criteria decision-making in the optimization of a hybrid renewable system," *Sustainable Cities and Society*, vol. 52, Jan. 2020, Art. no. 101780, <https://doi.org/10.1016/j.scs.2019.101780>.
- [16] P. Benítez, E. Rocha, H. Varum, and F. Rodrigues, "A dynamic multi-criteria decision-making model for the maintenance planning of reinforced concrete structures," *Journal of Building Engineering*, vol. 27, Jan. 2020, Art. no. 100971, <https://doi.org/10.1016/j.jobbe.2019.100971>.
- [17] D. Sabaei, J. Erkoyuncu, and R. Roy, "A Review of Multi-criteria Decision Making Methods for Enhanced Maintenance Delivery," *Procedia CIRP*, vol. 37, pp. 30–35, Jan. 2015, <https://doi.org/10.1016/j.procir.2015.08.086>.
- [18] E. K. Zavadskas and E. R. Vaidogas, "Multiattribute Selection from Alternative Designs of Infrastructure Components for Accidental Situations," *Computer-Aided Civil and Infrastructure Engineering*, vol. 24, no. 5, pp. 346–358, 2009, <https://doi.org/10.1111/j.1467-8667.2009.00593.x>.
- [19] R. Madlener, K. Kowalski, and S. Stagl, "New ways for the integrated appraisal of national energy scenarios: The case of renewable energy use in Austria," *Energy Policy*, vol. 35, no. 12, pp. 6060–6074, Dec. 2007, <https://doi.org/10.1016/j.enpol.2007.08.015>.
- [20] V. Dixit and M. K. Tiwari, "Project portfolio selection and scheduling optimization based on risk measure: a conditional value at risk approach," *Annals of Operations Research*, vol. 285, no. 1, pp. 9–33, Feb. 2020, <https://doi.org/10.1007/s10479-019-03214-1>.
- [21] C. Yi, "A Decision-Making Approach for R&D Project Selection in a Fuzzy Environment," in *2008 International Seminar on Business and Information Management*, Wuhan, China, Sep. 2008, vol. 1, pp. 372–375, <https://doi.org/10.1109/ISBIM.2008.178>.
- [22] N. N. Abbas and A. M. Burhan, "Investigating the Causes of Poor Cost Control in Iraqi Construction Projects," *Engineering, Technology & Applied Science Research*, vol. 12, no. 1, pp. 8075–8079, Feb. 2022, <https://doi.org/10.48084/etasr.4661>.
- [23] A. R. Radhi and B. A. Hamza, "Engineer's decision effect on delayed governmental construction project with budget abundance (case study)," *International Journal of Civil Engineering and Technology*, vol. 9, no. 6, pp. 1166–1175, Jun. 2018.
- [24] G. A. Fadhil and A. M. Burhan, "Developing Crisis Management System for Construction Projects in Iraq," *Journal of Engineering*, vol. 28, no. 1, pp. 33–51, Jan. 2022, <https://doi.org/10.31026/j.eng.2022.01.03>.
- [25] H. T. Almusawi and A. M. Burhan, "Developing a Model to Estimate the Productivity of Ready Mixed Concrete Batch Plant," *Journal of Engineering*, vol. 26, no. 10, pp. 80–93, Oct. 2020, <https://doi.org/10.31026/j.eng.2020.10.06>.
- [26] N. U. I. Soomro, A. H. Memon, N. A. Memon, and K. R. Memon, "Contractor's Selection Criteria in Construction Works in Pakistan," *Engineering, Technology & Applied Science Research*, vol. 10, no. 2, pp. 5520–5523, Apr. 2020, <https://doi.org/10.48084/etasr.3334>.
- [27] A. Daghour, K. Mansouri, and M. Qbadou, "Enhanced Model For Evaluating Information System Success: Determining Critical Criteria," *Engineering, Technology & Applied Science Research*, vol. 8, no. 4, pp. 3194–3198, Aug. 2018, <https://doi.org/10.48084/etasr.2148>.

Autonomous Navigation and Real Time Mapping Using Ultrasonic Sensors in NAO Humanoid Robot

Suresh Kumar

Department of Computer Systems Engineering
Sukkur IBA University
Sukkur, Pakistan
suresh@iba-suk.edu.pk

Malak Majeedullah

Department of Electrical Engineering
Sukkur IBA University
Sukkur, Pakistan
malakmajeedullah.be17@iba-suk.edu.pk

Abdul Baseer Buriro

Department of Electrical Engineering
Sukkur IBA University
Sukkur, Pakistan
abdul.baseer@iba-suk.edu.pk

Rohibullah

Department of Electrical Engineering
Sukkur IBA University
Sukkur, Pakistan
rohibullah.be17@iba-suk.edu.pk

Received: 5 July 2022 | Revised: 18 July 2022 | Accepted: 20 July 2022

Abstract-Mapping is an essential and basic requirement for a mobile robot in order to be able to navigate autonomously. This paper proposes a solution for autonomous navigation and real-time mapping using the virtual humanoid robot called NAO. The robot navigates through its environment using ultrasonic sensors only and develops a 2-D map of the environment. For implementation and testing, the Webots simulator was used. It provides real-time values, modification and designing of the 3-D world arena, and plugins for other parameters control. We test autonomous navigation in differently shaped environments. The proposed mathematical algorithm allows the autonomous navigation of the robot and calculates the position of the robot and the obstacles (if any). The results indicate that the algorithm can localize the robot within the environment whereas the accuracy in localization can be increased by adding a control constant to the orientation of the robot. The results demonstrate that the algorithm is more effective in the rectangular arena than in the triangular and pentagon arenas.

Keywords-robotics; mapping; humanoid; navigation

I. INTRODUCTION

Humans can navigate through unknown areas while avoiding collisions with other humans or objects. We are, also, capable to develop maps in our cognition of the known areas, which help us navigate. If we want robots to navigate around the world as humans do, then they must be capable of autonomous navigation, avoid unnecessary contacts with objects or humans, and develop maps. For navigation in outdoor environment, mobile robots are preferred. However, humanoid robots, due to their symmetrical structure to human beings, are preferred for indoor environments. This structure eliminates many singularity constraints and enables the robots to act in an environment designed specifically for humans [1]. In other words, one can say that humanoid robots can take the place of humans in many workspaces as these days robots are

performing very well in assisting humans in health, education, research, etc. [2].

For a humanoid robot to perform a task successfully in a real-world environment, stable dynamic biped locomotion is required [3]. Also, in order to work efficiently, a robot must know about its environment through maps, its own and obstacles' location in the environment. However, due to limited sensing capabilities, it is challenging for a robot to localize itself and detect obstacles in its environment. GPS has been used to determine the location of the robot, however, the GPS does not work in indoor environments or produces an error in location due to the absence of line of sight or reflected signal [4]. Furthermore, other sensors are required to detect the objects/obstacles in the environment. By adding more and more sensors, the complexity of the algorithms increases, adding delay in real-time response during navigation. In this paper, we propose an algorithm for obstacle detection and autonomous navigation and mapping of a humanoid robot by using ultrasonic sensors. For this purpose, we used a virtual humanoid, the NAO robot, for our experiments [5]. NAO is a humanoid robot with 25 degrees of freedom, dual vision cameras, force sensors on its feet, touch sensors in the head and arms and a pair of ultrasonic sensors on its chest. Apart from that, the robot has internal temperature and position sensors to detect joint motors' temperature and joint positions. The official vendor of the robot provides a simulator, Choregraphe, for the robot. However, for the experiments, we have used a third-party open-source simulator, Webots [6]. In comparison to Choregraphe, Webots provides extra features such as adding obstacles in the environment and tracking the odometry of the robot. The simulator also contains motion libraries to access robot joints and move them through high-level commands. During the motion, the motion library of the robot also controls physical the stability of the robot, thus, the robot does not fall

Corresponding author: Suresh Kumar

while walking. The robot can be programmed to reach a specific point in its environment by walking, in its frame of reference [7].

The purpose of this study is to propose a mathematical algorithm for the NAO robot to detect objects using ultrasonic sensors and localize the detected objects in the environment and localize itself using odometry. Furthermore, the algorithm creates a 2-D map of the space/environment in which the robot navigates.

II. LITERATURE REVIEW

Different researchers have worked on the mapping of NAO humanoid robots using the fusion of the different sensors, i.e. IR sensors, RGB camera, tactile sensors, and ultrasonic sensors [8]. Authors in [9] proposed a method for autonomous navigation of the NAO robot using a fusion of visual and robot odometry. Their approach improves robot pose estimation using the fusion of odometry compared to robot odometry. However, fusion makes the algorithm computational expensive. Furthermore, the experiment was conducted in a rectangular environment where the robot followed a predefined path, either straight or L-shaped, only, thus limiting the environment and walking length and direction. Authors in [10] demonstrated the navigation of indoor environment by NAO robot using robot's odometry. They used the vision of the robot only to confirm the target position and adjust in pose at any other location than the target position. The robot was tasked to reach for a door that contains a specific symbol. The robot navigates straight using odometry until it reaches the target. Although the experiment was performed using a real robot, however, it was performed in a controlled environment where no active object was present. This limits the capability of the algorithm to navigate and map in an environment with active objects present. Authors in [11] proposed a fuzzy logic-based obstacle avoidance algorithm for the virtual NAO robot. The algorithm decides the orientation and walking speed of the robot based on the data from ultrasonic sensors. They performed the experiment using a virtual robot in Webots simulator, as we do in this study. However, the scope of their study is limited to obstacle avoidance only, whereas our study focuses on autonomous navigation 2-D mapping, which contains obstacle avoidance as a part of the algorithm.

Apart from humanoid robots, mobile robots also have been used for testing algorithms for autonomous navigation and obstacle avoidance. Authors in [12] designed a fuzzy logic control system to steer a mobile robot for autonomous navigation and obstacle avoidance. However, they considered a simple two-wheeled mobile robot, which reduces the complexity of motion. Furthermore, the authors used simulated sensors to detect the position and angle of the obstacles with respect to the robot.

The above-mentioned studies either use a fusion of multiple sensors [9, 10] or limited scope of the robot is considered using ultrasonic sensors [11, 12]. Furthermore, using multiple sensors increases the complexity in getting data and computational cost. Also, dependency on many sensors can cause failure while performing a task, whereas the battery life is affected adversely [13].

III. METHODOLOGY

Two ultrasonic sensors, along with the ultrasonic transmitters, are placed on the chest of the robot. The sensors are in a distance of 0.0832m (8.32cm) apart from each other. Each sensor is able to detect 40KHz frequency with an effective cone angle of 60° and range from 0.25m to 2.55m [8]. The simulated robot is able to detect any object within this cone angle and range. It returns the distance of the object from the sensors, irrespective of its position. If there is no object within the range and cone angle, then the simulator returns the maximum distance, i.e. 2.55m. Since the two ultrasonic sensors return the distance from the object, thus it is challenging to locate the object within the space.

The proposed autonomous navigation algorithm lets robots make movements autonomously based on the sensor data. If the sensors detect any object at distance less than 0.8m, then the robot makes a turn, otherwise, it makes a forward move. The robot makes a left or right turn if an object is at a distance less than 0.8m on either the right or the left side respectively. If both sensors detect an object at a distance less than 0.8m then the robot makes a u-turn, i.e., a 180° turn. The distance, 0.8m, is selected for the robot's safety purpose as it should not strike the object while extending its arms. Figure 1 shows the flow diagram of the autonomous navigation.

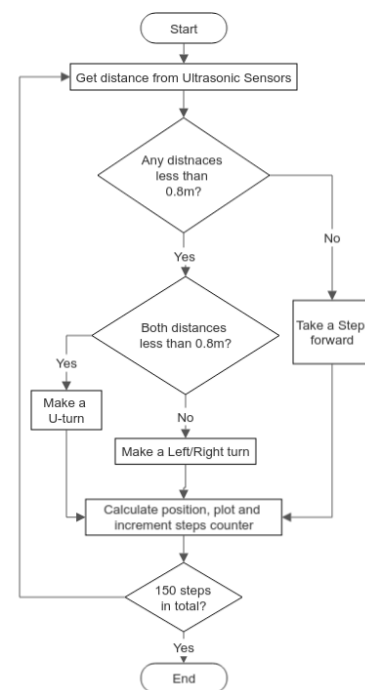


Fig. 1. Flow diagram of the autonomous navigation.

In order to locate the object, we assume that both sensors detect the same object at the same distance. In Figure 2, considering "O" as the object position, with respect to the center of the robot, L and R are the distance between the object and the robot detected by the sensors on either side and "D" is the distance between the object "O" and centre of the robot is given by (1):

$$\begin{aligned}
D_L &= \sqrt{L^2 - 0.0416^2} \\
D_R &= \sqrt{R^2 - 0.0416^2} \quad (1) \\
D &= \frac{D_L + D_R}{2}
\end{aligned}$$

where D_L , D_R the object's distance from the left and right sensor and D the object's distance from the robot.

The constant, 0.0416, in (1) is the distance (in meters) from the center of the robot to the center of the ultrasonic sensor on either side of the chest. In order to locate the object on the map, we need to consider the current position of the robot and its distance from the object. It should be noted that the robot is initially placed along the X-axis and Z-axis is on its left side whereas the Y-axis is perpendicular to the robot. In order to determine the position of the detected object, we use the distance calculated by both sensors and then add it to the existing position of the robot. The group (2) of equations provides the calculation details.

$$\begin{aligned}
OL_x &= R_x + D_L \cos(R_0) \\
OR_x &= R_x + D_R \cos(R_0) \\
OL_z &= R_z + D_L \sin(R_0) \\
OR_z &= R_z + D_R \sin(R_0) \quad (2) \\
O_x &= \text{Average}(OL_x + OR_x) \\
O_z &= \text{Average}(OL_z + OR_z)
\end{aligned}$$

where OL_x , OR_x the object's x coordinates with respect to sensors, OL_z , OR_z the object's z coordinates with respect to sensors, R_x , R_z , R_0 the robot's x , z coordinates, initially 0, and O_x and O_z the object's x , z coordinates.

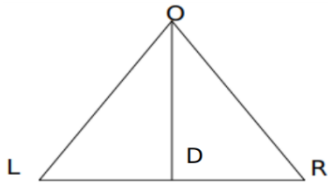


Fig. 2. Object localization using ultrasonic sensors.

The calculation is only made when the object is at a distance less than 0.8m. Objects beyond this range are ignored. For an object to be considered in the map, it must be detected by both sensors and ignored if detected by a single sensor. A nearby object is likely to be detected by both sensors.

In order to calculate the position of the object, we must know the current position of the robot. The robot's new x and z coordinates after making a motion, i.e. one step, left turn, right turn, or u-turn are given by:

$$R_x = (R_x) + S_s \cos(R_0 + \theta) \quad (3a)$$

$$R_z = (R_z) + S_s \sin(R_0 + \theta) \quad (3b)$$

where S_s is the step size of the robot and θ the current angle, +ve for left and -ve for right.

The position of a robot in its environment's Cartesian system is usually expressed in the position coordinates (x, y), and the orientation θ [14]. Initially, the robot's orientation and position in x and z (instead of y here) are 0. We conducted an experiment for calculating the step size and the angle of the robot when it walks straight or makes a turn as we observed deviation from the GPS position provided by the simulator and the actual location of the robot in the environment. We experimentally found the step size and effective angle of the ultrasonic sensors for the calculations in our algorithm.

IV. EXPERIMENTS AND RESULTS

In order to observe the robot's motion and behavior in the simulation, we controlled the robot manually by sending commands through a keyboard. First, we calculated the deviation in forwarding motion as mentioned in [10], hence, we designed an arena without boundary walls and obstacles, and allowed the robot to move straight forward on the x -axis only. After running the simulation for 150 steps, we observed that the robot did not follow the straight line but deviated from the desired path and the average deviation was 0.1856° per step. The deviation was calculated by taking the difference between the initial value of the inertial unit, yaw, and the final value. The deviation did not form a regular pattern but was random at every stage. One can get a different deviation value by running the simulation for more than 150 steps.

A. Step Size Experiment

The distance covered by the robot depends on the step size of the robot. We did an experiment to calculate the step size, which is mentioned in the reference manual as 0.088m. While performing the step size experiment, the initial coordinates were noted down, and then we sent the move forward command through the keyboard and noted down the final coordinates. The change in the distance gives us the step size of the robot and was found to be 0.086553m per step. The average of 150 steps was found to be 0.088m as claimed by the reference manual of the robot.

B. Rotation Angle Experiment

NAO robot can make a turn on either its left or right side depending upon the information received from the sensors. These turns are made using specific motion files designed by the developer in which the joints and their values, which are changed during the turn, are defined. In this experiment, we only considered 3 angles for the turns: 60° turn to the left side, 60° turn to the right side and 180° turn to the right side. The deviation in the 180° rotation was found to be 12° , which means the robot rotates by 192.56° rather than 180° while making a U-turn. For 60° rotation, the deviation was found to be 3° in both left and right turns. The rotation performed was at 57° rather than 60 degrees. The deviations can be observed in Figure 3. We tested the algorithm for autonomous navigation, localization and 2-D mapping in 3 different arenas. In the experiments, the robot position provided by the simulator GPS and the object position, set by the user, were considered ground truths. The graphs were plotted with calculated positions against the ground truths. The autonomous navigation was limited to 150 steps. The measurements on axes in all the Figures are given in meters.

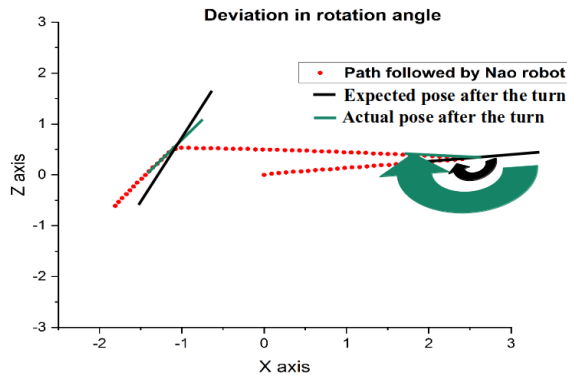


Fig. 3. Deviation in the angle while making turns.

C. Rectangular Arena

The rectangular arena was created with four walls, whereas the height of the walls was kept the same to that of the robot. The arena is 2.5m×2.5m area in size. The robot started from different points, i.e. the upper right corner, the lower left corner, and the center to observe if there were any changes. No significant change was observed in the results, thus we considered the center point as the starting point of the navigation. Figure 4 shows the simulated rectangular arena and the robot. The results of autonomous navigation and localization are plotted in Figure 5. The grey color shows the calculated path using the proposed algorithm and the red color path shows the simulator's GPS path followed by the robot. The green color represents the wall bounding the robot in the rectangular arena and the blue points on the map show the parts of the wall detected by the ultrasonic sensors of the robot as objects and plotted on the map with respect to the robot's position using the proposed algorithm. It is evident that the robot's position and orientation are very accurate while moving in a straight direction. However, a deviation can be seen after the robot is taking turns. This confirms the results shown in Figure 3. We found that the deviation varies in each turn. In order to remove this error, we calculated an average of the deviations of the turns the robot made during the 150 steps. The results improved after considering this offset in turns, as shown in Figure 6.



Fig. 4. The robot in the simulated rectangular arena.

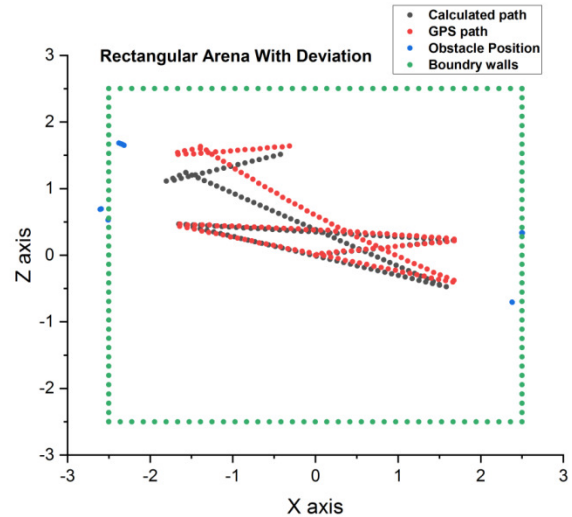


Fig. 5. Autonomous navigation in a rectangular arena.

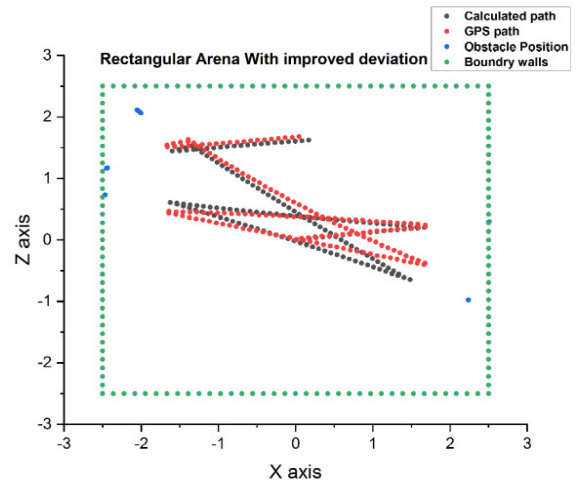


Fig. 6. Autonomous navigation after adding an offset.

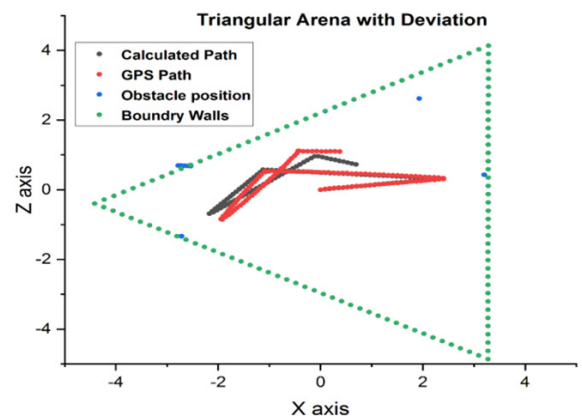


Fig. 7. Autonomous navigation in the triangular arena.

D. Triangular Arena

The experiment was repeated for the same number of steps in a triangular arena. The arena's area size was kept almost the same as that of the rectangular in the previous experiment.

Figure 7 shows the results obtained while navigating through the triangular arena. Figure 7 shows that the calculated path and GPS path of the robot has no change while moving in a straight direction. However, again, deviation occurred when the robot made turns.

E. Pentagon Arena

The arena of the third experiment was pentagon-shaped. In this arena, the robot was also allowed to autonomously navigate up to 150 steps in total. The results are shown in Figure 8.

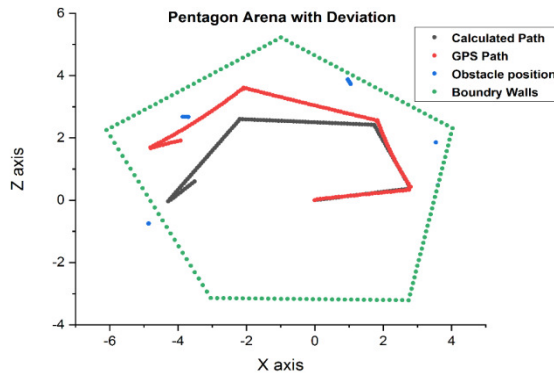


Fig. 8. Autonomous navigation in the pentagon arena.

Again, it is evident that the paths calculated through the algorithm and provided by the GPS are almost the same. However, deviation can again be observed after the robot takes a turn. The deviation kept increasing as the robot took more turns.

F. Adding a Kalman Filter

The Kalman Filter is a generic algorithm that is used to estimate a system variable while observing the measurement over time [15]. It is simple, consumes very small computational power, and is used with inaccurate or noisy measurements to estimate the state of that variable or another unobservable variable with greater accuracy. As the NAO robot moves, it encounters some deviations which do not form a regular pattern and hence in the long run will produce more deviations against the GPS values. We used a simple Kalman filter for one dimension which is very effective in computational cost and does not need any memory except the previous state.

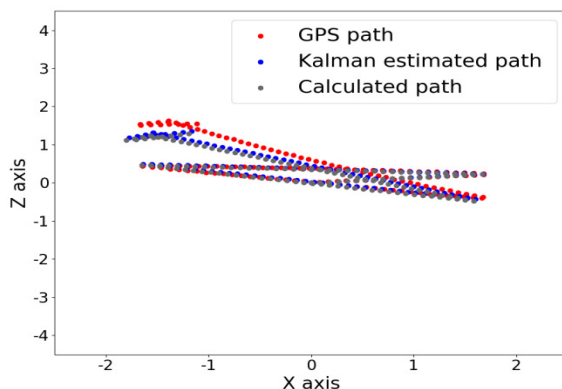


Fig. 9. Autonomous navigation using the Kalman filter.

The modified algorithm, with the Kalman filter, was tested in the rectangular arena. Figure 9 shows the results of this experiment. It is evident that the position calculation is not improved significantly after using the Kalman filter.

V. CONCLUSION

Using the Webots simulator, we designed a 2-D real-time mapping for a virtual NAO humanoid robot in different arenas using only ultrasonic sensors. All the graphs were plotted while the robot was navigating autonomously through the arena and were updated after each step. The results show that our algorithm is very simple in its calculations, yet it determines a more accurate position than the one provided by the GPS position of the simulator. Some deviation occurred in the position and orientation of the robot from the GPS values as the robot made turns. In Figure 3, we demonstrated that the robot is unable to make the turn at an exact angle and hence deviation is produced from the expected position.

The results demonstrate that the algorithm is able to localize the robot and obstacles in the environment while autonomously navigating through it. This localization is more accurate in the rectangular arena than in the triangular and pentagon arenas, maybe due to the acute angles and more angles in triangular and pentagon arenas respectively. However, further experiments may need to be conducted to build concrete reasoning.

We used the Kalman filter for one dimension variable to improve the results. However, it was evident that the filter did not significantly improve the results. The reason behind the negligible improvement from the Kalman filter is possibly the very small deviation in the calculated path compared to the simulator's GPS path. Furthermore, our experiment was limited to 150 steps. The filter may be effective for a higher number of steps. Anyhow, we do not consider the Kalman effective in our case.

Knowing the exact position of a robot, obstacles, computational cost, backup, and battery life are crucial for a robot to work in any environment. Hence we used only one sensor, the ultrasonic sensor, thus reducing computational cost and increasing battery life. This algorithm can also work as a backup if other sensors, such as the camera, fail. In the future, the work can be extended to improve the robot positioning further by improving the Kalman filter and its gain. Furthermore, the study will be extended to perform the experiments with real robots.

REFERENCES

- [1] K. P. Tee, R. Yan, Y. Chua, and Z. Huang, "Singularity-robust modular inverse kinematics for robotic gesture imitation," in *2010 IEEE International Conference on Robotics and Biomimetics*, Tianjin, China, Sep. 2010, pp. 920–925, <https://doi.org/10.1109/ROBIO.2010.5723449>.
- [2] A. Choudhury, H. Li, C. M. Greene, and S. Perumalla, "Humanoid Robot-Application and Influence," *Archives of Clinical and Biomedical Research*, vol. 2, no. 6, pp. 198–226, Dec. 2018, <https://doi.org/10.26502/acbr.50170059>.
- [3] N. L. A. Shaari, M. R. B. Razmi, M. F. Miskon, and I. S. M. Isa, "Parameter Study of Stable Walking Gaits for Nao Humanoid Robot," *International Journal of Research Engineering and Technology*, vol. 2, no. 9, pp. 16–23, Aug. 2013.

- [4] O. M. Mubarak, "The Effect of Carrier Phase on GPS Multipath Tracking Error," *Engineering, Technology & Applied Science Research*, vol. 10, no. 5, pp. 6237–6241, Oct. 2020, <https://doi.org/10.48084/etasr.3578>.
- [5] "NAO the humanoid and programmable robot," *SoftBank Robotics*. <https://www.softbankrobotics.com/emea/en/nao>.
- [6] "Webots: robot simulator," *Cyberbotics*. <https://cyberbotics.com/>.
- [7] "Cartesian control — Aldebaran 2.1.4.13 documentation," *Aldebaran*. <http://doc.aldebaran.com/2-1/naoqi/motion/control-cartesian.html>.
- [8] "Sonars — NAO Software 1.14.5 documentation," *Aldebaran*. http://doc.aldebaran.com/1-14/family/robots/sonar_robot.html.
- [9] Š. Fojtů, M. Havlena, and T. Pajdla, "Nao Robot Localization and Navigation Using Fusion of Odometry and Visual Sensor Data," in *Intelligent Robotics and Applications*, Montreal, Canada, Oct. 2012, pp. 427–438, https://doi.org/10.1007/978-3-642-33515-0_43.
- [10] C. Wei, J. Xu, C. Wang, P. Wiggers, and K. Hindriks, "An Approach to Navigation for the Humanoid Robot Nao in Domestic Environments," in *Towards Autonomous Robotic Systems*, Oxford, UK, Aug. 2014, pp. 298–310, https://doi.org/10.1007/978-3-662-43645-5_33.
- [11] O. Melinte, L. Vladareanu, and I.-A. Gal, "NAO robot fuzzy obstacle avoidance in virtual environment," *Periodicals of Engineering and Natural Sciences (PEN)*, vol. 7, no. 1, pp. 318–323, Apr. 2019, <https://doi.org/10.21533/pen.v7i1.359>.
- [12] B. Kasmi and A. Hassam, "Comparative Study between Fuzzy Logic and Interval Type-2 Fuzzy Logic Controllers for the Trajectory Planning of a Mobile Robot," *Engineering, Technology & Applied Science Research*, vol. 11, no. 2, pp. 7011–7017, Apr. 2021, <https://doi.org/10.48084/etasr.4031>.
- [13] S. Joshi and S. Talole, "An overview of energy systems in humanoid robots (Journal of Microelectronics and Solid State Devices)," *Journal of Microelectronics and Solid State Devices*, vol. 7, no. 3, pp. 12–19, 2020.
- [14] H. Medjoubi, A. Yassine, and H. Abdelouahab, "Design and Study of an Adaptive Fuzzy Logic-Based Controller for Wheeled Mobile Robots Implemented in the Leader-Follower Formation Approach," *Engineering, Technology & Applied Science Research*, vol. 11, no. 2, pp. 6935–6942, Apr. 2021, <https://doi.org/10.48084/etasr.3950>.
- [15] J. Humpherys, P. Redd, and J. West, "A Fresh Look at the Kalman Filter," *SIAM Review*, vol. 54, no. 4, pp. 801–823, Jan. 2012, <https://doi.org/10.1137/100799666>.

Statistical Modeling for Traffic Noise: The Case of Kirkuk City

Sundus Shakor Ali

Department of Civil Engineering
College of Engineering
University of Baghdad
Baghdad, Iraq

s.albayati1901m@coeng.uobaghdad.edu.iq

Amjad Hamad Khalil Albayati

Department of Civil Engineering
College of Engineering
University of Baghdad
Baghdad, Iraq

a.khalil@uobaghdad.edu.iq

Received: 2 July 2022 | Revised: 6 July 2022 | Accepted: 20 July 2022

Abstract—The auditory system can suffer from exposure to loud noise and human health can be affected. Traffic noise is a primary contributor to noise pollution. To measure the noise levels, 3 variables were examined at 25 locations. It was found that the main factors that determine the increase in noise level are traffic volume, vehicle speed, and road functional class. The data have been taken during three different periods per day so that they represent and cover the traffic noise of the city during heavy traffic flow conditions. Analysis of traffic noise prediction was conducted using a simple linear regression model to accurately predict the equivalent continuous sound level. The difference between the predicted and the measured noise shows that the model's accuracy is 93.93%. The results show the effectiveness of the suggested method and confirm its applicability in developing mitigation plans for both existing and future roadways. To test the effectiveness of the suggested method, the selected location of different road functional classifications of Kirkuk city in Iraq was studied. It was noticed that in all the selected sites, the noise level was observed to be above the permissible noise standard of the World Health Organization (WHO).

Keywords—noise level; traffic noise; road functionality; traffic volume; speed

I. INTRODUCTION

Noise is not only hard on our senses [1], our physical and emotional well-being also are also negatively affected [2]. Exposure to high noise levels, i.e. over 85dBA, for 8 hours or longer may be dangerous [3]. Expansion of cities, industries, and facilities put people's health at risk [4]. Generally, noise has significant effects on human health [5]. Table I shows the recommended noise level standards for several countries and the World Health Organization (WHO) [6]. Noise levels in Kirkuk city have been reported to be high, therefore, the situation requires evaluation. Vehicles are the main source of noise pollution [7]. For reducing the noise pollution caused by transportation in cities, it is necessary to predict traffic noise [8-10]. Research has been conducted to develop a traffic noise model for Surat's main arterial road in India and different variables affecting traffic noise were analyzed in [11]. The survey involved 3 arterial roads based on mixed traffic patterns

and a variety of land use patterns. The parameters were measured during peak hours. Multiple linear regression analysis was utilized and the model showed that the variables had a good relationship to the noise. A comprehensive noise prediction model was developed for 8 significant highways in the Indian states of Telangana and Andhra Pradesh in [8]. Each highway was measured for 7h each day. The variables include carriage width, traffic volume, and speed. The 15min interval model produced a negative relation against the 1h interval model. A traffic noise model was developed to measure the noise level of collector roads in Denpasar City, Indonesia in [13]. Measurements were conducted from 6:00 a.m. to 6:00 p.m. and 48 sets of data in total were obtained in 15min intervals. It was shown that if all the other variables remain constant, an increase of 100 motorcycles increases traffic noise by approximately 3dBA. In [14], the noise level was measured on the Asian Highway at the Golestan National Park, Iran. For the analysis of independent variables and noise, 76 sampling locations were selected between 0 and 250m from the road. At each sampling station, monitoring was done for one week with 15min periods between 8:00 a.m. and 8:00 p.m. while SPSS software was used for modeling. A model was developed in [15] to forecast traffic noise on the roadways of the Iranian city Ahvaz. On 7 roads of the city, 1344 observations were performed at 12 stations. During the model development, out of 15 variables, just 9 independent variables were used.

TABLE I. NOISE LEVEL STANDARDS

Noise level standard	Noise level (dBA)	
	Day time	Night time
WHO	55	45
Australia	45	35
Germany	45	35
Korea	50	45
Japan	45	35
India	55	45
Philippines	50	45

II. MATERIALS AND METHODS

To measure traffic noise in Kirkuk, 3 features were selected, road functionality, traffic volume, and speed, and their

Corresponding author: Amjad Hamad Khalil Albayati

impact on traffic noise was investigated. To measure the noise levels, the 3 variables were examined at 25 locations. At each road, functional classification, traffic volume, and speed survey were conducted and recorded at 15min intervals. Figure 1 displays the process for the suggested model starting with data collection using a sound level meter, variable selection analysis, model development, evaluation, and analysis of the findings. The obtained data include 3 variables: F (functional classification of the road), Q (traffic volume), and V (average speed of vehicles). Statistical analysis was designed to construct a noise level estimation model to highlight the effect of each variable on the noise level.

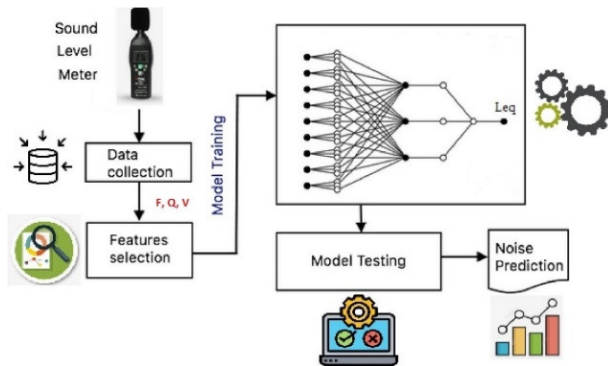


Fig. 1. Pipeline of the proposed model.

III. TRAFFIC NOISE DATA

The sound level meter (Figure 2) was used to measure the sound levels during peak hours. The average of maximum and minimum noise levels was calculated and plotted in a normal graph with respect to time. A tripod supported the device at 1m height and kept it at 6.5m away from the middle lane of the road as depicted in Figure 3.



Fig. 2. The sound level meter.

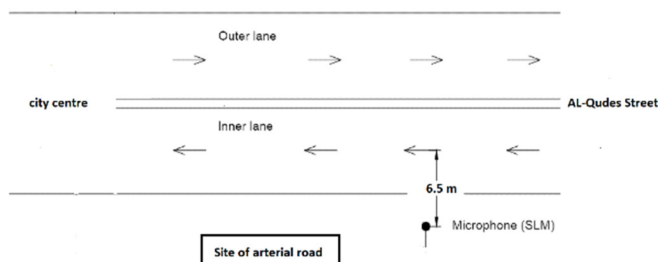


Fig. 3. A schematic diagram of the monitored site.

IV. SITE SELECTION

Kirkuk, located in the north of Iraq, was selected as a typical representative modern city to carry out the study on the aspect of traffic noise. Kirkuk witnessed extensive urban development over the past decades to become a node for commercial activity characterized by modern and beautiful buildings and modern sites. Traffic noise measurements were conducted at 25 locations on the main streets of Kirkuk, representing the classes of roads and zone types as shown in Figure 4. The data have been taken during 3 different periods of the day so that they may represent and cover the traffic noise of the city during heavy traffic flow conditions. The periods were: 8:00 a.m. to 9:00 a.m. (supposed to be the peak traffic hour density of the day), 1:00 p.m. to 2:00 p.m. (supposed to be the end of the governmental staff working hour), and 6:00 p.m. to 7:00 p.m. (time of the evening marketing). Measurements of the traffic count and speed were not taken during holidays [16, 17].

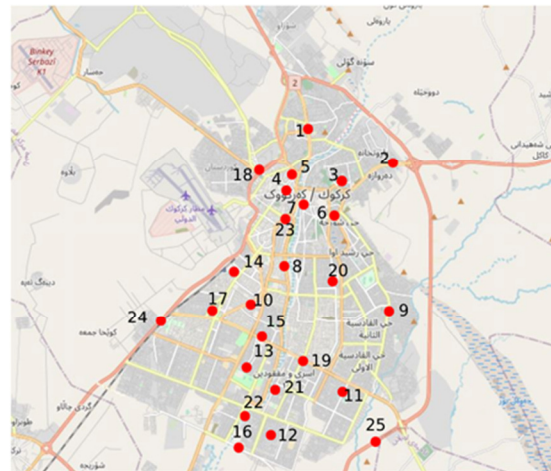


Fig. 4. Locations of data collection sites on Kirkuk city.

V. ROAD FUNCTIONAL CLASSIFICATION (F)

The road functional classification of a city is a channel for communication between the city's various parts and with nearby cities and urban areas. Factors like traffic volume and average speed are related to functionality. Therefore, functionality is associated with traffic noise [18]. The functionality variable was applied and 4 types of roads were considered according to their functionality: highway, arterial, collector, and local road. The highways and arterial roads recorded the highest noise level measurements since they are characterized by very congested traffic volumes and faster speeds.

VI. TRAFFIC VOLUME (Q)

The vehicles were counted within each time span of sound level measurement during observation. The traffic count was conducted manually by using a video camera [19] or by utilizing sensors on roads [20].

VII. VEHICLE SPEED (V)

It is the average measured speed of the cars. Vehicle speed can be manually measured by estimating the travel distance of

a car per second or by a velocity speed gun [21]. Bushnell 101911 (Figure 5) was used to detect the spot speed of passing vehicles. The gun was directed at the passing vehicle. The gun was designed to measure the speed in km/h. It delivers signals to moving objects and can detect any object running faster than 20km/h.



Fig. 5. The Bushnell speed gun.

VIII. NOISE LEVEL DESCRIPTOR (Leq)

The traffic noise statistical descriptors used in this study is the equivalent continuous sound level. Leq is often used in noise measurements [22]. The dBA is the most often used unit for sound measurement. Table II lists the independent variables (F, Q, and V) as well as the measured dependent variable (Leq) in relation to the sample values.

TABLE II. DATASET SAMPLE VALUES

F	Q	V	Leq
Highway (Erbil principal)	1424	80	78.19
Arterial (King Qazi street)	1309	63	78.86
Collector (University street)	895	53	76.52
Local (Iskan street)	122	31	68.27

IX. RESULTS AND DISCUSSION

As the road type is considered one of the primary noise sources, each road was statistically analyzed for noise response. The analysis revealed that the noise is very dependent on the functional classification of the road, especially the highway and arterial class, since they are designed to accommodate high speeds and are utilized in large-scale movements. There is a relationship between traffic volume and noise [23]. The noise level is more dependent on traffic volume followed by the road functional class. The study investigated the characteristics of traffic noise and found that traffic noise is closely related to traffic volume. The distribution of traffic noise in different regions is determined by the kinds of vehicles in the area and the density of a road network [24].

The speed variable also affects noise levels [25]. Reducing speed could decrease noise, moreover, noise reduction is achievable by traffic calming policies because it prevents forceful accelerations [26]. Both these claims are accurate in terms of producing sound pressure levels that the vehicles moving at a slower speed would produce less noise. Figures 6-9 show the relationship between each variable and the noise level (the plotted points refer to the average value of multiple readings).

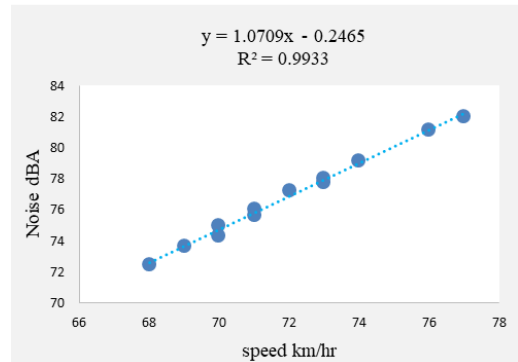
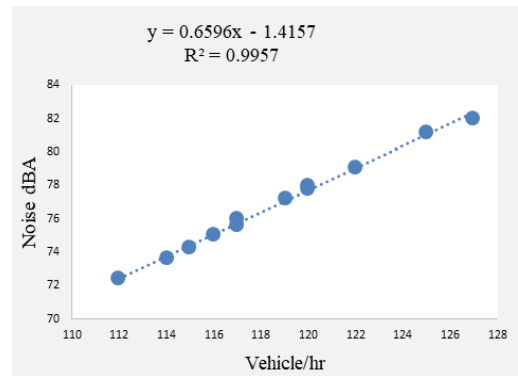


Fig. 6. Noise of the principal road (Erbil highway).

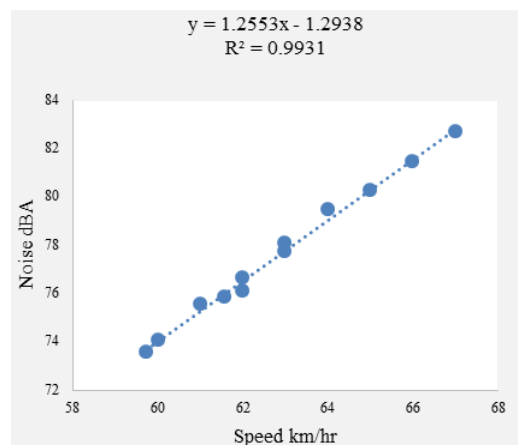
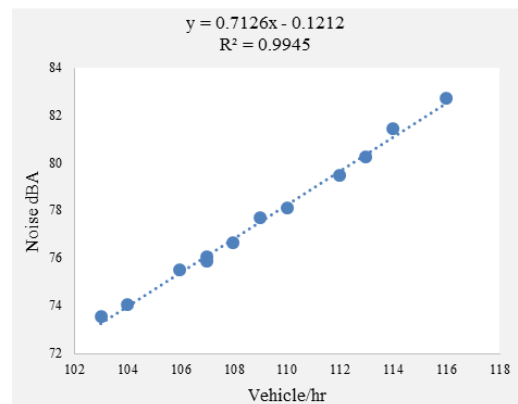


Fig. 7. Noise of the arterial road (King Qazi street).

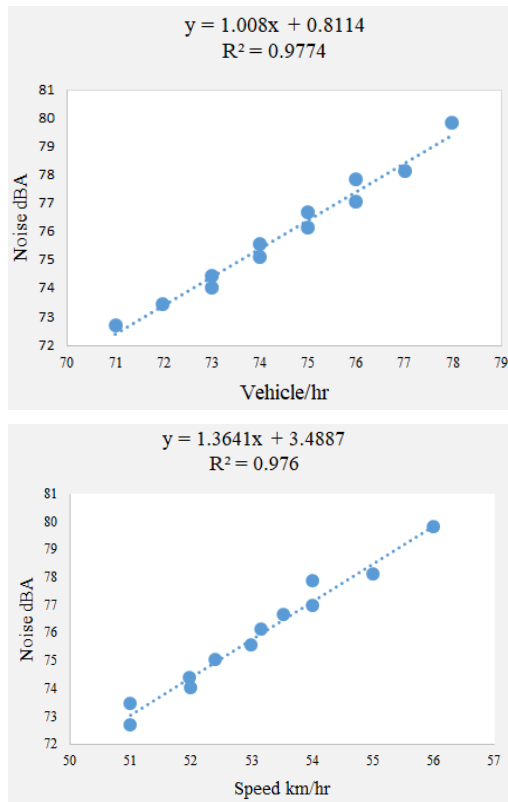


Fig. 8. Noise of the collector road (University street).

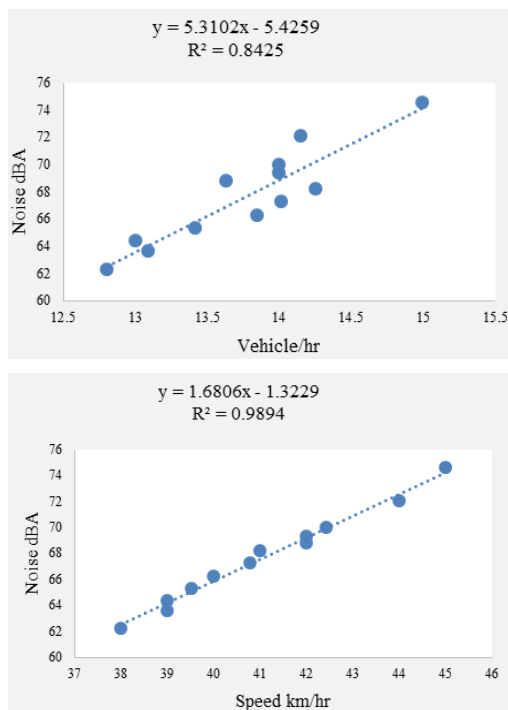


Fig. 9. Noise of the local road (Iskan street).

A statistical model was constructed to fit these parameters and connect them to the noise level. Simple linear regression

was used for formulating the model (using Minitab 21) and the output is the following model:

$$\text{Noise (dBA)} = 43.34 + 0.282 V + 0.000690 Q + 3.87 F \quad (1)$$

The noise level was reasonably predicted by the model, as shown in Figure 11. The model's effectiveness can be seen in the difference between the predicted and the measured noise. Plotting was done for the additional statistical indicators which show very good potential for prediction as depicted in Figure 12. It demonstrates the reliability of the predicted noise level within a given range. The accuracy of the model is important because it can then be used to plan noise abatement measures. The current study can be further expanded by adding additional features to these 3 variables.

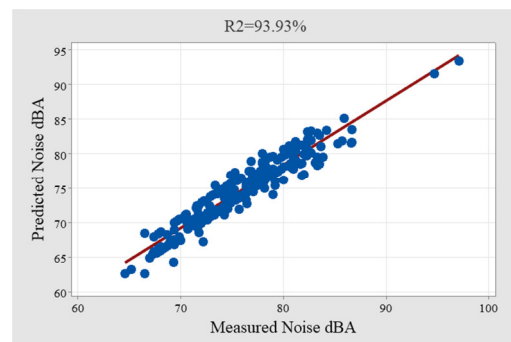


Fig. 10. Scatter of Leq dBA (measured vs predicted).

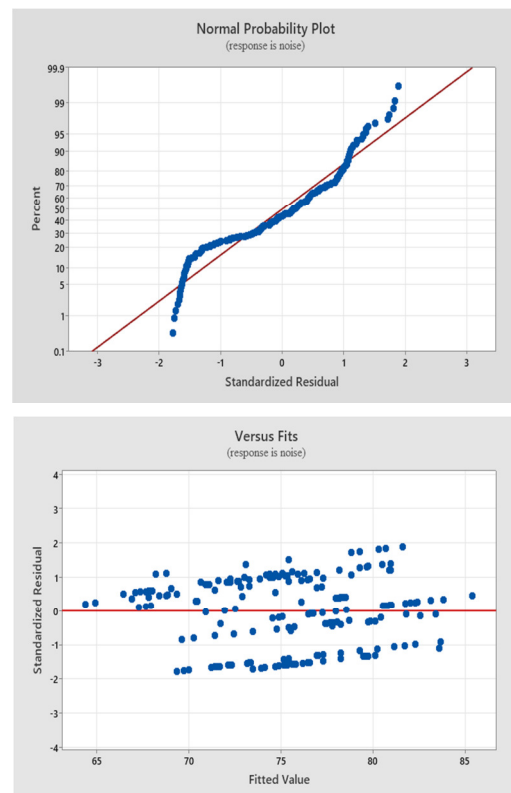


Fig. 11. Statistical indicators of the model.

X. CONCLUSION

Analysis of traffic noise prediction is carried out in the present work using a simple linear regression model to precisely predict the equivalent continuous sound level. The suggested method predicts the Leq dBA at various locations of Kirkuk city using 3 independent variables: road functionality, traffic volume, and average vehicle speed as essential features that affect the level of noise. It was confirmed that these variables are the main factors that influence the increase in noise level. The traffic noise can be predicted by using the formulated model with the aid of the suggested methods without using sound level devices. The output Leq value can be estimated with perfect accuracy by using the values of input variables. The model has predicted the level of noise with high accuracy (93.93%). This scenario implies an exact prediction that ranges within the bounds of the actual values. Measurements of traffic noise levels generally show levels above 70dBA at collector, arterial, and highway roads. These levels are generally higher than the accepted standard criteria of WHO. Moreover, Leq in the local streets of Kirkuk exceeded the limit recommended by the WHO for residential areas, except in relatively quiet locations during the off-peak hours.

REFERENCES

- [1] A. A. Faisal, L. P. J. Selen, and D. M. Wolpert, "Noise in the nervous system," *Nature Reviews Neuroscience*, vol. 9, no. 4, pp. 292–303, Apr. 2008, <https://doi.org/10.1038/nrn2258>.
- [2] M. M. Anees, M. Qasim, and A. Bashir, "Physiological and Physical Impact of Noise Pollution on Environment," *Earth Sciences Pakistan*, vol. 1, no. 1, pp. 8–10, 2017.
- [3] WHO, *United Nations road safety collaboration : a handbook of partner profiles*. Geneva, Switzerland: World Health Organization, 2005.
- [4] A. Debnath, P. K. Singh, and S. Banerjee, "Vehicular traffic noise modelling of urban area—a contouring and artificial neural network based approach," *Environmental Science and Pollution Research*, vol. 29, no. 26, pp. 39948–39972, Jun. 2022, <https://doi.org/10.1007/s11356-021-17577-1>.
- [5] A. Muzet, "Environmental noise, sleep and health," *Sleep Medicine Reviews*, vol. 11, no. 2, pp. 135–142, Apr. 2007, <https://doi.org/10.1016/j.smrv.2006.09.001>.
- [6] P. Kogan, J. P. Arenas, F. Bermejo, M. Hinalaf, and B. Turra, "A Green Soundscape Index (GSI): The potential of assessing the perceived balance between natural sound and traffic noise," *Science of The Total Environment*, vol. 642, pp. 463–472, Nov. 2018, <https://doi.org/10.1016/j.scitotenv.2018.06.023>.
- [7] S. M. Ali, A. R. Hama, and Y. M. Ali, "A study of Land Zoning in the base of Traffic Noise Pollution Levels using ArcGIS: Kirkuk City as a Case Study," *Al-Khwarizmi Engineering Journal*, vol. 13, no. 4, pp. 137–151, 2017, <https://doi.org/10.22153/kej.2017.06.002>.
- [8] N. Garg and S. Maji, "A critical review of principal traffic noise models: Strategies and implications," *Environmental Impact Assessment Review*, vol. 46, pp. 68–81, Apr. 2014, <https://doi.org/10.1016/j.eiar.2014.02.001>.
- [9] S. Kephelopoulou, M. Paviotti, F. Anfosso-Ledee, D. Van Maercke, S. Shilton, and N. Jones, "Advances in the development of common noise assessment methods in Europe: The CNOSSOS-EU framework for strategic environmental noise mapping," *Science of The Total Environment*, vol. 482–483, pp. 400–410, Jun. 2014, <https://doi.org/10.1016/j.scitotenv.2014.02.031>.
- [10] G. Dutilleul, J. Defrance, B. Gauvreau, and F. Besnard, "The revision of the French method for road traffic noise prediction," *The Journal of the Acoustical Society of America*, vol. 123, no. 5, May 2008, Art. no. 3150, <https://doi.org/10.1121/1.2933163>.
- [11] B. N. Tandel and J. Macwan, "Assessment and MLR modelling of urban traffic noise at major arterial roads of Surat, India," *Journal of Environmental Research And Development*, vol. 7, no. 4A, pp. 1–7, 2013.
- [12] A. Kamineni, S. K. Duda, V. Chowdary, and C. S. R. K. Prasad, "Modelling of Noise Pollution Due to Heterogeneous Highway Traffic in India," *Transport and Telecommunication*, vol. 20, no. 1, pp. 22–39, Feb. 2019, <https://doi.org/10.2478/tjt-2019-0003>.
- [13] P. A. Suthanaya, "Modelling Road Traffic Noise for Collector Road (Case Study of Denpasar City)," *Procedia Engineering*, vol. 125, pp. 467–473, Jan. 2015, <https://doi.org/10.1016/j.proeng.2015.11.125>.
- [14] S. Gharibi, M. Aliakbari, A. Salamanmahiny, and H. Varastehe, "Evaluation and Modelling of Traffic Noise on the Asian Highway in Golestan National Park, Iran," in *5th International Conference on Transportation and Traffic Engineering*, Lucerne, Switzerland, Jul. 2016, vol. 81, <https://doi.org/10.1051/mateconf/20168104008>.
- [15] E. M. R. Monazzam, M. S. Sekhavatjou, and Z. A. Chabi, "Designing a traffic noise prediction model for highways in iranian megacities [case study: Ahvaz City]," *International Journal of Environmental Research*, vol. 8, no. 2, pp. 427–434, 2014.
- [16] N. Hazim, L. Shbeeb, and Z. A. Salem, "Impact of Roadside Fixed Objects in Traffic Conditions," *Engineering, Technology & Applied Science Research*, vol. 10, no. 2, pp. 5428–5433, Apr. 2020, <https://doi.org/10.48084/etasr.3226>.
- [17] H. H. Mohammed and M. Q. Ismail, "Efficiency Assessment of a Signalized Roundabout and a Traffic Intersection in Baghdad City," *Engineering, Technology & Applied Science Research*, vol. 11, no. 6, pp. 7910–7916, Dec. 2021, <https://doi.org/10.48084/etasr.4564>.
- [18] G. R. Gozalo, J. M. B. Morillas, and V. G. Escobar, "Urban streets functionality as a tool for urban pollution management," *Science of The Total Environment*, vol. 461–462, pp. 453–461, Sep. 2013, <https://doi.org/10.1016/j.scitotenv.2013.05.017>.
- [19] D. Singh, R. Upadhyay, H. S. Pannu, and D. Leray, "Development of an adaptive neuro fuzzy inference system based vehicular traffic noise prediction model," *Journal of Ambient Intelligence and Humanized Computing*, vol. 12, no. 2, pp. 2685–2701, Feb. 2021, <https://doi.org/10.1007/s12652-020-02431-y>.
- [20] Z. Dai *et al.*, "Traffic parameter estimation and control system based on machine vision," *Journal of Ambient Intelligence and Humanized Computing*, May 2020, <https://doi.org/10.1007/s12652-020-02052-5>.
- [21] M. Alhamdany and A. H. K. Albayati, "Statistical Modeling of Time Headway on Urban Roads: A Case Study in Baghdad," *Engineering, Technology & Applied Science Research*, vol. 12, no. 3, pp. 8584–8591, Jun. 2022, <https://doi.org/10.48084/etasr.4878>.
- [22] "ANSI/ASA S12.9-2005/Part 4 (R2015) - Quantities and Procedures for Description and Measurement of Environmental Sound - Part 4: Noise Assessment and Prediction of Long-term Community Response." <https://webstore.ansi.org/Standards/ASA/ANSIASAS122005PartR2015>.
- [23] B. Wang and J. Kang, "Effects of urban morphology on the traffic noise distribution through noise mapping: A comparative study between UK and China," *Applied Acoustics*, vol. 72, no. 8, pp. 556–568, Jul. 2011, <https://doi.org/10.1016/j.apacoust.2011.01.011>.
- [24] E. M. Salomons and M. Berghauser Pont, "Urban traffic noise and the relation to urban density, form, and traffic elasticity," *Landscape and Urban Planning*, vol. 108, no. 1, pp. 2–16, Oct. 2012, <https://doi.org/10.1016/j.landurbplan.2012.06.017>.
- [25] H. M. Al-Mosawe, D. Alobaydi, and A. Albayati, "Development of Traffic Noise Prediction Model in an Educational Urban Area," *Civil Engineering Journal*, vol. 4, no. 11, pp. 2588–2595, Nov. 2018, <https://doi.org/10.28991/cej-03091183>.
- [26] H. Ryu, I. K. Park, B. S. Chun, and S. I. Chang, "Spatial statistical analysis of the effects of urban form indicators on road-traffic noise exposure of a city in South Korea," *Applied Acoustics*, vol. 115, pp. 93–100, Jan. 2017, <https://doi.org/10.1016/j.apacoust.2016.08.025>.

A Parametric Study of Fire-Damaged Reinforced Concrete Columns under Lateral Loads

Mohamed Baghdadi

LGC-ROI, Department of Civil Engineering
Faculty of Technology
University of Batna 2
Batna, Algeria
m.baghdadi@univ-batna2.dz

Mohamed S. Dimia

LGC-ROI, Department of Civil Engineering
Faculty of Technology
University of Batna 2
Batna, Algeria
ms.dimia@univ-batna2.dz

Djassem Baghdadi

Laboratory of Research in Civil Engineering
University of Mohamed Khider
Biskra, Algeria
djassem.baghdadi@univ-biskra.dz

Received: 2 July 2022 | Revised: 17 July 2022 | Accepted: 21 July 2022

Abstract-Columns are the structural members of buildings that ensure structural stability. A fire can severely affect the columns' structural performance by degrading the properties of their constituent materials, thereby reducing the strength capacity, stiffness, and stability. In seismic zones, the knowledge of the post-fire behavior of these elements is a fundamental requirement for a realistic seismic performance assessment. This study utilized numerical analysis using the parametric fire model of Eurocode-1 to estimate the post-fire axial and lateral performance of reinforced concrete columns. In the first step, the axial load-bearing capacity was evaluated from a parametric study for cantilever columns. In the second step, the lateral load capacity, force-displacement behavior, stiffness, ductility, energy dissipation capacity, and residual displacements were estimated to determine the impact of fire damage on the behavior of columns under lateral loads. The results showed that both the lateral load capacity and the ductility of the reinforced concrete columns decreased significantly due to fire exposure. This also indicated that fire damage decreases the vertical load-bearing capacity, and the reduction in lateral capacity was attributed to the loss of concrete's compressive strength. The column characteristics that significantly influence the residual response behavior were identified as section size, column height, axial load ratio, and concrete's compressive strength.

Keywords-natural fire; columns; post-fire behavior; fire damage; residual strength; lateral load capacity

I. INTRODUCTION

Fires and earthquakes are among the most severe conditions buildings may face. In the case of fire, the structural and nonstructural elements may undergo different changes depending on the intensity and exposure duration. The fire safety of Reinforced Concrete (RC) structures highly depends

on their fire resistance, which relies on the thermal conductivity and the resistance of load-bearing elements such as walls, columns, and beams. Fire damage leads to a decrease in the strength and deformation properties of structures. A Post-Fire Earthquake (PFE) is an eventual disaster, but its damage to RC members is complicated and usually affected by uncertain factors. The reinforced concrete structure can remain standing after a fire, or after an earthquake. The full or partial collapse of concrete buildings during a fire is rare, however, earthquakes following a fire can cause significant damage depending on the residual properties of the structural elements. In post-fire performance assessment, it should be decided whether to repair and strengthen or demolish and rebuild the entire structure, taking into account the earthquake loads during its remaining service life.

The behavior of a structure after a fire is related to its residual bearing capacity, so it is necessary to determine, quantify, and compare it with the safety levels. The study of the impact of earthquakes on structures damaged by real fires is a fundamental issue in assessing concrete's structural behavior in severe load combinations. Although the sequential application of these extreme loads may be too severe in most cases, this strategy may be appropriate for the design of important structures, where cost and technology are no barrier. However, current regulations do not consider fire and earthquake hazards [1]. Several studies investigated the influence of fire on the mechanical strength of RC members and structures [2-4]. Post-fire material tests showed that concrete's mechanical properties degrade after fire exposure and do not fully recover after cooling [5-7]. Different models were proposed in [8, 9] on the post-fire full stress-strain response of fire-damaged concrete and the residual stress-strain relationship after exposure to high

temperatures. Numerical investigations in [10, 11] evaluated the impact of fire duration and intensity on the residual load-bearing capacity and delayed failure of reinforced concrete columns. Experimental research and test results on the post-fire behavior of RC columns were presented in [12, 13]. A new modified finite element model was developed in [14] to predict the behavior and strength of concrete-filled steel tubular subjected to axial compression, considering the influence of some determinant parameters. A numerical study examined the fire behavior of thermally insulated strengthened RC beams subjected to fire exposure in [15]. The effect of fire on the flexural behavior of RC beams was studied in [16, 17].

An experimental study on the seismic behavior of high-performance concrete frames after a fire was presented in [18], showing that fire exposure can transform the failure mode of a frame subjected to reverse-cyclic loads from strong-column-weak-beam to strong-beam-weak-column with poor cyclic performance. Another study was conducted in [19] on the seismic performance of reinforced concrete beam-column joints after a fire and their practical strengthening. The performance of RC frame structures in post-earthquake fire loading and their failure times were analyzed in [20, 21]. In [22, 23], the seismic performance of RC short columns with light transverse reinforcement and RC beam-column joints under varying axial forces was investigated. Several studies on fire resistance and post-fire seismic behavior of concrete shear walls were carried out experimentally and numerically [24-27].

A limited number of studies attempted to estimate the post-fire lateral capacity performance of concrete columns. Although the behavior of reinforced concrete columns at elevated temperatures has been extensively investigated under service loads after cooling, studies on post-fire seismic behavior of RC structural elements are extremely rare. The results of [28, 29] evaluated the post-fire seismic performance of reinforced precast concrete columns damaged by fire to determine the impact of fire damage on force-displacement behavior, moment-curvature relationship, and residual displacements. An experimental study investigated the seismic performance of shear critical post-heated RC columns that had been repaired [30]. In [31], the results of a study on the seismic resistance of strengthened concrete members after fire exposure were presented. Furthermore, a numerical investigation of the response simulation of RC columns under lateral loads was conducted in [32]. In [33], the residual strength and lateral/seismic load capacity of RC columns after fire exposure were evaluated using numerical analysis.

This paper presents a numerical analysis that investigates the behavior of RC columns damaged by fire under vertical load and evaluate the lateral bearing capacity under horizontal loads, including a parametric study to identify the influential column characteristics. This study employed the structural analysis software SAFIR [34], which is capable of 3D simulation of building structures in fire. The parametric natural fire curves of Eurocode-1 were selected to perform the simulations.

II. EVALUATION OF VERTICAL RESIDUAL LOAD-BEARING CAPACITY OF COLUMNS

Each column was first subjected to constant loading, and then a section of the column was exposed to natural fire to assess its residual characteristics. Loading was applied in successive simulations in a decreasing and monotonous manner, and the time of the collapse was calculated for each loading level. The corresponding loading level represents the load-bearing capacity of the column to resist natural fire, including the heating and cooling phases.

A. Time-Temperature Curves Used

The fire curves were taken from the parametric fire model of Annex (A) of EN 1991-1-2(2002) [35] that represents the action of a natural fire, including the cooling phase. Figure 1 shows the various used fire curves, differing by the duration of the heating phase of 15, 30, 60, 90, and 120 minutes.

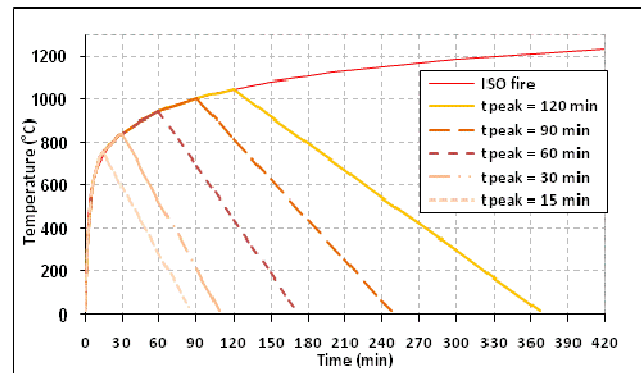


Fig. 1. Time-temperature curves.

B. Parametric Studies

The following parameters were considered to evaluate the total residual capacity:

- The section size of the column: 20×20cm, 30cm×30cm, 40×40cm, 60×60cm, and 80×80cm.
- The duration of the heating phase of the fire (t_{peak}): 15, 30, 60, 90, and 120 minutes to assess the influence of the maximum temperature on the residual characteristics.
- The height of the column: 3, 4, and 5m.
- The columns were cantilever, fixed in rotation at the bottom and free at the top.

C. Results and Discussions

1) Influence of the Effective Height of the Column

Table I shows the results for columns, considering their height, before and after fire exposure. A 30×30cm section was chosen to perform the simulations. For the same height, the influence of the maximum temperature during fire was considerable: a loss of 70% of vertical capacity (N_r) was found for the fire of $t_{peak}=60$ min for 3m columns. Considering the variation in column height for the same fire, the residual vertical capacity (N_r) of the 3m column was found to be greater than the 5m column's (about 90%).

TABLE I. VERTICAL LOAD BEARING CAPACITY BEFORE ($N_{20^\circ\text{C}}$) AND AFTER FIRE EXPOSURE (N_r) FOR COLUMNS

Height (m)	Before fire $N_{20^\circ\text{C}}$ (kN)	N_r (kN) after exposure				
		Fire of $t_{\text{peak}}=15\text{min}$	Fire of $t_{\text{peak}}=30\text{min}$	Fire of $t_{\text{peak}}=60\text{min}$	Fire of $t_{\text{peak}}=90\text{min}$	Fire of $t_{\text{peak}}=120\text{min}$
3	1978	798	669	589.5	559.5	540
4	1446	589.5	498	441	420	406.5
5	972	396	339	304.5	292.5	283.5

2) Influence of Section Size

Table II presents the results of different-sized sections having the same height (4m). For the 40×40cm section, a loss of 75% was found for a 60min fire and a loss of 85% was found for the section of 80×80cm. The maximum temperature during fire exposure and cooling time was among the most

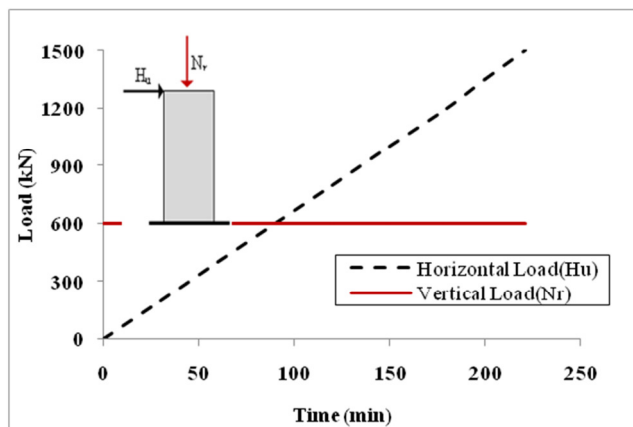
important parameters responsible for the degree of concrete damage. The greater the section size, the higher the temperature gradient during the cooling phase and therefore, the higher damage induced in the concrete. With natural cooling, the interior temperature gradient within the concrete can be higher than during the heating phase.

TABLE II. VERTICAL LOAD BEARING CAPACITY BEFORE ($N_{20^\circ\text{C}}$) AND AFTER FIRE EXPOSURE (N_r) OF SECTIONS

Section	Before fire $N_{20^\circ\text{C}}$ (kN)	N_r (kN) after exposure				
		Fire of $t_{\text{peak}}=15\text{min}$	Fire of $t_{\text{peak}}=30\text{min}$	Fire of $t_{\text{peak}}=60\text{min}$	Fire of $t_{\text{peak}}=90\text{min}$	Fire of $t_{\text{peak}}=120\text{min}$
sec20×20cm	295.5	123	108	99	96	93
sec30×30cm	1446	589.5	498	441	420	406.5
sec40×40cm	1725	652.5	537	466.5	439.5	421.5
sec60×60cm	8988	2847	2185.5	1776	1621.5	1521
sec80×80cm	16410	4689	3433.50	2658	2365.50	2175

III. LATERAL LOAD CAPACITY EVALUATION OF FIRE-DAMAGED RC COLUMNS

The horizontal load capacity was also evaluated to examine the column's behavior under combined vertical and horizontal loads, which is a real situation that a column must survive in frame structures. The lateral load was assumed to be a seismic load. This process utilized a numerical SAFIR model in a cold situation to investigate the lateral load response of the columns. The axial load was 25% and 50% of the residual vertical capacity N_r and was held constant throughout the analysis. The lateral load was applied horizontally at the top of the columns in displacement-controlled mode and incremented from zero up to the column failure, as shown in Figure 2. It was possible to estimate the maximum horizontal load H_u that the column can support. The horizontal load H_u represents the shear force that an earthquake can induce in a column.

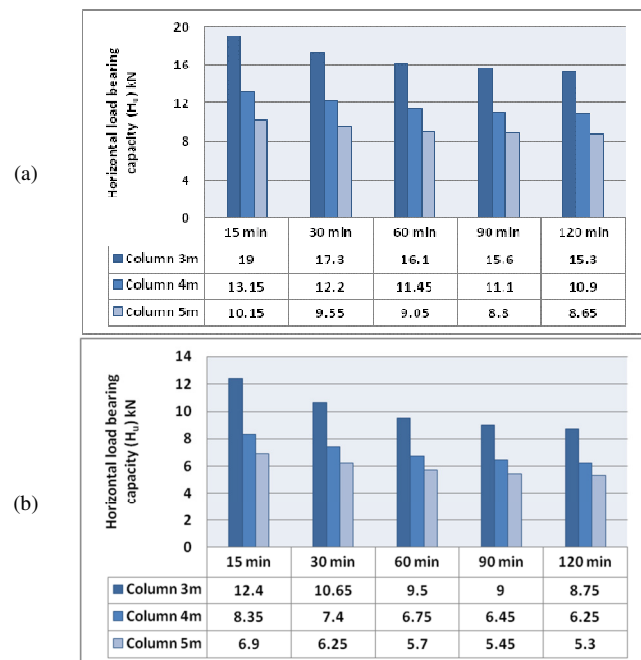
Fig. 2. Evolution of H_u and N_r .

A. Horizontal Load-Bearing Capacity (H_u) with Vertical Load

The column was subjected to both axial load and lateral deformation. The axial load used was the vertical load capacity of the column after fire exposure. Two loading rates were used: 25 and 50% of the residual bearing capacity.

1) Effect of Effective Height

For each fire and different heights, 44% and 42% loss of lateral capacity were found when applying 25% and 50% axial load of N_r respectively, as shown in Figure 3.

Fig. 3. H_u as a function of various heights for (a) 0.25 of N_r , (b) 0.5 of N_r .

However, as can be observed in Figure 3, the reductions in the lateral load capacities for the same height were less than the reductions in the compressive strength, which minimized the impact of the compressive strength on the column behavior.

2) Influence of the Size of the Sections

Figure 4 shows the evolution of H_u considering the effect of the section and the properties of the residual material after fire exposure. As the duration of fire increases, the residual properties of the material decrease, and a loss of 10% to 35% was evaluated for all columns considering the same height (4m). This degradation was due to the additional loss of the concrete's compressive resistance caused by the continuity of the evolution of temperatures in the massive sections. For the same fire, the horizontal load-bearing capacity of the column can increase by 97% depending on the section's dimensions.

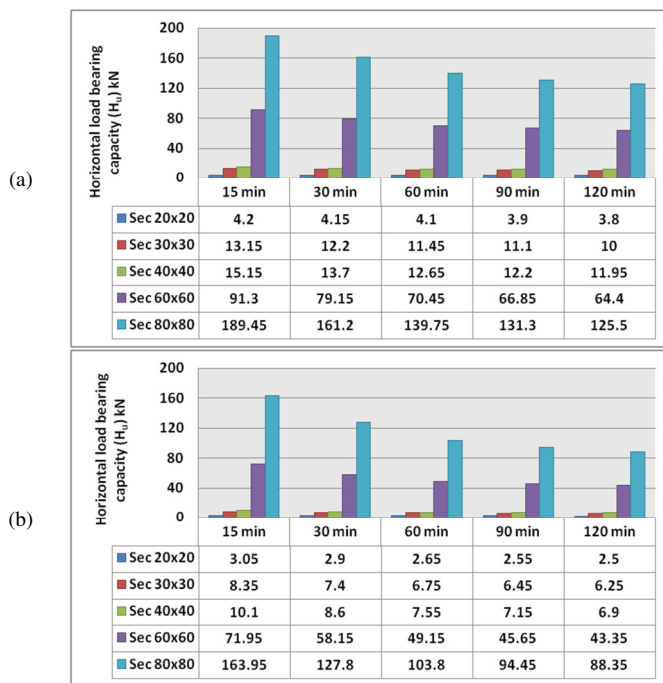


Fig. 4. H_u as a function of section size: (a) 0.25 of N_r , (b) 0.5 of N_r .

B. Evolution of the Maximum Lateral Displacement

1) Influence of the Height of the Column

Figure 5 shows the maximum lateral displacements at the top of the column for heights of 3, 4, and 5m using the same section of 30x30cm. Considering the residual resistance of the materials after the fire, the maximum lateral displacement was calculated for each fire. The results showed that the displacement value increased about 36% at the top of the 5m column compared to the reference column of 3m. The largest lateral displacement was 16cm for the 5m column exposed to fire with a heating phase (t_{peak}) of 15 minutes. Fire exposure has a greater effect on the residual compressive strength of concrete, and the structural response is governed by the geometrical properties of the column, such as inertia and height.

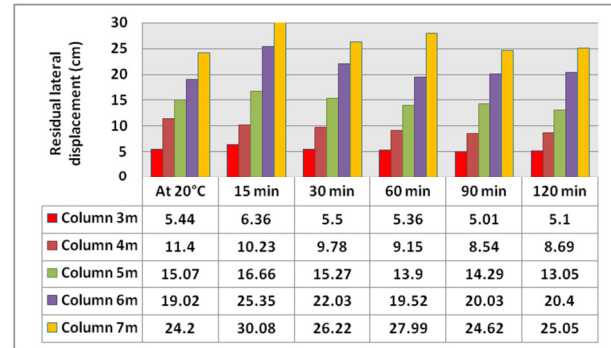


Fig. 5. Evolution of maximal lateral displacement.

2) Influence of the Sections of Columns

Figure 6 shows the influence of the section's size on the maximum lateral displacement. For the 20x20cm sections, the displacement increased gradually and its maximum was about 13cm. This growth was due to fire damage to the mechanical residual property of the materials, and the strength of the columns decreased following the degradation of the strength. For the 80x80cm sections, the displacement of 5cm has a small variation, showing that a column's behavior depends on its geometrical properties.

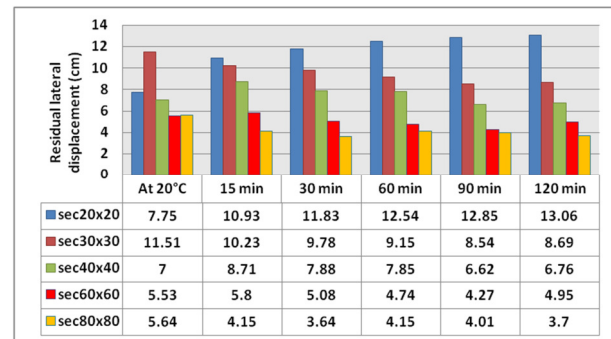


Fig. 6. Influence of section size on the maximum lateral displacement of a 4m column height.

C. Lateral Loads and Displacement Response Analysis

Horizontal displacements were calculated using the incremental method, evaluating the displacement for each time step. Figure 7 shows the load-lateral displacement which traces the development of lateral displacement on the top of columns under the incremental loading.

1) Energy Dissipation

The area enclosed by the curve and the horizontal axis in Figure 8 is defined as the energy dissipated by the columns, representing the ability to consume seismic energy through plastic deformations. Figure 7 shows that these curves are approximately straight lines before cracking. Within each curve, the decrease in secant stiffness caused by fire loading is somewhat insignificant, leading to small energy dissipation. However, they bend towards the displacement axis towards the end of loading. In other words, the top lateral displacements develop at accelerating rates before the failure of the column.

The curves indicate that the stiffness of an unheated column is higher than that of a heated one. This is because elevated temperatures cause more damage to the stiffness of the column subjected to greater temperature exposure (120min fire). Figure 8 also shows that the stiffness of the column exposed fires of 60, 90, and 120 minutes is very similar. This can be attributed to the damage caused by the high-temperature effect on the residual resistance of concrete. Among the curves presented, the stiffness of the column that has not been exposed to elevated temperature is the highest. The loading curves indicate that an elevated temperature has a significant effect under these conditions. Energy dissipation can be divided into two phases: pre-cracking and post-cracking. The energy dissipation capacity in the pre-cracking phase is very small.

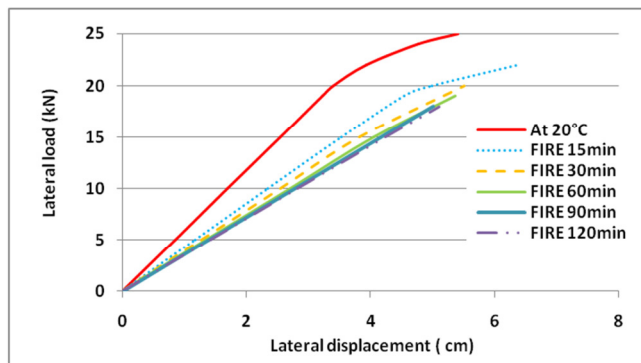


Fig. 7. Load-displacement curves of 3m columns.

TABLE III. DUCTILITY PARAMETERS OF THE COLUMNS

	Before fire (at 20°C)	After fire of $t_{peak}=15min$	After fire of $t_{peak}=30min$	After fire of $t_{peak}=60min$	After fire of $t_{peak}=90min$	After fire of $t_{peak}=120min$
Lateral yield displacement Δ_y (cm)	3.387	4.544	5.506	5.36	5.01	5.1
Lateral ultimate displacement Δ_u (cm)	5.405	6.368	5.506	5.36	5.01	5.1
Ductility factor: $\mu_d = \Delta_u / \Delta_y$	1.6	1.40	1	1	1	1

IV. CONCLUSIONS

The following remarks can be extracted from this study:

- The results showed that the lateral load capacity and ductility decreased substantially as a result of fire exposure.
- Post-fire lateral load capacities were not considerably affected by the increase in fire duration up to 60min. After 60min of fire exposure, a little reduction in the lateral load capacity of the column was observed, which minimized the impact of the concrete compressive strength loss on the post-fire lateral capacity of the columns.
- The reduction in lateral load capacity appeared to be caused by the residual properties of the concrete after fire exposure. For low axial loads (25% of N_r), the effects of vertical compressive load on the behavior of the columns were considerable.
- The energy dissipation of the columns was not significantly affected by fires with duration up to 30min. For a column

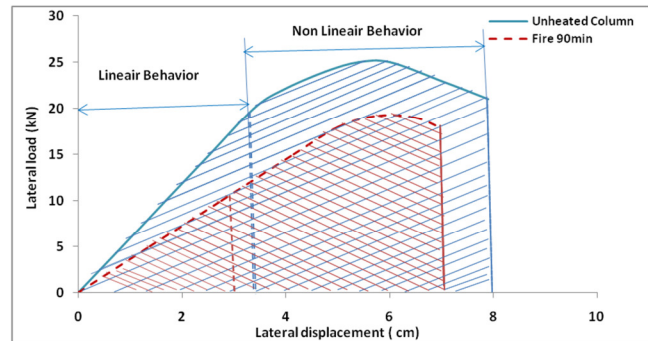


Fig. 8. Energy dissipated by the column.

2) Ductility Degradation

The displacement ductility factor μ_d , which is the ratio of the ultimate displacement Δ_u to the yield displacement Δ_y , was calculated for each column to compare the performance in terms of sustained ductility. Under a particular drift level, Table III shows that the ductility of the unheated column is about 60% of the fire-damaged column. The differences in ductility mainly reflect the effect of fire on mechanical properties. Furthermore, the differences in ductility mainly reflect that elevated temperature exposure reduces the capacity of the column. It can be concluded that the exposing temperature has a remarkable effect on the load-bearing capacity of the columns. The ductility of the columns was not found to be affected by fire exposure up to 30min.

subjected to a 90min fire, the reduction was about 25% compared to an unheated one, which was attributed to the loss of compressive strength. The stiffness of the column after a 30min fire was not affected. The slope of energy dissipation curves was confusing after a 30min fire.

- Ductility reduction was significantly affected compared to an unheated column after a 15min fire. This reduction was attributed to the post-fire loss in the mechanical properties of concrete. This can be explained by the greater loss in concrete's compressive strength and thereby the lower lateral load-bearing capacity of the columns.
- The application of the available Eurocode model for concrete after fire exposure resulted in a good estimation of the residual capacity of fire-damaged columns compared to the available existing results.

NOMENCLATURE

N_r = Vertical load-bearing capacity of a column.

H_u = Horizontal load-bearing capacity of a column.

t_{peak} = Time corresponding to the end of the heating phase - duration of the heating phase of the fire.

Δ_y = Lateral yield displacement.

Δ_u = Lateral ultimate displacement.

μ_d = Ductility factor.

REFERENCES

- [1] A. S. Usmani, "Research Priorities for Maintaining Structural Fire Resistance after Seismic Damage," presented at the 14th World Conference on Earthquake Engineering, Beijing, China, Oct. 2008.
- [2] D. Qin, P. Gao, F. Aslam, M. Sufian, and H. Alabduljabbar, "A comprehensive review on fire damage assessment of reinforced concrete structures," *Case Studies in Construction Materials*, vol. 16, Jun. 2022, Art. no. e00843, <https://doi.org/10.1016/j.cscm.2021.e00843>.
- [3] A. Agrawal and V. K. R. Kodur, "A Novel Experimental Approach for Evaluating Residual Capacity of Fire Damaged Concrete Members," *Fire Technology*, vol. 56, no. 2, pp. 715–735, Mar. 2020, <https://doi.org/10.1007/s10694-019-00900-1>.
- [4] J. Wróblewska and R. Kowalski, "Assessing concrete strength in fire-damaged structures," *Construction and Building Materials*, vol. 254, Sep. 2020, Art. no. 119122, <https://doi.org/10.1016/j.conbuildmat.2020.119122>.
- [5] R. Felicetti and P. G. Gambarova, "The Effects of High Temperature on the Residual Compressive Strength of High-Strength Siliceous Concretes," *Materials Journal*, vol. 95, no. 4, pp. 395–406, Jul. 1998, <https://doi.org/10.14359/382>.
- [6] J. Lee, Y. Xi, and K. Willam, "Properties of Concrete after High-Temperature Heating and Cooling," *Materials Journal*, vol. 105, no. 4, pp. 334–341, Jul. 2008, <https://doi.org/10.14359/19894>.
- [7] Y. N. Chan, G. F. Peng, and M. Anson, "Residual strength and pore structure of high-strength concrete and normal strength concrete after exposure to high temperatures," *Cement and Concrete Composites*, vol. 21, no. 1, pp. 23–27, Jan. 1999, [https://doi.org/10.1016/S0958-9465\(98\)00034-1](https://doi.org/10.1016/S0958-9465(98)00034-1).
- [8] A. Nassif, "Postfire full stress-strain response of fire-damaged concrete," *Fire and Materials*, vol. 30, no. 5, pp. 323–332, 2006, <https://doi.org/10.1002/fam.911>.
- [9] Y. F. Chang, Y. H. Chen, M. S. Sheu, and G. C. Yao, "Residual stress-strain relationship for concrete after exposure to high temperatures," *Cement and Concrete Research*, vol. 36, no. 10, pp. 1999–2005, Oct. 2006, <https://doi.org/10.1016/j.cemconres.2006.05.029>.
- [10] M. Salah Dimia, M. Guenfoud, T. Gernay, and J.-M. Franssen, "Collapse of concrete columns during and after the cooling phase of a fire," *Journal of Fire Protection Engineering*, vol. 21, no. 4, pp. 245–263, Nov. 2011, <https://doi.org/10.1177/1042391511423451>.
- [11] T. Gernay and M. Salah Dimia, "Structural behaviour of concrete columns under natural fires," *Engineering Computations*, vol. 30, no. 6, pp. 854–872, Jan. 2013, <https://doi.org/10.1108/EC-05-2012-0103>.
- [12] T. T. Lie, J. L. Woollerton, and Institut de recherche en construction (Canada), *Fire resistance of reinforced concrete columns, test results*. Ottawa, Canada: National Research Council of Canada, Institute for Research in Construction, 1988.
- [13] Y.-H. Chen, Y. F. Chang, G. C. Yao, and M.-S. Sheu, "Experimental research on post-fire behaviour of reinforced concrete columns," *Fire Safety Journal*, vol. 44, no. 5, pp. 741–748, Jul. 2009, <https://doi.org/10.1016/j.firesaf.2009.02.004>.
- [14] P. C. Nguyen, D. D. Pham, T. T. Tran, and T. Nghia-Nguyen, "Modified Numerical Modeling of Axially Loaded Concrete-Filled Steel Circular-Tube Columns," *Engineering, Technology & Applied Science Research*, vol. 11, no. 3, pp. 7094–7099, Jun. 2021, <https://doi.org/10.48084/etasr.4157>.
- [15] A. S. Ali and H. A. Al-Baghdadi, "Behavior of RC Beams Strengthened with NSM-CFRP Strips Exposure to Fire," *IOP Conference Series: Earth and Environmental Science*, vol. 856, no. 1, Jun. 2021, Art. no. 012035, <https://doi.org/10.1088/1755-1315/856/1/012035>.
- [16] H. M. Hekmet and A. F. Izzet, "Numerical Analysis of Segmental Post Tensioned Concrete Beams Exposed to High Fire Temperature," *Engineering, Technology & Applied Science Research*, vol. 9, no. 5, pp. 4759–4768, Oct. 2019, <https://doi.org/10.48084/etasr.3059>.
- [17] L. Ping, X. Jing, B. Othman, F. Yuefei, Z. B. A. Kadir, and X. Ping, "An Intercultural Management Perspective of Foreign Student's Adaptation in Chinese Universities: A Case Study of China Three Gorges University," *Engineering, Technology & Applied Science Research*, vol. 9, no. 2, pp. 3971–3977, Apr. 2019, <https://doi.org/10.48084/etasr.2589>.
- [18] X. Jianzhuang and X. Meng, "An experimental study on the seismic behavior of HPC frames after fire," *China Civil Engineering*, vol. 38, no. 8, pp. 36–42, 2005.
- [19] X. Liu, T. Gernay, L. Li, and Z. Lu, "Seismic performance of post-fire reinforced concrete beam-column joints strengthened with steel haunch system," *Engineering Structures*, vol. 234, May 2021, Art. no. 111978, <https://doi.org/10.1016/j.engstruct.2021.111978>.
- [20] M. Moradi, H. Tavakoli, and G. Abdollahzade, "Sensitivity analysis of the failure time of reinforcement concrete frame under postearthquake fire loading," *Structural Concrete*, vol. 21, no. 2, pp. 625–641, 2020, <https://doi.org/10.1002/suco.201900165>.
- [21] H. Mostafaei and T. Kabeyasawa, "Performance of a six-story Reinforced Concrete Structures in Post-Earthquake Fire," in *Proceedings of the 9th U.S. National and 10th Canadian Conference on Earthquake Engineering*, Toronto, Canada, Jul. 2010, Art. No. 659.
- [22] C. T. N. Tran and B. Li, "Seismic performance of RC short columns with light transverse reinforcement," *Structural Engineering and Mechanics*, vol. 67, no. 1, pp. 93–104, 2018, <https://doi.org/10.12989/sem.2018.67.1.093>.
- [23] Y. Hu, M. Maeda, Y. Suzuki, and K. Jin, "Seismic performance of exterior R/C beam-column joint under varying axial force," *Structural Engineering and Mechanics*, vol. 78, no. 5, pp. 623–635, 2021, <https://doi.org/10.12989/sem.2021.78.5.623>.
- [24] J. Zh. Xiao, J. Li, and F. Jiang, "Research on the seismic behavior of HPC shear walls after fire," *Materials and Structures*, vol. 37, no. 8, pp. 506–512, Oct. 2004, <https://doi.org/10.1007/BF02481574>.
- [25] G. R. Liu, "Experimental study on fire resistance and post-fire seismic behavior of concrete shear wall," Ph.D. dissertation, Dalian University of Technology, 2010.
- [26] S. Ni and A. C. Birely, "Post-fire seismic behavior of reinforced concrete structural walls," *Engineering Structures*, vol. 168, pp. 163–178, Aug. 2018, <https://doi.org/10.1016/j.engstruct.2018.04.018>.
- [27] M. Baghdadi, M. S. Dimia, M. Guenfoud, and A. Bouchair, "An experimental and numerical analysis of concrete walls exposed to fire," *Structural Engineering and Mechanics*, vol. 77, no. 6, pp. 819–830, Jan. 2021, <https://doi.org/10.12989/sem.2021.77.6.819>.
- [28] A. Ilki and U. Demir, "Factors Affecting the Seismic Behavior of Reinforced Concrete," *NED University Journal of Research - Special Issue on First South Asia Conference on Earthquake Engineering*, Feb. 2019.
- [29] U. Demir, M. F. Green, and A. Ilki, "Postfire seismic performance of reinforced precast concrete columns," *PCI Journal*, pp. 62–80, Nov. 2020.
- [30] C. G. Bailey and M. Yaqub, "Seismic strengthening of shear critical post-heated circular concrete columns wrapped with FRP composite jackets," *Composite Structures*, vol. 94, no. 3, pp. 851–864, Feb. 2012, <https://doi.org/10.1016/j.compstruct.2011.09.004>.
- [31] N. Benichou, H. Mostafaei, M. F. Green, and K. Hollingshead, "The impact of fire on seismic resistance of fibre reinforced polymer strengthened concrete structural systems," *Canadian Journal of Civil Engineering*, vol. 40, no. 11, pp. 1044–1050, Nov. 2013.
- [32] H. Mostafaei and J. K. Hum, "Response Simulation of Reinforced Concrete Columns Under Lateral Loads," National Research Council of Canada, Feb. 2010, <https://doi.org/10.4224/20375047>.
- [33] H. Mostafaei, F. J. Vecchio, and N. Bénichou, "Seismic Resistance of Fire-Damaged Reinforced Concrete Columns," in *Improving the Seismic Performance of Existing Buildings and Other Structures*, San

- Francisco, California, United States, Dec. 2009, pp. 1396–1407, [https://doi.org/10.1061/41084\(364\)128](https://doi.org/10.1061/41084(364)128).
- [34] J.-M. Franssen and T. Gernay, "Modeling structures in fire with SAFIR®: theoretical background and capabilities," *Journal of Structural Fire Engineering*, vol. 8, no. 3, pp. 300–323, Jan. 2017, <https://doi.org/10.1108/JSFE-07-2016-0010>.
- [35] *Eurocode 1: Actions on Structures: Part 1.2 General Actions : Actions on Structures Exposed to Fire*. London, UK: BSI, 2002.

Using Artificial Neural Networks for the Prediction of the Compressive Strength of Geopolymer Fly Ash

K. P. Rusna

Department of Civil Engineering
Coimbatore Institute of Technology
Coimbatore, Tamilnadu, India
rusnacbe19@gmail.com

V. G. Kalpana

Department of Civil Engineering
Coimbatore Institute of Technology
Coimbatore, Tamilnadu, India
kalpana@cit.edu.in

Received: 7 July 2022 | Revised: 19 July 2022 | Accepted: 20 July 2022

Abstract-Geopolymers are promising cement replacement materials as their use results in a considerable reduction of CO2 emissions. Geopolymer Fly ash (GF) is a widely used geopolymer due to its low cost and waste management achievement. The compressive strength of GF depends on variables such as curing time, curing temperature, NaOH molarity, the ratio of sodium silicate to sodium hydroxide, the ratio of fly ash to alkaline solution, etc. Artificial Neural Networks are employed to predict the strength of GF due to their accurate prediction capability as well as saving time and cost of experimental work. The obtained Root Mean Square Error (RMSE) and correction coefficient (R2) values were 4.47 and 0.972 respectively. The results illustrate the ability of the ANN model to be used as an efficient tool in predicting the compressive strength and determining the optimal values of GF parameters. The maximum strength of GF was observed for 2 hours curing time at 100°C, molarity of 10, fly ash to alkaline solution ratio of 3, and sodium silicate to sodium hydroxide ratio of 1.

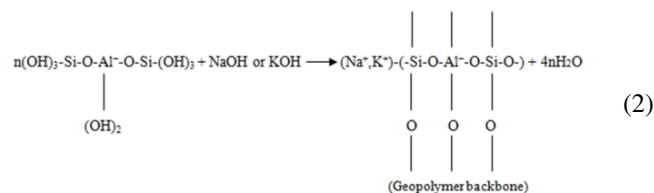
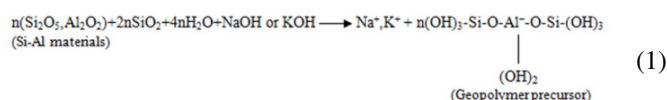
Keywords-fly ash; alkaline solution; geopolymer fly ash; Artificial Neural Networks (ANNs); compressive strength

I. INTRODUCTION

Climate warming is a serious global issue. The main reasons for climate warming are human activities that result in changes in the concentration of greenhouse gases such as CO₂ in the atmosphere [1]. One of the main sources of greenhouse gas emissions is the construction industry. The cement used in the construction sector produces significant amounts of CO₂ [2]. Therefore, the replacement of cement with eco-friendly alternatives such as fly ash, rice husk ash, and GGBS can significantly reduce the amount of CO₂ emissions [3-7].

Geopolymers are a new cement replacement material with promising performance for cement with less greenhouse gas emissions [8]. Geopolymer binders are produced through the reaction of aluminosilicate materials with alkaline solution. Fly ash, metakaoline, and ground granulated blast furnace slag are the most commonly used aluminosilicate materials. High strength is obtained with fly ash-based geopolymers [9]. Sodium hydroxide and sodium silicate or potassium hydroxide and potassium silicate mixtures are the most commonly used alkaline solutions [7]. Equations (1) and (2) explain the geopolymer material forming mechanism [10, 11]. The water

expelled during the chemical reaction leaves as nano-pores in the mix during curing time and imparts workability to the geopolymer mix during handling [12].



Investigating the mechanical properties of geopolymer materials by conducting experiments is time consuming and costly. There are many factors affecting the strength properties of geopolymers which make difficult their accurate estimation [13]. Mechanical modeling, analytical modeling, statistical methods, and artificial intelligence are the various methods used for the prediction of the strength properties of concrete [14]. Artificial intelligence is the most extensively used method for the prediction of the compressive strength of concrete. The use of ANNs is the most popular and widely used method in the area of artificial intelligence due to its easiness and prediction accuracy [15]. ANN modeling is a powerful machine learning technique that can solve various scientific problems [16]. In civil engineering, ANNs are widely used to predict the mechanical properties of concrete.

The compressive strength of concrete incorporated with fly ash admixture was predicted with Gene Expression Programming (GEP), ANNs, and Decision Tree (DT) algorithm in [17]. Soft-computing tools such as ANNs, Response Surface Methodology (RSM), and GEP have been applied to predict and analyze the compressive strength of alkali-activated strain-hardening geopolymer composites in [18]. The effect of parameters such as curing time, Ca(OH)_2 content, amount of superplasticizer, NaOH concentration, mould type, geopolymer type, $\text{H}_2\text{O/Na}_2\text{O}$ molar ratio, etc. on the compressive strength of different types of geopolymers were analyzed with ANNs in [9]. The influence of

sodium silicate to sodium hydroxide ratio and fly ash to alkaline solution ratio on the compressive strength of fly ash-based geopolymers was assessed using ANNs in [19]. Studies including the prediction of compressive strength of cement-based materials and geopolymer composites using ANNs are [20, 21].

In this study, ANNs are used to determine the compressive strength of geopolymer fly ash. Parameters such as NaOH molarity, $\text{Na}_2\text{SiO}_3/\text{NaOH}$ ratio, fly ash/alkaline solution ratio, curing temperature, and curing time influence the compressive strength of geopolymer fly ash. Parameter optimization is conducted using ANNs.

II. EXPERIMENTAL PHASE

A. Materials

Fly ash, sodium hydroxide (NaOH), and sodium silicate (Na_2SiO_3) solutions were used. The fly ash was collected from Mettur Thermal power plant, Tamilnadu, India and industrial grade chemicals Na_2SiO_3 and NaOH pellets were collected from coimbatore, Tamilnadu. The fly ash was class-F based on its chemical composition [22]. The specific gravity of fly ash was determined in accordance with IS1727 [23] and the value 2.12 was obtained. The chemical composition of Na_2SiO_3 solution used is $\text{SiO}_2=32.2\%$, $\text{Na}_2\text{O}=14.01\%$ and $\text{H}_2\text{O}=53.79\%$ by mass.



Fig. 1. Geopolymer fly ash cubes.

B. Sample Preparation and Testing

Sodium hydroxide solution and sodium silicate solution were mixed to prepare the alkaline solution. The alkaline solution was prepared one day before it was mixed with fly ash. Fly ash and alkaline solution were mixed and Geopolymer Fly ash (GF) cubes of $70.6\text{mm} \times 70.6\text{mm} \times 70.6\text{mm}$ were cast. The GF cubes were subjected to oven curing and were demolded. The compressive strength was tested after one day by keeping the cube specimens at room temperature. Figure 1 shows the Geopolymer Fly ash cubes ready for testing. The five considered parameters and their values are:

- Curing temperature: 50°C , 75°C , 100°C , 125°C , 150°C
- Curing time: 1hr, 2hr, 3hr
- Fly Ash/Alkaline Solution ratio (FA/AS): 2.5, 3, 3.5, 4
- $\text{Na}_2\text{SiO}_3/\text{NaOH}$ ratio: 1, 1.5, 2, 2.5
- Molarity of NaOH: 6M, 8M, 10M, 12M

III. MODELING PHASE

ANNs are used in this study to predict the compressive strength of GF.

A. Artificial Neural Networks

ANNs are a widely employed method in different fields of artificial intelligence [24]. ANNs are powerful machine learning methods for predicting and solving different scientific computations [16]. ANNs are widely used in the area of civil engineering for predicting concrete's mechanical properties. ANN modeling consists of two steps: 1) Network training with the available training data set and 2) the trained network is tested to compute the prediction accuracy.

B. Neural Network Model

A Back Propagation Network (BPN) was used in this study to train the ANN model. The BPN training set consists of two stages, the feed forward stage and the back propagation stage. In the feed forward stage, the input node is transferred by the input layer neurons to hidden layer neurons. Each hidden layer neuron calculates the weighted sum of its input, and the sum is transferred through its activation function and the activation value is given to the output layer. The output layer neurons compute the weighted sum of each neuron and the sum is transferred through its activation function, forming the network output value. The sigmoidal function is generally used as activation function. The output is given by:

$$f_j = \frac{1}{1 + \exp\left(-\sum w_{ji}o_i + b\right)} \quad (3)$$

where: w_{ji} is the connection weight from the lower layer neuron i to the upper layer neuron j , o_i is the output of the neuron i , and b is the bias value. In the second stage, the output layer transfers the network error to the input layer, and the network error is minimized to an acceptable level by adjusting the weights.

The utilized network consists of 5 neurons in the input layer, 5 neurons in the hidden layer, and 1 neuron in the output layer. The hidden neurons are arranged in 2 hidden layers to reduce the error percentage. Table I lists the ANN model parameters. The input layer consists of curing temperature, curing time, fly ash to alkaline solution ratio, sodium silicate to sodium hydroxide ratio, and NaOH molarity and the output layer represents the Compressive Strength (CS) of GF. The data set for preparing ANN model includes 63 experimental results provided in Table II. The ANN prediction accuracy is validated using 66% of the data for training and the remaining data for testing.

TABLE I. ANN MODEL PARAMETERS

Parameter	Value
Number of inputs	5
Number of hidden layers	3
Number of hidden layer units	8
Number of outputs	1
Network architecture	BPN
Training function	Sigmoidal function
Number of training	62
Number of testing	21

TABLE II. ONE DAY CS TEST RESULTS FOR GF CUBES

Sample No	Curing temperature (°C)	Curing time (hr)	FA/AS	Na ₂ SiO ₃ /NaOH	NaOH molarity	CS (N/mm ²)
1	50	1	3	2	10	0
2	50	2	3	2	10	0
3	50	3	3	2	10	0.71
4	100	1	3	2	10	4.50
5	100	2	3	2	10	25.08
6	100	3	3	2	10	24.28
7	150	1	3	2	10	7.50
8	150	2	3	2	10	21.16
9	150	3	3	2	10	0
10	100	2	2.5	2	10	6.76
11	100	2	3	2	10	25.08
12	100	2	3.5	2	10	22.28
13	100	2	4	2	10	11.33
14	100	2	3	1	10	28.25
15	100	2	3	1.5	10	31.47
16	100	2	3	2	10	25.08
17	100	2	3	2.5	10	17.48
18	100	2	3	1	8	14.64
19	100	2	3	1.5	8	23.43
20	100	2	3	2	8	17.19
21	100	2	3	2.5	8	14.10
22	100	2	3	1	12	22.07
23	100	2	3	1.5	12	28.44
24	100	2	3	2	12	25.46
25	100	2	3	2.5	12	22.21
26	50	1	3	1.5	10	0
27	50	2	3	1.5	10	0
28	50	3	3	1.5	10	2.95
29	100	1	3	1.5	10	2.90
30	100	2	3	1.5	10	31.47
31	100	3	3	1.5	10	30.27
32	150	1	3	1.5	10	9.71
33	150	2	3	1.5	10	26.22
34	150	3	3	1.5	10	0
35	100	2	2.5	1.5	10	13.09
36	100	2	3	1.5	10	31.47
37	100	2	3.5	1.5	10	30.29
38	100	2	4	1.5	10	20.02
39	75	2	3.5	1.5	12	5
40	100	2	3.5	1.5	12	26.4
41	125	2	3.5	1.5	12	32
42	150	2	3.5	1.5	12	30.5
43	125	1	3.5	1.5	12	16.7
44	125	2	3.5	1.5	12	27.1
45	125	3	3.5	1.5	12	26.2
46	125	2	3.5	1	12	17.5
47	125	2	3.5	1.5	12	21.5
48	125	2	3.5	2	12	20.2
49	125	2	3.5	2.5	12	16.8
50	100	2	1	3	6	25.9
51	100	2	1.5	3	6	23
52	100	2	2	3	6	18.33
53	100	2	2.5	3	6	11.59
54	100	1	1	3	8	2.2
55	100	1	1.5	3	8	9.1
56	100	1	2	3	8	4.2
57	100	1	2.5	3	8	3.8
58	100	1	1	3	10	11.5
59	100	1	2.5	3	10	4
60	100	1	1	3	12	11.8
61	100	1	1.5	3	12	9.5
62	100	1	2	3	12	3.8
63	100	1	2.5	3	12	3

IV. RESULTS AND DISCUSSION

A. Test Results

1) One Day Compressive Strength

The CS of the GF cubes was determined by following the ASTM C109 [25]. The one day compressive strength of 10M GF with different curing temperatures and curing times was obtained as shown in Figure 2. The GF cubes after 1 and 2hr of curing time at 50°C curing temperature were observed in wet condition and no strength was obtained. The strength was increased with rise in temperature and the maximum compressive strength of GF was observed for 100°C curing temperature. Similar results were reported in [26-28]. When the curing temperature became more than 100°C, a gradual decrease in strength was noticed. The curing time also showed influence on compressive strength and the maximum strength was observed for 2hrs curing time. Hence, the maximum value of 31.47N/mm² of strength was obtained for 100°C and 2hr curing time.

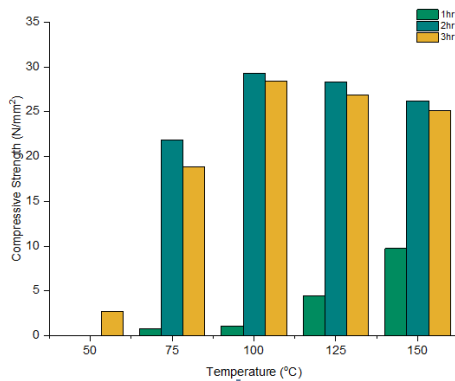


Fig. 2. One day compressive strength of GF with curing temperature and curing time.

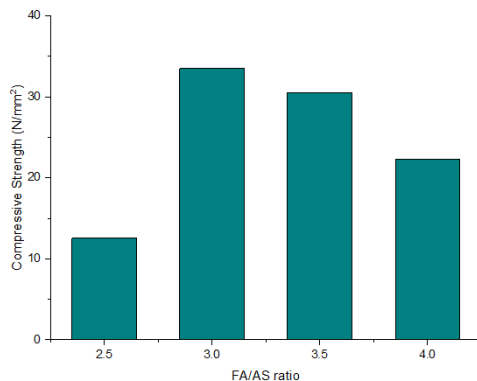


Fig. 3. One day compressive strength of GF with FA/SA ratio.

The one day compressive strength of 10M GF with different FA/AS ratios is shown in Figure 3. The FA/AS ratio was increased by 0.5 at 100°C curing temperature and 2hrs curing time. The maximum strength of GF was observed at the ratio of 3 as 31.47N/mm². The strength decreases beyond FA/AS ratio of 3. The one day CS of GF with different sodium silicate to sodium hydroxide ratios and NaOH molarities is shown in Figure 5. The maximum strength was observed for

Na₂SiO₃/NaOH ratio of 1 for every molarity. An increase in CS was observed with increase in molarity due to the increase of Na⁺ ions which enhance the geopolymer reaction [29, 31]. Maximum strength was observed in 10M GF cubes. Similar results were reported in [26-28]. When the molarity became more than 10M, a decrease in strength was observed due to the increase in the amount of OH⁻ ions which reduce the geopolymer reaction [26].

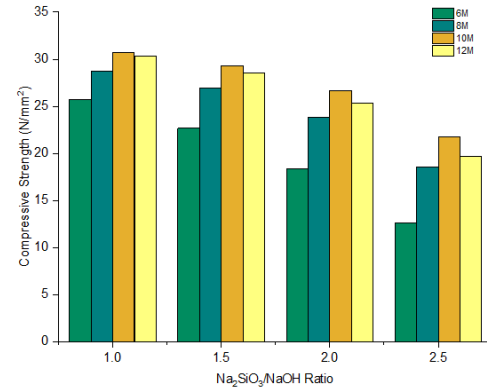


Fig. 4. The one day compressive strength of GF with curing temperature and curing time.

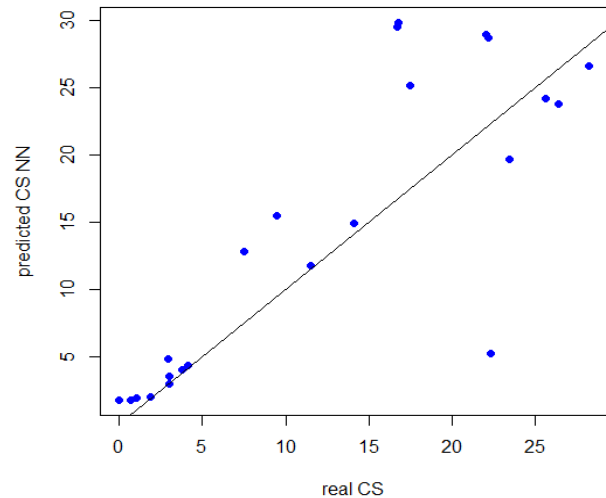


Fig. 5. Comparison between the ANN model predicted data and the experimental data.

B. Modeling Results

The most important step in ANN model development is the ANN architecture determination which suits the real problem. The ANN architecture L-5-4-3-1-1 was finalized after trial and error process. The performance of the ANN model was checked with the performance measures Root Mean Square Error (RMSE) and correction coefficient (R²) between the experimental results and the predicted results. They were computed by (4) and (5):

$$RMSE = \sqrt{\frac{\sum (x_i - y_i)^2}{n}} \quad (4)$$

$$R^2 = 1 - \frac{\sum (x_i - y_i)^2}{\sum y_i^2} \quad (5)$$

where x_i is the target value, y_i is the predicted value, and n is the number of test data.

TABLE III. EXPERIMENTAL AND PREDICTED VALUES

Experimental CS (N/mm ²)	ANN CS (N/mm ²)
0.71	1.14
7.5	18.7
23.43	18.54
28.25	25.17
17.48	24.15
22.07	26.014
22.21	25.98
2.9	5.06
25.66	26.08
22.32	25.03
26.4	26.08
16.7	24.01
16.8	24.01
3	3.98
1.9	0.234
4.1	4.06
5.9	7.74
13.8	5.3
11.5	6.82
5.2	9.87
1	0
14.1	14.5

Figure 5 represents the ANN model predicted data and the experimental data for the one day compressive strength test. The experimental compressive strength values and the corresponding ANN model predicted compressive strength values are given in Table III. The accuracy of the prediction is indicated by RMSE and R^2 . The RMSE and R^2 obtained values were 4.47 and 0.972 respectively, which show that the ANN is effective in the prediction of the CS of GF.

V. CONCLUSIONS

This study studies various factors affecting the compressive strength of geopolymers fly ash. The geopolymer fly ash was produced by mixing alkaline solution and fly ash. The factors considered in this study were curing temperature, curing time, fly ash to alkaline solution ratio, sodium silicate to sodium hydroxide ratio, and the molarity of sodium hydroxide. ANNs were employed in this study to predict the compressive strength of GF and the prediction accuracy was validated.

- The selected values of curing temperature were: 50, 75, 100, 125, and 150°C. The maximum compressive strength was observed at 100°C curing temperature.
- The values of curing time were as 1, 2, and 3hr. The maximum compressive strength was observed for 2hr curing time.
- The fly ash to alkaline solution ratio was 2.5, 3, 3.5, and 4. The maximum compressive strength was obtained for ratio equal to 3.

- The Na₂SiO₃/NaOH ratio was selected as 1, 1.5, 2, and 2.5. The maximum compressive strength was obtained for the ratio of 1.
- The molarity of NaOH varied as 6, 8, 10, and 12. The maximum compressive strength was obtained for 10M geopolymer fly ash.
- An ANN was developed to predict the compressive strength of GF. The accuracy of the model was evaluated with RMSE and R^2 . The obtained values were 4.47 and 0.972 respectively. These values of RMSE and R^2 confirm that the utilization of ANN for the prediction of the compressive strength of GF is a good choice due to its excellent correlation with the experimental results. This study suggests that ANNs are an effective tool in strength prediction of GF, reducing further the experimental cost and time.
- The geopolymer fly ash with its optimized parameters provides sufficient strength. Hence, it is applicable as a cement replacing material in concrete.

REFERENCES

- [1] A. M. Fathollahi-Fard, M. Hajiaghahi-Keshteli, and R. Tavakkoli-Moghaddam, "A bi-objective green home health care routing problem," *Journal of Cleaner Production*, vol. 200, pp. 423–443, Nov. 2018, <https://doi.org/10.1016/j.jclepro.2018.07.258>.
- [2] I. Tekin, O. Gencel, A. Gholampour, O. H. Oren, F. Koksall, and T. Ozbakkaloglu, "Recycling zeolitic tuff and marble waste in the production of eco-friendly geopolymer concretes," *Journal of Cleaner Production*, vol. 268, Sep. 2020, Art. no. 122298, <https://doi.org/10.1016/j.jclepro.2020.122298>.
- [3] M. A. Getahun, S. M. Shitote, and Z. C. Abiero Gariy, "Artificial neural network based modelling approach for strength prediction of concrete incorporating agricultural and construction wastes," *Construction and Building Materials*, vol. 190, pp. 517–525, Nov. 2018, <https://doi.org/10.1016/j.conbuildmat.2018.09.097>.
- [4] A. Saand, T. Ali, M. A. Keerio, and D. K. Bangwar, "Experimental Study on the Use of Rice Husk Ash as Partial Cement Replacement in Aerated Concrete," *Engineering, Technology & Applied Science Research*, vol. 9, no. 4, pp. 4534–4537, Aug. 2019, <https://doi.org/10.48084/etasr.2903>.
- [5] N. Bheel, A. W. Abro, I. A. Shar, A. A. Dayo, S. Shaikh, and Z. H. Shaikh, "Use of Rice Husk Ash as Cementitious Material in Concrete," *Engineering, Technology & Applied Science Research*, vol. 9, no. 3, pp. 4209–4212, Jun. 2019, <https://doi.org/10.48084/etasr.2746>.
- [6] S. Khoso, S. A. Abbasi, T. Ali, Z. Soomro, M. T. Naqash, and A. A. Ansari, "The Effect of Water-Binder Ratio and RHA on the Mechanical Performance of Sustainable Concrete," *Engineering, Technology & Applied Science Research*, vol. 12, no. 3, pp. 8520–8524, Jun. 2022, <https://doi.org/10.48084/etasr.4791>.
- [7] A. Mehta and R. Siddique, "Sustainable geopolymer concrete using ground granulated blast furnace slag and rice husk ash: Strength and permeability properties," *Journal of Cleaner Production*, vol. 205, pp. 49–57, Dec. 2018, <https://doi.org/10.1016/j.jclepro.2018.08.313>.
- [8] P. Duxson, A. Fernandez-Jimenez, J. L. Provis, G. C. Lukey, A. Palomo, and J. S. J. van Deventer, "Geopolymer technology: the current state of the art," *Journal of Materials Science*, vol. 42, no. 9, pp. 2917–2933, May 2007, <https://doi.org/10.1007/s10853-006-0637-z>.
- [9] A. Nazari and F. Pacheco Torgal, "Predicting compressive strength of different geopolymers by artificial neural networks," *Ceramics International*, vol. 39, no. 3, pp. 2247–2257, Apr. 2013, <https://doi.org/10.1016/j.ceramint.2012.08.070>.

- [10] J. Davidovits, "High-Alkali Cements for 21st Century Concretes," *Special Publication*, vol. 144, pp. 383–398, Mar. 1994, <https://doi.org/10.14359/4523>.
- [11] J. G. S. Van Jaarsveld, J. S. J. Van Deventer, and L. Lorenzen, "The potential use of geopolymeric materials to immobilise toxic metals: Part I. Theory and applications," *Minerals Engineering*, vol. 10, no. 7, pp. 659–669, Jul. 1997, [https://doi.org/10.1016/S0892-6875\(97\)00046-0](https://doi.org/10.1016/S0892-6875(97)00046-0).
- [12] D. Hardjito, S. E. Wallah, D. M. J. Sumajouw, and B. V. Rangan, "Fly Ash-Based Geopolymer Concrete," *Australian Journal of Structural Engineering*, vol. 6, no. 1, pp. 77–86, Jan. 2005, <https://doi.org/10.1080/13287982.2005.11464946>.
- [13] A. A. Shahmansouri, H. Akbarzadeh Bengar, and S. Ghanbari, "Compressive strength prediction of eco-efficient GGBS-based geopolymer concrete using GEP method," *Journal of Building Engineering*, vol. 31, Sep. 2020, Art. no. 101326, <https://doi.org/10.1016/j.jobbe.2020.101326>.
- [14] Z. H. Duan, S. C. Kou, and C. S. Poon, "Prediction of compressive strength of recycled aggregate concrete using artificial neural networks," *Construction and Building Materials*, vol. 40, pp. 1200–1206, Mar. 2013, <https://doi.org/10.1016/j.conbuildmat.2012.04.063>.
- [15] I. B. Topcu and M. Saridemir, "Prediction of properties of waste AAC aggregate concrete using artificial neural network," *Computational Materials Science*, vol. 41, no. 1, pp. 117–125, Nov. 2007, <https://doi.org/10.1016/j.commatsci.2007.03.010>.
- [16] A. Foucquier, S. Robert, F. Suard, L. Stephan, and A. Jay, "State of the art in building modelling and energy performances prediction: A review," *Renewable and Sustainable Energy Reviews*, vol. 23, pp. 272–288, Jul. 2013, <https://doi.org/10.1016/j.rser.2013.03.004>.
- [17] H. Song *et al.*, "Predicting the compressive strength of concrete with fly ash admixture using machine learning algorithms," *Construction and Building Materials*, vol. 308, Nov. 2021, Art. no. 125021, <https://doi.org/10.1016/j.conbuildmat.2021.125021>.
- [18] K. K. Yaswanth, J. Revathy, and P. Gajalakshmi, "Soft Computing Techniques for the Prediction and Analysis of Compressive Strength of Alkali-Activated Alumino-Silicate Based Strain-Hardening Geopolymer Composites," *Silicon*, vol. 14, no. 5, pp. 1985–2008, Apr. 2022, <https://doi.org/10.1007/s12633-021-00988-7>.
- [19] D. Tsamatsoulis, "Prediction of Cement Compressive Strength by Combining Dynamic Models of Neural Networks," *Chemical and Biochemical Engineering Quarterly*, vol. 35, no. 3, pp. 295–318, Oct. 2021, <https://doi.org/10.15255/CABEQ.2021.1952>.
- [20] H. Chen, C. Qian, C. Liang, and W. Kang, "An approach for predicting the compressive strength of cement-based materials exposed to sulfate attack," *PLOS ONE*, vol. 13, no. 1, Jan. 2018, Art. no. e0191370, <https://doi.org/10.1371/journal.pone.0191370>.
- [21] M. M. Yadollahi, A. Benli, and R. Demirboga, "Prediction of compressive strength of geopolymer composites using an artificial neural network," *Energy Materials*, vol. 10, no. 3, pp. 453–458, Sep. 2015, <https://doi.org/10.1179/1433075X15Y.0000000020>.
- [22] ASTM C618-19(2008), *Standard Specification for Coal Fly Ash and Raw or Calcined Natural Pozzolan for Use in Concrete*. West Conshohocken, PA, USA: ASTM International, 2008.
- [23] IS 1727 (1967), *Method of test for pozzolanic materials*. New Delhi, India: Bureau of Indian Standards, 1967.
- [24] A. Azadeh, J. Seif, M. Sheikhalishahii, and M. Yazdani, "An integrated support vector regression-imperialist competitive algorithm for reliability estimation of a shearing machine," *International Journal of Computer Integrated Manufacturing*, vol. 29, no. 1, pp. 16–24, Jan. 2016, <https://doi.org/10.1080/0951192X.2014.1002810>.
- [25] ASTM C109/C109M-20(2011), *Standard Test Method For Compressive Strength Of Hydraulic Cement Mortars (Using 2-In. Or [50-Mm] Cube Specimens)*. West Conshohocken, PA, USA: ASTM International, 2011.
- [26] S. Parvathy S, A. K. Sharma, and K. B. Anand, "Comparative study on synthesis and properties of geopolymer fine aggregate from fly ashes," *Construction and Building Materials*, vol. 198, pp. 359–367, Feb. 2019, <https://doi.org/10.1016/j.conbuildmat.2018.11.231>.
- [27] S. M. Rao and I. P. Acharya, "Synthesis and Characterization of Fly Ash Geopolymer Sand," *Journal of Materials in Civil Engineering*, vol. 26, no. 5, pp. 912–917, May 2014, [https://doi.org/10.1061/\(ASCE\)MT.1943-5533.0000880](https://doi.org/10.1061/(ASCE)MT.1943-5533.0000880).
- [28] U. S. Agrawal, S. P. Wanjari, and D. N. Naresh, "Characteristic study of geopolymer fly ash sand as a replacement to natural river sand," *Construction and Building Materials*, vol. 150, pp. 681–688, Sep. 2017, <https://doi.org/10.1016/j.conbuildmat.2017.06.029>.
- [29] P. Chindapasirt, C. Jaturapitakkul, W. Chalee, and U. Rattanasak, "Comparative study on the characteristics of fly ash and bottom ash geopolymers," *Waste Management*, vol. 29, no. 2, pp. 539–543, Feb. 2009, <https://doi.org/10.1016/j.wasman.2008.06.023>.
- [30] A. Sathonsaowaphak, P. Chindapasirt, and K. Pimraksa, "Workability and strength of lignite bottom ash geopolymer mortar," *Journal of Hazardous Materials*, vol. 168, no. 1, pp. 44–50, Aug. 2009, <https://doi.org/10.1016/j.jhazmat.2009.01.120>.

Application of a Seat-based Booking Control Mechanism in Rail Transport with Customer Diversion

Ahmet Z. Bulum

Department of Industrial Engineering
Karabuk University
Karabük, Turkey
ahmetbulum@karabuk.edu.tr

Muharrem Dugenci

Department of Industrial Engineering
Karabuk University
Karabük, Turkey
mdugenci@karabuk.edu.tr

Mumtaz Ipek

Department of Industrial Engineering
Sakarya University
Sakarya, Turkey
ipek@sakarya.edu.tr

Received: 1 July 2022 | Accepted: 10 July 2022

Abstract—The ticket booking control mechanism is a part of the Revenue Management (RM), commonly used in the airline industry. This study aims to optimize seat allocation in the railway industry and compare the performance of three booking control techniques by considering customer behavior. The preferences of customers who cannot find their desired ticket are considered as a customer diversion matrix, which also includes waiting and no-purchase probability. A Ticket Booking System (TBS) with buckets, which assigns seats to buckets, was adapted and implemented on the Turkish railway for the first time. A genetic algorithm that is specifically written to apply the TBS, including customer diversion, is used in simulations to obtain approximate solutions. It is seen that TBS gave successful results with a revenue increase of around 5.8%. We can also suggest, considering customer behavior, that the revenue can be raised by sales in periods.

Keywords—revenue management; railway transportation; customer behavior; genetic algorithm; seat inventory control

I. INTRODUCTION

Revenue Management (RM) can improve the profitability of firms in the service industry. RM has been used for pricing, forecasting, seat inventory control, and overbooking in airlines [1]. As a part of RM, seat inventory control or seat allocation deals with the decision to allocate a finite seat capacity optimal to demands [2]. Authors in [5] compared a deterministic linear and a probabilistic nonlinear programming model for the network problem with non-nested seat allocation. Authors in [6] suggested a multi-train seat inventory control model to control the seat inventory capacity among different trains. Authors in [7] proposed a stochastic dynamic model with some properties related to the profit-to-go functions. Authors in [8]

used three seat inventory control methods and modelled them under a single-fare class. With the spread of High-Speed Railway (HSR), RM's applicability in the railway industry has also increased [5, 10]. In the railway industry, RM is utilized as a management technique that aims to maximize the total revenue by finding an optimal strategy controlling the availability and/or the price of train tickets without any changes in the resources (e.g. adding trains or carriages) [11]. Articles regarding capacity allocation and prices in railway transport are mostly originated from countries where HSR is widely used [6, 8, 12–22]. While train tickets were sold formerly in railway stations or by authorized agents, online ticket reservation has become preferable nowadays. According to the classification in [23], there are different types of ticket booking mechanisms, such as Virtual Nesting (VN) and Partitioned Booking Limit Control (PBLC). VN, widely used in the airline industry, uses single-source nested controls to allocate each resource in the network. In practice, both the indexing process of VN and the control logic of mapping products to virtual classes is complex [23]. PBLC is a booking mechanism that allocates a fixed amount of capacity on each resource for every product offered, i.e. the seats are assigned to the tickets at the beginning of the booking horizon. Studies in which PBLC is used mainly aimed to find the optimal allocation of seats [5, 24, 25]. However, because of the fixed use of seats in PBLC, it is considered inefficient when the demand is stochastic and is seldom used in practice [23].

Customer behavior has been acknowledged as an important element for increasing revenue and has been included in modeling RM problems in some previous studies [26, 27]. Authors in [11] proposed a seat-based control mechanism and considered customers' purchase preferences as customer

behavior while optimizing seat allocation in China railway. Authors in [28, 29] proved that customer behavior is an essential factor affecting the ticket sale profit: the railway companies can collect more information with online reservation systems, such as the ticket booking time and purchase preferences of customers.

This research concentrates on evaluating the seat allocation performance of booking control mechanisms under diverse customer conditions. Unlike the previous studies, the diverted customer has more than two options: buying another ticket, waiting for an available seat, or leaving without buying. The customer diversion is utilized as a percentage matrix in this study. The ticket reservation process is utilized by the simulation method and a Genetic Algorithm (GA) is designed to cope with the complexity of the process. The methods were evaluated and compared through an experimental case and a real-world case using data from the Turkish railway. One contribution of this study is the application of customer diversion as customer behavior while optimizing seat allocation in the railway industry. Another contribution is the application of a ticket booking mechanism with buckets to the Turkish railway for the first time.

II. TICKET BOOKING MODELING WITH BUCKETS

Figure 1 shows an example of a railway line with three stops. In RM, resources are the seats in a train, and Resources 1 and 2 (Res1, Res2) consist of three seats. Products 1, 2 and 3 (Pr1, Pr2, Pr3) use the same seats but different resources. If a customer books a ticket for Pr3, for example Seat 1 (S1) will be occupied in Res1 and Res2. Then Res1 and Res2 have only two empty seats for booking, S2 and S3. But if the customer books a ticket for Pr1, then S1 will be removed only from Res1.

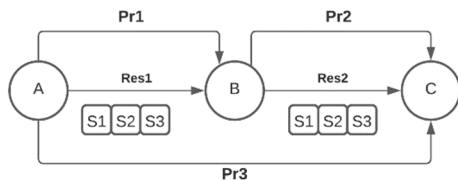


Fig. 1. A representative railway line with three stops.

A product is referred to the used resources, i.e. occupied seats in a train, between an Origin-Destination (O-D) pair. In the reservation process, customers send requests for products. After an accepted request, the seats related to that product will be assigned and occupied. Then different ticketing policies are involved: in PBLC a ticket will be printed immediately, but a ticket is generated before printing in the proposed ticket booking system with buckets (TBS). Modeling of the ticket booking process starts by allocating products and resources to the buckets. A bucket is a combination of tickets, and it contains a seat set and an offered product set. The bucket describes which products can be sold from the available resources [11]. The ticket pool is designed to collect the tickets generated for reusing. Some resources can remain unused after selling a ticket from a bucket. The remaining seats are assigned to appropriate products, which are collected in the ticket pool to sell additional tickets. Here, the exception is the ticket for travel from the first station to the last station.

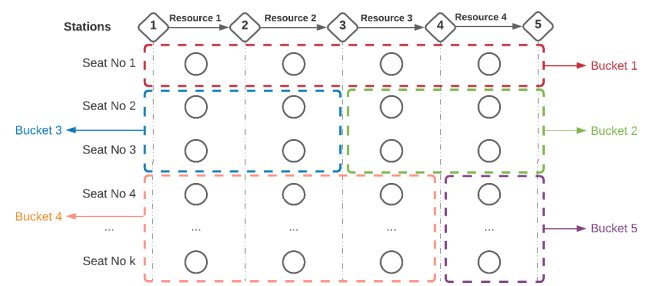


Fig. 2. The working mechanism of TBS.

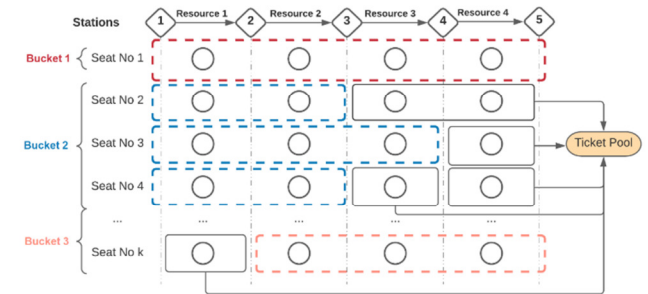


Fig. 3. The working mechanism of TBS.

Figures 2 and 3 show the different working mechanisms of PBLC and the proposed TBS. As seen in Figure 2, in PBLC all seats are assigned to some partitions and all tickets are generated and await their owner. However, in TBS, most seats are assigned to the buckets, and the remaining seats are sold by creating tickets according to the arriving passengers (Figure 3). The general assumptions of seat allocation problems are that the demand for cheap tickets is higher than for the expensive ones, and price-sensitive customers and long-distance travelers arrive earlier than the time-sensitive customers and short-distance travelers. The rules and assumptions made for TBS modeling are [11]: (1) The number of buckets is fixed during the ticket booking period, (2) a seat can be put in only a single bucket, (3) a product can relate to at most one bucket, (4) at the beginning of the reservation period, all the seats must be assigned to a bucket, (5) the ticket pool should be set to be empty before the ticket booking process starts, (6) the ticket pool has priority over the buckets for selling tickets, (7) demand for each product is assumed to be stochastic and representable by a probability distribution (mostly normal), (8) the number of seats is assumed to be fixed during the ticket booking period, and (9) no overbooking is considered. Tickets with lower prices to occupy the seats instead of more expensive ones are undesirable because airline or railway companies always prefer to sell seats at a higher price. Therefore, the allocation of products and seats in the buckets is the most critical factor affecting the profit.

III. FORMULATION AND SIMULATION STEPS

Two parameters must be set at the beginning of the booking horizon to start the ticket booking process: The number of seats reserved for each bucket rc_b and the product set for each bucket, which can be represented by the bucket-product

relationship δ_{kb} . The value of δ_{kb} is assumed to be equal to 1 if product k is in bucket b , and 0 otherwise. All necessary notations are given in Table I.

TABLE I. NOTATIONS

C	Total capacity of the train
n_{Buc}	Total number of buckets
n_{Prod}	Total number of products
b	Bucket number ($b=1, 2, \dots, n_{Buc}$)
k	Product number ($k=1, 2, \dots, n_{Prod}$)
c_b	Seat capacity for bucket b
δ	Bucket-product relation vector ($\delta \in \{0,1\}$)
Pr	Product vector
Buc	Bucket vector
Rev	Total revenue or sale income
t	A small time interval of the ticket booking time horizon T
R_t	Revenue of a time interval t
dec_{ij}	Diversion matrix for products
div_k	Number of the diverted customers of product k
rc_b	Remaining capacity of bucket b
p	Price vector for products/tickets
u	Product/ticket availability vector ($u \in \{0,1\}$)
$dmnd$	Demand vector for products/tickets
m	Mean demand vector for products/tickets
s	Standard deviation vector of demand for products/tickets
$rest_k$	Number of customers who did not buy a ticket for product k yet
rs	Random number representing customer requests a ticket for prod rs
$sale$	Income/revenue vector from sales of each product
TK	Ticket pool that contains the unoccupied seats or tickets
qtk_k	Quantity of seats in ticket pool for product k
$sold$	Vector indicating the number of tickets sold from each product

The objective of the seat allocation problem is to find an optimal combination of parameters (rc, δ) that maximizes total revenue $Rev(rc, \delta)$. It can be written as a mathematical formulation as follows:

$$\max_{rc, \delta} Rev(rc, \delta) \quad (1)$$

$$\sum_b^{n_{Buc}} rc_b = C \quad (2)$$

$$\sum_k^{n_{Prod}} \delta_{kb} \leq 1 \quad \forall b \quad (3)$$

where $rc_b \in Z^+$, $\delta_{kb} = \{0,1\}$, $b = 1, \dots, n_{Buc}$. The first constraint in (2) is for the capacity to ensure that each seat is placed in only one bucket. The second constraint (3) states that a product can be found in at most one bucket.

The ticket booking process begins when customers arrive to purchase tickets. In an appropriate sampling time, the customer arrival sequence can be approximated as a Bernoulli process. The ticket booking horizon is divided into t time intervals in the simulation process. If we assume that at most one customer can book a ticket in each time interval t , all the customers will arrive in the total ticket booking period T . Thus, $t = 1, 2, \dots, T$ and T are equal to the total number of customers.

If R_t denotes the revenue from ticket sale in time interval t , then the total revenue $Rev(rc, \delta)$ is expected to be the sum of each revenue in all time intervals. $Rev(rc, \delta)$ can be written as:

$$Rev(rc, \delta) = \text{Exp}\{\sum_{t=0}^T R_t | rc_{b,0} = c_b, qtk_{k,0} = 0\} \quad (4)$$

At the beginning of the booking process, the initial number of seats is determined and fixed, and the ticket pool is empty

($qtk_{k,0} = 0$ and $rc_{b,0} = c_b$ with $b = 1, \dots, n_{Buc}$ and $k = 1, \dots, n_{Prod}$). c_b represents the seat capacity of each bucket, $rc_{b,t}$ denotes the number of remaining seats in bucket b in time interval t and $qtk_{k,t}$ denotes the remaining number of product k in the ticket pool in time interval t .

Revenue in time interval t can be represented as:

$$R_t = \begin{cases} p_k \cdot u_{k,t}, & \text{if product } k \text{ is sold in period } t \\ 0, & \text{if no product is sold in } t \text{ or } rest_{k,t} = 0 \end{cases} \quad (5)$$

Revenue R_t depends on the ticket price (p) and the available product (u). The price of product k (p_k) is fixed during the ticket booking process, and $u_{k,t}$ denotes the availability of product k for booking in time interval t . The value of $u_{k,t}$ is 1 if the product k is available for booking in time interval t , and 0 otherwise (8). $rest_{k,t}$ represents the remaining demand, that has not been processed yet, from product k in time interval t and its value can be determined as:

$$rest_{k,t} = \begin{cases} rest_{k,t-1} - 1, & \text{if product } k \text{ is sold in time period } t \\ rest_{k,t} + 1, & \text{if } div_{k,t} \geq 1 \\ rest_{k,t}, & \text{otherwise} \end{cases} \quad (6)$$

$div_{k,t}$ denotes the number of diverted customers who could not find tickets for product k in time interval t . $div_{k,t}$ may increase by the customer diversion matrix dec_{ij} (will be discussed below) depending on the availability of product k in time interval t or decrease by 1 if the diverted customers find the ticket they want. Thus, the value of $div_{k,t}$ can be calculated by:

$$div_{k,t} = \begin{cases} div_{k,t} + dec_{kj} \mid j = 1, \dots, n_{Prod}, & \text{if } u_{k,t} = 0 \text{ and} \\ & \text{no product is sold in time period } t \\ div_{k,t} - 1, & \text{if product } k \text{ is sold in time period } t \end{cases} \quad (7)$$

The availability of a product for booking depends on whether it is offered by any bucket ($\sum rc_{b,t} \cdot \delta_{kb,t} > 0$) or if it is in the ticket pool ($qtk_{k,t} > 0$).

$$u_{k,t} = \begin{cases} 1, & \text{if } \sum rc_{b,t} \cdot \delta_{kb,t} > 0 \text{ or } qtk_{k,t} > 0 \\ 0, & \text{otherwise} \end{cases} \quad (8)$$

The remaining seat capacities (rc_b) and the remaining products in the ticket pool (qtk_k) in time interval $t+1$ depend on the sold product in time interval t . $rc_{b,t+1}$ and $qtk_{k,t+1}$ are determined as:

$$rc_{b,t+1} = \begin{cases} rc_{b,t} - 1, & \text{if product } k \text{ sold in time period } t \\ & \text{and } qtk_{k,t} = 0 \text{ and } \delta_{kb,t} = 1 \\ rc_{b,t}, & \text{otherwise} \end{cases} \quad (9)$$

$$qtk_{k,t+1} = \begin{cases} qtk_{k,t} - 1, & \text{if product } k \text{ is sold in time} \\ & \text{period } t \text{ and } qtk_{k,t} > 0 \\ qtk_{k,t} + \varphi_{k,t} \mid \forall k, & \text{if product } x \text{ is sold in time} \\ & \text{period } t \text{ and } qtk_{x,t} = 0 \\ qtk_{k,t}, & \text{otherwise} \end{cases} \quad (10)$$

$\varphi_{k,t} \in \{0,1\}$ (for $k = 1, \dots, n_{Prod}$) shows whether there are any available products left for booking when product x is sold. After product x is sold, more than one products can be

transferred to the ticket pool. In each time interval t , the maximum number of products to be transferred to the ticket pool is one less than the total number of products.

There are some restrictions in rail transport that are different from those in airlines. There can be as many passengers as the train capacity simultaneously during the whole trip, including the passengers who keep sitting, get on and off the train. These restrictions make the problem very difficult, especially as the number of stops and trains increases. So, revenues cannot be evaluated by simply calculating the difference between demand and capacity. Calculating the objective function by the booking process model can be difficult due to the curse of dimensionality. In addition, the fact that the number of products to be sold can be huge and it is challenging to express the parameter $\varphi_{k,t}$ analytically makes it very hard to find an absolute solution to the problem. Therefore, a GA was applied to solve the problem approximately, its steps will be described below.

A. Customer Diversion Matrix (CDM)

The author in [30] considered the buy-up possibility of customers, i.e. diversion. He defined diversion as the willingness of customers to purchase tickets in a different price class than they initially requested. Other studies with diversion are [31-33]. There are very few studies with customer diversion, and they are all related to the airline industry [34-37]. This study uses a CDM based on the customers' decisions. Table II shows an example of a CDM, which contains the diversion percentage of customers who decide to make a buy-up, wait, or buy nothing. CDM has as many rows as the number of products but has two more columns than the number of products. One of these two extra columns is for customers who prefer to wait and the other for customers who do not want to buy anything. It is not easy to create the dec_{ij} matrix. Whereas it was challenging to create an exact profile in the past, as most sales were made at the box offices in stations, nowadays, a lot of data about the booking process can be obtained thanks to online sales. dec_{ij} is the percentage of customers who want to buy a ticket from Product j because they could not buy a ticket from Product i . For instance, $dec_{23} = 0.4$ means that 40% of the customers who could not find any ticket from Product 2 decide to buy a ticket from Product 3. The total percentage of customers who decide to wait, buy-up, or buy nothing should always be 100%. In other words, the summation of each row in the diversion matrix never exceeds 100%. It is important to note here that in PBL and First-Come First-Served (FCFS), no waiting list is used, as all tickets are generated before the reservation period begins.

TABLE II. EXAMPLE MATRIX FOR DEC_{ij}

	1	2	3	4	5	6	7(w)	8(nb)
1	0	0	0	0	0	0	0	1
2	0.4	0	0	0	0	0	0	0.6
3	0	0.2	0	0	0	0	0.3	0.5
4	0.1	0.2*	0	0	0	0.2*	0	0.7
5	0	0.2	0	0.2	0	0	0.3	0.3
6	0	0	0	0.3	0	0	0.4	0.3

* Customers who cannot find Product (Ticket) 4 can make their trip by purchasing Ticket 2 and Ticket 6 together

B. Genetic Algorithm (GA)

The GA is an optimization method and one of the adaptive heuristic search algorithms. At first, the solution parameters are encoded in chromosomes. Each chromosome consists of a certain number of gene blocks representing the buckets, and is a solution candidate. The sum of the generated chromosomes constitutes the starting population. If we have a railway line with n stations and seat capacity C on a train, there will be $n-1$ resources and $n_{prod} = n(n-1)/2$ products. If the example from Section II is considered, Table III illustrates the way the products and buckets are encoded. There are 3 products and 2 buckets. Pr1 uses Res1 and Res2 and it is placed alone in Bucket 1 (Buc1). Zero stands for the absence of any candidates.

TABLE III. ENCODED BUCKETS AND PRODUCTS FOR A THREE-STOP LINE EXAMPLE

n=3	Stations from..to..	Encoded products	Encoded buckets
Pr1	1->3	Pr1=[1 2]	Buc1=[Pr1 0]
Pr2	1->2	Pr2=[1 0]	Buc2=[Pr2 Pr3]
Pr3	2->3	Pr3=[0 2]	

Buckets have a predetermined number of cells, symbolized as l_{Buc} . The number of seats, i.e. capacities of related buckets c_b , allocated for each bucket is placed in the last cell of a gene, so that the size of a gene should be $l_{Buc} + 1$. As seen in Table IV, a chromosome is encoded as an integer array with the genes arranged in a row. Therefore, the chromosome size depends on both the number of buckets used (n_{Buc}) and the size of a gene.

TABLE IV. ENCODED GENES AND CHROMOSOMES FOR A THREE-STOP LINE EXAMPLE

Parameters:	$l_{Buc}=2, n_{Buc}=2, C=100$		
Encoded buckets	Buc1=[Pr1 0]	Buc1=[Pr1 0]	Buc1=[0 Pr1]
	Buc2=[Pr2 Pr3]	Buc2=[Pr2 Pr3]	Buc2=[Pr2 0]
Encoded genes	Gene1=[Buc1 50]	Gene1=[Buc1 60]	Gene1=[Buc1 60]
	Gene2=[Buc2 50]	Gene2=[Buc2 40]	Gene2=[Buc2 40]
Encoded chromosomes	Cr1=[Gene1 Gene2]	Cr2=[Gene1 Gene2]	Cr3=[Gene1 Gene2]

Fitness: The performance of a chromosome is evaluated by fitness, which can be calculated using the objective function. Genetic operators expand the solution space by producing generations with better characteristics. Three basic genetic operators are selection, crossover, and mutation.

Selection: The selection process copies the existing chromosome to the next generation without making any changes in its genetic structure. We used the roulette method for selection in this research.

Crossover: Crossover is the formation of new individuals by randomly combining the structures of two individuals, namely chromosomes. We use the point-to-point uniform crossover rule, in which a coin is flipped for each gene to decide whether or not it will be included in the offspring. Since the chromosomes consist of the bucket and the number of seats allocated to it, the crossover was also performed in two steps according to the crossover rate.

Mutation: A mutation is performed by replacing one or more of the genes of an existing individual with entirely new

genes. We adopt the uniform mutation rule. The mutation also takes place in two steps. First step: The products in the genes of the randomly selected chromosome are replaced according to the mutation rate with new products that were never selected. Buckets with empty cells are filled and the filled ones can be empty. Second step: The number of seats in the randomly selected gene of the randomly selected chromosome is increased by 5 or decreased by 5. While performing this, it is essential to check that the number of seats does not fall below zero and does not exceed the capacity.

C. Simulations

In this research, ticket booking is treated as a time-dependent process. Only one customer arrives in a time interval t , which is a small part of the time horizon. So, the time horizon is divided into T time periods. The arrival of customers is simulated according to Poisson distribution. A random demand vector is generated with the average demand and standard deviation of demand provided. The customer behavior is simulated by using the CDM. The sales from any product depend on the sales from all other products. Therefore, in our model, the demand for a product consists of partially the customers who initially request that product and partially the customers diverting from other products. Several algorithms have been written in Matlab to simulate the booking process with the procedure shown in Table V. Various random demands are generated as over, under, and close or equal to the average demand to analyze the different scenarios.

In the beginning, the buckets used in the simulation have random initial values that come from the GA. After many simulation rounds, buckets with higher revenue can be achieved in GA via feedback of the simulation results. The values of the GA parameters, i.e. population size, mutation rate and crossover rate, were decided using the experimental design technique proposed by Taguchi [38]. Ticket requests are primarily responded to by sales from TK , i.e. ticket pool. If there is no appropriate ticket in TK , all the buckets are scanned for the product. It is not enough to find the product in a bucket, it is also necessary to have an empty seat for that bucket. After the sale from buckets, some seats can remain unoccupied. So these are added to TK for reuse next time. If there is no available seat for a product, customers who request a ticket for that product can either choose another product, wait for a seat for that ticket, or leave without purchasing (see Figure 4). The simulation algorithm runs until there is no demand and all ticket requests, positive or negative, are met. Evaluation and comparison of the techniques are made over a fictional railway line and a real-life example with different demand scenarios. We aim through simulations to observe how TBS differs from the other two ticket booking mechanisms and the effects of customer behavior on the booking process.

Apart from different random demand scenarios and random arrival sequences, special demand situations were also examined. We specifically set low, high, and equal-to-mean demand scenarios with appropriate random demands. Low and high demand represent the demand that is lower and higher than the capacity respectively. Equal-to-mean demand is equal or random but too close to the average historical demand. Each simulation has been run 100 times with various scenarios. The

exhibited results are the average values obtained at the end of the simulation trials.

TABLE V. SIMULATION STEPS

	Start
1.	Set initial parameters: $C, Buc, dmnd, dec_{ij}, TK$
2.	If there is no request for $Pr(rs)$ → Go to end
3.	Else
4.	If TK contains available resource(s) for $Pr(rs)$ → Sale from TK , go to line 2
5.	Else
6.	If Buc contains available resource(s) for $Pr(rs)$
7.	Sale from Buc
8.	If there is remaining resource(s)/seat(s) → Add the remaining resource(s)/seat(s) to TK , go to line 2
9.	Else
10.	If customer wants to buy nothing (with dec_{ij}) → Add $Pr(rs)$ to no-buy list, go to line 2
11.	Else if customer wants to wait (only in TBS !!!) → Add $Pr(rs)$ to wait list, go to line 2
12.	Else if the customer wants to buy another ticket → Distribute demand to re-buy list by dec_{ij} , go to line 2
13.	Else
14.	Add wait list and rebuy list to $dmnd$, go to line 2
	End

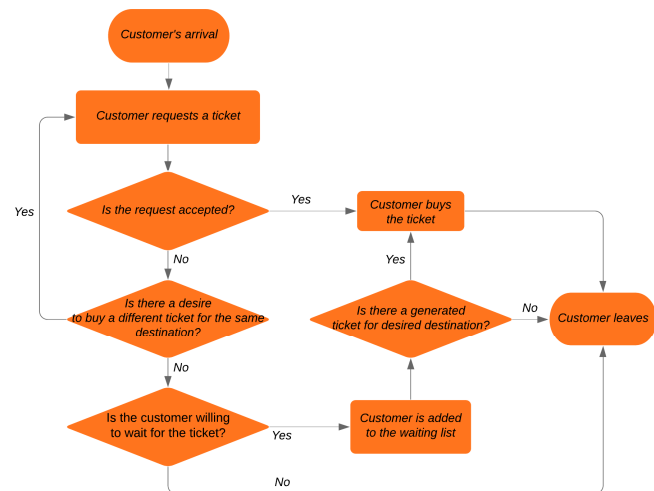


Fig. 4. Flowchart of the booking process steps with customer diversion.

IV. COMPUTATIONAL EXPERIMENTS

A. Fictive Railway Line Example

In this test example, there is a 5-stop railway line with a single train, whose seat capacity is 100. For the stations from A to E, the ticket price in US\$ and the demand information of the products is given in Table VI.

TABLE VI. TICKET FARES AND DEMAND INFORMATION

Products	1	2	3	4	5	6	7	8	9	10
	A-E	A-D	A-C	A-B	B-E	B-D	B-C	C-E	C-D	D-E
Price (\$)	80	50	30	20	70	40	20	60	30	40
Mean demand	75	50	13	5	38	25	5	37	12	63
St. dev. of demand	11.3	6.7	3.1	2.9	4.2	1.7	2.6	4.7	2.8	7.1

The diversion matrix of this example is generated from random values. As described above, the values in columns 11 and 12 of the 10×12-matrix are the waiting and non-purchase rates respectively. The results for different demand scenarios (under, over, and equal to the mean of the fictional demand) can be seen in Figures 5 and 6. The Figures show the expected revenue and the number of rejected requests for each scenario. In the Figures, TBS_axb stands for TBS with a buckets, each b cells long. The algorithm suggests 3 buckets with a length of 4 cells in this example, but we put some alternative bucket solutions in the Figures. As seen in Figure 5, in all demand levels, TBS gives a better performance than PBLC and FCFS. At every demand level, even if the arrival sequence of customers changes, the performance ranking by revenue is TBS > FCFS > PBLC. The way the integration of the customer's behavior into the booking process affects the income can be seen in Figure 5. While the effects of customer behavior are minimal on TBS, it appears to have the most significant impact on PBLC. Especially at low demand level, sales revenue is significantly increased in PBLC compared to the case without customer behavior. Figure 6 shows that considering customer behavior has not only resulted in improvement in revenue. The number of rejected customers decreased at all demand levels and for all techniques. The amount and rate of change vary according to the customers' demand and arrival sequence.

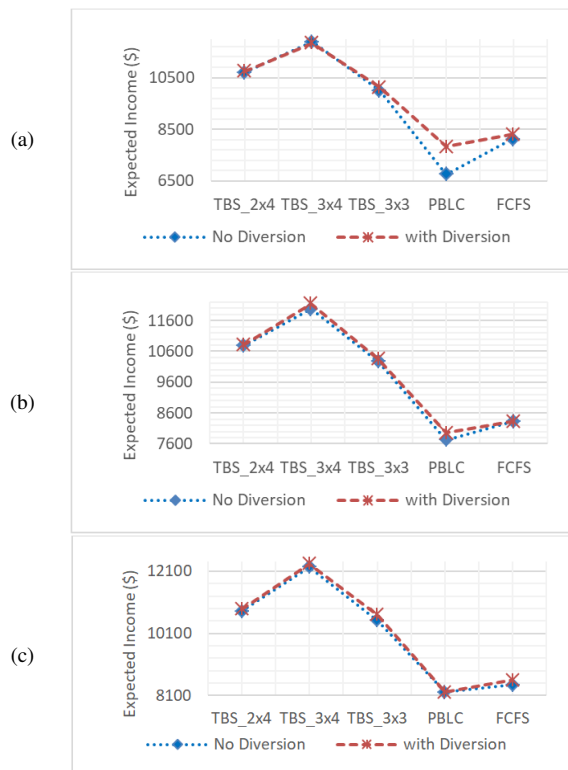


Fig. 5. Comparison of expected income with/without customer diversion: (a) Low demand, (b) mean-equal demand, and (c) high demand.

B. Real-life Railway Example

As a real-life example, the railway line between Ankara and Istanbul in Turkey was examined. The data were obtained from the statistical and annual reports published on the Turkish

national railway company website. The incompatible and irrelevant data were extracted or neglected. The company has 7 trains, each with 419 seats, daily departing from Ankara to Istanbul. There are 9 stations on the line, the first station is in Ankara and the last station is in Halkali in Istanbul. There are 36 products (see Table VII) and 8 resources in this example. Price and product numbers (in square brackets) of each O-D pair are listed in Table VII. Average demand and standard deviations of demand (shown in parentheses) of each product can be seen in Table VIII.

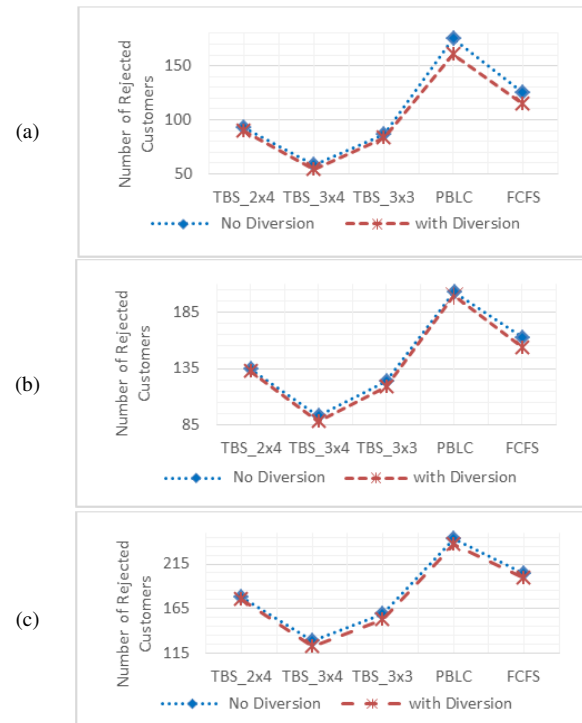


Fig. 6. Comparison graphs showing the number of rejected customers with/without customer diversion: (a) Low demand, (b) mean-equal demand, and (c) high demand.

TABLE VII. TICKET PRICE INFORMATION AND PRODUCT NUMBERS (IN SQUARE BRACKETS) FOR THE REAL-LIFE EXAMPLE

Price (TL)	Polatli	Eskisehir	Bozuyuk	Bilecik	Arifiye	Izmit	Istanbul (S.cesme)	Istanbul (Halkali)
Ankara	19.5 [8]	37.5 [7]	49.5 [6]	61.5 [5]	73.5 [4]	79.5 [3]	85.5 [2]	96 [1]
Polatli		28 [15]	43.5 [14]	55.5 [13]	61.5 [12]	67.5 [11]	79.5 [10]	90 [9]
Eskisehir			19.5 [21]	31.5 [20]	52.5 [19]	52.5 [18]	55.5 [17]	64 [16]
Bozuyuk				19.5 [26]	37.5 [25]	52.5 [24]	55.5 [23]	64 [22]
Bilecik					31.5 [30]	49.5 [29]	55.5 [28]	64 [27]
Arifiye						19.5 [33]	31.5 [32]	38.5 [31]
Izmit							19.5 [35]	26.5 [34]
Istanbul (S.cesme)								24 [36]

TABLE VIII. MEAN DEMAND AND STANDARD DEVIATION OF THE DEMAND (IN PARATHESIS) FOR GIVEN O-D PAIRS

Demand (Std.Dev.)	Polatli	Eskisehir	Bozuyuk	Bilecik	Arifiye	Izmit	Istanbul (S.cesme)	Istanbul (Halkali)
Ankara	8 (4.1)	121 (6.5)	4 (1.7)	6 (2.4)	7 (7.4)	15 (5.0)	219 (9.1)	32 (4.9)
Polatli		4 (4.0)	1 (1.4)	1 (2.8)	1 (1.7)	2 (2.2)	7 (6.6)	1 (7.0)
Eskisehir			1 (1.1)	2 (1.7)	7 (3.2)	17 (5.4)	112 (8.4)	13 (3.2)
Bozuyuk				1 (2.8)	1 (1.3)	1 (1.6)	3 (6.5)	3 (1.7)
Bilecik					2 (2.9)	2 (2.6)	6 (4.5)	4 (3.6)
Arifiye						1 (2.4)	6 (5.7)	4 (5.2)
Izmit							23 (7.4)	20 (10.9)
Istanbul (S.cesme)								1 (3.8)

The diversion matrix, for this example was created based on the opinions of expert. As mentioned above, the diversion data can be obtained online using new technologies and can be replaced easily in TBS. The matrix has a size of 36×38 and contains zero values for some products. Column 37 represents the rate of customers who desire to wait. Similarly, column 38 is the rate of customers who prefer to leave without purchasing. The simulation results are summarized in the tables according to the demand levels and whether customer behavior is considered. The obtained results are shown in Table IX and Figure 7 comparatively.

TABLE IX. CALCULATED EXPECTED REVENUES (IN TL), SOLD TICKETS AND REJECTED CUSTOMERS ACCORDING TO DEMAND SCENARIOS

Revenue (TL)				
Demand	Diversion	TBS 7x7	PBLC	FCFS
Low	No	36976	36976	36976
	Yes	36976	36976	36976
Mean-equal	No	39079	38084	37787
	Yes	39154	38159	37811
High	No	42567	40793	38663
	Yes	42634	41020	38742

Sold Tickets (pcs)				
Demand	Diversion	TBS 7x7	PBLC	FCFS
Low	No	589	589	589
	Yes	589	589	589
Mean-equal	No	624	618	617
	Yes	629	621	618
High	No	709	659	642
	Yes	719	664	644

Rejected customers (persons)				
Demand	Diversion	TBS 7x7	PBLC	FCFS
Low	No	0	0	0
	Yes	0	0	0
Mean-equal	No	35	41	42
	Yes	30	38	41
High	No	95	145	162
	Yes	85	140	160

The algorithm for TBS suggests 7 buckets with a length of 7 cells after trials of many bucket combinations. In low demand, the expected revenues of all booking techniques are the same or very close to each other. One reason for this may be that all customers can get the tickets they want due to the low demand and sufficient capacity. In high and mean-equal demand scenarios, the differences between the booking mechanisms are evident (Figure 7(b)-(c)). TBS shows clearly better performance than PBLC and FCFS. If we take the customer behavior into account in simulations, the changes in revenue can be seen in Figure 8. Again, there are no differences in revenue with or without customer diversion in low-demand scenarios and the reason explained above also applies here. In other demand levels, customer behavior shows its effect. Its most significant impact is on TBS, then on PBLC, and FCFS. In the simulation, experiments were carried out by diversifying customer arrivals. It has been observed that the effect of the changes in the customers' arrival is shallow, and there is no change in the performance order even though there are minor changes in the revenues. Figures 8 and 9 show that incorporating customer behavior into the system increased the expected revenues and decreased the number of rejected customers. In particular, the decrease in the number of rejected customers is quite evident, except for the low demand level (Figure 9(a)).

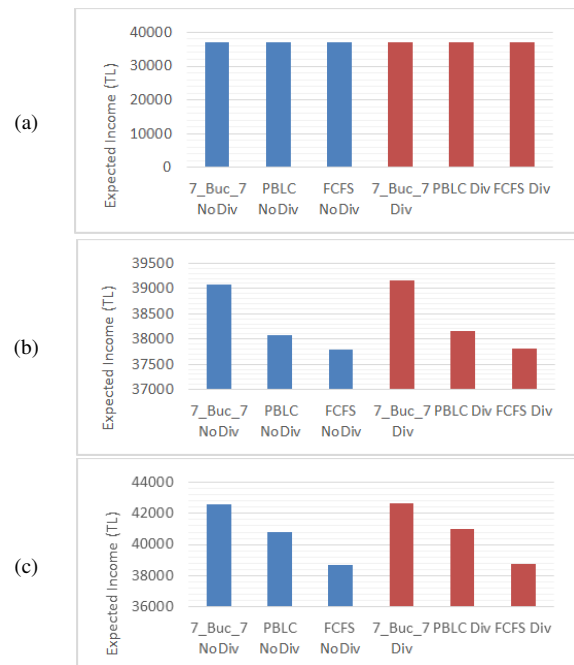


Fig. 7. Expected income with/without customer diversion according to the demand scenarios for the real-life example: (a) Low demand, (b) mean-equal demand, and (c) high demand.

C. Impact of Customer Behavior

Simulations were performed with different valued matrices of dec_{ij} to evaluate the customer behavior impact. The tests were carried out in two stages. First, simulations were run with different demand levels while keeping CDM constant. Changes were made in CDM in the second stage while keeping the demand constant.

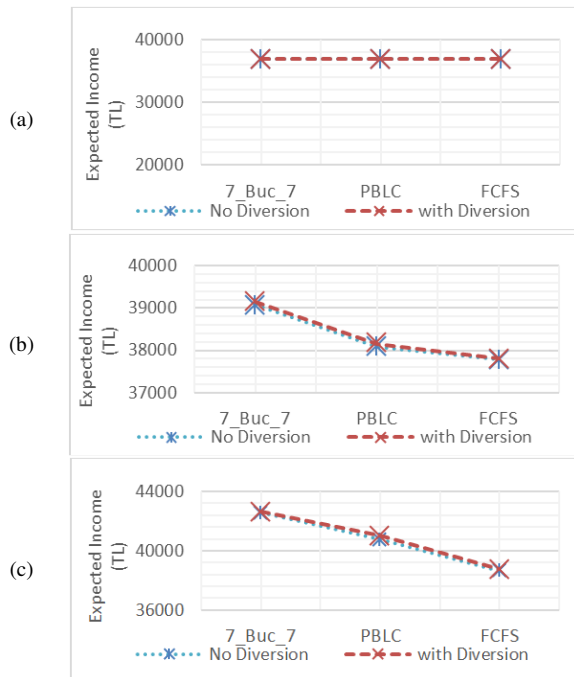


Fig. 8. Comparison of expected revenues with/without customer diversion according to the demand scenarios for the real-life example: (a) Low demand, (b) mean-equal demand, and (c) high demand.

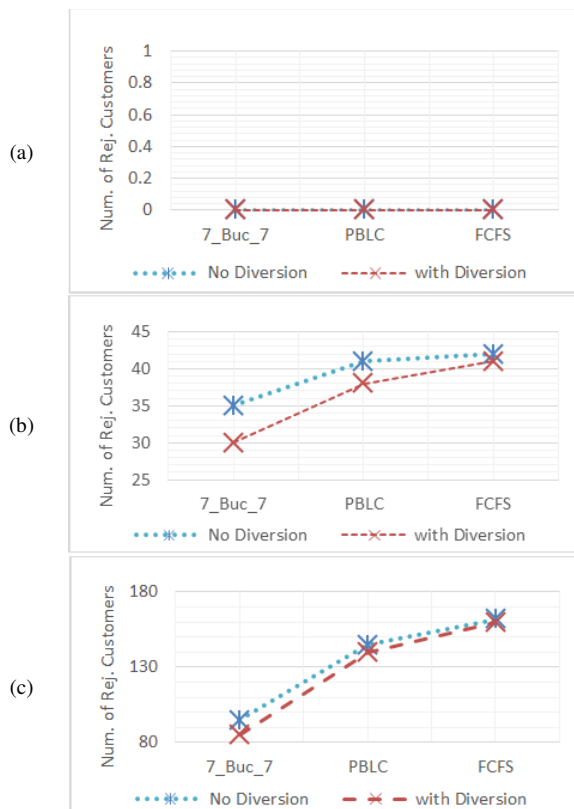


Fig. 9. Changes in the number of rejected customers with/without considering customer diversion according to the demand scenarios: (a) Low demand, (b) mean-equal demand, and (c) high demand.

As can be seen in Figure 10, in low demand, the revenue and the number of tickets sold are not affected by the customer behavior. As the demand increases, the change in income becomes more pronounced and is most significant in TBS. The impact of customer behavior on revenue and ticket sales was primarily monitored in above- and near-average demands. In the tests conducted with high demand, it has been observed that the effect of customer behavior decreases gradually due to the exhaustion of capacity if the demand is too high. In the second phase, changes were made in dec_{ij} by keeping the demand high above average and keeping it constant. It is important to note that the waiting behavior in the PBLC and FCFS methods does not affect revenue and ticket sales, because in these methods, after the capacity of a product is reached, the same product does not open for sale again. In TBS, the re-opening possibility is always present according to the order of the customer's arrival. Except for the waiting or no-buy columns, the changes are limited to cells with zero value. It would be easier to reduce the no-buy percentage by encouraging those who leave without buying anything to buy any product. The changes made in columns 1-36 (columns 37 and 38 are adjusted accordingly) had a more significant impact on revenue and ticket sales in PBLC and FCFS than in TBS.

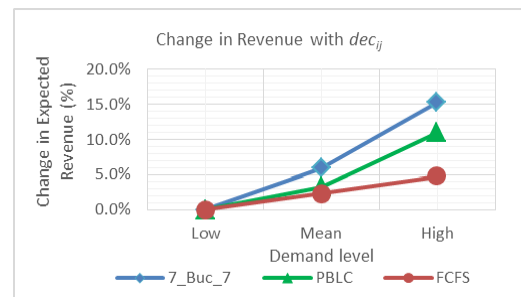


Fig. 10. Changes in the expected revenue with considering customer diversion according to the demand scenarios: (a) Low demand, (b) mean-equal demand, and (c) high demand.

The effect of changes made in the waiting and no-buy columns on revenue and sales can be analyzed by assigning a value of zero to the other columns. So, in Figures 11 and 12, W0/NB0 refers the results without CDM. In the expression W01/NB09, W01 represents that all cells in the waiting column get the value 0.1 and NB09 means that all cells in the no-buy column have the value 0.9. Similarly, numbers in other expressions (W0x/NB0y) represent ratios for columns 37 and 38. It should be noted that since the ratios in the cells represent a probability, their sum should not exceed 1, so the sum of each row cannot exceed 1. It has been observed that changes in the waiting column significantly impact the revenue and sales with TBS. This impact increases positively as the waiting rate increases (see Figures 11-12). In the tests with PBLC and FCFS, the slight changes in revenue and sales seen in the Figures can be interpreted as a result of the change in the no-buy percentage. The modification of CDM has a remarkable impact on revenue and ticket sales in TBS (up to 3.49% and 2.12% respectively) when the waiting rate (column 37) is changed. This will be instrumental for the development of a different sales strategy or policy to be based on the examination of the effects of customer behavior.

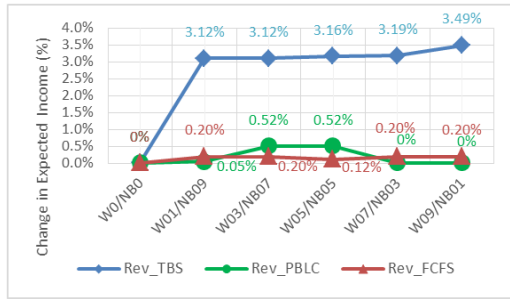


Fig. 11. Changes in expected revenue with various values of the dec_{ij} matrix (in percentage).

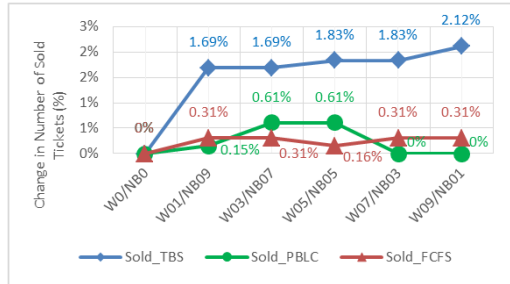


Fig. 12. Changes in the number of sold tickets with various values of the dec_{ij} matrix (in percentage).

V. CONCLUSION

The Turkish railway company sells 593 tickets and has an income of 36.866 TL on average in a day per train (2019). With the proposed algorithm (TBS), approximately 630 tickets can be sold in the case of average demand. An income raise of around 2100 TL per train can be expected with revenue up to 39000 TL, which is a good result compared to the current level. TBS gave the best results among the three examined methods. An annual revenue increase of 5.3M TL can be expected if our proposed model is implemented. Unlike previous research in which only the customers' choice of a train before departure has been taken into account, this study regards customers' preferences when they cannot find the ticket they want. This research concentrates on evaluating the performance of TBS under customer diversion conditions, which is utilized in our research as a percentage matrix. According to the experts' opinion, customers have 3 possibilities: Buying another product, waiting for a seat of the same product or not purchase anything when the desired ticket is unavailable. Adding customer behavior to the simulation process helps us find a better revenue-generating bucket.

This study is the first application of an alternative booking system for Turkish railways and implements a booking system with buckets in Turkish railways. This paper also contributes in terms of considering customer behavior in a booking system with buckets. To the best of our knowledge, customer diversion has never been applied before in the railway industry. The proposed TBS performs better than the PBL and the FCFS. When the demand is high, all methods have yielded their best results, i.e. the highest revenue. At low demand, the success of all techniques is very close to each other. The positive aspects of the TBS are the more profitable use of the empty seats with the ticket pool and the effective distribution of the capacity to

the products through the buckets. On the negative side, finding the optimum buckets takes time and processing power.

If we ignore the misleading results due to the missing data, we can say that the gain will improve with TBS with the available data, even in its pure form. If capacity cannot be increased, it may be wise to encourage customers to wait. Thus, empty seats can be sold to customers who prefer to wait for a second sale-period. Considering the effects of customer behavior, we can argue that selling tickets in two or more periods will increase revenue. In addition to the increase in revenue, the decrease in the number of rejected customers is obviously important in terms of customer satisfaction.

The seat allocation and ticketing processes of high-speed trains are similar to those on airplanes. For this reason, it would be appropriate for railway transportation companies to use technological advances in software to capture customer behavior more precisely. In the railway sector, hybrid algorithms can be tried with artificial intelligence on seat allocation and booking optimization.

ACKNOWLEDGEMENT

This paper is a part of the PhD thesis of Ahmet Z. Bulum in the Graduate Education Institute, Karabuk University, Karabuk 2021 [Advisor: Assoc. Prof. Dr. Muharrem Dugenci, Co-Advisor: Dr. Mumtaz Ipek].

DISCLOSURE STATEMENT

No potential conflict of interest was reported by the authors.

REFERENCES

- [1] J. I. McGill and G. J. van Ryzin, "Revenue Management: Research Overview and Prospects," *Transportation Science*, vol. 33, no. 2, pp. 233–256, May 1999, <https://doi.org/10.1287/trsc.33.2.233>.
- [2] R. Phillips, *Pricing and Revenue Optimization*. Stanford, CA, USA: Stanford Business Books, 2005.
- [3] S. L. Brumelle and J. I. McGill, "Airline Seat Allocation with Multiple Nested Fare Classes," *Operations Research*, vol. 41, no. 1, pp. 127–137, Feb. 1993, <https://doi.org/10.1287/opre.41.1.127>.
- [4] R. E. Curry, "Optimal Airline Seat Allocation with Fare Classes Nested by Origins and Destinations," *Transportation Science*, vol. 24, no. 3, pp. 193–204, Aug. 1990, <https://doi.org/10.1287/trsc.24.3.193>.
- [5] A. Ciancimino, G. Inzerillo, S. Lucidi, and L. Palagi, "A Mathematical Programming Approach for the Solution of the Railway Yield Management Problem," *Transportation Science*, vol. 33, no. 2, pp. 168–181, May 1999, <https://doi.org/10.1287/trsc.33.2.168>.
- [6] H. Luo, L. Nie, and Z. He, "Modeling of multi-train seat inventory control based on revenue management," in *International Conference on Logistics, Informatics and Service Sciences*, Sydney, NSW, Australia, Jul. 2016, pp. 1–6, <https://doi.org/10.1109/LISS.2016.7854371>.
- [7] Z. Xie, W. Zhu, and L. Zheng, "A Dynamic Railway Seat Allocation Problem," in *Industrial and Systems Engineering Research Conference*, Puerto Rico, PR, USA, Dec. 2013, pp. 3480–3489.
- [8] Y. Bao, J. Liu, M. Ma, and L. Meng, "Seat inventory control methods for Chinese passenger railways," *Journal of Central South University*, vol. 21, no. 4, pp. 1672–1682, Apr. 2014, <https://doi.org/10.1007/s11771-014-2109-y>.
- [9] P. Hetrakul and C. Cirillo, "A latent class choice based model system for railway optimal pricing and seat allocation," *Transportation Research Part E: Logistics and Transportation Review*, vol. 61, pp. 68–83, Jan. 2014, <https://doi.org/10.1016/j.tre.2013.10.005>.
- [10] A. Armstrong and J. Meissner, "Railway Revenue Management: Overview and Models," 2010. <https://eprints.lancs.ac.uk/id/eprint/49017>.

- [11] W. Yuan and L. Nie, "Optimization of seat allocation with fixed prices: An application of railway revenue management in China," *PLOS ONE*, vol. 15, no. 4, Apr. 2020, Art. no. e0231706, <https://doi.org/10.1371/journal.pone.0231706>.
- [12] C. Cizaire and P. Belobaba, "Joint optimization of airline pricing and fare class seat allocation," *Journal of Revenue and Pricing Management*, vol. 12, no. 1, pp. 83–93, Jan. 2013, <https://doi.org/10.1057/rpm.2012.27>.
- [13] G. Dutta and D. P. Marodia, "Comparison of forecasting techniques in revenue management for a national railway in an emerging Asian economy," *International Journal of Revenue Management*, vol. 8, no. 2, pp. 130–152, Jan. 2015, <https://doi.org/10.1504/IJRM.2015.070000>.
- [14] X. Wang, H. Wang, and X. Zhang, "Stochastic seat allocation models for passenger rail transportation under customer choice," *Transportation Research Part E: Logistics and Transportation Review*, vol. 96, pp. 95–112, Dec. 2016, <https://doi.org/10.1016/j.tre.2016.10.003>.
- [15] H. Jafarzadeh, N. Moradinasab, and M. Elyasi, "An Enhanced Genetic Algorithm for the Generalized Traveling Salesman Problem," *Engineering, Technology & Applied Science Research*, vol. 7, no. 6, pp. 2260–2265, Dec. 2017, <https://doi.org/10.48084/etasr.1570>.
- [16] T. Kara and M. C. Savas, "Design and Simulation of a Decentralized Railway Traffic Control System," *Engineering, Technology & Applied Science Research*, vol. 6, no. 2, pp. 945–951, Apr. 2016, <https://doi.org/10.48084/etasr.631>.
- [17] J. Zheng, J. Liu, and D. B. Clarke, "Ticket Fare Optimization for China's High-Speed Railway Based on Passenger Choice Behavior," *Discrete Dynamics in Nature and Society*, vol. 2017, Feb. 2017, Art. no. e6237642, <https://doi.org/10.1155/2017/6237642>.
- [18] J. Zheng and J. Liu, "The Research on Ticket Fare Optimization for China's High-Speed Train," *Mathematical Problems in Engineering*, vol. 2016, Aug. 2016, Art. no. e5073053, <https://doi.org/10.1155/2016/5073053>.
- [19] A. Nikseresh and K. Ziarati, "A Demand Estimation Algorithm for Inventory Management Systems Using Censored Data," *Engineering, Technology & Applied Science Research*, vol. 7, no. 6, pp. 2215–2221, Dec. 2017, <https://doi.org/10.48084/etasr.1517>.
- [20] Z. Xiaoqiang, M. Lang, and Z. Jin, "Dynamic pricing for passenger groups of high-speed rail transportation," *Journal of Rail Transport Planning & Management*, vol. 6, no. 4, pp. 346–356, Jan. 2017, <https://doi.org/10.1016/j.jrtpm.2017.01.001>.
- [21] M. Qin, Y. Li, and G. Che, "Railway passenger ticket pricing policy portfolio," in *International Conference on Logistics, Informatics and Service Sciences*, Sydney, NSW, Australia, Jul. 2016, pp. 1–5, <https://doi.org/10.1109/LISS.2016.7854432>.
- [22] G. Dutta and P. Ghosh, "A passenger revenue management system (RMS) for a National Railway in an Emerging Asian Economy," *Journal of Revenue and Pricing Management*, vol. 11, no. 5, pp. 487–499, Sep. 2012, <https://doi.org/10.1057/rpm.2012.10>.
- [23] K. T. Talluri and G. J. van Ryzin, *The Theory and Practice of Revenue Management*. Boston, MA, USA: Springer, 2005.
- [24] P.-S. You, "An efficient computational approach for railway booking problems," *European Journal of Operational Research*, vol. 185, no. 2, pp. 811–824, Mar. 2008, <https://doi.org/10.1016/j.ejor.2006.12.049>.
- [25] X. Jiang, X. Chen, L. Zhang, and R. Zhang, "Dynamic Demand Forecasting and Ticket Assignment for High-Speed Rail Revenue Management in China," *Transportation Research Record*, vol. 2475, no. 1, pp. 37–45, Jan. 2015, <https://doi.org/10.3141/2475-05>.
- [26] M. Riss, J. Cote, and G. Savard, "A new revenue optimization tool for high-speed railway: finding the right equilibrium between revenue growth and commercial objectives," in *8th World Congress on Railway Research*, Seoul, Korea, Dec. 2008.
- [27] P. Hetrakul, "Discrete choice models for revenue management," Ph.D. dissertation, University of Maryland, College Park, MD, USA, 2012.
- [28] S. S. Azadeh, M. Hosseinalifam, and G. Savard, "The impact of customer behavior models on revenue management systems," *Computational Management Science*, vol. 12, no. 1, pp. 99–109, Jan. 2015, <https://doi.org/10.1007/s10287-014-0204-z>.
- [29] W. L. Cooper, T. Homem-de-Mello, and A. J. Kleywegt, "Models of the Spiral-Down Effect in Revenue Management," *Operations Research*, vol. 54, no. 5, pp. 968–987, Oct. 2006, <https://doi.org/10.1287/opre.1060.0304>.
- [30] S.-W. Kim, "The impact of customer buying behavior on the optimal allocation decisions," *International Journal of Production Economics*, vol. 163, pp. 71–88, May 2015, <https://doi.org/10.1016/j.ijpe.2015.02.009>.
- [31] J. G. Wilson, C. K. Anderson, and S.-W. Kim, "Optimal booking limits in the presence of strategic consumer behavior," *International Transactions in Operational Research*, vol. 13, no. 2, pp. 99–110, 2006, <https://doi.org/10.1111/j.1475-3995.2006.00537.x>.
- [32] A. Sen and A. X. Zhang, "The newsboy problem with multiple demand classes," *IIE Transactions*, vol. 31, no. 5, pp. 431–444, May 1999, <https://doi.org/10.1023/A:1007549223664>.
- [33] P. P. Belobaba and L. R. Weatherford, "Comparing Decision Rules that Incorporate Customer Diversion in Perishable Asset Revenue Management Situations," *Decision Sciences*, vol. 27, no. 2, pp. 343–363, 1996, <https://doi.org/10.1111/j.1540-5915.1996.tb00856.x>.
- [34] I. S. Yeoman and U. McMahon-Beattie, "The turning points of revenue management: a brief history of future evolution," *Journal of Tourism Futures*, vol. 3, no. 1, pp. 66–72, Jan. 2017, <https://doi.org/10.1108/JTF-11-2016-0040>.
- [35] B. Vinod, "Evolution of yield management in travel," *Journal of Revenue and Pricing Management*, vol. 15, no. 3, pp. 203–211, Jul. 2016, <https://doi.org/10.1057/rpm.2016.15>.
- [36] A. K. Strauss, R. Klein, and C. Steinhardt, "A review of choice-based revenue management: Theory and methods," *European Journal of Operational Research*, vol. 271, no. 2, pp. 375–387, Dec. 2018, <https://doi.org/10.1016/j.ejor.2018.01.011>.
- [37] M.-E. A. Martinez, M.-A. G. Borja, and J.-A. M. Jimenez, "Yield Management As A Pricing Mechanism," *Review of Business Information Systems*, vol. 15, no. 5, pp. 51–60, Sep. 2011, <https://doi.org/10.19030/rbis.v15i5.6018>.
- [38] R. K. Roy, *Design of Experiments Using The Taguchi Approach: 16 Steps to Product and Process Improvement*. New York, NY, USA: Wiley, 2001.

The Effect of Spatial Configuration on the Movement Distribution Behavior

The Case Study of Constantine Old Town (Algeria)

Fouzia Fareh

LACOMOFA Laboratory
Department of Architecture
8 May 1945 Guelma University
Guelma, Algeria
fareh.fouzia@univ-guelma.dz

Djamel Alkama

LACOMOFA Laboratory
Department of Architecture
8 May 1945 Guelma University
Guelma, Algeria
alkama.djamel@univ-guelma.dz

Received: 30 June 2022 | Revised: 14 July 2022 | Accepted: 16 July 2022

Abstract-This study examines the correlation between spatial configuration and movement behavior within the traditional urban fabric of Constantine city. The distribution of pedestrian movement was modeled in relation to the syntactic measures of street networks. The results showed a significant correlation between pedestrian volume with integration and choice measures at the global scale (Rn), however, the local scale (R3) did not capture the variance and the presence of the movement. The measures of connectivity that are used to describe the density of street connections also revealed a weak association with the presence of people within the dense traditional layout of the research area. The results support the previous findings of space syntax theory, asserting the important role of the street network structure in assessing the configurational accessibility of a given spatial layout. However, we do not assert its exclusive role in determining the natural-movement patterns. Therefore, consideration should be given to more external indicators, like the interaction with land use and socioeconomic activities. We conclude that examining the network radius-based attributes of street configuration can provide a clear understanding of spatial variations in pedestrian activity within multi-scale walkable areas, which helps planners improve the livability of the city by designing more friendly walkable streets.

Keywords-movement; spatial configuration; walking; pedestrian volume; space syntax

I. INTRODUCTION

Walking is a freely and accessible mode of transportation. It has become a field with a great interest in socially engaged communities. Designing walkable places is gaining more attention for their positive outcomes related to sustainability, social life, health, and economy. Walkability has become one of the most investigated realms, not only in architecture and urban design, but also in the fields of public health and transportation [1]. Because of the growing knowledge of the walking advantages, the concept "walkable" has been newly labeled as encouraging physical activity [2]. Walkability is being evaluated as an "environmental justice issue" and it can be a good indicator of the physical quality of urban areas. As a result, there is an increasing demand to understand the

complexity behind the interaction between the different conditions of the built environment and the walking behavior of inhabitants [4-8]. Disciplines from various scientific fields, such as urban design and planning, architecture, traffic management, and public health are taking different approaches and implementing appropriate techniques to capture how people walk in the urban environment.

The association between the spatial configuration and pedestrian behavior at the street level has been investigated mostly within the conceptual and methodological framework of the space syntax approach [9-16]. This theoretical framework is based on a topological-visual analysis of the street network called the axial map, defined as the smallest set of straight axial lines covering the urban street network [12, 13, 17]. These studies have been conducted with respect to the concept of "natural movement," which means that the configuration of the street network determines extensively the distribution of movement within that network independently of other variables [17-20].

The prevalent assumption behind pedestrian volume modeling is that individuals tend to make their trips as short as possible by choosing a short trip length [21]. Therefore, street centrality indices are the most widely used measures to evaluate "natural movement." It is the calculation of the shortest paths between all the network's origin-destination pairs. Based on axial or segment lines, the centrality measures are defined mainly by two main values: first, the closeness of a given axial line to all other axial lines within the network and second, the degree to which a given axial line acts as an intermediary path within the network, or the so-called betweenness. Pedestrian volume models using the space syntax method through the integration level of the axial lines have revealed a squared correlation coefficient (R^2) ranging from 0.55 to 0.75 in London [13] and Dutch urban areas [22]. Nevertheless, there is divergence regarding the dominant role of the street network centrality measures in evaluating pedestrian movement activity, different movement volume models that were applied in different cities investigated other explanatory variables like land-use layout, which is described

as a non-negligible factor that has a crucial effect on pedestrian movement in urban space [23-26]. Other studies combined land use and spatial variables to explore the extent the built environment influences pedestrian patterns [1, 27-29]. These studies found that spatial configuration has a significantly greater correlation than land use does to pedestrian movement, but the possibility of combining them may produce greater results in capturing pedestrian movement volume [30]. The physical dimension of the street network can also influence the amount and presence of pedestrians. Many studies in this stream have emphasized an association with the sidewalk width, which tends to regulate the number of pedestrians on a given road [31, 32]. From the above, we can say that whatever the methodological framework used to evaluate pedestrian distribution, there is a consensus in the body of literature about the own social logic of space that affects human behavior, such as pedestrian movement from one place to another [33]. Therefore, a clear understanding of the precise nature of the relationship between spatial configuration and movement is more than necessary for better design and planning.

To address how people move in a dense urban area and by adopting appropriate measures which are sensitive to the spatial structure of street networks, we will explore in this study the movement behavior patterns related to syntactic attributes of Constantine's old town. We will attempt to clarify the extent the street network design affects pedestrian distribution movement at the scale of the town and neighborhoods. In doing so, we tend to enrich the body of literature that scrutinizes the aspects of the relationship that link movement behavior to spatial configuration as the long-term framework that influences the evolution of urban function.

II. METHODOLOGY

A. Study Area

Our research area is the old town of Constantine City in Algeria. It is the city's earliest settlement. It was founded on a rock at an altitude of 700 meters, surrounded by a cliff at a depth of 200 meters. The urban form is a mixture of different civilizations (Roman, Ottoman, and colonial). Each of them has left an imprint on the overall layout of the city. Its street network is mainly made up of an organic grid penetrated by long rectilinear commercial roads. At the back of the town, we find the residential neighborhoods as a compact fabric with winding and straight Derbs, or alleys, to allow transitioning from private to public spaces.



Fig. 1. The old town's street network in the context of Constantine city (© 2022 CNES/Airbus, Maxar Technologies).

Like in the Arab Medina configuration, the old town has busy roads and quiet parts [34]. It has also traditional markets, where artisans keep their workshops half inside, half on the street. A big part of the old town is car-free, which attracts daily familiar and unfamiliar visitors. The traditional town keeps confirming Constantine's urban and historical identity due to its outstanding location and unique spatial shape. Based on its specific urban network, we will attempt to investigate the walking behavior in such a complex fabric by exploring the extent this network affects the amount and the distribution of pedestrian movement.

B. Research Method

To investigate the effect of spatial layout configuration on pedestrian movement, we used the space syntax method by establishing an axial map based on the street network as demonstrated in Figure 2. An axial map is a set of axial lines that refers to an abstract representation of the street network. Each axial line represents the fewest and longest visible line of the street. It is equal to the smallest human-perceivable unit of space [21]. The next step was to generate a space syntax analysis by using Depth Map software (X) with the Space Syntax Toolkit, see Figures 2-4. Depth Map is a multi-platform software developed to perform multiple spatial network analyses in order to explore the complexity of social behavior in a given built environment. Normally, the preliminary results of the axial analysis will show how urban space is structured and how human behavior can be predicted. According to space syntax theory, there is a strong and significant relationship between spatial layout and movement patterns, or what we call "natural movement," which means that spatial configuration orients and regulates the presence and the distribution of movement in a given open space without the intervention of any other factors [11]. Based on this assumption, we will investigate the relationship between spatial pattern attributes and movement patterns in our research area. Through this work, we would like to assert that our objective is not to test the already well established Space Syntax principles, but rather to seek a new understanding of natural movement in different urban areas with different geographically and socially built environments.

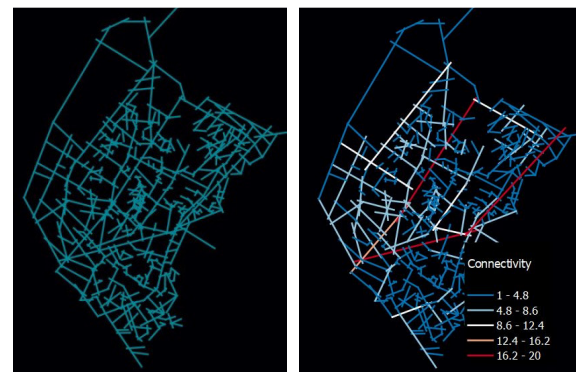


Fig. 2. Axial map (left) and connectivity map (right).

C. Data Collection

To realize our pedestrian movement model, we have used the gate count observation technique, which consists of

counting the average number of pedestrians per hour on a given axis of the spatial network. The measurement locations in the research area are selected according to the degree of the people's presence and use of street space, as shown in Figure 5. The street sample represents different syntactic measures and ranges from busy to lightly used. The counting was applied to specific points in each street axis, where an imaginary crossing line was drawn virtually from these points to the other side of the street space. The number of the moving pedestrians was recorded in a prepared table to be further analyzed. The counting was carried out for 5 minutes every hour for 6 hours (9-10, 10-11, 11-12, 2-3, 3-4, 4-5) at each location on major streets, and for 10 minutes every hour on minor streets to reduce the variance of movement values between different types of roads, see Figure 9. The counting was done simultaneously for all survey points on each street. The observations took place on sunny weekdays between 9 am and 5 pm. These times are chosen for two reasons: the operability of commercial activity during those time periods and because pedestrian traffic increases during rush hours, especially at the end of the workday and after school.

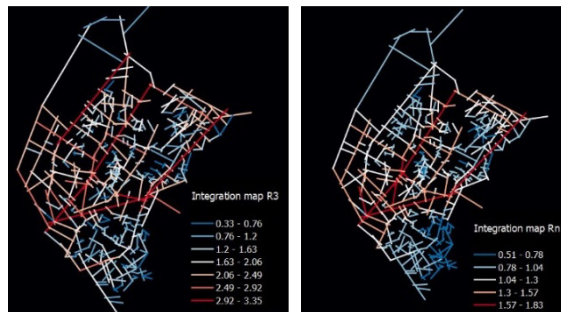


Fig. 3. Integration_(R3) map (left) and Integration_(Rn) map (right).

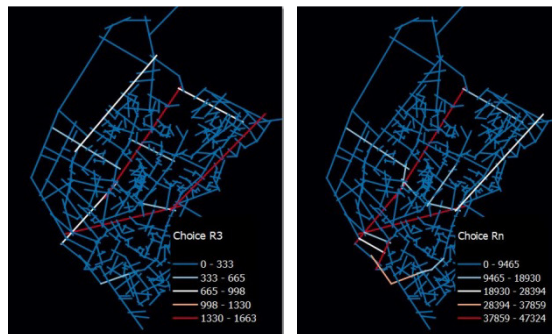


Fig. 4. Choice_(R3) map (left) and Choice_(Rn) map (right).

The entire research data set included 20 road segments where pedestrian movement volume was sampled in different parts of the town, namely: La Kasbah and Souika neighborhoods, La Rue De France street, Etrik Edjdida Street, Zighoud Youcef street, Eressif, and Souk Elasser sub-neighborhoods. The 20 sampled street segments were encoded according to the depth map output reference as the following: (26, 32, 34, 36, 38, 39, 43, 62, 80, 145, 174, 188, 227, 287, 289, 296, 308, 382, 383), see Figure 7. In order to explore the relationship between pedestrian movement and space configuration, an assumption of correlation was established

between the two variables by using the outcomes of gate count observation with the syntactic attributes of the research area. The association of variables was checked through the JMP package and was visualized through the Geographical Information System (GIS).

III. RESULTS AND DISCUSSION

In order to examine the effect of spatial configuration on natural movement patterns, and after making an axial analysis of the urban network, Pearson correlation was performed to test whether there is an association between the pedestrian volume and the syntactic properties of the urban layout as shown in Table II. The results showed significant disparities in pedestrian distribution among the different streets in the research area, Figure 6 illustrates the average pedestrian volume per road section in the research areas, where we observed a higher volume of pedestrian movement in the town's major commercial streets, such as La Rue De France, Etrik Edjdida, and Eressif streets, which are characterized by a high rate of retail and shops, compared to the other streets, such as Swika, Zighoud Youcef, and La Kasbah. Figure 8 shows the distribution frequency of the average pedestrian volume per hour. This distribution can be described as heavy-tailed, in other words, most of the survey points have a low volume, while only a few survey points have a high volume of pedestrian movement. This finding is mentioned in [32, 33], which found that a minor percentage of roads have significant traffic movement, whereas their majority have low traffic volumes. Since the pedestrian movement has a heavy-tailed distribution, it was normalized by using the log function (with the natural logarithm).

Figure 10 reveals the correlations between spatial configuration variables and pedestrian movement volume distribution. The results showed that the correlation with the street connectivity variable, which is based on the number of roads connected directly to each street, is not significant (P -value = 0.43), so there is no association between the number of pedestrians and the degree of connectivity in the street network. However, the pedestrian volume variable was found to positively and strongly correlate with two spatial variables, which are the global integration (with $r = 0.799$ and $p < 0.01$) and the global choice (with $r = 0.842$ and $p < 0.01$). These two spatial variables tend to have the highest squared correlation coefficient. The correlation model explained this association at 63% for integration and 70% for choice. Surprisingly, no correlation was found between movement distribution and spatial variables at the local scale (R3), corresponding to 400 meters, which is an appropriate distance for walking. The P -value in this case is ($P = 0.433$) for integration and ($P = 0.436$), so correlation is not significant at this level.

TABLE I. DESCRIPTIVE STATISTICS OF THE STUDY VARIABLES

Variable	N	Min	Max	Mean	Std. Deviation
Choice_Rn	20	28	1663	631.75	564.227
Choice_R3	20	3	1663	481.59	564.126
Integration_Rn	20	11.525	18.320	14.131	2.148
Integration_R3	20	2.257	33.549	21.436	9.619
Connectivity	20	3	20	9.24	5.618
Pedestrian Volume	20	383	3138	1215.24	918.610



Fig. 5. Survey points in the search area.

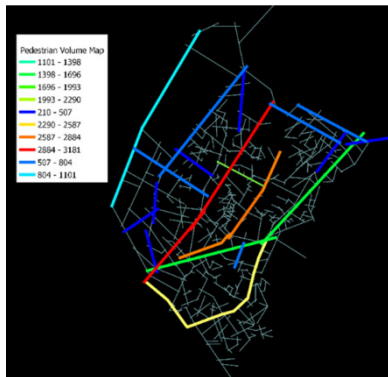


Fig. 6. The Average observed movement volume on 20 axes of the research area.

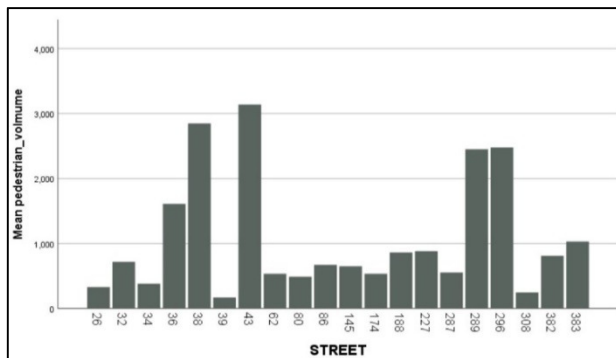


Fig. 7. The average pedestrian movement volume per street section.

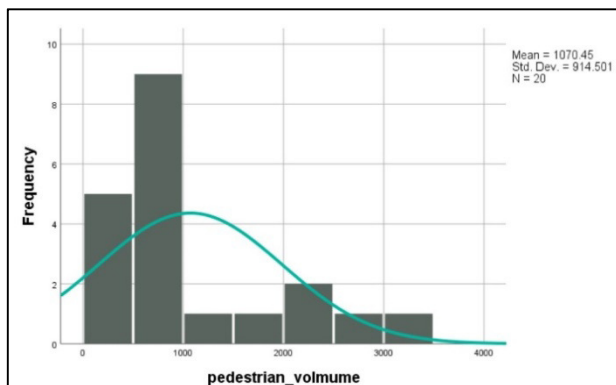


Fig. 8. Pedestrian volume frequency.

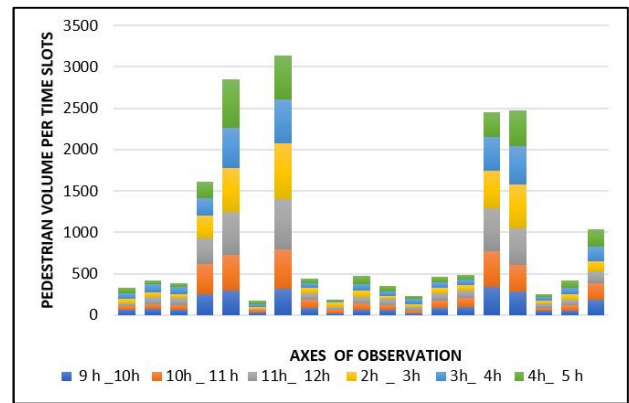


Fig. 9. Distribution of pedestrian volume on the six-time slots on each selected street.

TABLE II. PEARSON'S CORRELATIONS BETWEEN SPATIAL ATTRIBUTES AND PEDESTRIAN MOVEMENT VOLUME

Variable	P-value	Significance	(R)	(R ²)
Street Connectivity	0.434	Not significant	-0.436	0.190
Street Integration_Rn	0.000	Significant	0.799**	0.639
Street Integration_R3	0.433	Significant	-0.204	0.004
Street Choice_Rn	0.000	Highly significant	0.842**	0.709
Street Choice_R3	0.434	Not significant	-0.203	0.041

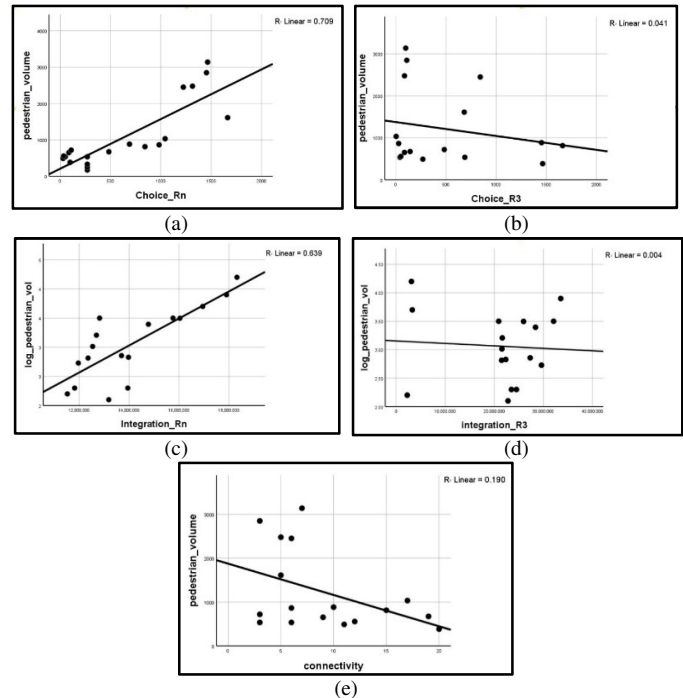


Fig. 10. Correlation of spatial variables with the average pedestrian volume per street: (a) Pedestrian volume per choice_Rn, (b) pedestrian volume per choice_R3, (c) pedestrian volume per integration_Rn, (d) pedestrian volume per integration_R3, (e) pedestrian volume per connectivity.

From the results, we conclude that the movement rate in the research area is showing a positive and significant correlation with spatial configuration only at the global scale. However,

the local scale configuration cannot capture the distribution of the natural movement. The old town has the potential to attract "through-movement" through the major streets because of its central location near the active and alive colonial center. Thus, configurational accessibility could be a need for a pedestrian-friendly environment. In other words, street networks with a high degree of configurational accessibility (in our case represented by Radius (n) integration) may satisfy one or more people's requirements when they are about to walk. However, walking in the old town's local neighborhoods cannot benefit from this potential because it is seen as confusing and difficult to grasp by unfamiliar users. But in some parts of the same neighborhoods, despite the fact that the attention of users can be evaded in dense and winding roads, as in the cases of Eressif and Rahbat Essouf, which are characterized by a high level of commercial activity and handicraft shops, we can still find a high rate of pedestrians. In other parts, however, walking activity is very low, especially in Swika neighborhood, which has some local socio-cultural features. From this, we can say that part of our results goes against the natural movement theory, which stipulates the exclusive role of spatial configuration in explaining the distribution patterns of movement.

IV. CONCLUSION

In this study, we have examined the correlation between spatial configuration and pedestrian traffic volume by using the configurational accessibility of the street network in the old town of Constantine city. The results showed that pedestrian volume in main commercial streets with a high rate of choice and integration is more significant. However, some segment streets located inside the local residential neighborhoods carry weaker pedestrian traffic. It was also observed that by going inside the dense residential fabric, where the network has a tree-like structure and the integration has its lowest values, movement distribution rates are significantly high, especially throughout the roads having commercial activities and craft shops as in Eressif, Rahbat Essouf, and a big part of Eswika neighborhood. Hence, we deduced that spatial configuration is an important but not sufficient parameter to capture movement behavior in all types and levels of configuration. In residential neighborhoods, for instance, walking depends more on previous experiences for wayfinding than on the street network configuration itself. However, movement in major business areas is generally captured by the spatial network configuration itself. These results do not totally agree with Hillier's to-movement principle, asserting the independent role of the street network design in explaining movement behavior. For that reason, consideration should be given to the correlation of more external indicators as the interaction between land use and population density, which will be investigated in further research. Finally, it can be said that examining the movement distribution patterns of a given spatial layout can provide a clear insight into understanding the dysfunction of certain urban fabrics that can be directly linked to the inequity of walking behavior.

The current study can be a contributing factor in revising the way settlements are planned or revitalizing the existing ones by mixing land use within the segregated urban fabrics

and designing streets in a way that allows safety and comfort, which will motivate walking activity, which in turn will regenerate livability.

REFERENCES

- [1] O. Ozer and A. S. Kubat, "Walkability: Perceived and measured qualities in action," *A/Z ITU Journal of the Faculty of Architecture*, vol. 11, no. 2, pp. 101–117, 2014.
- [2] A. S. Kubat, O. Ozer, and A. Ozbil, "Defining a strategical framework for urban pedestrianization projects," in *9th International Space Syntax Symposium*, Seoul, South Korea, Nov. 2013.
- [3] M. R. Greenberg and J. Renne, "Where does walkability matter the most? An environmental justice interpretation of New Jersey data," *Journal of Urban Health*, vol. 82, no. 1, pp. 90–100, Mar. 2005, <https://doi.org/10.1093/jurban/jti011>.
- [4] L. D. Frank *et al.*, "The development of a walkability index: application to the Neighborhood Quality of Life Study," *British Journal of Sports Medicine*, vol. 44, no. 13, pp. 924–933, Oct. 2010, <https://doi.org/10.1136/bjsm.2009.058701>.
- [5] F. Lima, N. Brown, and J. Duarte, "Urban Design Optimization: Generative Approaches towards Urban Fabrics with Improved Transit Accessibility and Walkability-generative approaches towards urban fabrics with improved transit accessibility and walkability," in *26th International Conference of the Association for Computer-Aided Architectural Design Research in Asia*, Hong Kong, China, Apr. 2021.
- [6] P. K. Maghelal and C. J. Capp, "Walkability: a review of existing pedestrian indices," *URISA Journal*, vol. 23, no. 2, pp. 5–20, Jul. 2011.
- [7] K. Manaugh and A. El-Geneidy, "Validating walkability indices: How do different households respond to the walkability of their neighborhood?," *Transportation Research Part D: Transport and Environment*, vol. 16, no. 4, pp. 309–315, Jun. 2011, <https://doi.org/10.1016/j.trd.2011.01.009>.
- [8] M. Socharoentum and H. A. Karimi, "Analyzing Personalized Walking in Smart Cities Through a Multi-Modal Transportation Simulation Environment," *International Journal On Advances in Internet Technology*, vol. 8, no. 3 & 4, pp. 93–100, 2015.
- [9] M. Bielik, R. Konig, S. Schneider, and T. Varoudis, "Measuring the Impact of Street Network Configuration on the Accessibility to People and Walking Attractors," *Networks and Spatial Economics*, vol. 18, no. 3, pp. 657–676, Sep. 2018, <https://doi.org/10.1007/s11067-018-9426-x>.
- [10] J. Hanson and B. Hillier, "The architecture of community: some new proposals on the social consequences of architectural and planning decisions," *Architecture et Comportement/Architecture and Behaviour*, vol. 3, no. 3, pp. 251–273, 1987.
- [11] B. Hillier and S. Iida, "Network and Psychological Effects in Urban Movement," in *International Conference on Spatial Information Theory*, Ellicottville, NY, USA, Sep. 2005, pp. 475–490, https://doi.org/10.1007/11556114_30.
- [12] B. Hillier, J. Hanson, and J. Peponis, "What do we mean by building function?," in *Designing for building utilisation*, London, UK: University College London, 1984, pp. 61–72.
- [13] B. Hillier, A. Penn, J. Hanson, T. Grajewski, and J. Xu, "Natural Movement: Or, Configuration and Attraction in Urban Pedestrian Movement," *Environment and Planning B: Planning and Design*, vol. 20, no. 1, pp. 29–66, Feb. 1993, <https://doi.org/10.1068/b200029>.
- [14] B. Jiang and C. Liu, "Street-based topological representations and analyses for predicting traffic flow in GIS," *International Journal of Geographical Information Science*, vol. 23, no. 9, pp. 1119–1137, Sep. 2009, <https://doi.org/10.1080/13658810701690448>.
- [15] A. Penn, B. Hillier, D. Banister, and J. Xu, "Configurational Modelling of Urban Movement Networks," *Environment and Planning B: Planning and Design*, vol. 25, no. 1, pp. 59–84, Feb. 1998, <https://doi.org/10.1068/b250059>.
- [16] A. van Nes and C. Yamu, "Space Syntax: A method to measure urban space related to social, economic and cognitive factors," in *The Virtual and the Real in Planning and Urban Design*, London, UK: Routledge, 2017, pp. 136–150.

- [17] B. Hillier, *Space is the machine: a configurational theory of architecture*. London, UK: Space Syntax, 2007.
- [18] J. Peponis, J. Wineman, S. Bafna, M. Rashid, and S. H. Kim, "On the Generation of Linear Representations of Spatial Configuration," *Environment and Planning B: Planning and Design*, vol. 25, no. 4, pp. 559–576, Aug. 1998, <https://doi.org/10.1068/b250559>.
- [19] A. Penn, "Space Syntax And Spatial Cognition: Or Why the Axial Line?," *Environment and Behavior*, vol. 35, no. 1, pp. 30–65, Jan. 2003, <https://doi.org/10.1177/0013916502238864>.
- [20] A. Turner, A. Penn, and B. Hillier, "An Algorithmic Definition of the Axial Map," *Environment and Planning B: Planning and Design*, vol. 32, no. 3, pp. 425–444, Jun. 2005, <https://doi.org/10.1068/b31097>.
- [21] B. Hillier, "The Hidden Geometry of Deformed Grids: Or, Why Space Syntax Works, When it Looks as Though it Shouldn't," *Environment and Planning B: Planning and Design*, vol. 26, no. 2, pp. 169–191, Apr. 1999, <https://doi.org/10.1068/b4125>.
- [22] S. Read, "Space Syntax and the Dutch City," *Environment and Planning B: Planning and Design*, vol. 26, no. 2, pp. 251–264, Apr. 1999, <https://doi.org/10.1068/b4425>.
- [23] P. P. Koh and Y. D. Wong, "Comparing pedestrians' needs and behaviours in different land use environments," *Journal of Transport Geography*, vol. 26, pp. 43–50, Jan. 2013, <https://doi.org/10.1016/j.jtrangeo.2012.08.012>.
- [24] Y. Lerman and I. Omer, "Urban area types and spatial distribution of pedestrians: Lessons from Tel Aviv," *Computers, Environment and Urban Systems*, vol. 55, pp. 11–23, Jan. 2016, <https://doi.org/10.1016/j.compenurbsys.2015.09.010>.
- [25] X. Liu and J. Griswold, "Pedestrian Volume Modeling: A Case Study of San Francisco," *Yearbook of the Association of Pacific Coast Geographers*, vol. 71, pp. 164–181, 2009.
- [26] J. Peponis, C. Ross, and M. Rashid, "The structure of urban space, movement and co-presence: The case of Atlanta," *Geoforum*, vol. 28, no. 3, pp. 341–358, Aug. 1997, [https://doi.org/10.1016/S0016-7185\(97\)00016-X](https://doi.org/10.1016/S0016-7185(97)00016-X).
- [27] I. Omer, Y. Rofo, and Y. Lerman, "The impact of planning on pedestrian movement: contrasting pedestrian movement models in pre-modern and modern neighborhoods in Israel," *International Journal of Geographical Information Science*, vol. 29, no. 12, pp. 2121–2142, Dec. 2015, <https://doi.org/10.1080/13658816.2015.1063638>.
- [28] A. Willis, N. Gjersoe, C. Havard, J. Kerridge, and R. Kukla, "Human Movement Behaviour in Urban Spaces: Implications for the Design and Modelling of Effective Pedestrian Environments," *Environment and Planning B: Planning and Design*, vol. 31, no. 6, pp. 805–828, Dec. 2004, <https://doi.org/10.1068/b3060>.
- [29] J. Zacharias, "Pedestrian Behavior Pedestrian Behavior and Perception in Urban Walking Environments," *Journal of Planning Literature*, vol. 16, no. 1, pp. 3–18, Aug. 2001, <https://doi.org/10.1177/08854120122093249>.
- [30] N. Roford and D. Ragland, "Pedestrian Volume Modeling for Traffic Safety and Exposure Analysis: The Case of Boston, Massachusetts," Apr. 2006, [Online]. Available: <https://escholarship.org/uc/item/61n3s4zr>.
- [31] J. Desyllas, E. Duxbury, E. Ward, and A. Hudson-Smith, "Pedestrian demand modelling of large cities: an applied example from London," Centre for Advanced Spatial Analysis, University College London, London, UK, Paper 62, Jun. 2003.
- [32] N. S. A. Sukor and S. F. M. Fisal, "Safety, Connectivity, and Comfortability as Improvement Indicators of Walkability to the Bus Stops in Penang Island," *Engineering, Technology & Applied Science Research*, vol. 10, no. 6, pp. 6450–6455, Dec. 2020, <https://doi.org/10.48084/etasr.3849>.
- [33] A. Rahmane and M. Abbaoui, "The Architectural Genotype Approach in Contemporary Housing (1995 to 2010): The Case Study of Setif, Algeria," *Engineering, Technology & Applied Science Research*, vol. 11, no. 1, pp. 6810–6818, Feb. 2021, <https://doi.org/10.48084/etasr.4006>.
- [34] E. Noaime *et al.*, "A Short Review of Influencing Factors of Islamic Architecture in Aleppo, Syria," *Engineering, Technology & Applied Science Research*, vol. 10, no. 3, pp. 5689–5693, Jun. 2020, <https://doi.org/10.48084/etasr.3447>.
- [35] B. Jiang, J. Yin, and S. Zhao, "Characterizing the human mobility pattern in a large street network," *Physical Review E*, vol. 80, no. 2, Aug. 2009, Art. no. 021136, <https://doi.org/10.1103/PhysRevE.80.021136>.
- [36] B. Jiang, "Head/Tail Breaks: A New Classification Scheme for Data with a Heavy-Tailed Distribution," *The Professional Geographer*, vol. 65, no. 3, pp. 482–494, Aug. 2013, <https://doi.org/10.1080/00330124.2012.700499>.

An Experimental and Analytical Study on the Seismic Performance of Piers with Different Foundation Bottom Widths

Takashi Nagao

Research Center for Urban Safety and Security
Kobe University
Kobe City, Japan
nagao@people.kobe-u.ac.jp

Yoshinao Kurachi

Technical Division
Oriental Shiraishi Corporation
Tokyo, Japan
yoshinao.kurachi@orsc.co.jp

Received: 17 May 2022 | Revised: 19 July 2022 | Accepted: 21 July 2022

Abstract—Piers can be severely damaged by earthquakes. When an action of a massive earthquake is assumed, the seismic performance of the pier can be improved by widening the foundation width. A previous horizontal loading study indicated that extending only the Foundation Bottom (FB) width, rather than the complete foundation, can boost seismic resilience while suppressing the increase in building cost. However, the research dealt with only two types of FB width, i.e. normal and widened, and the data for sufficiently assessing the inclination angle of the pier with loading were not obtained. In this study, to evaluate the seismic performance of piers with different FB widths in more detail, horizontal loading tests on piers with ordinary columnar foundations and two types of piers with widened FB were conducted, and the seismic resistance of the three pier types were compared. It was shown that horizontal displacement and inclination angle of the pier can be reduced by widening the FB. Furthermore, finite element analysis was carried out to reproduce the experimental results. The analysis results showed good agreement with the experimental results in terms of pier horizontal displacement and inclination angle.

Keywords—pier; foundation; seismic performance; finite element analysis

I. INTRODUCTION

The pier is a major port structure that facilitates cargo shipping. Since the pier is generally constructed on the soft ground in the coastal area, it can be damaged by earthquakes [1, 2]. Due to the enlargement of ships, the pier is required to be deeper in water depth, which brings about an increase in seismic load. In addition, a considerable lateral spreading pressure may act during a massive earthquake, which seismic design codes [3, 4] do not adequately account for [5]. Furthermore, the pier is strongly influenced by the ground deformation during earthquakes and undergoes residual displacement [6, 7], even when the structural member is not injured [8]. As a result, from the viewpoint of evaluating the serviceability of the pier, residual displacement needs to be assessed with high accuracy along with structural member safety. When the seismic resistance of the pier is insufficient against the reference earthquake, the cross-sectional width of

the foundation is increased to improve the seismic resistance in design practice, but the increase of the foundation width leads to a drastic increase in the construction cost. When a broad foundation is employed, the vertical subgrade reaction operating at the Foundation Bottom (FB) generates rotational resistance moment opposing the inclination of the pier. However, it should be noted that the subgrade reaction modulus decreases with increasing foundation width [9, 10]. As a way to increase the seismic resistance of the pier while keeping the rise of the construction cost mild, a method of widening only the FB was suggested in a previous study [11], and the horizontal loading test showed that the seismic performance is improved by widening the FB. However, in the previous study, only two varieties of FB width were handled, namely normal and widened, and data for adequately measuring the inclination angle of the pier with loads were not collected. In addition, there is no seismic design method that evaluates the seismic performance of a FB widened pier at the moment. In the current research, in order to assess the seismic performance of piers with different FB widths in more detail, new horizontal loading tests on piers with ordinary columnar foundations and two types of pier with widened FB were performed and the seismic resistance of the models was studied. Furthermore, for the development of the seismic design method of the FB widened pier, the findings of the experimental results were reproduced with two-dimensional Finite Element Analysis (FEA) and the reproducibility of the experimental results was demonstrated.

II. METHOD

Horizontal loading experiments of the pier using a mega torque motor were performed. Steel rigid frame models imitating piers with 150mm depth were put in the ground in a soil tank 900mm wide and 500mm deep (Figure 1). These dimensions were set considering the ease of performing the experiment and to prevent the bottom slab of the soil tank from suppressing the settlement of the pier foundation with loading. The pier model was installed in the central part of the soil tank in the depth direction to avoid the effect of ground confinement by the side wall of the soil tank. A steady brace was fitted to

Corresponding author: Takashi Nagao

prevent the pier model from tilting in the soil tank depth direction with loading. Figure 2 demonstrates the specifications of the model. A circular cross-section of 120mm in diameter was employed as the normal type, and pier models with the same shape of the column, FBs of 180mm in width and 120mm in depth were used as the widened 1 type, and FBs of 240mm in width and 120mm in depth were used as the widened 2 type. In the previous study [11], the scaling factor (prototype/model) was 100, whereas in this study, a reduced scaling factor of 50 was attained. The normal model weighs 20.145kg, the widened 1 model weighs 25.145kg, and the widened 2 model weighs 28.635kg.

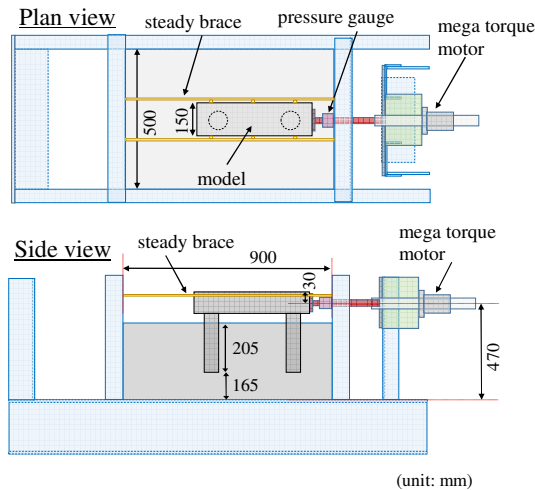


Fig. 1. Soil tank.

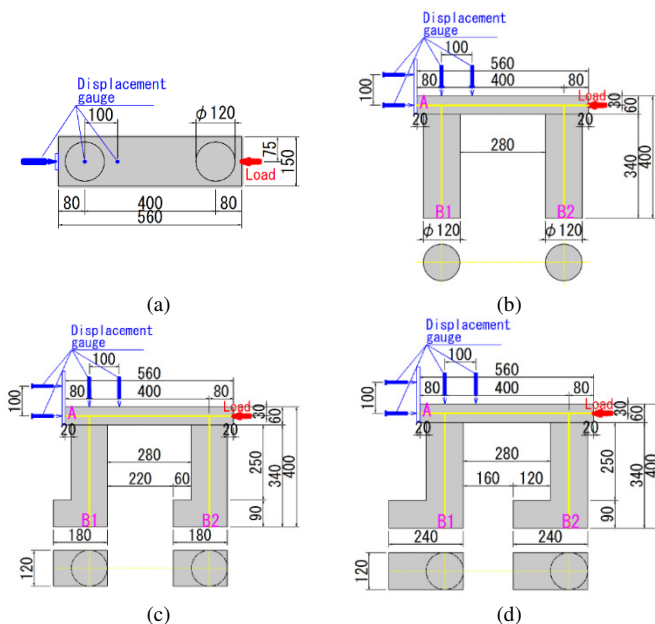


Fig. 2. Model specifications (unit: mm): (a) plan view, (b) side view: normal, (c) side view: widened 1, and (d) side view: widened 2.

The ground was prepared by air pluviation. Tohoku Silica Sand No. 6 in dry state was used. The target relative density of the ground was 77% which corresponds to the dense ground

condition. The foundation of the true pier is embedded into the bedrock to support the structure's weight. To simulate this situation, loading tests and shake table tests have often been performed in which the FB was fixed to the soil tank [12-16]. However, in such cases, the constraint of the FB due to the bedrock is excessively expressed, leading to no settlement or inclination of the foundation due to loading. The bedrock is a very rigid ground, but it slightly deforms when a load is applied from the FB, therefore, the pier is inclined during an earthquake. In this experiment, the FB of the pier model was not fastened to the soil tank but was put at a height of 165mm from the bottom end of the soil tank. The ground's thickness was 370mm. The loading was applied at a constant displacement speed of 1.3mm/s and the greatest displacement was 20mm, which is equivalent to 7m on a real scale by similitude [17] based on the scaling factor. The horizontal and vertical displacements of the pier and horizontal load were captured with a data logger. Displacement gauges were attached to the model superstructure to measure horizontal and vertical displacements. In [11], horizontal and vertical displacements were evaluated by one displacement gauge respectively. As a result, the displacement and inclination angle of the pier could not be accurately measured. In this research, horizontal and vertical displacements were evaluated by two displacement gauges. Noise in the observed data was eliminated similarly to [11] by executing fast Fourier transform and inverse fast Fourier transform after multiplying with a low-pass filter at 1Hz.

III. EXPERIMENTAL RESULTS

The time history of the loading of each case is depicted in Figure 3. In about 10 seconds after loading, the value of load decreased in each case. Because the loading was done at a constant displacement speed, the pier's displacement is progressing with decreasing load after roughly 10 seconds. This is because the main displacement mode of the pier changed from the inclination at the early stage of loading to the sliding in the latter half of loading.

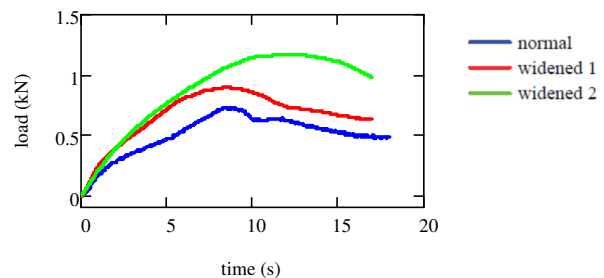


Fig. 3. Time history of load.

As previously stated, this test does not fix the FB of the pier to the soil tank, therefore, sliding happens in the pier. Since the FB of the actual pier is embedded into the bedrock, tilting of the pier occurs when lateral load is applied, but not sliding. Following that, we will focus on the results of the first half of loading. Based on the data of the four displacement gauges, the horizontal displacement at point A of the superstructure and

point B1 of the FB illustrated in Figure 2, and the inclination angle of the pier were determined (Figure 4). The tendency differs between the normal and widened types in the early stages of loading, although there is no significant variation in displacements between the two widened types. For the same load, the horizontal displacements at the FB (point B1) are almost the same, while the horizontal displacement of the superstructure (point A) is significant in the normal type and modest in the widened types. For this reason, the inclination angle of the normal type is larger than that of the widened types.

Figure 5 illustrates the piers' displacements when the load was 0.69kN, which was the maximum load observed for the normal type. Here, the displacements are magnified by a factor of 10. Both the horizontal displacement and inclination are large in the order of normal, widened 1, and widened 2 types. The horizontal displacements are 8.54, 4.84, and 4.28mm respectively and the inclination angles are 0.017, 0.008, and 0.006rad respectively. In the previous study [11], the widened type showed approximately 1/3 times the horizontal displacement compared with the normal type. In this study, the widened types have 1/2–1/3 times the horizontal displacements and 1/2 times the inclination angles compared with the normal type.

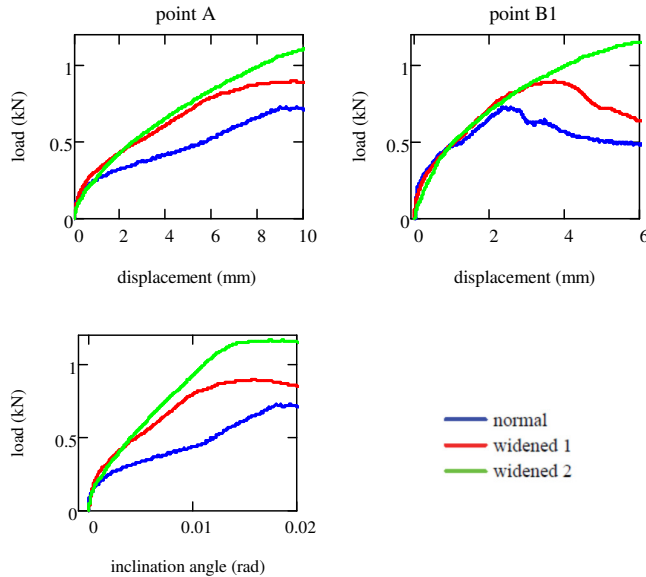


Fig. 4. Horizontal displacement and inclination angle.

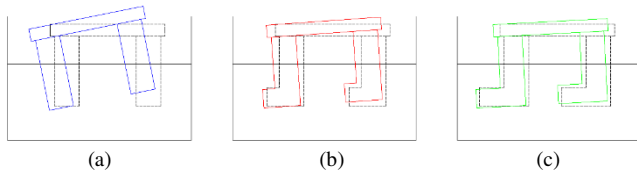


Fig. 5. Displacement of piers: (a) normal, (b) widened 1, (c) widened 2.

As was discussed in [10], when the FB is widened, the Rotational Resistance Moment (RRM) caused by the subgrade reaction acting at the FB surface increases and the shear

deformation at the soil under the FB decreases. In addition, as was discussed in [11], in the widened type, the rotational center is closer to the center of the superstructure when compared with the normal type, therefore, RRM arm length is larger than in the normal type. Those are the major reasons of the high seismic resistance of the FB widened pier when compared with the normal type. The variation in the seismic resistance of the two widened types is remarkable in the range where the horizontal displacement of the superstructure (point A) exceeds 6mm, which is equivalent to 2.1m on the real scale by the similitude [17]. The allowable displacement for quay wall during an earthquake is 1m or less in the seismic design code [6], therefore, this amount of displacement is greater than what is permitted in seismic design. As a result, widening the FB to 1.5 times the width of the foundation column would be sufficient to improve the seismic resilience of the pier.

IV. FINITE ELEMENT ANALYSIS

A. Analytical Method

Two-dimensional FEA was performed to reproduce the experimental results. The analysis code employed is FLIP [18], by which the seismic responses of port structures such as piers have been evaluated [8, 19]. The code employs a multi-spring model [20] to express the ground response under principal stress axes rotation. The nonlinearity of the ground is expressed as (1) using a hyperbolic model [21].

$$\frac{G}{G_0} = \frac{1}{1 + G_0 \gamma / \tau_m} \quad (1)$$

where G is the shear rigidity, G_0 is the initial shear rigidity, γ is the shear strain, and τ_m is the shear strength, which is calculated by [22]:

$$\tau_m = \sigma_m' \sin \phi \quad (2)$$

where σ_m' is the effective confining pressure and ϕ is the shear resistance angle.

The shear resistance angle of the ground is calculated using the relative density by referring to [22]. The ground shear rigidity G_m at each depth is calculated by [23]:

$$G_m = G_{ma} \left(\frac{\sigma_m'}{\sigma_{ma}'} \right)^{0.5} \quad (3)$$

where G_m is the shear rigidity, G_{ma} is the reference shear rigidity, σ_m' is the effective confining pressure, and σ_{ma}' is the reference effective confining pressure corresponding to the reference shear rigidity.

The shear rigidity of the ground is calculated by (4) using Young's modulus. Based on the results of a separate compression experiment, the Young's modulus was determined to be 2437kPa at the center depth of the ground.

$$G_m = \frac{E_m}{2(1+\nu)} \quad (4)$$

where E_m is the Young's modulus, G_m is the shear rigidity, and ν is the Poisson's ratio.

The superstructure and foundations of the pier are modeled by linear beam elements, and the variation in weights of each pier is expressed by changing the density of the foundation elements. Because the ground above the FB is assumed to act integrally with the pier in the widened types, the influence is accounted for in the foundation element densities. Tables I and II indicate the parameters of the ground and pier, respectively.

TABLE I. GROUND PARAMETERS

σ_{ms} (kPa)	2.06
G_{ms} (kPa)	916.2
ρ (t/m ³)	1.483
ϕ (°)	41.2
ν	0.33

ρ : density

TABLE II. PIER PARAMETERS

	Superstructure	Foundation		
		Normal	Widened 1	Widened 2
G (kPa)		7.69×10^7		
ν		0.33		
ρ (t/m ³)	2.624	0.827	2.172	3.112
A (m ²)	0.0090	0.0113		
I (m ⁴)	2.70×10^{-6}	1.02×10^{-5}		

ρ : density, A : area, I : moment of inertia

Soil-spring elements were arranged at the boundary between the foundation and the ground except for the FB. In two-dimensional analysis, this element reproduces the effect of the soil slipping through the columnar foundations with loading, and the soil-spring force estimated using (5) is proportional to the ratio of the soil's shear stress increment to shear strain increment ($d\tau/d\gamma$).

$$k_h = \alpha d\tau / \beta d\gamma \quad (5)$$

where k_h is the soil-spring modulus and α and β are the coefficients decided following the diameter and spacing of the foundation.

Since the soil elements exhibit nonlinear characteristics, the spring force reflects the effect of the decrease in the soil rigidity with loading. A frictional resistance force equivalent to the initial shear rigidity of the ground acts in the axial direction of the foundation until the shear stress reaches shear strength. At the FB, nonlinear spring elements with rigidity in three directions, i.e. axial spring, perpendicular to axial spring (shear spring), and rotational spring, are arranged. The axial spring's characteristic is defined as the relationship between the axial spring force and displacement difference. When the node of the FB is placed below the node of the ground element in contact with the FB, the displacement difference is described as negative. The subsidence of the FB is always accompanied by the same amount of subsidence of the ground due to loading; therefore, the displacement difference is not negatively generated. As a result, it was set to form a very large axial spring force when the displacement difference is in the negative range. In contrast, a positive displacement difference

corresponds to the circumstance in which the FB on the loading side floats up while the pier is inclined. Because there is no tensile force acting between the FB and the ground at that moment, the axial spring force is adjusted to practically zero when the displacement difference is positive. The shear spring expresses the sliding of the pier. First, maximum static friction force was assessed by assuming the friction coefficient between pier FB and the ground to be 0.5. The shear spring stiffness was set to be: (1) as much as the shear rigidity of the ground when the shear force was less than 0.5 times the maximum static friction force, (2) half of the shear rigidity of the ground when the shear force was 0.5–1.0 times the maximum static friction force, and (3) 5% of the shear rigidity of the ground when the shear force was more than the maximum static friction force. The rotational spring is bilinear, and the parameters were chosen to create the RRM in accordance with the FB width, as described in [10]. Figure 6 depicts the nonlinear spring elements' properties.

Figure 7 shows the FE mesh around the pier model. The soil mesh measures 15mm in height and 50mm in width. To account for the difference in ground rigidities in the vertical direction, the ground was divided into two elements: the top layer colored orange and the lower layer colored green, although the same parameters were applied to both soil elements. The side and bottom surface boundary conditions were designed to be fixed boundaries.

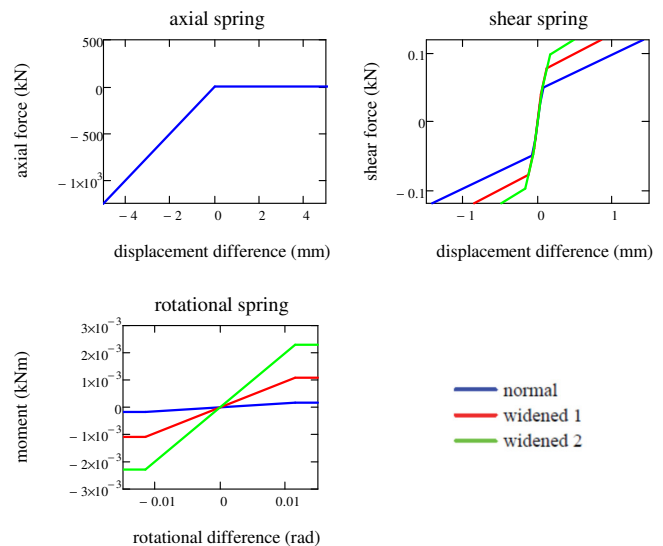


Fig. 6. Characteristics of nonlinear springs.

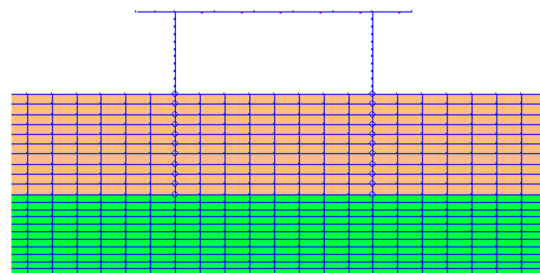


Fig. 7. FE mesh.

B. Analysis Results

Figure 8 compares the analysis results with the experimental results on the horizontal displacement of the superstructure (point A), vertical displacements of the FB (points B1 and B2), and inclination angle for the normal type. When settlement occurs, the vertical displacement is defined as negative. Early in the loading stage, the analytical findings of points A, B1, B2, and inclination angle showed fairly high agreement with the experimental data. However, they tended to be somewhat underestimated. In the latter half of the loading, the analysis results of the displacement and the inclination angle increased rapidly, and the deviation from the experimental results is large, because loading increased the shear stress of the soil element in contact with the FB, and the shear strain rose suddenly in the later part of loading due to the impact of the ground's nonlinear properties. Figure 9 depicts the time histories of vertical strain and shear strain of the soil element in contact with the FB (point B1). The normal strain grows steadily over time, but shear strain increases drastically when displacement and inclination in Figure 7 increase rapidly.

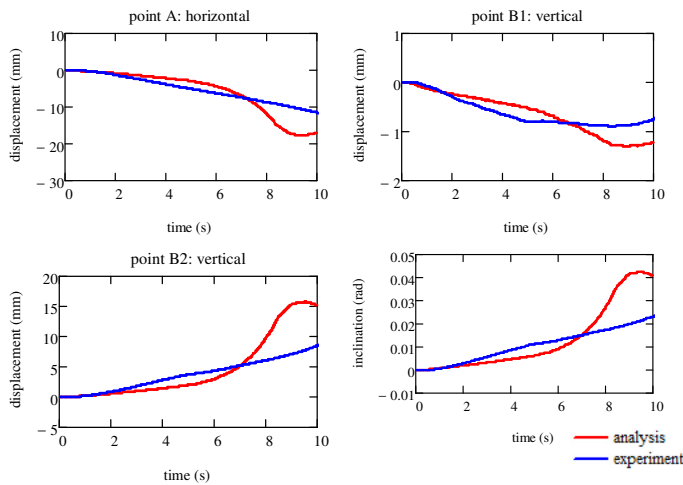


Fig. 8. Analysis results (normal type).

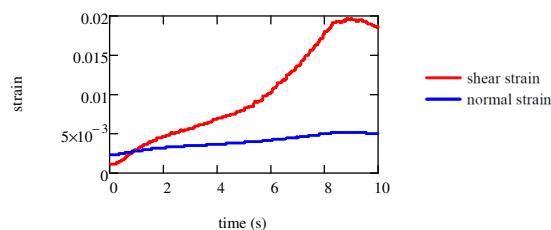


Fig. 9. Ground strain.

C. Discussion

The cause of the mismatch between the analysis and the experimental results in the latter half of loading is discussed in this section. In this analysis, the foundation is treated as a beam element with no breadth, such that the pier load operates as a concentrated load on the ground element in contact with the FB. As a result, the shear stress in the soil element tends to be overestimated. Because the FB has a width, a distributed load is

given to the ground, making the effect of ground nonlinearity unlikely to be realized. To enhance the reproducibility of the experimental results, this paper changes to an elastic element in which nonlinearity does not occur on the soil element below the FB. Figure 10 depicts the analysis findings. The FB subsidence understates the experimental results slightly since soil materials at the foundation's bottom edge do not exhibit nonlinear behavior, but reproducibility is greatly improved for horizontal displacement, vertical displacement, and pier inclination angle.

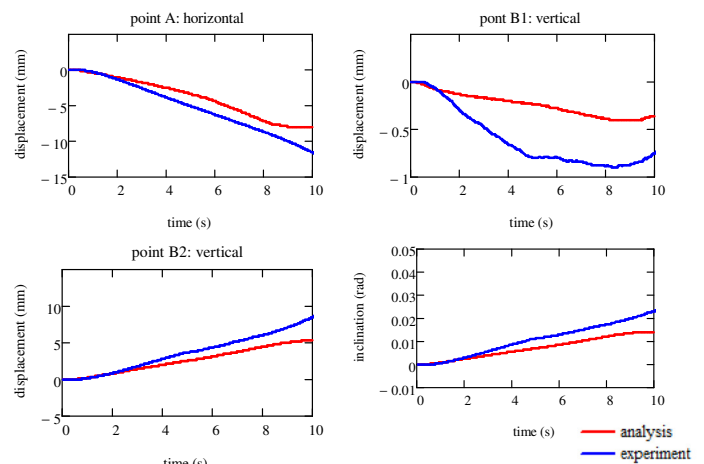


Fig. 10. Analysis results (normal type)/

Figures 11 and 12 demonstrate the analysis results of widened 1 and widened 2 types respectively using the soil element below the FB as an elastic element. Because the FB is wider in the widened types, it floats with loading at point B1, but this phenomenon cannot be recreated in the analysis because the foundation is modeled by beam elements. However, the floating of point B2 at the FB on the loading side is well reproduced, and the inclination of the superstructure (point A) is also very well reproduced. As a result of referring to the modeling in this study, it can be determined that accurate analysis can be carried out for the seismic response of the pier whose foundation is embedded into stiff ground.

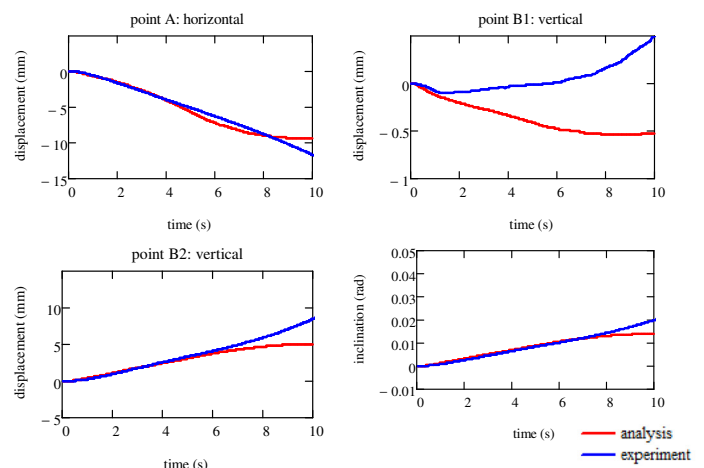


Fig. 11. Analysis results (widened 1 type).

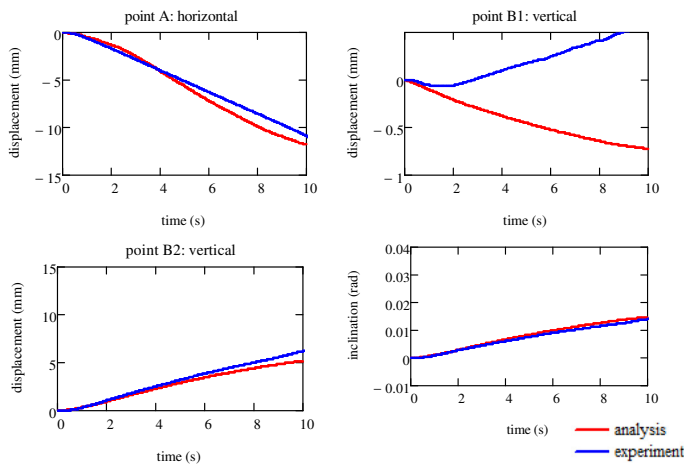


Fig. 12. Analysis results (widened 2 type).

V. CONCLUSION

In this study, in order to evaluate the seismic performance of piers with different FB widths in more detail, horizontal loading experiments for the pier with an ordinary columnar foundation and two types of the pier with widened FB were performed, and the seismic resistance difference of the three pier types was compared from the viewpoint of horizontal displacement and inclination angle. Two-dimensional FEA was used to replicate the experimental results, and the reproducibility of the experimental results was studied. The main conclusions obtained by this study are:

- Regarding the seismic performance of three pier types in which the FB width differs, there are large variations in the seismic performance between the normal type and the widened FB types, and displacement and inclination of the pier can be reduced by widening the FB. Because there is no significant difference in seismic performance between the two widened types within the range of displacement allowed in seismic design, it is recommended that the FB width should be about 1.5 times the foundation width of the columnar part to improve seismic performance while keeping the increase in construction cost to a minimum.
- The two-dimensional FEA modeling of the ground and pier enables us to evaluate accurately the response of the pier during horizontal loading. To avoid overestimating the shear strain produced in the ground at the FB when modeling the foundation with beam elements, the ground below the FB should be modeled as an elastic body, whereas nonlinearity should be considered for the ground above it. A suitable parameter setting approach for the spring element to be deployed at the soil-foundation boundary was presented. These findings pave the way for a rational seismic design method of the pier with widened FB.

ACKNOWLEDGMENTS

The authors are grateful to Yohei Ninomiya and Ryota Tsutaba for their help in carrying out the experiments.

REFERENCES

- [1] S. Werner, N. McCullough, W. Bruin, A. Augustine, G. Rix, B. Crowder, and J. Tomblin, "Seismic Performance of Port de Port-Au-Prince during the Haiti Earthquake and Post-Earthquake Restoration of Cargo Throughput", *Earthquake Spectra*, Vol. 27, No. S1, pp. 387–410, Oct. 2011, <https://doi.org/10.1193/1.3638716>.
- [2] T. Sugano, A. Nozu, E. Kohama, K. Shimosako, and Y. Kikuchi, "Damage to coastal structures", *Soils and Foundations*, Vol. 54, No.4, pp. 883–901, Aug. 2014, <https://doi.org/10.1016/j.sandf.2014.06.018>.
- [3] *Seismic Design of Piers and Wharves, ASCE/COPRI 61-14*, American Society of Civil Engineers, 2014.
- [4] *Technical standards and commentaries for port and harbour facilities in Japan*, Ports and Harbours Bureau, Ministry of Land, Infrastructure, Transport and Tourism, National Institute for Land and Infrastructure Management, Port and Airport Research Institute, The Overseas Coastal Area Development Institute of Japan, 2009.
- [5] T. Nagao and D. Shibata, "Experimental Study of the Lateral Spreading Pressure Acting on a Pile Foundation During Earthquakes", *Engineering, Technology & Applied Science Research* Vol. 9, No. 6, pp. 5021-5028, Dec. 2019, <https://doi.org/10.48084/etasr.3217>.
- [6] J. W. Yun and J. T. Han, "Dynamic behavior of pile-supported wharves by slope failure during earthquake via centrifuge tests", *International Journal of Geo-Engineering*, vol. 12, Nov. 2021, Art. no. 33, <https://doi.org/10.1186/s40703-021-00161-4>.
- [7] L. Su, J. Lu, A. Elgamal, and A. K. Arulmoli, "Seismic performance of a pile-supported wharf: Three-dimensional finite element simulation", *Soil Dynamics and Earthquake Engineering*, Vol. 95, pp. 167-179, Apr. 2017, <https://doi.org/10.1016/j.soildyn.2017.01.009>.
- [8] T. Nagao and P. Lu, "A simplified reliability estimation method for pile-supported wharf on the residual displacement by earthquake", *Soil Dynamics and Earthquake Engineering*, vol. 129, Feb. 2020, Art. no. 105904, <https://doi.org/10.1016/j.soildyn.2019.105904>.
- [9] T. Nagao, "Effect of Foundation Width on Subgrade Reaction Modulus", *Engineering, Technology & Applied Science Research* Vol. 10, No. 5, pp. 6253-6258, Oct. 2020, <https://doi.org/10.48084/etasr.3668>.
- [10] T. Nagao and R. Tsutaba, "Evaluation Methods of Vertical Subgrade Reaction Modulus and Rotational Resistance Moment for Seismic Design of Embedded Foundations", *Engineering, Technology & Applied Science Research* Vol. 11, No. 4, pp. 7386-7392, Aug. 2021, <https://doi.org/10.48084/etasr.4269>.
- [11] T. Nagao, "An Experimental Study on the Way Bottom Widening of Pier Foundations Affects Seismic Resistance", *Engineering, Technology & Applied Science Research* Vol. 10, No. 3, pp. 5713-5718, Jun. 2020, <https://doi.org/10.48084/etasr.3590>.
- [12] J. A. Knappett and S. P. G. Madabhushi, "Influence of axial load on lateral pile response in liquefiable soils, Part I: Physical modelling", *Geotechnique*, Vol. 59, No. 7, pp. 571-581, Sep. 2009, <https://doi.org/10.1680/geot.8.009.3749>.
- [13] D. Lombardi and S. Bhattacharya, "Evaluation of seismic performance of pile-supported models in liquefiable soils", *Earthquake Engineering & Structural Dynamics*, vol. 45, pp. 1019–1038, Feb. 2016, <https://doi.org/10.1002/eqe.2716>.
- [14] L. Su, L. Tang, X. Ling, C. Liu, and X. Zhang, "Pile response to liquefaction-induced lateral spreading: a shake-table investigation", *Soil Dynamics and Earthquake Engineering*, Vol. 82, pp. 196-204, Mar. 2016, <https://doi.org/10.1016/j.soildyn.2015.12.013>.
- [15] G. Li and R. Motamed, "Finite element modeling of soil-pile response subjected to liquefaction-induced lateral spreading in a large-scale shake table experiment", *Soil Dynamics and Earthquake Engineering*, vol. 92, pp. 573-584, Jan. 2017, <https://doi.org/10.1016/j.soildyn.2016.11.001>.
- [16] J. W. Yun and J. T. Han, "Dynamic behavior of pile-supported wharves by slope failure during earthquake via centrifuge tests", *International Journal of Geo-Engineering*, vol. 12, no. 33, Nov. 2021, <https://doi.org/10.1186/s40703-021-00161-4>.
- [17] S. Iai, "Similitude for Shaking Table Tests on Soil-Structure-Fluid Model in 1g Gravitational Field", *Soils and Foundations*, vol. 29, no. 1, pp. 105–118, Mar. 1989, <https://doi.org/10.3208/sandf1972.29.105>.

- [18] S. Iaf, K. Ichii, H. Liu, and T. Morita, "Effective Stress Analyses of Port Structures," *Soils and Foundations*, vol. 38, pp. 97–114, Sep. 1998, https://doi.org/10.3208/sandf.38.Special_97.
- [19] S. Iai, "Seismic Analysis and Performance of Retaining Structures," in *Geotechnical Earthquake Engineering and Soil Dynamics III*, Seattle, WA, USA, 1998, pp. 1020–1044.
- [20] I. Towhata and K. Ishihara, "Modelling soil behavior under principal stress axes rotation," in *International conference on numerical methods in geomechanics*, 1985, pp. 523–530.
- [21] B. O. Hardin and V. P. Drnevich, "Shear modulus and damping in soils: design equations and curves", Curves," *Journal of the Soil Mechanics and Foundations Division*, vol. 98, no. 7, pp. 667–692, Jul. 1972, <https://doi.org/10.1061/JSFEAQ.0001760>.
- [22] T. Morita, S. Iai, H. Liu, K. Ichi, and Y. Sato, "Simplified Method to Determine Parameter of FLIP," PARI Technical Note 0869, Jun. 1997.
- [23] I. Suetomi and N. Yoshida, "Nonlinear Behavior of Surface Deposit During the 1995 Hyogoken-Nambu Earthquake," *Soils and Foundations*, vol. 38, no. Special, pp. 11–22, 1998, https://doi.org/10.3208/sandf.38.Special_11.

An MPPT-based 31-Level ADC Controlled Micro-Inverter

Maulik J. Shah

Department of Electrical Engineering, CSPIT, CHARUSAT
Charotar University of Science and Technology
(CHARUSAT), CHARUSAT Campus
Changa, Gujarat, India
maulikniki@gmail.com

Kartik S. Pandya

Department of Electrical Engineering, CSPIT, CHARUSAT
Charotar University of Science and Technology
(CHARUSAT), CHARUSAT Campus
Changa, Gujarat, India
kartikpandya.ee@charusat.ac.in

Priyesh Chauhan

Electrical and Computer Science Engineering
Institute of Infrastructure, Technology, Research and Management
Gujarat, India
priyeshchauhan@iitram.ac.in

Received: 12 July 2022 | Revised: 22 July 2022 | Accepted: 24 July 2022

Abstract-This paper presents a 31-level micro-inverter with an innovative control scheme. The presented micro-inverter makes use of a single PV panel connected to an MPPT converter. Four half-bridge legs are connected in series to produce 31 levels at the inverter's output. At the output side of the micro-inverter, a single full-bridge power circuit is used to generate positive and negative half-cycles. A high-frequency transformer and a push-pull converter are used to generate the required isolated DC sources. The output of an Analog to Digital Converter (ADC) is used as a gate pulse for the half-bridge circuit power switching devices. PSIM software was used to simulate the proposed micro-inverter, and the results are discussed. Hardware prototypes were also created and the results are displayed.

Keywords-analog to digital converter; micro-inverter; MPPT; PV panel; Perturb and Observe

I. INTRODUCTION

A solar micro-inverter, also known as a micro-inverter, is a plug-and-play photovoltaic's component that transforms the Direct Current (DC) produced by a single solar module into Alternating Current (AC). Micro-inverters stand in contrast to traditional string and central solar inverters, which connect a single inverter to several solar panels. The output of multiple micro-inverters can be pooled and often sent into the power grid. Compared to normal inverters, micro-inverters provide several benefits. The key benefit is that they electrically isolate the panels from one another, so even a full module failure or minor quantities of shade, dust, or snow lines on one solar module do not significantly diminish the output of the entire array. By conducting Maximum Power Point Tracking (MPPT) for the modules it is attached to, each micro-inverter collects the most power possible. Since each inverter must be put next to a panel, one of the main drawbacks of a micro-inverter is that it has a greater initial equipment cost per peak Watt than a

central inverter of similar power (usually on a roof). Due to this, they are also more difficult to maintain and expensive to take apart and replace. In this proposed MPPT-based 31-level micro-inverter, the multi-level inverter is used to reduce the harmonics at the output. Figure 1 shows the basic block structure of the proposed micro-inverter.

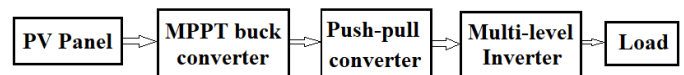


Fig. 1. Basic block structure of the proposed system.

There are many MPPT techniques available. Two common types are: conventional algorithms and intelligent control algorithms [1, 3]. In [1], a different comparative analysis of MPPT algorithms is presented. This paper simulated a 100kW grid-connected PV system with a beta control algorithm. Based on the previously known value, the accuracy of MPPT can be improved [7]. In the proposed inverter, the PV panel is used for MPPT with the Perturb and Observe (P&O) algorithm. A push-pull converter is used to separate a single source into many isolated DC sources. It employs a high-frequency transformer with a primary winding with a center tap and four different secondary windings. The isolated sources are used as asymmetric DC sources for the Multi-Level Inverter (MLI). Many MLI topologies are used nowadays to reduce the output voltage Total Harmonic Distortion (THD). Optimized topologies for MLI are represented in [2] with asymmetric and symmetric DC sources. The home type cascaded MLI with reduced power switching devices is presented in [4]. The asymmetric MLI gives higher output voltage levels than symmetric MLIs [5]. In the proposed topology, asymmetric power configuration is used for the generation of the 31-level output and a direct ADC control scheme is developed for the

inverter to get a 31-level output voltage. In this scheme, the output of the ADC is directly used as gate pulses of power switching devices in half-bridges.

II. MODELING OF THE PV MODULE

The equivalent circuit model for the PV module is shown in Figure 2. The equivalent circuit includes a current source in parallel with a diode and resistance. I_{ph} is the photo current, I_D is the diode current, R_{sh} and R_s show the shunt resistance and series resistance respectively [1, 3].

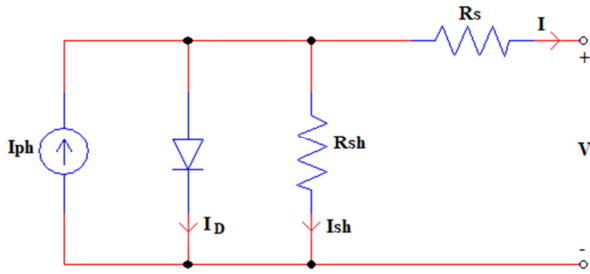


Fig. 2. Equivalent circuit for the PV cell.

$$I = I_{ph} - I_s \left(\exp \left(\frac{qV + qR_s I}{NKT} \right) - 1 \right) - \left(\frac{V + R_s I}{R_{sh}} \right) \quad (1)$$

where I is the load current, I_s the diode saturation current, and T is the cell temperature.

$$V = I_{ph} R_{sh} - I R_{sh} + I_s \left(\exp \left(\frac{qV + qR_s I}{NKT} \right) - 1 \right) - I R_s \quad (2)$$

By modifying (1), we get:

$$V = I_{ph} - I_s \left(\exp \left(\frac{qV + qR_s I}{NKT} \right) - 1 \right) - \frac{V}{R_{sh}} - \frac{R_s I}{R_{sh}} \quad (3)$$

$$I + \frac{R_s I}{R_{sh}} + I_s \left(\exp \left(\frac{qV + qR_s I}{NKT} \right) \right) = I_s - \frac{V}{R_{sh}} + I_{ph} \quad (4)$$

From (4) we will get:

$$\left(\frac{R_s + R_{sh}}{R_{sh} I_s} \right) I + \left(\exp \left(\frac{qV}{NKT} \right) \times \exp \left(\frac{R_s I}{NKT} \right) \right) = 1 - \frac{V}{R_{sh} I_s} + \frac{I_{ph}}{I_s} \quad (5)$$

An analytical solution for (5) is not possible. So, we ignore parameter R_s and thus we get:

$$I = \frac{1}{\left(\frac{R_{sh}}{R_{sh} I_s} \right)} - \left(1 - \frac{V}{R_{sh} I_s} \right) - \left(\exp \left(\frac{qV}{NKT} \right) \right) + \frac{I_{ph}}{I_s} \quad (6)$$

A. Maximum Power Point Tracking

MPPT is a method for maximizing energy extraction from variable power sources as conditions change. The main issue that MPPT attempts to solve is the fact that the efficiency of power transmission from the solar cell is dependent on the quantity of sunlight, the amount of shade, the temperature of the solar panel, and the electrical characteristics of the load. The load characteristic (impedance) that provides the maximum power transmission changes when these variables change. The system is optimized in order to maintain the best efficiency of power transfer as the load characteristic changes. The Maximum Power Point (MPP) refers to this ideal load property. Any enhancement to the MPPT's rise time will raise the system's efficiency and power extraction while also

increasing system reliability. There are many algorithms developed for MPPT, such as the P&O algorithm, the incremental conductance, and ripple correlation

B. Perturb and Observe (P&O)

By adjusting the voltage from the array by a little amount, the controller measures the power and, if it rises, tries more adjustments in that direction until the power stops rising. P&O is the most popular strategy because it is very simple to use, although it might lead to oscillations in the power output. Because it depends on the increase of the power versus voltage curve below the MPP and the decrease above that point, it is also known as the "hill climbing" approach. If a suitable predictive and adaptive hill climbing strategy is used, P&O method may produce top-level efficiency [1].

III. INVERTER WITH DIRECT ADC CONTROL SCHEME

All supplied DC sources in symmetric MLIs have the same magnitude, however in asymmetric MLIs, the magnitude of the supplied DC sources varies. DC sources are employed in asymmetric MLI binary or trinary types. DC sources in the binary pattern include V_{dc} , $2V_{dc}$, $4V_{dc}$, etc. DC sources of the trinary kind include V_{dc} , $3V_{dc}$, $9V_{dc}$, etc. However, the control strategy is quite complicated in trinary type power topologies and calls for a look-up table for switching power devices. Using an analog to digital conversion IC or an ADC channel built into a processor or microcontroller chip, the reference signal in binary-type DC sources can be converted directly. Using 4 isolated DC sources, an inverter with a total of 12 power switching components and 6 half-bridge MOSFET/IGBT driver circuits may provide an output voltage with 31 levels.

A. Direct ADC Control Scheme

There is no need for a triangular carrier wave in the direct ADC-controlled method. It produces n -bit controlled signals based on a look-up table for the sine wave's first half cycle. The resulting signals are immediately applied to the half-bridge of the inverter's gate pulses. As switching losses are reduced, an inverter's total efficiency also rises since the direct ADC method's switching frequency is lower than that of all PWM systems. The creation of gate pulses depends on the bit resolution of the ADC. The number of levels of the output voltage of the MLI is determined by the bit resolution of the ADC in this control system. As with 2-bit resolution, this will make only $(2 \times 2^2) - 1 = 7$ level output, a 3-bit resolution will make $(2 \times 2^3) - 1 = 15$ level output, and 4-bit will give $(2 \times 2^4) - 1 = 31$ levels.

IV. SIMULATIONS AND RESULTS

The simulation validation of the proposed micro-inverter topology was carried out in PSIM software. Figure 3 shows a complete simulated block diagram of the micro-inverter. A simulated block diagram contains a total of 3 subsystems and 1 PV panel. The MPPT converter is developed in the first subsystem S1. Subsystem S2 contains a push-pull converter with a high-frequency converter, and S3 includes a 31-level micro-inverter system.

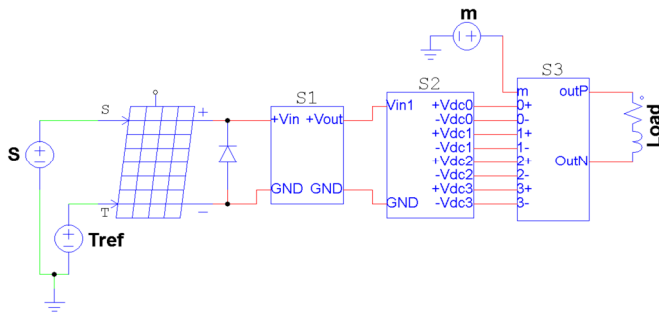


Fig. 3. Block diagram of the simulated system in PSIM.

A. PV panel and MPPT Converter

ASP-7-330 (Adani) PV panel was used for simulation in PSIM. Its specifications are given in Table I at 1000W/m² irradiance and 25°C cell temperature. In the simulation of the full system, the P&O algorithm is used for MPPT.

TABLE I. PV PANEL SPECIFICATIONS

Parameters	Value
Peak power (Pmax)	330W
Maximum Voltage (Vmpp)	37.21V
Maximum current (Impp)	8.87A
Open circuit voltage (Voc)	45.87V
Short circuit current (Isc)	9.42A
Module efficiency	16.84%

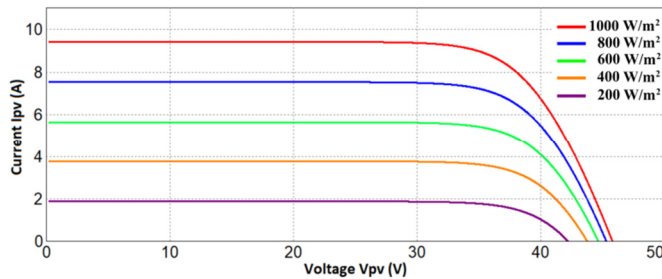


Fig. 4. I-V characteristics of the PV panel at 25°C at different irradiances.

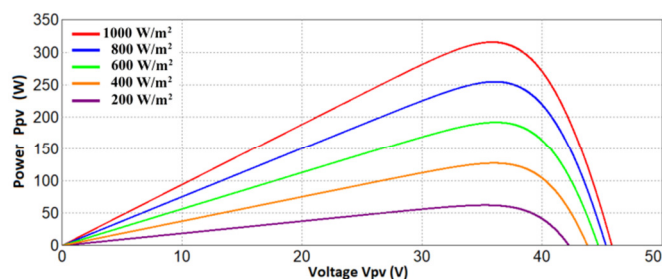


Fig. 5. P-V characteristics of the PV panel at 25°C at different irradiances.

Figures 4 and 5 show the obtained I-V and P-V characteristics at 25°C and at different irradiances: 200W/m² to 1000W/m² irradiance is taken at 25°C for I-V and P-V characteristics of the PV panel. Figure 6 represents the complete MPPT buck converter connected with PV panel. In this +Vin is coming from the positive terminal and GND is coming from the negative terminal of the PV panel. In MPPT block the P&O algorithm was developed in C language with the inputs the supply voltage (Vin) and current (I) of the PV panel. The switching frequency of the PWM pulse is 20kHz.

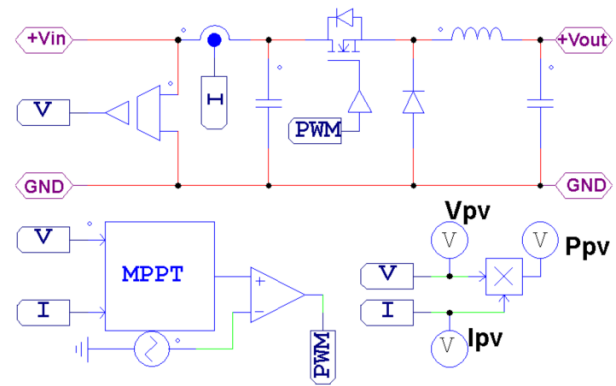


Fig. 6. Simulation diagram of the MPPT buck converter.

B. Push-Pull Converter with High-Frequency Transformer

The output of the MPPT converter +Vout and GND is connected to the supply of the push-pull converter. The push-pull converter is used to create isolated DC sources from a single source. It uses a high-frequency transformer with center tap primary winding and four numbers of secondary windings. Secondary winding turns are chosen such that it gives binary types of supply voltages like 12, 24, 48, and 96V. Each secondary winding is connected with a full-bridge diode rectifier to convert AC power into DC power. Each output is used as a power supply of the inverter half-bridges. Figure 8 shows the push-pull converter with a high-frequency transformer. Vdc0, Vdc1, Vdc2, and Vdc3 created the isolated DC sources in Figure 7. Figure 8 shows the output of the push-pull converter.

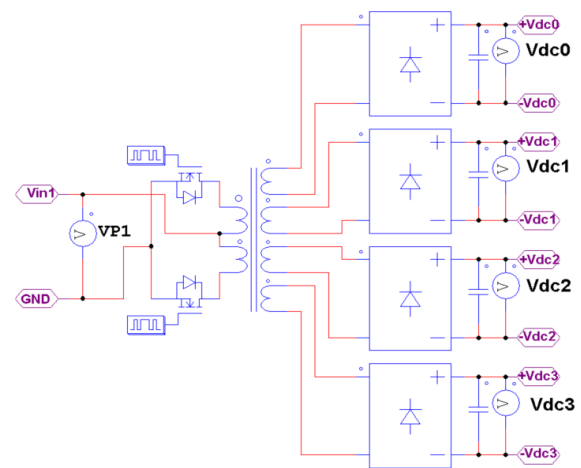


Fig. 7. Push-pull converter to create isolated DC sources.

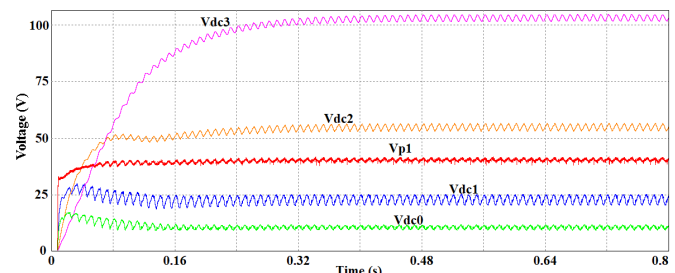


Fig. 8. Simulated output of the push-pull converter.

C. The 31-Level Inverter

One half-bridge circuit of the power switching device is connected to each DC source that is created by the push-pull converter. To generate the negative and positive cycle, one full-bridge circuit is employed. The full-bridge circuit's gate pulse is generated by the zero-crossing logic's output. Therefore, this H-switching bridge's frequency is comparable to its power frequency. The gate pulses of power switches S0 and S01 are working in inverting mode. Gate driver IC is used to generate the dead band in the gate pulses of these two switches. For S1-S11, S2-S21, S3-S31, and Sh1-Sh11, Sh2-Sh21, the same reasoning is used. Assuming $V_{dc0} = 12V$, $V_{dc1} = 24V$, $V_{dc2} = 48V$, and $V_{dc3} = 96V$ would follow. The power structure for the proposed 31-level inverter is shown in Figure 9.

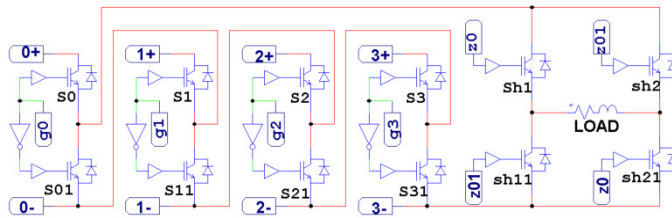


Fig. 9. Simulated power circuit of the 31-level inverter.

Switching appears to take the form of a binary conversation. Therefore, all DC sources are connected in series for the +15 Vdc output level. In the 4-bit binary, it is simply $(1111)_2$, which represents the states of power switches S3, S2, S1, and S0 respectively. Similar to the +10 Vdc case, the states are $(1010)_2$ in binary, meaning that switches S3 and S1 are in the on position, while S2 and S0 are in the off position. Figure 10(a) shows the simulated output voltage of the micro-inverter with a load of 65Ω connected in series with a $63.7mH$ inductor at modulation index 1.0. Figure 10(b) shows the zoomed view of the output voltage and Figure 11 shows the load current of the inverter. Figure 12 shows a comparison between the output voltage of the inverter and the grid voltage.

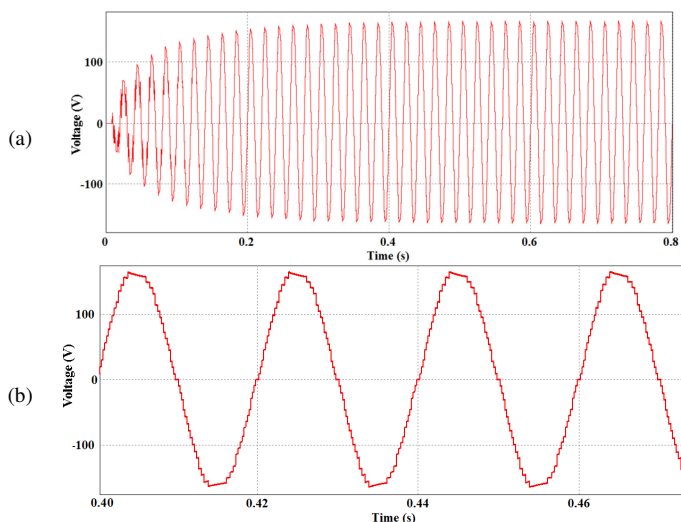


Fig. 10. (a) Output Voltage at $R=65\Omega$ and $L=63.7mH$ at modulation index $m=1.0$, (b) zoomed view of the output voltage.

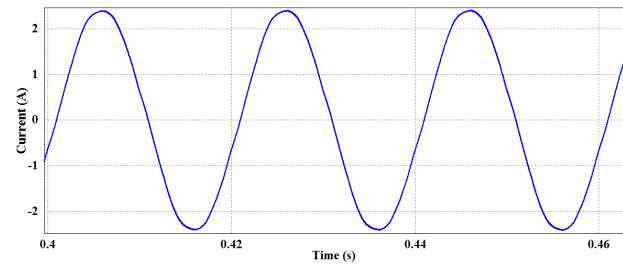


Fig. 11. Load current at $R=65\Omega$ and $L=63.7mH$ at $m=1.0$.

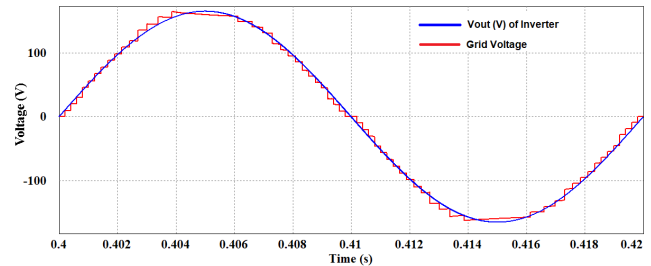


Fig. 12. Compared output Voltage of the inverter and grid voltage.

TABLE II. THD OF THE OUTPUT VOLTAGE AND LOAD CURRENT AT DIFFERENT MODULATION INDEX VALUES

Modulation Index (m)	THD (%)	
	Voltage (Vout)	Current (Iout)
1.0	3.16	0.82
0.9	3.67	1.23
0.8	3.93	1.12
0.7	4.95	1.67
0.6	5.40	1.76
0.5	6.42	1.69

Table II shows the % THD of the output voltage and load current concerning the fundamental components. It can be seen that THD will increase with the decrease in the modulation index value. As the modulation index is decreasing, the number of levels at the output side of the inverter decreases.

V. HARDWARE RESULTS

For the testing of the ADC control scheme, a hardware prototype of the inverter with isolated DC sources was developed. Each half-bridge MOSFET is driven by an IR 2104 half-bridge driver IC. So, the proposed MLI uses a total of 6 IR2104 driver ICs. A built-in dead-band facility exists between the top and lower MOSFETs of the IR2104 driver IC. Therefore, a dead band between two inverted gate pulses can be generated without the need for any additional hardware or software. For the 4 half-bridge circuits, IRFB4110 MOSFETs were used as power switching devices, and IRFP460N MOSFETs for full h-bridge circuits. To protect the microcontroller, 817 opto-coupler IC was used to isolate the gate pulses from the microcontroller. The hardware prototype was tested on resistive and inductive loads. Figure 13 shows the output of ADC that is used as gate pulses for four half-bridges. Figures 14 and 15 show the output voltage of an inverter at $m=1.0$ and $m=0.8$ respectively. Figure 16 shows the inverter output voltage in comparison with the grid voltage.

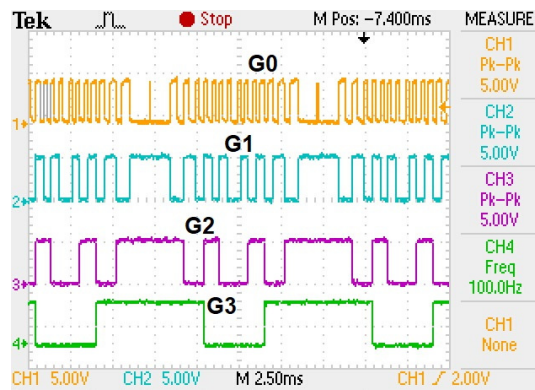


Fig. 13. Gate Pulses generated using ADC

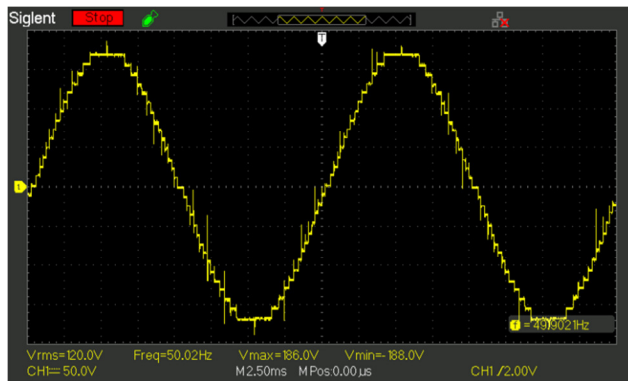
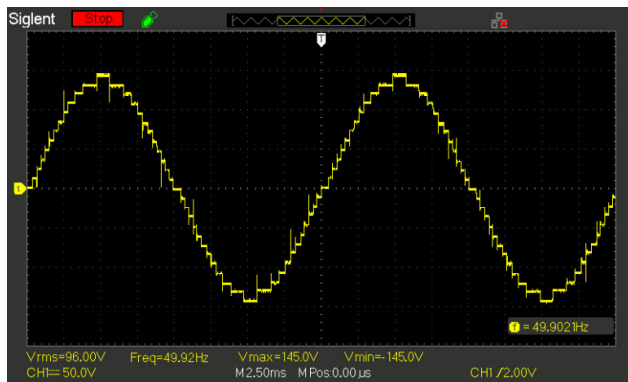
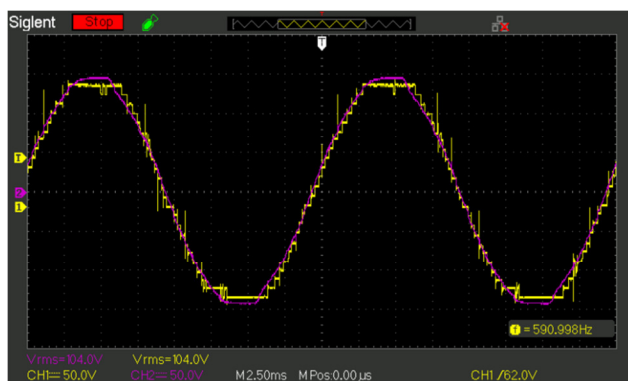
Fig. 14. Inverter output voltage at modulation index $m=1.0$.Fig. 15. Inverter output voltage at $m=0.8$.

Fig. 16. Inverter output voltage in comparison with the grid voltage. (yellow color: inverter output, purple color: grid voltage).

VI. CONCLUSION

In the proposed topology of the micro-inverter, the number of necessary DC power sources is reduced by using binary level DC sources. The inverter output voltage reached 31 levels utilizing only 4 isolated DC sources and direct ADC control. At modulation index $m=1$, the THD of the inverter output voltage was reduced to 2.11%. When compared to other control methods like SPWM, SVPWM, etc. the direct ADC control scheme utilized in this study is quite straightforward. Here, there is no need to contrast any carrier (triangular) wave with the reference sine wave. The direct ADC control approach makes it simple to create a grid connection for an inverter. The proposed MLI's RMS output voltage will fluctuate in line with variations in the grid's RMS voltage. The fundamental benefit of this control strategy is that the frequency of the grid and the output voltage are constantly synchronized.

REFERENCES

- [1] F. Z. Kebbab, L. Sabah, and H. Nouri, "A Comparative Analysis of MPPT Techniques for Grid Connected PVs," *Engineering, Technology & Applied Science Research*, vol. 12, no. 2, pp. 8228–8235, Apr. 2022, <https://doi.org/10.48084/etasr.4704>.
- [2] B. M. Manjunatha, S. N. Rao, A. S. Kumar, K. S. Zabeen, S. Lakshminarayanan, and A. V. Reddy, "An Optimized Multilevel Inverter Topology with Symmetrical and Asymmetrical DC Sources for Sustainable Energy Applications," *Engineering, Technology & Applied Science Research*, vol. 10, no. 3, pp. 5719–5723, Jun. 2020, <https://doi.org/10.48084/etasr.3509>.
- [3] M. T. Ahmed, M. R. Rashel, F. Faisal, and M. Tlemcani, "Non-iterative MPPT Method: A Comparative Study," *International Journal of Renewable Energy Research*, vol. 10, no. 2, pp. 549–557, Jun. 2020.
- [4] P. L. Kamani and M. A. Mulla, "A Home-type (H-type) Cascaded Multilevel Inverter with Reduced Device Count: Analysis and Implementation," *Electric Power Components and Systems*, vol. 47, no. 19–20, pp. 1691–1704, Dec. 2019, <https://doi.org/10.1080/15325008.2019.1660735>.
- [5] M. Farhadi Kangarlu and E. Babaei, "Cross-switched multilevel inverter: an innovative topology," *IET Power Electronics*, vol. 6, no. 4, pp. 642–651, 2013, <https://doi.org/10.1049/iet-pel.2012.0265>.
- [6] D. Shunmugham Vanaja and A. A. Stonier, "A novel PV fed asymmetric multilevel inverter with reduced THD for a grid-connected system," *International Transactions on Electrical Energy Systems*, vol. 30, no. 4, 2020, Apr. No. e12267, <https://doi.org/10.1002/2050-7038.12267>.
- [7] M. Chellal, T. F. Guimarães, and V. Leite, "Experimental Evaluation of MPPT algorithms: A Comparative Study," *International Journal of Renewable Energy Research (IJRER)*, vol. 11, no. 1, pp. 486–494, Mar. 2021.
- [8] V. Pakala and S. Vijayan, "A New DC-AC Multilevel Converter with Reduced Device Count," *International Journal of Intelligent Engineering and Systems*, vol. 10, no. 3, pp. 391–400, Jun. 2017, <https://doi.org/10.22266/ijies2017.0630.44>.
- [9] P. Manoharan, S. Rameshkumar, and S. Ravichandran, "Modelling and Implementation of Cascaded Multilevel Inverter as Solar PV Based Microinverter Using FPGA," *International Journal of Intelligent Engineering and Systems*, vol. 11, no. 2, pp. 18–27, Apr. 2018, <https://doi.org/10.22266/ijies2018.0430.03>.
- [10] M. Jagabar Sathik, N. Prabakaran, S. a. a. Ibrahim, K. Vijaykumar, and F. Blaabjerg, "A new generalized switched diode multilevel inverter topology with reduced switch count and voltage on switches," *International Journal of Circuit Theory and Applications*, vol. 48, no. 4, pp. 619–637, 2020, <https://doi.org/10.1002/cta.2732>.
- [11] D. A. Tuan, P. Vu, and N. V. Lien, "Design and Control of a Three-Phase T-Type Inverter using Reverse-Blocking IGBTs," *Engineering, Technology & Applied Science Research*, vol. 11, no. 1, pp. 6614–6619, Feb. 2021, <https://doi.org/10.48084/etasr.3954>.

- [12] J. Chakravorty and G. Sharma, "DVR with Modified Y Source Inverter and MCFC," *Engineering, Technology & Applied Science Research*, vol. 9, no. 1, pp. 3803–3806, Feb. 2019, <https://doi.org/10.48084/etasr.2522>.
- [13] S. Paul, P. Jacob, and J. Jacob, "Performance Comparison of Stand Alone Solar PV System with Variable Step Size MPPT," *International Journal of Renewable Energy Research (IJRER)*, vol. 10, no. 3, pp. 1277–1286, Sep. 2020, <https://doi.org/10.20508/ijrer.v10i3.11212.g8002>.
- [14] Z. Boumous and S. Boumous, "New Approach in the Fault Tolerant Control of Three-Phase Inverter Fed Induction Motor," *Engineering, Technology & Applied Science Research*, vol. 10, no. 6, pp. 6504–6509, Dec. 2020, <https://doi.org/10.48084/etasr.3898>.
- [15] U. B. Tayab and M. A. A. Humayun, "Modeling and Analysis of a Cascaded Battery-Boost Multilevel Inverter Using Different Switching Angle Arrangement Techniques," *Engineering, Technology & Applied Science Research*, vol. 7, no. 2, pp. 1450–1454, Apr. 2017, <https://doi.org/10.48084/etasr.1094>.

Deflection Reliability Analysis for Composite Steel Bridges

Duaa Mohammed

Department of Civil Engineering
College of Engineering
University of Baghdad
Baghdad, Iraq
d.rasol1901m@coeng.uobaghdad.edu.iq

Salah Al-Zaidee

Department of Civil Engineering
College of Engineering
University of Baghdad
Baghdad, Iraq
salah.r.al.zaidee@coeng.uobaghdad.edu.iq

Received: 18 June 2022 | Revised: 6 July 2022 | Accepted: 17 July 2022

Abstract-Reliability methods offer a very efficient serviceability assessment of structures with randomness due to geometry, material, and loading. Al-Awsej composite bridge in Diyala-Iraq with a span of 33.2m has been studied and its deflection reliability index for three lifespans was estimated and compared with the reliability target index. The reliability indices of the bridge have been evaluated through the First-Order Reliability Method (FORM) and Monte Carlo Simulation (MCS) method. MCS has adopted Matlab functions to generate pseudo-random numbers for the considered parameters, but it requires large sample sizes to estimate the small probabilities of failure. That leads to the use of the reduction variance methods such as the Importance Sampling (IS) method. Four cases of random loading were included: dead load and three cases of live loads, i.e. uniformly distributed load with knife-edge load, military load, and sidewalk load. Some assumptions are needed to assess the system behavior, where the bridge is represented as a parallel system with uncorrelated and perfect correlated girders. The reliability index of the composite bridge in the two cases was investigated for lifespans of 1, 10, and 50 years. For the uncorrelated case, the system shows the reliability index in the range of 5 and 4. In contrast, the correlated case offers a range between 4 and 2. With these assumptions, the results show that no failure occurs, hence the reliability index of the system is still within range of the target.

Keywords-steel girder bridge; statistical characteristics; FORM; MCs; importance sampling; parallel system; reliability

I. INTRODUCTION

Structure design is associated with a substantial level of uncertainty due to the limited information in the estimation of structural parameters. In practice, most structural engineering designs are based on deterministic parameters where structural performance is determined using a deterministic model for simplification and often ignore the variations in material properties, structure geometry, and applied loads. In previous studies, structural reliability methods that rationally evaluate the safety of complex structures or systems with unusual designs have been developed [1]. In this study, these methods will be used to assess the reliability of a bridge by determining the reliability indices of the steel girders considering the bridge

is a parallel system and comparing it with target reliability that ensures that structures meet the specified safety level. Thus, reliability is an approach to determine the relationship between an element and system reliability [2].

II. COURBON'S METHOD OF ANALYSIS

Courbon's method is one of the earliest rational analyses of bridges and is very popular due to its simplicity. The reaction factor for individual longitudinal girders is given by [3]:

$$R_i = \frac{P}{N} \left[1 + \left(\frac{N \times e \times x_i}{\sum x_i^2} \right) \right] \quad (1)$$

where R_i is the reaction load distribution factor of the girder, P the total concentrated live load on the span, N the number of longitudinal girders, e the eccentricity of live load to the axis of the bridge, and x_i is the distance from the girder to the central axis of the bridge.

III. LOAD APPLICATION

The applied loads on the composite bridge have been determined based on the Iraqi code specifications. The self-weight of the pavement, deck, sidewalk, supporting girders, and bracing have been determined depending on the cross-section dimensions and material densities. The own weight of the handrail has been estimated based on Iraqi standard specifications for road bridges [4]. Two cases, namely lane live and military load have been considered and applied according to the Iraqi standard. For a span of 33.2m, the lane load has a value of 28.7kN/m per lane with a Knife-Edge Load (KEL) of 120kN per lane. The military load consists of 900kN (Class 100) tracked vehicles. Two tracked vehicles have applied for a carriageway width of 9m [4].

IV. RELIABILITY ANALYSIS OF THE SYSTEM

Structural reliability analysis is based on the limit state design $g(\mathbf{X})$, where $\mathbf{X} = (X_1, X_2, \dots, X_n)$ represents the set of random variables that have some statistical information. The limit $g(\mathbf{X}) = 0$ separates the failure domain ($g(\mathbf{X}) < 0$) and the safety domain ($g(\mathbf{X}) > 0$) [7]. The probability of failure can be defined by:

$$P_f = P[g(\mathbf{X}) \leq 0] \quad (2)$$

The major source of uncertainty is actions with statistically independent maximums each year. The values of the probability of failure, P_{f_n} and of the reliability index, β_n for each reference period may be estimated using [5]:

$$P_{f_n} = 1 - (1 - P_{f_1})^n \quad (3)$$

and

$$\beta_n = -\Phi^{-1}(-P_{f_n}) \quad (4)$$

where Φ , and Φ^{-1} are the functions of the standard normal cumulative distribution.

The target reliability is a design constraint that ensures that structures meet the specified safety level. Table I shows the target values of reliability indices for various limit states and periods [6].

TABLE I. TARGET RELIABILITY INDICES

Reference period T (years)	Target reliability index β for serviceability	Target reliability index β for moment
1	2.9	4.7
10	2.2	4.2
50	1.5	3.8
100	1.1	3.6
200	0.6	3.5

V. RELIABILITY ANALYSIS METHODS

The evaluation of the failure probability of the structure in a closed-form is difficult and almost impossible. As a result, various analytical and numerical approaches have been developed, e.g. Taylor-series-based approaches, such as the First-Order Reliability Method (FORM), and simulation-based methods, such as Monte Carlo Simulation (MCS). The FORM approximation approaches are efficient for simple issues with few random variables, but for more complex problems with many random variables, MCS seem to be more reliable [7].

A. First-Order Reliability Method

It is possible to expand the original model into an infinite Taylor Series (TS) around the mean values:

$$g(\mathbf{X}) = g(\mu_X) + (X - \mu_X) \frac{dg}{dX} + \frac{1}{2} (X - \mu_X)^2 \frac{d^2g}{dX^2} + \dots + \frac{1}{n!} (X - \mu_X)^n \frac{d^ng}{dX^n} \quad (5)$$

where the function and derivatives are evaluated at μ_X . It is common to include only linear terms, assuming that random input variables are independent. A function $g(\mathbf{X})$ of N independent random variables can be approximated by linear terms of the TS, which are [8]:

$$E(Y) \approx g(\mu_{X_1}, \mu_{X_2}, \dots, \mu_{X_n}) \quad (6)$$

and

$$Var(Y) \approx \sum_{i=1}^N \sigma_{X_i}^2 \left(\frac{\partial g}{\partial X_i} \right)^2 \quad (7)$$

The limit state function is: $(x) = R - Q$, R , and Q both are random variables uncorrelated and assumed to be normally

distributed. The reliability index β is evaluated as a function of mean and standard deviations of resistance R and load Q as given by [8]:

$$\beta = \frac{\mu_R - \mu_Q}{\sqrt{\sigma_R^2 + \sigma_Q^2}} \quad (8)$$

B. Monte Carlo Method

The failure probability in MCS is the ratio of the number of samples in the failure domain to the total number of samples:

$$P_f = \frac{N_f}{N} = \frac{1}{N} \sum_{i=1}^N I[g(x) \leq 0] \quad (9)$$

where the sampling points x are generated according to the probability density function, N_f is the number of sampling points such that $g(x) \leq 0$, N is the total number of sampling points, $g(x)$ is the limit state, $I[g(x)]$ is an indicator function taking values of unity when are $g(x) \leq 0$ and zero otherwise. With increasing N , the accuracy of this estimation improves, and more simulations are needed to predict a smaller failure probability [9]. The required number of trials N of MCS is approximated by:

$$N \approx \frac{(1-P_f)}{(COV^2 \times P_f)} \quad (10)$$

where COV is the coefficient of variation of the response estimates smaller than 0.1 and P_f is usually between 10^{-2} to 10^{-6} . The total number required for that simulation is determined by:

$$N \approx \frac{(1-10^{-2})}{(0.1^2 \times 10^{-2})} \approx 9900 \quad (11)$$

C. Importance Sampling

The main idea of IS is to distribute the sampling points in the most important area so that the failure probability evaluation may be completed faster. The failure probability can be estimated as (9) is rewritten as follows:

$$P_f = \frac{1}{N} \sum_{j=1}^N I(x_j) \frac{f_X(x_j)}{h_X(x_j)} \quad (12)$$

where the sampling points x_j , $j = 1, \dots, N$ are generated according to the distribution h_X instead of f_X . The effectiveness of IS is dependent on choosing an adequate $h_X(x)$ so that the probabilistic sampling in (12) may be prioritized for the most important area, resulting in a higher convergence rate. Although no overall conclusion has been reached on the best choice of $h_X(x)$, it has been suggested that the Most Probable Point (MPP) and its surroundings can be a suitable selection for the most important area [10].

VI. SYSTEM RELIABILITY

The system reliability is affected by component reliability and several other parameters, such as the correlation among the component resistances and the system type. Structural system reliability is determined by considering the system failure rather than a single component failure [11]. The series system means that the entire system fails. The formula of the failure system for the statistically independent elements is given by:

$$P_f = 1 - \prod_{i=1}^n (1 - P_{f_i}) \quad (13)$$

where P_{f_i} and P_f are the probability of failure for the element i and the system respectively. The equation of the system failure for perfectly correlated elements can be defined as:

$$P_f = \max[P_{f_i}] \quad (14)$$

A parallel system is an overall system that fails after all its elements have failed. The probability of failure for the entire system when the elements are statistically independent and perfectly correlated respectively is defined as [11]:

$$P_f = \prod_{i=1}^n P_{f_i} \quad (15)$$

$$P_f = \min[P_{f_i}] \quad (16)$$

VII. CASE STUDY

The Al-Awsej composite bridge is constructed in Awsej valley at Diyala town in Iraq. It has 33.2m length and 14m width and consists of three longitudinal steel girders connected by steel bracings (2L100×10). The I-steel plate girders are non-symmetrically with an upper flange of 400×30mm and two lower flanges of 510×30mm and 490×30mm respectively. The floor bridge consists of a concrete deck slab with a thickness of 250mm and pavement bitumen of 60mm extending above a carriageway width of 9m, with a 2.5m sidewalk width and handrail of 1m on each side.

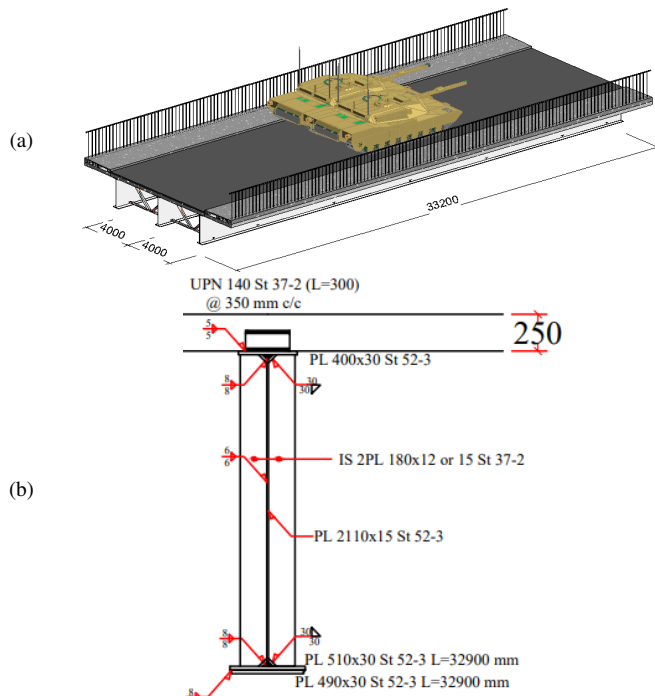


Fig. 1. The composite steel bridge.

VIII. STATISTICAL CHARACTERISTICS OF VARIABLES

In this article, the applied loads, beam span, cross-section dimensions, and modulus of elasticity are considered random variables. The statistical characteristics of these variables have been collected based on previous studies and are summarized in Table II.

TABLE II. STATISTICAL CHARACTERISTICS OF VARIABLES

Uncertainty	Mean/Nominal	COV	Distribution type
Weight of the deck slab	1.05	0.10	Normal
Weight of the girder	1.03	0.08	Normal
Weight of the pavement	1.00	0.25	Normal
Weight of the military	1.10	0.18	Lognormal
Uniform distribution with knife-edge live loads	1.10	0.18	Lognormal
Sidewalk live loads	1.10	0.18	Lognormal
Length of the girder	1.00	0.000502	Normal
Width of the Flange girder	1.00	0.00403	Normal
Thickness of the flange and web	1.05	0.044	Lognormal
Depth of the web girder	0.996	0.000486	Normal
Modulus of elasticity	0.993	0.034	Normal

IX. STATISTICAL PROPERTIES FOR THE DEFLECTION OF GIRDERS

Two methods have been used to analyze the exterior and interior girders: First-Order approximation and MCS.

A. First-Order Approximation Method

The determination of statistical characteristics of girder deflection has been determined due to the uncertainties in the moment of inertia I , span L , modulus of elasticity E , and loads. Self-weight and superimposed loads DL are considered uncertain due to the randomness in the weight of concrete deck slab, girders, and pavements. Randomness in the own weight of bracing, sidewalk, and handrail has been neglected. Live Load (LL) uncertainties have been considered for the cases of military, sidewalk, uniform distributed, and knife-edge loads. Table III provides the mean and standard deviation of deflection.

TABLE III. STATISTICAL CHARACTERISTICS OF THE GIRDER DEFLECTION - FORM

	Loads	Nominal (mm)	Mean (mm)	Standard deviation (mm)	COV
Exterior Girder	Self-weight and superimposed loads	70.44	70.72	7.10	0.10
	Military with sidewalk live loads	52.54	56.11	10.48	0.18
	Uniformly distributed with knife-edge and sidewalk live loads	61.26	65.45	12.22	0.18
Interior Girder	Self-weight and superimposed loads	51.95	51.60	6.50	0.13
	Military and sidewalk live loads	52.54	56.11	10.48	0.18
	Uniformly distributed with knife-edge and sidewalk live loads	49.11	52.45	9.80	0.18

B. Monte Carlo Simulation

The MCS was utilized for deflection of the exterior and interior girders. A Matlab code has been used to generate pseudo-random sampling. Six samples, each with a size of 1000, have been generated to include the randomness in the moment of inertia I , the span of the girder L , and the modulus of elasticity E .

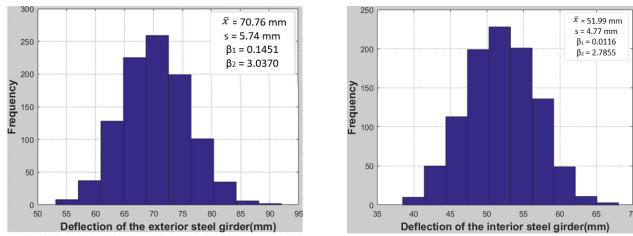


Fig. 2. Deflection sample for the case of dead and superimposed loads.

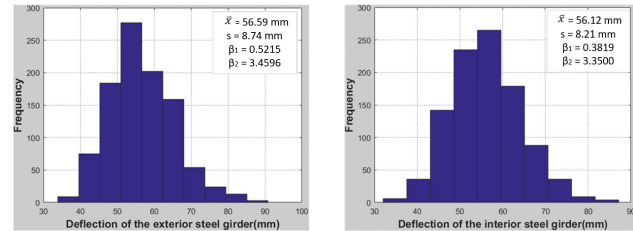


Fig. 3. Deflection sample for the case of military and sidewalk live loads.

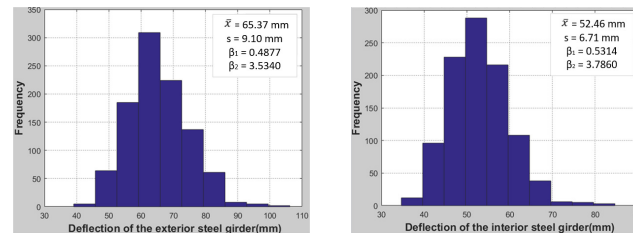


Fig. 4. Deflection sample for the case of uniform lane with knife-edge and sidewalk live loads.

Three samples have been considered for each of the exterior and interior girders. For each girder, the samples represent the randomness in dead loads, military with sidewalk loads, and uniform lane with knife-edge and sidewalk loads respectively. Table III shows that each random variable has been generated

based on preselected statistical parameters and probability density function. The sample data are presented in the histogram Figures 2-4, and the statistical characteristics for the deflection of the girders are shown in Table IV.

TABLE IV. STATISTICAL CHARACTERISTICS OF THE GIRDER DEFLECTION - MCS

Loads		Mean (mm)	Standard deviation (mm)	COV	Distribution type
Exterior Girder	Self-weight and superimposed loads	70.76	5.74	0.08	Normal
	Military and sidewalk live loads	56.59	8.74	0.15	Lognormal
	Uniformly distributed with knife-edge and sidewalk live loads	65.37	9.10	0.13	Lognormal
Interior Girder	Self-weight and superimposed loads	51.99	4.77	0.09	Normal
	Military and sidewalk live loads	56.12	8.21	0.15	Lognormal
	Uniformly distributed with knife-edge and sidewalk live loads	52.46	6.71	0.13	Lognormal

X. RELIABILITY ANALYSIS FOR STEEL GIRDER DEFLECTION

FORM and MCS methods have been adopted to estimate the reliability associated with girder deflection. Some assumptions have been adopted in the FORM, assuming all independent variables have a normal distribution. The mean and standard deviation of girders deflection in Table III have been used to evaluate the reliability index β and the probability of failure, P_f by:

$$\beta = \frac{\Delta_{Allowable\ max} - E(\Delta)}{s_{\Delta}} \quad (17)$$

where $\Delta_{Allowable\ max}$ represented a threshold limit of 80mm that was adopted as a camper in the design of the Al-Awsej bridge case study.

TABLE V. RELIABILITY INDEX AND PROBABILITY OF FAILURE BY FORM

Loads		1 year		10 years		50 years	
		P_f	β	P_f	β	P_f	β
Exterior Girder	Self-weight and superimposed loads	0.09	1.31	0.63	-0.34	0.99	-2.47
	Military with sidewalk live loads	0.001	3.09	0.009	2.33	0.048	1.66
	Uniform distributed with knife edge and sidewalk live loads	0.03	1.89	0.26	0.65	0.77	-0.75
Interior Girder	Self-weight and superimposed loads	6×10^{-6}	4.37	6×10^{-5}	3.84	0.0003	3.42
	Military and sidewalk live loads	0.001	3.09	0.009	2.33	0.048	1.66
	Uniformly distributed with knife edge and sidewalk live loads	0.0001	3.68	0.001	3.04	0.005	2.52

TABLE VI. RELIABILITY INDEX AND PROBABILITY OF FAILURE BY IS METHOD

Loads		N_f	1 year		10 years		50 years	
			P_f	β	P_f	β	P_f	β
Exterior Girder	Self-weight and superimposed loads	39	0.039	1.76	0.33	0.44	0.86	-1.09
	Military and sidewalk live loads	≈ 0	≈ 0	/	≈ 0	/	≈ 0	/
	Uniformly distributed with knife edge and sidewalk live loads	9	0.009	2.36	0.09	1.36	0.36	0.35
Interior Girder	Self-weight and superimposed loads	≈ 0	/	/	≈ 0	/	≈ 0	/
	Military and sidewalk live loads	≈ 0	/	/	≈ 0	/	≈ 0	/
	Uniformly distributed with knife-edge and sidewalk live loads	≈ 0	/	/	≈ 0	/	≈ 0	/

Regarding the live load deflection, R has been taken as the limit ratio of $L/375$ according to The American Association of State Highway and Transportation Officials (AASHTO) [12]. In the MCS method, importance sampling techniques have

been used to reduce the number of simulations. These methods rely on random sampling from random variable distributions to obtain the response uncertainty and the numerical estimate probability of failure. The assessment of the probability of

failure is based on the samples that exceed the threshold limit for girder deflection. The reliability index and probability of failure for exterior and interior girders for the three loading cases and through a lifetime of 1, 10, and 50 years are summarized in Tables V and VI. The results show that the first-order approximate analytical method has the ability to show the values of the probability of small failures, unlike MCS. Also, these Tables noted that the probability of failure increases with the passage of time thus, the reliability indices of the system decrease.

XI. RELIABILITY ANALYSIS FOR COMPOSITE BRIDGE DEFLECTION

The composite bridge has been simulated as a system of elements (girders). The live load was distributed to the girders

TABLE VII. RELIABILITY INDEX AND PROBABILITY OF FAILURE FOR PARALLEL BRIDGE DEFLECTION

Loads	One year		Ten year		fifty year	
	P_f	β	P_f	β	P_f	β
Uncorrelated, $\rho_{ij}=0$						
Self-weight and superimposed loads	5.42×10^{-8}	5.31	5.42×10^{-7}	4.88	2.70×10^{-6}	4.55
Military and sidewalk live loads	0.1×10^{-8}	5.99	0.1×10^{-7}	5.61	0.05×10^{-6}	5.33
Uniformly distributed with knife-edge and sidewalk live loads	8.41×10^{-8}	5.23	8.41×10^{-7}	4.79	4.20×10^{-6}	4.45
Perfect correlated, $\rho_{ij}=1$						
Self-weight and superimposed loads	6×10^{-6}	4.37	6×10^{-5}	3.84	0.0003	3.42
Military and sidewalk live loads	0.001	3.09	0.009	2.33	0.048	1.66
Uniformly distributed with knife edge and sidewalk live loads	0.0001	3.68	0.001	3.09	0.005	2.52

XII. CONCLUSION

A reliability analysis of Al-Awsej composite bridge has been performed in this paper, considering the randomness in geometry, material, and applied loads. The bridge is located in Diyala-Iraq and has a span of 33.2m. The main conclusions of the current study are:

- The first-order reliability method has estimated two moments (mean and standard deviation) of the girder deflection. At the same time, the MCS method determined four moments (mean, standard deviation, skewness, and peakedness) in addition to the distribution type.
- The MCS with IS method allowed the generation of 1000 pseudo-random samples instead of a large number of samples to estimate the probability of failure of a girder's deflection by distributing the failure sampling in the most crucial area. Hence, the failure probability evaluation was completed while saving cost and time.
- With an increase in the correlation between girders, the reliability decreases and the probability of failure increases.
- The reliability index of the deflection with two cases of correlation (uncorrelated and perfect correlated) was greater than the target reliability of the deflection.

REFERENCES

- [1] D. V. Ngo, K. V. Pham, D. D. Le, K. H. Le, and K. V. Huynh, "Assessing Power System Stability Following Load Changes and Considering Uncertainty," *Engineering, Technology & Applied Science Research*, vol. 8, no. 2, pp. 2758–2763, Apr. 2018, <https://doi.org/10.48084/etasr.1892>.
- [2] A. Nowak, "System reliability models for bridge structures," *Bulletin of the Polish Academy of Sciences, Technical Sciences*, vol. 52, no. 4, pp. 321–328, Dec. 2004.
- [3] M. G. Kalyanshetti and R. P. Shriram, "Study of Effectiveness of Courbon's Theory in the Analysis of T-beam Bridges," vol. 4, no. 3, pp. 1–4, Mar. 2013.
- [4] *Iraq Standard Specifications for Road Bridges Loading*. Baghdad, Iraq: Ministry of Housing and Construction, 1978.
- [5] E. Bastidas-Arteaga and A.-H. Soubra, "Reliability Analysis Methods," in *Stochastic Analysis and Inverse Modelling*, M. A. Hicks and C. Jommi, Eds. Grenoble, France: ALERT Doctoral School, 2014, pp. 53–77.
- [6] I. Lukačević, B. Androić, and D. Dujmović, "Assessment of reliable fatigue life of orthotropic steel deck," *Open Engineering*, vol. 1, no. 3, pp. 306–315, Sep. 2011, <https://doi.org/10.2478/s13531-011-0028-3>.
- [7] A. H.-S. Ang and W. H. Tang, *Probability Concepts in Engineering: Emphasis on Applications to Civil and Environmental Engineering*, 2nd ed. New York, NY, USA: Wiley, 2006.
- [8] S. S. Kar and L. B. Roy, "Probabilistic Based Reliability Slope Stability Analysis Using FOSM, FORM, and MCS," *Engineering, Technology & Applied Science Research*, vol. 12, no. 2, pp. 8236–8240, Apr. 2022, <https://doi.org/10.48084/etasr.4689>.
- [9] N. L. Tran and T. H. Nguyen, "Reliability Assessment of Steel Plane Frame's Buckling Strength Considering Semi-rigid Connections," *Engineering, Technology & Applied Science Research*, vol. 10, no. 1, pp. 5099–5103, Feb. 2020, <https://doi.org/10.48084/etasr.3231>.
- [10] M. Aldosary, J. Wang, and C. Li, "Structural reliability and stochastic finite element methods: State-of-the-art review and evidence-based comparison," *Engineering Computations*, vol. 35, no. 6, pp. 2165–2214, Jan. 2018, <https://doi.org/10.1108/EC-04-2018-0157>.
- [11] D. M. Frangopol, B. M. Kozy, B. Zhu, and S. Sabatino, "Bridge System Reliability and Reliability-Based Redundancy Factors," US Department of Transportation, Federal Highway Administration, Tech Report FHWA-HIF-19-093, Sep. 2019.
- [12] *AASHTO LRFD Bridge Design Specifications*, 8th ed. Washington DC, USA: AASHTO, 2017.

through a flexible medium and the deck slab and bracing were represented as the applied load to the girders.

In this case, the composite bridge can be considered as a parallel system. Hence, the reliability has been estimated with two instances of correlation: uncorrelated and perfect correlated. The composite bridge reliability depended on the probability of failure and the reliability index of the steel girders deflection. The results of MCS show that the probability of failure approaches zero, so the reliability of the parallel system was estimated based on the outcome of FORM (Table VII), which showed that the probability of failure increases with the passage of time, thus the reliability indices of the system decrease.

Correlation Analysis of Earthquake Intensity Measures and Engineering Demand Parameters of Reactor Containment Structure

Xuan-Hung Vu

Department of Civil Engineering, Vinh University
Vinh, Vietnam
vxhlkc@gmail.com

Van-Long Phan

Department of Civil Engineering, Vinh University
Vinh, Vietnam
phanlongkxd@vinhuni.edu.vn

Thanh-Tung Thi Nguyen

Department of Civil Engineering, Vinh University
Vinh, Vietnam
ntttung@gmail.com

Duy-Duan Nguyen

Department of Civil Engineering, Vinh University
Vinh, Vietnam
duyduankxd@vinhuni.edu.vn

Received: 4 July 2022 | Revised: 24 July 2022 | Accepted: 25 July 2022

Abstract—This study aims to analyze the correlation between earthquake Intensity Measures (IMs) and seismic responses of a reactor containment building in an APR-1400 nuclear power plant. A total of 20 IMs were employed to develop Seismic Demand Regression Models (SDRMs), which show the relationship between IMs and engineering demand parameters. A numerical model of the structure was constructed using the Lumped-Mass Stick Model (LMSM) in SAP2000. Additionally, a three-dimensional finite element model was developed to validate the simplified LMSM approach. A set of 90 ground motion records was used to perform a time-history analysis, where the motions cover a wide range of amplitude, intensity, epicenter distance, significant duration, and frequency of earthquakes. Engineering demand parameters were monitored in terms of floor accelerations and displacements. Consequently, strongly correlated IMs were identified based on the evaluation of SDRMs using four statistical indicators: coefficient of determination, standard deviation, practicality, and proficiency. The results showed that the strongest IMs were $S_a(T_1)$, $S_v(T_1)$, and $S_d(T_1)$ followed by ASI, EPA, PGA, and A95. On the other hand, the weakly correlated IMs were PGD, DRMS, SED, VRMS, PGV, HI, VSI, and SMV.

Keywords—reactor containment structure; earthquake intensity measure; seismic demand regression model; floor acceleration; floor displacement

I. INTRODUCTION

Currently, seismic design codes and guidelines use Peak Ground Acceleration (PGA) and Spectral Acceleration (S_a) as intensity measures. These parameters are widely employed to evaluate the probabilistic seismic damage of structures. However, each structure has specific characteristics, such as structural dimensions, material properties, and details. Therefore, the correlation between seismic structural responses and earthquake intensity measures may differ for different

structure types. Numerous studies evaluated the correlation between seismic Intensity Measures (IMs) and responses of different structures such as buildings [1-6], bridges [7-12], intake tanks [13], chimneys [14], and underground structures [15-17]. These studies concluded that PGA and S_a were not the optimal parameters to evaluate seismic responses and fragility analyses of structures. There is a need to systematically identify efficient earthquake IMs for seismic risk analysis of Nuclear Power Plants (NPPs), where the reactor containment building is one of the crucial structures.

Some studies investigated the interrelation of the responses of NPP structures and earthquake IMs. In [23], the correlation coefficients between typical IMs and seismic fragility of the Canada Deuterium Uranium reactor building were determined, pointing out that spectral acceleration $S_a(T_1)$ and spectral displacement at the fundamental period $S_d(T_1)$ are the most correlated IMs. In [24], time-history analysis was performed to recognize the strongly correlated earthquake IMs with the structural responses of base-isolated nuclear power plant structures, considering the high-frequency content of earthquakes. As a result, PGA, A95, and Sustained Maximum Acceleration (SMA) had the largest correlation with structural behaviors subjected to low-frequency earthquakes. Meanwhile, Specific Energy Density (SED), Characteristic Intensity (I_c), and Arias Intensity (I_a) were the strongest IMs under high-frequency ground motions. However, a systematic study on the correlation analysis between seismic IMs and structural behaviors of the 1400 NPP containment structure has not been performed. Since this structure is designed according to the US Nuclear Regulation Commission 1.60 (NRC 1.60) with $PGA=0.3g$, a selection of large ground motions is required, where the mean spectrum matches the design.

Moreover, a simplified numerical model called the Lumped Mass Stick Model (LMSM) and a full Three-Dimensional

Corresponding author: Duy-Duan Nguyen

Finite Element Model (3D FEM) have been used to evaluate nuclear structures [18]. However, since 3D FEM takes a long time for time-history analysis and occupies a large amount of memory, LMSM is preferred. Several studies demonstrated that LMSM was capable of evaluating fragility analyses of NPP structures [19-22]. This study conducted a correlation analysis between IMs and Engineering demand Parameters (EDPs) of reactor containment structures. A total of 20 IMs were considered to establish seismic demand regression models representing the relationship between IMs and EDPs. A numerical model of the containment structure was developed using the simplified LMSM in SAP2000. Additionally, a solid-based 3D FEM was built to validate the LMSM. A set of 90 seismic ground motion records was selected for time-history analysis. The EDPs were measured in terms of floor accelerations and displacements. Four statistical properties were used to evaluate the efficiency of seismic demand regression models, including coefficient of determination (R^2), standard deviation, practicality, and proficiency.

II. EARTHQUAKE INTENSITY MEASURES AND INPUT GROUND MOTIONS

This study selected 20 IMs to develop the seismic demand regression models, as shown in Table I. These IMs were classified in by amplitude, frequency, intensity, and energy.

TABLE I. CONSIDERED EARTHQUAKE INTENSITY MEASURES

No	Earthquake IMs	Formula	Unit	Ref.
1	Peak ground acceleration	$PGA = \max a(t) $	g	-
2	Peak ground velocity	$PGV = \max v(t) $	m/s	-
3	Peak ground displacement	$PGD = \max d(t) $	m	-
4	Root-mean-square of acceleration	$A_{rms} = \sqrt{\frac{1}{t_{tot}} \int_0^{t_{tot}} a(t)^2 dt}$	g	[25]
5	Root-mean-square of velocity	$V_{rms} = \sqrt{\frac{1}{t_{tot}} \int_0^{t_{tot}} v(t)^2 dt}$	m/s	[25]
6	Root-mean-square of displacement	$D_{rms} = \sqrt{\frac{1}{t_{tot}} \int_0^{t_{tot}} d(t)^2 dt}$	m	[25]
7	Arias intensity	$I_a = \frac{\pi}{2g} \int_0^{t_{tot}} a(t)^2 dt$	m/s	[26]
8	Characteristic intensity	$I_c = (A_{rms})^{2/3} \sqrt{t_{tot}}$	$m^{1.5}/s^{2.5}$	[27]
9	Specific energy density	$SED = \int_0^{t_{tot}} v(t)^2 dt$	m^2/s	-
10	Cumulative absolute velocity	$CAV = \int_0^{t_{tot}} a(t) dt$	m/s	[28]
11	Acceleration spectrum intensity	$ASI = \int_{0.1}^{0.5} S_a(\xi = 0.05, T) dT$	$g \cdot s$	[29]
12	Velocity spectrum intensity	$VSI = \int_{0.1}^{2.5} S_v(\xi = 0.05, T) dT$	m	[29]
13	Housner spectrum intensity	$HI = \int_{0.1}^{2.5} PS_v(\xi = 0.05, T) dT$	m	[30]
14	Sustained maximum acceleration	$SMA = \text{the } 3^{rd} \text{ of } PGA$	g	[31]
15	Sustained maximum velocity	$SMV = \text{the } 3^{rd} \text{ of } PGV$	m/s	[31]
16	Effective peak acceleration	$EPA = \frac{\text{mean}(S_a^{0.1-0.5}(\xi=0.05))}{2.5}$	g	[28]
17	Spectral acceleration at T_1	$S_a(T_1)$	g	[32]
18	Spectral velocity at T_1	$S_v(T_1)$	m/s	-
19	Spectral displacement at T_1	$S_d(T_1)$	m	-
20	A95 parameter	$A_{95} = 0.764 I_a^{0.438}$	g	[33]

A group of 90 ground motion records was selected from worldwide earthquakes provided by the PEER center, considering a wide range of amplitude, magnitude, epicentral distance, duration, fundamental period, and frequency. Figure 1 shows the response spectra of the 90 motion records. It should be noted that the mean spectrum of these motions is close to the design response spectrum of the US NRC 1.60 [34].

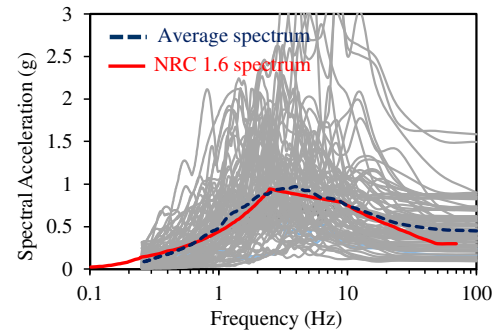


Fig. 1. Response spectra of 90 motion records.

III. FINITE ELEMENT MODEL OF CONTAINMENT STRUCTURE

The reactor containment structure in the Advanced Power Reactor 1400 (APR-1400) NPP was employed to develop the modeling. This structure is made of reinforced concrete with a cylinder and a top dome. The diameter and height of the cylinder are 47m and 54m respectively. The thickness of the RC cylinder wall is 1.22m. The radius and thickness of the dome are 23.2m and 1.07m respectively. Figure 2 shows the structural dimensions of the containment structure.

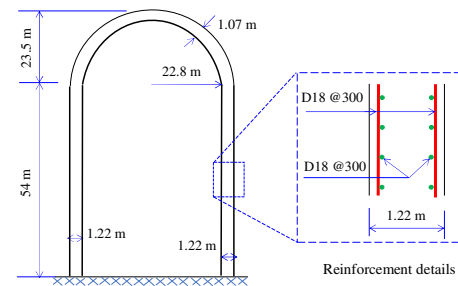


Fig. 2. Configurations of the containment structure.

Since the containment structure is a vertically symmetric cantilever column, its FEM can be developed using the simplified LMSM. This numerical model was based on beam elements with nodal masses assigned at the nodes of the elements. The model consisted of 14 beam elements, where their length was determined based on the change of vertical stiffness of the structure and the location where secondary systems are connected to the containment structure. The lumped masses and structural section properties of elements were calculated based on the real cross-section of the structure [35]. The LMSM of the containment structure was constructed in SAP2000, a commercial structural analysis program. Figure 3(a) shows the LMSM of the containment structure in SAP2000 and Table II shows the material properties.

3D FEM is known to be the most accurate numerical approach and was used to validate the simplified LSM. In this study, 3D FEM was developed using solid elements in ANSYS. The structural model was meshed into 13,571 prism elements, after conducting a sensitivity meshing analysis as shown in Figure 3(b). The elastic modulus of the material was 30,500MPa, Poisson's ratio was 0.17, and volumetric density was 24.0KN/m³.

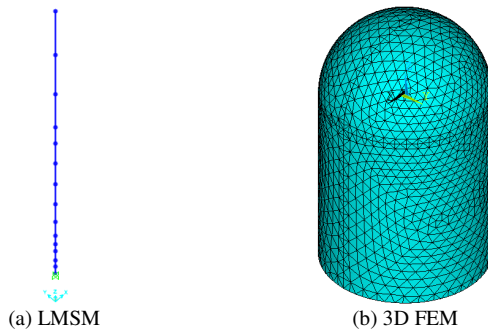


Fig. 3. Finite element models.

TABLE II. MATERIAL PROPERTIES USED IN LSM

Model	Elastic modulus (kN/m ²)	Volumetric density (kN/m ³)	Poisson's ratio
Containment structure	3.05E+07	0.00	0.170

IV. SEISMIC RESPONSES OF THE CONTAINMENT STRUCTURE

A series of linear time-history analyses was performed since the stiffness of the containment structure was very high and was expected to behave elastically under earthquakes. Acceleration records were imposed on the horizontal direction, and the effects of vertical motion were neglected. The EDPs (seismic responses) of the structure were quantified in terms of floor accelerations and displacements. These parameters are commonly used in structural and earthquake engineering analyses [36-38]. Figure 4 displays the time-history responses of the containment structure at the top and middle nodes using LSM and 3D FEM, showing that the results of the two models are highly compatible. Figure 5 shows the Floor Response Spectra (FRS) at different elevations of the structure, which also implies that LSM results are very close to 3D FEM and highlights the capability of the former to perform a seismic time-history analysis of the NPP structure.

V. SEISMIC DEMAND REGRESSION MODEL

The Seismic Demand Regression Model (SDRM) has been widely used to represent the relationship between earthquake IMs and EDPs. This model was also applied to seismic designs according to the probabilistic approach [6, 39]. The popular expression of SDRM is [7, 10, 40]:

$$S_D = a \times (IM)^b \quad (1)$$

where S_D is the mean seismic response of the structure, a and b are regression coefficients, and IM is the intensity measure considered. Equation (1) can be also written as:

$$\ln(S_D) = \ln(a) + b \times \ln(IM) \quad (2)$$

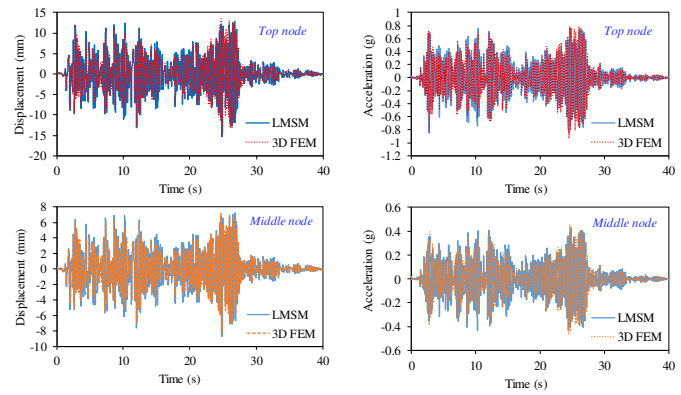


Fig. 4. Time-history responses of the structure subjected to the 1940 El Centro earthquake.

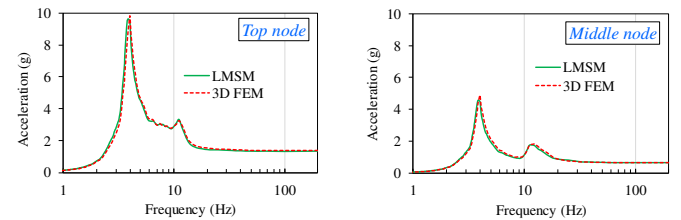


Fig. 5. FRS at different elevations of the structure under the 1940 El Centro earthquake.

A total of 40 SDRMs of the structure were constructed for 20 IMs and EDPs. Optimal IMs were evaluated using four statistical indicators: coefficient of determination (R^2), efficiency (standard deviation), practicality, and proficiency. It should be noted that R^2 represents the percentage of data closest to the regression line, and a higher R^2 value indicates a more optimal SDRM. On the contrary, efficiency denotes the scattering (standard deviation) of SDRM, and smaller efficiency indicates more optimal SDRMs. It practicality indicates the slope of the regression line, and smaller practicality means more correlated IM. Similarly, proficiency represents the balance between efficiency and practicality, and smaller proficiency means a more proficient SDRM.

Figure 6 shows the SDRMs for floor displacement for the 20 IMs. The results demonstrate that the IMs corresponding to SDRMs with the highest R^2 values and having the smallest scattering were: $S_a(T_I)$, $S_v(T_I)$, $S_d(T_I)$, ASI , EPA , PGA , and $A95$. Displacement-based regression models using $S_a(T_I)$, $S_v(T_I)$, and $S_d(T_I)$ had R^2 greater than 0.95. Similarly, R^2 values were also greater than 0.85 in acceleration-based regression models using $S_a(T_I)$, $S_v(T_I)$, $S_d(T_I)$. The trend of SDRMs was similar for both using floor displacement and acceleration as EDPs. Overall, a high correlation was observed for acceleration-based IMs, attributed to the large mass and stiffness of the investigated structure, so it was sensitive to acceleration rather than velocity and displacement [24]. Moreover, $S_a(T_I)$, $S_v(T_I)$, $S_d(T_I)$ had the strongest correlation with EDPs since they combine the earthquake characteristic and structural property (i.e. the fundamental period T_I).

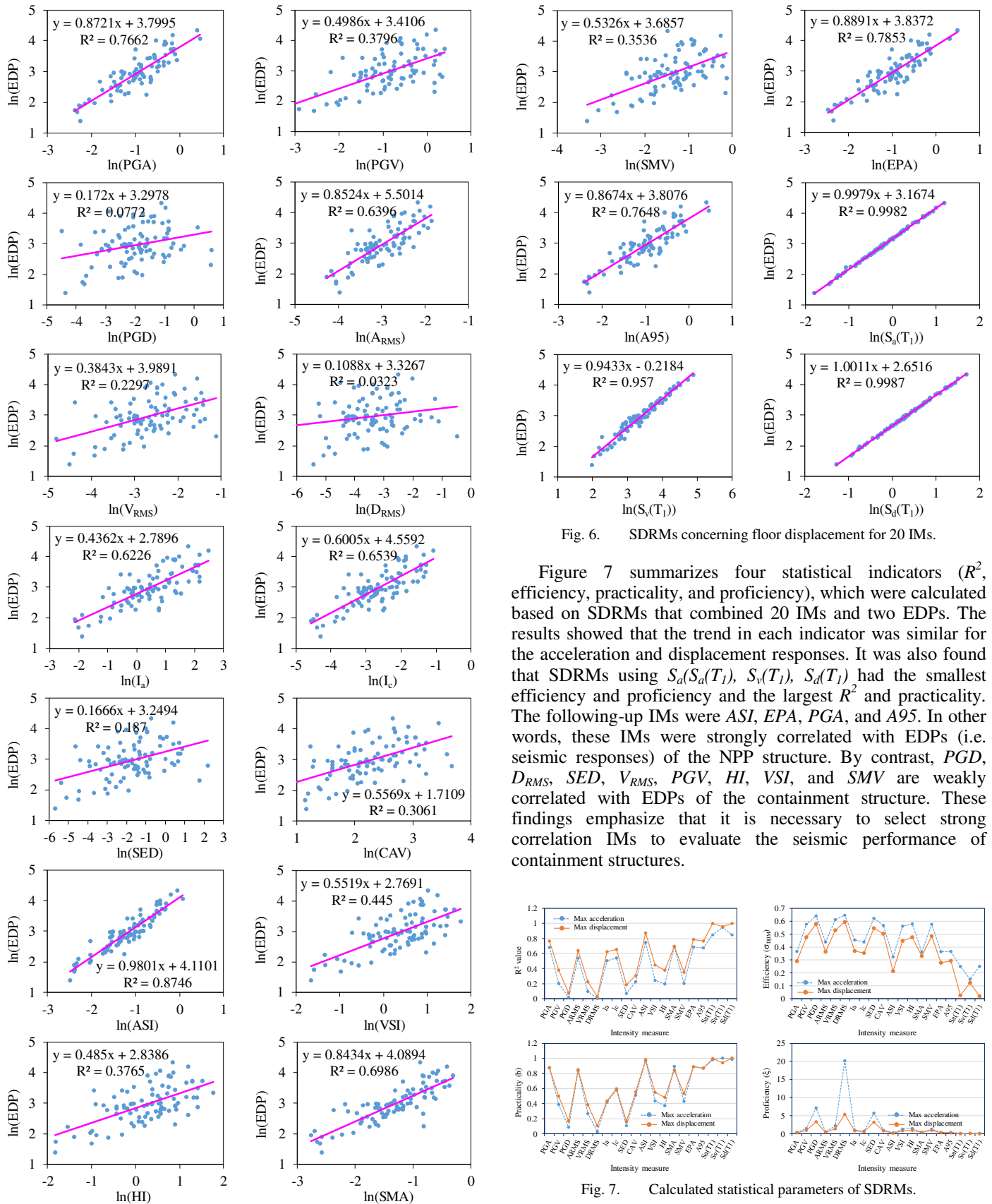


Fig. 6. SDRMs concerning floor displacement for 20 IMs.

Figure 7 summarizes four statistical indicators (R^2 , efficiency, practicality, and proficiency), which were calculated based on SDRMs that combined 20 IMs and two EDPs. The results showed that the trend in each indicator was similar for the acceleration and displacement responses. It was also found that SDRMs using $S_d(S_d(T_1))$, $S_v(T_1)$, $S_d(T_1)$ had the smallest efficiency and proficiency and the largest R^2 and practicality. The following-up IMs were AS_i , EPA , PGA , and $A95$. In other words, these IMs were strongly correlated with EDPs (i.e. seismic responses) of the NPP structure. By contrast, PGD , D_{RMS} , SED , V_{RMS} , PGV , HI , VSI , and SMV are weakly correlated with EDPs of the containment structure. These findings emphasize that it is necessary to select strong correlation IMs to evaluate the seismic performance of containment structures.

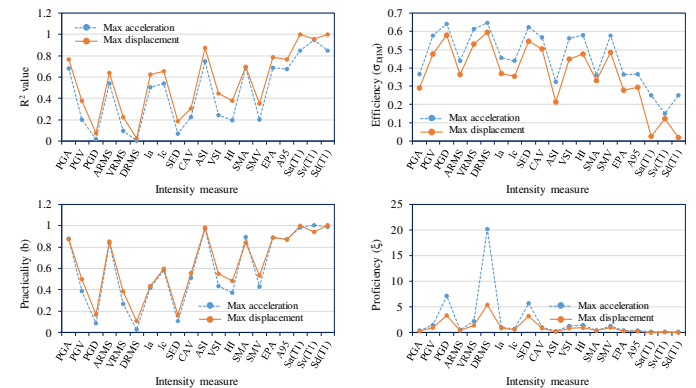


Fig. 7. Calculated statistical parameters of SDRMs.

VI. CONCLUSION

This study examined the correlation between earthquake IMs and EDPs of the containment structure of an APR-1400 NPP. Numerical modeling was developed using LSM and validated using a 3D FEM. A set of 90 ground motion records and 20 typical IMs were considered in time-history and correlation analyses. The correlation of IMs with EDPs was evaluated using statistical indicators. Based on the numerical results, the following conclusions can be drawn:

- LSM is reliable for performing time-history analysis of containment structures in NPPs.
- The strongest correlated IMs with EDPs of the containment structure were $S_d(T_1)$, $S_v(T_1)$, $S_d(T_1)$, followed by ASI , EPA , PGA , and $A95$.
- The weakest correlated IMs with EDPs of the containment structure were PGD , D_{RMS} , and SED , followed by V_{RMS} , PGV , HI , VSI , and SMV .
- It is necessary to select strongly correlated IMs to evaluate the seismic performance and fragility of NPP containment structures.

REFERENCES

- [1] A. Elenas and K. Meskouris, "Correlation study between seismic acceleration parameters and damage indices of structures," *Engineering Structures*, vol. 23, no. 6, pp. 698–704, Jun. 2001, [https://doi.org/10.1016/S0141-0296\(00\)00074-2](https://doi.org/10.1016/S0141-0296(00)00074-2).
- [2] V. V. Cao and H. R. Ronagh, "Correlation between seismic parameters of far-fault motions and damage indices of low-rise reinforced concrete frames," *Soil Dynamics and Earthquake Engineering*, vol. 66, pp. 102–112, Nov. 2014, <https://doi.org/10.1016/j.soildyn.2014.06.020>.
- [3] M. Ghayoomi and S. Dashti, "Effect of Ground Motion Characteristics on Seismic Soil-Foundation-Structure Interaction," *Earthquake Spectra*, vol. 31, no. 3, pp. 1789–1812, Aug. 2015, <https://doi.org/10.1193/040413EQS089M>.
- [4] K. Kostinakis, A. Athanatopoulou, and K. Morfidis, "Correlation between ground motion intensity measures and seismic damage of 3D R/C buildings," *Engineering Structures*, vol. 82, pp. 151–167, Jan. 2015, <https://doi.org/10.1016/j.engstruct.2014.10.035>.
- [5] A. Massumi and F. Gholami, "The influence of seismic intensity parameters on structural damage of RC buildings using principal components analysis," *Applied Mathematical Modelling*, vol. 40, no. 3, pp. 2161–2176, Feb. 2016, <https://doi.org/10.1016/j.apm.2015.09.043>.
- [6] J. R. Pejovic, N. N. Serdar, and R. R. Pejovic, "Optimal intensity measures for probabilistic seismic demand models of RC high-rise buildings," *Earthquakes and Structures*, vol. 13, no. 3, pp. 221–230, 2017, <https://doi.org/10.12989/eas.2017.13.3.221>.
- [7] J. E. Padgett, B. G. Nielson, and R. DesRoches, "Selection of optimal intensity measures in probabilistic seismic demand models of highway bridge portfolios," *Earthquake Engineering & Structural Dynamics*, vol. 37, no. 5, pp. 711–725, 2008, <https://doi.org/10.1002/eqe.782>.
- [8] Ö. Avşar and G. Özdemir, "Response of Seismic-Isolated Bridges in Relation to Intensity Measures of Ordinary and Pulselike Ground Motions," *Journal of Bridge Engineering*, vol. 18, no. 3, pp. 250–260, Mar. 2013, [https://doi.org/10.1061/\(ASCE\)BE.1943-5592.0000340](https://doi.org/10.1061/(ASCE)BE.1943-5592.0000340).
- [9] Y.-Y. Zhang, Y. Ding, and Y.-T. Pang, "Selection of Optimal Intensity Measures in Seismic Damage Analysis of Cable-Stayed Bridges Subjected to Far-Fault Ground Motions," *Journal of Earthquake and Tsunami*, vol. 09, no. 01, Mar. 2015, Art. no. 1550003, <https://doi.org/10.1142/S1793431115500037>.
- [10] V. Jahangiri, M. Yazdani, and M. S. Marefat, "Intensity measures for the seismic response assessment of plain concrete arch bridges," *Bulletin of Earthquake Engineering*, vol. 16, no. 9, pp. 4225–4248, Sep. 2018, <https://doi.org/10.1007/s10518-018-0334-8>.
- [11] C. Zelaschi, R. Monteiro, and R. Pinho, "Critical Assessment of Intensity Measures for Seismic Response of Italian RC Bridge Portfolios," *Journal of Earthquake Engineering*, vol. 23, no. 6, pp. 980–1000, Jul. 2019, <https://doi.org/10.1080/13632469.2017.1342293>.
- [12] B. Wei, Z. Hu, X. He, and L. Jiang, "Evaluation of optimal ground motion intensity measures and seismic fragility analysis of a multi-pylon cable-stayed bridge with super-high piers in Mountainous Areas," *Soil Dynamics and Earthquake Engineering*, vol. 129, Feb. 2020, Art. no. 105945, <https://doi.org/10.1016/j.soildyn.2019.105945>.
- [13] H. N. Phan and F. Paolacci, "Efficient Intensity Measures for Probabilistic Seismic Response Analysis of Anchored Above-Ground Liquid Steel Storage Tanks," in *Conference Proceedings - ASME 2016 Pressure Vessels and Piping Conference*, Vancouver, Canada, Dec. 2016, <https://doi.org/10.1115/PVP2016-63103>.
- [14] Y. Qiu, C. Zhou, and S. A. A., "Correlation between earthquake intensity parameters and damage indices of high-rise RC chimneys," *Soil Dynamics and Earthquake Engineering*, vol. 137, Oct. 2020, Art. no. 106282, <https://doi.org/10.1016/j.soildyn.2020.106282>.
- [15] Z. Chen and J. Wei, "Correlation between ground motion parameters and lining damage indices for mountain tunnels," *Natural Hazards*, vol. 65, no. 3, pp. 1683–1702, Feb. 2013, <https://doi.org/10.1007/s11069-012-0437-5>.
- [16] D. D. Nguyen, D. Park, S. Shamsher, V. Q. Nguyen, and T. H. Lee, "Seismic vulnerability assessment of rectangular cut-and-cover subway tunnels," *Tunnelling and Underground Space Technology*, vol. 86, pp. 247–261, Apr. 2019, <https://doi.org/10.1016/j.tust.2019.01.021>.
- [17] H. Shakib and V. Jahangiri, "Intensity measures for the assessment of the seismic response of buried steel pipelines," *Bulletin of Earthquake Engineering*, vol. 14, no. 4, pp. 1265–1284, Apr. 2016, <https://doi.org/10.1007/s10518-015-9863-6>.
- [18] D. D. Nguyen, B. Thusa, H. Park, M. S. Azad, and T. H. Lee, "Efficiency of various structural modeling schemes on evaluating seismic performance and fragility of APR1400 containment building," *Nuclear Engineering and Technology*, vol. 53, no. 8, pp. 2696–2707, Aug. 2021, <https://doi.org/10.1016/j.net.2021.02.006>.
- [19] T. K. Mandal, S. Ghosh, and N. N. Pujari, "Seismic fragility analysis of a typical Indian PHWR containment: Comparison of fragility models," *Structural Safety*, vol. 58, pp. 11–19, Jan. 2016, <https://doi.org/10.1016/j.strusafe.2015.08.003>.
- [20] T. T. Tran, A. T. Cao, T. H. X. Nguyen, and D. Kim, "Fragility assessment for electric cabinet in nuclear power plant using response surface methodology," *Nuclear Engineering and Technology*, vol. 51, no. 3, pp. 894–903, Jun. 2019, <https://doi.org/10.1016/j.net.2018.12.025>.
- [21] S. G. Cho and Y. H. Joe, "Seismic fragility analyses of nuclear power plant structures based on the recorded earthquake data in Korea," *Nuclear Engineering and Design*, vol. 235, no. 17, pp. 1867–1874, Aug. 2005, <https://doi.org/10.1016/j.nucengdes.2005.05.021>.
- [22] I. K. Choi, Y. S. Choun, S. M. Ahn, and J. M. Seo, "Seismic fragility analysis of a CANDU type NPP containment building for near-fault ground motions," *KSCE Journal of Civil Engineering*, vol. 10, no. 2, pp. 105–112, Mar. 2006, <https://doi.org/10.1007/BF02823928>.
- [23] C. Li, C. Zhai, S. Kunnath, and D. Ji, "Methodology for selection of the most damaging ground motions for nuclear power plant structures," *Soil Dynamics and Earthquake Engineering*, vol. 116, pp. 345–357, Jan. 2019, <https://doi.org/10.1016/j.soildyn.2018.09.039>.
- [24] D. D. Nguyen, B. Thusa, T. S. Han, and T. H. Lee, "Identifying significant earthquake intensity measures for evaluating seismic damage and fragility of nuclear power plant structures," *Nuclear Engineering and Technology*, vol. 52, no. 1, pp. 192–205, Jan. 2020, <https://doi.org/10.1016/j.net.2019.06.013>.
- [25] S. L. Kramer, *Geotechnical Earthquake Engineering*, 1st edition. Upper Saddle River, NJ, USA: Prentice Hall, 1996.
- [26] A. Arias, "Measure of Earthquake Intensity," in *Seismic Design for Nuclear Power Plants*, Cambridge, MA, USA: Massachusetts Institute of Technology Press, 1970, pp. 438–483.

- [27] Y.-J. Park, A. H.-S. Ang, and Y. K. Wen, "Seismic Damage Analysis of Reinforced Concrete Buildings," *Journal of Structural Engineering*, vol. 111, no. 4, pp. 740–757, Apr. 1985, [https://doi.org/10.1061/\(ASCE\)0733-9445\(1985\)111:4\(740\)](https://doi.org/10.1061/(ASCE)0733-9445(1985)111:4(740)).
- [28] J. R. Benjamin, "A Criterion for Determining Exceedances of the Operating Basis Earthquake," Electric Power Research Institute, Palo Alto, CA, USA, ERPINP-5930, 1988.
- [29] J. L. Von Thun, L. H. Roehm, G. A. Scott, and J. A. Wilson, "Earthquake Ground Motions for Design and Analysis of Dams," in *Earthquake Engineering and Soil Dynamics II - Recent Advances in Ground-Motion Evaluation*, Park City, UT, USA, 1988, pp. 463–481.
- [30] G. W. Housner, "Spectrum Intensities of Strong-Motion Earthquakes," C. M. Duke and M. Feigen, Eds. Los Angeles: Earthquake Engineering Research Institute, 1952, pp. 20–36.
- [31] O. W. Nuttli, "The relation of sustained maximum ground acceleration and velocity to earthquake intensity and magnitude," US Army Waterways Experimental Station, Vicksburg, MS, USA, Misc. Paper S-73-1 16, 1979.
- [32] N. Shome, C. A. Cornell, P. Bazzurro, and J. E. Carballo, "Earthquakes, Records, and Nonlinear Responses," *Earthquake Spectra*, vol. 14, no. 3, pp. 469–500, Aug. 1998, <https://doi.org/10.1193/1.1586011>.
- [33] S. K. Sarma and K. S. Yang, "An evaluation of strong motion records and a new parameter A95," *Earthquake Engineering & Structural Dynamics*, vol. 15, no. 1, pp. 119–132, 1987, <https://doi.org/10.1002/eqe.4290150109>.
- [34] "Design Response Spectra for Seismic Design of Nuclear Power Plants," Nuclear Regulatory Commission, Washington, DC, USA, Regulatory Guide 1.60 - Revision 2 2014–16297, Jul. 2014.
- [35] D.-D. Nguyen, T.-H. Lee, and V.-T. Phan, "Optimal Earthquake Intensity Measures for Probabilistic Seismic Demand Models of Base-Isolated Nuclear Power Plant Structures," *Energies*, vol. 14, no. 16, Jan. 2021, Art. no. 5163, <https://doi.org/10.3390/en14165163>.
- [36] D. D. Nguyen and C. N. Nguyen, "Seismic Responses of NPP Structures Considering the Effects of Lead Rubber Bearing," *Engineering, Technology & Applied Science Research*, vol. 10, no. 6, pp. 6500–6503, Dec. 2020, <https://doi.org/10.48084/etasr.3926>.
- [37] J. A. Alomari, "Effect of the Presence of Basements on the Vibration Period and Other Seismic Responses of R.C. Frames," *Engineering, Technology & Applied Science Research*, vol. 9, no. 5, pp. 4712–4717, Oct. 2019, <https://doi.org/10.48084/etasr.3005>.
- [38] P. C. Nguyen, B. Le-Van, and S. D. T. V. Thanh, "Nonlinear Inelastic Analysis of 2D Steel Frames: An Improvement of the Plastic Hinge Method," *Engineering, Technology & Applied Science Research*, vol. 10, no. 4, pp. 5974–5978, Aug. 2020, <https://doi.org/10.48084/etasr.3600>.
- [39] D.-D. Nguyen, B. Thusa, M. S. Azad, V.-L. Tran, and T.-H. Lee, "Optimal earthquake intensity measures for probabilistic seismic demand models of ARP1400 reactor containment building," *Nuclear Engineering and Technology*, vol. 53, no. 12, pp. 4179–4188, Dec. 2021, <https://doi.org/10.1016/j.net.2021.06.034>.
- [40] C. A. Cornell, F. Jalayer, R. O. Hamburger, and D. A. Foutch, "Probabilistic Basis for 2000 SAC Federal Emergency Management Agency Steel Moment Frame Guidelines," *Journal of Structural Engineering*, vol. 128, no. 4, pp. 526–533, Apr. 2002, [https://doi.org/10.1061/\(ASCE\)0733-9445\(2002\)128:4\(526\)](https://doi.org/10.1061/(ASCE)0733-9445(2002)128:4(526)).

Development of a Wide Bandwidth Massive Eight Dissimilar Radiating Element Multiband MIMO Antenna for mm-Wave Application

Shrenik Suresh Sarade
Electronics Engineering
Walchand College of Engineering
Sangli, India
shreniks2k7@rediffmail.com

Sachin D. Ruikar
Electronics Engineering
Walchand College of Engineering
Sangli, India
sachin.ruikar@walchandsangli.ac.in

Received: 10 June 2022 | Revised: 26 July 2022 | Accepted: 28 July 2022

Abstract-This paper proposes a massive MIMO antenna operating on 6GHz frequency as millimeter-wave. It consists of eight dissimilar-shaped radiating elements. The radiating element of the antenna is designed using square shape with different cut slots. Parasitic elements and defected ground structure are introduced for the enhancement of the correlation coefficients and total active reflection coefficients of the MIMO antenna. The rectangular shape parasitic elements are placed between the square radiating patches. The ground plane consists of rectangular shape defected ground structures. The antenna is constructed on the FR-4 substrate. Parameters such as isolation, cross-correlation, and bandwidth are enhanced. The obtained through simulations antenna parameters values of return loss, isolation, cross-correlation, total active reflection coefficients, and bandwidth are less than -10dB, less than -9.30dB, less than 0.16, less than 0.00015, and greater than 200MHz respectively. The antenna operates on various bands with fractional bandwidth greater than 3% for a frequency of 6GHz. This antenna is useful for a variety of applications in wireless systems.

Keywords-MIMO; DGS; TARC; CC; ECC

I. INTRODUCTION

Antennas are a crucial part of communication systems. An antenna is used to transport data from one location to another without interfering with the original signal. As a result, there is a need to build an antenna that meets the requirements of the communication system, such as size, weight, and signal quality. Multiple Input and Multiple Output (MIMO) antennas play an important role in the antenna field nowadays. Multiple antennas may be present at the transmitter and the receiver. The low data rate in Single Input and Single Output (SISO) system can be improved using an MIMO antenna system. The data rate of MIMO antenna grows linearly and depends on the number of patches in the antenna. The performance of the MIMO antenna differs with return loss, isolation, correlation coefficients, and total active reflection coefficients. In a MIMO antenna, multiple radiating patches are positioned on the same substrate in close proximity to one another. The close proximity of the square radiating patches influences the isolation (which becomes high) between the radiating patches

and the correlation coefficients become higher. There is a requirement of improvement in antenna's isolation, correlation coefficients, and data rate. To improve isolation and correlation coefficients, several studies employ Defective Ground Structure (DGS), Parasitic Elements (PEs), metamaterials, Decoupling Structure (DS), and Electromagnetic Band Gap (EBG) approaches. A DGS technique is used to improve isolation. Cut slots of various shapes are used in the ground plane [1-6]. To improve isolation, a decoupling structure is constructed that decouples the input of radiating patches from the matching network setup in [7-11]. PEs are used to improve the isolation between the patches in [12-17]. From the above literature survey, it can be concluded that there is a requirement to develop a massive MIMO antenna that operates on wide bandwidth multiband applications, with better TARC and better cross correlation.

A diverse shaped-element gigantic MIMO antenna is proposed in this work. It operates at multiband frequency with wide band operation. Parasitic elements and a defective ground structure are used to improve antenna parameters such as isolation, cross correlation, and total active reflection coefficients.

II. DESIGN OF THE MASSIVE MIMO ANTENNA

The concept of the MIMO antenna is explained above along with the literature survey. In this section, the massive MIMO antenna is designed and explained in detail. The designed antenna comprises of 8 square radiating patches with distinct cut slots for the 6GHz frequency, as shown in Figure 1. The antenna dimensions are provided in Figure 2. The antenna is developed using a FR-4 substrate with 1.6mm height h and 4.4 dielectric constant. The antenna's geometrical structure, i.e. length L_{re} and width W_{re} , was created using the square radiating patch transmission line model [20], which has the dimensions listed in Table I, which shows the measurements of 8 radiating elements with varying cut slots. A rectangular cut slot [20] is placed in patch-1 and patch-3, with length C and width D . A similar rectangular cut slot [20] is placed in patches-5, -7, and -8. A square cut slot is placed in patch-6, with both length and

Corresponding author: Shrenik Suresh Sarade

width C . The cut slot dimensions of the single patch are optimized using the equivalent circuit explained in Section III. Inset Feed Line (IFL) [20] with length C and width D is used to excite the antenna elements (dimensions listed in Table I). The

antenna's dimensions (FR-4 substrate) which consist of length E and width F of the patch are summarized in Table I. The distance between the parasitic elements and the radiating patches is less than half of the wavelength.

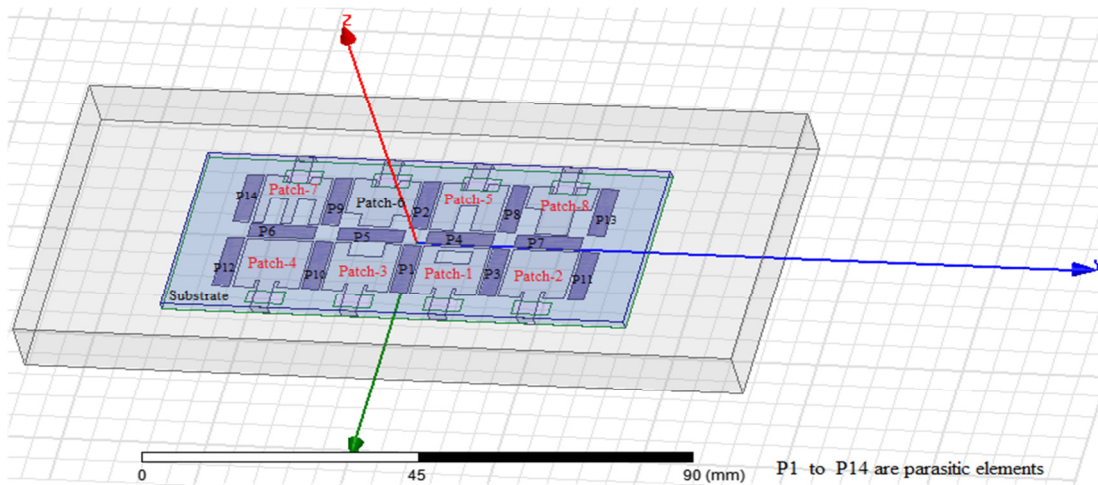


Fig. 1. Massive MIMO antenna with 8 distinct shaped components with PEs and a GDS.

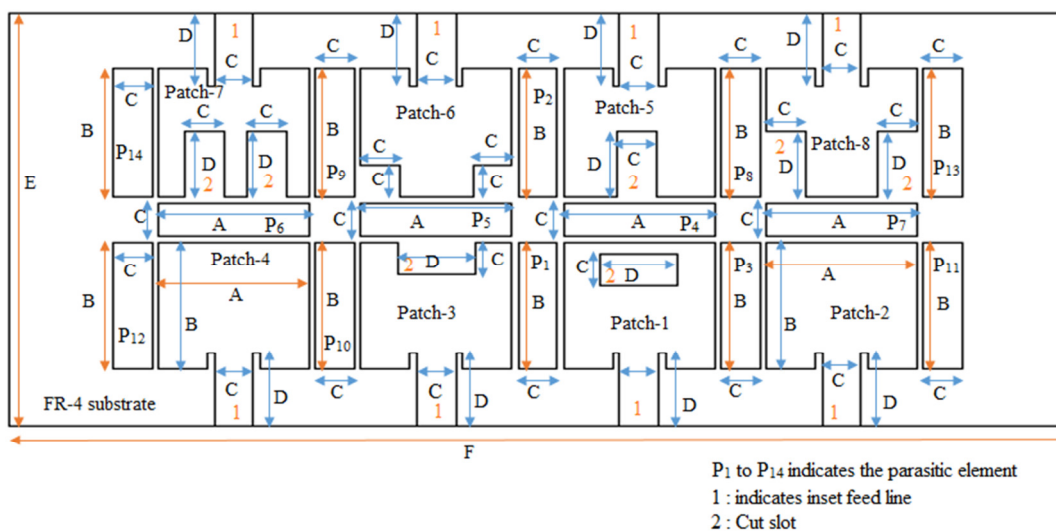


Fig. 2. The dimensions of the developed massive MIMO antenna.

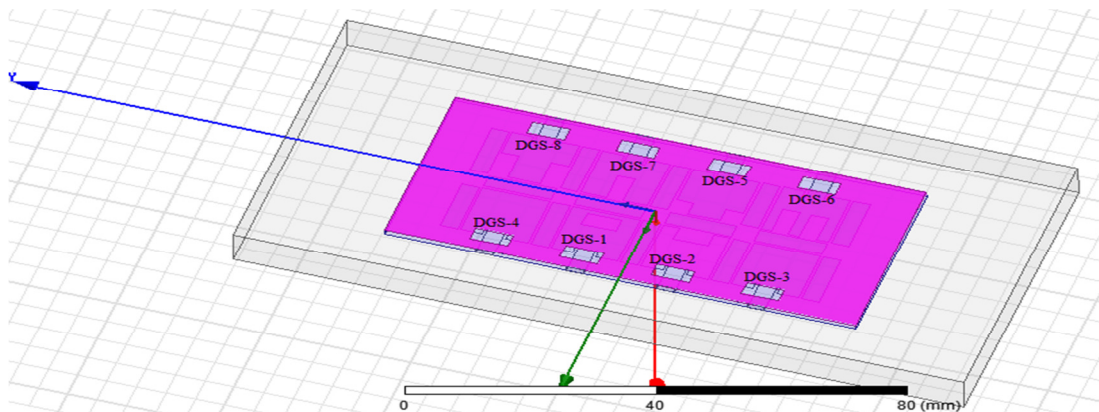


Fig. 3. The ground plane of antenna with DGS.

PEs and DGS improve the Total Active Reflection Coefficients (TARC), the Correlation Coefficient (CC), and the Envelope Correlation Coefficient (ECC) values between the radiating elements. Table I shows the size of parasitic elements (P1 to P14) [12-17]. As indicated in Figure 1, rectangular shaped Parasitic Elements (PEs) are used between the radiating patches. The PEs are used to negate parts of the coupled field between the elements because it creates an opposite coupling field, which lessens the original field and hence reduces total coupling on the antenna. The PE structure and the radiating patch are not physically related. Figure 3 depicts the antenna's ground plane, while Figure 4 depicts its dimensions. Table I shows the length D and width C of the DGS in the ground plane. The ground plane is made up of rectangular-DGS cut slots [1-6] that are utilized to improve isolation

TABLE I. ANTENNA DIMENSIONS

Sr. no.	Parameter	Dimensions (in mm)
1	Patch length (L_{re})	A = 11.38
2	Patch width (L_{re})	B = 11.38
3	Length of IFL	D = 6.41
4	Width of IFL	C = 2.942
5	Length of substrate	E = 36.522
6	Width of substrate	F = 80

III. EQUIVALENT CIRCUIT MODEL OF THE ANTENNA

In this section, the operation of the single radiating patch of the antenna is explained using the equivalent circuit model. That is applicable to all radiating patches. DGS and PEs are used in the development of the gigantic MIMO antenna. These two techniques are used to improve the antenna's isolation, TARC, CC, ECC, and bandwidth. The equivalent circuit mathematical model is used to describe how antennas work. The corresponding circuit of a single radiating patch is shown in Figure 5.

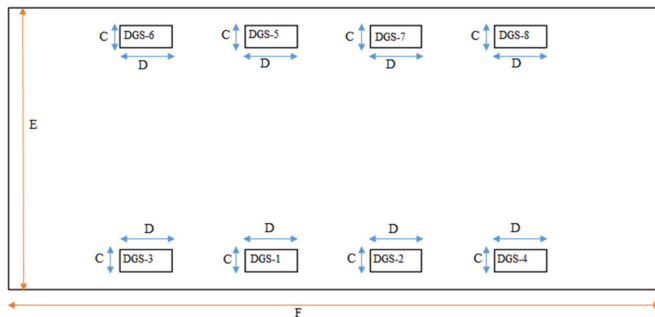


Fig. 4. The dimensions of the ground plane of the antenna with DGS.

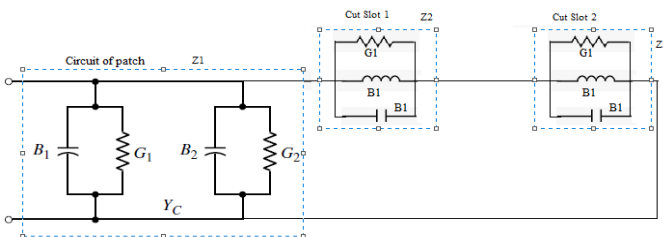


Fig. 5. Equivalent circuit model for square-radiating patch.

As shown in Figure 1, the antenna comprises of a square radiating patch with a cut slot. Figure 5 is divided into two parts: a square shape circuit with impedance Z_1 and rectangular cut slot-1 and 2 with impedance Z_2 and Z_3 . The inductor and capacitor values of the equivalent circuit [21] are used to compute the cut slot dimensions using (1) and (2):

$$G_1 = \frac{0.00833 W}{\lambda_0} [1 - 0.04167(k_0 H_{fr4})^2] \quad (1)$$

$$B_1 = \frac{0.00833 W}{\lambda_0} [1 - 0.636 \ln(k_0 H_{fr4})] \quad (2)$$

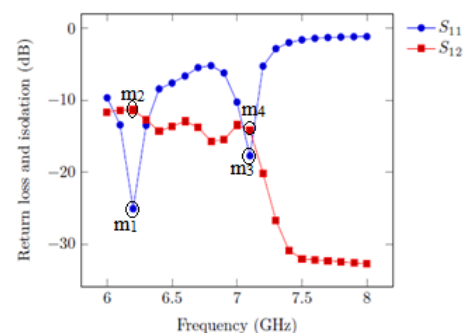
where G_1 is the resistive value of the circuit, B_1 is the capacitive or inductive value of the circuit, $W = L_{re}$ the width of the patch, h the height of the substrate, and k_0 constant.

Because the antenna elements have distinct cut slots, the antenna can function on many frequencies. This antenna's operating concept is similar to that of any other radiating patch, and cut slots are provided according to the desired frequency.

IV. RESULT ANALYSIS

The antenna is simulated using the High Frequency Structure Simulator (HFSS). Isolation, CC, ECC, TARC, and bandwidth [19] are the performance parameters of the MIMO antenna. The 8 radiating patches are arranged in a row (close to each other) which results in high level of isolation among the radiating patch. DGS and PE techniques are employed to improve the isolation between the radiating patches. The rectangular carved slit acts as a DGS in the ground. The DGS alters the properties of the transmission line's inductor and capacitor, resulting in a shift in the antenna's frequency response. A rectangular shaped PE is placed between the radiating elements to improve the antenna's isolation and bandwidth. It prevents the radiating energy passing from one element to the nearby element. The isolation performance between the parameters helps improve CC, ECC, and TARC.

The return loss (S_{11}) and the acquired isolation between the remaining elements of patch-1 are shown in Figure 6. The antenna operates on 6.2GHz (m_1) and 7.1GHz (m_3), with less than -17.50dB return loss (S_{11}), less than -11.25dB isolation (S_{12} (m_2 and m_4)), and 347.4MHz (5.79%) bandwidth. The isolation between the remaining patches, S_{13} , S_{14} , S_{15} , S_{16} , S_{17} , and S_{18} is less than -11.25dB (S_{12}).

Fig. 6. Return loss (S_{11}) and isolation of patch-1.

The antenna element bandwidth [18-20] is obtained at -10dB return loss. The return loss (S_{22}) and the isolation

between the remaining elements of patch-2 are shown in Figure 7. It operates on the 5.7GHz, with less than -24.79dB return loss (S_{22} (m_1)), less than -11dB isolation (S_{26} (m_2)), and 437.3MHz (7.289%) bandwidth. The isolation between the remaining patches such as S_{21} , S_{23} , S_{24} , S_{25} , S_{27} , and S_{28} is less than -11dB (S_{26}).

The return loss (S_{33}) and the isolation between the remaining elements of patch-3 are shown in Figure 8. It operates on 5.8GHz (m_1) and 6.9GHz (m_3), with less than -12.50dB return loss (S_{33}), less than -11.40dB isolation (S_{34} (m_2) and m_4)), and 403.32 MHz (6.72%) bandwidth. The isolation between the remaining patches such as S_{31} , S_{32} , S_{35} , S_{36} , S_{37} , and S_{38} is less than -11.40dB (S_{34}).

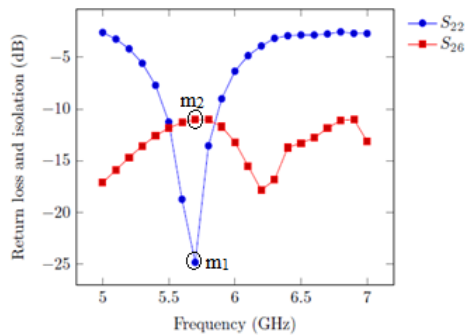


Fig. 7. Return loss (S_{22}) and isolation of patch-2.

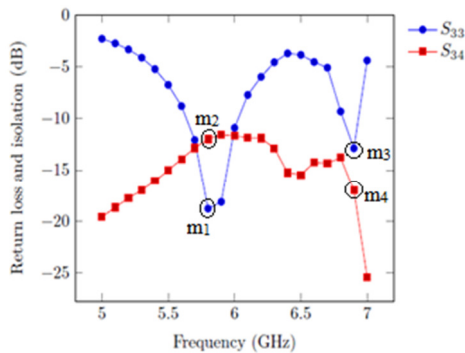


Fig. 8. Return loss (S_{33}) and isolation of patch-3.

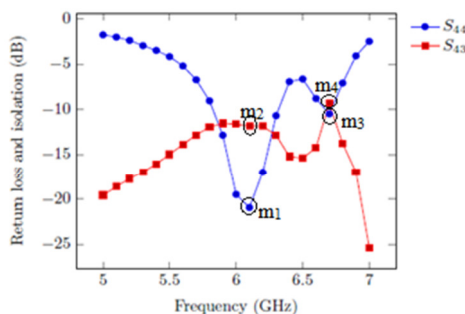


Fig. 9. Return loss (S_{44}) and isolation of patch-4.

The return loss (S_{44}) and the isolation between the remaining elements of patch-4 are shown in Figure 9. It operates on 6.1GHz (m_1) and 6.7GHz (m_3), with less than -10.25dB return loss (S_{44}), less than -9.35 dB isolation (S_{43} (m_2

and m_4)), and 488MHz (8.146%) bandwidth. The isolation between the remaining patches such as S_{41} , S_{42} , S_{45} , S_{46} , S_{47} , and S_{48} is less than -9.35 dB (S_{43}).

The return loss (S_{55}) and the isolation between the remaining elements of patch-5 are shown in Figure 10. It resonates on 5.8GHz (m_1) and 6.8GHz (m_3), with less than -18.50dB return loss (S_{55}), less than -9.70dB isolation (S_{51} 5.8GHz (m_2 and 5.8GHz m_4)), and 399MHz (6.65%) bandwidth. The isolation between the remaining patches such as S_{52} , S_{53} , S_{54} , S_{56} , S_{57} , and S_{58} is less than -11.33dB (S_{51}).

The return loss (S_{66}) and the isolation between the remaining elements of patch-6 are shown in Figure 11. It resonates on 5.8GHz (m_1), with less than -20.92dB return loss (S_{66}), less than -11.17dB isolation (S_{67} 5.8GHz (m_2)), and 425.76 MHz (7.096%) bandwidth. The isolation between the remaining patches such as S_{61} , S_{62} , S_{63} , S_{64} , S_{65} , and S_{68} is less than -11.33dB (S_{67}).

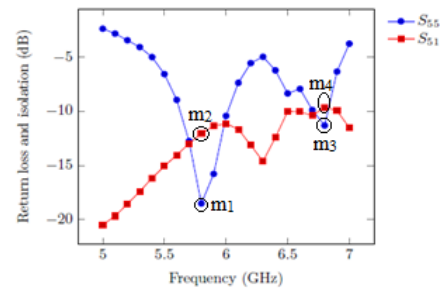


Fig. 10. Return loss (S_{55}) and isolation of patch-5.

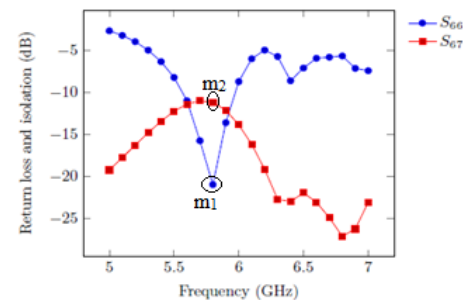


Fig. 11. Return loss (S_{66}) and isolation of patch-6.

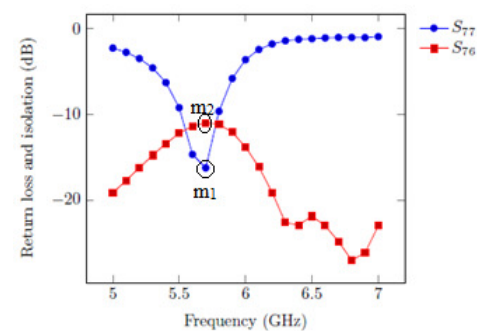


Fig. 12. Return loss (S_{77}) and isolation of patch-7.

The return loss (S_{77} (m_1)) and the isolation between the remaining elements of patch-7 are shown in Figure 12. It resonates at 5.7GHz, with less than -16.25dB return loss (S_{66}),

less than -10.98dB isolation ($S_{76}(m_2)$), and 297MHz (4.95%) bandwidth. The isolation between the remaining patches such as S_{71} , S_{72} , S_{73} , S_{74} , S_{75} , and S_{78} is less than -11.33dB (S_{76}).

The return loss (S_{88}) and the isolation between the remaining elements of patch-8 are shown in Figure 13. It resonates at 5.8GHz (m_1) and 6.8GHz (m_3), with less than -20.30dB return loss (S_{88}), less than -11.10dB isolation ($S_{84}(m_2$ and $m_4)$), and 379.2MHz (6.32%) bandwidth. The isolation between the remaining patches such as S_{81} , S_{82} , S_{83} , S_{85} , S_{86} , and S_{87} is less than -11.33dB isolation (S_{84}).

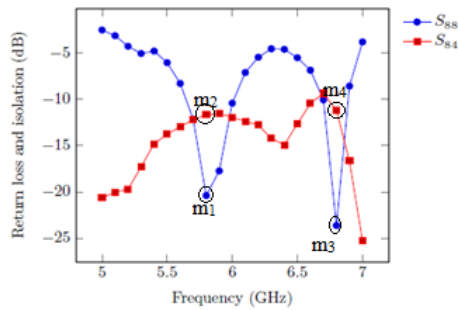


Fig. 13. Return loss (S_{88}) and isolation of patch-8.

The results of the antenna parameter investigation show that the gain attained is 2.69dB, as shown in Figure 14. Figure 15 shows the antenna radiation pattern. TARC is less than 0.16, CC is less than 0.0122, ECC is less than 0.00015, and DG is near to 9.9985 [20].

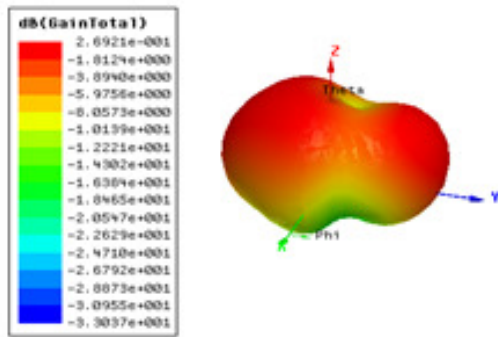


Fig. 14. Gain of the MIMO antenna.

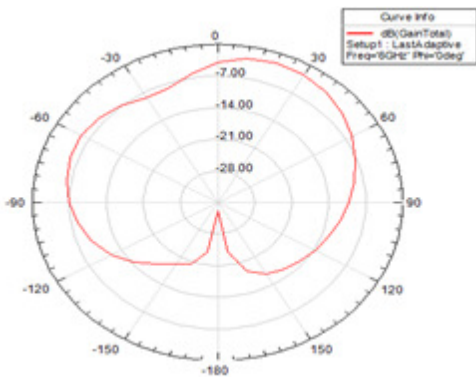


Fig. 15. Radiation pattern of the MIMO antenna.

V. COMPARISON

The proposed antenna's parameters are compared with other works in Table II. The comparison shows that the proposed antenna is developed for 8-different shaped radiating elements. It operates on the multiband frequency with a wide bandwidth.

TABLE II. COMPARISON OF THE PROPOSED ANTENNA WITH OTHER WORKS

Ref	Technique used	Parameter	Frequency band and bandwidth	Radiating patches
[1]	DGS	-10 dB RL, -12dB isolation	Single band and narrow band	Same shape 8-radiating patches
[7]	DGS	-20 dB RL, -15dB isolation	Dual band and narrow band	Same shape 8-radiating patches
[12]	PE	-10 dB RL, -10dB isolation	Dual band and wide band	Same shape 8-radiating patches
Proposed	DGS + PE	-10 dB RL, -9.30dB isolation	Multiband and wide band with better cross correlation	Different 8-shaped radiating patches

VI. CONCLUSION

The proposed 8 dissimilarized element antenna operates on various frequency bands for a wide bandwidth. The antenna parameters are enhanced using DGS and PEs. The proposed antenna operates at 5.7GHz, 5.8GHz, 6.1GHz, 6.2GHz, 6.7GHz, 6.8GHz, 6.9GHz, and 7.1GHz. The results obtained through simulations for various antenna parameter values show -10dB return loss, less than -9.30dB isolation, less than 0.16 CC, less than 0.0122 ECC, less than 0.00015 TARC, and bandwidth greater than 200MHz. The antenna operates on the various bands with fractional bandwidth greater than 3% for 6GHz frequency. This antenna is designed for various applications of communication systems with wide bandwidth operation.

REFERENCES

- [1] Y. Li, C.-Y.-D. Sim, Y. Luo, and G. Yang, "High-Isolation 3.5 GHz Eight-Antenna MIMO Array Using Balanced Open-Slot Antenna Element for 5G Smartphones," *IEEE Transactions on Antennas and Propagation*, vol. 67, no. 6, pp. 3820–3830, Jun. 2019, <https://doi.org/10.1109/TAP.2019.2902751>.
- [2] M. Y. Jamal, M. Li, and K. L. Yeung, "Isolation Enhancement of Closely Packed Dual Circularly Polarized MIMO Antenna Using Hybrid Technique," *IEEE Access*, vol. 8, pp. 11241–11247, 2020, <https://doi.org/10.1109/ACCESS.2020.2964902>.
- [3] W. Wang, Y. Wu, W. Wang, and Y. Yang, "Isolation Enhancement in Dual-Band Monopole Antenna for 5G Applications," *IEEE Transactions on Circuits and Systems II: Express Briefs*, vol. 68, no. 6, pp. 1867–1871, Jun. 2021, <https://doi.org/10.1109/TCSII.2020.3040164>.
- [4] J. C. Dash and D. Sarkar, "Microstrip Patch Antenna System With Enhanced Inter-Port Isolation for Full-Duplex/MIMO Applications," *IEEE Access*, vol. 9, pp. 156222–156228, 2021, <https://doi.org/10.1109/ACCESS.2021.3128997>.
- [5] M. O. Dwairi, "Increasing Gain Evaluation of 2x1 and 2x2 MIMO Microstrip Antennas," *Engineering, Technology & Applied Science Research*, vol. 11, no. 5, pp. 7531–7535, Oct. 2021, <https://doi.org/10.48084/etasr.4305>.

- [6] S. Dey, S. Dey, and S. K. Koul, "Isolation Improvement of MIMO Antenna Using Novel EBG and Hair-Pin Shaped DGS at 5G Millimeter Wave Band," *IEEE Access*, vol. 9, pp. 162820–162834, 2021, <https://doi.org/10.1109/ACCESS.2021.3133324>.
- [7] L. Cui, J. Guo, Y. Liu, and C.-Y.-D. Sim, "An 8-Element Dual-Band MIMO Antenna with Decoupling Stub for 5G Smartphone Applications," *IEEE Antennas and Wireless Propagation Letters*, vol. 18, no. 10, pp. 2095–2099, Jul. 2019, <https://doi.org/10.1109/LAWP.2019.2937851>.
- [8] M. Li and S. Cheung, "Isolation Enhancement for MIMO Dielectric Resonator Antennas Using Dielectric Superstrate," *IEEE Transactions on Antennas and Propagation*, vol. 69, no. 7, pp. 4154–4159, Jul. 2021, <https://doi.org/10.1109/TAP.2020.3044683>.
- [9] M. Li, M. Y. Jamal, L. Jiang, and K. L. Yeung, "Isolation Enhancement for MIMO Patch Antennas Sharing a Common Thick Substrate: Using a Dielectric Block to Control Space-Wave Coupling to Cancel Surface-Wave Coupling," *IEEE Transactions on Antennas and Propagation*, vol. 69, no. 4, pp. 1853–1863, Apr. 2021, <https://doi.org/10.1109/TAP.2020.3026897>.
- [10] H. Lin, Q. Chen, Y. Ji, X. Yang, J. Wang, and L. Ge, "Weak-Field-Based Self-Decoupling Patch Antennas," *IEEE Transactions on Antennas and Propagation*, vol. 68, no. 6, pp. 4208–4217, Jun. 2020, <https://doi.org/10.1109/TAP.2020.2970109>.
- [11] T. Pei, L. Zhu, J. Wang, and W. Wu, "A Low-Profile Decoupling Structure for Mutual Coupling Suppression in MIMO Patch Antenna," *IEEE Transactions on Antennas and Propagation*, vol. 69, no. 10, pp. 6145–6153, Jul. 2021, <https://doi.org/10.1109/TAP.2021.3098565>.
- [12] N. O. Parchin *et al.*, "Eight-Element Dual-Polarized MIMO Slot Antenna System for 5G Smartphone Applications," *IEEE Access*, vol. 7, pp. 15612–15622, 2019, <https://doi.org/10.1109/ACCESS.2019.2893112>.
- [13] W. Wang and Y. Zheng, "Wideband Gain Enhancement of a Dual-Polarized MIMO Vehicular Antenna," *IEEE Transactions on Vehicular Technology*, vol. 70, no. 8, pp. 7897–7907, Dec. 2021, <https://doi.org/10.1109/TVT.2021.3094879>.
- [14] S. Yang, L. Liang, W. Wang, Z. Fang, and Y. Zheng, "Wideband Gain Enhancement of an AMC Cavity-Backed Dual-Polarized Antenna," *IEEE Transactions on Vehicular Technology*, vol. 70, no. 12, pp. 12703–12712, Sep. 2021, <https://doi.org/10.1109/TVT.2021.3119643>.
- [15] Z. Akhter, R. M. Bilal, and A. Shamim, "A Dual Mode, Thin and Wideband MIMO Antenna System for Seamless Integration on UAV," *IEEE Open Journal of Antennas and Propagation*, vol. 2, pp. 991–1000, 2021, <https://doi.org/10.1109/OJAP.2021.3115025>.
- [16] Z. Chen, W. Zhou, and J. Hong, "A Miniaturized MIMO Antenna With Triple Band-Notched Characteristics for UWB Applications," *IEEE Access*, vol. 9, pp. 63646–63655, 2021, <https://doi.org/10.1109/ACCESS.2021.3074511>.
- [17] G. Kim and S. Kim, "Design and Analysis of Dual Polarized Broadband Microstrip Patch Antenna for 5G mmWave Antenna Module on FR4 Substrate," *IEEE Access*, vol. 9, pp. 64306–64316, 2021, <https://doi.org/10.1109/ACCESS.2021.3075495>.
- [18] H. Alsaif, "Extreme Wide Band MIMO Antenna System for Fifth Generation Wireless Systems," *Engineering, Technology & Applied Science Research*, vol. 10, no. 2, pp. 5492–5495, Apr. 2020, <https://doi.org/10.48084/etasr.3413>.
- [19] P. Bora, P. Pokkunuri, and B. T. P. Madhav, "The Design of Closed Square RR Loaded 2-Port MIMO for Dual Band Applications," *Engineering, Technology & Applied Science Research*, vol. 12, no. 2, pp. 8382–8387, Apr. 2022, <https://doi.org/10.48084/etasr.4760>.
- [20] S. S. Sarade and S. D. Ruikar, "A Different Shaped Radiating Element Wide Band Multi-Band Massive MIMO Antenna for 5G/WLAN applications with Enhanced Correlation Coefficient," *IOP Conference Series: Materials Science and Engineering*, vol. 1187, no. 1, p. 012017, Jun. 2021, <https://doi.org/10.1088/1757-899X/1187/1/012017>.
- [21] C. A. Balanis, *Antenna Theory: Analysis and Design*, 3rd ed. Hoboken, N.J, USA: Wiley, 2005.

An Enhanced Software Framework for Improving QoS in IoT

Uma Tomer

Faculty of Computer Applications
Manav Rachna International Institute of Research and
Studies, Faridabad
Haryana, India
uma.tomer@gmail.com

Parul Gandhi

Faculty of Computer Applications
Manav Rachna International Institute of Research and
Studies, Faridabad
Haryana, India
parul.fca@mriu.edu.in

Received: 20 May 2022 | Revised: 25 June 2022 | Accepted: 1 July 2022

Abstract-Internet of Things (IoT) and Artificial Intelligence (AI) with its subcomponents are the latest emerging technologies that make our daily lives easier. Quality of Service (QoS) plays a very important role in IoT due to the large number of interconnected nodes. QoS is inversely dependent on the node count, i.e. the increment of nodes causes hampering to QoS, as increasing the number of nodes increases the number of requests to the IoT server. An enhanced framework is strongly needed to control QoS in IoT applications. This study proposes and implements an enhanced framework using Matlab, to control the number of requests. The proposed model can improve QoS parameters like throughput, latency, and packet loss by reducing the number of requests generated by the end nodes without compromising the services to the end user. The results showed that QoS parameters improved in terms of throughput by 5-10%, packet loss by up to 6%, and packet latency by 4%. This model can also be tested in hardware and may provide a better QoS solution.

Keywords-QoS; packet loss; latency; throughput; QoL; PoE

I. INTRODUCTION

Technology is transforming daily life and the world is getting more and more digitized, as objects are interconnected to the internet to provide. Digital applications exploit networks, wireless sensors, Wireless Local Area Networks (WLANs), and the Internet to improve their performance. Everything related to IoT can be considered as an edge node that helps in sensing, measuring, and interpreting data, and therefore requires good internet connectivity [1-5]. The huge number of complex interactions between devices in edge nodes causes difficulties in achieving dynamic QoS requirements. Service-oriented IoT is based on dynamic services for various applications and software tools to process and monitor parameters. This technology faces many challenges such as power consumption, lack of compliance, botnet attack, real-time sensing, and failure of components [1]. Various architectures have been proposed for traditional networks, but the existing traditional QoS attributes are inappropriate, and more QoS attributes should be considered to include energy consumption, information accuracy, better utilization of the network, and IoT coverage [6]. To overcome these problems, a new QoS model is required to improve and balance data

accuracy and the quality of the data delivered to the sensors [6]. The accuracy of the information is the key to closing the gap between sensor data and the actual world [6].

IoT technology faces challenges such as standardization, cyber security, and energy management [6-8]. These problems motivated researchers to examine new IoT architectures for QoS, considering traditional and special attributes such as accuracy, energy consumption, and network optimization. This study proposes a three-layer architecture, i.e. sensor, network, and architecture, to achieve adequate performance depending on the demanded service. The Building Management System (BMS) is responsible for automatic regulation, control, and maintenance of predefined parameters to control functionality. It improves the Quality of Life (QoL) by improving the management system including transportation, smart grids, traffic lights, surveillance, and smart services. IoT-based systems can support these requirements easily by using Power over Ethernet (PoE), which offers an opportunity to revolutionize these devices. A survey study showed that buildings are responsible for consuming around 40% of the total energy consumption, but the BMS is increasing rapidly due to IoT applications. This study aims to:

- Investigate and analyze the main parameters that are vital for improving the performance of IoT QoS.
- Propose a framework to improve certain parameters of the IoT network, such as latency, throughput, and packet loss.
- Propose a novel algorithm to reduce the number of requests generated by IoT end-nodes and hence reduce the load of the IoT server.

II. RELATED WORKS

Although QoS for traditional networks has been explored a lot, the research on service-oriented IoT was comparatively less. A three-layered architecture was proposed for service-oriented IoT in [1], including the Application, Network, and Sensing Layers, to optimize scheduling performance and minimize resource costs. The Application Layer was used to explore optimal QoS-aware services using component services.

The Network layer was used to deal with the scheduling of heterogeneous network environments. The Sensing Layer was used to deal with information acquisition and resource allocation. Edge Computing improved the user experience by bringing computing resources closer to the location where IoT produces data [7]. IoT users face QoS hindrances for the isolated execution of their applications. The skillful pairing of cloudlets to IoT applications is the primary task to resolve QoS constraints. A bilateral solution for edge services was proposed in [7], taking into account the demands of QoS in terms of service response time and establishing the dynamic pricing of the edge service rooted in the motives of cloudlets, IoT users, and the system.

The existing energy management mechanism fails to estimate real-time computation and the mobility of battery-powered IoT [8]. This study presented real-time computations under QoS constraints for battery applications and proposed a mobility-aware network for lifetime maximization. This was performed in two stages, online and offline. The online stage included a time-efficient QoS for the execution of a task to the frequently changing QoS requirements, while optimal mobility maximized network lifetime in the offline stage. A QoS-constrained IoT system operating with Finite Block Length (FBL) codes was proposed in [9] to support low latency communications, studied the arrival model and the deadline limit, and presented a QoS-constrained throughput expression. This study proposed an optimal power control algorithm to maximize throughput while guaranteeing a certain reliability target.

Despite the enormous attempts in standardization to reach the full potential of IoT, many challenges still exist. In [10], the QoS parameters and metrics were highlighted to improve an IoT device, considering QoS metrics such as throughput, delay, and packet loss. As multimedia services demand equalized QoS, they can use Quality of Experience (QoE) to dynamically assign resources [11]. This study determined various methods to enhance QoE and presented a mathematical model to meet the desired QoS. As QoS factors have a strong influence on QoE, IoT services were examined by equating three fundamental metrics of QoS: small loss, latency, and jitter [12]. These studies show that there is room for further improvement in the QoS of IoT. As IoT applications are vital in different parts of life, such as health monitoring [13, 14] or intrusion detection [15], there is still a need to improve existing algorithms and improve the throughput, latency, packet loss, and performance of the IoT server by reducing the number of packets.

III. PERFORMANCE PARAMETERS FOR QoS OF IoT

IoT is expanding rapidly in wireless communications [16]. Cisco proposed a standard IoT framework having 7 IoT levels, distributed in 3 computational layers: Edge-side, Server/cloud-side, and User-side layer. These computational layers transform real-world data into application visions. The Edge-side layer consists of 3 different levels in the framework: Edge nodes, Communication, and Edge Computing. Edge nodes provide the intelligence to sense, measure, and connect the Internet gateway to the cloud [18]. IoT Information Communication Technology (ICT) transfers information human to human,

human to things, and things to things [19]. Edge-Computing is an emerging model that extends the cloud and its services to the edge of the network [20]. The Server/Cloud-side layer embeds data accumulation and abstraction, requiring high computational power, transmission cost, and delay [16]. To address the needs of non-real-time applications, real-time data is acquired in the data aggregation stage, which determines whether the data is relevant or not for the required application. The data abstraction stage conducts data preparation for the consumer application. The User-side layer consists of users and centers.

The performance parameters of QoS in IoT are latency, accuracy, and Packet Error Rate (PER). Latency is a measure of delay. In networking, latency is the measurement of data transmission to the target. In [21], the latencies of 3 Amazon Web Service (AWS) regions EAST-1, EAST-2, and WEST-2, and three Azure areas WEST, CENTRAL, and EAST were examined. To handle the latency of IoT instruments, it was noted that the aggregated processing latency in AWS was more than in Azure. The average latency was 45, 49, and 46ms for AWS EAST-1, EAST-2, and WEST-2 respectively, while 14, 12, and 4ms were the latencies for Azure WEST, CENTRAL, and EAST respectively. In [22], the analytical and downlink latency was compared, deriving expressions and highlighting performance tradeoffs in channel scheduling. The simulator was developed in Matlab and it was observed that it had a latency of 10ms.

Accuracy measures how close the displayed measurement is to the actual value of a signal. A framework was proposed in [23] to evaluate the accuracy by estimating the number of disk I/O per process. It was implemented with the INU emulator in Matlab by fixing 2 parameters: n as the number of buckets in the bucket array, and m as the number of buckets in each bucket subarray. Three simulations were performed for $t=1, 5$, and 10 minutes, and n and m were observed to be 20 and 5 respectively, to achieve accuracy. Piggybacking was used in [24] to improve accuracy. A comparison of the Shewhart and Least Mean Square (LMS) methods was performed for data-transmission reduction of the two datasets. For the indoor scenario, the numbers of transmissions were 408 and 58 for LMS and Shewhart respectively. For the outdoor scenario, the number of transmissions was 682 for LMS and 201 for Shewhart. During the measurements, it was observed that the current consumption increased with the increase in piggyback, and the battery life reduced.

PER is used to test the access terminal's receiver performance. A newscast approach was proposed in [25], using a moving average along with a network of devices to survey the PER of the current frame. This process can increase the probability of data renewal by providing the aimed number of encrypted yield packets to meet the number of required packets for appropriate data decoding and recovery. When using the legacy procedure, the data recovery probability strongly decreases accompanying the increase in packet inaccuracy. The packet error probability was between 0.1 and 0.3, and the PER was 0.012 for the legacy and 0.015 for the proposed model. PER in Wireless Sensor Network (WSN) for Heating, Ventilation, and Air Conditioning (HVAC) systems was

investigated in [26]. PER data were captured for 1 month. Temperature and humidity were collected and packet loss percentage was reported. The data were split into 3 classes: temperature and moisture (Class 1), neighbor node ID along with the number of hops (Class 2), amount of packets and small rebroadcast counts (Class 3). It was noticed that impenetrable node classification regionally can considerably reduce packet drain. The packet loss ratio of Class 1 was higher compared to the other two classes, possibly due to the large size of the packets. It was also deduced that a network could be simulated to decrease the leap counts by balancing the optimum count of nodes and separation.

IV. PROPOSED FRAMEWORK

An IoT network consists of a large number of interconnected devices. Some interconnections are based on local networking, and some of them require an Internet connection. The QoS of the IoT is based on the requests generated per unit of time for a particular IoT platform. An IoT platform can use Bluetooth, WiFi, Zigbee [27], or satellite networks [28]. Figure 1 shows the conventional and the proposed architecture of the IoT layer and the generation of a request to the IoT server. If the number of requests for a particular application can be reduced, then the QoS can be enhanced. There are many IoT platforms available on the market that focus on enhancing the devices to be served. The mutual benefit of an IoT hardware manufacturer and an IoT platform developer is that the more devices demanded, the more profit can be earned. But there is a very good scope for enhancing the QoS of a particular server by reducing its load.

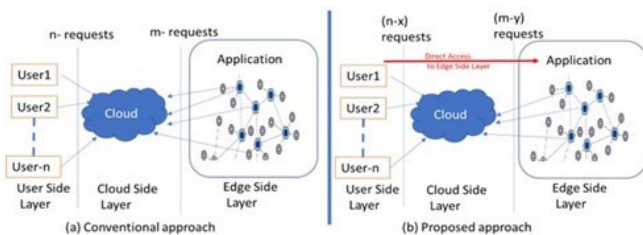


Fig. 1. (a) Conventional and (b) proposed IoT framework.

The proposed framework is based on a BMS application. Increasing the number of IoT devices requires a greater number of IoT devices connected to the IoT cloud, increasing the load of the server and compromising QoS as a greater number of requests is generated. Figure 1(a) shows the conventional approach of an IoT framework where both the user and the edge side layer generate requests to access the Internet. This may be to access the devices, log data to the cloud, etc. This generates a higher number of requests to the IoT service provider. Figure 1(b) shows the proposed approach of the IoT framework, which is based on user requirements. There are many tasks where the user is near to the edge side layer, so he can directly access the data from the edge side layer. In such cases, low-distance wireless communication can help a lot. Wi-Fi, Bluetooth, and Zigbee are some of the protocols which can be accessed locally, so some requests generated by this model could be handled locally by the user. This approach can significantly enhance the QoS by decreasing the load over the

IoT service platform. Figure 1(b) also shows that the number of requests generated by the edge side layer can also decrease due to the direct access to the user. Figure 2 shows the flowchart of the request generation and handling using the proposed IoT architecture. Users and devices generate requests in the application and session layers. The application and edge-side layers will check whether it is necessary to send these requests to the cloud server or not. After examining the type of request, if the request can be handled locally, then the network conditions will be checked. If the deployed network has some local networking with LAN WiFi, Bluetooth, or Zigbee, then the request will be checked and forwarded to the deployed network. Such requests can be handled locally, and there is no need to send them to the IoT platform server. If the request is not local, then the IoT platform has to be accessed. The same procedure must be followed if the network does not exhibit any local networking.

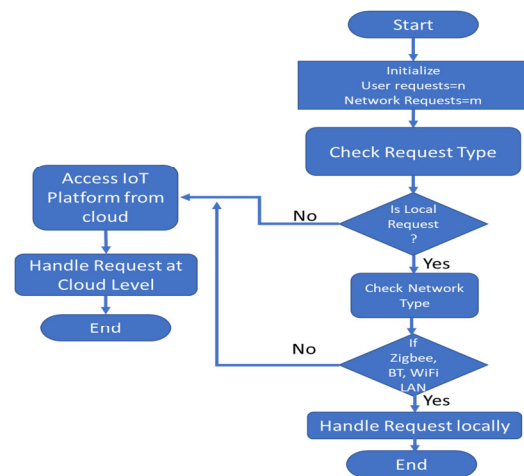


Fig. 2. Flowchart of the proposed IoT framework.

V. SIMULATION RESULTS

A simulation model was created to examine the proposed architecture. The numbers of requests generated by the user-side layer and the edge-side nodes were combined for the IoT service platform, and it was assumed that the number of service requests generated per node per unit of time was between 1 and 10, 30, and 50. In this scenario, the number of IoT nodes increases as time increases, and the load over the number of requests generated per unit of time can be formulated as:

$$R = \sum_{i=1}^n rand(R(i)) \quad (1)$$

where $R(i)$ is the number of requests generated by the i -node at any time t . Figure 3 shows the number of requests generated at any time t in a stochastic nature. The graph also shows that the number of requests continuously increases for an increasing number of IoT nodes. The number of requests was considered stochastic due to their random nature. As Figure 4 shows, applying the proposed method decreased the total number of requests. This was due to bypassing some user requests directly to the edge side layer. Figures 3 and 4 show that requests may proceed to 4500 requests per time unit using the conventional framework and a maximum of 2600 requests per time unit using the proposed method.

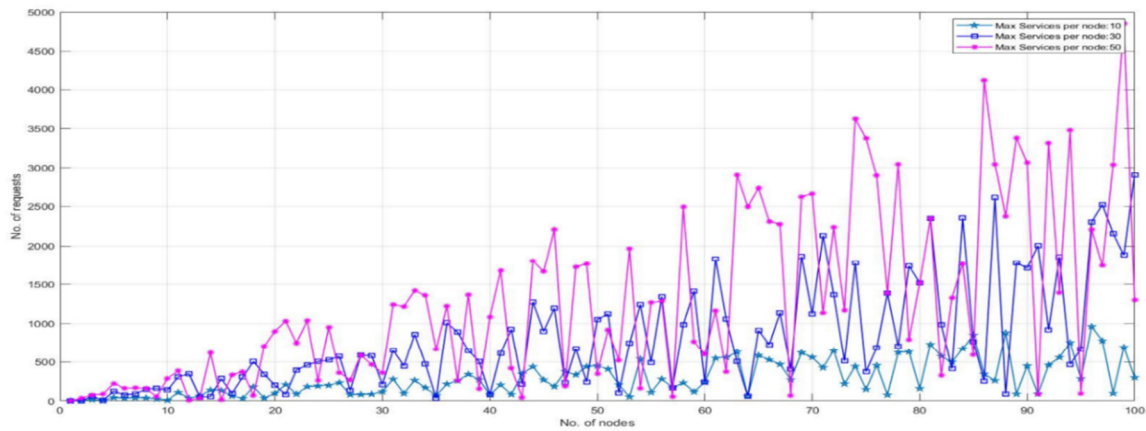


Fig. 3. Request generation by a conventional network of 100 nodes.

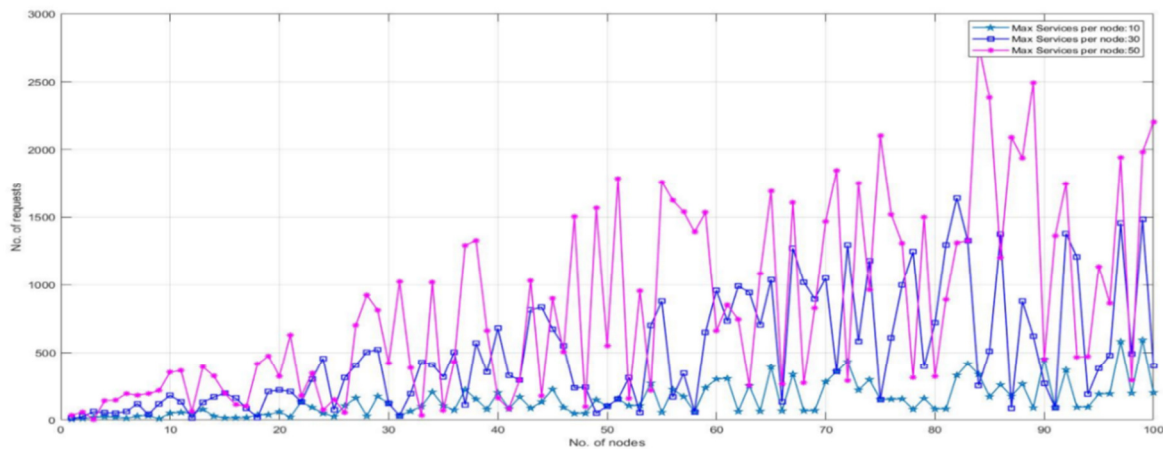


Fig. 4. Request generation by the proposed network of 100 nodes.

A test environment was built in Matlab to validate and justify the proposed method, considering a Wi-Fi network. This network requires a Wi-Fi Access Point (AP) and a Station Point (STA). A 12-node AP and a 24-node STA model were considered and used for the development of a Wi-Fi-enabled IoT model for a BMS application. Some network parameters were considered to examine the load sharing of the server. The IoT servers were accessed by the AP, which was responsible for sending and receiving data from the STAs to the server and vice versa. Figure 5 shows the throughput of 12 APs in the proposed and conventional approaches. The number of requests generated by the STAs was taken in two domains. In the first domain, the requests were forwarded to APs directly without using any filtration process, and in the second, the requests were forwarded to APs with the intelligent queuing process. This process followed the algorithm shown in Figure 3 to separate the server-oriented and local requests. Figure 5 shows that the throughput of the AP improved significantly in each node, increasing the quality of the network. Figures 6 and 7 show the packet loss and the average packet latency of STAs for both methods, considering again 24 STAs.

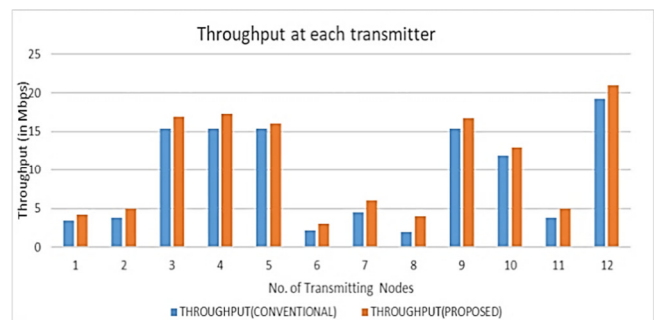


Fig. 5. Throughput of conventional and proposed scheme.

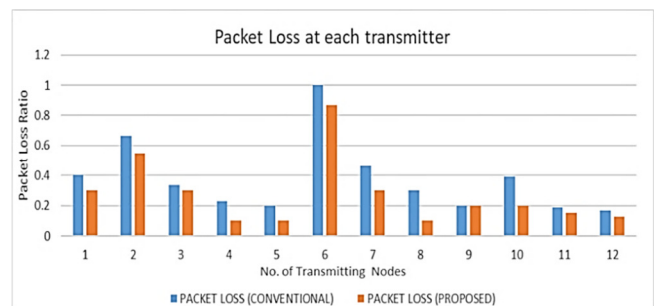


Fig. 6. Packet loss for conventional and proposed frameworks.

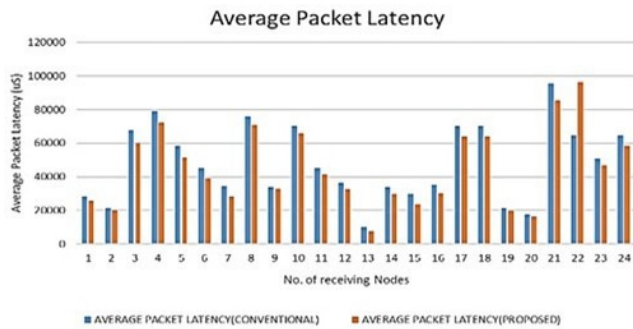


Fig. 7. Average packet latency for proposed and conventional schemes.

Figure 5 shows the reduction in packet loss for each node that functions as an STA. STAs are nodes that have some sensors, and may connect directly with the user based on the request type. Conventionally, each STA is supposed to provide and receive data from the server, and any request generated by the user or the STA pings the server and increases its load and packet latency. The proposed method reduced the number of requests to the server, and thus reduced the packet loss on each node. Figure 7 shows the average packet latency for the proposed and the conventional method. Average packet latency also decreased using the proposed algorithm, due to the smaller number of requests to the server. Packet latency is directly proportional to the number of requests generated by each STA. The number of requests generated for any IoT platform using the conventional approach increases significantly with the number of nodes, lowering the QoS parameters of the IoT network. As the increasing number of nodes in an IoT platform can't be controlled, the proposed approach can suit many applications. The proposed algorithm helps to lower the requests without limiting the number of nodes, and hence it can be very useful. Future work could investigate an AI-based intelligent approach to control the number of requests to the server at the device level. The nature of such a modification should have a very small memory footprint because of limited resources.

VI. CONCLUSION

Enhancing QoS without compromising the number of nodes is a challenge for IoT applications and the research society. The most important QoS parameters of an IoT network, i.e. packet loss, throughput, and latency, are directly proportional to the number of packets generated by the network. An intelligent model was proposed and investigated to reduce the requests to the server from the nodes. This model recognized requests that can be handled locally or should be forwarded to the server. The packet loss, throughput, and packet latency of the proposed model were examined using Matlab. The results showed that the proposed method minimized the number of requests by almost half on average of the conventional model. This enhanced the throughput of the networks by around 5- 10%, depending on the number of nodes, and decreased the average packet latency by 4%. The average packet loss also decreased by around 3-6%.

Dividing the number of requests to those to be handled locally and by the server can become smarter using AI and machine learning algorithms, which could be future work. AI

and machine learning algorithms can drastically enhance the proposed model and enhance the overall network performance. A trained neural network and a double Q method could enhance QoS. For validation, network tools like NS2, NS3, or a real-time physical network could be utilized.

REFERENCES

- [1] L. Li, S. Li, and S. Zhao, "QoS-Aware Scheduling of Services-Oriented Internet of Things," *IEEE Transactions on Industrial Informatics*, vol. 10, no. 2, pp. 1497–1505, Feb. 2014, <https://doi.org/10.1109/TII.2014.2306782>.
- [2] B. Guo, D. Zhang, Z. Wang, Z. Yu, and X. Zhou, "Opportunistic IoT: Exploring the harmonious interaction between human and the internet of things," *Journal of Network and Computer Applications*, vol. 36, no. 6, pp. 1531–1539, Nov. 2013, <https://doi.org/10.1016/j.jnca.2012.12.028>.
- [3] J.-S. Leu, C.-F. Chen, and K.-C. Hsu, "Improving Heterogeneous SOA-Based IoT Message Stability by Shortest Processing Time Scheduling," *IEEE Transactions on Services Computing*, vol. 7, no. 4, pp. 575–585, Jul. 2014, <https://doi.org/10.1109/TSC.2013.30>.
- [4] Y. Ding, Y. Jin, L. Ren, and K. Hao, "An Intelligent Self-Organization Scheme for the Internet of Things," *IEEE Computational Intelligence Magazine*, vol. 8, no. 3, pp. 41–53, Dec. 2013, <https://doi.org/10.1109/MCI.2013.2264251>.
- [5] P. Vlachas *et al.*, "Enabling smart cities through a cognitive management framework for the internet of things," *IEEE Communications Magazine*, vol. 51, no. 6, pp. 102–111, Jun. 2013, <https://doi.org/10.1109/MCOM.2013.6525602>.
- [6] D. Minoli, K. Sohraby, and B. Occhiogrosso, "IoT Considerations, Requirements, and Architectures for Smart Buildings—Energy Optimization and Next-Generation Building Management Systems," *IEEE Internet of Things Journal*, vol. 4, no. 1, pp. 269–283, Oct. 2017, <https://doi.org/10.1109/JIOT.2017.2647881>.
- [7] N. Sharghivand, F. Derakhshan, L. Mashayekhy, and L. Mohammad Khanli, "An Edge Computing Matching Framework with Guaranteed Quality of Service," *IEEE Transactions on Cloud Computing*, pp. 1–1, 2020, <https://doi.org/10.1109/TCC.2020.3005539>.
- [8] K. Cao, G. Xu, J. Zhou, T. Wei, M. Chen, and S. Hu, "QoS-Adaptive Approximate Real-Time Computation for Mobility-Aware IoT Lifetime Optimization," *IEEE Transactions on Computer-Aided Design of Integrated Circuits and Systems*, vol. 38, no. 10, pp. 1799–1810, Jul. 2019, <https://doi.org/10.1109/TCAD.2018.2873239>.
- [9] Y. Hu, Y. Li, M. C. Gursoy, S. Velipasalar, and A. Schmeink, "Throughput Analysis of Low-Latency IoT Systems With QoS Constraints and Finite Blocklength Codes," *IEEE Transactions on Vehicular Technology*, vol. 69, no. 3, pp. 3093–3104, Mar. 2020, <https://doi.org/10.1109/TVT.2020.2968463>.
- [10] A. Čolaković and M. Hadžialić, "Internet of Things (IoT): A review of enabling technologies, challenges, and open research issues," *Computer Networks*, vol. 144, pp. 17–39, Oct. 2018, <https://doi.org/10.1016/j.comnet.2018.07.017>.
- [11] M. Aazam and K. A. Harras, "Mapping QoE with Resource Estimation in IoT," in *2019 IEEE 5th World Forum on Internet of Things (WF-IoT)*, Limerick, Ireland, Apr. 2019, pp. 464–467, <https://doi.org/10.1109/WF-IoT.2019.8767254>.
- [12] A. Khamosh, M. A. Anwer, N. Nasrat, J. Hamdard, G. S. Gawhari, and A. R. Ahmadi, "Impact of Network QoS factors on QoE of IoT Services," in *2020 - 5th International Conference on Information Technology (InCIT)*, Chonburi, Thailand, Jul. 2020, pp. 61–65, <https://doi.org/10.1109/InCIT50588.2020.9310969>.
- [13] S. Javed, S. Ghazala, and U. Faseeha, "Perspectives of Heat Stroke Shield: An IoT based Solution for the Detection and Preliminary Treatment of Heat Stroke," *Engineering, Technology & Applied Science Research*, vol. 10, no. 2, pp. 5576–5580, Apr. 2020, <https://doi.org/10.48084/etasr.3274>.
- [14] Y. Djeldjeli and M. Zoubir, "CP-SDN: A New Approach for the Control Operation of 5G Mobile Networks to Improve QoS," *Engineering*,

- Technology & Applied Science Research*, vol. 11, no. 2, pp. 6857–6863, Apr. 2021, <https://doi.org/10.48084/etasr.4016>.
- [15] N. K. Al-Shammari, T. H. Syed, and M. B. Syed, "An Edge – IoT Framework and Prototype based on Blockchain for Smart Healthcare Applications," *Engineering, Technology & Applied Science Research*, vol. 11, no. 4, pp. 7326–7331, Aug. 2021, <https://doi.org/10.48084/etasr.4245>.
- [16] L. Atzori, A. Iera, and G. Morabito, "The Internet of Things: A survey," *Computer Networks*, vol. 54, no. 15, pp. 2787–2805, Oct. 2010, <https://doi.org/10.1016/j.comnet.2010.05.010>.
- [17] H. Yin, Z. Wang, and N. K. Jha, "A Hierarchical Inference Model for Internet-of-Things," *IEEE Transactions on Multi-Scale Computing Systems*, vol. 4, no. 3, pp. 260–271, Jul. 2018, <https://doi.org/10.1109/TMSCS.2018.2821154>.
- [18] Ian Beavers, "Intelligence at the Edge Part 1: The Edge Node," Northwood, MA, USA: Analog Devices Inc., 2017.
- [19] S. Al-Sarawi, M. Anbar, K. Alieyan, and M. Alzubaidi, "Internet of Things (IoT) communication protocols: Review," in *2017 8th International Conference on Information Technology (ICIT)*, Amman, Jordan, Feb. 2017, pp. 685–690, <https://doi.org/10.1109/ICITECH.2017.8079928>.
- [20] S. N. Shirazi, A. Gouglidis, A. Farshad, and D. Hutchison, "The Extended Cloud: Review and Analysis of Mobile Edge Computing and Fog From a Security and Resilience Perspective," *IEEE Journal on Selected Areas in Communications*, vol. 35, no. 11, pp. 2586–2595, Aug. 2017, <https://doi.org/10.1109/JSAC.2017.2760478>.
- [21] T. Vu, C. J. Mediran, and Y. Peng, "Measurement and Observation of Cross-Provider Cross-Region Latency for Cloud-Based IoT Systems," in *2019 IEEE World Congress on Services (SERVICES)*, Milan, Italy, Jul. 2019, vol. 2642–939X, pp. 364–365, <https://doi.org/10.1109/SERVICES.2019.00105>.
- [22] A. Azari, Č. Stefanović, P. Popovski, and C. Cavdar, "On the Latency-Energy Performance of NB-IoT Systems in Providing Wide-Area IoT Connectivity," *IEEE Transactions on Green Communications and Networking*, vol. 4, no. 1, pp. 57–68, Mar. 2020, <https://doi.org/10.1109/TGCN.2019.2948591>.
- [23] M. Shahzad and A. Ganji, "IoTm: A Lightweight Framework for Fine-Grained Measurements of IoT Performance Metrics," in *2018 IEEE 26th International Conference on Network Protocols (ICNP)*, Cambridge, UK, Sep. 2018, pp. 12–22, <https://doi.org/10.1109/ICNP.2018.00012>.
- [24] G. Tanganelli, C. Vallati, and E. Mingozzi, "CoAPthon: Easy development of CoAP-based IoT applications with Python," in *2015 IEEE 2nd World Forum on Internet of Things (WF-IoT)*, Milan, Italy, Sep. 2015, pp. 63–68, <https://doi.org/10.1109/WF-IoT.2015.7389028>.
- [25] S. Y. Jeon, J. H. Ahn, and T.-J. Lee, "Data Distribution in IoT Networks with Estimation of Packet Error Rate," in *2016 10th International Conference on Next Generation Mobile Applications, Security and Technologies (NGMAST)*, Cardiff, UK, Dec. 2016, pp. 94–98, <https://doi.org/10.1109/NGMAST.2016.25>.
- [26] F. H. Hung *et al.*, "Packet error rate analysis in IoT for industrial air conditioning system," in *IECON 2017 - 43rd Annual Conference of the IEEE Industrial Electronics Society*, Beijing, China, Jul. 2017, pp. 8367–8370, <https://doi.org/10.1109/IECON.2017.8217469>.
- [27] N. Chhabra, "Comparative Analysis of Different Wireless Technologies," *International Journal of Scientific Research in Network Security and Communication*, vol. 1, no. 5, pp. 13–17, 2013.
- [28] J. Zhou, X. Gong, L. Sun, Y. Xie, and X. Yan, "Adaptive Routing Strategy Based on Improved Double Q-Learning for Satellite Internet of Things," *Security and Communication Networks*, vol. 2021, Apr. 2021, Art. no. e5530023, <https://doi.org/10.1155/2021/5530023>.

Implementation of a High Power Quality BLDC Motor Drive Using Bridgeless DC to DC Converter with Fuzzy Logic Controller

Vishnu Gopan K.

Department of Electrical and Electronics Engineering
Coimbatore Institute of Technology, Coimbatore
Tamil Nadu, India
gopanlvishnu@gmail.com

J. Devi Shree

Department of Electrical and Electronics Engineering
Coimbatore Institute of Technology, Coimbatore
Tamil Nadu, India
devishreecit@gmail.com

Received: 20 July 2022 | Revised: 28 July 2022 | Accepted: 29 July 2022

Abstract—Electric motor drives based on electronic power converters having good power quality parameters are getting huge acceptance. Conventional Diode Bridge Rectifier (DBR) and DC to DC converter-based methods have become obsolete, as they provide low power quality indices which hamper the supply by introducing current harmonics and conduction losses. Although there are many developments in motors and control strategies, the risk and complexity of such drives become bottlenecks in implementation. This study implemented a drive scheme with a brushless DC Motor. The new improved bridgeless topology was modified with an advanced fuzzy logic controller to further improve its power quality and performance. Due to low power, a high-speed application of Brush Less (BLDC) motor was selected for the drive scheme. This combination could achieve almost Unity Power Factor (UPF) and significantly improve control compared to conventional topologies. A circuit-wise analysis was conducted to design the converter's components. The modifications were elaborated through mathematical expressions, and the parameters of power quality were analyzed and validated.

Keywords—Brush-Less Direct Current Motor (BLDC); Diode Bridge Rectifier (DBR); High-Frequency Transformer (HFT); Total Harmonic Distortion (THD); Discontinuous Inductor Current Mode (DICM); Bridgeless Dual Cuk (BDC); Fuzzy Logic Controller (FLC); Unity Power Factor (UPF)

I. INTRODUCTION

The need for quality AC supplies and their efficiency is becoming a primary concern in modern power electronics [1], especially in the development of various DC-DC and AC-DC converters. This paper discusses DC-DC converters, as they are more flexible and versatile in terms of power quality and efficiency. Improved power quality is mandatory for electrical equipment nowadays by the international Power Quality (PQ) standard IEC 61000-3-2. This standard also stipulates high power factor and low Total Harmonic Distortion (THD) of the AC main current for Class-A applications (<600W, <16A) [2]. Due to their advantages of high efficiency, high flux density per unit volume, low maintenance requirement, low EMI problems, high ruggedness, and a wide range of speed control,

Brush-Less DC (BLDC) motors are recommended for many low- and medium-power drive applications [3]. BLDC motors are used in numerous areas such as household applications [4], transportation (hybrid vehicles) [5], aerospace [6], heating, etc.

This study implemented and evaluated a variety of power electronic circuits to drive a BLDC motor. An AC Supply is essential for domestic loads. Conventionally, a Diode Bridge Rectifier (DBR), followed by a filter capacitor is used for the generation of a DC supply. Today, many applications continue to use them due to their simplicity of construction and cost-effective production. The high value of the filter capacitor draws a high non-sinusoidal current from the supply. In addition, DBRs with their inherent flaw of high conduction losses reduce the efficiency of converter circuits, and increased harmonic levels cause a rise in the THD levels between 45-65% [7]. Many Power Factor Correction (PFC) converters have been developed to reduce the THD levels to permissible limits and improve the power factor of the supply, and most of them serve their purpose on their performance levels. Therefore, more reliable drive control is performed through the control of the DC link voltage by controlling the switches on the PFC converter side [8]. To implement such a control, the converter has to be chosen from an array of DC-DC converters divided into isolated or nonisolated and bridged or bridgeless topologies [9, 10]. Moreover, it has to be decided in which mode the converter should operate to achieve Unity Power Factor (UPF).

This study selected a Cuk converter, after examining various topologies with different types of loads and applications of PFC converters, intending to improve the power quality of AC to DC conversion. This study also presents the bridgeless topology with a proposed modification. Additionally, a fuzzy logic-based advanced linguistic controller was implemented for the bridgeless topology to further enhance the performance of the converter and improve power quality at the main supply. The simulated results along with their mathematical validation, were used to analyze the improvements. Performance analysis and input power quality

of the operation of the converter were used to conduct the harmonic analysis of the topology. As there are many speed control drive schemes for various applications, this study allowed the operation of a motor drive with quick response and very low speed variations from the reference value. Moreover, the incorporation of FLC into a bridgeless configuration further improved performance and power quality.

II. CONFIGURATION

For speed control, the selection of the front-end converter and its operation configuration are equally important to achieve a high power factor at the supply mains. The Cuk converter was selected due to its many advantages [12]. There are multiple approaches for the conversion of AC input to variable DC for the drive scheme. A DBR followed by a high DC link capacitor was used, which due to its high losses was replaced by "DBR-Power Factor Correction (PFC)" converter configuration. In such circuits, the speed control of the drive can be achieved in several ways. One way is to control the switching of the 6 individual switches of the motor-end Voltage Source Inverter (VSI). Due to the increased number of control switches and the high frequency of motor operation, it is not preferred due to high switching losses [8]. Another solution could be a PFC converter to control the DC link voltage. The PFC converter can be controlled by 2 methods: a voltage follower or a current multiplier method [13]. These methods depend on which mode the PFC converters operate. This study discussed the 2 modes of operation and attempted to compare their results with the bridgeless topology. PID controllers were used for the three types of converters, using a linearized modeling technique to standardize the results.

In the voltage follower approach [13], the converter operates in DCM and is further divided into DICM and DVCM where the respective inductor currents or capacitive voltages become discontinuous during a switching period of the converter switch [13]. The advantage of this mode is that it requires only one sensor for control. The need for 2 voltage sensors and 1 current sensor makes this multiplier method more complex [13]. In this configuration, the converter operates in CCM and ensures more robust control [14]. The configuration consists of a DBR followed by a power factor correction Cuk converter designed to operate in CCM operation. The DC output of the converter is fed to the input side of the voltage source inverter that controls the speed of the BLDC motor. Even though both configurations have their advantages, the main drawback of lack of isolation between the high- and low-frequency switching parts hampers the smooth operation by introducing harmonics in the circuit. This reduces the converter's efficiency and the purported operation in power factor correction.

The proposed configuration, shown in Figure 1, resolves this inherent problem by providing high-frequency isolation [9]. This is done by providing 2 High-Frequency Transformers (HFT) in the respective positive and negative side converters of the modified Cuk converter topology. The modification of the proposed converter eliminates the need for a DBR and avoids any conduction losses. The converter operates in DICM, where the current through the output side inductor becomes discontinuous over a switching period. Three converters were constructed and analyzed in Matlab 2018 and their performance was compared during changes in speed conditions.

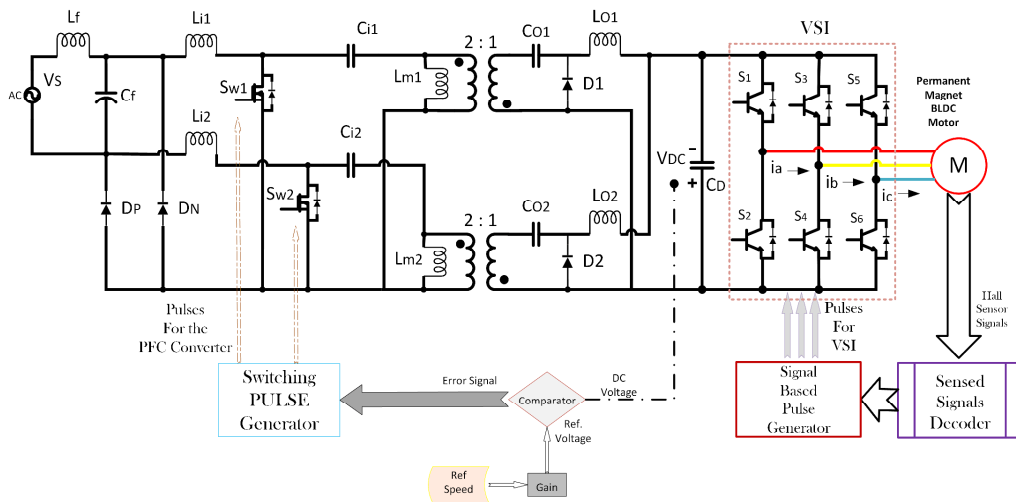


Fig. 1. Proposed isolated coupled Cuk converter-fed BLDC motor drive

III. OPERATION OF THE CONFIGURATION

The input side DBR was eliminated in the proposed converter-fed BLDC motor drive. This was achieved by incorporating another Cuk converter in parallel with the existing one so that one works in the positive half-cycle and the other in the negative half-cycle of the supply, by implementing a zero-crossing detector on the input side. Another major advantage of this method was that the AC input and the output

side BLDC motor drive were completely isolated with the help of an HFT. Hence, the speed control of the drive was hassle-free and the amount of noise present in the control signals could also be reduced. The converter was designed in such a way that the current through the output inductors $Lo1$ and $Lo2$ becomes discontinuous over a switching period in either half cycle of the input supply, as shown in Figure 2. Therefore, the converter operated in Discontinuous Inductor Current Mode

(DICM) [15]. Even though there are many categories of discontinuous conduction modes, such as DICM on input, DICM on output, and DCVM [16], applying DICM on the output side inductor was simpler and lowered harmonics. Several advantages can be gained by operating the rectifier in DICM, such as a natural near-unity power factor and at zero current the power switches are turned ON and the output diodes are turned OFF.

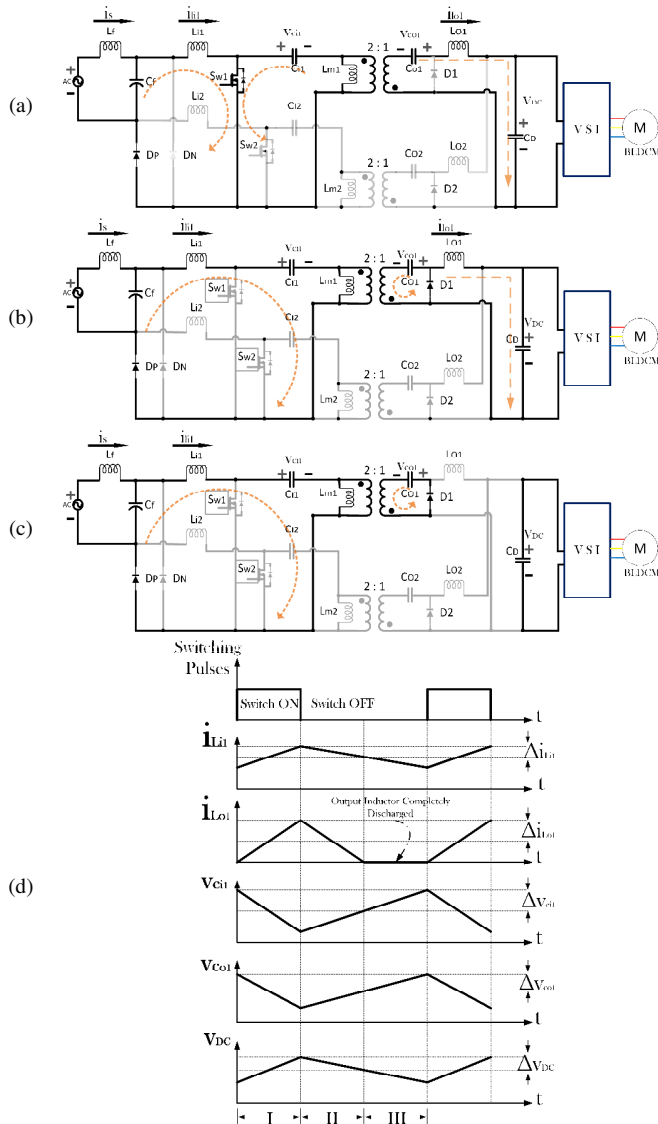


Fig. 2. Operating modes of the proposed converter at different intervals of the switching period during the positive half cycle: (a) switch closed, (b) switch open – inductor discharging, (c) switch closed – inductor fully discharged, and (d) associated waveforms.

In the first mode, switch $Sw1$ is turned ON and the inductors $L1$, $L2$, and magnetizing inductance $Lm1$ start charging. The capacitor $C1$ charges $Lm1$, and $C0$ delivers DC link voltage. In the second mode, the switch is being turned OFF, inductors $L1$ and $L2$ discharge thereby charging $C1$ and $C0$, and the magnetizing inductance $Lm1$ discharges

through Cd . In the third mode, the output side inductor $L2$ is completely discharged and the input inductor $L1$ and the magnetizing inductance of HFT $Lm1$ continue to discharge. Figure 3 shows the negative half operation of the converter. The converter operates in such a way that the input side energy storage components remain in non-conducting mode and the output side components remain non-discharged. The converter is designed so that the positive sinusoidal input from the AC supply at the fundamental frequency of 50Hz is split into a large number of cycles of operation of the upper Cuk converter switch.

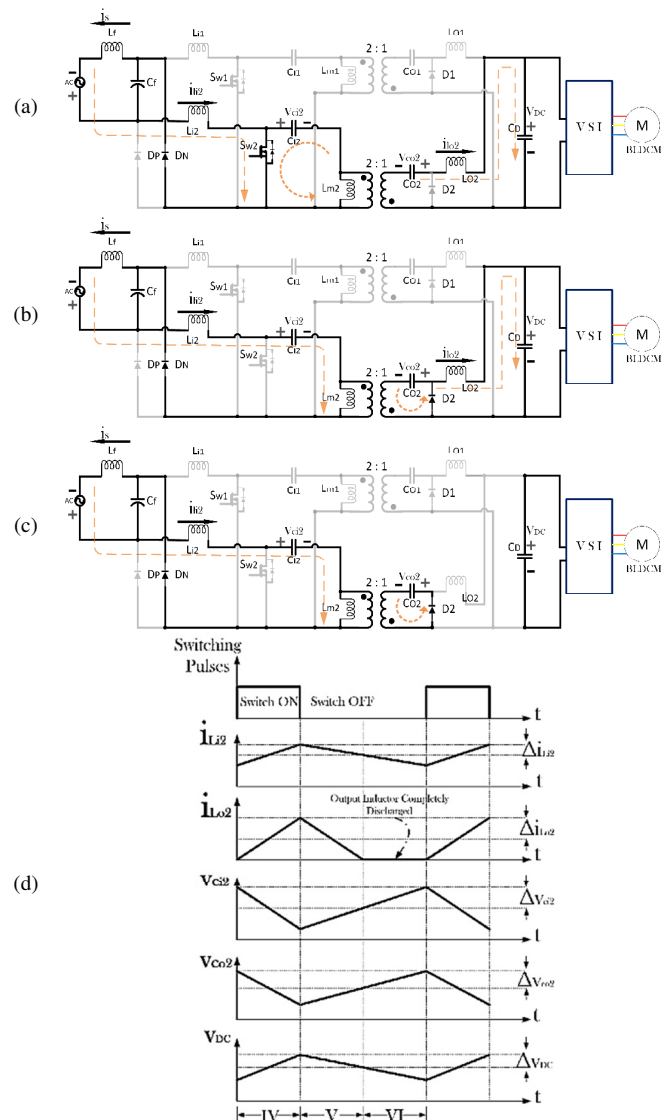


Fig. 3. Operating modes of the proposed converter at different intervals of the switching period during the negative half cycle: (a) switch closed, (b) switch open – inductor discharging, (c) switch closed – inductor fully discharged, and (d) associated waveforms.

A. Motor Speed Control

An electronic commutation of the BLDC motor includes the proper switching of the Voltage Source Inverter (VSI) to

draw a symmetrical DC from the DC link capacitor for 120° [17] and placed symmetrically at the center of the back Electro-Motive Force (EMF) of each phase. A Hall-effect position sensor was used to sense the rotor position on a span of 60°; which is required for the electronic commutation of the BLDC motor [18]. The front-end converter was controlled by feeding back the DC voltage. The control scheme was comprised of feedback DC voltage, reference voltage generator, and PWM generator. The reference voltage was obtained by multiplying the reference speed by the motor speed constant K_v :

$$V_{DC}^* = K_v \cdot \omega$$

This reference voltage was compared with the actual DC link value of the converter and the error was used for PWM generation in 3 different ways for the front-end converter switches to obtain speed control [19]. Table I illustrates the switching signals to be sent to the phase 3 VSI. The controller logic was designed to send the ON pulses to the respective switches following the rotor position in a single direction.

TABLE I. SWITCHING STATES FOR THE VSI

Angular Placement	State of Switches					
	T1	T2	T3	T4	T5	T6
NA	0	0	0	0	0	0
0-60	0	0	0	1	1	0
60-120	0	1	1	0	0	0
120-180	0	1	0	0	1	0
180-240	1	0	0	0	0	1
240-300	1	0	0	1	0	0
300-360	0	0	1	0	0	1
NA	0	0	0	0	0	0

IV. DESIGN

The basic CUK converter is shown in Figure 4.

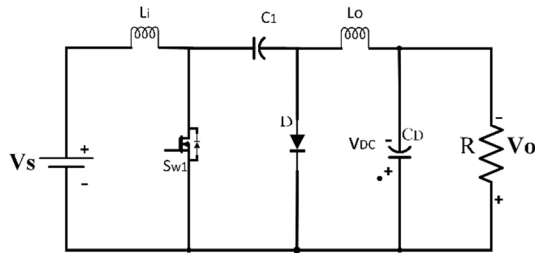


Fig. 4. CUK converter circuit.

For this Cuk converter, the output equation is given as [21]:

$$V_{DC} = -\frac{D}{1-D} V_{in}$$

In the case of the shown converter topology, the negative output at the output changes to a positive value by interchanging the terminals. In this type of arrangement, the average AC voltage applied across the input side can be obtained as:

$$V_{in}(t) = |V_m \sin(\omega t)| = |230\sqrt{2} \sin(340t)| \quad (1)$$

using the following parameter values: $V_{min}=100V$, $V_{max}=200V$, $V_{smin}=170V$, $V_{smax}=270V$, $P_{max}=250W$, and $P_{min}=125W$. The

selected switching frequency f_s was 20kHz for the operation of all 3 converters.

A. Design of the BDC Converter

The output voltage is obtained as [21]:

$$V_{DC} = \left[\frac{N_2}{N_1} \right] \frac{D}{(1-D)} V_{in} \quad (2)$$

Transformer ratio, $\left[\frac{N_2}{N_1} \right]$ was taken as 0.5. Let $D(t)$ be the instantaneous value of the duty ratio, then we have [16]:

$$D(t) = \frac{V_{DC}}{\left(\frac{N_2}{N_1} \right) V_{in}(t) + V_{DC}} = \frac{V_{DC}}{\left(\frac{N_2}{N_1} \right) |V_{in} \sin(\omega t)| + V_{DC}} \quad (3)$$

Instantaneous power is given by:

$$P_i = \left(\frac{P_{max}}{V_{DC,max}} V_{DC} \right) \quad (4)$$

1) Inductor Design [20]:

$$L_{i1} = L_{i2} = \frac{V_{in}(t) \cdot D(t)}{\eta I_{in}(t) f_s} = \frac{1}{\eta \cdot f_s} \left(\frac{V_s^2}{P_i} \right) \left(\frac{V_{DC}}{n V_{in}(t) + V_{DC}} \right) \quad (5)$$

where η is the input current ripple, which was taken as 50%, and n is the turns ratio of the HFT, taken as 1:2.

$$L_{o1} = L_{o2} = \left(\frac{V_s^2}{P_i} \right) \frac{V_{DC}}{2 V_{in}(t) f_s} \left(\frac{V_{DC}}{n V_{in}(t) + V_{DC}} \right) \quad (6)$$

Both equations are used under the assumption that $P_i = P_{i,max}$ and $V_{in} = \sqrt{2} V_{s,min}$. The value of the input side inductor was 7mH. The value of the output side inductor was obtained as 1.502mH for $V_{DC}=200V$, and 0.546mH for $V_{DC}=100V$, so a value lower than 0.546mH should be chosen. The selected value selected was 0.1mH. The magnetizing inductances are [16]:

$$L_{m1} = L_{m2} = \left(\frac{V_s^2}{P_i} \right) \frac{1}{\zeta \cdot f_s} \left(\frac{V_{DC}}{n V_{in}(t) + V_{DC}} \right) \quad (7)$$

where ζ is the permitted ripple current on the output side, taken as 50%, were obtained as 7mH.

2) Capacitor Design

$$C_{i1} = C_{i2} = \frac{n \cdot P_i}{k \cdot \sqrt{2} V_s \cdot f_s \cdot (n \sqrt{2} V_s + V_{DC})} \quad (8)$$

where $C_{i1}=C_{i2}=220nF$.

$$C_{o1} = C_{o2} = \frac{P_i}{x \cdot V_{DC} \cdot f_s \cdot (n \sqrt{2} V_s + V_{DC})} \quad (9)$$

where $C_{o1}=C_{o2}=2.2\mu F$. The output side DC link capacitor was given as:

$$C_D = \frac{I_{DC}}{2 \omega \Delta V_{DC}} = \left(\frac{P_i}{V_{DC}} \right) \frac{1}{(2 \omega \cdot \rho \cdot V_{DC})} \quad (10)$$

where k is the input side ripple voltage (25%), x is the ripple voltage at the converter side (10%), and $\rho = \Delta V_{DC}$ is the permitted output ripple (5%). The obtained value of CD was 1000 μF .

3) Filter Design

A low pass LC filter was used to avoid higher order harmonics in the supply system. The maximum value of the filter's capacitance was given by [13]:

$$C_{max} = \frac{I_m}{\omega_L V_m} \tan \theta = \frac{\sqrt{2} P_{max} / V_s}{\omega_L \sqrt{2} V_s} \tan \theta \quad (11)$$

where θ is the displacement angle between the fundamental value of supply voltage and supply current, taken as 2° . The maximum value of the filter capacitor was calculated using (11) at 574.4nF and was selected as 330nF. This value was selected for all 3 configurations as there is no variation in input voltage, and the capacitor always acts across one-half of the input supply at any given time. The value of the filter inductor was designed by considering the source impedance L_s as 4-5% of the base impedance. Hence, the additional value of required inductance was given as:

$$L_f = L_{req} + L_s \Rightarrow L_{req} = L_f - L_s$$

$$L_{req} = \frac{1}{4\pi^2 f_c^2 C_f} - 0.025 \left(\frac{1}{\omega_L} \right) \left(\frac{V_s^2}{P_o} \right) \quad (12)$$

where f_c is the cut-off frequency, selected such that $f_L < f_c < f_s$. Therefore, f_c was taken as $f_s/10$. Hence, the value of filter inductance was calculated using (20) as 3.77mH. Table II shows the motor operation details of the proposed topology.

TABLE II. MOTOR SPECIFICATIONS

Number of Poles	4
Rated Power	251.32 W
DC Rated Voltage	200V
Rated Torque	1.2Nm
Rated Speed	2000rpm
Back emf Constant, K_b	78V/Krpm
Torque Constant, K_t	0.74Nm/A
Per Phase Resistance	14.56Ω
Per Phase Inductance	25.71mH
Moment of Inertia, J	$1.3 \times 10^{-4} \text{ Kg m}^2$

V. FUZZY LOGIC CONTROLLER

The conventional PID controller has the inherent flaw of the limitation of operation range as it can only be tuned for a particular range or input-output combinations. The FLC [22], which uses linguistic variables to specify the wide range of inputs as its Membership Functions (MFs) can solve this problem of the PID controller and can operate effectively under the complete specified range of the DC voltage of the converter. The voltage range is split into segments and each segment is provided as a MF for the reference voltage and the actual output variables. These variables are considered the input variables of the FLC. Table III and Figures 5 and 6 illustrate the association of MFs to the two inputs to the FLC. From the inputs, FLC calculates the error and, based on the rule base shown in Table IV, it provides the apt duty ratio of the switching pulse, which is to be given to the converter switches. Duty ratios, ranging from 0 to 0.5, are divided into FLC MFs for the defuzzified output variable, as shown in Figure 7. Table V shows the fuzzy rule base defined for the FLC [23]. The selection of an appropriate output for the converter pulse duty ratio is decided on the error between the reference and the actual DC output voltage of the converter. The weightage and the point of selection of the exact value are decided based on the centroid method of FLC.

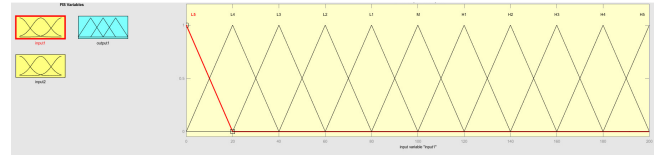


Fig. 5. Input 1 (ref. voltage) membership functions.

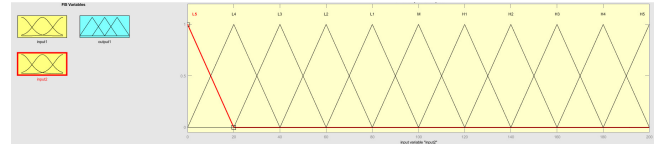


Fig. 6. Input 2 (actual voltage) membership functions.

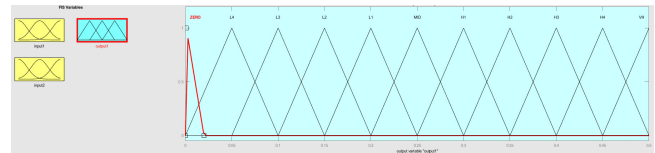


Fig. 7. De-fuzzified output (duty ratio output) membership functions.

TABLE III. FLC INPUT MFs AND RANGE

MF	Range of Voltage
L5	-20 to 20
L4	0 to 40
L3	20 to 60
L2	40 to 80
L1	60 to 100
M	80 to 120
H1	100 to 140
H2	120 to 160
H3	140 to 180
H4	160 to 200
H5	180 to 220

TABLE IV. FUZZY RULE BASE

		Input 1 MFs										
Input 2 MFs		L5	L4	L3	L2	L1	M	H1	H2	H3	H4	H5
	L5	ZER	ZER	ZER	ZER	ZER	ZER	ZER	ZER	ZER	ZER	ZER
	L4	L2	L3	L3	L4	L4	ZER	ZER	ZER	ZER	ZER	ZER
	L3	L2	L2	L2	L2	L4	L4	L4	L4	L4	L4	ZER
	L2	L1	L1	L1	L1	L2	L3	L4	L3	L4	L4	L4
	L1	MID	MID	L1	L1	L1	L1	L2	L2	L4	L3	L4
	M	H1	H1	H1	H1	H1	MID	L1	L1	L1	L2	L3
	H1	H1	H1	H1	H1	H1	H2	MID	L1	L1	L1	L2
	H2	H1	H1	H1	H1	H1	H2	H2	MID	MID	L1	L1
	H3	H2	H2	H1	H1	H1	H1	H1	H2	H1	MID	L1
	H4	H2	H2	H2	H2	H2	H2	H2	H2	H2	H1	MID
	H5	H2	H2	H2	H2	H2	H2	H2	H2	H2	H1	H1

VI. RESULTS AND DISCUSSION

The complete simulation schematics of the bridgeless dual Cuk converter controlled by the FLC are shown in Figure 8. As can be noted, the BDC Cuk converter has a significant advantage over the conventional bridge-type converters. The FLC converter performs efficiently with a fast response to inputs and gives good power quality indices. Figure 10 shows its output voltage response. As the FLC is mainly employed to improve power quality, the input side power quality parameters are very important.

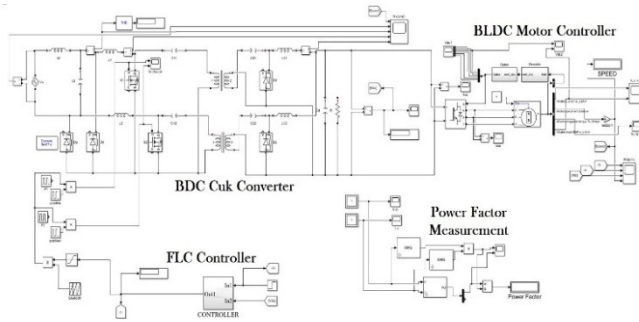


Fig. 8. Simulation diagram of the BDC converter with FLC.

Figure 9 shows the pure sinusoidal waveform of the supply current in the FLC-based converter compared to the partially sinusoidal current profile in the PID controller one.

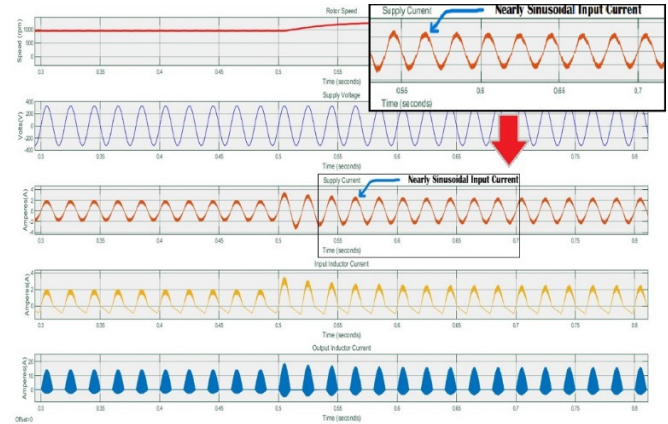


Fig. 9. Rotor speed, source voltage, source current, input inductor current, and output inductor current.

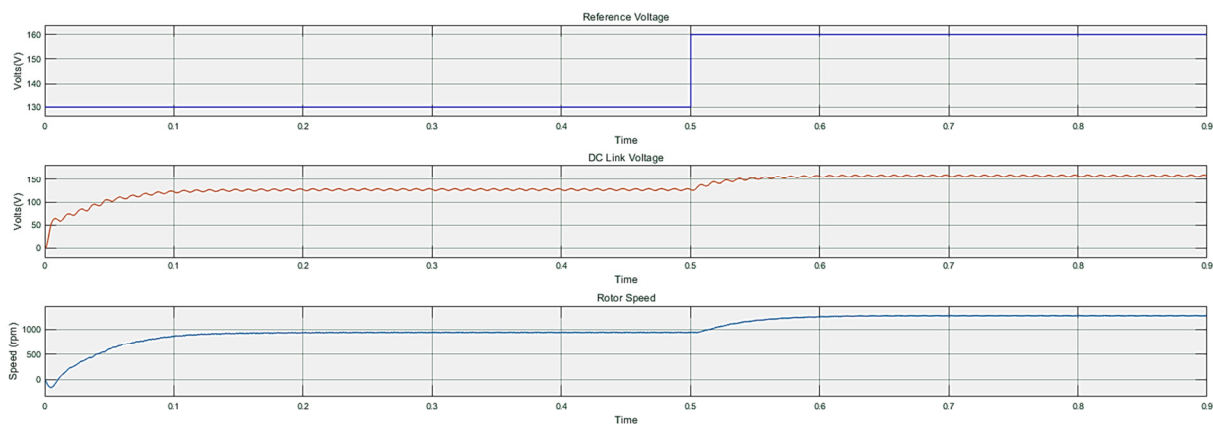


Fig. 10. Rotor speed output for the step reference voltage input.

A. THD Analysis

The harmonic content in the supply current can be determined by finding the THD value. This value was computed taking into account the percentage values of individual harmonic current components for the fundamental value. Also, some DC components may be present in the circuit due to switching losses or EMI, which should also be considered. By default, it was assumed to be 1%, unless it is present significantly. THD is the ratio of the root mean square sum of the individual harmonic components to the fundamental value. Either the percentile or the actual value of harmonics can be used. This study used harmonics as the percentage of the fundamental.

$$\text{THD}(\%) = \sqrt{\frac{(I_2^2 + I_3^2 + I_4^2 + \dots + I_n^2)}{I_1^2}} \times 100(\%) + \text{DC Component}(\%) \quad (13)$$

The DC component was not present in the harmonic analysis, so it was assumed to be 1%. From Table V we get:

$$\text{THD}(\%) = \sqrt{\frac{(3.2^2 + 1.2^2 + 0.8^2 + 0.6^2 + 0.3^2 + 0.2^2 + 0.15^2 + 0.1^2 + 0.15^2)}{100^2}} \times 100 ($$

THD(%) was 4.58%, which is close to the simulated value (3.98%). The analysis of the THD content on the supply current, shown in Figure 11, shows that the BDC converter with advanced FLC significantly improved the power quality

of the input supply. It can be noted that the THD levels significantly dropped to 3.98% compared to conventional converter topologies [10].

TABLE V. CURRENT HARMONICS IN BDC CONVERTER WITH FUZZY LOGIC CONTROLLER

Harmonic Order	Value (% of fundamental)
3	3.2
5	1.2
7	0.8
9	0.6
11	0.3
13	0.2
15	0.15
17	0.1
19	0.15
DC Component	1%

B. Power Factor

The BDC topology achieved a very high power factor, almost close to unity (0.99), compared to the other two conventional topologies with PFs of 0.95 and 0.97 respectively [10], as shown in Figure 12. Compared to conventional topologies, the proposed BDC scheme has the advantage of a

wide operating range because of the reduced stress on the operating components. Due to the single half-cycle specific operation of the converter, the BDC method used relatively fewer components at a time with minimal power rating.

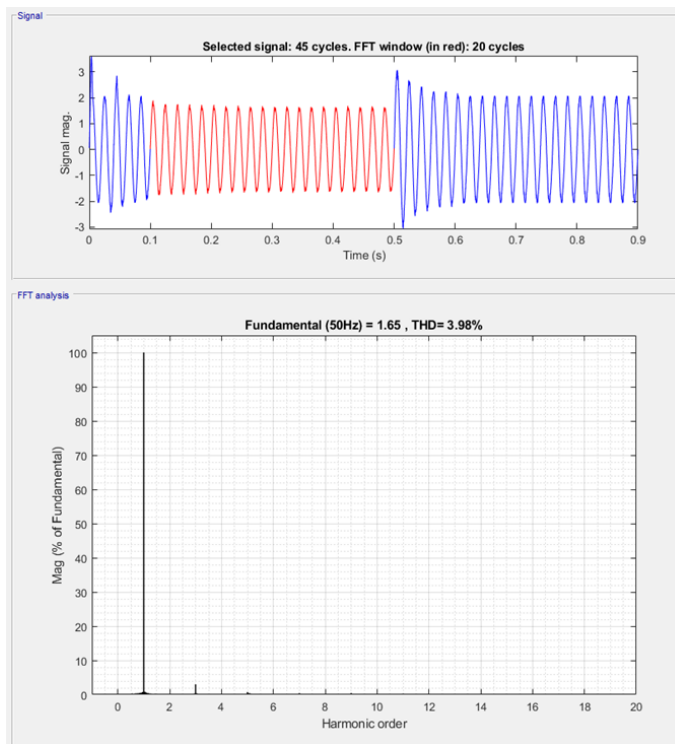


Fig. 11. THD analysis.

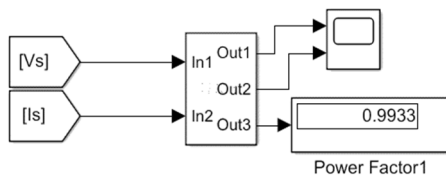


Fig. 12. Results of power factor analysis.

C. Efficiency

The performance of the three converters was examined to analyze their operation efficiency. As the VSI-fed BLDC motor part is the same for the three converters, the back end of the PFC converter was used to calculate the output power. Figure 13 shows that due to the absence of a current controller and the inherent conduction loss of the rectifier diodes, the overall efficiency was very low, ranging from 42.7% to an underwhelming 62.7%, even at the motor-rated voltage. The current multiplier method, due to the incorporation of the current controller and amidst the heavy conduction loss in the DBR, controlled the power loss and presented a much more efficient operation. The efficiency values were 51% at 40V DC and ranged to a maximum of 73.2% at the rated motor voltage of 200V DC. The proposed design rectified the issues of the previous topologies. The conduction loss is not a concern, as the DBR was eliminated, and the converter operation used a single sensor control for the same reason. The DCM operation resulted in a better power factor, and the power transfer was

smooth due to the coupled configuration of the Cuk converter. The efficiency of the converter was in the range of 88.7-96.1% at the rated motor voltage. Moreover, the life of the switching components can be extended because of the reduced transient time when the converter switches are subjected to switching stress due to the single half-cycle operation of each converter.

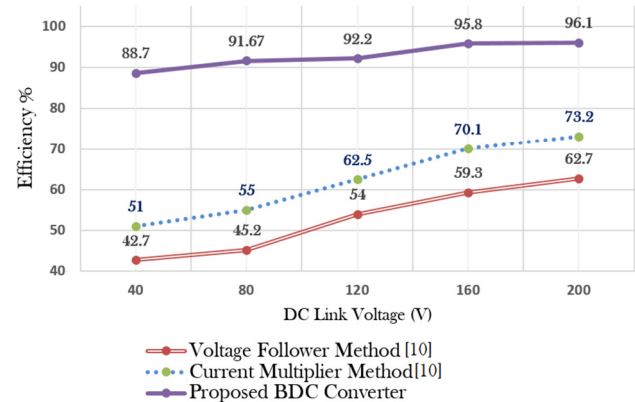


Fig. 13. Comparison of converter efficiency.

VII. CONCLUSION

The power quality of a new BLDC motor-based speed control drive was analyzed and the results showed that the proposed design attained significantly better power quality parameters compared to the conventional topologies [10]. The power factor and THD of conventional Cuk and proposed bridgeless dual Cuk converter topologies were analyzed using the simulated results for varying input conditions. The proposed method was portrayed to assert the merits of the BDC converter in attaining a power factor nearly unity for the drive. The fuzzy logic controller-based control strategy of the converter enhanced the performance of the modified Cuk converter and helped to achieve a very low THD value. The method was simulated using Matlab 2018 based on varying input conditions. The analysis proved experimentally that the BDC design was more efficient and the FLC-based BDC converter was the most efficient among other topologies and is suitable for modern variable speed electric drives that employ BLDC motors. The reduction of current sensors, one-cycle operation, and low current stress on the power electronic switches make it suitable for long-duration operation. Therefore, this topology is a notable choice for high-power motor drive schemes used in household and industrial equipment.

REFERENCES

- [1] V. V. Prabhakaran and A. Singh, "Enhancing Power Quality in PV-SOFC Microgrids Using Improved Particle Swarm Optimization," *Engineering, Technology & Applied Science Research*, vol. 9, no. 5, pp. 4616–4622, Oct. 2019, <https://doi.org/10.48084/etasr.2963>.
- [2] "Electromagnetic compatibility (EMC) - Part 3-2: Limits - Limits for harmonic current emissions (equipment input current ≤16 A per phase)," IEC, Geneva, Switzerland, International Standard IEC 61000-3-2, 2000.
- [3] C. Xiang, X. Wang, Y. Ma, and B. Xu, "Practical Modeling and Comprehensive System Identification of a BLDC Motor," *Mathematical Problems in Engineering*, vol. 2015, Apr. 2015, Art. no. e879581, <https://doi.org/10.1155/2015/879581>.

- [4] J. F. Gieras, Permanent Magnet Motor Technology: Design and Applications, Third Edition, 3rd ed. Boca Raton: CRC Press, 2009.
- [5] D. B. Minh, V. D. Quoc, and P. N. Huy, "Efficiency Improvement of Permanent Magnet BLDC Motors for Electric Vehicles," *Engineering, Technology & Applied Science Research*, vol. 11, no. 5, pp. 7615–7618, Oct. 2021, <https://doi.org/10.48084/etasr.4367>.
- [6] X. Huang, A. Goodman, C. Gerada, Y. Fang, and Q. Lu, "A Single Sided Matrix Converter Drive for a Brushless DC Motor in Aerospace Applications," *IEEE Transactions on Industrial Electronics*, vol. 59, no. 9, pp. 3542–3552, Sep. 2012, <https://doi.org/10.1109/TIE.2011.2171171>.
- [7] Y. Almalaq and M. Matin, "Two-Switch High Gain Non-Isolated Cuk Converter," *Engineering, Technology & Applied Science Research*, vol. 10, no. 5, pp. 6362–6367, Oct. 2020, <https://doi.org/10.48084/etasr.3826>.
- [8] S. B. Ozturk, O. Yang, and H. A. Toliyat, "Power Factor Correction of Direct Torque Controlled Brushless DC Motor Drive," in *2007 IEEE Industry Applications Annual Meeting*, New Orleans, LA, USA, Sep. 2007, pp. 297–304, <https://doi.org/10.1109/07IAS.2007.52>.
- [9] T. Sahu, Alok Sahu, M. K. Pradhan, "Enhanced Power Quality/Efficiency using Bridgeless Converter using Mo-SMPS," *International Journal of Engineering Trends and Technology - IJETT*, vol. 32, no. 6, pp. 266–271, Feb. 2016, <https://doi.org/10.14445/22315381/IJETT-V32P253>.
- [10] B. Singh, B. N. Singh, A. Chandra, K. Al-Haddad, A. Pandey, and D. P. Kothari, "A review of single-phase improved power quality AC-DC converters," *IEEE Transactions on Industrial Electronics*, vol. 50, no. 5, pp. 962–981, Jul. 2003, <https://doi.org/10.1109/TIE.2003.817609>.
- [11] V. Bist and B. Singh, "An Adjustable-Speed PFC Bridgeless Buck-Boost Converter-Fed BLDC Motor Drive," *IEEE Transactions on Industrial Electronics*, vol. 61, no. 6, pp. 2665–2677, Jun. 2014, <https://doi.org/10.1109/TIE.2013.2274424>.
- [12] S. Narthana, M. Shunmathi, P. Muthu Thiruvengadam, and S. Narthana, "Analysis of DC-DC Converter with High Step-up Gain for Alternative Energy Sources," *International Journal of Engineering Trends and Technology - IJETT*, vol. 69, no. 4, pp. 162–168, Apr. 2021, <https://doi.org/10.14445/22315381/IJETT-V69I4P223>.
- [13] V. Bist and B. Singh, "PFC Cuk Converter-Fed BLDC Motor Drive," *IEEE Transactions on Power Electronics*, vol. 30, no. 2, pp. 871–887, Oct. 2015, <https://doi.org/10.1109/TPEL.2014.2309706>.
- [14] L. Kathi, A. Ayachit, D. K. Saini, A. Chadha, and M. K. Kazimierzuk, "Open-loop small-signal modeling of cuk DC-DC converter in CCM by circuit-averaging technique," in *2018 IEEE Texas Power and Energy Conference (TPEC)*, College Station, TX, USA, Oct. 2018, <https://doi.org/10.1109/TPEC.2018.8312045>.
- [15] S. Buso, G. Spiazzi, and D. Tagliavia, "Simplified control technique for high-power-factor flyback Cuk and Sepic rectifiers operating in CCM," *IEEE Transactions on Industry Applications*, vol. 36, no. 5, pp. 1413–1418, Sep. 2000, <https://doi.org/10.1109/28.871291>.
- [16] V. Vlatkovic, D. Borojevic, and F. C. Lee, "Input filter design for power factor correction circuits," *IEEE Transactions on Power Electronics*, vol. 11, no. 1, pp. 199–205, Jan. 1996, <https://doi.org/10.1109/63.484433>.
- [17] Kanaiya G Bhatt and Yogesh Parmar, "Implementation of Brushless DC motor speed control on STM32F407 Cortex M4," *International Journal of Engineering Trends and Technology - IJETT*, vol. 53, no. 3, pp. 118–123, Nov. 2017, <https://doi.org/10.14445/22315381/IJETT-V53P221>.
- [18] Jagraj Singh and Manpreet Singh, "Comparison and Analysis of Different Techniques for Speed Control of Brushless DC Motor using Matlab Simulink," *International Journal of Engineering Trends and Technology - IJETT*, vol. 38, no. 7, pp. 373–379, Aug. 2016, <https://doi.org/10.14445/22315381/IJETT-V38P267>.
- [19] P. Yadav, R. Poola, and K. Najumudeen, "High dynamic performance of a BLDC motor with a front end converter using an FPGA based controller for electric vehicle application," *Turkish Journal of Electrical Engineering and Computer Sciences*, vol. 24, no. 3, pp. 1636–1651, Jan. 2016, <https://doi.org/10.3906/elk-1401-289>.
- [20] K. Gunasekaran and S. V. Thazhathu, "Improved resettable integrator control for a bridgeless interleaved AC/DC converter," *Turkish Journal of Electrical Engineering and Computer Sciences*, vol. 25, no. 5, pp. 3578–3590, Jan. 2017, <https://doi.org/10.3906/elk-1512-86>.
- [21] Muhammad H. Rashid, *Power electronics: circuits, devices, and applications*, Second edition. Englewood Cliffs, NJ, USA: Prentice Hall, 1993.
- [22] O. A. Heubo-Kwegna, "Fuzzy Logic versus Classical Logic: An Example in Multiplicative Ideal Theory," *Advances in Fuzzy Systems*, vol. 2016, Dec. 2016, Art. no. e3839265, <https://doi.org/10.1155/2016/3839265>.
- [23] R. O. Reddy, S. Kautish, V. P. Reddy, N. S. Yadav, M. M. Alanazi, and A. W. Mohamed, "Effects of Integrated Fuzzy Logic PID Controller on Satellite Antenna Tracking System," *Computational Intelligence and Neuroscience*, vol. 2022, Mar. 2022, Art. no. e7417298, <https://doi.org/10.1155/2022/7417298>.

An Empirical Framework for Recommendation-based Location Services Using Deep Learning

Vinita Rohilla

Department of Computer Science and Engineering, School of
Engineering and Technology, Sharda University, Greater
Noida, India and
Department of CSE, Maharaja Surajmal Institute of
Technology, New Delhi, India
vinita_rohilla@msit.in

Mandeep Kaur

Department of Computer Science and Engineering
School of Engineering and Technology
Sharda University
Greater Noida, India
mandeep.kaur@sharda.ac.in

Sudeshna Chakraborty

Department of Computer Science and Technology
Lloyd Institute of Engineering and Technology
Greater Noida, India
sudeshna2529@gmail.com

Received: 8 June 2022 | Revised: 8 July 2022 | Accepted: 10 July 2022

Abstract—The large amount of possible online services throws a significant load on the users' service selection decision-making procedure. A number of intelligent suggestion systems have been created in order to lower the excessive decision-making expense. Taking this into consideration, an RLSD (Recommendation-based Location Services using Deep Learning) model is proposed in this paper. Alongside robustness, this research considers the geographic interface between the client and the service. The suggested model blends a Multi-Layer-Perceptron (MLP) with a similarity Adaptive Corrector (AC), which is meant to detect high-dimensional and non-linear connections, as well as the location correlations amongst client and services. This not only improves recommendation results but also considerably reduces difficulties due to data sparseness. As a result, the proposed RLSD has strong flexibility and is extensible when it comes to leveraging context data like location.

Keywords—location services; recommendation system; deep learning; similarity corrector

I. INTRODUCTION

Numerous corporations and organizations have started to wrap their created business apps into more and more widespread multiple online services [1-4]. Many lightweight recommendation methods have also been created to reduce the expenses of consumer decision-making. Generally, by evaluating available client data, a recommender system can deduce a person's approximated tastes and preferences and then offer reliable suggestions [5-9]. It efficiently captures the relevant information and preferences of service clients. Location is an important component in decision recommendations since the Quality of Service (QoS) is sometimes significantly dependent on client or service location. Moreover, location-aware QoS data frequently contain

sensitive user information, such as a user's most recently requested service set, the amount of time it takes a user to summon a services located in a nation, etc. Service-Oriented Architecture (SOA) is commonly employed in decentralized computing environments [10], including cloud computing and mobile computing. Location-based services are more successful to provide recommendations based on user's interests [12, 13].

Collaborative Filtering (CF) is a popular way for creating a recommendation system. In recommendation systems, the current user-based CF mechanism seeks for a comparable user based on their prior behavior. The ideas must be according to the user's interest. For example, a user's visited locations are denoted by pins of various forms. The 4 customers check in at 9 distinct locations: 'Exhibition,' 'Hotel,' 'Campground,' 'Shopping Centre,' 'Cineplex,' 'Opera Cinema,' 'Cafe,' 'Library,' and 'College.' The CF approach often creates a similarity measure between various users and offers suggestions based on the maximum value. Let's create a suggestion for customer A1. We could observe that user A1's activities are more comparable to users A2's activities because both went into 'Cineplex,' 'Opera Cinema,' and 'Cafe.' Based on the activities of user A2, the CF technique now recommends 'Library' to user A1. Unfortunately, this is not the greatest fit for user A1 when user A1's visiting information indicates a preference in 'Entertainment' venues, like 'Gallery.' To address this constraint, we will construct an interested profile for every customer so that suggestions may be made as needed.

The following are the major contributions to this study:

- An RLSD framework is developed, which blends an MLP with a similarity Adaptive Corrector in a new way.

Corresponding author: Vinita Rohilla

- The performance of the suggested strategy was assessed and compared with 9 advanced options.
- The proposed technique not only improves recommendation performance, but it also significantly reduces difficulties due to data sparseness.

II. LITERATURE SURVEY

Authors in [14] focused mostly on the cold-start dilemma for service advice depending on user and service locations. To resolve this concern, they offered a service recommendation approach based on CF and geo location, which takes into account the characteristics of services at the edges, movement, and customer requests over time. To begin, they used a multidimensional weighted approach to synthesize the service quality for every dimension in different temporal chunks. In respect of recommendations accuracy, the empirical findings suggest that their multidimensional inverse similarity recommendation method (MDITCF) built on time-aware CF surpasses the Inverted CF recommendation method. Authors in [15] suggested a novel deep CF approach to service recommendations, dubbed Location-aware Deep CF (LDCF). These main advancements included in this approach are: 1) the location attributes are located into high-dimensional dense imbed matrices. MLP encapsulates the HD and non-linear features. Similarity ACs are integrated in the output nodes to first rectify the forecasting QoS. With this, LDCF not only understands the high-dimension and non-linear correlation among the user and services, but it can also dramatically reduce data sparseness. Extensive studies on a real-world Web service [15] database show that LDCF's recommendations efficiency clearly exceeds 9 state-of-the-art services recommendations approaches. Authors in [16] used location information in the factorization machine for QoS predictions, while contextualized information helps the CF similarity calculation. These computations understand the lower dimension and linear characteristics of customers and service providers. Authors in [17] suggested a tailored location-aware CF approach for web service recommendations. Picking comparable neighbors for the user based service the suggested technique takes advantage of both customer location and online services. The technique also incorporated an improved similarity metric for user and web services through accounting for their customized contribution. The test findings demonstrate that this methodology greatly increases QoS predictive performance and computing efficiency when compared to earlier CF-based systems.

III. PROPOSED METHODOLOGY

The major problem in recommending services is estimating QoS. CF is the most extensively utilized QoS predicting technology currently available. Conventional CF techniques, on the other hand, suffer from two flaws: 1) The similarity modeling approach used by conventional CF-based techniques can only gain knowledge of low-dimension and linear characteristics or features from previous networks of user and service and 2) the commonly used data sparseness dilemma in reality has a massive effect on recommendation systems' efficiency. This section provides a detailed description of the proposed model and methodology. The section briefly

describes the loss function, the optimizer, and the algorithm used in this work.

A. Deep Neural Networks

A Deep Neural Network (DNN) is one type of Neural Network with more than 2 layers: an input layer, at least one hidden layer, and an output layer. In a process known as "feature hierarchy," every layer conducts certain kinds of sorting and ordering. Handling with unorganized or unstructured input is among the most important applications of highly powerful neural network models [18].

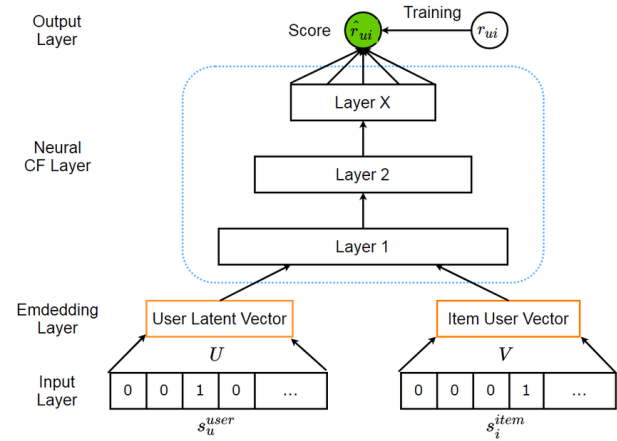


Fig. 1. Recommendation based location services based on deep learning architecture.

The RLSD model is a multiple-layered feed forward neural network with 3 main layers. An Input Layer is used to create the input variables needed from the Intermediate Layer and the similarities needed for the Output Nodes. The Intermediate Layer is employed for centralized training to ensure getting high-dimension and non-linear characteristics.

1) Input Layer

The Input layer's primary function is to regulate the initial Input. The Input contains user identification, location-based info, service identifiers, and service geo locations in Keras1's Embedding Layer, that may be thought as a special fully-connected layer lacking bias terms. Essentially, the Embedded Layer uses one-hot encoding on the inputs to build a '0' vector with a given dimension, while the vector's i -th point is set to 1 [19]. The category characteristics are translated to high-dimension fully connected embedding vectors using this procedure. The mapping procedure is depicted in (1) - (4):

$$I_u^k = f_1(P_1^T i_u + b_1) \quad (1)$$

$$G_u^k = f_1(P_1^T g_u + b_1) \quad (2)$$

$$I_s^k = f_1(Q_1^T i_s + b_1) \quad (3)$$

$$I_u^k = f_1(Q_1^T g_s + b_1) \quad (4)$$

where i_u and i_s are the user's identifier and the service's identifier, correspondingly, g_u and g_s are the initial inputs for the user's and service's location, P_1 and Q_1 are user's and service's embedding weighted matrices, b_1 is a bias term

initialized to 0, f_1 is the embedding layer's activation function, which is considered as the identity function for this work, I_u^k and G_u^k are the k -dimensional user_id and location embedding vector correspondingly, and U and S are the k -dimensional service_id and location embedding vector correspondingly.

These identifying feature vectors representations are integrated with the appropriate location features set to generate the user feature map and service feature map. Next, we append both feature maps to generate the intermediate layers input vector sequence. The equation is written in the following form:

$$U = \Phi(I_u^k, G_u^k) = \begin{bmatrix} I_u^k \\ G_u^k \end{bmatrix} \quad (5)$$

$$S = \Phi(I_s^k, G_s^k) = \begin{bmatrix} I_s^k \\ G_s^k \end{bmatrix} \quad (6)$$

$$X = \Phi(U, V) = \begin{bmatrix} u \\ v \end{bmatrix} \quad (7)$$

where Φ is the merge operation, U and S are user and service embedding vectors, and X is the input vector.

An Adaptive Corrector (AC) that computes similarities among user-location embedding and service-location embedding is present. The AC employs a similarity approach, including location similarities among consumers and services into the neural network's forward propagation phase. As a result, the AC bridges gaps across deep learning with CF. The AC's operation outcome is immediately transferred to the Output Nodes, bypassing the Intermediate Layer. The AC is adaptable and may be used for all other similarity computations like cosine and Euclidean similarity. Equations (8) and (9) describe the procedure:

$$O^{AC} = \text{cosider}(G_u, G_s) = \frac{G_u \cdot G_s}{\|G_u\| \|G_s\|} \quad (8)$$

$$O^{AC} = \text{cosider}(G_u, G_s) = \sqrt{G_u \cdot G_s} \quad (9)$$

where O^{AC} is the AC similarity output. Cosine and Euclidean similarities are both present in this. When no specific comment is made, (8) is applied to determine the cosine similarity outcome of the AC.

2) Intermediate Layer

The Intermediate Layer is responsible for processing the input vectors from the Input Nodes in order to capture non-linear information. The high-dimensional non-linear correlation among consumers and services is learned using a densely integrated MLP architecture in this work. First but foremost, we must select the non-linear activation. The activation function SeLU (Scaled Exponential Linear Unit) presents numerous benefits. It allows building a map featuring qualities that led to SNNs (Self-normalized Neural Networks). Secondly, in order for the DNN to train and learn many attributes, the network structure must adhere to the standard tower architecture [20]. Lastly, to avoid over fitting, we employ L2 regularization on weights. In the Intermediate Layer, the forward propagating of the input vector sequence is described by:

$$o_2^{mlp} = f_2(W_2^T x + b_2) \quad (10)$$

$$o_2^{mlp} = f_1(W_1^T f_2 o_{i-1}^{mlp} + b_1), I = 3, 4, \dots, N-1 \quad (11)$$

$$o^{mlp} = o_{n-1}^{mlp} \quad (12)$$

where o_{n-1}^{mlp} is the i th layer of the Intermediate Layer's output, b_1 the Intermediate Layer bias term, and o^{mlp} the Intermediate Layer's output.

3) Output Layer

The Output Layer is largely responsible for producing the overall forecast results. The FRLS paradigm divides users and services into two paths. We immediately combine the outcomes of these two paths, as in [20, 21]. We mix the similarity outcome o^{AC} with the output vector o^{mlp} to create a new output vector sequence o . Finally, FRLS makes the final projections using a single-layered neural network. Gaussian distribution is used to initialize the parameters of this layer, as illustrated in (13)-(14):

$$o = \Phi(o^{AC}, o^{mlp}) = \begin{bmatrix} o^{AC} \\ o^{mlp} \end{bmatrix} \quad (13)$$

$$\hat{Q}_{u,s} = f_n(W_n^T o + b_n) \quad (14)$$

where $\hat{Q}_{u,s}$ is the predicted QoS values of user u raising the s service, and b_n is the ordinary identity function that signifies the activation function of the last layer.

We get a typical matrix factorization network base Gaussian Matrix Factorization (GMF) distribution on one side and an MLP network on the other.

B. Multi-Layer Perceptron Networks

An MLP network is simply a formal moniker for the most fundamental type of DNN. An MLP network is made up of 5 dense hidden layers and the SeLu activation function. We began by embedding the user and items, then flattened and appended them. Afterwards, we added the first dropout layer, followed by 4 hidden layers with 64 neurons, 32 neurons, 16 neurons, 8 neurons, and finally one densely integrated neuron. Then a dropout and batch normalization layer was added between hidden layers 1 and 2 and 2 and 3. Lastly, we got our final output layer, which is nothing more than a one fully-connected neuron. We utilized log cosh as the error function and Nadam as optimizer.

C. Matrix Factorization Networks

A Gaussian MF networks is essentially a conventional point-wise MF that uses Stochastic Gradient Decent (Adam with this context) to approximate the factoring of a matrix (user×item) into two matrices, i.e. user×latent feature and latent feature×item.

D. Combining the two Networks: NeuMF

Finally, the Matrix factorization and MLP network are merged into the NeuMF network. Essentially, this merely appends the results of two networks. The two networks are then fused, and a single output node is added to the newly integrated model. From this, the configuration is like above, with a binary log cosh loss and the Nadam optimizer.

To improve the accuracy of representing probability distributions, many variants have been proposed. An alternative approach for improvement is through the reconstruction loss:

$$f(t; a) = \frac{1}{a} \log(\cosh(at)) = \frac{1}{a} \log \frac{e^{at} + e^{-at}}{2} \quad (15)$$

Nadam optimizer can be written as:

$$w_{t+1} = w_t - \frac{\alpha}{\sqrt{\hat{v}_t} + \epsilon} \left(\beta_1 \hat{m}_{t-1} + \frac{1 - \beta_1}{1 - \beta_1^t} \cdot \frac{\partial L}{\partial w_t} \right) \quad (16)$$

Nesterov is used by Nadam optimizer to modify the gradients 1 step forward by substituting the prior $m_vec(m_{t-1})$ in (16) with the current $m_vec(m_t)$:

$$w_{t+1} = w_t - \frac{\alpha}{\sqrt{\hat{v}_t} + \epsilon} \left(\beta_1 \hat{m}_t + \frac{1 - \beta_1}{1 - \beta_1^t} \cdot \frac{\partial L}{\partial w_t} \right) \quad (17)$$

Algorithm 1: RLSD (Recommendation based location services using the Deep Learning Algorithm).

Required: user_service request matrix (Rm), density of matrix (Dm), DNN topology design (t), learning rates (lr), decayed ratios (Dr), no. of iterations (Ni).

Output: Weighted matrix and the bias $P_1, Q_1, W_1, \dots, W_n, b_1, b_2, \dots, b_n$.

Strategy:

- step 1.** Scarce Rm based on Dm
- step 2.** Make training inputs entries for R_{train} and test input entries R_{test}
- step 3.** Create input attributes/features i_u, g_u, i_s, g_s ;
- step 4.** Construct the DNN using t and (10)-(12)
- step 5.** Set $P_1, Q_1, W_1, \dots, W_n$ according to the Gaussian distribution;
- step 6.** Set b_1, b_2, \dots, b_n to 0;
- step 7.** For each epoch = 1 to Ni do
- step 8.** For each user and service in R_{train} do
- step 9.** Create embedding vectors sequence using (1)-(4);
- step 10.** Create input vector sequence using (5)-(7)
- step 11.** Create the AC output from either (8) or (9)
- step 12.** Make prediction, $\hat{Q}_{u,s}$ using (13)-(14)
- step 13.** end for
- step 14.** Give lr and Dr to Nadam optimizer
- step 15.** Modify parameters of the model using the Nadam minimization (15)
- step 16.** for each user and service in R_{test} do
- step 17.** Use (20)-(21) to measure the performance of the model
- step 18.** end for
- step 19.** end for

IV. RESULTS AND DISCUSSION

This section discusses the experimentation results for location-based services on the WS-Dream dataset using Python programming. To assess the effectiveness of the proposed method, two evaluation measures are used.

A. Dataset

We ran tests upon the WS-Dream dataset which is a substantial Web services dataset gathered and managed in [22],

which consists of 19,74,675 QoS values from 339 users on 5,825 services. This dataset includes information on users' and services' locations. QoS data are presented in this work as a user-service matrix, with the row indicator representing the user identifier and the column indicator representing the services identifier. This work utilized response time and throughput as inputs to the RLSD.

B. Pre-processing

This research makes use of two spatially relevant dataset features/attributes: Country Name (CN) and Autonomous System Number (ASN). Users were spread throughout 30 nations and 136 ASNs, whereas services were spread across 990 ASNs across 73 countries, according to database figures. For CN, we utilized Sklearn3's category encoding to convert the classed characteristics into numerical embeddings, such that each classified attribute is expressed by a nation code. The data can be viewed like after pre-processing:

$$U = (U_ID, UASN, UCN) \quad (18)$$

$$S = (S_ID, SASN, SCN) \quad (19)$$

where U and S are the user input embedding vector and service input embedding vector correspondingly, U_ID is the user identifier, $UASN$ is an autonomous system numeric user code, UCN is the nationwide user code, and S_ID , $SASN$, and SCN are the same as above.

C. Parameter Setting

For CF methods (UPCC, LACF, IPCC, RegionKNN, etc.), the best- k value is set to 10, the learning rate is fixed at $1e^{-3}$, the total of implicit feature factors (size) is fixed to 10, the number of total iterations is fixed to 300, the regularization variables are fixed to 0.1, and the randomized factor for the rarefy matrix is fixed to 7. Deep learning techniques (NCF, RLSD), can be developed using the Keras API, wherein the Gaussian distribution function is utilized (average is 0, stdev is 0.01) to set the model hyper parameters and (15) to modify the hyper parameters. Then we configured the batch size to 256, learning rate to $1e^{-4}$, 4 MLPs, and Nadam optimizer.

D. Evaluation Metrics

The recommendation success of the specified approach is measured using two fundamental statistical evaluation metrics: Mean Absolute Error (MAE) and Root Mean Squared Error (RMSE):

$$MAE = \frac{\sum_{u,s} |Q_{u,s} - \hat{Q}_{u,s}|}{N} \quad (20)$$

$$RMSE = \sqrt{\frac{1}{N} \sum_{u,s} (Q_{u,s} - \hat{Q}_{u,s})^2} \quad (21)$$

where $Q_{u,s}$ is the QoS initial value for the user u raising the service s , $\hat{Q}_{u,s}$ is the QoS prediction value u raising the service s , and N is the overall QoS value.

Tables I and II show the obtained results by the algorithms performed in [21], with which the proposed model of this paper is compared to. The values in the Tables show that the proposed model is better in MAE and RMSE for response time (RT) and TP (throughput).

TABLE I. RESPONSE TIME EXPERIMENTAL RESULTS

Approach	Density									
	0.5		0.10		0.15		0.20		0.25	
	MAE	RMSE	MAE	RMSE	MAE	RMSE	MAE	RMSE	MAE	RMSE
UMEAN	0.876	0.853	0.873	1.857	0.874	1.857	0.873	1.858	0.874	1.858
IMEAN	0.703	0.567	0.686	1.542	0.684	1.533	0.681	1.529	0.680	1.525
UPCC	0.634	0.377	0.553	1.311	0.511	1.258	0.483	1.220	0.467	1.189
IPCC	0.633	1.397	0.591	1.341	0.507	1.258	0.454	1.208	0.431	1.175
UIPCC	0.624	1.386	0.579	1.328	0.498	1.247	0.448	1.197	0.425	1.165
RegionKNN	0.594	1.641	0.577	1.637	0.569	1.627	0.569	1.617	0.562	1.619
LACF	0.682	1.500	0.650	1.468	0.610	1.416	0.582	1.381	0.562	1.357
PMF	0.568	1.537	0.487	1.321	0.451	1.221	0.430	1.171	0.416	1.139
NCF	0.440	1.325	0.385	1.283	0.372	1.253	0.362	1.205	0.349	1.138
LDCF	0.246	0.7398	0.2787	0.895	0.2291	0.7573	0.2370	0.8004	0.2585	0.8819
RLSD (proposed)	0.1765	0.4977	0.1699	0.530	0.1892	0.6155	0.1831	0.5977	0.1710	0.5643

TABLE II. THROUGHPUT EXPERIMENTAL RESULTS

Approach	Density									
	0.5		0.10		0.15		0.20		0.25	
	MAE	RMSE	MAE	RMSE	MAE	RMSE	MAE	RMSE	MAE	RMSE
UMEAN	54.333	110.296	53.947	110.345	53.971	110.201	53.906	110.190	53.862	110.194
IMEAN	27.342	65.844	26.962	64.843	26.757	64.266	26.669	64.069	26.595	63.873
UPCC	27.559	60.757	22.687	54.598	20.525	50.906	19.243	48.834	18.253	47.135
IPCC	27.102	62.665	26.270	60.479	25.487	57.561	23.726	54.564	22.286	52.293
UIPCC	27.070	60.510	22.440	54.506	20.256	50.585	18.888	48.238	17.863	46.392
RegionKNN	26.857	69.614	25.352	68.015	24.947	67.365	24.687	66.923	24.746	66.831
LACF	27.419	65.770	24.847	62.057	22.943	58.816	21.562	56.507	20.587	54.785
PMF	18.943	57.020	16.004	47.933	14.668	43.642	13.988	41.652	13.398	40.025
NCF	15.468	49.703	13.616	46.034	12.284	42.317	11.833	41.263	11.312	39.534
LDCF	17.629	57.746	14.711	50.730	13.952	48.871	13.199	47.323	12.332	45.142
RLSD (proposed)	19.517	61.822	16.154	53.344	14.958	50.681	14.388	49.393	14.332	49.195

Figures 2 and 3 show the loss values obtained by both models in response time and throughput respectively. The lesser the loss value, the more accurate the simulation (unless the model was over fitted to the training set). The loss value can be computed during training and testing and is used to determine how good the model performs for the two different sets. Loss, like accuracy, is also not a proportion. It is the summarization of the errors incurred in training and test sets with each sample. It is clearly visible that the proposed RLSD model performed better than the existing methods by reducing the loss values in both response time and throughput.

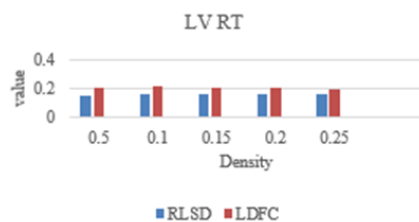


Fig. 2. Loss values of response time.

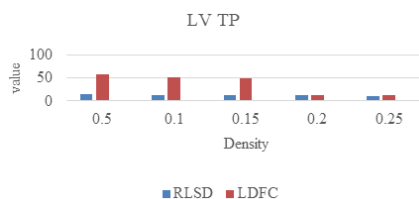


Fig. 3. Loss values of throughput.

V. CONCLUSION

A recommendation system is the backbone for retrieving and processing information that aims to forecast user interests. This study offers a novel deep learning-based approach called RLSD to provide recommendation services to predict QoS which incorporates a similarity AC to improve the prediction values. In the future, we plan to analyze and solve additional privacy concerns in location service recommendations, as well as improve the performance, using a parallel and distributed recommendations system to manage the required massive data. This model may also improve the results of [15, 23-29].

REFERENCES

- [1] Y. Wang, Z. Cai, Z.-H. Zhan, Y.-J. Gong, and X. Tong, "An Optimization and Auction-Based Incentive Mechanism to Maximize Social Welfare for Mobile Crowdsourcing," *IEEE Transactions on Computational Social Systems*, vol. 6, no. 3, pp. 414-429, Jun. 2019, <https://doi.org/10.1109/TCSS.2019.2907059>.
- [2] Y. Zhang, Y. Zhou, F. Wang, Z. Sun, and Q. He, "Service recommendation based on quotient space granularity analysis and covering algorithm on Spark," *Knowledge-Based Systems*, vol. 147, pp. 25-35, May 2018, <https://doi.org/10.1016/j.knosys.2018.02.014>.
- [3] S. Zhang, X. Li, Z. Tan, T. Peng, and G. Wang, "A caching and spatial K-anonymity driven privacy enhancement scheme in continuous location-based services," *Future Generation Computer Systems*, vol. 94, pp. 40-50, May 2019, <https://doi.org/10.1016/j.future.2018.10.053>.
- [4] S. Zhang, G. Wang, and Q. Liu, "A Dual Privacy Preserving Scheme in Continuous Location-Based Services," in *IEEE Trustcom/BigDataSE/ICSS*, Sydney, NSW, Australia, Aug. 2017, pp. 402-408, <https://doi.org/10.1109/Trustcom/BigDataSE/ICSS.2017.264>.
- [5] L. Qi, R. Wang, C. Hu, S. Li, Q. He, and X. Xu, "Time-aware distributed service recommendation with privacy-preservation," *Information*

- Sciences*, vol. 480, pp. 354–364, Apr. 2019, <https://doi.org/10.1016/j.ins.2018.11.030>.
- [6] W. Dou, X. Zhang, J. Liu, and J. Chen, "HireSome-II: Towards Privacy-Aware Cross-Cloud Service Composition for Big Data Applications," *IEEE Transactions on Parallel and Distributed Systems*, vol. 26, no. 2, pp. 455–466, Oct. 2015, <https://doi.org/10.1109/TPDS.2013.246>.
 - [7] Y. Xu, L. Qi, W. Dou, and J. Yu, "Privacy-Preserving and Scalable Service Recommendation Based on SimHash in a Distributed Cloud Environment," *Complexity*, vol. 2017, Dec. 2017, Art. no. e3437854, <https://doi.org/10.1155/2017/3437854>.
 - [8] A. Ramlatchan, M. Yang, Q. Liu, M. Li, J. Wang, and Y. Li, "A survey of matrix completion methods for recommendation systems," *Big Data Mining and Analytics*, vol. 1, no. 4, pp. 308–323, Dec. 2018, <https://doi.org/10.26599/BDMA.2018.9020008>.
 - [9] Y. Zhang *et al.*, "Covering-Based Web Service Quality Prediction via Neighborhood-Aware Matrix Factorization," *IEEE Transactions on Services Computing*, vol. 14, no. 5, pp. 1333–1344, Sep. 2021, <https://doi.org/10.1109/TSC.2019.2891517>.
 - [10] I. M. Delamer and J. L. M. Lastra, "Service-Oriented Architecture for Distributed Publish/Subscribe Middleware in Electronics Production," *IEEE Transactions on Industrial Informatics*, vol. 2, no. 4, pp. 281–294, Aug. 2006, <https://doi.org/10.1109/TII.2006.885188>.
 - [11] B. AlBanna, M. Sakr, S. Moussa, and I. Moawad, "Interest Aware Location-Based Recommender System Using Geo-Tagged Social Media," *ISPRS International Journal of Geo-Information*, vol. 5, no. 12, Dec. 2016, Art. no. 245, <https://doi.org/10.3390/ijgi5120245>.
 - [12] N. Kumar, A. Hashmi, M. Gupta, and A. Kundu, "Automatic Diagnosis of Covid-19 Related Pneumonia from CXR and CT-Scan Images," *Engineering, Technology & Applied Science Research*, vol. 12, no. 1, pp. 7993–7997, Feb. 2022, <https://doi.org/10.48084/etasr.4613>.
 - [13] A. B. S. Salamh and H. I. Akyuz, "A Novel Feature Extraction Descriptor for Face Recognition," *Engineering, Technology & Applied Science Research*, vol. 12, no. 1, pp. 8033–8038, Feb. 2022, <https://doi.org/10.48084/etasr.4624>.
 - [14] M. Yu, G. Fan, H. Yu, and L. Chen, "Location-based and Time-aware Service Recommendation in Mobile Edge Computing," *International Journal of Parallel Programming*, vol. 49, no. 5, pp. 715–731, Oct. 2021, <https://doi.org/10.1007/s10766-021-00702-5>.
 - [15] N. Kumar and D. Aggarwal, "LEARNING-based Focused WEB Crawler," *IETE Journal of Research*, pp. 1–9, Feb. 2021, <https://doi.org/10.1080/03772063.2021.1885312>.
 - [16] Y. Yang, Z. Zheng, X. Niu, M. Tang, Y. Lu, and X. Liao, "A Location-Based Factorization Machine Model for Web Service QoS Prediction," *IEEE Transactions on Services Computing*, vol. 14, no. 5, pp. 1264–1277, Sep. 2021, <https://doi.org/10.1109/TSC.2018.2876532>.
 - [17] J. Liu, M. Tang, Z. Zheng, X. Liu, and S. Lyu, "Location-aware and personalized collaborative filtering for web service recommendation," *IEEE Transactions on Services Computing*, vol. 9, no. 5, pp. 686–699, Sep. 2016, <https://doi.org/10.1109/TSC.2015.2433251>.
 - [18] U. Khan, K. Khan, F. Hassan, A. Siddiqui, and M. Afaq, "Towards Achieving Machine Comprehension Using Deep Learning on Non-GPU Machines," *Engineering, Technology & Applied Science Research*, vol. 9, no. 4, pp. 4423–4427, Aug. 2019, <https://doi.org/10.48084/etasr.2734>.
 - [19] L. Zhang, T. Luo, F. Zhang, and Y. Wu, "A Recommendation Model Based on Deep Neural Network," *IEEE Access*, vol. 6, pp. 9454–9463, 2018, <https://doi.org/10.1109/ACCESS.2018.2789866>.
 - [20] X. He, L. Liao, H. Zhang, L. Nie, X. Hu, and T.-S. Chua, "Neural Collaborative Filtering," in *26th International Conference on World Wide Web*, Perth, Australia, Apr. 2017, pp. 173–182, <https://doi.org/10.1145/3038912.3052569>.
 - [21] H.-J. Xue, X.-Y. Dai, J. Zhang, S. Huang, and J. Chen, "Deep matrix factorization models for recommender systems," in *26th International Joint Conference on Artificial Intelligence*, Melbourne, Australia, Aug. 2017, pp. 3203–3209.
 - [22] Z. Zheng, H. Ma, M. R. Lyu, and I. King, "QoS-Aware Web Service Recommendation by Collaborative Filtering," *IEEE Transactions on Services Computing*, vol. 4, no. 2, pp. 140–152, Apr. 2011, <https://doi.org/10.1109/TSC.2010.52>.
 - [23] N. Kumar, M. Gupta, D. Sharma, and I. Ofori, "Technical Job Recommendation System Using APIs and Web Crawling," *Computational Intelligence and Neuroscience*, vol. 2022, Jun. 2022, Art. no. e7797548, <https://doi.org/10.1155/2022/7797548>.
 - [24] N. Kumar, "Segmentation based Twitter Opinion Mining using Ensemble Learning," *International Journal on Future Revolution in Computer Science & Communication Engineering*, vol. 3, no. 9, pp. 1–9, Sep. 2017.
 - [25] N. Kumar and P. Dahiya, "Weighted similarity page rank: an improvement in WPR and WSR," *International Journal of Computer Engineering and Applications*, vol. 11, no. 8, pp. 1–11, 2017.
 - [26] J. Mor, N. Kumar, and D. Rai, "Effective presentation of results using ranking & clustering in meta search engine," *COMPUSOFT, An international journal of advanced computer technology*, vol. 7, no. 12, Art. no. 2957, 2018.
 - [27] J. Mor, D. D. Rai, and D. N. Kumar, "An XML based Web Crawler with Page Revisit Policy and Updation in Local Repository of Search Engine," *International Journal of Engineering & Technology*, vol. 7, no. 3, pp. 1119–1123, Jun. 2018, <https://doi.org/10.14419/ijet.v7i3.12924>.
 - [28] N. Kumar and P. Singh, "Meta Search Engine with Semantic Analysis and Query Processing," *International Journal of Computational Intelligence Research*, vol. 13, no. 8, pp. 2005–2013, 2017, <https://doi.org/10.37622/IJCIR/13.8.2017.2005-2013>.
 - [29] N. Kumar, "Document Clustering Approach for Meta Search Engine," *IOP Conference Series: Materials Science and Engineering*, vol. 225, Dec. 2017, Art. no. 012291, <https://doi.org/10.1088/1757-899X/225/1/012291>.

The Feasibility of Applying Waste Concrete as Coarse Aggregates in New Concrete

Tien Hong Nguyen

Faculty of Construction

Vinh University

Vinh City, Vietnam

tienhongkxd@vinhuni.edu.vn

Thi Thanh Tung Nguyen

Faculty of Construction

Vinh University

Vinh City, Vietnam

ntttung@gmail.com

Thi Thu Hien Nguyen

Faculty of Construction

Vinh University

Vinh City, Vietnam

thuhien.tvna@gmail.com

Van Tien Phan

Faculty of Construction

Vinh University

Vinh City, Vietnam

vantienkxd@vinhuni.edu.vn

Received: 17 July 2022 | Revised: 26 July 2022 | Accepted: 27 July 2022

Abstract-This paper presents a study on the possibility of replacing natural coarse aggregates with recycled aggregates in concrete in terms of strength, namely compressive strength and flexural strength. The concrete was designed to have a 25MPa compressive strength and an 8cm slump. The replacement rates of natural aggregates with recycled coarse aggregates were 0%, 10%, 15%, and 20%. The test samples were compressed to determine their strength value after 28 days of curing. The research results give a more complete assessment of the efficiency of the use of recycled raw aggregates instead of natural aggregates in concrete. The results indicate that using recycled aggregates is feasible due to the small decrease in concrete strength. The experiment shows that up to 20% replacement, the recorded reduction in the strength of concrete is lower than 15%. However, it is indispensable that the strength of concrete should be enhanced when recycled aggregates are used. According to previous works, fiber reinforcement may be an effective solution. Therefore, to further develop research using recycled aggregates, it is necessary to consider using different fibers to strengthen the concrete. The fiber content can be used in the range of 0-1% of the weight of concrete.

Keywords-compressive strength; flexural strength; waste concrete; demolishing work

I. INTRODUCTION

Recycling of waste construction materials from demolishing works in order to reduce the environmental impact has been investigated by numerous researchers [1-5]. The use sustainable construction materials coming from demolishing works, like recycled concrete, could help produce sustainable materials with advantages such as good quality and low cost while reducing the environmental impact. Besides, the growth in population in big cities leads to continuously rising in the demand of construction materials, which leads to a negative impact on the environment.

Aggregates in concrete are prepared by crushing rocks into different sizes, then sieving and classifying particle sizes according to standards, and mixing to ensure a standard grading curve. This process poses many serious health and environmental hazards, and disrupts ecosystems, necessitating the search for alternative sources of aggregates. On the other hand, the volume of waste concrete generated from the dismantled works is very large and the produced materials are considered waste. As a hard material like stone, waste concrete can be used as aggregates for new concrete. The possibility of replacing natural coarse aggregates with recycled aggregates in concrete has been evaluated by many authors on many aspects. Authors in [2] found that recycled coarse aggregates and natural aggregates can be mixed in a proportionate ratio to be used in pavement and building construction. Various strength tests, including compressive and tensile strength tests of cylinder with 0, 25, 50, 75, and 100% recycled coarse aggregate replacement were performed. Authors in [1] investigated the use of recycled concrete in improving the quality and enhancing the mechanical and microstructure properties of concrete [1]. The designed concrete strength is 35MPa with a fixed water to cement ratio of 0.48. Various characteristics of concrete, including density, workability, temperature, compressive strength, split tensile strength, flexural strength, and microstructural analysis, were investigated. In [6], the authors fully replaced natural coarse aggregates with recycled coarse aggregates and they investigated the bulk density and the compressive strength of concrete for various curing durations. The results show that bulk density and compressive strength of concrete with recycled coarse aggregates were lower than those of concrete using natural coarse aggregates. Authors in [7] carried out various experiments to determine the properties of concrete made with crushed concrete as coarse aggregates. It was found that the recycled coarse aggregates have lower specific gravity

and higher absorption capacity than the original crushed granite aggregates. The use of recycled coarse aggregates leads to reduced compressive strength up to 25%, reduced modulus of elasticity up to 30%, improved damping capacity up to 30%, and higher amounts of drying shrinkage and creep.

To summarize, it is possible to produce concrete with recycled aggregate as coarse aggregates. The quality of the original concrete from which the recycled aggregates are produced seems to have little influence upon the properties of the produced concrete [7]. However, the study and evaluation of the feasibility of using recycled aggregates in concrete needs to be further studied in terms of strength, including compressive strength, split tensile strength, and bending strength.

II. EXPERIMENTAL SETUP

Before casting, slump measurement was performed to determine the slump of concrete in fresh state. Concrete with slump values that are too low or too high can be identified and corrected prior use. Compression test was carried out on cubical specimens. In the present research, cube specimens with size 15×15×15cm were used. Compression experiments were conducted by loading the cube specimens between two plates, and then applying force by moving the crossheads together. During the test, the specimens were compressed and the applied load was recorded. The yield strength and compressive strength of concrete were then measured. Flexural strength is a measure of the tensile strength of concrete. Unreinforced concrete beams sized 10×10×40cm were used. The peak force when the beam specimen begins to appear failure in bending was measured.

After curing at room temperature for 28 days, the concrete samples were tested for compressive strength and flexural strength. The experimental setup is shown in Figures 1 and 2.



Fig. 1. Four-point bending test.

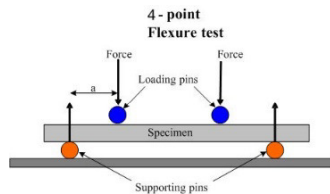


Fig. 2. Compressive test.

In this study, all concrete sample constituents were acquired from local sources, namely Vietnamese standard Portland cement, river sand used as fine aggregates, local natural-crushed rock used as coarse aggregates with diameters ranging from 5 to 20 mm (Table I).

Four cements sets with 0%, 10%, 15%, and 20% of recycled coarse aggregates were cast. Each set consisted of 5 specimens. The specimens were cast in composite molds and compacted through an external vibration machine. The specimens were demolded at least 24h later.

TABLE I. MIX COMPONENTS OF CONCRETE (PER 1m³)

Content of recycled aggregates	Cement (kg)	Sand (kg)	Natural aggregates (kg)	Recycled aggregates (kg)	Water (kg)
0%	292.5	648.3	1216.3	0	195
10%	292.5	648.3	1094.7	121.6	195
15%	292.5	648.3	1033.9	182.4	195
20%	292.5	648.3	973	243.3	195

III. RESULTS AND DISCUSSION

The failure loading values, recorded in the compression test are presented in Table II. These values will be used to calculate the compressive strength of concrete for various percentages of recycled aggregates. The compressive strength values of concrete, calculated according to the Vietnamese standard 3118:1993, are shown in Table II.

TABLE II. FAILURE LOADS IN COMPRESSION TEST

Percentage of recycled aggregates	Specimen	Failure load (kN)	Compressive strength (MPa)
0%	1	505.2	22.45
	2	512.7	22.78
	3	501.3	22.28
	4	499.9	22.22
	5	510.4	22.68
10%	1	497.2	22.1
	2	479.2	21.3
	3	490.5	21.8
	4	489.1	21.74
	5	482.4	21.44
15%	1	455.2	20.23
	2	465.8	20.7
	3	472.4	21.0
	4	477.7	21.23
	5	485.1	21.56
20%	1	460.3	20.46
	2	427.4	19.0
	3	435.5	19.36
	4	418.7	18.61
	5	422.9	18.79

The compressive strength of concrete using different contents of recycled aggregates is plotted in Figure 3. It can be easily seen that using recycle aggregates leads to a decrease of the compressive strength of concrete, although the result arrangement varies in several specimens corresponding to the usage of recycle aggregates. However, the compressive strength of concrete generally decreases with the increasing use of recycled aggregates. This result is in agreement with the results of [3, 5-7].

The drop in percentage of the average compressive strength of concrete using various contents of recycled aggregates was calculated. The result is plotted in Figure 4. We can see that the drop rate of compressive strength of concrete is almost linearly declining with the increase of the using rate of recycled

aggregates, with less than 15% reduction in strength when 20% recycled aggregates are used. From this, the use of recycled coarse aggregates can be considered feasible.

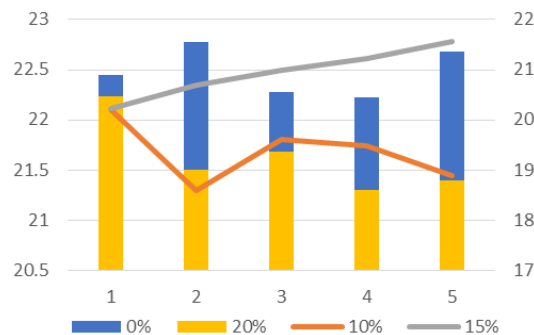


Fig. 3. Compressive strength of concrete samples using recycled aggregates.

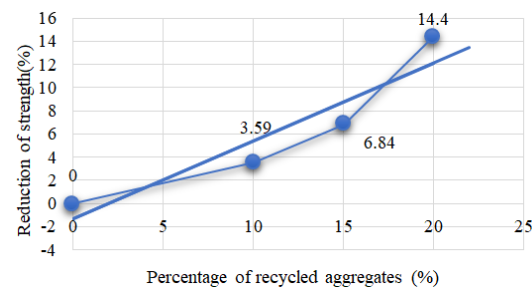


Fig. 4. The drop rate in the compressive strength of concrete using recycled aggregates.

The destructive forces, recorded in the 4-point flexural test, are presented in Table III. The flexural strength, defined as the maximum stress in a material just before it yields in a bending test, was calculated according to the Vietnamese standard 3119:1993.

TABLE III. DESTRUCTIVE FORCES AND FLEXURAL STRENGTH OF CONCRETE

Percentage of recycled aggregates	Specimen	Load (kN)	Flexural strength (MPa)
0%	1	1003.61	3.16
	2	1013.7	3.19
	3	1138.1	3.59
	4	1026.25	3.23
	5	1009.8	3.18
10%	1	987.34	3.11
	2	968.25	3.05
	3	972.21	3.06
	4	979.08	3.08
	5	991.06	3.12
15%	1	932.5	2.94
	2	955.01	3.01
	3	960.23	3.02
	4	934.1	2.94
	5	963.17	3.03
20%	1	872.6	2.75
	2	889.13	2.8
	3	905.74	2.85
	4	919.2	2.89
	5	879.04	2.77

The flexural strength of concrete using different content values of recycled aggregates is plotted in Figure 5. It indicates that using recycle aggregates leads to a slight decrease of flexural strength. The drop in the percentage of the average flexural strength using various content values of recycled aggregates was calculated and the result is plotted in Figure 6. It indicates that the drop rate of compressive strength of concrete is almost linearly declining with the increase of the using rate of recycled aggregates, with less than 15% reduction in flexural strength when 20% recycled aggregates are used. So, the use of recycled coarse aggregate can be considered feasible in terms of flexural strength.

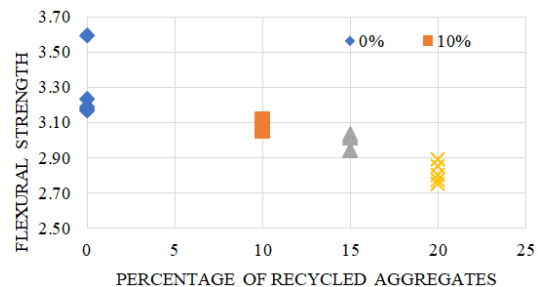


Fig. 5. Flexural strength of concrete samples using recycled aggregates.

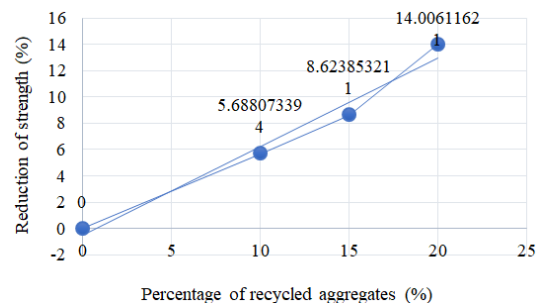


Fig. 6. The drop rate in the flexural strength of concrete using recycled aggregates.

Thus, in order to be able to use recycled aggregates in concrete, it is necessary to find solutions to enhance its compressive and flexural strength. Fiber reinforcement may be considered for the enhancement of the strength of concrete [8-10]. The quantity of fibers has been selected as 0.5% and 1.0% of the weight of concrete [8]. It has been concluded that increased quantity of fibers, improves the flexural strength of concrete beams [8]. Therefore, to further develop the research in the use of recycled aggregates, it is necessary to consider using different fibers to strengthen the cement. The fiber content can be used in the range of 0-1% of the weight of concrete.

IV. CONCLUSION

In this paper, the compressive strength and flexural strength of concrete with recycled aggregates have been investigated. The recycled aggregates came from demolition works, and were used at different contents, namely 0%, 10%, 15%, and 20%. The results indicate that using recycled aggregates is feasible because of the low decrease of concrete strength. The experiment shows that for up to 20% of recycled

concrete used, the recorded reduction in the strength of concrete is lower than 15%. However, it is indispensable that the strength of concrete should be enhanced when recycled aggregates are used. According to previous studies, fiber reinforcement may be an effective solution. Therefore, to further develop the research on the use of recycled aggregates, it is necessary to consider the use of different fibers to strengthen concrete. The fiber content can be used in the range of 0-1% of the weight of concrete.

REFERENCES

- [1] M. T. El-Hawary, C. Koenke, A. El-Nemr, and N. F. Hanna, "Using Recycled Concrete as a Replacement for Coarse Aggregate in the Production of Green Concrete," in *Sustainable Issues in Infrastructure Engineering*, Cham, Switzerland, 2021, pp. 127–151, https://doi.org/10.1007/978-3-030-62586-3_9.
- [2] B. Panda, N. T. Imran, and K. Samal, "A Study on Replacement of Coarse Aggregate with Recycled Concrete Aggregate (RCA) in Road Construction," in *Recent Developments in Sustainable Infrastructure*, Singapore, 2021, pp. 1097–1106, https://doi.org/10.1007/978-981-15-4577-1_91.
- [3] D. D. Nguyen and V. T. Phan, "Compressive Strength Studies on Recycled Binder Concrete," *Engineering, Technology & Applied Science Research*, vol. 11, no. 4, pp. 7332–7335, Aug. 2021, <https://doi.org/10.48084/etasr.4230>.
- [4] V. T. Phan and T. H. Nguyen, "The Influence of Fly Ash on the Compressive Strength of Recycled Concrete Utilizing Coarse Aggregates from Demolition Works," *Engineering, Technology & Applied Science Research*, vol. 11, no. 3, pp. 7107–7110, Jun. 2021, <https://doi.org/10.48084/etasr.4145>.
- [5] X. H. Vu, T. C. Vo, and V. T. Phan, "Study of the Compressive Strength of Concrete with Partial Replacement of Recycled Coarse Aggregates," *Engineering, Technology & Applied Science Research*, vol. 11, no. 3, pp. 7191–7194, Jun. 2021, <https://doi.org/10.48084/etasr.4162>.
- [6] H. Opara, U. Eziefula, and C. Ugwuogbu, "Experimental study of concrete using recycled coarse aggregate," *International Journal of Materials and Structural Integrity*, vol. 10, no. 4, pp. 123–132, Dec. 2016.
- [7] R. Sri Ravindrarajah and C. T. Tam, "Properties of concrete made with crushed concrete as coarse aggregate," *Magazine of Concrete Research*, vol. 37, no. 130, pp. 29–38, Mar. 1985, <https://doi.org/10.1680/mac.1985.37.130.29>.
- [8] A. Namdar, I. B. Zakaria, A. B. Hazeli, S. J. Azimi, A. S. B. A. Razak, and G. S. Gopalakrishna, "An experimental study on flexural strength enhancement of concrete by means of small steel fibers," *Frattura ed Integrità Strutturale*, vol. 7, no. 26, pp. 22–30, Sep. 2013, <https://doi.org/10.3221/IGF-ESIS.26.03>.
- [9] S. T. Kang, B. Y. Lee, J.-K. Kim, and Y. Y. Kim, "The effect of fibre distribution characteristics on the flexural strength of steel fibre-reinforced ultra high strength concrete," *Construction and Building Materials*, vol. 25, no. 5, pp. 2450–2457, May 2011, <https://doi.org/10.1016/j.conbuildmat.2010.11.057>.
- [10] H. binti Hashim *et al.*, "Improving the mechanical properties of polycaprolactone using functionalized nanofibrillated bacterial cellulose with high dispersibility and long fiber length as a reinforcement material," *Composites Part A: Applied Science and Manufacturing*, vol. 158, Jul. 2022, Art. no. 106978, <https://doi.org/10.1016/j.compositesa.2022.106978>.

Levy Enhanced Cross Entropy-based Optimized Training of Feedforward Neural Networks

Kartik Pandya

M & V Patel Department of Electrical Engineering
FTE, CSPIT, CHARUSAT
Changa, India
kartikpandya.ee@charusat.ac.in

Dharmesh Dabhi

M & V Patel Department of Electrical Engineering
FTE, CSPIT, CHARUSAT
Changa, India
harmeshdabhi.ee@charusat.ac.in

Pratik Mochi

M & V Patel Department of Electrical Engineering
FTE, CSPIT, CHARUSAT
Changa, India
vipul.rajput@djmit.ac.in

Vipul Rajput

Department of Electrical Engineering
Dr. Jivraj Mehta Institute of Technology
Mogar, India
vipulrajput16986@gmail.com

Received: 11 July 2022 | Revised: 27 July 2022 | Accepted: 1 August 2022

Abstract—An Artificial Neural Network (ANN) is one of the most powerful tools to predict the behavior of a system with unforeseen data. The feedforward neural network is the simplest, yet most efficient topology that is widely used in computer industries. Training of feedforward ANNs is an integral part of an ANN-based system. Typically an ANN system has inherent non-linearity with multiple parameters like weights and biases that must be optimized simultaneously. To solve such a complex optimization problem, this paper proposes the Levy Enhanced Cross Entropy (LE-CE) method. It is a population-based meta-heuristic method. In each iteration, this method produces a "distribution" of prospective solutions and updates it by updating the parameters of the distribution to obtain the optimal solutions, unlike traditional meta-heuristic methods. As a result, it reduces the chances of getting trapped into local minima, which is the typical drawback of any AI method. To further improve the global exploration capability of the CE method, it is subjected to the Levy flight which consists of a large step length during intermediate iterations. The performance of the LE-CE method is compared with state-of-the-art optimization methods. The result shows the superiority of LE-CE. The statistical ANOVA test confirms that the proposed LE-CE is statistically superior to other algorithms.

Keywords—artificial neural networks; cross entropy method; feedforward neural networks; Levy step; training

I. INTRODUCTION

The Artificial Neural Network (ANN) [1] is the one of the most popular Artificial Intelligence methods. It is inspired from the communication and computation abilities of the human brain and it mimics the learning techniques of human brain to find out relationships between the input and the output (target) variables of a test system. The human brain consists of millions of neurons which are interconnected in a complex network which takes input signal to perform voice recognition, image

classifications, etc. at remarkable speed and accuracy. Similarly, an ANN may consist of many neurons which are subjected to input signals through the connection links. Every connection link has an associated weight, which is multiplied with the signal. Weights are the control variables which are used to solve the optimization problem. Weights and biases are updated in every iteration to finally obtain their optimal values which will minimize the Mean Square Error (MSE) function. This procedure is known as the training (learning) of an ANN.

A. Related Work

Feedforward Neural Networks (FNNs) with two layers are a widely used ANN topology [2]. It has been proved that two-layer FNNs can approximate any nonlinear or linear function with a good accuracy [3]. Training is an integral part of FNNs. Various optimization methods have been suggested in the literature to train FNN. Back Propagation (BP) is a popular gradient-based classical optimization method to train FNNs. But it is susceptible to slow convergence [4] and may get trapped into local minima [5]. Newton's method [6] is another classical method which has quadratic convergence that largely depends upon the choice of initial starting point (guess). A wrong initial guess will lead to a local optima of the problem under consideration. The last two decades, population-based meta-heuristic methods that solve the FNN training problem effectively have emerged. Authors in [7] proposed the use of ANNs to detect the vibration of the rotor shaft of a gas turbine. Authors in [8] suggested the use of Genetic Algorithm (GA) to precisely recognize sign gesture using feature extraction, but mutation strategy makes GA very time consuming and it is preferred for binary solution sets. Also, it is vulnerable to premature convergence. Authors in [9] proposed a new approach to address the optimal design of a FNN using self-adaptive penalty functions. Authors in [10] proposed a Particle Swarm Optimization (PSO)-based neuro-fuzzy model to

enhance dynamic voltage stability of a wind connected grid. Authors in [11] proposed a PSO-powered back-propagation neural network load-shedding strategy in the post-fault condition in a microgrid. Another AI method is Gravitational Search Algorithm (GSA) [12], which has been inspired from the law of gravity and mass interactions. Even though it is a simple method, the unbalance between the application of gravitational law and mass interactions may create premature convergence. Differential Evolutionary (DE) method [13] is another powerful method which uses mutation, crossover, and selection operators on various vectors to get optimal solutions, but the selection of crossover rate greatly affects its convergence. PSO [14] is one of the most popular meta-heuristic methods, as it is easily implementable and it has less parameters to be tuned.

B. Aims and Objectives

The related work (literature survey) reveals that many classical optimization methods suffer from premature convergence, whereas artificial intelligence methods are population-based with generated randomly initial solutions, and as a result, in each simulation run it gives different optimal solutions. So, the aim and objective of this research is to suggest a proper solution methodology which trains an ANN more effectively and with better accuracy. This paper proposes the Levy Enhanced Cross Entropy (LE-CE) optimization method, which is an extension of the Cross Entropy (CE) method. The contributions of this paper are summarized below.

C. Research Outline

- The LE-CE method is proposed for the optimization of the weights and biases of the ANN with the aim to minimize the MSE function.
- The incorporation of Levy flight increases the global exploration capability of the CE method, which improves the quality of the solution.
- The LE-CE method has fewer parameters to be tuned, so it is a fast method.
- The practical Iris classification system is used to check the effectiveness of the LE-CE method.
- The performance of the LE-CE method is compared with the WCCI 2018 award winning EVDEPSO [15] and GECCO 2019 award winning HL_PS_VNSO [16] computational intelligence methods.
- The LE-CE method outperformed the compared methods in terms of optimal solutions.
- ANOVA statistical test and Tukey's HSD test also proved that the proposed method is statistically different from the other compared methods.

II. LEVY ENHANCED CROSS ENTROPY METHOD FOR TRAINING FNNs AND ENCODING STRATEGY

CE method was proposed by Rubinstein [17]. It is a population-based meta-heuristic optimization method similar to the Differential Evolutionary method. However, unlike traditional meta-heuristic methods which directly update

prospective solutions (particles) to obtain sub-optimal solutions, this method produces a distribution of prospective solutions and updates it by updating the parameters like mean and standard deviation of each dimension to obtain sub-optimal solutions. As a result, it decreases the probability of getting stuck into local minima. It has a very few parameters to be tuned and it can be easily executed. The basics of LE-CE method are explained below.

The population of particles is randomly generated and they obey the probability distribution function (pdf) $f(\cdot; \Phi)$, where Φ is the vector of parameters which are to be optimized. Generally, $f(\cdot; \Phi)$ is the Gaussian distribution parameterized by its mean m and variance σ^2 , i.e. $\Phi = (m, \sigma^2)$. Secondly, a threshold value (χ) of the fitness function is selected and only those particles whose fitness values are less than the set threshold value, i.e. $f(x) < \chi$ are considered in the subsequent iterations. Such particles are known as elite particles μ_e . Then, the new parameterized distribution function $f(\cdot; \phi^n)$ with elite particles is updated in such a way that it coincides the target distribution function $f(\cdot; \phi^*)$ by minimizing the Kullback-Leibler (KL) divergence. This procedure finishes one iteration. In the subsequent iterations, a family of distribution functions $f(\cdot; \phi^{(1)}) \dots f(\cdot; \phi^*)$ are produced in accordance with $\chi^{(1)} \dots \chi^{(*)}$ to reach the sub-optimal distribution function $f(\cdot; \phi^*)$. The following section shows the step-by-step implementation of LE-CE.

1) Step 1: Initialization of Mean and Standard Deviation for Each Dimension

Assume iteration $iter=0$, Total no. of iterations $iter_{max} = 500$, No. of particles N , Dimension (control variables) of the problem D , elite particles μ_e (20% of N), smoothing parameters α_s and β_s , $m_e^{(iter)} \in \mathbb{R}^D$ is the mean value of the search distribution for each dimension at iteration $iter$, $\sigma^{(iter)} \in \mathbb{R}^+$ is the standard deviation at iteration $iter$. x_{min} and x_{max} are the minimum and maximum limits of the D^{th} dimension particle. Mean and standard deviation of population are initialized as:

$$m_e^{(0)} = 0.5 * (x_{min} + x_{max}) \quad (1)$$

$$\sigma^{(0)} = 0.25 * (x_{max} - x_{min}) \quad (2)$$

2) Step 2: Generate the Population of Particles

The generation of the population of particles from the sampling distribution $\text{Normal}(m_e^{(iter)}, \sigma^{2(iter)})$ occurs as:

$$x_i^{(iter+1)} = m_e^{(iter)} + \sigma^{(iter)} \text{randn}() \quad \text{for } i = 1, \dots, N \quad (3)$$

where N is the population size, $x_i^{(iter+1)} \in \mathbb{R}^D$ is the i^{th} particle obtained at iteration $(iter+1)$, $m_e^{(iter)} \in \mathbb{R}^D$ is the mean value of the search distribution for each dimension at iteration $iter$, $\sigma^{(g)} \in \mathbb{R}^+$ is step-size (standard deviation) at iteration $iter$,

randn() is a normally distributed random variable with parameters Normal(0,1).

3) Step 3: Fitness Function Evaluations

The fitness values of the whole population are determined as follows:

The FNN consists of n_i input nodes, h_i hidden nodes, and o_i output nodes. In each iteration of learning, the output of each hidden nodes is calculated using (4):

$$f(y_k) = 1 / \left(1 + \exp \left(- \left(\sum_{j=1}^{n_i} w_{jk} * x_j - \theta_k \right) \right) \right), \quad (4)$$

$$k = 1, 2, \dots, h_i$$

where $y_k = \sum_{j=1}^{n_i} w_{jk} x_j - \theta_k$, w_{jk} is the connection weight from the j^{th} node from the input layer to the k^{th} node in the hidden layer, θ_k is the bias of the k^{th} hidden node, and x_j is the j^{th} input.

The final output is calculated following the output of hidden nodes as given by (5):

$$o_l = \sum_{j=1}^{h_i} w_{lk} * f(y_k) - \theta_l, \quad l = 1, 2, \dots, o_i \quad (5)$$

where w_{lk} is the connection weight between the k^{th} hidden node to the l^{th} output node and θ_l is the bias of the l^{th} output node.

Eventually, the mean square error (e_i) is calculated from:

$$e_i = \sum_{j=1}^{h_i} (o_j^l - d_j^l)^2 \quad (6)$$

$$e = \sum_{t=1}^T \frac{e_t}{t} \quad (7)$$

where t represents the training samples and d_j^l is the desired output of the j^{th} input when the l^{th} training sample is considered.

So, the fitness function of the j^{th} training sample can be defined as follows:

$$\text{Fitness}(x_j) = e(x_j) \quad (8)$$

4) Step 4: Ranking of Fitness Functions

Sort (rank) all fitness function values in ascending order as given in (9):

$$f(x_1) < f(x_2) < \dots < f(N) \quad (9)$$

where $f(x_j)$ is the fitness of the j^{th} particle and x_1 is a Global Best (G_{Best}) particle having the best (minimum) fitness among all particles. Consider the top best 20%-30% of the particles as elite particles.

5) Step 5: Updating Mean and Standard Deviation of the Elite Particles

The mean ($m_{i\mu}^{(iter+1)}$) of the selected elite particles is found by:

$$m_{i\mu}^{(iter+1)} = \frac{1}{\mu_e} \sum_{j=1}^{\mu_e} x_{j:N}^{(iter+1)} \quad (10)$$

where $x_{j:N}^{(iter+1)}$ is the j^{th} best particle among the whole population at $iter+1$ iteration. The index $j:N$ denotes the index of the j^{th} rank particle. Standard deviation ($\sigma_{i\mu}^{(iter+1)}$) (step-length) of elite particles is found by (11):

$$\sigma_{i\mu}^{(iter+1)} = \sqrt{\frac{1}{\mu_e - 1} \sum_{j=1}^{\mu_e} (x_{j:N}^{(iter+1)} - m_{i\mu}^{(iter+1)})^2} \quad (11)$$

6) Step 6: Apply Smoothing of Mean and Standard Deviation of the Whole Population

As elite particles are in the vicinity of optimal solutions, more smoothing (weightage) is applied to their mean value as compared to mean of whole population as per (12):

$$m_e^{(iter+1)} = \alpha m_{i\mu}^{(iter+1)} + (1 - \alpha) m_e^{(iter+1)} \quad (12)$$

where $\alpha = 0.9, \beta = 0.1$ are the smoothing parameters.

Similarly, the standard deviation of the elite particles should be updated to a very small extent as they lie near the optimal solutions. So, less smoothing is applied to them as compared to the standard deviation of all particles which requires more exploration of the search space and thus more smoothing as given in (13):

$$\sigma^{(iter+1)} = \beta \sigma_{i\mu}^{(iter+1)} + (1 - \beta) \sigma_{tu}^{(iter+1)} \quad (13)$$

7) Step 7: Apply Levy Flight for Global Exploration

Levy flight [18-19] is a random walk whose length is derived from the Levy distribution as described in (14), where u and v are obtained from the normal distribution. Many species (e.g. swordfish and silky sharks) use Levy flights to search for food. The function of Levy step is to efficiently explore the search space by taking a large step size during the intermediate iterations to obtain the global optimum solution.

$$\text{Levy-step} = \frac{u}{|v|^{1/\beta}} \quad (14)$$

where:

$$u = \text{rand}(0,1) * \text{Sigma} \quad (15)$$

$$v = \text{rand}(0,1) \quad (16)$$

$$\text{Sigma} = \left\{ \frac{\Gamma(1 + \beta) * \sin(\Pi * \beta)}{\Gamma[(1 + \beta) / 2] * \beta * 2^{(\beta-3)}} \right\}^{1/\beta} \quad (17)$$

where $\beta (=3/2)$ is a Levy coefficient and:

$$m_e^{(iter+1)} = m_e^{(iter)} + Levy - step \quad (18)$$

8) Step 8: Increment of Iteration Count

Set $iter := iter + 1$ and go to Step 2 until the maximum number of iterations is reached.

The detail flowchart of the LE-CE method to train FNNs is shown in Figure 1.

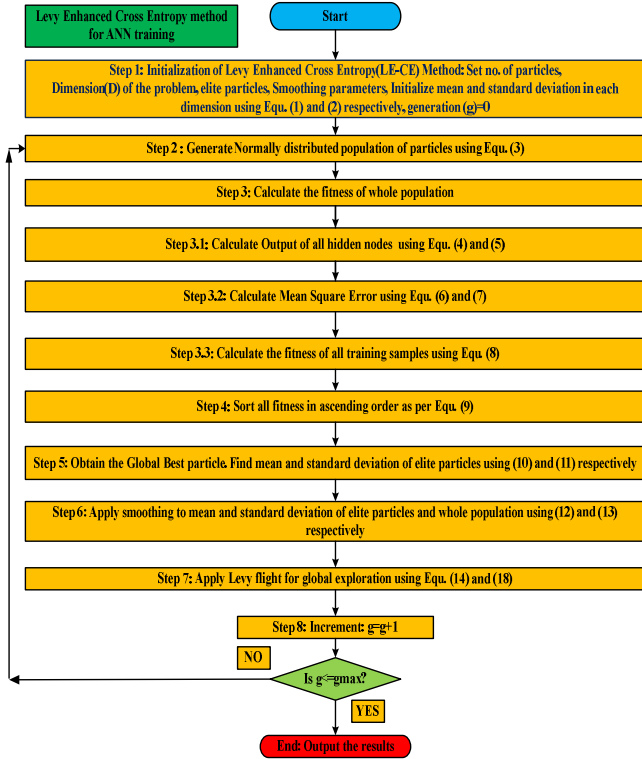


Fig. 1. Flowchart of the LE-CE method for training FNNs.

III. ANN ENCODING STRATEGY

Figure 2 shows the typical structure of an ANN. It consists of 2 input nodes, 3 hidden nodes, and 1 output node. For the training of ANN, the most popular matrix encoding method is used in this paper as follows:

$$particle(:, i) = [w_1, B_1, w_2^T, B_2] \quad (20)$$

$$w_1 = \begin{bmatrix} w_{13} & w_{23} \\ w_{14} & w_{24} \\ w_{15} & w_{25} \end{bmatrix}, B_1 = \begin{bmatrix} \theta_1 \\ \theta_2 \\ \theta_3 \end{bmatrix}, w_2^T = \begin{bmatrix} w_{36} \\ w_{46} \\ w_{56} \end{bmatrix}, B_2 = [\theta_4] \quad (21)$$

where w_1 is the weight matrix of the hidden layer, B_1 is the bias matrix of the hidden layer, w_2 is the weight matrix of the output layer, w_2^T is the transpose of the w_2 matrix, and B_2 is the bias matrix of the hidden layer.

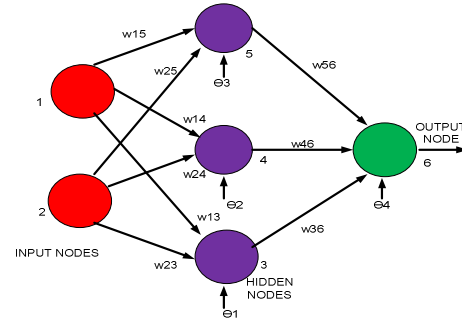


Fig. 2. ANN typical structure.

IV. SIMULATION RESULTS AND DISCUSSION

The performance of the proposed LE-CE algorithm is not tested on a small system because, as per the no-free lunch theorem [20], the average performance of all the optimization methods remains the same for small test systems which consist of a small number of control variables. So, in order to check the effectiveness of the proposed LE-CE algorithm, it is tested on the practical Iris classification [21] problem and its output results, convergence, and statistical results are compared with WCCI 2018 international award winning EVDEPSO [15] and GECCO 2019 international award winning HL_PS_VNSO [16] computational intelligence methods. Both these methods had secured 2nd ranks in the aforementioned conference competitions.

EVDEPSO (Enhanced Velocity Differential Evolution Particle Swarm Optimization), is a meta-heuristic iterative method which has been inspired from the behavior of bird flocking and fish schooling. Mathematically, each bird represents the prospective solution of the optimization problem and its position is adjusted depending upon the position of the best bird and their past best positions in every iteration to obtain optimal solutions. The process is continued until no significant improvement in the optimal solutions is observed. The detail theory of EVDEPSO is available in [15]. HL_PS_VNSO (Hybrid Levy Particle Swarm Variable Neighbourhood Search Optimization) algorithm is a hybridization of PSO and variable neighborhood search algorithm. Its key elements are Perception, Cooperation, and the Levy step. It consists of a Perception term for the local exploitation of search space in which a particle follows its personal best position, a Cooperation term in which the particle follows the global best particle with mutated weights, and the Levy step to globally explore the search space. Its detail theory is given in [16].

A. Practical Iris Classification Problem

The Iris classification problem was used in [21]. The Iris dataset contains 4 features (length and width of sepals and petals) of 3 species of Iris (Iris setosa, Iris virginica, and Iris versicolor) as shown in [22, 23]. The data contains 150 samples. These measures were used initially to create a linear model to classify the species in machine learning. Different hidden nodes such as $H=4, 5, 6, 7, 8, 9, 10, 11, 12, 13, 14$, and 15 were set to test the performance of the algorithms. The simulation results have been performed on Matlab 2017a

environment, Intel CORE i5 with 16 GB RAM. All tested methods find the optimal combinations of the weights and biases which results into minimum error of the FNN. A total of 20 trials were executed as the LE-CE is a meta-heuristic method and as a result in every simulation run it yields different optimal solutions. Finally, the mean recognition rate was obtained from the results of the 20 trials. Table I shows that the proposed LE-CE outperforms the other methods in recognizing the output correctly with different hidden nodes in all cases, due to fact that LE-CE method's mean and standard deviation updating using smoothing parameters yield better solutions as the elite particles are in the vicinity of the optimal solution (as per (12) and (13)). Also, CE is powered by Levy flight, which has the ability to take larger step size during optimization. As a result, the search space is being explored more efficiently. So, LE-CE yields better solutions as compared to original CE method and other tested algorithms.

TABLE I. MEAN RECOGNITION RATE WITH DIFFERENT HIDDEN NODES

Hidden nodes (H)	LE-CE (%)	CE (%)	EVDEPSO (%)	HL_PS_VNSO (%)
4	99.92	98.32	90.12	89.14
5	100	97.25	91.18	87.17
6	99.45	95.36	92.78	89.35
7	100	96.65	90.07	90.14
8	99.32	93.45	91.95	87.88
9	100	92.32	90.45	83.41
10	99.12	93.85	88.35	87.12
11	99.85	92.65	91.98	83.45
12	100	96.36	89.45	76.3
13	99.85	94.36	90.42	86.32
14	100	93.95	88.01	83.25
15	99.36	94.15	91.05	87.05

It is cleared from Table II that the proposed LE-CE outperforms the other methods in all 12 cases for average MSE, std. dev MSE, and best MSE. Hidden nodes are increased from 4 to 15 in each case. As a result, the complexity of the ANN increases as more mathematical equations have to be solved by the algorithm. Also, the convergence characteristics of LE-CE for different hidden nodes are better than the compared algorithms' as shown in Figures 3-5, because, unlike other meta-heuristic methods, the LE-CE method is a tuning free algorithm and its adaptive mean and standard deviation updating strategy makes it quite suitable to obtain optimal solutions. Traditional CE has not a Levy flight step, so its performance remains inferior to LE-CE. EVDEPSO's and HLPVSNSO's performance is worse than LE-CE's because both these methods have a large number of parameters to be tuned which affects convergence, whereas LE-CE has a very small number of parameters to be tuned and it searches solutions by updating the mean and standard deviation of elite particles. As a result, it can achieve better solutions as compared to the other tested algorithms.

Figures 3-5 clearly show that the LE-CE has better convergence characteristics as compared to the other methods for the set termination criteria. The other methods have many step length updating operators, which increase the computational burden on the algorithm.

TABLE II. AVERAGE, STANDARD DEVIATION, AND BEST MSE IN 20 INDEPENDENT RUNS WITH DIFFERENT HIDDEN NODES

Hidden nodes (H)	Algorithm	Average MSE	Std dev MSE	Best MSE
4	LE-CE	1.9021e-02	1.1905e-03	1.3538e-02
	CE	2.1926e-02	2.0907e-03	1.4538e-02
	EVDEPSO	2.7048e-02	2.0825e-02	7.0291e-03
	HL_PS_VN SO	4.1936e-02	1.0413e-02	4.0013e-02
5	LE-CE	1.8127e-02	1.6252e-03	1.3085e-02
	CE	1.9457e-02	1.7267e-03	1.6525e-02
	EVDEPSO	2.4756e-02	1.7638e-02	1.3629e-02
	HL_PS_VN SO	4.4355e-02	1.1071e-02	4.0770e-02
6	LE-CE	1.3593e-02	2.2182e-03	1.2013e-02
	CE	1.6932e-02	2.0082e-03	1.5113e-02
	EVDEPSO	1.8453e-02	7.2653e-03	1.6253e-02
	HL_PS_VN SO	1.0441e-01	1.0374e-01	4.4510e-02
7	LE-CE	1.3682e-02	1.2446e-03	1.2128e-02
	CE	2.6122e-02	1.0746e-03	2.4358e-02
	EVDEPSO	1.7691e-02	4.0023e-03	1.4523e-02
	HL_PS_VN SO	5.5226e-02	6.6222e-03	5.0238e-02
8	LE-CE	1.7042e-02	3.2045e-03	1.2511e-02
	CE	1.8142e-02	6.2545e-03	1.3011e-02
	EVDEPSO	2.1454e-02	6.0198e-03	2.0378e-02
	HL_PS_VN SO	4.7541e-02	7.2863e-03	3.8607e-02
9	LE-CE	1.3294e-02	3.2993e-03	1.0070e-02
	CE	1.6302e-02	6.5093e-03	1.0670e-02
	EVDEPSO	5.0615e-02	1.2549e-02	5.0301e-02
	HL_PS_VN SO	3.8314e-02	1.3757e-02	3.0293e-02
10	LE-CE	1.2521e-02	1.0021e-03	1.1021e-02
	CE	1.8221e-02	1.1821e-03	1.4321e-02
	EVDEPSO	3.9265e-02	1.3342e-02	3.0427e-02
	HL_PS_VN SO	4.4245e-02	1.3204e-02	4.3230e-02
11	LE-CE	1.2646e-02	1.8009e-03	1.0840e-02
	CE	1.5246e-02	2.1709e-03	1.0880e-02
	EVDEPSO	1.4203e-02	1.2120e-02	1.0393e-03
	HL_PS_VN SO	4.1536e-02	6.7323e-03	3.7538e-02
12	LE-CE	1.2006e-02	2.2091e-03	1.0049e-02
	CE	1.6806e-02	2.9391e-03	1.3849e-02
	EVDEPSO	1.7889e-02	6.9515e-03	1.3409e-02
	HL_PS_VN SO	1.2098e-01	1.3702e-01	1.0316e-02
13	LE-CE	1.1753e-02	1.3090e-03	1.0021e-02
	CE	2.3453e-02	1.8740e-03	2.2422e-02
	EVDEPSO	1.8013e-02	5.0128e-03	1.5113e-02
	HL_PS_VN SO	3.1724e-01	1.3744e-01	3.0250e-02
14	LE-CE	1.1270e-02	1.0086e-03	1.0592e-02
	CE	2.6250e-02	1.0186e-03	2.3592e-02
	EVDEPSO	1.5241e-02	1.0171e-03	1.1297e-02
	HL_PS_VN SO	4.3257e-02	1.0214e-02	4.1200e-02
15	LE-CE	1.2189e-02	1.3530e-03	1.1509e-02
	CE	3.3589e-02	2.7530e-03	3.1725e-02
	EVDEPSO	2.145e-02	2.5846e-03	2.1153e-02
	HL_PS_VN SO	5.3539e-02	6.2441e-02	5.2546e-02

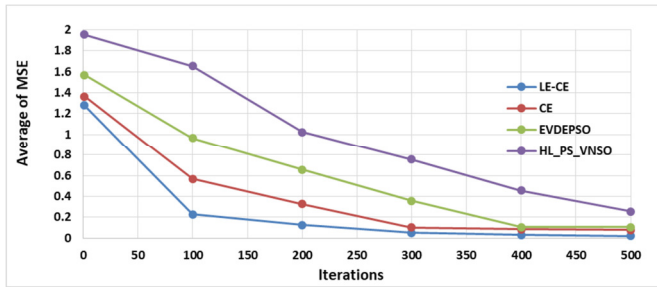


Fig. 3. Convergence curve with 5 hidden nodes.

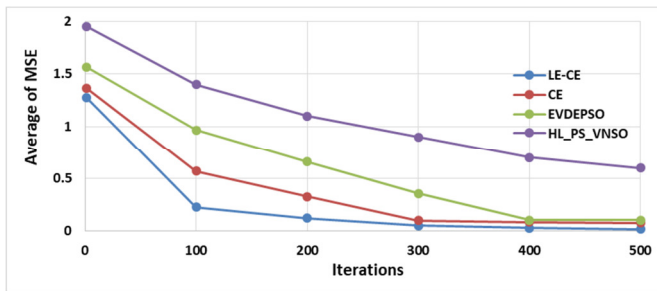


Fig. 4. Convergence curve with 11 hidden nodes.

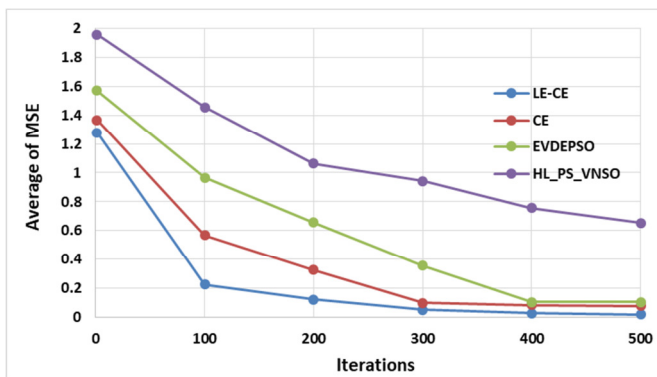


Fig. 5. Convergence curve with 15 hidden nodes.

V. STATISTICAL ANALYSIS

A. One-Way ANOVA Statistical Test

The ANOVA statistical test [24] is used to verify whether the MSE of all algorithms evaluated for each simulation run shows any significant difference. In this test, the degree of significance is set to 0.05 to check the statistical difference between the tested algorithms. During the comparison, if it is found that the P-value is less than 0.05, then it is inferred that all tested algorithms are substantially different from one another. From Table III, it is seen that the F-ratio value is 6.75541. The P-value is 0.000758. So, the result is significant at $p < 0.05$. This implies that at least one of the means of the groups is significantly different from the others. However, it is not known which group(s) contribute to this difference, hence Tukey's Honestly Significant Difference (HSD) test was carried out.

B. Tukey's Honestly Significant Difference Test

To further check the statistical difference between two algorithms, the pairwise comparison test entitled Tukey's HSD

test [25] was carried out. In this test, the first step is to find the critical value (Q_{crit}) from the studentized range distribution table [26] based on the $a=4$ treatments (algorithms) and $DF=44$ Degrees of Freedom. The critical value obtained from the studentized range distribution table is 3.777. Then, the Q_{ij} is calculated as per (22) for all the pairwise comparisons with the proposed algorithm. The result values are given in Table IV.

$$Q_{i,j} = \frac{|\bar{y}_i - \bar{y}_j|}{\sqrt{\frac{(MS)}{N_{Runs}}}} \quad (22)$$

where $i, j = 1, \dots, a, i \neq j$. is the difference between the optimal fitness values of the compared pair of algorithms.

TABLE III. RESULTS OF THE ONE-WAY ANOVA STATISTICAL TEST

Variation	Sum of square due to source (SS)	DF	Mean sum of square due to source (MS)	F ratio value	P-value	F crit
Between algorithms	0.03278	3	0.0109	6.7554	0.00075	2.816
Within algorithms	0.07117	44	0.0016			
Total	0.10395	47				

TABLE IV. TUKEY HSD TEST RESULTS

Pairwise comparisons	Q (Statistic)
LE-CE and CE	0.61
LE-CE and EVDEPSO	0.85
LE-CE and HL_PS_VNSO	5.64

Table IV reveals that for all pairwise treatments, the proposed algorithm is substantially statistically different from the other algorithms.

The algorithm has been developed in Matlab environment and the source codes can be provided to the enthusiastic learner by the main author upon request.

VI. CONCLUSION

The Levy Enhanced Cross Entropy method to train feedforward neural network has been proposed in this paper. The LE-CE method has less parameters to be tuned and its adaptive updating for mean and standard deviation of the solutions make it quite powerful in terms of local exploitation and global exploration of the solution space. To further improve its global search exploration, the CE method is powered by the Levy flight. The simulation on the practical Iris test system reveals that the proposed LE-CE method outperforms the contemporary optimization methods in terms of solution quality, iterations, average MSE, standard deviation MSE, and best MSE. The proposed method is confirmed to be statistically different from the other compared optimization methods. The proposed method can be used in highly complex nonlinear ANN systems. In the future, the same algorithm will be applied to train more realistic training sets of neural networks with hundreds of variables and constraints.

REFERENCES

- [1] C.-J. Lin, C.-H. Chen, and C.-Y. Lee, "A self-adaptive quantum radial basis function network for classification applications," in *International Joint Conference on Neural Networks (IEEE Cat. No.04CH37541)*, Budapest, Hungary, Jul. 2004, vol. 4, pp. 3263–3268, <https://doi.org/10.1109/IJCNN.2004.1381202>.
- [2] S. Mirjalili, S. Z. Mohd Hashim, and H. Moradian Sardroudi, "Training feedforward neural networks using hybrid particle swarm optimization and gravitational search algorithm," *Applied Mathematics and Computation*, vol. 218, no. 22, pp. 11125–11137, Jul. 2012, <https://doi.org/10.1016/j.amc.2012.04.069>.
- [3] K. Hornik, M. Stinchcombe, and H. White, "Multilayer feedforward networks are universal approximators," *Neural Networks*, vol. 2, no. 5, pp. 359–366, Jan. 1989, [https://doi.org/10.1016/0893-6080\(89\)90020-8](https://doi.org/10.1016/0893-6080(89)90020-8).
- [4] J.-R. Zhang, J. Zhang, T.-M. Lok, and M. R. Lyu, "A hybrid particle swarm optimization-back-propagation algorithm for feedforward neural network training," *Applied Mathematics and Computation*, vol. 185, no. 2, pp. 1026–1037, Feb. 2007, <https://doi.org/10.1016/j.amc.2006.07.025>.
- [5] M. Gori and A. Tesi, "On the Problem of Local Minima in Backpropagation," *IEEE Transactions on Pattern Analysis and Machine Intelligence*, vol. 14, no. 1, pp. 76–86, Jan. 1992, <https://doi.org/10.1109/34.107014>.
- [6] L. V. Kantorovich, "Functional analysis and applied mathematics," *Uspekhi Matematicheskikh Nauk*, vol. 3, no. 6, pp. 89–185, 1948.
- [7] E. A. Ogbonnaya, E. M. Adigio, H. U. Ugwu, and M. C. Anumiri, "Advanced Gas turbine rotor shaft fault diagnosis using artificial neural network," *International Journal of Engineering and Technology Innovation*, vol. 3, no. 1, pp. 58–69, 2013.
- [8] R. Kaluri and P. Reddy CH, "Optimized feature extraction for precise sign gesture recognition using self-improved genetic algorithm," *International Journal of Engineering and Technology Innovation*, vol. 8, no. 1, pp. 25–37, 2018.
- [9] M. Njah and R. E. Hamdi, "A Constrained Multi-Objective Learning Algorithm for Feed-Forward Neural Network Classifiers," *Engineering, Technology & Applied Science Research*, vol. 7, no. 3, pp. 1685–1693, Jun. 2017, <https://doi.org/10.48084/etasr.968>.
- [10] D. N. Truong and V. T. Bui, "Hybrid PSO-Optimized ANFIS-Based Model to Improve Dynamic Voltage Stability," *Engineering, Technology & Applied Science Research*, vol. 9, no. 4, pp. 4384–4388, Aug. 2019, <https://doi.org/10.48084/etasr.2833>.
- [11] L. T. H. Nhung, T. T. Phung, H. M. V. Nguyen, T. N. Le, T. A. Nguyen, and T. D. Vo, "Load Shedding in Microgrids with Dual Neural Networks and AHP Algorithm," *Engineering, Technology & Applied Science Research*, vol. 12, no. 1, pp. 8090–8095, Feb. 2022, <https://doi.org/10.48084/etasr.4652>.
- [12] E. Rashedi, H. Nezamabadi-pour, and S. Saryazdi, "GSA: A Gravitational Search Algorithm," *Information Sciences*, vol. 179, no. 13, pp. 2232–2248, Jun. 2009, <https://doi.org/10.1016/j.ins.2009.03.004>.
- [13] R. Storn and K. Price, "Differential Evolution – A Simple and Efficient Heuristic for global Optimization over Continuous Spaces," *Journal of Global Optimization*, vol. 11, no. 4, pp. 341–359, Dec. 1997, <https://doi.org/10.1023/A:1008202821328>.
- [14] J. Kennedy and R. Eberhart, "Particle swarm optimization," in *International Conference on Neural Networks*, Perth, WA, Australia, Dec. 1995, vol. 4, pp. 1942–1948, <https://doi.org/10.1109/ICNN.1995.488968>.
- [15] D. Dabhi and K. Pandya, "Enhanced Velocity Differential Evolutionary Particle Swarm Optimization for Optimal Scheduling of a Distributed Energy Resources With Uncertain Scenarios," *IEEE Access*, vol. 8, pp. 27001–27017, 2020, <https://doi.org/10.1109/ACCESS.2020.2970236>.
- [16] D. Dabhi and K. Pandya, "Uncertain Scenario Based MicroGrid Optimization via Hybrid Levy Particle Swarm Variable Neighborhood Search Optimization (HL_PS_VNSO)," *IEEE Access*, vol. 8, pp. 108782–108797, 2020, <https://doi.org/10.1109/ACCESS.2020.2999935>.
- [17] R. Y. Rubinstein, "Optimization of computer simulation models with rare events," *European Journal of Operational Research*, vol. 99, no. 1, pp. 89–112, May 1997, [https://doi.org/10.1016/S0377-2217\(96\)00385-2](https://doi.org/10.1016/S0377-2217(96)00385-2).
- [18] C. T. Brown, L. S. Liebovitch, and R. Glendon, "Levy Flights in Dobe Ju/'hoansi Foraging Patterns," *Human Ecology*, vol. 35, no. 1, pp. 129–138, Feb. 2007, <https://doi.org/10.1007/s10745-006-9083-4>.
- [19] X. S. Yang, "Random Walks and Levy Flights," in *Nature-Inspired Metaheuristic Algorithms*, 2nd ed., Cambridge, UK: Luniver Press, 2010, pp. 11–19.
- [20] D. H. Wolpert and W. G. Macready, "No free lunch theorems for optimization," *IEEE Transactions on Evolutionary Computation*, vol. 1, no. 1, pp. 67–82, Apr. 1997, <https://doi.org/10.1109/4235.585893>.
- [21] R. A. Fisher, "The Use of Multiple Measurements in Taxonomic Problems," *Annals of Eugenics*, vol. 7, no. 2, pp. 179–188, 1936, <https://doi.org/10.1111/j.1469-1809.1936.tb02137.x>.
- [22] "The Iris Dataset," *Gist*. <https://gist.github.com/curran/a08a1080b88344b0c8a7>.
- [23] K. Thirunavukkarasu, A. S. Singh, P. Rai, and S. Gupta, "Classification of IRIS Dataset using Classification Based KNN Algorithm in Supervised Learning," in *4th International Conference on Computing Communication and Automation*, Greater Noida, India, Dec. 2018, pp. 1–4, <https://doi.org/10.1109/CCAA.2018.8777643>.
- [24] E. Ostertagova and O. Ostertag, "Methodology and Application of Oneway ANOVA," *American Journal of Mechanical Engineering*, vol. 1, no. 7, pp. 256–261, Jan. 2013, <https://doi.org/10.12691/ajme-1-7-21>.
- [25] H. Abdi and L. J. Williams, "Tukey's Honestly Significant Difference (HSD) Test," in *Encyclopedia of Research Design*, Thousand Oaks, CA, USA: SAGE, 2010.
- [26] H. L. Harter, "Critical Values for Duncan's New Multiple Range Test," *Biometrics*, vol. 16, no. 4, pp. 671–685, 1960, <https://doi.org/10.2307/2527770>.

Investigating the Deflection and Strain of Reinforced Green Concrete Beams Made with Partial Replacement of RCA under Sustained Loading

Abdul Hafeez Buller

Department of Civil Engineering
Faculty of Engineering
International Islamic University
Malaysia, Selangor, Malaysia
ah.buller@quest.edu.pk

Nadiah Md. Husain

Department of Civil Engineering
Faculty of Engineering
International Islamic University
Malaysia, Selangor, Malaysia
drnadiah@iium.edu.my

Mehboob Oad

Department of Civil Engineering,
Quaid-e-Awam University of
Engineering, Science and
Technology, Nawabshah, Pakistan
engrmahbooboad04@gmail.com

Bashir Ahmed Memon

Department of Civil Engineering
Quaid-e-Awam University of Engineering, Science and
Technology
Nawabshah, Pakistan
bashir_m@hotmail.com

Irum Naz Sodhar

Department of Computer Science
Faculty of Information and Communication Technology
International Islamic University Malaysia
Selangor, Malaysia
iram10akber@gmail.com

Received: 30 June 2022 | Revised: 12 July 2022 | Accepted: 1 August 2022

Abstract-Artificial intelligence (AI) and statistical methods are used in various fields and have played a vital role in investigating the deflection and strain of reinforced green concrete beams made with partial replacement of recycled concrete aggregates under sustained loading. The methods used to assess structural contributors are time-saving and cost-effective compared to experimental evaluation. This study investigated the numerical modeling of reinforced concrete beams produced by replacing 50% of coarse natural aggregates with demolished vintage concrete under sustained loading. Multivariate regression analysis was used to determine the mathematical equations for long-term deflection and stress from experimental data of 6, 9, and 12 months of loading. Three software suites were used for the regression analysis, namely NCSS, Matlab, and Microsoft Excel. Six beams were cast using demolished concrete as 50% of coarse aggregates to test and validate the regression equations, where three of them were examined for two months of sustained loading and the other three for three months. The regression results were in accordance with the experimental observations with a maximum error of 10.34%. Therefore, the provided regression equations for deflection and pressure could be used to estimate the parameters of reinforced concrete beams.

Keywords-Artificial Intelligence (AI); green concrete; long-term loading; numerical modeling; recycled concrete aggregates; sustained loading

I. INTRODUCTION

Many structural engineering challenges remain outstanding although the sector grows its interest in technological solutions [1]. Most of these problems are hard optimization problems [2],

making them relatively difficult to resolve, as an increase in the dimensionality of a problem increases its complexity [3]. Conventional optimization strategies cannot tackle complicated issues for numerous reasons, especially in the case of the referred curse of dimensionality. Furthermore, investigating the use of gradient-primarily based strategies for engineering problems with neighborhood solutions is time-consuming, as these methods depend on the region of the initial issue [4]. All these drawbacks made researchers to extend machine learning methods consisting of metaheuristic or hybrid methods [5] to resolve engineering problems. Estimation of concrete properties, particularly green concrete, before and after hardening is a key effort to ensure its quality [6]. Green concrete is preferred as it is environmentally friendly and preserves the natural constituents of conventional concrete, but it requires extensive research to determine its behavior under different conditions. On the other hand, the experimental assessment of required parameters is not only time-consuming, but also requires much care, labor, and cost. Moreover, any inaccuracy in an experimental setup or procedure requires repetition and modification. Therefore, an alternative tool is required to avoid these problems. The best option is numerical analysis, carried out by mathematical modeling of the required parameters based on experimental data. Regression analysis is the most widely used method for this purpose [7].

Many concrete manufacturing methods have been proposed using domestically available substances or waste [8]. The use of demolished concrete as coarse aggregates in new concrete could reduce the environmental impact due to the transport of natural coarse aggregates and the waste dumping in landfills. In

Corresponding author: Abdul Hafeez Buller

addition, it could help reduce waste control issues and the overall cost of the structure. Various proportions of recyclable aggregates from demolished concrete [9, 10] or plastics [11] have been investigated in concrete mixtures, examining their compressive and tensile strength. In [12], a relationship between the cylindrical and cubic compressive strength of concrete using recycled concrete as coarse aggregate was presented, using regression analysis of the experimental observations of 400 samples. Regression analysis is a process of predicting the deviation in the dependent variables for the deviation of the independent variables. This process is effectively used in civil engineering to determine mathematical equations for different properties based on experimental observations. In [13], a regression model was presented considering the variable workability of recycled aggregate concrete. In [14], regression analysis was used to model concrete delivery and placement, while in [15] the cost estimation of a project was studied using the same method.

Traditional strategies for modeling and optimizing complicated structures require huge amounts of computing resources. AI-based methods can provide valuable alternatives to efficiently solve issues in civil engineering [16], while many studies examined concrete's strength using numerical modeling. In [17], the age and curing period of concrete were used to predict its strength, finding correlation coefficients equal to 0.995 and 0.994 for 7 and 28 days of curing and demonstrating the validity of the model. In [18], a combination of multivariate regression analysis and neural networks was investigated to study the strength of concrete with mineral admixtures. The concrete samples, using fly ash and a blast furnace, were cast and cured from 3 to 180 days, followed by nondestructive testing. Laboratory results were used as data for numerical modeling, and the neural network showed better performance. However, the combination of both methods was more suitable for non-linear relationships of the parameters. Numerical modeling of the relationships between the properties of demolished concrete, recycled aggregates, and recycled concrete aggregate and the flexural behavior of amorphous concrete are some other examples of regression analysis studies [19-23]. Numerical modeling of several aspects of normal and recycled aggregate concrete under short-term loading has been investigated in several studies. However, very few studies are available on the numerical modeling of concrete behavior when using green concrete produced by demolished concrete as coarse aggregates. This study presents a regression analysis of the deflection and strain of reinforced green concrete beams under sustained long-term loads (6, 9, and 12 months) [24-26]. NCSS [27], Matlab 2016 [28], and Microsoft Excel 2016 were used to perform regression analysis, and their results were compared. To validate the results, 6 RC green concrete beams were cast and tested. A comparison of the test with the predicted results showed very good agreement between the two sets.

II. METHOD AND ANALYSIS

Regression analysis is a statistical method to estimate a relationship between two or more variables and can be used to predict future values from available datasets. The method mainly depends on a dependent or target variable and

independent or predictor variables. This process requires the declaration of dependent and independent variables, and then it fits the data for regression and gives the coefficients of a mathematical equation along with the statistical analysis of the data. This study used a dataset from experimental investigations of long-term deflection and strain under sustained load for 6, 9, and 12 months [24-26]. These studies used reinforced concrete beams cast using 50% replacement of natural coarse aggregates with demolished concrete. The beams were tested in frames with a constant central point load maintained with the help of screw jacks and load cells. The central point deflection was monitored and recorded on daily basis. The strain was measured at 11 locations along the central line (depth) of the beam, and then all these values were averaged. Six beams were used for each loading duration, three made from all-natural coarse aggregates (NAB) and three with an equal dosage of natural and recyclable aggregates (RAB). Figure 1 shows the plot of deflection in mm of all beams versus time in days and the proportion of recyclable aggregates (%). Similarly, Figure 2 shows the average recorded strain in all beams. Both figures show the results of beams cast with all-natural and recyclable aggregates on the same axis.

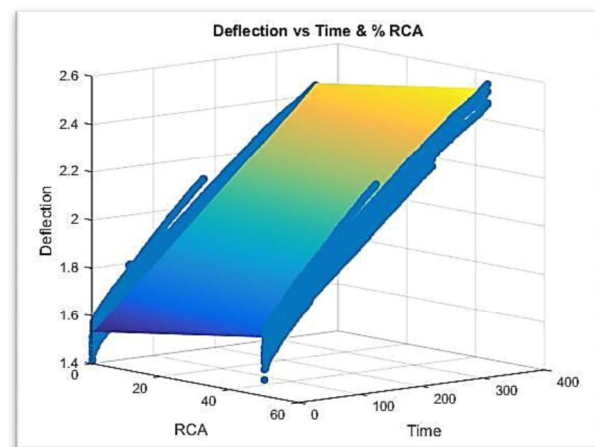


Fig. 1. Deflection in all beams.

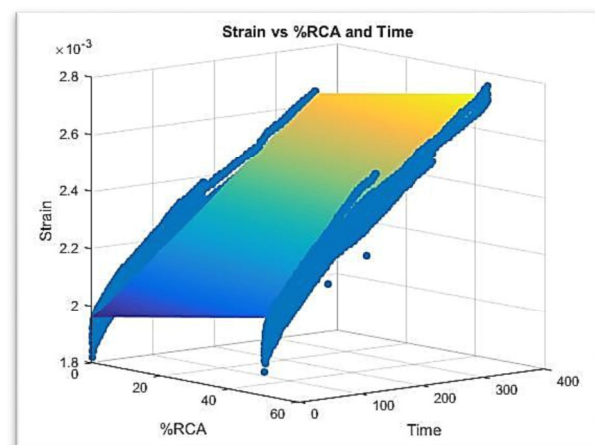


Fig. 2. Strain in all beams.

At first, a regression equation was produced for deflection, considering the proportion of recyclable aggregates (0 or 50) and time as independent variables. Initially, the load was also considered as an independent variable, but as it was the same throughout the sustained load duration, it had no impact and was removed from the list of variables. Similarly, a regression equation was investigated for strain. In this process, the strain was considered as the dependent variable while all the other parameters were kept constant. Although several software suites are available for regression analysis, this study used NCSS, Matlab, and Microsoft Excel. NCSS and Matlab have been widely used for statistical analysis. The coefficients of the regression equation for the deflection and the strain, generated by NCSS, along with standard error are given in Tables I and II.

TABLE I. COEFFICIENTS AND STANDARD ERROR FOR DEFLECTION USING NCSS

Independent variable	Regression coefficient	Standard error	Lower 95% conf. limit	Upper 95% conf. limit
Intercept	1.519958	0.0067	1.5067	1.5331
Time	0.017779	0.0002	0.0173	0.0182
RCA%	0.002341	0.0001	0.0021	0.0025

TABLE II. COEFFICIENTS AND STANDARD ERROR FOR STRAIN USING NCSS

Independent Variable	Regression Coefficient	Standard Error	Lower 95% Conf. Limit	Upper 95% Conf. Limit
Intercept	0.001953044	3.42×10^{-6}	0.00195	0.00195
Time	1.336448×10^{-5}	1.20×10^{-7}	1.31×10^{-7}	1.35×10^{-5}
RCA%	2.200535×10^{-6}	6.56×10^{-8}	6.56×10^{-8}	2.33×10^{-6}

Regression analysis on experimental observations for deflection and strain in Matlab produced the coefficients of regression equations given in Table III. Finally, regression analysis was conducted in Microsoft Excel, and the coefficients obtained for deflection and strain are shown in Tables IV and V.

TABLE III. COEFFICIENTS FOR DEFLECTION AND STRAIN USING MATLAB

Independent variable	Regression coefficient	
	Deflection	Strain
Intercept	1.5309459	0.0019583
Time	0.0025159	1.8728203×10^{-6}
RCA%	0.0022354	2.1973138×10^{-6}

TABLE IV. MS EXCEL REGRESSION RESULTS FOR DEFLECTION

Description	Regression coefficient	Standard error	P-value	Lower 95%	Upper 95%
Intercept	1.531000785	0.001403289	0	1.528249712	1.533751858
Time	0.002515843	7.07153×10^{-6}	0	0.00250198	0.002529707
RCA %	0.002234576	2.66382×10^{-5}	0	0.002182353	0.002286799

TABLE V. MS EXCEL REGRESSION RESULTS FOR STRAIN

Description	Regression coefficient	Standard error	P-value	Lower 95%	Upper 95%
Intercept	0.001958191	1.23844×10^{-6}	0	0.001955763	0.001960619
Time	1.87426×10^{-6}	6.24082×10^{-9}	0	1.86202×10^{-6}	1.88649×10^{-6}
RCA %	2.19487×10^{-6}	2.3509×10^{-8}	0	2.14878×10^{-6}	2.24096×10^{-6}

The regression coefficients obtained from NCSS were used to write the regression equations for deflection and strain in (1) and (2), respectively:

$$\delta = 1.530946 + 0.0022354 \times RCA + 0.0025159 \times T \quad (1)$$

$$\varepsilon = 0.0019583 + 2.19731379 \times 10^{-6} \times RCA + 1.8728203 \times 10^{-6} \times T \quad (2)$$

where δ represents deflection, ε denotes strain, RCA is used for proportions of recyclable aggregates (0 for 0%, 50 for 50%, etc), and T is time in days. Similarly, the coefficients given in Table III, obtained from regression analysis in Matlab, were used in (3) and (4):

$$\delta = 1.5309459 + 0.0022354 \times RCA + 0.0025159 \times T \quad (3)$$

$$\varepsilon = 0.0019583 + 2.1973138 \times 10^{-6} \times RCA + 1.8728203 \times 10^{-6} \times T \quad (4)$$

Similarly, the regression coefficients given in Tables IV and VI obtained using Microsoft Excel can be used for the respective regression equations for strain and deflection. These equations were used to predict the deflection and strain values. To further validate the performance of the equations, six beams were cast and cured for 28 days. The proportion of recycled aggregates in the beams was 50%. Three beams were tested for 2 months of sustained load, and the other three were tested for 3 months. The load and loading mechanism was maintained the same with the test results used to develop the regression equations. Figure 3 shows the loading system.



Fig. 3. Loading system.

III. RESULTS AND DISCUSSION

Several statistical parameters were computed and compared in regression analysis to check the authenticity of the process. The R-square value is one among them and is presented along with the standard error in Table VI. The R-square values obtained from the regression analysis by NCSS are equal to 0.953 and 0.9496 for deflection and strain. This shows that about 95% of deflection and 96% of strain predicted values are around the mean value. The normal probability plots of deflection and strain are shown in Figures 4 and 5. Both figures also verify that the vast majority of data points fall in a close band, indicating a good agreement of predicted and test values.

A similar observation was made for the R-square value obtained from the Matlab regression analysis. Similarly to the above, Microsoft Excel R-square values were equal to 0.9645 and 0.9525 for deflection and strain. These values also show that about 96% of the data points are close to the mean.

Additionally, the p -value for all variables computed by the software was nearly zero. Both R-square and p values show the validity of the developed regression equations.

TABLE VI. SUMMARY REPORT

Software	NCSS		MATLAB		EXCEL	
Dependent variable	Deflection	Strain	Deflection	Strain	Deflection	Strain
R²	0.9530	0.9496	0.951	0.9642	0.9645	0.9526
Adj R²	0.9527	0.9496	0.951	0.9642	0.9645	0.9526
Standard error	0.0022	8.66×10^{-7}	-	-	0.0467	4.12×10^{-5}

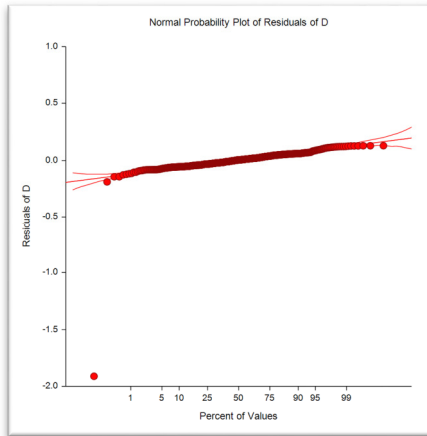


Fig. 4. Normal probability plot of deflection (NCSS).

The three sets of regression coefficients have very minor or ignorable differences, showing the similarity of the capabilities of these suites for the purpose. The regression equations were then used to predict the deflection and stress of the concrete beams and compare them to the experimental results. Table VII shows the error in the computed values. It can be observed that the maximum error in deflection computations is about 12%, whereas in stress is about 10%, proving the validity of the regression equations. The regression analysis cannot only save from the experimental procedures but additionally provides results in little time. To further verify the validity of the equations, six reinforced concrete beams were prepared and tested with the same conditions. Table VIII shows the variables, numerical results, and experimental observations.

TABLE VIII. DATA AND RESULTS FOR TEST BEAMS

#	Variables			Deflection			Strain			
	T	RCA	Lab	NCSS	MATLAB	EXCEL	Lab	NCSS	MATLAB	EXCEL
B1	60	40	1.58	1.7713	1.7713	1.7713	0.00211	0.002159	0.002159	0.002164
B2	60	40	1.59				0.00212			
B3	60	40	1.59				0.00211			
B4	90	40	1.83	1.8468	1.8468	1.8468	0.0022	0.002215	0.002215	0.002219
B5	90	40	1.85				0.0023			
B6	90	40	1.85				0.0023			

IV. CONCLUSION

This study used regression analysis to investigate the numerical modeling of deflection and strain under sustained long-term loads of reinforced green concrete beams, using

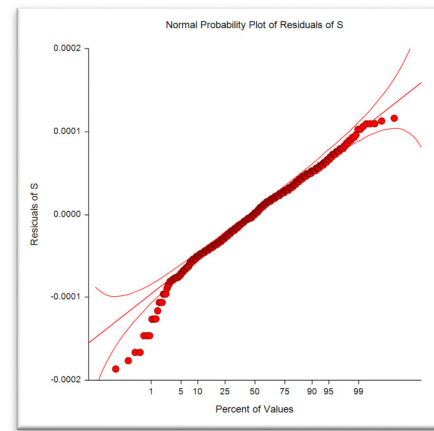


Fig. 5. Normal probability plot of strain (NCSS).

TABLE VII. ERROR % IN PREDICTED VALUES OF DEFLECTION AND STRAIN

Description	Deflection		Strain	
	Maximum (%)	Minimum (%)	Maximum (%)	Minimum (%)
NCSS	12.30248	-6.03898	10.107397	-4.82636
MATLAB	12.348812	-6.09497	10.0916	-4.84347
Excel	12.30491	-6.0357	10.29922	-4.85232

It may be noted that almost the same deflection results were produced by all three equation sets. The same strain value was calculated using the regression equations of NCSS and Matlab, whereas a slightly higher strain value was calculated using the strain equation developed by Excel. The percentage difference with the other two regression models was about 2%, which is negligible. In comparison to the findings with the average values of test results of the beams loaded for 2 months, it was observed that the regression value of deflection was about 11.8% higher than the average test results. The difference in strain for the beams was recorded as equal to 2%. The difference between regression and average test observations of deflection and strain for reinforced concrete beams loaded for 3 months was recorded equal to 1% for both parameters. Therefore, it can be concluded that the regression equations predicted very well the long-term deflection and strain of the reinforced green concrete beams under sustained load, even beyond the data set.

three software suites, namely NCSS, Matlab, and Microsoft Excel. The experimental results of 6, 9, and 12 months of loading were used as input variables to develop regression equations for deflection and strain. It was observed that all software suites used developed almost similar regression

equations. The use of regression equations to predict the parameters showed good agreement between the two sets with a maximum error of 12.34%. Further validation of the regression equations was performed by casting and testing six additional reinforced green concrete beams. The numerical results of these beams were observed to be 12% higher than the experimental results. Therefore, the regression equations may be confidently used to predict the deflection and strain of proposed beams under long-term loading.

REFERENCES

- [1] V. Plevris and G. C. Tsiatas, "Computational Structural Engineering: Past Achievements and Future Challenges," *Frontiers in Built Environment*, vol. 4, Apr. 2018, <https://doi.org/10.3389/fbuil.2018.00021>.
- [2] P. Mohapatra, K. Nath Das, and S. Roy, "A modified competitive swarm optimizer for large scale optimization problems," *Applied Soft Computing*, vol. 59, pp. 340–362, Oct. 2017, <https://doi.org/10.1016/j.asoc.2017.05.060>.
- [3] Y. Sun, T. Yang, and Z. Liu, "A whale optimization algorithm based on quadratic interpolation for high-dimensional global optimization problems," *Applied Soft Computing*, vol. 85, Dec. 2019, Art. no. 105744, <https://doi.org/10.1016/j.asoc.2019.105744>.
- [4] H. Gupta, P. P. Bansal, and R. Sharma, "Development of high performance hybrid fiber reinforced concrete using different fine aggregates," *Advances in concrete construction*, vol. 11, no. 1, pp. 19–32, 2021, <https://doi.org/10.12989/acc.2021.11.1.019>.
- [5] C. C. Ruiz, J. L. Caballero, J. H. Martinez, and W. A. Aperador, "Algorithms to measure carbonation depth in concrete structures sprayed with a phenolphthalein solution," *Advances in concrete construction*, vol. 9, no. 3, pp. 257–265, 2020, <https://doi.org/10.12989/acc.2020.9.3.257>.
- [6] B. A. Memon, M. Oad, A. H. Buller, S. A. Shar, A. S. Buller, and F.-R. Abro, "Effect of Mould Size on Compressive Strength of Green Concrete Cubes," *Civil Engineering Journal*, vol. 5, no. 5, pp. 1181–1188, May 2019, <https://doi.org/10.28991/cej-2019-03091322>.
- [7] A. H. Buller, A. Memon, A. S. Buller, and Irum Naz Sodhar, "Modeling Fire Effect of Reinforced Recycled Aggregate Concrete Beams by Regression Analysis," *International Journal on Emerging Technologies*, vol. 12, no. 1, pp. 97–102, 2021, <https://doi.org/10.13140/RG.2.2.29740.39048>.
- [8] B. B. Mukharjee and S. V. Barai, "Performance assessment of nano-Silica incorporated recycled aggregate concrete," *Advances in concrete construction*, vol. 8, no. 4, pp. 321–333, 2019, <https://doi.org/10.12989/acc.2019.8.4.321>.
- [9] M. Oad and B. A. Memon, "Compressive Strength of Concrete Cylinders using Coarse Aggregates from Old Concrete," in *Abstract Proceedings of 1st National Conference on Civil Engineering (NCCE 2013-14)*, Apr. 2014.
- [10] S. A. Shohana, M. I. Hoque, and M. H. R. Sobuz, "Experimental investigation on hardened properties of recycled coarse aggregate concrete," *Advances in concrete construction*, vol. 10, no. 5, pp. 369–379, 2020, <https://doi.org/10.12989/acc.2020.10.5.369>.
- [11] M. Ashok, P. Jayabalan, V. Saraswathy, and S. Muralidharan, "A study on mechanical properties of concrete including activated recycled plastic waste," *Advances in concrete construction*, vol. 9, no. 2, pp. 207–215, 2020, <https://doi.org/10.12989/acc.2020.9.2.207>.
- [12] A. H. Buller, M. Oad, and B. A. Memon, "Relationship between Cubical and Cylindrical Compressive Strength of Recycled Aggregate Concrete," *IJIRMPs - International Journal of Innovative Research in Engineering & Multidisciplinary Physical Sciences*, vol. 7, no. 2, pp. 14–19, Apr. 2019, <https://doi.org/10.17605/OSF.IO/QKJU6>.
- [13] P. Chopra, R. K. Sharma, and M. Kumar, "Predicting Compressive Strength of Concrete for Varying Workability Using Regression Models," *International Journal of Engineering and Applied Sciences*, vol. 6, no. 4, pp. 10–22, Dec. 2014, <https://doi.org/10.24107/ijeas.251233>.
- [14] P. Dunlop and S. Smith, "Estimating key characteristics of the concrete delivery and placement process using linear regression analysis," *Civil Engineering and Environmental Systems*, vol. 20, no. 4, pp. 273–290, Dec. 2003, <https://doi.org/10.1080/1028660031000091599>.
- [15] G. H. Kim, S. H. An, and K. I. Kang, "Comparison of construction cost estimating models based on regression analysis, neural networks, and case-based reasoning," *Building and Environment*, vol. 39, no. 10, pp. 1235–1242, Oct. 2004, <https://doi.org/10.1016/j.buildenv.2004.02.013>.
- [16] P. Lu, S. Chen, and Y. Zheng, "Artificial Intelligence in Civil Engineering," *Mathematical Problems in Engineering*, vol. 2012, Dec. 2012, Art. no. e145974, <https://doi.org/10.1155/2012/145974>.
- [17] M. F. M. Zain, S. M. Abd, K. Sopian, M. Jamil, and A. I. Che-Ani, "Mathematical regression model for the prediction of concrete strength," in *Proceedings of the 10th WSEAS international conference on Mathematical methods, computational techniques and intelligent systems*, Stevens Point, Wisconsin, USA, Jul. 2008, pp. 396–402.
- [18] U. Atici, "Prediction of the strength of mineral admixture concrete using multivariable regression analysis and an artificial neural network," *Expert Systems with Applications*, vol. 38, no. 8, pp. 9609–9618, Aug. 2011, <https://doi.org/10.1016/j.eswa.2011.01.156>.
- [19] A. H. Buller, M. Oad, and B. A. Memon, "Flexural Strength of Reinforced Concrete RAC Beams Exposed to 6-hour Fire – Part 2: Rich Mix," *Engineering, Technology & Applied Science Research*, vol. 9, no. 1, pp. 3814–3817, Feb. 2019, <https://doi.org/10.48084/etasr.2494>.
- [20] A. H. Buller, B. A. Memon, and M. Oad, "Effect of 12-hour fire on Flexural Behavior of Recyclable Aggregate Reinforced Concrete Beams," *Civil Engineering Journal*, vol. 5, no. 7, pp. 1533–1542, Jul. 2019, <https://doi.org/10.28991/cej-2019-03091350>.
- [21] A. S. Buller, F.-R. Abro, T. Ali, S. H. Jakhriani, A. H. Buller, and Z. Ul-Abdin, "Stimulated autogenous-healing capacity of fiber-reinforced mortar incorporating healing agents for recovery against fracture and mechanical properties," *Materials Science-Poland*, vol. 39, no. 1, pp. 33–48, Mar. 2021, <https://doi.org/10.2478/msp-2021-0009>.
- [22] E. Ekinici, İ. Türkmen, and E. Birhanli, "Mechanical and durability characteristics of GGBS-based self-healing geopolymer mortar produced using by an endospore-forming bacterium," *Journal of Building Engineering*, vol. 57, Oct. 2022, Art. no. 104944, <https://doi.org/10.1016/j.jobbe.2022.104944>.
- [23] A. H. Buller, M. Oad, B. A. Memon, and S. Sohu, "24-hour Fire Produced Effect on Reinforced Recycled Aggregates Concrete Beams," *Engineering, Technology & Applied Science Research*, vol. 9, no. 3, pp. 4213–4217, Jun. 2019, <https://doi.org/10.48084/etasr.2764>.
- [24] M. Oad, A. H. Buller, B. A. Memon, and N. A. Memon, "Impact of Long-Term Loading on Reinforced Concrete Beams Made with Partial Replacement of Coarse Aggregates with Recycled Aggregates from Old Concrete," *Engineering, Technology & Applied Science Research*, vol. 9, no. 1, pp. 3818–3821, Feb. 2019, <https://doi.org/10.48084/etasr.2498>.
- [25] M. Oad, A. H. Buller, B. A. Memon, N. A. Memon, and S. Sohu, "Long Term Impact in Reinforced Recycled Concrete Beams Under 9-Month Loading," *Engineering, Technology & Applied Science Research*, vol. 9, no. 3, pp. 4140–4143, Jun. 2019, <https://doi.org/10.48084/etasr.2697>.
- [26] M. Oad, B. A. Memon, A. H. Buller, and N. A. Memon, "Flexural Behavior of RC Beams Made with Recycled Aggregates Under 12-Month Long Term Loading," *Engineering, Technology & Applied Science Research*, vol. 9, no. 5, pp. 4631–4635, Oct. 2019, <https://doi.org/10.48084/etasr.3013>.
- [27] NCSS, "Statistical Software | Sample Size Software | NCSS." NCSS. Available: <https://www.ncss.com/>.
- [28] Mathworks, "MATLAB - MathWorks." Available: <https://www.mathworks.com/products/matlab.html>.

Multi-Criteria Decision Making in the Milling Process Using the PARIS Method

Hong Ky Le

Vinh Long University of Technology Education
Vinh Long, Vietnam
kylh@vlute.edu.vn

Received: 8 July 2022 | Revised: 25 July 2022 | Accepted: 25 July 2022

Abstract-The Multi-Criteria Decision-Making (MCDM) process of milling SNCM439 steel is presented in this study. In this experimental study, 3 cutting tool parameters, namely the number of pieces, cutting piece material, and tip radius were considered and 3 cutting mode parameters, i.e. cutting speed, feed rate, and depth of cut changed in each experiment. SR and MRR are selected as the output parameters of the milling process. The PARIS method was used for MCDM, in which, the weights of SR and MRR were determined by 3 methods, namely AW, EW, and MW. Twenty-seven sets of ranking results for 27 alternatives (experiments) are presented. The GINI index was used to evaluate the stability of ranking alternatives. The results have determined the value of 6 input parameters to ensure the minimum SR and the maximum MRR simultaneously.

Keywords-MCDM; PARIS; average weight; entropy weight; Merce weight; GINI index; milling

I. INTRODUCTION

Milling the plane with a face milling cutter is a machining method that gives the highest productivity of all cutting machining methods, because it has many teeth simultaneously involved in cutting and a tool with a large diameter can be chosen [1-3]. Therefore, this method is increasingly used in machine manufacturing. Thanks to the development of machine tools as well as cutting tool manufacturing technology, the accuracy of this method is increasingly improved. This method is even used instead of grinding when it is necessary to machine surfaces that require high precision. In addition, the residual stress on the surface layer of the part during milling is usually compressive residual stress, whereas the residual stress on the surface layer during grinding is usually tensile residual stress. This is also the advantage of milling over the grinding method. Among many criteria to evaluate the machining process, such as MRR, surface hardness, cutting force, cutting heat, etc., SR and MRR are the two most used parameters in published documents. This can be easily understood because MRR is an important parameter to evaluate cutting productivity, while SR is a parameter that has a great influence on the workability as well as the life of the product. On the other hand, determining the value of SR and MRR is also quite simple, specifically an SR measuring device is quite more popular than a force measuring device or a heat measuring device, and MRR can be calculated from simple

math formulas. As with most machining processes, it is desirable to have minimum SR and maximum MRR when milling the plane with a face mill. However, these requirements cannot be achieved simultaneously with each specific machining condition. Some examples to support this statement follow. In [4], when performing 27 tests of milling SCM440 steel, the one with the smallest SR was also the one with the smallest MRR. When performing 9 tests for milling 060A4 steel, the one with the smallest SR is had a very small MRR [5]. Among 27 SKD11 steel milling experiments, the one with the smallest SR almost had the smallest MRR [6], etc. Thus, in cases like these it is necessary to define an experiment where SR is considered smallest and MRR is considered maximum, i.e. an MCDM [4-6] problem. There are various mathematical methods that support MCDM such as: SAW, WASPAS, TOPSIS, VIKOR, MOORA, COPRAS, PIV, PSI, EDAS, MARCOS, CODAS, WASPAS, WPAS, etc. These methods have been widely applied to MCDM in many different fields. The common feature of these methods is that each method gives only one set of ranking results for the alternatives.

The PARIS method was first proposed in 2020 by Ardil [7]. PARIS is also an MCDM method, but, unlike the above techniques, it performs threefold data normalization in 3 different ways. In addition, for each data normalization method, the ranking of the alternatives is performed in 3 stages. Thus, when applying this method, 9 different ratings will be conducted for the alternatives. In the next section of this paper, this method will be presented in detail. This method has been applied to make multi-criteria decisions in some specific cases such as: When deciding in choosing 1 of 6 aircraft types, each aircraft is evaluated through 7 criteria. The PARIS method was applied to accomplish this in [7]. In this study, two methods, i.e. AW and EW were used to determine the weights for 7 criteria. The TOPSIS method was also used and compared with the PARIS method. When using the PARIS method with two different weighting methods (AW and EW) it gave 18 ranking options. When using the TOPSIS method with two different weighting methods two ranking options were proposed. An interesting result was obtained that all 20 ranking options identified the best aircraft according to the 7 given criteria. Besides, Ardil also used the PARIS method [8] to decide which one of the 3 types of military aircraft to choose. In this case, each aircraft is evaluated on 7 criteria. AW and EW were again

Corresponding author: Hong Ky Le

used to determine the weights of the criteria and TOPSIS was also used and compared with the PARIS method. The calculated results showed that all 20 ranking options (including 18 options of PARIS and 2 options of TOPSIS) identified the same best aircraft. In [9], the PARIS method was also used to select 1 out of 5 software candidates, considering 8 criteria. In total, there were 31 sub-criteria out of which 8 were applied. In addition, 3 different sets of weights that are random numbers (RN) have been assigned to the criteria. The calculated results showed 27 rating options. In particular, the different best alternatives depended on the random weights assigned to the criteria.

The above results show that the use of PARIS method is quite effective. However, the PARIS method has only been used in the mentioned studies. Up to now, and to the best of our knowledge, there have been no studies using this method in MCDM for the milling process and mechanical processing in general. AW, EW, and RN methods were used to determine the weights for the criteria in the above studies when applying the PARIS method. This is understandable because AW is the simplest method to determine the weights for criteria where the weights of the criteria are equal, and EW is a method with high accuracy that has been widely used. Its use is recommended in MCDM [10]. The RN method was used because out of the 31 criteria for software evaluation, there are both qualitative and quantitative criteria. However, for quantitative criteria it is not necessary to use this method. The MW weighting method was first proposed in 2021 [11]. It has been used in several studies to determine weights in MCDM [12, 13]. However, this method has not been used to determine weights for the criteria of any milling process. Therefore, the use of the MW method for determining the weights for the criteria of the milling process along with the two methods already used (AW and EW) ensures the novelty of the current study. The use of 3 methods of determining weights in a study is the basis for assessing the stability in determining the best solution.

SNCM439 steel (according to JIS standard - Japan) is a high-alloy steel and products like gears, wood cutters, dies, etc. are usually made from it. This steel is equivalent to some steels according to other standards such as, AISI - 4340, EN - 36CrNiMo4, BS - EN24, JIS - SNCM439, DIN - 150Cr14, GOST - 9CrSi (or 9XC or 9HS or 9KHS). There have been a few studies regarding the milling of this steel (or equivalent steels). In [14], the authors investigated the influence of the parameters of the MQL-type cooling lubrication on SR when hard milling of 9CrSi steel. In [15], the Response Surface Method (RSM) and an Artificial Neural Network (ANN) model were combined to predict the value of tool wear and cutting force for the dry milling of EN24 steel. In [16], the shear force and friction force were investigated when milling EN24 steel with different cooling lubrication conditions. In [17], the optimal values of cutting speed, feed rate, and depth of cut were determined to ensure minimum SR when milling EN24 steel. The influence of cutting speed, feed rate, and depth of cut on SR on cutting temperature when hard milling AISI-4340 steel were investigated in [18]. In [19], it was determined that the value of cutting speed, feed rate, and depth of cut improve the surface hardness when milling AISI-4340 steel. Research on milling steel SNCM439 (or equivalent steels) has been

conducted in a number of studies as described above. However, to date, there has not been any research done in MCDM when machining this steel. This is the reason that this steel was chosen as the research object in this paper.

Like the SR parameter, the MRR is a very common parameter used to evaluate the milling process. This parameter reflects the processing capacity. Considering both SR and MRR in a study makes both economic and technical implications. That is why this study has selected both SR and MRR as the criteria to evaluate the milling process. Besides, the three cutting parameters (cutting speed, feed rate, and depth of cut) that have been investigated in many studies, the parameters of the cutting tool (number of inserts, cutting tool material, and nose radius) are also parameters that have a great influence on the surface roughness during milling [20-22]. However, until now, no study has been found that considers all 6 of these parameters during the milling process. Therefore, the consideration of all these 6 parameters is also a novelty of this work.

This study will conduct SNCM439 steel milling experiments. In each experiment, 6 parameters will be changed including cutting speed, feed rate, depth of cut, number of inserts, insert material, and nose radius. SR and MRR were selected as the two output criteria. PARIS method is used for MCDM with 3 weighting methods including AW, EW, and MW.

II. THE PARIS METHOD

The PARIS method is performed according to the following steps [7].

Step 1: Building of the decision matrix.

$$X = \begin{bmatrix} x_{11} & x_{12} & x_{1j} & x_{1n} \\ x_{21} & x_{22} & x_{2j} & x_{2n} \\ x_{i1} & x_{i2} & x_{ij} & x_{in} \\ x_{m1} & x_{m2} & x_{mj} & x_{mn} \end{bmatrix} \quad (1)$$

In which: m is the number of options, $i = 1, 2, \dots, m$ and n is the number of criteria, $j = 1, 2, \dots, n$.

If x_{ij} is negative then do the calculation $x'_{ij} = x_{ij} = \min(x_{ij})$, then x'_{ij} is used to calculate the next steps.

Step 2: Normalizing the decision matrix.

Normalizing way 1 (Vector normalization):

$$r_{ij} = \frac{x_{ij}}{\sqrt{\sum_{i=1}^m x_{ij}^2}} \quad \text{If } j \text{ is the criterion, the bigger the better} \quad (2)$$

$$r_{ij} = 1 - \frac{x_{ij}}{\sqrt{\sum_{i=1}^m x_{ij}^2}} \quad \text{If } j \text{ is the criterion, the smaller the better} \quad (3)$$

Normalizing way 2 (Linear normalization):

$$r_{ij} = \frac{x_{ij}}{x_j^{\max}} \quad \text{If } j \text{ is the criterion, the bigger the better} \quad (4)$$

$$r_{ij} = \frac{x_j^{\min}}{x_{ij}} \quad \text{If } j \text{ is the criterion, the smaller the better} \quad (5)$$

Normalizing way 3 (Max - Min linear normalization):

$$r_{ij} = \frac{x_{ij} - x_j^{\min}}{x_j^{\max} - x_j^{\min}} \quad \text{If } j \text{ is the criterion, the bigger the better} \quad (6)$$

$$r_{ij} = \frac{x_j^{\max} - x_{ij}}{x_j^{\max} - x_j^{\min}} \quad \text{If } j \text{ is the criterion, the smaller the better} \quad (7)$$

Step 3: Calculating of the weighted normalized value:

$$z_{ij} = \omega_j \cdot r_{ij} \quad (8)$$

Step 4: Summarizing the weighted normalized values as:

$$\pi_i^\omega = \sum_{j=1}^n \omega_j \cdot r_{ij} \quad (9)$$

where $i = 1, 2, \dots, m; j = 1, 2, \dots, n$.

Step 5: Rank the alternatives. The solution with the largest value of π_i^ω is the best solution.

Step 6: Identify the elements of the reference ideal solution:

$$z_j^* = \{z_1^*, \dots, z_j^*\} = \{(max_i z_{ij} \mid j \in B), (min_i z_{ij} \mid j \in C)\} \quad (10)$$

where B represents a criterion as large as possible, C represents a criterion as small as possible.

Step 7: Calculate the distance from the reference ideal solution:

$$\pi_i^* = \sum_{j=1}^n (z_j^* - z_{ij}) \quad (11)$$

Step 8: Rank the alternatives according to the principle that the one with the smallest value of π_i is the best one.

Step 9: Calculate the distance from the alternatives to the ideal solution:

$$R_i = \sqrt{(\pi_i^\omega - \pi_i^{\omega, \max})^2 + (\pi_i^* - \pi_i^{*, \min})^2} \quad (12)$$

Step 10: Rank the alternatives according to the principle that the one with the smallest R_i value is the best one.

III. METHODS OF DETERMINING WEIGHTS

A. The Average Weight Method

AW is determined according to the following formula [23]:

$$w_j = \frac{1}{n} \quad (13)$$

where n is the number of criteria.

B. The Entropy Weighted Method

EW is determined according to the following steps [10].

Step 1: Determine the normalized values for the indicators:

$$p_{ij} = \frac{x_{ij}}{m + \sum_{i=1}^m x_{ij}^2} \quad (14)$$

where x_{ij} is the value of criterion j corresponding to option i and m is the number of alternatives.

Step 2: Calculate the value of the Entropy measure for each indicator with:

$$me_j = -\sum_{i=1}^m [p_{ij} \cdot \ln(p_{ij})] - \left(1 - \sum_{i=1}^m p_{ij}\right) \cdot \ln\left(1 - \sum_{i=1}^m p_{ij}\right) \quad (15)$$

Step 3: Calculate the weight for each indicator:

$$w_j = \frac{1 - me_j}{\sum_{j=1}^m (1 - me_j)} \quad (16)$$

C. The MEREC Weight Method

MW is determined according to the following steps [11]:

Step 1: Is similar to step 1 of the PARIS method.

Step 2: Calculate the normalized values according to:

$$h_{ij} = \frac{\min x_{ij}}{x_{ij}} \quad \text{If } j \text{ is the criterion, the bigger the better.} \quad (17)$$

$$h_{ij} = \frac{x_{ij}}{\max x_{ij}} \quad \text{If } j \text{ is the criterion, the smaller the better} \quad (18)$$

Step 3: Calculate the overall efficiency of the alternatives according to:

$$S_i = \ln \left[1 + \left(\frac{1}{n} \sum_{j=1}^n |\ln(h_{ij})| \right) \right] \quad (19)$$

Step 4: Calculate the performance of the alternatives according to:

$$S'_{ij} = \ln \left[1 + \left(\frac{1}{n} \sum_{k \neq j} |\ln(h_{ik})| \right) \right] \quad (20)$$

Step 5: Calculate the absolute value of the deviations according to:

$$E_j = \sum_i |S'_{ij} - S_i| \quad (21)$$

Step 6: Calculate the weight for the criteria according to:

$$w_j = \frac{E_j}{\sum_k E_k} \quad (22)$$

IV. MILLING EXPERIMENT

A. Experimental Design

Experiments were carried out on a 3-axis machining center. The values of the 6 input parameters are presented in Table I [1, 24]. As the number of inserts varies in each experiment, 3 different types of inserts have been used. In addition, each type of tool head has several insert positions of 2, 3, and 4. All 3 types of cutters have a diameter of 40mm. The basic geometrical parameters of the selected insert types are the same. Specifically, the main cutting angle is 90° , the main cutting-edge length is 10mm, and the blade width is 6.8mm [24]. The Taguchi method was used for the experimental design due to its advantages [25, 26]. In this experiment, an experimental matrix of 27 experiments was designed (Table II).

TABLE I. INPUT PARAMETERS

Parameter	Symbol	Unit	Value at level		
			1	2	3
Number of insert	N	-	2	3	4
Insert material	M	-	TiN	TiCN	TiAlN
Nose radius	r	mm	0.3	0.5	0.8
Cutting speed	v_c	m/min	120	150	180
Feed rate	v_f	mm/min	300	400	500
Depth of cut	a_p	mm	0.2	0.35	0.5

TABLE II. EXPERIMENTAL MATRIX AND RESULTS

Trial	N	M	r (mm)	v_c (m/min)	v_f (mm/min)	a_p (mm)	MRR (mm ³ /min)	SR (μ m)
1	2	TiN	0.3	120	300	0.2	2400	2.287
2	2	TiN	0.3	120	400	0.35	5600	3.152
3	2	TiN	0.3	120	500	0.5	10000	4.017
4	2	TiCN	0.5	150	300	0.2	2400	1.377
5	2	TiCN	0.5	150	400	0.35	5600	2.242
6	2	TiCN	0.5	150	500	0.5	10000	3.107
7	2	TiAlN	0.8	180	300	0.2	2400	0.490
8	2	TiAlN	0.8	180	400	0.35	5600	1.240
9	2	TiAlN	0.8	180	500	0.5	10000	2.105
10	3	TiN	0.5	180	300	0.35	4200	0.245
11	3	TiN	0.5	180	400	0.5	8000	0.793
12	3	TiN	0.5	180	500	0.2	4000	1.163
13	3	TiCN	0.8	120	300	0.35	4200	1.104
14	3	TiCN	0.8	120	400	0.5	8000	1.969
15	3	TiCN	0.8	120	500	0.2	4000	2.339
16	3	TiAlN	0.3	150	300	0.35	4200	0.838
17	3	TiAlN	0.3	150	400	0.5	8000	1.703
18	3	TiAlN	0.3	150	500	0.2	4000	2.073
19	4	TiN	0.8	150	300	0.5	6000	0.345
20	4	TiN	0.8	150	400	0.2	3200	0.456
21	4	TiN	0.8	150	500	0.35	7000	0.890
22	4	TiCN	0.3	180	300	0.5	6000	0.611
23	4	TiCN	0.3	180	400	0.2	3200	0.241
24	4	TiCN	0.3	180	500	0.35	7000	0.624
25	4	TiAlN	0.5	120	300	0.5	6000	0.657
26	4	TiAlN	0.5	120	400	0.2	3200	1.027
27	4	TiAlN	0.5	120	500	0.35	7000	1.892

B. Results and Discussion

The SR for each experiment can be seen presented in Table II. These values are the mean values of at least 3 consecutive measurements. In addition, the MRR at each experiment is also been summarized in Table II. The values are calculated by (23), where v_f , a_p and b_w are the feed rate, the depth of cut, and the wide cut respectively.

$$MRR = v_f \cdot a_p \cdot b_w \quad (23)$$

The extent and influence of the parameters on SR are shown in Figure 1. From this graph, it is shown that:

- The number of inserts, cutting speed, and feed rate have a great influence on SR. The nose radius and depth of cut also affect the SR, but to a lesser extent than the 3 mentioned above parameters. The insert material has no significant effect on SR.
- When the number of insert increases, the SR decreases. This can be explained by the fact that as the number of inserts increases, each area of the machined surface is cut more than once. That means that after a insert cuts off a

layer of the material, the metal layer on the surface of the part will be elastically deformed. This metal is then removed by other cuttings, which causes the SR to decrease.

- As the cutting speed increases, the cutting tool rotates at a faster speed. Then a point on the surface of the workpiece will be repeatedly cut by the cutting edges, even the undulations caused by plastic deformation will be eliminated, which leads to a reduced SR. The case is similar with the increasing of the number of inserts discussed above.
- As the feed rate increases, the time the cutting tool is in contact between an area of the part surface and the cutting edge decreases, causing plastic layers of metal on the surface to not be removed, leading to an increase in SR. Increasing the nose radius will cause the SR to decrease. It can be understood that the height of the surface undulation is inversely proportional to the nose radius, as discussed in [27]. Furthermore, the large SR at large feed rates and small nose radius are also consistent with the SR calculation formula used in some studies [27]:

$$R_a = 1000 \cdot 0.0321 \cdot v_f^2 / r$$

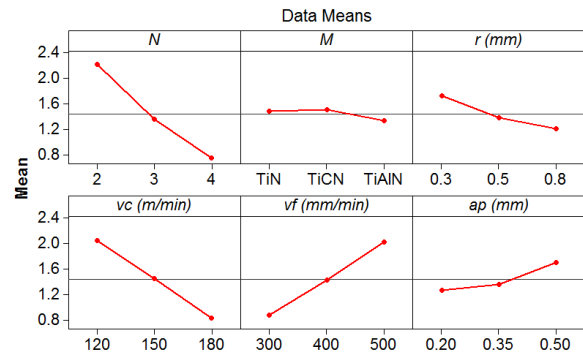


Fig. 1. Main effects plot for surface roughness.

From Figure 1, if the SR has a small value, choose a large cutting speed, a small feed rate, and a small depth of cut. However, according to (23), when the feed rate and cutting depth are small, the MRR will also be small, which is undesirable. Therefore, choosing the value of the cutting parameters to ensure that the SR is small and the MRR is large, it is necessary to make the right decisions. This right decision can be made with a MCDM method. In this problem, the PARIS method will be used.

V. MULTI-CRITERIA DECISION MAKING

A. Determining the Weights of the Criteria

Equation (1) is used to build the decision matrix. The last two columns in Table II are the decision matrix. Equation (13) was applied to determine the weights of the criteria according to the AW method. In addition, (14)-(16) are used to determine the weights for the criteria according to the EW method. Equations (17)-(22) determine the weights of the criteria of the MW method. The results are shown in Table III.

TABLE III. CRITERIA WEIGHTS

Method	Ra	MRR
AW	0.5	0.5
EW	0.6859	0.3141
MW	0.3663	0.6337

B. Applying the PARIS Method

Equations (2) and (3) are used to normalize the matrix in way 1. Equations (4) and (5) are applied to normalize the matrix in way 2. Equations (6) and (7) are used to normalize the matrix in way 3. The results are presented in Table V.

TABLE IV. VALUE OF Z_j^*

Normalization	SR	MRR
Way 1	0.255	0.200
Way 2	0.030	0.500
Way 3	0.000	0.500

To rank the alternatives for weight calculation according to the AW method we apply (8) to calculate the weighted normalized value (z_{ij}) and (9) to calculate the weighted normalized sum (π_i^0). The results are presented in Table VI. The results of ranking the alternatives according to the value of π_i^0 are also presented in this Table. Equation (10) was applied to determine the factors of the ideal solution (z_j^*) and the results are presented in Table IV. Equation (11) is used to determine the distance from the reference ideal solution (π_i). The results are presented in Table VII. The results of ranking the alternatives according to the value of π_i are also presented in this Table. The distance from the alternatives to the ideal solution (R_i) is calculated by (12). The results are presented in

Table VIII. The results of ranking options according to the value of R_i are also shown in this Table.

TABLE V. NORMALIZED MATRICES

Trial.	Way 1		Way 2		Way 3	
	SR	MRR	SR	MRR	SR	MRR
1	0.721	0.096	0.105	0.240	0.458	0.000
2	0.616	0.224	0.076	0.560	0.229	0.421
3	0.511	0.400	0.060	1.000	0.000	1.000
4	0.832	0.096	0.175	0.240	0.699	0.000
5	0.727	0.224	0.107	0.560	0.470	0.421
6	0.622	0.400	0.078	1.000	0.241	1.000
7	0.940	0.096	0.492	0.240	0.934	0.000
8	0.849	0.224	0.194	0.560	0.735	0.421
9	0.744	0.400	0.114	1.000	0.506	1.000
10	0.970	0.168	0.984	0.420	0.999	0.237
11	0.903	0.320	0.304	0.800	0.854	0.737
12	0.858	0.160	0.207	0.400	0.756	0.211
13	0.866	0.168	0.218	0.420	0.771	0.237
14	0.760	0.320	0.122	0.800	0.542	0.737
15	0.715	0.160	0.103	0.400	0.444	0.211
16	0.898	0.168	0.288	0.420	0.842	0.237
17	0.793	0.320	0.142	0.800	0.613	0.737
18	0.747	0.160	0.116	0.400	0.515	0.211
19	0.958	0.240	0.699	0.600	0.972	0.474
20	0.944	0.128	0.529	0.320	0.943	0.105
21	0.892	0.280	0.271	0.700	0.828	0.605
22	0.926	0.240	0.394	0.600	0.902	0.474
23	0.971	0.128	1.000	0.320	1.000	0.105
24	0.924	0.280	0.386	0.700	0.899	0.605
25	0.920	0.240	0.367	0.600	0.890	0.474
26	0.875	0.128	0.235	0.320	0.792	0.105
27	0.770	0.280	0.127	0.700	0.563	0.605

TABLE VI. SOME PARAMETERS IN PARIS RANKED BY THE VALUE OF π_i^0

Trial	Way 1				Way 2				Way 3			
	z_{ij}		π_i^0	Rank	z_{ij}		π_i^0	Rank	z_{ij}		π_i^0	Rank
	SR	MRR			SR	MRR			SR	MRR		
1	0.361	0.048	0.409	27	0.053	0.120	0.173	27	0.229	0.000	0.229	27
2	0.308	0.112	0.420	26	0.038	0.280	0.318	21	0.115	0.211	0.325	26
3	0.255	0.200	0.455	23	0.030	0.500	0.530	8	0.000	0.500	0.500	18
4	0.416	0.048	0.464	22	0.088	0.120	0.208	26	0.350	0.000	0.350	24
5	0.363	0.112	0.476	21	0.054	0.280	0.334	19	0.235	0.211	0.446	22
6	0.311	0.200	0.511	18	0.039	0.500	0.539	7	0.120	0.500	0.620	10
7	0.470	0.048	0.518	16	0.246	0.120	0.366	17	0.467	0.000	0.467	20
8	0.424	0.112	0.537	12	0.097	0.280	0.377	16	0.368	0.211	0.578	13
9	0.372	0.200	0.572	7	0.057	0.500	0.557	4	0.253	0.500	0.753	2
10	0.485	0.084	0.569	8	0.492	0.210	0.702	1	0.499	0.118	0.618	11
11	0.452	0.160	0.612	1	0.152	0.400	0.552	5	0.427	0.368	0.795	1
12	0.429	0.080	0.509	19	0.104	0.200	0.304	22	0.378	0.105	0.483	19
13	0.433	0.084	0.517	17	0.109	0.210	0.319	20	0.386	0.118	0.504	17
14	0.380	0.160	0.540	11	0.061	0.400	0.461	13	0.271	0.368	0.640	9
15	0.358	0.080	0.438	25	0.052	0.200	0.252	25	0.222	0.105	0.327	25
16	0.449	0.084	0.533	14	0.144	0.210	0.354	18	0.421	0.118	0.539	15
17	0.396	0.160	0.556	9	0.071	0.400	0.471	12	0.306	0.368	0.675	8
18	0.374	0.080	0.454	24	0.058	0.200	0.258	24	0.257	0.105	0.363	23
19	0.479	0.120	0.599	3	0.349	0.300	0.649	3	0.486	0.237	0.723	4
20	0.472	0.064	0.536	13	0.264	0.160	0.424	14	0.472	0.053	0.524	16
21	0.446	0.140	0.586	4	0.135	0.350	0.485	10	0.414	0.303	0.717	5
22	0.463	0.120	0.583	5	0.197	0.300	0.497	9	0.451	0.237	0.688	6
23	0.485	0.064	0.549	10	0.500	0.160	0.660	2	0.500	0.053	0.553	14
24	0.462	0.140	0.602	2	0.193	0.350	0.543	6	0.449	0.303	0.752	3
25	0.460	0.120	0.580	6	0.183	0.300	0.483	11	0.445	0.237	0.682	7
26	0.437	0.064	0.501	20	0.117	0.160	0.277	23	0.396	0.053	0.449	21
27	0.385	0.140	0.525	15	0.064	0.350	0.414	15	0.281	0.303	0.584	12

TABLE VII. π_i^* VALUES AND RATINGS

Trial	Way 1		Way 2		Way 3	
	π_i^*	Rank	π_i^*	Rank	π_i^*	Rank
1	0.047	27	0.357	27	0.271	27
2	0.035	26	0.212	21	0.175	26
3	0.000	23	0.000	8	0.000	18
4	-0.009	22	0.322	26	0.150	24
5	-0.020	21	0.196	19	0.054	22
6	-0.055	18	-0.009	7	-0.120	11
7	-0.063	16	0.164	17	0.033	20
8	-0.081	12	0.153	16	-0.078	13
9	-0.116	7	-0.027	4	-0.253	2
10	-0.114	8	-0.172	1	-0.118	6
11	-0.156	1	-0.022	5	-0.295	1
12	-0.054	19	0.226	22	0.017	19
13	-0.061	17	0.211	20	-0.004	17
14	-0.085	11	0.069	13	-0.140	10
15	0.018	25	0.278	25	0.173	25
16	-0.078	14	0.176	18	-0.039	15
17	-0.101	9	0.059	12	-0.175	9
18	0.002	24	0.272	24	0.137	23
19	-0.144	3	-0.119	3	-0.223	4
20	-0.081	13	0.106	14	-0.024	16
21	-0.130	4	0.045	10	-0.217	5
22	-0.127	5	0.033	9	-0.188	7
23	-0.094	10	-0.130	2	-0.053	14
24	-0.147	2	-0.013	6	-0.252	3
25	-0.125	6	0.047	11	-0.182	8
26	-0.046	20	0.253	23	0.051	21
27	-0.069	15	0.116	15	-0.084	12

TABLE VIII. R_i VALUES AND RATINGS

Trial	Way 1		Way 2		Way 3	
	R_i	Rank	R_i	Rank	R_i	Rank
1	0.287	27	0.748	27	0.976	27
2	0.271	26	0.543	21	0.750	18
3	0.221	23	0.243	8	0.418	3
4	0.209	22	0.699	26	0.912	26
5	0.193	21	0.521	19	0.681	14
6	0.143	18	0.231	7	0.343	2
7	0.132	16	0.475	17	0.860	25
8	0.106	12	0.459	16	0.624	13
9	0.056	7	0.204	4	0.298	1
10	0.060	8	0.000	1	0.700	15
11	0.000	1	0.212	5	0.427	4
12	0.145	19	0.563	22	0.757	19
13	0.134	17	0.541	20	0.737	17
14	0.101	11	0.340	13	0.454	6
15	0.246	25	0.637	25	0.834	24
16	0.111	14	0.492	18	0.724	16
17	0.078	9	0.327	12	0.444	5
18	0.223	24	0.627	24	0.814	22
19	0.018	3	0.074	3	0.563	10
20	0.107	13	0.393	14	0.791	21
21	0.037	4	0.306	10	0.499	8
22	0.041	5	0.289	9	0.569	11
23	0.088	10	0.059	2	0.781	20
24	0.014	2	0.224	6	0.495	7
25	0.045	6	0.309	11	0.570	12
26	0.156	20	0.600	23	0.820	23
27	0.123	15	0.408	15	0.536	9

TABLE IX. RANKING WHEN THE WEIGHTS ARE DETERMINED WITH THE EW METHOD

Trial	Ranking by value of π_i^*			Ranking by value of π_i^*			Ranking by value of R_i		
	Way 1	Way 2	Way 3	Way 1	Way 2	Way 3	Way 1	Way 2	Way 3
1	25	27	26	25	27	25	25	27	27
2	26	23	27	26	23	27	26	23	24
3	27	13	25	27	13	26	27	13	13
4	20	26	20	20	2	20	20	26	26
5	21	22	22	21	22	22	21	22	17
6	23	12	21	23	12	21	23	12	3
7	10	9	13	10	9	13	10	9	22
8	12	17	14	12	17	14	12	17	12
9	17	11	10	17	11	10	17	11	1
10	4	1	5	2	1	5	2	1	14
11	3	6	1	4	6	1	4	6	2
12	16	20	17	15	20	17	15	20	18
13	13	19	15	13	19	15	13	19	16
14	18	15	16	18	15	16	18	15	5
15	24	25	24	24	25	24	24	25	25
16	11	16	11	11	16	11	11	16	15
17	14	14	12	16	14	12	16	14	4
18	22	24	23	22	24	23	22	24	23
19	1	3	2	1	3	2	1	3	8
20	9	5	9	9	5	9	9	5	20
21	8	10	7	8	10	7	8	10	7
22	5	7	4	6	7	4	6	7	9
23	7	2	8	5	2	8	5	2	19
24	2	4	3	3	4	3	3	4	6
25	6	8	6	7	8	6	7	8	10
26	15	21	18	14	21	19	14	21	21
27	19	18	19	19	18	18	19	18	11

TABLE X. RANKING WHEN THE WEIGHTS ARE DETERMINED WITH THE MW METHOD

Trial	Ranking by value of π_i^0			Ranking by value of π_i^*			Ranking by value of R_i		
	Way 1	Way 2	Way 3	Way 1	Way 2	Way 3	Way 1	Way 2	Way 3
1	27	27	27	27	27	27	27	27	27
2	24	18	22	24	18	22	24	18	15
3	14	3	9	14	3	10	14	3	3
4	25	26	26	25	26	26	25	26	26
5	20	17	16	20	17	17	20	17	14
6	10	2	3	9	2	3	10	2	2
7	21	21	23	21	21	23	21	21	25
8	13	15	13	13	15	14	13	15	13
9	2	1	1	2	1	1	2	1	1
10	11	5	14	11	5	15	11	5	16
11	1	6	2	1	6	2	1	6	4
12	19	22	20	19	22	8	19	22	19
13	18	20	18	18	20	19	18	20	18
14	9	10	7	10	10	7	9	10	6
15	26	24	25	26	25	25	26	24	23
16	16	19	15	16	19	16	16	19	17
17	6	9	5	6	9	5	6	9	5
18	23	23	24	23	23	24	23	23	21
19	5	4	8	5	4	9	5	4	10
20	17	16	19	17	16	20	17	16	22
21	4	11	6	4	11	6	4	11	8
22	7	12	10	7	12	11	7	12	11
23	15	8	17	15	8	18	15	8	20
24	3	7	4	3	7	4	3	7	7
25	8	13	11	8	13	12	8	13	12
26	22	25	21	22	24	21	22	25	24
27	12	14	12	12	14	13	12	14	9

The ranking results in Tables V-X show 27 different ranking options. From these results it is shown that:

- 22/27 times experiment #1 was determined to be the worst. In this experiment, $MRR = 2400\text{mm}^3/\text{min}$ was one of the 3 smallest values in Table II (equal to the MRR in experiments #4 and #7). In addition, $Ra = 2.287\mu\text{m}$ is very large compared to the surface texture in other experiments (only smaller than the surface texture in 4 experiments: #2, #3, #5, and #15). That allows the claim that the experiment #1 is the worst to be entirely reasonable.
- 8/27 times determined experiment #9, 6/27 times determined experiment #10, 10/27 times determined experiment #11, and 3/27 times determined experiment #19 as the best. Thus, determining which experiment is the best would not be achieved if the work stopped here. To determine the best experiment, in addition to the ranking results, it is also necessary to add the stability of the ratings. In this study, the GINI index value will be used to determine the stability in ranking the alternatives [29]. The GINI index value is determined by [29, 30]:

$$D(R) = \frac{4}{(m-1)(z^2 - \left|\sin(\frac{\pi}{z})\right|)} \sum_{h=1}^{z-1} \sum_{l=h+1}^z |R_h - R_l| \quad (24)$$

where m is the number of options, z is the number of MCDM methods used, R_h and R_l are the ranking values of the alternatives of the decision method h and l , and $D(R) \in [0,1]$. When $D(R) = 0$, the rank of an alternative is the same when ranking by different methods. In contrast, when $D(R) = 1$, the ranking of the alternatives is most different when using different ranking methods. When comparing two alternatives,

the one with the smaller GINI index value is the better one. Equation (24) has been applied to calculate the GINI index value for the data in Tables V-X. The results are presented in Table XI.

TABLE XI. GINI INDEX VALUE OF THE ALTERNATIVES

Experiment	GINI index	Experiment	GINI index
1	0.002536	15	0.003381
2	0.018808	16	0.015427
3	0.048605	17	0.017751
4	0.018174	18	0.004861
5	0.012468	19	0.013314
6	0.040152	20	0.019231
7	0.01754	21	0.019019
8	0.014159	22	0.015216
9	0.019442	23	0.040997
10	0.032967	24	0.012046
11	0.016272	25	0.015216
12	0.018597	26	0.016061
13	0.014582	27	0.011834
14	0.017117		

The results in Table XI show that:

- In experiment #1, the minimum GINI index value is 0.002536. This proves that experiment #1 has the highest stability when ranking in different times. Up to 22/27 options confirmed this experiment as the worst (ranked 27th), 4/27 options indicate that this experiment is the second worst (ranked 26), and 1/27 indicates that this experiment is the third worst (ranked 25). On the other hand, 27th or 26th or 25th ranking is very close. That proves that experiment #1 has the highest stability when ranking according to different options.

- In experiment #3, the largest GINI index value was 0.048605, proving that this experiment has the lowest rank stability when ranking according to the alternatives. According to the data in Tables VI, VIII-XI, experiment #3 came 5 times at the 3rd place, 3 times at the 8th, 1 time at the 9th, 1 time 10th, 4 times came at the 13th, 3 times at the 14th place, 2 at the 18th, 3 at the 23rd place, and 1 at the 25th, 26th time, and 27th place. So, the stability in the ranking of experiment #3 is very weak. This experiment ranked in a variety of categories, with both good (3) and bad (27) ranks.
- Among the 4 experiments #9, #10, #10 and #19, experiment #19 has the smallest GINI index value. That proves that experiment #19 has a higher stability rating than the other 3 experiments. Thus experiment #19 is the best of these 4 experiments and it is also the best of the 27 experiments performed. The best values of the input parameters to ensure minimum SR and maximum MRR at the same time are: 4 as the number of inserts, TiN as the insert material, 0.8mm nose radius, 150m/min cutting speed, 30mm/min feed rate, and 0.5 mm depth of cut.
- The use of different weighting methods leads to different ranking orders. Responding to different data normalization ways will result in different ranking orders for the alternatives. However, the simultaneous use of multiple weighting and multiple data normalization methods to give different ranking results, and then the use of the GINI index to choose the best solution will form the basis for determining which option is the best.

VI. CONCLUSIONS

In this study, 27 SNCM439 steel milling experiments were performed. At each experiment, 6 parameters were considered: number of inserts, cutting material, nose radius, cutting speed, feed rate, and depth of cut. SR and MRR were determined in each experiment. The PARIS method was used to rank the alternatives, and the stability in ranking was evaluated by the GINI index. Some drawn conclusions are:

- The number of inserts, cutting speed, and feed rate have a great influence on surface roughness. Increasing the number of inserts or cutting speed reduces the surface roughness, while increasing the feed rate increases it. The nose radius and depth of cut also affect the surface roughness. Surface roughness is reduced if the tip radius is increased, or the depth of cut is decreased. On the other hand, the insert material does not significantly affect surface roughness.
- The use of 3 data normalization methods is what distinguishes the PARIS method from other methods. For each data normalization method, the PARIS method also gives 3 ranking results for the alternatives. This is also its difference from the other MCDM methods.
- The combination of the PARIS method and 3 different weighting methods (AW, EW, and MW) resulted in 27 different ranking options. The combination of the PARIS method and the GINI index to determine the best solution has higher reliability instead of using just one method that only gives a ranking solution for the alternatives.

- To ensure minimum SR and maximum MRR simultaneously, it is recommended to use the TiN insert with parameter values of the number of inserts, tool radius, cutting speed, feed rate, and depth of cut respectively as 4 pieces, 0.8mm, 150m/min, 30mm/min, and 0.5mm.

NOMENCLATURE

PARIS	Preference Analysis for Reference Ideal Solution
SAW	Simple Additive Weighting
WASPAS	Weighted Aggregates Sum Product Assessment
TOPSIS	Technique for Order of Preference by Similarity to Ideal Solution
VIKOR	Vlsekriterijumska optimizacija i kompromisno resenje in Serbian
MOORA	Multiobjective Optimization On the basis of Ratio Analysis
COPRAS	COMplex Proportional ASsessment
PIV	Proximity Indexed Value
PSI	Preference Selection Index
EDAS	Evaluation based on Distance from Average Solution
MARCOS	Measurement Alternatives and Ranking according to COMpromise Solution
CODAS	COMbinative Distance based Assessment
WASPAS	Weighted Aggregated Sum Product Assessment
WPAS	Weighted Product Assessment
MCDM	Multi-Criteria Decision-Making
MEREC	Method based on the Removal Effects of Criteria
AW	Average Weight
EW	Entropy Weight
MW	Merec Weight

REFERENCES

- [1] D. D. Trung, "Application of EDAS, MARCOS, TOPSIS, MOORA and PIV Methods for Multi-Criteria Decision Making in Milling Process," *Strojnicki casopis - Journal of Mechanical Engineering*, vol. 71, no. 2, pp. 69–84, Nov. 2021, <https://doi.org/10.2478/scjme-2021-0019>.
- [2] T. H. Le, V. B. Pham, and T. D. Hoang, "Surface Finish Comparison of Dry and Coolant Fluid High-Speed Milling of JIS SDK61 Mould Steel," *Engineering, Technology & Applied Science Research*, vol. 12, no. 1, pp. 8023–8028, Feb. 2022, <https://doi.org/10.48084/etasr.4594>.
- [3] V. C. Nguyen, T. D. Nguyen, and D. H. Tien, "Cutting Parameter Optimization in Finishing Milling of Ti-6Al-4V Titanium Alloy under MQL Condition using TOPSIS and ANOVA Analysis," *Engineering, Technology & Applied Science Research*, vol. 11, no. 1, pp. 6775–6780, Feb. 2021, <https://doi.org/10.48084/etasr.4015>.
- [4] N. V. Cuong and N. L. Khanh, "Parameter Selection to Ensure Multi-Criteria Optimization of the Taguchi Method Combined with the Data Envelopment Analysis-based Ranking Method when Milling SCM440 Steel," *Engineering, Technology & Applied Science Research*, vol. 11, no. 5, pp. 7551–7557, Oct. 2021, <https://doi.org/10.48084/etasr.4315>.
- [5] H. L. H. Anh, T. K. Tuan, N. H. Quang, N. H. Luan, T. M. Truong, and N. T. Q. Dung, "Optimization of Milling Process by Taguchi-PSI Method," *E3S Web of Conferences*, vol. 309, Sep. 2021, Art. no. 01019, <https://doi.org/10.1051/e3sconf/202130901019>.
- [6] D. D. Trung, N. V. Thien, and N.-T. Nguyen, "Application of TOPSIS Method in Multi-Objective Optimization of the Grinding Process Using Segmented Grinding Wheel," *Tribology in Industry*, vol. 43, no. 1, pp. 12–22, 2021, <https://doi.org/10.24874/ti.998.11.20.12>.
- [7] C. Ardil, "Aircraft Selection Process Using Preference Analysis for Reference Ideal Solution (PARIS)," *International Journal of Aerospace and Mechanical Engineering*, vol. 14, no. 3, pp. 80–90, 2020.
- [8] C. Ardil, "A Comparative Analysis of Multiple Criteria Decision Making Analysis Methods for Strategic, Tactical, and Operational Decisions in Military Fighter Aircraft Selection," *International Journal of Aerospace and Mechanical Engineering*, vol. 14, no. 7, pp. 275–288, Oct. 2021.

- [9] C. Ardil, "Software Product Quality Evaluation Model with Multiple Criteria Decision Making Analysis," *International Journal of Computer and Information Engineering*, vol. 14, no. 12, pp. 486–502, Jan. 2022.
- [10] D. Duc Trung, "A combination method for multi-criteria decision making problem in turning process," *Manufacturing Review*, vol. 8, Sep. 2021, Art. no. 26, <https://doi.org/10.1051/mfreview/2021024>.
- [11] M. Keshavarz-Ghorabae, M. Amiri, E. K. Zavadskas, Z. Turskis, and J. Antucheviciene, "Determination of Objective Weights Using a New Method Based on the Removal Effects of Criteria (MERECE)," *Symmetry*, vol. 13, no. 4, Apr. 2021, Art. no. 525, <https://doi.org/10.3390/sym13040525>.
- [12] M. Keshavarz-Ghorabae, "Assessment of distribution center locations using a multi-expert subjective-objective decision-making approach," *Scientific Reports*, vol. 11, no. 1, Sep. 2021, Art. no. 19461, <https://doi.org/10.1038/s41598-021-98698-y>.
- [13] K. Sabaghian, K. Khamforoosh, and A. Ghaderzadeh, "Presentation of a new method based on modern multivariate approaches for big data replication in distributed environments," *PLOS ONE*, vol. 16, no. 7, Jun. 2021, Art. no. e0254210, <https://doi.org/10.1371/journal.pone.0254210>.
- [14] Q.-M. Nguyen, H.-T. Nguyen, N.-A.-V. Le, T.-N. Nguyen, T.-H.-T. Dang, and T.-V. Do, "Investigation on the Effect of Nanofluid-MQL Parameters on Surface Roughness During Milling of Hardened 9CrSi Steel," in *2nd Annual International Conference on Material, Machines and Methods for Sustainable Development*, Nha Trang, Vietnam, Nov. 2020, pp. 311–316, https://doi.org/10.1007/978-3-030-69610-8_43.
- [15] S. Saikumar and M. S. Shunmugam, "Investigations into high-speed rough and finish end-milling of hardened EN24 steel for implementation of control strategies," *The International Journal of Advanced Manufacturing Technology*, vol. 63, no. 1, pp. 391–406, Nov. 2012, <https://doi.org/10.1007/s00170-012-3915-8>.
- [16] G. K. Gupta, "Investigation of cutting and frictional force components in dry, wet and cryogenic machining of EN24 STEEL," in *2nd International Conference and Exhibition on Mechanical & Aerospace Engineering*, Philadelphia, PHL, USA, Sep. 2014.
- [17] B. Singh, R. Khanna, K. Goyal, and P. Kumar, "Optimization of Input Process Parameters in CNC Milling Machine of EN24 Steel," *International Journal of Research in Mechanical Engineering and Technology*, vol. 4, no. 1, pp. 40–47, 2014.
- [18] S. S. Muhamad, J. A. Ghani, A. Juri, and C. H. C. Haron, "Dry and cryogenic milling of AISI 4340 alloy steel," *Jurnal Tribologi*, vol. 21, pp. 1–12, Jan. 2019.
- [19] S. S. Muhamad, J. A. Ghani, C. H. C. Haron, and H. Yazid, "Cryogenic milling and formation of nanostructured machined surface of AISI 4340," *Nanotechnology Reviews*, vol. 9, no. 1, pp. 1104–1117, Jan. 2020, <https://doi.org/10.1515/ntrev-2020-0086>.
- [20] D. D. Trung, "Influence of Cutting Parameters on Surface Roughness during Milling AISI 1045 Steel," *Tribology in Industry*, vol. 42, no. 4, pp. 658–665, 2020, <https://doi.org/10.24874/ti.969.09.20.11>.
- [21] R. K. Bhushan, "Impact of nose radius and machining parameters on surface roughness, tool wear and tool life during turning of AA7075/SiC composites for green manufacturing," *Mechanics of Advanced Materials and Modern Processes*, vol. 6, no. 1, Aug. 2020, <https://doi.org/10.1186/s40759-020-00045-7>.
- [22] N. C. Tampu, G. Brabie, and B. A. Chirita, "Influence of Inserts Number on Surface Quality in Milling," *Applied Mechanics and Materials*, vol. 809–810, pp. 177–182, 2015, <https://doi.org/10.4028/www.scientific.net/AMM.809-810.177>.
- [23] R. M. Dawes and B. Corrigan, "Linear models in decision making," *Psychological Bulletin*, vol. 81, no. 2, pp. 95–106, 1974, <https://doi.org/10.1037/h0037613>.
- [24] D. Trung, "Multi-objective optimization of SKD11 Steel Milling Process by Reference Ideal Method," *International Journal of Geology*, vol. 15, pp. 1–16, Apr. 2021, <https://doi.org/10.46300/9105.2021.15.1>.
- [25] M. S. Phadke, *Quality Engineering Using Robust Design*, Illustrated edition. Hoboken, NJ, USA: Prentice Hall, 1989.
- [26] D. D. Trung, "The combination of Taguchi – Entropy – WASPAS – PIV methods for multi-criteria decision making when external cylindrical grinding of 65G steel," *Journal of Machine Engineering*, vol. 21, no. 4, pp. 90–105, 2021.
- [27] T. V. Dich, N. T. Binh, N. T. Dat, N. V. Tiep, and T. X. Viet, *Manufacturing technology*. Ha Noi, Vietnam: Science and Technics Publishing House, 2003.
- [28] M. P. Groover, *Fundamentals of Modern Manufacturing: Materials, Processes, and Systems*. Hoboken, NJ, USA: Prentice Hall, 1996.
- [29] L. Ceriani and P. Verme, "The origins of the Gini index: extracts from Variabilita e Mutabilita (1912) by Corrado Gini," *The Journal of Economic Inequality*, vol. 10, no. 3, pp. 421–443, Sep. 2012, <https://doi.org/10.1007/s10888-011-9188-x>.
- [30] S. Coutu, L. Rossi, D. A. Barry, and N. Chevre, "Methodology to account for uncertainties and tradeoffs in pharmaceutical environmental hazard assessment," *Journal of Environmental Management*, vol. 98, pp. 183–190, May 2012, <https://doi.org/10.1016/j.jenvman.2012.01.001>.

Improvement of Sliding Mode Control Strategy Founded on Cascaded Doubly Fed Induction Generator Powered by a Matrix Converter

Amar Maafa

Department of Electrical Engineering
Akli Mohand Oulhadj University
Bouira, Algeria
ommafa@univ-bouira.dz

Hacene Mellah

Department of Electrical Engineering
Akli Mohand Oulhadj University
Bouira, Algeria
h.mellah@univ-bouira.dz

Kaci Ghedamsi

Laboratoire de Maîtrise des Energies Renouvelables
Bejaia University, Algeria
kghedamsi@yahoo.fr

Djamel Aouzellag

Laboratoire de Maîtrise des Energies Renouvelables
Bejaia University, Algeria
aouzellag@hotmail.com

Received: 1 July 2022 | Revised: 29 July 2022 | Accepted: 31 July 2022

Abstract-The current paper presents a Sliding Mode Controller (SMC) for indirect field-oriented Cascaded Doubly Fed Induction Generator (CDFIG) powered through a Matrix Converter (MC). The proposed SMC employs a continuous control strategy to accomplish free chattering fractional-order sliding-mode control and to ensure that the control of the first DFIG stator's reactive and active power is separated. An MC is used to control the current provided to the second stator of the CDFIG as an alternative to standard voltage source inverters. The two MCs are controlled via Space-Vector Pulse-Width Modulation (SVPWM) and Indirect Field Oriented Control (IFOC). The proposed Wind Power Generation System (WPGS) is used with the purpose to ensure Maximum Power Point Tracking (MPPT) sensing under various disturbance variables such as turbulent wind. The simulation results prove the efficiency and robustness of the proposed method.

Keywords- *Sliding Mode Control (SMC); Wind Power Generation System (WPGS); Cascaded Doubly Fed Induction Generator (CDFIG); Matrix Converter (MC)*

I. INTRODUCTION

The current interest in wind energy comes from the need to develop less expensive, clean, and sustainable WPGSs [1], while reducing maintenance cost and increasing availability and production [2], hence, the need for the research regarding electromechanical converters of high reliability [2]. Many WTs are equipped by DFIGs [3] to produce electrical energy [4-9]. Furthermore, brushes and slip-rings, are fitted with wound-rotor induction machines, which may pose maintenance issues. In addition, because of its similar characteristics, a CDFIG is a strong candidate for DFIG replacement [10-15].

In this work, a perturbation observer-based SMC of CDFIG associated with MC for optimal power extraction is proposed.

Corresponding author: Amar Maafa

To govern the active and reactive power injection to the electrical power grid via the WPGS, controllers with dynamical variable structure and adaptive control are applied. The purpose of this of this technology is to achieve chatter-free fractional order SMC as well as decoupled active and reactive power regulation in the stator. The three-phase MC is among the recent generations of the conventional direct-power AC-AC converter. There are nine bidirectional switches in total. The MC has various advantages over traditional AC-AC converter topologies, including the ability to reverse the power flow via the MC, i.e. it can operate in all four quadrants of the voltage-current plane, allowing it to operate with both modes, either with a generator or with a motor. Assuming hypothetical zero-loss switches, the instantaneous power input should be equalized to the power output due to the lack of energy storage devices. On the other hand, it is not required that the input and output reactive powers are in agreement. On the MC inputs and depending on the load to be supplied, it is possible to modify and preset the phase angle between the voltages and currents, which does not have to be the same as the output [16-18].

The extensive research on MC began with [19]. This method was founded on a duty-cycle matrix technics and it is introduced using time domain quantities. SVM is a modulation solution, based on the representation of space vectors in complex space [20-22]. Direct SVM (DSVM) [23] and Indirect SVM (ISVM) [24] are two techniques that have been developed. The ISVM approach is investigated in this study. ISVM is a modulation approach that divides the input current and output voltage control into two phases. To regulate the entire MC, two transfer matrices are required, and the well-known SVM approach is used for the rectifying and inverting stages respectively [14].

II. DESCRIPTION OF THE WPGS

The direct MC is made up of 9 bidirectional switches that allow any input phase a, b, c to be connected to any output phase A, B, C. According to Figure 1, each output phase contains a set of 3 switches connected to the 3 input phases. The sinusoidal output voltage with variable frequency and/or magnitude must be calculated from the input voltages defined by a constant frequency and magnitude [14]. There are 2 major limitations on how an MC may operate: (a) no short circuits are permitted in the 3 input phases and (b) no circuits with 3 output phases may ever be opened [25].

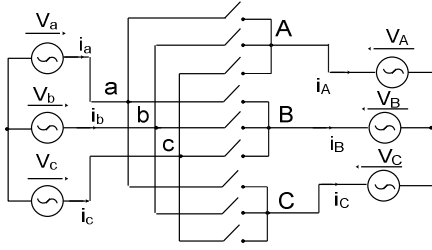


Fig. 1. Matrix converter topology.

A. Space Vector Modulation (SVM)

The MC is represented as a two-level converter connected by an imaginary DC link in order to employ the SVPWM: the first level acts as an input rectifier with the current link and the second level acts as an output voltage source inverter [17, 26]. For further information, the interested reader is directed to [2, 21-27].

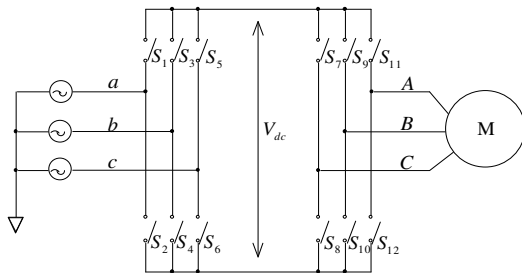


Fig. 2. Power circuit topology of the 3x3 IMC.

B. SVM for the Rectifier Stage

The following transformation is used to describe the input current space vector I_{in} as a space vector:

$$I_{in} = \frac{2}{3} (I_a + I_b e^{j\frac{2\pi}{3}} + I_c e^{-j\frac{2\pi}{3}}) \quad (1)$$

The neighboring switching vectors I_γ and I_δ are multiplied with the corresponding duty cycles d_γ and d_δ to create I^* .

$$I^* = d_\gamma I_\gamma + d_\delta I_\delta \quad (2)$$

Figure 3 shows the reference current vector synthesis.

C. SVM For the Inverter Stage

The output voltage vector is represented as:

$$V_{out} = \frac{2}{3} (V_A + V_B e^{j\frac{2\pi}{3}} + V_C e^{-j\frac{2\pi}{3}}) \quad (3)$$

Two consecutive switching vectors v_α and v_β with duty cycles d_α and d_β synthesize the reference output voltage space vector as follows:

$$V^* = d_\alpha v_\alpha + d_\beta v_\beta \quad (4)$$

The active vectors' duty cycle is computed as:

$$\begin{cases} d_\alpha = \frac{T_\alpha}{T_s} = m_v \sin(\frac{\pi}{3} - \theta_v) \\ d_\beta = \frac{T_\beta}{T_s} = m_v \sin(\theta_v) \\ d_0 = \frac{T_0}{T_s} = 1 - (d_\alpha + d_\beta) \end{cases} \quad (5)$$

where θ_v represents the angle between the reference voltage vector and the actual hexagon sector. The appropriate voltage transmission ratio is determined by the voltage adjustment indicator denoted as m_v [28]. In this application, for all MC bidirectional switches, it is necessary to create a single modulation mechanism from the two separate space vector modulations.

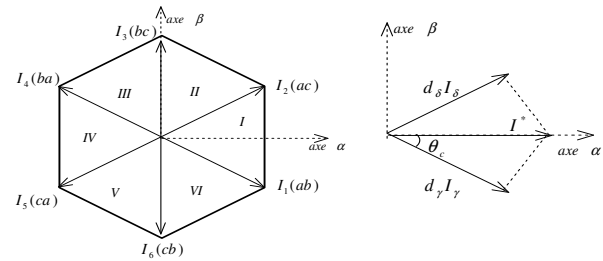


Fig. 3. Reference current vector synthesis.

D. Model of CDFIG

The CDFIG consists of 2 induction generators, with p1 and p2 being their pole-pairs, connected in cascade to remove the brushes and copper rings in the Conventional Doubly Fed Induction Machine (DFIM) [2, 13, 29]. Figure 4 shows the mechanical and electric coupling of two wound rotors. In a synchronously rotating d-q frame, the mathematical model of the electrical machine is detailed in [2]. The purpose of the choosing of a d-q reference frame where the d-axis is in agreement with the first stator flux is to have its quadrature component equal to zero [18].

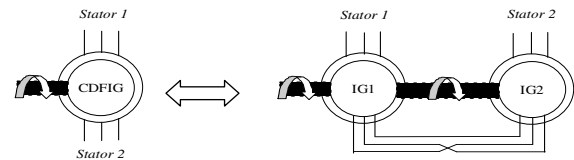


Fig. 4. Mechanical and electric coupling of two IG equivalents to the CDFIG.

The second stator's active and reactive powers, voltages, and currents can be written in accordance with the rotor currents as follows:

$$\begin{cases} v_{ds2} = R_{s2}i_{ds2} + (L_{s2} - C \cdot L_{m2}) \frac{di_{ds2}}{dt} \\ \quad - s \cdot \omega_s (L_{s2} - C \cdot L_{m2}) \cdot i_{qs2} \\ v_{qs2} = R_{s2}i_{qs2} + (L_{s2} - C \cdot L_{m2}) \frac{di_{qs2}}{dt} \\ \quad + s \cdot \omega_s (L_{s2} - C \cdot L_{m2}) \cdot i_{ds2} + s \cdot \frac{L_{m1}V_s}{L_{s1}} \end{cases} \quad (6)$$

$$\begin{cases} P_{s1} = -C \cdot V_s \frac{L_{m1}}{L_{s1}} i_{qs2} \\ Q_{s1} = \frac{V_s^2}{\omega_s \cdot L_{s1}} \left(1 + \frac{C \cdot L_{m1}^2}{L_{s1} \cdot L_{m2}} \right) - C \cdot V_s \frac{L_{m1}}{L_{s1}} i_{ds2} \end{cases} \quad (7)$$

where $s = (\omega_s - (p_1 + p_2) \cdot \Omega_r) / \omega_s$ and $C = L_{m2} / (L_{r1} + L_{r2} - \frac{L_{m1}^2}{L_{s1}})$. The sliding surfaces $S(i_{ds2})$, $S(i_{qs2})$ relative to stator currents are defined as:

$$\begin{cases} S(i_{qs2}) = i_{qs2_ref} - i_{qs2} \\ S(i_{ds2}) = i_{ds2_ref} - i_{ds2} \end{cases} \quad (8)$$

For the chosen variables to converge to their reference values, both surfaces must be zero:

$$\begin{cases} \dot{S}(P) = \frac{d}{dt}(i_{qs2_ref} - i_{qs2}) = 0 \\ \dot{S}(Q) = \frac{d}{dt}(i_{ds2_ref} - i_{ds2}) = 0 \end{cases} \quad (9)$$

The control algorithm is defined by the relations:

$$\begin{cases} V_{qs2} = V_{qs2_eq} + V_{qs2_n} \\ V_{ds2} = V_{ds2_eq} + V_{ds2_n} \end{cases} \quad (10)$$

$$\begin{cases} V_{qs2_eq} = R_{s2}i_{qs2} - L_{s1} \frac{L_{s2} - CL_{m2}}{CV_s L_{m1}} \dot{P}_{s1_ref} \\ \quad - s \omega_{s1} (L_{s2} - CL_{m2}) i_{ds2} + \frac{L_{m1}}{L_{s1}} C s V_s \\ V_{qs2_n} = K_1 (L_{s2} - CL_{m2}) \operatorname{sgn}(S(i_{qs})) \end{cases} \quad (11)$$

$$\begin{cases} V_{qs2_eq} = R_{s2}i_{qs2} - L_{s1} \frac{L_{s2} - CL_{m2}}{CV_s L_{m1}} \dot{P}_{s1_ref} \\ \quad - s \omega_{s1} (L_{s2} - CL_{m2}) i_{ds2} + \frac{L_{m1}}{L_{s1}} C s V_s \\ V_{qs2_n} = K_1 (L_{s2} - CL_{m2}) \operatorname{sgn}(S(i_{qs})) \end{cases} \quad (12)$$

where V_{qs2_eq} , V_{ds2_eq} are the equivalent control voltages used to maintain the variable to be controlled on the sliding surface, V_{qs2_n} , V_{ds2_n} are switching control voltages used to check the convergence condition because the parameters of the system are imprecise. An SMC block diagram applied to the CDFIG is schematized in Figure 6 according to (11)-(12). The goal is to capture the maximum aerodynamic power without exceeding the allowable power of the converter. Furthermore, the pitch angle is raised to lose aerodynamic power when the power converter's maximum rating is reached [2]. The SMC of CDFIG with MPPT using MC is shown in Figure 8.

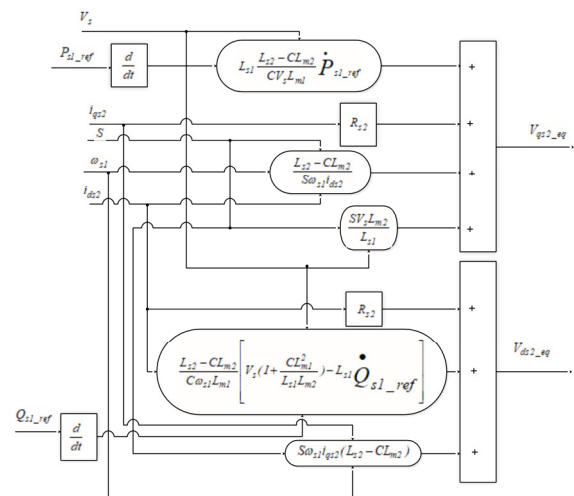


Fig. 5. The equivalent control voltage's structure.

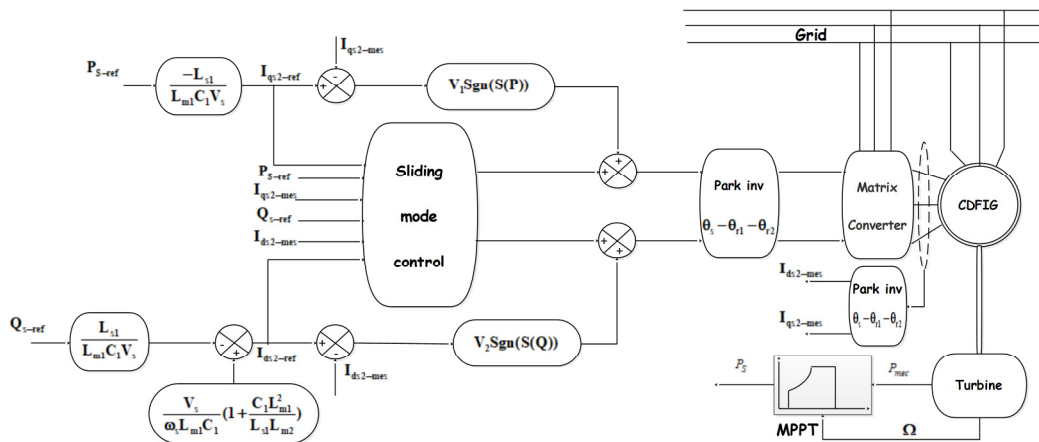


Fig. 6. Sliding mode control block diagram of the CDFIG.

III. SIMULATION RESULTS AND DISCUSSION

The proposed WPGS was realized in Matlab/Simulink environment as presented in Figure 7, according to the control block diagram illustrated in Figure 6. We employed the DFIG parameters listed in [2]. In this section, the simulation of a

direct grid connection of CDFIG through the first stator that is controlled through its second stator winding via AC/AC direct converter is presented. The considered system is controlled with the purpose to generate maximum energy while minimizing loads.

is clearly evident that a portion of the active power exceeding 1.5MW is transmitted to the grid from the second stator side of the CDFIG. The first stator's voltage and current curves are illustrated in Figure 14. As we can see, the sinusoidal current and voltage are in phase opposition as illustrated in Figure 15.

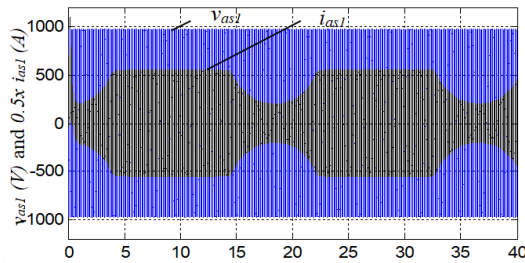


Fig. 14. First stator voltage and current.

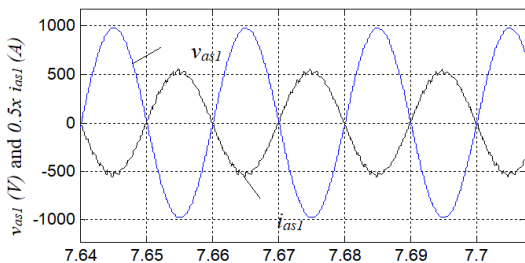


Fig. 15. Zoom first stator voltage and current.

The voltage and current curves of the second stator are depicted in Figure 16. We can conclude that according to the slip s value, the frequency of the voltage and the current change, as depicted in Figures 17 and 8. Furthermore, in the case of synchronous operation mode, the slip is equal to zero and the voltage and current of the second stator have continuous forms as illustrated in Figure 19.

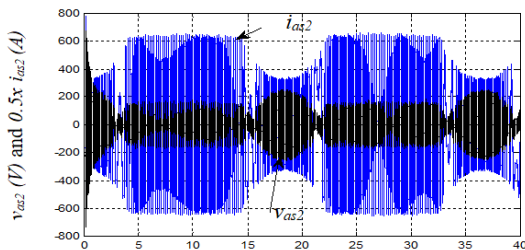


Fig. 16. Second stator voltage and current.

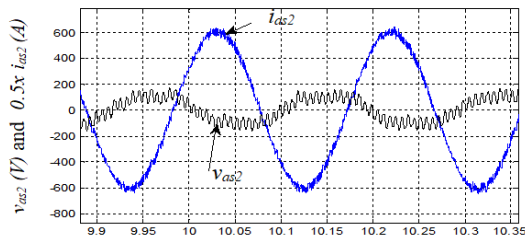


Fig. 17. Zoom second stator voltage and current ($S > 0$).

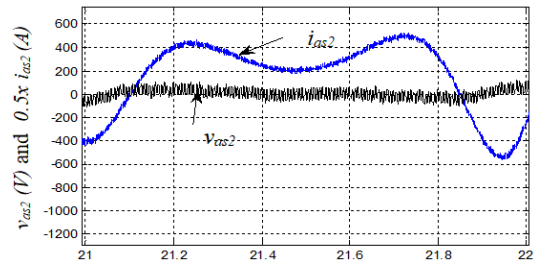


Fig. 18. Zoom second stator voltage and current ($S = 0$).

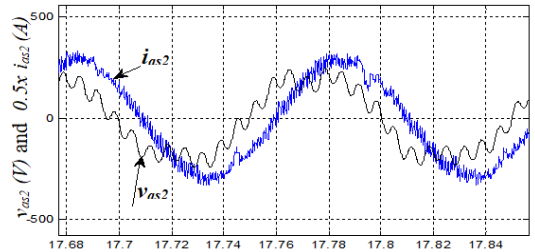


Fig. 19. Zoom second stator voltage and current ($S < 0$).

Many studies have dealt with DFIG control issues for several applications and many approaches have been proposed [30-35]. A very interested work is proposed in [30], where the authors propose SMC and an update of SMC, called terminal SMC to control the output voltage of CDFIG. Authors in [31] present a grid synchronization method founded on SMC for sub- and super-synchronous mode. A promising technique called super twisting sliding mode control was applied in [32-34] with the purpose of power control. All these works ignore pitch control and the CDFIG is not supplied via an MC. In contrast, authors in [35] use SMC with an MC but for a motor application.

IV. CONCLUSION

In this paper, an SMC for indirect field-oriented CDFIG associated with MC was proposed. The suggested SMC is intended to lower chattering phenomena levels, and this has been confirmed by the simulation results of a nonlinear controlled system. The recommended MC was simulated, and the results demonstrate that it is capable of controlling the secondary side voltage and frequency even in an operational situation with bidirectional power flow. The goal of the pitch controller is to capture the maximum aerodynamic power without exceeding the power allowable of the converter. The results of the simulation showed that the active and reactive powers closely match their reference values. A near unity input power factor has been achieved by carefully managing MC's input power factor. The lack of any energy storage element in MC preserves and prolongs the life of the proposed structure. The wind speed is applied in such a way, as to have the three operating modes of the WT, namely synchronous, hyper-synchronous, and hypo-synchronous. The results obtained in this study can be found with DFIG instead of CDFIG, but CDFIG has the advantages of reducing the maintenance cost, eliminating the contacts between copper rings and brushes, and reducing the size of the gearbox in the WPGS.

REFERENCES

- [1] H. Mellah, S. Arslan, H. Sahraoui, K. E. Hemsas, and S. Kamel, "The Effect of Stator Inter-Turn Short-Circuit Fault on DFIG Performance Using FEM," *Engineering, Technology & Applied Science Research*, vol. 12, no. 3, pp. 8688–8693, Jun. 2022, <https://doi.org/10.48084/etasr.4923>.
- [2] A. Maafa, D. Aouzellag, K. Ghedamsi, and R. Abdessemed, "Cascaded doubly fed induction generator with variable pitch control system," *Revue Roumaine des Sciences Techniques*, vol. 61, no. 4, pp. 361–366, 2016.
- [3] P. D. Chung, "Smoothing the Power Output of a Wind Turbine Group with a Compensation Strategy of Power Variation," *Engineering, Technology & Applied Science Research*, vol. 11, no. 4, pp. 7343–7348, Aug. 2021, <https://doi.org/10.48084/etasr.4234>.
- [4] F. Poitiers, T. Bouaouiche, and M. Machmoum, "Advanced control of a doubly-fed induction generator for wind energy conversion," *Electric Power Systems Research*, vol. 79, no. 7, pp. 1085–1096, Jul. 2009, <https://doi.org/10.1016/j.epsr.2009.01.007>.
- [5] D. Aouzellag, K. Ghedamsi, and E. M. Berkouk, "Network power flux control of a wind generator," *Renewable Energy*, vol. 34, no. 3, pp. 615–622, Mar. 2009, <https://doi.org/10.1016/j.renene.2008.05.049>.
- [6] M. Adjoudj, M. Abid, A. Aissaoui, H. Bounoua, and Y. Ramdani, "Sliding mode control of a doubly fed induction generator for wind turbines," *Revue Roumaine des Sciences Techniques*, vol. 51, no. 1, pp. 15–24, 2011.
- [7] K. Ghedamsi, D. Aouzellag, and E. M. Berkouk, "Control of wind generator associated to a flywheel energy storage system," *Renewable Energy*, vol. 33, no. 9, pp. 2145–2156, Sep. 2008, <https://doi.org/10.1016/j.renene.2007.12.009>.
- [8] A. Djoudi, S. Bacha, H. Iman-Eini, and T. Rekioua, "Sliding mode control of DFIG powers in the case of unknown flux and rotor currents with reduced switching frequency," *International Journal of Electrical Power & Energy Systems*, vol. 96, pp. 347–356, Mar. 2018, <https://doi.org/10.1016/j.ijepes.2017.10.009>.
- [9] M. Rahimi, "Improvement of energy conversion efficiency and damping of wind turbine response in grid connected DFIG based wind turbines," *International Journal of Electrical Power & Energy Systems*, vol. 95, pp. 11–25, Feb. 2018, <https://doi.org/10.1016/j.ijepes.2017.08.005>.
- [10] R. Cardenas, R. Pena, P. Wheeler, J. Clare, A. Munoz, and A. Sureda, "Control of a wind generation system based on a Brushless Doubly-Fed Induction Generator fed by a matrix converter," *Electric Power Systems Research*, vol. 103, pp. 49–60, Oct. 2013, <https://doi.org/10.1016/j.epsr.2013.04.006>.
- [11] M. El Achkar, R. Mbayed, G. Salloum, S. Le Ballois, and E. Monmasson, "Generic study of the power capability of a cascaded doubly fed induction machine," *International Journal of Electrical Power & Energy Systems*, vol. 86, pp. 61–70, Mar. 2017, <https://doi.org/10.1016/j.ijepes.2016.09.011>.
- [12] L. Bouchaoui, K. Hemsas, H. Mellah, and S. Benlahneche, "Power transformer faults diagnosis using undestructive methods (Roger and IEC) and artificial neural network for dissolved gas analysis applied on the functional transformer in the Algerian north-eastern: a comparative study," *Electrical Engineering & Electromechanics*, no. 4, pp. 3–11, Apr. 2021, <https://doi.org/10.20998/2074-272X.2021.4.01>.
- [13] K. Protsenko and D. Xu, "Modeling and Control of Brushless Doubly-Fed Induction Generators in Wind Energy Applications," *IEEE Transactions on Power Electronics*, vol. 23, no. 3, pp. 1191–1197, Feb. 2008, <https://doi.org/10.1109/TPEL.2008.921187>.
- [14] M. Moazen, R. Kazemzadeh, and M.-R. Azizian, "Mathematical modeling and analysis of brushless doubly fed reluctance generator under unbalanced grid voltage condition," *International Journal of Electrical Power & Energy Systems*, vol. 83, pp. 547–559, Dec. 2016, <https://doi.org/10.1016/j.ijepes.2016.04.050>.
- [15] M. Adamowicz and R. Strzelecki, "Cascaded doubly fed induction generator for mini and micro power plants connected to grid," in *13th International Power Electronics and Motion Control Conference*, Poznan, Poland, Sep. 2008, pp. 1729–1733, <https://doi.org/10.1109/EPEPMC.2008.4635516>.
- [16] N. Taib, B. Metidji, and T. Rekioua, "Performance and efficiency control enhancement of wind power generation system based on DFIG using three-level sparse matrix converter," *International Journal of Electrical Power & Energy Systems*, vol. 53, pp. 287–296, Dec. 2013, <https://doi.org/10.1016/j.ijepes.2013.05.019>.
- [17] N. Mohan, T. M. Undeland, and W. P. Robbins, *Power Electronics: Converters, Applications, and Design*, 3rd ed. New York, NY, USA: Wiley, 2002.
- [18] A. Djahbar, B. Benziane, and A. Zegaoui, "A Novel Modulation Method for Multilevel Matrix Converter," *Energy Procedia*, vol. 50, pp. 988–998, Jan. 2014, <https://doi.org/10.1016/j.egypro.2014.06.118>.
- [19] A. Alesina and M. G. B. Venturini, "Analysis and design of optimum-amplitude nine-switch direct AC-AC converters," *IEEE Transactions on Power Electronics*, vol. 4, no. 1, pp. 101–112, Jan. 1989, <https://doi.org/10.1109/63.21879>.
- [20] V. T. Ha, P. T. Giang, and V. H. Phuong, "T-Type Multi-Inverter Application for Traction Motor Control," *Engineering, Technology & Applied Science Research*, vol. 12, no. 2, pp. 8321–8327, Apr. 2022, <https://doi.org/10.48084/etasr.4776>.
- [21] A. Benachour, E. M. Berkouk, and M. Mahmoudi, "A new direct torque control of induction machine fed by indirect matrix converter," *Revue Roumaine des Sciences Techniques*, vol. 62, pp. 25–30, Jan. 2017.
- [22] F. Yue, P. W. Wheeler, and J. C. Clare, "Relationship of Modulation Schemes for Matrix Converters," in *3rd IET International Conference on Power Electronics, Machines and Drives - PEMD 2006*, Dublin, Ireland, Apr. 2006, pp. 266–270, <https://doi.org/10.1049/cp:20060113>.
- [23] D. Casadei, G. Grandi, G. Serra, and A. Tani, "Space vector control of matrix converters with unity input power factor and sinusoidal input/output waveforms," in *Fifth European Conference on Power Electronics and Applications*, Brighton, UK, Sep. 1993, vol. 7, pp. 170–175.
- [24] L. Huber and D. Borojevic, "Space vector modulated three-phase to three-phase matrix converter with input power factor correction," *IEEE Transactions on Industry Applications*, vol. 31, no. 6, pp. 1234–1246, Aug. 1995, <https://doi.org/10.1109/28.475693>.
- [25] P. Bunpakdee, J. Theeranan, and C. Jeraputra, "Experimental Validation of Vector Control of a Matrix Converter Fed Induction Generator for Renewable Energy Sources," *Procedia Computer Science*, vol. 86, pp. 397–400, Jan. 2016, <https://doi.org/10.1016/j.procs.2016.05.043>.
- [26] S. M. Dabour, A. S. Abdel-Khalik, S. Ahmed, A. M. Massoud, and S. M. Allam, "Common-mode voltage reduction for space vector modulated three- to five-phase indirect matrix converter," *International Journal of Electrical Power & Energy Systems*, vol. 95, pp. 266–274, Feb. 2018, <https://doi.org/10.1016/j.ijepes.2017.08.020>.
- [27] D. Varajao and R. E. Araujo, "Modulation Methods for Direct and Indirect Matrix Converters: A Review," *Electronics*, vol. 10, no. 7, Jan. 2021, Art. no. 812, <https://doi.org/10.3390/electronics10070812>.
- [28] A. Abdelrehim, S. D. Erfan, M. El-Habrouk, and K. H. Youssef, "Indirect 3D-Space Vector Modulation for Matrix Converter," *Engineering, Technology & Applied Science Research*, vol. 8, no. 2, pp. 2847–2852, Apr. 2018, <https://doi.org/10.48084/etasr.2007>.
- [29] A. Maafa, D. Aouzellag, K. Ghedamsi, and R. Abdessemed, *Modélisation et contrôle en puissance d'une cascade de deux machines asynchrones doublement alimentées (CDFIG)*. Batna, Algeria: University of Batna 2, 2010.
- [30] H. Zahedi Abdolhadi, G. Arab Markadeh, and S. Taghipour Boroujeni, "Sliding Mode and Terminal Sliding Mode Control of Cascaded Doubly Fed Induction Generator," *Iranian Journal of Electrical and Electronic Engineering*, vol. 17, no. 3, pp. 1955–1955, Sep. 2021, <https://doi.org/10.22068/IJEEE.17.3.1955>.
- [31] X. Yan and M. Cheng, "A Robust Grid Synchronization Method for Cascaded Brushless Doubly Fed Induction Generator," in *22nd International Conference on Electrical Machines and Systems*, Harbin, China, Aug. 2019, pp. 1–6, <https://doi.org/10.1109/ICEMS.2019.8922507>.
- [32] X. Yan and M. Cheng, "A Robustness-Improved Control Method Based on ST-SMC for Cascaded Brushless Doubly Fed Induction Generator,"

- IEEE Transactions on Industrial Electronics*, vol. 68, no. 8, pp. 7061–7071, Dec. 2021, <https://doi.org/10.1109/TIE.2020.3007087>.
- [33] R. Sadeghi, S. M. Madani, M. Ataei, M. R. Agha Kashkooli, and S. Ademi, "Super-Twisting Sliding Mode Direct Power Control of a Brushless Doubly Fed Induction Generator," *IEEE Transactions on Industrial Electronics*, vol. 65, no. 11, pp. 9147–9156, Aug. 2018, <https://doi.org/10.1109/TIE.2018.2818672>.
- [34] O. Moussa, R. Abdessemed, and S. Benagguene, "Super-twisting sliding mode control for brushless doubly fed induction generator based on WECS," *International Journal of System Assurance Engineering and Management*, vol. 10, no. 5, pp. 1145–1157, Oct. 2019, <https://doi.org/10.1007/s13198-019-00844-3>.
- [35] H. Wang *et al.*, "A Cascade PI-SMC Method for Matrix Converter-Fed BDFIM Drives," *IEEE Transactions on Transportation Electrification*, vol. 7, no. 4, pp. 2541–2550, Sep. 2021, <https://doi.org/10.1109/TTE.2021.3061742>.

Analysis of a Frictionless Electro Viscoelastic Contact Problem with Signorini Conditions

Abla Boulaouad

Department of Mathematics
Ferhat Abbas University Setif 1
Setif, Algeria
a_boulaouad@yahoo.fr

Abbes Ourahmoun

Institute of Optics and Precision Mechanics
Ferhat Abbas University Setif 1
Setif, Algeria
abbes.ourahmoun@univ-setif.dz

Touffik Serrar

Department of Mathematics
Ferhat Abbas University Setif 1
Setif, Algeria
touffik.serrar@univ-setif.dz

Received: 10 July 2022 | Revised: 27 July 2022 | Accepted: 31 July 2022

Abstract-This study considered a mathematical model to describe the process of a quasi-static contact between a piezoelectric body and an electrically conductive foundation. The behavior of the material was modeled with a nonlinear electro-viscoelastic constitutive law, the contact was frictionless, and the result was described with the Signorini condition. A variational formulation was derived for the problem, proving the existence and uniqueness of a weak solution of the model. The proof was based on arguments for nonlinear equations with maximal monotone operators.

Keywords-electro-viscoelastic materials; frictionless contact; Signorini conditions; maximal monotone operators; weak solution

I. INTRODUCTION

Considerable progress has been achieved recently in modeling, mathematical analysis, and numerical simulations of various contact processes and, as a result, a general mathematical theory of contact mechanics is currently emerging. Mathematical structures underlie general contact problems with different constitutive laws for materials, varied geometries, and different contact conditions, [1, 2]. The piezoelectric effect is characterized by the coupling between the mechanical and electrical properties of materials. The appearance of electric charges on some crystals submitted to the action of body forces and surface tractions was observed and their dependence on the deformation process was examined. Conversely, it was proved experimentally that the action of an electric field on the crystals may generate strain and stress. A deformable material having such behavior is called a piezoelectric material. Piezoelectric materials are used extensively as switches in many engineering systems such as radio electronics, electro acoustics, and measuring equipment. Some general models for electro-elastic materials can be found

in [3, 4]. A static frictional contact problem for electro-elastic materials was considered in [5, 6].

II. NOTATIONS AND PRELIMINARIES

This study considered a body made of a piezoelectric material that occupies the domain with a smooth boundary $\partial\Omega=\Gamma$ and a unit normal ν . A body force of f_0 density acts on the body and has volume-free electric charges of q_0 density, constrained mechanically and electrically on the boundary. To describe these conditions, a partition of Γ was considered into three open disjoint parts Γ_1, Γ_2 , and Γ_3 . A partition of $\Gamma_1 \cup \Gamma_2$ was in two open parts Γ_a and Γ_b . It was assumed that $meas\Gamma_1 > 0$ and $meas\Gamma_a > 0$. The spatial and time variables were denoted as $x \in \Omega \cup \Gamma$ and $t \in [0, T]$ respectively. The body was clamped on Γ_1 and the displacement field vanished there. Surface tractions of density f_2 act on Γ_2 . It was also assumed that the electrical potential vanishes on Γ_a and a surface-free electrical charge of density q_2 is prescribed on Γ_b . The notation S^d was used for the space of second-order symmetric tensors on \mathbb{R}^d , while \cdot and $\|\cdot\|$ represent the inner product and the Euclidean norm on S^d and \mathbb{R}^d respectively, where:

$$\begin{aligned} u \cdot v &= u_i v_i, \quad \|v\| = (v \cdot v)^{\frac{1}{2}}, \quad \forall u, v \in \mathbb{R}^d \\ \sigma \cdot \tau &= \sigma_{ij} \tau_{ij}, \quad \|\sigma\| = (\sigma \cdot \sigma)^{\frac{1}{2}}, \quad \forall \sigma, \tau \in S^d \end{aligned} \quad (1)$$

where $i, j=1, \dots, d$. The summation over repeated indices is used and the index which follows a comma indicates a partial derivative. Let $\Omega \subset \mathbb{R}^d$ be a bounded domain, $x = (x_i)$ a point in $\Omega \cup \Gamma$, while $\nu = \nu_i$ denotes the outward unit normal at Γ . Also, the inner products on the Hilbert spaces $L^2(\Omega)^d$ and $L^2(\Gamma)^d$ are given by:

$$(u, v)_{L^2(\Omega)^d} = \int_{\Omega} u \cdot v dx ; (u, v)_{L^2(\Gamma)^d} = \int_{\Gamma} u \cdot v da \quad (2)$$

The associated norms will be denoted by $\|\cdot\|_{L^2(\Omega)^d}$ and $\|\cdot\|_{L^2(\Gamma)^d}$ respectively. The closed subspace of $H^1(\Omega)^d$ is defined by:

$$V = \{v \in H^1(\Omega)^d : v = 0 \text{ on } \Gamma_1\} \quad (3)$$

$$Q = \{\tau = (\tau_{ij}) / \tau_{ij} \in L^2(\Omega)^d : \tau_{ij} = \tau_{ji}\} \quad (4)$$

which are Hilbert spaces with the following scalar products:

$$(u, v)_V = \int_{\Omega} \varepsilon(u) \cdot \varepsilon(v) dx, (\sigma, \tau)_Q = \int_{\Gamma} \sigma \cdot \tau dx \quad (5)$$

The associated norms are $\|\cdot\|_V$ and $\|\cdot\|_Q$, respectively. The deformation tensor $\varepsilon : H^1(\Omega)^d \rightarrow Q$ is given by:

$$\varepsilon(v) = (\varepsilon_{ij}(v)), \varepsilon_{ij}(v) = \frac{1}{2}(v_{ij} + v_{ji}); \forall v \in H^1(\Omega)^d \quad (6)$$

Therefore $(V, \|\cdot\|_V)$ is a real Hilbert space. Moreover, by Sobolev's trace theorem, a constant C_0 exists which depends only on Ω , Γ_1 , and Γ_3 such that:

$$\|v\|_{L^2(\Gamma_3)^d} \leq C_0 \|v\|_V, \forall v \in V \quad (7)$$

given a Hilbert space X , for a function $\phi : X \rightarrow]-\infty, +\infty]$:

$$\text{Dom}(\phi) = \{u \in X : \phi(u) \neq \infty\},$$

$$\partial\phi u = \{f \in X : \phi(v) - \phi(u) \geq (f, v - u), \forall u, v \in X\}.$$

so, the following existence and uniqueness result can be concluded:

Lemma: Let X be a real Hilbert space and let $\phi : X \rightarrow]-\infty, +\infty]$ be a convex proper lower semicontinuous function. Then for every $f \in L^2(0, T, X)$ and $u_0 \in \text{Dom}(\phi)$, a unique function $u \in W^{1,2}(0, T, X)$ exists which satisfies:

$$\begin{aligned} \dot{u}(t) + \partial\phi u(t) \ni f(t), \text{ a.e. } t \in (0, T), \\ u(0) = u_0. \end{aligned} \quad (8)$$

More details can be found in [7].

III. PROBLEM STATEMENT

This section describes the process model and clarifies the assumptions about the data. The process starts from the physical framework, and the law of behavior and the conditions of contact should be specified. It was supposed that the body was electro-viscoelastic, rested on a rigid foundation by the part Γ_3 of its border, this contact was affected without friction, and the tangential movements were completely free. Additionally, as the quasistatic case was studied, the body Ω had a behavior law of the form of (9), see [8-10]. Under these considerations, the studied mechanical problem can be formulated as follows:

Problem 1. Find the displacement field $u : \Omega \times \mathbb{R}_+ \rightarrow \mathbb{R}^d$, the stress field $\sigma : \Omega \times \mathbb{R}_+ \rightarrow S^d$, the electric potential $\varphi : \Omega \times [0, T] \rightarrow \mathbb{R}$, and the electrical displacements field $D : \Omega \times [0, T] \rightarrow \mathbb{R}^d$, such that:

$$\sigma = \mathcal{A}\varepsilon(u) + \mathcal{F}\varepsilon(u) - \varepsilon^* E(\varphi) \text{ in } \Omega \times (0, T) \quad (9)$$

$$D = \mathcal{E}(u) + \beta E(\varphi) \text{ in } \Omega \times (0, T) \quad (10)$$

$$\text{Div} \sigma + f_0 = 0 \text{ in } \Omega \times (0, T) \quad (11)$$

$$\text{div} D = q_0 \text{ in } \Omega \times (0, T) \quad (12)$$

$$u = 0 \text{ on } \Gamma_1 \times (0, T) \quad (13)$$

$$\sigma_v = f_2 \text{ on } \Gamma_2 \times (0, T) \quad (14)$$

$$\begin{cases} u_v \leq 0, \sigma_v \leq 0 \\ u_v \sigma_v = 0, \sigma_\tau = 0 \end{cases} \text{ on } \Gamma_3 \times (0, T) \quad (15)$$

$$\varphi = 0 \text{ on } \Gamma_a \times (0, T) \quad (16)$$

$$D \cdot v = q_2 \text{ on } \Gamma_b \times (0, T) \quad (17)$$

$$u = u_0 \text{ in } \Omega \quad (18)$$

Equations (9) and (10) represent the constitutive electro-viscoelastic law, (11) and (12) represent the equilibrium equations, (13) and (14) are the boundary conditions in displacement and traction respectively. The boundary condition (15) represents the conditions of contact without Signorini friction, (16) and (17) are the electrical boundary conditions, and (18) represents the initial condition. It should be noted that $\sigma = (\sigma_{ij})$ is the stress tensor, $\varepsilon(u)$ denotes the linearized strain tensor, \mathcal{A} and $\mathcal{E} = (e_{ijk})$ represent the third-order piezoelectric tensor, \mathcal{E}^* is its transpose, $\beta = (b_{ij})$ denote the electric permittivity tensor, and $D = (D_1, \dots, D_d)$ is the electric displacement vector. The tensors \mathcal{E} and \mathcal{E}^* satisfy:

$$\mathcal{E} \sigma \cdot v = \sigma \cdot \mathcal{E}^* v; \forall (\sigma_{ij}) \in S^d, v \in \mathbb{R}^d$$

and Div and div denote the divergence operator for tensor and vector-valued function. For the electric displacement field, two Hilbert spaces were used.

$$\mathcal{W} = L^2(\Omega)^d; \mathcal{W}^1 = \{D \in \mathcal{W} : \text{div} D \in L^2(\Omega)\}$$

endowed with the inner products:

$$(D, E)_{\mathcal{W}} = \int_{\Omega} D_i E_i dx$$

$$(D, E)_{\mathcal{W}^1} = (D, E)_{\mathcal{W}} + (\text{div} D, \text{div} E)_{L^2(\Omega)}$$

The electric potential field was defined by:

$$\mathcal{W} = \{\psi \in H^1(\Omega) : \psi = 0 \text{ on } \Gamma_a\}$$

Since $\text{meas} \Gamma_a > 0$ the Friedrichs-Poincaré inequality holds, thus:

$$\|\nabla \psi\|_{\mathcal{W}} \geq c_F \|\psi\|_{H^1(\Omega)}; \forall \psi \in \mathcal{W}.$$

The assumptions on the problem data were listed for the study of problem \mathcal{P} . Then, the viscosity \mathcal{A} , the operator of elasticity \mathcal{F} , the piezoelectric tensor \mathcal{E} , and the electric permittivity tensor β satisfy the following properties:

$$\begin{cases} (a). \mathcal{A} = (a_{ijkl}) : \Omega \times S^d \rightarrow S^d \\ (b). a_{ijkl} = a_{lijlk} \in L^2(\Omega) \\ (c). \text{There exist } m_A > 0 \text{ such that} \\ a_{ijkh} \tau_{ijkh} \geq m_A \|\tau\|^2; \forall \tau \in S^d, \text{ a.e. } x \in \Omega \end{cases} \quad (19)$$

$$\left\{ \begin{array}{l} (a). \mathcal{F} : \Omega \times S^d \rightarrow S^d. \\ (b). \text{There exist } L_{\mathcal{F}} > 0 \text{ such that} \\ \|\mathcal{F}(x, \varepsilon_1) - \mathcal{F}(x, \varepsilon_2)\| \leq L_{\mathcal{F}} \|\varepsilon_1 - \varepsilon_2\|, \\ \forall \varepsilon_1, \varepsilon_2 \in S^d, a. e. x \in \Omega. \\ (c). \text{The mapping } x \rightarrow \mathcal{F}(x, \varepsilon) \\ \text{is measurable on } \Omega, \forall \varepsilon \in S^d, \\ (d). \text{The mapping } x \rightarrow \mathcal{F}(x, 0) \in \mathcal{H}. \end{array} \right. \quad (20)$$

$$\left\{ \begin{array}{l} (a). \mathcal{E} = (e_{ijk}) : \Omega \times S^d \rightarrow \mathbb{R}^d \\ e_{ijk} = e_{ikj} \in L^\infty(\Omega) \end{array} \right. \quad (21)$$

$$\left\{ \begin{array}{l} (a). \beta = (\beta_{ij}) : \Omega \times \mathbb{R}^d \rightarrow \mathbb{R}^d. \\ \beta_{ij} = \beta_{ji} \in L^\infty(\Omega). \\ (b). \text{There exist } m_\beta > 0 \text{ such that} \\ \beta_{ij} E_i E_j \geq m_\beta \|E\|^2 \\ \forall E \in \mathbb{R}^d, p. p. x \in \Omega \end{array} \right. \quad (22)$$

The densities of body forces and surface tractions have regularity:

$$f_0 \in W^{1,1}(0, T; L^2(\Omega)^d), f_2 \in W^{1,1}(0, T; L^2(\Gamma_2)^d) \quad (23)$$

and surface free charge densities satisfy:

$$q_0 \in W^{1,1}(0, T; L^2(\Omega)), q^2 \in W^{1,1}(0, T; L^2(\Gamma_a)) \quad (24)$$

$$q_2(t) = 0 \text{ on } \Gamma_3; \forall t \in [0, T] \quad (25)$$

Condition (19) allows providing the space V with the scalar product and the associated norm defined by:

$$(u, v)_V = (\mathcal{A}\varepsilon(u), \mathcal{A}\varepsilon(v))_{\mathcal{H}}; \|u\|_V = \sqrt{(u, u)_V} \quad (26)$$

This norm on V is equivalent to that of $H^1(\Omega)^d$. Convex K which will be the space of admissible displacements, i.e. compatible with the connections (boundary conditions and unilateral conditions):

$$K = \{v \in V; v \leq 0 \text{ on } \Gamma_3\} \quad (27)$$

Finally, the following assumption was made:

$$u_0 \in K \quad (28)$$

For the rest, the following functional space was considered:

$$W = \{\psi \in H^1(\Omega) \mid \psi = 0 \text{ on } \Gamma_a\}$$

The operator A was said to be maximal monotone if it is monotone and if for all x and y in space X :

$$\langle y - A\zeta, x - \zeta \rangle \geq 0 \text{ for all } \zeta \in \text{dom}(A) \Rightarrow y \in Ax$$

Now all the necessary ingredients are available to provide a weak formulation of problem \mathcal{P} and present the main result of the existence and uniqueness of the weak solution.

IV. VARIATIONAL FORMULATION

This section starts by giving a variational formulation in terms of displacement and electric potential. Once this weak formulation is established, a result of the existence and uniqueness of the weak solution emerges:

Let $f : [0, T] \rightarrow V$ et $q : [0, T] \rightarrow W$ be the functional

$$(f(t), v)_V = \int_{\Omega} f_0(t) \cdot v dx + \int_{\Gamma_2} f_2(t) \cdot v da \quad (29)$$

$$(q(t), \psi)_W = \int_{\Omega} q_0(t) \cdot \psi dx - \int_{\Gamma_2} q_2(t) \cdot \psi da \quad (30)$$

for all $v \in V, \psi \in W, t \in [0, T]$. The conditions (23) and (24) imply:

$$f \in W^{1,1}(0, T; V), q \in W^{1,1}(0, T; W) \quad (31)$$

Using Green's formula and assuming that (u, σ, ϕ, D) are regular functions satisfying (11) and (17):

$$u(t) \in K, (\sigma(t), \varepsilon(v) - \varepsilon(u(t)))_H \geq (f(t), u(t) - v)_V \quad (32)$$

$$(D(t), \nabla \psi)_{L^2(\Omega)^d} + (q(t), \psi)_W = 0 \quad (33)$$

for all $v \in K, \psi \in W$ and $t \in [0, T]$. Now, putting (9) in (32), (10) in (33), and keeping in mind that $E(\phi) = -\nabla \phi$ as well as the initial condition (18), the variational formulation of the mechanical problem \mathcal{P} can be obtained in terms of displacement and electric potential following:

Problem 2: Find the displacement field $u : [0, T] \rightarrow V$ and electric potential $\phi : [0, T] \rightarrow W$ such that:

$$\left\{ \begin{array}{l} u(t) \in K, (\mathcal{A}\varepsilon(\dot{u}(t)), \varepsilon(v) - \varepsilon(u(t)))_{\mathcal{H}} + \\ (\mathcal{F}\varepsilon(u(t)), \varepsilon(v) - \varepsilon(u(t)))_{\mathcal{H}} + \\ (E^* \nabla \phi(t), \varepsilon(v) - \varepsilon(u(t)))_{\mathcal{H}} \geq (f(t), v - u(t))_V \\ \forall v \in K, p. p. t \in [0, T], \end{array} \right. \quad (34)$$

$$\left\{ \begin{array}{l} (\beta \nabla \phi(t), \nabla \psi)_{L^2(\Omega)^d} - (\varepsilon \varepsilon(u(t)) - \nabla \psi)_{L^2(\Omega)^d} = \\ (q(t), \psi)_W; \forall \psi \in W, \forall t \in [0, T], \end{array} \right. \quad (35)$$

$$u(0) = u_0 \quad (36)$$

The well-posedness of the above \mathcal{P}^V problem is examined in the next section.

V. EXISTENCE RESULT

This section states and proves the existence and the uniqueness of the result.

Theorem 1: Assume that (19), (25), and (28) are verified. Then the variational problem \mathcal{P}^V has a unique solution (u, ϕ) , having the regularity:

$$u \in W^{1,\infty}(0, T; V), \phi \in W^{1,\infty}(0, T; W) \quad (37)$$

A quadruplet (u, σ, ϕ, D) satisfying the (9) and (10) is called a weak solution to the mechanical problem \mathcal{P} . It can be concluded from Theorem 1 that problem \mathcal{P} admits a unique solution. Regarding the regularity of the weak solution, it follows to refer to the regularity of the element $(u, \phi) \in W^{1,\infty}(0, T; V) \times W^{1,\infty}(0, T; W)$, to the constitutive laws (9) and (10), and also to the hypotheses (19) and (22). Then:

$$\sigma \in L^\infty(0, T; H), D \in L^\infty(0, T; L^2(\Omega)^d)$$

Now, taking $v = u(t) \pm z$, where $z \in C_0^\infty(\Omega)^d$ in (32) and $\psi \in C_0^\infty(\Omega)$ in (33), and using the notations (29) and (30) we get:

$$\text{Div}\sigma(t) + f_0(t) = 0, \text{div}D(t) = q_0(t)$$

for all $t \in [0, T]$. From (23) and (18), it follows that $\text{Div}\sigma \in L^\infty(0, T; L^2(\Omega)^d)$ and $\text{div}D \in L^\infty(0, T; L^2(\Omega))$, and therefore:

$$\sigma \in L^\infty(0, T; \mathcal{H}_1), D \in L^\infty(0, T; W) \quad (38)$$

So, it is concluded that the solution (u, σ, ϕ, D) of problem \mathcal{P} will have regularity (37) and (38).

Proof: The abstract result will be used to obtain the existence and the uniqueness of the solution. For that, let's suppose in the continuation that the hypotheses (19), (25), and (28) are verified. Using the Riesz representation theorem, the operators $\mathcal{B}: W \rightarrow W$ and $\mathcal{C}: V \rightarrow W$ are defined as follows:

$$(\mathcal{B}\varphi, \psi)_W = (\beta \nabla \phi, \nabla \psi)_{L^2(\Omega)^d} \quad (39)$$

$$(\mathcal{C}v, \varphi)_W = (\mathcal{E}\varepsilon(v), \nabla \varphi)_{L^2(\Omega)^d} \quad (40)$$

for all $\varphi, \psi \in W, v \in V$. From (22), it is deduced that \mathcal{B} is a linear, symmetric, and positive operator. Consequently, \mathcal{B} is a revertible and continuous operator on W . Now, using (26) and (21), it follows that \mathcal{C} is a linear and continuous operator on V . Let $\mathcal{C}^*: W \rightarrow V$ be the adjoint of \mathcal{C} . So:

$$(\mathcal{C}^*\varphi, v)_V = (E^*\nabla\phi, \varepsilon(v))_H; \forall v \in V, \varphi \in W \quad (41)$$

Let $t \in [0, T]$. By putting (39) and (40) in (35) we have:

$$(\varphi(t), \psi)_W = (\mathcal{C}u(t), \psi)_W + (q(t), \psi)_W, \forall \psi \in W$$

Consequently,

$$\varphi(t) = \mathcal{C}u(t) + q(t)$$

On the other hand, $\mathcal{B}: W \rightarrow W$ is invertible. The previous equation then becomes:

$$\phi(t) = \mathcal{B}^{-1}\mathcal{C}u(t) + \mathcal{B}^{-1}q(t) \quad (42)$$

Using (42) in (34) and the definitions of operators $\mathcal{B}, \mathcal{C}, \mathcal{C}^*$ given by (39-41) we get:

$$\begin{aligned} u(t) \in K, & \left(\mathcal{A}\varepsilon(\dot{u}(t)), \varepsilon(v) - \varepsilon(u(t)) \right)_{\mathcal{H}} + \\ & \left(\mathcal{F}\varepsilon(u(t)), \varepsilon(v) - \varepsilon(u(t)) \right)_{\mathcal{H}} + \\ & (\mathcal{C}^*\mathcal{B}^{-1}\mathcal{C}u(t), v - u(t))_V \geq (f(t) - \mathcal{B}^{-1}q(t), v - u(t))_V \\ & \forall v \in V, p.p. t \in [0, T] \end{aligned} \quad (43)$$

Let the operator $L: V \rightarrow V$ be defined by:

$$L(v) = \mathcal{C}^*\mathcal{B}^{-1}\mathcal{C}(v); \forall v \in V \quad (44)$$

and keeping in mind the properties of the operators \mathcal{B}, \mathcal{C} , and \mathcal{C}^* , it is deduced that L is a linear operator, continuous on V .

$$\|Lu_1 - Lu_2\|_V \leq \|L\| \|u_1 - u_2\|_V; \forall u_1, u_2 \in V \quad (45)$$

$\mathcal{G}: V \rightarrow V$ denotes the operator based on the representation of Riesz given by:

$$(\mathcal{G}u, v)_V = (\mathcal{F}\varepsilon(u), \varepsilon(v))_{\mathcal{H}} + (Lu, v)_V; \forall u, v \in V \quad (46)$$

Now, taking into account (19), (20), (26), and (46) we have:

$$\|\mathcal{G}u^1 - \mathcal{G}u^2\|_V \leq \left(\frac{L_{\mathcal{F}}}{m_{\mathcal{A}}} + \|L\| \right) \|u^1 - u^2\|_V, \forall u_1, u_2 \in V \quad (47)$$

This relation proves that the \mathcal{G} is a Lipschitz operator. Now, let the function $f: [0, T] \rightarrow V$ given by:

$$\mathcal{F}(t) = f(t) - \mathcal{C}^*\mathcal{B}^{-1}q(t); \forall t \in [0, T] \quad (48)$$

Using (39) and the fact that $\mathcal{C}^*\mathcal{B}^{-1}$ is linear and continuous, it comes by observing (48) that:

$$f \in W^{1,1}(0, T; V) \quad (49)$$

On the other hand, the operator:

$$\mathcal{G} + \left(\frac{L_{\mathcal{F}}}{m_{\mathcal{A}}} + \|L\| \right) I: V \rightarrow V \quad (50)$$

is a Lipschitz operator on V .

Now, the indicator function $\psi_K: V \rightarrow]-\infty, +\infty]$ of the set K is introduced as well as its sub-differential $\partial\psi_K$. Being the set K non-empty, closed, and convex, the sub-differential $\partial\psi_K$ is a strongly monotone operator on the space V . The domain of this sub-differential is thus: $D(\partial\psi_K) = K$. It can be said that the sum:

$$\partial\psi_K + \mathcal{G} + \left(\frac{L_{\mathcal{F}}}{m_{\mathcal{A}}} + \|L\| \right) I: K \subset V \rightarrow 2^V$$

is a strongly monotone operator. Being the hypotheses (49) and (28) satisfied, (8) can be applied with:

$$X = V; A = \partial\psi_K + \mathcal{G}; D(A) = K \subset V \rightarrow 2^V$$

and:

$$\omega = \frac{L_{\mathcal{F}}}{m_{\mathcal{A}}} + \|L\|$$

This result deduces that there is a unique element $u \in W^{1,\infty}(0, T; V)$ which verifies:

$$\dot{u}(t) + \partial\psi_K(u(t)) + \mathcal{G}u(t) \ni f(t) \text{ p.p. } t \in (0, T) \quad (51)$$

and:

$$u(0) = u_0 \quad (52)$$

In addition, for all $g \in V$ there is the equivalence:

$$g \in \partial\psi_K(u) \Leftrightarrow u \in K, (g, v - u)_V; \forall v \in K$$

The differential inclusion (51) is equivalent to the variational inequality:

$$\begin{aligned} u(t) \in K, & (\dot{u}(t), v - u(t))_V + (\mathcal{G}u(t), v - u(t))_V \\ & \geq (f(t), v - u(t))_V \forall v \in K, p.p. t \in (0, T). \end{aligned} \quad (53)$$

From (53), (46), and (26) comes that u satisfies the inequality:

$$\begin{aligned} u(t) \in K, & (\mathcal{A}\varepsilon(\dot{u}(t)), \varepsilon(v) - \varepsilon(u(t)))_{\mathcal{H}} \\ & + (\mathcal{F}\varepsilon(u(t)), \varepsilon(v) - \varepsilon(u(t)))_{\mathcal{H}} + (Lu(t), v - u(t))_V \\ & \geq (f(t), v - u(t))_V; \forall v \in K, p.p. t \in (0, T). \end{aligned} \quad (54)$$

From (53), (46), (44), and (48), it is concluded that u satisfies (43). Let φ be the function given by (42). Using (43), (52), and (42), it follows that (u, φ) is the solution to the variational problem \mathcal{P}^V . Regarding the regularity of the function φ , it follows to refer to the regularity of the element

$u \in W^{1,\infty}(0, T; V)$ and to the hypotheses (42) and (31). Then it is obtained that function φ has the regularity $\varphi \in W^{1,\infty}(0, T; W)$.

A solution (u, φ) of regularity $u \in W^{1,\infty}(0, T; V)$, $\varphi \in W^{1,\infty}(0, T; W)$ was just shown. The uniqueness part of the function φ is deduced from the uniqueness of the function $u \in W^{1,\infty}(0, T; V)$ solution of (51) and (53) given by Lemma 1, thus taking into account (42).

VI. CONCLUSION

This paper investigated a mathematical model to describe the quasistatic contact between a piezoelectric body and a deformable foundation. The contact was frictionless and described with Signorini conditions. The proof of the existence and the uniqueness of the weak solution was presented using a classical result of elliptic variational inequalities and a maximal monotone operator.

REFERENCES

- [1] Y. Letoufa, H. Benseridi, S. Boulaaras, and M. Dilmi, "On the asymptotic behavior of solutions of anisotropic viscoelastic body," *Boundary Value Problems*, vol. 2021, no. 1, Nov. 2021, Art. no. 89, <https://doi.org/10.1186/s13661-021-01567-w>.
- [2] R. D. Mindlin, "Elasticity, piezoelectricity and crystal lattice dynamics," *Journal of Elasticity*, vol. 2, no. 4, pp. 217–282, Dec. 1972, <https://doi.org/10.1007/BF00045712>.
- [3] S. Drabla and Z. Zellagui, "Analysis of a Electro-Elastic Contact Problem with Friction and Adhesion," *Mathematica*, vol. 24, no. 1, pp. 75–99, Mar. 2009.
- [4] O. Chau, M. Shillor, and M. Sofonea, "Dynamic frictionless contact with adhesion," *Zeitschrift für angewandte Mathematik und Physik ZAMP*, vol. 55, no. 1, pp. 32–47, Jan. 2004, <https://doi.org/10.1007/s00033-003-1089-9>.
- [5] O. Chau, J. R. Fernández, W. Han, and M. Sofonea, "Variational and numerical analysis of a dynamic frictionless contact problem with adhesion," *Journal of Computational and Applied Mathematics*, vol. 156, no. 1, pp. 127–157, Jul. 2003, [https://doi.org/10.1016/S0377-0427\(02\)00909-3](https://doi.org/10.1016/S0377-0427(02)00909-3).
- [6] S. Drabla and Z. Zellagui, "Variational Analysis and the Convergence of the Finite Element Approximation of an Electro-Elastic Contact Problem with Adhesion," *Arabian Journal for Science and Engineering*, vol. 36, no. 8, pp. 1501–1515, Dec. 2011, <https://doi.org/10.1007/s13369-011-0131-z>.
- [7] S. Migórski, A. Ochal, and M. Sofonea, *Nonlinear Inclusions and Hemivariational Inequalities: Models and Analysis of Contact Problems*. New York, NY, USA: Springer Science & Business Media, 2012.
- [8] A. Guediri, A. Guediri, and S. Touil, "Modeling and Comparison of Fuzzy-PI and Genetic Control Algorithms for Active and Reactive Power Flow between the Stator (DFIG) and the Grid," *Engineering, Technology & Applied Science Research*, vol. 12, no. 3, pp. 8640–8645, Jun. 2022, <https://doi.org/10.48084/etasr.4905>.
- [9] A. Z. Al-Khazaal and N. Ahmad, "A Study of the Impact of Iron Content on the Thermal Response of the sPP/Fe Composites," *Engineering, Technology & Applied Science Research*, vol. 12, no. 3, pp. 8555–8558, Jun. 2022, <https://doi.org/10.48084/etasr.4884>.
- [10] T. N. Le, H. M. V. Nguyen, T. A. Nguyen, T. T. Phung, and B. D. Phan, "Optimization of Load Ranking and Load Shedding in a Power System Using the Improved AHP Algorithm," *Engineering, Technology & Applied Science Research*, vol. 12, no. 3, pp. 8512–8519, Jun. 2022, <https://doi.org/10.48084/etasr.4862>.

AUTHORS PROFILE

Abla Boulaouad, M.C. of mathematics scale functional analysis option, Faculty of Technology, University Ferhat Abbas Setif 1, Algeria, and Member of the Mathematics Laboratory LAMA.

Abbes Ourahmoun, Institute of Optics and Precision Mechanics, University Ferhat Abbas Setif 1, Setif, Algeria

Touffik Serrar, Department of Mathematics, University Ferhat Abbas Setif 1, Setif, Algeria.

Assessing Critical Criteria for Historical Archeological Buildings in Iraq

Oday Hammoody Abdullah
Department of Civil Engineering
University of Baghdad
Baghdad, Iraq
10984@uotechnology.edu.iq

Wadhah Amer Hatem
Baquba Technical Institute
Middle Technical University
Baghdad, Iraq
wadhah1970wadhah@gmail.com

Received: 18 June 2022 | Revised: 13 July 2022 | Accepted: 14 July 2022

Abstract-This research was conducted to identify and evaluate the relative importance of the criteria in an archaeological building. Open and closed questionnaires were used and interviews with experts and specialists from many ministries and governorates were conducted to identify the most important criteria. The aim determines what factors influence historic archaeological building success, and which criteria should be used to determine the best response. The data were analyzed with the SPSS V25 program using the Relative Importance Index (RII) method to determine the relative importance of the considered 15 variables. RII allows the identification of the most important criteria based on responses from participants, and it is a useful tool for prioritizing indicators rated on Likert-type scales. The data were analyzed using a formula from a previous study's relative index analysis method. Providing information on a database of historic old buildings ranked first with RII = 92%, and providing information on the changes taking place in old buildings ranked second with RII = 88%.

Keywords-construction projects; historic archaeological buildings; relative importance index

I. INTRODUCTION

Architectural and art historians, historical geographers, and local historians are among those who study the environment of historical archaeological buildings [1]. Archaeological discoveries of buried structures are frequently dismissed in favor of artifacts recovered from buried deposits associated with them [2]. The original architectural and structural system of approximately 25% of structures changes by restoration [3]. As a result, in some historical archaeology overviews, the study of buildings is virtually invisible. Instead, surveys of vernacular architecture studies are being conducted [4]. Others, aware of the importance of more integrated archaeology of buildings, find such perspectives strangely limited, whether in interpretations of Neolithic Europe or descriptions of mediaeval Britain [5]. Archaeologists around the world have used a variety of methods to focus their research and cultural resource management efforts on building remains that have survived above or below ground as wall foundations, floor surfaces, or post holes over the past 40 years, despite the general lack of attention paid to the study of buildings in the mainstream historical archaeology literature. Some of this

material is reviewed in [6]. We argue that built structures are an important part of the material remains of the past 500 years and that their study should be integrated with the study of sites, artifacts, and landscapes. To quantify the relative importance indices of an exhaustive list of the criteria of historical archaeological building in Malaysia, the Relative Importance Index (RII) technique was used in [7]. The paper is divided into five sections based on the importance of historical, archaeological building factors. In this study, the RII technique was used to rank historical and archaeological building criteria [8]. The survey's findings revealed that ignorance of planning and building regulations, insufficient housing schemes, unrealistic zoning, and the location of land are important factors that influence unauthorized building sitting [9]. Data from previous related studies were analyzed using a formula for the relative index analysis method for historical/archaeological buildings. The results revealed that site maintenance ranked first (RII = 0.836), warranty clauses in contract specifications to incorporate construction quality ranked second (RII = 0.830), and construction personnel training ranked third (RII = 0.826) [10]. The RII of the main criteria in descending order in [11] is: Experience & Past Performance (EP), Financial Stability (FS), Personnel Capabilities (PC), Equipment Capabilities (EC), Managerial Capabilities (MC), Health & Safety (HS), Past Relationships (RR), and Geographic Location of contractor (GL) [11].

II. IDENTIFYING IMPORTANT CRITERIA FOR HISTORICAL ARCHEOLOGICAL BUILDINGS

Because different criteria apply to different areas, different authors considered different criteria for historical buildings. Previous research has identified a number of critical standards for historical and archaeological constructions (see Table I).

III. RESEARCH OBJECTIVES

The research objectives are:

- To determine the factors that should be examined and taken into account when recommending a historical or archaeological structure.
- Criteria ranking according to their RII values.

TABLE I. IDENTIFIED CRITERIA FROM PREVIOUS STUDIES

No.	Criterion	Symbol	Ref.
1	Providing information or a database of historical old buildings	C01	[10]
	There are differences and intersections between architectural, construction, electrical and other disciplines	C02	
	Existence of complete plans as a reality for the old buildings	C03	
2	Having a regular maintenance system	C04	[11]
	Providing a schedule to determine the times of processing materials for maintenance	C05	
3	Existence of a facility management system	C06	[12]
	Availability of specialized staff using BIM technology	C07	
	There is coordination between the members of the team that design the architectural, construction, electrical, and other specializations	C08	
4	Presence of information on the changes taking place in old buildings, including additions and removals through time	C09	[13]
	Existence of a facility management system	C10	
	Availability of specialized staff using BIM technology in the department	C11	
5	Provides 3D models of old buildings	C12	[14]
	There is documentation of information on ancient buildings	C13	
	Damage and lost items are controlled on site	C14	
	There is continuous work to improve the quality of the design	C15	

IV. RESEARCH METHODOLOGY

The following points describe briefly the methodology of the current research:

- Obtaining the necessary information and data during theoretical and field research on the study topic and using the research map to locate the historical/archaeological structure criteria.
- Using an open questionnaire to collect data from a group of experts to identify the criteria.
- Determining the criteria and selecting the study sample by using a closed questionnaire to collect data from the open questionnaire.
- Ranking the criteria with the RII method from higher to lower importance on the given scale, i.e. 1-very low, 2-low, 3-medium, 4-high, and 5-very high.

V. PILOT STUDY FOR THE CLOSED QUESTIONNAIRE FORM

A pilot study can be used to validate and evaluate closed questionnaires. Risk is vital to contractors, clients, and consultants within the construction industry; however, the problems of risk assessment are complex and poorly understood in practice [15]. A questionnaire run that includes testing of question formulation is known as a pilot study, in which the effectiveness of various data collection methods is assessed by identifying and testing the most challenging inquiries [16]. In this phase, the questions are checked for clarity and any issues that may arise are discovered. An assessment group with at least 15 years of experience was used

for this pilot study's closed questionnaire distribution. Evaluation and assessment of the validity of the closed questionnaire form was carried out by experts, who confirmed the validity and suitability of the sections of the closed questionnaire form. All suggestions and comments were collected and rated, and all suggestions and proposed changes were discussed [17].

VI. CLOSED QUESTIONNAIRE FORM DISTRIBUTION

Closed questionnaires were handed out to a selected group of participants. Fifty survey forms were collected out of 60 sent forms and some samples were excluded due to lack of data and information. In the end, 45 closed questionnaire forms were considered and analyzed.

VII. QUANTITATIVE ANALYSIS DATA

Quantitative data were gathered and analyzed using a statistical program (IBM/SPSS V25). The factors were calculated for ranking using the RII technique. RII was used to rank the importance of each recommendation provided by the respondents [18]. The RII of the criteria is calculated by [19]:

$$RII = \left(\frac{\sum W}{A \cdot N} \right) \quad (1)$$

where RII ranges from 0 to 1, W is the weight given to the factors by the responders, ranging from 1 to 5 (1 is less important and 5 is highly important), A is the total number of responses for that factor or option, and Z is the highest weight (in this case, 5).

VIII. RELIABILITY AND VALIDITY TESTS

Validity and reliability consider the most important method conditions for research tool design. Therefore, validity and reliability of the closed questionnaire forms must be provided before any statistical analyses data. The value of Reliability can be founded by finding the value of (Cronbach's Alpha, α) [20].

1) Reliability of Closed Questionnaire

The term "reliability" refers to the measurement of true results and the stability and equality checks. Reliability is a necessary, but not sufficient factor in determining the viability of a tool for measuring historical building criteria.

2) Validity of Closed Questionnaire

More than any single statistical tool, it is necessary to establish a relationship between the assessment and the behavior it is meant to measure in order to determine its validity. It is critical that the test be valid to use and interpret the results correctly. Validity is equal to the square root of the coefficient of reliability [21]:

$$V = \sqrt{\alpha} \quad (6)$$

where V is the validity and α the reliability.

IX. STATISTICAL ANALYSIS

The top test criteria were determined using the SPSS V25 statistical program. The results are provided in the form of tables to make them more understandable and straightforward. Following the distribution and collection of completed

questionnaire forms, the next step was to determine a specific method for statistical and measurement purposes to complete the calculations and data analysis.

1) Reliability

Most the social science research situations use the Cronbach's alpha. If it is more than 0.7, then the consistency index shows high reliability and it would be acceptable [18]. Table II shows the closed questionnaire's reliability for each criterion.

TABLE II. CRONBACH'S ALPHA FOR THE CLOSED QUESTIONNAIRE

No.	Criterion	Cronbach's Alpha { α }
1	C01	0.920
	C02	0.810
	C03	0.780
2	C04	0.800
	C05	0.70
3	C06	0.77
	C07	0.87
	C08	0.88
4	C09	0.90
	C10	0.65
	C11	0.95
5	C12	0.88
	C13	0.75
	C14	0.77
	C15	0.70

2) Validity

Table III shows the validity of each criterion for the historical archaeological building in the closed questionnaire.

TABLE III. VALIDITY

No.	Criterion	α	Validity coefficient
1	C01	0.920	0.959
	C02	0.810	0.900
	C03	0.780	0.883
2	C04	0.800	0.894
	C05	0.700	0.836
3	C06	0.770	0.877
	C07	0.870	0.932
	C08	0.880	0.938
4	C09	0.900	0.948
	C10	0.680	0.824
	C11	0.950	0.974
5	C12	0.880	0.938
	C13	0.750	0.866
	C14	0.770	0.877
	C15	0.700	0.836

X. ANALYSIS OF THE CLOSED QUESTIONNAIRE FORMS

The first stage of a closed questionnaire is a description of the sample members' general experience. The second stage is an assessment of the criteria. Respondents were asked to mark (spot) the criteria of historical archaeological buildings that they thought were important in a closed questionnaire and RIIs were calculated. The analysis and discussion of the results will be according to the parts mentioned, so each axis will be analyzed and discussed separately.

A. Part One: (Personal Information)

Part one includes the personal information in closed questionnaire forms.

1) Scientific Qualifications

Table IV shows the frequency distribution of respondents according to their scientific qualification.

TABLE IV. SCIENTIFIC QUALIFICATIONS

Scientific qualification	Frequency	Percentage
BSc	23	51.00%
MSc	12	27.00%
PhD	10	22.22%
Total	45	100.00%

2) Engineering Specialization

Table V shows the engineering specialization of the respondents.

TABLE V. ENGINEERING SPECIALIZATION

Engineering specialization	Frequency	Percentage
Civil	24	53.33%
Electricity	6	13.33%
Architectural	5	11.11%
Mechanical	4	8.89%
Environment	3	6.67%
Chemical	3	6.67%
Total	45	100.00%

3) Actual Experience

Table VI shows the experience of the respondents.

TABLE VI. EXPERIENCE

Actual experience	Frequency	Percentage
(15-20)	15	33.33%
(21-25)	5	11.11%
(26-30)	11	24.45%
More than 30	14	31.11%
Total	45	100.00%

4) Labor Sector

The respondents' distribution according to the labor sector is shown in Table VII.

TABLE VII. LABOR SECTOR

Labor sector	Frequency	Percentage
Public	35	77.78%
Private	10	22.22%
Total	45	100.00%

B. Part Two: Evaluation of the Criteria

Part two includes the evaluation of the criteria for historical archaeological buildings from the respondents. Each question will be analyzed by RII to find the criteria ranking. Table VIII shows the analysis and ranking of the criteria from higher to lower importance.

TABLE VIII. CRITERIA ANALYSIS AND RANGING BY RII FOR HISTORICAL ARCHAEOLOGICAL BUILDINGS

Criterion	Very high	High	Medium	Low	Very low	Ranking
C01	30	12	3	0	0	92%
C09	26	15	3	1	0	88%
C15	21	16	8	0	0	86%
C10	21	14	8	2	0	84%
C02	12	28	4	1	0	82%
C03	8	30	7	0	0	80%
C11	7	29	9	0	0	79%
C08	15	15	10	5	0	78%
C12	8	23	13	1	0	76%
C06	8	21	15	1	0	75%
C04	10	19	10	6	0	74%
C07	7	17	20	1	0	73%
C05	13	13	11	5	3	72%

XI. CONCLUSION

The development of a set of evaluation criteria for historical and archaeological structures is described in this paper. Based on a thorough literature review, fieldwork, and discussion with selected experts from many governorates, a total of 15 criteria were identified in this study. RII calculation and analysis was used to rank the criteria from the most to the least important. The researchers were able to compare the relative importance of the criteria as perceived by respondents using these rankings. The first criterion is the provision of information or a database of old historical buildings which received the 92% of the vote, indicating that this criterion is very important. Most of the criteria are construction activities, indicating that respondents agreed that historical and archaeological building criteria should be implemented. Ministries and local governments can use the findings of this study to develop historical and archaeological structures, as well as using it as a pilot study to get feedback from a group of experts. Experts were contacted to assess the questionnaire's validity and to confirm the suitability of the items for the research goals in order to identify any flaws in the questionnaire.

ACKNOWLEDGEMENT

This project is supported by the Ministry of Planning, Iraq, and the University of Baghdad.

REFERENCES

- [1] E. Ziglio, *Gazing into the Oracle: The Delphi Method and its Application to Social Policy and Public Health*, 1st ed. London, UK: Jessica Kingsley, 1996.
- [2] O. P. Akadiri, "Development of a Multi-Criteria Approach for the Selection of Sustainable Materials for Building Projects," Ph.D. dissertation, University of Wolverhampton, Wolverhampton, UK, 2011.
- [3] H. I. Polat, "A Classification Study on the Development Stages of Construction Technologies in Turkey," *Engineering, Technology & Applied Science Research*, vol. 7, no. 5, pp. 1909–1913, Oct. 2017, <https://doi.org/10.48084/etasr.1606>.
- [4] S. Balubaid *et al.*, "Assessment Index Tool for Green Highway in Malaysia," *Jurnal Teknologi*, vol. 77, no. 16, Nov. 2015, <https://doi.org/10.11113/jt.v77.6405>.
- [5] J. M. Bryce, *Developing Sustainable Transportation Infrastructure Exploring the Development and Implementation of a Green Highway Rating System*. Washington, DC, USA: ASTM International, 2008.
- [6] A. L. Delbecq and A. V. D. Ven, *Group techniques for program planning: A guide to nominal group and Delphi processes*. Glenview, IL, USA: Scott, Foresman, 1975.
- [7] G. Fernández-Sánchez and F. Rodríguez-López, "A methodology to identify sustainability indicators in construction project management—Application to infrastructure projects in Spain," *Ecological Indicators*, vol. 10, no. 6, pp. 1193–1201, Nov. 2010, <https://doi.org/10.1016/j.ecolind.2010.04.009>.
- [8] A. Griffith and K. Bhutto, "Better environmental performance: A framework for integrated management systems (IMS)," *Management of Environmental Quality: An International Journal*, vol. 20, no. 5, pp. 566–580, Jan. 2009, <https://doi.org/10.1108/14777830910981230>.
- [9] R. E. Anderson, R. L. Tatham, W. C. Black, and J. F. Hair, *Multivariate Data Analysis*, 5th ed. Upper Saddle River, NJ: Prentice Hall College Div, 1998.
- [10] K. Nikumbh and P. D. Aher, "A review paper - Study of green highway rating system," *International Research Journal of Engineering and Technology*, vol. 4, no. 5, pp. 2014–2018, 2017.
- [11] A. Khoso, N. Memon, S. Sohu, F. H. Siddiqui, and J. Khan, "Decision Criteria For Assessment Of Contractors In Prequalification Phase Of Public Projects," *International Journal of Advanced Science and Technology*, vol. 29, no. 11s, pp. 2624–2635, Jun. 2020.
- [12] S. R. Sahamir, R. Zakaria, G. Alqaifi, N. I. A. Abidin, and R. R. M. Rooshdi, "Investigation of Green Assessment Criteria and Sub-criteria for Public Hospital Building Development in Malaysia," *Chemical Engineering Transactions*, vol. 56, pp. 307–312, Mar. 2017, <https://doi.org/10.3303/CET1756052>.
- [13] M. Soderlund, "Sustainable Roadway Design - A Model For An Environmental Rating System," M.S. thesis, University of Washington, Washington DC, USA, 2007.
- [14] M. Loosemore and T. Uher, *Essentials of Construction Project Management*. NewSouth Publishing, 2003.
- [15] U. H. Issa, M. A. Farag, L. M. Abdelhafez, and S. A. Ahmed, "A Risk Allocation Model for Construction Projects in Yemen," *Civil and Environmental Research*, vol. 7, no. 3, pp. 78–88, 2015.
- [16] N. M. N. Saeed and A. S. Hasan, "The Effect of Total Quality Management on Construction Project Performance," *Journal of Science and Technology*, vol. 17, no. 2, pp. 11–30, 2012, <https://doi.org/10.20428/jst.v17i2.93>.
- [17] J. D. Princy and S. Shanmugapriya, "A Probabilistic Fuzzy Logic Approach to Identify Productivity Factors in Indian Construction Projects," *Journal of Construction Engineering and Project Management*, vol. 7, no. 3, pp. 39–55, 2017, <https://doi.org/10.6106/JCEPM.2017.9.29.039>.
- [18] J. N. Gatitu, C. K. Kabubo, and P. Ajwang, "Approaches on Mitigating Variation Orders in Road Construction Industry in Kenya: The Case of Kenya National Highways Authority (KeNHA)," *Engineering, Technology & Applied Science Research*, vol. 10, no. 5, pp. 6195–6199, Oct. 2020, <https://doi.org/10.48084/etasr.3737>.
- [19] R. A. Majeed and H. K. Breesam, "The criteria for selecting the landfill sites in Baghdad governorate," *IOP Conference Series: Materials Science and Engineering*, vol. 1090, no. 1, Nov. 2021, Art. no. 012013, <https://doi.org/10.1088/1757-899X/1090/1/012013>.
- [20] F. Magalhaes, *Facing the Challenges of Informal Settlements in Urban Centers: The Re-urbanization of Manaus, Brazil*. Washington DC, USA: Inter-American Development Bank.
- [21] R. A. Majeed and H. K. Breesam, "Application of SWARA Technique to Find Criteria Weights for Selecting Landfill Site in Baghdad Governorate," *IOP Conference Series: Materials Science and Engineering*, vol. 1090, no. 1, Nov. 2021, Art. no. 012045, <https://doi.org/10.1088/1757-899X/1090/1/012045>.
- [22] M. A. Akhund, H. U. Imad, N. A. Memon, F. Siddiqui, A. R. Khoso, and A. A. Panhwar, "Contributing Factors of Time Overrun in Public Sector Construction Projects," *Engineering, Technology & Applied Science Research*, vol. 8, no. 5, pp. 3369–3372, Oct. 2018, <https://doi.org/10.48084/etasr.2276>.

A Study of Isotherms and Kinetics of *Mangifera Indica* Bark Adsorbent Used for Fluoride Removal from Drinking Water

Abhishek Kumar

Department of Civil Engineering
National Institute of Technology Patna
Patna, India
abhishek.ce18@nitp.ac.in

Nityanand Singh Maurya

Department of Civil Engineering
National Institute of Technology Patna
Patna, India
nsmaurya@nitp.ac.in

Received: 14 July 2022 | Revised: 26 July 2022 | Accepted: 2 August 2022

Abstract-In this paper, we have investigated the bark of mango (*Mangifera Indica*) as an adsorbent for fluoride removal. Chemical treatment and aluminum hydroxide coating increased the adsorption capacity of the adsorbent from 0 to 15mg/g. Aluminum hydroxide-coated adsorbent (Al-MIBAC) was subjected to a batch study by considering different operational parameters such as adsorbent dose, reaction time, and pH. The kinetics of the adsorbent strongly followed second-order behavior, indicating the chemo-sorption adsorption process. The R2 value for Langmuir isotherm is 0.999 and it was found to be fitted well with the experimental data. It is hence assumed that the adsorption of fluoride is homogeneous and monolayer. The maximum fluoride adsorption amount of Al-MIBAC was 56.81mg/g, which was superior to those of other adsorbents derived from bark. Al-MIBAC was highly effective in reducing the fluoride concentration from 20mg/L to less or equal to 1.5mg/L which is safe for drinking purposes.

Keywords-adsorption; Al-MIBAC; activated carbon; fluoride removal; isotherm; kinetics; mangifera indica

I. INTRODUCTION

Fluoride is a well-known pollutant present in drinking water. As per WHO, the allowable limit of fluoride concentration in drinking water is 1.5mg/L, whereas BIS, recommended 1mg/L [1]. Fluoride is beneficial for the bones and teeth if present in acceptable limits, otherwise it may cause dental and skeletal fluorosis, brittle bones, thyroid disorder, Alzheimer's syndrome, arthritis, brain damage, infertility, cancer, osteoporosis, and damage DNA structure [2, 3]. Natural process such as weathering and leaching of fluoride rich minerals, and anthropogenic processes like industrial discharging, biomass burning, mining, and extensive use of fertilizers are major sources of fluoride contamination in groundwater [4]. Authors in [5] reported the appearance of excessive fluoride concentration in drinking water in more than 25 countries. Approximately 200 million people around the world are facing serious problems of very high fluoride exposure through drinking water [5]. Therefore, there is a high priority to deal with this problem, to ensure safe drinking water

[6]. For this purpose, several methods such as precipitation, electro-coagulation, ion-exchange, membrane technology, and adsorption have been used to remove such pollutants [7]. Each of them has some benefits and drawbacks [8]. Precipitation/coagulation and electrocoagulation produce huge amounts of sludge. In ion-exchange process, the high operational cost is a major drawback. Membrane process has high initial and maintenance cost coupled with wasting huge amounts of water. Frequent fouling or scaling results in reduced useful life of membrane filters [7]. Among all the removal methods, adsorption is eco-friendly, with low cost, is less tedious in operation, and possesses high removal capacity [9]. Several studies have been conducted on various types of adsorbents, such as biological materials (bio-adsorbents), metal hydroxides and oxides, geomaterials, industrial by-products, etc. The best outcome and greatest adsorption capability among the adsorbents mentioned above are demonstrated by carbonaceous materials, particularly those loaded with oxides and hydroxides of metals. Activated carbon derived from Indian mulberry (*Morinda Tinctoria*), Gular bark (*Ficus racemosa*), Babool bark (*Acacia nilotica* bark), and *Mangifera indica* bark have been previously used in the removal of fluoride from drinking water [10-12, 14]. To enhance the performance, activated carbon has also been treated with metal hydroxides and oxides, such as Al-impregnated eucalyptus bark ash, aluminum hydroxide coated *Morinda Tinctoria* bark, etc. [11, 13].

In the present study, a novel adsorbent is proposed and prepared using aluminum hydroxide coated activated carbon of mango (*mangifera indica*) bark for the effective removal of fluoride from drinking water. The parameters considered were pH, adsorbent dose, and reaction time. Three widely used kinetics and isotherm models were employed to the experimental data. This paper will investigate the mechanism of adsorption followed between adsorbent's surface and fluoride ions. The developed adsorbent exhibits an adsorption capacity of 56.81mg/g which is significantly higher in comparison to many other materials as presented in Table I.

TABLE I. ADSORPTION CAPACITY OF DIFFERENT PLANT BARKS

Adsorbent	Reaction Time	Dose (g/L)	Adsorption capacity (mg/g)	Ref.
AC acacia nilotica bark	8 h	5	1.891	[10]
AC morinda tinctoria	60 min	0.1	26.028	[11]
Al-impregnated eucalyptus bark ash	30 min	0.1	3.922	[13]
AC ficus- racemosa plant	60 min	4	1.549	[12]
AC mangifera bark	90 min	2	1.862	[14]
Al (OH) ₃ coated mango bark	24 h	0.3	56.81	Present work

II. MATERIALS AND METHODS

A. Plant Description

There is a variety of plant barks indicated in the literature and tested against the adsorption of fluoride present in surface or ground water. In the present study, *Mangifera Indica* (mango) Bark (MIB) was used to prepare the adsorbent. *Mangifera indica*, an evergreen tree of anacardiaceae family is commonly found in tropical regions like India. It grows to a height of 10-45 m, dome shaped with dense foliage, typically heavy branched from a stout trunk. Different parts of *mangifera indica* have different pharmacological and therapeutic properties: the juice of unripe mango fruit is used in heat strokes, the seeds are used in asthma and astringent treatment, fumes of burning leaves are used for hiccups, and the bark is used in the treatment of menorrhagia, anaemia, scabies, cutaneous infections, syphilis, diabetes, diarrhoea, etc. [15, 16].

B. Bark Collection

The bark was carefully removed from the stem, without disturbing its inner parts, from the top (25 cm below the lowest branch) to the bottom (25 cm above the highest root). The cut width was not larger than 20 cm, thus the environmental impact of mango stem bark collection was minimal.

C. Chemicals

Analytical grade chemicals were used in the present study. Sodium fluoride (NaF), aluminum sulphate ($\text{Al}_2(\text{SO}_4)_3 \cdot 16\text{H}_2\text{O}$), sodium hydroxide (NaOH), and hydrochloric acid (HCl) were obtained from the local market. Test solutions were prepared using distilled water.

D. Preparation of the Activated Carbon

After collection, the MIB was cut into small pieces and dried in hot air oven at 65°C to remove moisture. The dried bark was powdered using a kitchen grinder. To obtain the desired particle size bark powder, the grinded bark was sieved using a 425 µm mesh size. For removal of dust and color, it was shocked in diluted nitric acid solution for 24 hours with occasional mixing and was washed several times with distilled water until the wash water pH approached neutral value. The washed MBI powder was dried in hot air oven. To obtain activated carbon from the MBI, it was placed in muffle furnace under anoxic condition at 450°C for 1 hour with uniform increase in temperature of 2°C/min.

E. Coating of Aluminium Hydroxide on Activated Carbon

Firstly 600 mL, 0.6M aluminum sulphate solution were poured into the beaker, followed by the slow addition of 100 gm ready MIBAC to the beaker as shown in [17]. Proper mixing was done to ensure complete mixing of MIBAC into the aluminum sulphate solution. Afterwards, 3M of sodium hydroxide were slowly added into the mixture. Sodium hydroxide reacts with aluminum sulphate and precipitates of aluminium hydroxide were formed. The precipitates were deposited on the MIBAC surface. The pH of the reaction mixture controls the addition of sodium hydroxide, which stopped once the pH reached the target range of 5-7. The resultant mixture contains aluminum hydroxide coated MIBAC and sodium salt. This slurry was filtered with vacuum pressure filter. The filtered materials were dried at 110 °C to complete the coating of aluminum hydroxide. To eliminate the sodium sulphate salt before conducting further tests, the Al-coated MIBAC was thoroughly rinsed with distilled water. Washing continued until the output water contained less than 1 mg/L of sulphate ions. The washed MIBAC was dried at 65 °C for 12 hours and was stored in an air tight bottle for adsorption experiments [17].

III. EXPERIMENTAL PROCEDURE

A. Fluoride Stock and Test Solution Preparation

An amount of 2.21g sodium fluoride were dissolved in 1 L distilled water, to make a stock solution of 100 mg/L concentration stored in 1 L reagent bottle. To prepare the test solution the fluoride stock solution was diluted 5 times to achieve 20 mg/L concentration.

B. Adsorption Experiment

Batch adsorption equilibrium isothermal study was conducted by adding an appropriate dose of adsorbent in 200 ml reagent bottles containing 100 ml fluoride solution of 20 mg/L concentration. The bottles were loaded on an orbital shaker at 100 revolution per minutes at 25 ± 2 °C. By ensuring adequate reaction time, the resultant mixture was separated using 0.45 µm Whatman's filter paper and the filtrate was collected for residual fluoride. Kinetics experiment was performed in a cylindrical vessel of 2 L capacity. A speed-controlled mixer was used to mix the solution at the desired mixing speed. The experiment was conducted at adsorbent dose of 0.3 g/L, initial concentration 20 mg/L, and initial pH 6.5. The cylindrical vessel was partially submerged in water bath to maintain a constant temperature of 30 ± 2 °C. To study the effect of the initial pH on the removal percentage, the pH was adjusted from 2.35 to 10.25 using 0.1M NaOH and 0.1M HCl solutions. To determine the effect of adsorbent dose on fluoride removal and adsorption capacity, 100 ml of fluoride solution having 20 mg/L concentration reacted with different adsorbent doses of 100, 300, 600, 900, and 1200 mg/L. The experiments were performed in triplicates. The fluoride adsorption capacity was calculated as:

$$q_e = \frac{(C_i - C_e) \times V}{W} \quad (1)$$

where C_i and C_e are the initial and equilibrium concentrations of test solution, q_e is the equilibrium adsorption capacity

(mg/g), W is the mass of the adsorbent (mg), and V the volume of test solution (ml) [18].

The percentage removal was calculated from (2):

$$\% \text{ Removal} = \frac{C_i - C_e}{C_i} \times 100 \quad (2)$$

IV. RESULTS AND DISCUSSION

A. Batch Adsorption Studies

1) Effect of pH on the Removal of Fluoride

In order to investigate the effect of initial pH on fluoride removal from drinking water, the initial pH of the fluoride solution varied pH from 2.35 to 8.49 using 0.1M NaOH and 0.1M HCl solutions. The initial concentration of fluoride and the adsorbent dose were kept similar at all pH values. Figure 1 indicates that fluoride removal efficiency is a function of pH and maximum fluoride removal took place at pH=5.35. Authors in [19] observed maximum removal efficiency at pH=7 during the adsorption of fluoride on aluminum hydroxide-coated activated carbon of morinda tinctoria. Authors in [8] also reported maximum adsorption at pH=6 for a composite adsorbent prepared activated carbon of egg cell and rice straw. At lower pH values, removal efficiency decreases due to the formation of weak hydrofluoric acid and complexations of fluoride ions with aluminium [19]. After pH=5.35, continuous decrease in fluoride removal was observed. The main reason behind this decrease is the repulsive force between the hydroxide and fluoride ions available on the adsorbent surface and aqueous solution. It was also reduced due to the competition of hydroxide and fluoride ions to bind on the surface of Al-MIBAC [20].

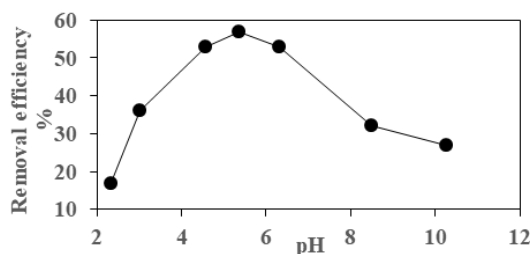


Fig. 1. Effect of pH.

2) Effect of the Adsorbent Dose on Fluoride Removal

To investigate the impact of adsorbent dose on fluoride removal from polluted drinking water, varying adsorbent doses of 0.3 g/L to 1.2 g/L, at pH 6.5, and temperature $25 \pm 2^\circ\text{C}$ were mixed with 20 mg/L initial fluoride concentration. From Figure 2, it is observed that removal efficiency increases drastically from 21 to 86.5%, when the dose of the adsorbent increased from 0.1g/L to 0.9 g/L. Further increase of the dose up to 1.2 g/L results to gradual increase to 90%. The rise in removal efficiency with increasing adsorbent dose is caused by the increase of the presence of active sites. However, with increase in adsorbent dose, the amount of fluoride absorbed per unit weight of the adsorbent decreased. This decrease may be caused by the increase of adsorbent-adsorbent contact instead of fluoride contact with adsorbent surface. As a result,

adsorbent-adsorbent contact causes the adsorbent particles to aggregate [21]. Because of this overlap, there are fewer active sites on the adsorbent particles' surface, which inhibits the surface area from growing as a result of increased adsorbent dosages. Authors in [22] reported similar results during the adsorption of fluoride on potent nanocrystalline hydroxyapatite surface.

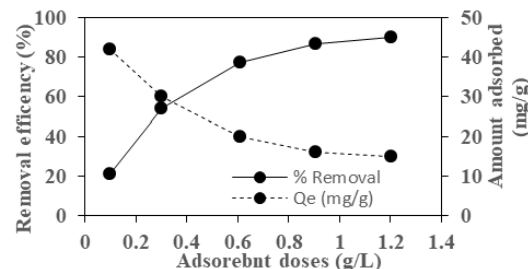


Fig. 2. Dose effect.

B. Batch Adsorption Equilibrium Isotherm

Fluoride removal capacity was investigated by varying the dose of adsorbent from 0.3 g/L to 1.2 g/L at 20 mg/L initial fluoride concentration, initial pH 6.5, contact time 24 hours, and $25 \pm 2^\circ\text{C}$ temperature. Three commonly used isotherm models namely Langmuir, Freundlich and Temkin isotherm models were employed to fit the experimental data. The related parameters are presented in Table II.

TABLE II. OBTAINED ISOTHERM PARAMETERS

Isotherm	Parameters	Value
Langmuir	K_L	0.182
	Q_m	56.81
	R^2	0.9991
Freundlich	K_f	11.3516
	n	2.0157
	R^2	0.9812
Temkin	A_T	1.5478
	B	13.249
	R^2	0.9975

1) Langmuir Isotherm Model (LIM)

LIM considers a specific number of active adsorption sites present on the surface of the adsorbent. Only one adsorbate molecule can be absorbed by each active site. The adsorption process may be considered completed if all the active sites are occupied by the adsorbate. This adsorption is monolayer in nature with constant adsorption energy [23]. The linear form of LIM is expressed as:

$$\frac{C_e}{q_e} = \frac{1}{K_L q_m} + \frac{C_e}{q_m} \quad (3)$$

where q_m is the maximum adsorption capacity, C_e is the equilibrium concentration, K_L is the Langmuir constant, q_m and K_L are calculated by plotting the graph between $\frac{C_e}{q_e}$ vs C_e (Figure 3). The values of q_m and K_L obtained from LIM are 56.81 and 0.182 respectively. The regression coefficient R^2 is 0.9991 indicating a very good fit. Authors in [8, 11] reported that aluminium impregnated composite adsorbent follows the Langmuir isotherm.

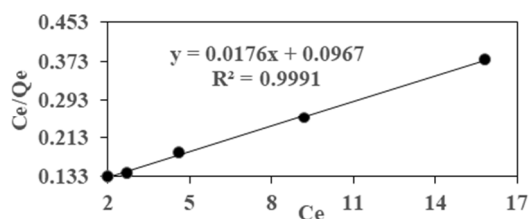


Fig. 3. Langmuir isotherm.

2) Freundlich Isotherm Model (FIM)

FIM is an empirical model applicable for multilayer adsorption process. It considers heterogeneous absorbent surface with varying affinity for adsorption. The experimental data were employed in FIM to obtain the value of Freundlich constants (n) and (K_F) [23]. This model is expressed as:

$$\ln q_e = \ln K_F + \frac{1}{n} \ln C_e \quad (4)$$

The graph between $\ln q_e$ and $\ln C_e$ is shown in Figure 4. The values of Freundlich constant and exponent were determined by slope and intercept respectively.

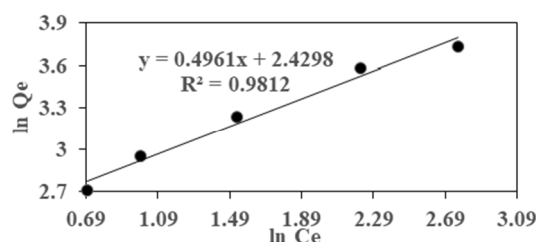


Fig. 4. Freundlich isotherm.

3) Temkin Isotherm Model (TIM)

TIM was proposed in 1940. This model describes that the heat of adsorption between adsorbate and adsorbent molecule decreases linearly due to the interactions between adsorbed molecules on the surface [24]. TIM model is expressed as:

$$q_e = \frac{RT}{b_T} \ln A_T + \frac{RT}{b} \quad (5)$$

$$q_e = B \ln A_T + B \ln C_e \quad (6)$$

where $B = \frac{RT}{b_T}$, b_T is the Temkin isotherm constant, A_T is the binding constant at equilibrium (L/g), B is a constant corresponding to the heat of sorption (J/mol), R is the universal gas constant (J/mol K), and T the temperature in Kelvin.

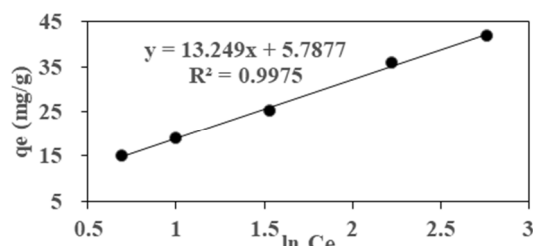


Fig. 5. Temkin isotherm.

The R^2 value of TIM is 0.997 and fitted well with the experimental data. To evaluate the B and A_T , a graph q_e vs $\ln C_e$ is plotted Figure 5. The obtained values of B and A_T from slope and intercept are 13.294 J/mol and 1.5478 L/g. Among the models applied to the experimental data in the present study, Langmuir was the better fitted model with $R^2 = 0.9991$ regression. Thus, LIM describes better the adsorption isotherm behavior as compared to TIM ($R^2 = 0.9975$) and FIM ($R^2 = 0.9812$).

C. Kinetics Study

Adsorption kinetics provides relations between reaction time and adsorption capacity (Figure 6). The effect of reaction time on fluoride adsorption was observed by changing reaction time from 5 min to 37 hours, with initial fluoride concentration of 20 mg/L, at pH=6.5 and temperature $30 \pm 2^\circ\text{C}$. Kinetics also provides information about the mechanism of adsorption, the surface, and the nature of the adsorbent. The linear from of the three kinetics models, namely Pseudo First Order (PFO), Pseudo Second Order (PSO), and Intra-Particle Diffusion (IPD) model were employed on the experimental data.

1) Pseudo First Order

PFO is based on the assumption that the change in solute uptake rate over time is directly proportional to the difference in saturation concentration and quantity of the solid uptake with time. The linear from of PFO is:

$$\ln(q_e - q_t) = \ln q_e - K_1 t \quad (7)$$

where q_e and q_t are the adsorption capacity at equilibrium and at time t (mg/g), K_1 is the rate constant, and t is the reaction time. The plot $\ln(q_e - q_t)$ vs t , gives slope = -0.0015 and intercept = 2.3169 with a regression coefficient $R^2 = 0.5675$, indicating that PFO does not fit the observed data.

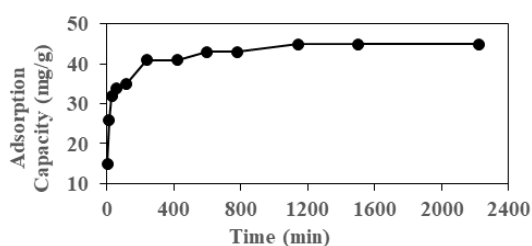


Fig. 6. Adsorption capacity.

2) Pseudo Second Order

It is based on the assumption that the rate-limiting step is chemical sorption or chemisorption and predicts the behavior over the whole range of adsorption. In this condition, the adsorption rate is dependent on the adsorption capacity, not on the concentration of the adsorbent. The main difference of PSO over PFO is that, in PSO equilibrium, the adsorption capacity is obtained from the model and does not need to be calculated theoretically from adsorption experiments [25]. The linear from of PSO is:

$$\frac{t}{q_t} = \frac{1}{K_2 q_e^2} + \frac{t}{q_e} \quad (8)$$

where K_2 is a second order rate constant (mg/g min).

The linear fit as per (8) is given in Figure 7, and indicates excellent fit with a very high regression coefficient $R^2 = 0.9996$. The adsorption capacity obtained from PSO kinetics is 45.24 mg/g and $K_2 = 1.063 \times 10^{-3}$. The lower value of K_2 indicates that the rate of fluoride sorption is fast.

3) Intra-Particle Diffusion

The mass transfer diffusion model [26] is described by:

$$q_t = K_p t^{0.5} + C \quad (9)$$

where K_p is the intra-particle diffusion rate constant and C is a constant related to boundary layer thickness

If IPD controls the adsorption process, the q_t vs $t^{0.5}$ plot will be a straight line indicating IPF is a rate determining step. However, if nonlinearity is observed, it would indicate that several processes control the mechanism involved in rate limiting steps. From the plot in Figure 8 between q_t and $t^{0.5}$, it is observed that three steps control the adsorption process. Each step among the three is the rate limiting step at specific time intervals. The rate of adsorption calculated from the slope of linear portion, if the slope is increased at a sharp rate, the adsorption is faster. As a result, the beginning of the straight line with a steep slope passing close to the origin indicates that the rate of initial diffusion through micropores and mesopores is high. The second straight portion of plots indicates fluoride diffusion through micropores and the last straight segments represents the modest adsorption on the adsorbent [8]. It is reported that pseudo second order are best fitted during adsorbent kinetics of fluoride on aluminum hydroxide coated activated carbon prepared from bark of morinda tinctoria [11]. Authors in [8] also reported that during the adsorption, second order kinetics nicely fit the kinetics of fluoride on aluminum impregnated composite adsorbent.

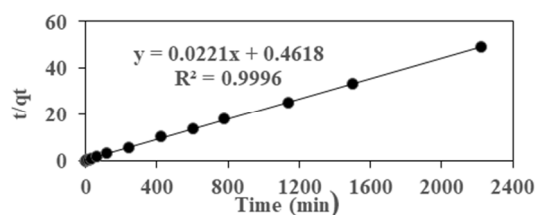


Fig. 7. Pseudo second order.

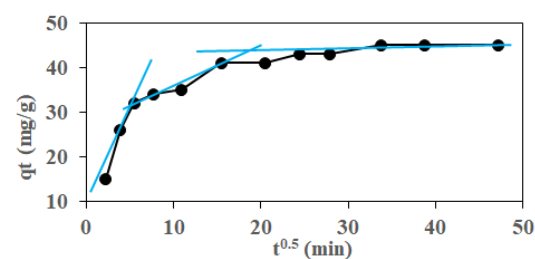


Fig. 8. Intra-particle diffusion model.

V. CONCLUSION

Mangifera indica, commonly known as mango, is a significant herb in the ayurvedic and traditional medicine. In this study, we used *mangifera indica* bark for fluoride removal

from drinking water. Its fluoride adsorption efficiency was improved by chemical treatment. Aluminum hydroxide coated mangifera bark adsorbent was developed for fluoride removal. Aluminum coating on the activated Carbon of MIBAC not only increased the affinity towards fluoride, but also increased the adsorbent surface, thus improving its adsorption capacity. A batch study on Al-MIBAC was conducted by considering different operational parameters like dose, reaction time, and initial pH at constant temperature of $25 \pm 2^\circ\text{C}$. The best fitted kinetics of Al-MIBAC was the second order kinetics with $R^2 = 0.9996$. All analyzed models fitted good, but the Langmuir model exhibited the best fit with the experimental data with $R^2 = 0.9991$, which indicates monolayer and homogeneous adsorption. Temkin and Freundlich isotherms also assumed to contribute partially in the adsorption.

REFERENCES

- [1] S. Ayoob and A. K. Gupta, "Fluoride in Drinking Water: A Review on the Status and Stress Effects," *Critical Reviews in Environmental Science and Technology*, vol. 36, no. 6, pp. 433–487, Dec. 2006, <https://doi.org/10.1080/106433806006078112>.
- [2] A. Ghosh, K. Mukherjee, S. K. Ghosh, and B. Saha, "Sources and toxicity of fluoride in the environment," *Research on Chemical Intermediates*, vol. 39, no. 7, pp. 2881–2915, Sep. 2013, <https://doi.org/10.1007/s11164-012-0841-1>.
- [3] A. N. Laghari, Z. A. Siyal, D. K. Bangwar, M. A. Soomro, G. D. Walasai, and F. A. Shaikh, "Groundwater Quality Analysis for Human Consumption: A Case Study of Sukkur City, Pakistan," *Engineering, Technology & Applied Science Research*, vol. 8, no. 1, pp. 2616–2620, Feb. 2018, <https://doi.org/10.48084/etasr.1768>.
- [4] B. Karthikeyan and E. Lakshmanan, "Fluoride in Groundwater: Causes, Implications and Mitigation Measures," in *Fluoride Properties, Applications and Environmental Management*, S. D. Monroy, Ed. 2011, pp. 111–136.
- [5] N. Adimalla, S. Venkatayogi, and S. V. G. Das, "Assessment of fluoride contamination and distribution: a case study from a rural part of Andhra Pradesh, India," *Applied Water Science*, vol. 9, no. 4, May 2019, Art. no. 94, <https://doi.org/10.1007/s13201-019-0968-y>.
- [6] K. Praveen and L. B. Roy, "Assessment of Groundwater Quality Using Water Quality Indices: A Case Study of Paliganj Distributary, Bihar, India," *Engineering, Technology & Applied Science Research*, vol. 12, no. 1, pp. 8199–8203, Feb. 2022, <https://doi.org/10.48084/etasr.4696>.
- [7] S. Ayoob, A. K. Gupta, and V. T. Bhat, "A Conceptual Overview on Sustainable Technologies for the Defluoridation of Drinking Water," *Critical Reviews in Environmental Science and Technology*, vol. 38, no. 6, pp. 401–470, Sep. 2008, <https://doi.org/10.1080/10643380701413310>.
- [8] A. Saini, P. H. Maheshwari, S. S. Tripathy, S. Waseem, A. Gupta, and S. R. Dhakate, "A novel alum impregnated CaO/ carbon composite for defluoridation of water," *Groundwater for Sustainable Development*, vol. 14, Aug. 2021, Art. no. 100622, <https://doi.org/10.1016/j.gsd.2021.100622>.
- [9] M. Mohapatra, S. Anand, B. K. Mishra, D. E. Giles, and P. Singh, "Review of fluoride removal from drinking water," *Journal of Environmental Management*, vol. 91, no. 1, pp. 67–77, Oct. 2009, <https://doi.org/10.1016/j.jenvman.2009.08.015>.
- [10] T. Akafu, A. Chimdi, and K. Gomoro, "Removal of Fluoride from Drinking Water by Sorption Using Diatomite Modified with Aluminum Hydroxide," *Journal of Analytical Methods in Chemistry*, vol. 2019, Dec. 2019, Art. no. 4831926, <https://doi.org/10.1155/2019/4831926>.
- [11] A. Amalraj and A. Pius, "Removal of fluoride from drinking water using aluminum hydroxide coated activated carbon prepared from bark of Morinda tinctoria," *Applied Water Science*, vol. 7, no. 6, pp. 2653–2665, Oct. 2017, <https://doi.org/10.1007/s13201-016-0479-z>.
- [12] S. Ravulapalli and R. Kunta, "Defluoridation studies using active carbon derived from the barks of Ficus racemosa plant," *Journal of Fluorine*

- Chemistry, vol. 193, pp. 58–66, Jan. 2017, <https://doi.org/10.1016/j.jfluchem.2016.11.013>.
- [13] S. B. Ghosh and N. K. Mondal, "Application of Taguchi method for optimizing the process parameters for the removal of fluoride by Al-impregnated Eucalyptus bark ash," *Environmental Nanotechnology, Monitoring & Management*, vol. 11, May 2019, Art. no. 100206, <https://doi.org/10.1016/j.enmm.2018.100206>.
- [14] A. Rastogi and S. K. Gupta, "Defluoridation Studies of Ground Water Using Natural Adsorbent Prepared From Mango Bark," *International Journal of Chemical & Petrochemical Technology*, vol. 8, no. 1, pp. 1–8, Jan. 2018, <https://doi.org/10.24247/ijcptfeb20181>.
- [15] K. Shah, M. B. Patel, R. J. Patel, and P. K. Parmar, "Mangifera Indica (Mango)," *Pharmacognosy Review*, vol. 4, no. 7, pp. 42–48, 2010, <https://doi.org/10.4103/0973-7847.65325>.
- [16] P. Scartezzini and E. Speroni, "Review on some plants of Indian traditional medicine with antioxidant activity," *Journal of Ethnopharmacology*, vol. 71, no. 1, pp. 23–43, Jul. 2000, [https://doi.org/10.1016/S0378-8741\(00\)00213-0](https://doi.org/10.1016/S0378-8741(00)00213-0).
- [17] V. Ganvir and K. Das, "Removal of fluoride from drinking water using aluminum hydroxide coated rice husk ash," *Journal of Hazardous Materials*, vol. 185, no. 2, pp. 1287–1294, Jan. 2011, <https://doi.org/10.1016/j.jhazmat.2010.10.044>.
- [18] S. Ayoob, A. K. Gupta, P. B. Bhakat, and V. T. Bhat, "Investigations on the kinetics and mechanisms of sorptive removal of fluoride from water using alumina cement granules," *Chemical Engineering Journal*, vol. 140, no. 1, pp. 6–14, Jul. 2008, <https://doi.org/10.1016/j.cej.2007.08.029>.
- [19] A. M. Raichur and M. Jyoti Basu, "Adsorption of fluoride onto mixed rare earth oxides," *Separation and Purification Technology*, vol. 24, no. 1, pp. 121–127, Jun. 2001, [https://doi.org/10.1016/S1383-5866\(00\)00219-7](https://doi.org/10.1016/S1383-5866(00)00219-7).
- [20] S. M. Maliyekkal, S. Shukla, L. Philip, and I. M. Nambi, "Enhanced fluoride removal from drinking water by magnesia-amended activated alumina granules," *Chemical Engineering Journal*, vol. 140, no. 1, pp. 183–192, Jul. 2008, <https://doi.org/10.1016/j.cej.2007.09.049>.
- [21] N. Rajamohan, R. R. Kannan, and M. Rajasimman, "Kinetic Modeling and Effect of Process Parameters on Selenium Removal Using Strong Acid Resin," *Engineering, Technology & Applied Science Research*, vol. 6, no. 4, pp. 1045–1049, Aug. 2016, <https://doi.org/10.48084/etasr.635>.
- [22] B. Nayak, A. Samant, R. Patel, and P. K. Misra, "Comprehensive Understanding of the Kinetics and Mechanism of Fluoride Removal over a Potent Nanocrystalline Hydroxyapatite Surface," *ACS Omega*, vol. 2, no. 11, pp. 8118–8128, Nov. 2017, <https://doi.org/10.1021/acsomega.7b00370>.
- [23] S. Raghav and D. Kumar, "Adsorption Equilibrium, Kinetics, and Thermodynamic Studies of Fluoride Adsorbed by Tetrametallic Oxide Adsorbent," *Journal of Chemical & Engineering Data*, vol. 63, no. 5, pp. 1682–1697, May 2018, <https://doi.org/10.1021/acs.jced.8b00024>.
- [24] A. O. Dada, A. P. Olalekan, A. M. Olatunya, and O. Dada, "Langmuir, Freundlich, Temkin and Dubinin–Radushkevich Isotherms Studies of Equilibrium Sorption of Zn²⁺ Unto Phosphoric Acid Modified Rice Husk," *IOSR Journal of Applied Chemistry*, vol. 3, no. 1, pp. 38–45, 2012, <https://doi.org/10.9790/5736-0313845>.
- [25] Y. S. Ho and G. McKay, "A Comparison of Chemisorption Kinetic Models Applied to Pollutant Removal on Various Sorbents," *Process Safety and Environmental Protection*, vol. 76, no. 4, pp. 332–340, Nov. 1998, <https://doi.org/10.1205/095758298529696>.
- [26] J. C. Morris and W. J. Weber, "Removal of Biologically-Resistant Pollutants from Waste Waters by Adsorption," in *Advances in Water Pollution Research*, London, UK, Sep. 1962, pp. 231–266, <https://doi.org/10.1016/B978-1-4832-8391-3.50032-4>.

A Numerical Model for Heat and Moisture Transfer in Porous Media of Building Envelopes

Talita Scussiato

Civil Engineering Department
Aeronautics Institute of Technology
Sao Jose dos Campos, Brazil
talita.scussiato@gmail.com

William Hideki Ito

Civil Engineering Department
Aeronautics Institute of Technology
Sao Jose dos Campos, Brazil
ito.william@yahoo.com

Jaqueline Ramis

Civil Engineering Department
Aeronautics Institute of Technology
Sao Jose dos Campos, Brazil
jacramis23@gmail.com

Paulo Ivo Braga de Queiroz

Civil Engineering Department
Aeronautics Institute of Technology
Sao Jose dos Campos, Brazil
pi@ita.br

Received: 1 January 2022 | Revised: 2 February 2022 | Accepted: 3 March 2022

Abstract-This study presents a one-dimensional quantitative analysis of unsaturated flow in natural stones using a numerical model (Finite Difference Method) and a mass balance for the heat flow. For that, we considered heat and moisture transfer between the external environment and a porous media (sandstone and limestone) with homogeneous characteristics. For unsaturated water flow, Richards' equation and the formulation proposed by Gardner for volumetric water content and hydraulic conductivity were considered. The results of the numerical analysis showed that the evaporation of porewater throughout summer days (January 3rd and 4th) considerably reduced the temperature of the roof by about 8°C. The accumulated conductive heat flow and the volumetric water content also had a reduction due to the evaporation process. This fact indicates that evaporation can be useful in providing thermal comfort and, consequently, in improving the energetic efficiency of buildings with natural stones as envelope.

Keywords-Richards' equation; heat transfer; thermal comfort; porous Media

I. INTRODUCTION

Natural stones are used as major components of building envelopes of several historical constructions. The porosity of these natural stones can be greater than those found in other cladding materials, which might influence the decrease of water content absorbed by the capillarity due to evaporation. Some studies have suggested that the moisture transfer between cladding materials and the external environment plays a major role in the thermal comfort inside these buildings [1]. The use of evaporative processes in roofs to enhance thermal comfort in buildings is not an innovation per se, and numerical and experimental modeling of these solutions is frequent in research nowadays. A review of the evaporative method to improve thermal comfort due to the reduction of heat flux through the roof was discussed in [2], whereas authors in [3]

presented a review of evaporative cooling systems for buildings. Numerical studies became more frequent in the literature due to the improvement of personal computer processing capacity in recent years. Authors in [4] presented a model based on the Finite Differences Method to evaluate the external surface temperature of a roof using the accumulated internal surface heat flux and the evaporation rate. Authors in [5] carried out a two-dimensional numerical model of evaporation on a plate of the heat exchanger. They showed that ambient temperature, relative humidity, and wind speed have a significant impact on the evaporation and on the reduction of plate temperature. Authors in [6] showed the efficiency of Phase Change Materials (PCM) in the thermal comfort of buildings. Similar results were achieved by other researchers, e.g. in [7-12] among others.

Moisture exchange with the external environment has a great importance to the thermal comfort inside buildings, mainly because the water absorbed by the pores of the rock (or other cladding materials like concrete) migrates to the surface and evaporates. As a result, the absorption of the latent heat cools it [4, 8]. Since the reduction of CO₂ emissions has become a priority to many countries due to the concern of climate change, many studies have focused on improving thermal comfort in building environment with minimal energy consumption. Meantime, there are only a few researches that take in account the influence of the moisture in thermal flow. Following this trend and improving the works already done in this field, the present paper suggests a novel method to evaluate the evaporative process applied to thermal exchanges in a building's roof. To do so, we present a numerical study where we solved the Richard's equation by Finite Difference Method in a one-dimensional model. We compared two types of material envelop in two different days, one humid and other

Corresponding author: Talita Scussiato

dry, and analyzed the influence of external weather conditions in the variation of internal temperature.

II. THEORETICAL FRAMEWORK

Modeling heat and moisture transfer in porous materials is considered a complex task mainly because several phenomena must be evaluated, such as:

- Energy balance
- Solar and nocturnal atmospheric radiation
- Gray body radiation emission by the roof
- Heat conduction in roof slab
- Convective heat transfer between roof and atmosphere
- Heat transfer in evaporative processes
- Water flow in unsaturated porous media.

The following sections briefly describe each of these processes and their equations adopted in this work.

A. Energy Balance

In steady-state conditions, the energy flow balance is written as the sum of the heat flows involved in the thermal exchanges, as indicated in Figure 1 and expressed in (1)

$$q''_I + q'' + q''_c - q''_r = q''_e \quad (1)$$

where q''_I is the solar radiation flow, q'' is the conductive heat flow, q''_c is the convective heat flow, q''_r is the gray body radiation flow, and q''_e is the evaporative heat flow.

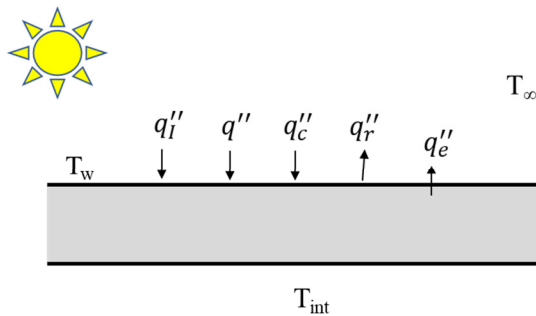


Fig. 1. Heat flow on the roof of a building.

Solar radiation is by far the most important heat source in buildings. For this reason, there are several models available to calculate this parameter [14], which have been used [15] to study the sol-air temperature in a natural stone (marble). Following the work of [13], the authors evaluated the induced stress by daily variation of temperature in external façades using a model developed by [16], which is the model that supported the development of the simplified model by [14] for clear-sky radiation. According to several solar radiation models, a building envelope (wall or roof) absorbs 3 different types of radiation from its surroundings, as shown in (2):

$$q''_I = \alpha_r (I_D \cdot \cos \theta_z + I_d + I_R) \quad (2)$$

where α_r is the shortwave radiation absorbance, I_D is the direct solar radiation attenuated by the atmosphere, θ_z is the zenith angle, I_d is the diffuse sky radiation, and I_R is the solar radiation reflected by surrounding buildings.

Night sky radiation can be considered by (3) [17]:

$$q''_{I, noct} = (1 + KG^2) \cdot 8.78 \times 10^{-13} T_\infty^{5.852} RH^{0.07195} \quad (3)$$

where KG is an index that depends on the cloud cover, T_∞ is the air temperature, and RH is the relative humidity.

Radiation energy is transmitted via electromagnetic waves, and it can be represented by gray body radiation. It is defined by the modified Stefan law presented in (4) [18]:

$$q''_r = \sigma \varepsilon T_w^4 \quad (4)$$

where ε is the radiation emissivity, σ is the Stefan-Boltzmann constant ($5.67 \times 10^{-8} \text{ W/m}^2 \text{ K}^4$), and T_w is the surface temperature of the outer (outdoor) portion of the roof.

Fourier law describes heat conduction in a continuum medium, and it can be represented by (5) and (6):

$$q'' = -\frac{l}{R_w} (T_{int} - T_w) \quad (5)$$

where T_{int} is the indoor temperature, R_w is the thermal resistance of the roof, and l is the roof slab thickness.

The hypothesis of steady-state flow assumed in the present work seems reasonable, since a great part of the transient condition (over 90%) is dissipated in less than two hours.

Convective heat transfer between roofs and the external environment can be calculated by two distinct formulations: artificially or naturally induced convection. Both models assess the convective heat transfer by (6):

$$q''_c = h_c (T_\infty - T_w) \quad (6)$$

where h_c is the convective heat transfer coefficient.

Heat transfer by forced convection was estimated through a dimensionless model in [10, 20], where h_c is estimated by (7) for Nusselt number (Nu):

$$Nu = h_c \frac{L_{eq}}{k_a} = 0.036 \cdot Pr^{0.43} (Re^{0.8} - 9200) \left(\frac{\mu_\infty}{\mu_w} \right)^{0.25} \quad (7)$$

where L_{eq} is the equivalent length, k_a is the air thermal conductivity, Pr is the Prandtl number, Re is the Reynolds number, μ_∞ is the absolute air viscosity in the atmosphere, and μ_w is the absolute air viscosity at the roof temperature. The viscosity correction $\left(\frac{\mu_\infty}{\mu_w} \right)^{0.25}$ can be neglected for gases.

The equivalent length refers to the longest building length in the wind direction for a finite length building, expressed by:

$$L_{eq} = \min \left[\frac{B}{\sin \theta}, \frac{L}{\cos \theta} \right] \quad (8)$$

where B is the building plan width, L is the building plan length, and θ is the wind direction.

The free convection coefficient is estimated by the model presented in [20, 21]:

$$Nu = c(Gr \cdot Pr)^n \quad (9)$$

$$Sh = c(Gr \cdot Sc)^n \quad (10)$$

where Gr is the Grashof number, Sh is the Sherwood number, and c and n are constants (see Table I).

Grashof number (Gr) is defined by (11) [17]:

$$Gr = \beta g L_{eq}^3 \frac{(T_w - T_\infty)}{v^2} \quad (11)$$

where g is the gravitational acceleration (9.81 m/s^2) and β is the coefficient of the thermal expansion of the air, which is the inverse of the temperature for an ideal gas.

The estimates of the evaporative flux and the heat transfer due to this process are calculated using an iterative process, given that one depends on the other. According to the model presented in [22], the evaporation flow is estimated in a very similar way to the convective flow process, which involves forced or free convection. The evaporative flow is calculated by:

$$F_{ev} = - \left(\frac{Sh \cdot D_v \cdot (\chi_w - \chi_\infty)}{L_{eq}} \right) \quad (12)$$

where F_{ev} is the evaporative mass flux, D_v is the molecular diffusivity of water vapor in the air, and χ_w, χ_∞ are the mass concentration of water vapor at the surface and in the free atmosphere respectively.

In this study, the forced convection uses the dimensionless Sherwood number (Sh) for mass transfer, as presented in (13):

$$Sh = 0.036 Sc^{0.43} (Re^{0.8} - 9200) \quad (13)$$

where Sc is the Schmidt number.

Mass concentration of water vapor (absolute humidity or χ) can be expressed as in:

$$\chi = \frac{M_w \cdot u_v^{air}}{RT} \quad (14)$$

where M_w is the molar mass of water, u_v^{air} is the partial pressure of water vapor, and R is the universal gas constant.

TABLE I. CONSTANTS c AND n FOR FREE CONVECTION ON A HORIZONTAL PLATE AT UNIFORM TEMPERATURE BY [20, 21]

Surface orientation	$Gr \cdot Pr$	c	n	Regime
Hot surface up	10^5 to 2×10^7	0.54	1/4	Laminar
Cold surface down	2×10^7 to 3×10^{10}	0.14	1/3	Turbulent
Hot surface down or cold surface up	3×10^5 to 3×10^{10}	0.27	1/4	Laminar

The partial pressure of water vapor (u_v^{air}) is calculated with the relative humidity (RH) given by:

$$RH = \frac{u_v^{air}}{u_{v0}^{air}} \quad (15)$$

where u_{v0}^{air} is the saturation pressure of water vapor. In the present study, this variable is given by Tetens equation, as shown in [23, 24]:

$$u_{v0}^{air} = 0.61078 \exp \left(\frac{17.27 \cdot T}{T + 237.3} \right) \quad (16)$$

where T is the temperature ($^\circ\text{C}$).

According to [22], the difference of air density above the roof must be considered for simultaneous heat and water vapor transfer analysis. Hence, the concept of virtual temperature is introduced to conveniently express the difference in density between dry and moist air at temperature T . This relationship is represented by:

$$T_v = \left(\frac{T}{1 - (1 - \varepsilon_w) \frac{u_v^{air}}{\bar{u}_a}} \right) \approx T \left(1 + (1 - \varepsilon_w) \frac{u_v^{air}}{\bar{u}_a} \right) \quad (17)$$

where ε_w is the ratio of molecular weights of water vapor and air, taken as 0.622, and \bar{u}_a is the absolute pressure of the air-vapor mixture. Hence, $T_w - T_\infty$, in (11) should be replaced by:

$$T_{vw} - T_{v\infty} \approx (T_w - T_\infty) + \frac{0.38(T_w u_{vw}^{air} - T_\infty u_{v\infty}^{air})}{\bar{u}_a} \quad (18)$$

where u_{vw}^{air} and $u_{v\infty}^{air}$ are the partial vapor pressure near the roof and in the atmosphere respectively.

Heat loss/gain due to evaporation/condensation is expressed by:

$$q''_e = h_{vap} \cdot F_{ev} \quad (19)$$

where h_{vap} is the enthalpy of water evaporation.

B. Water Flow in Unsaturated Porous Media

A great number of numerical models considering the unsaturated flow in porous media rely on Richards' equation, which can be represented in a mixed form by [25]:

$$\frac{\partial \theta_w}{\partial t} = \frac{\partial}{\partial z} \left[K(\psi) \frac{\partial (\psi + z)}{\partial z} \right] \quad (20)$$

where θ_w is the volumetric water content, t is the time, K is the hydraulic conductivity and ψ is the water matric suction, that is, the difference between air pressure and pore water pressure.

The unsaturated formulation was proposed by Gardner [35] where the volumetric water content of a porous medium can be estimated as:

$$\theta_w = \theta_r + (\theta_s - \theta_r) e^{\alpha \psi} \quad (21)$$

where θ_r is the residual water content, θ_s is the saturated water content, α is the air entry suction parameter, and ψ is the matric suction.

In the formulation proposed by [35], water hydraulic conductivity (K) is represented by:

$$K = k_s e^{\alpha \psi} \quad (22)$$

where k_s is the saturated hydraulic conductivity.

III. MATERIALS AND METHODS

The input data used in this work are representative of a typical summer day in Brazil. The analysis was conducted using porous rock materials (sandstones and limestones), which are used in several historical buildings. A C++ code was implemented to solve the differential equations.

C. Assumptions Assumed Prior to the Analysis

The following assumptions were considered to simplify the modeling:

- The flow is one-dimensional
- The heat flow is in steady-state condition
- The water flow is in a transient regime
- The airflow is negligible
- The indoor temperature (T_{int}) is constant at 23°C
- The porous media are considered homogeneous
- The thermal conductivity of the porous media is constant concerning the volumetric water content and temperature.

D. Weather Data

In the present study, meteorological data of Ouro Preto – Minas Gerais, Brazil (latitude: 20°23'8", longitude: 43°30'13", altitude: 1.200m above sea level) are considered. The location was chosen because many of the preserved historical buildings in Brazil are located in this area. Meteorological data, including wind velocity (U) and direction (θ), relative humidity (RH), and air temperature (T_∞) were obtained from a weather station at the Federal University of Ouro Preto. The proposed methodology was applied in the interval between January 3rd, 2013 and January 4th, 2013, to evaluate the evaporative-cooling roof effect. The input data used in this paper are presented in Figure 2. On January 3rd, the air temperature varied from 27°C to 17°C, mean wind velocity was about 3.8m/s from 10:00 to 19:00, relative humidity varied from 34% to 100%, and the maximum solar radiation of 870W/m² occurred at 11:13. Similar behavior was verified for January 4th, in which the air temperature varied from 25°C to 17°C and the mean wind velocity was about 4m/s, relative humidity varied from 55% to 100%, and the solar radiation was almost coincident with the preceding day. According to these data, we can conclude that January 4th was wetter, colder, and less windy than January 3rd.

E. Heat Flow and Evaporation

Considering an internal environment with constant temperature $T_{int}=23^\circ\text{C}$, a quasi-Newton-Raphson scheme was used to find temperature T_w , as shown in (23):

$$T_{w,i+1} = \frac{\frac{1}{R_w}T_{int} + q''_l + hT_\infty + 3\sigma\epsilon T_w^4 - h_{vap}F_{ev}}{\frac{1}{R_w} + h + 4\sigma\epsilon T_w^3} \quad (23)$$

F. Porous Roof Slab

Sandstone and limestone slabs are the unsaturated porous media considered in this study. Both materials were assumed to be homogeneous and without cracks. They were chosen because they are abundant in Southeast Brazil, where Ouro Preto is located. In order to characterize two hypothetical constructions with these materials, some of their properties were taken from the literature (Table II). Both models have a thickness of 0.1m, a building plan width B of 8m, and a building plan length L of 10m. Figure 3 shows the water retention curves of sandstone and limestone used, obtained by the use of van Genuchten parameters [33] described in [32].

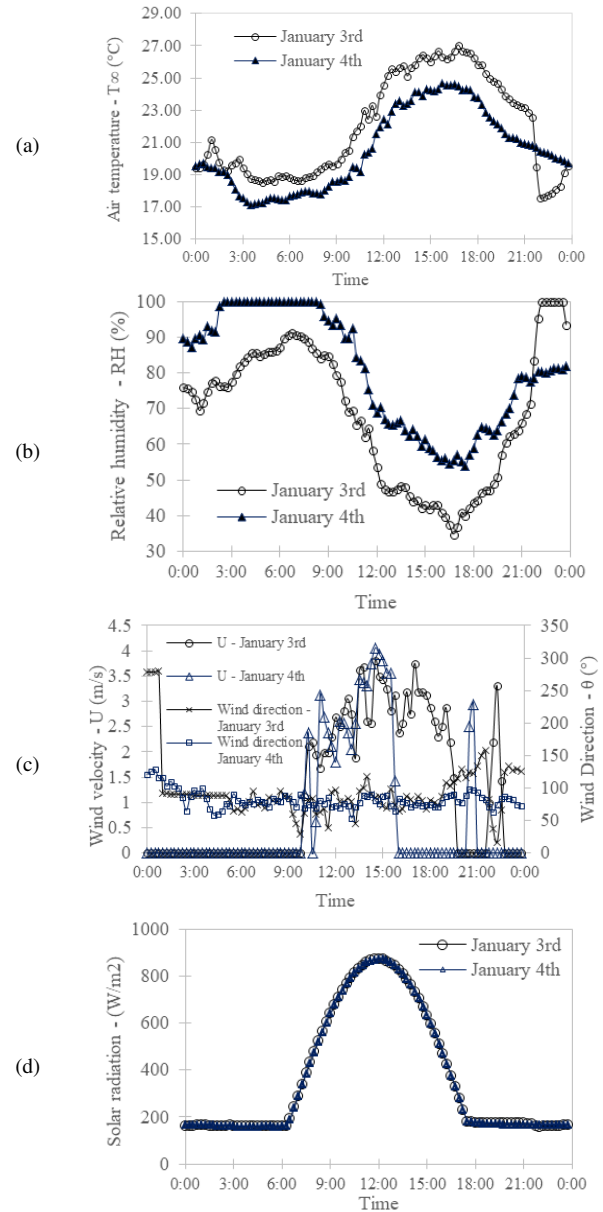


Fig. 2. Environmental conditions for January 3rd and 4th, 2013: (a) Air temperature, (b) relative humidity, (c) wind velocity and direction, (d) solar radiation ($I_D \cdot \cos \theta_z$) where θ_z is the zenith angle.

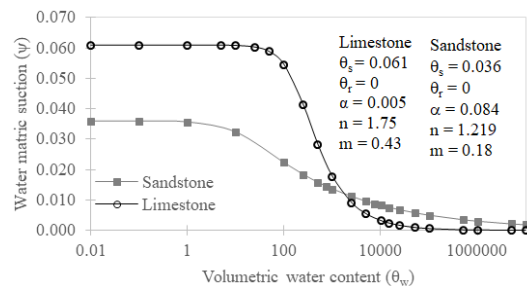


Fig. 3. Water retention curve for limestone and sandstone fitted with the van Genuchten (VG) model.

TABLE II. PROPERTIES OF SANDSTONE AND LIMESTONE USED IN THIS STUDY

Parameter	Sandstone	Limestone	Unit	Ref.
Thermal conductivity (k_r)	1.83	2.5	W/m.K	[26, 27]
Radiation emissivity (ϵ)	0.935	0.87	-	[28, 29]
Saturated hydraulic conductivity (k_s)	8×10^{-5}	5×10^{-7}	m/s	[30, 31]*
Saturated water content (θ_s)	0.036	0.061	-	[32]
Residual water content (θ_r)	0	0	-	[32]
Air-entry parameter (α)	0.084	0.005	m^{-1}	[32]
Porosity (n_p)	3.4	1.75	%	[32]
Bulk density (ρ_b)	2.35	2.3	g/cm^3	[32]
*mean value				

G. Unsaturated Flow

The calculation of unsaturated flow was based on the work developed by Mannich [34]:

$$\theta_w = \theta_r + (\theta_s - \theta_r)e^{\alpha\psi}, K = k_s e^{\alpha\psi}$$

Mannich uses a finite volume in spatial discretization and a Crank-Nicholson scheme in time. In this scheme, the equations system is solved simultaneously and the Richards' equation (20) can be rewritten as (24):

$$C(\psi) \frac{\partial \psi}{\partial t} = \frac{\partial q}{\partial z} \quad (24)$$

where q and $C(\psi)$ can be defined as:

$$q = K(\psi) \frac{\partial \psi}{\partial z} + K(\psi), C(\psi) = \frac{\partial \theta}{\partial \psi} \quad (25)$$

The equation for internal nodes, representing the capillary potential calculated at the end of the time interval, can be expressed as:

$$P_i \psi_i^{j+1} = W_i \psi_{i-1}^{j+1} + E_i \psi_{i+1}^{j+1} + B_i \quad (26)$$

where ψ_i^j is the matric suction in grid node i at time j .

The coefficients of (26) are expressed as:

$$W_i = \frac{k_{i-\frac{1}{2}}^{j+1}}{\Delta z^2}, E_i = \frac{k_{i+\frac{1}{2}}^{j+1}}{\Delta z^2}, P_i = \frac{C_i^{j+\frac{1}{2}}}{\Delta t} + W_i + E_i \quad (27)$$

$$B_i = \frac{C_i^{j+\frac{1}{2}} \psi_i^j}{\Delta t} + \frac{1}{\Delta z} \left[k_{i+\frac{1}{2}}^j \left(\frac{\psi_{i+1}^j - \psi_i^j}{\Delta z} + 1 \right) - k_{i-\frac{1}{2}}^j \left(\frac{\psi_i^j - \psi_{i-1}^j}{\Delta z} + 1 \right) + k_{i+\frac{1}{2}}^{j+1} + k_{i-\frac{1}{2}}^{j+1} \right] \quad (28)$$

Half indexes like in $k_{i-\frac{1}{2}}^{j+1}$ denote that the hydraulic conductivity is calculated with the average suction between ψ_{i-1}^{j+1} and ψ_i^{j+1} . Hence, $C_i^{j+\frac{1}{2}}$ is the derivative $C = \frac{\partial \theta_w}{\partial \psi}$ calculated with the average suction $\psi = \frac{\psi_{i-1}^{j+1} + \psi_i^{j+1}}{2}$.

The bottom of the slab was taken as a moist environment, where $\psi_0 = B_0 = 0$, $W_0 = 0$, $E_0 = 0$, and $P_0 = 0$.

For the top of the slab, evaporative mass flux (F_{ev}) was imposed, which means that the coefficients of (26) become

$$W_n = 1, E_n = 0, P_n = 1, \text{ and } B_n = \left(\frac{q^j - k_{n-\frac{1}{2}}^j}{k_{n-\frac{1}{2}}^j} \right) \Delta z.$$

The coefficient q^j is represented by:

$$q^j = F_{ev} \quad (29)$$

For the finite element difference grid, the time interval (Δt) considered was of 15 minutes over the course of a day, and the space interval (Δz) was 0.01m for a total thickness $L=0.1$ m for sandstone roof slab. The main goal of the proposed methodology is the consideration of the evaporative processes through the coefficients of water flow in the heat flux.

IV. RESULTS AND DISCUSSION

A. Roof Temperature

Figures 4 and 5 show, respectively, the results of the temperatures calculated for January 3rd and 4th in sandstone and limestone hypothetical roofs. The external air temperatures are also plotted. Two different conditions were considered: with and without evaporation. From 12:00 AM to 6:00 AM, the external air temperature was about 20°C, but the theoretical temperature on the external surface of the roof was about 13°C for sandstone and 15°C for limestone. These almost constant temperatures are explained by the absence of direct solar irradiation. However, from 6:00 AM to 4:00 PM, the temperature of the roof rises until it reaches a peak, and then it falls. During a great part of this interval, the temperature calculated for the external surface of the roof is higher than the external air temperature for both conditions (with and without considering evaporation). Temperature differences occur due to the solar radiation effect, which starts to increase at 6:00 AM and reaches its peak around 12:00 PM (coinciding with maximum roof temperature). After that, the solar radiation continuously decreases until it becomes negligible. From 4:00 PM on, the roof temperature is lower than the temperature of the air for both hypotheses (with and without evaporation).

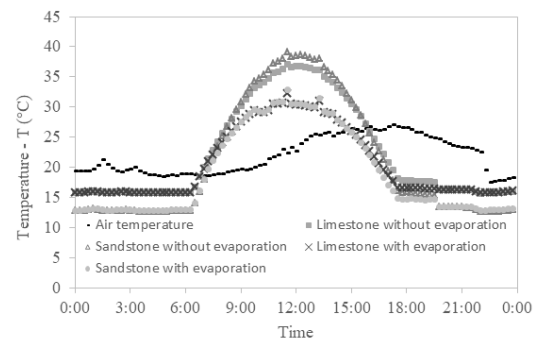


Fig. 4. Temperature of the roof and air on a sunny day (January 3rd).

These results show that the theoretical temperature is almost the same for both materials if the evaporation effect is considered. Without this effect, the difference in temperature reaches 2°C. This can be explained by solar radiation, which was the major phenomenon involved in the calculation. The value of shortwave radiation absorbance (α) used was the same for both materials. The reduction of temperature due to evaporation on January 3rd and 4th (Figures 4 and 5), was about 8°C-7°C for sandstone and 6°C-5°C for limestone. In Figure 4, the outliers observed at 11:30 AM and at 01:15 PM can be explained by the changes in wind direction.

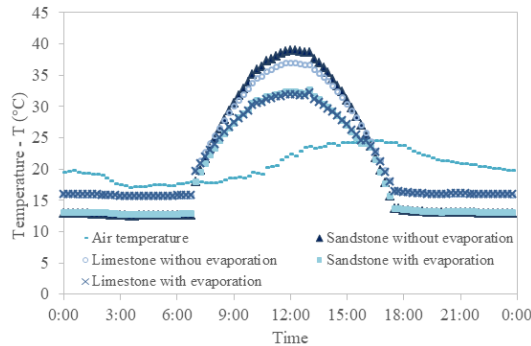


Fig. 5. Temperature in the roof and air on a mild and humid summer day (January 4th).

B. Heat Transfer

Figure 6 presents the conductive heat flow calculated for the examples described above. One can notice that the accumulated conductive heat flow is positive until 9:00 am. Afterward, a reduction in accumulated heat flow from 9:00 AM to 15:00 PM on January 4th is noticeable. Then, it asymptotically stabilizes near -0.4 and -0.2 for conditions neglecting and considering the evaporation effect respectively. This phenomenon occurred due to the absence of wind during this period. Without wind, the roof's temperature does not change, and the system does not exchange heat."

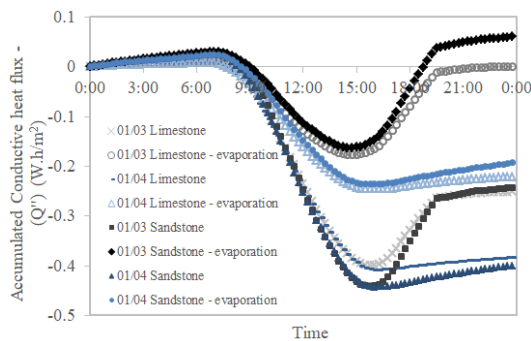


Fig. 6. Accumulated conductive heat flow in sandstone and limestone roofs on two different summer days (January 3rd and 4th).

On January 3rd, the decrease in accumulated heat flux occurred until 03:00 PM. It reached a minimum, and then increased until 06:00 PM, and stabilized in -0.25 for both materials. This happened in a condition without evaporation, and 0 for limestone and 0.05 for sandstone when the

evaporation process was taken into consideration. This occurred because the system only reaches stability when wind velocity is zero. The cumulative conductive heat flow is lower for processes that consider the evaporative effect than for those which do not, mainly because the roof loses a lesser amount of energy to the environment due to the lower gradient of temperature between the surfaces. Similarly, if evaporation is not considered, the heat flow is higher because the temperature of the external surface of the roof is also higher. Therefore, it is possible to conclude that the evaporation process causes the reduction of temperature, that is, it consumes heat.

C. Water Flow

Figure 7 shows the cumulated evaporative rate through roof thickness throughout the day. We can see that the maximum evaporation rate is close to 4.5L/m² for sandstone on a summer day in Ouro Preto (January 3rd). The minimum evaporative rate of 2.5L/m² was verified for limestone on January 4th. One can notice that the cumulated evaporative rate was smaller on January 4th than on January 3rd in both materials. The difference occurred due to the difference in the temperature verified in these two days, which was 2°C lower on January 3rd. The relative humidity was 20% higher and there was less wind throughout the day. It can be pointed out that, for January 4th, the accumulated evaporative rate was smaller than on January 3rd for both materials, because on the 4th the temperature was 2°C lower, the relative humidity 20% higher, and there was less wind during that day.

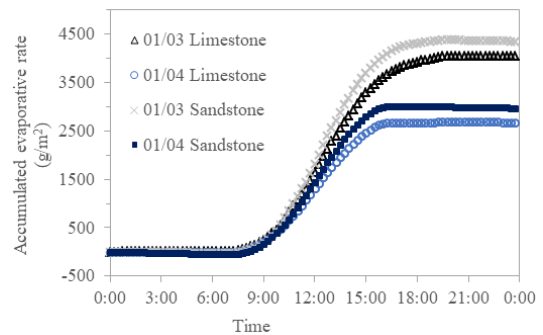


Fig. 7. The accumulated evaporative rate in sandstone and limestone roofs on January 3rd and 4th.

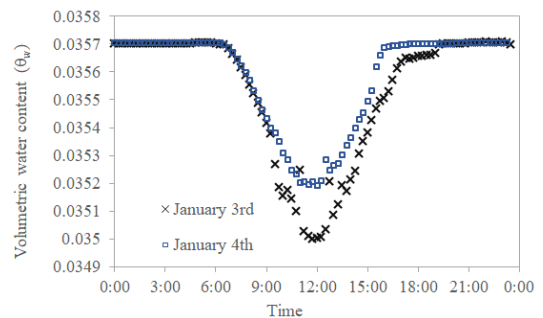


Fig. 8. Volumetric water content (θ_v) on January 3rd in sandstone roof.

Figures 8 and 9 show the volumetric water content for sandstone and limestone roofs on January 3rd and 4th respectively. It is noticeable that the volumetric water content

did not reduce significantly due to the evaporation on sandstone (about 2%). On the other hand, for the limestone roof model, the reduction was of about 15% on January 3rd around 12:00 pm.

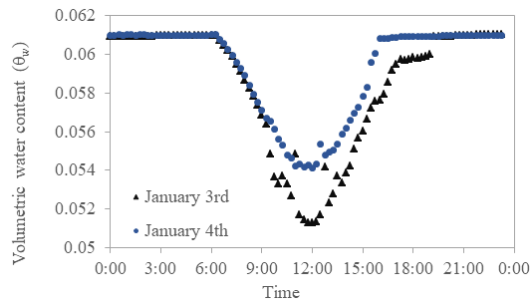


Fig. 9. Volumetric water content (θ_v) on January 4th in limestone roof.

D. Discussion

The current study uses weather data and properties of facade materials to calculate roof temperature. Its main purpose is to model how evaporative roofs improve thermal comfort in buildings. Following the world trend of NZEB (Net Zero Energy Buildings) [35], this study shows that the internal environment temperature may be reduced by the evaporative process. The choice of appropriate envelope material can reduce the use of air-conditioning. The main contribution presented here is the method of accounting for the evaporative process in the boundary condition of water flow in a finite volume scheme for unsaturated materials. Similar works [1, 34] do not consider the coupled effects of water flow and evaporation associated to heat flow.

V. CONCLUSION

This study presented a numerical calculation, in one-dimensional Finite Difference Method, for unsaturated flow using Richards' equation and Gardner's formulation for volumetric water content and saturated hydraulic conductivity. For the heat flow, the balance of 5 heat fluxes (solar radiation, conductive, convective, gray body radiation, and evaporative) were considered. The heat and moisture transfer model was carried out for 2 different natural stones (sandstone and limestone) in a hypothetical building located at a historical city in Brazil (Ouro Preto-MG) and under two conditions: with and without evaporation.

This study showed that, for both materials, the evaporation process of the porewater throughout the day considerably reduces the temperature of the roof. Around 12:00 pm, the roof temperature dropped approximately by 8.5°C on January 3 and 7.5°C on January 4 due to the evaporation of the water contained within the pores of the sandstone roof. The temperature was 2°C higher on sandstone roofs when compared to limestone roofs. On January 3, during an entire summer day, we observed a maximum accumulated evaporation rate of about 4.5L/m² of sandstone roof area. Moreover, the maximum reduction of water content for the limestone roof was about 15%, around 12:00 pm.

The numerical analysis results show that the evaporation of porewater throughout summer days considerably reduces the temperature of the roof and the accumulated conductive heat flow. The results indicate that evaporative processes can be useful in order to provide hygrothermal comfort with energetic efficiency for buildings having sandstone or limestone as envelope material for the summer day design conditions.

ACKNOWLEDGEMENT

The authors are grateful to Maria Luiza Teófilo Gandini and Gilberto Queiroz da Silva for providing the data of the weather station of Ouro Preto Federal University.

REFERENCES

- [1] L. Zhang, R. Zhang, Y. Zhang, T. Hong, Q. Meng, and Y. Feng, *The Impact of Evaporation Process on Thermal Performance of Roofs Model Development and Numerical Analysis*. Berkeley, CA, USA: Lawrence Berkeley National Laboratory, 2016.
- [2] G. N. Tiwari, A. Kumar, and M. S. Sodha, "A review—Cooling by water evaporation over roof," *Energy Conversion and Management*, vol. 22, no. 2, pp. 143–153, Jan. 1982, [https://doi.org/10.1016/0196-8904\(82\)90036-X](https://doi.org/10.1016/0196-8904(82)90036-X).
- [3] P. M. Cuce and S. Riffat, "A state of the art review of evaporative cooling systems for building applications," *Renewable and Sustainable Energy Reviews*, vol. 54, pp. 1240–1249, Feb. 2016, <https://doi.org/10.1016/j.rser.2015.10.066>.
- [4] L. Zhang, X. Liu, Q. Meng, and Y. Zhang, "Experimental study on the impact of mass moisture content on the evaporative cooling effect of porous face brick," *Energy Efficiency*, vol. 9, no. 2, pp. 511–523, Apr. 2016, <https://doi.org/10.1007/s12053-015-9377-8>.
- [5] N. Grich, W. Foudhil, S. Harmand, and S. B. Jabrallah, "Numerical simulation of water spray transport along a plate of a heat exchanger," *Journal of Thermal Analysis and Calorimetry*, vol. 143, no. 5, pp. 3887–3895, Mar. 2021, <https://doi.org/10.1007/s10973-020-09356-w>.
- [6] N. B. Khedher, "Numerical Study of the Thermal Behavior of a Composite Phase Change Material (PCM) Room," *Engineering, Technology & Applied Science Research*, vol. 8, no. 2, pp. 2663–2667, Apr. 2018, <https://doi.org/10.48084/etasr.1824>.
- [7] S. Ahmadi, M. Irandoost Shahrestani, S. Sayadian, M. Maerefat, and A. Haghighi Poshtiri, "Performance analysis of an integrated cooling system consisted of earth-to-air heat exchanger (EAHE) and water spray channel," *Journal of Thermal Analysis and Calorimetry*, vol. 143, no. 1, pp. 473–483, Jan. 2021, <https://doi.org/10.1007/s10973-020-09268-9>.
- [8] J. I. Kindangen and M. K. Umboh, "Design of evaporative-cooling roof for decreasing air temperatures in buildings in the humid tropics," *AIP Conference Proceedings*, vol. 1818, no. 1, Mar. 2017, Art. no. 020023, <https://doi.org/10.1063/1.4976887>.
- [9] T. Chati, K. Rahmani, T. T. Naas, and A. Rouibah, "Moist Air Flow Analysis in an Open Enclosure. Part A: Parametric Study," *Engineering, Technology & Applied Science Research*, vol. 11, no. 5, pp. 7571–7577, Oct. 2021, <https://doi.org/10.48084/etasr.4344>.
- [10] P. Tewari, S. Mathur, and J. Mathur, "Thermal performance prediction of office buildings using direct evaporative cooling systems in the composite climate of India," *Building and Environment*, vol. 157, pp. 64–78, Jun. 2019, <https://doi.org/10.1016/j.buildenv.2019.04.044>.
- [11] E. Zanchini and C. Naldi, "Energy saving obtainable by applying a commercially available M-cycle evaporative cooling system to the air conditioning of an office building in North Italy," *Energy*, vol. 179, pp. 975–988, Jul. 2019, <https://doi.org/10.1016/j.energy.2019.05.065>.
- [12] W. Aich, "3D Buoyancy Induced Heat Transfer in Triangular Solar Collector Having a Corrugated Bottom Wall," *Engineering, Technology & Applied Science Research*, vol. 8, no. 2, pp. 2651–2655, Apr. 2018, <https://doi.org/10.48084/etasr.1857>.

- [13] J. E. Ramis, "Modelagem da transferência de calor em lajes de cobertura de terminais de passageiros aeroportuários," Ph.D. dissertation, Instituto Tecnológico de Aeronáutica, São José dos Campos, Brasil, 2016.
- [14] ASHRAE, *Fundamentals: 2001 Ashrae Handbook, Inch-Pound Edition*. New York, NY, USA: American Society of Heating, Refrigerating and Air-Conditioning Engineers, 2001.
- [15] W. H. Ito *et al.*, "On the Thermal Stresses Due to Weathering in Natural Stones," *Applied Sciences*, vol. 11, no. 3, Jan. 2021, Art. no. 1188, <https://doi.org/10.3390/app11031188>.
- [16] M. Iqbal, *An Introduction To Solar Radiation*. New York, NY, USA: Academic Press, 1983.
- [17] M. A. Goforth, G. W. Gilchrist, and J. D. Sirianni, "Cloud effects on thermal downwelling sky radiance," in *Proceedings of SPIE*, Orlando, FL, USA, Apr. 2002, vol. 4710, pp. 203–213, <https://doi.org/10.1117/12.459570>.
- [18] T. L. Bergman, F. P. Incropera, D. P. DeWitt, and A. S. Lavine, *Fundamentals of Heat and Mass Transfer*, 7th edition. Hoboken, NJ, USA: John Wiley & Sons, 2011.
- [19] S. Whitaker, *Elementary Heat Transfer Analysis*. New York, NY, USA: Pergamon, 1976.
- [20] M. N. Ozisik, *Heat Transfer: A Basic Approach*, International Ed edition. New York, NY, USA: McGraw-Hill, 1985.
- [21] W. H. McAdams, *Heat transmission*, 3rd edition. New York, NY, USA: McGraw-Hill, 1954.
- [22] J. Monteith and M. Unsworth, *Principles of Environmental Physics: Plants, Animals, and the Atmosphere*, 4th edition. Amsterdam, Boston: Academic Press, 2013.
- [23] O. Tetens, "Über einige meteorologische Begriffe," *Zeitschrift Geophysic*, vol. 6, pp. 297–309, 1930.
- [24] F. W. Murray, "On the Computation of Saturation Vapor Pressure," *Journal of Applied Meteorology and Climatology*, vol. 6, no. 1, pp. 203–204, Feb. 1967, [https://doi.org/10.1175/1520-0450\(1967\)006<0203:OTCOSV>2.0.CO;2](https://doi.org/10.1175/1520-0450(1967)006<0203:OTCOSV>2.0.CO;2).
- [25] L. A. Richards, "Capillary conduction of liquids through porous mediums," *Physics*, vol. 1, no. 5, pp. 318–333, Nov. 1931, <https://doi.org/10.1063/1.1745010>.
- [26] M. N. Ozisik, *Heat Conduction*, 2nd ed. New York, NY, USA: Wiley, 1993.
- [27] J. Thomas, R. R. Frost, and R. D. Harvey, "Thermal conductivity of carbonate rocks," *Engineering Geology*, vol. 7, no. 1, pp. 3–12, Jun. 1973, [https://doi.org/10.1016/0013-7952\(73\)90003-3](https://doi.org/10.1016/0013-7952(73)90003-3).
- [28] C. D. Kern, *Evaluation of Infrared Emmission of Clouds and Ground as Measured by Weather Satellites*. Office of Aerospace Research, US Air Force, 1965.
- [29] E. Barreira, E. Bauer, N. Mustelier, and V. Freitas, "Measurement of materials emissivity – Influence of the procedure," in *13th International Workshop on Advanced Infrared Technology & Applications*, Pisa, Italy, Sep. 2015.
- [30] M. Farzamian, F. A. Monteiro Santos, and M. A. Khalil, "Estimation of unsaturated hydraulic parameters in sandstone using electrical resistivity tomography under a water injection test," *Journal of Applied Geophysics*, vol. 121, pp. 71–83, Oct. 2015, <https://doi.org/10.1016/j.jappgeo.2015.07.014>.
- [31] P. A. Domenico and F. W. Schwartz, *Physical and chemical hydrogeology*. New York, NY, USA: Wiley, 1990.
- [32] K. Parajuli, M. Sadeghi, and S. B. Jones, "A binary mixing model for characterizing stony-soil water retention," *Agricultural and Forest Meteorology*, vol. 244–245, pp. 1–8, Oct. 2017, <https://doi.org/10.1016/j.agrformet.2017.05.013>.
- [33] M. Th. van Genuchten, "A Closed-form Equation for Predicting the Hydraulic Conductivity of Unsaturated Soils," *Soil Science Society of America Journal*, vol. 44, no. 5, pp. 892–898, 1980, <https://doi.org/10.2136/sssaj1980.03615995004400050002x>.
- [34] M. Mannich, "Desenvolvimento de Solucoes Analiticas e Numericas da Equacao de Richards," Ph.D. dissertation, Universidade Federal do Parana, Curitiba, Brazil, 2008.
- [35] W. R. Gardner, "Some Steady-State Solutions of the Unsaturated Moisture Flow Equation with Application to Evaporation from a Water Table," *Soil Science*, vol. 85, pp. 228–232, Apr. 1958, <https://doi.org/10.1097/00010694-195804000-00006>.

Feature Extraction of EEG Signals for Seizure Detection Using Machine Learning Algorithms

Mohammed A. Alsuwaiket

Department of Computer Science and Engineering Technology
Hafar Al Batin University
Hafar Al Batin, Saudi Arabia
Malsuwaiket@uhb.edu.sa

Received: 18 July 2022 | Revised: 1 August 2022 | Accepted: 2 August 2022

Abstract—Epilepsy is a central nervous system disorder in which brain activity becomes abnormal and causes periods of unusual behavior and sometimes loss of awareness. Epilepsy is a disease that may affect males or females of all ethnic groups and ages. Detecting seizures is challenging due to the difference in human behaviors and brain signals. This paper aims to automate the extraction of electroencephalogram (EEG) signals without referring to doctors using two feature extraction methods, namely Wavelet Packet decomposition (WPD) and Genetic Algorithm-Based Frequency-Domain Feature Search (GAFDS). Three machine learning algorithms were applied, namely Conventional Neural Networks (CNNs), Support Vector Machine (SVM), and Random Forest (RF) to diagnose epileptic seizures. The results achieved from the classifiers show a higher accuracy rate using CNNs as a classifier and GAFDS as feature extraction reaching 97.93% accuracy while the accuracy rate of the SVM and RF was 94.49% and 88.03% respectively.

Keywords—EEG; CNN; SVM; seizure; feature extraction

I. INTRODUCTION

Epilepsy disorder is considered one of the most common brain diseases. According to the World Health Organization (WHO), this disease affects about sixty million people. Epilepsy is a brain disorder that causes the recurrent occurrence of epileptic seizures that can cause a possible dangerous life-threatening situation [1]. Brain seizures occur when a temporary and unexpected electrical disruption occurs in the brain along with the discharging of an excessive neuronal apparent in an EEG signal representative of the electrical activity in the brain. EEGs are most used in specifying brain disorders and predicting epileptic seizures. Epileptic seizure signals can be detected using image scanning of the EEG data, but unfortunately, this commonly requires a few days to collect the data. In addition, it also needs medical experts to study the length of the recorded EEG signals [2]. Improving the automated systems that detect seizures will reduce the error that could happen during the data reading process and will decrease the possibility of wrong decisions [3, 4]. Recently, other automated seizure detection systems, that use different methods and techniques like Machine Learning (ML) algorithms, have emerged.

The EEG signal has three characteristics that interpret signals as an intricate problem. The first characteristic is the non-stationary and stochastic signal behavior. The main reason for the non-stationary EEG signals is the brain neural activity that might not be in a coherent structure and thus neural charges/discharges of the same fraction of scalp change with different intensity levels over time [5]. The second characteristic is the low Signal to Noise Ratio (SNR). EEG signals usually maintain a low SNR because electrode conductivity on the scalp is affected by body motion, eye blinking, muscle movement, or other dynamic transitions in the environment. The third characteristic is the non-linearity of the EEG signals. The human brain is a complex system and EEG signals can be seen as a linear model, whereas some researchers have shown that EEG signals fit better in non-linear models [6].

A seizure is a transient extravagant electrical discharge of neurons in the human brain. Video monitoring is the most reliable technique for seizure diagnosis [7]. However, EEG signals are used for detection and seizure treatments. Also, exploring EEG epileptic records enables neurologists to determine the seizure type and its location in the brain. Seizure occurrences in EEG appear as low-frequency abnormal neuronal activities, such as spikes, which might be predominated by high-frequency oscillations and sudden changes in signal amplitude [8]. Early seizure detection several hours before its onset is possible by monitoring spike discharge activities and amplitude dynamics of slow waves before seizure occurrences. There are multiple seizure diagnosis tools, such as CT-scan, MRI, ultrasound, EEG, and Positron Emission Tomography (PET), where ultrasounds, CT-scan, and MRI are too expensive and may not be utilized for extensive assessment. Thus, EEG could be one of the most utilized tools to assess epilepsy patients [4].

Some researchers tried to detect and select features according to the redundancy and relevancy assessment in seizure monitoring to lower computational complexity. This paper intends to extract the EEG features using two different feature extraction methods and apply two ML algorithms to achieve the best diagnosis of epileptic seizures. The main aim of this paper can be achieved through pre-processing of the

EEG signals using different filters, then using two feature extraction methods, namely WPD and GAFDS to extract the main features from the EEG signal. Principal Component Analysis (PCA) method will be used to select the most useful features needed for the classification phase. Finally, SVM, RF, and CNN ML algorithms will be applied, and the results will be compared in terms of accuracy, speed, and complexity and the best classifier among them will be selected for EEG signal diagnosis.

Many researchers focused on the use of one classifier with or without the use of any feature extraction methods. Furthermore, there is no comprehensive comparison between the used classifiers or feature extraction methods with the evaluation for the running model from run time or performance perspectives. Authors in [9, 10] aimed to apply CNNs to detect epileptic seizures automatically by utilizing EEG signals to assist neurologists in the diagnostic process. This technique includes creating input data for the CNN model to detect the seizure accurately. The results showed that CNN has the ability to categorize the EEG signals and detect epileptic seizures with high accuracy. The effectiveness of different ML algorithms such as RF, SVM, and k-Nearest Neighbor (k-NN) was tested in [11, 12] to choose the best method with the best performance in detecting epileptic seizures. The ML algorithms were applied to pre-processed data and then to the original dataset. The results showed high accuracy of the RF, SVM, and k-NN with values 98.52%, 98.17%, and 96.52% respectively. Authors in [13] proposed an automated scheme to identify seizures. They used the SVM classifier with a Bayesian optimization algorithm to optimize the SVM hyper-parameters and integrated the Quadratic Linear Discriminant Analysis (QLDA) and Linear Discriminant Analysis (LDA) to match the findings. The proposed model was tested on a public dataset. The individual level of accuracy of the techniques was 97.05%, 76.41%, and 80.79% for SVM, LDA, and QLDA respectively. Epileptic seizure detection was achieved in [14] by applying both extreme gradient boosting (XGBoost) and Complementary Ensemble Empirical Mode Decomposition (CEEMD). Two EEG datasets were used to estimate the performance of the suggested model. The results showed that the CEEMD-XG boost model is a promising method for epileptic seizure detection. In [15], selection and feature extraction methods were used and ML algorithms were applied to the diagnosis monitoring knowledge system.

II. RESEARCH METHODOLOGY

The proposed methodology of this paper, as shown in Figure 1, starts with the raw data obtained from the EEG dataset. The dataset will be prepared and cleaned by removing the unwanted and noisy data. After that, the data will be ready for the preprocessing phase to be extracted by the proposed feature extraction methods (WPD, GAFDS). Then, the preprocessed data will be passed by the PCA feature selection method. Finally, the selected features will be applied to the proposed ML algorithms (SVM, CNN), and the results will be evaluated and compared. The following sections will go through all the phases mentioned in the proposed methodology in detail.

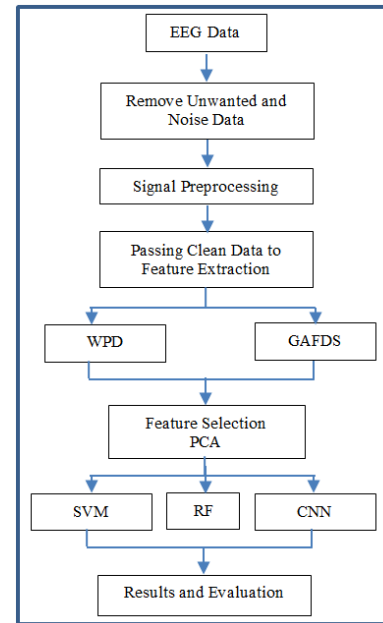


Fig. 1. The proposed methodology.

III. EEG DATASET DESCRIPTION

EEG data have been collected from the Children's Hospital Boston [16], consisting of EEG recordings from pediatric subjects with intractable seizures. Recordings, grouped into 23 cases, were collected from 22 subjects (5 males, with ages from 3 to 22 and 17 females, with ages from 1.5 to 19). Each case in the data files contains between 9 and 40 continuous .edf files from a single subject. In most cases, the .edf files contain 1 hour of digitized EEG signals, although those belonging to some cases are 2 and 4 hours long. Occasionally, files in which seizures are recorded are shorter. All signals were sampled at 256 samples per second with 16-bit resolution. Most files contain 23 EEG signals (24 or 26 in a few cases). One file in the dataset called RECORDED contains a list of all 664 .edf files included in this collection, and the file RECORDS-WITH-SEIZURES lists the 129 of those files that contain one or more seizures. In all, these records include 198 seizures (182 in the original set of 23 cases) [16].

IV. SIGNAL PREPARATION AND PRE-PROCESSING

In this paper, the preparation phase is used to clean the data by denoising the signals, removing the noise, and selecting the channels and signals that will be used. Denoising will be based on signal filters to remove the artifacts and EEG noise from the device and brain signals. The particles are isolated from the signal during the pre-processing phase to observe the artifact-free EEG signals. This method is achieved by filtering the data using the EEG signals acquired from multiple electrodes using a belt pass filter, a Common Spatial Pattern (CSP) filter, a broad Laplacian filter, and an Optimized Spatial Pattern (OSP) filter, which can then be transformed into the surrogate channel. With the use of a Finite Impulse Response (FIR) filter, the pure channel data will be small after artifact elimination. In the categorization process, obtaining relevant information is the main issue, and the epilepsy seizure data will be utilized and the whole bio-physical data will be transformed using Matlab.

During the pre-processing phase, the noise will be eliminated from the original signal to acquire the noise-free signal.

V. FEATURE EXTRACTION

Feature extraction is a process that removes the corresponding information or functions from the signal to easily explain the features. Therefore, the perception of an input signal is a significant operation. The extract of knowledge describes the physiology and pathology of the brain. It includes many variables which involve a huge memory or a strong data processing algorithm [17]. A function extraction method is required for this context to overwhelm these variables or to read the data accurately. The feature collection reduces the dimension of feature space, making it simpler to train and implement results. In this study, two feature extraction methods will be applied to the EEG dataset, WPD and GAFDS.

A. Wavelet Packet Decomposition (WPD)

WPD is a wavelet transition under which more filters than other methods are utilized. Wavelet packets constitute a peculiar linear wavelet mixture. They form bases that maintain much of their parent wavelets' orthogonality, smoothness, and positions. The linear combination coefficients are determined with a recursive algorithm that allows the study tree's root in each newly computed wavelet packet chain [5].

B. Genetic Algorithm –Based Frequency-Domain Feature Search (GAFDS)

The Genetic Algorithm (GA) uses the chance optimization approach for the analysis and demonstrates global optimization strength. The frequency domain is a coordinate system in signal processing, which defines the frequency characteristics of the signal. A frequency spectrogram represents the relationship between the frequency and the amplitude of the signals, often used for the study of signals. The GAFDS system adopts GA to look for the proper description of frequency spectrum characteristics [18].

VI. MACHINE LEARNING ALGORITHMS

Supervised ML algorithms are the best classification technique to find whether the data are classified as a seizure or not. In ML, the classification of EEG signals deals with the categorizing a set of classes to which a new reading belongs, based on a training set of EEG feature sets containing occurrences whose class relationship is identified [19]. Classification will be done to segment the data that will be tested with obtained data from several classifiers. Due to this, it is likely to identify if the information is of seizure or not. SVM, RF, and CNNs will be implemented in this paper. For software setup, Anaconda Python 3.7 was used for the experimental work. Keras has added due to its success and broad support for various learning styles, design features, and hypermeters. Libraries such as Panda's data storage, NumPy for multidimensional arrays, and Scikit Learn for data analysis were enabled. The ML classifiers have been trained, tested, and classified via the Sklearn machine libraries.

A. Support Vector Machine (SVM)

SVM is an ML technique used for classification and regression. SVM is effective in high-dimensional spaces and in

cases where the number of dimensions is greater than the number of samples. SVM includes a separating hyperplane used to differentiate between the plots or classes. The selection of the hyperplane is done according to the best separating area [20]. The classification method used in SVM (Figure 2) distinguishes a collection of binary labeled workout data and a maximum distance hyperplane and shows the seizure, non-seizure, and support vector points. The extracted confusion matrix from performing the SVM classifier and the comparison of the 2 feature extraction methods can be seen in Table I. GAFDS showed better results with accuracy near 94.5% compared with the WPD which showed a lower accuracy of 92.95%.

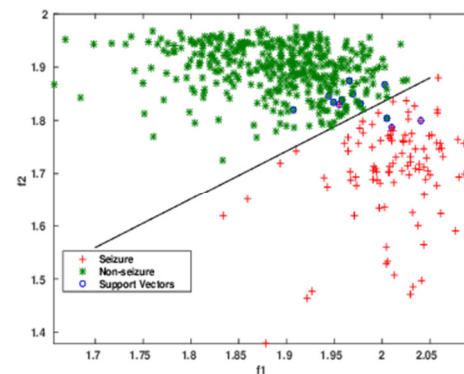


Fig. 2. SVM algorithm for EEG data.

TABLE I. SVM CLASSIFIER CONFUSION MATRIX

Feature extraction	Number of artifacts	Accuracy %	Precision %	Recall %	f1-score %
GAFDS	64,512	94.49	97	98	97
WPD	64,512	92.95	96	97	96

TABLE II. RF CLASSIFIER CONFUSION MATRIX

Feature extraction	Number of artifacts	Accuracy %	Precision %	Recall %	f1-score %
GAFDS	64,512	88.03	88	98	93
WPD	64,512	87.07	88	97	92

B. Random Forest (RF)

RF is a popular supervised ML technique used in classification and regression problems. It creates decision trees on various instances and takes their vote for classification and average in the case of regression. RF can handle datasets containing continuous variables as in the case of regression and categorical variables as in the case of classification. It performs better in classification problems [21]. With the RF classifier, the data need to be segmented into different sets. We start from calling the Sklearn's ensemble library to call the RF classifier. The function will load the data and split them into training and testing sets. The labeled data will start to train using the maximum iteration number that can be reached. This threshold has been set to 80%. Different types of feature extractions have been used to support the classifier. A total of 150 trees, with max depth = 12, and 50 nodes were used. The extracted confusion matrix from the RF classifier and the comparison of the 2 feature extraction methods can be seen in Table II. The

RF confusion matrix shows the metric values for both feature extraction methods. GAFDS showed better results with accuracy of 88.03% whereas WPD showed a lower accuracy of 87.07%.

C. Conventional Neural Networks (CNNs)

This paper utilizes a simple CNN to classify epileptic seizures [22, 23]. The diagnosis of epileptic seizure affects the identification and different characteristic of the EEG signals as discussed above. Furthermore, it needs a method for classifying epileptic seizures. Figure 3 shows the EEG signals classifications using CNN.

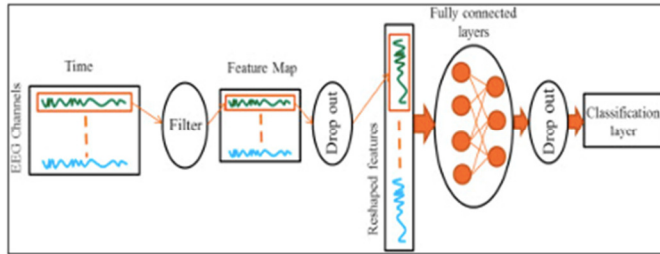


Fig. 3. EEG signal classifications using CNN.

Table III shows the CNN parameters that have been used for testing the proposed method. All layers have been chosen based on the dataset size without affecting the performance, run time, and accuracy results. The extracted confusion matrix from the CNN classifier and the comparison of the 2 feature extraction methods can be seen in Table IV. The CNN confusion matrix and the used parameters show the metric values for both feature extraction methods used in this paper. GAFDS showed better accuracy results.

TABLE III. CNN PARAMETERS

Input Layer	Hidden layer	Neurons	Epochs	Output layer
Based features	10	50	30	Based features
Based features	20	100	30	Based features
Based features	30	150	30	Based features
Based features	40	200	30	Based features
Based features	50	300	30	Based features

TABLE IV. CNN CLASSIFIER CONFUSION MATRIX

Feature extraction	Number of artifacts	Accuracy %	Precision %	Recall %	f1-score %
GAFDS	10	94.8	97	96	96
	20	95.34	97	97	97
	30	96.52	97	98	98
	40	96.88	97	99	98
	50	97.93	97	100	99
WPD	10	94.34	97	95	96
	20	95.07	97	96	97
	30	95.41	97	97	97
	40	96.3	97	98	97
	50	97.6	97	99	98

VII. RESULTS AND EVALUATION

In this paper, EEG signals were used as the data source. The proposed method used and compare different ML

techniques. The experiment uses Python programming language and an Intel i7 processor. The data were split into two sets, the first set (70%) for training and the second (30%) for testing. Table V and Figure 4 show the obtained results, which show that CNN had the best results for both feature extraction methods, followed by the SVM. RF had the lowest accuracy compared with the other ML algorithms in both feature extraction methods.

TABLE V. COMPREHENSIVE RESULTS

Feature extraction	Number of artifacts	Accuracy %	Precision %	Recall %	f1-score %
SVM	GAFDS	94.49	97	98	97
	WPD	92.95	96	97	96
RF	GAFDS	88.03	88	98	93
	WPD	87.07	88	97	92
CNN	GAFDS	97.93	97	100	99
	WPD	97.6	97	99	98

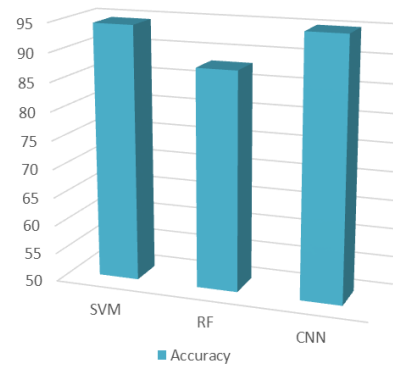


Fig. 4. Accuracy results for 70% training and 30% testing of EEG signals.

According to the obtained results for classifying EEG data for different size datasets using different ML algorithms, there are considerable differences among the results: some had low and some high accuracy. There are various reasons for such results, such as the use of different EEG data collection and screening methods, the selection of different EEG data features, the use of different EEG data formatting methods, and finally the different classification techniques and their parameters. EEG data classification accuracy is commonly relatively below. The reason behind that is the bulk of noise and artifacts which appear in the EEG signals and are not easy to avoid and hence make their analysis difficult. There are certain methods available to remove the artifacts from the EEG data as discussed above. However, this may cause losing some valuable data and affect the classification accuracy results.

VIII. CONCLUSIONS AND FUTURE WORK

In this paper, different methods of pre-processing for the EEG signals and two feature extraction methods were applied to extract the main features from the EEG signal. PCA was used to select the most useful features needed for the classification phase. The goal of this study was to test various ML techniques for the classification of EEG data. Three ML algorithms, i.e. SVM, RF, and CNN were used in the experiments. The chosen methods were analyzed using EEG data obtained from a children's hospital in Boston, including

EEG reports from children with intractable seizures. The chosen algorithms were built, and the results were compared in terms of accuracy and other evaluation methods, and the best classifier among all methods was selected for EEG signal diagnosis.

The CNN gave the best results in EEG data classification with. It should be noted that the findings are fully disparate when it comes to classifying EEG data separately for each subject. This means that the specific participants have major variations. Another important finding is that centered brain activities for a particular target will lead to greater accuracy than various brain activities for multiple targets. For future work, the use of other methods such as fuzzy logic [24], decision tree algorithm [25], and other supervised ML methods such as k-NN, Naïve Bayes, and logistic regression [26-28] is recommended.

REFERENCES

- [1] Z. Wang, G. Healy, A. F. Smeaton, and T. E. Ward, "A review of feature extraction and classification algorithms for image RSVP based BCI," in *Signal Processing and Machine Learning for Brain-Machine Interfaces*, T. Tanaka and A. Mahnaz, Eds. Stevenage, England: The Institute of Engineering and Technology, 2018, pp. 243–270.
- [2] Y. Zhang, Y. Zhang, J. Wang, and X. Zheng, "Comparison of classification methods on EEG signals based on wavelet packet decomposition," *Neural Computing and Applications*, vol. 26, no. 5, pp. 1217–1225, Jul. 2015, <https://doi.org/10.1007/s00521-014-1786-7>.
- [3] S. Raghu, N. Sriraam, and G. P. Kumar, "Effect of Wavelet Packet Log Energy Entropy on Electroencephalogram (EEG) Signals," *International Journal of Biomedical and Clinical Engineering*, vol. 4, no. 1, pp. 32–43, Jan. 2015, <https://doi.org/10.4018/IJBCE.2015010103>.
- [4] D. A. Torse and V. V. Desai, "Design of adaptive EEG preprocessing algorithm for neurofeedback system," in *International Conference on Communication and Signal Processing*, Melmaruvathur, India, Apr. 2016, pp. 392–395, <https://doi.org/10.1109/ICCSP.2016.7754164>.
- [5] V. Krishnan and B. Anto P, "Features of wavelet packet decomposition and discrete wavelet transform for malayalam speech recognition," *International Journal of Recent Trends in Engineering*, vol. 1, no. 2, pp. 93–96, 2009.
- [6] H. Shimizu, K. Yasuoka, K. Uchiyama, and S. Shioya, "Bioprocess Fault Detection by Nonlinear Multivariate Analysis: Application of an Artificial Autoassociative Neural Network and Wavelet Filter Bank," *Biotechnology Progress*, vol. 14, no. 1, pp. 79–87, 1998, <https://doi.org/10.1021/bp9701372>.
- [7] U. R. Acharya, S. L. Oh, Y. Hagiwara, J. H. Tan, and H. Adeli, "Deep convolutional neural network for the automated detection and diagnosis of seizure using EEG signals," *Computers in Biology and Medicine*, vol. 100, pp. 270–278, Sep. 2018, <https://doi.org/10.1016/j.compbiomed.2017.09.017>.
- [8] S. Ruder, "An overview of gradient descent optimization algorithms," arXiv, Jun. 15, 2017, <https://doi.org/10.48550/arXiv.1609.04747>.
- [9] P. Boonyakitanont, A. Lek-uthai, K. Chomtho, and J. Songsiri, "A Comparison of Deep Neural Networks for Seizure Detection in EEG Signals," bioRxiv, Jul. 15, 2019, Art. no. 702654, <https://doi.org/10.1101/702654>.
- [10] L. Chaari, Ed., *Digital Health Approach for Predictive, Preventive, Personalised and Participatory Medicine*. New York, NY, USA: Springer, 2019.
- [11] Seferkurnaz and A. A. Saleh, "Comparative and Analysis Study of normal and epileptic seizure EEG signals by using various classification Algorithms," *IOSR Journal of Computer Engineering*, vol. 20, no. 4, pp. 23–33, Jul. 2018, <https://doi.org/10.9790/0661-2004012333>.
- [12] M. Zhou *et al.*, "Epileptic Seizure Detection Based on EEG Signals and CNN," *Frontiers in Neuroinformatics*, vol. 12, Dec. 2018, Art. no. 95, <https://doi.org/10.3389/fninf.2018.00095>.
- [13] A. Nandy, M. A. Alahe, S. M. Nasim Uddin, S. Alam, A.-A. Nahid, and Md. A. Awal, "Feature Extraction and Classification of EEG Signals for Seizure Detection," in *International Conference on Robotics, Electrical and Signal Processing Techniques*, Dhaka, Bangladesh, Jan. 2019, pp. 480–485, <https://doi.org/10.1109/ICREST.2019.8644337>.
- [14] J. Wu, T. Zhou, and T. Li, "Detecting Epileptic Seizures in EEG Signals with Complementary Ensemble Empirical Mode Decomposition and Extreme Gradient Boosting," *Entropy*, vol. 22, no. 2, Feb. 2020, Art. no. 140, <https://doi.org/10.3390/e22020140>.
- [15] H. Liu, L. Xi, Y. Zhao, and Z. Li, "Using Deep Learning and Machine Learning to Detect Epileptic Seizure with Electroencephalography (EEG) Data," arXiv, Oct. 06, 2019, <https://doi.org/10.48550/arXiv.1910.02544>.
- [16] A. L. Goldberger *et al.*, "PhysioBank, PhysioToolkit, and PhysioNet: components of a new research resource for complex physiologic signals," *Circulation*, vol. 101, no. 23, pp. E215–220, Jun. 2000, <https://doi.org/10.1161/01.cir.101.23.e215>.
- [17] K. Ueki and T. Kobayashi, "Fusion-Based Age-Group Classification Method Using Multiple Two-Dimensional Feature Extraction Algorithms," *IEEE Transactions on Information and Systems*, vol. E90-D, no. 6, pp. 923–934, Jun. 2007.
- [18] T. Wen and Z. Zhang, "Effective and extensible feature extraction method using genetic algorithm-based frequency-domain feature search for epileptic EEG multiclassification," *Medicine*, vol. 96, no. 19, May 2017, Art. no. e6879, <https://doi.org/10.1097/MD.0000000000006879>.
- [19] J. Seo, T. H. Laine, and K.-A. Sohn, "Machine learning approaches for boredom classification using EEG," *Journal of Ambient Intelligence and Humanized Computing*, vol. 10, no. 10, pp. 3831–3846, Oct. 2019, <https://doi.org/10.1007/s12652-019-01196-3>.
- [20] Y.-D. Cai, G.-P. Zhou, and K.-C. Chou, "Support Vector Machines for Predicting Membrane Protein Types by Using Functional Domain Composition," *Biophysical Journal*, vol. 84, no. 5, pp. 3257–3263, May 2003, [https://doi.org/10.1016/S0006-3495\(03\)70050-2](https://doi.org/10.1016/S0006-3495(03)70050-2).
- [21] M. Al Lababede, A. Blasi, and M. Alsuaiket, "Mosques Smart Domes System using Machine Learning Algorithms," *International Journal of Advanced Computer Science and Applications*, vol. 11, no. 3, pp. 373–378, Mar. 2020, <https://doi.org/10.14569/IJACSA.2020.0110347>.
- [22] R. Aroud, A. Blasi, and M. Alsuaiket, "Intelligent Risk Alarm for Asthma Patients using Artificial Neural Networks," *International Journal of Advanced Computer Science and Applications*, vol. 11, no. 6, pp. 95–100, Jun. 2020, <https://doi.org/10.14569/IJACSA.2020.0110612>.
- [23] A. Blasi, "Performance Increment of High School Students using ANN model and SA algorithm," *Journal of Theoretical and Applied Information Technology*, vol. 95, no. 11, pp. 2417–2425, Jan. 2017.
- [24] A. Blasi, "Scheduling Food Industry System using Fuzzy Logic," *Journal of Theoretical and Applied Information Technology*, vol. 96, no. 19, pp. 6463–6473, Oct. 2018.
- [25] A. H. Blasi, M. A. Abbadi, and R. Al-Huweimel, "Machine Learning Approach for an Automatic Irrigation System in Southern Jordan Valley," *Engineering, Technology & Applied Science Research*, vol. 11, no. 1, pp. 6609–6613, Feb. 2021, <https://doi.org/10.48084/etasr.3944>.
- [26] A. H. Blasi and M. Alsuaiket, "Analysis of Students' Misconducts in Higher Education using Decision Tree and ANN Algorithms," *Engineering, Technology & Applied Science Research*, vol. 10, no. 6, pp. 6510–6514, Dec. 2020, <https://doi.org/10.48084/etasr.3927>.
- [27] M. Alsuaiket, A. H. Blasi, and K. Altarawneh, "Refining Student Marks based on Enrolled Modules' Assessment Methods using Data Mining Techniques," *Engineering, Technology & Applied Science Research*, vol. 10, no. 1, pp. 5205–5210, Feb. 2020, <https://doi.org/10.48084/etasr.3284>.
- [28] M. Alsuaiket, A. H. Blasi, and R. A. Al-Msie'deen, "Formulating Module Assessment for Improved Academic Performance Predictability in Higher Education," *Engineering, Technology & Applied Science Research*, vol. 9, no. 3, pp. 4287–4291, Jun. 2019, <https://doi.org/10.48084/etasr.2794>.

Reliability Analysis of an Uncertain Single Degree of Freedom System Under Random Excitation

Mohammed S. M. Noori

Department of Civil Engineering

College of Engineering

University of Baghdad

Baghdad, Iraq

m.noori1901m@coeng.uobaghdad.edu.iq

Rafaa M. Abbas

Department of Civil Engineering

College of Engineering

University of Baghdad

Baghdad, Iraq

dr.rafaa@coeng.uobaghdad.edu.iq

Received: 10 July 2022 | Revised: 4 August 2022 | Accepted: 7 August 2022

Abstract—In practical engineering problems, uncertainty exists not only in external excitations but also in structural parameters. This study investigates the influence of structural geometry, elastic modulus, mass density, and section dimension uncertainty on the stochastic earthquake response of portal frames subjected to random ground motions. The North-South component of the El Centro earthquake in 1940 in California is selected as the ground excitation. Using the power spectral density function, the two-dimensional finite element model of the portal frame's base motion is modified to account for random ground motions. A probabilistic study of the portal frame structure using stochastic finite elements utilizing Monte Carlo simulation is presented using the finite element program ABAQUS. The dynamic reliability and probability of failure of stochastic and deterministic structures based on the first-passage failure were examined and evaluated. The results revealed that the probability of failure increases due to the randomness of stiffness and mass of the structure. The influence of uncertain parameters on reliability analysis depends on the extent of variance in structural parameters.

Keywords—reliability; Monte Carlo simulation; uncertain system; random excitation; stochastic; finite element analysis

I. INTRODUCTION

In practical engineering problems, the external excitations, such as wind loading and seismic waves, and the parameters of a structure exhibit uncertainty. Structural parameter uncertainty may strongly influence structural response and reliability [1]. Earthquakes are the most disastrous natural phenomena. Therefore, the seismic response of many types of structures and buildings has been widely investigated. However, most modeling attempts of seismic random response analysis of structures belong to deterministic models in which all structural parameters were regarded as deterministic parameters. From another aspect, most engineering structures can be classified as random due to the variability in their geometric or material properties. Therefore, the problem of stochastic structures subject to stochastic seismic excitation is of great importance [2]. Considering that ground motion induced by an earthquake represents a type of random excitation, the theory and methods of random vibration should be applied to analyze the seismic

response of structures. The random excitation is usually specified regarding its Power Spectral Density (PSD) [3]. The random vibration theoretical framework has been well established. The dynamic analysis of systems with deterministic structural parameters to random excitations is available. However, the dynamic analysis of systems with stochastic structural parameters under random excitations has not been developed to the same extent [4]. A natural frequency represents one of the most influencing parameters on system response. Uncertainty in the natural frequency can arise from uncertainties in the stiffness or inertia properties of the structure. In this case, probabilistic-based analysis methods should be utilized. Thus, the considered statistical parameters associated with the distribution of random variables should be determined. In general, the stochastic finite element-based method is a probabilistic analysis method and is well suited to deal with random parameter problems [5]. Given the random nature of loading, material specifications, and implementation issues, probabilistic-based analysis should be utilized. Thus, considering the statistical parameters associated with the distribution of random variables should be determined. The reliability-based analysis is a new approach to structural analysis and design that takes uncertainty into account [6].

A survey of previous studies indicated that structural reliability methods have been mainly developed for rationally evaluating the safety of deterministic structures with excitation. However, the studies on nondeterministic structures to investigate statistical uncertainty characteristics are limited. The current study emphasizes on reliability analysis of a stochastic structure with uncertain parameters and excitation to assess the reliability and safety of this system. To achieve the goal of this study, a single degree of freedom system subject to seismic base excitation is examined using a probabilistic finite element ABAQUS code using Monte Carlo Simulation (MCS) and Python script to generate pseudo-random values for the considered random parameters.

II. RANDOM EXCITATION

The stochastic earthquake analysis in this study is based on the stationary assumption, in which the statistical parameters'

mean and variance do not vary with time. A stationary model makes them less sophisticated, simplifies computations, and gives satisfactory results [7]. As a single record is insufficient for producing general conclusions, an ergodicity assumption is applied. Moreover, only one earthquake record from the local area can be utilized. The PSD function of acceleration seismic motion is assumed to be in the form of a filtered Gaussian white noise ground motion. The model was suggested in [8, 9] and was later modified in [10]. This model can be expressed as:

$$S_{\ddot{X}_g}(\omega)_{CP} = \frac{1+4\xi_g^2(\omega/\omega_g)^2}{[1-(\omega/\omega_g)^2]^2+4\xi_g^2(\omega/\omega_g)^2} \frac{(\omega/\omega_f)^2}{[1-(\omega/\omega_f)^2]^2+4\xi_f^2(\omega/\omega_f)^2} S_0 \quad (1)$$

where ξ_g , ω_g , ξ_f , and ω_f represent the damping ratio and natural frequency of the soil and high pass filter respectively, and S_0 is the intensity of the white noise of ground motion. To estimate the filter parameters, the method of the spectral moment [11] is the key statistical parameter of the PSD function [12]. The i^{th} spectral moment λ_i is defined as:

$$\lambda_i = \int_0^\infty \omega^i G(\omega) d\omega \quad (2)$$

The variance of the excitation is the zero spectral moment:

$$\lambda_0 = \sigma_0^2 = \int_0^\infty G(\omega) d\omega \quad (3)$$

The central frequency, ω_c , and the shape factor, δ , of the random process can be directly evaluated from the first few spectral moments:

$$\omega_c = \sqrt{\lambda_2/\lambda_0}, \quad (4)$$

$$\delta = \sqrt{1 - (\lambda_1^2/\lambda_2\lambda_0)} \quad (5)$$

As the central frequency and shape factor are functions of the spectral moments (λ_0 , λ_1 , and λ_2), they are expressed in terms of the filter parameters, i.e. ω_g , ξ_g , and S_0 . Hence, they can be computed by matching the variance of acceleration, the central frequency, and the shape factor of the actual and theoretical PSD.

III. STATIONARY RANDOM VIBRATION ANALYSIS

The equation of motion for a Single Degree of Freedom (SDOF) structure subjected to random ground acceleration is:

$$m\ddot{X}(t) + c_0\dot{X}(t) + kX(t) = -m\ddot{X}_g(t) \quad (6)$$

where \ddot{X}_g , m , c_0 , and k are the ground acceleration process, structural mass, viscous damping, and elastic stiffness respectively. The PSD of the displacement response may be represented as in (7) if the ground motion acceleration (\ddot{X}_g) is considered a stationary Gaussian random process [10].

$$S_{yy}(\omega) = H(\omega) H(\omega)^* S_{\ddot{X}_g}(\omega) \quad (7)$$

where $S_{\ddot{X}_g}(\omega)$ is the PSD function of the (\ddot{X}_g), $H(\omega)$ is the frequency response function as in (8), and (*) stands for complex conjugate:

$$H(\omega) = \frac{1}{\omega_j^2 - \omega^2 + 2i\xi_j\omega_j\omega} \quad (8)$$

where ω_j and ξ_j are the j^{th} order inherence frequency and mode damping of structure respectively. The mean square and the root mean square of the relative displacement can be expressed as in (9) and (10) respectively [10]:

$$\sigma_x^2 = \int_{-\infty}^{\infty} S_{yy}(\omega) d\omega \quad (9)$$

$$\sigma_x = \sqrt{\int_{-\infty}^{\infty} S_{yy}(\omega) d\omega} \quad (10)$$

IV. MONTE CARLO SIMULATION

Although being a highly time-consuming computational method, the MCS method is considered one of the most powerful and accurate simulation tools to estimate numerically the reliability and failure probability of uncertain structures [18]. This method is used to calculate the response uncertainty and the numerical estimate of failure probability. It uses random sampling from random variable distributions. The "crude" or "direct" MCS, which is a pseudo-random sampling, is the basic version [13]. In MCS, the failure probability is described as:

$$\hat{p}_f = \frac{N_f}{N} \quad (11)$$

where N is the total number of samples and N_f is the number of samples in the failure domain.

MCS is a most general approach for the Stochastic Finite Element Method (SFEM) [14]. The deterministic FEM and the MCS technique are merged in this methodology. SFEM can express randomness in one or more of the main components of the classic FEM, such as geometry, material properties, and external forces [15].

V. DYNAMIC RELIABILITY

The reliability of a system is closely related to the concept of level crossing. This case is particularly true for first-passage failure, in which the system is considered to fail only when a particular stress process or displacement $X(t)$ reaches a critical level b in the time interval $[0, T]$. When the structural response of a deterministic structural parameter is a stationary Gaussian process, the crossing time of the response $x(t)$ and limit b submit to the Poisson process. The dynamic probability of failure of a SDOF structure can then be obtained from [16]:

$$p_f(t) \approx 1 - \exp\left\{-v_0 T \exp\left[-\frac{1}{2}\left(\frac{b}{\sigma_x}\right)^2\right]\right\} \quad (12)$$

$$R(t) \approx \exp\left\{-v_0 T \exp\left[-\frac{1}{2}\left(\frac{b}{\sigma_x}\right)^2\right]\right\} \quad (13)$$

where T is the duration of the stationary process, σ_x is a root mean square of the response, and v_0 is zero mean cross rate expressed as follows:

$$v_0 = \frac{1}{2\pi} \sqrt{\frac{\lambda_2}{\lambda_0}} \quad (14)$$

where λ_0 and λ_2 are zero and the second spectral moment respectively, defined as follows:

$$\lambda_m = \int_0^{\omega_c} \omega^m G_s(\omega) d\omega \quad \text{For } m = 0, 1, 2 \quad (14)$$

When the structural parameters and the excitation are random, the system reliability may be evaluated by calculating the probability of an equivalent extreme-value event. Hence, the seismic excitation and structural response are assumed to have a zero mean. y_e and σ_x are the extreme value and standard division of structural response $y(t)$ respectively. The dimensionless parameters are explained below [16].

$$\eta = \frac{y_e}{\sigma_x} \quad (15)$$

Assuming a Poisson process for the number of horizontal crossings, taking parameter uncertainty into account, the estimated mean of the extreme value is:

$$E(\eta) = (\sqrt{2 \ln v_0 T} + \frac{0.5772}{\sqrt{2 \ln v_0 T}}) \quad (16)$$

and the variance of η is:

$$\sigma^2(\eta) = \frac{\pi^2}{6} \frac{\sigma_x^2}{(2 \ln v_0 T)} \quad (17)$$

The extreme value of the stochastic process $y(t)$ is expressed as:

$$y_e = E(\eta) \times \sigma_x \quad (18)$$

The limit state function of the inter-story drift system is expressed as:

$$G(\Delta) = R(\Delta) - Q(\Delta) \quad (19)$$

where $R(\Delta)$ is the structure drift limit equal to 0.01, 0.015, and 0.02 from story height, and $Q(\Delta)$ represents the extreme value of the structural drift because of the loading, including the uncertainties of the structural parameters. Limit state function $G(\Delta) \leq 0$ is the failure state, and $G(\Delta) > 0$ is a safe state. Table I shows the target reliability of the steel structure system.

TABLE I TARGET RELIABILITY INDICES [17]

Component type	Loading condition		
	D+(L or S)	D+L+W	D+L+E
Members	3.0	2.5	1.75
Connections	4.5	4.5	4.5

VI. NUMERICAL EXAMPLE

A numerical example is presented and analyzed to demonstrate the reliability analysis for a case study of a simple frame structure, as shown in Figure 1. The stochastic response due to the uncertainty in structure physical properties and seismic excitation force is taken into account.

A. Proposed Structural System

Uncertainty and reliability analysis have been executed for an interior frame of the shear building system, as shown in Figure 1. The floor system consists of a concrete slab 200mm thick supported by 3 steel girders with a W12×190 cross-section and the girders are supported by steel columns with a W10×33 cross-section, as shown in Figure 2. In addition to the own weight, uniformly distributed pressures of 2 and 1kPa were adopted for the superimposed and live loads respectively.

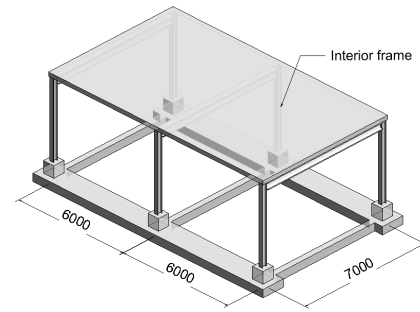


Fig. 1. One-story two-bay frame.

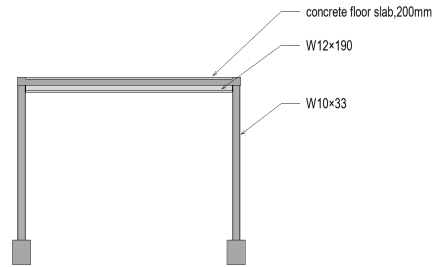


Fig. 2. Interior frame.

B. Random Ground Motion

In this study, the North-South component of the 1940 El Centro earthquake was chosen as the ground motion. Using the spectral moment method, the acceleration spectral density function parameters of filtered white noise ground motion have been estimated, as shown in Figure 3. The calculated values of natural frequency and the damping ratio for the first and second filters were $\omega_g = 18.5 \text{ rad/s}$, $\xi_g = 0.43$, and $\omega_f = 1.5 \text{ rad/s}$, and $\xi_f = 0.6$ respectively. The intensity factor of the earthquake was $S_0 = 0.00282 \text{ m}^2/\text{s}^3$.

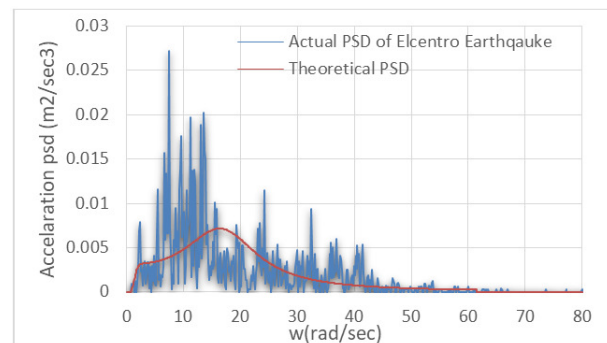


Fig. 3. Actual and theoretical PSD of the El-Centro earthquake.

C. Stochastic Earthquake Analysis with Deterministic Structural Parameters

The dynamic characteristics of the deterministic portal frame structures have been analyzed with ABAQUS finite element software [18]. The two-dimension portal frame has been modeled with wire part B21, as shown in Figure 4. The inertia mass has been selected based on the effective weight of the concrete slab, superimposed, and a quarter of the live load according to ASCE7-16. The girder and columns were

discretized using a mesh size of 100mm. A rigid body constraint has been adopted for the girder. In addition, the density of the column has been reduced to achieve the assumption of a shear frame of the rigid girder supported by weightless columns with fixed supports. The structure's natural frequency was obtained by modal analysis, and two values were extracted, as shown in Figure 5 and Table II.

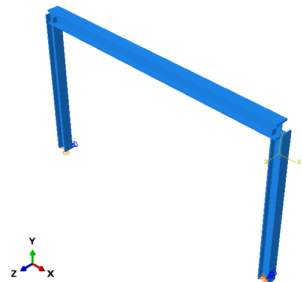


Fig. 4. 3D portal frame view.

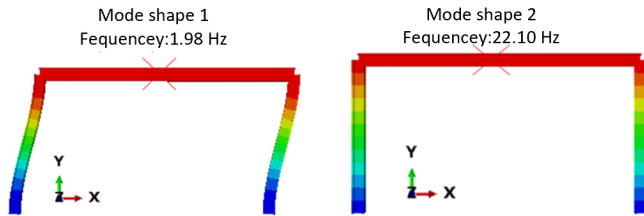


Fig. 5. First two mode shapes.

TABLE II NATURAL FREQUENCY AND MASS PARTICIPATION FACTOR

Mode	Frequency (Hz)	Frequency (rad/sec)	Mass participation factor	Direction
1	1.98	12.46	99%	Along x-direction
2	22.10	138.85	99%	Along y-direction

Random vibration analysis was conducted with a base motion of the portal frame in the x-direction. The frequency range of interest and the response have been set. Hence, the PSD of the relative displacement was obtained as shown in Figure 6. One peak detected in the vibration responses refers to the resonance occurrence at the first natural frequency of the investigated system.

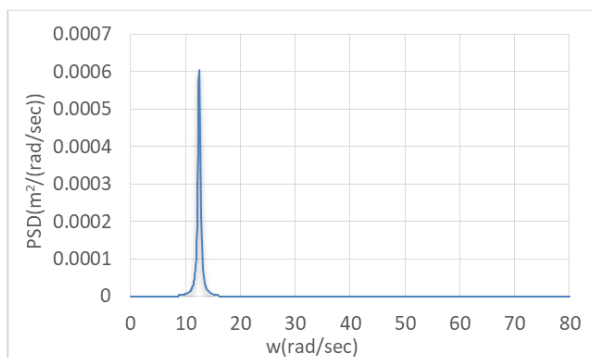


Fig. 6. Response PSD of relative displacement.

By integrating the response PSD, the mean square and Root Mean Square (RMS), of relative displacement were $7.48 \times 10^{-5} \text{m}^2$ and $8.65 \times 10^{-3} \text{m}$ respectively. The displacement resistance limit of the structure has been taken from ASCE 7–16 structural design codes, where the allowable story drift is related to the risk categories and the structural system. Thus, this research intends to investigate the different allowable limits, i.e. 1.0%, 1.5%, and 2%, of story height. The probability of failure of the system has been estimated for 3 response intervals of 10, 15, and 20s, as shown in Figure 7. Based on this estimate, the reliability index was obtained and is presented in Table II. The results showed that the probability of failure slightly increased when the response time increased. Therefore, the reliability index of the system was not significantly affected. From another aspect, comparing the reliability index with the target reliability shown in Table I reveals that the structure meets the specified safety level.

TABLE III FAILURE PROBABILITY AND RELIABILITY INDEX FOR A DETERMINISTIC SYSTEM

Threshold	10s		15s		20s	
	<i>pf</i>	β	<i>pf</i>	β	<i>pf</i>	β
0.01H	1.11×10^{-3}	3.06	1.66×10^{-3}	2.94	2.21×10^{-3}	2.85
0.015H	5.32×10^{-9}	5.72	7.98×10^{-9}	5.65	1.06×10^{-8}	5.60
0.02H	≈ 0	—	≈ 0	—	≈ 0	—

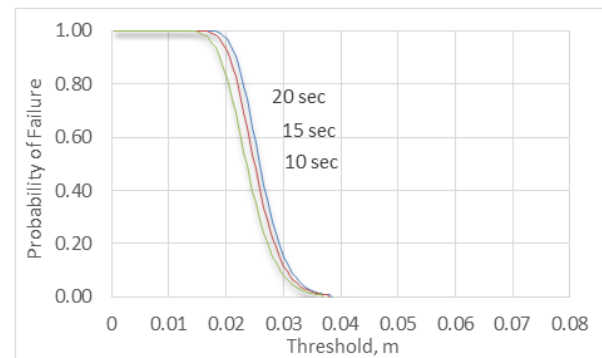


Fig. 7. First-passage failure for the three-time response interval.

D. Stochastic Earthquake Analysis with Nondeterministic Structural Parameters

To illustrate the effect of the randomness of structural parameters, including stiffness k and mass m on the natural frequency and random seismic response, MCS was performed to update the random variables of interest for each Finite Element Analysis (FEA) trial. Python programming was used to develop the deterministic FE model, and then, the random input variables of interest were updated based on the idea of parameter updating functionality. In this study, the cross-section dimensions, modulus of elasticity, column length, and the applied load were considered as random variables. Table IV shows the statistical characteristics of these parameters.

Probabilistic modal analyses of random structural parameters of the interior portal frame were estimated using SFEM with python script coding. Matlab function was used to generate 5000 pseudo-random samples of cross-section dimensions, modulus of elasticity, column length, and

structural effective mass. Figure 8 depicts the natural frequency result obtained from the sample data. Mean value, standard deviation, and coefficient of variance were 12.34rad/sec, 1.3576, and 0.109 respectively. Notably, the mean value for the natural frequency is very close to that shown in Table II for the deterministic analysis, indicating the validity of the dynamic analysis with random properties and excitation. Due to the randomness in the natural frequency, the system response was affected.

Figure 9 shows the RMS of relative displacement. Mean, standard deviation, and Cov were 0.0105m, 0.0016, and 0.1483 respectively. The results for the coefficient of variance indicate the effectiveness of randomness in the stochastic structure properties and excitation on the response properties.

TABLE IV STATISTICAL CHARACTERISTICS OF VARIABLES

Random variables		Mean/nominal	COV	Distribution type	Ref.
Cross section dimension	Depth of the web	1.0009	0.004	Normal	[20]
	Width of the flange	1.0139	0.009	Normal	
	Thickness of the flange	0.9927	0.044	Normal	
	Thickness of the web	1.054	0.037	Normal	
Modulus of elasticity		0.993	0.034	Normal	[21]
Column length		1	0.07	Lognormal	[22]
Load	Weight of a girder	1.03	0.1	Normal	[23]
	Weight of a slab	1.05	0.1	Normal	
	Superimposed load	1.03	0.1	Normal	
	Live load	1	0.1	Gumbel	

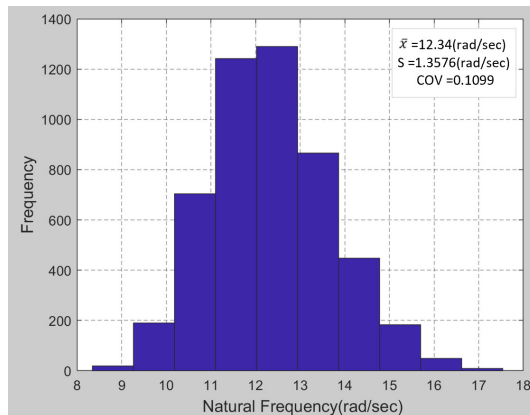


Fig. 8. Histogram of the first natural frequency.

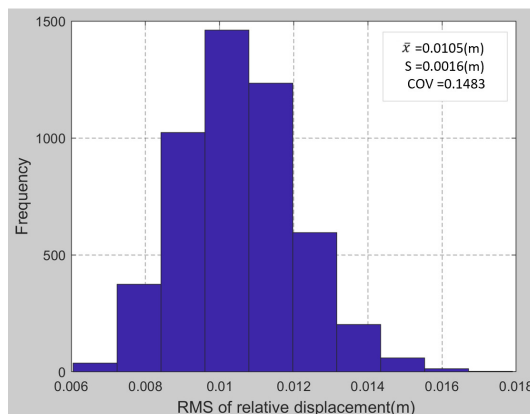


Fig. 9. Histogram of the RMS of the relative displacement.

Figures 8 and 9 show the failure probability estimates for the threshold level of 1%, and Table IV presents the summary. Notably, the Monte Carlo estimate for 1.5% and 2% levels is not shown in the Figure because the sample size is not large enough to provide sufficiently accurate estimates for the probability of failure corresponding to this threshold level. The results revealed that randomness in the system's stiffness and mass influences the system's reliability. Moreover, generally, the probability of failure increased due to the randomness in the stiffness and mass of the structure. This conclusion is confirmed by comparing the results presented in Tables III and V for deterministic and stochastic systems. The Probability Density Function (PDF) in Figure 10 shows that the distribution ranges of the equivalent extreme value have a trend of moving toward the right-hand side with increasing response time intervals. This case accords to the trends of increasing the probability of failure. The cumulative density function in Figure 11 shows the boundary between the safe and failure domains, which is described by the limit of 0.04m on the x-axis.

TABLE V FAILURE PROBABILITY AND RELIABILITY INDEX FOR A STOCHASTIC SYSTEM

Threshold	10s		15s		20s	
	pf	β	pf	β	pf	β
0.01H	2.8×10^{-3}	2.77	9.4×10^{-3}	2.34	21.4×10^{-3}	2.02

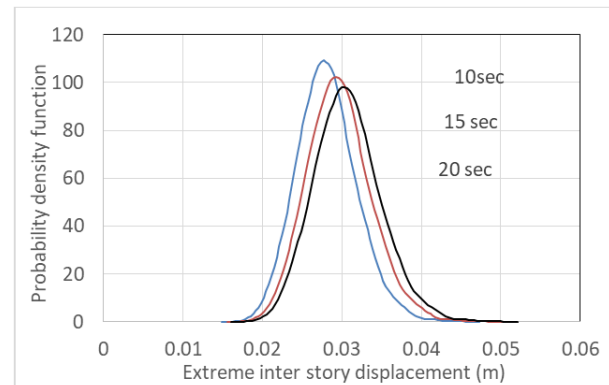


Fig. 10. Probability density function for the extreme value of drift.

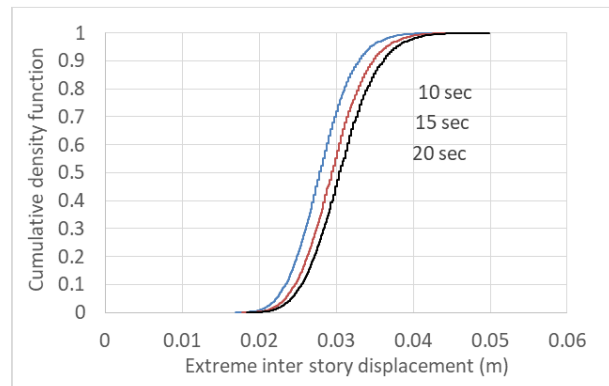


Fig. 11. Cumulative density function for the extreme value of drift.

VII. CONCLUSIONS

In this study, a reliability analysis of portal frames excited by random ground motion with deterministic and stochastic structural parameters was performed. The following conclusions can be drawn:

- The probability of failure and the reliability index of the deterministic structure were affected slightly by the excitation time interval. The probability of failure increased and the reliability index decreased with increasing time interval.
- The reliability index of the deterministic structure was greater than the target reliability index for members subject to seismic base motion.
- The results for the mean values of the dynamic response for the SDOF system with random properties and excitation correlate well with the deterministic analysis results.
- Randomness in the system's stiffness and mass influences the system's reliability and probability of failure. Generally, the probability of failure increased due to the randomness in stiffness and mass of the structure.

REFERENCES

- [1] J. Li and S. Liao, "Response analysis of stochastic parameter structures under non-stationary random excitation," *Computational Mechanics*, vol. 27, no. 1, pp. 61–68, Jan. 2001, <https://doi.org/10.1007/s004660000214>.
- [2] J. Dai, W. Gao, N. Zhang, and N. Liu, "Seismic random vibration analysis of shear beams with random structural parameters," *Journal of Mechanical Science and Technology*, vol. 24, no. 2, pp. 497–504, Feb. 2010, <https://doi.org/10.1007/s12206-009-1210-x>.
- [3] M. R. Machado, L. Khalij, and A. T. Fabro, "Dynamic Analysis of a Composite Structure under Random Excitation Based on the Spectral Element Method," *International Journal of Nonlinear Sciences and Numerical Simulation*, vol. 20, no. 2, pp. 179–190, Apr. 2019, <https://doi.org/10.1515/ijnsns-2018-0050>.
- [4] W. Gao and N. J. Kessissoglou, "Dynamic response analysis of stochastic truss structures under non-stationary random excitation using the random factor method," *Computer Methods in Applied Mechanics and Engineering*, vol. 196, no. 25, pp. 2765–2773, May 2007, <https://doi.org/10.1016/j.cma.2007.02.005>.
- [5] S. Adhikari and B. Pascual, "The 'damping effect' in the dynamic response of stochastic oscillators," *Probabilistic Engineering Mechanics*, vol. 44, pp. 2–17, Apr. 2016, <https://doi.org/10.1016/j.probengmech.2015.09.017>.
- [6] M. H. Soltani and S. H. Ghasemi, "Structural Drift Corresponding to the Critical Excitations," *Journal of Structural Engineering and Geo-Techniques*, vol. 10, no. 2, pp. 27–34, Dec. 2020.
- [7] K. Hacıfendioglu, H. B. Başağa, and S. Banerjee, "Probabilistic analysis of historic masonry bridges to random ground motion by Monte Carlo Simulation using Response Surface Method," *Construction and Building Materials*, vol. 134, pp. 199–209, Mar. 2017, <https://doi.org/10.1016/j.conbuildmat.2016.12.101>.
- [8] K. Kiyoshi, "Semi-empirical Formula for the Seismic Characteristics of the Ground," *Bulletin of the Earthquake Research Institute, University of Tokyo*, vol. 35, no. 2, pp. 309–325, Sep. 1957, <https://doi.org/10.15083/0000033949>.
- [9] H. Tajimi, "Statistical Method of Determining the Maximum Response of Building Structure During an Earthquake," *Proceedings of the 2nd WCEE*, vol. 2, pp. 781–798, 1960.
- [10] R. W. Clough and J. Penzien, *Dynamics of Structures*. New York: McGraw-Hill College, 1975.
- [11] S. P. Lai, "Statistical characterization of strong ground motions using power spectral density function," *Bulletin of the Seismological Society of America*, vol. 72, no. 1, pp. 259–274, Feb. 1982, <https://doi.org/10.1785/BSSA0720010259>.
- [12] E. H. Vanmarcke, "Chapter 8 - Structural Response to Earthquakes," in *Developments in Geotechnical Engineering*, vol. 15, C. Lomnitz and E. Rosenblueth, Eds. Elsevier, 1976, pp. 287–337.
- [13] S. S. Kar and L. B. Roy, "Probabilistic Based Reliability Slope Stability Analysis Using FOSM, FORM, and MCS," *Engineering, Technology & Applied Science Research*, vol. 12, no. 2, pp. 8236–8240, Apr. 2022, <https://doi.org/10.48084/etasr.4689>.
- [14] J. D. Arregui-Mena, L. Margetts, and P. M. Mummery, "Practical Application of the Stochastic Finite Element Method," *Archives of Computational Methods in Engineering*, vol. 23, no. 1, pp. 171–190, Mar. 2016, <https://doi.org/10.1007/s11831-014-9139-3>.
- [15] D. T. Hang, X. T. Nguyen, and D. N. Tien, "Stochastic Buckling Analysis of Non-Uniform Columns Using Stochastic Finite Elements with Discretization Random Field by the Point Method," *Engineering, Technology & Applied Science Research*, vol. 12, no. 2, pp. 8458–8462, Apr. 2022, <https://doi.org/10.48084/etasr.4819>.
- [16] Y. K. Wen and H.-C. Chen, "On fast integration for time variant structural reliability," *Probabilistic Engineering Mechanics*, vol. 2, no. 3, pp. 156–162, Sep. 1987, [https://doi.org/10.1016/0266-8920\(87\)90006-3](https://doi.org/10.1016/0266-8920(87)90006-3).
- [17] W. T. Segui, *Steel Design*, 5th ed. Mason, OH, USA: Cengage Learning, 2013.
- [18] N. L. Tran and T. H. Nguyen, "Reliability Assessment of Steel Plane Frame's Buckling Strength Considering Semi-rigid Connections," *Engineering, Technology & Applied Science Research*, vol. 10, no. 1, pp. 5099–5103, Feb. 2020, <https://doi.org/10.48084/etasr.3231>.
- [19] "Abaqus Analysis User's Guide (6.14)," *Simulia*. <http://130.149.89.49:2080/v6.14/books/usb/default.htm>.
- [20] Z. Kala, J. Melcher, and L. Puklicky, "Material and geometrical characteristics of structural steels based on statistical analysis of metallurgical products," *Journal of Civil Engineering and Management*, vol. 15, no. 3, pp. 299–308, Sep. 2009.
- [21] S. Zhang and W. Zhou, "System Reliability Assessment of 3d Steel Frames Designed Per AISC LRFD Specifications," *Advanced Steel Construction*, vol. 9, no. 1, pp. 77–89, 2016, <https://doi.org/10.1016/J.JCSR.2016.01.009>.
- [22] M. M. A. Moghaddam and M. Moudi, "Analysis of beam failure based on reliability system theory using monte carlo simulation method," in *International Conference on Applied Computer Science - Proceedings*, Jan. 2010, pp. 516–519.
- [23] A. S. Nowak and K. R. Collins, *Reliability of Structures*. New York, NY, USA: McGraw-Hill, 2000.
- [24] S. G. Buonopane and B. W. Schafer, "Reliability of Steel Frames Designed with Advanced Analysis," *Journal of Structural Engineering*, vol. 132, no. 2, pp. 267–276, Feb. 2006, [https://doi.org/10.1061/\(ASCE\)0733-9445\(2006\)132:2\(267\)](https://doi.org/10.1061/(ASCE)0733-9445(2006)132:2(267)).

Effects of Inrush Current on the Hysteresis Loop and Load Influences on the Transient Current of a Single-Phase Transformer

Abdelghani Yahiou

Automatic Laboratory of Sétif (LAS)
Department of Electrical Engineering
University of Bouira
Bouira, Algeria
abdelghani.yahiou@univ-bouira.dz

Hacene Mellah

Automatic Laboratory of Sétif (LAS)
Department of Electrical Engineering
University of Bouira
Bouira, Algeria
h.mellah@univ-bouira.dz

Abdelhafid Bayadi

Automatic Laboratory of Sétif (LAS)
Department of Electrical Engineering
University of Sétif-1
Sétif, Algeria
a_bayadi@univ-setif.dz

Mokhtar Abid

Department of Automatic and Electrical Engineering
University of Blida-1
Blida, Algeria
oussama.electrotechnique@gmail.com

Received: 15 July 2022 | Revised: 4 August 2022 | Accepted: 7 August 2022

Abstract—When putting any unloaded transformer into service, a high-value current that can be very dangerous, called the inrush current, appears. The latter may cause problems and consequences in the electrical system. The challenges of visualizing the effects of transient regimes on the iron core's characteristics and the influence of the type of load on inrush current characteristics are covered in this study. The main purpose of this paper is to treat the influence of this transient phenomenon on the hysteresis loop of a single-phase transformer, in terms of its size, area, or position, and therefore, the influence of the load on the transient regime. A general study of the electromagnetic characteristics of the transformer iron core will be presented. Then, using the ATP-EMTP program, the purpose of the realized simulations is to visualize the relationship between the hysteresis loop and the magnetizing inrush current in the transient state. The results show the decrease of the hysteresis loop area and their shift with respect to the origin of the axes following the increase in the transient inrush current peak. As the second part of this article, there is a study of the influence of the load on the transient regime, i.e. inrush current. This is accomplished by adding a load with different configurations and various connections. The purpose is to find the effect of the load on the reduction of the transient inrush current phenomenon.

Keywords—transformer; inrush current; transient regime; hysteresis loop; load influence; ATP-EMTP

I. INTRODUCTION

Inrush current is caused by the saturation of a power transformer due to variations in the magnetization voltage [1, 2]. When an unloaded transformer is energized, a transient

phenomenon called inrush current may appear in the excited circuit side. Therefore, necessary research must be carried out in order to anticipate a suitable protecting system for the transformer. There are many works in the literature that fall into this framework, such as [3-5], where many numerical and analytical tools have been developed. Furthermore, the majority of studies on the field of transformer transient study are in the context of finding effective and inexpensive techniques to reduce this inrush current. Among these methods, there is the technique proposed in [6], in which four different methods to reduce the inrush current were compared. The required result is the ability to use the circuit breakers with an independent pole, as well as the ability to deem the residual flux in the iron core of the transformer. The measurement and simulation studies performed in [7, 8] consist pioneering work, simulation, and measurements, in the area of inrush current reduction in three- and single- phase transformers. Taking into account the residual flux values, the authors propose three schemes in this technique, by closing the circuit breakers in a synchronous, quick, and delayed manner. Authors in [9] utilized the technique of making a modification in the transformer bobbin. This is intended to decrease the inrush current peaks by increasing the transient inductance value. Taking into account the phase shift between the three phases of the transformer during its energization, the authors in [10-13] introduce a resistance between the ground and the transformer neutral. Authors in [14], while taking into account the switching moment, used the reversed flux technique to investigate the reduction of the inrush current using an existed photovoltaic generator. The idea proposed in [15], is in the

same context with what was accomplished in [10-13], where the residual flux is taken into account, and a controlled circuit breaker is used to isolate the neutral of the three-phase transformer with respecting of the three phases sequential. Authors in [16] present several methods to protect and reduce the various interactions of transformer relays as well as the introduction and removal of the load in a random or studied manner by the circuit breakers. Authors in [17] depended on formal methods to solve differential equations based on the equivalent circuit represented using the state space equation. Authors in [18] raised the resistance value of the transformer winding, using the transformer tap changer to reduce the effect of the inrush current power system as well as mitigating its peak value. The main contribution in [19] is the application of a technique using a real-time measurement setup to eliminate the sympathetic inrush current. The latter results from the interaction of two transformers, one is energized and the second is already supplied. Moreover, there is a comparison of the results (measurement and simulation) to prove the efficacy of the proposed technique found in [20] to mitigate also this sympathetic inrush current. Authors in [21] presented an important technique in the field of inrush current mitigation, especially by using renewable energies, where the reverse flux is applied. Authors in [22] presented a review of some factors which affect the resistance during breakdown of transformer oil. Authors in [23] exposed a generator differential protection relay system, its disadvantages and its advantages. In [24], a real power transformer was used in the experiments, and a UHF-PD detection system was built.

The supply of the transformer primary, under its nominal voltage, is accompanied by a transient regime during which the intensity of the inrush current can take values much higher than those of the nominal intensity, depending on the instant of appreciation of the voltage and the induction remanence of the magnetic circuit. Hence the need to predetermine through the study of the transient regime the approximate value of this inrush current which may be greater than or equal to several times the current of the transformer [25]. Holcomb in [5] is considered among the first who raised the idea of the inrush current calculation, but without going far. The author studied only a method to compute the peak inrush current for the first and any succeeding cycle, without considering its effect on hysteresis loop. In [25], the authors used a developed model to estimate the inrush current and hysteresis loop. However, they did not make a comparison between the relationships of the position of the hysteresis loop wave according to the corresponding inrush current. The same weakness was observed in [26, 27], where the authors estimated the saturation curve from the inrush current waveform. This major drawback of these previous works has been studied and dealt with in the present work, where the comparison has been made between different effects of transformer energization on the nature of the iron core. Authors in [28] exploited a real model of a transformer to study different phenomena such as the application of the nonlinear load. However, limited their study to the load effects on the steady-state regime.

The first part of this paper is devoted to the study of the transient inrush current effect on the hysteresis loop of a transformer. Therefore, a quick rundown is presented on how

to identify the equivalent circuit parameters for the used transformer and the iron core magnetizing characteristic (air core-inductance). Then, a simulation using ATP-EMTP program is performed using the nonlinear Type 98 inductance and the nonlinear Type 92 resistance, as well as the system that measures the hysteresis cycle (flux-current). Finally, the presented simulation results show the variation of the area of the hysteresis cycle and the shift of this loop according to the increase and decrease of the inrush current peak. A comparison is made with respect to the hysteresis cycle in the steady state. The next part is devoted to the study of the load insertion effect on the transient inrush current of a transformer. Simulation is done using the same model and the same transformer characteristics, only a load with different values of impedance and different connections is added in the secondary side. The simulation results show the variation of the inrush current waveforms with the application of deferent types of loads.

II. MATERIALS AND METHODS

This section is devoted to a presentation of the real transformer used in the simulation, the identification of the parameters of its equivalent circuit, and the representation of the model with nonlinear parameters. The single-phase transformer (Figure 1) used in the simulations of this paper is manufactured by the company DELORENZO, Italy and is available at the Laboratory of the Power System, University of Sétif 1. All the experimental tests of this paper were carried out in this laboratory. Table I shows some parameter values of the used transformer. The parameters of the transformer equivalent circuit obtained by applying the classical equations are presented in Table II. The study of any transformer transient regime such as ferro-resonance and inrush current requires careful modeling of the iron core nonlinearities and precision in the equivalent circuit parameters of the transformer determination.



Fig. 1. The used transformer.

TABLE I. TEST TRANSFORMER NAMEPLATE DATA.

Power (VA)	Frequency (Hz)	Phase	Voltage ratio (kV)	Turn (tr)	Current Ratio (A)	Class (isolated)
2000	050	01	0.22/0.025	0330/0037	9.10/080	E

TABLE II. TRANSFORMER PARAMETERS

Parameter	Value
Shunt resistance R_m	2847.05Ω
Shunt reactance X_m	609.72Ω
Equivalent resistance R_{eq}	3.48Ω
Equivalent reactance X_{eq}	2.69Ω

A. Nonlinearities of the Iron Core

The representation of the transformer model with linear resistors and inductances does not reflect the actual behavior of the electrical transformer. So, the effects of hysteresis and saturation must be introduced using non-linear branch elements. Figure 2 shows the saturation curve $\lambda = f(i_r)$ which represents the air core inductance. The nonlinear resistance characteristic $v = f(i_{lr})$ is depicted in Figure 3. Both figures use the data of [1].

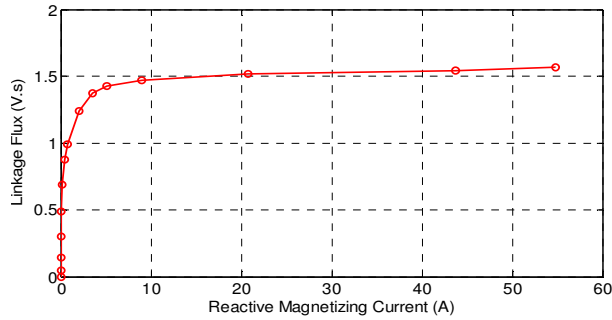


Fig. 2. Air core inductance characteristic $\lambda = f(i_r)$ [1].

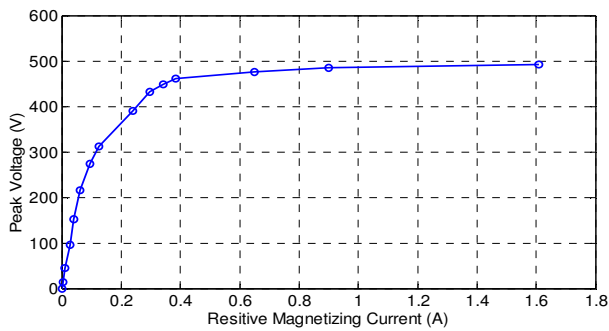


Fig. 3. Nonlinear resistance characteristic $\lambda = f(i_r)$ [1].

The curves of Figures 2 and 3 are computed by the method based on the improved technique presented in [20, 29], and they have been inserted in the transformer models (saturable) found in ATP-EMTP program to simulate the effect of the inrush current phenomenon on the hysteresis loop.

B. Residual Flux

Residual flux plays a basic role in the occurrence of inrush current in an unloaded transformer. It represents a continuous flux value that persists in the magnetic circuit, which can generate an inrush current after switching off if the transformer is not completely demagnetized [30, 31]. The instantaneous equation for flux in the iron core is:

$$\lambda_{\text{core}}(t) = \lambda_R + \int_{t_{\text{close}}}^t u_{\text{coil}}(t) dt \quad (1)$$

$$\lambda_{\text{core}} = -\lambda_{\text{max}} \cos(\omega * t) + \lambda_{\text{max}} \cos(\omega * t_{\text{close}}) + \lambda_R$$

C. Simulation of the Influence of the Inrush Current on the Hysteresis Loop

In this section, the simulation and the results will be presented in detail. Figure 4 shows the simulation diagram using the ATP-EMTP program to visualize the influence of the transient inrush current on the hysteresis loop.

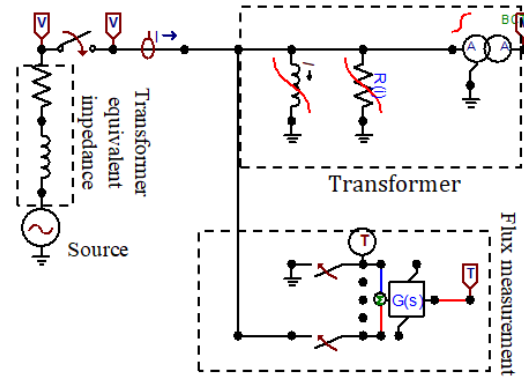


Fig. 4. Simulation diagram.

III. RESULTS

A. Steady State

In the steady state, a voltage source is placed in the primary of the test transformer while the secondary is unloaded. The obtained simulated magnetizing current curve is shown in Figure 5 and the corresponding hysteresis loop curve is shown in Figure 6.

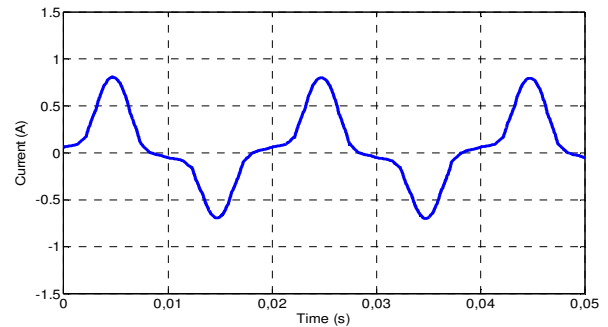


Fig. 5. Unloaded steady state current waveform.

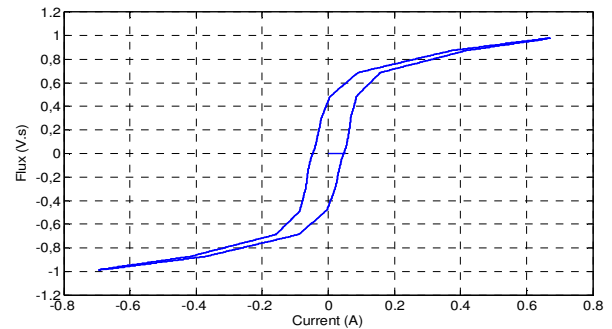


Fig. 6. Unloaded steady state hysteresis loop.

It should be noted that the current waveform in the no-load state is distorted non-sinusoidal due to the harmonics caused by the non-linearity of the transformer core. Figure 6 represents the variation of the flux as a function of current in the unloaded test. It should be noted that the hysteresis loop is symmetrical with respect to the origin of the reference. The surface occupied by this loop is approximately bounded from -1.2 to 1.2A and beyond this interval we enter the saturation phase. This area represents the losses in the iron core.

B. Transient Regime (Inrush Current)

In these applications, the simulation time is fixed to 2s, and a controlled circuit breaker is exploited to vary the closing time and see the first peak of the inrush current and its attenuation up to the magnetizing current until reached the steady state. The hysteresis loop corresponding to each closing time of the circuit breaker will be drawn.

1) Closing Time $t_f = 0.5808s$

When the circuit breaker closes at $t_f = 0.5808s$, the first peak of inrush current is reached at 2.25A, and continue to decrease until the steady state current, as shown in Figure 7. The hysteresis loop is distorted and asymmetrical with respect to the origin. The saturation phase in the positive part follows the inrush current peak of 2.25A corresponding to a flux value of 1.26V.s. While the current of the negative part does not exceed the value of -0.2A and the flux the value of -0.3V.s. Figure 8 shows the complete hysteresis loop.

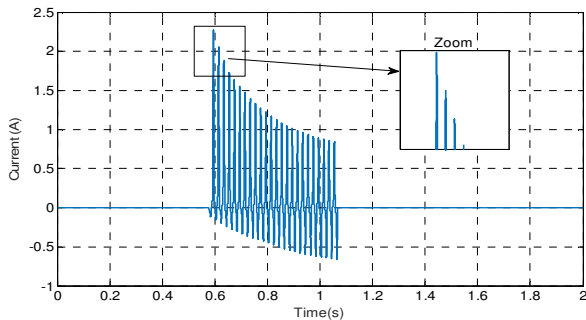


Fig. 7. Transient inrush current for closing time $t_f = 0.5808 s$.

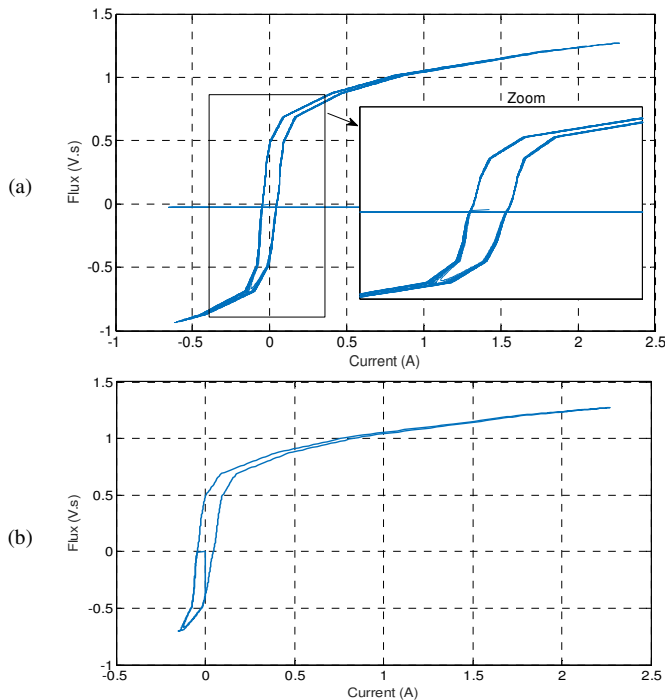


Fig. 8. Hysteresis loop at $t_f = 0.5808s$ for (a) several periods, (b) one period.

2) Closing Time $t_f = 0.5828s$

When the circuit breaker closes at $t_f = 0.5828s$, the first peak of inrush current is reached at 18.72A and continues to decrease until the steady state current, as shown in Figure 9. The inrush current peak is very large in this application compared to the peak in the first application. This leads the hysteresis loop to withdraw completely to the positive part according to the direction of the inrush current. For the positive part, it follows the inrush current peak of 18.72A corresponding to a flux value of 1.52V.s, while that of the negative part does not exceed the values of -0.03A and -0.38V.s. Figure 10 shows the complete hysteresis loop.

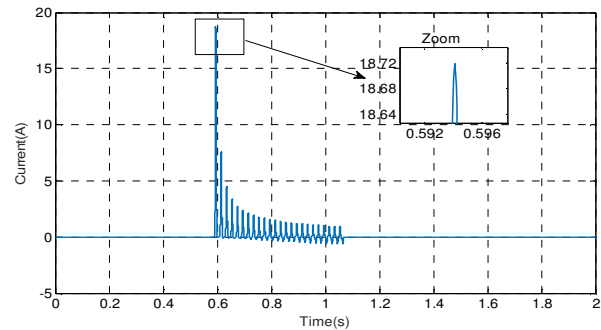


Fig. 9. Transient inrush current for closing time $t_f = 0.5828s$.

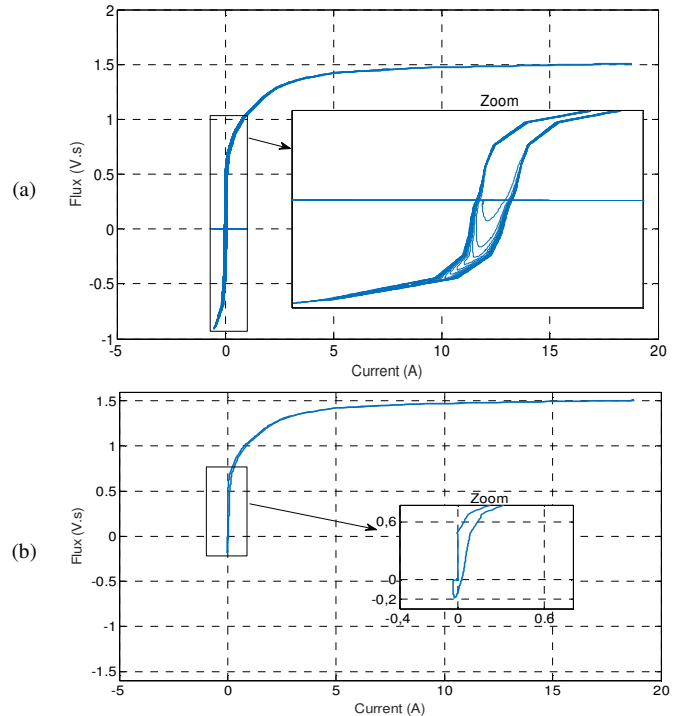


Fig. 10. Hysteresis loop at $t_f = 0.5828s$ for (a) several periods, (b) one period.

3) Closing Time $t_f = 0.5848s$

When the circuit breaker closes at $t_f = 0.5848s$ the first peak of inrush current reached 26.50A and continued to decrease until the steady state current, as shown in Figure 11. When compared to the peak in the previous application, the inrush current peak is considerably large. According to the direction

of the inrush current, this causes the hysteresis loop to entirely retreat to the positive part. The inrush current peak of 26.50A, corresponding to a flux value of 1.57V.s, is followed by the positive portion. The negative component, on the other hand, does not surpass the current value of -0.03A and flux value of -0.18V.s. The whole hysteresis loop is shown in Figure 12.

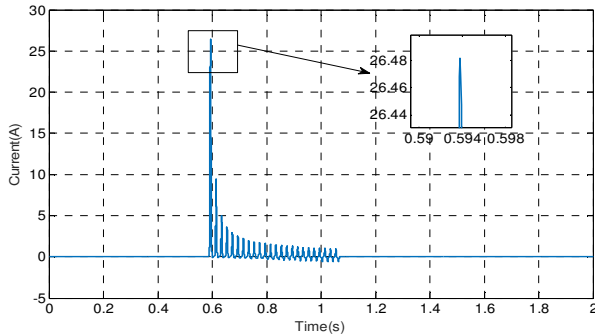


Fig. 11. Transient inrush current for closing time $t_f = 0.5848$ s.

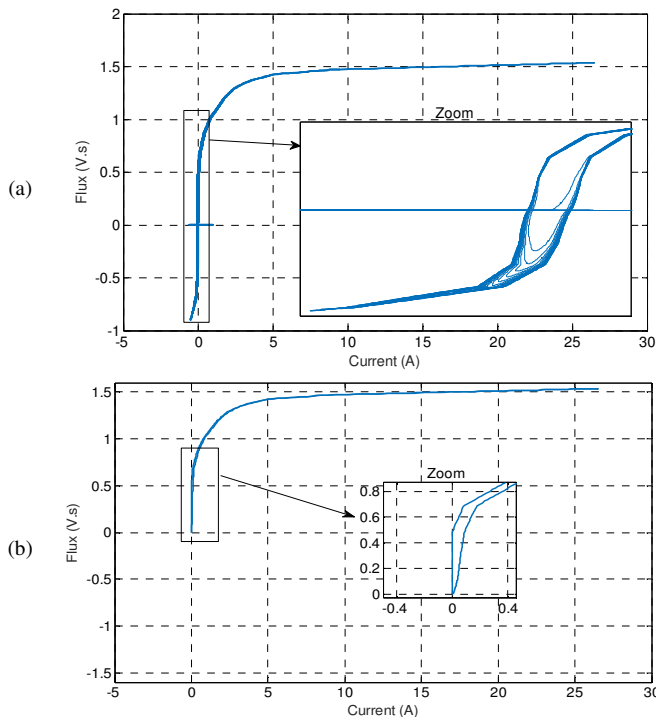


Fig. 12. Hysteresis loop at $t_f = 0.5848$ s for (a) several periods, (b) one period.

IV. LOAD EFFECTS ON THE INRUSH CURRENT

The goal is to apply different loads with different values in the secondary side of the transformer to observe the influence of this variation on the transient inrush current phenomenon. The simulation is carried out using the model of Figure 4, and the same transformer characteristics, but with adding load.

A. Resistive Load

In the first application, and after the unloaded operating of the transformer as seen in the first part of this article, a pure resistance load is added in the secondary side. Figure 13 shows a comparison between transient current waveforms with

different proportions of resistive load (100%, 50%, and 120% of the nominal resistive load).

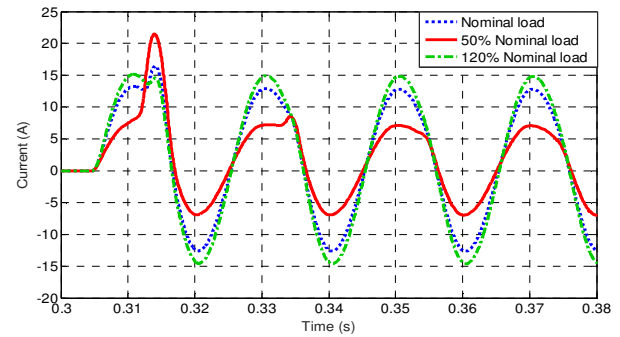


Fig. 13. Primary current waveforms for the resistive load.

B. R-L load

In the second application, a resistance-inductance (R-L) load is added in the secondary side. Figure 14 shows a comparison between transient current waveforms with different proportions of R-L load.

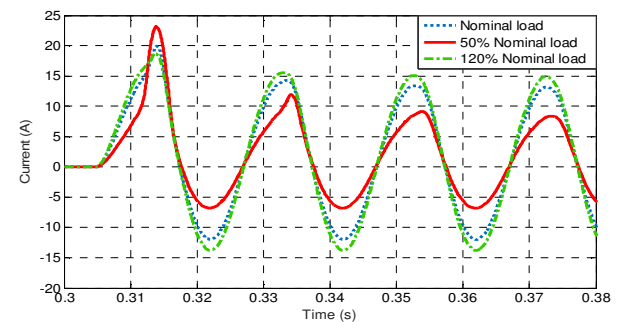


Fig. 14. Primary current waveforms for the R-L load.

C. R-L-C Load

In the last application, a resistance-inductance-capacitance (R-L-C) load is added in the secondary side. Figure 15 shows a comparison between transient current waveforms with different proportions of R-L-C load (100%, 50%, and 120% of the nominal R-L-C load). The values of Figures 13-15 are summarized in Table III.

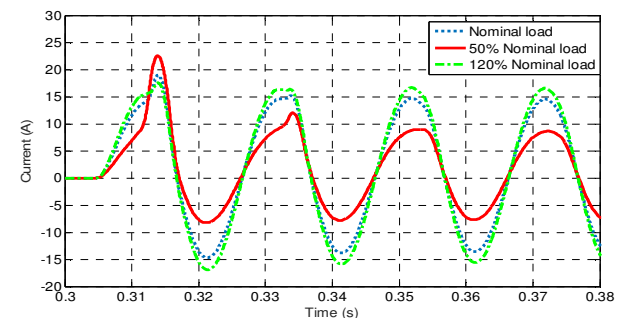


Fig. 15. Primary current waveforms for the R-L-C load.

TABLE III. CURRENT VALUES FOR DIFFERENT LOAD VALUES

	Resistive load	R-L load	R-L-C load	
Inrush current first peak (A).	16.48	19.9	18.4	Nominal load
Steady state current (A)	12.73	12.04	13.8	
Inrush current first peak (A)	21.45	23.13	22.57	50% of nominal load
Steady state current (A)	7.037	6.82	7.9	
Inrush current first peak (A)	15.14	18.70	17.5	120% of nominal load
Steady state current (A)	14.74.	14.74	15.79	

V. DISCUSSION

From the obtained results in the first part, it can be concluded that the transient inrush current of the transformer has a direct influence on the hysteresis loop waveform. This impact results in the reduction of the area of this loop according to the increase of the inrush current peak, therefore it can explain the reduced iron core losses with the inrush current appearance. Moreover, there is a withdrawal of the hysteresis loop according to the direction of the transient inrush current, which means that the hysteresis loop shifts towards the value and direction of the peak inrush current. On the other hand, Figures 13-15 represent the transient currents waveforms when different types of loads at 50% and 120% of the nominal values are inserted. The figures show that the energization of transformer lightly loaded causes transient inrush current almost similar to that of energizing an unloaded transformer. Moreover, the energization of a highly loaded transformer causes transient inrush current much less to that acquired after energizing an unloaded transformer. The above applications, by adding load in its various forms and values, prove that a decrease in the load leads to an increase in the transient inrush current. On the other hand, the current in the steady state (after removing the transient regime) is proportional to the value of the load. In the unloaded test, when the current waveform takes its permanent regime, it was not sinusoidal. However, adding load leads to the return of the sinusoidal waveform after crossing the transient regime. These simulations prove that the transformer loading decreases the amplitude of the transient inrush current. So, it can be concluded that the inrush current exists only at energization of an unloaded or lightly.

VI. CONCLUSION

This work is concerned with the visualization of the effect of transient regimes on the characteristics of the iron core, as well as the influence of the load on the inrush current characteristics. In the present paper, a summary of the parameter identification method of the transformer equivalent circuit has been presented and a magnetizing characteristic representing the transformer iron core has been illustrated. Parameter identification was achieved using classical tests such as open circuit and short-circuit. A simulation using ATP-EMTP was performed using the Type 98 nonlinear inductance and the Type 92 nonlinear resistance, and a system that measures the hysteresis cycle (flux-current). Finally, the simulation results were presented and show the variation of the

area of the hysteresis cycle and the shift of this loop according to the increase and decrease of the inrush current peak. The comparison was conducted with respect to the hysteresis cycle in steady state. Energizing an unloaded transformer causes transients at large amplitudes, with the effect of the non-linear behavior of the magnetic circuit on the current waveform occurring in this mode of operation. Increasing the load value decreases the transient regime. Therefore, the application of the load restores the sinusoidal waveform of the steady state current. Regarding future research, we intend to concentrate on experiments in order to confirm the present simulation results and to adopt this approach to large power transformers.

REFERENCES

- [1] A. Yahiou, "Contribution a l'etude et a l'analyse du regime transitoire dans les transformateurs de puissance : cas du courant d'appel," M.S. thesis, Universite Ferhat Abbas de Setif, Setif, Algeria, 2012.
- [2] A. Yahiou, A. Bayadi, and B. Babes, "Point on Voltage Wave Switching for Sympathetic Inrush Current Reduction," in *International Conference on Applied Smart Systems*, Medea, Algeria, Nov. 2018, pp. 1-4, <https://doi.org/10.1109/ICASS.2018.8651972>.
- [3] G. Bertagnolli, *The ABB Approach to Short-circuit Duty of Power Transformers*. Zurich, Switzerland: ABB, 2007.
- [4] T. R. Specht, "Transformer Magnetizing Inrush Current," *Transactions of the American Institute of Electrical Engineers*, vol. 1, no. 70, pp. 323-328, 1951, <https://doi.org/10.1109/T-AIEE.1951.5060409>.
- [5] J. E. Holcomb, "Distribution Transformer Magnetizing Inrush Current," *Transactions of the American Institute of Electrical Engineers. Part III: Power Apparatus and Systems*, vol. 80, no. 3, pp. 697-702, Apr. 1961, <https://doi.org/10.1109/AIEEPAS.1961.4501117>.
- [6] R. Cano-Gonzalez, A. Bachiller-Soler, J. A. Rosendo-Macias, and G. Alvarez-Cordero, "Controlled switching strategies for transformer inrush current reduction: A comparative study," *Electric Power Systems Research*, vol. 145, pp. 12-18, Apr. 2017, <https://doi.org/10.1016/j.epsr.2016.11.018>.
- [7] J. H. Brunke and K. J. Frohlich, "Elimination of transformer inrush currents by controlled switching. I. Theoretical considerations," *IEEE Transactions on Power Delivery*, vol. 16, no. 2, pp. 276-280, Apr. 2001, <https://doi.org/10.1109/61.915495>.
- [8] J. H. Brunke and K. J. Frohlich, "Elimination of transformer inrush currents by controlled switching. II. Application and performance considerations," *IEEE Transactions on Power Delivery*, vol. 16, no. 2, pp. 281-285, Apr. 2001, <https://doi.org/10.1109/61.915496>.
- [9] C.-K. Cheng, T.-J. Liang, J.-F. Chen, S.-D. Chen, and W.-H. Yang, "Novel approach to reducing the inrush current of a power transformer," *IEE Proceedings - Electric Power Applications*, vol. 151, no. 3, pp. 289-295, May 2004, <https://doi.org/10.1049/ip-epa:20040223>.
- [10] S. J. Arand, M. Saeedi, and S. Masoudi, "Transformer Inrush Current Mitigation Using Controlled Switching and Magnetic Flux Shunts," *International Journal of Energy and Power Engineering*, vol. 2, no. 2, pp. 46-53, Apr. 2013, <https://doi.org/10.11648/j.ijepe.20130202.13>.
- [11] S. G. Abdulsalam and W. Xu, "A Sequential Phase Energization Method for Transformer Inrush Current Reduction—Transient Performance and Practical Considerations," *IEEE Transactions on Power Delivery*, vol. 22, no. 1, pp. 208-216, Jan. 2007, <https://doi.org/10.1109/TPWRD.2006.881450>.
- [12] H. A. Abdulsalam and A. Y. Abdelaziz, "A New Strategy for Selection of Switching Instant to Reduce Transformer Inrush Current in a Single-phase Grid-connected Photovoltaic System," *Electric Power Components and Systems*, vol. 43, no. 11, pp. 1297-1306, Jul. 2015, <https://doi.org/10.1080/15325008.2015.1027424>.
- [13] Y. Cui, S. G. Abdulsalam, S. Chen, and W. Xu, "A sequential phase energization technique for transformer inrush current reduction - Part I: Simulation and experimental results," *IEEE Transactions on Power Delivery*, vol. 20, no. 2, pp. 943-949, Apr. 2005, <https://doi.org/10.1109/TPWRD.2004.843467>.

- [14] W. Xu, S. G. Abdulsalam, Y. Cui, and X. Liu, "A sequential phase energization technique for transformer inrush current reduction - Part II: theoretical analysis and design guide," *IEEE Transactions on Power Delivery*, vol. 20, no. 2, pp. 950–957, Apr. 2005, <https://doi.org/10.1109/TPWRD.2004.843465>.
- [15] R. Cano-Gonzalez, A. Bachiller-Soler, J. A. Rosendo-Macias, and G. Alvarez-Cordero, "Inrush current mitigation in three-phase transformers with isolated neutral," *Electric Power Systems Research*, vol. 121, pp. 14–19, Apr. 2015, <https://doi.org/10.1016/j.epsr.2014.11.031>.
- [16] S. Schramm, C. Sihler, and S. Rosado, "Limiting Sympathetic Interaction Between Transformers Caused by Inrush Transients," in *International Conference on Power Systems Transients*, Delft, Netherlands, Jun. 2011.
- [17] U. Rudez and R. Mihalic, "Sympathetic inrush current phenomenon with loaded transformers," *Electric Power Systems Research*, vol. 138, pp. 3–10, Sep. 2016, <https://doi.org/10.1016/j.epsr.2015.12.011>.
- [18] J. Pontt, J. Rodriguez, J. San Martin, and R. Aguilera, "Mitigation of Sympathetic Interaction between Power Transformers Fed by Long over Head Lines Caused by Inrush Transient Currents," in *IEEE Industry Applications Annual Meeting*, New Orleans, LA, USA, Sep. 2007, pp. 1360–1363, <https://doi.org/10.1109/07IAS.2007.211>.
- [19] A. Yahiou, A. Bayadi, and B. Babes, "Mitigation of Sympathetic Inrush Current in Transformer Using the Technique of Point on Voltage Wave Control Switching," in *International Conference on Communications and Electrical Engineering*, El Oued, Algeria, Dec. 2018, pp. 1–6, <https://doi.org/10.1109/CCEE.2018.8634501>.
- [20] A. Yahiou, A. Bayadi, and B. Babes, "Modified method for transformer magnetizing characteristic computation and point-on-wave control switching for inrush current mitigation," *International Journal of Circuit Theory and Applications*, vol. 47, no. 10, pp. 1664–1679, 2019, <https://doi.org/10.1002/cta.2682>.
- [21] H. A. Abdelsalam, A. Ahmed, and A. Y. Abdelaziz, "Mitigation of Transformer Inrush Current Using PV Energy," *Recent Advances in Communications and Networking Technology (Discontinued)*, vol. 4, no. 2, pp. 95–102, <https://doi.org/10.2174/2215081104666150822001924>.
- [22] M. Danikas, R. Sarathi, and S. Morsalin, "A Short Review of Some of the Factors Affecting the Breakdown Strength of Insulating Oil for Power Transformers," *Engineering, Technology & Applied Science Research*, vol. 10, no. 3, pp. 5742–5747, Jun. 2020, <https://doi.org/10.48084/etasr.3554>.
- [23] K. H. Le and P. H. Vu, "Performance Evaluation of a Generator Differential Protection Function for a Numerical Relay," *Engineering, Technology & Applied Science Research*, vol. 9, no. 4, pp. 4342–4348, Aug. 2019, <https://doi.org/10.48084/etasr.2754>.
- [24] H. Fan, J. Hu, H. Liu, Y. Yin, and M. Danikas, "UHF PD Experiments on Real Power Transformer and its Frequency Characteristics Results," *Engineering, Technology & Applied Science Research*, vol. 6, no. 1, pp. 906–912, Feb. 2016, <https://doi.org/10.48084/etasr.608>.
- [25] S. Sahoo, N. Abeywickrama, T. Bengtsson, and R. Saers, "Understanding the Sympathetic Inrush Phenomenon in the Power Network using Transformer Explorer," in *4th International Conference on Condition Assessment Techniques in Electrical Systems*, Chennai, India, Nov. 2019, pp. 1–5, <https://doi.org/10.1109/CATCON47128.2019.CN0031>.
- [26] J. Faiz and S. Saffari, "Inrush Current Modeling in a Single-Phase Transformer," *IEEE Transactions on Magnetics*, vol. 46, no. 2, pp. 578–581, Oct. 2010, <https://doi.org/10.1109/TMAG.2009.2032929>.
- [27] S. G. Abdulsalam, W. Xu, W. L. A. Neves, and X. Liu, "Estimation of transformer saturation characteristics from inrush current waveforms," *IEEE Transactions on Power Delivery*, vol. 21, no. 1, pp. 170–177, Jan. 2006, <https://doi.org/10.1109/TPWRD.2005.859295>.
- [28] R. Oyanagi, T. Noda, and M. Ichikawa, "A Method for Estimating the Current-Flux Curve of a Single-Phase Transformer for Electromagnetic Transient Simulations of Inrush Currents," *Electrical Engineering in Japan*, vol. 204, no. 2, pp. 13–24, 2018, <https://doi.org/10.1002/eej.23102>.
- [29] H. Altun, S. Sunter, and O. Aydogmus, "Modeling and analysis of a single-phase core-type transformer under inrush current and nonlinear load conditions," *Electrical Engineering*, vol. 103, no. 6, pp. 2961–2972, Dec. 2021, <https://doi.org/10.1007/s00202-021-01283-9>.
- [30] W. L. A. Neves and H. W. Dommel, "On modelling iron core nonlinearities," *IEEE Transactions on Power Systems*, vol. 8, no. 2, pp. 417–425, Feb. 1993, <https://doi.org/10.1109/59.260845>.
- [31] T. Liu, "Manoeuvre controlee des transformateurs de puissance avec flux remanent," Ph.D. dissertation, Supélec, Paris, France, 2011.

Langmuir-Hinshelwood-Hougen-Watson Heterogeneous Kinetics Model for the Description of Fe (II) Ion Exchange on Na-X Zeolite

Sanarya K. Kamal

Chemical Engineering Department

College of Engineering

University of Baghdad

Baghdad, Iraq

sanarya.kamal1507d@coeng.uobaghdad.edu.iq

Ammar S. Abbas

Chemical Engineering Department

College of Engineering

University of Baghdad

Baghdad, Iraq

ammarabbas@coeng.uobaghdad.edu.iq

Received: 26 June 2022 | Revised: 14 July 2022 | Accepted: 29 July 2022

Abstract-This study aimed to investigate the kinetics of the anion exchange step of ferrous ions with Na-X zeolite in a temperature range of 20 and 80°C for a period of up to 8 hours. A ferrous sulfate heptahydrate solution was used as a ferrous ion source to exchange with the sodium of the Na-X zeolite. The results showed a change in the physical appearance of the zeolite with the progress of the ion exchange process. The catalyst color was observed with the progress of the ion exchange time and changed from yellow to brown. The ferrous ion exchanged contents increased with temperature and reached 0.519 at 80°C after 8 hours. A kinetic model based on the Langmuir-Hinshelwood-Hougen-Watson model was suggested and developed to describe the ion-exchange process. The proposed model was solved numerically, and the results indicated its ability to describe the experimental results with high correlation coefficients. Finally, the activation energy for the forward reaction was 31590.7J/mole compared to 28105.5J/mole for the backward, and the frequency factors for the forward and backward reactions were investigated.

Keywords-Fe exchanged; Na-X zeolite; ion exchange; anion capacity

I. INTRODUCTION

Zeolites are microporous, crystalline aluminosilicates with a unique mix of physical and chemical properties that make them excellent for a wide range of uses in industry [1-3], agriculture, medicine [4], and environmental pollution cleanup [5]. Na-X zeolites are synthetic zeolites that have been used and investigated in industrial chemicals as ion exchangers, sorbents [5, 6], and catalysts [7] due to their significant void volume of 50% of the frame structure, their ion exchange capacity, shape selectivity, and solid acid sites [8, 9]. The structure of Na-X zeolites is a Faujasite framework with a cage made up $\text{Na}_{86}[(\text{AlO}_2)_{86}(\text{SiO}_2)_{106}]\cdot\text{H}_2\text{O}$ with a ratio of 1-1.5 joined together by bridging oxygen atoms resulting in a 12-ring pore opening and 3-dimensional channel system [10].

The negative charges of AlO_4 units are balanced by sodium cations (Na^+) which are exchanged by other cations such as

CO^{2+} , Cu^{2+} , Zn^{2+} , and Cr^{3+} ions in the solution [11, 12]. Because of the destruction of the zeolite framework, the exchange capacity of Na-X zeolites makes them particularly effective adsorbents or catalysts. Metal-containing zeolites are especially appealing [13]. Iron-containing zeolites can be used as heterogeneous Fenton or photo-Fenton catalysts [14] and utilized to remove organic pollutants in water treatment plants [15, 16]. Transition metal-containing zeolites are manufactured using a variety of methods including: (i) ion exchange from aqueous solution [11, 17, 18] or solid-state reaction [19], (ii) hydrothermal synthesis [20], and (iii) adsorption and decomposition of volatile organometallic compounds [21, 22]. Ion exchange from an aqueous solution is frequently used to introduce transition metal ions into Na-X zeolites. The mechanics and outcomes are not always straightforward. Transition metal ions may usually replace only a portion of the original cations, which are mainly sodium ions [23].

Ferrous ions (Fe (II)), which are frequently introduced into Na-X zeolites by ion exchange, can coordinate with oxygen atoms more selectively than filling the shell cations and have easy access to other oxidation states [24], so their introduction into zeolites leads to new mechanisms for their function as sorbents [14] and catalysts [25]. However, because ion exchange is reversible, once adsorbed nuclides in water are exchanged by other cations (Na^+ , Ca^{2+} , Mg^{2+} , etc.) [26]. This research aimed to study the effect of temperature and time on the Fe (II) exchange process with Na on the X zeolite. A heterogeneous kinetics model was developed to describe the exchange process based on the heterogeneous Langmuir-Hinshelwood-Hougen-Watson (LHHW) approach.

II. EXPERIMENTAL PROCESS

The zeolite used was the type Na-X zeolite (commercial grain, Si/Al ratio 1.75, pore volume $0.2733\text{cm}^3/\text{g}$, surface area $450\text{m}^2/\text{g}$, initial $\text{Na}=14.719\%$), which was crushed and then sieved with 200 mesh strainers to homogenize its size. 40g of zeolite were weighed and then washed with distilled water. Afterward, they were washed with deionized water at various

times, the Na-X zeolite was filtered by filter paper (Chm F1002 filter paper, 150mm, penetration range (7-8 μ m)), went through a Buckner funnel, a vacuum pump, and then was dried at 60°C overnight in an oven (Memmert, Sigma, England UK). Na-X was mashed by crushing until powder again. The activation process was carried out using a 0.1N chloride acid solution (36.5% HCl, USA) to clean the pore surface of zeolite and remove impurities. The cleaning HCl acid solution was mixed with Na-X zeolite in a 10:1 ratio (v/w ratio) and stirred with a hot plate magnetic stirrer (Thermo Fisher Scientific Inc, USA) for 1 hour at 250rpm at 25°C [27]. The HCl solution was separated from the Na-X zeolite using filter paper, washed with distilled water, and stopped until a neutral pH=7 was obtained. The activated Na-X zeolite was dried at 60°C overnight. The calcination of the cleaning Na-X zeolite samples was obtained at 550°C for 3 hours with a furnace (Carbonite, Sigma, England UK). After cooling, the samples were stored in a desiccator to prevent water absorption. Then, Na-X zeolite containing a high sodium weight percentage (14.719%) was exposed to an ion exchange procedure with ferrous sulfate heptahydrate ($\text{FeSO}_4 \cdot 7\text{H}_2\text{O}$, India) to replace the sodium from Na-X zeolite. This procedure was carried out in beakers with a volume of 0.5lt, under controlled temperatures (20, 40, 60, and 80°C) and were stirred again. 5g of dried Na-X zeolite were added to 100ml of a 0.319M solution and maintained at the required temperature with constant stirring at 300rpm for 8 hours. Subsequently, exchanged Na-X zeolite samples were taken from the ion-exchanged solution and filtered, washed several times with distilled water to remove the Fe (II) that was not exchanged, and taken to an oven to dry at 60°C overnight. The samples were calcined in a furnace at 550°C for 3 hours, and were left to cool inside desiccator until they reached room temperature. The concentration of Fe (II) in the exchange solution was measured using atomic absorption spectrophotometry (VarianAA240FS, Australia), and the amount of exchange Fe (II) was determined. The atomic absorption spectrophotometry was tested at North Gas Company (Ministry of Oil, Iraq).

III. RESULTS AND DISCUSSION

The ion exchange reaction was carried out between Na-X zeolite and ferrous sulfate solution with a stoichiometric amount of Fe/Na at different temperatures for a processing time up to 8 hours. At first, the color of the catalyst was observed with the progression of the ion exchange process. A darker yellowish-brown product was generally obtained with increasing ion-exchange time and processing temperature. Figure 1 depicts three zeolites: original Na-X zeolite, activated Na-X zeolite, and X zeolite after Fe (II) ions were exchanged for 8 hours at 80°C. The color change of the treated zeolite indicated that Fe-13X was formed.

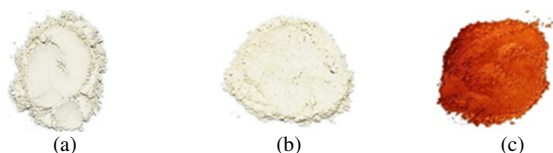


Fig. 1. Color of (a) Na-X Zeolite, (b) Na-X activated, and (c) Modified Fe-13X for 8 hours at 80°C.

The amount of Fe (II) conversion versus time and temperature by ion exchange reaction is shown in Figure 2. Figure 2 shows that the Fe (II) ion exchange (conversion) increased with the reaction time and temperature, and the results showed a rapid increase during the first 0.25h, after which the conversion increased slowly and reached a similar to the equilibrium state at the end of the studied time. The conversion accelerated with the reaction time as the temperature increased. The conversion was 0.179 after 0.25h of reaction at 20°C, whereas it was 0.415 after the same period at 80°C, while the higher required value of Fe (II) conversion was 0.519 obtained after 8h of ion exchange at 80°C. These results agree with the Cobalt exchange on Na-X zeolite previously found in [28].

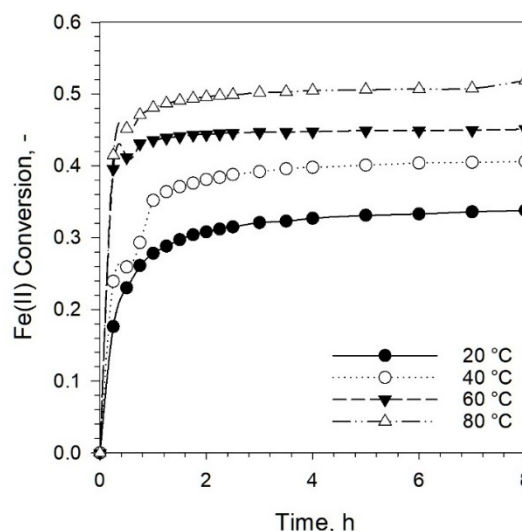
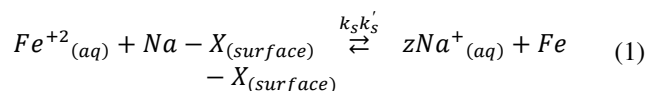


Fig. 2. Fe (II) conversion on the Na-X zeolite versus time at different temperatures.

Langmuir-Hinshelwood-Hougen-Watson (LHHW) kinetics model assumes that before the surface reaction, the Fe (II) is adsorbed onto the catalyst surface. The final stage of the mechanism involves the desorption of Na ions. The surface reaction (1) was assumed to be the rate-controlling step, and the LHHW kinetics model performing the ion exchange can be written as (2) - (11).



$$-r_{\text{Fe}^{+2}_s} = k_s \left(C_{\text{Fe}^{+2}_s} C_{\text{Na-X}_s} - \frac{1}{K_s} C_{z\text{Na}^{+}_s} C_{\text{Fe-X}_s} \right) \quad (2)$$

The adsorbed phase concentrations can be written as:

$$C_{\text{Fe}^{+2}_s} = K_{\text{Fe}^{+2}} C_{\text{Fe}^{+2}} C_v \quad (3)$$

$$C_{z\text{Na}^{+}_s} = K_{z\text{Na}^{+}} C_{z\text{Na}^{+}} C_v \quad (4)$$

Substituting these values in (3) and (4) into (2) gives:

$$-r_{Fe^{+2}s} = k_s \left(K_{Fe^{+2}} C_{Fe^{+2}} C_v K_{Na-X} C_{Na-X} C_v - \frac{1}{K_s} K_{ZNa^+} C_{ZNa^+} C_v K_{Fe-X} C_{Fe-X} C_v \right) \quad (5)$$

Now,

$$C_{Fe^{+2}o} = C_{Fe^{+2}s} + C_{ZNa^+s} + C_v \quad (6)$$

which can be simplified into:

$$C_{Fe^{+2}o} = C_v (K_{Fe^{+2}} C_{Fe^{+2}} + K_{ZNa^+} C_{ZNa^+} + 1) \quad (7)$$

Finally, solving for C_v gives:

$$C_v = \frac{C_{Fe^{+2}o}}{(K_{Fe^{+2}} C_{Fe^{+2}} + K_{ZNa^+} C_{ZNa^+} + 1)} \quad (8)$$

By substituting and simplifying, this can be rewritten as:

$$-r_{Fe^{+2}s} = k_s K_{Fe^{+2}} K_{ZNa^+} (C_{Fe^{+2}o}) \left(\frac{\frac{C_{Fe^{+2}} C_{Na-X}}{K_{ZNa^+}} \frac{C_{ZNa^+} C_{Fe-X}}{K_s K_{Fe^{+2}}}}{1 + K_{Fe^{+2}} C_{Fe^{+2}} + K_{ZNa^+} C_{ZNa^+}} \right) \quad (9)$$

$$K_s = \frac{C_{ZNa^+s}}{C_{Fe^{+2}s}} = \frac{k_s}{k_s} \quad (10)$$

$$K = \frac{K_{Fe^{+2}}}{K_{ZNa^+}} \cdot K_s \quad (11)$$

where $C_{Fe^{+2}}$ is the concentration of Fe (II) in the solution, C_{Na-X} is the concentration of the catalyst Na-X zeolite, C_{ZNa^+} is the concentration of Na^+ in the solution, C_{Fe-X} is the concentration of Fe exchanged on the zeolite, k_s is the forward surface reaction rate constant, k_s' is the backward surface reaction constant, K_s is the equilibrium constant for exchange surface reaction, and K_{Fe} and K_{Na} are the equilibrium constants for Fe (II), and Na^+ respectively. The correlation coefficient (R^2) is presented in (12):

$$R^2 = \frac{(\sum_{i=1}^n (r_{Fe^{+2}exp} - \bar{r}_{Fe^{+2}exp})(r_{Fe^{+2}cal} - \bar{r}_{Fe^{+2}cal}))^2}{\sum_{i=1}^n (r_{Fe^{+2}exp} - \bar{r}_{Fe^{+2}exp})^2 \times \sum_{i=1}^n (r_{Fe^{+2}cal} - \bar{r}_{Fe^{+2}cal})^2} \quad (12)$$

where $r_{Fe^{+2}exp}$ is the experimental reaction rate, $r_{Fe^{+2}cal}$ is the calculated reaction rate from the model, and $(\bar{})$ represents average value. The kinetics equation was solved numerically using the damped least-squares method with the Levenberg-Marquardt algorithm by finding the reaction rate constant and

the values of the equilibrium constants at each temperature, which gives a reaction rate approximating the experimental reaction speed, which was obtained by maximizing the R^2 value (12) at each temperature. Figure 3 shows the relationship between the reaction rate values calculated from the model and the experimental values. Figure 3 also shows that the model rate values were slightly higher than the experimental rates at low reaction rate values, but in general, the model excellently described the experimental results with a high R^2 .

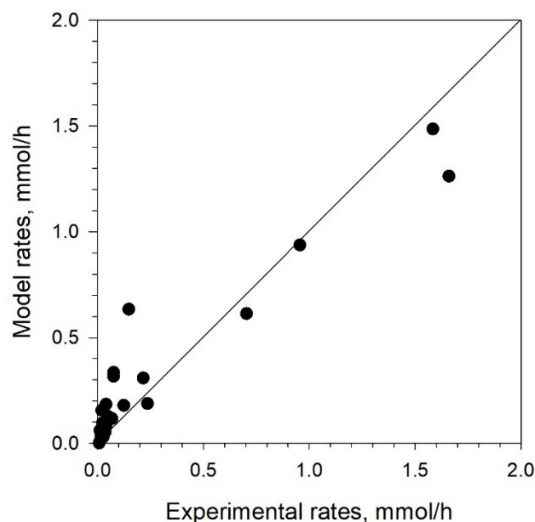


Fig. 3. Relation between the experimental and model rates.

The results of the model solution, including the values of the reaction rate and the equilibrium constants, and the values of R^2 for each temperature, are summarized in Table I. As can be noted, the values of k_s , k_s' , and K_s increased with the temperature of the ion exchange process. The increase in the values of k_s , k_s' , and K_s with increasing temperature and the values of k_s remaining higher than the values of k_s' , indicated that the reaction of ion exchange of Fe (II) with sodium improved with increasing temperature. The results of the model solution also showed that the values of K_{Fe} and K_{Na} lowered with the increase in temperature, indicating that the quantities at the catalyst surface of these two substances decrease with temperature rise.

TABLE I. REACTION RATE CONSTANT VS DIFFERENT TEMPERATURES

Temperature, °C	k_s , 1/liter.mmol.h	K_s	k_s' , 1/liter.mmol.h	K_{Fe}	K_{Na}
20	10.1997	1.1318	9.0119	59.9865	1.8494
40	63.5805	1.2086	52.607	21.3015	1.6658
60	84.7414	1.2661	66.931	5.4395	1.3750
80	100.6624	1.4658	68.674	4.3195	1.2513

Activation energies and frequency pre-exponential factors were calculated for both the forward and backward reaction constants (k_s , or k_s') using the Arrhenius equation [29]. The linear form of the Arrhenius equation is:

$$\ln(k_i) = \ln(A) - \frac{E}{RT} \quad (13)$$

where k_i is the rate constant (k_s , or k_s'), T is the absolute temperature in Kelvin, A is the pre-exponential factor for the

chemical reaction, E is the reaction activation energy, and R is the general gas constant. Figure 4 shows the linear form of the Arrhenius equation, and the activation energy and frequency factor values were calculated for each of the forward and the backward reactions of the ion exchange process.

The activation energies were 31590.7J/mole for the forward reaction and 28105.5J/mole for the backward. The value of the frequency factor for the forward reaction was higher than for

the backward (6596171.7 versus 1418343.2). The large value of the activation energy of the forward reaction relative to the backward supports the fact that the ion exchange process improves with increasing temperature, which was experimentally observed.

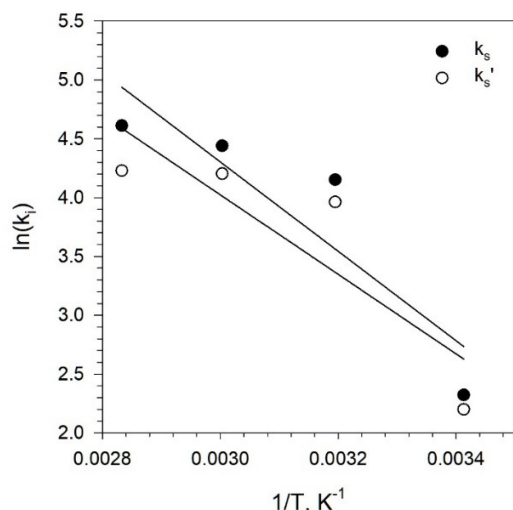


Fig. 4. Arrhenius plot of Fe exchange kinetics.

IV. CONCLUSION

The Fe (II) exchanged Na-X zeolite was prepared by the ion exchange method from a $\text{FeSO}_4 \cdot 7\text{H}_2\text{O}$ solution. The catalyst color changed from yellow to dark brown with the ion exchange progress and increased temperature. The Fe (II) exchanged contents increased with temperature and reached 0.519 at 80°C after 8 hours. An LHHW heterogeneous kinetics model was developed and used to describe the ion-exchange experimental data. The results indicated the ability of the model to describe the experimental results with high correlation coefficients. In general, the values of the reaction constant and reaction equilibrium constant increased with temperature, while the equilibrium constants of the reactant and the products on the zeolite surface decreased. The activation energies were 31590.7J/mole and 28105.5J/mole for the forward and backward reactions, therefore, it can be concluded that higher temperature improves the ion exchange process.

REFERENCES

- [1] A. H. A. K. Mohammed and M. M. Abdul-Raheem, "Adsorption of BTX Aromatic from Reformate by 13X Molecular Sieve," *Iraqi Journal of Chemical and Petroleum Engineering*, vol. 9, no. 4, pp. 13–20, Dec. 2008.
- [2] A. H. A. K. Mohammed and M. K. Baki, "Separation Benzene and Toluene from BTX using Zeolite 13X," *Iraqi Journal of Chemical and Petroleum Engineering*, vol. 9, no. 3, pp. 21–25, Sep. 2008.
- [3] A. H. El-Sinawi, "Production of Hydrogen from Poly Ethylene Terephthalate (PET) using CT 434 ZSM-5 Catalyst at Considerably Low Temperatures," *Engineering, Technology & Applied Science Research*, vol. 6, no. 6, pp. 1269–1273, Dec. 2016, <https://doi.org/10.48084/etasr.822>.
- [4] A. Elfiad, D. C. Boffito, S. Khemassia, F. Galli, S. Chegrouche, and L. Meddour-Boukhobza, "Eco-friendly synthesis from industrial wastewater of Fe and Cu nanoparticles over NaX zeolite and activity in 4-nitrophenol reduction," *The Canadian Journal of Chemical*

Engineering, vol. 96, no. 7, pp. 1566–1575, 2018, <https://doi.org/10.1002/cjce.23083>.

- [5] S. K. A. Barno, H. J. Mohamed, S. M. Saeed, M. J. Al-Ani, and A. S. Abbas, "Prepared 13X Zeolite as a Promising Adsorbent for the Removal of Brilliant Blue Dye from Wastewater," *Iraqi Journal of Chemical and Petroleum Engineering*, vol. 22, no. 2, pp. 1–6, Jun. 2021, <https://doi.org/10.31699/IJCPE.2021.2.1>.
- [6] R. T. Yang, *Adsorbents: Fundamentals and Applications*. Hoboken, NJ, USA: John Wiley & Sons, 2003.
- [7] "Comparative Study on the Catalytic Performance of a 13X Zeolite and its Dealuminated Derivative for Biodiesel Production," *Bulletin of Chemical Reaction Engineering & Catalysis*, vol. 16, no. 4, pp. 763–772, Aug. 2021, <https://doi.org/10.9767/bcrec.16.4.11436.763-772>.
- [8] K. Y. Foo and B. H. Hameed, "The environmental applications of activated carbon/zeolite composite materials," *Advances in Colloid and Interface Science*, vol. 162, no. 1, pp. 22–28, Feb. 2011, <https://doi.org/10.1016/j.cis.2010.09.003>.
- [9] A. Corma, "State of the art and future challenges of zeolites as catalysts," *Journal of Catalysis*, vol. 216, no. 1, pp. 298–312, May 2003, [https://doi.org/10.1016/S0021-9517\(02\)00132-X](https://doi.org/10.1016/S0021-9517(02)00132-X).
- [10] B. A. Alshahidy and A. S. Abbas, "Preparation and modification of 13X zeolite as a heterogeneous catalyst for esterification of oleic acid," *AIP Conference Proceedings*, vol. 2213, no. 1, Mar. 2020, Art. no. 020167, <https://doi.org/10.1063/5.0000171>.
- [11] S. Bendenia, K. Marouf-Khelifa, I. Batonneau-Gener, Z. Derriche, and A. Khelifa, "Adsorptive properties of X zeolites modified by transition metal cation exchange," *Adsorption*, vol. 17, no. 2, pp. 361–370, Apr. 2011, <https://doi.org/10.1007/s10450-011-9336-4>.
- [12] J. R. Ugal, M. Mustafa, and A. A. Abdulhadi, "Preparation of Zeolite Type 13X from Locally Available Raw Materials," *Iraqi Journal of Chemical and Petroleum Engineering*, vol. 9, no. 1, pp. 51–56, Mar. 2008.
- [13] P. C. Silva, N. P. Ferraz, E. A. Perpetuo, and Y. J. O. Asencios, "Oil Produced Water Treatment Using Advanced Oxidative Processes: Heterogeneous-Photocatalysis and Photo-Fenton," *Journal of Sedimentary Environments*, vol. 4, no. 1, pp. 99–107, Mar. 2019, <https://doi.org/10.12957/jse.2019.40991>.
- [14] S. Navalon, M. Alvaro, and H. Garcia, "Heterogeneous Fenton catalysts based on clays, silicas and zeolites," *Applied Catalysis B: Environmental*, vol. 99, no. 1, pp. 1–26, Aug. 2010, <https://doi.org/10.1016/j.apcatb.2010.07.006>.
- [15] H. A. Maddah, "Numerical Analysis for the Oxidation of Phenol with TiO₂ in Wastewater Photocatalytic Reactors," *Engineering, Technology & Applied Science Research*, vol. 8, no. 5, pp. 3463–3469, Oct. 2018, <https://doi.org/10.48084/etasr.2304>.
- [16] R. M. Galvin, "Evaluating Pollutants of Emerging Concern in Aquatic Media Through E-PRTR Regulation. A Case Study: Cordoba, Spain, 2009-2018," *Engineering, Technology & Applied Science Research*, vol. 9, no. 5, pp. 4795–4800, Oct. 2019, <https://doi.org/10.48084/etasr.3130>.
- [17] S. Bendenia, K. Marouf-Khelifa, I. Batonneau-Gener, Z. Derriche, and A. Khelifa, "Adsorptive properties of X zeolites modified by transition metal cation exchange," *Adsorption*, vol. 17, no. 2, pp. 361–370, Apr. 2011, <https://doi.org/10.1007/s10450-011-9336-4>.
- [18] N. Rajamohan, R. R. Kannan, and M. Rajasimman, "Kinetic Modeling and Effect of Process Parameters on Selenium Removal Using Strong Acid Resin," *Engineering, Technology & Applied Science Research*, vol. 6, no. 4, pp. 1045–1049, Aug. 2016, <https://doi.org/10.48084/etasr.635>.
- [19] R. M. Haniffa and K. Seff, "Partial structures of solid-state copper(II)-exchanged zeolite Y and its D₂O sorption complex by pulsed-neutron diffraction," *Microporous and Mesoporous Materials*, vol. 25, no. 1, pp. 137–149, Dec. 1998, [https://doi.org/10.1016/S1387-1811\(98\)00196-6](https://doi.org/10.1016/S1387-1811(98)00196-6).
- [20] P. Feng, X. Bu, and G. D. Stucky, "Hydrothermal syntheses and structural characterization of zeolite analogue compounds based on cobalt phosphate," *Nature*, vol. 388, no. 6644, pp. 735–741, Aug. 1997, <https://doi.org/10.1038/41937>.
- [21] J. G. Jee, M. K. Park, H. K. Yoo, K. Lee, and C. H. Lee, "Adsorption and Desorption Characteristics of Air on Zeolite 5A, 10X, and 13X Fixed

- Beds," *Separation Science and Technology*, vol. 37, no. 15, pp. 3465–3490, Jan. 2002, <https://doi.org/10.1081/SS-120014437>.
- [22] W. Shen and B. J. Shen, "Synthesis and Characterization of Composite Structure Zeolite Y," *Advanced Materials Research*, vol. 233–235, pp. 1790–1793, 2011, <https://doi.org/10.4028/www.scientific.net/AMR.233-235.1790>.
- [23] F. Heinrich, C. Schmidt, E. Löffler, and W. Grünert, "A highly active intra-zeolite iron site for the selective catalytic reduction of NO by isobutane," *Catalysis Communications*, vol. 2, no. 10, pp. 317–321, Dec. 2001, [https://doi.org/10.1016/S1566-7367\(01\)00056-5](https://doi.org/10.1016/S1566-7367(01)00056-5).
- [24] S. Kumar and S. Jain, "History, Introduction, and Kinetics of Ion Exchange Materials," *Journal of Chemistry*, vol. 2013, Oct. 2013, Art. no. e957647, <https://doi.org/10.1155/2013/957647>.
- [25] I. C. Ostroski, M. A. S. D. Barros, E. A. Silva, J. H. Dantas, P. A. Arroyo, and O. C. M. Lima, "A comparative study for the ion exchange of Fe(III) and Zn(II) on zeolite NaY," *Journal of Hazardous Materials*, vol. 161, no. 2, pp. 1404–1412, Jan. 2009, <https://doi.org/10.1016/j.jhazmat.2008.04.111>.
- [26] M. N. Rashed and P. N. Palanisamy, "Introductory Chapter: Adsorption and Ion Exchange of Zeolites for Treatment of Polluted Water," in *Zeolites and Their Applications*, London, UK: InTechOpen, 2018.
- [27] H. Nasution, H. Harahap, S. Pandia, D. M. Putra, and M. T. A. Fath, "Characterizations of activated zeolite using hydrolysis method," *AIP Conference Proceedings*, vol. 2175, no. 1, Nov. 2019, Art. no. 020019, <https://doi.org/10.1063/1.5134583>.
- [28] H.-L. Tran, M.-S. Kuo, W.-D. Yang, and Y.-C. Huang, "Study on Modification of NaX Zeolites: The Cobalt (II)-Exchange Kinetics and Surface Property Changes under Thermal Treatment," *Journal of Chemistry*, vol. 2016, Mar. 2016, Art. no. e1789680, <https://doi.org/10.1155/2016/1789680>.
- [29] O. Levenspiel, *Chemical Reaction Engineering*. New York, NY, USA: John Wiley & Sons, 1998.

A New Assessment Parameter to Determine the Efficiency of a Hybrid Vehicle

Khaled R. M. Mahmoud

University of Jeddah
Jeddah, Saudi Arabia
mrmahmoud@uj.edu.sa

Samy M. Ghania

University of Jeddah
Jeddah, Saudi Arabia
sghania@uj.edu.sa

Received: 25 July 2022 | Revised: 4 August 2022 | Accepted: 7 August 2022

Abstract-This paper presents a new evaluation technique for the determination of the efficiency of a hybrid vehicle. First, the savings in fuel consumption is estimated in the ideal case considering the vehicle runs through a standard driving cycle and the engine runs at the lowest specific fuel consumption all the time. The hybridization efficiency can be defined as the ratio between the fuel savings in hybrid mode to the ideal savings according to the standard driving cycle. A case study was conducted with a medium-size passenger car according to the new European standard driving cycle. The results showed that the new proposed evaluation criterion is very effective for evaluating hybrid vehicles.

Keywords-fuel consumption; hybridization efficiency; standard driving cycle

I. INTRODUCTION

The growing use of transportation based on fossil fuels has forced scientists and policymakers to take measures that would reduce the negative environmental and climate impacts, the demand for oil production, and increased fuel prices [1-3]. At present, the consumption of the transport sector represents two-thirds of the global consumption of petroleum, and passenger cars and light commercial transport represent half of that consumption. Therefore, the seek for alternative solutions that are highly efficient, smart, safe and clean has been among the challenges that draw the attention of researchers in both environmental and transportation fields [4-6]. Hence, the development of innovative technologies of hybrid electric vehicles is a potential environmentally friendly and cost-effective solution along with their applicability. Logically, there is an urgent need to switch from conventional Internal Combustion Engine (ICE) vehicles to hybrid vehicles. Nowadays, hybrid vehicles contribute significantly to the reduction of emissions, especially in urban areas. The use of hybrid vehicle technologies has recently accelerated not only for passenger cars but also for heavy vehicles [7-9].

Many factors affect the fuel economy of passenger cars include traffic conditions, road geometry, and vehicle running modes such as idling, cruise, load, acceleration, and so on. The combination of these conditions can be summarized in two cases: city and highway driving. Driving a vehicle on the highways means with semi constant engine speed and load is

often associated with an economic performance featured by moderate fuel consumption with lower exhaust emissions per kilometer. City driving is usually recalling different engine modes especially idling, acceleration, and deceleration modes where low speeds and light or no loads which means low efficiency and excessive emission levels. So, the electric motor is the suitable alternative solution to reduce emissions and fuel consumption. Also, the possibility of using brake regeneration energy as a further energy source helps reduce fuel consumption by up to 15% [10-12].

Increase in intelligent technology used in hybrid vehicles such as the reduction of battery mass and the increased performance leads to increased number of hybrid vehicles in the auto market [13-16]. Many studies indicated a significant rise in the number of hybrid vehicles due to the expected improvement in fuel consumption and reducing harmful emissions. Some studies considered fuel consumption is little affected when running over vehicles for standard driving highway cycles and the effect is considerable within city roads [17-19]. The hybrid vehicle system operates the ICE mostly in the high efficiency and low consumption range. In addition, the batteries of the hybrid system are charged to reach the area of minimum fuel consumption whenever possible [20-22]. However, the main source of energy in hybrid vehicle systems is the ICE, and hybrid system deployment is one of the methods proven effective in achieving operating points close to the optimal operating point inherent to minimum specific fuel consumption for ICE operation most of the time [23, 24]. In other words, the main goal of the hybridization of vehicles is to operate the vehicle under the most economical operating conditions or as close to the highest efficiency range as possible [25, 26].

Usually, hybrid vehicles work on the basis that the efficiency of ICEs is relatively low and varies depending on the engine load and speed. On the other hand, the electric motor has high engine power and efficiency [27]. The operation of hybrid vehicles is an attempt to operate the vehicle engine in a high efficiency state as much as possible. The low energy demand at low vehicle speeds, especially in urban areas, requires low engine power. So, the battery motor is sufficient and efficient to power the vehicle, in what is called tailpipe zero emission mode. When the vehicle is running at a high

speed (70-120km/h), and the engine is running in a high efficiency range, then the ICE can be relied upon to power the vehicle, which is known as the gasoline mode [28]. For high loads, it is possible to rely on both the ICE and the electric motor. The battery charging strategy is based on the use of the difference between the torque at maximum efficiency and the actual torque of the vehicle to charge the batteries. Hybrid vehicles are characterized by the fact that they use the energy resulting from regenerative braking energy recovery to charge the batteries and use it later when needed in the vehicle's motion, resulting in additional savings in fuel consumption [5, 29].

The common evaluation parameter of hybrid vehicles is the degree of hybridization, defined as the ratio between the power of the battery pack and the sum of battery reverse power and ICE power [30]. In the same context, the degree of hybridization is defined as the ratio of the power developed by an electric motor in a hybrid vehicle to the total power consumed [31]. Similarly, authors in [5, 32] have defined Hybridization Factor (HF) as the ratio of electric motor power to the sum of electric motor power and ICE power.

The degree of hybridization indicates the degree of improvement over the traditional situation but does not provide sufficient information on whether this improvement has reached or is close to the ideal degree. Researchers have evaluated hybrid vehicles using the terms "hybridization degree" or "hybridization factor". This definition is limited to indicating the rate of reduction in fuel consumption compared to conventional vehicles. However, can the rate of the improvement increase and to what extent has this improvement reached its maximum value? The performance of any thermal or mechanical system is evaluated by calculating the efficiency, using the ratio between the actual case and the ideal condition, and for hybrid vehicles, the parameters for the ideal condition are not available until the efficiency is calculated. Therefore, a new evaluation is needed to calculate the efficiency of hybridization because of the special working of that type of car. The current evaluation of the hybrid vehicles has some shortages. It adds a considerable amount of electric power to the main driving power of the internal combustion engine to save fuel consumption, but it does not provide how close this saving is to the deal saving of the fuel consumption.

In this paper, hybrid vehicles are evaluated by calculating the efficiency of the vehicles when it runs over a complete standard driving cycle, as the term efficiency gives a more realistic impression of how close the system is to the ideal state. Therefore, a new evaluation was needed to estimate the efficiency of hybridization. Therefore, a new evaluation parameter will be introduced to evaluate the hybrid vehicles in terms of hybridization efficiency. This parameter is applied through a case study of a medium passenger car that undergoes the New European Driving Cycle (NEDC).

II. METHODOLOGY

The new method for evaluating hybrid vehicles is based on the determination of hybridization efficiency. The new method can be applied according to the following steps:

- Calculating the total energy E required to run through the whole driving cycle:

$$E = \int_0^t P(t)dt \quad (1)$$

where E is the required energy to complete the driving cycle, $P(t)$ is the required power, and t is the total time of the driving cycle.

- Calculating the required fuel consumption when the vehicle runs whole driving cycle in conventional mode, β_c in liters.
- Calculating the required fuel consumption when the vehicle runs the same driving cycle with hybrid mode, β_h in liters.
- Minimum track fuel consumption β_{min} can be achieved considering the ideal case that the engine is running at minimum specific fuel consumption $bsfc_{min}$.
- The minimum fuel consumption can be expressed as

$$\beta_{min} = \frac{E \cdot bsfc_{min}}{\rho_f} \quad (2)$$

where ρ_f is the fuel density.

As shown in Figure 1, it is considered that the fuel consumption with the conventional case is at 0% hybridization efficiency, while the 100% hybridization efficiency is at minimum fuel consumption. Normally, the fuel consumption in the hybrid condition lies between the conventional and the ideal cases. From Figure 1, the similarity of the triangles led to the following equation to calculate the hybridization efficiency.

$$\eta_h = \frac{\beta_c - \beta_h}{\beta_c - \beta_{min}} \quad (3)$$

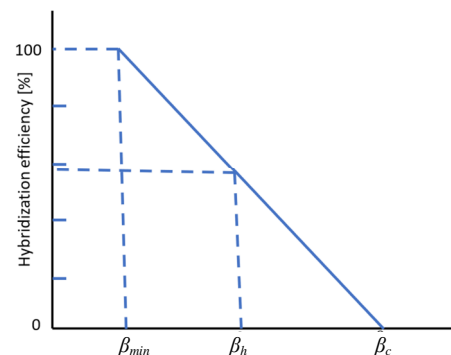


Fig. 1. Variation of the hybridization efficiency with fuel consumption.

The engine fuel consumption map can provide the brake specific fuel consumption $bsfc$ at any point coordinated by engine speed and brake mean effective pressure (sometimes engine torque). Driving cycles are defined as a set of vehicle speed data points as a function of driving cycle time. In this study, the NEDC [35] is used as the standard driving cycle. The evaluation of vehicle performance while moving along a driving cycle depends on how many liters of fuel are consumed to drive a complete cycle. Brake specific fuel consumption varies according to the equivalent torque of a revolution. The vehicle specifications are shown in Table I. The engine fuel map of the vehicle used in this study is shown in Figure 2.

TABLE I. VEHICLE SPECIFICATIONS

Displacement	cm ³	1498
Bore/ Stroke	mm	73.0/89.4
Tire radius	mm	320
Projected area	m ²	2.1
Coefficient of air resistance	--	0.32
Gear ratios		3.643, 2.08, 1.361, 1.024, 0.83, and 0.686
Final drive ratio		4.105
Coefficient of rotating parts \square		1.05
Gross vehicle mass (conventional)	kg	1285
Gross vehicle mass (hybrid)	kg	1515

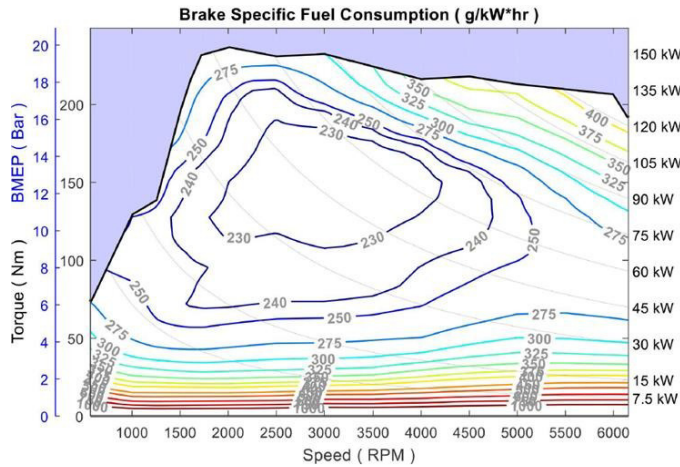


Fig. 2. Engine fuel consumption map.

The batteries specifications used in this study are:

- No of batteries: 38

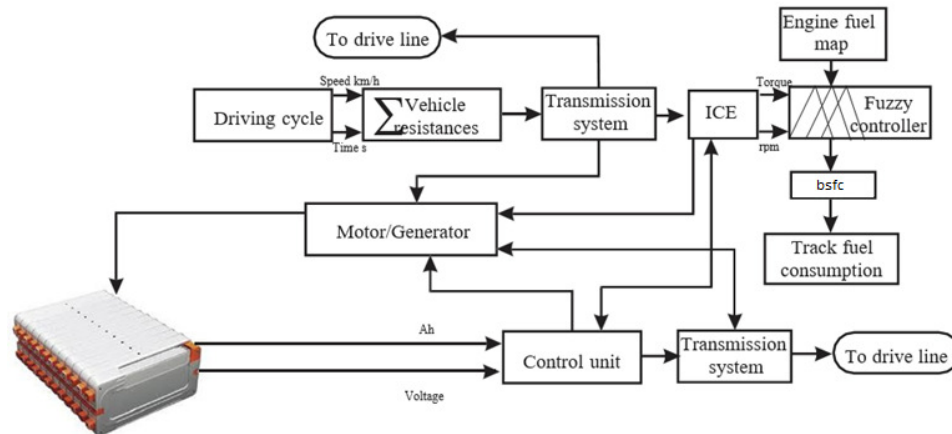


Fig. 3. Schematic diagram of the power flow chart of the hybrid vehicle.

The track fuel consumption of the conventional vehicle running the whole NEDC in ml/s is plotted in Figure 6. The fuel consumption ranges from 0.12ml/s (idle case) to 3.4ml/s. In the urban region, there are four similar ranges with maximum values of about 1.5ml/s, while in the highway region, the enroute fuel consumption in ml/s is relatively higher. The total fuel consumption in conventional condition, β_c in liters, can be calculated as the integration of fuel

consumption with driving cycle time. In this case, it is 0.826lt. The track fuel consumption of the hybrid vehicle without regenerative braking energy recovery when running through the entire NEDC is plotted in Figure 7. The State Of Charge (SOC) is assumed to be 100% at the beginning of the driving cycle. In urban areas, the vehicle is driven by the electric motor (tailpipe zero emission mode). SOC reaches about 60% at urban areas within the period of 0-840s of the driving cycle time.

- Battery voltage: 8.4V
- Battery ampere-hours: 8.4Ah

Figure 3 illustrates the power flow of the model. A Matlab/Simulink model is built with the vehicle speed of the input driving cycle, and the model running time is the driving cycle time. The vehicle resistances are evaluated and the corresponding engine torque and power are calculated. The engine torque, the corresponding engine revolutions, and engine fuel map data are the inputs of the fuzzy controller to calculate the brake specific fuel consumption. Using (6) from [34], the track's fuel consumption can be calculated.

III. RESULTS

The total energy required to complete the entire drive cycle is a key parameter for evaluating hybridization efficiency. The total energy can be calculated by integrating the engine power. The nominal power required to operate the vehicle throughout the NEDC is shown in Figure 4. The energy required to achieve the cycle is shown in Figure 5 with and without brake energy recovery. In these Figures, there are four similar urban zones between 0s and about 800s, and the vehicle travels in the highway zone after this period. The maximum power in the highway zone can be about twice that in the urban zone. In the same context, the maximum negative power of the highway zone is higher than twice the value in the urban zone. However, the total energy required by the vehicle to achieve the NEDC without brake energy recovery is about 6000kJ, while, the total energy required to achieve the NEDC with brake energy regeneration is reduced by about 15% without brake energy regeneration. These results agree with [7, 32].

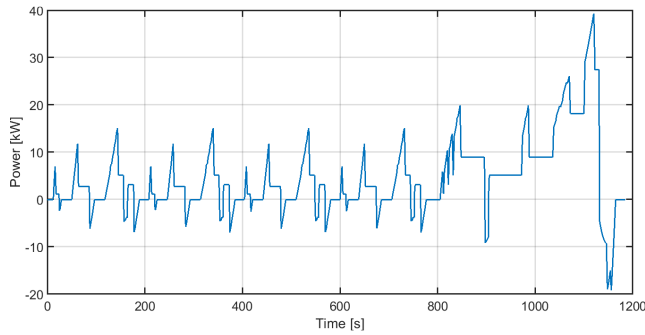


Fig. 4. Engine power variations within a cycle time of NEDC.

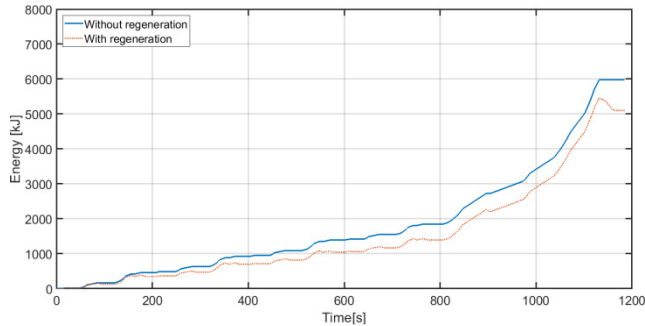


Fig. 5. Vehicle energy variations within the NEDC cycle time.

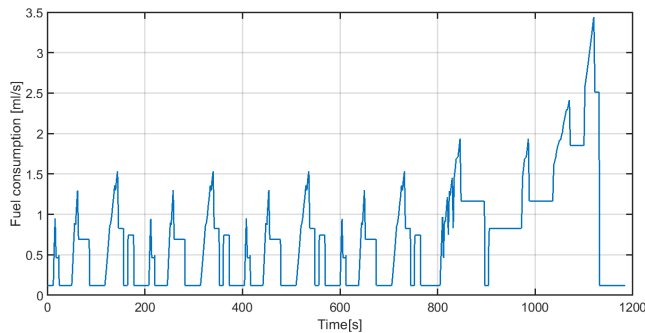


Fig. 6. Fuel consumption of the conventional vehicle according to NEDC.

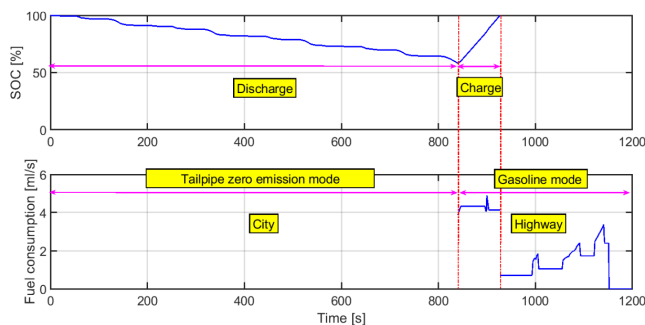


Fig. 7. Fuel consumption and SOC of the hybrid vehicle without regenerative brake energy recovery running over the NEDC.

On the highway, the vehicle's engine performs two tasks: it mainly drives the vehicle and the rest of the maximum engine torque is used to charge the batteries. A time period of about 70s is sufficient in this case to recharge the batteries and bring the SOC back to 100%. The average fuel consumption during this period is about 4.3ml/s. Finally, in the last period, the vehicle runs in gasoline mode, as this is economically feasible

on the highway. The total fuel consumption on the highway when the vehicle is driven in gasoline mode and the batteries are recharged to 100% within SOC is about 0.67lt, which is about 19% lower than the conventional vehicle. These results are in accordance with [33, 34]. The fuel consumption for the hybrid vehicle for the case of brake regeneration energy recovery is shown in Figure 8. When the vehicle is driven in the urban area in the tailpipe zero -emission mode, the SOC decreases from 100% to about 72%. When the vehicle is on the highway, in addition to charging the batteries, it also takes 55s to recharge the SOC to 100%. The total fuel consumption required for highway driving, in addition to battery charging, is about 0.583lt, which is 35% less than the conventional vehicle and about 13% less than the hybrid vehicle without regenerative braking energy recovery.

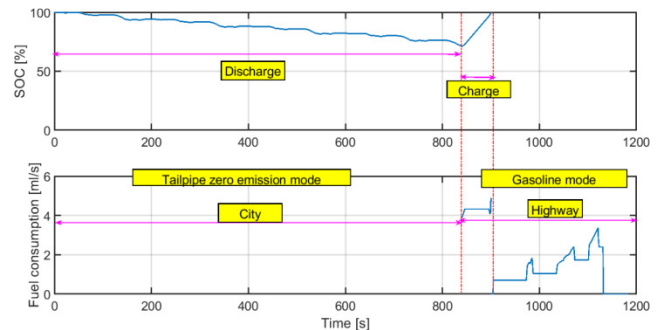


Fig. 8. Fuel consumption and SOC of the hybrid vehicle with regenerative brake energy recovery according to the NEDC.

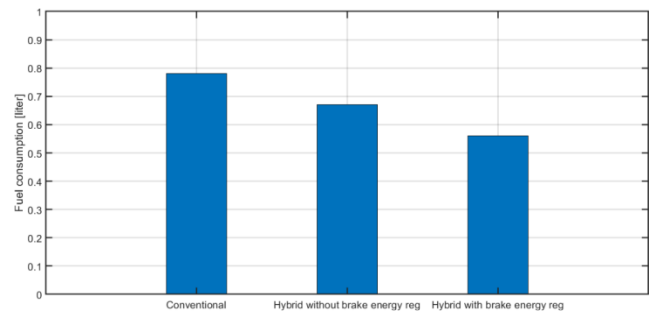


Fig. 9. Track fuel consumption of the vehicle according to the NEDC.

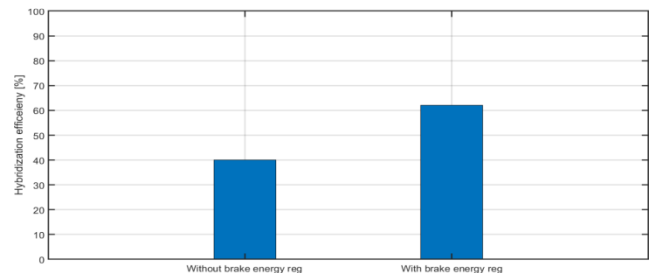


Fig. 10. Hybridization efficiency of the vehicle according to the NEDC.

It can be concluded that this comparison shows a significant improvement when using the hybrid system with and without brake energy regeneration. But have these improvements reached the maximum limits, or can the fuel savings be increased? This evaluation method does not give us an

indication of the fuel economy in the ideal case. Equation (3) was applied to evaluate the proposed new evaluation parameter and the result is shown in Figure 10. It shows the relationship between hybridization efficiency in the two usage modes and the non-use of brake energy recovery for both driving cycles. Efficiency is a measurable and easily understood concept that provides a clear indication of the extent to which the hybridization efficiency reaches the ideal state.

Figure 11 shows the degree of hybridization of the vehicle crossing the whole NEDC with and without brake regeneration energy. Looking in depth at the current assessment, there are some shortcomings, which are the extent to which the optimum reduction in fuel consumption can be reached. The expression in terms of efficiency provides a clear picture of how close this is to the ideal case.

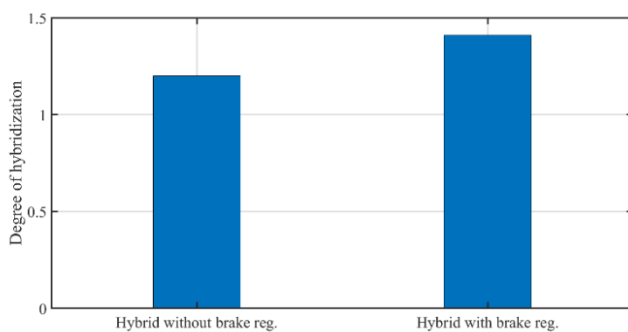


Fig. 11. Degree of hybridization according to the NEDC (current assessment).

IV. CONCLUSIONS

In this paper, the status of hybrid vehicle evaluation was reviewed. It was found that there are some shortcomings in the current evaluation parameters, regardless of the degree of hybridization or the hybridization factor. These inadequacies, since the fuel economy savings are given as a percentage of the conventional condition, do not refer to the ideal conditions (the concept of efficiency). Therefore, a new evaluation parameter can be used to evaluate the hybridization efficiency with reference to the ideal condition. Hybridization efficiency can be calculated by dividing the fuel economy in hybrid mode by the maximum economy in the ideal condition when the vehicle runs the entire standard driving cycle. Hybridization efficiency gives a tangible and accurate comparative formula for evaluating hybrid vehicles. In this study, two case studies are presented with a mid-size passenger car in the full NEDC driving cycle with and without brake energy regeneration. The results show that the new factor, hybridization efficiency, is very effective and provides tangible and logical results. The hybridization efficiency is about 40% and 61% without and with regenerative braking energy respectively, when the vehicle goes through the whole NEDC driving cycle.

ACKNOWLEDGEMENT

This work was funded by the University of Jeddah, Jeddah, Saudi Arabia, under grant No. (UJ-21-DR-39). The authors thank the University of Jeddah for the technical and financial support.

REFERENCES

- [1] J. Cao, J. Peng, and H. He, "Modeling and Simulation Research on Power-split Hybrid Electric Vehicle," *Energy Procedia*, vol. 104, pp. 354–359, Dec. 2016, <https://doi.org/10.1016/j.egypro.2016.12.060>.
- [2] A. Dubray and P. Beguery, "Energy Management Strategy of Hybrid Electric Vehicles and Driving Cycles," *IFAC Proceedings Volumes*, vol. 33, no. 17, pp. 1131–1136, Jul. 2000, [https://doi.org/10.1016/S1474-6670\(17\)39564-2](https://doi.org/10.1016/S1474-6670(17)39564-2).
- [3] H. Liu, J. Zhao, T. Qing, X. Li, and Z. Wang, "Energy consumption analysis of a parallel PHEV with different configurations based on a typical driving cycle," *Energy Reports*, vol. 7, pp. 254–265, Nov. 2021, <https://doi.org/10.1016/j.egypro.2020.12.036>.
- [4] M. Mourad and K. Mahmoud, "Investigation into SI engine performance characteristics and emissions fuelled with ethanol/butanol-gasoline blends," *Renewable Energy*, vol. 143, pp. 762–771, Dec. 2019, <https://doi.org/10.1016/j.renene.2019.05.064>.
- [5] M. E. Bendib and A. Mekias, "Solar Panel and Wireless Power Transmission System as a Smart Grid for Electric Vehicles," *Engineering, Technology & Applied Science Research*, vol. 10, no. 3, pp. 5683–5688, Jun. 2020, <https://doi.org/10.48084/etasr.3473>.
- [6] A. Khadhraoui, T. Selmi, and A. Cherif, "Energy Management of a Hybrid Electric Vehicle," *Engineering, Technology & Applied Science Research*, vol. 12, no. 4, pp. 8916–8921, Aug. 2022, <https://doi.org/10.48084/etasr.5058>.
- [7] S. Changizian, P. Ahmadi, M. Raeesi, and N. Javani, "Performance optimization of hybrid hydrogen fuel cell-electric vehicles in real driving cycles," *International Journal of Hydrogen Energy*, vol. 45, no. 60, pp. 35180–35197, Dec. 2020, <https://doi.org/10.1016/j.ijhydene.2020.01.015>.
- [8] G. Fontaras, P. Pistikopoulos, and Z. Samaras, "Experimental evaluation of hybrid vehicle fuel economy and pollutant emissions over real-world simulation driving cycles," *Atmospheric Environment*, vol. 42, no. 18, pp. 4023–4035, Jun. 2008, <https://doi.org/10.1016/j.atmosenv.2008.01.053>.
- [9] K. Mahmud, G. E. Town, S. Morsalin, and M. J. Hossain, "Integration of electric vehicles and management in the internet of energy," *Renewable and Sustainable Energy Reviews*, vol. 82, pp. 4179–4203, Feb. 2018, <https://doi.org/10.1016/j.rser.2017.11.004>.
- [10] C. Lv, J. Zhang, Y. Li, and Y. Yuan, "Mechanism analysis and evaluation methodology of regenerative braking contribution to energy efficiency improvement of electrified vehicles," *Energy Conversion and Management*, vol. 92, pp. 469–482, Mar. 2015, <https://doi.org/10.1016/j.enconman.2014.12.092>.
- [11] S. Zhou, P. Walker, and N. Zhang, "Parametric design and regenerative braking control of a parallel hydraulic hybrid vehicle," *Mechanism and Machine Theory*, vol. 146, Apr. 2020, Art. no. 103714, <https://doi.org/10.1016/j.mechmachtheory.2019.103714>.
- [12] L. Li, Y. Zhang, C. Yang, B. Yan, and C. Marina Martinez, "Model predictive control-based efficient energy recovery control strategy for regenerative braking system of hybrid electric bus," *Energy Conversion and Management*, vol. 111, pp. 299–314, Mar. 2016, <https://doi.org/10.1016/j.enconman.2015.12.077>.
- [13] W. Gu, D. Zhao, and B. Mason, "A Review of Intelligent Road Preview Methods for Energy Management of Hybrid Vehicles," *IFAC-PapersOnLine*, vol. 52, no. 5, pp. 654–660, Jan. 2019, <https://doi.org/10.1016/j.ifacol.2019.09.104>.
- [14] S. Sharma, A. K. Panwar, and M. M. Tripathi, "Storage technologies for electric vehicles," *Journal of Traffic and Transportation Engineering*, vol. 7, no. 3, pp. 340–361, Jun. 2020, <https://doi.org/10.1016/j.jtte.2020.04.004>.
- [15] K. Uddin, M. Dubarry, and M. B. Glick, "The viability of vehicle-to-grid operations from a battery technology and policy perspective," *Energy Policy*, vol. 113, pp. 342–347, Feb. 2018, <https://doi.org/10.1016/j.enpol.2017.11.015>.
- [16] A. Rabbani and M. Rokni, "Dynamic characteristics of an automotive fuel cell system for transitory load changes," *Sustainable Energy Technologies and Assessments*, vol. 1, pp. 34–43, Mar. 2013, <https://doi.org/10.1016/j.seta.2012.12.003>.

- [17] A. Al-Samari, "Study of emissions and fuel economy for parallel hybrid versus conventional vehicles on real world and standard driving cycles," *Alexandria Engineering Journal*, vol. 56, no. 4, pp. 721–726, Dec. 2017, <https://doi.org/10.1016/j.aej.2017.04.010>.
- [18] P. Plotz, S. A. Funke, and P. Jochem, "Empirical Fuel Consumption and CO2 Emissions of Plug-In Hybrid Electric Vehicles," *Journal of Industrial Ecology*, vol. 22, no. 4, pp. 773–784, 2018, <https://doi.org/10.1111/jiec.12623>.
- [19] J. Rios-Torres, J. Liu, and A. Khattak, "Fuel consumption for various driving styles in conventional and hybrid electric vehicles: Integrating driving cycle predictions with fuel consumption optimization," *International Journal of Sustainable Transportation*, vol. 13, no. 2, pp. 123–137, Feb. 2019, <https://doi.org/10.1080/15568318.2018.1445321>.
- [20] A. Tchetchik, L. I. Zvi, S. Kaplan, and V. Blass, "The joint effects of driving hedonism and trialability on the choice between internal combustion engine, hybrid, and electric vehicles," *Technological Forecasting and Social Change*, vol. 151, Feb. 2020, Art. no. 119815, <https://doi.org/10.1016/j.techfore.2019.119815>.
- [21] F. Salek, M. Zamen, S. V. Hosseini, and M. Babaie, "Novel hybrid system of pulsed HHO generator/TEG waste heat recovery for CO reduction of a gasoline engine," *International Journal of Hydrogen Energy*, vol. 45, no. 43, pp. 23576–23586, Sep. 2020, <https://doi.org/10.1016/j.ijhydene.2020.06.075>.
- [22] D. A. Howey, R. F. Martinez-Botas, B. Cussons, and L. Lytton, "Comparative measurements of the energy consumption of 51 electric, hybrid and internal combustion engine vehicles," *Transportation Research Part D: Transport and Environment*, vol. 16, no. 6, pp. 459–464, Aug. 2011, <https://doi.org/10.1016/j.trd.2011.04.001>.
- [23] H. Choi and I. Oh, "Analysis of product efficiency of hybrid vehicles and promotion policies," *Energy Policy*, vol. 38, no. 5, pp. 2262–2271, May 2010, <https://doi.org/10.1016/j.enpol.2009.12.014>.
- [24] P. Leiby and J. Rubin, "Understanding the Transition to New Fuels and Vehicles: Lessons Learned from Analysis and Experience of Alternative Fuel and Hybrid Vehicles," in *The Hydrogen Energy Transition*, D. Sperling and J. S. Cannon, Eds. Burlington, MA, USA: Academic Press, 2004, pp. 191–212.
- [25] L. Youngjae, K. Gangchul, and P. Youngdug, "The Influence of Operating Conditions on Fuel Economy of the Hybrid Electric Vehicle," *Transactions of the Korean Society of Automotive Engineers*, vol. 13, no. 3, pp. 35–40, 2005.
- [26] B. Y. Liaw and M. Dubarry, "From driving cycle analysis to understanding battery performance in real-life electric hybrid vehicle operation," *Journal of Power Sources*, vol. 174, no. 1, pp. 76–88, Nov. 2007, <https://doi.org/10.1016/j.jpowsour.2007.06.010>.
- [27] F. Leach, G. Kalghatgi, R. Stone, and P. Miles, "The scope for improving the efficiency and environmental impact of internal combustion engines," *Transportation Engineering*, vol. 1, Jun. 2020, Art. no. 100005, <https://doi.org/10.1016/j.treng.2020.100005>.
- [28] Y. Wang *et al.*, "Fuel consumption and emission performance from light-duty conventional/hybrid-electric vehicles over different cycles and real driving tests," *Fuel*, vol. 278, Oct. 2020, Art. no. 118340, <https://doi.org/10.1016/j.fuel.2020.118340>.
- [29] Y.-T. Zhang, C. G. Claudel, M.-B. Hu, Y.-H. Yu, and C.-L. Shi, "Develop of a fuel consumption model for hybrid vehicles," *Energy Conversion and Management*, vol. 207, Mar. 2020, Art. no. 112546, <https://doi.org/10.1016/j.enconman.2020.112546>.
- [30] R. Capata and A. Coccia, "Procedure for the Design of a Hybrid-Series Vehicle and the Hybridization Degree Choice," *Energies*, vol. 3, no. 3, pp. 450–461, Mar. 2010, <https://doi.org/10.3390/en3030450>.
- [31] O. M. Govardhan, "Fundamentals and Classification of Hybrid Electric Vehicles," *International Journal of Engineering and Techniques*, vol. 3, no. 5, pp. 194–198, 2017.
- [32] J. M. Tyrus, R. M. Long, M. Kramskaya, Y. Fertman, and A. Emadi, "Hybrid electric sport utility vehicles," *IEEE Transactions on Vehicular Technology*, vol. 53, no. 5, pp. 1607–1622, Sep. 2004, <https://doi.org/10.1109/TVT.2004.832418>.
- [33] P. Lijewski, M. Kozak, P. Fuc, L. Rymaniak, and A. Ziolkowski, "Exhaust emissions generated under actual operating conditions from a hybrid vehicle and an electric one fitted with a range extender," *Transportation Research Part D: Transport and Environment*, vol. 78, Jan. 2020, Art. no. 102183, <https://doi.org/10.1016/j.trd.2019.11.012>.
- [34] K. Ahn and H. A. Rakha, "A Simple Hybrid Electric Vehicle Fuel Consumption Model for Transportation Applications," in *Applied Electromechanical Devices and Machines for Electric Mobility Solutions*, London, UK: IntechOpen, 2019.
- [35] A. S. Khameesa and M. R. Altaay, "Evaluating the Efficiency of Finance Methods in Residential Complex Projects in Iraq," *Engineering, Technology & Applied Science Research*, vol. 12, no. 1, pp. 8080–8084, Feb. 2022, <https://doi.org/10.48084/etasr.4663>.

AUTHORS PROFILE



Khaled R. M. Mahmoud, is a professor in the Mechanical and Materials Engineering Department, College of Engineering, University of Jeddah, Saudi Arabia. He received his Ph.D. degree from the Heinz Nixdorf Institute, University of Paderborn, Paderborn, Germany in 2005. He has pioneered research in vehicle dynamics and vehicle braking systems and has published more than 35 research articles. He has reviewed several research papers in ISI journals, in fields such as Energy Conversion and Management and Vehicle Dynamics. His current research interests lie on the dynamics of hybrid vehicle systems and internal combustion engines fueled by alternative fuels.



Samy M. Ghania was born in Egypt, in 1971. He received the B.Sc., M.Sc., and Ph.D. degrees in Electrical Engineering from the Faculty of Engineering, Benha University, Cairo, Egypt, in 1995, 2001, and 2005 respectively. In July 2006, he joined the University of Waterloo, Waterloo, ON, Canada, as a Postdoctoral Fellow. He is currently working as a Professor of Electrical Engineering at the University of Jeddah, Saudi Arabia. He has published several papers in international journals and conferences in electrical machines, drives, interference, and electromagnetic simulation, and effects on the human body. He has carried several projects on electrical machine control using micro-controllers, DSP, programmable logic control, and renewable energy resources. His areas of interest include modeling and simulation of electrical machines, drives for electrical vehicles, and its control systems.

Steel Fiber Addition in Eco-Friendly Zero-Cement Concrete: Proportions and Properties

Ali N. Hussein

Department of Civil Engineering
University of Kerbala
Kerbala Iraq
ali.naser@s.uokerbala.edu.iq

Zainab M. R. Abdul Rasoul

Department of Civil Engineering
University of Kerbala
Kerbala Iraq
zainabm@uokerbala.edu.iq

Aymen J. Alsaad

Department of Civil Engineering
University of Kerbala
Kerbala Iraq
aymen.alsaad@uokerbala.edu.iq

Received: 4 July 2022 | Revised: 20 July 2022 | Accepted: 23 July 2022

Abstract—The main objective of this paper is to study the behavior of eco-friendly zero-cement concrete, its proportions, and its properties. The experimental program involves casting and testing many specimens divided into three main groups according to the percentage of added steel fibers in order to investigate the effect of steel fibers on the density, compressive strength, modulus of elasticity, and splitting tensile strength of concrete. The experimental outcomes indicated that the percentage of steel fibers has a small impact on the dry density: adding 0.5% and 1% of steel fibers increased the dry density by about 0.9% and 1.6% respectively. The percentage of steel fibers has an important impact on the compressive strength: after 28 days, steel fibers increased the compressive strength by about 4.9% and 12.8% for added steel fiber percentages of 0.5% and 1%. Also, the results indicated that steel fiber had an important impact on the splitting tensile strength in concrete after 28 days of curing: adding 0.5% and 1% steel fibers increased the splitting tensile strength by about 11.8% and 23.2% respectively. Finally, adding steel fibers has an impact on the modulus of elasticity: after 28 days, adding 0.5% and 1% steel fibers improved the modulus of elasticity approximately by 1.7% and 5%.

Keywords—eco-friendly concrete; Pozzolime concrete; steel fibers; mechanical properties

I. INTRODUCTION

Global attention in eco-friendly and sustainable building materials has increased over the last decades and new constructional adhesives to replace conventional cement are researched. Researchers are being urged to investigate alternatives, such as the reinstitution of lime Pozzolanic systems. Lime might be considered an ecologically friendly binder due to its low energy needs, limited CO₂ emissions during production, and carbonation-induced CO₂ uptake through setting [1]. Lime natural Pozzolans are ancient building materials that were utilized in the process of building

using masonry. The use of lime natural Pozzolanic materials had ceased to exist due to the development of inorganic bindings due to their sluggish setting and hardening. After the discovery of Portland cement in the nineteenth century, the use of natural pozzolan-lime binding materials decreased considerably. The environmental repercussions of the Portland cement production process have increased interest in lime-natural Pozzolan cement during the last 50 years [2]. Kadum [3], created Pozzolime, a unique, sustainable binder composed of hydrated-lime, silica fumes, and fly ashes. Many studies have shown that the addition of fibers, especially steel fibers, to concrete can reduce the requirement for conventional reinforcement in certain circumstances. Steel fibers increase the post-cracking tension response and cracking control qualities of reinforced concrete [4]. Utilizing deformed fibers, like those that are hooked, corrugated, or twisted, can further boost the mechanical strength of composite materials. Reportedly, deformed steel fibers give 3 to 7 times the fiber-matrix binding strength of straight fibers. Several factors, including fiber shape, fiber length, and curing conditions, influence the degree to which mechanical properties are enhanced [5]. Fibers are typically added to Fiber-Reinforced Cementitious Composites (FRCCs) in order to restrict the volumetric ratio of the mix to 3% in order to address mixing and casting issues such as fiber floating and balling.

Pozzolans are natural or man-made materials that are not cementitious on their own but, because they are made of aluminosilicates, they create hydraulic cement when mixed with lime hydrates. Authors in [6] investigated the viability of employing Pozzolans derived from natural sources in Algeria. This Pozzolanic material is seldom used in concrete, so its features have not been thoroughly examined. To learn more about the effectiveness of Pozzolan concrete, 6 concrete mixes were tested: one with Portland cement (as a reference), and 5

Corresponding author: Ali N. Hussein

with 10, 20, 30, 40, and 50% Pozzolan substitution of cement. To make lightweight aggregate concrete, shattered Pozzolan was used as the Lightweight Aggregates (LA), and fine sand was added to all mixes (LAC). Workability and density of fresh concrete mixes were evaluated. The compressive strength, splitting tensile strength, and flexural strength of hardened concrete samples were measured after 3, 7, 28, 90, and 365 days. All the concrete mixes had a constant cementitious material concentration of 400kg/m³. The findings of this experiment indicated that the inclusion of Pozzolan at 20% of the weight of cement results in the greatest gain in strength among the evaluated mixes.

The experimental results of [7-12] showed that the addition of fly ash particles had little effect on the mechanical properties of normal concrete, while steel fibers had the greatest effect. The highest increase was reported in compressive and flexural strength.

II. EXPERIMENTAL WORK

A. Materials

1) Hydrated Lime

In Pozzolime concrete compositions, hydrated lime is utilized. The main component of hydrated lime is calcium hydroxide (Ca(OH)₂). The utilized hydrated lime was manufactured at a lime factory in Karbala and conforms to the Iraqi standard IQS No. 807 /2004 [13]. Table I displays the chemical analyses, chemical composition, and physical properties.

TABLE I. CHEMICAL AND PHYSICAL TEST VALUES OF HYDRATED LIME*

	Components	Results %	Limits IQS NO. 807
Chemical analysis	CaO + MgO	73.1	Min. 65%
	SiO ₂	2.28	
	Al ₂ O ₃	1.08	
	Fe ₂ O ₃	0.23	
	MgO	0.46	5% Max.
	Fe ₂ O ₃ +Al ₂ O ₃ + SiO ₂	3.60	5% Max.
	SO ₃	0.2	
	Loss on ignition	22.8	
	Ca(OH) ₂	92.49	85% Min
	CaO % activity	70.12	
Physical test	CO ₂ %	2.27	5% Max.
	Residue on 90µm	2.2	10% Max.
	Slaking time	24	Min
	Fineness m ² /kg	361	

* The tests were carried out in Karbala plant for cement and lime

2) Cement

This study utilized Portland cement, since it is readily accessible on the market. The used cement was utilized in the production of earlier concrete mixtures. The chemical and physical characteristics agree to the limitations of Iraqi standard No.5/1984 type V [14] (see Tables II and III).

3) Fine Aggregates

Local fine sand complying to zone two of the IQS No. 45 was utilized as FA [15]. According to the findings, the FA satisfies the grading requirements of this standard.

TABLE II. CHEMICAL COMPOSITION AND MAIN COMPOUNDS OF SULFATE-RESISTING PORTLAND CEMENT*

Oxides composition	Content %	Limits of Iraqi standard No.5/1984
CaO	62.15	---
SiO ₂	19.88	---
Al ₂ O ₃	3.5	---
Fe ₂ O ₃	4.7	---
MgO	3.23	< 5.00
SO ₃	1.84	< 2.50
Na ₂ O	0.26	
K ₂ O	0.51	
L.O.I.	1.25	< 4.00
Insoluble residue	0.80	< 1.5
Lime Saturation Factor	0.928	0.66-1.02
Main compounds (Bogue's equations)		
C ₃ S	54.51	---
C ₂ S	18.77	---
C ₃ A	1.51	< 3.50
C ₄ AF	14.14	---

* Chemical analysis was carried out in the Karbala Laboratory

TABLE III. PHYSICAL PROPERTIES OF CEMENT

Physical properties	Test results	Limits of Iraqi standard No.5/1984
Surface area (Blaine) m ² /kg	282	≥ 250
Setting time (Vicat)	Initial setting, hrs: min	≥ 45 min
	Final setting, hrs: min	≤ 10 hrs
Compressive strength, MPa	3 days	≥ 15.00
	7 days	≥ 23.00
Soundness (autoclave) %	0.13	≤ 0.8

4) Coarse Aggregates

All mixtures contained local river gravel broken to a maximum size of 12.5mm as Coarse Aggregates (CA). The grading of CA corresponds to the Iraqi standard IQS No.45/1984 [15]. The CA properties were determined at the Karbala construction laboratory.

TABLE IV. CHEMICAL ANALYSIS OF SILICA FUME*

No.	Components	Silica fume %	ASTM C1240 limitations
1	CaO	1.22	
	SiO ₂	91.05	≥ 85
	Al ₂ O ₃	0.018	
	Fe ₂ O ₃	0.012	
	MgO	0.01	
	SO ₃	0.225	
	Na ₂ O	0.205	
	K ₂ O	0.155	
	Loss on ignition	2.975	≤ 6
	Moisture content	0.68	≤ 3
2	Activity index with Portland cement at 7 days	132.4	≥ 105
	Percentage retained on 45µm (No. 325) sieve, max, %	7	≤ 10
	Surface area (Blaine) m ² /kg	20000	≥ 15000

*The tests was carrying by the manufacturer

5) Silica Fume

Silica fume is a by-product of the production of silicon composites in electrical arched furnaces and may be utilized as a cementitious additive to improve the performance of concrete [16]. Densified micro-silica fume from Mega-Add MC (D) type was utilized in this study. Its Pozzolanic activity index is 132.4% after 7 days. Table IV displays the chemical and particular surface of the utilized silica fume, which conforms to ASTM C1240 [17].

6) High-Range Water Reducing Admixture

As shown in Table V, this additive belongs to the 3rd generation of superplasticizers. The admixture satisfies the standards of ASTM C 494 type G [18].

TABLE V. TECHNICAL DESCRIPTION OF THE ADDITIVE *

Chemical Base	Polycarboxylic ether based
Appearance/color	Amber homogenous liquid
Density	1.082 - 1.142 kg/liter, at 20°C
Chlorine content%	< 0.1
Alkaline content%	< 3
Recommended dosage	(0.5 - 1.5) of binder weight %

*Manufacturer data sheet

TABLE VI. POZZOLIME CONCRETE MIX PROPORTIONS AND PROPERTIES

Mixing	Materials						Slump mm	Compressive strength, 28 days (MP)a
	Hydrate lime (kg/m ³)	Cement (kg/m ³)	Silica fume (kg/m ³)	FA (kg/m ³)	CA (kg/m ³)	W/B ratio by wt.		
Mix1	225	-	225	625	945	0.45	100	24.3
Mix2	310	25*	110	600	940	0.5	115	23.8

* for accelerated setting time

C. Casting and Curing of Specimens

All steel molds (cylinders and cubes) were cleaned and their inside was completely lubricated to prevent the concrete from adhering to the molds after setting. The concrete was poured in two layers before being compacted with a tamping rod or vibrating machine to exclude as much air as possible [19-21]. The samples' top surfaces were then troweled, and in order to avoid the loss of mixing water and moisture from the top surface and plastic shrinkage breaking, they were protected with polythene sheets for 24 hours.



Fig. 1. The tested specimens.

The samples were then demolded and completely submerged in tap water until testing time. The curing schedule

7) Water

Tap water was utilized for mixing and curing. The molten salts comprise fewer than one thousand parts per million. Distilled water was utilized for concrete mixing and curing.

8) Steel Fibers

Micro-steel fibers of the RC 59/13 BN type, with low carbon content, and with both straight ends were utilized. The fibers have a length of 13mm, diameter of 0.22mm, aspect ratio of 59, tensile strength of 2850MPa, and density of 7.85g/cm³.

B. Mix Proportion

Authors in [3] have invented a sustainable binder known as Pozzolime. This binder consists of hydrated-lime, silica-fume; and does not include Portland cement. Table VI displays the proportions chosen for two Pozzolime mixtures, mix1 and mix2, based on the work of [3]. Using a small quantity of cement in mix2 hastened setting time. Firstly, 6 cubes were tested for compressive strength (f_{cu}) for each mix, and the results show that the value of f_{cu} for mix2 was 15.4 and 18.3MPa for age of 7 and 14 days respectively, while the f_{cu} for mix1 was 16.6 and 18.6MPa respectively. So, mix1 was chosen for the rest of the experimental work.

for pervious concrete was 7 and 28 days of water curing. Figure 1 shows the tested specimens. Control specimens were also used in this research, so the total samples used were 9 cubes (10×10×10cm) for the density test, 27 cubes (10×10×10cm) for the compressive strength test, 27 cylinders (30×15cm) for the splitting tensile strength test, and 27 cylinders (30×15cm) for the modulus of elasticity test.

III. RESULTS AND DISCUSSION

A. Dry Density

Concrete's dry density following ASTM C138 [22] was determined using a cylinder mold. The specimens were evaluated after 28 days of water curing. The density of hardened concrete was determined using the subsequent procedures:

$$\gamma_{dry} = W_{dry} / Vol \quad (1)$$

where γ_{dry} is the dry density (kg/m³), W_{dry} the oven-dry mass (kg), and Vol the volume of the specimens (m³).

B. Compressive Strength

Compressive strength testing was determined in accordance with the BS EN 12390.0 [23] using a standard hydraulic digit ELE machine of 2000kN capacity at a loading rate of about 0.30MPa/s. At each test, the average value of 3 tested cubes was determined. The tests on Pozzolime concrete were conducted after 7 and 28 days of curing.

C. Splitting Tensile Strength (f_{ct})

Splitting tensile strength tests were based on ASTM C 496/C496M-(2011) [24]. A hydraulic digital testing ELE machine of 2000kN capacity was used to load the cylinders constantly up to failure at a loading rate of 2.2kN/sec. The mean splitting tensile strength was calculated using the average of 3 cylinders.

D. Modulus of Elasticity (E_c)

The modulus of elasticity of concrete (E_c) was tested using 3 concrete cylinders in accordance with ASTM C-469-(2002), [25]. E_c is calculated from the stress-strain diagram using a compress meter gauge with a length of 20cm and an accuracy of 0.001mm. The load was applied at a steady rate up to 40% of the maximum load.

All laboratory tests values for concrete mix1 are shown in Tables VII and VIII.

TABLE VII. TEST RESULTS OF CONCRETE MIX1

Property	Steel fibers (%)	Density (kg/m ³)	Increase in density (%)
Fresh density	0	2283	Ref.
Fresh density	0.5	2288	0.2
Fresh density	1	2292	0.4
Dry density	0	2250	Ref.
Dry density	0.5	2270	0.9
Dry density	1	2285	1.6
Oven density	0	2150	Ref.
Oven density	0.5	2200	2.3
Oven density	1	2225	3.5

Table VII indicates that the steel fiber percentage has a small effect on the fresh density: the increase of the percentage increased the fresh density by about 0.2, and 0.4% for added steel fiber percentage of 0.5 and 1% with respect to the reference specimens. Also, the steel fiber percentage has a small impact on dry density. Steel fibers increased dry density by about 0.9 and 1.6% for 0.5 and 1% added steel fiber percentage. Steel fibers had a higher impact on the oven density: steel fibers increased the oven density by about 2.3 and 3.5% for 0.5 and 1% added steel fiber percentage. Figure 2 shows the impact of steel fiber percentage on concrete density.

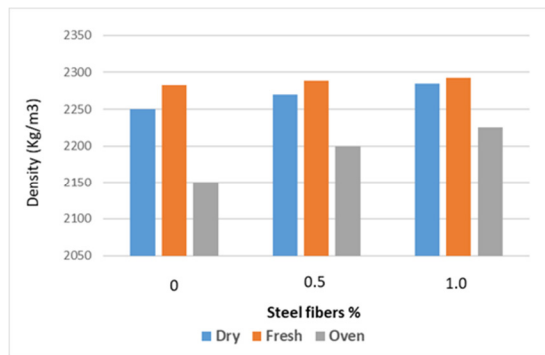


Fig. 2. The impact of steel fiber percentage on concrete density.

Table VII indicates that the steel fiber percentage has an important impact on compressive strength: steel fibers

increased compressive strength by about 2.4 and 16.3% when 0.5 and 1% steel fibers were added at curing age of 7 days. This is comparable to [7], which shows that the percentage of 2% steel fibers increased the compressive strength by about 10.8%. Adding steel fibers increased the compressive strength by about 4.1, and 37.6% for 0.5 and 1% steel fiber addition at 14 days. At 28 days, the respective increase percentages were 4.9 and 12.8%. Figure 3 shows the effect of steel fiber percentage on concrete compressive strength at various ages.

TABLE VIII. RESULTS OF LABORATORY TESTS FOR CONCRETE MIX1

Property	Steel fiber (%)	Result (MPa)	Increase (%)
f_{cu} , 7 days	0	16.6	Ref.
	0.5	17	2.4
	1	19.3	16.3
f_{cu} , 14 days	0	18.6	Ref.
	0.5	22.7	4.1
	1	25.6	37.6
f_{cu} , 28 days	0	24.3	Ref.
	0.5	25.5	4.9
	1	27.4	12.8
f_{ct} , 7 days	0	2.11	Ref.
f_{ct} , 14 days	0.5	2.36	11.8
f_{ct} , 28 days	1	2.6	23.2
E_c , 7 days	0	23800	Ref.
E_c , 14 days	0.5	24200	1.7
E_c , 28 days	1	25000	5

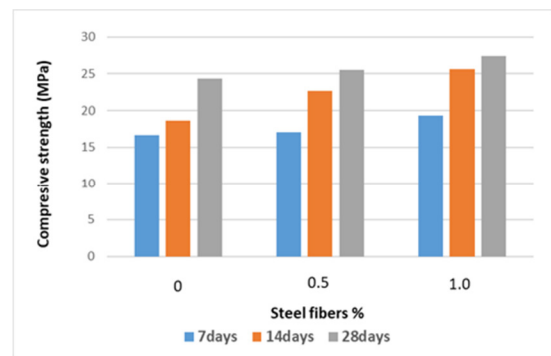


Fig. 3. The impact of steel fiber percentage on concrete compressive strength at various ages.

Also, Table VIII indicates that the steel fiber percentage has a significant impact on splitting tensile strength (f_{ct}) for 28 days curing age. Steel fiber 0.5 and 1% addition increased f_{ct} by about 11.8 and 23.2%. Finally, the addition of steel fibers has an impact on E_c after 28 days of curing. Steel fiber 0.5 and 1% addition increased E_c by about 1.7 and 5%.

IV. PARAMETRIC STUDY

Figures 4, 5, 6, and 7 indicate the impact of steel fiber percentage on density, compressive strength, splitting tensile strength, and modulus of elasticity respectively. The relation between the steel fibers percentage and splitting tensile strength was linear, while the relation between steel fiber percentage and compressive strength and modulus of elasticity was nonlinear for specimens cured for 28 days.

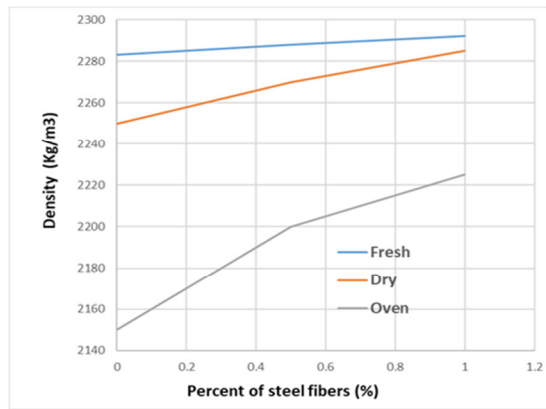


Fig. 4. Impact of steel fiber percentage on density.

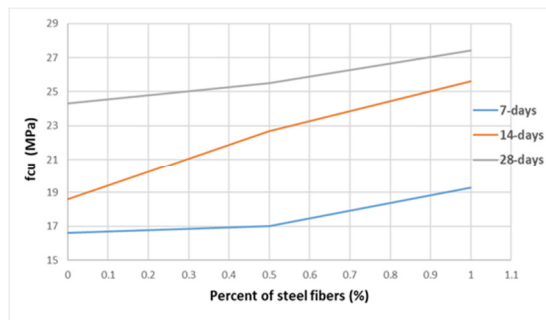


Fig. 5. Impact of steel fiber percentage on compressive strength.

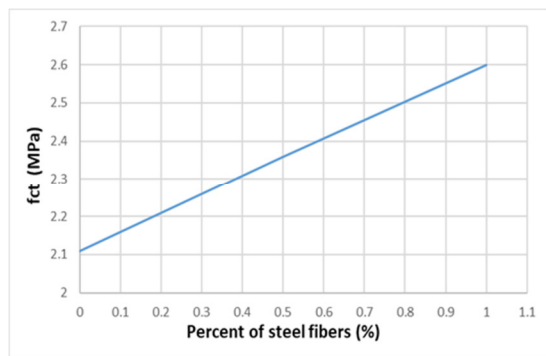


Fig. 6. Impact of steel fiber percentage on splitting tensile strength after 28 days of curing.

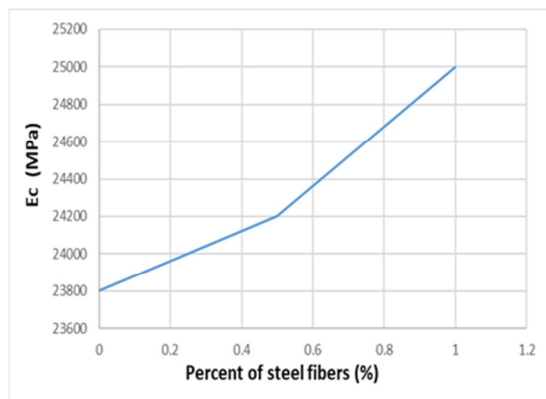


Fig. 7. Effect of steel fiber percentage on the modulus of elasticity after 28 days of curing.

V. CONCLUSIONS

- Steel fiber percentage had a minor influence on fresh density. Adding 0.50 and 1.0% steel fiber to the reference specimen enhanced the fresh density by 0.2% and 0.4% respectively.
- Steel fiber percentage had a marginal impact on dry density. Adding 0.5 and 1.0% steel fibers to the reference specimen raised the dry density by 0.9% and 1.6% respectively.
- Steel fiber percentage had a larger influence on oven density. Adding 0.5 and 1% steel fibers raised oven density by 2.3% and 3.5% respectively.
- Steel fiber percentage had an important impact on compressive strength. Adding 0.50 and 1.0% steel fibers increased compressive strength by 2.4% and 16.3% respectively, after 7 days of curing. Adding 0.50 and 1.0% steel fibers increased compressive strength by 4.1% and 37.6% at 14 days and 4.9% and 12.8% at 28 days.
- Steel fiber percentage had a substantial influence on splitting tensile strength at 28 days. Adding 0.50 and 1.0% steel fibers enhanced splitting tensile strength by 11.8% and 23.2% respectively.
- Steel fiber percentage affects the modulus of elasticity at 28 days. Adding 0.50 and 1.0% steel fibers increased the modulus of elasticity by 1.7% and 5% respectively..

VI. RECOMMENDATIONS FOR FUTURE WORK

- Studying eco-friendly zero-cement concrete proportions and properties under the effects of high-temperature.
- Studying slurry Infiltrated Fiber Concrete (SIFCON) proportions and properties under the effects of high-temperature.

REFERENCES

- [1] A. J. Alsaad, T. S. Al-Attar, and B. S. Al-Shathir, "Utilization of Mineral Sequestration for CO₂ Capturing in Car Parks and Tunnels," *Engineering and Technology Journal*, vol. 38, no. 5, pp. 728–737, May 2020, <https://doi.org/10.30684/etj.v38i5A.594>.
- [2] A. Moropoulou, A. Cakmak, K. C. Labropoulos, R. Van Grieken, and K. Torfs, "Accelerated microstructural evolution of a calcium-silicate-hydrate (C-S-H) phase in pozzolanic pastes using fine siliceous sources: Comparison with historic pozzolanic mortars," *Cement and Concrete Research*, vol. 34, no. 1, pp. 1–6, Jan. 2004, [https://doi.org/10.1016/S0008-8846\(03\)00187-X](https://doi.org/10.1016/S0008-8846(03)00187-X).
- [3] N. Kadum, T. al-Attar, and Z. Al-Azzawi, "Evaluation of pozzolime mixtures as a sustainable binder to replace portland cement in structural concrete," *MATEC Web of Conferences*, vol. 120, 2017, Art. no. 02009, <https://doi.org/10.1051/mateconf/201712002009>.
- [4] S. P. Shah and B. V. Rangan, "Fiber Reinforced Concrete Properties," *Journal Proceedings*, vol. 68, no. 2, pp. 126–137, Feb. 1971, <https://doi.org/10.14359/11299>.
- [5] G. K. Mohammed, K. F. Sarsam, and I. N. Gorgis, "Flexural Performance of Reinforced Concrete Built-up Beams with SIFCON," *Engineering and Technology Journal*, vol. 38, no. 5, pp. 669–680, May 2020, <https://doi.org/10.30684/etj.v38i5A.501>.
- [6] M. Mouli and H. Khelafi, "Performance characteristics of lightweight aggregate concrete containing natural pozzolan," *Building and Environment*, vol. 43, no. 1, pp. 31–36, Jan. 2008, <https://doi.org/10.1016/j.buildenv.2006.11.038>.

- [7] N. A. Farhan, M. N. Sheikh, and M. N. S. Hadi, "Engineering Properties of Ambient Cured Alkali-Activated Fly Ash-Slag Concrete Reinforced with Different Types of Steel Fiber," *Journal of Materials in Civil Engineering*, vol. 30, no. 7, Jul. 2018, Art. no. 04018142, [https://doi.org/10.1061/\(ASCE\)MT.1943-5533.0002333](https://doi.org/10.1061/(ASCE)MT.1943-5533.0002333).
- [8] Q. Wang, Y. Yi, G. Ma, and H. Luo, "Hybrid effects of steel fibers, basalt fibers and calcium sulfate on mechanical performance of PVA-ECC containing high-volume fly ash," *Cement and Concrete Composites*, vol. 97, pp. 357–368, Mar. 2019, <https://doi.org/10.1016/j.cemconcomp.2019.01.009>.
- [9] M. A. Faris *et al.*, "Comparison of Hook and Straight Steel Fibers Addition on Malaysian Fly Ash-Based Geopolymer Concrete on the Slump, Density, Water Absorption and Mechanical Properties," *Materials (Basel, Switzerland)*, vol. 14, no. 5, Mar. 2021, Art. no. 1310, <https://doi.org/10.3390/ma14051310>.
- [10] B. Ali, S. S. Raza, R. Kurda, and R. Alyousef, "Synergistic effects of fly ash and hooked steel fibers on strength and durability properties of high strength recycled aggregate concrete," *Resources, Conservation and Recycling*, vol. 168, May 2021, Art. no. 105444, <https://doi.org/10.1016/j.resconrec.2021.105444>.
- [11] M. Shariq, S. Pal, R. Chaubey, and A. Masood, "An experimental and analytical study into the strength of hooked-end steel fiber reinforced HVFA concrete," *Advances in concrete construction*, vol. 13, no. 1, pp. 35–43, 2022, <https://doi.org/10.12989/acc.2022.13.1.035>.
- [12] M. H. Kumar, I. Saikrishnamacharyulu, N. R. Mohanta, A. Ashutosh, P. Mishra, and S. Samantaray, "Mechanical behaviour of high strength concrete modified with triple blend of fly ash, silica fume and steel fibers," *Materials Today: Proceedings*, Apr. 2022, <https://doi.org/10.1016/j.matpr.2022.03.528>.
- [13] *Iraqi specification no 807: Lime Used in Buildings*. 2004.
- [14] *Iraqi specification Standard no 5: Portland Cement*. 1984.
- [15] *Iraqi Specification Standard no 45: Natural Aggregate Resources Used in Buildings and Concrete*. 1984.
- [16] P. K. Mehta and P. J. M. Monteiro, *Concrete: Microstructure, Properties, and Materials*, 4th ed. New York, NY, USA: McGraw Hill, 2013.
- [17] *ASTM C1240-20: Standard Specification for Silica Fume Used in Cementitious Mixtures*. ASTM International, 2020.
- [18] *ASTM C494/C494M-13: Standard Specification for Chemical Admixtures for Concrete*. ASTM International, 2013.
- [19] A. M. Al-Hilali, A. F. Izzet, and N. Oukaili, "Static Shear Strength of a Non-Prismatic Beam with Transverse Openings," *Engineering, Technology & Applied Science Research*, vol. 12, no. 2, pp. 8349–8353, Apr. 2022, <https://doi.org/10.48084/etasr.4789>.
- [20] B. F. Abdulkareem, A. F. Izzet, and N. Oukaili, "Post-Fire Behavior of Non-Prismatic Beams with Multiple Rectangular Openings Monotonically Loaded," *Engineering, Technology & Applied Science Research*, vol. 11, no. 6, pp. 7763–7769, Dec. 2021, <https://doi.org/10.48084/etasr.4488>.
- [21] H. M. Hekmet and A. F. Izzet, "Performance of Segmental Post-Tensioned Concrete Beams Exposed to High Fire Temperature," *Engineering, Technology & Applied Science Research*, vol. 9, no. 4, pp. 4440–4447, Aug. 2019, <https://doi.org/10.48084/etasr.2864>.
- [22] *ASTM C138/C138M-17a: Standard Test Method for Density (Unit Weight), Yield, and Air Content (Gravimetric) of Concrete*. ASTM International, 2017.
- [23] *BS EN 12390-3:2019 - TC: Testing hardened concrete - Compressive strength of test specimens*. BSI, 2019.
- [24] *ASTM C496/C496M-17: Standard Test Method for Splitting Tensile Strength of Cylindrical Concrete Specimens*. ASTM International, 2017.
- [25] *ASTM C469/C469M-14: Standard Test Method for Static Modulus of Elasticity and Poisson's Ratio of Concrete in Compression*. ASTM International, 2014.

Heat Transfer Enhancement in a Receiver Tube of Solar Collector Using Various Materials and Nanofluids

Djemaa Guerraiche

Applied Energy Physics Laboratory (LPEA)
Department of Physics
Faculty of Matter Sciences
University of Batna 1
Batna, Algeria
d.guerraiche@gmail.com

Khelifa Guerraiche

Mechanical Engineering Department
Faculty of Technology
University of Batna 2
Batna, Algeria
guer.khelifa@yahoo.com

Zied Driss

Laboratory of Electromechanical Systems (LASEM)
National School of Engineers of Sfax (ENIS)
University of Sfax, Sfax, Tunisia
zied.driss@enis.tn

Atef Chibani

Department of Chemical Engineering
University Salah Boubnider Constantine 3
Constantine, Algeria
chibaniatef@gmail.com

Slimane Merouani

Department of Chemical Engineering
University Salah Boubnider Constantine 3
Constantine, Algeria
s.merouani@yahoo.fr

Cherif Bougriou

Mechanical Engineering Department
Faculty of Technology, University of Batna 2
Batna, Algeria
c.bougriou@univ-batna2.dz

Received: 21 July 2022 | Revised: 5 August 2022 | Accepted: 8 August 2022

Abstract—The solar flux distribution on the Parabolic Trough Collector (PTC) absorber tube is extremely non-uniform, which causes non-uniform temperature distribution outside the absorber tube. Therefore, it generates high thermal stress which causes creep and fatigue damage. This presents a challenge to the efficiency and reliability of parabolic trough receivers. To override this problem, we have to homogenize the heat flux distribution and enhance the heat transfer in the receiver's absorber tube to improve the performance of the PTC. In this work, 3D thermal and thermal stress analyses of PTC receiver performance were investigated with a combination of Monte Carlo Ray-Trace (MCRT), Computational Fluid Dynamics (CFD) analysis, and thermal stress analysis using the static structural module of ANSYS. At first, we studied the effect of the receiver tube material (aluminium, copper, and stainless steel) on heat transfer. The temperature gradients and the thermal stresses were compared. Second, we studied the effect of the addition of nanoparticles on the working Heat Transfer Fluid (HTF), employing an Al_2O_3 - H_2O based nanofluid at various volume concentrations. To improve the thermal performance of the PTC, a nanoparticle volume concentration ratio of 1%–6% is required. The results show that the temperature gradients and thermal stresses of stainless steel are significantly higher than those of aluminium and copper. From the standpoint of thermal

stress, copper is recommended as the tube receiver material. Using Al_2O_3 in water as an HTF increases the average output temperature by 2%, 6%, and 10% under volume concentrations of 0%, 2%, and 6% respectively. The study concluded that the thermal efficiency increases from 3% to 14% for nanoparticle volume fractions ranging from 2% to 6%.

Keywords—heat transfer; nanofluids; solar concentrator; receiver; non-uniform heat flux; temperature gradients

I. INTRODUCTION

The use of renewable energies has become essential to the reduction of the consumption of fossil resources and the production of carbon dioxide (CO_2), which is the main gas responsible for the greenhouse effect. The technology of Concentrated Solar Power (CSP) can meet the demands for thermal and electrical energy. The benefits of using a CSP technology with a PTC system are: it is best suited for a wide range of industrial applications and can contribute to thermal energy production, which can have significant economic, environmental, and social implications [1]. Recently, the PTC has been developing towards a higher concentration ratio and operating temperature for the purposes of reducing the

investment cost and improving its thermal efficiency, especially at high temperatures. This is an important goal in order for these technologies to be energetically and financially viable [2]. However, the PTC suffers from several problems and failures, especially concentrated solar Non-Uniform Heat Flux (NUHF) distribution on the outer surface of the absorber tube. In addition, the heat flux is small near the top wall where the collimated energy is incident and is large near the bottom wall [3]. NUHF causes high local temperature and big temperature gradient in solar receivers due to the restricted thermal conductivity of the receiver tube and the thermal convection capacity inside the tube, producing an increase in thermal stress. This causes the absorber tube to deviate from the focal plane and large increase in optical losses because the selective coating degrades when the local temperature is too high, limiting the maximum working temperature. All these issues represent challenges that will have a long-term impact on the PTC's efficiency and safety [4]. Authors in [5] discovered that the maximum temperature differential for safe functioning of receiver tubes is around 50K. Furthermore, strong temperature gradients have many repercussions circumferentially, which may be summed by the deflection of the absorber tube. This causes the absorber tube to deviate from the concentrator's focus line, causing optical loss. When the local temperature is too high, the selective coating degrades, limiting the maximum operating temperature. As a result of the thermal breakdown of the HTF, hydrogen production and penetration occur [6], resulting in increasing heat loss, material degradation, heat stress, and deformation of the absorber tube. These pose significant obstacles to the concentrated solar system's safe and efficient functioning. To solve this issue, we must homogenize the heat flow distribution by flattening the temperature distribution, lowering the peak temperature and the temperature gradient. Recent studies have concentrated on improving thermal transfer and thermal distribution uniformity. A simple solution to flattening the temperature distribution is to homogenize the flow distribution. Heat transfer enhancement technology can reduce thermal losses and thermal stress while increasing heat transfer rates between the absorber tube and HTF at a low cost. The solutions can be roughly classified into three groups: Improvements to the tube's thermal conductivity, collector optimization to homogenize solar energy, and augmentation of convective heat transfer within the absorber tube [7].

Receiver tubes are subjected to a harsh operating environment. To alleviate the extreme operating conditions and ensure the receiver's durability, dependability, and integrity throughout its lifecycle, special consideration was required when selecting the receiver material. High corrosion resistance, optimal physical and mechanical properties, excellent fabricability, and a higher capacity for flux density are all critical criteria. Several solutions have been adopted by enhancing the thermal conductivity of the absorber tube and employing an absorber with thermal compensator and heat transfer improvement techniques [8]. Using selective materials, solution techniques aimed to improve the thermal conductivity of the absorber tube have been proposed for the PTC receiver. Authors in [9] conducted a structural and thermal analysis of a PTC absorber tube to investigate the effect of material

variations on temperature distribution flattening. Steel, copper, aluminium, and bimetallic materials (Cu-Fe) have been investigated. They concluded that when using copper, the circumferential temperature non-uniformity was less bending due to less thermal load than using steel. Using a bimetallic tube improves temperature distribution and reduces maximum deflection by 45–49%. Authors in [2] presented an experimental investigation in which the steel tube was replaced with a copper tube. The reduced bending of the absorber tube was caused by the lower circumferential temperature variations due to copper's strong thermal conductivity.

II. HOMOGENIZING SOLAR FLUX DISTRIBUTION

A more straightforward way to flatten the temperature distribution appears to be the homogenization of the flux distribution. Several researchers proposed innovative concentrators for flux homogenization. The heat flow gradient in the absorber tube must be reduced and homogenized. Authors in [10] proposed improvements based on the conventional PTC and a secondary reflector was added overhead the tube. The numerical results showed that the heat flux gradient was reduced by 70.37%, and the temperature gradient from 159.39K to 24.16K. Authors in [11] used a variable focus PTC, in which the focal length varied as a function of the reflector's motion relative to the receiver, significantly enhanced the flux distribution's homogeneity. Authors in [12] placed a secondary reflector within the annular gap in order to reflect more sun rays onto the top of the absorber. Authors in [13] investigated the heat flux distribution on the outside surface of the PTC absorber tube in order to lower the tube's temperature gradient by relocating the absorber tube away from the focal line and toward the parabola and adding a secondary reflector. The results show that installing another reflector overhead the absorber tube improves the heat flux distribution and reduces heat flux gradient by 70.37%.

III. HEAT TRANSFER ENHANCEMENT AND OPTIMIZATION

Heat transfer improvement might result in a more uniform temperature distribution in the metal tube, reducing thermal deformation in the receiving tube. For the PTC receiver, a number of strategies for enhancing convective heat transfer have been proposed. Authors in [14] used an absorber with a thermal compensator at the parabolic dish concentrated solar receiver, which contains a Phase Change Material (PCM) to produce uniform heat distribution. Thermal performance is improved by using PCMs as thermal energy storage. Homogeneous temperature distribution was observed on the PCM integrated receiver in the absence of solar radiation. A non-uniform temperature distribution was discovered during the charging of the PCM included within the solar receiver. Authors in [15] presented a novel PTC receiver design based on a concentric absorber tube filled with PCM. The absorber was regarded as a component of transitory thermal heat storage. The results validated the suggested design and verified that combining PTC and PCM in the receiver peripheral can improve the thermal performance of the provided system. In [16], for solar cascade heat collection, a new PTC with a concentric receiver tube based on two HTFs, Syltherm-800 oil, was presented. The findings revealed that the absorber tube's peak temperature and circumferential temperature gradient

were lower than regular PTC at the same mass flow rate. The absorber tube's maximum temperature and temperature difference lowered to 66K and 65K respectively. For the PTC receiver, several strategies for improving convective heat transfer have been proposed. This technology employs helical swirl generators, treated areas, vortex generators, displacement increase devices, extended surfaces, jagged surfaces, and nanoparticles [17]. According to these studies, the peak temperature and temperature gradient can be minimized. In [18], the impact of swirl inserts with and without nanofluids on PTCs with non-uniform heating flux was examined. The results showed that combining the swirl inserts and nanofluids improved the Nusselt number by 57.4% while the maximum reduction in thermal losses was 23%. The Nusselt number, on the other hand, was enhanced by 15.57% when utilizing nanofluid only.

The working fluid is one of the most important components of a solar receiver since it plays an important role in heat transmission. During the last 25 years, nanotechnology has found applications in solar energy production. The use of nanofluids has transformed material science, and they have been used as potential alternative fluid solutions for increasing the efficiency and profitability of thermal systems. Adding nanoparticles to the heating fluid presents the best solution to improve thermal conductivity and thermo-physical and heat transfer properties of the fluid [19]. In fact, nanofluids have a favorable effect on the performance of the PTC. The heat transfer performance obtainable with nanofluids is known to surpass the performance of heat transfer liquids available today [20]. The most used nanofluids contain nanoparticles such as Al, Fe_2O_3 , Al_2O_3 , Cu, TiO_2 , and SiO_2 [21]. Some studies on the use of nanofluids for solar energy harvesting are available in the literature. For example, authors in [22] investigated the application of nanofluids in concentrating a solar PTC. The effect of several nanofluids employed as working fluid on the performance of solar thermal collectors was studied experimentally. Authors in [23] discussed the progressive application of nanofluids in solar collectors with different thermophysical properties. In addition, they evaluated the performance of different types of solar collectors. Authors in [24] proposed a mathematical model for the investigation of the effect of nanofluid concentration on PTC. They found that using nanofluids in a PTC improves its thermal efficiency. Authors in [25] presented an experimental study of the heat transfer and friction factor of silver nanofluids in a PTC receiver with twisted tape inserts. They confirmed that using nanofluids increases the heat transfer performance of the receiver. Authors in [26] confirmed that the performance of concentrating solar thermal systems with a nanofluid as working fluid has an excellent potential for power tower applications improving efficiency by 5%–10%. Authors in [27] investigated the performance of nanofluids on PTC systems and improved the efficiency by at least 5% [27]. Authors in [28] presented an experimental study to evaluate the thermal efficiency of a PTC using nanoparticles of alumina (Al_2O_3) in water with a volume fraction of 1% and 3% as HTF. The results showed that with nanofluid as working fluid, the maximum efficiencies were 52.4% and 57.7%, while for water, these efficiencies were 40.8% and 46.5% for 3% and 1%

volume fraction respectively. PTC thermal enhancement has recently attracted considerable attention. The enhancement of PTC performance can be achieved by modifying the material, modifying the geometry, and using nanofluids instead of conventional base fluids. Even so, utilizing nanofluids on PTCs provided a positive result. These results are still facing several breaking points in the method of using a HTF [29]. Finding the optimal configuration of various parameters, such as receiver formation and geometry, receiver size and material, HTF, and regulation of the maximum heat flow, is one of the most challenging and important research purposes for enhanced thermal systems to further improve efficiency and profitability through innovation in design and application of new fluids and new materials.

This work presents a three-dimensional numerical study of the thermal and thermal stress performance of a PTC. In order to attain this goal, the suggested approach consists of two main steps. The impact of the absorber tube material on heat transmission was investigated in the first step. The performance of PTC receivers was studied using a combination of Monte Carlo Ray-Trace (MCRT), Computational Fluid Dynamics (CFD) simulation using Ansys Fluent software, and thermal stress analysis using ANSYS' static structural module. We will solve the temperature distributions in the heat transfer analysis, and the thermal stress analysis will use the interpolated temperature distributions specified at the nodes of the CFD meshes as input data for the nodes. A comparative study of numerous materials, such as copper, aluminum, and stainless steel, is employed and compared to find which is ideal for a small-sized PTC under actual NUHF. Second, the effect of the addition of nanoparticles on the working fluid, employing Al_2O_3 -H₂O based nanofluid at various volume concentrations is carried out. The computational model is developed in Ansys Fluent environment.

IV. PHYSICAL MODEL

Figure 1 shows the physical model considered in this work. The PTC system consists of a mirror folded into a parabolic shape with a heat collecting element at its focus. In the numerical study, the rim angle (Φ_r) of the collector is 90° and the total aperture area ($A_p = W \times L$) is 1.80m². The receiver of the parabolic trough solar collector consists of a metallic tube that is enclosed in a glass envelope. The absorber tube is coated with a selective coating that has a high absorptivity of the incoming solar radiation and a low emissivity of infrared radiation. The geometrical dimensions and optical properties of the PTC system are defined in Table I. In this work, a three-dimensional analysis of the thermal losses and thermal stress performance of a solar PTC receiver was investigated through studying the influence of the receiver tube, material type, and the nanofluid used as the working fluid. To improve the thermal performance of the PTC and homogenize the flux distribution for flattening the temperature distribution, various types of materials were used for the receiver heat transfer enhancement, namely copper, stainless steel, aluminium, and water containing nanoparticles of Al_2O_3 . 321H stainless steel was used for the absorber tube due to its low bending behavior and high strength capability [30]. The thermal properties of absorber materials are given in Table II. In these conditions, the

concentration ratio and the mass flow rate are equal to 0%–6% and 0.005kg/s respectively. For our analysis, the solar collector shown in Figure 2 was chosen as the geometrical model in the simulations.

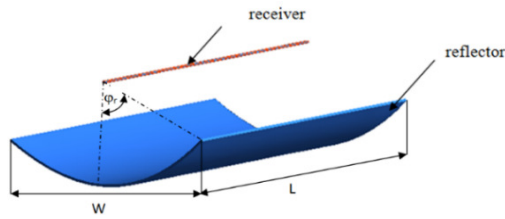


Fig. 1. View of the parabolic trough collector and its components.

TABLE I. GEOMETRICAL PARAMETERS OF THE PTC [15]

Receiver tube	
Inner diameter of receiver tube	0.027 m
Outer diameter of receiver tube	0.028 m
Inner diameter of pyrex cover	0.048 m
Outer diameter of pyrex cover	0.050 m
Collector	
Focal length, f	0.25 m
Aperture width, w	1.0 m
Rim angle, ϕ_r	90°
Length, L	1.80 m
Geometrical concentration ratio, C	13
Mirrors reflectivity, ρ	0.91
Slope error σ_{slope}	2 mrad
Specularity error σ_{spec}	2 mrad

TABLE II. STEEL, ALUMINA, AND COPPER ABSORBER TUBE PHYSICALS PARAMETERS [30]

Parameter	321H Stainless steel	Alumina	Copper
Density (kg.m^{-3})	8030	3850	8978
Conductivity ($\text{W.m}^{-1}\text{.K}^{-1}$)	17.3	36	387.6
Specific heat ($\text{J.kg}^{-1}\text{.K}^{-1}$)	512	773	381

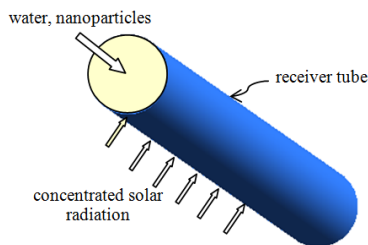


Fig. 2. Receiver parabolic trough solar collector geometry.

V. NUMERICAL MODEL AND MATHEMATICAL FORMULATION

A three-dimensional optic-thermal coupling model is used to analyze the heat transfer process in a PTC system employing Al_2O_3 /water nanofluid as the HTF. The Monte Carlo Ray Trace (MCRT) code is used to calculate a realistic non-uniform solar radiation heat flux distribution on the outside wall of the absorber tube to expose the optical features of the proposed PTC system. The solar flux distribution created using the MCRT approach was regarded as heat flux boundary conditions in the steady state heat transfer investigation for

CFD analysis. In the estimation of heat flux distributions, actual variables such as sun shape, incidence angle, optical characteristics, and numerous optical defects, were taken into consideration. The expected Direct Normal Irradiance (DNI) was 1000W/m^2 . The thermal performance of the PTC was studied utilizing a Computational Fluid Dynamics (CFD) software tool and a nanofluid as the working fluid. The Reynolds averaged Navier-Stokes equations were solved using the finite volume approach in the commercial computational fluid dynamics package Ansys Fluent 16.0. The finite volume approach was used to discretize the governing equations of continuity, nanoparticle conservation, momentum, and energy. The convective and diffusive components in momentum and energy equations were discretized using the second-order upwind approach. For pressure discretization, the PRESTO scheme was utilized. The SIMPLE method was used to solve the velocity pressure coupling problem. Nanofluid flow modeling is classified into two categories: the single-phase flow in which the base fluid and the suspended nanoparticles are assumed homogenous, taking into consideration the thermal characteristics of the nanofluid and relying on published correlations, and two-phase flow which separates the base fluid from the suspended nanoparticles. FLUENT supports three models: Volume Of Fluid (VOF), mixed, and Eulerian. The single-phase method was utilized in this study, which is regarded as an accurate method when the nanoparticle concentration and diameter are less than 10% and 100nm respectively. [31].

VI. MESH INDEPENDENCE VERIFICATION

A three-dimensional geometry was created, and a tetrahedral mesh was placed over the absorber tube's fluid domain. Figure 3 depicts the absorber tube's mesh geometry. A grid independence test was performed to ensure that the mesh value is not affected by the grid. Table III shows the results of the mesh sensitivity study for the output temperature of a working fluid.

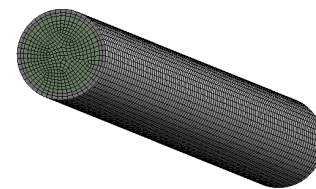


Fig. 3. 3D meshing of the absorber tube.

TABLE III. GRID INDEPENDENCE STUDY

Grid	Outlet temperature (K)
182680	328.12
256660	327.55
365760	326.51
406460	326.50

VII. HEAT TRANSFER FLUID PROPERTIES

Water with Al_2O_3 , a frequently used and affordable nanoparticle, was employed as the base fluid in this study. The nanofluids' qualities are determined by the thermophysical parameters of the base fluid, the volume concentration ratio of

nanoparticles, and the temperature. Table IV lists the characteristics of Al_2O_3 nanoparticles [32].

TABLE IV. PROPERTIES OF THE Al_2O_3 NANOPARTICLES

	Density (kg.m^{-3})	Conductivity ($\text{W.m}^{-1}\text{K}^{-1}$)	Specific heat ($\text{J.kg}^{-1}\text{K}^{-1}$)
Al_2O_3	3850	36	773

Nanofluid density, heat capacitance, dynamic viscosity, and thermal conductivity are determined from the following equations [33]. The density of the nanofluid is determined by:

$$\rho_{nf} = (1-f)\rho_f + f\rho_p \quad (1)$$

where ρ , f , p , nf and ϕ denote the density, base fluid, nanoparticle, and nanofluid and the volumetric concentration of Al_2O_3 in the base fluid respectively. The ratio between the thermal conductivities of the nanofluid K and the base fluid K_f is defined as follows:

$$\frac{K}{K_f} = \frac{\tau + (\eta - 1) - (\eta - 1)(1 - \tau)\phi}{\tau + (\eta - 1) + (1 - \tau)\phi} \quad (2)$$

The ratio between the thermal conductivities of the particles K_p and the base fluid is defined as:

$$\tau = K_p / K_f \quad (3)$$

The aspect ratio is given by (4), where ξ is the sphericity:

$$\eta = \xi/3 \quad (4)$$

The viscosity of the nanofluid is defined by:

$$\frac{\mu_{nf}}{\eta_{bf}} = 1 + 2.5\phi \quad (5)$$

The specific heat of the nanofluid is given by:

$$C_{p,nf} = (1-\phi)C_{p,f} + \phi C_{p,p} \quad (6)$$

VIII. THERMAL PERFORMANCE

The thermal efficiency η_{th} of the PTC system is determined as follows:

$$\eta_{th} = \frac{Q_u}{Q_s} \quad (7)$$

where Q_u is the useful gained thermal energy and Q_s is the available solar energy:

$$Q_s = A_a \times I_b \quad (8)$$

where A_a is the the aperture area of the solar collector:

$$A_a = w \times L \quad (9)$$

The useful gained thermal energy Q_u is determined based on the mass flow rate of the HTF, mass flow rate, and the fluid temperatures at the inlet and outlet, T_{in} and T_{out} [34]:

$$Q_u = \dot{m} C_p (T_{out} - T_{in}) \quad (10)$$

where \dot{m} , C_p , T_{out} , and T_{in} are the mass flow rate, specific heat capacity, and inlet and outlet heat transfer fluid temperature.

The conventional definition of the local convective heat transfer coefficient can be calculated in terms of the inner wall temperature of the absorber tube T_w , surface heat flux q'' , and the average temperature T_{ave} of the inlet and the outlet:

$$h_f = \frac{q''}{(T_w - T_{ave})} \quad (11)$$

IX. HYDRAULIC PERFORMANCE

The pressure drop in the solar absorber tube can be determined as follows [35]:

$$\Delta P = P_{av,inl} - P_{av,out} \quad (12)$$

The friction factor coefficient is computed as:

$$f = \frac{2}{\left(\frac{L}{D_i}\right)} \frac{\Delta P}{\rho U^2} \quad (13)$$

Several correlations and data from the literature were utilized to validate the numerical model's conclusions. To obtain the heat transfer performance in a parabolic trough receiver tube, the friction factor was calculated using the correlation of [36]:

$$f = 0.173 \text{Re}^{-0.1974} \quad (14)$$

The average Nu is expressed as:

$$\text{Nu} = \frac{h_f \cdot D_i}{k_f} \quad (15)$$

where k_{eff} is the effective thermal conductivity ($\text{Wm}^{-1}\text{K}^{-1}$).

$$\text{Nu} = \frac{(f/8)(\text{Re}-1.00)\text{Pr}}{1+12.7((f/8)^{0.5})(\text{Pr}^{2/3}-1)} \quad (16)$$

with $\text{Pr} \leq 2000$ and $10^3 \leq \text{Re} \leq 5 \times 10^6$.

The Reynolds number is given by:

$$\text{Re} = \frac{\rho \cdot U \cdot D_i}{\mu} \quad (17)$$

X. BOUNDARY CONDITIONS

For the intake and outlet of the absorber tube, constant mass flow rate, temperature, and outflow boundary conditions were adopted. To generate more realistic findings, a non-uniform heat flow profile around the perimeter of the receiver's absorber tube was examined. SolTrace calculates the solar heat flux density to derive the heat flux distribution profile under direct normal irradiation of 1000W/m^2 . The flux is centered on the lowest half, which is facing the PTC's mirror. The heat flow density is really low in the higher section. In reality, the radiation that comes into contact with the face in this section is direct radiation.

XI. OPTICAL MODELLING (SOLAR HEAT FLUX DENSITY)

For the optical modeling of the collector, SolTrace software was used to predict the effective heat flux falling on the bottom of the absorber tube and to find the effective rays concentrating on the receiver tube using the Monte Carlo ray tracing algorithm. The sun form is characterized by a Gaussian distribution with a standard deviation of 2mrad. Mirror secularity and slope flaws were both taken into account. The efficient rays focused on the outer surface of the absorber tube were discovered using the Monte Carlo ray tracing approach. Figure 4 depicts the distribution of the solar heat flow around the outside wall of the receiving tube. The flux is concentrated on the lower part which is facing the PTC's mirror. For the upper part, the heat flux density is very low (direct solar radiation). Data polynomial functions were created into a macro in Fluent CFD simulation as a User Defined Function (UDF), which is used as the boundary condition input for the heat flux wall on the absorber tube's outer surface as seen in Figure 5. No-slip conditions were applied to all solid surfaces.

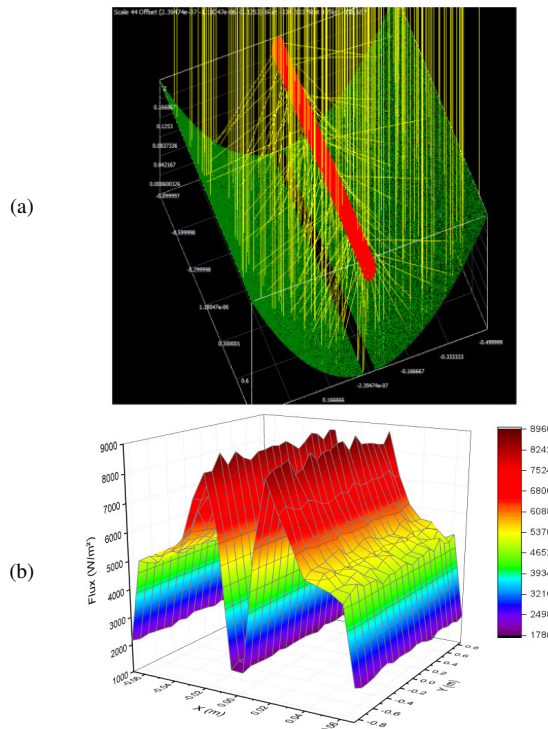


Fig. 4. (a) Ray tracing parabolic reflector and absorber tube surface, (b) 3-dimensional view of the heat flux distribution on the absorber tube surface.

XII. MODEL VALIDATION

To confirm the solution's validity, the precision of the computational modeling was calculated and a comparison with previously reported experimental and theoretical correlations for the local Nusselt variation and pressure drop were performed. The model's validity is evaluated using the experimental data from [38]. The geometry and thermal boundary conditions are nearly identical to those in this simulation.

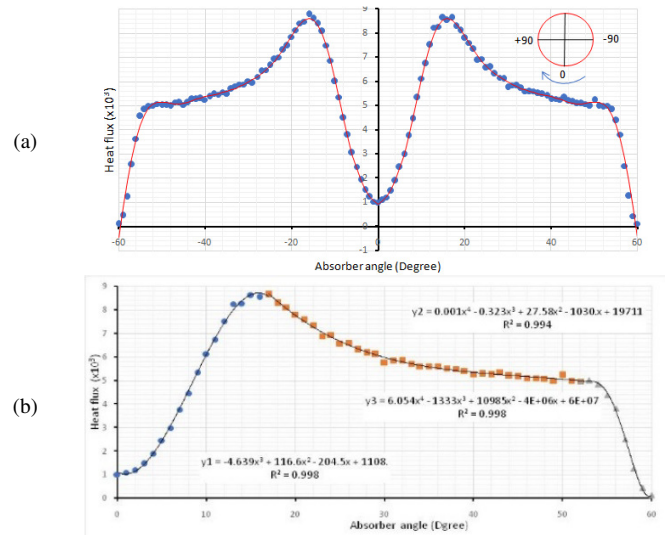


Fig. 5. (a) Circumferential heat flux distribution on the absorber tube. (b) polynomial functions of heat flux profile on the outer surface of the absorber.

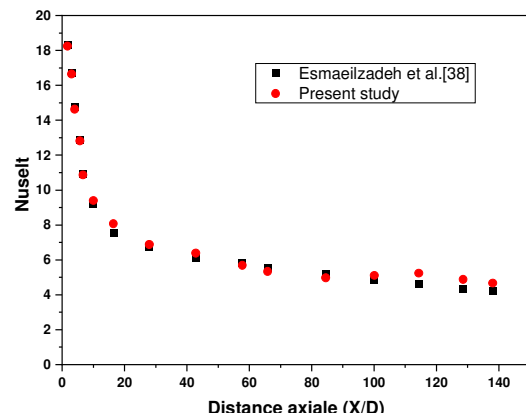


Fig. 6. Comparison of the obtained Nusselt number with [38].

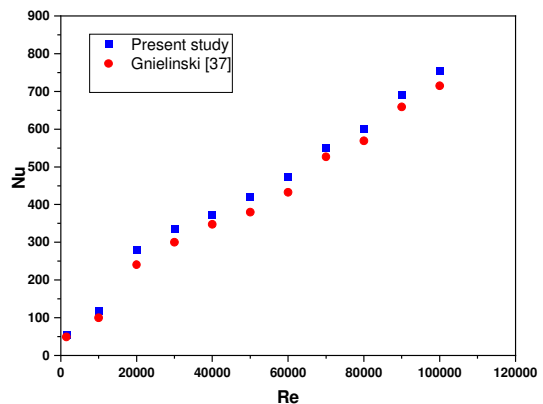


Fig. 7. Comparison of Nu with the result of [37].

The authors in [38] investigated the effect of incorporating Al_2O_3 nanoparticles into pure water on the hydrodynamic and heat transfer parameters of laminar flow at $\text{Re} = 799.53$ inside horizontal flow with uniform heat flux of 9000W/m^2 on the outer pipe wall. According to Figure 6, the current study's modeling results match the experimental results of [38]. Numerical results deviate from experimental data by

approximately 3.5% for the estimation of Nu when $\phi=1\%$. Gnielinski correlations were used to validate the results of our numerical study for heat transfer when $\phi=0\%$ [37] given by (16). As shown in Figure 7, the present study results are shown to be in good agreement with the given correlations. The friction factors were compared with the results from [36], given by (14). Excellent agreement was obtained, as shown in Figure 8, with a deviation of less than 3%. The results indicate that the model and the calculation process are appropriate and acceptable.

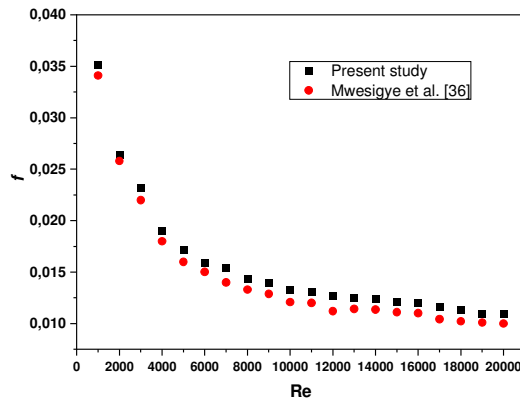


Fig. 8. Validation of present study friction factor with [36] for $\phi=4\%$.

XIII. RESULTS AND DISCUSSION

As a heat flux boundary condition, a UDF was used to connect the acquired heat flux profile to a CFD. Figure 9 depicts the heat flux distribution and temperature distribution on the outer surface of the absorber tube. For typical working condition of HTF inlet mass flow rate, DNI, and HTF inlet temperature of 0.005m/s, 1000W/m², and 300K respectively, the performance of the solar collector was tested using water as HTF.

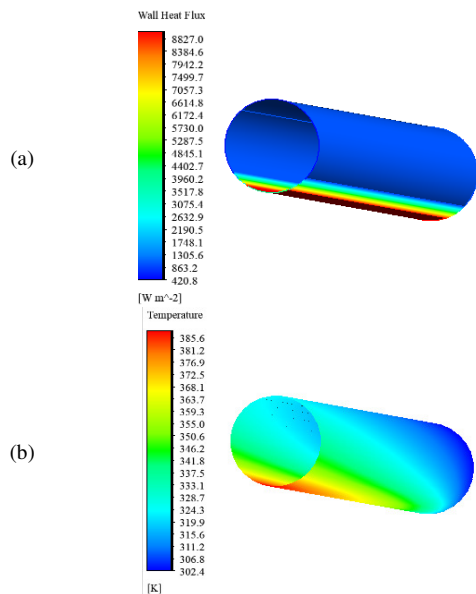


Fig. 9. (a) CFD heat flux, (b) temperature distributions on the outer surface of the absorber tube.

A. Effect of the Absorber Tube Material

Figure 10 depicts the temperature distribution on the outside of the absorber tube for various materials. When the thermophysical properties of the absorber vary and the distribution of heat flux on the outer wall changes, the temperature distribution varies over the entire tube wall. Due to its lower thermal conductivity, the steel absorber tube has a poor circumferential temperature distribution. Copper has higher thermal properties than stainless steel, but it has a higher self-weight and lower mechanical strength [3].

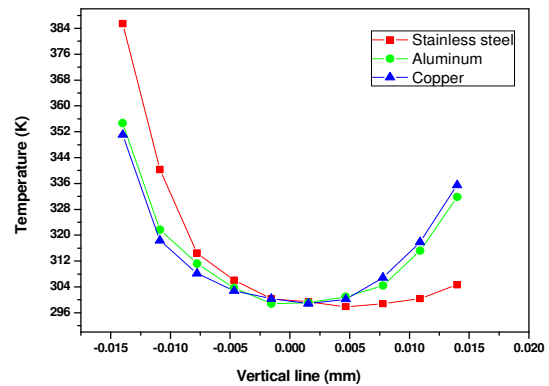


Fig. 10. Distribution of the outlet temperature.

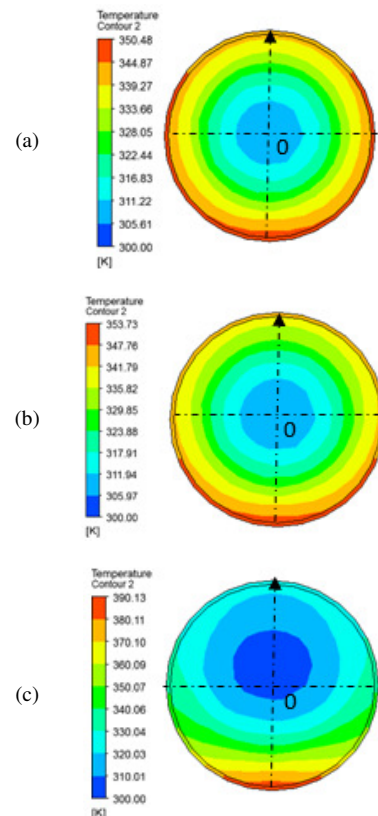


Fig. 11. Temperature variation from bottom wall to top wall of the absorber: (a) Cooper, (b) aluminium, (c) stainless stell.

Figure 11 shows the temperature profiles around the diameter of the inner surface of the absorber tube at the outlet

section. Among the three materials, the temperature of stainless steel is the maximum due to its low thermal conductivity. The temperature gradients with stainless steel are much higher than those of aluminium and copper. The radial temperature distribution is asymmetrical. This can cause higher thermal stresses and reduce the durability of the absorber tube. Circumferential temperature distribution of different absorber tubes is presented in Figure 12 for different absorber tube materials.

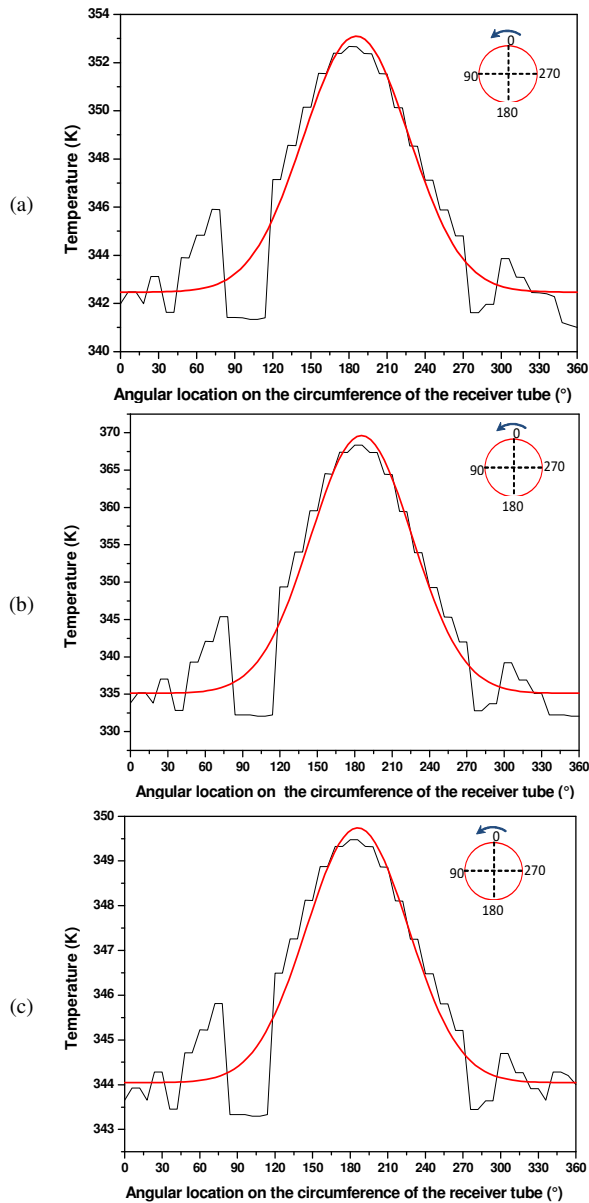


Fig. 12. Circumferential temperature distribution on absorber tube at outlet section ($Re=1400$): (a) Stainless steel, (b) aluminium, (c) copper.

The temperature distributions changed with angle ϕ for the three materials. The top wall ($\phi=0^\circ$) temperature remains approximately constant, while for the bottom wall ($\phi=180^\circ$) it is maximum with a very significant gradient. This part of the absorber tube receiver concentrated solar radiation. The stainless-steel has the greatest maximum temperature. The

maximum circumferential temperature of stainless steel and aluminium is approximately 10% and 6% higher than the maximum temperature obtained using copper. The temperature gradients of the stainless-steel tube receiver are much greater than those of the aluminium and copper tube receivers. It can be seen that copper has better circumferential temperature distribution than other materials. The circumferential temperature difference (ΔT_c) is 34K, 10K, and 6K for stainless steel, aluminium, and copper respectively.

As can be seen in Figure 13, the temperature increases along the length of the tube from the inlet to the outlet. Due to the non-uniform circumferential heat flux distribution, temperature variation in the z direction is negligible compared to the circumferential direction temperature variation. The temperature profiles increase almost linearly and cannot create any stresses. The stress distributions are fully dependent on the wall temperature.

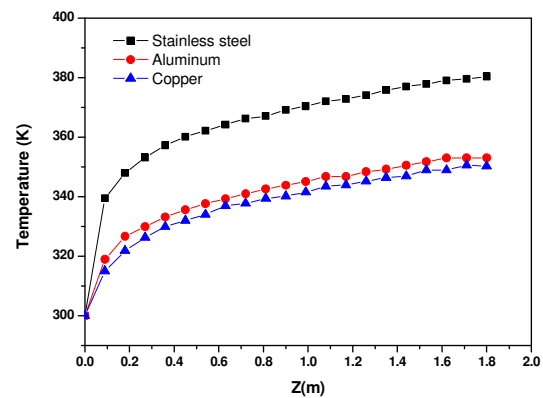


Fig. 13. Axial temperature profiles at the tube inner surface (bottom wall).

B. Thermal Stress Analysis

When the temperature of a continuous body varies in the presence of constraints, thermal stress can arise. In the present study, thermal stress analysis was conducted along the heat transfer fluid's current. The static structural module of ANSYS was used. The thermal stress of the tubes in the thermoelastic model is totally determined by the temperature profiles. The temperature data from the tubes obtained from the thermal model could be used as the boundary conditions in the thermoelastic model's nodes. In addition, the material tube was supposed to be isotropic and elastically deformed under temperature load. The stress levels and distributions are determined by the combined effects of circumferential axial and radial temperature gradients on the PTC receiver tube.

Figure 14 shows the axial stress profiles for the three different materials on the inner surface tube along the length direction at bottom wall. Stainless steel axial compressive stress values are significantly higher than the ones of aluminium and copper. The axial stress values of all materials are close to zero at the inlet and outlet ends, and they increase rapidly to higher values that are close to the profile's peak compressive axial stress values. The temperature profiles along the axial direction at the tube inner surface illustrated in Figure 13 can explain these phenomena. As can be seen from this Figure, the temperature profiles at the tube receiver ends

increase almost linearly along the axial direction, which cannot create any stresses and the stress distributions are fully dependent on the wall temperature. Figure 15 shows the radial stress profiles on the inner surface tube along the axial direction for the different material conditions at bottom wall. The radial stresses act as tensile stress at the tube outlet and inlet ends for all the three material, and then the radial stress values suddenly change to compressive stress. The radial stress values are approximately constant from $z = 0.1$ m to $z = 1.7$ m, which is near to zero. The highest maximum radial stress is 3.2 MPa in stainless steel. The maximum radial stress for aluminium and copper conditions is very small, at about 1.6 MPa and 0.6 MPa, respectively.

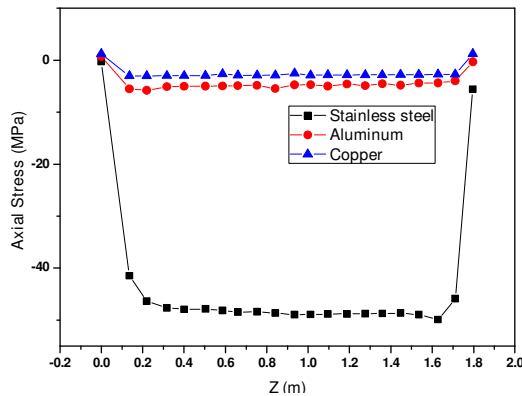


Fig. 14. Axial stress profiles on the inner surface tube along the length direction at bottom wall.

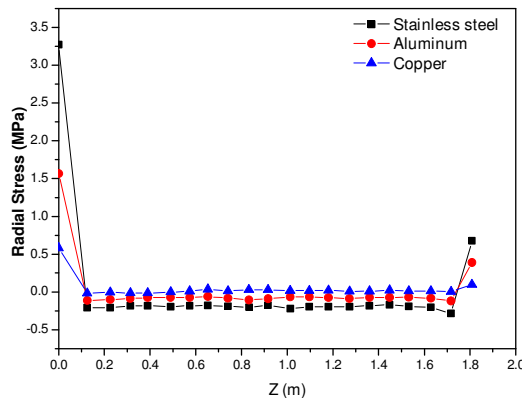


Fig. 15. Radial stress profiles on the inner surface tube at bottom wall.

As can be seen in Figure 16, the circumferential stress of the absorber tube is greatest at a circumference angle of the bottom wall because the temperature there is the highest hence the stress created in this area is the greatest. As the temperature drops, the circumferential stress decreases. The circumferential stress is lower at the top surface of the absorber tube, where the temperature is lower. On the other hand, the temperature difference between the local temperatures of the wall and the fluid influences local heat transfer from the wall, resulting in greater strain at the tube's bottom. Maximum stress is found in stainless steel and the lowest stress in copper.

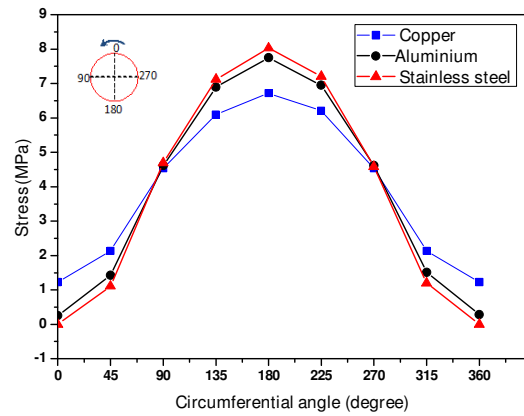


Fig. 16. Circumferential stress distribution of the absorber tube.

C. Effect of the Al_2O_3 Concentration

A numerical simulation with three different volumetric concentrations of Al_2O_3 , equal to 2%, 4%, and 6%, is used to investigate the influence of Al_2O_3 volume fraction on the performance of the solar receiver when the mass flowrate of the HTF is 5g/s. In order to investigate the solar receiver's performance, a non-uniform solar radiation heat flux distribution on the outer wall of the absorber tube is used as a boundary condition. Figures 17 and 18 depict the effects of Al_2O_3 volume fractions on the temperature distributions of the absorber wall with nanoparticle volume fractions ranging from 0% to 6%.

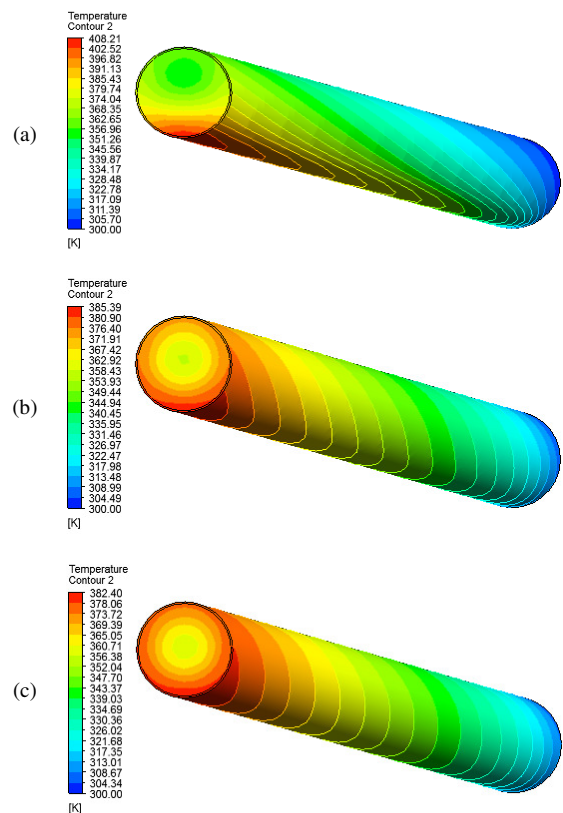


Fig. 17. Temperature distribution vs. nanoparticle concentration ($Re=1300$): (a) $\phi=1\%$, (b) $\phi=2\%$, (c) $\phi=6\%$.

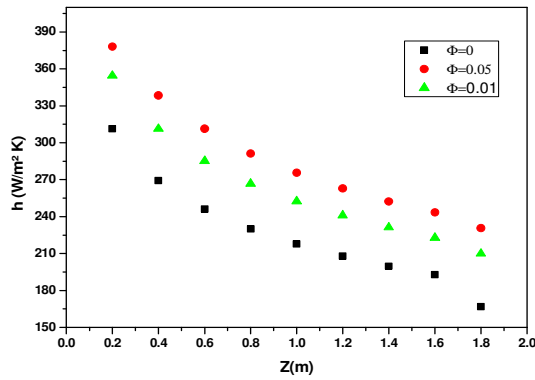


Fig. 18. Average and maximum temperature distribution of the absorber wall under different volume fractions of Al_2O_3 ($\text{Re}=1300$).

According to these findings, the average and maximum temperatures of the absorber tube fall noticeably as the volume fraction increases. As the volume percentages of Al_2O_3 grow from 0% to 6%, the maximum temperature drops from 408.4K to 382K. As a result, the thermal gradients in the absorber tube and the receiver's heat loss are decreased.

Figure 19 shows the axial variation of the local Nusselt number for different volume fractions of Al_2O_3 nanoparticles. From the results, it is clear that the addition of nanoparticles to the base fluid has a direct effect in the field of heat transfer. In these conditions, the Nusselt number of the nanofluid is greater than that of pure water. It increases significantly with an increasing volume concentration of nanoparticles. So, it is confirmed that the suspension of nanoparticles in its base fluid gives a remarkable increase in heat exchange.

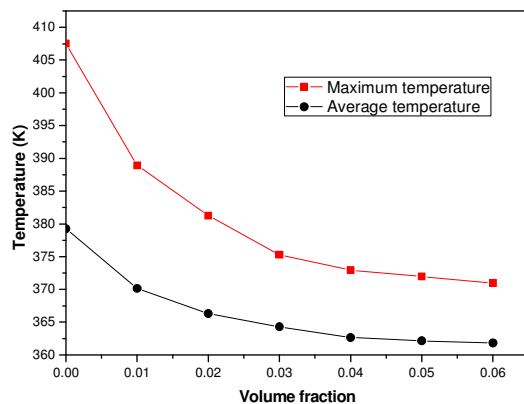


Fig. 19. Variation of local Nusselt number ($\text{Re}=1300$).

Figure 20 illustrates the axial variation of the convection heat transfer coefficients along the axial direction of the absorber tube for $\text{Re}=1300$ and different volume concentrations of nanoparticles. It is obvious that the convection heat transfer coefficient increases as the volume fraction of the nanoparticles increases. The main reason is that when the volume percentage of nanoparticles increases, the thermophysical properties of the fluid improve.

Figure 21 shows the axial temperature variation for different Al_2O_3 nanoparticle volume fraction. It is clear that the growth in the shape of the curves is due to the increase in the

volume fraction of the Al_2O_3 nanoparticles, due to their effective thermal conductivity, which is higher than water's. This generates an increase in the exchange coefficient h and in the temperature values. At outlet ($Z=1.8\text{m}$), the temperature reaches $T=318\text{K}$ for $\phi=6\%$ and $T=310\text{K}$ for $\phi=0\%$.

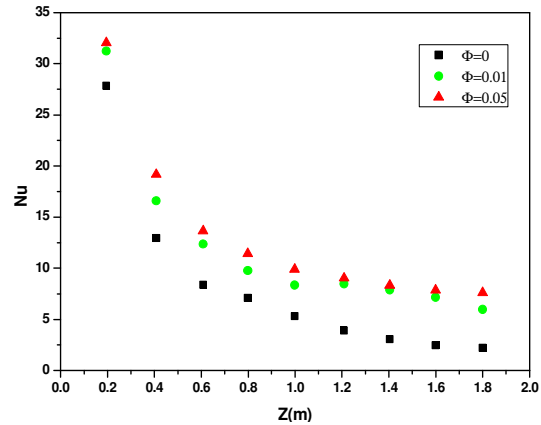


Fig. 20. Variation of the heat transfer coefficients ($\text{Re}=1300$).

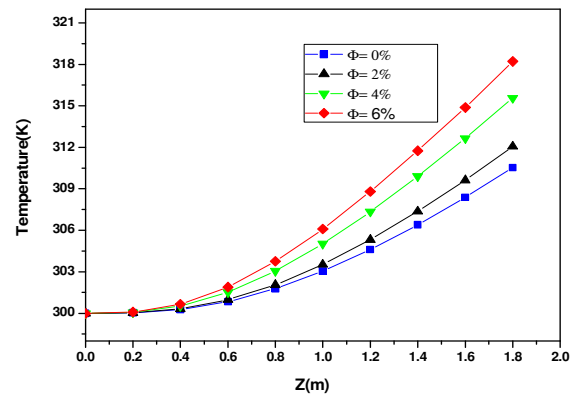


Fig. 21. Axial temperature for different volume fractions of Al_2O_3 .

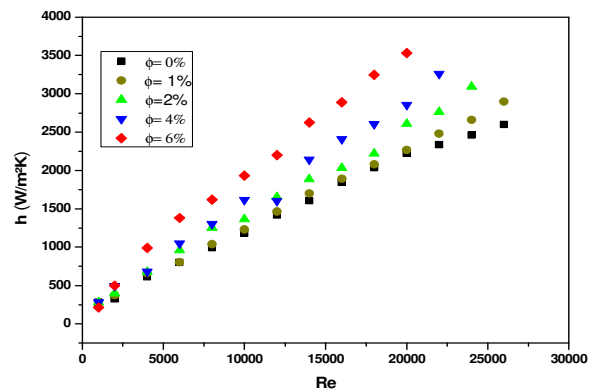


Fig. 22. Heat transfer coefficient vs. nanoparticle volume fraction and Reynolds number for $T_{\text{ini}}=300\text{K}$.

Figure 22 shows the heat transfer coefficient as a function of Re and nanoparticle volume fraction at inlet temperature $T_{\text{ini}}=300\text{K}$. As shown in the Figure, using nanofluids improves heat transfer performance when compared to the base fluid ($\phi=0\%$). It can be seen that the heat transfer coefficient

increases by 48%, 38%, and 33% as the volume fraction increases by 8%, 6%, and 4% respectively, especially at higher Reynolds number values. As a result, the improvement in heat transfer performance must be greater than the increase in pump capacity for the usage of nanofluids to be economically viable.

It is vital to understand pressure drop in order to build the best pump available. The pressure drop is also explored in this work. The pressure drop between the collector's intake and output ports was determined using the simulation data. Figure 23 shows that when the volume fraction grows, the pressure drop increases dramatically, especially at higher Reynolds numbers. When the particle volumetric concentration in the nanofluid increases, the density and viscosity rise, causing an increase in pressure drop. This increases flow resistance and necessitates more pumping power. This causes an increase in flow resistance and needs additional pumping force.

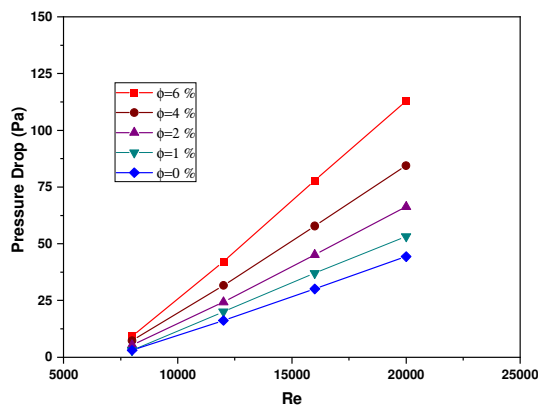


Fig. 23. Pressure drop in the absorber tube vs. nanoparticle volume fraction and Reynolds number.

Figure 24 shows the change in the velocity profile. The profile is tested at axial locations $z = 0, 0.1, 0.6, 1.2, 1.80\text{m}$ and for volume concentrations of 1%, 2%, and 6%. The velocity of the working fluid is constant at the inlet. From this section and beyond the velocity increases, and the profile becomes less flattened. The maximum velocity is not reached at the center, and it is pushed down, due to the fact that the fluid is heated asymmetrically because the solar heat flux distribution is not uniform. There is an angle towards the end of the entering area. An increase in particle volume fraction is, therefore, advantageous in terms of energy utilization. A higher temperature rise of the nanofluid will lead to higher collector thermal efficiency. However, increased particle loading also increases fluid viscosity, which affects pressure drop.

According to Figure 25, the collector's efficiency decreases considerably as the volume fraction increases due to the nanofluid's increased heat conductivity. The thermal efficiency decreases continually as Re increases. Pressure drop increases significantly at much higher Re values, therefore, the increase in pumping power outweighs by far the gain in thermal performance, leading to lower efficiency. It is concluded that for nanoparticle volume fractions ranging from 2 to 6%, thermal efficiency increases by 3 to 14%.

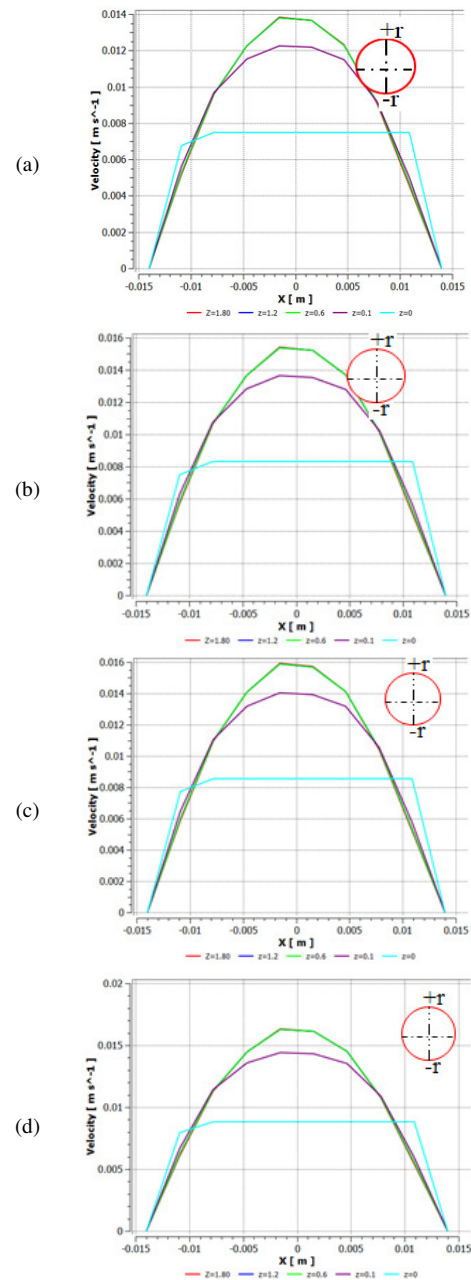


Fig. 24. Velocity profiles for (a) $\phi=6\%$, (b) $\phi=4\%$, (c) $\phi=2\%$, (d) $\phi=0\%$.

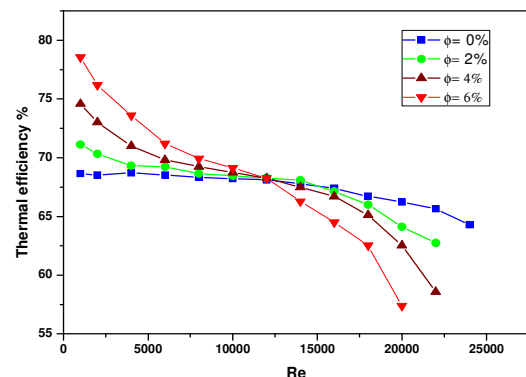


Fig. 25. Thermal efficiency vs. volume fraction and Re for $T_{inl}=300\text{K}$.

XIV. CONCLUSION

In this paper, 3-dimensional numerical simulation of a PTC system under solar NUHF on the outer surface of the absorber tube were used to evaluate the influence of material selection on the thermal and the thermal stresses of tube receivers. Moreover, the use of Al_2O_3 /water nanofluid as HTF was proposed to improve the performances of the PTC system. This study is a preliminary overview of the key parameters which promote the optimization of the absorber tube by homogenizing heat flux distribution, reducing peak temperature and decreasing the temperature gradient to reduce thermal stresses, which are generated by the high temperature gradients. Three materials (copper, stainless steel, and aluminum) and nanoparticles of Al_2O_3 with concentration ratios ranging from 0% to 6 % were used. The results confirmed that:

- Receiver tube material selection is critical for ensuring reliability. The temperature gradients with stainless steel are much higher than those with aluminum and copper gradients, which can cause higher thermal stresses and reduces durability of the absorber tube.
- The maximum circumferential temperature of stainless steel and aluminium is approximately 10% and 6% higher than the maximum temperature obtained using copper. The temperature gradient of the stainless-steel tube receivers is much greater than those of the aluminum and copper tube receivers. Copper has a better circumferential temperature distribution than the other materials. For stainless steel, aluminium, and copper, the circumferential temperature difference (ΔT) is 34K, 10K, and 6K respectively. Copper is the recommended material as the receiver tube material from the point of view of thermal stress.
- The temperature gradient and the maximum temperature in the absorber are greatly reduced by using Al_2O_3 /water as HTF. The temperature gradient and the maximum temperature in the absorber decrease with the Al_2O_3 particle concentration.
- Increase in nanoparticle volume fraction by 1%, 2%, and 6% increases the average of output temperatures by 2%, 6%, and 10% respectively.
- Heat transfer coefficient increases by 48%, 38% and 33% as the volume fraction increases to 8%, 6%, and 4% respectively, especially at higher Reynolds numbers. The study concluded that for nanoparticle volume fractions ranging from 2% to 6%, thermal efficiency increases by 3% to-14%.

In future work, the study will be focused towards the effect of other receiver tube material and the results will be used for the design and manufacturing of a more efficient parabolic trough solar receiver.

REFERENCES

- [1] N. B. Khedher, "Experimental Evaluation of a Flat Plate Solar Collector Under Hail City Climate," *Engineering, Technology & Applied Science Research*, vol. 8, no. 2, pp. 2750–2754, Apr. 2018, <https://doi.org/10.48084/etasr.1957>.
- [2] R. Almanza, A. Lentz, and G. Jimenez, "Receiver behavior in direct steam generation with parabolic troughs," *Solar Energy*, vol. 61, no. 4, pp. 275–278, Oct. 1997, [https://doi.org/10.1016/S0038-092X\(97\)88854-8](https://doi.org/10.1016/S0038-092X(97)88854-8).
- [3] H. Price *et al.*, "Advances in Parabolic Trough Solar Power Technology," *Journal of Solar Energy Engineering*, vol. 124, no. 2, pp. 109–125, Apr. 2002, <https://doi.org/10.1115/1.1467922>.
- [4] M. A. Irfan and W. Chapman, "Thermal stresses in radiant tubes due to axial, circumferential and radial temperature distributions," *Applied Thermal Engineering*, vol. 29, no. 10, pp. 1913–1920, Jul. 2009, <https://doi.org/10.1016/j.applthermaleng.2008.08.021>.
- [5] P. Wang, D. Y. Liu, and C. Xu, "Numerical study of heat transfer enhancement in the receiver tube of direct steam generation with parabolic trough by inserting metal foams," *Applied Energy*, vol. 102, pp. 449–460, Feb. 2013, <https://doi.org/10.1016/j.apenergy.2012.07.026>.
- [6] Y.-L. He, K. Wang, Y. Qiu, B.-C. Du, Q. Liang, and S. Du, "Review of the solar flux distribution in concentrated solar power: Non-uniform features, challenges, and solutions," *Applied Thermal Engineering*, vol. 149, pp. 448–474, Feb. 2019, <https://doi.org/10.1016/j.applthermaleng.2018.12.006>.
- [7] S. Khanna, V. Sharma, S. Singh, and S. B. Kedare, "Explicit expression for temperature distribution of receiver of parabolic trough concentrator considering bimetallic absorber tube," *Applied Thermal Engineering*, vol. 103, pp. 323–332, Jun. 2016, <https://doi.org/10.1016/j.applthermaleng.2016.04.110>.
- [8] W. Fuqiang, T. Zhexiang, G. Xiangtao, T. Jianyu, H. Huaizhi, and L. Bingxi, "Heat transfer performance enhancement and thermal strain restrain of tube receiver for parabolic trough solar collector by using asymmetric outward convex corrugated tube," *Energy*, vol. 114, pp. 275–292, Nov. 2016, <https://doi.org/10.1016/j.energy.2016.08.013>.
- [9] Y. Aldali, T. Muneer, and D. Henderson, "Solar absorber tube analysis: thermal simulation using CFD," *International Journal of Low-Carbon Technologies*, vol. 8, no. 1, pp. 14–19, Mar. 2013, <https://doi.org/10.1093/ijlct/ctr039>.
- [10] M. R. Haddouche and A. Benazza, "Numerical Investigation and Solar Flux Distribution Analysis of Parabolic Trough Solar Collector by Adding Secondary Reflector," *Instrumentation Measure Metrologie*, vol. 18, pp. 275–280, Aug. 2019, <https://doi.org/10.18280/im.180307>.
- [11] C.-Y. Tsai and P. D. Lin, "Optimized variable-focus-parabolic-trough reflector for solar thermal concentrator system," *Solar Energy*, vol. 86, no. 5, pp. 1164–1172, May 2012, <https://doi.org/10.1016/j.solener.2012.01.009>.
- [12] E. Bellos and C. Tzivanidis, "Investigation of a booster secondary reflector for a parabolic trough solar collector," *Solar Energy*, vol. 179, pp. 174–185, Feb. 2019, <https://doi.org/10.1016/j.solener.2018.12.071>.
- [13] Z. Wu, S. Li, G. Yuan, D. Lei, and Z. Wang, "Three-dimensional numerical study of heat transfer characteristics of parabolic trough receiver," *Applied Energy*, vol. 113, pp. 902–911, Jan. 2014, <https://doi.org/10.1016/j.apenergy.2013.07.050>.
- [14] R. Senthil, C. Rath, and M. Gupta, "Enhancement of uniform temperature distribution on the concentrated solar receiver with integrated phase change material," *International Journal of Mechanical Engineering and Technology*, vol. 8, no. 9, pp. 315–320, Sep. 2017.
- [15] D. Guerraiche, C. Bougriou, K. Guerraiche, L. Valenzuela, and Z. Driss, "Experimental and numerical study of a solar collector using phase change material as heat storage," *Journal of Energy Storage*, vol. 27, Feb. 2020, Art. no. 101133, <https://doi.org/10.1016/j.est.2019.101133>.
- [16] P. Liu, Z. Dong, H. Xiao, Z. Liu, and W. Liu, "Thermal-hydraulic performance analysis of a novel parabolic trough receiver with double tube for solar cascade heat collection," *Energy*, vol. 219, Mar. 2021, Art. no. 119566, <https://doi.org/10.1016/j.energy.2020.119566>.
- [17] M. Keshavarz Moraveji and S. Razvarz, "Experimental investigation of aluminum oxide nanofluid on heat pipe thermal performance," *International Communications in Heat and Mass Transfer*, vol. 39, no. 9, pp. 1444–1448, Nov. 2012, <https://doi.org/10.1016/j.icheatmass.2012.07.024>.
- [18] N. Abed, I. Afgan, H. Iacovides, A. Cioncolini, I. Khurshid, and A. Nasser, "Thermal-Hydraulic Analysis of Parabolic Trough Collectors

- Using Straight Conical Strip Inserts with Nanofluids," *Nanomaterials*, vol. 11, no. 4, Apr. 2021, Art. no. 853, <https://doi.org/10.3390/nano11040853>.
- [19] H. A. Fakhim, "An Investigation of the Effect of Different Nanofluids in a Solar Collector," *Engineering, Technology & Applied Science Research*, vol. 7, no. 4, pp. 1741–1745, Aug. 2017, <https://doi.org/10.48084/etasr.1283>.
- [20] H. B. Lanjwani, M. S. Chandio, K. Malik, and M. M. Shaikh, "Stability Analysis of Boundary Layer Flow and Heat Transfer of Fe₂O₃ and Fe-Water Base Nanofluid over a Stretching/Shrinking Sheet with Radiation Effect," *Engineering, Technology & Applied Science Research*, vol. 12, no. 1, pp. 8114–8122, Feb. 2022, <https://doi.org/10.48084/etasr.4649>.
- [21] K. Boukerma and M. Kadja, "Convective Heat Transfer of Al₂O₃ and CuO Nanofluids Using Various Mixtures of Water-Ethylene Glycol as Base Fluids," *Engineering, Technology & Applied Science Research*, vol. 7, no. 2, pp. 1496–1503, Apr. 2017, <https://doi.org/10.48084/etasr.1051>.
- [22] T. P. Otanicar, P. E. Phelan, R. S. Prasher, G. Rosengarten, and R. A. Taylor, "Nanofluid-based direct absorption solar collector," *Journal of Renewable and Sustainable Energy*, vol. 2, no. 3, May 2010, Art. no. 033102, <https://doi.org/10.1063/1.3429737>.
- [23] S. Hassani, R. Saidur, S. Mekhilef, and A. Hepbasli, "A new correlation for predicting the thermal conductivity of nanofluids; using dimensional analysis," *International Journal of Heat and Mass Transfer*, vol. 90, pp. 121–130, Nov. 2015, <https://doi.org/10.1016/j.ijheatmasstransfer.2015.06.040>.
- [24] V. Verma and L. Kundan, "Thermal Performance Evaluation of a Direct Absorption Flat Plate Solar Collector (DASC) using Al₂O₃-H₂O Based Nanofluids," *IOSR Journal of Mechanical and Civil Engineering*, vol. 6, no. 2, pp. 29–35, 2013.
- [25] D. R. Waghole, R. M. Warkhedkar, V. S. Kulkarni, and R. K. Shrivastva, "Experimental Investigations on Heat Transfer and Friction Factor of Silver Nanofluid in Absorber/Receiver of Parabolic Trough Collector with Twisted Tape Inserts," *Energy Procedia*, vol. 45, pp. 558–567, Jan. 2014, <https://doi.org/10.1016/j.egypro.2014.01.060>.
- [26] R. A. Taylor *et al.*, "Applicability of nanofluids in high flux solar collectors," *Journal of Renewable and Sustainable Energy*, vol. 3, no. 2, Mar. 2011, Art. no. 023104, <https://doi.org/10.1063/1.3571565>.
- [27] T. Sokhansefat, A. B. Kasaeian, and F. Kowsary, "Heat transfer enhancement in parabolic trough collector tube using Al₂O₃/synthetic oil nanofluid," *Renewable and Sustainable Energy Reviews*, vol. 33, pp. 636–644, May 2014, <https://doi.org/10.1016/j.rser.2014.02.028>.
- [28] T. Yousefi, F. Veysi, E. Shojaeizadeh, and S. Zinadini, "An experimental investigation on the effect of Al₂O₃-H₂O nanofluid on the efficiency of flat-plate solar collectors," *Renewable Energy*, vol. 39, no. 1, pp. 293–298, Mar. 2012, <https://doi.org/10.1016/j.renene.2011.08.056>.
- [29] M. Mahmoodi and S. M. Hashemi, "Numerical study of natural convection of a nanofluid in C-shaped enclosures," *International Journal of Thermal Sciences*, vol. 55, pp. 76–89, May 2012, <https://doi.org/10.1016/j.ijthermalsci.2012.01.002>.
- [30] R. Forristall, "Heat Transfer Analysis and Modeling of a Parabolic Trough Solar Receiver Implemented in Engineering Equation Solver," National Renewable Energy Lab, Golden, CO, United States, NREL/TP-550-34169, Oct. 2003. <https://doi.org/10.2172/15004820>.
- [31] Y. Wang, Q. Liu, J. Lei, and H. Jin, "Performance analysis of a parabolic trough solar collector with non-uniform solar flux conditions," *International Journal of Heat and Mass Transfer*, vol. 82, pp. 236–249, Mar. 2015, <https://doi.org/10.1016/j.ijheatmasstransfer.2014.11.055>.
- [32] S. El Becaye Maiga, C. Tam Nguyen, N. Galanis, G. Roy, T. Mare, and M. Coqueux, "Heat transfer enhancement in turbulent tube flow using Al₂O₃ nanoparticle suspension," *International Journal of Numerical Methods for Heat & Fluid Flow*, vol. 16, no. 3, pp. 275–292, Jan. 2006, <https://doi.org/10.1108/09615530610649717>.
- [33] R. Ekciler, K. Arslan, O. Turgut, and B. Kursun, "Effect of hybrid nanofluid on heat transfer performance of parabolic trough solar collector receiver," *Journal of Thermal Analysis and Calorimetry*, vol. 143, no. 2, pp. 1637–1654, Jan. 2021, <https://doi.org/10.1007/s10973-020-09717-5>.
- [34] K. Wang, Y. He, and Z. Cheng, "A design method and numerical study for a new type parabolic trough solar collector with uniform solar flux distribution," *Science China Technological Sciences*, vol. 57, no. 3, pp. 531–540, Mar. 2014, <https://doi.org/10.1007/s11431-013-5452-6>.
- [35] M. S. Bretado de los Rios, C. I. Rivera-Solorio, and A. J. Garcia-Cuellar, "Thermal performance of a parabolic trough linear collector using Al₂O₃/H₂O nanofluids," *Renewable Energy*, vol. 122, pp. 665–673, Jul. 2018, <https://doi.org/10.1016/j.renene.2018.01.094>.
- [36] A. Mwesigye, T. Bello-Ochende, and J. P. Meyer, "Heat transfer and thermodynamic performance of a parabolic trough receiver with centrally placed perforated plate inserts," *Applied Energy*, vol. 136, pp. 989–1003, Dec. 2014, <https://doi.org/10.1016/j.apenergy.2014.03.037>.
- [37] V. Gnielinski, "On heat transfer in tubes," *International Journal of Heat and Mass Transfer*, vol. 63, pp. 134–140, Aug. 2013, <https://doi.org/10.1016/j.ijheatmasstransfer.2013.04.015>.
- [38] E. Esmaeilzadeh, H. Almohammadi, Sh. Nasiri Vatan, and A. N. Omrani, "Experimental investigation of hydrodynamics and heat transfer characteristics of γ -Al₂O₃/water under laminar flow inside a horizontal tube," *International Journal of Thermal Sciences*, vol. 63, pp. 31–37, Jan. 2013, <https://doi.org/10.1016/j.ijthermalsci.2012.07.001>.

Statistical Analysis of Component Deviation from Job Mix Formula in Hot Mix Asphalt

Saba S. Almasoudi

Department of Civil Engineering
College of Engineering
University of Baghdad

s.khudair1901m@coeng.uobaghdad.edu.iq

Amjad Hamad Khalil Albayati

Department of Civil Engineering
College of Engineering
University of Baghdad

a.khalil@uobaghdad.edu.iq

Received: 26 July 2022 | Accepted: 3 August 2022

Abstract—The main objective of this research is to find out the effect of deviation in the aggregate gradients of asphalt mixtures from the Job Mix Formula (JMF) on the general mixture performance. Three road layers were worked on (wearing layer, binder layer, and base layer) and statistical analysis was performed for the data of completed projects in Baghdad city and the sieve that carried the largest number of deviations for each layer was identified. No.8 sieve (2.36mm), No.50 sieve (0.3mm), and 3/8" sieve (9.5mm) had the largest number of deviations in the wearing layer, the binder layer, and the base layer respectively. After that, a mixture called Mix 1, was made. This mixture was selected from a number of completed mixtures, and it represents the worst mixture. Mix 1 was compared with two other mixtures, Mix 2 and Mix 3, Mix 2 representing the middle of JMF for the gradients of aggregates, and Mix 3 is the same as Mix 1 except for the sieve that contains the largest number of deviations, so the gradient of aggregates for it is the middle of JMF. Fifteen Marshall specimens were made for each mixture and for each layer in order to know the differences in Marshall properties between the mixtures. Also, 6 specimens were made for each mixture (the total is 18 specimens for each layer) to check the indirect tensile strength, for the purpose of knowing mixtures susceptibility to moisture. Finally, 1 specimen was made for each mixture for repeated load test for the purpose of knowing the performance of the mixtures with respect to permanent deformation. The tests showed that the performance of Mix 2 and Mix 3 was improved in comparison with Mix 1. The deviation of the aggregate gradients in specific sieves may be higher than the limits of the JMF or it may be less, and in both cases, the implementation of a mixture like Mix 1 for the streets is bad for the performance of the road and failures occur due to the wrong implementation of the JMF. On the other hand, there are much better mixtures in all respects such as Mix 2 and Mix 3, and if they are implemented on the streets, they will certainly have much better.

Keywords—hot mix asphalt; JMF; deviation; aggregate gradations

I. INTRODUCTION

Road construction industry faces the challenge of designing and constructing high-performance asphalt materials to meet the ever-growing demand of increasing traffic volumes and axle loadings. Quality control over the production of hot

asphalt compounds is a significant issue. When the asphalt components are manufactured to have high performance under weather and road conditions, this increases asphalt pavement life and consequently reduces additional maintenance and rehabilitation costs.

One of the most important issues that affect pavement design is the occurrence of defects. The reasons for these defects may be the quality of the used materials, laboratory equipment, unqualified staff, the lack and delay of necessary maintenance after the implementation of the pavement, wrong construction, or a flaw or wrong execution of the JMF resulting in aggregate gradients that do not conform to JMF contain deviations. Generally, the deviations in aggregate gradations are not accidental, but are caused by external factors [1]. The method to verify that the produced mix complies with the project specifications is the JMF or dense gradation mix submittal. A successful mix design should meet the suggested proportion of aggregates and asphalt binder. This suggested mixture also includes the type of asphalt binder, the aggregate gradation, and the permissible specification bands for inherent material and production variability. The mix designer is free to select a specific JMF gradation, and the manufacturer is expected to produce the mix according to this JMF gradation closely [2]. The Iraqi standard specifications for roads and bridges, SCRB R/9 2003, allowed some tolerances in JMF with regard to the following properties: coarse aggregate gradients, fine aggregate gradients, filler content, asphalt concrete content, and mixing temperature (Table I) [3]. The characteristics of the asphalt mixture's components have a significant and obvious impact on the performance of the pavement, especially the aggregates that make up a significant portion of the asphalt mixture. Aggregates are the largest and most important volumetric component of the asphalt mixture and its performance and are the basis of the homogeneous and solid texture of the asphalt mixture.

In addition to serving as the base for the design of asphalt mixtures, aggregates play a significant role in determining the quality of the road, the loads applied on it, and the nature of road layers. The type and viscosity of the asphalt used are impacted by the gradient of the aggregates and internal friction. The fundamental concept of choosing the aggregate quality and

size is to get the highest consistency and homogeneity of the asphalt mixture, creating the perfect layer to receive and distribute the load of wheels and vehicles on the sub base without failures [4-6].

TABLE I. ALLOWED TOLERANCES FROM JMF [3]

Sieve size	Tolerance
Aggregate materials passing through sieve 4.75mm (No.4) or larger	±6%
Aggregate materials passing through sieve 2.36mm (No.8) to sieve 0.3mm (No.50)	±4%
Filler passing through sieve 0.075mm (No.200)	±1.5%
Asphalt	±0.3%
Mixing temperature	±15°C

Aggregate gradation, which is measured by sieve analysis, is the distribution of aggregate particle size. While aggregates of varying size made the mixture have fewer voids, the aggregates that have no variety in sizes make the compacted mass to have more voids due to the uniformity of the particles. Aggregate gradation significantly affects Hot Mix Asphalt (HMA) properties. The component content in the HMA mixture has been shown to have an impact on the mixture's structure and properties, which in turn affects the dependability and durability of the pavement [7]. It is concluded that the deviations related to the gradient of the asphalt mixture aggregates are considered to be effective and common deviations, which requires taking appropriate procedures to avoid these failures, including doing the correct JMF in a manner appropriate to the use of the intended layer in addition to the use of materials that successfully pass laboratory testing and ensure the correct implementation of the required thickness and compaction, thus, improving the quality and performance of the implemented road in a way that meets its purpose [8].

In order to find some performance requirements, designers are interested in aggregate gradation. For good permanent deformation resistance, Superpave defines the "Restricted Zone" within the gradation of aggregates and recommends that the limited area should not be violated. Depending on the nominal maximum particle size, the restricted zone is between the mid-size particles (4.75 or 2.36mm), and the 0.3mm at the maximum dense line [9-11]. Aggregate gradation determines how well an asphalt pavement performs. Any changes in aggregate gradation cause changes in many factors, such as directions and contact points, which in turn affect the performance of asphalt pavements [12]. Authors in [13] showed the use of 4 different aggregate gradations and the wheel tracking test showed that they were superior to fine aggregates regarding permanent deformation. Authors in [14] showed that aggregate gradation was a significant factor of the perfect mixture. With three grades and various percentages, they produced a hot and a warm mix of asphalt from a single source. The test results showed that the aggregate gradations had a variety of effects on the introduced mixtures' rutting resistance, particularly their sensitivity to moisture. Authors in [15] examined the way aggregate gradation affects the different characteristics of asphalt concrete mixtures. The effects of different aggregate types and gradations on the mixing properties have been investigated for blends with fine, medium, and coarse aggregate gradations. The mixtures' asphalt content

remained constant at the job mix design content. They looked at the properties of Marshall stability, Marshall flow, unit weight, air voids, and mineral aggregates. Analysis of the different aggregate types made clear that the fine-coarse and coarse-fine variations had the greatest impact on the mix. Authors in [16] estimated the effect of asphalt and aggregate gradation type on HMA found in asphalt concrete mixtures. Additionally, the effect of the aggregate characteristics on the Marshall mix properties was investigated. Finally, an estimation of the relationship between rutting potential and HMA mixing was made. The study showed that characteristic mineral aggregates had a significant influence on the construction of local highways, giving the possibility to develop resistance to various externally applied loads and environmental conditions. Furthermore, it illustrated how aggregate properties have a long-term impact on the way hot-mix asphalt is deformed.

Many studies have been conducted to identify the effect of aggregate gradation on moisture susceptibility and permanent deformation of HMA. Rutting has recently taken over as the main mode of flexible pavement failure as a result of increased truck tire pressure and the lack of maintenance [17]. Rutting is mainly brought on by the accumulation of permanent deformations in the pavement or its layers. Heavy axle loads and high tire pressure contribute significantly to rutting in the flexible pavement surface layer. High tire pressure increases stress and reduces the area of contact between the tire and the pavement, which aggravates deformation in flexible pavements. Additionally, the pavements' top layer is significantly impacted by environmental conditions [18]. The asphalt mixtures used in road construction must be resistant to cracking and permanent deformations. They are composed of voids, aggregates, and binder. To obtain relevant properties that affect the way the asphalt behaves, appropriate materials must first be chosen in advance, and their proportions in the asphalt mixture must be determined. It's essential to know how asphalt mixtures are built in, in addition to how they are produced [6]. It is widely accepted that coarser gradation results in an HMA mixture that is more rut resistant. However, some studies have discovered that mixtures with finer gradations have lower rut potential [19]. Authors in [20] observed that, a significant contributing factor to the asphalt binder film's loss of adhesion may be the fine aggregates. They also noted that the presence of crushed sand may reduce moisture damage and that maximum aggregate size and mixture gradation have a significant impact on rutting resistance.

II. DATA USED AND MOST COMMON DEVIATIONS

For the purpose of knowing the sieve that carries the largest number of deviations in the aggregate gradients (the most frequent) and for the three considered layers (wearing, binder, and base layer) a data set was acquired from road projects implemented in Baghdad governorate. The data were randomly selected. Data were taken from 140 wearing layer specimens, 33 binder layer specimens, and 30 base layer specimens. The percentage of passing through each sieve can be easily plotted for each sieve and the conclusion is that the largest number of deviations in the aggregate gradients from JMF of wearing layer were sieve No.8 (2.36mm) for the wearing layer, No.50

(0.3mm) for the binder layer, and sieve 3/8" (9.5mm) for the base layer.

III. SELECTION OF AGGREGATE GRADATIONS

The sieve that has the largest number of deviations in aggregate gradations was determined for each considered layer. Figures 1-3 show the aggregate gradients for the worst implemented chosen mixture, and the amount of its deviation from Iraqi specification for roads and bridges (SCRB) and JMF. This mixture was called Mix 1. The performance of this mixture (Mix 1) was compared with mixtures without or less errors and deviations, in order to determine how bad these mixtures are being implemented. Another mixture, called Mix 2, was made. Its aggregate gradients represent the midpoint of the JMF for Mix 1. A third mixture, called Mix 3, was prepared with the same gradations of aggregates as Mix1, except for the sieve containing the largest number of deviations (the sieve that deviates from the JMF). So we have:

- Mix 1: as it is.
- Mix 2: mean of JMF.
- Mix 3: as it is, mid for deviated sieve.

The above were implemented on all layers (wearing, binder and base). Figures 1-3 show the gradations of aggregates for each mixture and for each layer.

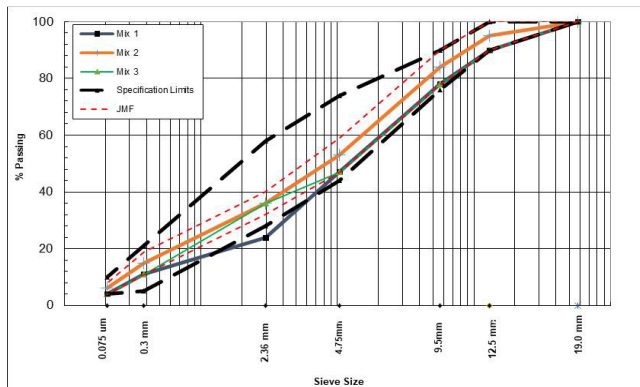


Fig. 1. Wearing layer aggregate gradients.

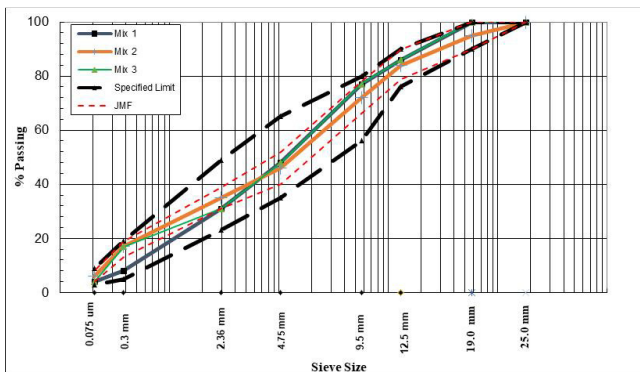


Fig. 2. Binder layer aggregate gradients.

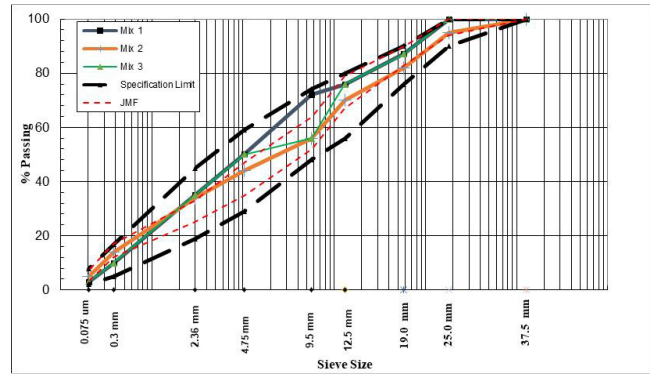


Fig. 3. Base layer aggregate gradients.

IV. MATERIAL CHARACTERIZATION

A. Aggregates

Crushed quartz was used as aggregates in this research. In the city of Baghdad, this aggregate type is frequently used in asphalt mixtures. Routine tests were performed on the aggregates to assess their physical characteristics. Table II provides a summary of the results along with the specification limits established by the SCR. The test results indicate that the selected aggregates meet the SCR specifications.

TABLE II. PHYSICAL PROPERTIES OF AGGREGATES

Property	Coarse aggregates	Fine aggregates	SCR
Bulk specific gravity (ASTMC127 and C128)	2.646	2.63
Apparent specific gravity (ASTMC127 and C128)	2.656	2.667
Percent water absorption (ASTM C127 and C128)	0.14	0.523
Percent wear (Los-Angeles Abrasion) (ASTM C131)	19.69		30 Max
Fractured pieces (%)	98		90 min
Sand Equivalent(ASTM D 2419)		55	45 min Superpave (SP-2)
Soundness loss by sodium sulfate solution, %(C-88)	3.4		12 Max

TABLE III. PHYSICAL PROPERTIES OF AC 40/50

Tests	Unit	40/50 AC specification	SCR specification
Penetration at 25°C, 100gm, 5sec (ASTM-D5)	0.1mm	45	40-50
Softening point R&B (ASTM-D36)	°C	48
Specific gravity at 25°C (ASTM-D70)	1.04
Flash point (ASTM-D92)	°C	290	Min. 232
Ductility (ASTM-D113)	cm	132	Min. 100
Residue from thin film oven test (ASTM-D1754)			
Retained penetration ,% of original (ASTM-D5)	0.1mm	59	Min. 55
Ductility at 25°C, 5cm/min, (ASTM-D113)	cm	90	Min. 25

B. Asphalt Cement

The penetration grade (40/50) of asphalt cement, which is frequently used in paving construction projects in Iraq, was considered in this study. For the purpose of determining the fundamental physical characteristics of asphalt cement, a number of ASTM tests were carried out. The asphalt cement used in this study complies with the necessary (SCR/R9 2003 Revision) specification, as shown in Table III.

C. Filler

The filler is a non-plastic material passing through sieve No.200 (0.075mm). The filler used in this work is limestone dust. Its physical properties are presented in Table IV.

TABLE IV. PHYSICAL PROPERTIES OF MINERAL FILLER.

Property	Test result
Specific gravity	2.78
Passing sieve No.200 (0.075mm)	85

V. SPECIMEN PREPARATION AND TESTING PROCEDURE

To evaluate the performance of the three mixtures, three types of tests were performed, the Marshall test (ASTM D6926-2010a) in order to obtain the optimum asphalt content, density, stability, flow, and other properties, indirect tensile strength test (ASTM- D-4867-96) in order to evaluate the moisture sensitivity of the mixes, and finally the repeated load test for permanent deformation evaluation.

A. Marshall Test

In Marshall design there are two kinds of test: stability-flow tests and density voids tests. The Marshall method (ASTM D6927) is used to determine the optimum asphalt content of the HMA pavement. For the purpose of calculating the optimum asphalt content, 5 different percentage values 4, 4.3, 4.6, 4.9 and 5.2%, were used for asphalt cement (binder course), while 3.4, 3.7, 4, 4.3, and 4.6% were used for base course, and 4.3, 4.6, 4.9, 5.2, and 5.5% were used for the wearing course. Three specimens were prepared for each ratio. Therefore, 15 specimens were prepared for each mix, i.e. 45 specimens for each layer (to a total of 135 specimens for the three layers). The aggregate gradations for all mixtures (Mix 1, Mix 2, Mix 3) and for all layers were as explained above and the Marshall specimens were made after the calculation of the optimum asphalt content for each mixture. The Marshall test steps have been performed.

B. Indirect Tensile Strength Test

To assess the moisture sensitivity of mixes, Indirect Tensile Tests (ITSs), according to ASTM- D-4867-96 were performed for each mix: two subsets, 3 specimens each were compacted with blow range between 30 to 50 for wearing course, binder course, and base course. So, 6 specimens were prepared for each mixture and for each layer, to a total of 54 specimens. The first subset was tested in a dry condition (soaked in water for 2hr at 25°C). The second subset was tested in wet condition, i.e. it was inundated for 24hr at 60°C followed by 25°C for 2hr in water bath. The Marshall device applies a compressive load to a cylindrical specimen through two diametrically opposed rigid strips consisting of 10×10mm (0.39×0.39in) rectangular

steel bars of 102mm (4in) diameter specimens to induce tensile stress along the diametric vertical axis of the test specimen. A series of splitting tensile strength tests were conducted at a constant strain rate of 2in/min vertically until vertical cracks appeared and the sample failed. The peak compressive load was recorded and used to calculate the tensile strength of the specimen using (1):

$$S_t = 2 P_u / \pi t D \quad (1)$$

where S_t is the tensile strength (Psi), P_u is the max. load (lb), t is specimen's height immediately before tensile test (in), and D is specimen's diameter (in.).

The Tensile Strength Ratio (TSR, %) was calculated by:

$$TSR = (S_{tm} / S_{td}) \times 100 \quad (2)$$

where S_{tm} is the average tensile strength of the moisture conditioned subset (Psi) and S_{td} is the average tensile strength of the dry subset (Psi).

C. Repeated Load Test

A total of 9 cylindrical specimens (1 specimen for each mix for the 3 layers) were fabricated to investigate the effect of deviation in the gradation of aggregates on permanent deformation of asphalt concrete mixture at 40°C. The cylindrical specimens produced for this study had initial dimensions of 101.6mm (4in) diameter × 152.4mm (6in) height. The tests were performed at single stress level of 20Psi (138kPa). Repeated compressive loading for 10,000 repetitions was conducted with a loading cycle of 60 cycles per minute in duration and consisting of a 0.1s load period followed by a 0.9s rest period (the 0.1s load duration was selected in order to simulate the loading of truck moving at the highway with a speed of 50km/hr). This test was applied to determine the permanent deformation characteristics of paving materials. Permanent axial deformation was recorded throughout the test using Linear Variable Differential Transducer (LVDT) to measure the deformation in the upper face of the sample via a data acquisition system. A Pneumatic Repeated Load System (PRLS) apparatus manufactured under the auspices of University of Baghdad's Civil Engineering Department was used to calculate the permanent strain values [21]. The values of the permanent strain were obtained at 1, 2, 10, 100, 500, 1000, 2000, 3000, 4000, 5000, 6000, 7000, 8000, 9000, and 10000 load repetitions. The permanent strain (ϵ_p) was calculated by:

$$\epsilon_p = \frac{P_d \times 10^6}{h} \quad (3)$$

where ϵ_p is the axial permanent microstrain, P_d is the axial permanent deformation, and h is the specimen's height.

Authors in [22, 23] suggested a log-log relationship between ϵ_p and N , as in (4):

$$\epsilon_p = a N^b \quad (4)$$

where N is the number of load repetitions, and a and b are positive regression constants. As depicted in Figure 4, the parameter a is the intercept with the permanent strain axis, and b is the slope of the linear portion of the logarithmic relationship.

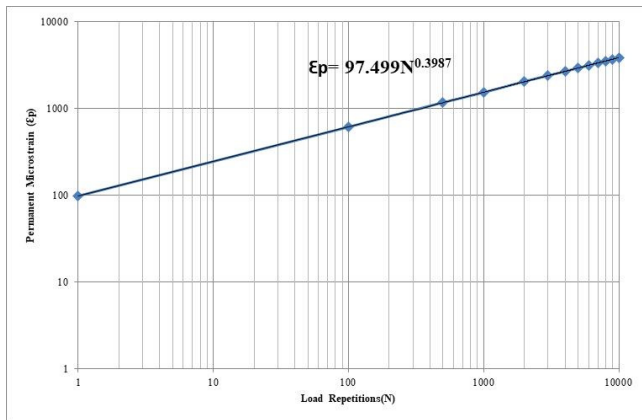


Fig. 4. Log-log relationship between permanent microstrain and number of load repetitions.

VI. RESULTS AND DISCUSSION

As mentioned above, Mix 1 is the mixture that has already been implemented in some of the streets of the city of Baghdad. This mixture shows some deviations in the gradients of the aggregates from the mixing equation and for the 3 layers of the road. These deviations surely did not occur intentionally, but due to defects in the JMF specified for each project, implementation errors, or errors of weighing and determining the exact amount of aggregate required for each sieve and for each mixture. Some of these deviations were beyond the upper limits of the mixing equation and even exceeded the amount of tolerance specified according to the SCRB. On the other hand, some of the deviations were less than the minimum limit of the mixing equation. Both cases can cause defects in the mixture.

The occurrence of defects in the aggregate gradients prescribed for a particular road, means an increase or decrease of fine or coarse materials in the mixture, leading to problems in the mixture and weakened performance of the road, making it prone to failures. This was made clear from the test results. To clarify the difference between the performance of the 3 mixtures, the results of each test and for each layer, will be discussed.

For the wearing course, the deviated sieve is sieve No. 8 (2.36mm). For Mix 1, the passing percentage of aggregates for this sieve is 24%, which is outside the lower limit of JMF (it is even outside the tolerance limit ± 4) and is also less than the lower limit of Iraqi standard specifications, which is 28%.

For binder course, in Mix 1, the value of the aggregates that passed through the sieve No. 50 is 8%, which is less than the lower limit of the JMF and its tolerance limit, but within the limits of the Iraqi specification, as the percentage of passing through sieve No. 50 of binder course according to it must be within 5-19%.

For base course, in Mix 1, the transit ratio of aggregates to a 3/8" sieve was 72%, which is outside the upper limits of the mixing equation, and the tolerance limits of the mixing equation, but it is within the limits of SCRB, as the value of aggregates for this sieve and the base layer according to the SCRB is from 48 to 74%.

Mix 2 is the best (ideal) mixture. Figures 5-11 show how the properties of Mix 2 and Mix 3 were significantly improved in comparison to Mix 1. The values of stability, flow, and density of the asphalt mixture improved. Also, an increase in the ITR value was observed, which means more moisture resistance. A decrease in the values of slope and intercept was also noticed for Mix 2 and Mix 3 compared to Mix 1 for all the considered layers of the road (wearing, binder and base). The higher the value of the intercept, the larger is the strain and hence the larger the potential for permanent deformation [24], while slope b represents the rate of change in the permanent strain as a function number of loading cycles (N) in the log-log scale. High-slope values of a mix indicate an increase in the material deformation rate, hence less resistance against rutting. A mix with a low slope value is preferable as it prevents the occurrence of the rutting distress mechanism [25].

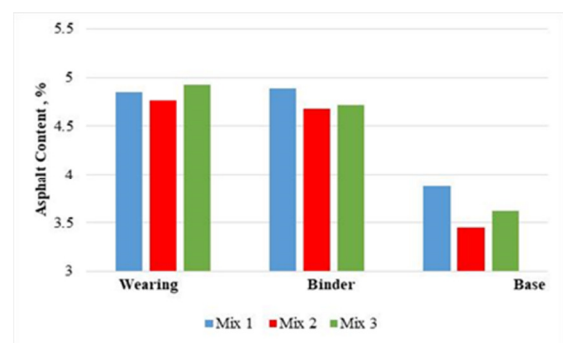


Fig. 5. Tests results of asphalt concrete percentage for each layer.

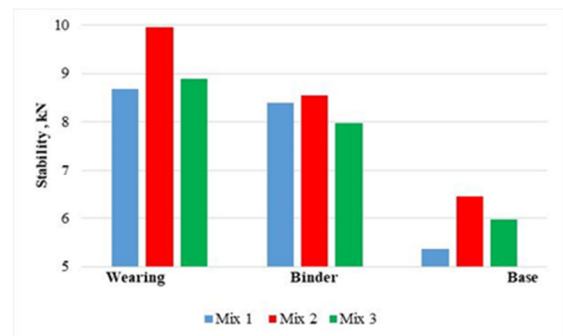


Fig. 6. Tests results of Marshall stability for each layer.

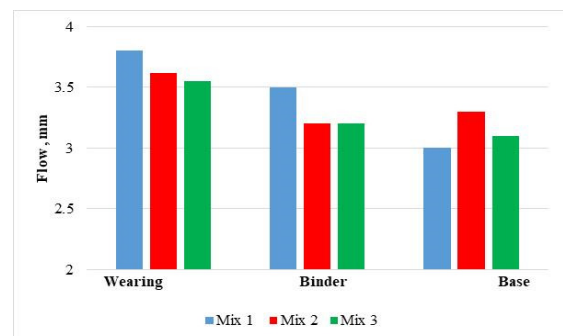


Fig. 7. Tests results of Marshall flow for each layer.

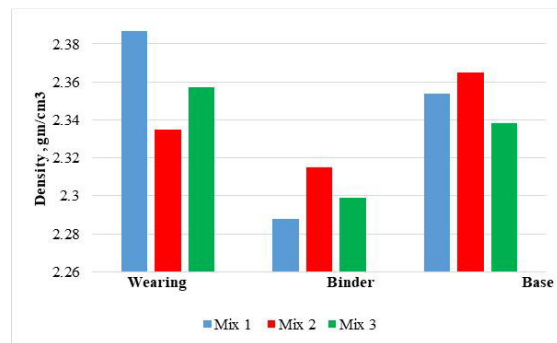


Fig. 8. Tests results of Marshall density for each layer.

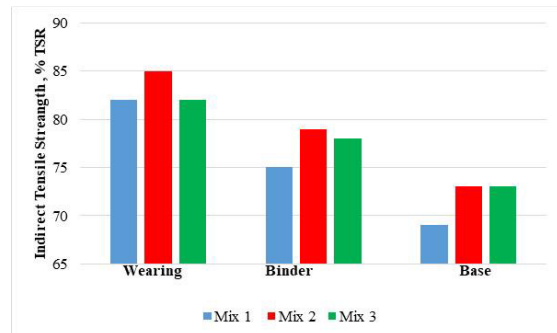


Fig. 9. Tests results of indirect TSR for each layer.

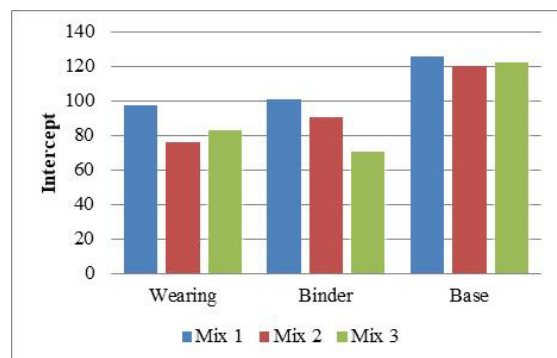


Fig. 10. Intercept value from log-log relationship between microstrain and load repetition for each layer.

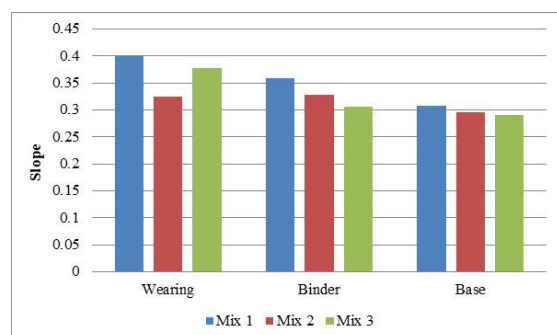


Fig. 11. Slope value from log-log relationship between microstrain and load repetition for each layer.

VII. CONCLUSION

In this research, three types of mixtures and three pavement layers were studied. The first mixture is already implemented

in some of the road projects in the city of Baghdad, and it shows deviations in the aggregate gradients from the mixing equations, suffering from weak performance and noticeable failures in some roads. Knowing the importance of adjusting the aggregate gradients in the asphalt mixture according to the specifications, noticeable performance improvement was noticed when Mix 2 and Mix 3 were produced (correcting deviant aggregate gradients according to the mixing equations). Even if it is difficult to implement Mix 2 (which represents the gradients of aggregates at the mean values of the mixing equation), it is possible to implement Mix 3, which is closer to the reality of implementation, and all its properties are better than Mix 1, guaranteeing an improvement in road performance, fewer failures, and greater durability.

REFERENCES

- [1] Y. H. Huang, *Pavement analysis and design*. Hoboken, NJ, USA: Prentice Hall, 1993.
- [2] H. M. A. A. Kareem and A. H. K. Albayati, "The Possibility of Minimizing Rutting Distress in Asphalt Concrete Wearing Course," *Engineering, Technology & Applied Science Research*, vol. 12, no. 1, pp. 8063–8074, Feb. 2022, <https://doi.org/10.48084/etasr.4669>.
- [3] *Standards and Specifications for Roads and Bridges (Section R9)*. Baghdad, Iraq: State Commission of Roads and Bridges, Ministry of Housing and Construction, 2003.
- [4] T. D. White, S. R. Johnson, and J. J. Yzenas, *Aggregate Contribution to Hot Mix Asphalt (HMA) Performance*. West Conshohocken, PA, USA: ASTM International, 2001.
- [5] M. A. Al-Jumaily, "A Study into the Merits of Using Recycled Hot-Mixes in the Construction of Surface Course Pavement in Iraq," M.S. thesis, University of Technology, 1998.
- [6] N. Zavrtanik, A. Ljubic, and G. Turk, "Statisticka odstupanja u analizama svojstava asfaltnih mjesavina," *Gradevinar*, vol. 67, no. 12, pp. 1199–1206, 2015, <https://doi.org/10.14256/JCE.1176.2014>.
- [7] J. Braziliunas and H. Sivilevicius, "Statistical analysis of component deviation from job-mix formula in hot mix asphalt," in *8th International Conference on Environmental Engineering*, Vilnius, Lithuania, Dec. 2011, pp. 1044–1050.
- [8] H. H. Joni, "Most Distresses Causes in Flexible Pavement For Baghdad Streets At Last Years," *Engineering and Technology Journal*, vol. 28, no. 18, pp. 894–906, 2010.
- [9] P. S. Kandhal and L. A. Cooley, "The Restricted Zone in the Superpave Aggregate Gradation Specification," National Academy Press, Washington, DC, USA, NCHRP REPORT 464, 2001.
- [10] L. T. de Souza, "Investigation of aggregate angularity effects on asphalt concrete mixture performance using experimental and virtual asphalt samples," M.S. thesis, University of Nebraska, 2009.
- [11] H. Al-Mosawe, N. Thom, G. Airey, and A. Al-Bayati, "Effect of aggregate gradation on the stiffness of asphalt mixtures," *International Journal of Pavement Engineering and Asphalt Technology*, vol. 16, no. 2, pp. 1–10, Dec. 2015, <https://doi.org/10.1515/ijpeat-2015-0008>.
- [12] H. Al-Mosawe, N. Thom, G. Airey, and A. Albayati, "Linear viscous approach to predict rut depth in asphalt mixtures," *Construction and Building Materials*, vol. 169, pp. 775–793, Apr. 2018, <https://doi.org/10.1016/j.conbuildmat.2017.11.065>.
- [13] M. A. Ahmed and M. I. E. Attia, "Impact of Aggregate Gradation and Type on Hot Mix Asphalt Rutting In Egypt," *International Journal of Engineering Research and Applications*, vol. 3, no. 4, pp. 2249–2258, 2013.
- [14] E. Sangsefidi, H. Ziari, and A. Mansourkhaki, "The effect of aggregate gradation on creep and moisture susceptibility performance of warm mix asphalt," *International Journal of Pavement Engineering*, vol. 15, no. 2, pp. 133–141, Feb. 2014, <https://doi.org/10.1080/10298436.2012.752824>.
- [15] A. H. M. Afaf, "Effect of aggregate gradation and type on hot asphalt concrete mix properties," *Journal of Engineering Sciences*, vol. 42, no.

- 3, pp. 567–574, May 2014, <https://doi.org/10.21608/jesaun.2014.115005>.
- [16] A. F. Al-Ani, "The effect of aggregate gradation and asphalt type on Marshall Properties and permanent deformation parameters of asphalt concrete mixes," *Association of Arab Universities Journal of Engineering Sciences*, vol. 25, no. 1, pp. 195–212, Apr. 2018.
- [17] O. M. Kunene and D. Allopi, "Comparison Between Conditions of Major Roads Within and Outside the Port of Durban," *Engineering, Technology & Applied Science Research*, vol. 3, no. 1, pp. 363–367, Feb. 2013, <https://doi.org/10.48084/etasr.263>.
- [18] F. Alzaidy and A. H. K. Albayati, "A Comparison between Static and Repeated Load Test to Predict Asphalt Concrete Rut Depth," *Engineering, Technology & Applied Science Research*, vol. 11, no. 4, pp. 7363–7369, Aug. 2021, <https://doi.org/10.48084/etasr.4236>.
- [19] E. Vivar and J. Haddock, "HMA Pavement Performance and Durability," Purdue University, West Lafayette, IN, USA, FHWA/IN/JTRP-2005/14 2-11–14, SPR-2646, 2006, <https://doi.org/10.5703/1288284313391>.
- [20] C. Pan and T. White, "Conditions for Stripping Using Accelerated Testing," Purdue University, West Lafayette, IN, USA, FHWA/IN/JTRP-97/13, Feb. 1999, <https://doi.org/10.5703/1288284313476>.
- [21] A. Albayati, "Permanent Deformation Prediction of Asphalt Concrete Under Repeated Loading," University of Baghdad, Baghdad, Iraq, 2006, <https://doi.org/10.13140/RG.2.1.2630.8242>.
- [22] T. L. J. Wasage, G. Ong, T. Fwa, and S. Tan, "Laboratory evaluation of rutting resistance of geosynthetics reinforced asphalt pavement," *Journal of the Institution of Engineers*, vol. 1, no. 2, pp. 29–44, Jan. 2004.
- [23] C. L. Monismith, N. Ogawa, and C. R. Freeme, "Permanent deformation characteristics of subgrade soils in repeated loading," in *54th Annual Meeting of the Transportation Research Board*, Washington, DC, USA, Jan. 1975, pp. 1–17.
- [24] M. W. Witczak and K. Kaloush, "Specimen Geometry and Aggregate Size Effects in Uniaxial Compression and Constant Height Shear Tests," in *Asphalt Paving Technology 2000*, Reno, NV, USA, Mar. 2000, pp. 733–793.
- [25] W. A. Gul, "Effect of recycled cement concrete content on rutting behavior of asphalt concrete," M.S. thesis, Middle East Technical University, Ankara, Turkey, 2008.

Assessment of an Assumed Strain-based Quadrilateral Membrane Element

Abdelhak Kherfi

Laboratory of Development in
Mechanics and Materials (LDMM)
University of Djelfa
Djelfa, Algeria
a.ak.k65@gmail.com

Khelifa Guerraiche

Mechanical Engineering
Department, Faculty of Technology,
University of Batna 2, Batna, Algeria
NMISSI Laboratory, Faculty of
Science and Technology, Biskra
University, Biskra, Algeria
guer.khelifa@yahoo.com

Kamel Zouggar

Laboratory of Mechanics of
Structures and Solids (LMSS)
Faculty of Technology, Djillali
Liabès University of Sidi Bel-Abbès,
Sidi Bel Abbès, Algeria
zouggar.kamel.zk@gmail.com

Received: 6 July 2022 | Revised: 31 July 2022 | Accepted: 4 August 2022

Abstract—This paper describes the development of a simple quadrilateral strain-based element for plane stress and strain problems. This element has five nodes, four located at its corners and one at the center. Each of the four corner nodes had two essential external degrees of freedom (u, v), while the center node had three degrees of freedom (u, v, θ); the static condensation method was used for the internal node. This element was used for both linear and dynamic analysis. Its performance was assessed using a variety of membrane and axisymmetric analysis problems. The obtained results demonstrated the good performance and accuracy of the proposed element.

Keywords—strain approach; drilling rotation; quadrilateral element; linear analysis; dynamic analysis; axisymmetric

I. INTRODUCTION

Numerical methods, such as finite elements, finite volumes, finite differences, and discrete element methods are powerful and efficient computational tools for solving engineering problems. However, the finite element method is the most popular because of its robust mathematical basis and applicability, which is reflected in its extensive use in various applications [1-3]. In [4], the linear (constant-strain) triangle and the bilinear rectangle were formulated, based on the displacement approach in standard elements, whereas in [5] the standard bilinear quadrilateral was produced. They have been extensively used as plane-stress, plane-strain, and axisymmetric-solid models for two-dimensional structures. However, computational experience soon showed that these elements are excessively stiff for problems where linear strain gradients dominate the response. Furthermore, over-rigidity grows rapidly as the rate of aspect degrades. These behaviors are referred to as mesh distortions and bending problems.

Much effort has been put into improving these or creating new simple elements. Some studies showed that other strategies, such as hybrid stress elements [6-8], assumed strain or enhanced assumed strain elements [9-11], quasi-conforming elements [12, 13], and generalized conforming elements [14-16] provide special advantages compared to classic finite

elements. The development of efficient and straightforward finite elements to analyze structures is a primary motivation for scientific research in solid mechanics. A class of elements was developed using the strain-based approach. This approach produces displacement fields enriched by higher-order terms, without the necessity of introducing non-essential degrees of freedom, hence obtaining elements with more accurate results on displacements. The resulting elements from this approach are free from shear locking and parasitic shear. The state of strains for this approach is composed of rigid body motions, constant strains, and higher-order strains. This approach was used in [17] for curved structures, and it was extended for plan elasticity [11, 18-21]. A summary of this early work was presented in [22, 23], with three-dimensional elasticity problems [24-26], plate bending [9, 27-30], and shell structures [31-34]. Other studies presented the treatment of non-linear problems [31, 35-36], composite materials [37], functionally graded plates [29, 38], and fracture mechanics [39]. These elements are stable and have good efficiency, and the strain approach is very practical for the development of robust finite elements which are insensitive to common problems such as mesh sensitivity and different locking problems.

This paper presents a quadrilateral element based on strain formulation. The proposed element has two degrees of freedom (u, v) at each of the corner nodes. Moreover, to enrich the strain field (ϵ_x, ϵ_y , and γ_{xy}) of the element, an internal node was introduced with three degrees of freedom (u, v, θ) to improve accuracy and reduce computational effort for the analysis of the plane structure, which will be subsequently eliminated by static condensation [11, 18]. After condensation, the element becomes a simple four-node quadrilateral element. Each node contains the two essential translational degrees of freedom, and hence the element is free of any parasitic and shear problems and is insensitive to mesh distortion. Various numerical problems (plane elasticity, axisymmetric, and dynamics) verified the high accuracy and efficiency of the proposed element compared to other existing plane elements.

II. FORMULATION OF THE DEVELOPED ELEMENT

The proposed Strain Based Five Node (SBFN) element is quadrilateral with two degrees of freedom at each of the corner nodes, corresponding to two translations (u , v), and additional in-plane translations (u , v) associated with the rotation degree of freedom θ_z at the internal node, as shown in Figure 1.

A. Case of Plane Elasticity

The strain components relations and compatibility equation for plan elasticity are respectively given as:

$$\begin{cases} \varepsilon_x = \frac{\partial u}{\partial x} \\ \varepsilon_y = \frac{\partial v}{\partial y} \\ \gamma_{xy} = \frac{\partial u}{\partial y} + \frac{\partial v}{\partial x} \end{cases} \quad (1)$$

$$\frac{\partial^2 \varepsilon_x}{\partial y^2} + \frac{\partial^2 \varepsilon_y}{\partial x^2} - \frac{\partial^2 \gamma_{xy}}{\partial x \partial y} = 0 \quad (2)$$

where u and v are the displacements in the x and y axes respectively, ε_x and ε_y are the normal strains, and γ_{xy} is the shear strain. The rigid body modes displacement field is determined by setting the three deformations in (1) to zero, followed by integration:

$$\begin{cases} u = a_1 - a_3 y \\ v = a_2 + a_3 x \\ \theta = a_3 \end{cases} \quad (3)$$

The following equation is used for the element's drilling degree of freedom:

$$\theta = \frac{1}{2} \left(\frac{\partial v}{\partial x} - \frac{\partial u}{\partial y} \right) \quad (4)$$

Figure 1 shows the geometry of the proposed SBFN element and the corresponding nodal displacements:

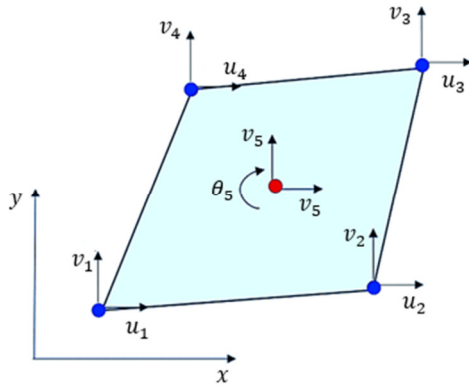


Fig. 1. The strain based five node element.

The SBFN element has eleven independent degrees of freedom, and therefore the displacement field should contain eleven independent constants. Since the three constants a_1 , a_2 , and a_3 represent the displacement field of the rigid body modes, as shown in (3), the remaining eight constants a_4 , a_5, \dots, a_{11} denote the imposed strains of the elements that are expressed as:

$$\begin{cases} \varepsilon_x = a_4 + a_5 y + a_8 x + \frac{a_{10}}{2} (x^2 + y^2) \\ \varepsilon_y = a_6 + a_7 x + a_9 y + \frac{a_{10}}{2} (x^2 + y^2) \\ \gamma_{xy} = 2a_{11} + 2a_{10} (x^2 - y^2 + y - x + xy) \end{cases} \quad (5)$$

The strain functions for the present element, given above, satisfy the compatibility equation (2). These can be written in matrix form:

$$\{\varepsilon\} = [Q]\{a\} \quad (6)$$

where $[Q]$ presents the matrix relating the strain fields to the unknown constants, given by:

$$[Q] = \begin{pmatrix} 0 & 0 & 0 & 1 & y & 0 & 0 & x & 0 & \frac{x^2}{2} + \frac{y^2}{2} & 0 \\ 0 & 0 & 0 & 0 & 0 & 1 & x & 0 & -y & \frac{x^2}{2} + \frac{y^2}{2} & 0 \\ 0 & 0 & 0 & 0 & 0 & 0 & 0 & 0 & 0 & 2x^2 + 2xy - 2x - 2y^2 + 2y & 2 \end{pmatrix} \quad (7)$$

Integrating (5) and substituting (3), the final displacement functions can be obtained:

$$\begin{cases} u = a_1 - a_3 y + a_4 x + a_5 xy - \frac{y^2}{2} a_7 + \frac{y^2}{2} a_8 + \left(\frac{x^3}{6} + \frac{xy^2}{2} - \frac{2y^3}{3} + y^2 \right) a_{10} + a_{11} y \\ v = a_2 + a_3 x - \frac{x^2}{2} a_5 + a_6 y + a_7 xy - \frac{y^2}{2} a_9 + \left(\frac{2x^3}{3} + \frac{yx^2}{2} - x^2 + \frac{y^3}{6} \right) a_{10} + a_{11} x \\ \theta = a_3 - a_5 x + a_7 y + a_{10} (x^2 + y^2 - y - x) \end{cases} \quad (8)$$

These can be written in matrix form as:

$$\{u\} = [T]\{a\} \quad (9)$$

where $[T]$ is expressed as:

$$[T] = \begin{pmatrix} [P] \\ [R] \end{pmatrix} \quad (10)$$

and:

$$[P] = \begin{pmatrix} 1 & 0 & -y & x & xy & 0 & -\frac{y^2}{2} & \frac{x^2}{2} & 0 & \frac{x^3}{6} + \frac{xy^2}{2} - \frac{2y^3}{3} + y^2 & y \\ 0 & 1 & x & 0 & -\frac{x^2}{2} & y & xy & 0 & -\frac{y^2}{2} & \frac{y^3}{6} + \frac{yx^2}{2} + \frac{2x^3}{3} - x^2 & x \end{pmatrix} \quad (11)$$

$$[R] = \begin{pmatrix} 0 & 0 & 1 & 0 & -x & 0 & y & 0 & 0 & x^2 - x + y^2 - y & 0 \end{pmatrix} \quad (12)$$

The nodal displacements and the vector coefficients $\{a\}$ are related as:

$$\{q_e\} = [C]\{a\} \quad (13)$$

where:

$$\{q_e\} = \{u_1, v_1, u_2, v_2, u_3, v_3, u_4, v_4, u_5, v_5, \theta_5\}^T \quad (14)$$

$$\{a\} = \{a_1, a_2, a_3, a_4, a_5, a_6, a_7, a_8, a_9, a_{10}, a_{11}\}^T \quad (15)$$

where $[C]$ (11×11) is the matrix that relates nodal displacements to the constants (a_1 to a_{11}) as follows:

$$[C] = \begin{pmatrix} [P(x_1, y_1)] \\ [P(x_2, y_2)] \\ [P(x_3, y_3)] \\ [P(x_4, y_4)] \\ [P(x_5, y_5)] \\ [R(x_5, y_5)] \end{pmatrix} \quad (16)$$

From (13), the following can be obtained:

$$\{a\} = [C]^{-1}\{q_e\} \quad (17)$$

By substituting (17) into (6) and (9):

$$\{U\} = [P][C]^{-1}\{q_e\} = [N]\{q_e\} \quad (18)$$

and:

$$\{\varepsilon\} = [Q][C]^{-1}\{q_e\} = [B]\{q_e\} \quad (19)$$

where:

$$[N] = [P][C]^{-1}; [B] = [Q][C]^{-1} \quad (20)$$

The stress-strain relationship is given by:

$$\{\sigma\} = [D]\{\varepsilon\} \quad (21)$$

where $[D]$ is the elasticity matrix given in Appendix A for plane stress and plane strain, respectively. The procedures to obtain the element stiffness matrix, are:

The standard weak form for static can be expressed as:

$$\int_{V_e} \delta\{\varepsilon\}^T \{\sigma\} dV = \int_{V_e} \delta\{U\}^T \{f_v\} dV \quad (22)$$

By substituting (18), (19), and (21) into (22) we get:

$$\delta\{q_e\}^T \left(\int_{V_e} [B]^T [D] [B] dV \right) \{q_e\} = \delta\{q_e\}^T \left(\int_{V_e} [N]^T \{f_v\} dV \right) \quad (23)$$

where:

$$[K_e] = \left(\int_{V_e} [B]^T [D] [B] dV \right) \quad (24)$$

$$[K_e] = t \cdot [C]^{-T} \left(\iint [Q]^T \cdot [D] \cdot [Q] dx dy \right) [C]^{-1} \quad (25)$$

where t is the thickness:

$$[K_e] = t \cdot [C]^{-T} [K_0] [C]^{-1} \quad (26)$$

$$[K_0] = \iint [Q]^T \cdot [D] \cdot [Q] dx dy \quad (27)$$

Using numerical integration:

$$[K_0] = \int_{-1}^1 \int_{-1}^1 [Q]^T [D] [Q] \det[J] d\xi d\eta \quad (28)$$

where J presents the Jacobean. The element nodal body forces vector is:

$$\{F_b\} = \int_{V_e} [N]^T \{f_v\} dV = [C]^{-T} \left(\int_{V_e} [P]^T \{f_v\} dV \right) \quad (29)$$

After assembly over all elements, the global stiffness $[K]$ is used in global equations for static, given as:

$$[K]\{q\} = [F] \quad (30)$$

B. Case of Axisymmetric Formulation

The strain components in the case of axisymmetric formulation are given as:

$$\begin{cases} \varepsilon_r = \frac{\partial u}{\partial r} \\ \varepsilon_z = \frac{\partial v}{\partial z} \\ \gamma_{rz} = \frac{\partial u}{\partial z} + \frac{\partial v}{\partial r} \\ \varepsilon_\theta = \frac{u}{r} \end{cases} \quad (31)$$

and the element stiffness matrix in the axisymmetric case is:

$$[K_e] = \left(\int_{V_e} [B]^T [D] [B] r \cdot dV \right) \quad (32)$$

where r is the radial coordinate, and $[D]$ is the axisymmetric elasticity matrix given in the Appendix. It is worth noting here that the integrals calculations in the used programs use the Gauss numerical integration. In the case of forced vibration, the complex response method is used [48].

III. NUMERICAL VALIDATION

Several tests were selected to evaluate the accuracy of the element with different analyses such as plane strain, plane stress, axisymmetric, and dynamic. A comparative study was conducted between the proposed and the following elements:

TABLE I. ELEMENTS USED IN THE COMPARATIVE STUDY

SBQM [19]	5-node quadrilateral element with in-plane rotation based on the strain approach.
Q4	Standard four-node quadrilateral element.
Q8	Standard eight-node quadrilateral element.
Q6 [20]	Quadrilateral element with six nodes.
FRQ [10]	4-node quadrilateral element based on the "Plane Fiber Rotation" concept.
Q4WT [21]	Quadrilateral element with four nodes with incompatible modes.
Q4PS [21]	4-node quadrilateral hybrid element.
CPS8 [19]	Classic 8-node quadrilateral element in-plane stress with exact integration (Abaqus).
SBRIER [40]	Element with strain field at four nodes with in-plane rotation.
Q4CST [20]	The constant strain quadrilateral.
QM5 [20]	Plane stress element and Verbeke plate element boundary element formulation.
SBQ5 [41]	Strain-based quadrilateral element with five nodes.
SBE [42]	Strain Based Element.
CQUAD4 [43]	MSC/NASTRAN

A. Linear Elasticity Tests

1) Macneal's Beam

The sensitivity of the proposed element to mesh distortion was evaluated using the Macneal beam. Three distinct meshes (rectangular, parallelogram, and trapezoidal) were adopted. The Macneal and Harder test [44] is well-known as the standard for testing the mesh distortion sensitivity. There were two loading cases under consideration: pure bending and transverse linear bending. Figure 2 shows the appropriate mechanical and geometrical data, while Tables II and III show the results obtained by the proposed versus the other elements.

TABLE II. NORMALIZED DEFLECTION FOR MACNEAL'S ELONGATED BEAM SUBJECTED TO END SHEAR

Element	Force shearing at the free end P=1		
	Mesh Type		
	Rectangular (a)	Parallelogram (b)	Trapezoidal (c)
SBQM [19]	0.993	0.964	0.972
Q4	0.093	0.035	0.003
Q8	0.951	0.919	0.854
SBE [42]	1	0.976	0.978
SBFN	0.993	0.993	0.994
Reference solution [44]	- 0.1081		

TABLE III. NORMALIZED DEFLECTION FOR MACNEAL'S ELONGATED BEAM SUBJECTED TO END PURE BENDING

Element	Pure bending moment $M=0.2$		
	Mesh Type		
	Rectangular (a)	Parallelogram (b)	Trapezoidal (c)
SBQM [19]	1	1	1
Q4	0.093	0.031	0.022
Q8	1	0.994	0.939
SBE [42]	1	0.989	0.989
SBFN	1	1	1
Reference solution [44]	- 0.0054		

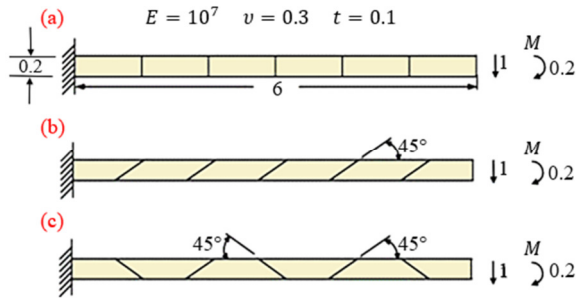


Fig. 2. McNeal's cantilever beam: (a) rectangular (b) trapezoidal (c) parallelogram.

Low sensitivity to mesh distortion was observed for the strain-based elements SBQM, SBE, and for the standard eight-node quadrilateral element Q8 for both loading cases in trapezoidal and parallelogram mesh. A neglected sensitivity in all mesh types was registered for the SBFN element, and more accuracy was observed in cases (b) and (c) compared to the other elements. However, the transverse shears locking resulting from over rigidity of the standard four-node quadrilateral element Q4 affected its results.

2) Beam In-Plane Bending

The proposed element was validated in the console beam problem subjected to a uniform vertical load using [21] and [10]. The vertical displacement at the beam's free end was computed using five meshes, as shown in Figure 3. Timoshenko's beam theory was implemented for a reference solution:

$$V_c^{ref} = \frac{L^3}{3EI} + \frac{6P_z L}{5GA} \quad (33)$$

Table IV shows the results obtained from the SBFN element for several meshes (M1, M2, M3, M4, and M5). The obtained results were compared to some other membrane element outcomes, allowing to note the following:

- SBFN gave more accurate results than the Q4, FRQ, and SBRIEIR elements.
- Similar results were noticed for Q4WT, Q4PS, and Q8 elements for regular meshes M1, M2, and M3.
- The SBFN element was more insensitive to distorted meshes than other membrane elements for M4 and M5 meshes.

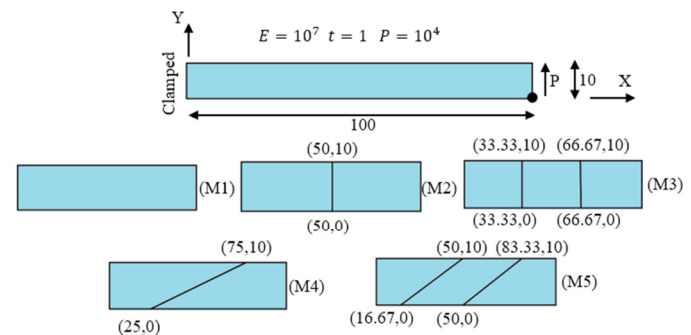


Fig. 3. Beam in-plane bending (data and meshes).

TABLE IV. VERTICAL DISPLACEMENT OF A BEAM IN PLANE BENDING

Mesh Type	FRQ [10]	Q4 [21]	Q4WT [21]	Q4PS [21]	Q8 [21]	SBRIEIR [19]	SBQM [19]	SBFN
M1	2.76	0.10	3.03	3.03	3.03	2.86	3.02	3.03
M2	3.44	0.38	3.78	3.78	3.7	3.57	3.77	3.78
M3	3.56	0.75	3.92	3.92	3.84	3.71	3.91	3.91
M4	1.09	0.12	0.30	0.49	0.64	2.92	3.04	4.53
M5	1.61	0.22	1.79	1.94	1.76	3.04	3.14	4.27
Reference solution [21]	4.03							

3) Cook's Skew Beam

The non-prismatic beam is a popular benchmark problem for evaluating planar elements. Several studies [45-57] have treated this problem. Due to the lack of an analytical solution, the reference solution was obtained using the CPS8 element of ABAQUS with a 64x64 mesh. The mechanical properties, the geometrical, and the loading data used in the treated structure are presented in Figure 4. The results of the vertical deflection at point C are shown in Table V. The SBFN element provided a good agreement with the reference solution, although the mesh was coarse compared to the Q4, SSQUAD [14], CQUAD4 [43], SBQM [19], and CPS8 [19] elements.

TABLE V. TIP VERTICAL DEFLECTION OF THE COOK'S SKEW BEAM

Element	Mesh - Vertical displacement at point C			
	2x2	4x4	8x8	16x16
Q4	11.80	18.29	22.08	23.43
SSQUAD [14]	25.65	24.27	24.01	23.96
CQUAD4 [43]	21.05	23.02	23.69	23.94
SBQM [19]	23.2173	23.4350	23.7376	23.9817
CPS8 [19]	23.35	24.54	23.8793	23.8596
SBFN	23.9298	23.9282	23.9267	23.9411
Reference solution [48]	23.9652			

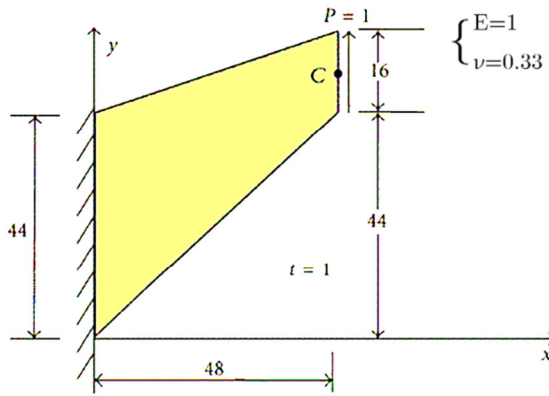


Fig. 4. Cook's skew beam.

B. Axisymmetric Elasticity Test

1) Simply Supported Circular Plate Uniformly Loaded

A simply supported circular plate under uniform load having a thickness $t=1$ was considered. Two distinguishable meshes were used for the discretization of the plate. At first, a rectangular mesh with a distortion $e=0$ followed by a trapezoidal mesh with a distortion $e=0.025$ was applied, as shown in Figure 5. The exact solution was taken from [49] as:

$$w(r) = \frac{p \cdot r_0^4}{64 \cdot D(1+\nu)} \left[2 \cdot (3\nu) \cdot \left(1 - \left(\frac{r}{r_0} \right)^2 \right) - (1+\nu) \cdot \left(1 - \left(\frac{r}{r_0} \right)^4 \right) \right] \quad (34)$$

$$\begin{cases} w_{\max} = w(0) \\ w_{\max} = \frac{p \cdot r_0^4 (5+\nu)}{64 \cdot D \cdot (1+\nu)} \end{cases} \quad (35)$$

where p and r_0 are respectively the uniform load and radius of the plate, and D is the flexural rigidity expressed as:

$$D = \frac{Eh^3}{12(1-\nu^2)} \quad (36)$$

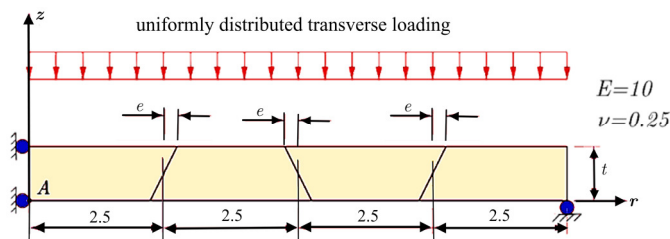


Fig. 5. Simply supported uniformly loaded circular plate.

TABLE VI. NORMALIZED VERTICAL DISPLACEMENT AT THE CENTER 'A' FOR THE UNIFORMLY LOADED CIRCULAR PLATE

Element	Mesh type - u_{zA}	
	Rectangular	Trapezoidal
Q4	0.696	0.694
Q8	1.0079	1.0183
SBFN	0.9889	0.989
Reference solution [49]	-738.280	

Table VI shows the obtained results of displacement. It can be noted that the SBFN element gave excellent results close to the exact solution, similar to those provided by the Q8 element,

whereas the Q4 element gave poor results. The SBFN element gave the best results for the cases where bending was dominant.

1) Axisymmetric Cylindrical Shell

A thin cylindrical shell $R/e = 168$ was subjected to a moment in the end [20], as shown in Figure 6. This is a problem of a thin shell with axisymmetric loading where the exact solution can be found using the theory of shells in the infinite length case. A quadrilateral element through the thickness was used. The result of the theoretical solution of the shells [49] was used to compare with the numerical radial displacement for the formulated and various types of elements. The obtained results are shown in Table VII and Figure 7. The formulated element provided excellent results, which will be more pronounced in bending cases.

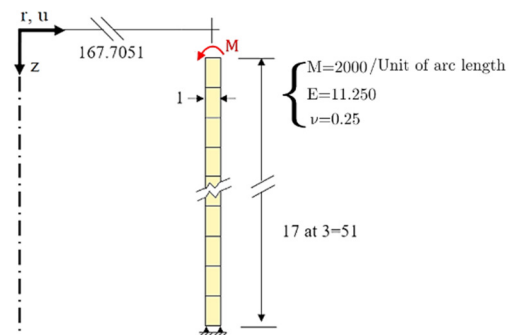


Fig. 6. Cylindrical shell analysis.

TABLE VII. RADIAL DISPLACEMENTS (U) FOR THE AXISYMMETRIC CYLINDRICAL SHELL

Z	Radial displacements u					
	Q4CST [19]	QM5 [19]	Q4 [19]	Q6 [19]	SBFN	Analytical solution [19]
0	39.97	98.56	46.47	100.01	100.08	100.00
3	26.04	47.87	29.17	48.98	49.01	48.88
6	14.98	13.49	15.69	14.19	14.40	14.31
9	6.56	-7.29	5.69	-6.54	-6.54	-6.57
12	0.47	-17.77	-1.31	-17.15	-17.17	-17.16
15	-3.65	-21.17	-5.82	-20.70	-20.72	-20.68
18	-6.16	-20.21	-8.35	-19.88	-19.90	-19.85
21	-7.40	-16.97	-9.39	-16.83	-16.80	-16.75
24	-7.68	-12.92	-9.33	-12.85	-12.86	-12.82
27	-7.27	-8.98	-8.55	-9.00	-9.01	-8.95
30	-6.40	-5.65	-7.32	-5.72	-5.73	-5.63
33	-5.27	-3.12	-5.87	-3.23	-3.24	-3.06

The obtained results clearly show that the Q4 and Q4CST elements gave very erroneous values. These elements have difficulty representing the bending phenomena. SBFN, QM5, and Q6 showed very good levels of accuracy with the theoretical solution. The excellent results are remarkable for the formulated element in the case where bending is predominant.

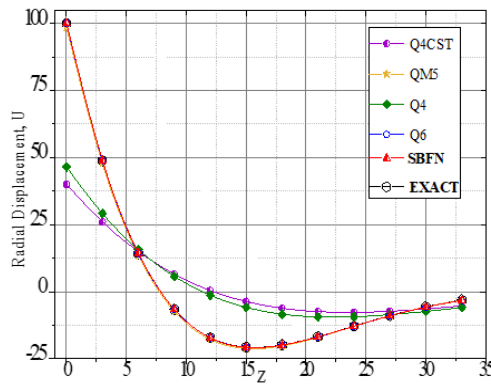


Fig. 7. Radial displacements (u) for the axisymmetric cylindrical shell.

C. Dynamic Numerical Validation

1) Forced Vibration of a Rectangular Solid in-Plane Strain

This benchmark tested the proposed element in a rectangular beam in-plane strain case to analyze forced vibrations using the complex response method. The modeled results were compared with those obtained by Q8 [50] and Q4, SBQ5, and SBRIE [41]. Fig. 9. Figure 8 shows the geometric components of the evaluated beam and its mechanical properties. The beam was subjected to a vertical harmonic force $F = \cos(\omega t)$, where force-frequency was 0.3, time step was $1/20$, the period was $2\pi/\omega$, and the ratio of depreciation was 5%. Figure 9 shows the displacements for step time results. It is noticed that the proposed SBFN agreed well with the Q8 element.

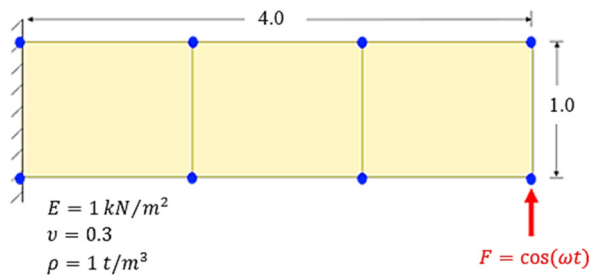


Fig. 8. Geometrical and mesh presentation of the console beam subjected to forced vibration.

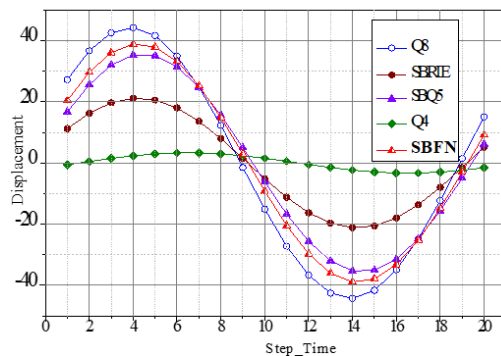


Fig. 9. Displacement as a function of time for a console beam.

IV. CONCLUSION

This study proposed a new quadrilateral plane element using an assumed strain approach. Rigid body motions, constant strain, and application of compatibility conditions to the assumed strain field guaranteed and optimized monotonic convergence to the solution. The formulated element had five nodes with eleven degrees of freedom, whereas the fifth node of the element was located in the center having three degrees of freedom (u, v, θ). This central node was eliminated using the static condensation method. Therefore, the proposed became a simple four-node element with two essential degrees of freedom (u, v) in each of the four corner nodes. The SBFN linear quadrilateral element showed acceptable performance, was insensitive to mesh distortion, and had an excellent convergence characteristic in all numerical examples. The proposed membrane element's precision was often close to that of the second-order quadrilateral plane element Q8, in static and dynamic analysis for plane and axisymmetric structures. Furthermore, the obtained numerical results of the proposed element were consistent and give better results when bending dominated.

APPENDIX

For the case of plane stress problem, the elasticity matrix $[D]$ is:

$$[D] = \frac{E}{(1-\nu^2)} \begin{bmatrix} 1 & \nu & 0 \\ \nu & 1 & 0 \\ 0 & 0 & \frac{1-\nu}{2} \end{bmatrix} \quad (A.1)$$

For the case of plane strain problem, the elasticity matrix $[D]$ is:

$$[D] = \frac{E}{(1+\nu)(1-2\nu)} \begin{bmatrix} (1-\nu) & \nu & 0 \\ \nu & (1-\nu) & 0 \\ 0 & 0 & \frac{(1-2\nu)}{2} \end{bmatrix} \quad (A.2)$$

For the case of axisymmetric problem, the elasticity matrix $[D]$ is:

$$[D] = \frac{E(1-\nu)}{(1+\nu)(1-2\nu)} \begin{bmatrix} 1 & \frac{\nu}{1-\nu} & \frac{\nu}{1-\nu} & 0 \\ \frac{\nu}{1-\nu} & 1 & \frac{\nu}{1-\nu} & 0 \\ \frac{\nu}{1-\nu} & \frac{\nu}{1-\nu} & 1 & 0 \\ 0 & 0 & 0 & \frac{1-2\nu}{2(1-\nu)} \end{bmatrix} \quad (A.3)$$

REFERENCES

- [1] A. G. da S. Jr, J. A. Martins, and E. C. Romão, "Numerical Simulation of a One-Dimensional Non-Linear Wave Equation," *Engineering, Technology & Applied Science Research*, vol. 12, no. 3, pp. 8574–8577, Jun. 2022, <https://doi.org/10.48084/etasr.4920>.
- [2] F. Khelil, M. Belhouari, N. Benseddig, and A. Talha, "A Numerical Approach for the Determination of Mode I Stress Intensity Factors in PMMA Materials," *Engineering, Technology & Applied Science Research*, vol. 4, no. 3, pp. 644–648, Jun. 2014, <https://doi.org/10.48084/etasr.442>.
- [3] A. Boulouar, N. Benseddig, and M. Mazari, "Two-dimensional Numerical Estimation of Stress Intensity Factors and Crack Propagation in Linear Elastic Analysis," *Engineering, Technology & Applied Science Research*, vol. 3, no. 5, pp. 506–510, Oct. 2013, <https://doi.org/10.48084/etasr.363>.

- [4] M. J. Turner, R. W. Clough, H. C. Martin, and L. J. Topp, "Stiffness and Deflection Analysis of Complex Structures," *Journal of the Aeronautical Sciences*, vol. 23, no. 9, pp. 805–823, 1956, <https://doi.org/10.2514/8.3664>.
- [5] I. C. Taig and R. I. Kerr, "Some Problems in the Discrete Element Representation of Aircraft Structures," in *Matrix Methods of Structural Analysis*, F. de Veubeke, Ed. Oxford, UK: Pergamon Press, 1964, pp. 267–316.
- [6] K. Y. Sze, "On immunizing five-beta hybrid-stress element models from 'trapezoidal locking' in practical analyses," *International Journal for Numerical Methods in Engineering*, vol. 47, no. 4, pp. 907–920, 2000, [https://doi.org/10.1002/\(SICI\)1097-0207\(20000210\)47:4<907::AID-NME808>3.0.CO;2-A](https://doi.org/10.1002/(SICI)1097-0207(20000210)47:4<907::AID-NME808>3.0.CO;2-A).
- [7] W. Chen and Y. K. Cheung, "Axisymmetric solid elements by the generalized hybrid method," *Computers & Structures*, vol. 27, no. 6, pp. 745–752, Jan. 1987, [https://doi.org/10.1016/0045-7949\(87\)90287-2](https://doi.org/10.1016/0045-7949(87)90287-2).
- [8] K. Y. Sze and C. L. Chow, "An incompatible element for axisymmetric structure and its modification by hybrid method," *International Journal for Numerical Methods in Engineering*, vol. 31, no. 2, pp. 385–405, Feb. 1991, <https://doi.org/10.1002/nme.1620310211>.
- [9] F. Boussem and L. Belounar, "A Plate Bending Kirchhoff Element Based on Assumed Strain Functions," *Journal of Solid Mechanics*, vol. 12, no. 4, pp. 935–952, Dec. 2020, <https://doi.org/10.22034/jsm.2020.1901430.1601>.
- [10] R. Ayad, "Éléments finis de plaque et coque en formulation mixte avec projection en cisaillement," Ph.D. dissertation, University of Compiègne, 1993.
- [11] K. Guerraiche, "Elements finis d'Elasticite Plane et de Volume Bases Sur l'Approche en Deformation," Ph.D. dissertation, University Mohamed Khider - Biskra, 2014.
- [12] Y. Long and Y. Xu, "Generalized conforming quadrilateral membrane element with vertex rigid rotational freedom," *Computers & Structures*, vol. 52, no. 4, pp. 749–755, Aug. 1994, [https://doi.org/10.1016/0045-7949\(94\)90356-5](https://doi.org/10.1016/0045-7949(94)90356-5).
- [13] W. Changsheng, Q. Zhaohui, Z. Xiangkui, and H. Ping, "Quadrilateral 4-node Quasi-Conforming Plane Element with Internal Parameters," *Chinese Journal of Theoretical and Applied Mechanics*, vol. 46, no. 6, pp. 971–976, Nov. 2014, <https://doi.org/10.6052/0459-1879-14-167>.
- [14] M. Rezaiee-Pajand and M. Yaghoobi, "Formulating an effective generalized four-sided element," *European Journal of Mechanics - A/Solids*, vol. 36, pp. 141–155, Nov. 2012, <https://doi.org/10.1016/j.euromechsol.2012.02.012>.
- [15] M. S. Djoudi and H. Bahai, "A cylindrical strain-based shell element for vibration analysis of shell structures," *Finite Elements in Analysis and Design*, vol. 40, no. 13, pp. 1947–1961, Aug. 2004, <https://doi.org/10.1016/j.finel.2003.11.008>.
- [16] A. B. Sabir and A. C. Lock, "A curved, cylindrical shell, finite element," *International Journal of Mechanical Sciences*, vol. 14, no. 2, pp. 125–135, Feb. 1972, [https://doi.org/10.1016/0020-7403\(72\)90093-8](https://doi.org/10.1016/0020-7403(72)90093-8).
- [17] D. G. Ashwell, A. B. Sabir, and T. M. Roberts, "Further studies in the application of curved finite elements to circular arches," *International Journal of Mechanical Sciences*, vol. 13, no. 6, pp. 507–517, Jun. 1971, [https://doi.org/10.1016/0020-7403\(71\)90038-5](https://doi.org/10.1016/0020-7403(71)90038-5).
- [18] A. B. Sabir and A. Sfindji, "Triangular and rectangular plane elasticity finite elements," *Thin-Walled Structures*, vol. 21, no. 3, pp. 225–232, Jan. 1995, [https://doi.org/10.1016/0263-8231\(94\)00002-H](https://doi.org/10.1016/0263-8231(94)00002-H).
- [19] A. Belounar, "Eléments finis membranaires et flexionnels à champ de déformation pour l'analyse des structures," Ph.D. dissertation, University Mohamed Khider - Biskra, 2019.
- [20] S. J. Fennes, N. Perrone, and A. R. Robinson, *Numerical and Computer Methods in Structural Mechanics*. New York, NY, USA: Elsevier, 2014.
- [21] J.-L. Batoz and G. Dhatt, *Modélisation des structures par éléments finis*. Sainte-Foy, France: Presses Université Laval, 1990.
- [22] M. Rezaiee-Pajand, N. Gharai-Moghaddam, and M. Ramezani, "Review of the strain-based formulation for analysis of plane structures Part II: Evaluation of the numerical performance," *Iranian Journal of Numerical Analysis and Optimization*, vol. 11, no. 2, pp. 485–511, Sep. 2021, <https://doi.org/10.22067/ijnao.2021.70940.1051>.
- [23] D. Boutagouga, "A Review on Membrane Finite Elements with Drilling Degree of Freedom," *Archives of Computational Methods in Engineering*, vol. 28, no. 4, pp. 3049–3065, Jun. 2021, <https://doi.org/10.1007/s11831-020-09489-z>.
- [24] M. T. Belarbi and A. Charif, "Développement d'un nouvel élément hexaédrique simple basé sur le modèle en déformation pour l'étude des plaques minces et épaisses," *Revue Européenne des Éléments Finis*, vol. 8, no. 2, pp. 135–157, Jan. 1999, <https://doi.org/10.1080/12506559.1999.10511361>.
- [25] K. Guerraiche, L. Belounar, and L. Bouzidi, "A New Eight Nodes Brick Finite Element Based on the Strain Approach," *Journal of Solid Mechanics*, vol. 10, no. 1, pp. 186–199, Mar. 2018.
- [26] L. Belounar and K. Guerraiche, "A new strain based brick element for plate bending," *Alexandria Engineering Journal*, vol. 53, no. 1, pp. 95–105, Mar. 2014, <https://doi.org/10.1016/j.aej.2013.10.004>.
- [27] L. Belounar and M. Guenfoud, "A new rectangular finite element based on the strain approach for plate bending," *Thin-Walled Structures*, vol. 43, no. 1, pp. 47–63, Jan. 2005, <https://doi.org/10.1016/j.tws.2004.08.003>.
- [28] F. Boussem, A. Belounar, and L. Belounar, "Assumed strain finite element for natural frequencies of bending plates," *World Journal of Engineering*, vol. ahead-of-print, no. ahead-of-print, Jan. 2021, <https://doi.org/10.1108/WJE-02-2021-0114>.
- [29] A. Belounar, F. Boussem, M. N. Houhou, A. Tati, and L. Fortas, "Strain-based finite element formulation for the analysis of functionally graded plates," *Archive of Applied Mechanics*, vol. 92, no. 7, pp. 2061–2079, Jul. 2022, <https://doi.org/10.1007/s00419-022-02160-y>.
- [30] A. Belounar, S. Benmebarek, and L. Belounar, "Strain based triangular finite element for plate bending analysis," *Mechanics of Advanced Materials and Structures*, vol. 27, no. 8, pp. 620–632, Apr. 2020, <https://doi.org/10.1080/15376494.2018.1488310>.
- [31] M. S. Djoudi and H. Bahai, "A shallow shell finite element for the linear and non-linear analysis of cylindrical shells," *Engineering Structures*, vol. 25, no. 6, pp. 769–778, May 2003, [https://doi.org/10.1016/S0141-0296\(03\)00002-6](https://doi.org/10.1016/S0141-0296(03)00002-6).
- [32] M. Bourezane M, "An Efficient Strain Based Cylindrical Shell Finite Element," *Journal of Solid Mechanics*, vol. 9, no. 3, pp. 632–649, Jan. 2017.
- [33] A. Mousa, "Strain-Based Finite Element Analysis of Stiffened Cylindrical Shell Roof," *American Journal of Civil Engineering*, vol. 5, no. 4, Jul. 2017, <https://doi.org/10.11648/j.ajce.20170504.15>.
- [34] H. Guenfoud, M. Himeur, H. Ziou, and M. Guenfoud, "A consistent triangular thin flat shell finite element with drilling rotation based on the strain approach," *International Journal of Structural Engineering*, vol. 9, no. 3, 2018, <https://doi.org/10.1504/IJSTRUCTE.2018.093673>.
- [35] A. B. Sabir and M. S. Djoudi, "Shallow shell finite element for the large deflection geometrically nonlinear analysis of shells and plates," *Thin-Walled Structures*, vol. 21, no. 3, pp. 253–267, Jan. 1995, [https://doi.org/10.1016/0263-8231\(94\)00005-K](https://doi.org/10.1016/0263-8231(94)00005-K).
- [36] C. Rebiai and L. Belounar, "A new strain based rectangular finite element with drilling rotation for linear and nonlinear analysis," *Archives of Civil and Mechanical Engineering*, vol. 13, no. 1, pp. 72–81, Mar. 2013, <https://doi.org/10.1016/j.acme.2012.10.001>.
- [37] A. Belounar, L. Belounar, and A. Tati, "An assumed strain finite element for composite plates analysis," *International Journal of Computational Methods*, Jul. 2022, <https://doi.org/10.1142/S0219876222500347>.
- [38] A. Belounar, F. Boussem, and A. Tati, "A Novel C0 Strain-Based Finite Element for Free Vibration and Buckling Analyses of Functionally Graded Plates," *Journal of Vibration Engineering & Technologies*, Jun. 2022, <https://doi.org/10.1007/s42417-022-00577-x>.
- [39] M. Rezaiee-Pajand, N. Gharai-Moghaddam, and M. Ramezani, "Strain-based plane element for fracture mechanics' problems," *Theoretical and Applied Fracture Mechanics*, vol. 108, Aug. 2020, Art. no. 102569, <https://doi.org/10.1016/j.tafmec.2020.102569>.
- [40] A. B. Sabir, "A Rectangular and Triangular Plane Elasticity Elements with Drilling Degrees of Freedom," in *Proceedings of the Second International Conference on Variational Methods in Engineering*, 1985, pp. 17–25.

- [41] L. Bouzidi, L. Belounar, and K. Guerraiche, "Presentation of a new membrane strain-based finite element for static and dynamic analysis," *International Journal of Structural Engineering*, vol. 10, no. 1, pp. 40–60, Jan. 2019, <https://doi.org/10.1504/IJSTRUCTE.2019.101431>.
- [42] C. Rebiai, N. Saidani, and E. Bahloul, "A New Finite Element Based on the Strain Approach for Linear and Dynamic Analysis," *Research Journal of Applied Sciences, Engineering and Technology*, vol. 11, no. 6, pp. 639–644, Jul. 2015.
- [43] R. Winkler and D. Plakomytis, "A New Shell Finite Element with Drilling Degrees of Freedom and its Relation to Existing Formulations," in *Proceedings of the VII European Congress on Computational Methods in Applied Sciences and Engineering (ECCOMAS Congress 2016)*, Crete Island, Greece, 2016, pp. 2803–2842, <https://doi.org/10.7712/100016.1998.11192>.
- [44] R. H. Macneal and R. L. Harder, "A proposed standard set of problems to test finite element accuracy," *Finite Elements in Analysis and Design*, vol. 1, no. 1, pp. 3–20, Apr. 1985, [https://doi.org/10.1016/0168-874X\(85\)90003-4](https://doi.org/10.1016/0168-874X(85)90003-4).
- [45] Y. K. Cheung, Y. X. Zhang, and W. J. Chen, "A refined nonconforming plane quadrilateral element," *Computers & Structures*, vol. 78, no. 5, pp. 699–709, Dec. 2000, [https://doi.org/10.1016/S0045-7949\(00\)00049-3](https://doi.org/10.1016/S0045-7949(00)00049-3).
- [46] W. Zouari, F. Hammadi, and R. Ayad, "Quadrilateral membrane finite elements with rotational DOFs for the analysis of geometrically linear and nonlinear plane problems," *Computers & Structures*, vol. 173, pp. 139–149, Sep. 2016, <https://doi.org/10.1016/j.compstruc.2016.06.004>.
- [47] P. G. Bergan and C. A. Felippa, "A triangular membrane element with rotational degrees of freedom," *Computer Methods in Applied Mechanics and Engineering*, vol. 50, no. 1, pp. 25–69, Jul. 1985, [https://doi.org/10.1016/0045-7825\(85\)90113-6](https://doi.org/10.1016/0045-7825(85)90113-6).
- [48] R. D. Cook, D. S. Malkus, M. E. Plesha, and R. J. Witt, *Concepts and Applications of Finite Element Analysis, 4th Edition*. Hoboken, NJ, USA: John Wiley & Sons, Ltd, 2001.
- [49] S. Timoshenko and S. Woinowsky-krieger, *Theory of Plates and Cells*. New York, NY, USA: Mc Graw-Hill, 1959.
- [50] I. M. Smith, D. V. Griffiths, and L. Margetts, *Programming the Finite Element Method*. Chichester, UK: John Wiley & Sons, 2013.

Development of a Wire Mesh Composite Material for Aerospace Applications

Siva Chakra Avinash Bikkina

Department of Electrical, Electronics and Communication
Engineering, GITAM Deemed to be University
Visakhapatnam, India
sbikkina@gitam.in

Pappu V. Y. Jayasree

Department of Electrical, Electronics and Communication
Engineering, GITAM Deemed to be University
Visakhapatnam, India
jpappu@gitam.edu

Received: 13 July 2022 | Revised: 9 August 2022 | Accepted: 14 August 2022

Abstract—The electrical conductivity of Fiber-Reinforced Polymers (FRPs) may be used to reduce the dangers of lightning strikes, radar radiation, and aerial radio frequency transmitters. Metal Matrix Composites (MMCs) were created to guard against Electromagnetic Interference (EMI) in the aircraft's electric and electrical systems. High-Intensity Radiated Field Protection (HIRFP) aircrafts are required to be manufactured from a metal matrix consisting of Al6061, Al2O₃, and Fly Ash (FA) to keep up with the ever-increasing needs of industry. The current work considered three MMC combinations. MMC1 is AL6061+10% and Al2O₃+5% FA, MMC2 consists of AL6061+15 and Al2O₃+5% FA, and MMC3 of AL6061+20% and Al2O₃+5% FA. These MMCs made the shielding more effective at different percentages. The material electrical properties were interpreted based on experiments. Analytical approaches include the testing of the electrical parameters of materials to measure the shielding effectiveness. The calculated shielding efficiencies MMC1-55.7dB, MMC2-57.2dB, and MMC3-59.1dB allow the composites to be employed in aircrafts. This indicates that, for specific applications like HIRFPs, the constructed MMCs perform well.

Keywords—Metal Matrix Composites (MMCs); reinforcement; Al₂O₃; fly ash

I. INTRODUCTION

Frequent lightning strikes can harm commercial airliners. Lightning's high-intensity fields interfere with the electronic devices of the in-built guidance and communication systems [1-2]. The damage caused by lightning to aircrafts varies significantly with altitude and flight duration [3]. With its precise rigidity, strength, and lightweight, FRPs are ideal for aircraft reinforcement [4]. The materials used in their construction have sufficient mechanical qualities and low energy consumption per unit. However, they have low electrical conductivity, and the electric field cannot travel through it, resulting in delamination and embrittlement when lightning hits an aircraft [5]. Aluminum composites have great promise since their fundamental qualities may be enhanced by reinforcing with other materials. Metals including titanium, nickel, magnesium, copper, and aluminum have all been utilized to create metal matrix composites. As a result of its low density, high strength, low electrical conductivity, and high reflectivity, aluminum is the material of choice [6]. Authors in

[7] studied various physical models based on the electrical qualities of lightning strike protection. With its low density, particular corrosion resistance, high strength, and solid electrical qualities, Al6061 was developed as an alternative to FRPs [8]. Since many incident EM waves are arbitrarily oriented, an evaluation of wire mesh's shielding effectiveness for normal incidence might be generalized to all practical applications. The study is based on TL modelling in the situation of normal incidence. It is an arbitrary perspective because the polarized electric and magnetic fields in this situation are normal or vertical to the plane. The referenced research analyzed the oblique impact of lightning's EM waves on aircraft. Authors in [9] created a lightning-proof carbon filter epoxy pre-preg laminate with a 55dB SE.

The novelty of the proposed research work is the protection of the electronic components of the aircraft from the lightning strike effect. To protect from this effect, a MMC (Al6061) with a variety of Al₂O₃/FA particle reinforced was considered. Electrical conductivity, permeability, and permittivity were measured after reinforcing Al6061 with varying concentrations of considered and 5% FA. The shielding effectiveness of the composite material was calculated with the TL method. Simulations were performed to determine the efficiency of shielding against X-band electromagnetic radiation with oblique incidence. The whole process was well-organized, from the preparation of the materials to the efficiency assessment of the shielding, and to result analysis.

II. UTILIZED MATERIALS

Aluminum oxide (Al₂O₃) has a density of 0.0039kg/cc³, and is employed as a reinforcing material because of its high corrosion resistance and high-temperature tolerance. As a result, the Al₂O₃ particles in hybrid composites are also used as load-bearing and electrical conductivity components in metals. Al₂O₃ and Al6061 may be used in aircraft design because of their low cost [10-11]

FA is a byproduct of coal-fired thermal power plants. In recent decades, carbon fibers have been used as a reinforcing material for aluminum-based metal matrix composites. To prevent Al₄C₃, FA may be used for aluminum metal matrix composites reinforced with silicon carbide (SiC) [14]. A

substance's absorption capacity may be increased to enhance the shielding qualities of the substance. Only 5% FA may be utilized in the composite since it affects the material's tensile strength [12-13].

III. COMPOSITE MATERIAL PREPARATION

As indicated in Figure 1, stir casting was used to add micro-sized Al_2O_3 and FA to the Al6061 metal matrix composite to improve its electrical and mechanical characteristics. A composite is formed when two or more materials are combined, as shown in Table I. The fabricated materials made from stir casting are shown in Figure 2. Stir casting is the most cost-effective technique for synthesizing particle-reinforced composites, and this is how the proposed MMC is made. A furnace, a feeder for reinforcing ingredients, and a stirrer were used in the stir casting process to create the composite. The stirrer comes with a rod and blades for stirring. A resistance-heated muffle furnace was used to heat 1kg of Al6061 alloy to 720°C in a ceramic crucible. Before casting, the Al 6061 alloy was warmed to 600°C to remove any gases and moisture from the reinforcing particles (Al_2O_3 and FA). This prevents temperature drops during the casting process. The stirrer's alumina-coated blades are used to avoid ferrous ions.



Fig. 1. Experimental setup for reinforcement using stir casting.



Fig. 2. Fabricated material from stir casting.

FA (5wt%) and varied quantities of Al_2O_3 (5wt%) were used to make the composites described in Table I. The liquid composite was mixed with all the reinforcing elements and was then poured into a steel mold warmed to 250°C to prevent condensation from forming. The metal cools in the atmosphere before solidifying. The mold was emptied of the solidified composite. The other specimens were made with the same process but with varied quantities of reinforcing materials.

TABLE I. METAL MATRIX REPRESENTATION

Material and weight percentages combined	Representation
AL6061+10% Al_2O_3 +5% FA	MMC-1
AL6061+15% Al_2O_3 +5% FA	MMC-2
AL6061+20% Al_2O_3 +5% FA	MMC-3

IV. ELECTRICAL PARAMETER CALCULATION

The Transmission/Reflection method utilized by a E8263B Agilent Technologies Vector Network Analyzer (VNA) was used to determine the permeability (μ), permittivity (ϵ), and conductivity (σ), of the MMCs (Figure 3). In order to create the incident electromagnetic wave, a piece of MMC was put into the waveguide [14-15]. To analyze the electrical properties of the composite, a waveguide measuring $22.86\text{mm} \times 10.16\text{mm}$ was implanted in the test specimens. The MMC samples utilized in the waveguide are shown in Figure 2, and the experimental setup for the transmission/reflection approach is shown in Figure 3. We conducted the experiment in the X-band and determined the VNA levels for a range of frequencies. The results of the VNA are shown in Figures 6–9. They provide evidence that μ , σ , and ϵ have a connection to periodicity. It is important to note that the electrical characteristics of MMC vary with its operating frequency. The degree to which a given material may operate as a shield depends on the values of μ , σ , and ϵ in the MMC ratio.



Fig. 3. Transmission/Reflection method experimental setup.

V. THEORETICAL ANALYSIS OF SHIELDING EFFECTIVENESS FOR WIRE MESH METAL MATRIX COMPOSITES

The Shielding Efficiency (SE) [17] statistic is often used to evaluate a material's shielding capacity. Figure 4 shows the mesh surface with an oblique incidence of electromagnetic (EM) waves [16]. The mesh surface with an oblique incidence of EM wave is shown in Figure 4. The ratio of received power before and after shielding is used to quantify EM shielding effectiveness. In (1), p_r represents the received power before the area was shielded, and p_s represents the measured power after the region was shielded. The same approach is used to protect against electric and magnetic fields and is effective in both application circumstances.

$$SE(\text{dB}) = 10 \log_{10} \left(\frac{p_r}{p_s} \right) \quad (1)$$

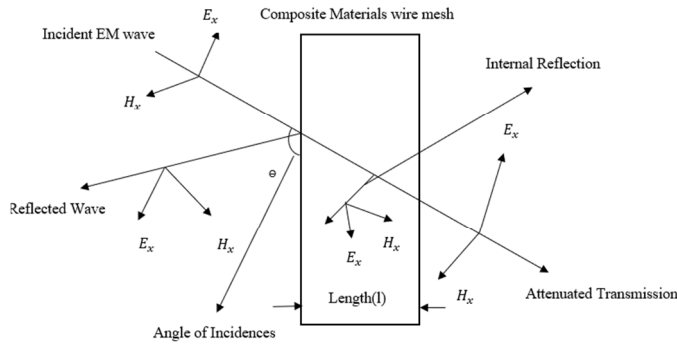


Fig. 4. Representation of oblique incidences for WMMC.

Simple in design, the Wire Metal Matrix Mesh Composite (WMMC) is made up of parallel MMC wires that are equally spaced apart. This means that the effectiveness of WMMC as a radiation shield depends on parameters such as the distance between the wires, their thickness, the wave's incidence angle, etc. It is possible to increase the SE of such a mesh by using additional orthogonal wires to the initial set of wires. Electromagnetic shielding effectiveness is examined when mesh apertures are small in contrast to the operating wavelength of the screen. The impedance of a wire-mesh screen sheet is used to measure its impedance [18-19]. When an electromagnetic wave with a relatively low frequency strikes a mesh, a reactive field is formed near the mesh surface. Without a screen, this reactive field diminishes exponentially with distance [19]. As can be seen in Figure 1 of [22], a mesh with a square aperture length a_s and wire radius r_w has a shielding efficacy [20-22] that may be defined as:

$$z_{s1} = z'_w a_s + j\omega L_s \quad (2)$$

$$z_{s2} = z_s - \frac{j\omega L_s}{2} \sin^2 \theta \quad (3)$$

The following calculations show that the transmission coefficients for polarization T_1 and T_2 represent TE and TM modes and can be calculated for a range of frequencies and incidence angles.

$$T_1 = \frac{2\left(\frac{z_{s1}}{z_0}\right) \cos \theta}{1 + 2\left(\frac{z_{s1}}{z_0}\right) \cos \theta} \quad (4)$$

$$T_2 = \frac{2\left(\frac{z_{s2}}{z_0}\right) \cos \theta}{1 + 2\left(\frac{z_{s2}}{z_0}\right) \cos \theta} \quad (5)$$

where θ is the incidence angle, calculated from the flat sheet's regular, z_0 is the free-space impedance, and z_{s1} and z_{s2} are the eigenvalues of TE and TM mesh impedance operators respectively. The sheet inductance L_s is calculated from:

$$L_s = \frac{\mu_0 \cdot a_s}{2\pi} \ln(1 - e^{-\frac{2\pi r_s}{a_s}})^{-1} \quad (6)$$

The wire impedance per unit length z'_w depends on the resistance per unit length, τ_w is a time constant and I_0 and I_1 are first kind Bessel functions.

$$z'_w = r'_w \frac{(\sqrt{j\omega\tau_w}) \cdot I_0(\sqrt{j\omega\tau_w})}{2 \cdot I_1(\sqrt{j\omega\tau_w})} \quad (7)$$

$$SE = -10 \log_{10} \left(\left(\frac{1}{2} T_1^2 \right) + \left(\frac{1}{2} T_2^2 \right) \right) \quad (8)$$

$$T_{total} = -SE \quad (9)$$

Since no noticeable change occurred for the frequencies and structures under examination when the skin effect was included in (7), the DC wire resistance was included as an approximation to the wire impedance (6). Consequently, it becomes straightforward to determine the SE of a particular mesh (with square openings) under various situations (and in different directions).

VI. SIMULATION RESULTS

A. Electrical Parameter Measurements

The connection between an electrical parameter of a composite material and its frequency may be deduced from the vector analyzer's output considering the electrical characteristics of conductivity, permeability, and permittivity. As a direct result of the material's permeability and permittivity, its electrical properties are intimately linked. The essential portion of the permittivity of lossless materials displays the quantity of stored electrical energy.

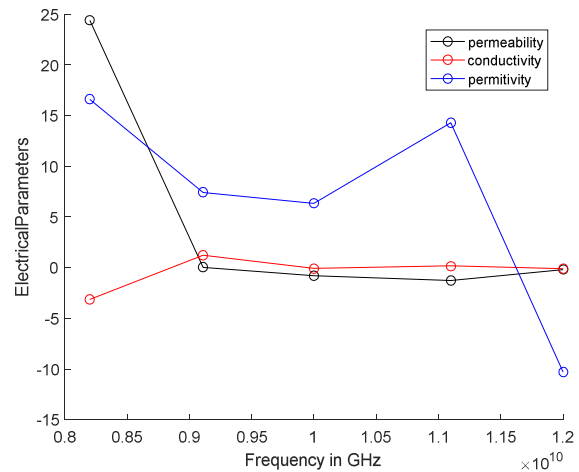


Fig. 5. Electrical parameters of pure AL6061.

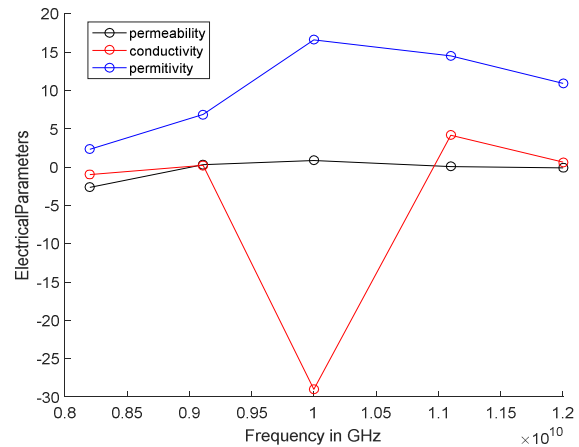


Fig. 6. Electrical parameters of MMC-1.

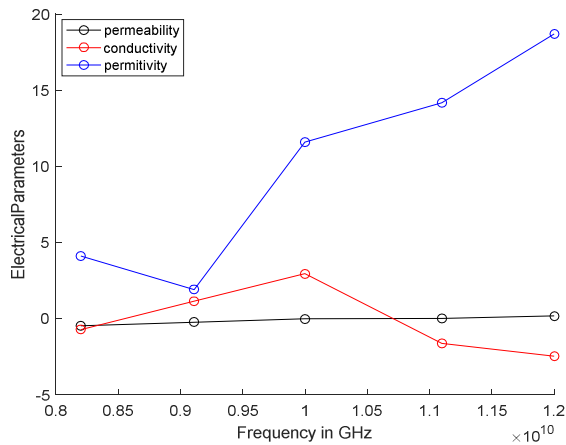


Fig. 7. Electrical parameters of MMC-2.

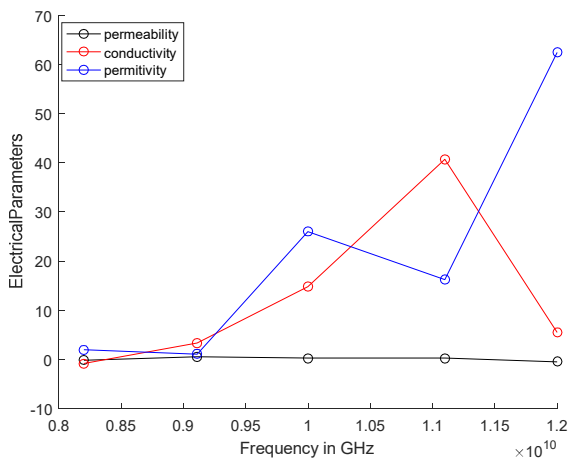


Fig. 8. Electrical parameters of MMC-3.

The imaginary part of permeability is used to quantify the power lost due to magnetic fields, which is crucial for calculating the magnetic energy stored in a material. A VNA having a waveguide or coaxial construction and working at 8–12GHz may be used to assess scattering properties (X-band frequency). To calculate the reflection coefficient equation's value, $|S_{11}|$ and $|S_{21}|$ were plugged into the calculator's bar. The VNA results are shown in Figures 5-8.

B. Shielding Effectiveness Measurement

Most electromagnetic signal occurrences on the mesh surface were oblique in practice, as described in the literature. Using a range of angles from 0 to 90°, the shielding performance of each composite was evaluated. As the incidence angle increases, so does the shielding, as shown by the relationship between the electromagnetic mesh surface and the incidence angle. The stimulated results of pure AL6061 and MMC are represented in Figures 9-12. At increasing incidence angles, the shielding efficiency of pure AL6061 and composites supported by varying proportions of Al_2O_3 and FA as shown in Table II. SE decreases as the incidence angle becomes normal to the mesh material. Al_2O_3 and FA have been used in this study to support AL6061 alloys. Shielding relies on absorption and reflection for its success. Permeability may be

used to measure the material's ability to absorb. Depending on the conductivity of the substance, the reflectance of the object changes. The material's excellent permeability and conductivity result in high absorption and reflection losses. The composite material's permittivity improves as a result of the Al_2O_3 growing proportion. Also, the whole composite's absorption loss rises. For aviation applications of 48.83dB, the effective shielding effectiveness is considered adequate [29-30]. The material's excellent permeability and conductivity result in high absorption and reflection losses. The composite's 55.7dB shielding value at a 20° angle of incidence aided by Al_2O_3 (10%) and FA (5%) reinforcement resulted in reflection and only absorption from the FA. By increasing the Al_2O_3 and FA content by 15% and 20%, 57.6dB and 59.1dB increase in shielding value is respectively obtained. The material will no longer be suitable for aviation applications if the percentage exceeds that level.

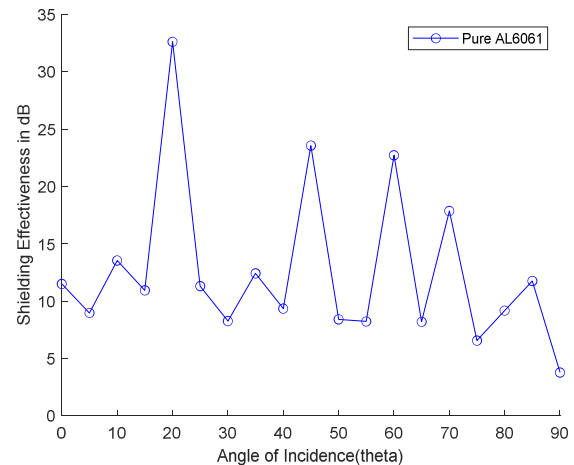


Fig. 9. Shielding effectiveness of pure AL6061.

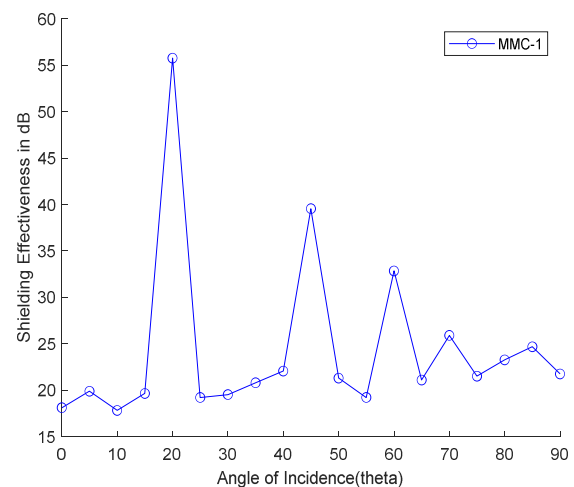


Fig. 10. Shielding effectiveness of MMC-1.

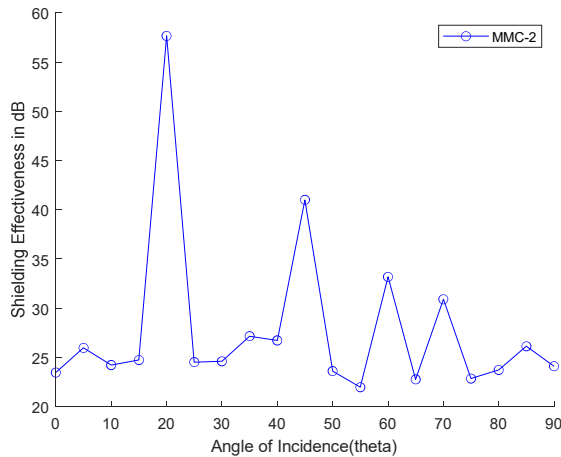


Fig. 11. Shielding effectiveness of MMC-2.

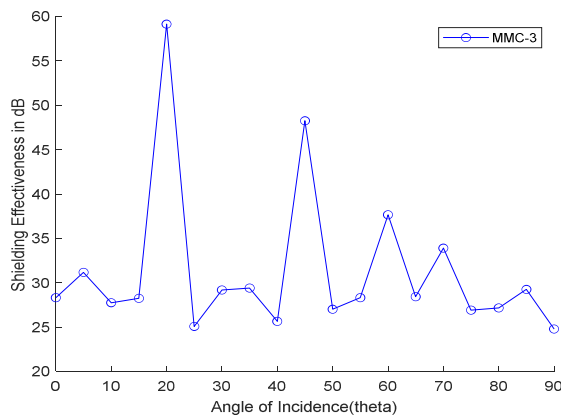


Fig. 12. Shielding effectiveness of MMC-3.

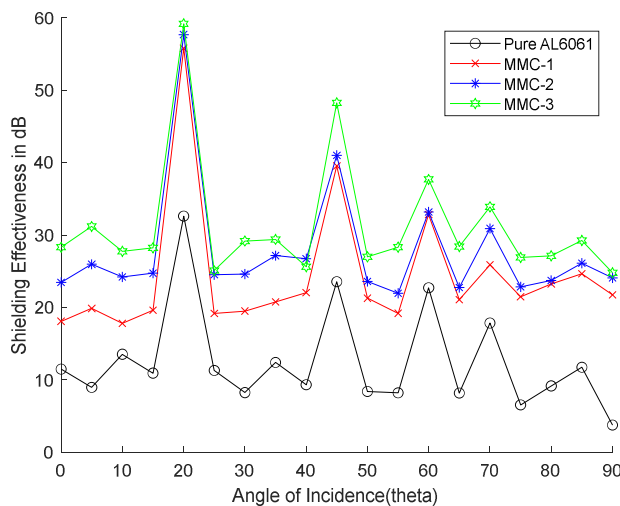


Fig. 13. Shielding effectiveness comparison of MMCs with Pure AL6061.

The FA content of all combinations is fixed to 5%. If the concentration is more, the material strength decreases, and the material properties are lost. Shielding increases by around 20% for incidence angles of 45°, 60°, 70°, and 85°, but as the incidence angle increases, the values decrease. Table II shows

the comparison of the results of the present work with other known works and Table III exhibits the shielding effectiveness of MMCs with different angle of incidences.

TABLE II. COMPARISON OF SHIELDING EFFECTIVENESS VALUES

Reference	Material	Frequency	Shielding effectiveness
[23]	Al ₂ O ₃ /FeSiAl/flaky graphite	X band	30.4
[24]	Ti ₃ Si(Al)C ₂ /Al ₂ O ₃	X band	42.1
[25]	Al ₂ O ₃	X band	29-32
Present work	Al6061/ Al ₂ O ₃ /FA	X band	59.1

TABLE III. RELATIONSHIP BETWEEN THE SHIELDING PROPERTIES OF VARIOUS REINFORCED MATERIALS AND AL6061 COMPOSITE AT VARIOUS INCIDENCE ANGLES

Material	Incidence angle				
	20°	45°	60°	70°	85°
Pure AL6061	32.62	23.48	22.72	17.86	11.77
MMC-1	55.7	39.5	32.8	25.8	24.6
MMC-2	57.6	41	33.1	30.9	26.17
MMC-3	59.1	48.2	37.6	33.8	29.3

VII. CONCLUSION

Composite materials with strong SE are well-known in aerial applications. The WMCs developed in this work will give SE up to 59.1dB. Electromagnetic shielding is evaluated from different perspectives (20°, 45°, 60°, 70°, and 85°). These MMCs have an SE of more than 55dB. So, these materials are more suitable for protecting aircrafts from lightning strikes. MMCs structure has physical flexibility and less weight, so they are more suited to protect large structures than metal sheets. Compared to metal-coated windows, wire mesh screens offer a unique advantage. The proposed WMMC has lower SE than metallic sheets. According to the literature, using a material with a 50dB shielding efficiency for aircraft surfaces provides good lightning protection. Regarding high-intensity radiation fields, the shielding of prepared compositions may be used in airborne radars and wind turbine systems. Any mix of materials may be employed to satisfy the demands of different applications. A variety of aluminum composite materials may be treated to provide the appropriate shielding.

REFERENCES

- [1] M. A. Uman and V. A. Rakov, "The interaction of lightning with airborne vehicles," *Progress in Aerospace Sciences*, vol. 39, no. 1, pp. 61–81, Jan. 2003, [https://doi.org/10.1016/S0376-0421\(02\)00051-9](https://doi.org/10.1016/S0376-0421(02)00051-9).
- [2] A. Larsson, "The interaction between a lightning flash and an aircraft in flight," *Comptes Rendus Physique*, vol. 3, no. 10, pp. 1423–1444, Dec. 2002, [https://doi.org/10.1016/S1631-0705\(02\)01410-X](https://doi.org/10.1016/S1631-0705(02)01410-X).
- [3] M. Jaroszewski, S. Thomas, and A. V. Rane, "Recent progress in electromagnetic absorbing materials," in *Advanced Materials for Electromagnetic Shielding: Fundamentals, Properties, and Applications*, New York, NY, USA: John Wiley & Sons, 2018, pp. 147–166.
- [4] Y. Guo, Y. Xu, Q. Wang, Q. Dong, X. Yi, and Y. Jia, "Eliminating lightning strike damage to carbon fiber composite structures in Zone 2 of aircraft by Ni-coated carbon fiber nonwoven veils," *Composites Science and Technology*, vol. 169, pp. 95–102, Jan. 2019, <https://doi.org/10.1016/j.compscitech.2018.11.011>.
- [5] M. Gagne and D. Theriault, "Lightning strike protection of composites," *Progress in Aerospace Sciences*, vol. 64, pp. 1–16, Jan. 2014, <https://doi.org/10.1016/j.paerosci.2013.07.002>.

- [6] G. Moona, R. Walia, R. Vikas, and R. Sharma, "Aluminium metal matrix composites: A retrospective investigation," *Indian Journal of Pure and Applied Physics*, vol. 56, pp. 164–175, Jan. 2018.
- [7] Z. M. Gizatullin, R. M. Gizatullin, and M. G. Nuriev, "Technique of physical modeling of lightning strike effects on aircraft," *Russian Aeronautics (Iz VUZ)*, vol. 59, no. 2, pp. 157–160, Apr. 2016, <https://doi.org/10.3103/S106879981602001X>.
- [8] B. V. Ramnath *et al.*, "Aluminium metal matrix composites—A review," *Reviews on Advanced Materials Science*, vol. 38, pp. 55–60, 2014.
- [9] B. Zhang, S. A. Soltani, L. N. Le, and R. Asmatulu, "Fabrication and assessment of a thin flexible surface coating made of pristine graphene for lightning strike protection," *Materials Science and Engineering: B*, vol. 216, pp. 31–40, Feb. 2017, <https://doi.org/10.1016/j.mseb.2017.02.008>.
- [10] V. V. Vani and S. K. Chak, "The effect of process parameters in Aluminum Metal Matrix Composites with Powder Metallurgy," *Manufacturing Review*, vol. 5, 2018, Art. no. 7, <https://doi.org/10.1051/mfreview/2018001>.
- [11] G. Pitchayapillai, P. Seenikannan, K. Raja, and K. Chandrasekaran, "Al6061 Hybrid Metal Matrix Composite Reinforced with Alumina and Molybdenum Disulphide," *Advances in Materials Science and Engineering*, vol. 2016, Nov. 2016, Art. no. e6127624, <https://doi.org/10.1155/2016/6127624>.
- [12] A. Dey and K. M. Pandey, "Characterisation of fly ash and its reinforcement effect on metal matrix composites: A review," *Reviews on Advanced Materials*, vol. 44, pp. 168–181, 2016.
- [13] A. K. Senapati, P. C. Mishra, and B. C. Routara, "Use of Waste Flyash in Fabrication of Aluminium Alloy Matrix Composite," *International Journal of Engineering and Technology*, vol. 6, no. 2, pp. 905–912, 2014.
- [14] U. C. Hasar, "Permittivity Measurement of Thin Dielectric Materials from Reflection-Only Measurements Using One-Port Vector Network Analyzers," *Progress In Electromagnetics Research*, vol. 95, pp. 365–380, 2009, <https://doi.org/10.2528/PIER09062501>.
- [15] A. P. Alegaonkar and P. S. Alegaonkar, "Nanocarbons: Preparation, assessments, and applications in structural engineering, spintronics, gas sensing, EMI shielding, and cloaking in X-band," in *Nanocarbon and its Composites*, A. Khan, M. Jawaid, Inamuddin, and A. M. Asiri, Eds. Sawston, UK: Woodhead Publishing, 2019, pp. 171–285.
- [16] L. F. Liu and Q. S. Zhang, "Analysis of Electromagnetic Shielding Effectiveness of Metal Material," *Advanced Materials Research*, vol. 538–541, pp. 655–659, 2012, <https://doi.org/10.4028/www.scientific.net/AMR.538-541.655>.
- [17] D. Mansson and A. Ellgardt, "Comparing analytical and numerical calculations of shielding effectiveness of planar metallic meshes with measurements in cascaded reverberation chambers," *Progress In Electromagnetics Research C*, vol. 31, pp. 123–135, 2012, <https://doi.org/10.2528/PIERC12061506>.
- [18] P. S. Spandana and P. V. Y. Jayasree, "A Mathematical Approach to the Effect of Mobile Position on Human Head Against RF Radiation," *Progress In Electromagnetics Research C*, vol. 121, pp. 127–144, 2022, <https://doi.org/10.2528/PIERC22051604>.
- [19] P. S. Spandana and P. V. Y. Jayasree, "Numerical Computation of SAR in Human Head with Transparent Shields Using Transmission Line Method," *Progress In Electromagnetics Research M*, vol. 105, pp. 31–45, Jul. 2021.
- [20] K. F. Casey, "Electromagnetic shielding behavior of wire-mesh screens," *IEEE Transactions on Electromagnetic Compatibility*, vol. 30, no. 3, pp. 298–306, Dec. 1988, <https://doi.org/10.1109/15.3309>.
- [21] S. S. Pudipeddi, P. V. Y. Jayasree, and S. G. Chintala, "Polarization Effect Assessment of Sub-6 GHz Frequencies on Adult and Child Four-Layered Head Models," *Engineering, Technology & Applied Science Research*, vol. 12, no. 4, pp. 8954–8959, Aug. 2022, <https://doi.org/10.48084/etasr.5096>.
- [22] H. M. El-Maghrabi, "Electromagnetic Shielding Effectiveness Calculation for Cascaded Wire-Mesh Screens with Glass Substrate," *The Applied Computational Electromagnetics Society Journal*, vol. 33, no. 6, pp. 641–647, 2018.
- [23] L. Zhou *et al.*, "Dielectric properties and electromagnetic interference shielding effectiveness of Al₂O₃-based composites filled with FeSiAl and flaky graphite," *Journal of Alloys and Compounds*, vol. 829, Jul. 2020, Art. no. 154556, <https://doi.org/10.1016/j.jallcom.2020.154556>.
- [24] N. Dong *et al.*, "Fabrication and electromagnetic interference shielding effectiveness of Ti₃Si(Al)₂C₂ modified Al₂O₃/SiC composites," *Ceramics International*, vol. 42, no. 8, pp. 9448–9454, Jun. 2016, <https://doi.org/10.1016/j.ceramint.2016.03.001>.
- [25] L. Zhu *et al.*, "Significantly enhanced electromagnetic interference shielding in Al₂O₃ ceramic composites incorporated with highly aligned non-woven carbon fibers," *Ceramics International*, vol. 45, no. 10, pp. 12672–12676, Jul. 2019, <https://doi.org/10.1016/j.ceramint.2019.03.079>.

Thermodynamic and Performance Assessment of an Innovative Solar-Assisted Tri-Generation System for Water Desalination, Air-Conditioning, and Power Generation

A. Fouda

Department of Mechanical and Materials Engineering
Faculty of Engineering, University of Jeddah
Jeddah, Saudi Arabia
aafoudah@uj.edu.sa

H. F. Elattar

Department of Mechanical and Materials Engineering
Faculty of Engineering, University of Jeddah
Jeddah, Saudi Arabia
hfalattar@uj.edu.sa

Saeed Rubaiee

Department of Mechanical and Materials Engineering
Department of Industrial and Systems Engineering
Faculty of Engineering, University of Jeddah
Jeddah, Saudi Arabia
salrubaiee@uj.edu.sa

Abdullah S. Bin Mahfouz

Department of Chemical Engineering
Faculty of Engineering, University of Jeddah
Jeddah, Saudi Arabia
asbinmahfouz@uj.edu.sa

Abdullah M. Alharbi

Department of Industrial and Systems Engineering
Faculty of Engineering, University of Jeddah
Jeddah, Saudi Arabia
amealharbi@uj.edu.sa

Received: 3 August 2022 | Revised: 14 August 2022 | Accepted: 15 August 2022

Abstract—An innovative tri-generation system powered by solar energy for water desalination, air-conditioning, and electrical power production is proposed and investigated numerically in this paper. The system is designed for small and medium-sized buildings in countries that are rich in solar energy but poor in fossil fuels and water resources. The devised system includes a solar system (evacuated tube collectors and thermal energy storage unit), an Organic Rankine Cycle (ORC), a Humidification and Dehumidification (HDH) water desalination system, and a Desiccant Cooling System (DCS). A detailed parametric study of the developed system is carried out for a wide range of operating conditions and design parameters on the system's productivity and performance parameters. It is found that: (i) The proposed tri-generation system can deliver high electrical power, fresh water, space cooling capacity, and Energy Utilization Factor (EUF) of 104.5kW, 72.37kg/h, 25.48kW, and 0.2643 respectively. In comparison to the basic system, the EUF_{imp} and ASC_{sav} parameters were enhanced having maximum values of 69.9% and 41.14% respectively. General numerical correlations derived from the numerical data can predict the system productivity and performance parameters within reasonable error.

Keywords—tri-generation; organic Rankine cycle; humidification-dehumidification; desiccant cooling system

I. INTRODUCTION

Due to the increasing population and pollution, the needs for fresh water productivity, electricity generation, and air conditioning have dramatically increased. The heat rejection to the environment can be overcome by double-use systems that integrate desalination and power systems, in which the low-grade heat rejected from the power cycle is used to drive the desalination system. This significantly improves the energy efficiency of the combined plant [1-7]. On the other hand, dual solar-powered systems can play a key part in reducing CO₂ emissions. In addition, the integration of Concentrated Solar Power (CSP) and cogeneration systems can reduce the unit product costs of water and electricity with current developments in CSP technology [8]. Solar electricity and desalination systems can offer economic solutions to meet the increasing demands for both electricity and freshwater in dry arid regions such as the Gulf and MENA (Middle East and North Africa). To face the problem of rising temperatures, it is also necessary to adapt the air to achieve thermal comfort,

which can be accomplished by using a desiccant air conditioner, which is distinguished by not producing polluting gases such as chlorofluorocarbons, which are produced by traditional air conditioning systems. A hybrid system of air conditioning and desalination units was employed to lower the use of electricity in desalination and air conditioning systems. In hybrid air conditioners, renewable energy is also used to minimize the rate of power consumption. Several researchers combined air conditioning and refrigeration systems with HDH water desalination systems in different configurations to obtain hybrid systems for cooling and air conditioning [9–12]. The effects of system configuration, operating conditions, and geometric parameters have been investigated. Authors in [13] proposed a low-energy HDH and A/C hybrid system using an efficient design of dehumidifier (strips-finned helical coil) and packing pad material (cellulose paper in bee-hive structure). The integrated cooling or heating, fresh water generation and power systems, known as tri-generation plants, are an efficient method intended to have a lower consumption of primary energy and reduce greenhouse gas emissions. The processes and technologies for trigeneration that are currently available can provide a number of benefits [14, 15]: increasing global energy efficiency while expanding the use of renewable energy sources, lowering environmental impact in terms of carbon dioxide equivalent emissions, and reducing electrical system overloads and blackouts. Tri-generation techniques are used in several areas, including buildings, industries, and manufacturing [16].

Few researchers have concentrated on tri-generation system modeling. Previous research has looked into multi-generation facilities for electricity, cooling or heating, and freshwater generation that are combined with renewable energy resources. Authors in [17] investigated a multi-generation system that generates electrical power, freshwater, space cooling, and industrial heating using geothermal, solar, and ocean thermal energy conversion as energy inputs. Authors in [18] created a tri-generation facility that includes a flat plate solar collector field, a Kalina electrical power generation cycle, and a multi-stage desalination unit. A thermodynamic analysis of a polygeneration system comprising a Solar Power System (SPS), a Multi Effect Desalination (MED) system, and an Absorption Refrigeration System (ARS) was given in [19]. Solar energy is used to power the plant, which is supplemented by a natural gas heater. The impacts of various design and operating parameters on the plant's energy and exergetic parameters are investigated using a parametric study. Authors in [20] created a new tri-generation system for freshwater, electricity, and cooling production. A HDH unit is used as a binary cycle in this trigeneration system. According to the literature review, there are several cogeneration systems integrated with ORC/HDH and DCS/HDH, and a few trigeneration systems for power, freshwater, and cooling load integrated with MED/SRC/ARS and HDH/ORC/ECC, including CPVT, biogas, biomass boilers, and geothermal wells. So, tri-generation systems have not been extensively investigated up to now. For this aim, a new trigeneration set-up on the basis of an ORC, a DCS, and a HDH unit is designed to generate power, cooling, and freshwater. ORC power generation is only appropriate for small-scale applications and

low operating temperatures [21]. Low-temperature energy utilization (e.g. waste energy, solar energy), simplicity, and low operating and installation costs are advantages of HDH water desalination. A desiccant air conditioner is a type of air conditioner that does not emit polluting gases like chlorofluorocarbons. CPVT, on the other hand, is an appealing technology due to its efficiency, but its dependability and economic feasibility have yet to be proven [22]. These restrictions inspire the authors to investigate the design of a tri-generation system that can supply small-scale continuous daylight electrical power, cooling, and desalination using solar energy sources.

The energy analysis of a tri-generation system comprising evacuated tube collectors, a thermal energy storage unit, an ORC, a HDH, and a DCS is presented in the current study. To the best of our knowledge, no previous research has looked into such a complex system. The paper will present the following that will help in the design of the proposed system: (i) Extensive energy mathematical modeling, (ii) the effect of various design and operating parameters on the proposed system's performance, (iii) evaluation of the system and comparison with the basic system, (iv) numerical correlations for the system's productivity and performance parameters in terms of the studied parameters.

II. SYSTEM DESCRIPTION

The proposed tri-generation system, depicted in Figure 1, can produce electricity, cooling, and potable water by combining ORC with DCS and an HDH desalination unit. The solar system includes an evacuated tube solar collector and a thermal storage tank. For the solar field loop, a thermal oil (Therminol-VP1) is used as a working fluid because it is able to remain in the liquid phase in temperatures up to 400°C [23]. The system can be decomposed into four main loops: two closed loops (solar fluid loop and ORC fluid loop) and two open loops (air loop and water loop). In the solar field loop, evacuated tubes solar collectors are used to gather the solar radiation through which the thermal oil flows, which is used to charge the storage tank during the sunlight period (state points 23 and 24). The thermal storage tank is used to supply the proposed system with constant demand during daylight. The thermal oil is used to transfer heat from/to the thermal storage tank to/from the ORC (i.e. evaporator) at state points 25 and 26. In the closed ORC fluid loop, heat is transferred from the secondary fluid to the ORC working fluid through the evaporator where it is boiled and superheated at state point 19. Then, the superheated ORC fluid expands in the turbine, producing the required electrical load in a generator. Low-grade superheated organic fluid (state point 20) is rejected from the turbine and sent to the condenser (triple channel heat exchanger) where it gets condensed at state point 17 and supplies the DCS and HDH units with the required heat to keep the temperature of state points 8 and 15 the same. After that, the ORC liquid is pressurized by the pump and sent to the evaporator (state point 18) for a gain and the cycle is completed. For the ORC in the present study, n-Octane was selected as the working fluid since it has the best performance among other organic fluids [24] due to its thermodynamic properties (e.g. $T_{cr} = 296.2^{\circ}\text{C}$ and $P_{cr} = 2497\text{kPa}$).

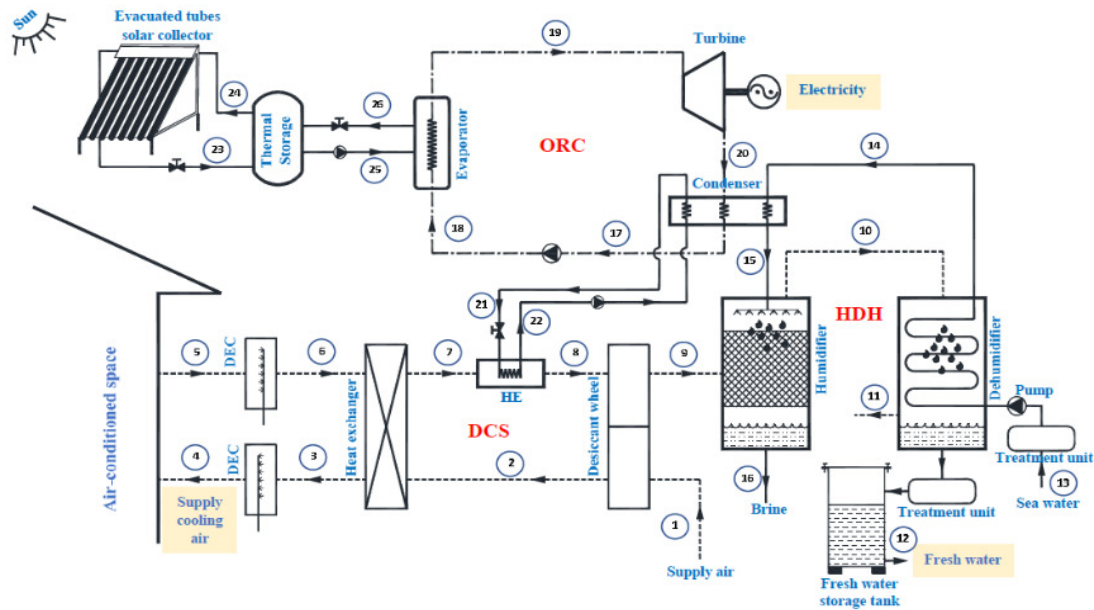


Fig. 1. Proposed tri-generation system layout.

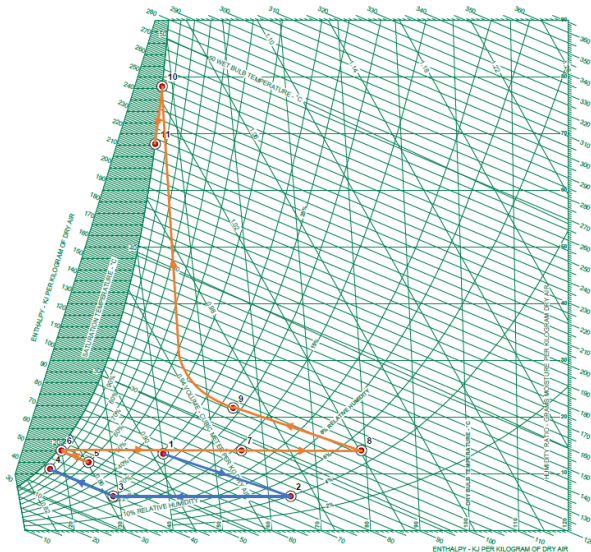


Fig. 2. Proposed tri-generation system psychrometric cycles.

In the air loop, process air enters the desiccant wheel at state point 1, where it is dehumidified and heated to state point 2. The process air input to the heat exchanger is at state point 2, and it is sensibly cooled to state point 3. After that, the process air enters the direct evaporative cooler at state point 3, where it is cooled and humidified before being delivered to the air-conditioned space at state point 4. At state point 5, the return air from the room inlet is directed to the direct evaporative cooler, where the air is cooled and humidified to state point 6. At this point, the return air inlet to the heat exchanger cools the process supply air, where the return air is sensibly heated to state point 7. At state point 7, the return air (regeneration air) goes through the heat exchanger, which recovers a portion of the ORC condenser heat, and the regeneration air is sensibly heated to the desired regeneration temperature at state point 8. After that, the regeneration air from state point 8 enters the

reactivation portion of the desiccant wheel, where it is cooled and humidified to state point 9 via the desiccant wheel. The humidifier receives the hot regeneration air from the desiccant wheel on a continual basis, humidifying it at state point 10 before flowing to the dehumidifier, where it is cooled and dehumidified at state point 11. In Figure 2, the psychrometric cycle depicts the passage of air through the proposed tri-generation system.

In the water loop, sea water at state point 13 is pumped by a feed water pump to the dehumidifier coil in order to dehumidify the process air for producing fresh water. The seawater exits the dehumidifier at state point 14, where it is preheated during the air dehumidification process. This preheated water flows through an ORC condenser and the heat recovered from the condenser is used to reheat the sea water to state point 15, and then it passes through the humidifier to humidify the air, where part of the water evaporates and is carried out of the humidifier by the incoming air, and the remaining part is drained as a brine at state point 16.

III. MATHEMATICAL MODEL AND THERMODYNAMICS ANALYSIS

The proposed tri-generation system is powered by solar energy for water desalination, air-conditioning, and power generation and it is integrated with a thermal energy storage unit. The system is simulated using the developed computer programs in C++ programming language and Engineering Equation Solver (EES) software based on the energy and mass balances for all system components. The tri-generation system is divided into three subsystems: ORC, HDH, and DCS in order to calculate the thermodynamic properties and subsystems and the whole system performance. In the simulating model procedure, the energy and mass conservation and first and second laws of thermodynamics are applied on each system components. The developed model is based on the following assumptions:

- All system processes are considered in steady state conditions.
- Leakage (air/water) in the system components is neglected.
- The temperatures of the blowdown water leaving the humidifier and the air wet-bulb temperature are equal.
- The mass flow rates of process air ($\dot{m}_{p,a}^*$), return air ($\dot{m}_{R,a}^*$), and water (\dot{m}_w^*) are equal.
- The temperatures of the air (t_8) and water (t_{15}) leaving the condenser of ORC are equal.
- The temperatures of the fresh water and the air wet-bulb at the dehumidifier exit are equal.
- The ORC fluid's state at the turbine inlet is superheated based on the different values of P_{18} and t_{19}
- The electrical generator efficiency of the ORC is 95%.
- The isentropic efficiency of the turbine and the pump is 75%.
- The effectiveness of all the heat exchangers is 80%.
- The efficiency of direct evaporative coolers used in the DCS is 90%.

In order to investigate and present the system performance, the Energy Utilization Factor (EUF), electrical power generation (\dot{W}_{net}^*), thermal efficiency of the ORC (η_{ORC}), fresh water productivity (\dot{m}_{fresh}^*), Gain Output Ratio (GOR), space cooling capacity ($\dot{Q}_{cooling}^*$), the coefficient of performance of DCS (COP_{DCS}), space supply air temperature and humidity ratio (t_4 and w_4), and area of solar collectors (A_{PSC}) are considered. In the present tri-generation system, electrical power, space cooling capacity, and fresh water productivity are being produced simultaneously from the single solar energy source.

A. Solar Radiation

The technique and complete calculation for obtaining the daily average solar intensity I_T for Jeddah are given in [25]. The I_T incidents on the surfaces of the air and water solar collectors (south oriented with a zero-tilt angle) are calculated for the weather conditions of Jeddah city, KSA on July 21 by regression analysis and are given by:

$$I_T (W/m^2) = 10602.89 - 4332.31\tau + 614.44\tau^2 - 34.45\tau^3 + 0.66\tau^4 \quad (1)$$

where τ represents the hour of day measured from 7:00 to 13:00. In the current work the daily average solar intensity is taken as $I_{T,avg,daily} = 750 W/m^2$.

B. Organic Rankine Cycle

- Evaporator energy balance:

$$\dot{Q}_{Evap}^* = \dot{m}_{ORC}^* (h_{19} - h_{18}) \quad (2)$$

$$\dot{m}_{ORC}^* (h_{19} - h_{18}) = \dot{m}_{oil}^* (h_{25} - h_{26}) \quad (3)$$

$$\eta_{SC,PS} = \frac{\dot{Q}_{Evap}^*}{I_{T,avg,daily} A_{PSC}} \quad (4)$$

where the average annual value of thermal efficiency of the evacuated tube solar collector is 63.2% [75].

- Condenser energy balance:

$$\dot{Q}_{Cond}^* = \dot{m}_{ORC}^* (h_{20} - h_{17}) \quad (5)$$

$$\varepsilon_{HE} = \left(\frac{\dot{m}_w^* (h_{15} - h_{14}) + \dot{m}_{R,a}^* (h_8 - h_7)}{\dot{m}_{ORC}^* (h_{20} - h_{17})} \right) \quad (6)$$

$$MR = \frac{\dot{m}_{ORC}^*}{\dot{m}_{R,a}^* + \dot{m}_w^*} \quad (7)$$

- Turbine power:

$$\dot{W}_t^* = \dot{m}_{ORC}^* (h_{19} - h_{20}) \eta_t \eta_g \quad (8)$$

- Pump power:

$$\dot{W}_p^* = \dot{m}_{ORC}^* v_{17} (P_{18} - P_{17}) / \eta_p \quad (9)$$

$$\dot{W}_p^* = \dot{m}_{ORC}^* (h_{18,a} - h_{17}) \quad (10)$$

- ORC net power and thermal efficiency:

$$\dot{W}_{net}^* = \dot{W}_t^* - \dot{W}_p^* \quad (11)$$

$$\eta_{ORC} = \frac{\dot{W}_{net}^*}{\dot{Q}_{Evap}^*} \quad (12)$$

C. Desiccant Cooling System

The desiccant wheel is the main component of the DCS. The model developed in [27] is carried out in the present work to simulate the desiccant wheel. The related energy balance and governing equations for the components of DCS are given below.

- Combined potential of the desiccant wheel:

$$F_{1,i} = \left[-\frac{2865}{(t_i + 273.15)^{1.49}} \right] + 4.344 [w_i / 1000]^{0.8624} \quad (13)$$

$$F_{2,i} = \left[\frac{(t_i + 273.15)^{1.49}}{6360} \right] - 1.127 [w_i / 1000]^{0.07969} \quad (14)$$

- Desiccant wheel's efficiency:

$$\eta_{F1} = \frac{F_{1,2} - F_{1,1}}{F_{1,8} - F_{1,1}} \quad (15)$$

$$\eta_{F2} = \frac{F_{2,2} - F_{2,1}}{F_{2,8} - F_{2,1}} \quad (16)$$

The efficiencies of the desiccant wheel are considered to be at the high level and about $\eta_{F1} = 0.05$ and $\eta_{F2} = 0.95$ [28].

- Energy and mass balances of the desiccant wheel:

$$\dot{m}_{P,a} (h_2 - h_1) = \dot{m}_{R,a} (h_8 - h_9) \quad (17)$$

$$\dot{m}_{P,a} (w_1 - w_2) = \dot{m}_{R,a} (w_9 - w_8) \quad (18)$$

- Heat exchanger:

$$\dot{m}_{P,a} c_{p,ma} (t_2 - t_3) = \dot{m}_{R,a} c_{p,ma} (t_7 - t_6) \quad (19)$$

$$\varepsilon_{HE} = \frac{\dot{m}_{P,a} c_{p,ma} (t_2 - t_3)}{C_{\min} (t_2 - t_6)} \quad (20)$$

where $C_{\min} = \min\{\dot{m}_{P,a} c_{p,ma}, \dot{m}_{R,a} c_{p,ma}\}$.

- Direct evaporative coolers:

$$\eta_{DEC(P,a)} = \frac{t_3 - t_4}{t_3 - t_{3,wb}} \quad (21)$$

$$\eta_{DEC(P,a)} = \frac{w_4 - w_3}{w_{4,ideal} - w_3} \quad (22)$$

$$\eta_{DEC(R,a)} = \frac{t_5 - t_6}{t_5 - t_{5,wb}} \quad (23)$$

$$\eta_{DEC(R,a)} = \frac{w_6 - w_5}{w_{6,ideal} - w_5} \quad (24)$$

- Regeneration energy, space cooling capacity, and coefficient of performance:

$$\dot{Q}_{in,DCS} = \dot{m}_{R,a} (h_8 - h_7) \quad (25)$$

$$\dot{Q}_{cooling} = \dot{m}_{P,a} (h_5 - h_4) \quad (26)$$

$$COP_{DCS} = \frac{\dot{Q}_{cooling}}{\dot{Q}_{in,DCS}} \quad (27)$$

D. Humidification Dehumidification System (HDH)

The energy balance of the humidifier is given as:

$$\dot{m}_{R,a} (h_{10} - h_9) = \dot{m}_w h_{15} - \dot{m}_{brine} h_{16} \quad (28)$$

where $\dot{m}_{brine} = \dot{m}_w - \dot{m}_{makeup}$.

The mass flow rate of the makeup water (sea or brackish water) supplied to the system is given as:

$$\dot{m}_{makeup} = \dot{m}_{R,a} (w_{10} - w_9) \quad (29)$$

The energy balance of the dehumidifier is given as:

$$\dot{m}_{R,a} (h_{10} - h_{11}) = \dot{m}_w (h_{14} - h_{13}) + \dot{m}_{fresh} h_{12} \quad (30)$$

$$\varepsilon_{deh} = \frac{\dot{m}_w c_{p,w} (t_{14} - t_{13})}{C_{\min} (t_{10} - t_{13})} \quad (31)$$

where $h_{12} = c_{p,w} t_{11}$ and $C_{\min} = \min\{\dot{m}_w c_{p,w}, \dot{m}_{R,a} c_{p,ma}\}$.

The condensate water mass flow rate leaving the dehumidifier is calculated as:

$$\dot{m}_{fresh} = \dot{m}_{R,a} (w_{10} - w_{11}) \quad (32)$$

The gain output ratio for the system is given by:

$$GOR = \frac{\dot{m}_{fresh} h_{fg}}{\dot{m}_w (h_{15} - h_{14}) + \dot{m}_{R,a} (h_9 - h_1)} \quad (33)$$

E. System Performance Parameters and Evaluation

The EUF of the proposed tri-generation and its corresponding basic system are expressed below:

$$EUF_{PS} = \frac{\dot{m}_{fresh} h_{fg} + \dot{Q}_{cooling} + W_{net}}{\dot{Q}_{Evap}} \quad (34)$$

$$EUF_{BS} = \frac{\dot{m}_{fresh} h_{fg} + \dot{Q}_{cooling} + W_{net}}{\dot{Q}_{Evap} + \dot{m}_w (h_{15} - h_{14}) + \dot{m}_{R,a} (h_8 - h_7)} \quad (35)$$

$$\eta_{SC,BS} = \frac{\dot{Q}_{Evap} + \dot{m}_w (h_{15} - h_{14}) + \dot{m}_{R,a} (h_8 - h_7)}{I_{T,avg,daily} A_{bSC}} \quad (36)$$

For evaluating the system performance, the EUF improvement and the saving in the area of the solar collectors can be expressed as:

$$EUF_{imp} = \frac{EUF_{PS} - EUF_{BS}}{EUF_{BS}} \quad (37)$$

$$A_{SC,sav} = \frac{A_{SC,BS} - A_{SC,PS}}{A_{SC,BS}} \quad (38)$$

The system governing equations are solved by using C++ and EES to calculate the system performance and productivity parameters for different ranges of design and operating conditions as given in Table I.

TABLE I. STUDIED AND OPERATING PARAMETER VALUES

Parameter	Value
Turbine inlet temperature, t_{19}	170-195°C
Ambient air inlet temperature, t_1	25-45°C
Ambient air inlet humidity, w_1	12-20g/kg
Sea water inlet temperature, t_{13}	15-25°C
Evaporation pressure of ORC, P_{18}	200-400kPa
Condensation pressure of ORC, P_{17}	5-20kPa
ORC fluid mass flow rate, \dot{m}_{ORC}	0.5-1.3kg/s
Mass flow rate ratio, MR	0.1-0.6

IV. MODEL VALIDATION

To approve the developed thermodynamic models in the present work and to determine their degree of accuracy, model validation is applied and the results of the current work are compared with those reported in the literature. The validation of the current thermodynamic models with previously published data in [27, 29, 30] for HDH, ORC, and DCS subsystems is shown in Figure 3. It can be seen that there is good agreement between the current study's results and those previously reported in the literature.

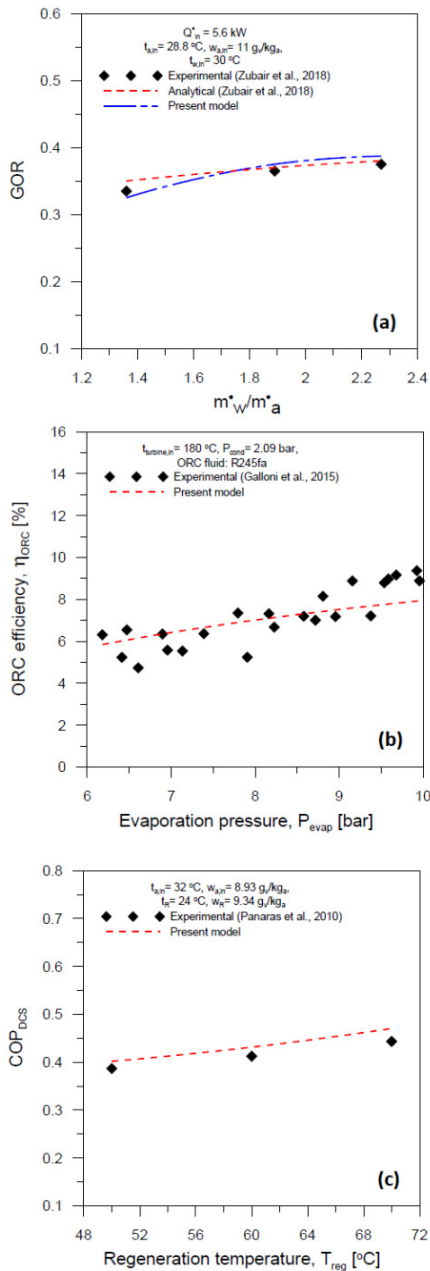


Fig. 3. Validation of the present model with the previously published data for (a) HDH, (b) ORC, (c) DCS.

V. RESULTS AND DISCUSSION

A comprehensive parametric study was conducted to study the effects of operating parameters on the performance of the proposed tri-generation system. For this purpose, the effects of turbine inlet temperature (t_{19}) of the ORC, ambient air inlet temperature and humidity ratio (t_1 and w_1), evaporation pressure (P_{18}) of the ORC, condensation pressure (P_{17}) of the ORC and mass flow rate ratio (MR) on the main productivity and performance parameters (\dot{W}_{net} , \dot{h}_{ORC} , \dot{m}_{fresh} , GOR, $\dot{Q}_{cooling}$, COP_{DCS} , t_4 , w_4 , EUF_{PS} , and A_{PSC}) in addition to system assessment parameters (EUF_{imp} , $A_{SC,sav}$) are presented in Figures 4-10. The other parameters remain constant when a certain operating parameter is changed, in order to examine its

effect. The performance parameters of the tri-generation system are investigated and evaluated with n-Octane as the working fluid in the ORC.

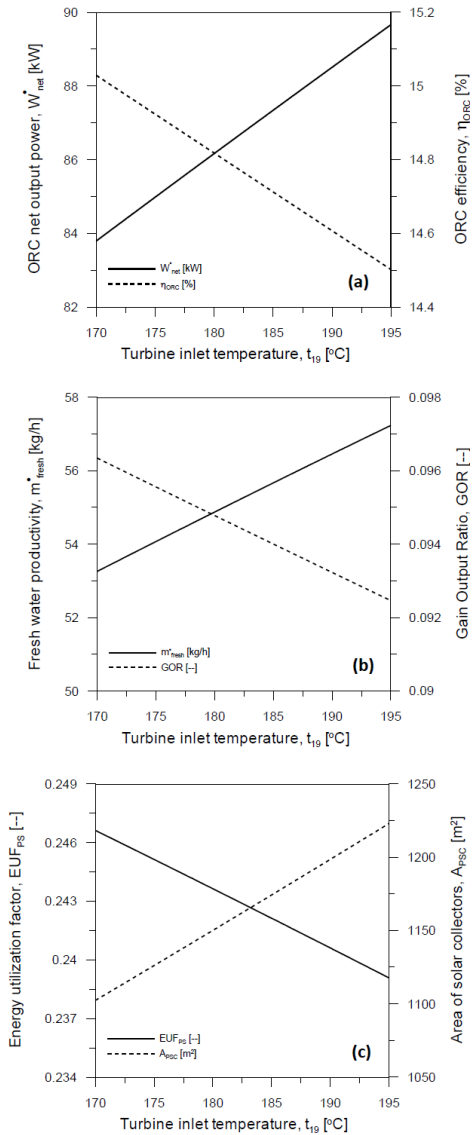


Fig. 4. Influence of t_{19} on the proposed system performance parameters.

A. Effects of Turbine Inlet Temperature

Figure 4 shows the effects of turbine inlet temperature (t_{19}) of the ORC on the main productivity and performance parameters of the proposed tri-generation system. t_{19} is increased from the fluid's saturated vapour temperature (170°C) to the superheated temperature (195°C). As shown in Figure 4, increasing t_{19} raises \dot{W}_{net} , \dot{m}_{fresh} , and A_{PSC} . The increase of the ORC turbine power, required input solar energy, and reject energy of the ORC condenser with increasing t_{19} , leading to the increase of ORC net output power, required area of solar collectors, humidification capacity of the air in the humidifier, and space cooling capacity. Also, the increase in heat input to ORC, HDH, and DCS with increasing turbine

inlet temperature, leads to the reduction of h_{ORC} , GOR , and EUF_{PS} . It is found that the highest values of \dot{W}_{net} , h_{ORC} , \dot{m}_{fresh} , GOR , EUF_{PS} , and A_{PSC} are 89.66kW, 15.03%, 57.23kg/h, 0.09634, 0.2466, and 1223m² respectively, while their lowest are 83.8kW, 14.5%, 53.26kg/h, 0.09246, 0.2391, and 1102m². Furthermore, increasing t_{i9} from 170°C to 195°C increased net output power, fresh water productivity, and space cooling capacity by 7%, 7.5%, and 10.3% respectively.

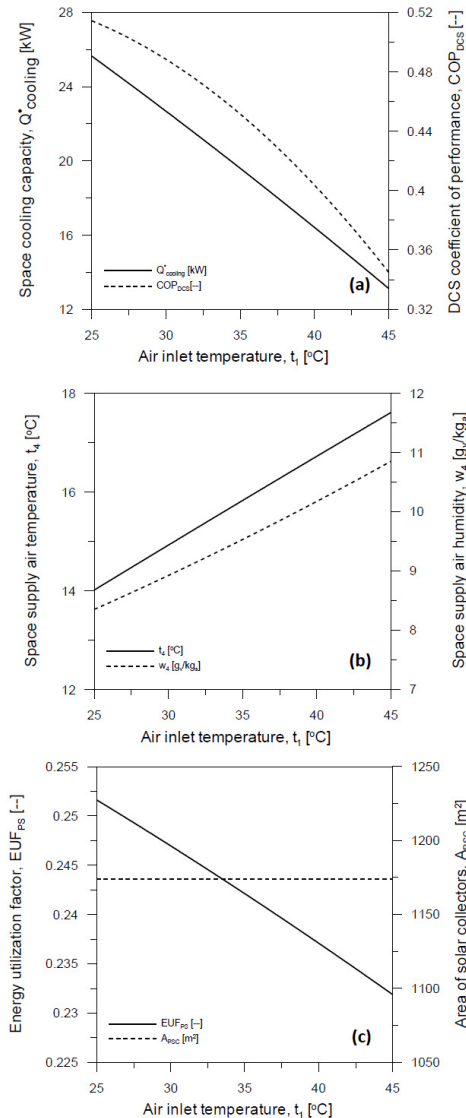


Fig. 5. Influence of t_i on the proposed system performance parameters.

B. Effect of Air Inlet Temperature

The effect of the air inlet temperature on the main productivity and performance parameters of the proposed tri-generation system are given in Figure 5, which shows that as the air inlet temperature rises, the $\dot{Q}_{cooling}$, COP_{DCS} , and EUF_{PS} decrease while t_4 and w_4 increase, due to the increased required regeneration energy in DCS with increasing air inlet temperature, while the heat rejected in the condenser of ORC is fixed, leading to poor DCS performance. In addition, the

highest obtained values of $\dot{Q}_{cooling}$, COP_{DCS} , t_4 , w_4 and EUF_{PS} are 25.64kW, 0.5146, 17.61°C, 10.85g/kg_a and 0.2516 respectively, while the lowest are 13.13kW, 0.3446, 14.02°C, 8.354g/kg_a and 0.2319, where A_{PSC} is kept constant at 1174m². Furthermore, the fresh water productivity, \dot{m}_{fresh} , improved by 2.2% and the space cooling capacity, $\dot{Q}_{cooling}$, dropped by 48.9% with an increase of t_i from 25°C to 45°C.

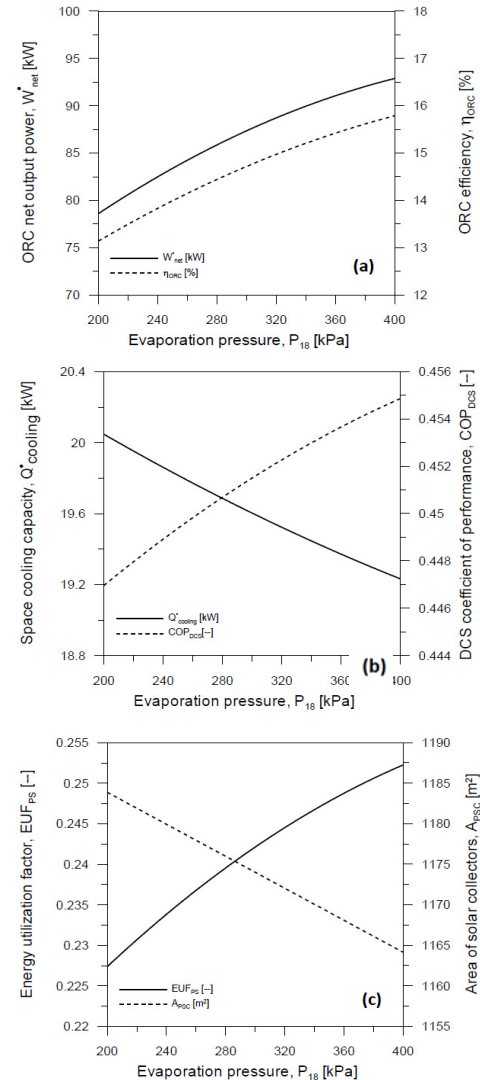


Fig. 6. Influence of P_{18} on the proposed system performance parameters.

C. Effect of Evaporation Pressure

The influence of the ORC evaporation pressure on the main productivity and performance parameters of the proposed tri-generation system is presented in Figure 6. The increase of \dot{W}_{net} , h_{ORC} , COP_{DCS} , and EUF_{PS} with the rise of the evaporation pressure can be seen. This occurs due to the decrease in heat input in the evaporator and heat reject in the condenser of ORC and the increased output power of the turbine. Figures 5(b)-(c) show the decrease of $\dot{Q}_{cooling}$ and A_{PSC} with the increase of the evaporation pressure. This can be attributed to the decrease of input heat to the ORC evaporator and the rejected heat from the condenser, which leads to a decrease in the humidification

capacity of the air inside the humidifier and the fresh water yield in the dehumidifier. Hence, lower fresh water production rate can be obtained. Additionally, this reduces the regeneration energy of DCS and the required area of solar collectors. The highest obtained values of \dot{W}_{net} , h_{ORC} , $\dot{Q}_{cooling}$, COP_{DCS} , EUF_{PS} , and A_{PSC} are 92.97kW, 15.8%, 20.05kW, 0.4469, 0.2524, and 1184m² respectively, while their lowest values are 87.34kW, 13.12%, 19.23kW, 0.4549, 0.2272, and 1164m². Furthermore, \dot{W}_{net} improved by 6.4%, and \dot{m}_{fresh} and $\dot{Q}_{cooling}$ dropped by 3.2% and 4.2% respectively when P_{17} increased from 200 to 400kPa.

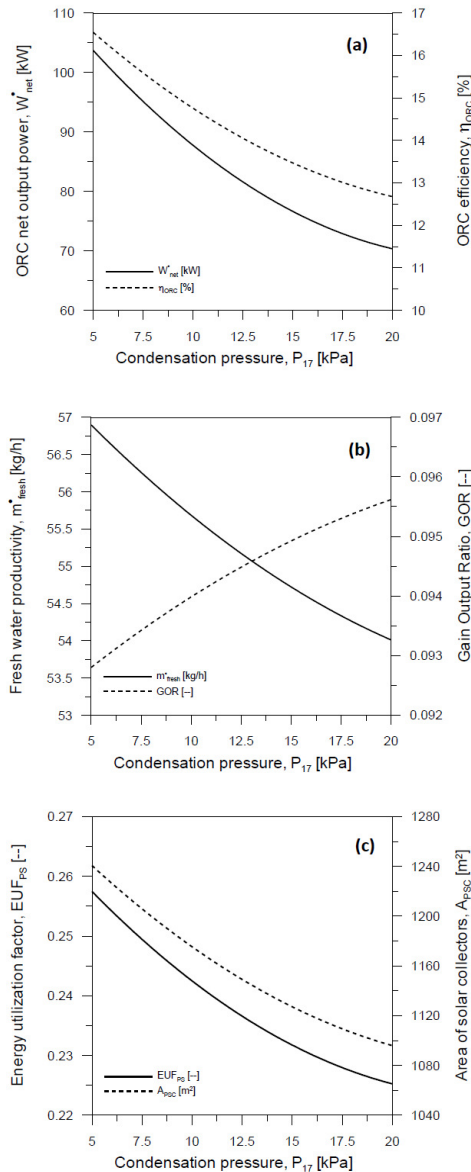


Fig. 7. Influences of P_{17} on the proposed system performance parameters.

D. Effects of ORC Condensation Pressure

Figure 7 shows the influence of ORC condensation pressure (P_{17}) on the proposed system performance and productivity parameters. \dot{W}_{net} , h_{ORC} , \dot{m}_{fresh} , EUF_{PS} , and A_{PSC} decrease as P_{17} increases. The reduction in net output power with increasing

P_{17} is caused by the reduction in enthalpy difference across the turbine that leads to a reduction in ORC thermal efficiency. Decreasing the fresh water rate with rising condenser pressure is expected because of the reduced amount of heat recovered from the condenser to water and air streams before entering the humidifier, which lessens the amount of water evaporation and consequently reduces the amount of fresh water produced at the dehumidifier. The reduction in EUF_{PS} is attributed to the reducing of \dot{W}_{net} and \dot{m}_{fresh} with increasing P_{17} , which overcomes the reduction in the total input power of the system. The reduction in A_{PSC} with rising P_{17} is due to the reduction in the heat added to the evaporator at the same solar intensity input to the solar collectors. While Figure 7(b) displays increasing GOR with rising P_{17} , the increase in GOR is due to a decrease in both fresh water production rate and heating input power to the system that is needed to raise the temperatures of seawater and air to the humidifier inlet. The disadvantage of a decrease in fresh water production rate cannot compensate for the benefit of a decrease in system input power. It is observed that the highest \dot{W}_{net} , \dot{m}_{fresh} , and EUF_{PS} obtained at $P_{17} = 5$ kPa are 104.5kW, 56.9 kg/h, and 0.2582 respectively, while the A_{PSC} reduction is 11.98% when the condenser pressure increases from 5 to 20kPa.

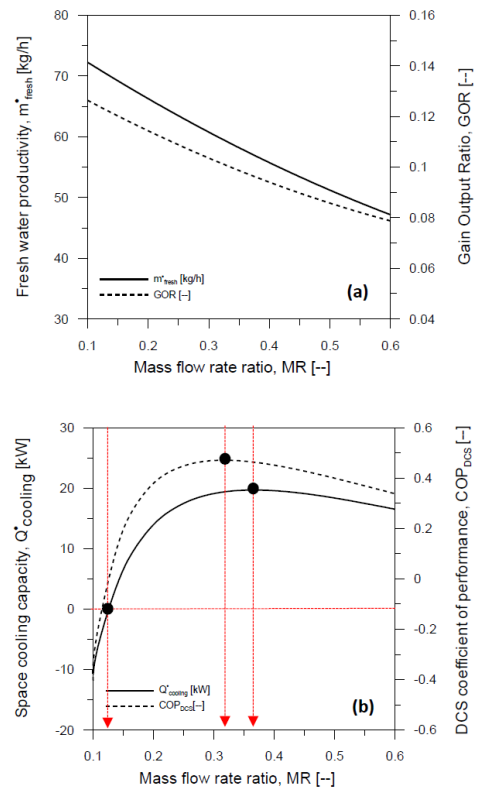


Fig. 8. Influence of MR on the proposed system performance parameters.

E. Effects of Mass Flow Rate Ratio

Figure 8 shows the influence of mass flow rate ratio (MR) on the proposed system performance and productivity parameters. Figure 8(a) shows the decrease of \dot{m}_{fresh} and GOR with increasing MR. Increasing MR means lowering both the air and seawater mass flow rates equally (i.e. $\dot{m}_a = \dot{m}_w$) while

keeping \dot{m}_{ORC} constant and equal to 1kg/s, results in a lower rate of evaporation in the humidifier and a lower rate of condensation in the dehumidifier, and thus lower GOR. Figure 8(b) shows that $\dot{Q}_{cooling}$ and COP_{DCS} increase with increasing MR until they reach their highest values and then they decrease with increasing MR. Increasing MR has two opposing effects: i) it decreases the air mass flow rate and ii) it decreases the supply air enthalpy to the conditioned space, increasing the enthalpy difference across the conditioned space. As observed in Figure 8(b), for MR=0.38, the increase in enthalpy difference across the conditioned space overcomes the reduction in air mass flow rate, which results in higher $\dot{Q}_{cooling}$ and subsequently COP_{DCS} , and vice versa for MR>0.38. Furthermore, MR=0.125 leads to negative cooling capacity, which isn't recommended for cooling and dehumidifying applications through the conditioned space. It's noticed from Figure 8 that the maximum \dot{m}_{fresh} and $\dot{Q}_{cooling}$ obtained are 72.13kg/h and 19.7kW and \dot{m}_{fresh} improved by 52.7% when MR dropped from 0.6 to 0.1.

F. Effects of Ambient Air Humidity Ratio

Figure 9 depicts the effects of ambient air humidity ratio (w_I) variation with MR on the proposed system performance parameters. $\dot{Q}_{cooling}$, COP_{DCS} , and EUF_{PS} increase with increasing MR until they reach their highest values, and then they decrease with increasing MR for any w_I . Also, it is found that they drop with increasing w_I for any MR. Increasing w_I for the same MR increases the enthalpy of supply air, which reduces the air enthalpy difference through the conditioned space, which adversely effects the conditioned space cooling capacity as well as COP_{DCS} as seen in Figures 9(a)-(b). Moreover, the system operation conditions with MR less than 0.11, 0.15, 0.2, 0.25, at $w_I = 14, 16, 18, \text{ and } 20 \text{ g/kg}_a$ respectively, are not recommended for cooling and dehumidifying applications due to the negative cooling capacity for the conditioned space. Furthermore, the highest values of $\dot{Q}_{cooling}$ that can be obtained are 26.46, 21.65, 17.93, 14.97, and 12.47kW at MR = 0.2667, 0.3222, 0.3778, 0.4889, 0.5444, and $w_I = 12, 14, 16, 18, \text{ and } 20 \text{ g/kg}_a$ respectively. While increasing w_I causes a decrease in EUF_{PS} because total system power output decreases when compared to the total system input power. Increasing w_I causes a decrease in $\dot{Q}_{cooling}$ and an increase in \dot{m}_{fresh} but \dot{W}_{net} doesn't change, and the increase in \dot{m}_{fresh} can't compensate for the reduction in $\dot{Q}_{cooling}$, which results in an adverse effect on EUF_{PS} as shown in Figure 9(c). At MR= 0.19, 0.24, 0.2667, 0.3222, 0.3778, and $w_I = 12, 14, 16, 18, \text{ and } 20 \text{ g/kg}_a$, the optimum EUF_{PS} values are 0.2643, 0.2526, 0.2435, 0.2356, and 0.2286. Additionally, w_I has no effect on the A_{PSC} due to the independence of w_I on the heating energy needed at the ORC evaporator.

G. System Assessment and Evaluation

To the best of our knowledge there are no tri-generation systems for power generation, A/C, and freshwater production systems available in the literature using ORC, DCS, and HDH combined integrated systems with the same operating conditions. Therefore, the performance of the proposed system is compared with the performance of a basic tri-generation system in which the needed heating sources for the three subsystems are taken separately from one source (i.e. solar

collector system) that gathers the whole three subsystems into one basic tri-generation system, and the used system performance parameters are EUF_{BS} and A_{BSC} (see (34)-(35)). Therefore, the proposed system can be evaluated and assessed at different significant influencing operating parameters (t_{I9} , P_{I8} , and P_{I7}) by using two important dimensionless performance and design parameters: Energy Utilization Factor improvement, EUF_{imp} (36), and solar collector area saving $A_{SC,sav}$ (37). As seen in Figures 10(a)-(b), EUF_{imp} and $A_{SC,sav}$ are enhanced with increasing t_{I9} and P_{I7} , due to the prevailing total energy output increment and solar collector area reduction of the proposed system than the basic system with increasing t_{I9} and P_{I7} , and the maximum values of EUF_{imp} that can be obtained are 68.4% and 69.9% at $t_{I9} = 195^\circ\text{C}$ and $P_{I7} = 20\text{kPa}$.

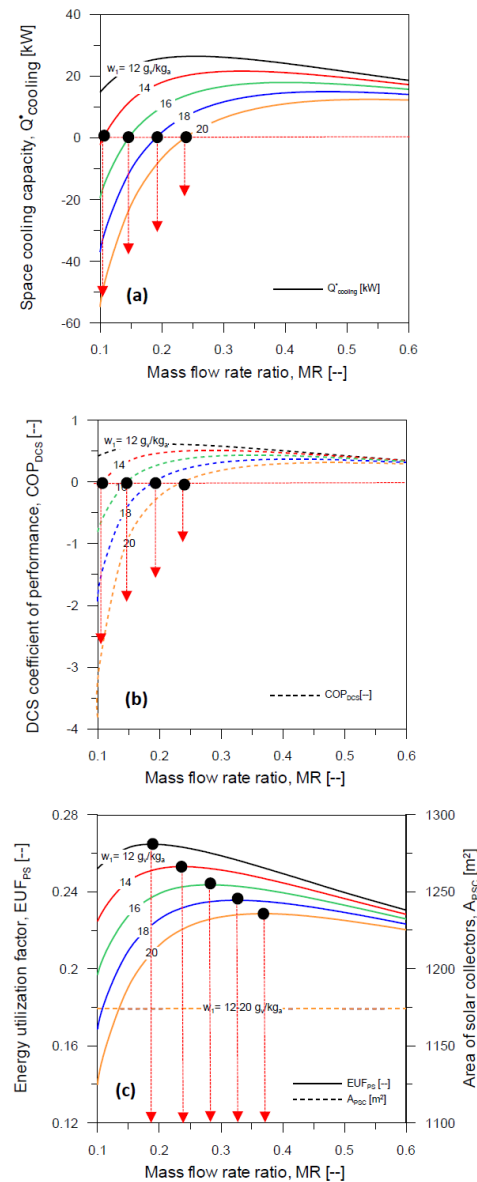


Fig. 9. Influence of w_I on the proposed system performance parameters at MR values.

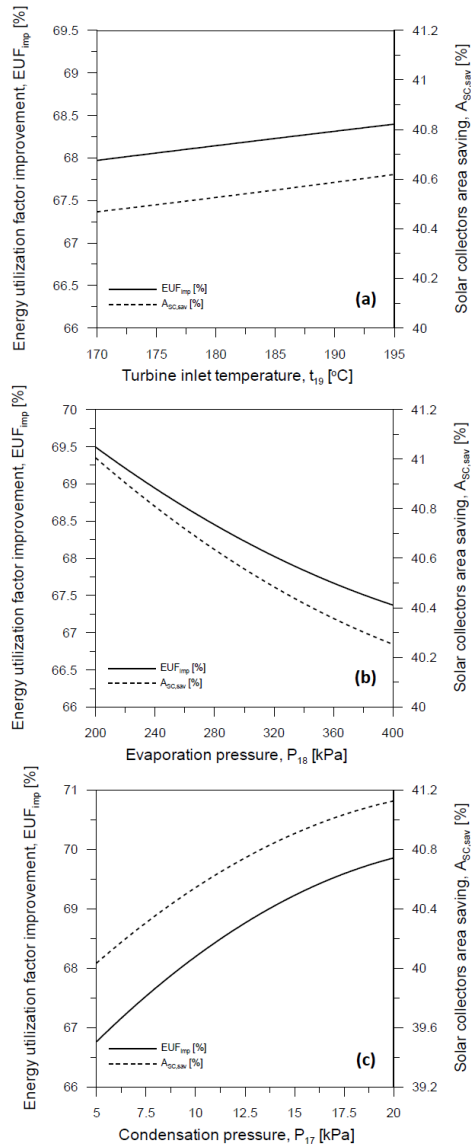


Fig. 10. Influences of studied system parameters on EUF_{imp} and $A_{SC,sav}$ of the proposed tri-generation system.

Similarly, the maximum values of $A_{SC,sav}$ that can be obtained are 40.62% and 41.14% at $t_{19} = 195^{\circ}\text{C}$ and $P_{17} = 20\text{kPa}$ respectively. In addition, Figure 10(b) shows that increasing P_{18} has an adverse effect on EUF_{imp} and $A_{SC,sav}$ due to the advantage of EUF_{PS} increase and A_{PSC} reduction with rising P_{18} that can't compensate for the increasing of EUF_{BS} and decreasing of A_{BSC} that lead to decreasing EUF_{imp} and $A_{SC,sav}$ with rising P_{18} .

Table II illustrates the different values for EUF_{imp} and $A_{SC,sav}$ as system evaluation parameters for different operation and design parameters (t_1 , t_{13} , \dot{m}_{ORC} , MR, w_1) that have no variation effects on EUF_{imp} and $A_{SC,sav}$ within their studied ranges. According to the Table, the maximum EUF_{imp} and $A_{SC,sav}$ obtained are 69.9% and 41.14% at $t_{19} = 185^{\circ}\text{C}$, $P_{18} = 300\text{kPa}$, and $P_{17} = 20\text{kPa}$, and the minimum values obtained are 66.7% and 40.01% at $t_{19} = 185^{\circ}\text{C}$, $P_{18} = 300\text{kPa}$, and $P_{17} = 5\text{kPa}$ for all studied ranges of t_1 , \dot{m}_{ORC} , MR, and w_1 .

TABLE II. PROPOSED SYSTEM ASSESSMENT AND EVALUATION FOR DIFFERENT PARAMETER VALUES

Parameter	t_{19} [°C]	P_{18} [kPa]	P_{17} [kPa]	EUF_{imp} [%]	$A_{SC,sav}$ [%]
t_1 (25-45 °C) t_{13} (15-25 °C) \dot{m}_{ORC} (0.5-1.3 kg/s) MR (0.1-0.6) w_1 (12-20 g/kg _a)	170	300	10	67.97	40.47
	185	300	10	68.23	40.56
	195	300	10	68.4	40.62
	185	200	10	69.51	41.01
	185	400	10	67.36	40.25
	185	300	5	66.7	40.01
	185	300	20	69.9	41.14

H. Numerical Correlations Prediction

The numerical results are regressed to obtain new numerical correlations for the proposed tri-generation productivity and performance parameters (\dot{W}_{net} , \dot{m}_{fresh} , $\dot{Q}_{cooling}$, T_4 , W_4 , A_{PSC} , and EUF_{PS}) in terms of all studied design and operating parameters. The obtained correlations with their errors are shown in Figure 11, and the presented correlations are valid in the ranges given in Table I, and the values of $t_{19,max}$, $t_{1,max}$, $t_{13,max}$, $\dot{m}_{ORC,max}$, $w_{1,max}$ are 195°C , 45°C , 25°C , 1.3kg/s , and 20 g/kg_a respectively.

Numerical correlations	Error
$\dot{W}_{net} [kW] = 44.92 \left(\frac{P_{18}}{P_{17}} \right)^{0.28} \left(\frac{t_{19}}{t_{19,max}} \right)^{0.49} \left(\frac{\dot{m}_{ORC}}{\dot{m}_{ORC,max}} \right)$	Predicts 100% of the numerical results within error $\pm 3\%$.
$A_{PSC} [m^2] = 1248.15 \left(\frac{P_{18}}{P_{17}} \right)^{0.071} \left(\frac{t_{19}}{t_{19,max}} \right)^{0.75} \left(\frac{\dot{m}_{ORC}}{\dot{m}_{ORC,max}} \right)$	Predicts 100% of the numerical results within error $\pm 3\%$.
$t_4 [^{\circ}\text{C}] = 16.4 MR^{-0.21} \left(\frac{P_{18}}{P_{17}} \right)^{-0.005} \left(\frac{t_{19}}{t_{19,max}} \right)^{-0.16} \left(\frac{t_1}{t_{1,max}} \right)^{0.38} \left(\frac{t_{13}}{t_{13,max}} \right)^{-0.045} \left(\frac{w_1}{w_{1,max}} \right)^{0.44}$	Predicts 100% of the numerical results within error $\pm 2.7\%$.
$w_4 [g_v / kg_a] = 9.1 MR^{-0.36} \left(\frac{P_{18}}{P_{17}} \right)^{-0.01} \left(\frac{t_{19}}{t_{19,max}} \right)^{-0.26} \left(\frac{t_1}{t_{1,max}} \right)^{0.46} \left(\frac{t_{13}}{t_{13,max}} \right)^{-0.08} \left(\frac{w_1}{w_{1,max}} \right)^{0.54}$	Predicts 100% of the numerical results within error $\pm 5\%$.
$EUF_{PS} [-] = 0.143 MR^{-0.04} \left(\frac{P_{18}}{P_{17}} \right)^{0.11} \left(\frac{t_{19}}{t_{19,max}} \right)^{-0.28} \left(\frac{t_1}{t_{1,max}} \right)^{-0.14} \left(\frac{t_{13}}{t_{13,max}} \right)^{-0.1} \left(\frac{w_1}{w_{1,max}} \right)^{-0.17}$	Predicts 99% of the numerical results within error $\pm 5\%$.
$\dot{m}_{fresh} [kg / h] = 50.75 MR^{-0.25} \left(\frac{P_{18}}{P_{17}} \right)^{0.02} \left(\frac{t_{19}}{t_{19,max}} \right)^{0.5} \left(\frac{t_1}{t_{1,max}} \right)^{0.034} \left(\frac{t_{13}}{t_{13,max}} \right)^{-0.45} \left(\frac{w_1}{w_{1,max}} \right)^{0.042} \left(\frac{\dot{m}_{ORC}}{\dot{m}_{ORC,max}} \right)$	Predicts 97% of the numerical results within error $\pm 5\%$.
$\dot{Q}_{cooling} [kW] = 16.68 MR^{0.22} \left(\frac{P_{18}}{P_{17}} \right)^{-0.013} \left(\frac{t_{19}}{t_{19,max}} \right)^{0.27} \left(\frac{t_1}{t_{1,max}} \right)^{-1.034} \left(\frac{t_{13}}{t_{13,max}} \right)^{0.17} \left(\frac{w_1}{w_{1,max}} \right)^{-1.35} \left(\frac{\dot{m}_{ORC}}{\dot{m}_{ORC,max}} \right)$	Predicts 90% of the numerical results within error $\pm 15\%$.

Fig. 11. Numerical correlation predictions and their errors.

VI. CONCLUSION AND RECOMMENDATIONS

In this article, an innovative combined ORC, DCS, and HDH tri-generation solar-driven plant for electrical power, cooling, and desalinated water production was presented. The proposed system recovers the ORC condenser heat to be used as a heating source and prime mover of the DCS and HDH sub

systems. The proposed system's performance was evaluated and compared with the basic tri-generation system to find the optimum system operation conditions. The major concluding remarks of the current study are:

- The proposed tri-generation system can produce electrical power and fresh water and carry out the space cooling load while keeping comfortable conditions inside the space.
- The net output power increases with increasing turbine inlet temperature, ORC evaporation pressure, and ORC fluid flow rate, and it decreases with ORC condensation pressure and does not affect ambient air inlet temperature, or mass flow rate ratio.
- Fresh water productivity improved with rising turbine inlet temperature and ambient air inlet temperature, while it decreased with mass flow rate ratio, ORC condensation pressure, and ORC evaporation pressure.
- Space cooling load is enhanced at higher turbine inlet temperature, ORC fluid flow rate, and mass flow rate ratio and it decreases with increasing ambient air humidity ratio, ORC condensation pressure, and ORC evaporation pressure.
- The proposed system can provide maximum electrical power, fresh water, cooling capacity, and energy utilization factor of 104.5kW, 72.37kg/h, 25.48kW, and 0.2421 respectively at $t_{19} = 185^{\circ}\text{C}$, $t_1 = 35^{\circ}\text{C}$, $w_1 = 15\text{g}_v/\text{kg}_a$, $t_{13} = 20^{\circ}\text{C}$, $P_{18} = 300\text{kPa}$, $P_{17} = 10\text{kPa}$, $\text{MR} = 0.4$, and $\dot{m}_{\text{ORC}} = 1\text{kg/s}$.
- With increasing t_{19} from 170°C to 195°C , net output power, fresh water productivity, and space cooling capacity improved by 7%, 7.5%, and 10.3% respectively.
- \dot{m}_{fresh} increased by 2.2% and space cooling capacity \dot{Q}_{cooling} decreased by 48.9% when t_1 increased from 25 to 45°C .
- Increasing P_{18} from 200 to 400kPa, \dot{m}_{fresh} and \dot{Q}_{cooling} dropped by 3.2% and 4.20% respectively.
- MR should be 0.21 at $w_1 = 15\text{g}_v/\text{kg}_a$ for cooling applications because the supply air humidity ratio (w_4) should be equal to or less than the room humidity ratio ($w_5 = 12\text{g}_v/\text{kg}_a$). Moreover, the system operation conditions with MR less than 0.11, 0.15, 0.2, 0.25, at $w_1 = 14, 16, 18$, and $20\text{g}_v/\text{kg}_a$ respectively, are not recommended for cooling and dehumidifying applications due to the negative cooling capacity for the conditioned space.
- The energy utilization factor increased as the ORC evaporation pressure and mass flow rate ratio increased (for $\text{MR} = 0.2667$ at $w_1 = 15\text{g}_v/\text{kg}_a$), and decreased as the ORC condensation pressure, ambient air inlet temperature and humidity, turbine inlet temperature, and mass flow rate ratio decreased.
- The highest energy utilization factor attained is 0.2643 at $t_{19} = 185^{\circ}\text{C}$, $t_1 = 35^{\circ}\text{C}$, $t_{13} = 20^{\circ}\text{C}$, $P_{17} = 10\text{kPa}$, $P_{18} = 300\text{kPa}$, $\dot{m}_{\text{ORC}} = 1\text{kg/s}$, $\text{MR} = 0.19$, and $w_1 = 12\text{g}_v/\text{kg}_a$.
- With increasing turbine inlet temperature and ORC condensation pressure, system evaluation performance parameters (EU_{imp} and $A_{\text{SC},\text{sav}}$) improved, but they dropped at higher ORC evaporation pressure. At $t_{19} = 185^{\circ}\text{C}$, $P_{18} = 300\text{kPa}$, and $P_{17} = 20\text{kPa}$, the maximum EU_{imp} and $A_{\text{SC},\text{sav}}$ obtained are 69.9% and 41.14% respectively.
- Finally, general numerical correlations obtained from the numerical data can predict the system's productivity and system performance parameters with reasonable error.

Experimental and transient analyses using more heat recovery approaches are recommended as future work for the proposed system.

ACKNOWLEDGEMENT

This work was funded by the University of Jeddah, Jeddah, Saudi Arabia, under grant No. UJ-20-015-DR. The authors thank the University for the technical and financial support.

NOMENCLATURE

A	Area, m^2
C_p	Specific heat, kJ/kg K
F_1, F_2	Combined potential, -
h_{fg}	Water latent heat of evaporation, kJ/kg
h	Specific enthalpy, kJ/kg
I_T	Total solar intensity, W/m^2
\dot{m}	Mass flow rate, kg/s
\dot{Q}	Heat transfer rate, kW
t	Temperature, $^{\circ}\text{C}$
W	Humidity ratio, g_v/kg_a
\dot{W}	Power, kW
β	Tilt angle, $^{\circ}$
η	Efficiency
η_{F1}, η_{F2}	Efficiency of the desiccant wheel
ε	Effectiveness
τ	Time, hours

Subscript

a	Air/dry air/actual
atm	Atmosphere
avg	Average
BS	Basic system
BSC	Basic Solar Collectors
$cond$	Condenser
$Evap$	Evaporator
g	Generator
hum	Humidifier
HE	Heat exchanger
$i = 1, 2, 3$	Index referring to various positions of the desiccant system
imp	Improvement
in	Input
ma	Moist air
v	Water vapour
reg	Regeneration
R, a	Return air
P, a	Process air
P	Pump
PS	Proposed system
PSC	Proposed solar collectors
SC	Solar collectors
Sav	Saving

<i>t</i>	Turbine
<i>w</i>	Seawater
<i>1, 2, 3,</i>	State points

Abbreviations

<i>DCS</i>	Desiccant Cooling System
<i>DEC</i>	Direct Evaporative Cooler
<i>EUF</i>	Energy Utilization Factor
<i>COP</i>	Coefficient Of Performance
<i>GOR</i>	Gain Output Ratio
<i>HDH</i>	Humidification Dehumidification
<i>KSA</i>	Kingdom of Saudi Arabia
<i>ORC</i>	Organic Rankine Cycle
<i>MR</i>	Mass flow rate ratio

REFERENCES

- [1] Y. Wang and N. Lior, "Performance analysis of combined humidified gas turbine power generation and multi-effect thermal vapor compression desalination systems — Part 1: The desalination unit and its combination with a steam-injected gas turbine power system," *Desalination*, vol. 196, no. 1, pp. 84–104, Sep. 2006, <https://doi.org/10.1016/j.desal.2006.01.010>.
- [2] Y. Wang and N. Lior, "Performance analysis of combined humidified gas turbine power generation and multi-effect thermal vapor compression desalination systems," *Desalination*, vol. 1–3, no. 207, pp. 243–256, 2007, <https://doi.org/10.1016/j.desal.2006.06.013>.
- [3] R. Chacartegui, D. Sanchez, N. di Gregorio, F. J. Jimenez-Espadafor, A. Munoz, and T. Sanchez, "Feasibility analysis of a MED desalination plant in a combined cycle based cogeneration facility," *Applied Thermal Engineering*, vol. 29, no. 2, pp. 412–417, Feb. 2009, <https://doi.org/10.1016/j.applthermaleng.2008.03.013>.
- [4] E. A. Al-Ammar, N. H. Malik, and M. Usman, "Application of using Hybrid Renewable Energy in Saudi Arabia," *Engineering, Technology & Applied Science Research*, vol. 1, no. 4, pp. 84–89, Aug. 2011, <https://doi.org/10.48084/etasr.33>.
- [5] J. B. V. Subrahmanyam, P. Alluvada, Bandana, K. Bhanupriya, and C. Shashidhar, "Renewable Energy Systems: Development and Perspectives of a Hybrid Solar-Wind System," *Engineering, Technology & Applied Science Research*, vol. 2, no. 1, pp. 177–181, Feb. 2012, <https://doi.org/10.48084/etasr.104>.
- [6] A. Belkadi, D. Mezghani, and A. Mami, "Energy Design and Optimization of a Greenhouse: A Heating, Cooling and Lighting Study," *Engineering, Technology & Applied Science Research*, vol. 9, no. 3, pp. 4235–4242, Jun. 2019, <https://doi.org/10.48084/etasr.2787>.
- [7] M. Ray, P. Samal, and C. K. Panigrahi, "Implementation of a Hybrid Technique for the Predictive Control of the Residential Heating Ventilation and Air Conditioning Systems," *Engineering, Technology & Applied Science Research*, vol. 12, no. 3, pp. 8772–8776, Jun. 2022, <https://doi.org/10.48084/etasr.5027>.
- [8] P. Palenzuela, G. Zaragoza, and D.-C. Alarcon-Padilla, "Characterisation of the coupling of multi-effect distillation plants to concentrating solar power plants," *Energy*, vol. 82, pp. 986–995, Mar. 2015, <https://doi.org/10.1016/j.energy.2015.01.109>.
- [9] A. Fouda, S. A. Nada, and H. F. Elattar, "An integrated A/C and HDH water desalination system assisted by solar energy: Transient analysis and economical study," *Applied Thermal Engineering*, vol. 108, pp. 1320–1335, Sep. 2016, <https://doi.org/10.1016/j.applthermaleng.2016.08.026>.
- [10] H. F. Elattar, A. Fouda, and S. A. Nada, "Performance investigation of a novel solar hybrid air conditioning and humidification–dehumidification water desalination system," *Desalination*, vol. 382, pp. 28–42, Mar. 2016, <https://doi.org/10.1016/j.desal.2015.12.023>.
- [11] S. A. Nada, H. F. Elattar, and A. Fouda, "Energy-efficient hybrid A/C and freshwater production system proposed for high latent load spaces," *International Journal of Energy Research*, vol. 43, no. 13, pp. 6812–6826, 2019, <https://doi.org/10.1002/er.4677>.
- [12] H. F. Elattar, S. A. Nada, A. Al-Zahrani, and A. Fouda, "Humidification-dehumidification water desalination system integrated with multiple evaporators/condensers heat pump unit," *International Journal of Energy Research*, vol. 44, no. 8, pp. 6396–6416, 2020, <https://doi.org/10.1002/er.5368>.
- [13] S. A. Nada, A. Fouda, M. A. Mahmoud, and H. F. Elattar, "Experimental investigation of air-conditioning and HDH desalination hybrid system using new packing pad humidifier and strips-finned helical coil," *Applied Thermal Engineering*, vol. 185, Feb. 2021, Art. no. 116433, <https://doi.org/10.1016/j.applthermaleng.2020.116433>.
- [14] M. Jradi and S. Riffat, "Tri-generation systems: Energy policies, prime movers, cooling technologies, configurations and operation strategies," *Renewable and Sustainable Energy Reviews*, vol. 32, pp. 396–415, Apr. 2014, <https://doi.org/10.1016/j.rser.2014.01.039>.
- [15] S. Sibilio, A. Rosato, G. Ciampi, M. Scorpio, and A. Akisawa, "Building-integrated trigeneration system: Energy, environmental and economic dynamic performance assessment for Italian residential applications," *Renewable and Sustainable Energy Reviews*, vol. 68, pp. 920–933, Feb. 2017, <https://doi.org/10.1016/j.rser.2016.02.011>.
- [16] G. Leonzio, "An innovative trigeneration system using biogas as renewable energy," *Chinese Journal of Chemical Engineering*, vol. 26, no. 5, pp. 1179–1191, May 2018, <https://doi.org/10.1016/j.cjche.2017.11.006>.
- [17] M. S. Azhar, G. Rizvi, and I. Dincer, "Integration of renewable energy based multigeneration system with desalination," *Desalination*, vol. 404, pp. 72–78, Feb. 2017, <https://doi.org/10.1016/j.desal.2016.09.034>.
- [18] B. Ghorbani, M. Mehrpooya, and M. Sadeghzadeh, "Developing a tri-generation system of power, heating, and freshwater (for an industrial town) by using solar flat plate collectors, multi-stage desalination unit, and Kalina power generation cycle," *Energy Conversion and Management*, vol. 165, pp. 113–126, Jun. 2018, <https://doi.org/10.1016/j.enconman.2018.03.040>.
- [19] AymanO. Abdelhay, HassanE. S. Fath, and S. A. Nada, "Solar driven polygeneration system for power, desalination and cooling," *Energy*, vol. 198, May 2020, Art. no. 117341, <https://doi.org/10.1016/j.energy.2020.117341>.
- [20] T. Gholizadeh, M. Vajdi, and H. Rostamzadeh, "A new trigeneration system for power, cooling, and freshwater production driven by a flash-binary geothermal heat source," *Renewable Energy*, vol. 148, pp. 31–43, Apr. 2020, <https://doi.org/10.1016/j.renene.2019.11.154>.
- [21] I. Dincer and M. Demir, "4.8 Steam and Organic Rankine Cycles," in *Comprehensive Energy Systems*, Amsterdam, Netherlands: Elsevier, 2018, pp. 264–311.
- [22] I. K. Karathanassis, E. Papanicolaou, V. Belessiotis, and G. C. Bergeles, "Design and experimental evaluation of a parabolic-trough concentrating photovoltaic/thermal (CPVT) system with high-efficiency cooling," *Renewable Energy*, vol. 101, pp. 467–483, Feb. 2017, <https://doi.org/10.1016/j.renene.2016.09.013>.
- [23] M. A. Sharaf Eldean and A. M. Soliman, "Study of Using Solar Thermal Power for the Margarine Melting Heat Process," *Journal of Solar Energy Engineering*, vol. 137, no. 2, Sep. 2014, Art. no. 021004, <https://doi.org/10.1115/1.4028367>.
- [24] M. Yari, L. Ariyanfar, and E. A. Aghdam, "Analysis and performance assessment of a novel ORC based multi-generation system for power, distilled water and heat," *Renewable Energy*, vol. 119, pp. 262–281, Apr. 2018, <https://doi.org/10.1016/j.renene.2017.12.021>.
- [25] A. Fouda, S. A. Nada, H. F. Elattar, S. Rubaiee, and A. Al-Zahrani, "Performance analysis of proposed solar HDH water desalination systems for hot and humid climate cities," *Applied Thermal Engineering*, vol. 144, pp. 81–95, Nov. 2018, <https://doi.org/10.1016/j.applthermaleng.2018.08.037>.
- [26] L. M. Ayompe and A. Duffy, "Thermal performance analysis of a solar water heating system with heat pipe evacuated tube collector using data from a field trial," *Solar Energy*, vol. 90, pp. 17–28, Apr. 2013, <https://doi.org/10.1016/j.solener.2013.01.001>.
- [27] G. Panaras, E. Mathioulakis, V. Belessiotis, and N. Kyriakis, "Theoretical and experimental investigation of the performance of a desiccant air-conditioning system," *Renewable Energy*, vol. 35, no. 7, pp. 1368–1375, Jul. 2010, <https://doi.org/10.1016/j.renene.2009.11.011>.

- [28] N. Wang *et al.*, "Performance assessment of PCM-based solar energy assisted desiccant air conditioning system combined with a humidification-dehumidification desalination unit," *Desalination*, vol. 496, Dec. 2020, Art. no. 114705, <https://doi.org/10.1016/j.desal.2020.114705>.
- [29] S. M. Zubair, M. A. Antar, S. M. Elmutasim, and D. U. Lawal, "Performance evaluation of humidification-dehumidification (HDH) desalination systems with and without heat recovery options: An experimental and theoretical investigation," *Desalination*, vol. 436, pp. 161–175, Jun. 2018, <https://doi.org/10.1016/j.desal.2018.02.018>.
- [30] E. Galloni, G. Fontana, and S. Staccone, "Design and experimental analysis of a mini ORC (organic Rankine cycle) power plant based on R245fa working fluid," *Energy*, vol. 90, pp. 768–775, Oct. 2015, <https://doi.org/10.1016/j.energy.2015.07.104>.

A Theoretical-Experimental Study of the Influence of FDM Parameters on PLA Spur Gear Stiffness

Dragos Gabriel Zisopol
Mechanical Engineering Department
Petroleum- Gas University
Ploiesti, Romania
zisopol@zisopol.ro

Dragos Valentin Iacob
Production Department
Marelli
Ploiesti, Romania
dragoshicb@gmail.com

Alexandra-Ileana Portoaca
Mechanical Engineering Department
Petroleum – Gas University
Ploiesti, Romania
alexandra.portoaca@upg-ploiesti.ro

Received: 6 July 2022 | Revised: 24 July 2022 and 7 August 2022 | Accepted: 15 August 2022

Abstract—This paper studies the influence of FDM (Fused Depositing Modeling) parameters on gear stiffness made of Polyactic Acid (PLA). 3D printing parameters must be optimized because they influence the physical, mechanical, and quality characteristics of the additive manufactured part along with its functionality. The objective of this research is to optimize FDM parameters in order to obtain the highest stiffness. In this context, we used Finite Element Analysis (FEA) and we made experimental tests to validate its results. The experimental tests are divided into two categories, gears with the same parameters and gears with the same layer height and variable filling percentage. The average results of gear stiffness with the same parameters are 8.18% highest than the average results of gear stiffness with the same layer height and variable filling percentages.

Keywords—3D printing; FDM parameters; FDM parameters; stiffness; spur gears; FEA

I. INTRODUCTION

The term additive manufacturing encompasses a set of technologies and processes that use different materials to make objects by depositing material in successive layers. Due to the recent improvements in additive technologies, they are used in many fields of activity. Initially, they were suitable for rapid prototyping of models, now they are used for sophisticated applications such as unique parts, custom products, medical implants, etc. [1-4]. Compared to formative and subtractive manufacturing, additive manufacturing technologies have many advantages: material waste is negligible, realization of very complex objects without bases and fasteners, cost-effective manufacturing, simplicity in use, etc. [5, 6]. In this paper we show that FDM 3D printing with PLA can be a good solution for plastic gears and we also find the optimal parameters for FDM printed gears. The novelty of this article consists in determining the influence of FDM parameters, the

height of the deposited PLA layer, and the percentage of filling for spur gears with straight teeth, on the rigidity gear assembly. The rigidity of PLA gear assembly, 3D-printed by FDM, is theoretically determined using FEA and experimentally validated using a device designed and manufactured by the authors, whereas the recording of the results was realized by a digital torque wrench [7, 9].

II. FDM 3D PRINTING OF SPUR GEARS

PLA filament with a diameter of 1.75mm, Verbatim brand, was the material used for FDM 3D printing of the spur gears with straight teeth. The printing methodology is shown in Figure 1.

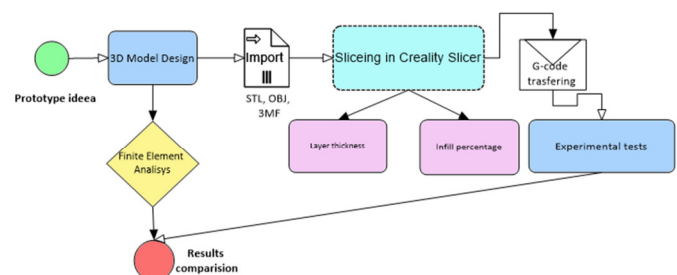


Fig. 1. Study methodology.

2D and later 3D models of straight-tooth cylindrical gears were made in the CAD Solidworks program. Figure 2 shows the 2D model of the drive gear module 1 with 30 straight teeth (R1) and Figure 3 shows the 2D model of the drive wheel module 1 with 60 straight teeth (R2). Both were designed in Solidworks. Using the same software, the two CAD files corresponding to the 3D models obtained were saved with the STL extension.

Corresponding author: Dragoș Valentin Iacob

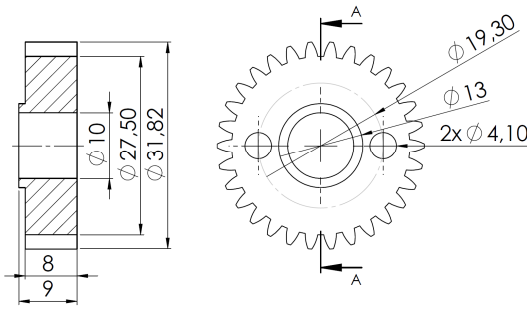


Fig. 2. Leading spur gear (R1).

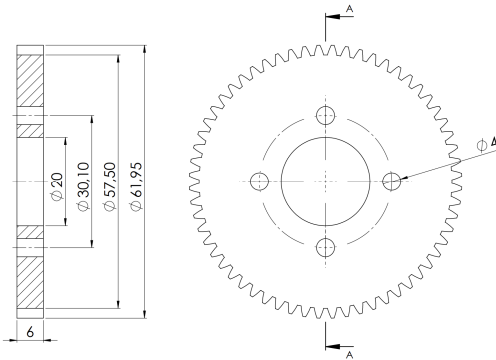


Fig. 3. Driven spur gear (R2).

Using the Creality Slicer program of the Creality CR-X printer, the two files with the STL extension corresponding to the straight-tooth cylindrical gears shown in Figures 2 and 3, after entering the 3D printing parameters, were transformed into a G-file Code (Figure 4).

```

M190 S60.000000
M109 S200.000000
;Sliced at: Sun 09-01-2022 15:54:02
;Basic settings: Layer height: 0.1 Walls: 0.8 Fill: 100
;Print time: 5 hours 54 minutes
;Filament used: 8.525m 25.0g
;Filament cost: None
;M190 S60 ;Uncomment to add your own bed temperature line
;M109 S200 ;Uncomment to add your own temperature line
G21 ;metric values
G90 ;absolute positioning
M82 ;set extruder to absolute mode
M107 ;start with the fan off

G28 X0 Y0 ;move X/Y to min endstops
G28 Z0 ;move Z to min endstops

G1 Z15.0 F3000 ;move the platform down 15mm

G92 E0 ;zero the extruded length
G1 F200 E3 ;extrude 3mm of feed stock
G92 E0 ;zero the extruded length again
G1 F3000
;Put printing message on LCD screen
M117 Printing...

;Layer count: 88
;LAYER:0
M106 S127
G0 F3000 X118.843 Y146.229 Z0.300
;TYPE:SKIRT
G1 F1500 X118.581 Y146.502 E0.01888
G1 X118.362 Y146.826 E0.03839

```

Fig. 4. G-Code commands.

The parameters of 3D printing of cylindrical gears, presented in Table I, are grouped in two categories, constant process parameters and variable technological parameters. The first parameters category refers to the orientation of the parts, the printing speed (V_p), the extruder temperature (T_e), the

printing bed temperature (T_p), and the model used for filling. Variable technological parameters refer to the height of the deposited layer (H_s) and the percentage of filling, (P_u) [1]. Also, the number of gear pairs tested is mentioned. Data in Table I were used to reveal constant parameters and parameters varied to test different layer thicknesses and infill percentages.

TABLE I. 3D PRINTING PARAMETERS

Constant parameters	Variable parameters			Spur gears	
	Layer height (H_s)	Infill percentage (P_u)			
Building orientation X, Y	(mm)	(%)			(pieces)
Extrusion temperature (T_e) – 210 °C	0.10	50	75	100	27
	0.15				27
Bed temperature (T_p) – 60 °C					
Speed (V_p) – 80 mm/s	0.20				27
Filling model – Lines 45°					

Figure 5 shows the set of cylindrical gears with straight teeth R1 and R2, created with the Creality Slicer [3]. The G-Code file was transferred to the Creality CR-X printer on which 162 straight-tooth cylindrical gears were made of PLA (81 R1 and 81 R2), according to the data centralized in Table I.

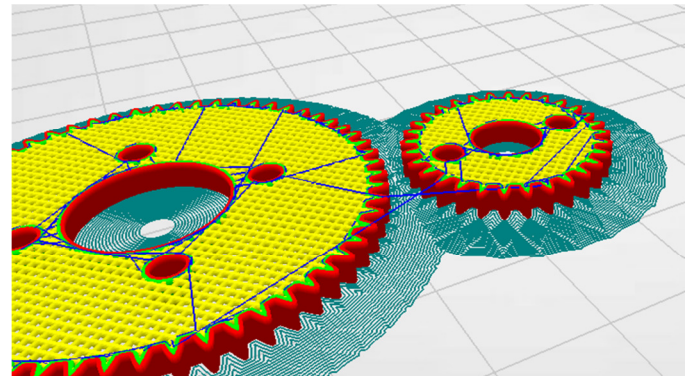


Fig. 5. R1 and R2 spur gears, in Creality Slicer.

III. STIFFNESS DETERMINATION OF THE 3D PRINTED SPUR GEAR

The stiffness of the PLA 3D printed spur gears was theoretically determined using FEA applied in Solidworks 2016 and experimentally validated using the device in Figure 8 designed and manufactured by the authors.

A. Theoretical Study

For FEA of stiffness gears with straight in Solidworks 2016 a torque R1 equal to 0.0022kN·m was applied (minimum value at which teeth yielded). The FEA results of the stiffness of the straight-tooth cylindrical gears of PLA (R1 and R2) are shown in Figures 5 and 6. The equivalent Von Mises stress obtained is 2.225MPa and the maximum linear displacement is 1.208mm.

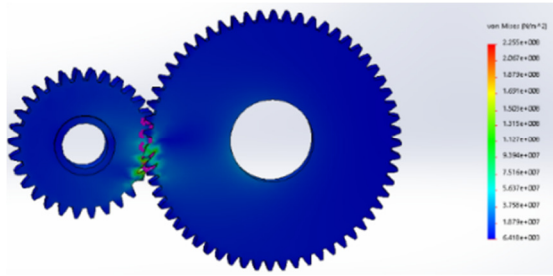


Fig. 6. Equivalent Von Mises stress.

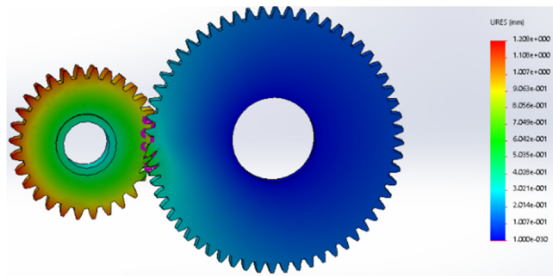


Fig. 7. Maximum linear displacement.

B. Experimental Tests

For the experimental determination of the gear stiffness of the gears, the authors designed and made the device shown in Figure 8.

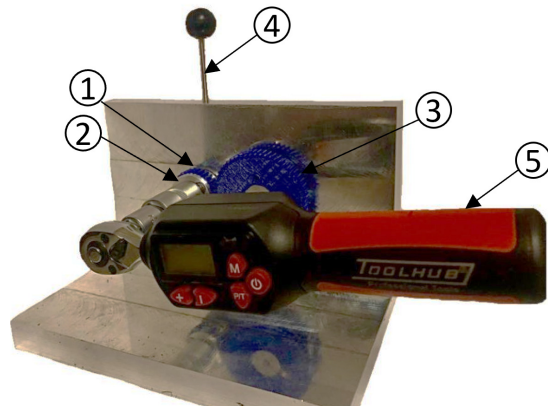
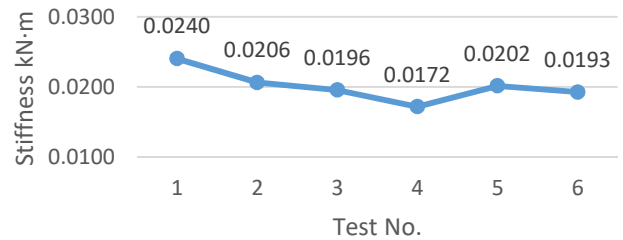
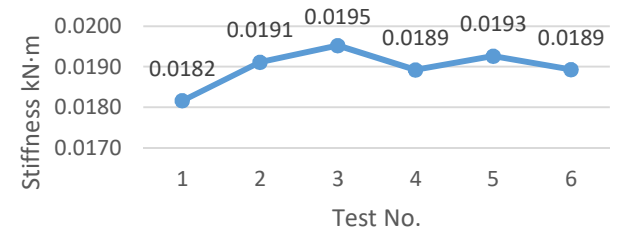
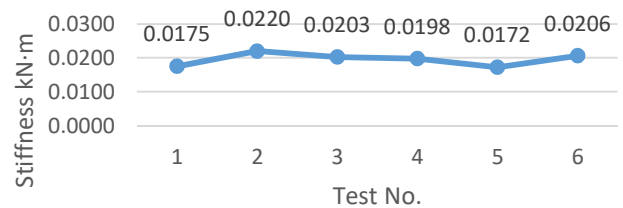
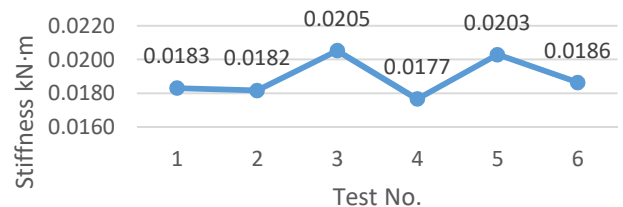
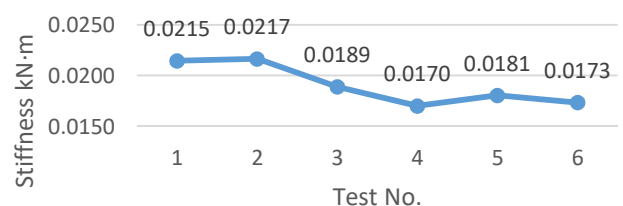


Fig. 8. Gear stiffness determination device: 1 – leading gear (R1); 2 – washer; 3 – driven wheel (R2); 4– locking rod; 5 – digital torque wrench.

The stiffness of the leading gear R1 (1), fixed to the device by the washer (2) and locked by the rod (4), with the driven gear R2 (3) was determined by the digital torque wrench (5) by recording the maximum torque corresponding to the gear assembly failure. A total of 162 experimental tests were performed on the device in Figure 8, using cylindrical gears with straight teeth with the parameters shown in Table I.

C. Results and Discussion

The results obtained from the experimental determinations performed on the device in Figure 8 are shown graphically in Figures 9-36. The averages of the results obtained from the experimental determinations; are presented in Figure 36.

Fig. 9. Gear stiffness R1 ($H_s = 0.10\text{mm}$, $P_u = 100\%$) with R2 ($H_s = 0.10\text{mm}$, $P_u = 100\%$).Fig. 10. Gear stiffness R1 ($H_s = 0.10\text{mm}$, $P_u = 75\%$) with R2 ($H_s = 0.10\text{mm}$, $P_u = 75\%$).Fig. 11. Gear stiffness R1 ($H_s = 0.10\text{mm}$, $P_u = 50\%$) with R2 ($H_s = 0.10\text{mm}$, $P_u = 50\%$).Fig. 12. Gear stiffness R1 ($H_s = 0.15\text{mm}$, $P_u = 100\%$) with R2 ($H_s = 0.15\text{mm}$, $P_u = 100\%$).Fig. 13. Gear stiffness R1 ($H_s = 0.15\text{mm}$, $P_u = 75\%$) with R2 ($H_s = 0.15\text{mm}$, $P_u = 75\%$).

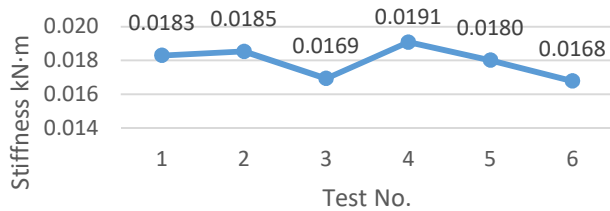


Fig. 14. Gear stiffness R1 ($H_s = 0.15\text{mm}$, $P_u = 50\%$) with R2 ($H_s = 0.15\text{mm}$, $P_u = 50\%$).

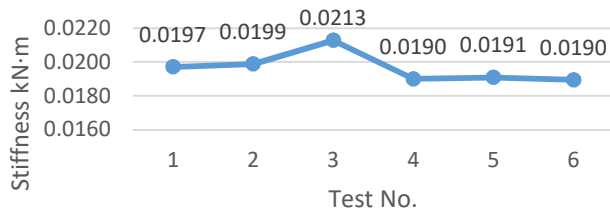


Fig. 15. Gear stiffness R1 ($H_s = 0.20\text{mm}$, $P_u = 100\%$) with R2 ($H_s = 0.20\text{mm}$, $P_u = 100\%$).

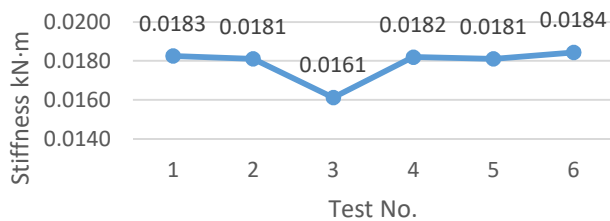


Fig. 16. Gear stiffness R1 ($H_s = 0.20\text{mm}$, $P_u = 75\%$) with R2 ($H_s = 0.20\text{mm}$, $P_u = 75\%$).

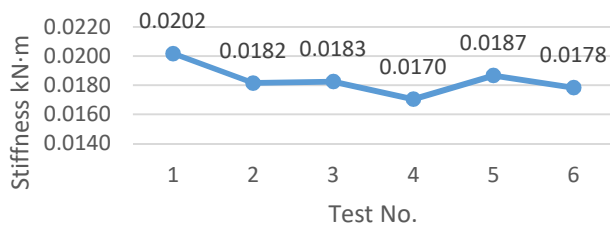


Fig. 17. Gear stiffness R1 ($H_s = 0.20\text{mm}$, $P_u = 50\%$) with R2 ($H_s = 0.20\text{mm}$, $P_u = 50\%$).

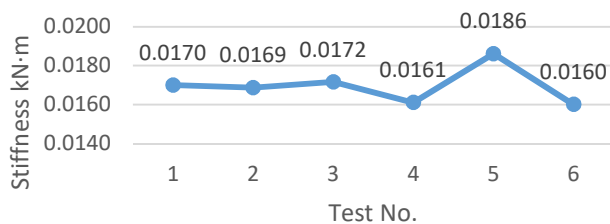


Fig. 18. Gear stiffness R1 ($H_s = 0.10\text{mm}$, $P_u = 100\%$) with R2 ($H_s = 0.10\text{mm}$, $P_u = 75\%$).

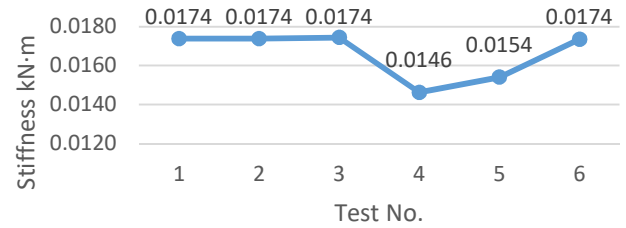


Fig. 19. Gear stiffness R1 ($H_s = 0.10\text{mm}$, $P_u = 100\%$) with R2 ($H_s = 0.10\text{mm}$, $P_u = 50\%$).

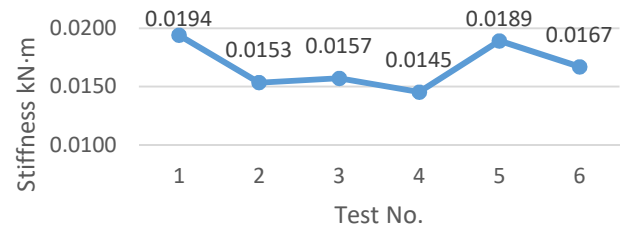


Fig. 20. Gear stiffness R1 ($H_s = 0.10\text{mm}$, $G_u = 75\%$) with R2 ($H_s = 0.10\text{mm}$, $P_u = 100\%$).

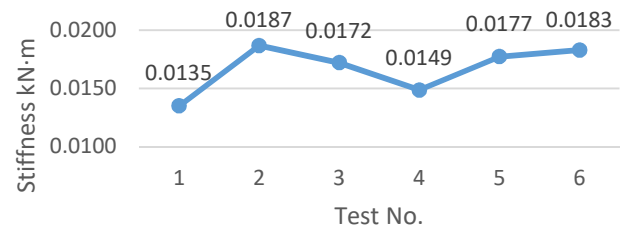


Fig. 21. Gear stiffness R1 ($H_s = 0.10\text{mm}$, $P_u = 75\%$) with R2 ($H_s = 0.10\text{mm}$, $P_u = 50\%$).

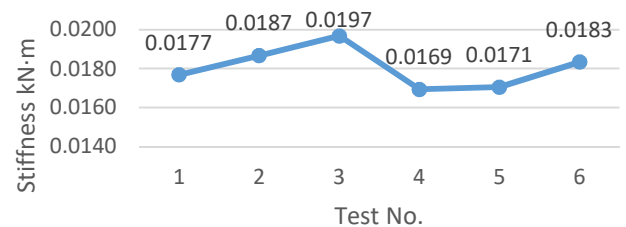


Fig. 22. Gear stiffness R1 ($H_s = 0.10\text{mm}$, $P_u = 50\%$) with R2 ($H_s = 0.10\text{mm}$, $P_u = 100\%$).

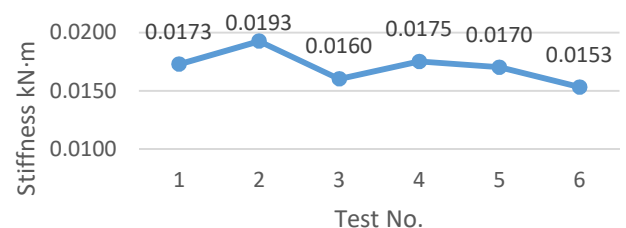


Fig. 23. Gear stiffness R1 ($H_s = 0.10\text{mm}$, $P_u = 50\%$) with R2 ($H_s = 0.10\text{mm}$, $P_u = 75\%$).

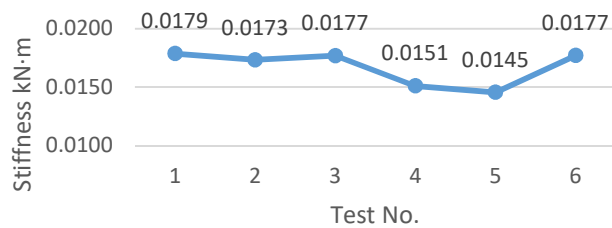


Fig. 24. Gear stiffness R1 ($H_s = 0.15\text{mm}$, $P_u = 100\%$) with R2 ($H_s = 0.15\text{mm}$, $P_u = 75\%$).

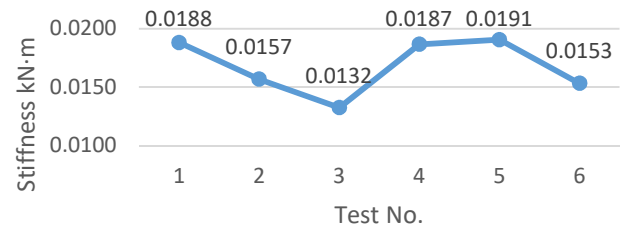


Fig. 29. Gear stiffness R1 ($H_s = 0.15\text{mm}$, $P_u = 50\%$) with R2 ($H_s = 0.15\text{mm}$, $P_u = 75\%$).

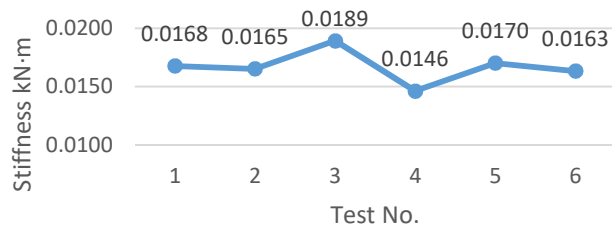


Fig. 25. Gear stiffness R1 ($H_s = 0.15\text{mm}$, $P_u = 100\%$) with R2 ($H_s = 0.15\text{mm}$, $P_u = 50\%$).

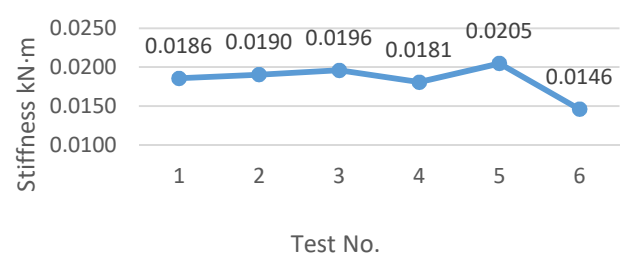


Fig. 30. Gear stiffness R1 ($H_s = 0.20\text{mm}$, $P_u = 100\%$) with R2 ($H_s = 0.15\text{mm}$, $P_u = 75\%$).

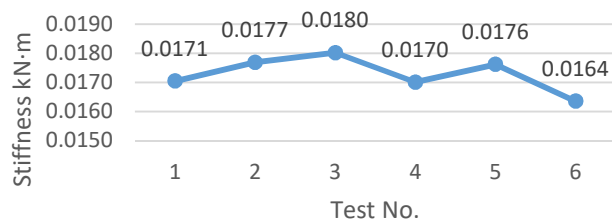


Fig. 26. Gear stiffness R1 ($H_s = 0.15\text{mm}$, $P_u = 75\%$) with R2 ($H_s = 0.15\text{mm}$, $P_u = 100\%$).

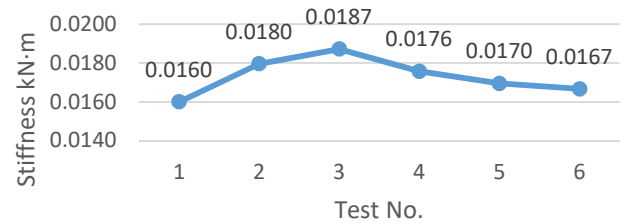


Fig. 31. Gear stiffness R1 ($H_s = 0.20\text{mm}$, $P_u = 100\%$) with R2 ($H_s = 0.15\text{mm}$, $P_u = 50\%$).

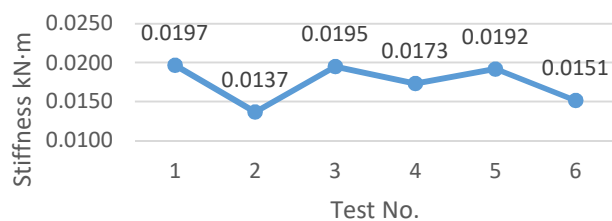


Fig. 27. Gear stiffness R1 ($H_s = 0.15\text{mm}$, $P_u = 75\%$) with R2 ($H_s = 0.15\text{mm}$, $P_u = 50\%$).

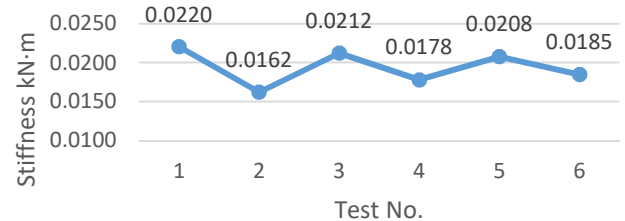


Fig. 32. Gear stiffness R1 ($H_s = 0.20\text{mm}$, $P_u = 75\%$) with R2 ($H_s = 0.15\text{mm}$, $P_u = 100\%$).

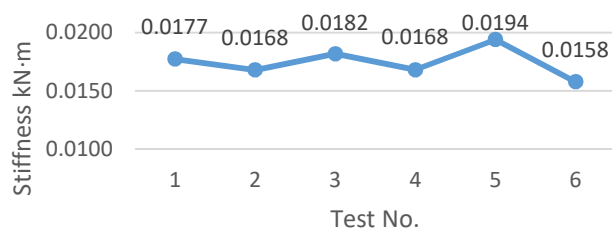


Fig. 28. Gear stiffness R1 ($H_s = 0.15\text{mm}$, $P_u = 50\%$) with R2 ($H_s = 0.15\text{mm}$, $P_u = 100\%$).

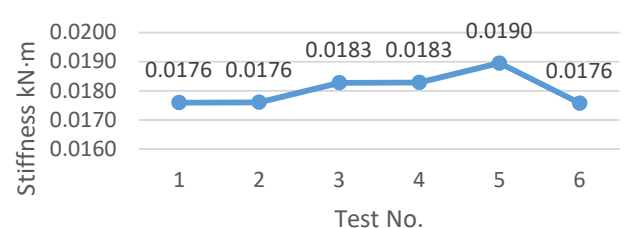


Fig. 33. Gear stiffness R1 ($H_s = 0.20\text{mm}$, $P_u = 75\%$) with R2 ($H_s = 0.15\text{mm}$, $P_u = 50\%$).

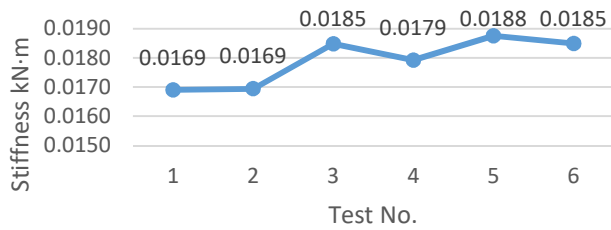


Fig. 34. Gear stiffness R1 ($H_s = 0.20\text{mm}$, $P_u = 50\%$) with R2 ($H_s = 0.15\text{mm}$, $P_u = 100\%$).

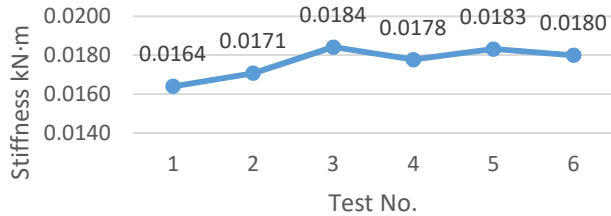


Fig. 35. Gear stiffness R1 ($H_s = 0.20\text{mm}$, $P_u = 50\%$) with R2 ($H_s = 0.15\text{mm}$, $P_u = 75\%$).

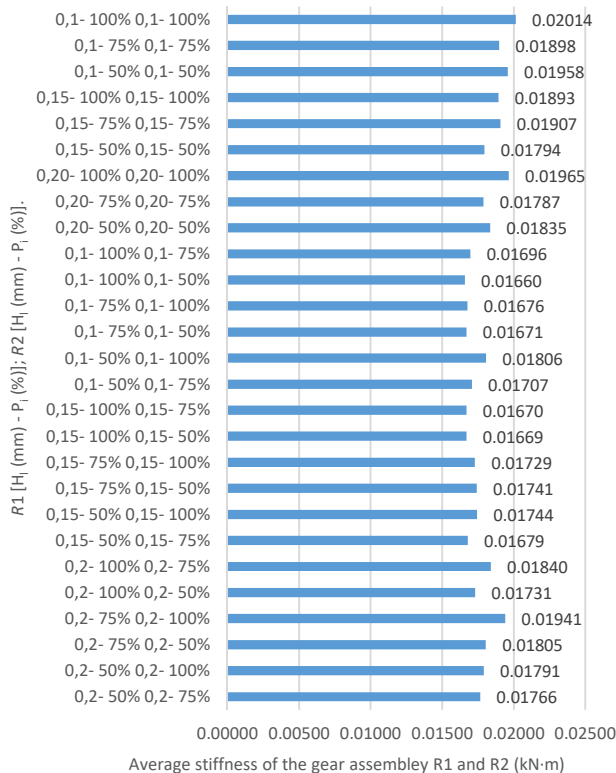


Fig. 36. Average stiffness of the R1 and R2 gear assembly.

The rigidity of the assembly of cylindrical gears was theoretically determined using FEA in Solidworks and experimentally validated using the device shown in Figure 8. The theoretical study of the gears stiffness revealed results that are presented in Figures 6 and 7, validated by the experimental

results presented in Figures 9-36. It was found out that the percentage difference was 9.49%. Analyzing the results of the 162 experimental tests, an average value of the stiffness of the cylindrical gears with straight teeth $0.01791\text{kN}\cdot\text{m}$ was obtained. For cylindrical gears, the minimum value of gear stiffness is $0.01323\text{kN}\cdot\text{m}$ and was obtained for the gear with R1 ($H_s = 0.15\text{mm}$, $P_u = 50\%$) and R2 ($H_s = 0.15\text{mm}$, $P_u = 75\%$) and the maximum value of the gear stiffness is $0.02402\text{kN}\cdot\text{m}$ and was obtained for the gear with R1 ($H_s = 0.10\text{mm}$, $P_u = 100\%$) and R2 ($H_s = 0.10\text{mm}$, $P_u = 100\%$). The height of the deposited layer (H_s) and the percentage of filling (P_u) influence the stiffness of the cylindrical gears assembly with straight teeth. Increasing the height of the deposited layer from $H_s = 0.10\text{mm}$ to $H_s = 0.15\text{mm}$ increases the stiffness of the gear by 2.34% and increasing from $H_s = 0.10\text{mm}$ to $H_s = 0.20\text{mm}$ increases stiffness by 4.02%. The increase of the filling percentage from $P_u = 50\%$ to $P_u = 75\%$ increases gear stiffness by 0.08% and the increase from $P_u = 50\%$ to $P_u = 100\%$ by 4.84%. The rigidity of the gears assembly with straight teeth is influenced by the percentage of filling (P_u) by 5.44% more than it is influenced by the height of the deposited layer (H_s). The novelty of this work consists in obtaining results of the maximum torque that can be applied to various printed gears characterized by different layer thicknesses and infill percentages until it deforms irreversibly in order to protect the energy source used in practical applications. There is a limited number of studies conducted on the subject. In [10], 6 types of PLA, from different producers, 2 types of ABS and 3 types of nylon all printed with the same parameters were compared and an optimal type of PLA that crushed at $0.018\text{kN}\cdot\text{m}$ torque was.

IV. CONCLUSIONS

The objective of the current study was to determine an optimal combination of gear characterization by the printing and tested parameters. Furthermore, the result is similar to other studies using different PLA producers [10], so the study is considered valid. The paper reveals the maximum torque supported by 3D printed PLA (with certain parameters) and helps in choosing efficient variants of construction depending of the requirements of the application. The study is recommended to be applied to other types of 3D printed gears from various materials, using different additive manufacturing technologies.

REFERENCES

- [1] D. G. Zisopol, I. Nae, A. I. Portoaca, and I. Ramadan, "A Theoretical and Experimental Research on the Influence of FDM Parameters on Tensile Strength and Hardness of Parts Made of Polylactic Acid," *Engineering, Technology & Applied Science Research*, vol. 11, no. 4, pp. 7458–7463, Aug. 2021, <https://doi.org/10.48084/etasr.4311>.
- [2] D. G. Zisopol, I. Nae, A. I. Portoaca, and I. Ramadan, "A Statistical Approach of the Flexural Strength of PLA and ABS 3D Printed Parts," *Engineering, Technology & Applied Science Research*, vol. 12, no. 2, pp. 8248–8252, Apr. 2022, <https://doi.org/10.48084/etasr.4739>.
- [3] A. Portoaca, I. Nae, D. Zisopol, and I. Ramadan, "Studies on the influence of FFF parameters on the tensile properties of samples made of ABS," Iasi, Romania, Oct. 2021.
- [4] D. G. Zisopol, A. I. Portoaca, I. Nae, and I. Ramadan, "A Comparative Analysis of the Mechanical Properties of Annealed PLA," *Engineering, Technology & Applied Science Research*, vol. 12, no. 4, pp. 8978–8981, Aug. 2022, <https://doi.org/10.48084/etasr.5123>.

- [5] H.-J. Dennig, L. Zumofen, and A. Kirchheim, "Feasibility Investigation of Gears Manufactured by Fused Filament Fabrication," in *Industrializing Additive Manufacturing*, Cham, 2021, pp. 304–320, https://doi.org/10.1007/978-3-030-54334-1_22.
- [6] J. C. Camargo, Á. R. Machado, E. C. Almeida, and E. F. M. S. Silva, "Mechanical properties of PLA-graphene filament for FDM 3D printing," *The International Journal of Advanced Manufacturing Technology*, vol. 103, no. 5, pp. 2423–2443, Aug. 2019, <https://doi.org/10.1007/s00170-019-03532-5>.
- [7] O. Luzanin, D. Movrin, and M. Plancak, "Effect of layer thickness, deposition angle, and infill on maximum flexural force in FDM-built specimens," *Journal for Technology of Plasticity*, vol. 39, Jan. 2014.
- [8] M. Sharma, V. Sharma, and P. Kala, "Optimization of process variables to improve the mechanical properties of FDM structures," *Journal of Physics: Conference Series*, vol. 1240, Apr. 2019, Art. no. 012061, <https://doi.org/10.1088/1742-6596/1240/1/012061>.
- [9] O. A. Mohamed, S. H. Masood, and J. L. Bhowmik, "Optimization of fused deposition modeling process parameters: a review of current research and future prospects," *Advances in Manufacturing*, vol. 3, no. 1, pp. 42–53, Mar. 2015, <https://doi.org/10.1007/s40436-014-0097-7>.
- [10] "Angus Deveson is creating 3D Printing Videos," *Patreon*. <https://www.patreon.com/makersmuse>.

Static and Dynamic Behavior of Circularized Reinforced Concrete Columns Strengthened with Hybrid CFRP

Zena H. Abdulghafoor

Department of Civil Engineering

University of Baghdad

Baghdad, Iraq

z.abdulghafar1901m@coeng.uobaghdad.edu.iq

Hayder A. Al-Baghdadi

Department of Civil Engineering

University of Baghdad

Baghdad, Iraq

baghdadi.hayder@coeng.uobaghdad.edu.iq

Received: 26 June 2022 | Revised: 14 July 2022 and 5 August 2022 | Accepted: 14 August 2022

Abstract-In this study, three strengthening techniques, near-surface mounted NSM-CFRP, NSM-CFRP with externally bonding EB-CFRP, and hybrid CFRP with circularization were studied to increase the seismic performance of existing RC slender columns under lateral loads. Experimentally, 1:3 scale RC models were studied and subjected to both lateral static load and seismic excitation. In the dynamic test, a model was subjected to El Centro 1940 NS earthquake excitation by using a shaking table. According to the test results, the strengthening techniques showed a significant increase in load carrying capacity, of about 86.6%, and 46.6%, for circularization and NSM-CFRP respectively, of the reference unstrengthened columns. On the other hand, columns strengthened with hybrid NSM-CFRP and EB-CFRP showed a different failure mode. Dynamically, the lateral drift was decreased by about 75%, 47%, and 49% for earthquake amplitudes of 0.05g, 0.15g, and 0.32g respectively. Finally, it was concluded, depending on the static and dynamic analyses, that the circularization process showed a significant increase in lateral load-bearing capacity.

Keywords-circularization; strengthening; CFRP; NSM; dynamic; slender column

I. INTRODUCTION

Most structures in Iraq were built exclusively for gravity loads only, posing a significant problem when minimizing earthquake hazards is concerned. Improved design standards and procedures can keep the damage to newer buildings to a manageable level in the event of a moderate to severe earthquake [1]. In this work, three strengthening techniques, externally bonding EB-CFRP, near-surface mounted NSM-CFRP, and hybrid CFRP with circularization were studied to increase the seismic performance of existing RC slender columns under lateral loads. After reviewing the literature regarding the CFRP strengthening techniques, and to the best of our knowledge, there is no previous work that studied the strengthening of slender columns under seismic excitation with the use of a circularization technique. Therefore, the main aims of this study are: (i) to understand the behavior of several types of strengthened Reinforced Concrete (RC) slender columns

being subjected to different amplitudes of the El-Centro 1940 earthquake, and (ii) assessing the efficacy of the strengthening techniques after exposure to seismic excitation.

Prior to the '70s, the majority of structures were built to withstand gravity stresses. While these structures did well under such pressures, their performance under seismic loads was doubtful. Due to the ever-aging infrastructure and losses caused by significant catastrophic events worldwide, there is an increasing demand for the introduction of inexpensive and speedier retrofitting approaches. Due to their increased strength, light weight, durability, corrosion resistance, and aesthetic appeal, Carbon Fiber Reinforced Polymers (CFRPs) are being used more and more for strengthening and retrofitting RC structures [3]. Many strengthening techniques have been developed and used to repair and rehabilitate earthquake-damaged and seismically deficient structures. The identification of an effective rehabilitation method is directly related to the outcome of a seismic evaluation of the structure and is based on the consideration of many factors, including the type of structure, its rehabilitation objective, strengthening scheme effectiveness, constructability, and cost. It is possible to employ FRP materials and systems to enhance the overall seismic performance of a structure by modifying individual components. There are many advantages of using FRP reinforcement strengthening to effectively decrease brittle failure mechanisms at the component level. Shear failure of unconfined beam-column junctions, shear failure of beams, columns, or both, and lap splice failure are all possible. FRP strengthening may also be used to raise the inelastic rotational capacity of reinforced concrete members, as well as:

- To increase the flexural capacity of RC members and prevent flexural steel bars from buckling.
- To improve the overall behavior of reinforced concrete structures exposed to seismic events by increasing the structure's global displacement and energy dissipation capabilities.

Corresponding author: Zena H. Abdulghafoor

FRP shear strengthening and confinement have a minor impact on the structure's stiffness or mass. A reevaluation of the seismic demand after strengthening is usually not necessary in such circumstances. FRP strengthening of local components may be combined with other typical global upgrading approaches when structural stiffness has to be enhanced [4].

Many columns have a rectangular or square cross-section because it is simpler and less expensive to construct. Some columns have non-regular cross-sections, such as hexagons and other shapes. As a consequence, the goal of this research is to investigate the process of converting existing non-circular columns to circular ones and then wrapping the changed circular elements with sheet reinforcement. Modifying rectangular or square members into circular columns may be done in various ways. These approaches may essentially be divided into two categories

- A circular mold is used to encircle the non-circular compression element. After that, a rich concrete mix is poured to fill the gaps between the mold and the non-circular compression parts.
- To generate a circular cross-section, adhesives are used to adhere previously cast and cured concrete segments to the faces of the non-circular compression component (or column) [5].

Furthermore, authors in [6] found that using the circularization technique to change the form of square (non-circular) compression members to a circular shape eliminates stress concentration zones that appear at the corners of externally constrained square compression members.

II. EXPERIMENTAL PROCEDURE

A. Methodology

In the experimental work, 8 square concrete columns were casted for laboratory experiments with length and width of 130×130mm and height of 1500mm. The experimental tests are categorized into two main groups, each group with 4 columns (Figure 1):

- 4 specimens were tested statically.
- 4 specimens were tested dynamically.

All column specimens were designed with a normal concrete strength of $f_c = 30\text{MPa}$. For the circularization process, plain concrete was used with concrete strength of $f_c = 30\text{MPa}$.

B. Concrete Casting

Self-Compacting Concrete (SCC) with a compressive strength of 30MPa was used to cast the square columns due to the small cross-section of the column and the difficulty of using a vibration [7]. SCC is more workable and its production makes less noise [8]. Figure 5 shows the models after casting. Table I lists the details of the concrete mix.

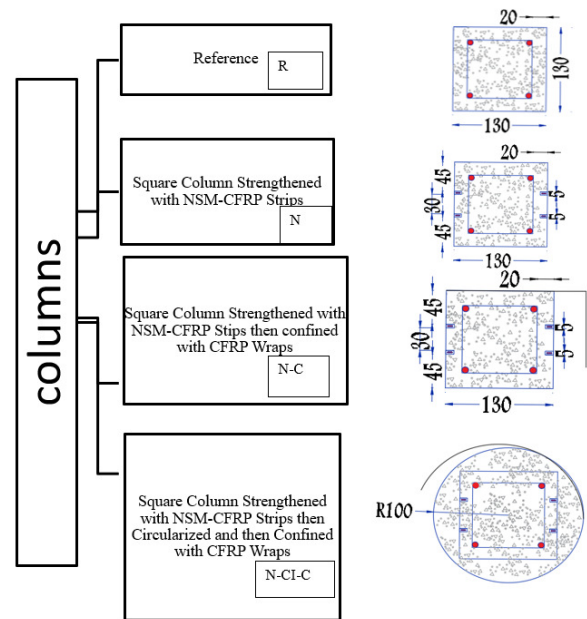


Fig. 1. Experimental matrix.

TABLE I. DETAILS OF MIX DESIGN

Materials	Final mix (kg, m ³)
Cement: Sand: Gravel (ratio by weight)	1:1.25:1.25
Water/Cementitious materials ratio	0.4125
Water	165
Cement	400
Sand	500
Gravel	500
Viscocrete 5930 IQ	8 ml / kg of cement
Rapid-1	2.6ml / kg of cement

C. Strengthening Methods

1) NSM CFRP Strengthening Method

The grooves were formed by a diamond blade cutter. The groove size is about 10mm in depth and 5mm in width. The longitudinal distance of the groove is 1250mm with an embedded length of 300mm, so the grooves were extended below the top face of the foundation block by 300mm by drilling holes along the grooves at the foundation, and the spacing between the two grooves was 30mm. The dimensions of the grooves were calculated according to ACI-440.2R-17. Figures 2-4 show the columns' specifications. The grooves were filled with the adhesive material, Sikadur 30LP, after mixing the epoxy adhesive according to supplier recommendations; components A (white) and B (black) were mixed in (3:1) proportion with an electric mixer until the color became a uniform grey.

The CFRP strip was inserted into the middle of the groove and was pressed gently so that it was completely covered by epoxy, and then the surface was leveled and pressed well by hand [9]. Finally, the columns were cured for 7 days according to the product datasheet before being tested to achieve the maximum strengthening level, as shown in Figure 6.

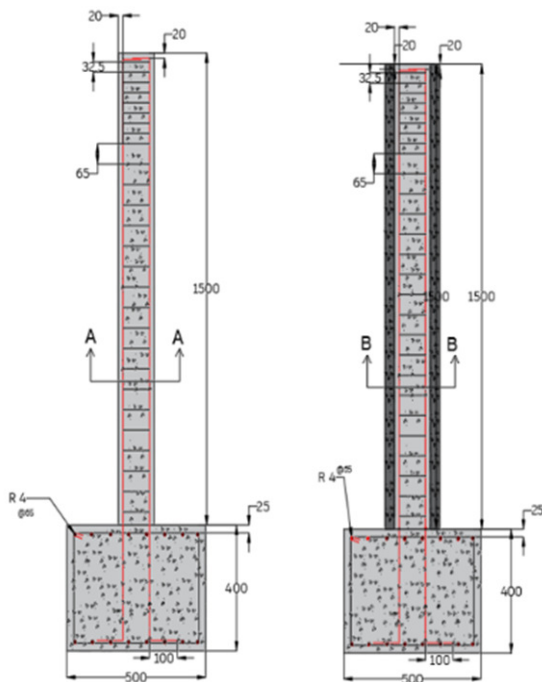


Fig. 2. The column models. All dimensions in mm.

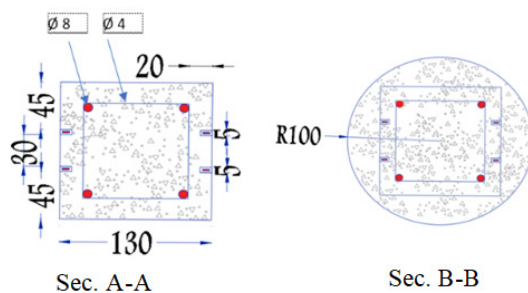


Fig. 3. The column sections. All dimensions in mm.

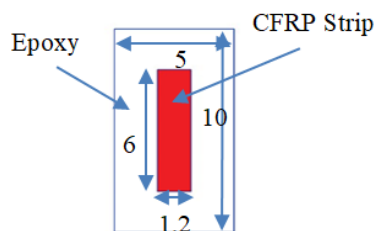


Fig. 4. Groove details. All dimensions in mm.



Fig. 5. The column models after casting.



Fig. 6. NSM-CFRP technique procedure.

2) Strengthening Technique with Circularization

Cylindrical formworks were used to change the shape of the square columns from a square cross-sectional into a circular cross-sectional shape. The molds had dimensions of 20cm diameter and 150cm height. For this study, the direct circularization method was used. In this method, the square columns were cast first. After sufficient time had passed, the cylindrical molds were put outside the square columns to perform the shape modification process. Finally, it should be noted that, like the square members, the casting of circularization concrete was done vertically. The advantage of applying the direct circularization method is that the surface of final circularized columns is almost a perfect cylinder with no discontinuities or distortions. Square columns that are circularized by the direct circularization method are shown in Figure 7.



Fig. 7. Circularization and CFRP-EB technique.

3) Strengthening with External Confinement Technique

The dry layup technique was used to wrap the columns using epoxy resin. First, the epoxy resin (Sikadur 330) was prepared by mixing the two components of the product, A and B, in 1:4 proportions. After putting components A and B of the epoxy in one container following the proportions recommended by the product datasheet, slow mixing rate was applied by hand with a spatula. When applying the epoxy resin to the surface, the resin was spread evenly throughout the model's surface with a tiny brush. After that, one layer of CFRP was applied to the specimens' surface. A small, serrated roller was utilized to ensure good resin impregnation inside the CFRP layer and to prevent any air bubbles from forming or get trapped inside the epoxy. Furthermore, the development

length for CFRP wraps is mandated by ACI-440.2R-17, and is equal to 73mm [10]. A 100mm overlap was adopted for every single layer to ensure more confinement effectiveness. They were additionally arranged around the specimens like hoops. In order to prevent any air bubbles from being caught, the serrated roller spun in the fibers' direction, the EB process is shown in Figure 7. Additionally, according to the product datasheet, it should be noted that CFRP wraps were left for 7 days to develop full bonding strength [11]. Figure 8 shows the final shape of the models.



Fig. 8. Final shape of column models.

III. STATIC TEST

To study the performance of the RC columns before and after strengthening, all columns, which included 1 column reference column and 3 strengthened columns, were loaded up to failure by applying incremental monotonic static load horizontally over the tipping point of the column where the steel cap was put to prevent local crushing. The load was measured by the testing machine's load cell, and displacement data were recorded by an LVDT placed in the free end of the column. All specimens were tested in the structural laboratory of the Department of Civil Engineering, University of Baghdad.

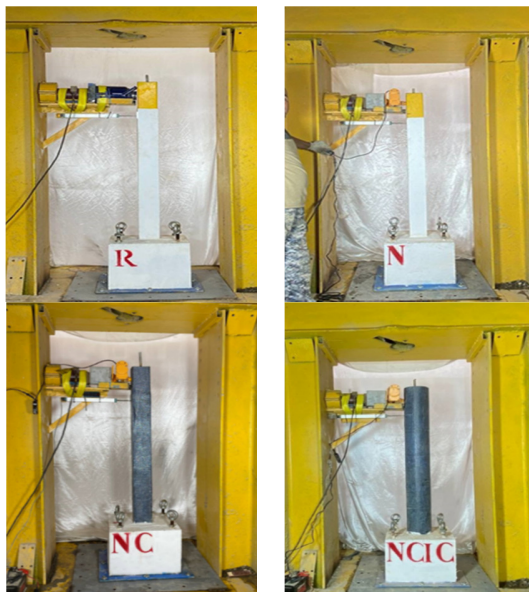


Fig. 9. Static test.

For each specimen, the base was screwed on all sides with a steel plate which was fixed on the frame floor by welding to avoid uplifting. An electric control jack applied the lateral load with a capacity of 40kN, which was connected to a load cell with a 200kN capacity. Figure 9 shows the static test.

A. Static Results

Table II lists the results of the models after being subjected to static lateral force. Figures 10-11 show the load-displacement curve of the models and the comparison with the reference model.

TABLE II. STATIC TEST RESULTS

Column code	Ultimate load P_u (kN)	Load P_u (kN) at 60mm	Δu (mm)	% Increase in load at 60mm
R	4.11	3.15	124	/
N	4.67	4.62	72.9	46.6
N-C	3.66	3.42	203.8	8.57
N-CI-C	6.52	5.88	100.5	86.6

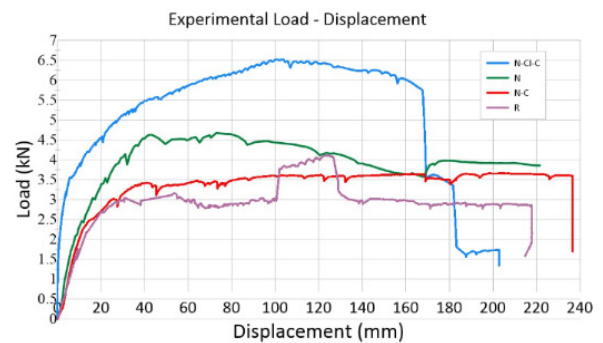


Fig. 10. Load displacement of models.

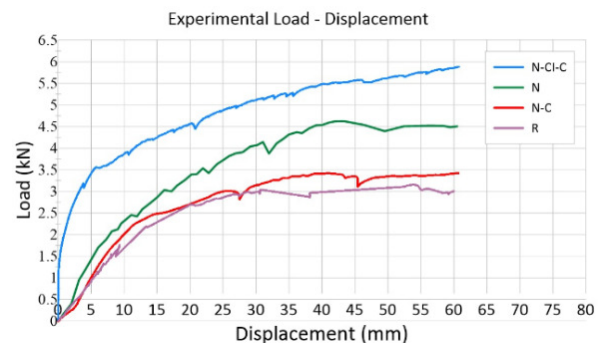


Fig. 11. Load displacement of models at 60mm displacement.

B. Static Test Results and Discussion

Table II and Figures 10-11 lead to the conclusion that a major increase in the load-bearing capacity was detected by the column N-CI-C due to the circularization technique that provided more rigidity in comparison to the column R. Column N also showed a significant increase in the load-bearing capacity but less than column N-CI-C. In contrast, the column N-C showed a different failure mode, in which it doesn't increase the load-bearing capacity. Figure 11 shows the load displacement of the models for 60mm displacement due to the serviceability limit [12].

IV. DYNAMIC TEST

One column from each group was tested using the shaking table developed in [13], utilizing the time history analysis method to simulate the seismic excitation. Two LVDTs were put at the top and the base of the columns to assess the displacement after the seismic excitation with 3 amplitudes, 0.05g, 0.15g, and 0.32g, to study the behavior of the columns that were strengthened with different techniques, as shown in Figure 12. In this study, an additional mass was used to simulate the loads subjected to the column, so it was assumed that the load on the prototype is 2543kg, and the weight of the mass model is 282.6kg, according to [14]. For mass similitude, additional weight was added in the form of steel plates at the free end of the column models, which were made up for the weight deficiency of 22mm thickness and 15kg weight each.



Fig. 12. Dynamic test.

1) Dynamic Test Results and Discussions

Table III lists the results of the 4 models after being subjected to El Centro seismic excitation. Each column was subjected to three amplitudes, 0.05g, 0.15g, and 0.32g. Figures 13 to 21 show the displacement-time curve of all models and the comparison with the reference model.

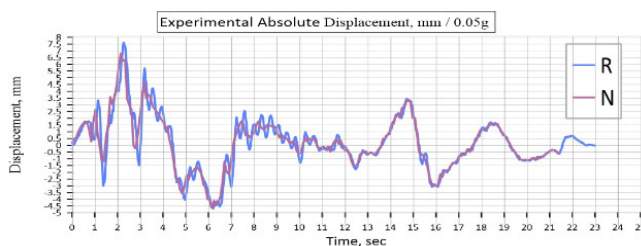


Fig. 13. Time-displacement of R and N models with 0.05g excitation.

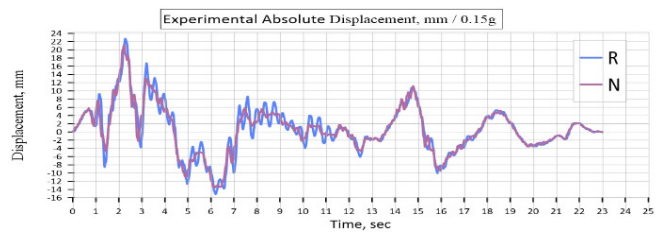


Fig. 14. Time-displacement of R and N models with 0.15g excitation.

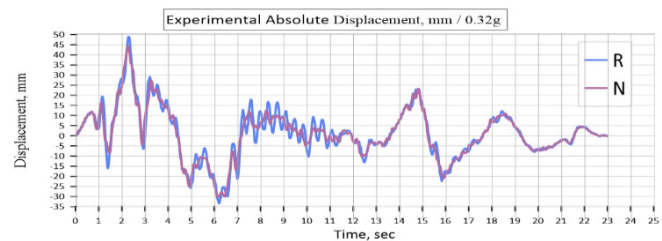


Fig. 15. Time-displacement of R and N models with 0.32g excitation.

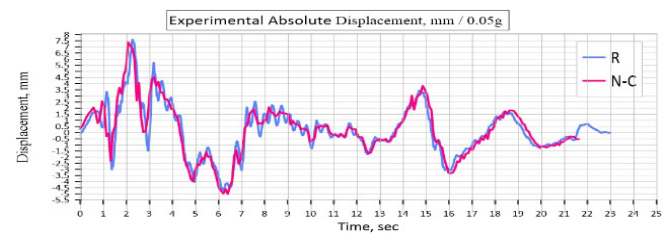


Fig. 16. Time-displacement of R and N-C models with 0.05g excitation.

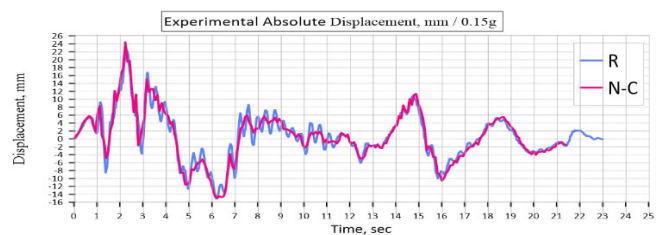


Fig. 17. Time-displacement of R and N-C models with 0.15g excitation.

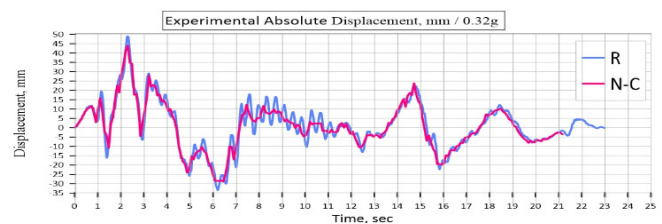


Fig. 18. Time-displacement of R and N-C models with 0.32g excitation.

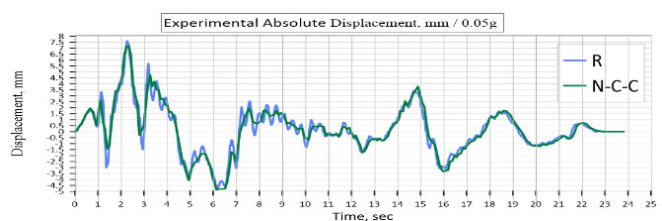


Fig. 19. Time-displacement of R and N-CI-C models with 0.05g excitation.

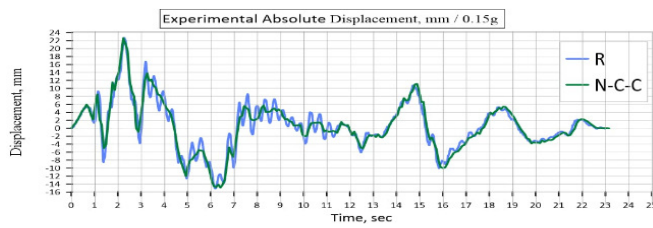


Fig. 20. Time-displacement of R and N-CI-C models with 0.15g excitation.

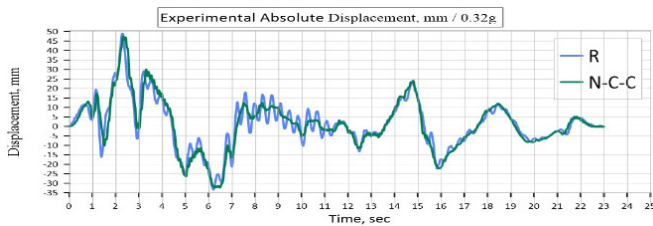


Fig. 21. Time-displacement of R and N-CI-C models with 0.32g excitation.

TABLE III. DYNAMIC TEST RESULTS

Column code	Earthquake amplitude (g)	Absolute displacement (mm)		Relative displacement (mm)	
		Max.	Min.	Max.	Min.
R	0.05	7.607	-4.685	2.059	-2.289
	0.15	22.69	-15.12	5.127	-5.968
	0.32	48.96	-33.41	5.801	-7.821
N	0.05	6.909	-4.621	0.973	-0.911
	0.15	21.08	-13.51	2.233	-3.882
	0.32	44.33	-30.31	3.901	-6.019
N-C	0.05	7.384	-5.117	0.924	-1.807
	0.15	24.4	-14.93	3.912	-3.187
	0.32	43.9	-28.9	4.115	-6.501
N-CI-C	0.05	7.352	-4.8	0.413	-0.551
	0.15	22.63	-14.8	3.11	-2.54
	0.32	46.05	-32.3	2.322	-3.924

Table III and Figures 13-21 showed that a major reduction in the displacement was detected by the column N-CI-C due to the circularization technique that provided more rigidity compared to the column R. Column N also showed a significant reduction in the displacement, but less than N-CI-C. In contrast, the column N-C showed a different failure mode, which doesn't enhance the dynamic response.

V. CONCLUSIONS

In this study, the behavior of slender columns strengthened with strengthening techniques was studied. Two approaches were adopted. In the dynamic test approach, a column model was subjected to El Centro 1940 NS earthquake excitation by using a shaking table. In the static test approach, a column model was subjected to a lateral load and tested up to failure. Depending on the experimental test results the main conclusions can be summarized as:

In the static test, the strengthening techniques showed significant increase in load carrying capacity, of about 86.6%, and 46.6%, for circularization with NSM-CFRP and NSM-CFRP respectively, of the reference unstrengthened columns.

In the dynamic test, columns that were strengthened with hybrid NSM-CFRP and EB-CFRP showed a different failure mode. Dynamically, the lateral drift was decreased by about 75%, 47%, and 49% for earthquake amplitudes of 0.05g, 0.15g, and 0.32g respectively.

The circularization process effectively avoided stress concentration zones that would otherwise occur when a non-circular column was wrapped in CFRP. As a result, the load-carrying capacity and dynamic response improved.

ACKNOWLEDGMENT

The authors wish to thank the Department of Civil Engineering at the University of Baghdad for their assistance.

REFERENCES

- [1] *Seismic Evaluation and Retrofit of Existing Buildings*. American Society of Civil Engineers, 2014.
- [2] M. Saadi and D. Yahiaoui, "The Effectiveness of Retrofitting RC Frames with a Combination of Different Techniques," *Engineering, Technology & Applied Science Research*, vol. 12, no. 3, pp. 8723–8727, Jun. 2022, <https://doi.org/10.48084/etasr.4979>.
- [3] M. Fahim, F. Alam, H. Khan, I. U. Haq, S. Ullah, and S. Zaman, "The Behavior of RC Beams Retrofitted with Carbon Fiber Reinforced Polymers (CFRP)," *Engineering, Technology & Applied Science Research*, vol. 12, no. 3, pp. 8701–8706, Jun. 2022, <https://doi.org/10.48084/etasr.4926>.
- [4] K. Soudki and T. Alkhrdaji, "Guide for the Design and Construction of Externally Bonded FRP Systems for Strengthening Concrete Structures (ACI 440.2R-02)," in *Structures Congress 2005*, Apr. 2012, [https://doi.org/10.1061/40753\(171\)159](https://doi.org/10.1061/40753(171)159).
- [5] V. L. Doan, "Behaviour of shape-modified columns confined with carbon fibre-reinforced polymer under eccentric loading," M.S. thesis, University of Wollongong, Wollongong, Australia, 2013.
- [6] Z. Yan, "Shape modification of rectangular columns confined with FRP composites," Ph.D. dissertation, University of Utah, Salt Lake City, UT, USA, 2005.
- [7] M. Nuruzzaman, J. O. Camargo Casimiro, and P. K. Sarker, "Fresh and hardened properties of high strength self-compacting concrete using by-product ferromagnetic slag fine aggregate," *Journal of Building Engineering*, vol. 32, Nov. 2020, Art. no. 101686, <https://doi.org/10.1016/j.jobbe.2020.101686>.
- [8] J. Abd and I. K. Ahmed, "The Effect of Low Velocity Impact Loading on Self-Compacting Concrete Reinforced with Carbon Fiber Reinforced Polymers," *Engineering, Technology & Applied Science Research*, vol. 11, no. 5, pp. 7689–7694, Oct. 2021, <https://doi.org/10.48084/etasr.4419>.
- [9] C. Maheswaran, S. Prakash Shanmugam, V. Mahadik, and A. Sharma, "Experimental and Numerical Studies on Effectiveness of Hybrid FRP Strengthening on Behavior of RC Columns under High Eccentric Compression," *Journal of Bridge Engineering*, vol. 24, no. 6, Jun. 2019, [https://doi.org/10.1061/\(ASCE\)BE.1943-5592.0001420](https://doi.org/10.1061/(ASCE)BE.1943-5592.0001420).
- [10] R. Abokwiek, "Strengthening of Reinforced Concrete Columns Using Composite of Near Surface Mounted CFRP Strips and Fabric," M.S. thesis, American University of Sharjah, Sharjah, United Arab Emirates, 2016.
- [11] Ü. Karagöz İşleyen and H. İ. Kesik, "Experimental and numerical analysis of compression and bending strength of old wood reinforced with CFRP strips," *Structures*, vol. 33, pp. 259–271, Oct. 2021, <https://doi.org/10.1016/j.istruc.2021.04.070>.
- [12] *ASCE 7 standard*. ASCE, 2016.
- [13] H. Al-Baghdadi, "Nonlinear Dynamic Response of Reinforced Concrete Buildings to Skew Seismic Excitation," Ph.D. dissertation, University of Baghdad, Baghdad, Iraq, 2014.
- [14] H. Harris and G. M. Sabnis, *Structural Modeling and Experimental Techniques*, 2nd ed. Boca Raton, FL, USA: CRC Press, 1999.

The Effects of Superstatistics Properties on Hot Plasma

Samia Dilmi

Laboratory of Operator Theory and
PDE, Faculty of Exact Sciences
University of El Oued
El-Oued, Algeria
samia-dilmi@univ-eloued.dz

Fadhila Khalfaoui

Laboratory of Operator Theory and
PDE, Faculty of Exact Sciences
University of El Oued
El-Oued, Algeria
fadhila-khalfaoui@univ-eloued.dz

Abdelmalek Boumali

Laboratory of Applied and
Theoretical Physics
University LarbiTébessi
Tébessa, Algeria
boumali.abdelmalek@gmail.com

Received: 26 July 2022 | Revised: 5 August 2022 | Accepted: 16 August 2022

Abstract—The electron impact ionization is a crucial atomic process in the collisional radiative model and the study of ionization balance. The superstatistics theory, which was originally proposed for the study of non-equilibrium complex systems, has recently been extended to studies of small systems interacting with a finite environment due to their interesting statistical behavior. This paper introduces the superstatistics formalism in the case of ionization rates with different values of the dynamical parameter q and shows how it affects the calculation of the ionization rates for Li^+ . Moreover, the distribution function for the effective Boltzmann factor of superstatistics was swapped.

Keywords—ionization rates; Boltzmann factor; superstatistics; code FAC; cross-section

I. INTRODUCTION

Electron impact ionization of neutral atoms has been proven to be significant in a variety of fields, including mass spectrometry and plasma physics [1]. Thomson utilized the ionization of atoms by charge impact in the early 1910s. Since then, many others, have amended it [2, 3]. Furthermore, electron-impact ionization has been used to measure a detailed ionization spectrum and cross-sections using various methods [4]. Plasma is important in nuclear physics because many studies showed that it can take various shapes, including non-equilibrium plasma that is used to change the characteristics of the surface [5, 6]. The characteristics of non-equilibrium plasmas are known through the ionization of atoms and molecules by electron impact, which has great practical significance. Experimental data, which include laboratory plasma at low and high temperatures, atmospheric physics, and mass spectrometry, are also significant as they can be compared to theoretical predictions [7, 8].

Ionization occurs when an electron collides with a neutral particle with sufficient energy to produce a positive ion and a free electron [9]. Superstatistics is a subfield of statistical physics or mechanics that studies nonlinear and non-equilibrium systems [10]. It is characterized by the use of a superposition of several distinct statistical models to attain the desired nonlinearity. In ordinary statistical terms, this is similar

to compounding the distributions of random variables, and it can be thought of as a simple case of a doubly stochastic model [11, 12]. Furthermore, superstatistics contends that in systems with temperature fluctuations, coarse-grained measurements of the energy performed over spatial and temporal scales are larger than those determined through the correlation properties of the temperature.

Yield statistical distributions can be considered as a superposition of canonical distributions. Superstatistics [10, 13-17] is a powerful modeling and/or analysis technique for complex systems with two or more distinct time scales in dynamics. The fundamental idea is to consider a superposition of several systems in local equilibrium, each with its inverse temperature, and then take an average over the fluctuating that are disseminated according to some probability density for theoretical modeling. In general, the parameter does not have to be an inverse temperature but could be any system parameter that shows large-scale fluctuations, such as energy dissipation in a turbulent flow or financial market volatility [18]. Finally, all relevant expectation values for the complex system are averaged over this distribution. Several applications have been previously described, including modeling the statistics of classical turbulent flow [19, 20], quantum turbulence [21], spacetime granularity [22], stock price changes [23, 24], virus infection pathways [25], and more [4, 25-27].

Once incorporated into the fluctuating parameter, superstatistical systems are efficiently described by more general measures than the Boltzmann–Gibbs entropy. The following question can be asked: What entropy statistics appear in the case of a fluctuating control parameter? This study aimed to develop a generalization of the Beck-Cohen superstatistics that makes possible to appropriately consider such fluctuations. The main idea was to use superstatistics to replace the distribution function via the effective Boltzmann factor and introduce the superstatistics formalism in the case of ionization rates with different values of q .

II. SUPERSTATISTICS

Long-range interactions between different ions and electrons dominate in the plasma state, causing these systems to

be in highly non-equilibrium states. Even when these systems achieve a steady state, they do not adhere to Boltzmann-Gibbs statistics [14]. The following critical question is asked: Do these steady-state plasmas have a well-determined temperature? Superstatistics was introduced in 2003 as an interesting suggestion for the treatment of non-equilibrium steady-state systems [10] and depends on ordinary Boltzmann statistics, which are formed as a tool to study systems with complex dynamics and non-equilibrium [15]. In a non-Boltzmann-Gibbs distribution, where the systems are out of equilibrium and non-extensive, superstatistics displays a relative motion to explain the gain of it [27]. These statistics admit the superposition of canonical ensembles at different temperatures [28]. Superstatistics is a branch of statistical mechanics that occurs in non-equilibrium and stable states with large parameter fluctuations. They were named superstatistics because they are a type of "statistics of statistics" [28]. Superstatistics systems are a superposition of two (or more) different statistics: one is given by ordinary Boltzmann factor, and the other by large-scale fluctuations of one (or many) intensive parameters, e.g. the inverse temperature [29]. Since then, it has been used to describe a wide variety of dynamic structures with changing environmental conditions [30]. This new type relies on ordinary statistical mechanics, described by the ordinary Boltzmann factor $e^{-\beta E}$, thus an effective Boltzmann factor $B(E)$ for the full system can be defined as [31]:

$$B(E) = \int_0^\infty f(\beta) e^{-\beta E} d\beta = \langle e^{-\beta E} \rangle \quad (1)$$

where $f(\beta)$ is the normalized probability distribution, E is the effective energy in each cell, and $\beta = \frac{1}{K_B T}$ is approximately a constant. At the same time, the normalized probability distribution must be realized by probability density [10]:

$$f(\beta) = \delta(\beta - \beta_0) \quad (2)$$

where β_0 is the average of β (fixed constant) and δ is the Dirac delta. The probability density $f(\beta)$ has to provide the following conditions:

1. It must be a normalized probability density, it may be a physically relevant density from statistics, such as Gaussian, uniform, etc. [32].
2. When there are no fluctuations in intensive quantities, the new statistics decrease to Boltzmann-Gibbs statistics [33, 34], and has to be normalizable [34].

There are two types of superstatistics:

- Type-A superstatistics, where the Boltzmann factor is normalized to yield the stationary long-term probability distribution [35]:

$$P(E) = \frac{1}{Z(\beta)} B(E) e^{-\beta E} \quad (3)$$

- Type-B superstatistics: As the distribution in type A is not properly normalized, a better way of writing would be [36]:

$$P(E) = \int \frac{e^{-\beta E}}{Z(\beta)} f(\beta) d\beta \quad (4)$$

$$Z(\beta) = \int_0^\infty B(E) dE \quad (5)$$

where $Z(\beta)$ is the normalization constant of $e^{-\beta E}$ for a given β .

This approximation represents the leading order correction to ordinary statistical mechanics for a nonhomogeneous system with small temperature fluctuations. Following this approximation, it was demonstrated that the generalized Boltzmann factor for any distribution is given by the following:

$$B(E) = e^{-\beta_0 E} \left(1 + \frac{1}{2} \sigma^2 E^2 + \sum_{r=3}^\infty \frac{(1)^r}{r!} \langle (\beta - \beta_0)^r \rangle E^r \right) \quad (6)$$

with average $\langle \beta \rangle = \beta_0 = \int_0^\infty \beta f(\beta) d\beta$, and variance $\sigma^2 = \langle \beta^2 \rangle - \langle \beta \rangle^2$. The zeroth-order approximation to $B(E)$ corresponds, as is expected, to the "pure" Boltzmann statistic: $B(E_n) \sim e^{-\langle \beta \rangle E_n}$. This universality indicated that the superstatistics theory is restricted by two universal parameters (β, q) with:

$$q = \frac{\langle \beta^2 \rangle}{\langle \beta \rangle^2} \quad (7)$$

In (7), the parameter q is simply the coefficient of variation of the distribution $f(\beta)$ defined by the standard deviation to mean ratio. The fluctuation of the intensive parameter β is controlled by this parameter. If there are no fluctuations, $q=1$ [10]. To easier deal with the Boltzmann factor, it was imposed into a general form as [10]:

$$B(E) = e^{-\beta_0 E} \left(1 + \frac{1}{2} (q-1) \beta_0^2 E^2 + g(q) \beta_0^3 E^3 \dots \right) \quad (8)$$

where the function $g(q)$ is determined by the used superstatistics. The following can be obtained:

$$g(q) = 0 \quad (\text{uniform and 2-level}) \quad (9)$$

$$= -\frac{1}{3} (q-1)^2 \quad (\text{Gamma}) \quad (10)$$

$$= -\frac{1}{3} (q^3 - 3q + 2) \quad (\text{log-normal}) \quad (11)$$

$$= -\frac{1}{3} \frac{(q-1)(5q-6)}{3-q} \quad (\text{F-distribution}) \quad (12)$$

Finally, superstatistics has become a hot topic in recent years, with applications in a variety of fields of physics [37].

III. CALCULATION OF THE IONIZATION RATES FROM SUPERSTATISTICS DISTRIBUTIONS

This study aims to calculate the ionization rates from superstatistics distributions. Free electrons are represented by a specific energy distribution within the plasma. The ionization rates were calculated through the integration of a cross-section of a collision that depends on energy over the energy distribution functions. The ionization rates by electron impact were calculated by averaging the product of the electron's velocity and the ionization cross-section. An ionizing collision results in an electron impact process, resulting in a low-energy electron and an atomic ion if an electron receives sufficient energy (via super-elastic collisions), which is equivalent to the neutral atom's ionizing potential. The ionization rates for direct ionization are defined by [38, 39]:

$$\tau = \int v \sigma(\varepsilon) F(\varepsilon) d\varepsilon \quad (13)$$

where v is the velocity of the incident electron, $\sigma(\varepsilon)$ is the impact ionization cross sections calculated by the FAC code [40, 41], $F(\varepsilon)$ is the electron energy distribution function, and ε is the energy of the impacting electron.

The associated rate coefficients could be represented by a simple analytical formula using the appropriate approximation for the energy dependency of the cross-sections. Two types of distribution functions were used in previous studies for the ionization rates: Maxwellian and non-Maxwellian. Indeed, superstatistics provides an effective description of their tools, having demonstrated their adaptability in advanced research. As a result, the calculations were extended to the case of plasma by replacing $F(\varepsilon)$ in (13) with the effective Boltzmann factor $B(E)$ using the superstatistics distribution function. The FAC code [40] was used for the calculation of the Li^+ cross-sections, where the relativistic Distorted Wave (DW) approximation method with an interpolation-factorization method [42] was used. The type of most physically pertinent averaging process for a generic system with intense parameter fluctuations is an intriguing question. The answer to this question depends on the physical problem under consideration. Depending on the underlying microscopic dynamics, different non-equilibrium systems may necessitate different types of superstatistics. When using the effective Boltzmann factor:

$$\tau = \int v \sigma(E) B(E) dE \quad (14)$$

the ionization rates become:

$$\tau = \int_0^\infty v \sigma(E) e^{-\beta_0 E} \left(1 + \frac{1}{2}(q-1)\beta_0^2 E^2 + g(q)\beta_0^3 E^3 \right) dE \quad (15)$$

where $g(q)$ refers to the previously shown superstatistics formulas.

IV. RESULTS AND DISCUSSION

The above definitions can be used to obtain the results of measuring the ionization rates of Li^+ for the Gamma, log-normal, and F-distributions for various values of q in Figures 1, 2, and 3. Li^+ ionization rates were calculated using (15) and the various $g(q)$ functions, which rely on the superstatistics concept. The values of the rate coefficients in Figures 1-3 increase very quickly at low temperatures. In the case of high temperatures, the ionization rate curves were very sensitive to q values, and the curves gradually moved away from each other as the q values increased. There is a convergence of the curves for the same distribution and a lot of coordination between the curves for all three functions, especially for low values of q .

In general, the behavior of all superstatistics at high temperatures differs, as it is strongly dependent on the $f(\beta)$ function, but the behavior at low temperatures is universal. Furthermore, it should be noted that the first-order corrections to the Boltzmann factor $e^{-\beta_0 E}$ for the above distribution functions can be written in a universal form. The physical meaning of this broadly defined parameter q is simply the coefficient of variation of the distribution $f(\beta)$, defined by the standard deviation/mean ratio. If there are no fluctuations in β , q equals to 1.

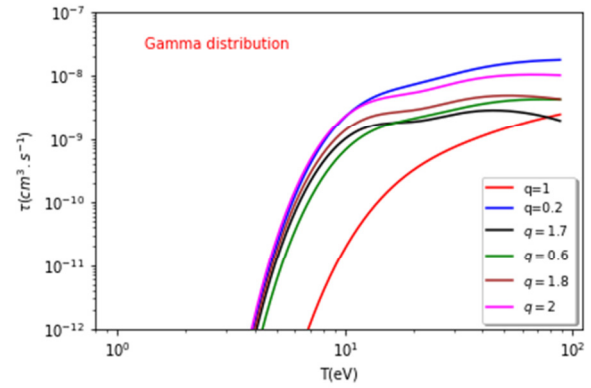


Fig. 1. Ionization rates of Li^+ obtained by the Gamma distribution with different values of q .

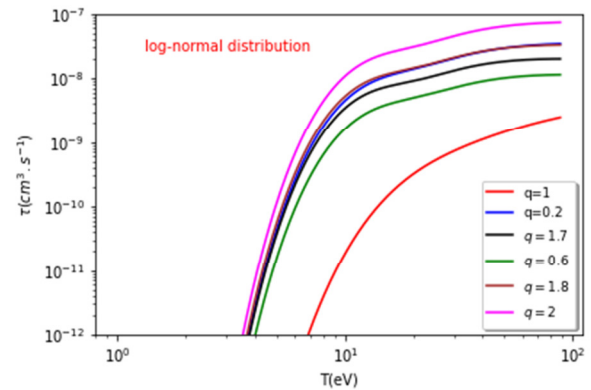


Fig. 2. Ionization rates of Li^+ obtained by the log-normal distribution with different values of q .

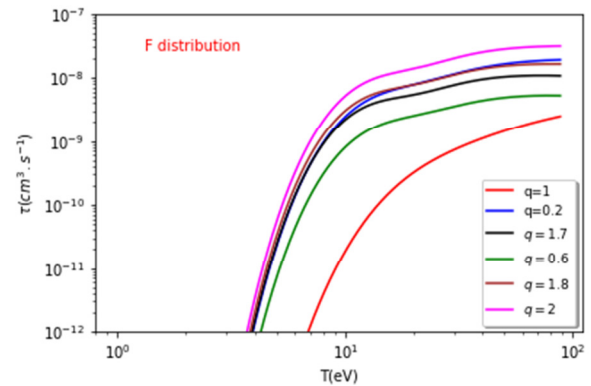


Fig. 3. Ionization rates of Li^+ obtained by the F-distribution with different values of q .

V. CONCLUSION

This study used the FAC code for the calculation of the cross-sections of Li^+ . The Maxwellian distribution function of energy was replaced by an effective Boltzmann factor for various distribution functions to estimate ionization rates from cross-sections. As superstatistics and Maxwellian statistics have similarities when q is close to 1, the results showed a good agreement between the designed curves for various values of q . However, instead of applying deviations to a

superstatistical non-equilibrium system, they were applied to an ordinary statistical mechanics equilibrium system with an inverse temperature. Moreover, superstatistics theory requires the presence of temporally local equilibrium within the plasma, which appears to be a non-equilibrium thermodynamic system. Thus, the introduction of superstatistics formalism in the case of ionization rates with different values of q was limited to agreement with other statistics. The connection between the Maxwellian distributions and the Beck-Cohen superstatistics can be noted, as the relationship between the superstatistics approach and the different values of q on the calculation of lithium ionization rates Li^+ was shown.

The dynamic parameter q of (7) can be defined in superstatistics methods. It was shown that all superstatistics have universal behavior for small variances in the fluctuations. There were differences of large variance that gave information on the underlying complex dynamics [43]. In general, different types of superstatistics may be required for complex non-equilibrium problems. The Tsallis statistics are just one example of many new statistical methods that could be used [36]. There is no reason to believe that other superstatistics would not exist in nature.

REFERENCES

- [1] A. J. Murray, "(e,2e) ionization studies of alkaline-earth-metal and alkali-earth-metal targets: Na, Mg, K, and Ca, from near threshold to beyond intermediate energies," *Physical Review A*, vol. 72, no. 6, Dec. 2005, Art. no. 062711, <https://doi.org/10.1103/PhysRevA.72.062711>.
- [2] H. Deutsch and T. D. Märk, "Calculation of absolute electron impact ionization cross-section functions for single ionization of He, Ne, Ar, Kr, Xe, N and F," *International Journal of Mass Spectrometry and Ion Processes*, vol. 79, no. 3, pp. R1–R8, Nov. 1987, [https://doi.org/10.1016/0168-1176\(87\)83009-4](https://doi.org/10.1016/0168-1176(87)83009-4).
- [3] X. Llovet, C. J. Powell, F. Salvat, and A. Jablonski, "Cross Sections for Inner-Shell Ionization by Electron Impact," *Journal of Physical and Chemical Reference Data*, vol. 43, no. 1, Mar. 2014, Art. no. 013102, <https://doi.org/10.1063/1.4832851>.
- [4] V. Jonauskas *et al.*, "Electron-impact ionization of W^{5+} ," *Physical Review A*, vol. 100, no. 6, Dec. 2019, Art. no. 062701, <https://doi.org/10.1103/PhysRevA.100.062701>.
- [5] F. Mehmood, T. Kamal, and U. Ashraf, "Generation and Applications of Plasma (An Academic Review)," Oct. 2018, <https://doi.org/10.20944/preprints201810.0061.v1>.
- [6] A. Alogla, M. a. H. Eleiwa, and H. Alshortan, "Design and Evaluation of Transmitting Antennas for Solar Power Satellite Systems," *Engineering, Technology & Applied Science Research*, vol. 11, no. 6, pp. 7950–7956, Dec. 2021, <https://doi.org/10.48084/etasr.4607>.
- [7] L. J. Kieffer and G. H. Dunn, "Electron Impact Ionization Cross-Section Data for Atoms, Atomic Ions, and Diatomic Molecules: I. Experimental Data," *Reviews of Modern Physics*, vol. 38, no. 1, pp. 1–35, Jan. 1966, <https://doi.org/10.1103/RevModPhys.38.1>.
- [8] M. Alhamdany and A. H. K. Albayati, "Statistical Modeling of Time Headway on Urban Roads: A Case Study in Baghdad," *Engineering, Technology & Applied Science Research*, vol. 12, no. 3, pp. 8584–8591, Jun. 2022, <https://doi.org/10.48084/etasr.4878>.
- [9] A. Chachereau and S. Pancheshnyi, "Calculation of the Effective Ionization Rate in Air by Considering Electron Detachment From Negative Ions," *IEEE Transactions on Plasma Science*, vol. 42, no. 10, pp. 3328–3338, Jul. 2014, <https://doi.org/10.1109/TPS.2014.2354676>.
- [10] C. Beck and E. G. D. Cohen, "Superstatistics," *Physica A: Statistical Mechanics and its Applications*, vol. 322, pp. 267–275, May 2003, [https://doi.org/10.1016/S0378-4371\(03\)00019-0](https://doi.org/10.1016/S0378-4371(03)00019-0).
- [11] A. F. Tseluyko, V. T. Lazurik, D. L. Ryabchikov, V. I. Maslov, and I. N. Sereda, "Experimental study of radiation in the wavelength range 12.2–15.8 nm from a pulsed high-current plasma diode," *Plasma Physics Reports*, vol. 34, no. 11, pp. 963–968, Nov. 2008, <https://doi.org/10.1134/S1063780X0811010X>.
- [12] A. F. Tseluyko *et al.*, "Influence of plasma nucleus form on radiation orientation in high-current pulse plasma diode," *Problems of Atomic Science and Technology*, no. 6, pp. 176–178, 2010.
- [13] C. Beck, E. G. D. Cohen, and H. L. Swinney, "From time series to superstatistics," *Physical Review E*, vol. 72, no. 5, Nov. 2005, Art. no. 056133, <https://doi.org/10.1103/PhysRevE.72.056133>.
- [14] H. Touchette and C. Beck, "Asymptotics of superstatistics," *Physical Review E*, vol. 71, no. 1, Jan. 2005, Art. no. 016131, <https://doi.org/10.1103/PhysRevE.71.016131>.
- [15] C. Mark, C. Metzner, and B. Fabry, "Bayesian inference of time varying parameters in autoregressive processes," Oct. 2009, 2014, <https://doi.org/10.48550/arXiv.1405.1668>.
- [16] R. Hanel, S. Thurner, and M. Gell-Mann, "Generalized entropies and the transformation group of superstatistics," *Proceedings of the National Academy of Sciences*, vol. 108, no. 16, pp. 6390–6394, Apr. 2011, <https://doi.org/10.1073/pnas.1103539108>.
- [17] A. M. Reynolds, "Superstatistical Mechanics of Tracer-Particle Motions in Turbulence," *Physical Review Letters*, vol. 91, no. 8, Aug. 2003, Art. no. 084503, <https://doi.org/10.1103/PhysRevLett.91.084503>.
- [18] M. Ausloos and K. Ivanova, "Dynamical model and nonextensive statistical mechanics of a market index on large time windows," *Physical Review E*, vol. 68, no. 4, Oct. 2003, Art. no. 046122, <https://doi.org/10.1103/PhysRevE.68.046122>.
- [19] C. Beck, "Statistics of Three-Dimensional Lagrangian Turbulence," *Physical Review Letters*, vol. 98, no. 6, Feb. 2007, Art. no. 064502, <https://doi.org/10.1103/PhysRevLett.98.064502>.
- [20] C. Beck and S. Miah, "Statistics of Lagrangian quantum turbulence," *Physical Review E*, vol. 87, no. 3, Mar. 2013, Art. no. 031002, <https://doi.org/10.1103/PhysRevE.87.031002>.
- [21] P. Jizba and F. Scardigli, "Special relativity induced by granular space," *The European Physical Journal C*, vol. 73, no. 7, Jul. 2013, Art. no. 2491, <https://doi.org/10.1140/epjc/s10052-013-2491-x>.
- [22] S. Rizzo and A. Rapisarda, "Environmental Atmospheric Turbulence at Florence Airport," *AIP Conference Proceedings*, vol. 742, no. 1, pp. 176–181, Dec. 2004, <https://doi.org/10.1063/1.1846475>.
- [23] P. Rabassa and C. Beck, "Superstatistical analysis of sea-level fluctuations," *Physica A: Statistical Mechanics and its Applications*, vol. 417, pp. 18–28, Jan. 2015, <https://doi.org/10.1016/j.physa.2014.08.068>.
- [24] Y. Ito, "Heterogeneous anomalous diffusion in view of superstatistics," *Physics Letters A*, vol. 378, no. 41, pp. 3037–3040, Aug. 2014, <https://doi.org/10.1016/j.physleta.2014.08.022>.
- [25] K. Briggs and C. Beck, "Modelling train delays with q-exponential functions," *Physica A: Statistical Mechanics and its Applications*, vol. 378, no. 2, pp. 498–504, May 2007, <https://doi.org/10.1016/j.physa.2006.11.084>.
- [26] L. Leon Chen and C. Beck, "A superstatistical model of metastasis and cancer survival," *Physica A: Statistical Mechanics and its Applications*, vol. 387, no. 13, pp. 3162–3172, May 2008, <https://doi.org/10.1016/j.physa.2008.01.116>.
- [27] D. N. Sob'yanin, "Hierarchical maximum entropy principle for generalized superstatistical systems and Bose-Einstein condensation of light," *Physical Review E*, vol. 85, no. 6, Jun. 2012, Art. No. 061120, <https://doi.org/10.1103/PhysRevE.85.061120>.
- [28] G. C. Yalcin and C. Beck, "Environmental superstatistics," *Physica A: Statistical Mechanics and its Applications*, vol. 392, no. 21, pp. 5431–5452, Nov. 2013, <https://doi.org/10.1016/j.physa.2013.06.057>.
- [29] K. Ourabah and M. Tribeche, "Fractional superstatistics from a kinetic approach," *Physical Review E*, vol. 97, no. 3, Mar. 2018, Art. no. 032126, <https://doi.org/10.1103/PhysRevE.97.032126>.
- [30] M. Baus and C. F. Tejero, Eds., *Equilibrium Statistical Physics*. Berlin, Heidelberg: Springer, 2008.
- [31] T. D. Märk, "Cluster ions: Production, detection and stability," *International Journal of Mass Spectrometry and Ion Processes*, vol. 79,

- no. 1, pp. 1–59, Oct. 1987, [https://doi.org/10.1016/0168-1176\(87\)80022-8](https://doi.org/10.1016/0168-1176(87)80022-8).
- [32] G. C. Yalcin and C. Beck, "Currents in complex polymers: An example of superstatistics for short time series," *Physics Letters A*, vol. 376, no. 35, pp. 2344–2347, Jul. 2012, <https://doi.org/10.1016/j.physleta.2012.05.057>.
- [33] H. Touchette and C. Beck, "Asymptotics of superstatistics," *Physical Review E*, vol. 71, no. 1, Jan. 2005, Art. no. 016131, <https://doi.org/10.1103/PhysRevE.71.016131>.
- [34] A. Boumali, F. Serdouk, and S. Dilmi, "Superstatistical properties of the one-dimensional Dirac oscillator," *Physica A: Statistical Mechanics and its Applications*, vol. 553, Sep. 2020, Art. no. 124207, <https://doi.org/10.1016/j.physa.2020.124207>.
- [35] S. Sargolzaeipor, H. Hassanabadi, and W. S. Chung, "q-deformed superstatistics of the Schrödinger equation in commutative and noncommutative spaces with magnetic field," *The European Physical Journal Plus*, vol. 133, no. 1, Jan. 2018, Art. no. 5, <https://doi.org/10.1140/epjp/i2018-11827-1>.
- [36] C. Tsallis and A. M. C. Souza, "Constructing a statistical mechanics for Beck-Cohen superstatistics," *Physical Review E*, vol. 67, no. 2, Feb. 2003, Art. no. 026106, <https://doi.org/10.1103/PhysRevE.67.026106>.
- [37] F. Sattin, "Bayesian approach to superstatistics," *The European Physical Journal B - Condensed Matter and Complex Systems*, vol. 49, no. 2, pp. 219–224, Jan. 2006, <https://doi.org/10.1140/epjb/e2006-00038-8>.
- [38] S. B. Hansen and A. S. Shlyaptseva, "Effects of the electron energy distribution function on modeled x-ray spectra," *Physical Review E*, vol. 70, no. 3, Sep. 2004, Art. no. 036402, <https://doi.org/10.1103/PhysRevE.70.036402>.
- [39] A. Escarguel, F. B. Rosmej, C. Brault, T. Pierre, R. Stamm, and K. Quotb, "Influence of hot electrons on radiative properties of a helium plasma," *Plasma Physics and Controlled Fusion*, vol. 49, no. 1, pp. 85–93, Sep. 2006, <https://doi.org/10.1088/0741-3335/49/1/006>.
- [40] *Flexible Atomic Code (FAC)*. <https://www-amdis.iaea.org/FAC/>.
- [41] M. F. Gu, "The flexible atomic code," *Canadian Journal of Physics*, vol. 86, no. 5, pp. 675–689, May 2008, <https://doi.org/10.1139/p07-197>.
- [42] W. Lotz, "Electron-Impact Ionization Cross-Sections and Ionization Rate Coefficients for Atoms and Ions," *The Astrophysical Journal Supplement Series*, vol. 14, May 1967, <https://doi.org/10.1086/190154>.
- [43] N. B. Serradj, A. D. K. Ali, and M. E. A. Ghernaout, "A Contribution to the Thermal Field Evaluation at the Tool-Part Interface for the Optimization of Machining Conditions," *Engineering, Technology & Applied Science Research*, vol. 11, no. 6, pp. 7750–7756, Dec. 2021, <https://doi.org/10.48084/etasr.4235>.

The Mechanical Properties of Ferrocement Mortar with Waste Plastic Fibers at Elevated Temperatures

Farah A. Al-Fahdawi
Department of Civil Engineering
University of Anbar
Anbar, Iraq
far20e1013@uoanbar.edu.iq

Abdulkader I. Al-Hadithi
Department of Civil Engineering
University of Anbar
Anbar, Iraq
abdulkader.alhadithi@uoanbar.edu.iq

Jamal A. Al-Asafi
Department of Civil Engineering
University of Anbar
Anbar, Iraq
jamal.Khalaf@uoanbar.edu.iq

Received: 21 July 2022 | Revised: 31 July 2022 | Accepted: 10 August 2022

Abstract-The main aim of the current research was to investigate the behavior of ferrocement mortar reinforced with waste plastic fibers at elevated temperatures. The use of PET residues in ferrocement mortar at normal temperatures could be a viable option. However, the utilization of PET-containing ferrocement mortar in high-temperature applications requires more research. In this study, one reference mix was made along with 3 other mixes containing Polyethylene Terephthalate (PET) fiber by volumetric ratios of 0.5, 0.75, and 1%. Compressive and flexural strength tests were performed on the samples before and after being exposed to elevated temperatures. Each batch of ferrocement mortar samples was heated to the requisite temperature for roughly 60 minutes, then was progressively cooled to room temperature before being tested. The compressive and flexural strengths of some samples were evaluated at room temperature (25°C). Other samples were evaluated after being exposed to high temperatures in an electric furnace (100°C, 200°C, 400°C, and 600°C). Both compressive and flexural strengths were found to be significantly reduced after being exposed to a temperature greater than 400°C. Results proved that the addition of 0.75% PET was determined as the optimum percentage that enhanced the mechanical properties of the produced ferrocement mortar at 25°C. At 200°C, the ferrocement mortar samples retained their original color. As a result of the combustion of PET fibers, black spots formed on the top surfaces of the tested specimens that were heated to 400°C.

Keywords-elevated temperature; ferrocement mortar; flexural strength; compressive strength; PET; mechanical properties

I. INTRODUCTION

Ferrocement is a thin water-cement mortar that has been reinforced with close layers. It is considered the best regarding the resistance to compression, tensile strength, and fracture parameters. Also it is light weight, easy to operate, and economical. Ferrocement technology was introduced in the

'70s; damaged parts of concrete structures were reinforced with this mortar [1]. Cement mortars are a main component of the construction industry, used in many applications and in the manufacturing of ferrocement elements [2]. The mortar is the resulting material for the proposed mixture (intimate mixture) of sand grains, binder, and water. Its properties depend mainly on the nature of the compounds of the binder in it [3]. Cement mortar is used as a binder for building units in walls or to protect building surfaces. When making ferrocement, the mortar has a 95% or more effect on the behavior of the final product. Ferrocement mortar has practical uses in strengthening concrete structures damaged by loads and stresses.

Managing waste is a global major challenge, as various human activities result to the production of significant amounts of waste of different kinds [4]. The residues of mineral water bottles and PET beverage containers consist a major source of solid trash. Sustainable materials are being developed with economic and environmental benefits in order to reduce pollution, including CO₂ emissions, and recycle waste by incorporating environmentally friendly materials into civil engineering projects. The use of post-consumer plastics in concrete production is an economical alternative and consumption of resources. The global widespread use of PET as well as the long-term degradation of this plastic type in nature has prompted researchers to investigate PET recycling solutions. The incorporation of plastic waste into concrete to enhance the qualities of hardened concrete and solve the problem of brittleness has garnered considerable research interest. The inclusion of plastic wastes, such as polypropylene fibers, in concrete can prevent cracking and improve the resistance of concrete components to cracking [5]. The usage of hand-cut PET fibers with length of 6cm, width of 1.2cm, and various geometric shapes, increases the strength of hardened concrete [6].

Corresponding author: Farah A. Al-Fahdawi

When structural elements deteriorate as a result of exposure to high temperatures, the risk of a structure collapsing increases. As a result, the selection of fire-resistant materials to limit heat damage to structural elements is critical. The research on the behavior of concrete at elevated temperatures has showed that elevated temperatures degrade the mechanical characteristics of concretes. The behavior of concrete at high temperatures depends on a few parameters, including the constituents of the materials used for the concrete mixture and the permeability of the concrete [7]. Exposure to temperatures above 300°C can drastically reduce the mechanical characteristics of concrete. The calcium hydroxide content of the cement material can be dehydrated at temperatures above 400°C. Consequently, the water vaporizes, which causes the physical qualities of concrete to deteriorate [8].

The effect of rising temperatures on the characteristics of strengthened cement mortar by adding waste plastic fibers from soft drink bottle recycling is studied in this paper. These fiber types were added in volumetric proportions (0.5%, 1%, 1.5%, and 2%) and a reference mixture was utilized for comparison. The specimens of cement mortar from each group were heated to the desired temperature before being evaluated. Some samples were tested for compressive and flexural strength at room temperature, while others were studied after being exposed to increased temperatures of 100, 200, 400, and 700°C. After exposure to temperatures over 400°C, the compressive and flexural strength values decline significantly [9]. The main objective of this study is to investigate experimentally the effect of high temperatures on the mechanical properties of concrete and the effect of the added fibers to the ferrocement mortar as a solution to increase the resistance and to control cracking during fire exposure.

II. MATERIALS

A. Cement

Ordinary Portland Cement (OPC) Type I with 3.15g/cm³ specific gravity was used as a binder in all mixes. Cement is the most important component in concrete production [10]. The physical properties of OPC are shown in Table I, according to the Iraqi [IQS No.5/ 2019].

TABLE I. PHYSICAL CHARACTERISTICS OF OPC

Physical characteristics	Test result	IQS, No.5/ 2019
Fineness using Blain method (cm ² /g)	3344	>2500cm ² /gm
Initial setting time (min)	164	>45min
Final setting time (min)	222	<600min
Soundness (mm)	1	<10mm

B. Fine Aggregates

Local sand passing through 2.36mm with specific gravity of 2.65g/cm³ was used. Table II shows the characteristics of the used sand according to the Iraqi specifications [11].

TABLE II. CHARACTERISTICS OF FINE AGGREGATES

Type aggregate	Sand
Passing Sieve	2.36
Specific gravity	2.65
Salt content %	0.11

C. Water

Tap water was used to create and cure concrete in this research.

D. Polyethylene Terephthalate (PET)

The type of waste plastic considered in this study came from waste plastic soft drink bottles. The waste plastic bottles were sliced to small uniform pieces with an average length equal to 30mm, width equal to about 3mm, and thickness equal to 0.3mm. The density of the waste plastic fibers was 1300kg/m³, the aspect ratio was 28, and the tensile strength 103Mpa. The volumetric ratios used in this study were 0, 0.5%, 0.75%, and 1%.

III. TYPES OF MOLDS

A total of 120 cube and prism specimens were cast. The dimensions were 70×70×70mm cubes for compressive strength testing and 40×40×160 mm prisms for flexural strength testing.

IV. MIX DESIGN

Several experimental mixtures were produced to choose the optimal mixing water ratio by using a mold of mortar 50×50×50mm to determine the compressive strength after 7 days. The chosen design was 1:3:0.45 cement, fine aggregates, and water/cement ratio respectively by weight. The designed strength was 30MPa.

V. CASTING AND CURING

To prevent the mortar from adhering to the inside surfaces of the molds, they were cleaned and pre-coated with coating oil. All the specimens were covered with nylon sheets to avoid water evaporation immediately after the concrete was mixed. The samples were de-molded and immediately submerged in the treatment water basin for 28 days after the nylon sheets were removed.

VI. HEATING PROCESS

At the age of 28 days, the specimens were withdrawn from the water cure and were left to dry in the laboratory for one day. The concrete specimens were then dried in a vented oven before being exposed to high temperatures. The first group with 24 cube and prism samples (3 samples for each mixture) was assessed and utilized as a comparison standard at room temperature (25°C). In the laboratory furnace, 4 more groups were exposed to temperatures of 100, 200, 400, and 600°C for 1h. After the exposure, the specimens were allowed to cool at room temperature before being tested.

VII. TESTING PROGRAM

A. Compressive Strength Test

Based on [12], compressive tests on the cubic samples were carried out to find the concrete's compressive strength after 28 water-curing days. All samples were tested in the ELE-Digital testing compression machine with a maximum capacity of 2000KN at the rate of 3KN/s. Three cubes were tested for each case (room temperature, 100°C, 200°C, 400°C, and 600°C) and the average strength was considered.

B. Flexural Strength Test

Flexural strength was measured according to [13]. A machine with a capacity of 5KN was used to determine flexural strength (Center-Point Loading Method) on the prismatic samples after 28 water-curing days. Three prisms were tested for case and their average strength was considered.

VIII. RESULTS AND DISCUSSION

Figure 1 shows the relationship between temperature and compressive strength for all ferrocement mortar mixes. In general, it can be clearly seen that all cement mortar mixes exhibited a loss in compressive strength as temperature increased. As the temperature increases above 400°C there is a major decrease in compressive strength, which can be attributed to the loss of cement paste plasticity at high temperatures [14]. At room temperature (about 25°C), the mixes with V_f value equal to 0.75% exhibited higher compressive strength by 17.63% than the reference ferrocement mortar mix. At the same temperature, the mix with $V_f = 1\%$ had lower compressive strength than the reference mix by 12.28%. That decrease in compressive strength might be caused by the forming of segregations on the mixes containing waste plastic fibers, leading to form stiff bonds about these bulks. Also, the plastic fibers reduced the density of cubes, and that leads to a decrease of the compressive strength of the composite [15]. Using of waste plastic fiber with $V_f = 1\%$ increased the porous inside the mortar structure and that reduced the compressive strength.

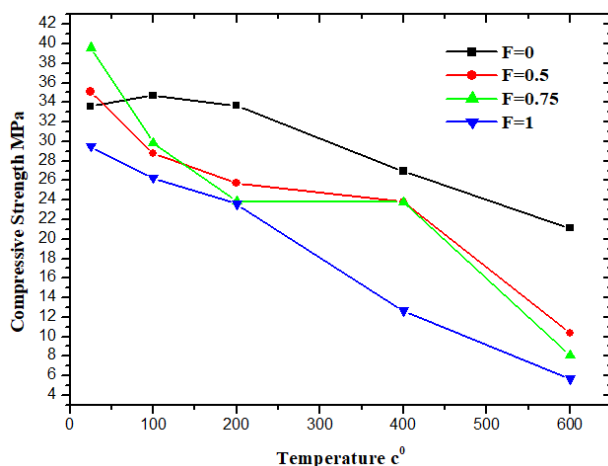


Fig. 1. Relationship between temperature and compressive strength for all ferrocement mortar mixes.

Flexural strength results of ferrocement mortar mixtures at the age of 28 days are shown in Figure 2, which shows a decrease in flexural strength with the elevation of temperature for all 4 mixes. As the temperature increases above 400°C there is a major decrease in flexural strength. At room temperature, the addition of waste plastic fiber to mixes had a positive effect on flexural strength in compared with the reference mix, in accordance with the findings of [16]. This can be attributed to the increase of homogeneity, the decrease in voids, and the increase of the bond strength between the waste plastic fibers

and the other components of concrete mixture. Fibers resist the generation of cracks and bridging of these cracks. The test results showed increase in flexural strength by 2.81%, 5.45%, and 1.08% when waste plastic fibers were added by V_f equal to 0.5%, 0.75%, 1% respectively. When the volumetric ratio of waste plastic fibers is equal to 1%, the decreasing in flexural strength is still greater than that of the reference mixture. The reason for this is that increasing the volumetric ratios of fiber reduces flexural strength due to the irregular distribution of fibers. The samples (cubes and prisms) which were heated to a temperature equal to 200°C maintained their original color, while in specimens heated to 400°C, black spots appeared on the top surfaces of the cubes due to the burning of PET. At 700°C, the black spots disappeared due to the evaporation of the burned PET residuals and the specimens suffered noticeable color changes with a spalling occurred on the samples surfaces.

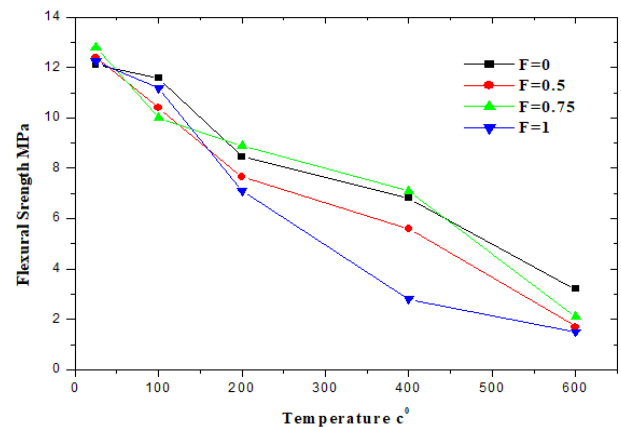


Fig. 2. Relationship between temperature and flexural strength for all ferrocement mortar mixes.

IX. CONCLUSIONS

The following conclusions could be drawn from the current research work:

- The addition of PET fibers is an effective method for recycling plastic waste.
- The compressive and flexural strength values of reference cement mortar and mortar containing waste plastic fibers reduced by an amount depending on the value of the exposing temperature.
- For specimens evaluated at temperatures up to 200°C, the loss in compressive strength was relatively small.
- A severe decrease in the compressive and flexural strength values occurred when the specimens were exposed to temperatures higher than 400°C.
- The samples which were heated to temperature equal to 200°C maintained their original color and no apparent visual discoloration occurred in the ferrocement mortar.
- Due to the combustion of PET fibers, black patches form on the surfaces of mortar cubes and prisms heated to 400°C.

- At 700°C the black spots disappear due to the evaporation of the burned PET residuals and the specimens suffered noticeable color changes with a spalling occurring on the sample surfaces.

REFERENCES

- [1] L. M. Jiang, F. H. Tang, and M. L. Ou, "Experimental Research on the Strengthening of RC Columns by High Performance Ferrocement Laminates," *Advanced Materials Research*, vol. 243–249, pp. 1409–1415, 2011, <https://doi.org/10.4028/www.scientific.net/AMR.243-249.1409>.
- [2] N. A. Memon, A. H. Larik, M. A. Bhutto, N. A. Lakho, M. A. Memon, and A. N. Memon, "Effect of Prepackaged Polymer on Compressive, Tensile and Flexural Strength of Mortar," *Engineering, Technology & Applied Science Research*, vol. 8, no. 3, pp. 3044–3047, Jun. 2018, <https://doi.org/10.48084/etasr.2039>.
- [3] P. Ellis, "The Analysis of Mortar: The Past 20 Years," *Building Conservation*. <https://www.buildingconservation.com/articles/mortar/mortar.htm>.
- [4] O. M. Okeyinka and O. J. Idowu, "Assessment of the Suitability of Paper Waste as an Engineering Material," *Engineering, Technology & Applied Science Research*, vol. 4, no. 6, pp. 724–727, Dec. 2014, <https://doi.org/10.48084/etasr.485>.
- [5] S. Zhang and B. Zhao, "Influence of polypropylene fibre on the mechanical performance and durability of concrete materials," *European Journal of Environmental and Civil Engineering*, vol. 16, no. 10, pp. 1269–1277, Nov. 2012, <https://doi.org/10.1080/19648189.2012.709681>.
- [6] C. Marthong and D. K. Sarma, "Influence of PET fiber geometry on the mechanical properties of concrete: an experimental investigation," *European Journal of Environmental and Civil Engineering*, vol. 20, no. 7, pp. 771–784, Aug. 2016, <https://doi.org/10.1080/19648189.2015.1072112>.
- [7] S. P. Shah, *High Performance Concrete: Properties and Applications*. New York, NY, USA: McGraw-Hill, 1994.
- [8] R. Feasey and A. Buchanan, "Post-flashover fires for structural design," *Fire Safety Journal*, vol. 37, no. 1, pp. 83–105, Feb. 2002, [https://doi.org/10.1016/S0379-7112\(01\)00026-1](https://doi.org/10.1016/S0379-7112(01)00026-1).
- [9] S. Nasir, B. I. Al-Hadithi, and A. I. Al-Hadithi, "The Effects of Adding Waste Pet Fibers on the Some Mechanical Properties of Cement Mortar under Exposure to Elevated Temperature," *Journal of Engineering and Applied Sciences*, vol. 13, no. 11, pp. 3985–3996, 2018, <https://doi.org/10.36478/jeasci.2018.3985.3996>.
- [10] A. Saand, T. Ali, M. A. Keerio, and D. K. Bangwar, "Experimental Study on the Use of Rice Husk Ash as Partial Cement Replacement in Aerated Concrete," *Engineering, Technology & Applied Science Research*, vol. 9, no. 4, pp. 4534–4537, Aug. 2019, <https://doi.org/10.48084/etasr.2903>.
- [11] *Iraqi Specification No. 45 - Aggregates from natural sources for concrete and construction*. Baghdad, Iraq, 1984.
- [12] EN 12390-3:2019 - Testing hardened concrete - Part 3: Compressive strength of test specimens. CEN, 2019.
- [13] *Standard Test Method for Flexural Strength of Concrete (Using Simple Beam With Center-Point Loading)*. ASTM International, 2015.
- [14] A. S. M. A. Awal and I. A. Shehu, "Performance evaluation of concrete containing high volume palm oil fuel ash exposed to elevated temperature," *Construction and Building Materials*, vol. 76, pp. 214–220, Feb. 2015, <https://doi.org/10.1016/j.conbuildmat.2014.12.001>.
- [15] A. I. Al-Hadithi, A. T. A. Ejbari, and G. S. Jameel, "Behaviour of Waste Plastic Fiber Concrete Slabs Under Low Velocity Impact," *Iraqi Journal of Civil Engineering*, vol. 9, no. 1, pp. 135–148, 2013.
- [16] A. A. Chyad, "Flexural Strength and Impact Behavior of Ferrocement Members Containing Waste Materials," M.S. thesis, University of Anbar, Ramadi, Iraq, 2021.

A Hybrid Metaheuristic and Deep Learning Approach for Change Detection in Remote Sensing Data

Yacine Slimani

Department of Computer Science
Laboratory of Intelligent Systems
University of Ferhat Abbas Setif 1
Setif, Algeria
slimaniy09@univ-setif.dz

Rachid Hedjam

Department of Computer Science
Sultan Qaboos University
Muscat, Oman
rachid.hedjam@squ.edu.om

Received: 6 August 2022 | Revised: 17 August 2022 | Accepted: 20 August 2022

Abstract—This study aimed to adapt Convolutional Neural Networks (CNN) to solve the problem of change detection using remote sensing imagery. Specifically, the goal was to investigate the impact of each CNN layer to detect changes between two satellite images acquired on two different dates. As low-level CNN layers detect fine details (small changes) and higher-level layers detect coarse details (large changes), the idea was to assign a weight to each layer and use a genetic algorithm based on a training dataset to generalize the detection process on the test dataset. The results showed the effectiveness of the proposed approach based on two real-life datasets.

Keywords—change detection; remote sensing; deep learning; convolutional neural networks; genetic algorithms

I. INTRODUCTION

The aim of binary Change Detection (CD) in remote sensing is to compare two images acquired at two different dates to detect meaningful differences [1]. Usually, two CD approaches are used: supervised or unsupervised. Supervised CD requires temporal reference data for the training phase [2, 3], while unsupervised CD is based on a direct comparison of input images without using labeled data [4-6]. In general, unsupervised binary CD techniques consist of two steps: i) compute the difference between the features of the two input images to generate a difference image or change index, and ii) generate the binary change map by segmenting (thresholding) the difference image computed in the first step into change and no-change regions. However, traditional CD methods that use handcrafted features are not effective in complex situations, because the designed features cannot accurately capture high- and medium-level image representations [7]. Recently, deep learning has emerged and has become a state-of-the-art approach for CD. Deep learning is very effective in extracting representative features from low, middle, and higher image representation levels. The advantages of deep learning are that, it learns discriminant features and computes them automatically without relying on the involvement of an expert.

Several deep-learning methods for CD have been proposed. In [8], a method was proposed to compute the difference image using a backpropagation algorithm and a deep belief network.

A deep belief network learns low and high-level features around a pixel neighborhood and the backpropagation algorithm builds the difference image using training samples. Finally, a simple segmentation algorithm was used to compute the binary change map. A method was proposed in [9] that combined deep features, saliency detection, and Convolutional Neural Networks (CNNs) to compute the change. A patch-based Siamese Neural Network was presented in [10], where external images, whose textures resembled the changing area, were used to generate genuine and imposter pair samples for the training process. A method that combined CNN features to create a single higher feature vector was proposed in [7], using the pixel-wise Euclidean distance between the extracted feature vectors after having been transformed into matrices to compute the change map. A review of the deep learning-based CD methods can be found in [11].

This study extends [12] and is related to [7]. The difference between this study and [7] lies in the combination process of the CNN layers. In [7], all CNN layers were combined into a single feature vector, but this study proposes the assignment of weights to the CNN layers before combining them. In [12], the weights were binary (i.e. 1 for considering a layer and 0 for not) and assigned manually. This study used a Genetic Algorithm (GA) to automatically learn the weights based on training data. The GA aims to find the best weights that lead to the best match between the CD reference (ground truth) and the change map detected by the proposed algorithm. Therefore, the weight vector can be seen as a mask, where the goal is to demonstrate that the layers can be assigned different weights before being combined to detect different regions that represent the changes between the two input images. The assumption was that, to detect large changes, high-level layers are assigned higher weights, i.e. considered more.

II. THE PROPOSED APPROACH

Usually, the spatial changes in remote sensing images are specific patterns with special features in terms of color, shape, and texture. Therefore, their CNN characteristics are different from those of the same location in the image before the change. In other terms, an unchanged spatial area between the two

inputs should have almost similar CNN features, whereas the changed areas have different. Thus, it seems reasonable to compute the features of the two input images using the same CNN structures and then compute their difference to generate the difference image, where the brighter pixels represent the changed areas due to the larger difference values. To detect the changed areas, the difference image can be segmented by a thresholding method into "changed" and "unchanged" classes. In a CNN, the lower layers capture low-level image features such as edges, color, and gradient orientation, while the mid-high level layers capture coarse patterns of the images that can represent whole objects in the images [13]. Since the changes are almost a random natural process, they may affect areas with different sizes from fine to coarse. Therefore, detecting changes between the two input images based on the difference between their last CNN feature is not effective. To overcome this limitation, a new change detection method was proposed, which is an improvement over [7]. The procedure obeys the following: i) extract low, mid and higher features from each image using a pre-trained CNN (e.g. VGG19 [14]), ii) resize the layers to the same size and combine them into a single feature vector for each image, iii) reshape the two feature vectors into square matrices, and finally iv) compute the Euclidean distance between the two matrices to generate the difference image, which will be segmented into two classes, "changed" and "unchanged".

In [12], a binary weight was assigned manually to each layer to include it or not in the combination process of the layers. In other terms, the binary vector of weights played a mask role that allowed or prevented some layers from the combination process. If the weight of a given layer was equal to one (1), it meant that this layer was included in the combination process, while if it was equal to zero (0) it was not. Assigning weights to layers is application dependent. In practice, it is best to consider high-level layers when detecting large changes, while low-level layers should be taken into account when detecting minor changes.

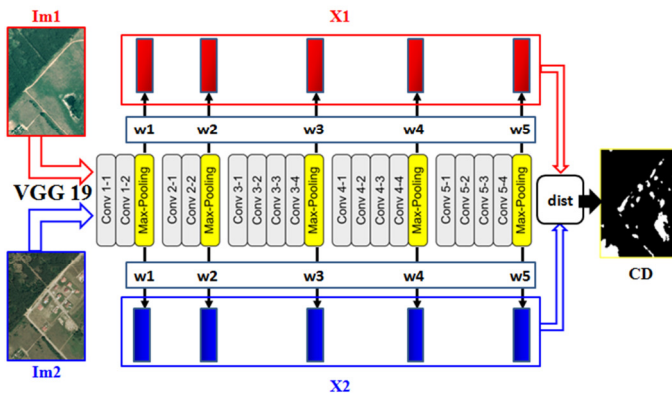


Fig. 1. Convolutional feature-based change detection with VGG19.

In the training phase, N image tuples were used $\{(Im1; Im2; Tr)\}_{i=1..N}$, where $Im1$ and $Im2$ are the images before and after a change and Tr is the corresponding ground truth. Each image is divided into M patches of size $d \times d$. In other terms, there is a set of $S=N \times M$ patches before the change, i.e. $\{P_{j1},$

$j=1..S\}$, a set of patches after the change, i.e. $\{P_{j2}, j=1..S\}$, and the same number of ground truth patches. Each patch is fed to a VGG19 CNN to extract 5 feature maps from 5 different layers. This study used the 3rd, 6th, 10th, 14th, and 18th layers of the VGG19. From each input patch, 5 layers (feature maps) were extracted and resized to the same size.

Formally, let $[X_{j11}, X_{j12}, X_{j13}, X_{j14}, X_{j15}]$ be the list of the feature maps extracted from P_{j1} , and $[X_{j21}, X_{j22}, X_{j23}, X_{j24}, X_{j25}]$ be the list of the feature maps extracted from P_{j2} . Thus, the corresponding weighted feature maps are:

$$F_{j1} = [w_1 \times X_{j11}, w_2 \times X_{j12}, w_3 \times X_{j13}, w_4 \times X_{j14}, w_5 \times X_{j15}]$$

$$F_{j2} = [w_1 \times X_{j21}, w_2 \times X_{j22}, w_3 \times X_{j23}, w_4 \times X_{j24}, w_5 \times X_{j25}]$$

where $W=[w_1, w_2, \dots, w_5]$ are the continuous weights learned by a GA. The difference image for the j^{th} patch-pair is then computed as follows (see Figure 2):

$$DI_j = \text{dist}(F_{j1}, F_{j2})$$

$$= \sqrt{\sum_{k=1}^5 (w_k \times X_{j1k} - w_k \times X_{j2k})^2} \quad (1)$$

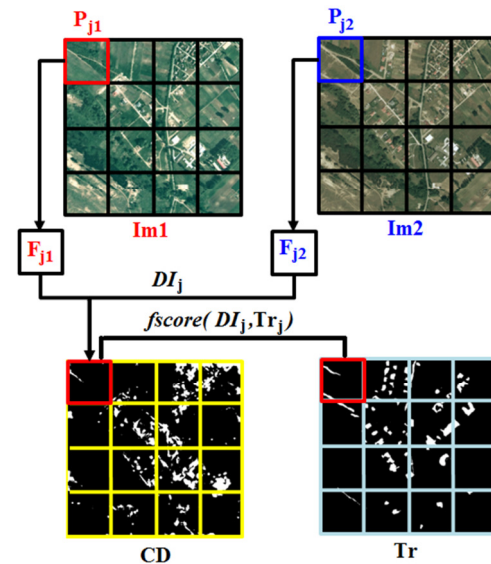


Fig. 2. CNN-based features vectors process.

The goal is to learn the weight vector W using a GA that maximizes the fitness (f-score) between the detected change and the corresponding ground truth for all the patches used in the training phase [15]. Once the optimal weights are learned, they will be used in the test phase. The overall GA for learning the weights, shown in Figure 3, was:

- Step 1 (Initialize population): The first step of GA is to randomly create and initialize the chromosomes of the initial population. Nb_Ind vectors $W = \{W^{(i)} | i = 1..Nb_Ind\}$ are generated. Each $W^{(i)}$ is a chromosome with five (5) real-valued genes $[w_k^{(i)} | k = 1..5]$.

- Step 2 (Evaluation): The fitness function measures the fitness of the change map between each pair of the patch and the corresponding ground truth patches as follows:

$$Fitness(W^{(i)}) = \frac{\sum_{j=1}^S fscore(DI_j, Tr_j)}{S} \quad (2)$$

Algorithm 1: GA-based Learning Process.

```

Data: BasImages, NB Ind, NB Gen, ProbSelect,
        ProbCross, ProbMutation
Result: W
/*CurrentGeneration = InitGeneration(NB Ind)*;/
for i=1..NB Ind do
  for Gene j=1..5] do
    Wj = random(0, 1);
  end
  CurrentGeneration[i]=W;
end
/*Evaluation of population*/;
for i=1..NB Ind do
  Fitness[i] = CNN(CurrentGeneration[i]);
end
OldGeneration = Sort(CurrentGeneration);
foreach Generation [i=1..NB Gen] do
  /*Selection(ProbSelect)*;/
  for i=1..NB Ind*ProbSelect do
    CurrentGeneration.Append(OldGeneration[i])
  end
  /*Crossover(ProbCross)*;/
  for i=1..NB Ind*ProCross do
    WFather = Select(OldGeneration);
    WMother = Select(OldGeneration);
    for Gene j=1..5] do
      Wj = Choice(WFather[j], WMother[j])
    end
    CurrentGeneration.Append(W)
  end
  /*Duel(ProbDuel)*;/
  for i=1..NB Ind*ProCross do
    Ind1 = Select(OldGeneration);
    Ind2 = Select(OldGeneration);
    if Fitness[Ind1] > Fitness[Ind2] then
      W = OldGeneration[Ind1];
    else
      W = OldGeneration[Ind2];
    end
    CurrentGeneration.Append(W)
  end
  /*Mutation(ProbMutation)*;/
  for i=1..NB Ind*ProbMutation do
    Ind Mut = randint(0, NB Ind);
    W = CurrentGeneration[Ind Mut];
    Gene Mut = randint(0, 5);
    WGene Mut = random(0, 1);
  end
  /*Evaluation of population*/;
  for i=1..NB Ind do
    Fitness[i] = CNN(CurrentGeneration[i]);
  end
  OldGeneration = Sort(CurrentGeneration)
end
return best(W)

```

Fig. 3. GA-based learning process algorithm.

- Step 3 (Selection): The elitism selection method selects the best $W^{(i)}$ chromosomes from the previous population to integrate them into the next population. According to the best fitness function values $Fitness(W^{(i)})$, a portion of ($ProbSelect\%$) from the precedent population was selected to breed a new generation.
- Step 4 (Crossover): The crossover method creates a portion of ($ProbCross\%$) from the precedent population. A one-point crossover method was used.
- Step 5 (Mutation): The goal of this function was to introduce diversity into the population. A portion of ($ProbMut\%$) was chosen and a random value was assigned to one randomly chosen gene.

- Redo steps 2, 3, 4, and 5 until stability (no change in the fitness) (see Algorithm 1). Finally, the best W is chosen to be used in the test phase.

III. EXPERIMENTATION AND EVALUATION

A. Dataset Description

Two datasets were used to evaluate the proposed change detection framework, namely the SZTAKI AirChange Benchmark set [16] and the Onera Satellite Change Detection dataset [17]. The SZTAKI AirChange Benchmark set contains 13 aerial image pairs of 952×640 pixels with a resolution of 1.5m/pixel, and binary change masks (a ground truth defined by experts). The Onera Satellite Change Detection dataset consists of 24 pairs of multispectral images taken using the Sentinel-2 satellites between 2015 and 2018. The locations were picked from all over the world, Brazil, the United States, Europe, the Middle East, and Asia. For each location, registered pairs of 13-band multispectral satellite images are required. The images vary in spatial resolution between 10m, 20m, and 60m. The pixel-level change ground truth is provided for the image pairs. The annotated changes focus on urban changes, such as new buildings or new roads.

B. GA Parameter Setting

In the training phase, a pre-trained VGG19 was used to extract the feature maps. The GA requires several parameters to search for the optimal layer weights:

- Number of generations $Nb_Gen=200$
- Number of Individuals $Nb_Ind=100$
- Probability of selection $ProbSelect=40\%$
- Probability of crossover $ProbCross=40\%$
- Probability of mutation $ProbMutation=20\%$

C. Results, Evaluation, and Comparison to Other Methods

The proposed method was compared with two classes of existing change detection methods, traditional and deep learning based. The traditional methods were the Iteratively Reweighted Multivariate Alteration Detection Method (IMAD) for change detection [18], Slow Feature Analysis (SFA) algorithm for change detection [19], Principal Component Analysis and k-means clustering (PCA-Kmeans) [20], and Change Vector Analysis (CVA) [21]. The deep learning-based methods were two simple CNN-based without layer weighting: the VGG19 [7], and the ResNet50 [22].

Table I shows the change detection results using different methods in terms of f-score, recall, precision, and accuracy, based on the SZTAKI dataset. Based on f-score and accuracy, the proposed method gave the best results with the test images Szada3, Tiszadob2, and Archive (accuracy was 0.90, 0.85, and 0.85 respectively). In the case of the Szada4 image, the proposed method gave better results than the original VGG19 algorithm (accuracy was 0.70 versus 0.69) but had lower accuracy than IMAD, which can be justified by the poor quality of the ground truth.

TABLE I. CHANGE DETECTION RESULTS OF THE SZTAKI AIRCHANGE DATASET

Images	Methods	f-score	Recall	Precision	Accuracy	White pixels detected
Szada3	IMAD	0.45	0.63	0.35	0.86	4261
	ISFA	0.35	0.38	0.33	0.89	2553
	PCA-Kmeans	0.37	0.50	0.29	0.84	3368
	CVA	0.16	0.60	0.09	0.42	4062
	VGG 19	0.31	0.32	0.30	0.87	2166
	ResNet50	0.41	0.66	0.29	0.82	4462
	Proposed	0.45	0.45	0.44	0.90	3078
Szada4	IMAD	0.57	0.50	0.67	0.78	14438
	ISFA	0.42	0.39	0.45	0.67	11350
	PCA-Kmeans	0.59	0.57	0.61	0.76	16548
	CVA	0.38	0.57	0.29	0.45	16418
	VGG 19	0.27	0.20	0.45	0.69	5646
	ResNet50	0.50	0.45	0.57	0.73	12884
	Proposed	0.30	0.24	0.48	0.70	6865
Tiszadob2	IMAD	0.39	0.48	0.32	0.70	7608
	ISFA	0.36	0.47	0.29	0.66	7555
	PCA-Kmeans	0.48	0.63	0.39	0.74	10011
	CVA	0.32	0.67	0.21	0.45	10734
	VGG 19	0.23	0.17	0.36	0.78	2664
	ResNet50	0.36	0.36	0.37	0.75	5769
	Proposed	0.44	0.35	0.60	0.85	4945
Archive	IMAD	0.40	0.45	0.36	0.76	6392
	ISFA	0.31	0.22	0.56	0.83	3118
	PCA-Kmeans	0.40	0.46	0.35	0.76	6544
	CVA	0.31	0.71	0.20	0.45	10092
	VGG 19	0.31	0.20	0.65	0.84	2863
	ResNet50	0.45	0.48	0.42	0.80	6776
	Proposed	0.32	0.21	0.70	0.85	2958

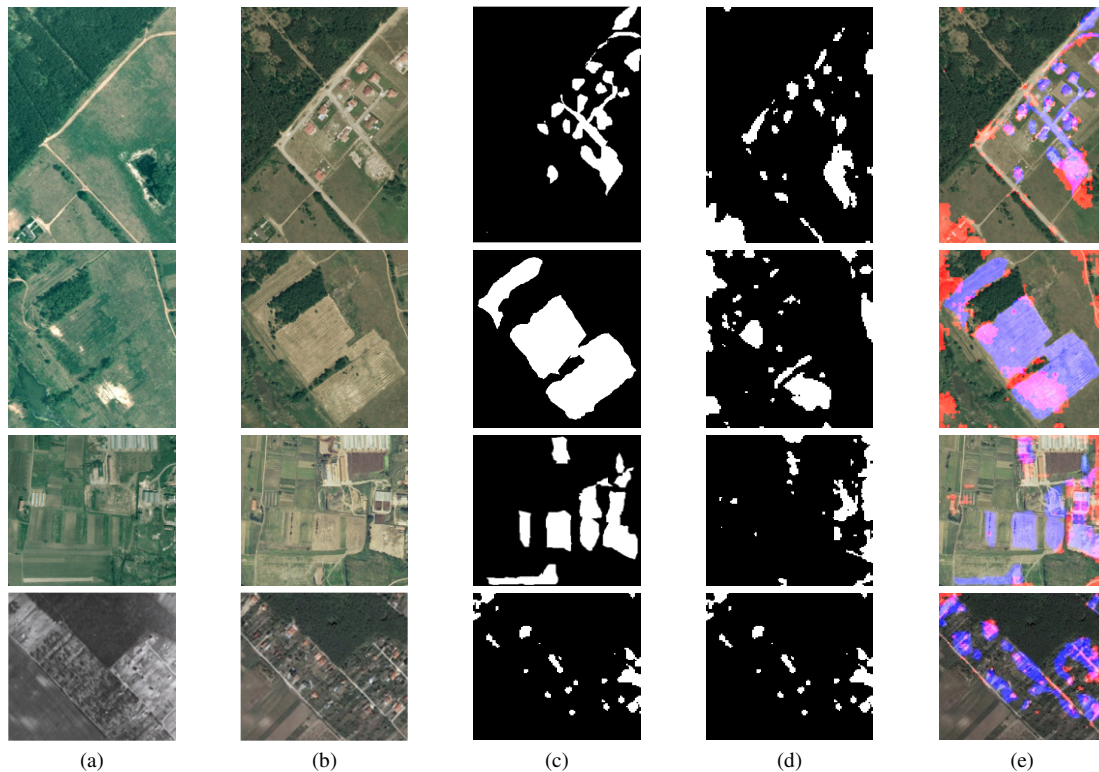


Fig. 4. Subjective results. From left to right: (a) image (1) before change, (b) image (2) after change, (c) ground-truth, (d) CD map, (e) overlay of CD on image (2). Images from SZTAKI, from top to bottom, Szada3, Szada4, Tiszadob2, Archive.

TABLE II. CHANGE DETECTION RESULTS OF THE ONERA SATELLITE DATASET

Images	Methods	f-score	Recall	Precision	Accuracy	White pixels detected
Beirut	IMAD	0.46	0.58	0.39	0.90	2262
	ISFA	0.42	0.94	0.27	0.80	3682
	PCA-Kmeans	0.54	0.71	0.43	0.90	2804
	CVA	0.17	0.82	0.09	0.35	3231
	VGG 19	0.26	0.17	0.53	0.92	670
	ResNet50	0.43	0.55	0.36	0.89	2165
Chongqing	Proposed	0.55	0.57	0.67	0.94	2252
	IMAD	0.56	0.75	0.45	0.94	1897
	ISFA	0.52	0.77	0.39	0.93	1943
	PCA-Kmeans	0.42	0.53	0.35	0.93	1340
	CVA	0.07	0.50	0.04	0.36	12682
	VGG 19	0.22	0.19	0.27	0.93	492
Las Vegas	ResNet50	0.36	0.45	0.31	0.92	1125
	Proposed	0.41	0.43	0.44	0.94	1095
	IMAD	0.60	0.61	0.59	0.92	3183
	ISFA	0.33	0.55	0.24	0.77	2858
	PCA-Kmeans	0.54	0.49	0.60	0.91	2558
	CVA	0.17	0.65	0.10	0.37	3346
Montpellier	VGG 19	0.37	0.42	0.32	0.85	2196
	ResNet50	0.64	0.94	0.48	0.89	4853
	Proposed	0.40	0.46	0.49	0.90	2362
	IMAD	0.67	0.65	0.69	0.92	4141
	ISFA	0.62	0.54	0.72	0.92	3451
	PCA-Kmeans	0.69	0.76	0.62	0.91	4825
	CVA	0.26	0.75	0.16	0.47	4725
	VGG 19	0.51	0.40	0.71	0.90	2554
	ResNet50	0.63	0.63	0.62	0.91	4014
	Proposed	0.44	0.35	0.60	0.85	4945

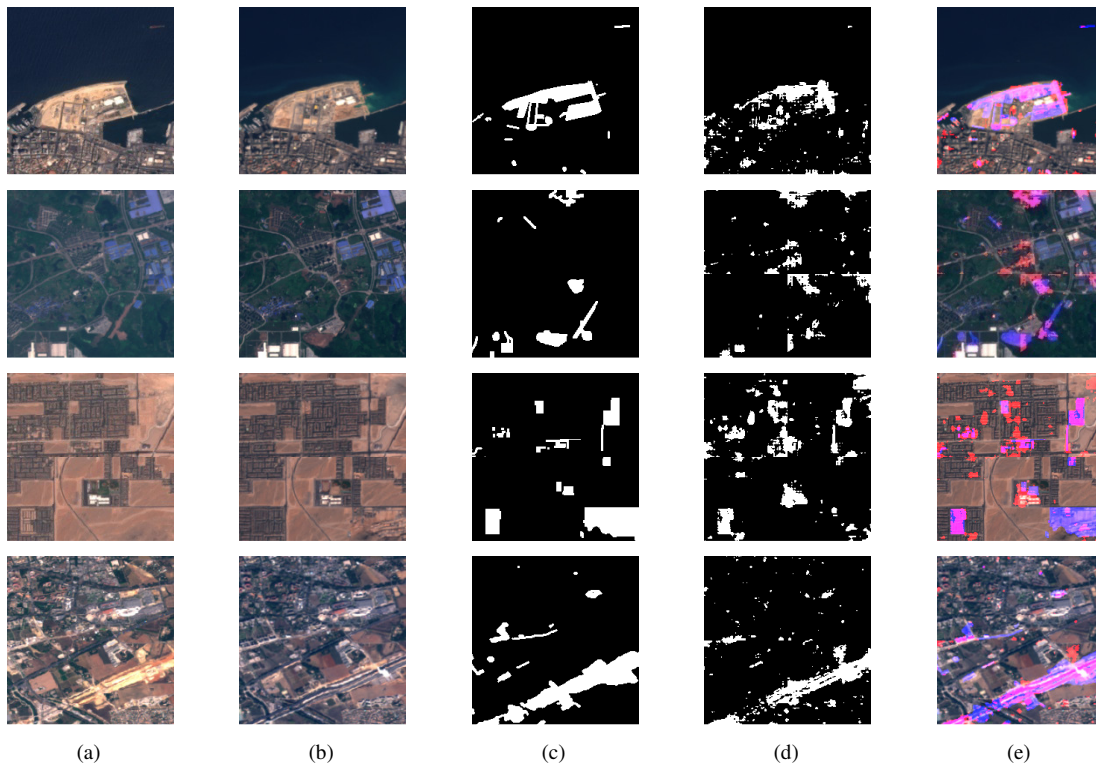


Fig. 5. Subjective results. From left to right: (a) image (1) before change, (b) image (2) after change, (c) ground-truth, (d) CD map, (e) overlay of CD on image (2). Images from Onera. From top to bottom, Beirut, Chongqing, Las Vegas, Montpellier.

Table II shows the change detection results of the different methods in terms of f-score, recall, precision, sensitivity, and accuracy, based on the Onera Satellite dataset. The proposed

method was again better than VGG19 in any case, and it was the best for Beirut and Chongqing test images, but weaker than IMAD for Las Vegas and Montpellier.

Figures 4 and 5 show the results of change detection on the test image from the SZTAKI and the Onera datasets respectively. The last column shows the overlay of the change detection map on the image after the change, where the changes are highlighted in red and the ground truth is highlighted in cyan blue. It can be noted that most of the changes that occurred were detected. Unfortunately, the method detected unwanted changes, which means that it triggered more false alarms. Finally, the results obtained show that the proposed method gave better results than [7] and [12], unveiling the problem with the weight of the layer. Moreover, the GA learning phase made it possible to detect fine and coarse details, by finding the best weight vector.

IV. CONCLUSION

This paper presented an artificial intelligence-based change detection approach for remote sensing. The challenge of finding the best weighted CNN layers to the change detection problem was solved using a genetic algorithm. The proposed approach combines a CNN (pre-trained VGG19) and genetic algorithm to build a near-optimal weight vector. This vector was combined with the feature maps to compute their difference and produce the change map. The purpose of this study was to investigate the adaptation of CNNs to detect changes in remote-sensing images. Two datasets were used to show that it is recommended to specify the CNN layers to be used to detect different changes. More precisely, detecting small changes requires the use of the first CNN layers, whereas large changes require the use of the last layers. Therefore, a natural way to solve this problem is to use a meta-heuristic optimization method to find the best weights for the layers to be combined to generate the relevant feature maps. Future work could investigate other CNN architectures and metaheuristic search methods and extend the work on a larger number of datasets.

REFERENCES

- [1] P. Coppin, E. Lambin, I. Jonckheere, and B. Muys, "Digital change detection methods in natural ecosystem monitoring: a review," in *Analysis of Multi-Temporal Remote Sensing Images*, vol. Volume 2, Singapore: World Scientific, 2002, pp. 3–36.
- [2] B. Demir, F. Bovolo, and L. Bruzzone, "Classification of Time Series of Multispectral Images With Limited Training Data," *IEEE Transactions on Image Processing*, vol. 22, no. 8, pp. 3219–3233, Dec. 2013, <https://doi.org/10.1109/TIP.2013.2259838>.
- [3] J. Collomb, P. Baland, P. Francescato, Y. Gardet, D. Leh, and P. Saffré, "Thermomechanical Optimization and Comparison of a Low Thermal Inertia Mold with Rectangular Heating Channels and a Conventional Mold," *Advances in Materials Science and Engineering*, vol. 2019, May 2019, Art. no. e3261972, <https://doi.org/10.1155/2019/3261972>.
- [4] T. L. Dammalage and N. T. Jayasinghe, "Land-Use Change and Its Impact on Urban Flooding: A Case Study on Colombo District Flood on May 2016," *Engineering, Technology & Applied Science Research*, vol. 9, no. 2, pp. 3887–3891, Apr. 2019, <https://doi.org/10.48084/etasr.2578>.
- [5] S. Liu, L. Bruzzone, F. Bovolo, and P. Du, "Unsupervised Multitemporal Spectral Unmixing for Detecting Multiple Changes in Hyperspectral Images," *IEEE Transactions on Geoscience and Remote Sensing*, vol. 54, no. 5, pp. 2733–2748, Feb. 2016, <https://doi.org/10.1109/TGRS.2015.2505183>.
- [6] X. Zheng, X. Chen, X. Lu, and B. Sun, "Unsupervised Change Detection by Cross-Resolution Difference Learning," *IEEE Transactions on Geoscience and Remote Sensing*, vol. 60, pp. 1–16, 2022, <https://doi.org/10.1109/TGRS.2021.3079907>.
- [7] A. M. E. Amin, Q. Liu, and Y. Wang, "Convolutional neural network features based change detection in satellite images," in *First International Workshop on Pattern Recognition*, Jul. 2016, vol. 10011, pp. 181–186, <https://doi.org/10.1117/12.2243798>.
- [8] G. Cao, B. Wang, H.-C. Xavier, D. Yang, and J. Southworth, "A new difference image creation method based on deep neural networks for change detection in remote-sensing images," *International Journal of Remote Sensing*, vol. 38, no. 23, pp. 7161–7175, Dec. 2017, <https://doi.org/10.1080/01431161.2017.1371861>.
- [9] D. Peng and H. Guan, "Unsupervised change detection method based on saliency analysis and convolutional neural network," *Journal of Applied Remote Sensing*, vol. 13, no. 2, May 2019, Art. no. 024512, <https://doi.org/10.1117/1.JRS.13.024512>.
- [10] R. Hedjam, A. Abdesselam, and F. Melgani, "Change Detection from Unlabeled Remote Sensing Images Using SIAMESE ANN," in *IGARSS 2019 - 2019 IEEE International Geoscience and Remote Sensing Symposium*, Yokohama, Japan, Jul. 2019, pp. 1530–1533, <https://doi.org/10.1109/IGARSS.2019.8898672>.
- [11] L. Khelifi and M. Mignotte, "Deep Learning for Change Detection in Remote Sensing Images: Comprehensive Review and Meta-Analysis," *IEEE Access*, vol. 8, pp. 126385–126400, 2020, <https://doi.org/10.1109/ACCESS.2020.3008036>.
- [12] Y. Slimani and R. Hedjam, "Which Cnn Layer For Which Change? A Cnn Adaptation Approach For Change Detection In Remote Sensing Data," in *2020 Mediterranean and Middle-East Geoscience and Remote Sensing Symposium (M2GARSS)*, Tunis, Tunisia, Mar. 2020, pp. 5–8, <https://doi.org/10.1109/M2GARSS47143.2020.9105168>.
- [13] M. D. Zeiler, G. W. Taylor, and R. Fergus, "Adaptive deconvolutional networks for mid and high level feature learning," in *2011 International Conference on Computer Vision*, Aug. 2011, pp. 2018–2025, <https://doi.org/10.1109/ICCV.2011.6126474>.
- [14] S. Sahel, M. Alsahafi, M. Alghamdi, and T. Alsubait, "Logo Detection Using Deep Learning with Pretrained CNN Models," *Engineering, Technology & Applied Science Research*, vol. 11, no. 1, pp. 6724–6729, Feb. 2021, <https://doi.org/10.48084/etasr.3919>.
- [15] B. K. Alsaidi, B. J. Al-Khafaji, and S. A. A. Wahab, "Content Based Image Clustering Technique Using Statistical Features and Genetic Algorithm," *Engineering, Technology & Applied Science Research*, vol. 9, no. 2, pp. 3892–3895, Apr. 2019, <https://doi.org/10.48084/etasr.2497>.
- [16] C. Benedek and T. Sziranyi, "Change Detection in Optical Aerial Images by a Multilayer Conditional Mixed Markov Model," *IEEE Transactions on Geoscience and Remote Sensing*, vol. 47, no. 10, pp. 3416–3430, Jul. 2009, <https://doi.org/10.1109/TGRS.2009.2022633>.
- [17] B. L. Saux, R. C. Daudt, A. Boulch, and Y. Gousseau, "OSCD - Onera Satellite Change Detection," IEEE, Oct. 09, 2019, Accessed: Aug. 21, 2022. [Online]. Available: <https://iee-dataport.org/open-access/oscd-onera-satellite-change-detection>.
- [18] A. A. Nielsen, "The Regularized Iteratively Reweighted MAD Method for Change Detection in Multi- and Hyperspectral Data," *IEEE Transactions on Image Processing*, vol. 16, no. 2, pp. 463–478, Oct. 2007, <https://doi.org/10.1109/TIP.2006.888195>.
- [19] C. Wu, B. Du, and L. Zhang, "Slow Feature Analysis for Change Detection in Multispectral Imagery," *IEEE Transactions on Geoscience and Remote Sensing*, vol. 52, no. 5, pp. 2858–2874, Feb. 2014, <https://doi.org/10.1109/TGRS.2013.2266673>.
- [20] T. Celik, "Unsupervised Change Detection in Satellite Images Using Principal Component Analysis and k-Means Clustering," *IEEE Geoscience and Remote Sensing Letters*, vol. 6, no. 4, pp. 772–776, Jul. 2009, <https://doi.org/10.1109/LGRS.2009.2025059>.
- [21] W. A. Malila, "Change Vector Analysis: An Approach for Detecting Forest Changes with Landsat," in *Symposium on Machine Processing of Remotely Sensed Data and Soil Information Systems and Remote Sensing and Soil Survey Proceedings*, Jun. 1980, pp. 326–335.
- [22] K. L. de Jong and A. Sergeevna Bosman, "Unsupervised Change Detection in Satellite Images Using Convolutional Neural Networks," in *2019 International Joint Conference on Neural Networks (IJCNN)*, Budapest, Hungary, Jul. 2019, pp. 1–8, <https://doi.org/10.1109/IJCNN.2019.8851762>.

Simulated Photogrammetric Data for Testing the Performance of Photogrammetric Instruments and Systems

Khalid L. A. El-Ashmawy

Department of Civil Engineering
College of Engineering and Islamic Architecture
University of Umm Al-Qura
Makkah, Saudi Arabia
khalid85_2002@yahoo.com

Received: 26 July 2022 | Revised: 12 August 2022 | Accepted: 18 August 2022

Abstract—The generation of mathematical photograms (photos) as data is universally accepted as the basis for photogrammetric studies. New development in the field of computer technology has had a major influence on photogrammetry. This paper aims to describe the development of a computer system called SimuPhotos designed to produce simulated data in different forms for testing photogrammetric methodologies, software, and instruments. SimuPhotos is capable of generating photogrammetric blocks with different specifications. It generates the simulated data for the whole block, strips, or selected photos. The simulated free error data include the camera interior orientation parameters, ground coordinates of points, and for each photograph, camera exterior orientation parameters, and the photo coordinates of imaged points. To increase the capabilities of the developed system, it has a special error generator to get normally distributed error(s) with arbitrary mean(s) and standard deviation(s). The obtained errors are then, if required, applied to the error-free photo and ground coordinates of points. The developed system interfaces CAD technology to generate simulated photogrammetric data in DXF and raster formats which are suitable for testing the photogrammetric instruments and softcopy systems. SimuPhotos has been used for testing the analytical photogrammetric system PhotoMap. The results showed that PhotoMap is free of system error and is functional. Also, the results showed that SimuPhotos can effectively provide a convenient, economical, and accurate testing tool for photogrammetric systems. The developed system is quite versatile and affordable.

Keywords—simulated photogrammetric data; numerical data; graphical data; SimuPhoto; testing photogrammetric systems; softcopy photogrammetry

I. INTRODUCTION

Photogrammetry has experienced significant changes caused by advances in optics, electronics, imaging techniques and computer technology. It is applied in the form of mechanical systems such as stereo plotters, combinations of mechanical and computerized systems such as analytical plotters, and fully computerized systems like softcopy systems.

Testing the results of the developed software or the performance (calibration) of the instrument's mechanism requires error free and well-defined input and output data in a compatible form. Generally, data enter the available photogrammetric system in the form of paper-based photographs, diapositives, or numbers or pixels. The data of actual photographs are characteristically incomplete because the object coordinates of all image points are unknown. Furthermore, the actual data are full of errors that disturb the results of computations and analysis, and it is difficult to estimate how the data, the geometry of the problem, the software, and the instrument's mechanism might affect the results.

The main sources of actual data errors are the variation of the irregular photo errors from one photo to the next, the correlation of the irregular errors and the difficulty of determining their degree, incomplete elimination of systematic errors, investigation of undetected errors, poor image quality and control data, poor image identification, and inadequate redundancy of control data [1]. The specifications of data required for photogrammetric research studies include high quality stereo photographs from cameras of precisely known interior orientation, considerably more than the minimum required ground control data, so that a large number of check points may be selected for the study of error vectors. Ground control data must be of considerably higher precision than the errors expected and ground control points must be suitably located, precisely described, and unmistakably identified on the photographs [2]. Actual photographs taken with the best photogrammetric cameras on the best quality film may not meet the above specifications. Further, available methods of ground survey cannot produce control data of the highest desired precision (1/10 micron in photo coordinates and equivalent in ground control for studying the effects of computational rounding off, and photogrammetric errors). On the other hand, entering the actual photo in pixel form causes a series of problems to image matching [3-6]. These problems

include foreshortened effects such as changing the value of the sampled gray level due to the elements smaller than pixel size, lab processing noise, e.g. scratches or spots on the photographic material due to uneven processing or aging chemicals, digital camera radiometric calibration differences like integration time, gray level range definition and exposure setting, digital camera noise during image digitization and textural problems such as existence of distinguishable structures, repetitive texture, hanging surfaces, ambiguous levels, and thin objects.

Fortunately, the problems of non-availability of error free photogrammetric data and using actual photographs for testing the photogrammetric systems and instruments can be alleviated by a combination of the simulated data generation through software and merging them with the capabilities of the Computer Aided Drafting (CAD) technology for preparation of the data in a compatible form for the photogrammetric instruments and systems. This paper deals with:

- The development, description and evaluation of a system called SimuPhotos for automatic generation of simulated photogrammetric data in numerical and graphical forms. SimuPhotos is an acronym that specifies the generation of simulated photographs for testing the available photogrammetric instruments, methodologies, and systems.
- The use of the capabilities of SimuPhotos for testing the results of a photogrammetric system called PhotoMap [2].

II. CONCEPT OF GENERATING THE SIMULATED PHOTOGRAMMETRIC DATA

A block of simulated photographs for aerial platforms is planned to be obtained in much the same way as in actual photography. The present work is limited to near vertical photography. A set of mathematical photogrammetric data should consist of the following values for strips or photogrammetric blocks:

- Interior orientation of camera selected for photography.
- Ground coordinates of each exposure station.
- Angular orientation of each photograph.
- Ground coordinates of some ground points.
- Photo coordinates of all ground points available within the format of each photograph.

To provide a means for performing computational operations, for generating the mathematical photogrammetric data, the following steps are taken:

- Adopting standard specifications for longitudinal and lateral overlaps, camera angular orientations (ω , ϕ , κ), camera displacements (b_y, b_z), etc.
- Assignment of the ground coordinates (X_o, Y_o, Z_o) to each camera station in the block.
- Assignment of height values and planimetric positions to the ground points.

- Computation of photo coordinates of image points on each photograph using the collinearity condition [7].

III. SPECIFICATIONS FOR GENERATING THE SIMULATED DATA

The specifications for generating the simulated photogrammetric data include built-in and floating specifications. Built-in specifications outline the general layout of the ground, the location of points whose values are fixed during the computational session, and the proposed photography. Floating specifications refer to camera specifications and the terrain type. Their values can be changed by the researcher, depending on the study aims and the available data.

A. Built-in Specifications

The following specifications were taken into account during the development of the software. They outline the general layout of the simulated block:

- Unit block: The maximum size of the block has been adopted to be 5 strips of 21 photographs each, to a total of 105 photographs. This block size represents the average size that is generally used in photogrammetric practice. A strip of 21 photographs may be considered as of medium length. The ground area covered by a block is variable depending on the camera and format used.
- Scale: The hypothetical ground system is chosen such that photos of near-vertical specification are produced at an approximate scale of 1:1. This decision conforms to the International Society of Photogrammetry's relevant resolution on the desirability of reporting all photogrammetric errors at the negative scale [8].

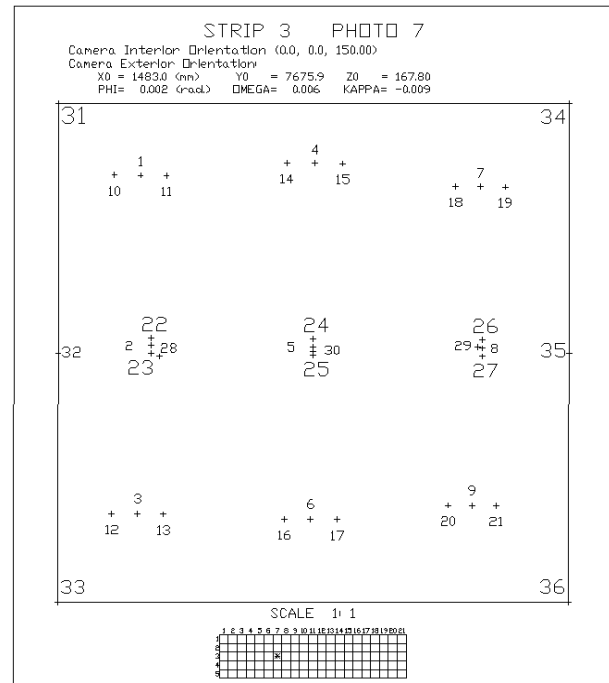


Fig. 1. Points transferred per photograph (single photograph numbering system).

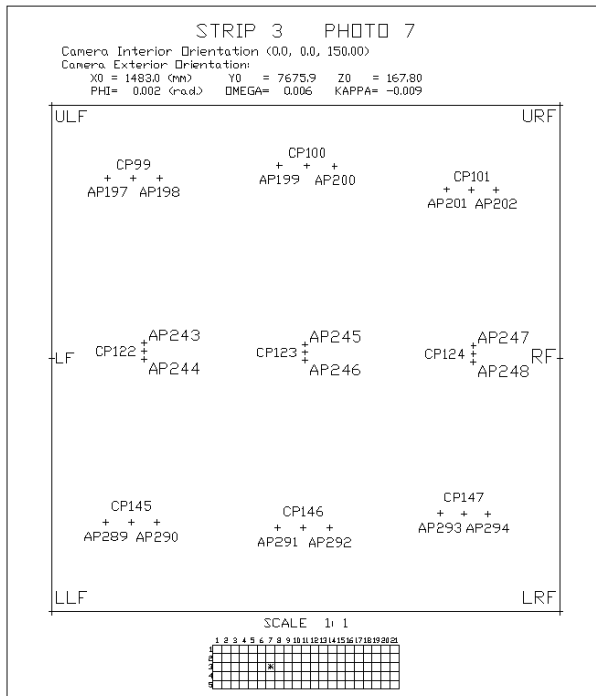


Fig. 2. Points transferred per photograph (block numbering system).

- Precision of image coordinates: The photo coordinates of the image points are computed mathematically to a precision of ± 0.1 micron. A precision of about ± 0.1 micron may be considered high enough to reduce into insignificance the effect of image errors on photogrammetric data processing [8].
- Numbering code for strip and photos: For identifying each photograph, an alpha-numerical code system is used. Strips and photographs are identified by serial numbers 1 to 5 and 1 to 21 respectively.
- Number of points transformed per photo: On each photograph, as shown in Figure 1, 30 points are selected for transformation from ground system into the photo coordinate system and 6 points (31-36) for transformation from the photo coordinate system to the ground system. Of the 30 points, 9 (points 1-9) are primary, 18 (points 10-27) auxiliary, 2 (points 28 and 29) are transferred principal points from preceding and following photographs, and one is the nadir point (point 30). Points 31-36 are the image (fiducial) points and their ground coordinates help in defining the extent of the photograph's ground coverage. For photogrammetric studies, primary points may be used as orientation points, while auxiliary points may be used as auxiliary orientation and scale transfer points [2].
- Numbering codes for points: Points are identified by 2 numbering systems, single photograph and block numbering. In single photograph numbering system, as shown in Figure 1, the points are directly identified by serial numbers (1 to 36). This numbering system is suitable for all single photograph studies, for example, studying the effects of dimensional distortions [9]. In the block numbering system, the alpha-numerical code system is used

for identifying each point of the block points. Each of the three longitudinal sections of a strip has $(n+2)$ and $2(n+2)$ primary and auxiliary points respectively, n being the number of photographs per strip. For a block with m laterally overlapping strips, there are $(n+2)(2m+1)$ and $2(n+2)(2m+1)$ primary and auxiliary block points respectively. Thus, the block has $23 \times 11 = 253$ and $2 \times 23 \times 11 = 506$ primary and auxiliary points, and each strip 69 and 138 primary and auxiliary points, which are common with the adjoining strip. To differentiate the primary points from the auxiliary points, CP and AP numbering codes are added to their numbers respectively as shown in Figure 2.

- The block numbering system is suitable for block studies such as determination of strip deformations, studying the effects of systematic and random errors on the results of block adjustment, comparison of the results of the different procedures of block adjustment, e.g. sequential and bundle, and helping in the development of new methodologies for block adjustment and investigation of the effect of changing one or all block specifications on the results.
- Ground coordinates of block points: The planned X and Y coordinates of the perspective center of the first photo of the first strip in the block are taken as the coordinates of block origin (X_{G_o} , Y_{G_o}).
- Applied mathematical model: As mentioned above, perfect perspective projection (collinearity condition [7]) from ground to photograph and from photograph to ground, and absence of all error sources have been assumed for generating the mathematical photogrammetric data.

B. Floating Specifications

Floating specifications can be changed, depending on the study and the available data and are entered to the software operating system by editing the data file.

- Camera focal length and format: These values depend on the camera used.
- X and Y ground coordinates of block origin: X and Y ground coordinates of block points and camera stations are referred to the coordinates of block origin X_{G_o} , Y_{G_o} .
- Height variation: Height variation of ground points is taken as a percentage of the flying height. This factor defines the terrain type.
- Longitudinal and lateral overlaps: These are entered as percentages of the width of the photograph (longitudinal%, lateral%), and are necessary for strips and block formations, and photogrammetric studies.
- Flight specifications: These include the values of b_y , b_z , ω , ϕ and κ for each of 105 photographs of the block.

IV. THE SIMUPHOTOS SYSTEM

Software suites designed to support CAD have become popular. The most well-known software package in this regard is AutoCAD, from Autodesk, Inc. [10]. Of equal importance has been the development of software designed to utilize efficient user interfaces, e.g. window-driven and menus [11]. These advances in technology have enabled the development of the SimuPhotos system. The applied methodologies in SimuPhotos development provide automatic generation of the simulated data in numerical and graphical forms. The numerical form enables the testing of analytical processing methodologies and systems. The graphical form in drawing exchange format (DXF) and numerical forms are used for testing photogrammetric instruments, e.g. stereoplotters and

analytical plotters. Furthermore, the graphical form is suitable for testing the digital systems by scanning the plotted photos using CCD cameras or scanners. Also, the graphical form in DXF format can be directly converted to pixel or raster format using the capabilities of software such as CorelDraw [12] and AutoCAD [10]. One of the most important aspects of automatic generation of graphical simulated data is the prevention of manual graphical presentation, e.g. using hand or software drawing of the numerical simulated data which is time consuming and may have additional mistakes. The structure of generating the simulated data process is shown in Figure 3. Four main modules (generating simulated photos MathP module, generating AutoCAD files DXFGEN module, control interface, and AutoCAD software) can be seen.

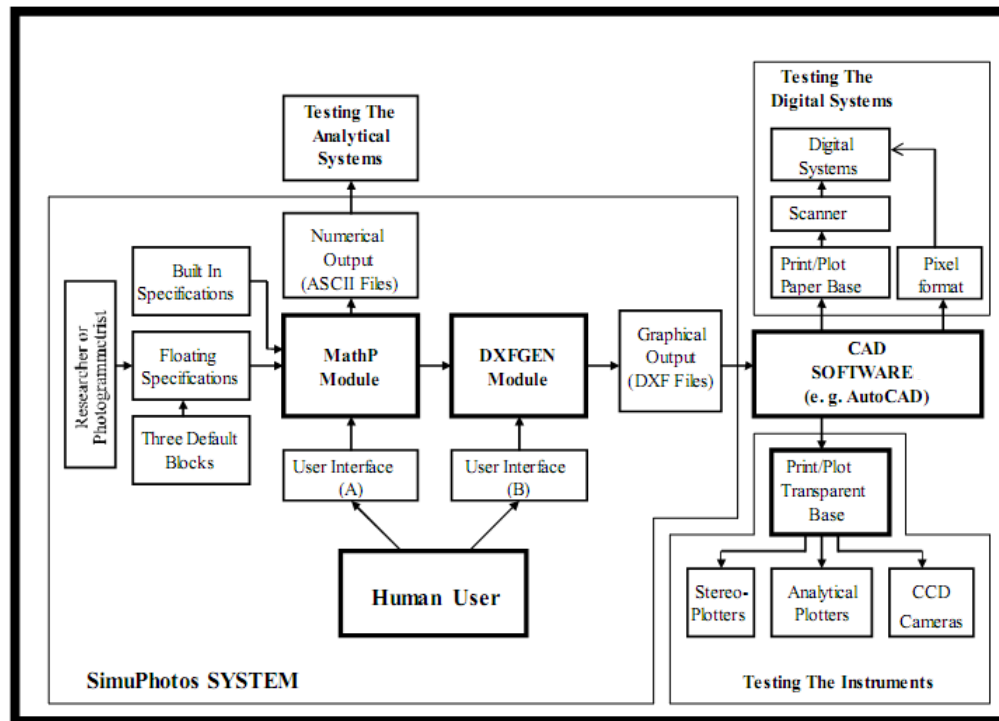


Fig. 3. SimuPhotos system architecture and its intermediate communication to the hardcopy devices.

Central to the system is the MathP module that reads the floating block specifications from the input data file (3 data files are available to the system) and uses these specifications along with built-in block specifications for generating the free error simulated photos. The module has a special error generator to get normally distributed error(s) with arbitrary mean(s) and standard deviation(s). The obtained errors are then, if it is required, applied to the error free photo and the ground coordinates of points of the generated blocks. MathP module stores the generated data in ASCII format for further processing. MathP module is a window-driven program consisting of two master windows. The main master window consists of 5 menus, depending upon the user's choice. These menus are basically for generating the simulated data for the whole block, selected strips and selected photos, helping the user and exiting to the system main window. The second master window consists of 2 menus for choosing the

numbering system, single photo or block numbering system. Also, the user interface helps the user to move across the generated data and send the required data to the available hardcopy interfaces.

The DXFGEN module reads the generated data and prepares the suitable AutoCAD drawing files in DXF format. A menu pad is provided, allowing the user to work without knowledge of AutoCAD command sequences. Each key on this pad invokes a different mapping function. Map scale, legends, title blocks, border, and coordinate gridding can be entered. The DXFGEN module is supported by default values for automatic map generation without user choices.

The main functions of using AutoCAD are (1) enabling the user to add his modification(s) to the resulting map, (2) sending the generated maps to the hardcopy interfaces, and (3)

converting the DXF file into a raster format file, such as BMP, JPG, PNG, and TIFF, with the required resolution.

The SimuPhotos system generates the necessary data for both analytical and digital processing systems. Basically, these data are classified as numerical and graphical simulated data.

- Numerical simulated data: They include photos per each strip, ground coordinates of the origin point, camera format, height variation, and camera interior orientation parameters and Photo-Oriented Elements (which include photo and strip numbers, camera exterior orientation parameters, point numbers with respect to the chosen numbering system, and photo and ground coordinates of points).
- Graphical simulated data: They consist of the generated maps for location of the camera stations, location of points and for each photo, showing the image locations and their numbers as indicated in Figures 1 and 2.

V. TESTING PHOTOMAP

The PhotoMap system [2] is an analytical data processing and presentation photogrammetric system. PhotoMap is under continuous development and new capabilities are developed and added to widen its applications. PhotoMap contains 7 modules namely BUNDLE [2], Self-Calibration [9], DLT [13], Coplanarity [9], Distance-Control [14], No-Control [15], INTERSECTION [2] and GENERATE [2]. SimuPhotos was used for generating the necessary data for testing all computational stages of the developed modules of PhotoMap. The BUNDLE, Self-Calibration, DLT, Coplanarity, Distance-Control modules were developed to generate control points, compute the parameters of camera exterior orientation, and store the output in the system data bank. The INTERSECTION module utilizes the computed/known parameters of camera exterior orientation for computing the object coordinates of desired number of points for specific application. These are stored in the system data bank. The GENERATE module reads the stored data in the system data bank and generates the desired graphical output in digital format compatible with the available CAD and DTM (Digital Terrain Model) packages for plotting and statistical error analysis. The most important function of GENERATE module is its ability to generate the maps in DXF file format which is suitable for many commercially available GIS (Geographic Information System) packages.

Testing a photogrammetric system is a complex task. It includes the availability of appropriate data for testing, decisions regarding the number and type of tests to be accomplished, photogrammetric tasks for each test to be achieved, and many other considerations. After completing the development stages, PhotoMap was subjected to a series of tests. These tests provided an opportunity to verify that the developed system satisfies the required general performance, specifically the flexibility and feasibility of photogrammetric data processing. Testing the system error and functionality of BUNDLE and INTERSECTION modules could be offered right here.

System errors consist of (a) error due to the rounding off of values throughout intermediate computations which may be

minimized by using double precision computations as far as possible and (b) errors because of truncation of higher order terms while forming the linearized observation equations from the nonlinear condition equations. For instance, in bundle adjustment the errors in triangulation process may be generated because of the use of simplified linearized correction equations derived from the non-linear collinearity condition equations by truncating a few terms [2, 7].

A. Planning for Testing PhotoMap

The simulated photogrammetric block utilizing the depicted specifications in Table I was used for testing the system error of PhotoMap.

TABLE I. SPECIFICATIONS FOR THE USED SIMULATED PHOTOGRAMMETRIC BLOCK

Specification	Value
a. Photograph scale	1:1
b. Camera format	230.0*230.0 mm
c. Camera focal length	150.00 mm
d. Longitudinal and Lateral overlaps	65% and 30% respectively
e. Total number of points available per model	18
f. Terrain configuration	Hilly type with height variation of 25% of flying height.

B. Testing the Results of BUNDLE Module

BUNDLE module carries the photogrammetric operations using the following methodologies [2]:

- Exterior orientation determination,
- Bundle block adjustment.

Each of these methodologies has been independently tested for the system error as described below.

1) Testing the System Error for Camera Exterior Orientation Determination

The available 18 points in the model were considered control points and this control distribution pattern was used to test the results of camera exterior orientation determination. Error free photo and ground coordinates of the 18 control points and their a priori standard deviations were processed simultaneously in the BUNDLE module. The known quantities were photo and ground coordinates of the control points and camera interior orientation parameters. The unknowns to be estimated were the 6 exterior orientation parameters of each photograph. The residual errors between the actual and the computed values of camera exterior orientation parameters were found out, along with standard errors [16] as tabulated in Table II.

TABLE II. PHOTOMAP SYSTEM ERROR FOR CAMERA EXTERIOR ORIENTATION DETERMINATION

Standard Errors					
Camera ground coordinates (μm)			Orientation angle (rad)		
σ_x	σ_y	σ_z	σ_ϕ	σ_ω	σ_κ
0.001	0.001	0.001	0.000	0.000	0.000

* Values at 1:1 photograph scale

These standard errors are small and negligible, and it can be concluded that BUNDLE module is free from system error for camera exterior orientation determination.

2) Testing the System Error for BUNDLE Block Adjustment

For testing the results of bundle block adjustment, suitable location and number of control points were chosen [2]. The block size was 5 strips, each with 21 photographs. In this case, the block contained 253 and 506 control and check points respectively. Error free photo coordinates of control and check points, ground coordinates of the control points and their standard deviations were processed simultaneously with the BUNDLE module. The output was the adjusted camera exterior orientation parameters and the ground coordinates of the check points. Table III lists the standard errors for camera exterior orientation parameters and ground coordinates of the check points.

TABLE III. PHOTOMAP SYSTEM ERROR FOR BUNDLE BLOCK ADJUSTMENT

a. Camera exterior orientation parameters					
Standard error					
Camera Ground Coordinates (μm)			Orientation Angle (rad)		
σ_x	σ_y	σ_z	σ_ϕ	σ_ω	σ_κ
0.002	0.002	0.003	0.000	0.000	0.000
b. Ground coordinates of check points					
Standard error (μm)*					
σ_x	σ_y	σ_z			
0.001	0.001	0.002			

* Values at 1:1 photograph scale

These results lead to following conclusions:

- The bundle block adjustment has system error for the Z coordinate larger than for planimetric (X, Y) coordinates which was expected [9, 14, 15] and
- The maximum system error is $0.002\mu\text{m}$ for the ground coordinates of check points, which is negligible.

From the above, it is obvious that the BUNDLE module is free from system error and that it is functional.

C. Testing the System Error of the INTERSECTION Module

The ground coordinates of the 18 points of each model for which image coordinates were known, were computed with the INTERSECTION module. The error free values of camera exterior orientation parameters for each photograph as generated by SimuPhotos were used. The residual errors between the actual and the computed ground coordinates of these intersected points were obtained for computing the shown standard errors in Table IV.

TABLE IV. PHOTOMAP ERROR FOR TESTING SPACE INTERSECTION METHODOLOGY

Standard error of ground coordinates of check points (μm)*		
σ_x	σ_y	σ_z
0.002	0.002	0.004

* Values at 1:1 photograph scale

The results indicate negligible standard errors and hence the INTERSECTION module of PhotoMap is also free from system error in performing space intersection operation and is functional.

VI. CONCLUSIONS

This paper discusses a new application of CAD technology for automatic preparation of the necessary data for calibrating photogrammetric instruments. Using the colored facilities of the hardcopy devices, inkjet or laser printer or plotter, the gray level of graphical simulated data can be changed. SimuPhotos provides a real time solution for testing the photogrammetric systems and eliminates the need of manufactured plates which are costly and not always available, and preventing manual graphical presentation such as using hand or software drawing of the numerical simulated data which is time consuming and may pose additional mistakes. The numerical and graphical simulated data are useful for academic studies such as error behavior investigations, determination of the suitable number of control points and their location, testing the results of the suggested methodologies of data processing, etc.

The PhotoMap testing results clearly showed that SimuPhotos system can effectively provide a convenient, economic, and accurate testing tool for photogrammetric systems. Moreover, the results showed that PhotoMap is free of system errors and is functional. SimuPhotos provides a window-driven system that is both portable and suitable for use by non-technical users after a short training period.

The developed system is quite versatile and provides an affordable tool to the researchers in universities and academic canters.

REFERENCES

- [1] F. J. Doyle, "Fictitious data generator for analytical aerotriangulation," *Photogrammetria*, vol. 21, no. 5, pp. 179–194, Oct. 1966, [https://doi.org/10.1016/0031-8663\(66\)90011-1](https://doi.org/10.1016/0031-8663(66)90011-1).
- [2] K. L. A. El-Ashmawy, "A Cost-Effective Photogrammetric System for Engineering Applications," Ph.D. dissertation, University of Roorkee, Roorkee, India, 1998.
- [3] S. Rani, Y. Chabarra, and K. Malik, "An Improved Denoising Algorithm for Removing Noise in Color Images," *Engineering, Technology & Applied Science Research*, vol. 12, no. 3, pp. 8738–8744, Jun. 2022, <https://doi.org/10.48084/etasr.4952>.
- [4] S. Banerjee, A. Bandyopadhyay, A. Mukherjee, A. Das, and R. Bag, "Random Valued Impulse Noise Removal Using Region Based Detection Approach," *Engineering, Technology & Applied Science Research*, vol. 7, no. 6, pp. 2288–2292, Dec. 2017, <https://doi.org/10.48084/etasr.1609>.
- [5] R. Vadhi, V. S. Kilari, and S. S. Kumar, "An Image Fusion Technique Based on Hadamard Transform and HVS," *Engineering, Technology & Applied Science Research*, vol. 6, no. 4, pp. 1075–1079, Aug. 2016, <https://doi.org/10.48084/etasr.707>.
- [6] Yu. B. Blokhinov, D. A. Gribov, and A. S. Chernyavskiy, "Image matching problem for certain cases of perspective photography," *Journal of Computer and Systems Sciences International*, vol. 47, no. 6, pp. 959–973, Dec. 2008, <https://doi.org/10.1134/S1064230708060105>.
- [7] S. K. Ghosh, *Fundamentals of Computational Photogrammetry*, 1st ed. New Delhi, India: Concept Publishing Company Pvt. Ltd., 2005.
- [8] *Manual of Photogrammetry*. Bethesda, MD, USA: ASPRS, 2004.
- [9] K. L. A. El-Ashmawy, "Coplanarity Condition for Photogrammetric Simultaneous and Self Calibration Block Adjustments," *International*

- Journal of Advances in Scientific Research and Engineering*, vol. 7, no. 2, May 2021, <https://doi.org/10.31695/IJASRE.2021.33970>.
- [10] I. Autodesk, *Autocad Reference Manual*. Sausalito, CA, USA: Autodesk, Inc., 1986.
- [11] K. Gregory, *Using Visual C++ 6*, Special edition. Indianapolis, IN, USA: Que Pub, 1998.
- [12] *CorelDRAW® 2020 User Guide*. Corel Corporation, 2020.
- [13] K. L. A. El-Ashmawy, "Using direct linear transformation (DLT) method for aerial photogrammetry applications," *Geodesy and Cartography*, vol. 44, no. 3, pp. 71–79, Oct. 2018, <https://doi.org/10.3846/gac.2018.1629>.
- [14] K. L. A. El-Ashmawy, "Block Adjustment Using Control Distances Constraint," *International Journal of Innovation Scientific Research and Review*, vol. 3, no. 3, pp. 948–953, Mar. 2021.
- [15] K. L. A. El-Ashmawy, "Photogrammetric block adjustment without control points," *Geodesy and Cartography*, vol. 44, no. 1, pp. 6–13, Apr. 2018, <https://doi.org/10.3846/gac.2018.880>.
- [16] C. D. Ghilani, *Adjustment Computations: Spatial Data Analysis*, 6th ed. Wiley, 2017.

Data Mining Regarding Cyberbullying in the Arabic Language on Instagram Using KNIME and Orange Tools

Shumaa Saeed Alzahrani

Computer Science and Engineering Department
College of Computers and Information Systems
Umm Al-Qura University
Makkah, Saudi Arabia
shayma.s.s.alzahrani@gmail.com

Received: 20 July 2022 | Revised: 15 August 2022 | Accepted: 22 August 2022

Abstract-This paper deals with data mining on verbal bullying by Instagram users. It tracks people who repeatedly have abusive behavior and may cause harm to other persons or groups. In this work, a dataset holding verbal bullying in the Arabic language was extracted from Instagram comments, and the entries were classified as regular verbal bullying and suspicious verbal bullying. KNIME and Orange open source data mining tools were utilized to discover comments that involved verbal bullying on Instagram and to delete previous comments while users sent their comments automatically and immediately. Classification algorithms Rule-Based in KNIME and Select Rows in Orange were used.

Keywords-KNIME tool; Orange tool; Instagram; data mining; Instagram comments; cyberbullying; verbal bullying

I. INTRODUCTION

Social media platforms have developed rapidly during the last few years. One of them is the Instagram. It is free, contains online data, and provides an easy form of communication. Users can talk in private and upload, tag, like, comment on, and share posts. Machine learning powers the app. Instagram's feed ranking is constantly adapting and improving based on new data [1]. The Instagram algorithm predicts how much you care about a post. This way, one can find and classify bullies based on trending [1]. Also, the people who use offensive or abusive words can be identified with data mining tools.

A. How the Instagram Algorithm Works

Six key factors influence the Instagram algorithm for feed posts: interest, relationship, timeliness, frequency, following, and usage. The Instagram algorithm is constantly changing. The more the Instagram algorithm "likes" a post, the higher it will appear in your feed. This phenomenon is based on the "past behavior on similar content and possibly machine vision analyzing the post's actual content." What you see in your Instagram feed is a mixture of all your behaviors on Instagram [1]: the people you communicate with, the stories you watch, the individuals you are tagged with, and the topics you

comment and like. Comments, likes, reshares, and views are the most critical engagements for feed rating, which is beneficial when you prepare content and captions [1].

B. Comment of All Lengths Count as Engagement

The Instagram algorithm counts comments that are less than 3 words in length. Instagram comments have become essential sources of knowledge for making fast and informed decisions and understanding how people behave in the real world. National and human rights organizations are now tracking social media [2].

C. Motivation

Bullying includes repetitive and violent physical, verbal, or emotional actions. In this paper, the target goal is verbal bullying, which includes calling names, mocking, taunting, threatening, or verbally assaulting. Bullying can make you feel powerless, ashamed, depressed, or even suicidal. Detecting bullying can assist authorities in taking appropriate action by copying data, deleting them from public comments, or imposing fines. Using social media sites as data providers may be an effective mechanism for protecting ourselves.

Due to the evolving technology, bullying is no longer confined to schoolyards or street corners but can happen at home via phone calls, texts, emails, and social media. Cyberbullies stalk, attack, or humiliate victims using digital technology. Cyberbullying, unlike conventional bullying, does not involve face-to-face contact and is not limited to a few people at a time. It also does not necessitate physical strength or many bullies. The embarrassment can be shared by hundreds or thousands of people online with just a few clicks. Cyberbullying may involve sending threatening or degrading messages via text, email, social media posts, or instant messaging, as well as breaking into an email account or stealing someone's online identity. Some cyberbullies may set up a website or a social media account to harass a victim. The approaches used to cyberbully are as diverse and creative as the technologies accessible to bullies. The effects of cyberbullying

and traditional bullying are similar. They make victims feel angry, hurt, scared, powerless, hopeless, lonely, embarrassed, and guilty. A victim's mental health is likely to deteriorate, and the victim is more likely to experience mental health issues like low self-esteem, depression, PTSD, or anxiety. Because most cyberbullying on Instagram is anonymous, the victims do not know who is targeting them, which can make them feel even more threatened, and it can embolden bullies, who think that because they are anonymous online, they are less likely to be exposed. While cyberbullies cannot see the victim's reaction, they will sometimes go deeper with their harassment or mockery than they would if the victims were personally present.

Arabic speakers post both formal and informal comments in social media. The formal form of Arabic is Modern Standard Arabic (MSA), while the informal form is the regional dialects (DA), the spoken language used for everyday contact in Arab countries. Compared to the most common languages, such as English, dealing with Arabic text poses substantial challenges. Arabic has a wide range of grammatical forms, word synonyms, and meanings, dependent on factors such as word order and diacritics. There is an additional difficulty when dealing with dialect or colloquial language, commonly used in Instagram comments.

D. Research Questions

The main goal of this paper is to demonstrate the ability to detect verbal cyberbullying from social media comments, with Instagram being used as a case study. To identify bullies' comments, suspicious verbal cyberbullying terms, and verbal cyberbullying words, the following are the key research questions and sub-questions I hope to answer:

- RQ1: How can an Arabic dataset of verbal cyberbullying be built?
- RQ1.1: How can an Arabic dataset involving verbal cyberbullying in different dialects be built?
- RQ1.2: How can a verbal cyberbullying dataset be appropriate for this study?
- RQ1.3: How can the reliability of dataset classes be ensured?
- RQ2: How is verbal cyberbullying distinguished from non-related event comments?
- RQ2.1: What is the most effective tool for detecting verbal cyberbullying?
- RQ2.2: What are the best machine learning tools that improve the performance of the approaches?

E. Research Goals

This section addresses the paper's research objectives, followed by a discussion of the targets and their justifications. The following are the main objectives of this paper:

- To create an Arabic Instagram dataset of verbal cyberbullying comments that identifies known and suspicious verbal cyberbullying words in comments in Arabic.

- To determine the best method for detecting verbal cyberbullying by comparing KNIME and Orange tools results to discover the most successful supervised learning strategy.

Most relevant studies have created Instagram datasets for testing verbal cyberbullying detection approaches. Many datasets have been built for commonly used languages such as English, but Arabic has received less attention. To the best of my knowledge, no one has performed or identified verbal cyberbullying detection in Arabic. As a result of the increasing demand for Arabic datasets, I created a dataset specifically to assess my targeted verbal cyberbullying detection system. Because unsupervised methods are typically ineffective at detecting verbal cyberbullying, researchers must monitor their approaches. Most unsupervised approaches use burst detection, which compares constructed words to verbal bullying word frequencies in comments. The burst behavior of specific words may not be verbal cyberbullying. For instance, not all sentences in Arabic that include animal words (حيوان) are verbal cyberbullying. Table I shows examples of verbal cyberbullying-related comments and non-related verbal cyberbullying comments.

TABLE I. INSTAGRAM COMMENT EXAMPLES

Non-related verbal cyberbullying comment	"Mara [a type of rodent] animal" "حيوان المارا"
Related verbal cyberbullying comment	"An animal, may God suffice us of him" "حيوان حسبي الله عليه"

Both comments in Table I use the same word. This word may indicate bursts, but it is not always indicative of verbal cyberbullying. Compared to unsupervised approaches, the detection domain of supervised approaches is small.

II. RELATED WORK

Most published studies concentrate on cyberbullying identification strategies for commonly used languages like English, with Arabic gaining less attention. The first subsection of this chapter is a related work overview of the most influential cyberbullying identification studies in English social media or SNS. The following subsection presents studies on cyberbullying identification in Arabic social media or SNS. In terms of cyberbullying detection, I have divided the reviewed papers into supervised and unsupervised approaches.

Authors in [11] proposed a solution to dispose of verbal cyberbullying. They suggested using a new feature selection technique for the closest neighbor classifier, which involves summarizing the original training materials using a measure of sentence importance. The two measures of sentence similarity used in their method for summarizing a single document were the frequency of the terms in a sentence and the similarity of that sentence to other sentences. After the researchers ranked all sentences, they chose the best-ranking sentences for a summary (within a threshold limitation). The researchers took every document's summary from the corpus and entered it into a new document used for summarization evaluation. In [12], the effort focused on classifying documents, a guided learning technique. Text preprocessing, feature extraction, and classification are the phases that make up the document

categorization process. The study evaluated the performance of two classifiers (KNN and Naive Bayes) and specific feature selection strategies with or without combining accuracy, average precision, precision, and recall. The researchers trained each experiment's classifiers using a custom data set. The results showed that the Naive Bayes classifier outperformed the other classifiers in several instances. In [13], the authors employed the comparative study's performance evaluation metrics of accuracy, precision, and F-measure. Three algorithms were used for cyberbullying classification, i.e. Naive Bayes, SVM, and C4.5.

A. Event Detection in Arabic Social Media

In [6], the researchers built a text corpus focusing on two common Arabic dialects on Twitter. They proposed a 3-level hierarchical annotation schema for hate and offensive language characterization. For hate speech, their emphasis was on 4 types: religion, ethnicity, nationality, and gender, for offensive speech, they focused on posts containing nonacceptable language or general profanity. Based on machine learning (SVM, Naive Bayes, logistic regression) and deep learning (CNN, LSTM, and GRU), they trained numerous 2-class, 3-class, and 6-class hate speech classifiers using a panoply of feature extraction techniques, including unigram, word, and character n-grams and word embeddings (random, skip-gram, CBOW, and fastText) and contextual word embedding (multilingual BERT). The researchers observed that deep learning was superior to machine learning across the 3 classification tasks. In deep neural networks, the CNN+mBERT model outperformed all the other learned models across the 3 prediction tasks, with 87.05% for the 2-class task, 78.99% for the 3-class task, and 75.51% for the 6-class task. In [7], the researchers presented a scheme to detect cyberbullying messages in Arabic social media streams (Twitter and YouTube). The detection algorithm used a corpus of offensive words most used among Arab youth. The proposed scheme involved the following steps: (i) data cleaning and preprocessing, (ii) extracting bullying keywords and attributing weights, (iii) detecting cyberbullying comments, and (iv) calculating the bullying strength and classifying the comments. This scheme only focused on labeling the comments as bullying or non-bullying and decision making.

B. Existing Arabic Datasets

Authors in [3] published one of the first studies on Arabic abusive language identification, which included the development of an Arabic dataset of abusive comments. The dataset contained 1,100 tweets gathered from controversial accounts and hashtags. Three annotators classified the dataset as pornographic, offensive, or clean. The authors used a pattern-based Twitter search to build a seed word list of 228 obscene Arabic words for classification. Then, based on their use of obscene words in the seed list, they separated Twitter users into clean and obscene. They also compiled a longer list of potentially obscene terms by removing only unigram and bigram words. They assessed the utility of both lists as features for categorizing tweets as obscene or clean. Experiments revealed that combining the seed word list with the extended list generated the best F1 score of 60%. Authors in [4] presented a more detailed dataset for religious hate speech in

dialectal Arabic. The dataset comprised 6,600 tweets using religious-related keywords. The researchers used crowdsourcing to classify the tweets as hateful or not and if they were religious extremist targets. They looked at various features, including lexicon-based and n-gram features, as well as standard machine learning algorithms. They also used neural networks like GRU and LSTM to evaluate their theories. Their experiments showed that GRU had the highest prediction accuracy of 77%. Authors in [5] created the Levantine Hate Speech and Abusive Behavior (L-HSAB) Twitter dataset, which included 5,812 tweets categorized as average, hateful, or abusive. The researchers divided the learning tasks into 2-class (abusive, normal) and 3-class classification tasks (abusive, hateful, normal) for model validation. They tried various n-gram ranges, such as unigrams, bigrams, and trigrams, as functions. They compared SVM and Naive Bayes classification performance and found that Naive Bayes outperformed SVM with an F1 score of 89.6% for 2-class classification and 74.4% for 3-class classification.

III. ARABIC CYBERBULLYING DATASET

One of the difficulties in detecting Arabic cyberbullying is the small number of Arabic datasets. To detect cyberbullying, I wanted to create a dataset with comments written in MSA, Saudi, and other dialects. In this section, the dataset of Arabic comments from Instagram that I made to detect cyberbullying is presented and the research question and sub-questions RQ1, RQ1.1, RQ1.2, and RQ1.3 will be answered.

A. Verbal Cyberbullying Instagram Comment Collection

Two key measures were followed to establish a dataset to detect cyberbullying. In the first step, comments by keywords were manually collected. In the second step, the collected comments were filtered into two classes: bully or positive. The other way was by verbal keywords. The comments were manually collected from the Instagram website through the author's personal account. The reason for choosing Instagram was because it has a high volume of cyberbullying comments, although it is not open source. Thus, I created the dataset in an Excel file to use in KNIME and Orange tools. Comments were collected for a period of 11 months between January and November of 2021. By using search terms for cyberbullying, a keywords list was prepared, for example:

- غبي- غبية- غيبة- اغبياء-أغبياء-اغبياء باعبي-ياغيه يا أغبياء- ي غبي-ي { These words mean stupid in different ways in the Arabic language.
- يا حمار- يا حمار يا حماره- يا حماره- يا حماره- انتي حماره- انتي حماره- لانتك حمار {حمار-إنّ حمار -ي حمار -ي حماره – انتي حماره-انتي حماره- لانك حمار
These words mean donkey in different ways in the Arabic language.

Cyberbullying comments were collected based on a set of keyword lists related to calling names, mocking, taunting, threatening, or verbally assaulting in singular and plural. There were approximately 1,500 comments received for cyberbullying, with about 1,000 comments filtered by 1,857 keywords. Figure 1 shows a part of this dataset. Most comments were collected in 6 months. They were saved in an Excel spreadsheet, which is an excellent choice for storing

Instagram data in tables. In addition, because Excel is a spreadsheet that consists of field and value pairs, storing comments is easy.

Comments	Verbal Bullying
1	عليون ساترين
2	يا كوازيه
3	صدام بالمداد طمو عليك يا كراويد
4	البنته دوراوت بنت الخرد تلتجوتيه بيوم
5	كبي تحبين علي ع المرافين يمكن حرفي لان التي عجوز شماء كل هذا لان هاتج علاوي
6	هتدين يا جي هند حدها سوق الجمعة ينسها
7	ما احبها
8	والتي طافط الغره اتتم الكوتين كل سنه مزارين من دوله
9	تحيون الرزايل
10	زابه
11	طير
12	طاح حطج
13	الله من التلق
14	شكستين
15	فارغه
16	اروي تصلي المصربين
17	لا تصلقون الا طميه
18	كلم فاضي
19	مات حالج
20	اصداك لا تملطين هههههه
21	مارت عن هوا دارج هههههه

Fig. 1. A section of table comments and verbal bullying keywords.

IV. PROPOSED APPROACHES

The goal was to examine cyberbullying comments using keywords and categorize them into two types: cyberbullying (known and suspicious) and non-cyberbullying. I used KNIME and Orange tools to evaluate two different methods. Both tools detect cyberbullying comments distinguishable from non-cyberbullying comments by performing workflows using many nodes to classify data. The two tools were evaluated and compared. In this section, the RQ2, RQ2.1, RQ2.2 question and sub-questions will be addressed.

A. Utilized Methodologies

In cyberbullying detection, classification is usually used for specific cyberbullying detection, while clustering is generally used for unspecific cyberbullying detection. Two methods were assessed to detect cyberbullying on Instagram. The comments were manually gathered and the dataset was created. The suggested methods aimed to identify a specific form of cyberbullying.

As a result, only supervised learning methods were used. Because social media features such as follower counts, mention counts, and message lengths do not apply to the cyberbullying detection task, I focused the cyberbullying detection task on the textual content of the comments. The first method used the KNIME tool to identify cyberbullying and non-cyberbullying comments. The second method used the Orange tool. The two methods were compared to see if breaking down the issue of cyberbullying identification into two phases improved its effectiveness. Regarding the negative impact of noisy and informal comment text in both proposed methods, writing the keywords in different ways, such as in chatting manners, to detect relevant comments more effectively, is recommended.

B. Data Mining Tools

In this paper, cyberbullying is detected through data mining using the open-source tools KNIME and Orange. The reason behind the existence of these tools is the existence of massive amounts of data. As a result, the traditional statistics methods are no longer useful. In the late '80s, many pieces of research appeared to solve these problems, in addition to searching for solutions that combined several disciplines, including statistics, databases, artificial intelligence, distinguishing different

models, or analog computing. Then, data mining and knowledge discovery emerged, which proved to be successful solutions for analyzing vast amounts of data by transforming them from accumulated and incomprehensible data into valuable information that could be exploited and used [8]. Data mining is the process of analyzing data from different perspectives, drawing relationships between them, and summarizing them into useful information.

1) KNIME Tool

KNIME makes understanding data and developing data science workflows and reusable components accessible by being intuitive, transparent, and constantly incorporating new technologies [9].

2) Orange Tool

The Orange tool is open-source machine learning and data visualization software. With a comprehensive and diverse toolbox, it builds data analysis workflows visually [10]. Data visualizations that are parts of the Orange help find hidden data patterns, provide intuition behind data analysis procedures, or support collaboration between data scientists and domain experts. Scatter plots, box plots, and histograms are among the visualization widgets available, as are model-specific visualizations such as dendrograms, silhouette plots, and tree visualizations. Many other visualization tools, such as network visualizations, word clouds, and geographical maps are available as add-ons. Interactive visualizations allow exploratory data analysis. A user can pick interesting data subsets directly from plots, graphs, and data tables and mine them in downstream widgets. For instance, a user can perform cross-validation logistic regression on a data set and map some misclassifications to the two-dimensional projection. It is simple to transform Orange into a tool that allows domain experts to explore their data, even if they have little experience with statistics or machine learning.

C. Cyberbullying Approaches

1) KNIME Tool

a) Phase 1

The workflow in Figure 2 represents the data flow between different nodes, starting with Excel Reader, then moving on to Tika Language Detector (to recognize used languages), Column Filter, Filter Apply Row Splitter, Row Filter, Rule-based Row Filter, and finally Excel Writer.

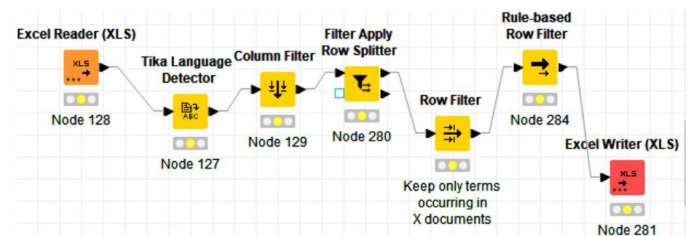


Fig. 2. The workflow of extracting bullying terms by rule.

The working of nodes 128, 127, and 281 has been explained above.

- Column Filter: This node allows columns to be filtered from the input table while the remaining columns are passed to the output table. Within the dialog, columns can be moved between the Include and Exclude list.
 - Filter Apply Row Splitter: This node splits the input according to the filter definitions, either given in the input table itself or optional as an additional model input. Filter definitions are only applied if an additional model is provided as input. If the input contains a filter defined on a column not present in the input table, the node will not fail but will display a warning message.
 - Row Filter (Figure 3): This node allows for row filtering according to specific criteria. It can include or exclude certain ranges (by row number), rows with a particular row ID, or rows with a specific value in a selectable column (attribute). The node does not change the domain of the data table. In other words, the upper and lower bounds or the possible values in the table spec are not adapted, even if one of the bounds or values is fully filtered out. Figure 3 shows the configuration dialog of the node.
 - Rule-based Row Filter (Figure 4): This node takes a list of user-defined rules and tries to match them to each row in the input table. The row is selected for inclusion if the first matching rule has a TRUE outcome. Otherwise (i.e. if the first matching rule yields FALSE), it will be excluded. If no rule matches, the row will be excluded. Inclusion and exclusion may be inverted (see the options in Figure 4).
- In the dialog in Figure 4, I used the simple rule **\$Col0\$ IN ("Bully") => TRUE** to extract just cyberbullying comments by classifying the comments as bullying (1) or positive (0). Figure 5 shows a part of the cyberbullying comment results using the rule Bully term, which extracted 999 comments out of 1,500.
- | | | |
|-----|-------|--|
| 981 | Bully | سيحان الله الرجال المغازل والنسونجي يعترف من |
| 982 | Bully | واضح عينه زايغه |
| 983 | Bully | طبيب جسمك كله تضاريس البسي شي يستر ويرتب |
| 984 | Bully | ابو الحريم |
| 985 | Bully | تغير راس بالكامل |
| 986 | Bully | واضح من شكله نسونجي لو قعدت مع زوجها الاول |
| 987 | Bully | شكله بيتزوجها (👍👍👍👍👍) مايفور احد ه |
| 988 | Bully | بدنه، فلة الخشم شكده (👍👍👍👍👍) |

In the dialog in Figure 4, I used the simple rule **\$Col0\$ IN ("Bully") => TRUE** to extract just cyberbullying comments by classifying the comments as bullying (1) or positive (0). Figure 5 shows a part of the cyberbullying comment results using the rule Bully term, which extracted 999 comments out of 1,500.

[illegible]

Fig. 5. Part of cyberbullying comments results by Bully term.

b) Phase 2

The workflow in Figure 6 represents the flow data to extract cyberbullying comments by verbal bullying keywords.

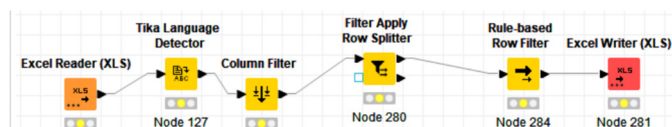


Fig. 6. The workflow used to extract cyberbullying by VB Keywords.

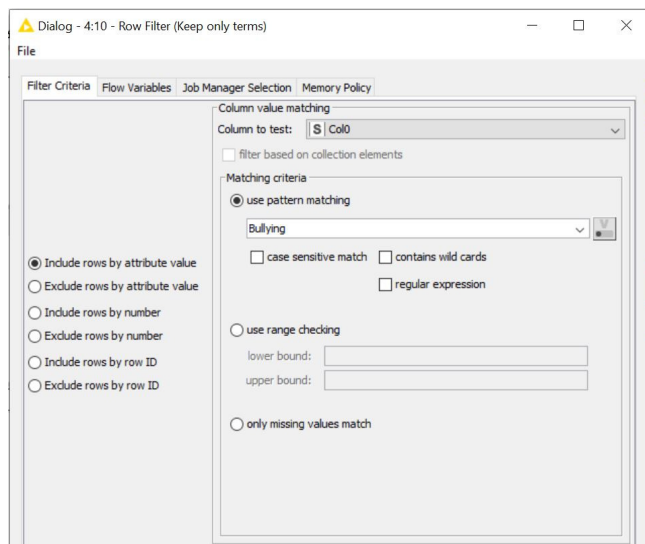


Fig. 3. Row Filter output.

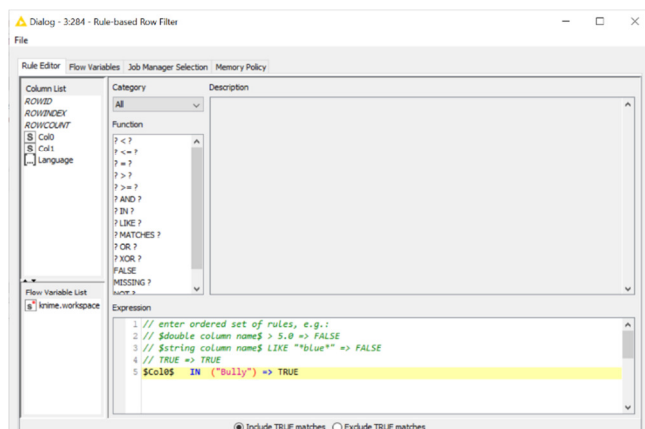


Fig. 4. Ruled-based Row Filter output.

1043 الكرف والتمش وتبين نتيجة في أقل من اسبوعين وتثبت حتى لو سببتها ترانسلي خاص (⊖) 1044
1045 تشرف بخدمته جميعاً (بحوث واجبات أنشطة) ♥ 1046
1047 في جلب الجامعة ؟ فجمعا جوداتها يعني ما من ضمن الباثات اى مايفرجو صحاره .. وغير كذا 1048
1049 شغلوا كل دقيقه في حياتكم الجامعيه والبسطو فيها فاعده افرأ تعلقاكم وكنت منخرجه في 10 1050
1051 كنت كتلك صام بالله اعد الايام والاقول براى مادرت اى كنت في نعمه (⊕) 1052
1053 اهل برفاك وبومضاك والطلب اهل في التناكب براى ادى الحين وكل صافى وايت ساجده ادى 1054
1055 لله الحمد لله ، والعكس والله انا ندانه على الوظيفه كرت ماى ندانه اى ضيعت وفي وعمره 1056
1057 لو موجود الصي ماراحو به في الجوع خلاهم ياكلون منه 1058
1059 الكرف الافضل خارج الجامعة صافى كرت تندر حتى اسعاهها معقوله لان كفتريات الجامعة لو 1060
1061 سندوشات وبفوف ودر ولا كل شى اى كفى صافى ربه ايت اكله محبيه ومعتومه 1062
1063 اهل الى كرتيه جودوا للهلالللى بى حلق الحوص من سناك سلفط وجيه ريسيه تحليه 1064
1065 الى والى كذا افصحيه برفر قهوه بش اه شى طعمه كونك توب لان كل م ذقت شى بالجامعه م بيع 1066
1067 حلى حلى قهوه وخصوصا الشاء العربى (⊕) والله يوفقك بشروعك 1068
1069 جيبى الى بيت مكرونه بشملى وفطابى ركفته وكذا 1070
1071 جيبى اى تذاكر بيليزيز 1072
1073 لمضاربع المهاجم .. كذا الغلات ، المكنى الاستعانة بفرق يسليا لاجاز مهاجم اى اكمل وه 1074
1075 لطلاب الاجابات الجامعيه - عربى / انجليزى صالة المحتوى بعيدا عن النقل والتشابهات ؛جوده 1076
1077 يدري بس لاجز لاجز لاجز في الاختبار 1078
1079 لطلاب خاص لى يسعدك لى اسوعمره 1080
1081

Fig. 7. Results extract cyberbullying comments by VB Keywords.

The results in Figure 7 represent 1,061 cyberbullying comments, 64 of them being positive. The KNIME tool is inaccurate because it does not deal perfectly with Arabic (as with English). Phase1 in KNIME has 999 right results out of 1500. In phase 2 there are 61 wrong comments.

2) Orange Tool

a) *Phase 1*

The workflow in Figure 8 represents extracting cyberbullying comments by using the Bully term through a categorical type target role in the file node description. The file classifies bully and positive comments. The results are fairly accurate. There were 999 cyberbullying comments out of 1,498, and the workflow ignored the rest.

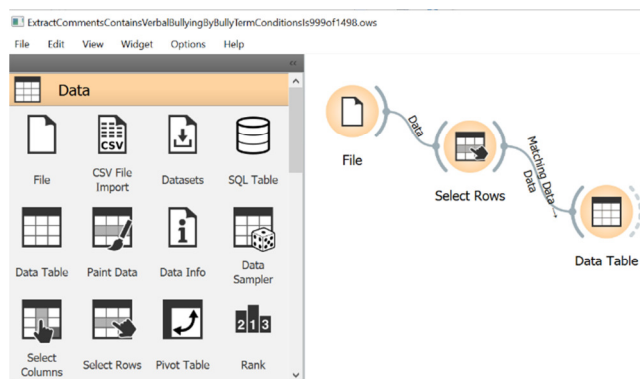


Fig. 8. Workflow for classifying cyberbullying and non-cyberbullying comments by the Bully term.

The Select Rows dialog in Figure 9 represents the condition pattern in which the classification is a column in the original file and the type of condition. Bully is one of the values in the classification column. The other value is Positive for non-cyberbullying comments.

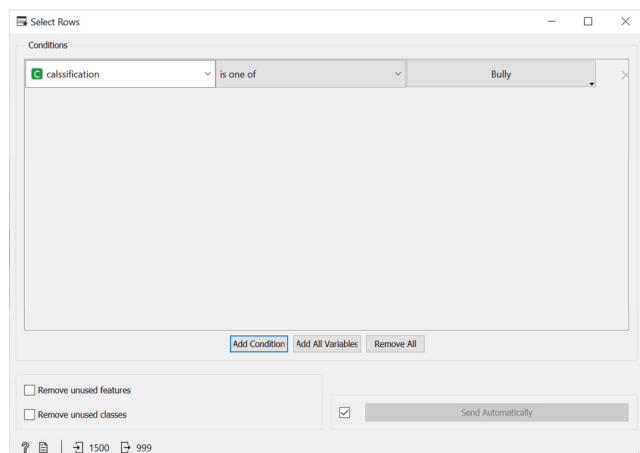


Fig. 9. Select Rows dialog with condition pattern.

Figure 10 displays the results for extracting 999 cyberbullying comments by Bully term out of 1,500 comments.

b) Phase 2

I changed the Select Rows node description in Figure 8. I

used the condition in Select Rows node that the verbal bullying must contain the cyberbullying called (اوعى تسدى المصريين ،ايران)
 ماتتلام فيكم عبل، اسنوت مثل الموميا، اسلوبها زج، اسلوبج الخايس، اصصايك
 لانتجلطين ههههههه، اعطنها اكبر من حجمها، افلس اخلاقيا من بعد ماافلس فنيا ،
 اقربي وجهك ، اذا تسنل على صراويل الراقين اسنل امك عنها اسنل محتفضه فيهم
 (الذكركه

Data Table (1)

Info

999 instances
2 features (49.9 % missing data)
No target variable.
1 meta attribute

Variables

☒ Show variable labels (if present)

☐ Visualize numeric values

☒ Color by instance classes

Selection

☒ Select full rows

Restore Original Order

☒ Send Automatically

	Comments	calsification	Feature 1
973	كل واحد تهول	Bully	?
974	ي مرضيه لونها	Bully	?
975	🤔🤔🤔🤔🤔...	Bully	?
976	التمر عموما	Bully	?
977	ابتلعشيا بالهالينا	Bully	?
978	حد يقههما هذا	Bully	?
979	قطيعه صغ حرو	Bully	?
980	لزام افكت تخاف	Bully	?
981	سبحان الله الرجا	Bully	?
982	واضح عبه رايحه	Bully	?
983	طيب جسمك كله	Bully	?
984	ابو الحريم	Bully	?
985	تعبير راس الكامل	Bully	?
986	واضح من شكله	Bully	?
987	شكله بيزوجها	Bully	?
988	بدون فلتر الحشم	Bully	?
989	!!!! شوفوا الفلتر	Bully	?
990	تدرون من اسوااا	Bully	?
991	طائر فيها عكس	Bully	?
992	راحت سوت وجه	Bully	?
993	بيسببياااااااااااا	Bully	?
994	بع يغ باربي	Bully	?
995	لو اناك يكتلمي	Bully	?
996	اففففففففففففففف	Bully	?
997	الشبان المراهقين	Bully	?
998	... التعليقات بدل م	Bully	?
999	... والله م تلقينها	Bully	?

Fig. 10. Data Table node results for extracting 999 cyberbullying comments by Bully term.

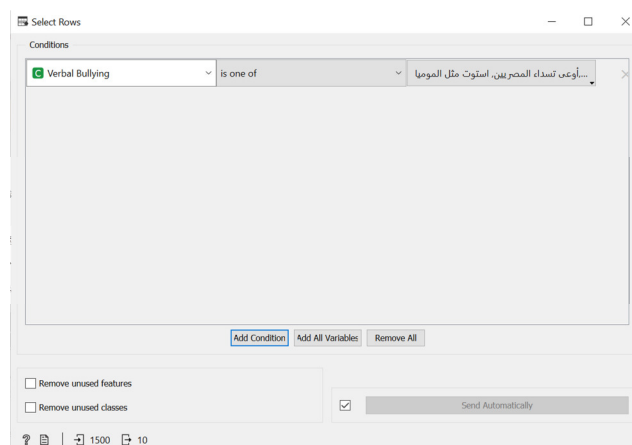


Fig. 11. Extracting cyberbullying comments with more than one VB keyword.

[illegible]

Fig. 12. Result of extracting cyberbullying comments with more than one VB keywords.

The output in Figure 12 represents 10 chosen rows applied by the condition in the original file of 1,500 comments classified as cyberbullying

c) Phase 3

I changed the condition in the Select Rows node description in Figure 8. I used the condition in the Select Rows node that the comment must contain the cyberbullying term (تتفون مذلولين), as shown in Figure 13. The output in Figure 14 represents one row in the original file of 1,500 comments classified as cyberbullying.

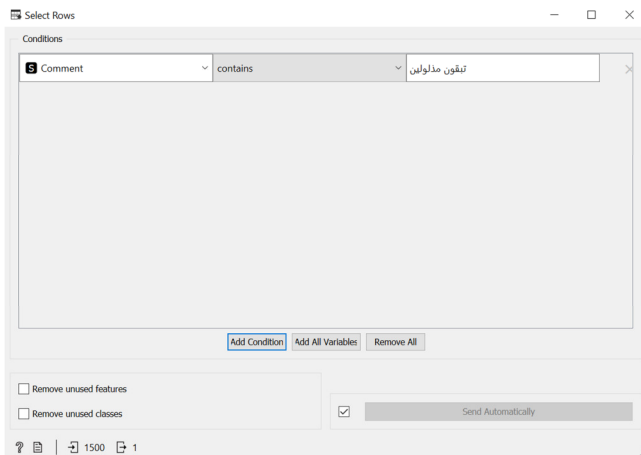


Fig. 13. Select Rows with condition comment contains VB keywords.

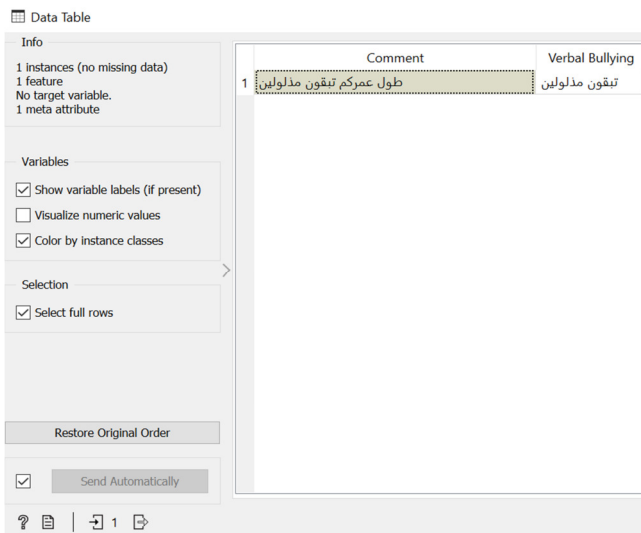


Fig. 14. Workflow result.

Phase 1 in Orange tool has a right result. Phase 2 extracts cyberbullying comments by just one cyberbullying term. In Phase 3, only the right answer can be shown when the cyberbullying terms are less than 100.

D. Comparison and Evaluation

In this paper, Orange and KNIME tools were used to classify Instagram comments under the cyberbullying and non-cyberbullying categories. Two data mining methods were applied: the first used two classes, Bully and Positive. The second used VB keywords. Each tool has its advantages and

disadvantages. The advantages of the KNIME tool are that it can deal with an extensive dataset, different types of files, a huge variety of components, has easy code-to-write conditions that make the tool more developed, and has excellent performance. The disadvantages are the need to use a special node to define the language, accurate results within the English language but inaccurate results within the Arabic language, the inability to use the Remove Punctuation node to get the correct result in the Arabic language, and unclear descriptions for using the tool. The advantages of the Orange tool are the lack of need to define the language, accurate results when the VB keywords are less than 100, easy dealing with nodes, and easy understanding of the concepts of the tool. The disadvantages are that it cannot deal with a large dataset, every single VB keyword must be chosen every time, and it cannot make a condition with comments containing more than one VB.

TABLE II. COMPARISON BETWEEN KNIME AND ORANGE

Tool	Algorithm	Phase1	Phase2	Phase3	Notes
KNIME	Rule-based	999 of 1500	1061 of 1500		Phase2 has wrong result
Orange	Select Rows	999 of 1500	Cyberbullying term<100 of 1500	1 of 1500	Phase2 allows small data. Phase3 allows one condition every time

E. Conclusion

Orange and KNIME tools were used in this paper to data mine cyberbullying comments and distinguish them from non-cyberbullying comments on Instagram. I extracted cyberbullying in two ways, one using VB keywords and the other classifying comments as Bully or Positive. In KNIME, I got inaccurate data results within the large dataset, while in Orange, I got accurate data results with less than 100 VB keywords. The results in both tools in the second way were accurate.

V. CONCLUSIONS AND FUTURE WORK

The driving question behind this study is "How can you detect cyberbullying in social media?" In this paper, emphasis was given on detecting name calling, mocking, taunting, threatening, or verbal abuse on Instagram. I addressed a complex problem in Arabic social media and carried out the key research goals.

To assess cyberbullying detection methods, I created a cyberbullying dataset that included written comments in MSA, Saudi, and other Arabic dialects. I created the dataset taking cyberbullying into consideration. I evaluated two supervised learning approaches to detect cyberbullying—the KNIME tool and the Orange tool. The keywords were the same in both approaches, as they are on social media. Both methods produced positive evaluation outcomes. Regarding detecting

cyberbullying, the Orange tool outperformed the KNIME tool. To address the issue of cyberbullying detection tasks, I suggest using the KNIME tool with raw data.

Regarding future work on cyberbullying detection, the following two directions are suggested for further investigation:

- Dataset expanding. A second version of the cyberbullying keyword dataset can be published by extracting extra samples and performing labeling process (known verbal, suspicious verbal, and non-cyberbullying).
- Cyberbullying detection in audio files using the KNIME tool with the created cyberbullying keywords dataset.

The utilized cyberbullying detection approach will be used in the future on the Twitter platform with its open-source API.

REFERENCES

- [1] J. Warren, "This Is How the Instagram Algorithm Works in 2022," *Later.com*, Jun. 21, 2022. <https://later.com/blog/how-instagram-algorithm-works/>.
- [2] F. Chen and D. B. Neill, "Human Rights Event Detection from Heterogeneous Social Media Graphs," *Big Data*, vol. 3, no. 1, pp. 34–40, Mar. 2015, <https://doi.org/10.1089/big.2014.0072>.
- [3] H. Mubarak, K. Darwish, and W. Magdy, "Abusive Language Detection on Arabic Social Media," in *Proceedings of the First Workshop on Abusive Language Online*, Vancouver, BC, Canada, Dec. 2017, pp. 52–56, <https://doi.org/10.18653/v1/W17-3008>.
- [4] K. E. Abdelfatah, G. Terejanu, and A. A. Alhelbawy, "Unsupervised Detection of Violent Content in Arabic Social Media," in *Computer Science & Information Technology (CS & IT)*, Mar. 2017, pp. 01–07, <https://doi.org/10.5121/csit.2017.70401>.
- [5] L. Kaati, E. Omer, N. Prucha, and A. Shrestha, "Detecting Multipliers of Jihadism on Twitter," in *2015 IEEE International Conference on Data Mining Workshop (ICDMW)*, Aug. 2015, pp. 954–960, <https://doi.org/10.1109/ICDMW.2015.9>.
- [6] S. Alsafari, S. Sadaoui, and M. Mouhoub, "Hate and offensive speech detection on Arabic social media," *Online Social Networks and Media*, vol. 19, Sep. 2020, Art. no. 100096, <https://doi.org/10.1016/j.osnem.2020.100096>.
- [7] D. Mouheb, R. Ismail, S. A. Qaraghuli, Z. A. Aghbari, and I. Kamel, "Detection of Offensive Messages in Arabic Social Media Communications," in *2018 International Conference on Innovations in Information Technology (IIT)*, Aug. 2018, pp. 24–29, <https://doi.org/10.1109/INNOVATIONS.2018.8606030>.
- [8] A. Sayed, "Data mining tool open source: Analytical evaluation study," *Journal of Taibah University Arts and Humanities*, vol. 5, no. 10, pp. 791–865, Jun. 2016, <https://doi.org/10.12816/0032954>.
- [9] "Data Analytics Platform: Open Source Software Tools," *KNIME*. <https://www.knime.com/knime-analytics-platform>.
- [10] "Orange Data Mining." <https://orangedatamining.com/>.
- [11] S. R. Basha, J. K. Rani, and J. J. C. P. Yadav, "A Novel Summarization-based Approach for Feature Reduction Enhancing Text Classification Accuracy," *Engineering, Technology & Applied Science Research*, vol. 9, no. 6, pp. 5001–5005, Dec. 2019, <https://doi.org/10.48084/etasr.3173>.
- [12] S. R. Basha and J. K. Rani, "A Comparative Approach of Dimensionality Reduction Techniques in Text Classification," *Engineering, Technology & Applied Science Research*, vol. 9, no. 6, pp. 4974–4979, Dec. 2019, <https://doi.org/10.48084/etasr.3146>.
- [13] M. Alghobiri, "A Comparative Analysis of Classification Algorithms on Diverse Datasets," *Engineering, Technology & Applied Science Research*, vol. 8, no. 2, pp. 2790–2795, Apr. 2018, <https://doi.org/10.48084/etasr.1952>.

Motivation of Female Engineers in the Construction Industry in Bosnia and Herzegovina

Edina Hodzic

Architecture Department
International Burch University
Sarajevo, Bosnia and Herzegovina
edinahodzic11@hotmail.com

Ahmed El Sayed

Architecture and Civil Engineering Department
International Burch University
Sarajevo, Bosnia and Herzegovina
ahmed.elsayed@ibu.edu.ba

Adnan Novalic

Architecture Department
International Burch University
Sarajevo, Bosnia and Herzegovina
adnan.novalic@ibu.edu.ba

Received: 16 June 2022 | Revised: 6 July 2022 | Accepted: 13 July 2022

Abstract-Female engineers go through different stages during their professional careers due to natural life processes and factors. In developing countries, it is not rare for managers to avoid hiring female engineers, due to these factors and the conservative belief that construction is a male-dominated industry. In Bosnia and Herzegovina (B&H) there are a few studies that refer to the motivation in the construction industry, but none that refer to the position of women in the construction industry and their motivation based on the selected demographic factors. This study aims to fill this research gap, utilizing quantitative research methods. The sample included female engineers of different profiles, working in the construction industry, who were required to fulfill the Multidimensional Work Motivation Scale (MWMS). The five considered demographic factors are age, family status, number of children, education level, and professional experience. The results of this research showed that family status does not affect any motivation dimension, whereas professional experience affects all motivation dimensions except the identified regulations. External-material regulations consist the most influential motivation dimension for female engineers in the construction industry in B&H, whereas amotivation, and introjected regulations were the least. It is recommended for managers and human resources to use the findings of this research in order to keep the female construction engineers motivated and satisfied in their workplace or to know what motivation dimensions to use during the hiring process.

Keywords-motivation; female engineers; construction industry; Bosnia and Herzegovina

I. INTRODUCTION

Motivation is an important factor, but yet it is a vague concept in work [1]. Various profiles of engineers require diverse motivation systems, but there is not a standard motivation model that could be used for all engineers. The reason for that is that the profiles of engineers change over

time, due to the nature of human life. In Bosnia and Herzegovina (B&H) only a few studies refer to the motivation in the construction industry [2]. To the best of our knowledge, there is no study that refers to the motivation of women in the construction industry, based on specific demographic factors. That is why this study will fill that research gap and aims to find out what motivates female construction engineers in B&H. A relevant study that was conducted in Nigeria resulted that financial reward is mostly used to motivate supervisors, whereas contractors prefer nonfinancial incentives. An important result is that in Nigeria construction industry, motivation of workers is not related to their needs [3]. The motivational factor that has the largest influence on female engineers is good work discipline, whereas the leading factor for motivation of male engineers is company name and stability [4]. Authors in [5] discovered 5 key motivational factors: achievement, proper recognition and awards, interesting work, involvement in decision making, and adequate training and development. During the last 50 years, the productivity in construction has remained low and when compared to other industries it can be said that the construction industry has fallen behind [6]. The top five most frequent problems that women in construction encounter are [7]:

- Slow advancement in career that leads to disappointment with the industry and construction culture.
- Difficulties with work-family balance.
- Attitude barriers that were the result of the male workers' domination in the construction industry.
- "Job hopping" to overcome barriers caused by slow progress and inflexible work structure.
- The culture because it consists of disputes, aggression and large percentage of men.

Still, the main reason why women are withdrawing from the construction industry and why women are not looking at it as viable career is culture. The potential solution for this, offered by some papers, is that the substantial change in the culture of the construction industry and its first impression will be needed in order to bring and keep large number of women at all levels [7].

A. Female Engineers in the Construction Industry

When the construction industry exhibited the greatest degree of vertical segregation by sex, women were less than 1% of the employed in construction trades in UK [8]. Construction's negative public image is that it is dirty and dangerous which results in a decrease of women's participation [9]. It is interesting to mention that previously conducted studies on women's construction careers did not reflect the nature of women's careers and why women encounter barriers more often and advance more slowly than their male coworkers [10]. A lawsuit was filed against the USA Department of Labor for its failure to fulfill its duties that prohibit discrimination in employment decisions on the basis of race, religion, gender, or national origin for federal construction contractors and subcontractors who do over \$10,000 in government business in one year. This action resulted in the establishment of regulations that were issued to integrate women into the construction industry by requiring specific steps [11].

Three out of five women that were interviewed in [12] stated that they had experienced harassment on the construction site, such as whistling, cat calls, a constant feeling to prove oneself, and so on. Career frustration and increased intentions to leave the industry are some of the factors that have been connected to the lower number of entries of female engineers in the construction industry [13]. It is important for construction managers to understand that what motivates male engineers, does not have to apply for female engineers. Women have different perceptions and priorities than male engineers, which results in different ways of motivation [14]. Promotion of STEM (Science, Technology, Engineering, and Mathematics) careers is more common these days than it was in the past. But there are not so many opportunities to bring in and explain construction management to new generations. So again, girls are deprived because chances are quite low for them to have some practical experience with construction or buildings design in comparison to the boys [15]. The main focus on how to transform the construction industry is through building relationships between the industry itself and universities [16, 17]. In the education process, ways to motivate workers should also be included because having qualified manpower is very important for the achievement of quality [18].

Effective construction project management is crucial in order to have good performance [19]. Employers could support female engineers in construction management by making the environment more respectful for them. It is concluded that it is imperative for the management to support women, create respectful environment with zero tolerance for harassment and try to provide them quality training opportunities in order for them to grow and develop their professional career [12].

B. Maslow's Theory

Motivation gives a goal that a person seeks to achieve. Every person has that need and if that need is withheld it will have a mobilizing effect, and if satisfied, a new goal of satisfying a new need on the hierarchy will be set [20]. Two main conclusions that can be derived from Maslow's need hierarchy are [21]:

- Satisfaction of one need does not serve as motivator.
- When needs on the lower part of the hierarchy become satisfied, then the next needs on the hierarchy determine the person's behavior.

Authors in [22] used motivation factors from Maslow's theory in the construction industry. It can be said that motivation is a main reason for the increased productivity of workers. It consists of powers and mechanisms that serve to direct a person's behavior in a desired way. This means that all the activities in the purpose of convincing and encouraging workers are the reasons they do their tasks willingly.

C. The Effect of Demographic Factors on Motivation

The relationship between motivation factors and gender in the case of engineers in the construction industry was tested in [14]. The results of that research showed no difference in the factors that motivate and demotivate them. It was also concluded that different things attract males and females to the workplace. The findings of [23] state that the age has very low level of influence on motivation, while education level has a large impact on achieving organizational goals. The professional qualification does have an influence on motivation, even when in relation with professional experience. Additionally, the overall motivation is not statistically impacted by the relationship between the age of the workers and the years they spent in a company. It is important to add that safety is the only motivational factor that depends on the age of the respondents because employees with different professional experiences do not have similar attitudes towards safety [23]. Factors such as the working hours, recognition received for a job well done, and colleague relationships play a major role in motivating engineers [24].

D. Literature Review Summary

The summarized findings of the literature review are:

- The motivational factor that has the most influence on female engineers is the good discipline at work.
- It is imperative for the management to support women in construction industry by:
 1. Creating respectful environment with zero tolerance for harassment (solving the "being ignored at meetings" issue).
 2. Providing quality training opportunities for continued professional development.
- Professional qualification has an influence on motivation, but none when in relation with professional experience.
- Safety is the only motivational factor that depends on the age of employees.

II. RESEARCH METHODOLOGY

The target population for this study consists of female engineers in Bosnia and Herzegovina that work or are educated in construction related fields. They have to have at least a bachelor's degree in construction related fields such as architecture, civil, mechanical, or electrical engineering. No other minimal requirements were taken into consideration. Sampling included all kinds of construction companies, architecture studios, schools, universities, and all other job positions where female construction engineers work. Snowballing technique was used. No names will be mentioned for confidentiality reasons.

Data collection started on 18th of December, 2021. The questionnaire consisted of the Multidimensional Work Motivation Scale (MWMS) with a total of 19 items and 5 demographic factors. The questionnaire was made by using google forms, and all questions were marked as required fields to be answered. Questions were answered in a Likert scale of 5 points, ranging from 1 for strongly disagree to 5 for strongly agree [25]. The online questionnaire was made in English and Bosnian. On the 13th of March, 2022 there were 200 respondents who filled out the questionnaire. The data collection process lasted for 2 months and 26 days.

Due to the established effect of demographics on the motivation in the literature findings and because women go through different phases in life, from being only a worker to being a worker, wife, and a mother by going through physical and mental changes, the following demographic factors were chosen in order to find solutions to the research problem: age, family status, number of children, educational level, and professional experience. The hypotheses assumed in this study, are:

- Hypothesis 1 (H1): Professional experience, as a demographic factor of female construction engineers in B&H, has a larger effect on intrinsic regulations than on other motivation dimensions.
- Hypothesis 2 (H2): Education level, as a demographic factor of female construction engineers in B&H, has a larger effect on external regulations - social than on other motivation dimensions.
- Hypothesis 3 (H3): Family status, as a demographic factor of female construction engineers in B&H, has a larger effect on external regulations - material than on other motivation dimensions.
- Hypothesis 4 (H4): Family status in relation with the number of children has a larger effect on identified regulations than on other motivation dimensions.
- Hypothesis 5 (H5): Education level in relation with professional experience has a larger effect on external regulations - social than on other motivation dimensions.

The research questions of this paper are:

1. The demographic factor amotivation, as a motivation dimension for female engineers in construction industry in B&H, could be used?

2. The demographic factor external regulations - social, as motivation dimension for female engineers in construction industry in B&H, could be used?
3. The demographic factor external regulations – material, as motivation dimension for female engineers in construction industry in B&H, could be used?
4. The demographic factor introjected regulations, as motivation dimension for female engineers in construction industry in B&H, could be used?
5. The demographic factor intrinsic regulations, as motivation dimension for female engineers in construction industry in B&H, could be used?
6. Which demographic factor is the most common and which is the least common effect on motivation dimensions of MWMS scale for female construction engineers in B&H?
7. What motivation dimension is most widely used for motivating female construction engineers in B&H and what the least?

In this paper, the motivational dimensions are the dependent variables and the demographic factors the independent variables, meaning that the motivational dimensions used in this research depend on the demographic factors. There are 19 items that are sorted in 6 different dimensions in the MWMS [26]:

1. Amotivation
2. External material regulations
3. External social regulations
4. Introjected regulations
5. Identified regulations
6. Intrinsic motivation

The MWMS dimensions and their questions are given below [26].

A. Amotivation

MWMS1: I don't put any effort on the current job, because I really feel that I'm wasting my time at work.

MWMS2: I do put a little effort on the current job, because I don't think this work is worth putting efforts into.

MWMS3: I don't put any effort on the current job, because I don't know why I'm doing this job, it is a pointless job.

B. External Regulations - Social

MWMS4: I put an effort in the current job to get others' approval (e.g. supervisor, colleagues, family, clients).

MWMS5: I put an effort in the current job because others will respect me more.

MWMS6: I put an effort in the current job to avoid being criticized by others.

C. External Regulations - Material

MWMS7: I put an effort in the current job because others will reward me financially only if I put enough effort in it (e.g. employer, supervisor).

MWMS8: I put an effort in the current job because others offer me greater job security if I put enough effort in it.

MWMS9: I put an effort in the current job because I risk losing my job if I don't put enough effort in it.

D. Introjected Regulations

MWMS10: I put an effort in the current job because I have to prove to myself that I can.

MWMS11: I put an effort in the current job because it makes me feel proud of myself.

MWMS12: I put an effort in the current job because otherwise I will feel ashamed.

MWMS13: I put an effort in the current job because otherwise I will feel bad about myself.

E. Identified Regulations

MWMS14: I put an effort in the current job because I personally consider it important to put efforts in this job.

MWMS15: I put an effort in the current job because putting efforts in this job aligns with my personal values.

MWMS16: I put an effort in the current job because putting efforts in this job has personal significance to me.

F. Intrinsic Motivation

MWMS17: I put an effort in the current job because I have fun while doing it.

MWMS18: I put an effort in the current job because what I do in my work is exciting.

MWMS19: I put an effort in the current job because the work I do is interesting

III. RESULTS AND DISCUSSION

Tests for analyzing the hypotheses will be chosen based on the types of included variables. Regression test will be used for the hypotheses where an independent continuous variable affects a dependent continuous variable. When an independent categorical variable affects a multiple dependent continuous variables, the one-way MANOVA (multivariate analysis of variance) will be applied, whereas MANCOVA (multivariate analysis of covariance) will be applied when categorical and continuous variables affect multiple dependent continuous variables. The dependent variables are amotivation, external regulations – social, external regulations – material, introjected regulations, identified regulations, and intrinsic regulations. A total of 200 female engineers filled out the questionnaire. Those engineers are architects, civil engineers, electrical engineers and mechanical engineers. The demographic questions were year of birth, family status, number of children, educational level, and professional experience. The range of respondents' years of birth is 1959-1999. This shows that there

is a 40-year difference between the youngest and the oldest female engineer in the construction industry that participated in this research.

A. Reliability

For testing and measuring reliability, Cronbach's alpha coefficient was used. IBM SPSS statistics software showed the results of the reliability test and the results of Exploratory Factor Analysis (EFA). Cronbach's alpha for all dimensions ranges from 0.759-0.922. Reliability is good if Cronbach's alpha values are higher than 0.7 [27]. A conclusion can be made that the alpha coefficients are reliable as they are all higher than 0.7 (Table I). The minimum accepted loading of EFA is 0.4 [28]. The analysis was carried out for all items of 6 the dimensions of MWMS. The EFA results showed that all correlations (loadings) for the given items regarding all variables in the MWMS scale are above the minimum value of 0.4. This shows that the validity of the questionnaire for all variables is satisfactory.

TABLE I. VALUES OF CRONBACH'S ALPHA COEFFICIENT AND INTERNAL CONSISTENCY [27]

Cronbach's alpha	Internal consistency
$\alpha \geq 0.90$	Excellent
$0.90 \geq \alpha \geq 0.80$	Good
$0.80 \geq \alpha \geq 0.70$	Acceptable
$0.70 \geq \alpha \geq 0.60$	Questionable
$0.60 \geq \alpha \geq 0.50$	Poor
$0.50 < \alpha$	Unacceptable

B. Testing the Hypotheses

In statistics, it can be stated that the population mean lies within a 95% confidence interval. This means that as an approximate population number, the mean of the sample size can be used [29]. The following significant terms are used in reporting [29]:

- $p < 0.05$ (significant at 5%) "The difference was significant"
- $p < 0.01$ (significant at 1%) "The difference was highly significant".

1) Testing Hypothesis 1

Professional experience, as a demographic factor of female engineers in B&H construction industry, has a larger effect on intrinsic regulations than on other motivation dimensions. In the case of Hypothesis 1, the independent discrete variable is professional experience, whereas motivation dimensions are dependent continuous variables, linear regression was used for testing. The confidence interval is 95%. The significance level or P-value is higher than 0.05 for all factors, except for identified regulation, which is 0.126 which means that professional experience has no significant effect on identified regulations [29]. This leads to the conclusion that the identified regulations should not be used as a motivation dimension regarding the professional experience of female engineers in the construction industry. The value of R-square will tell the strength of correlation.

TABLE II. CORRELATION OF DETERMINATION [30]

R-squared value	Strength of association
$r^2=0$	No correlation
$0 < r^2 < 0.25$	Very weak correlation
$0.25 \leq r^2 < 0.50$	Weak correlation
$0.50 \leq r^2 < 0.75$	Moderate correlation
$0.75 \leq r^2 < 0.90$	Strong correlation
$0.90 \leq r^2 < 1$	Very strong correlation
$r^2=1$	Perfect correlation

TABLE III. HYPOTHESIS 1 - R SQUARE & ASSOCIATION STRENGTH

Dependent variables	Independent variable: Professional experience		
	R square	Adjusted R square	Strength of association
Amotivation	0.015	0.010	very weak
External regulations-social	0.044	0.040	weak
External regulations-material	0.051	0.046	weak
Introjected regulations	0.020	0.015	very weak
Intrinsic regulation	0.059	0.054	moderate

When comparing the adjusted R square of the dependent variables, it can be said that intrinsic regulations is the most associated with the other motivation dimensions. It has a moderate correlation with the age of female engineers. Based on the results in this section, it can be concluded that Hypothesis 1 is accepted.

2) Testing Hypothesis 2

Education level, as a demographic factor of female engineers in B&H construction industry, has a larger effect on external regulations - social than on other motivation dimensions. Education level is, as a family status, a categorical independent variable. The hypothesis of the effect of the independent categorical variable on dependent continuous variable will be tested and one-way MANOVA was used. The results showed that education level, as a demographic factor of female engineers in the construction industry in B&H, affects both external regulations, but does not affect any other motivation dimension. Since both external regulations are affected by the education level, then the amount of effect that education level has on them should be measured.

TABLE IV. PARTIAL ETA SQUARED - EFFECT SIZE [29]

Partial eta squared	Effect size
0.01	Small effect
0.06	Moderate effect
0.14	Large effect

TABLE V. PARTIAL ETA SQUARED – HYPOTHESIS 2

Dependent Variables	Association strength
External regulations-social	0.091
External regulations-material	0.054

The effect of education level on external regulation – material is small, very close to being moderate. On the other side, external regulations – social is moderately affected by the education level, since partial eta squared is larger than 0.06 [29]. From the results and the information presented in this section, it can be stated that Hypothesis 2 is accepted.

3) Testing Hypothesis 3

Family status, as a demographic factor of female engineers in B&H construction industry, has a larger effect on external regulations - material than on other motivation dimensions. After the conducted MANOVA, the significance level is one of the most important parts of the results. Those results are shown in Table VI. Based on them, it can be seen that family status does not affect any motivation dimension if confidence interval is 95% [29]. Then, Hypothesis 3 is rejected.

TABLE VI. ONE-WAY MANOVA RESULTS - HYPOTHESIS 3

Dependent Variables	Significance value
	Number of children
Amotivation	0.110
External regulations-social	0.184
External regulations-material	0.272
Introjected regulations	0.850
Identified regulations	0.071
Intrinsic regulations	0.072

4) Testing Hypothesis 4

Family status in relation with the number of children has a larger effect on identified regulations than on other motivation dimensions. MANCOVA will be used for this hypothesis because independent variables are categorical and continuous and affect multiple dependent continuous variables. Table VII shows the MANCOVA results. When the number of children and family status are in relation, they do not have an effect on any motivation dimension [29]. With that result, Hypothesis 4 is rejected.

TABLE VII. ONE-WAY MANCOVA RESULTS - HYPOTHESIS 4

Dependent variables	Significance value	
	Family status	Number of children
Amotivation	0.333	0.592
External regulations-social	0.488	0.491
External regulations-material	0.393	0.093
Introjected regulations	0.817	0.613
Identified regulations	0.624	0.076
Intrinsic regulations	0.580	0.119

5) Testing Hypothesis 5

Education level in relation with professional experience has a larger effect on external regulations - social than on other motivation dimensions.

TABLE VIII. ONE-WAY MANCOVA RESULTS - HYPOTHESIS 5

Dependent variables	Significance value	
	Education level	Professional experience
Amotivation	0.646	0.295
External regulations-social	0.004	0.318
External regulations-material	0.147	0.076
Introjected regulations	0.661	0.215
Identified regulations	0.331	0.577
Intrinsic regulations	0.840	0.007

The results show that education level in relation with professional experience does not affect external regulations – material as it did on its own. It affects only external regulations – social. Professional experience in relation with education

level affects only intrinsic regulations, whereas on its own it affects all regulations except the identified regulations. As mentioned, education level in relation with professional experience affects only external regulations – social [29]. This leads to the conclusion that Hypothesis 5 is accepted.

6) Research Questions

Amotivation could only be used for female engineers with regard to their professional experience. The findings state that external regulations – social, as motivation dimension, is the most useful for motivating with regard to the education level of female engineers in the construction industry in B&H. External regulations – material is affected by all demographic factors except family status. This means that this motivation dimension could be used for any of these demographic factors. Based on the results, introjected regulations could only be used for motivating when it comes to professional experience. For all demographic factors except family status and education level, intrinsic motivation regulations could be used. Family status does not affect any motivation dimension, whereas professional experience affects all motivation dimensions except the identified regulations. External – material regulations is the most influential motivation dimension for female engineers in the construction industry in B&H, whereas identified regulations, amotivation, and introjected regulations are used the least.

7) Summary

This section will show the comparison between the findings of the current research and the literature findings.

TABLE IX. RESULTS COMPARISON WITH LITERATURE FINDINGS

Research results	Literature findings
External – material regulations have the most impact on motivation dimension for female engineers in construction industry in B&H	The motivational factor that has the most influence on female engineers is good discipline at work
Both external regulations are affected by education level, but when in relation with professional experience it affects only external regulations - social	Professional qualification has an influence on motivation, but none when in relation with professional experience

Table X shows the status of hypothesis testing and the explanations in case a hypothesis was rejected.

TABLE X. HYPOTHESES RESULT SUMMARY

Hypothesis	Status	Association
H1	Accepted	Moderate association (adjusted R square)
H2	Accepted	Moderate association (partial eta squared)
H3	Rejected	Family status does not affect any motivation dimension
H4	Rejected	Family status and number of children in relation do not affect any motivation dimension
H5	Accepted	Decreased association with external regulations – social (from moderate when on its own to weak when in relation).

IV. CONCLUSION

When education level is used as a demographic factor of female construction engineers in B&H, both external

regulations could be used for motivation. Intrinsic regulations is the most associated with professional experience than other motivation dimensions, since it has moderate association. Family status does not affect any motivation dimension, whereas professional experience affects all motivation dimensions except the identified regulations. External – material regulations is the most influential motivation dimension for female engineers in the construction industry in B&H, whereas identified regulations, amotivation, and introjected regulations are used the least.

To the best of our knowledge, there are no studies that refer to the motivation of women in the construction industry in B&H, based on the selected demographic factors. The current study fills that research gap. The results of this research could be used in construction companies in order to motivate their female engineers. Regarding the demographic factors used, the motivation dimension for each employee should be found. It would be a duty of management or human resources to update these applications as female engineers go through different stages in their professional careers due to natural life processes and factors and their motivation regulation might change. Hopefully, many female engineers in the construction industry in B&H may find this research useful to find ways of self-motivation. When analyzing whether to stay in the construction industry or how to develop their career, this research may lead to desired outcomes for female construction engineers. Additionally, managers and human resources can now find what motivates their female construction engineers in order to keep them satisfied in their workplace or to know what motivation dimensions to use during the hiring process.

REFERENCES

- [1] M. Yazdanifar, "Effect of Social Capital on Innovation: A Mediating Role of Employee Motivation," *Engineering, Technology & Applied Science Research*, vol. 8, no. 4, pp. 3098–3102, Aug. 2018, <https://doi.org/10.48084/etasr.1730>.
- [2] A. El Sayed, S. Spago, F. Catovic, and A. Novalic, "New Approaches and Techniques of Motivation for Construction Industry Engineers in B&H," in *International Conference "New Technologies, Development and Applications"*, Sarajevo, Bosnia and Herzegovina, Jun. 2019, pp. 736–745, https://doi.org/10.1007/978-3-030-18072-0_85.
- [3] A. Funso, L. Sammy, and M. Gerryshom, "Application of Motivation in Nigeria Construction Industry: Factor Analysis Approach," *International Journal of Economics and Finance*, vol. 8, no. 5, pp. 271–276, 2016.
- [4] P. T. R. S. Sugathadasa, M. Lakshitha, A. Thibbotuwawa, and K. A. C. P. Bandara, "Motivation factors of engineers in private sector construction industry," *Journal of Applied Engineering Science*, vol. 19, no. 3, pp. 795–806, 2021, <https://doi.org/10.5937/jaes0-29201>.
- [5] M. H. Momade and M. R. Hainin, "Identifying Motivational and Demotivational Productivity Factors in Qatar Construction Projects," *Engineering, Technology & Applied Science Research*, vol. 9, no. 2, pp. 3945–3948, Apr. 2019, <https://doi.org/10.48084/etasr.2577>.
- [6] J. E. Barg, R. Ruparathna, D. Mendis, and K. N. Hewage, "Motivating Workers in Construction," *Journal of Construction Engineering*, vol. 2014, Jul. 2014, Art. no. e703084, <https://doi.org/10.1155/2014/703084>.
- [7] C. L. Menches and D. M. Abraham, "Women in Construction—Tapping the Untapped Resource to Meet Future Demands," *Journal of Construction Engineering and Management*, vol. 133, no. 9, pp. 701–707, Sep. 2007, [https://doi.org/10.1061/\(ASCE\)0733-9364\(2007\)133:9\(701\)](https://doi.org/10.1061/(ASCE)0733-9364(2007)133:9(701)).
- [8] S. L. Fielden, M. J. Davidson, A. W. Gale, and C. L. Davey, "Women in construction: the untapped resource," *Construction Management and*

- Economics*, vol. 18, no. 1, pp. 113–121, Jan. 2000, <https://doi.org/10.1080/014461900371004>.
- [9] S. Barthorpe, R. Duncan, and C. Miller, "The pluralistic facets of culture and its impact on construction," *Property Management*, vol. 18, no. 5, pp. 335–351, Jan. 2000, <https://doi.org/10.1108/02637470010360632>.
- [10] A. R. J. Dainty, R. H. Neale, and B. M. Bagilhole, "Comparison of Men's and Women's Careers in U.K. Construction Industry," *Journal of Professional Issues in Engineering Education and Practice*, vol. 126, no. 3, pp. 110–115, Jul. 2000, [https://doi.org/10.1061/\(ASCE\)1052-3928\(2000\)126:3\(110\)](https://doi.org/10.1061/(ASCE)1052-3928(2000)126:3(110)).
- [11] "Advisory Committee on Construction Safety and Health (ACCSH) | Occupational Safety and Health Administration." <https://www.osha.gov/advisorycommittee/accsh> (accessed Aug. 26, 2022).
- [12] K. Scott W., W. Stephanie, and S. April E., "Women in U.S. Construction Management Positions: A Qualitative Look at Motivations, Challenges and Considerations," in *Creative Construction e-Conference*, Jul. 2020, pp. 167–175, <https://doi.org/10.3311/CCC2020-037>.
- [13] V. Francis, "What influences professional women's career advancement in construction?," *Construction Management and Economics*, vol. 35, no. 5, pp. 254–275, May 2017, <https://doi.org/10.1080/01446193.2016.1277026>.
- [14] G. L. Gilbert and D. H. T. Walker, "Motivation of Australian white-collar construction employees: a gender issue?," *Engineering Construction and Architectural Management*, vol. 8, no. 1, pp. 59–66, 2001, <https://doi.org/10.1046/j.1365-232x.2001.00185.x>.
- [15] K. Stephenson, "Breaking Down Gender Bias in the Construction Industry," *Building Energy*, vol. 36, no. 1, pp. 53–54, 2017.
- [16] Z. Al-Gasim, A. A. Senin, and M. E. bin Yusoff, "A Review and Comprehensive Analysis of the Performance of University – Construction Industry Collaboration," *Civil Engineering Journal*, vol. 7, no. 4, pp. 763–774, Apr. 2021, <https://doi.org/10.28991/cej-2021-03091688>.
- [17] P. K. Oad, S. Kajewski, A. Kumar, and B. Xia, "Bid evaluation and assessment of innovation in road construction industry: A systematic literature review," *Civil Engineering Journal (Iran)*, vol. 7, no. 1, pp. 179–196, Jan. 2021.
- [18] T. Bangia and R. Raskar, "Cohesive Methodology in Construction of Enclosure for 3.6m Devasthal Optical Telescope," *HighTech and Innovation Journal*, vol. 3, no. 2, pp. 162–174, Feb. 2022, <https://doi.org/10.28991/HIJ-2022-03-02-05>.
- [19] H. A. Sulieman and F. A. Alfaraidy, "Influences of Project Management Capabilities on the Organizational Performance of the Saudi Construction Industry," *Engineering, Technology & Applied Science Research*, vol. 9, no. 3, pp. 4144–4147, Jun. 2019, <https://doi.org/10.48084/etasr.2740>.
- [20] P. Cardoso, C. Dominguez, and A. Paiva, "Hints to Improve Motivation in Construction Companies," *Procedia Computer Science*, vol. 64, pp. 1200–1207, Jan. 2015, <https://doi.org/10.1016/j.procs.2015.08.513>.
- [21] R. Kreitner, *Organizational behavior*, 9th ed. Boston, MA, USA: McGraw-Hill, 2010.
- [22] A. Kazaz, E. Manisali, and S. Ulubeyli, "Effect of basic motivational factors on construction workforce productivity in Turkey," *Journal of Civil Engineering and Management*, vol. 14, no. 2, pp. 95–106, Jan. 2008, <https://doi.org/10.3846/1392-3730.2008.14.4>.
- [23] S. Urosevic and N. Milijic, "Influence of Demographic Factors on Employee Satisfaction and Motivation," *Organizacija*, vol. 45, no. 4, pp. 174–182, Aug. 2012.
- [24] G. L. Smithers and D. H. T. Walker, "The effect of the workplace on motivation and demotivation of construction professionals," *Construction Management and Economics*, vol. 18, no. 7, pp. 833–841, Oct. 2000, <https://doi.org/10.1080/014461900433113>.
- [25] A. Joshi, S. Kale, S. Chandel, and D. Pal, "Likert Scale: Explored and Explained," *British Journal of Applied Science & Technology*, vol. 7, no. 4, pp. 396–403, Jan. 2015, <https://doi.org/10.9734/BJAST/2015/14975>.
- [26] M. Gagne *et al.*, "The Multidimensional Work Motivation Scale: Validation evidence in seven languages and nine countries," *European Journal of Work and Organizational Psychology*, vol. 24, no. 2, pp. 178–196, Mar. 2015, <https://doi.org/10.1080/1359432X.2013.877892>.
- [27] L. J. Cronbach and R. J. Shavelson, "My Current Thoughts on Coefficient Alpha and Successor Procedures," *Educational and Psychological Measurement*, vol. 64, no. 3, pp. 391–418, Jun. 2004, <https://doi.org/10.1177/0013164404266386>.
- [28] J. F. Hair, *Multivariate data analysis*, 7th ed. Hoboken, NJ, New Jersey: Prentice Hall, 2010.
- [29] H. Coolican, *Research Methods and Statistics in Psychology*, 6th edition. New York, NY, USA: Psychology Press, 2014.
- [30] "Interpreting the Correlation - Year 12 Mathematical Applications." <https://sites.google.com/site/year12mathematicalapplications/statistics-and-working-with-data/linear-correlation/interpreting-the-correlation> (accessed Aug. 26, 2022).

A Fast Digital Phase Frequency Detector with Preset Word Frequency Searching in ADPLL for a UHF RFID Reader

Syaza Norfilsha Ishak

Institute of Microengineering & Nanoelectronics (IMEN)
Universiti Kebangsaan Malaysia
Bangi, Malaysia
syazanorfilsha@gmail.com

Jahariah Sampe

Institute of Microengineering & Nanoelectronics (IMEN)
Universiti Kebangsaan Malaysia
Bangi, Malaysia
jahariah@ukm.edu.my

Nazrul Anuar Nayan

Faculty of Engineering and Built Environment
Universiti Kebangsaan Malaysia
Bangi, Malaysia
nazrul@ukm.edu.my

Zubaida Yusoff

Faculty of Engineering
Multimedia University
Cyberjaya, Malaysia
zubaida@mmu.edu.my

Received: 15 July 2022 | Revised: 9 August 2022 | Accepted: 10 August 2022

Abstract—An All-Digital Phase-Locked Loop (ADPLL) is an architecture that is widely employed in the communication system due to the advancement of the Complementary Metal-Oxide-Semiconductor (CMOS) technology process. A 2.4GHz Radio Frequency Identification (RFID) system needs a frequency synthesizer in the local oscillator architecture of the transceiver to generate a stable frequency tuning range. Therefore, in this paper, a Digital Phase-Frequency Detector (DPFD) is designed to achieve the phase and frequency acquisition in the ADPLL system. The proposed DPFD is divided into two main parts, the first is the Phase Detector (PD) and the second is the Frequency Detector (FD). The PD has managed to detect the presence of the phase difference by recognizing two different input signals. The FD, on the other hand, is capable to detect the higher frequency by identifying the output signals from the PD in digital formation. In addition, a control unit module is developed to control and adjust the Preset Word (PW) for the system by using a binary search scheme. Comparison results show that the final value of the PW from the simulation is the same as from the manual calculation (theoretical values). The digital PFD and the PW control modules are designed and simulated by using Verilog HDL code. These two designed modules will be integrated into the targeted ADPLL to achieve fast locking performance and ultra-low power for Ultra-High Frequency (UHF) RFID applications.

Keywords—RFID; all-digital PLL; ADPLL; digital PFD; frequency synthesizer; local oscillator; binary search

I. INTRODUCTION

Internet-of-Things (IoT) is a main component of the application system of a smart city. Radio Frequency Identification (RFID) is one of the integration applications that work with the IoT that is widely employed in the biomedical

and healthcare industries. With the IoT, we can monitor a patient's health such and observing his severe or chronic disease [1] and tracking medical members and properties through smart application devices by using Wireless Sensor Network (WSN) nodes [2, 3] or RFID tags that are connected to the server. RFID is a system that aims to exchange identification information or data from the tag to the RFID reader through an RF transceiver antenna [4] to carry out specific applications based on the data stored in the tag [5]. Presently, RFID technology system devices have been developed to accommodate low-power devices with enhanced data transfer capabilities [6].

Figure 1 depicts the typical transceiver of the 2.4GHz RFID reader and includes some basic blocks such as an RF antenna, a receiver block, a transmitter block, a switch, and a Local Oscillator (LO). In the transceiver, the LO plays a crucial role in the architecture by providing the tuning frequencies for the transmitter and the receiver. Furthermore, in the 2.4GHz applications, a frequency synthesizer is required to produce a varying high-frequency range of the LO. PLL is commonly used in the frequency synthesizer. Based on the literature, the PLL is built either in analogue, mixed-analogue-digital, or fully digital. In the analogue PLL, the configuration typically consists of a Voltage-Controlled Oscillator (VCO), a Phase-Frequency Detector (PFD), an analogue Loop Filter (LF) [7] or a charge-pump loop filter [8], and a fractional divider at the feedback loop. Nevertheless, the trend of implementing the digital circuitry using the Very Large-Scale Integration (VLSI) is gradually increased due to the advancement of the CMOS technology process because of its advantages over the analogue counterparts [9], such as the fast acquisition of the phase and the frequency, the smaller size, and the low power

consumption. Besides, the ADPLL has a better performance of a less complex design, better jitter, high stability, and good locking-in time [10].

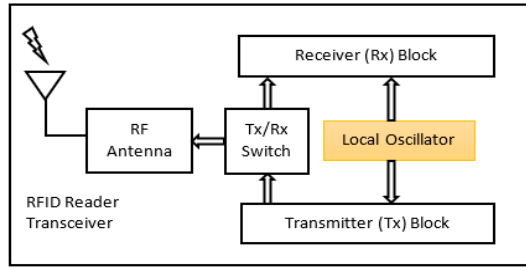


Fig. 1. RFID reader transceiver.

Currently, the advanced transceiver's requirement no longer can be met by the analogue PLL [11] because the analogue parts in the PLL are very sensitive to a wide range of design constraints as compared to the digital parts. For instance, the operating DC bias voltage shifts, the challenge of building Higher Order Filters (HOFs), the requirement for the initial and the recurring calibration for the devices, etc. [12]. On top of that, due to its low mobility process, the analogue part is typically difficult to reuse across process technologies. Nearly every analogue part needs to be modified or redesigned, and more advanced technology requirements to be implemented or imported for the sake of cost saving or performance enhancement. Furthermore, the fabrication of the analogue or mixed-analogue-digital devices is typically more expensive since the capacitors required for the analogue circuits require additional processing procedures. Thus, the transition of the analogue or mixed-analogue-digital PLL to the ADPLL gradually increases. The ADPLL is more desirable in deep submicron process technology and it is also much preferred in the RFID application system. It is because of the advancement of digital over analogue circuits in lower voltage operation and higher tolerance to the on-chip noise, where the low supply voltage and high noise immunity are very demanding [13-15]. The Process, Voltage, and Temperature (PVT) variations [16] form one crucial issue in the ADPLL design, especially in settling the time performance. However, the pre-setting and the estimating oscillator tuning word technique as introduced in [16, 17] may solve the PVT issue. Moreover, the voltage variation in the DCO can be reduced by the supply noise cancellation technique [18, 19]. This shows that the ADPLL design is robust.

Some research works on the fast-locking techniques have been reported. The authors in [17] improved the locking process in their proposed ADPLL system by improving the Oscillation Tuning Word (OTW) using the estimation and pre-set technique and the frequency search is utilizing one by one step. In [12, 13, 20] the frequency search is defined by a binary search scheme. Both techniques are reliable to be implemented in future design but in terms of the fast-locking performance, the binary search scheme is preferred. In this paper, the digital phase and frequency detector designs are presented in the first part. In the second part, the PW for the DCO operation will be investigated and discussed.

II. ADPLL ARCHITECTURE

The ADPLL architecture is constructed with a Digital Phase-Frequency Detector (DPFD), a Control Unit (CU), a DCO, and a divider at the loop feedback as can be seen in [21]. The DPFD is an important part of the ADPLL architecture which determines the difference and mismatch of the phase and frequency of two input signals, namely the frequency reference signal and the divided DCO output frequency signal. The DPFD has been redesigned and restructured by many researchers [12, 22-25] to achieve fast detection and acquisition performance in ADPLL. The Time-to-Digital Converter (TDC) is a famous design architecture for developing a DPFD. It has good measurement capabilities for the time difference between the edge of the two input signals [26] and it also performs well in terms of resolution [27]. Reviews have been conducted in [28] about the phase-frequency detector in various ADPLL design topologies. In [24], the use of a bang-bang PFD in ADPLL is quite attractive due to the better phase locking-in time, good jitter performance, and small area as compared to the use of the full-ranged TDC. In addition, the calibrating process is needed in the ADPLL design [24] to minimize the quantization noise if the TDC is used in the design. In this paper, the Phase Detector (PD) and Frequency Detector (FD) as DPFD and frequency searching by using a bisection scheme are proposed to achieve fast locking detection in ADPLL.

III. CIRCUIT IMPLEMENTATION

A. Proposed Phase Detector Design

In this part, a new design of a PFD is proposed, which combines the phase and the frequency block to accomplish fast acquisition performance, as shown in Figure 2. This is an extension work from [21], but major improvements have been made. The proposed design comprises two main parts: the PD and the FD. The output of this PFD will be converted into digital form.

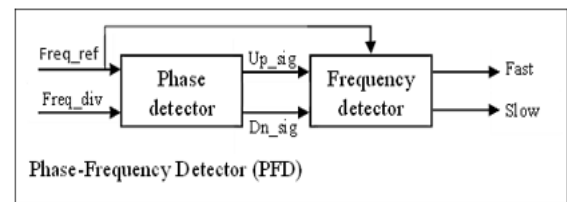


Fig. 2. The proposed DPFD design.

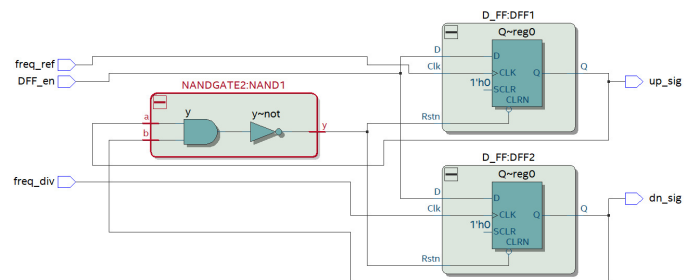


Fig. 3. Logic diagram of the PD.

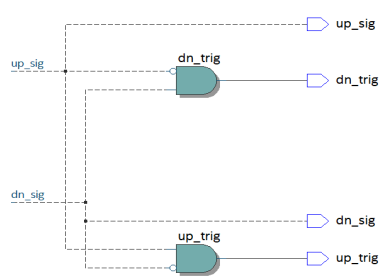


Fig. 4. The logic diagram to overcome a dead zone in PD.

The PD design in this work is adapted from [21], consisting of two D-flip-flops and a NAND gate at the feedback. This configuration design is chosen due to the dead zone problem, and it is quite a famous design in phase error detection between the reference signal clock and the divided DCO signal clock. Based on Figure 3, the PD block detects two input signals: the reference frequency clock (freq_ref) and the divided DCO frequency clock (freq_div). The PD block generates the output signals that are called up_sig and dn_sig. In the initial state, both up_sig and dn_sig pulses are zero until either the positive edge of freq_ref or freq_div is received. The output of up_sig will be triggered if the PD detects the positive edge of freq_ref is leading the freq_div. On the other hand, the production of dn_sig will be triggered if the PD detects the opposite operation. The logic diagram in Figure 4 is the extension circuit of the proposed PD design. This circuit is added to eliminate the dead zone pulses that produced from the logic diagram in Figure 3. The purpose of the added circuit is to produce a stable output for the controller block in the next work. This circuit also generates output signals namely up_trig and dn_trig.

B. Modified Frequency Detector Design

The other part of the proposed PFD block is the FD. The FD in this work is an improved design based on the previous work of [21] as illustrated in Figure 5. It receives the signal of up_trig and dn_trig from the previous PD block that synchronizes with the reference frequency clock and produces two exclusive outputs of "slow" and "fast" signals. The proposed FD is constructed utilizing the frequency comparison technique as described in [10], whereby a comparator is employed to compare two generated signals and produced two output signals. Figure 6 depicts the proposed design's flowchart for the frequency acquisition step. It is aimed to lock the DCO target frequency to the reference frequency clock by ignoring the phase recognition. As soon as the system starts, all variables are set to zero and the counters are assigned for the reference clock, the up_trig, and the dn_trig. After that, the inputs reference clock, up_trig, and dn_trig go through a counting process. At the 14th cycle of the reference clock, the signal of the "complete clock" will be activated, allowing the system to do comparisons between the up_trig and the dn_trig. In this comparison process, the system will be checking the output counter for both up_trig and dn_trig. If the system detects the counting of up_trig is more than dn_trig, the "fast" signal will be activated, while if the opposite operation is detected, the "slow" signal will be triggered.

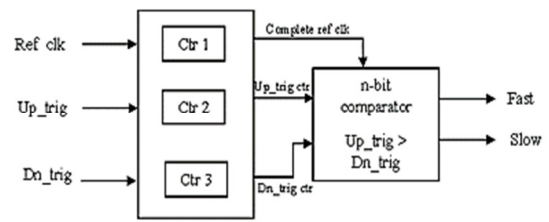


Fig. 5. The proposed FD design block diagram.

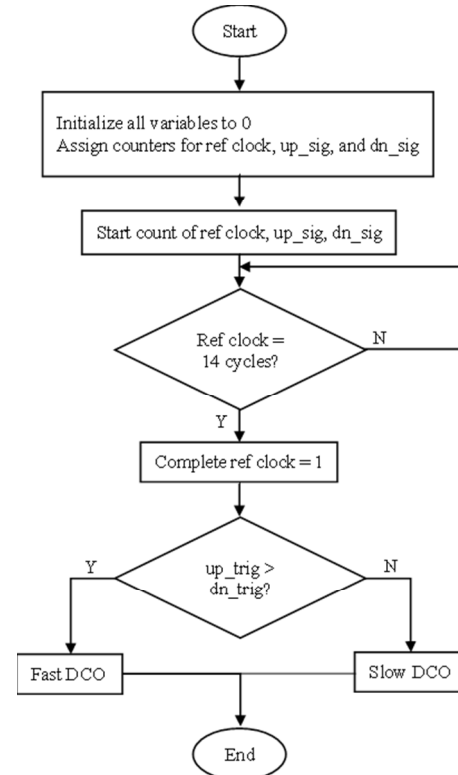


Fig. 6. FD design flowchart.

Therefore, three counters (Ctr1, Ctr2, Ctr3) are employed to count the frequency cycles of the three input signals to execute the frequency acquisition step. Ctr1 is used to track the reference frequency clock, while the other two counters (Ctr2 and Ctr3) are used to count up_trig and dn_trig pulses. Additionally, the proposed FD includes an n-bit comparator, which compares the output of the two counters from up_trig and dn_trig and as a result, generates the "fast" and "slow" signals. In further development, the DCO will be operated via two of these output signals. The definition of "fast" and "slow" correspond to the accelerating and the decelerating of the operation frequency at the DCO, respectively.

C. Control Unit

A CU is another approach to filter the bit control in the ADPLL instead of using the Digital Loop Filter (DLF). There are many considerations in designing the DLF to achieve fast locking performance, such as by considering a proper loop gain selection for the gain controller [25], a dynamic filter bandwidth adjustment [29, 30], a voltage buffer amplifier, etc. and these make the design complex and unstable. Hence, to

overcome these problems, a CU design is chosen because of the advantages of a simpler and a more stable design as compared to the DLF. A CU is a module that can change the PW of the DCO adjustment operation frequency to achieve fast locking performance. There are two methods to lock the PLL, first, the locking time approach in digital PLL, as shown in Figure 7, introduces gradual frequency changes until the target frequency is reached. This search type is a simple search scheme, but it takes a long time to lock the phase and frequency of the ADPLL. The second approach is by using a binary search scheme. It is a fast-searching algorithm, where the frequency changing process depends on certain rules or conditions and is quite popular and used in many research works. Many binary scheme approaches have been reported, but the method in [31] is more attractive for the PW value calculation because of the successful lock-in time reduction of 80-90% in the design. The design searches the target frequency by using the bisection scheme in the PW calculation. The frequency changing process is shown in Figure 8. The binary search performs faster-locking time process in ADPLL as compared to the linear frequency search.

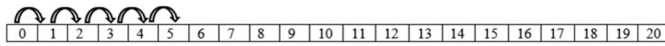


Fig. 7. Linear or sequential frequency search.

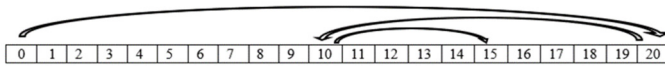


Fig. 8. Binary frequency search.

In this work, the PW calculation is adjusted using the bisection scheme which is an iteration process that determines the estimated roots from a given range of values [32]. To realize the operation of the bisection scheme, the maximum and the minimum frequency determination should be initialized. According to Figure 8, it is assumed that the frequency control has 21 words, including the word 0. If the target frequency is increased, the PW would be increased by half and vice versa. The equation of the bisection scheme can be written as follows:

When the target frequency increases:

$$f_{dco}^{n+1} = f_{min} + \frac{f_{max} - f_{min}}{2} \quad (1)$$

where $f_{min} = f_{dco}^n$.

When the target frequency decreases:

$$f_{dco}^{n+1} = f_{max} - \frac{f_{max} - f_{min}}{2} \quad (2)$$

where $f_{max} = f_{dco}^n$.

In (1)-(2), f_{dco}^{n+1} is the frequency control word for the next state, and f_{dco}^n is the frequency control word for the current state.

The increase or the decrease in target frequency is a rule condition of the system that is produced by our digital PFD. Moreover, the increase in target frequency represents the "fast" signal that is triggered in the FD, while the decrease in target

frequency represents the "slow" signal that is produced by the FD. However, to program the equation as in (1) and (2) into our ADPLL system by using the Verilog HDL code is very tricky due to the division operator. Thus, the equations are reformed as follows:

When the "fast" signal is triggered:

$$PresetWord_{n+1} = PresetWord_n + PWspan \quad (3)$$

When the "slow" signal is triggered:

$$PresetWord_{n+1} = PresetWord_n - PWspan \quad (4)$$

where $PresetWord_{n+1}$ is the frequency control word for the next state, and $PresetWord_n$ is the frequency control word for the current state.

IV. SIMULATION RESULTS AND ANALYSIS

The simulations in this paper are conducted using the Verilog HDL code and they are divided in three parts: the PD simulations, the FD simulations, and the PW calculations simulations.

A. PD Simulations

The PD simulations are conducted in two operations: A) Freq_ref is faster than Freq_div, and B) Freq_ref is slower than Freq_div. The simulation setup for A and B are set as follows:

- A: Reference frequency = 40MHz, assumed DCO divided frequency = 35.7MHz.
- B: Reference frequency = 40MHz, assumed DCO divided frequency = 43.48MHz.

Figure 9 shows the timing diagram of the PD block in this work. The circuit in Figure 4 is added to the PD block to minimize the dead zone problem to produce a stable system indicated as 1 in Figure 10. The new output signals of the PD are produced and named up_trig and dn_trig. After the circuit in Figure 5 is added to the PD design, the dead zone signal is removed from the system indicated as 2 in Figure 9.

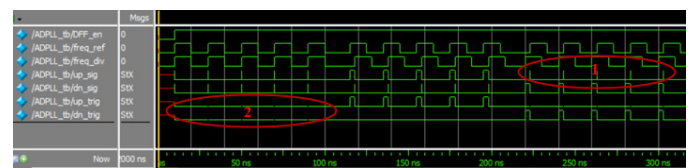


Fig. 9. Simulation result of the circuit in Figure 4 added into the PD.

Figures 10 and 11 show the simulation results for the two setups. The results show that the up_trig signal goes up when the freq_ref signal is faster than the freq_div and the dn_trig signal goes up when the freq_div is faster than the freq_ref. Both up_trig and dn_trig signals are presented as pulse signals. The pulse width (w_{pulse}) for the up_trig and dn_trig signals represent the phase differences or phase error (ϕ_{error}) between the freq_ref and the freq_div. The relationship between the pulse width for up_trig and dn_trig is directly proportional to the phase error as shown in (5), where the smaller the pulse width of up_trig and dn_trig, the smaller the phase error between the freq_ref and the freq_div.

$$w_{pulse} \propto \phi_{error} \quad (5)$$

The second stage output for both results is presented as up_trig and dn_trig. The results clearly show that the strike pulse at the first stage output has no longer appears at the second stage output. Therefore, the proposed PD in this work achieved a stable signal for the frequency detection.

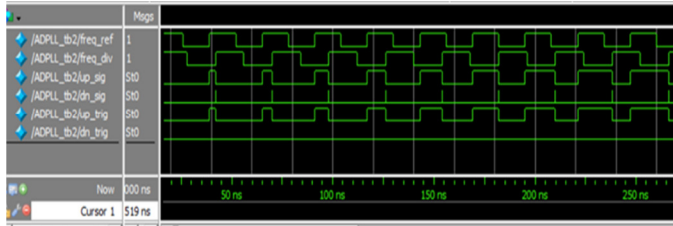


Fig. 10. The simulation result for freq_ref is faster than freq_div.

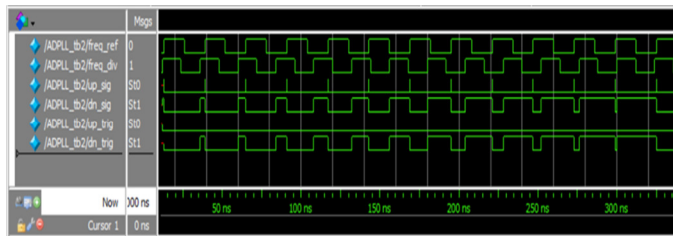


Fig. 11. The simulation result for freq_div is faster than freq_ref.

B. FD Simulations

The FD simulations are conducted in two operations. The first operation is set up for when freq_ref is faster than freq_div and the second operation is set up for when freq_div is faster than freq_ref. For this part, the FD design is integrated with the PD design by using the Verilog HDL code. The RTL view of the circuit is shown in Figure 12. The simulation frequencies setup is the same as in the previous part. Figure 13 shows the simulation result for freq_ref faster than freq_div while the simulation result in Figure 14 shows the situation when freq_ref is slower than freq_div. It should be noted that the system for this part will compare the frequency of the freq_ref and freq_div without taking into account the phase alignment but only taking into account the pulses of the output signal frequency. The output pulses will be counted and the system will compare which counter will produce the highest value. In Figure 13, the system detects that the frequency of up_trig pulses is higher than dn_trig pulses through the output counter. According to the flowchart in Figure 6, when the up_trig pulses produce the higher one, the system will send the "fast" signal to the DCO. Thus, the "fast" signal is triggered in Figure 13 after the signal of counting freq_ref is completed, while in Figure 14, the opposite operation is detected and the dn_trig count pulses are higher than the up_trig-count pulses. In this situation, the "slow" instruction will be sent to the DCO. Based on the FD simulation results, the fast detection performance is achieved because of the FD system can complete at thirteenth cycles of the freq_ref.

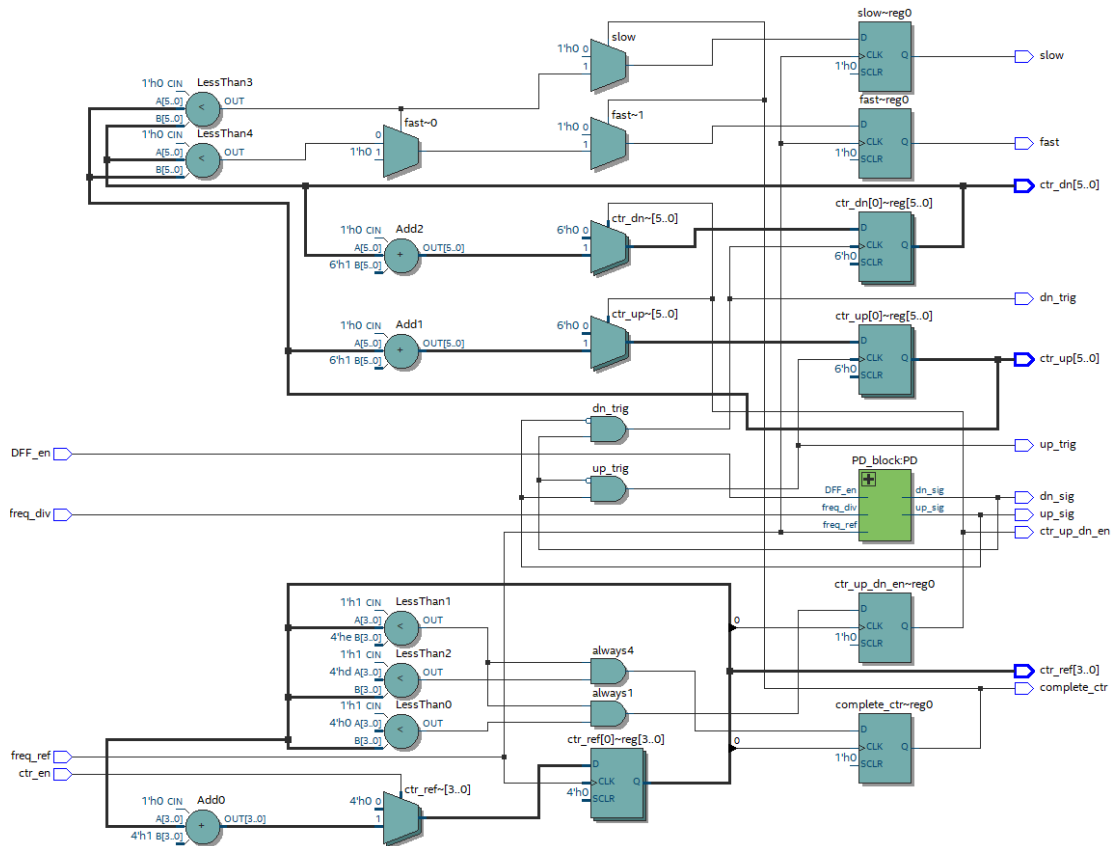


Fig. 12. The RTL view for PD and FD design architecture in Verilog HDL.

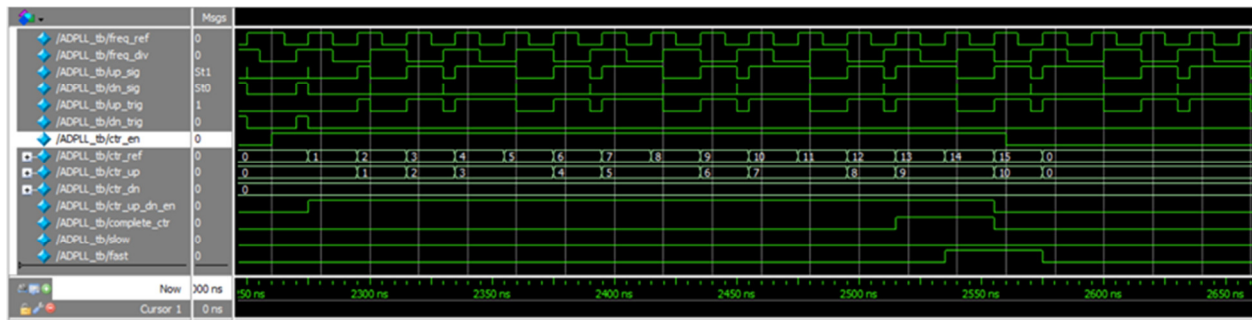


Fig. 13. The simulation result for FD design when up_trig pulses are higher than dn_trig pulses.

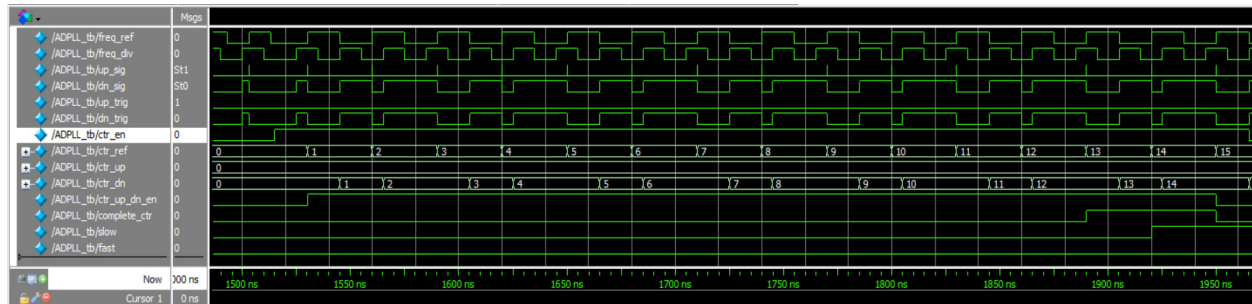


Fig. 14. The simulation result for FD design when dn_trig pulses are higher than up_trig pulses.

TABLE I. SUMMARY OF THE PW USING MANUAL CALCULATIONS FOR THE PROPOSED SYSTEM

Input									Output								
1	2	3	4	5	6	7	8	9	PW1	PW2	PW3	PW4	PW5	PW6	PW7	PW8	Final_PW
0	0	0	0	1	1	1	0	1	159	239	279	299	289	284	281	282	281
0	0	0	1	1	1	0	0	0	159	239	279	259	249	244	246	247	248
0	1	1	1	0	1	1	1	1	159	79	39	19	29	24	21	20	19

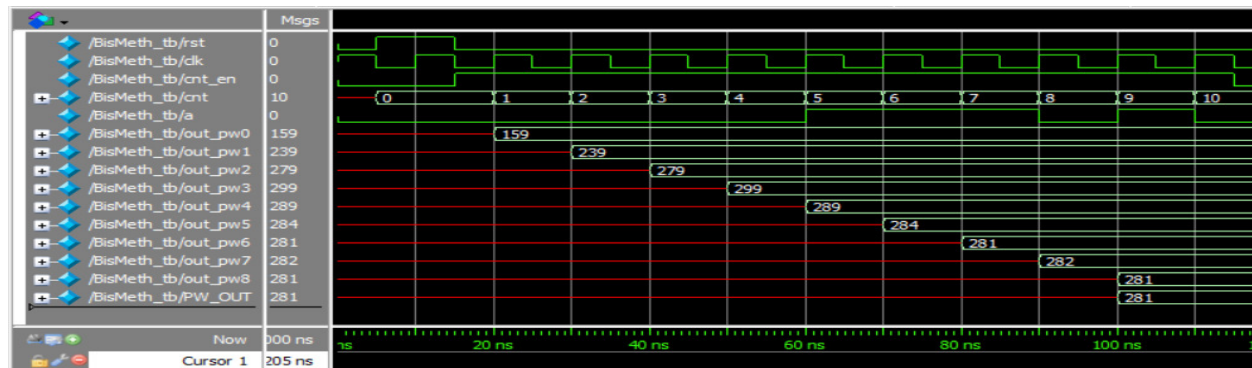


Fig. 15. System testing for input 000 011 101.

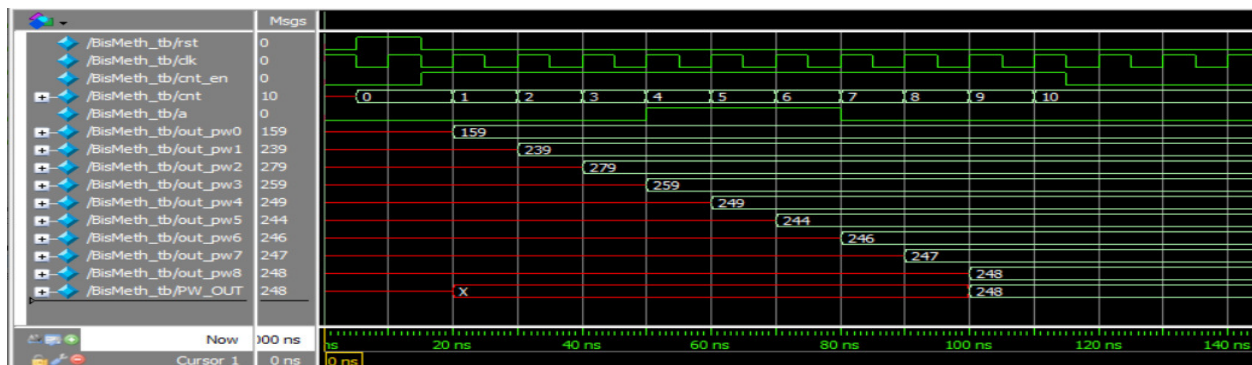


Fig. 16. System testing for input 000 111 000.

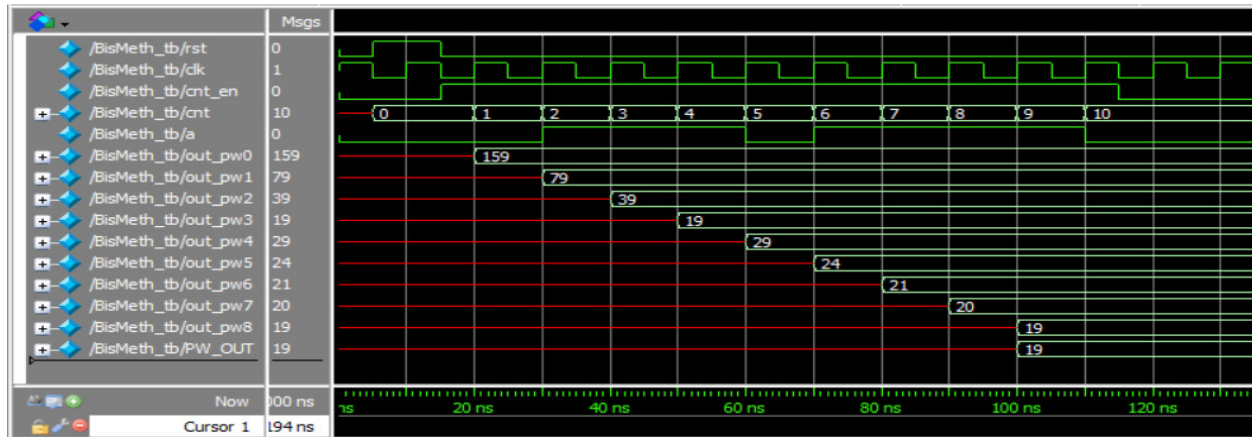


Fig. 17. System testing for input 011 101 111.

C. Simulations of the PW Calculations

In this work, the module of PW calculations is presented using the Verilog HDL coding. The system receives the signal from the PFD block, which is a "slow" or "fast" signal. Nevertheless, in the testing platform, the "slow" and "fast" signals are represented as a binary form of 0 and 1 respectively. The manual calculation of the PW for the proposed system is presented in Table I. Only 3 tests are shown in this section to prove that the proposed system produces the same output as the theoretical values. Nine detections of input are developed in the system. When the system detects the binary 0, the PW is increased and when the binary 1 is detected, the PW is decreased. There are also 9 PW outputs presented and the 9th detection is the last detection, which produced the final PW for the DCO operation. Figures 15 - 17 show the simulation results for the testing input of 000 011 101, 000 111 000, and 011 101 111 respectively. Based on the PW shown at the bottom list for each Figure, the values are matched with the manual calculation as in Table I. Thus, the proposed design shows that the PW searching is achieved very fast and only takes 9 cycles to calculate the desired value. Based on the proposed design, the good results of the PD and the FD simulation and the PW searching are presented. In this work, the dead zone problem is considered in order to achieve the phase acquisition step and system stability.

The dead zone occurs when the PFD is unable to distinguish the phase mismatch of the positive or the negative edges of the two input signals and it may lock to the incorrect phase [33]. The incorrect phase-locked may degrade the phase noise performance. Thus, to achieve better phase acquisition performance, the proposed PD design architecture has successfully removed the dead zone pulses as presented in [34]. Furthermore, the proposed FD design has adopted the frequency acquisition step technique to achieve locking mechanism and system accuracy. Our proposed FD is able to count and compare the frequency pulses of each signal directly. Our design improved the PFD block of the work of [31] where their ADPLL did not consider the frequency acquisition step.

Next, the PW frequency searching in the proposed work is to achieve the target frequency and it is based on the binary search algorithm and the changing frequency step of the

proposed PW is using a bisection scheme calculation. In our PW design, the large frequency step takes place in the early PW calculation, and it saves a lot of time to reach the target frequency which takes only 9 steps for 320 frequency control codes. Our frequency searching is simpler as compared to using the oscillator tuning word (OTW) algorithm in [16, 35].

V. CONCLUSION

A digital PFD for the RFID-ADPLL architecture is proposed and designed in this paper with the Verilog HDL system. The design of the PFD is divided into two main parts, which are the phase-detection and frequency-detection to achieve the phase acquisition and the frequency acquisition respectively. The proposed PD module consists of two components of D-flip-flop and a NAND gate at the reset feedback. The outputs of the up_trig and dn_trig signals are well-produced by eliminating the dead zone signal and presented a stable output for the FD module. In addition, the FD module is designed by comparing the counting value of the up_trig and the dn_trig signals. As a result, the "fast" and "slow" signals are produced at the thirteenth cycle of freq_ref and represent the increase and decrease of the operation of the future DCO respectively. Moreover, to search the target frequency for the DCO, a binary search scheme is used to calculate the PW for controlling the DCO operation in the future. The manual calculation of the PW has also been tabulated for the theoretical comparison. The comparison shows that the PW calculation in simulations is matched with the theoretical values and finished the calculation at the ninth cycle detection of freq_ref. Based on the results of the DPFD and the PW searching, fast detection performance is achieved in this work. In future research work, the control code output generated from the proposed digital PFD and the PW searching will be connected to the DCO block

ACKNOWLEDGMENT

This work is funded by the Malaysian Ministry of Education under the grant FRGS/1/2018/TK04/UKM/02/1.

REFERENCES

- [1] G. Maniam, J. Sampe, R. Jaafar, and M. Ibrahim, "Smart Monitoring System for Chronic Kidney Disease Patients based on Fuzzy Logic and IoT," *International Journal of Advanced Computer Science and*

- Applications, vol. 13, no. 2, pp. 324–333, Jan. 2022, <https://doi.org/10.14569/IJACSA.2022.0130238>.
- [2] N. H. Mohd Yunus, J. Sampe, J. Yunas, A. Pawi, and Z. A. Rhazali, "MEMS based antenna of energy harvester for wireless sensor node," *Microsystem Technologies*, vol. 26, no. 9, pp. 2785–2792, Sep. 2020, <https://doi.org/10.1007/s00542-020-04842-5>.
 - [3] N. H. Mohd Yunus, J. Yunas, A. Pawi, Z. A. Rhazali, and J. Sampe, "Investigation of Micromachined Antenna Substrates Operating at 5 GHz for RF Energy Harvesting Applications," *Micromachines*, vol. 10, no. 2, Feb. 2019, Art. no. 146, <https://doi.org/10.3390/mi10020146>.
 - [4] K. Mekki, O. Necibi, C. Boussetta, and A. Gharsallah, "Miniaturization of Circularly Polarized Patch Antenna for RFID Reader Applications," *Engineering, Technology & Applied Science Research*, vol. 10, no. 3, pp. 5655–5659, Jun. 2020, <https://doi.org/10.48084/etasr.3445>.
 - [5] T. N. T. Mohamad, J. Sampe, and D. D. Berhanuddin, "Architecture of Micro Energy Harvesting Using Hybrid Input of RF, Thermal and Vibration for Semi-Active RFID Tag," *Engineering Journal*, vol. 21, no. 2, pp. 183–197, Mar. 2017, <https://doi.org/10.4186/ej.2017.21.2.183>.
 - [6] C. Bredendiek et al., "A 61-GHz SiGe Transceiver Frontend for Energy and Data Transmission of Passive RFID Single-Chip Tags With Integrated Antennas," *IEEE Journal of Solid-State Circuits*, vol. 53, no. 9, pp. 2441–2453, Sep. 2018, <https://doi.org/10.1109/JSSC.2018.2843348>.
 - [7] M. Faseehuddin, M. A. Albrni, J. Sampe, and S. H. M. Ali, "Novel VDBA based universal filter topologies with minimum passive components," *Journal of Engineering Research*, vol. 9, no. 3B, pp. 110–130, Sep. 2021, <https://doi.org/10.36909/jer.v9i3B.8781>.
 - [8] E. Ali, D. Narwani, A. M. Bughio, N. Nizamani, S. H. Siyal, and A. R. Khatri, "Analyzing the Impact of Loop Parameter Variations on the Transient Response of Second Order Voltage-Switched CP-PLL," *Engineering, Technology & Applied Science Research*, vol. 11, no. 1, pp. 6687–6690, Feb. 2021, <https://doi.org/10.48084/etasr.3969>.
 - [9] J. Sampe, M. Faseehuddin, and S. H. M. Ali, "Design of ultra-low voltage CCII utilizing level shifting technique and a dual mode multifunction universal filter as an application," *Journal of Engineering Research*, vol. 6, no. 2, pp. 155–175, Sep. 2018.
 - [10] J. Dunning, G. Garcia, J. Lundberg, and E. Nuckolls, "An all-digital phase-locked loop with 50-cycle lock time suitable for high-performance microprocessors," *IEEE Journal of Solid-State Circuits*, vol. 30, no. 4, pp. 412–422, Apr. 1995, <https://doi.org/10.1109/4.375961>.
 - [11] J. Bae, S. Radhapuram, I. Jo, T. Kihara, and T. Matsuoka, "A low-voltage design of controller-based ADPLL for implantable biomedical devices," in *IEEE Biomedical Circuits and Systems Conference*, Atlanta, GA, USA, Oct. 2015, pp. 1–4, <https://doi.org/10.1109/BioCAS.2015.7348405>.
 - [12] M.-L. Lin, S.-C. Huang, and J.-C. Liu, "Digital-only PLL with adaptive search step," *International Journal of Electronics*, vol. 101, no. 6, pp. 865–876, Jun. 2014, <https://doi.org/10.1080/00207217.2014.896036>.
 - [13] H.-J. Hsu and S.-Y. Huang, "A Low-Jitter ADPLL via a Suppressive Digital Filter and an Interpolation-Based Locking Scheme," *IEEE Transactions on Very Large Scale Integration (VLSI) Systems*, vol. 19, no. 1, pp. 165–170, Jan. 2011, <https://doi.org/10.1109/TVLSI.2009.2030410>.
 - [14] M. Kumm, H. Klingbeil, and P. Zipf, "An FPGA-Based Linear All-Digital Phase-Locked Loop," *IEEE Transactions on Circuits and Systems I: Regular Papers*, vol. 57, no. 9, pp. 2487–2497, Sep. 2010, <https://doi.org/10.1109/TCSL.2010.2046237>.
 - [15] W. Liu, W. (R.) Li, P. Ren, C. L. Lin, S. Zhang, and Y. Wang, "An 11-bit and 39 ps resolution time-to-digital converter for ADPLL in digital television," *International Journal of Electronics*, vol. 97, no. 4, pp. 381–388, Apr. 2010, <https://doi.org/10.1080/00207210903325237>.
 - [16] K. Okuno, S. Izumi, K. Masaki, H. Kawaguchi, and M. Yoshimoto, "A Fast Settling All Digital PLL Using Temperature Compensated Oscillator Tuning Word Estimation Algorithm," *IEICE Transactions on Fundamentals of Electronics, Communications and Computer Sciences*, vol. E98.A, no. 12, pp. 2592–2599, 2015, <https://doi.org/10.1587/transfun.E98.A.2592>.
 - [17] G. Yu, Y. Wang, H. Yang, and H. Wang, "Fast-locking all-digital phase-locked loop with digitally controlled oscillator tuning word estimating and presetting," *IET Circuits, Devices & Systems*, vol. 4, no. 3, pp. 207–217, May 2010, <https://doi.org/10.1049/iet-cds.2009.0173>.
 - [18] A. Elshazly, R. Inti, W. Yin, B. Young, and P. K. Hanumolu, "A 0.4-to-3GHz digital PLL with supply-noise cancellation using deterministic background calibration," in *IEEE International Solid-State Circuits Conference*, San Francisco, CA, USA, Feb. 2011, pp. 92–94, <https://doi.org/10.1109/ISSCC.2011.5746233>.
 - [19] J. Liu et al., "15.2 A 0.012mm² 3.1mW bang-bang digital fractional-N PLL with a power-supply-noise cancellation technique and a walking-one-phase-selection fractional frequency divider," in *IEEE International Solid-State Circuits Conference Digest of Technical Papers*, San Francisco, CA, USA, Feb. 2014, pp. 268–269, <https://doi.org/10.1109/ISSCC.2014.6757429>.
 - [20] C.-C. Chung and C.-Y. Ko, "A Fast Phase Tracking ADPLL for Video Pixel Clock Generation in 65 nm CMOS Technology," *IEEE Journal of Solid-State Circuits*, vol. 46, no. 10, pp. 2300–2311, Jul. 2011, <https://doi.org/10.1109/JSSC.2011.2160789>.
 - [21] S. N. Ishak, J. Sampe, F. H. Hashim, and M. Faseehuddin, "Digital Phase-Frequency Detector in All-Digital PLL-based Local Oscillator for Radio Frequency Identification System Transceiver," in *18th International Colloquium on Signal Processing & Applications*, Selangor, Malaysia, Dec. 2022, pp. 231–236, <https://doi.org/10.1109/CSPA55076.2022.9781829>.
 - [22] I.-C. Hwang, S.-H. Song, and S.-W. Kim, "A digitally controlled phase-locked loop with a digital phase-frequency detector for fast acquisition," *IEEE Journal of Solid-State Circuits*, vol. 36, no. 10, pp. 1574–1581, Jul. 2001, <https://doi.org/10.1109/4.953487>.
 - [23] C.-C. Chung, W.-S. Su, and C.-K. Lo, "A 0.52/1 V Fast Lock-in ADPLL for Supporting Dynamic Voltage and Frequency Scaling," *IEEE Transactions on Very Large Scale Integration (VLSI) Systems*, vol. 24, no. 1, pp. 408–412, Jan. 2016, <https://doi.org/10.1109/TVLSI.2015.2407370>.
 - [24] J. K. Sahani, A. Singh, and A. Agarwal, "A fast locking and low jitter hybrid ADPLL architecture with bang bang PFD and PVT calibrated flash TDC," *AEU - International Journal of Electronics and Communications*, vol. 124, Sep. 2020, Art. no. 153344, <https://doi.org/10.1016/j.aue.2020.153344>.
 - [25] W.-B. Yang, H.-H. Wang, H.-I. Chang, and Y.-L. Lo, "A fast-locking all-digital PLL with dynamic loop gain control and phase self-alignment mechanism for sub-GHz IoT applications," *Japanese Journal of Applied Physics*, vol. 59, no. SG, Nov. 2020, Art. no. SGG08, <https://doi.org/10.35848/1347-4065/ab7276>.
 - [26] B. Zhao and D. L. Yan, "A low-power digital design of all digital PLL for 2.4G wireless communication applications," in *International Symposium on Integrated Circuits*, Singapore, Singapore, Dec. 2016, pp. 1–4, <https://doi.org/10.1109/ISICIR.2016.7829674>.
 - [27] L. Ferreira, M. Moreira, B. Souza, S. Ferreira, F. Baumgratz, and S. Bampi, "Review on the Evolution of Low-power and Highly-linear Time-to-Digital Converters - TDC," in *11th Latin American Symposium on Circuits & Systems*, San Jose, Costa Rica, Feb. 2020, pp. 1–4, <https://doi.org/10.1109/LASCAS45839.2020.9068950>.
 - [28] S. N. Ishak, J. Sampe, Z. Yusoff, and M. Faseehuddin, "All-Digital Phase Locked Loop (ADPLL) Topologies For RFID System Application: A Review," *Jurnal Teknologi (Sciences and Engineering)*, vol. 84, no. 1, pp. 219–230, 2021, <https://doi.org/10.11113/jurnalteknologi.v84.17123>.
 - [29] J.-M. Lin and C.-Y. Yang, "A Fast-Locking All-Digital Phase-Locked Loop With Dynamic Loop Bandwidth Adjustment," *IEEE Transactions on Circuits and Systems I: Regular Papers*, vol. 62, no. 10, pp. 2411–2422, Jul. 2015, <https://doi.org/10.1109/TCSL.2015.2477575>.
 - [30] H. E. Taheri, "A 4-4.8GHz Adaptive Bandwidth, Adaptive Jitter Phase Locked Loop," *Engineering, Technology & Applied Science Research*, vol. 7, no. 2, pp. 1473–1477, Apr. 2017, <https://doi.org/10.48084/etasr.1099>.
 - [31] X. Deng, H. Li, and M. Zhu, "A Novel Fast-Locking ADPLL Based on Bisection Method," *Electronics*, vol. 10, no. 12, Jan. 2021, Art. no. 1382, <https://doi.org/10.3390/electronics10121382>.

- [32] A. Ersöz and M. Kurban, "Bisection Method and Algorithm for Solving the Electrical Circuits," presented at the 2nd International Eurasian Conference on Mathematical Sciences and Applications, Sarajevo, Bosnia-Herzegovina, Aug. 2013.
- [33] T. Azadmousavi, M. Azadbakht, E. Najafi Aghdam, and J. Frounchi, "A novel zero dead zone PFD and efficient CP for PLL applications," *Analog Integrated Circuits and Signal Processing*, vol. 95, no. 1, pp. 83–91, Apr. 2018, <https://doi.org/10.1007/s10470-018-1118-4>.
- [34] P. Muppala, S. Ren, and G. Y.-H. Lee, "esign of high-frequency wide-range all digital phase locked loop in 90 nm CMOS," *Analog Integrated Circuits and Signal Processing*, vol. 75, no. 1, pp. 133–145, Apr. 2013, <https://doi.org/10.1007/s10470-013-0043-9>.
- [35] G. Yu, Y. Wang, H. Yang, and H. Wang, "A fast-locking all-digital phase-locked loop with a novel counter-based mode switching controller," in *IEEE Region 10 Conference*, Singapore, Singapore, Jan. 2009, pp. 1–5, <https://doi.org/10.1109/TENCON.2009.5396168>.

Settling Time Optimization of a Critically Damped System with Input Shaping for Vibration Suppression Control

Minh-Duc Duong

School of Electrical and Electronic Engineering
Hanoi University of Science and Technology
Hanoi, Vietnam
duc.duongminh@hust.edu.vn

Quy-Thinh Dao

School of Electrical and Electronic Engineering
Hanoi University of Science and Technology
Hanoi, Vietnam
thinh.daoquy@hust.edu.vn

Trong-Hieu Do

School of Electrical and Electronic Engineering
Hanoi University of Science and Technology
Hanoi, Vietnam
hieu.dotrong@hust.edu.vn

Received: 5 August 2022 | Revised: 23 August 2022 | Accepted: 24 August 2022

Abstract—The input shaping technique is widely used as feedforward control for vibration suppression of flexible dynamic systems. The main disadvantage of the input shaping technique is the increasing system time response since the input shaper contains time delay parts. However, with the same reference input, the actuator effort in the case of using an input shaper is smaller than the one in the case without an input shaper. Thus, it is possible to decrease the system response time by designing the feedback controller to maximize the actuator effort. This paper proposes a design approach to design the Proportional-Derivative (PD) controller for position control of the actuator so that the settling time of the flexible system with input shaper is minimized. The actuator system with a PD controller is equivalent to a critically damped system, and the condition for the controller gains is established. In addition, the settling time and actuator effort with shaped step input are calculated. The controller gains can be determined by solving the settling time optimization problem with the actuator effort constraint. The effectiveness of the proposed approach is verified via experiments with an overhead crane model.

Keywords—flexible system; input shaping; PD controller; settling time optimization; overhead crane

I. INTRODUCTION

The vibration of flexible dynamic systems such as live load and flexible beam systems [1-3] and flexible robot manipulator and cranes [4-12] often causes a decrease in operation speed and accuracy. Due to sensor noise and unmodeled flexible dynamic problems, vibration suppression control using feedback control has often substantial limitations [4-7]. Open-loop control is effective and widely used for the vibration suppression control of flexible machines. If the vibration dynamics are known with some confidence, then several

techniques for modifying commands can suppress the system's vibration [8-13]. Among them, input shaping [13], which convolves a sequence of impulses with the command signal, is one of the most attractive techniques. Various improvements and applications of input shaping have been reported [14, 15]. The input shaping technique has also been used along with feedback control to optimize the system performance [16-24]. In [16-18], the concurrent design of the Proportional-Derivative (PD) controller and input shaping was considered. The PD controller parameters were chosen to fasten the feedback system response, and the input shaping was designed to eliminate the natural vibration frequency of the PD feedback control system. The same idea was deployed in [19] for the combination of input shaping technique and a Linear Quadratic Regulator (LQR) feedback control system. These works only considered the single mode vibration. The design technique was proposed for a feedback control system with multi-mode vibration in [20-21]. The vibration model uncertainty was also considered when combining input shaping and feedback controller [22-24].

The above mentioned studies used input shaping that eliminates the vibration of the feedback system to optimize the system performance, not to suppress the vibration of a flexible system. In general, the vibration suppression control of a flexible dynamic system includes a feedback control part for actuator position control and a feed-forward control part for vibration control, as shown in Figure 1. When using an Input Shaper (IS) as feed-forward control, the IS only depends on the vibration model, not the feedback system. The feedback control is usually designed independently with the feed-forward controller. This design method is simple but does not optimize the system performance.

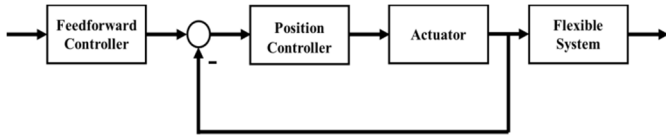


Fig. 1. Feed-forward control structure for vibration suppression control.

Since the IS includes time delay parts that slow down the system, various efforts have been made to shorten the delay, see [14] for more details. However, most of them have not considered combining a feedback controller to reduce the system response. In this paper, a design technique to optimize the time performance of the system with the IS is proposed. At first, the IS is designed using the vibration's parameters. Next, the PD controller is chosen to minimize settling time while keeping the actuator effort within the acceptable range. For this purpose, design techniques such as the one in [16] can be applied. However, that technique can only be applied to an under-damped feedback system. In many applications, the under-damped system is not expected since the existence of overshoot may cause limit excess. Thus, in this paper, we consider a design technique for a critically damped system. The PD feedback controller is designed to optimize the settling time, in consideration that the IS has been added to shape the input. The actuator effort is used as a design constraint. The settling time and actuator effort calculation are established such that the optimization problem can be easily solved by an optimization toolbox.

II. INPUT SHAPING METHOD

Input preshaping [13] is a feed-forward control technique for vibration suppression. The idea of input preshaping method is to cancel the vibration of an impulse input by generating another impulse that causes the inverse phase vibration with the first one. Let's consider a simple vibratory system that can be expressed as second order system as following:

$$G_s = \frac{Y(s)}{V(s)} = \frac{\omega_0^2}{s^2 + 2\omega_0\xi_0 s + \omega_0^2} \quad (1)$$

where ω_0 is the undamped natural frequency, ξ_0 is the damping ratio of the system, $Y(s)$ and $V(s)$ are the Laplace transforms of output $y(t)$ and input $v(t)$ respectively. If an impulse input with amplitude A_i is put into the system at time t_i , then the output response $y(t)$ is calculated as:

$$y(t) = B_i \cdot \sin(\alpha \cdot t + \phi_i) \quad (2)$$

where $B_i = A_i \cdot \frac{\omega_0}{\sqrt{1-\xi_0^2}} e^{-\xi_0\omega_0(t-t_i)}$, $\alpha = \omega_0\sqrt{1-\xi_0^2}$, and

$$\phi_i = \omega_0\sqrt{1-\xi_0^2}t_i.$$

In order to suppress the vibration caused by the impulse, we consider applying a second impulse to the system. Then the response of two impulses is calculated as:

$$y = B_1 \cdot \sin(\alpha \cdot t + \phi_1) + B_2 \cdot \sin(\alpha \cdot t + \phi_2) \quad (3)$$

Using the trigonometric relation, we can obtain:

$$y = B \cdot \sin(\alpha \cdot t + \phi_{th}) \quad (4)$$

where:

$$\begin{cases} B = \sqrt{(B_1 \sin \phi_1 + B_2 \sin \phi_2)^2 + (B_1 \cos \phi_1 + B_2 \cos \phi_2)^2} \\ \phi_{th} = \tan^{-1} \left(\frac{B_1 \sin \phi_1 + B_2 \sin \phi_2}{B_1 \cos \phi_1 + B_2 \cos \phi_2} \right) \end{cases}$$

By setting the response of two impulses equal to zero after applying the last impulse, we can easily obtain (supposing that the time of applying the first impulse is $t_1 = 0$ and the impulse amplitude are normalized $A_1 + A_2 = 1$):

$$\begin{bmatrix} A_i \\ t_i \end{bmatrix} = \begin{bmatrix} \frac{1}{1+K} & \frac{K}{1+K} \\ 0 & \Delta t \end{bmatrix} \quad (5)$$

$$\text{where } \begin{cases} K = \frac{-\pi D}{e^{\sqrt{1-D^2}}} \\ \Delta t = \frac{\pi}{\omega_0 \sqrt{1-D^2}} \end{cases}.$$

The two-impulse shaper is called the Zero Vibration (ZV) shaper. In general, if we apply N impulses with amplitude A_i and at time t_i ($i = 1, \dots, N$), then the response of N impulses is calculated as:

$$y = \sum_{i=1}^N y_i(t) = \sum_{i=1}^N B_i \cdot \sin(\alpha \cdot t + \phi_i) \quad (6)$$

$$\text{where } \begin{cases} B = \sqrt{(\sum_{i=1}^N B_i \sin \phi_i)^2 + (\sum_{i=1}^N B_i \cos \phi_i)^2} \\ \phi_{th} = \tan^{-1} \left(\frac{\sum_{i=1}^N B_i \sin \phi_i}{\sum_{i=1}^N B_i \cos \phi_i} \right) \end{cases}$$

By setting the amplitude and its derivative equal to zero after applying the last impulse, we can obtain the result for 3 impulses ($N=3$) as follows:

$$\begin{bmatrix} A_i \\ t_i \end{bmatrix} = \begin{bmatrix} \frac{1}{(1+K)^2} & \frac{2K}{(1+K)^2} & \frac{K^2}{(1+K)^2} \\ 0 & \Delta t & 2\Delta t \end{bmatrix} \quad (7)$$

The three-impulse shaper or Zero Vibration Derivative (ZVD) shaper is more robust than the ZV shaper. More results can be seen in [14, 15]. By convolving the reference input and the above impulse series, the vibration can be suppressed. This paper will apply vibration suppression control using input preshaping with two and three impulses. It is noted that the response of the system with input preshaping is slower than that without input preshaping. The delay time is Δt with ZV and $2\Delta t$ with ZVD input preshaping.

III. CONTROLLER DESIGN

In a flexible system, the actuator, such as an electrical motor, is controlled by a motor driver under velocity control mode. The actuator then can be modeled as follows:

$$\frac{X(s)}{U(s)} = G_p(s) = \frac{K_c}{(T_c s + 1)s} \quad (8)$$

where K_c is the gain and T_c is time constant of the system, $U(s)$ and $X(s)$ are the Laplace transforms of control voltage input $u(t)$ and actuator position $x(t)$ respectively.

The system structure is shown in Figure 2, where $G_{PD}(s)$ is the transfer function of the feedback controller, $G_p(s)$ is the transfer function of the plant (actuator and driver). The IS includes N impulses designed based on the flexible system's vibration frequency and damping. We consider the system step

input to design the PD controller for position control. System response and settling time are calculated. In addition, the actuator effort is also determined. Then the settling time optimization with actuator effort constraint can be established, and the selection of PD controller parameters can be made by solving this optimization problem.

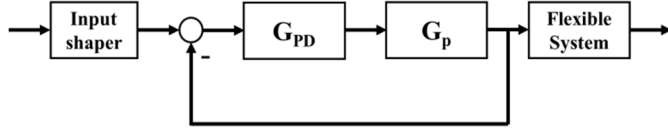


Fig. 2. Input shaper – PD feedback control structure.

A. System Output Response

The PD controller can be described by the following transfer function:

$$G_{PD}(s) = K_D s + K_P \quad (9)$$

where $K_P \geq 0$ is the proportional gain and $K_D \geq 0$ is the derivative gain. Then, the transfer function of the closed-loop system is:

$$G_{CL} = \frac{G_p G_{PD}}{G_p G_{PD} + 1} = \frac{\frac{K_c K_D}{T_c} s + \frac{K_c K_P}{T_c}}{s^2 + \frac{K_c K_P + 1}{T_c} s + \frac{K_c K_P}{T_c}} \quad (10)$$

By setting: $\frac{K_c K_D}{T_c} = M$ and $\frac{K_c K_P}{T_c} = N$ we have:

$$G_{CL} = \frac{Ms + N}{s^2 + \frac{MT_c + 1}{T_c} s + N} = \frac{X(s)}{R(s)} \quad (11)$$

Because the underdamped system is not expected, the denominator of $G_{CL}(s)$ must have negative real roots. In addition, we require minimum response time. Thus, the denominator should have double negative roots. The condition for being double root is:

$$\left(\frac{MT_c + 1}{2T_c}\right)^2 = N \Leftrightarrow \left(\frac{K_c K_D + 1}{2T_c}\right)^2 = \frac{K_c K_P}{T_c} \quad (12)$$

Now, we introduce an input step with magnitude L into the system at time t_0 , $R(s) = \frac{Le^{-t_0 s}}{s}$, the response of the feedback system is:

$$X(s) = \frac{Le^{-t_0 s}}{s} \frac{Ms + N}{s^2 + \frac{MT_c + 1}{T_c} s + N} \quad (13)$$

Thus, the response of the system with single step input can be expressed as:

$$x(t) = \frac{LM}{a^2} \left[\alpha - \alpha e^{-a(t-t_0)} + a(a-\alpha)(t-t_0)e^{-a(t-t_0)} \right] \quad (14)$$

where $a = \frac{M \cdot T_c + 1}{2T_c}$ and $\alpha = \frac{N}{M}$.

Since the overshoot is not expected to appear, $x(t)$ must be a non-decreasing or non-increasing function in the region $t \geq t_0$. Thus, the root t_r of equation $\dot{x}(t) = 0$ must be outside the region $t \geq t_0$, or $t_r < t_0$. Solving the equation $\dot{x}(t) = 0$ we obtain $t_r = t_0 + \frac{a}{a-\alpha}$. Thus:

$$t_r < t_0 \Leftrightarrow \frac{a}{a-\alpha} < 0 \Leftrightarrow a < \alpha \Leftrightarrow \frac{K_D^2}{T_c} < K_P \quad (15)$$

From the system response with single step input (14), the response of the system with convolved step command after step k is:

$$y(t) = \frac{LM}{a^2} \left[\alpha \sum_{j=1}^k L_i - \alpha \sum_{j=1}^k L_i e^{-a(t-t_j)} + a(a-\alpha) \sum_{j=1}^k L_i (t-t_j) e^{-a(t-t_j)} \right] \quad (16)$$

Since $\frac{M}{a^2} \alpha = 1$, the response $y(t)$ can be rewritten as:

$$y(t) = L \sum_{j=1}^k L_j - L \sum_{j=1}^k L_j e^{-a(t-t_j)} + L(M-a) \sum_{j=1}^k L_j (t-t_j) e^{-a(t-t_j)} \quad (17)$$

B. Settling Time

Settling time is a primary concern for most industrial applications. The faster the settling time, the higher throughput and accuracy are. The system is defined to be settled when the output response falls below a certain percentage (usually 5% or 2%) of the step magnitude. The settling time is the required time for the output curve to reach and stay within a range of a certain percentage (usually 5% or 2%) of the final value. In this paper, we use the range of 5% to calculate settling time. We can describe the definition of settling time t_s as the following conditions:

$$1 - \frac{y(t)}{L} \leq 0.05, \forall t \geq t_s \quad (18)$$

$$1 - \frac{y(t_s)}{L} = 0.05 \quad (19)$$

It is obvious that settling time is determined after the final step. Thus, the output $y(t)$ to calculate settling time is the output with N steps. Since $\sum_{j=1}^N L_i = 1$, and substituting (17) into (19), we have:

$$1 - \frac{y(t_s)}{L} = \sum_{j=1}^N L_j e^{-a(t_s-t_j)} - (M-a) \sum_{j=1}^N L_j (t_s-t_j) e^{-a(t_s-t_j)} = 0.05 \quad (20a)$$

Moreover, since $t_s > t_n$, it can make the approximation $e^{-a(t_s-t_j)} \cong 0$ and $(t_s-t_j)e^{-a(t_s-t_j)} \cong 0$ with $j < N$. Then (20a) becomes:

$$L_n [e^{-a(t_s-t_n)} - (M-a)(t_s-t_n)e^{-a(t_s-t_n)}] = 0.05 \quad (20b)$$

Using the Lambert W function $W(z)$ (i.e. $z = W(z)e^{W(z)}$) [25], the settling time t_s can be determined as:

$$t_s = t_n + \frac{1}{M-a} - \frac{1}{a} W\left(\frac{0.05a e^{\frac{M-a}{a}}}{a(M-a)}\right) \quad (21)$$

C. Actuator Effort

With reference input as step input, we are also interested in the actuator effort when designing the controller. According to Figure 2, with the input $R(s)$, the actuator effort can be determined as:

$$U(s) = \frac{G_{PD}}{G_{PD} \cdot G_p + 1} \cdot R(s) = \frac{s(T_c s + 1)(K_c K_D s + K_c K_P)}{T_c s^2 + (K_c K_D + 1)s + K_c K_P} \cdot R(s) \quad (22)$$

If the input $r(t)$ is the step input with magnitude L at the time t_0 , $R(s) = \frac{Le^{-t_0s}}{s}$, then:

$$U(s) = Le^{-t_0s} \frac{(T_c s + 1)(K_c K_D s + K_c K_P)}{T_c s^2 + (K_c K_D + 1)s + K_c K_P} \quad (23)$$

The actuator effort can be calculated as:

$$u(t) = L \frac{K_P T_c - K_c K_D^2}{T_c} [e^{-a(t-t_0)} + (\alpha_1 - a)(t - t_0)e^{-a(t-t_0)}] \quad (24)$$

where $\alpha_1 = \frac{K_P - K_c K_P K_D}{T_c K_P - K_c K_D^2}$. Then, the actuator effort with convolved step command after step k is:

$$u(t) = \frac{K_P T_c - K_c K_D^2}{T_c} \times \sum_{j=1}^k L_j [e^{-a(t-t_j)} + (\alpha_1 - a)(t - t_j)e^{-a(t-t_j)}] \quad (25)$$

The actuator effort $u(t)$ can be represented as the form:

$$u(t) = P_k e^{-at} + Q_k t e^{-at} \quad (26)$$

where:

$$P_k = \frac{K_P T_c - K_c K_D^2}{T_c} \sum_{j=1}^k L_j [1 - (\alpha_1 - a)t_j] e^{at_j}$$

$$Q_k = \frac{K_P T_c - K_c K_D^2}{T_c} \sum_{j=1}^k L_j (\alpha_1 - a) e^{at_j}$$

To find the maximum value of $u(t)$, we solve the equation:

$$\dot{u}(t) = [(-aP_k + Q_k) - aQ_k t] e^{-at} = 0 \quad (27)$$

Thus, the maximum value of $u(t)$ can be obtained at time:

$$t_{ku} = \frac{Q_k - aP_k}{aQ_k} \quad (28)$$

It is noted that we can only consider $u(t)$ after step k , and $u(t)$ is decreased when $t > t_{ku}$. Therefore, the maximum value of actuator effort U_{kmax} is calculated as:

$$U_{kmax} = \begin{cases} P_k e^{-at_k} + Q_k t_k e^{-at_k} & \text{if } t_{ku} \leq t_k \\ P_k e^{-at_{ku}} + Q_k t_{ku} e^{-at_{ku}} & \text{if } t_{ku} > t_k \end{cases} \quad (29)$$

To guarantee that $u(t)$ is within the allowable actuator effort range, the following constraint is required after the step corresponding to each impulse:

$$U_{kmax} \leq U_{max} \text{ for all } k = 1, \dots, N \quad (30)$$

where U_{max} is the maximum allowable actuator effort.

D. Controller Designing

The designing process of actuator position control using a PD controller and vibration suppression control using input shaping for a flexible dynamic system is:

Step 1: Determine the system vibration parameters, including natural vibration frequency and damping factor.

Step 2: Choose the appropriate input preshaping techniques such as ZV, ZVD, etc. See [14, 15] for more details about IS techniques.

Step 3: Choose the PD controller parameters K_P and K_D to minimize the system settling time by solving the following

optimization problem: minimizing (21) with constraints (12), (15), and (30).

IV. APPLICATION TO OVERHEAD CRANE

Figure 3 describes the overhead crane. In this figure, x is the cart's position, l is the rope length, m is the load mass, M is the cart mass, and θ is the angle between the rope and the vertical axis (Y axis). According to [26], the overhead crane linearized model can be described as:

$$F_x = (M + m)\ddot{x} + b_x \dot{x} + ml\ddot{\theta} \quad (31)$$

$$-\ddot{x} = l\ddot{\theta} + b_\theta \dot{\theta} + g\theta \quad (32)$$

where b_x and b_θ are the equivalent viscous damping of the cart and the load respectively. It can be seen that (31) describes the relation between the input force and the cart's position. The load angle plays the role of disturbance. Equation (32) describes the effect of the cart's motion to the vibration of the load.

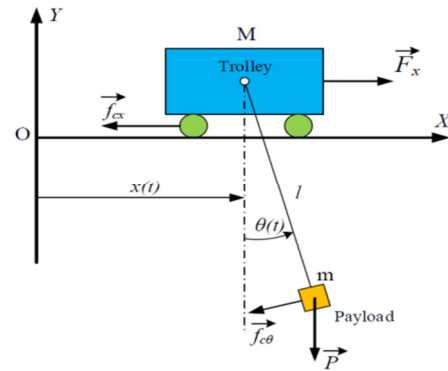


Fig. 3. Overhead crane model.

In practice, the cart is controlled by a motor with a driver. That can allow us to control the velocity of the cart. Therefore, to control the cart's position, we use the motor model with a driver instead of (31). The cart plays the role of an actuator in a flexible system and has (8) as the transfer function. The control of the overhead crane is to move the load to the desired position while suppressing the load vibration. To control the cart's position precisely, a PD controller is used. In addition, to suppress the load vibration, input preshaping is applied.

The actual experiments are conducted with the overhead crane model shown in Figure 4. The vibration model can be calculated from (32), however, the model's parameters may not be precise. Thus, we measured the sway angle and identified the natural vibration frequency and damping factor. The experiment parameters are shown in Table I.

TABLE I. EXPERIMENT PARAMETERS

Parameter	Values
K_c	4
T_c	0.2
ω_0	4.45 rad/s
ξ_0	0.007
g	9.81 m/s ²
U_{max}	10 V

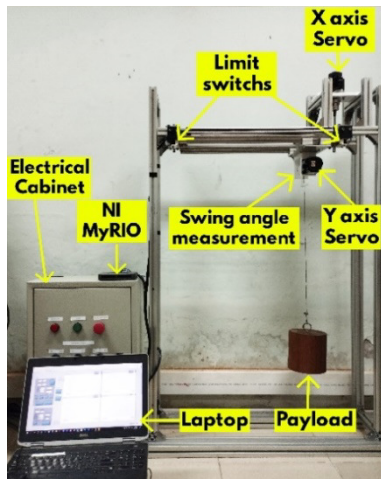


Fig. 4. Experimental crane system.

Then, two types of input shaping including ZV and ZVD can be designed using (5) for ZV and (7) for ZVD. Using the designed ISs, the PD controllers that optimize the settling time were calculated. We call them optimized PD-ZV and optimized PD-ZVD. In addition, the PD controller that optimizes the settling time of the feedback system using step input only and with the same constraint is also calculated. We call it optimized PD without IS. The ISs (5) and (7) are then applied to the optimized PD without IS. We call them ZV-optimized PD and ZVD-optimized PD without IS. The results are shown in Table II.

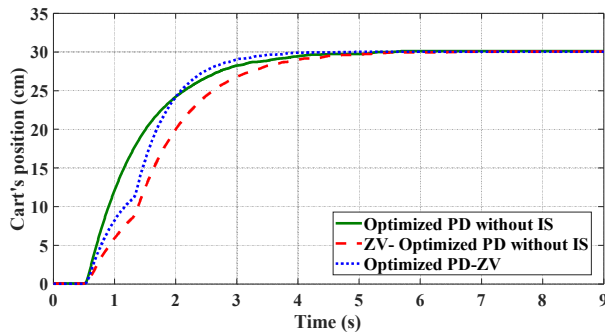


Fig. 5. Cart's position in three cases: optimized PD without IS, ZV-optimized PD without IS, and optimized PD-ZV.

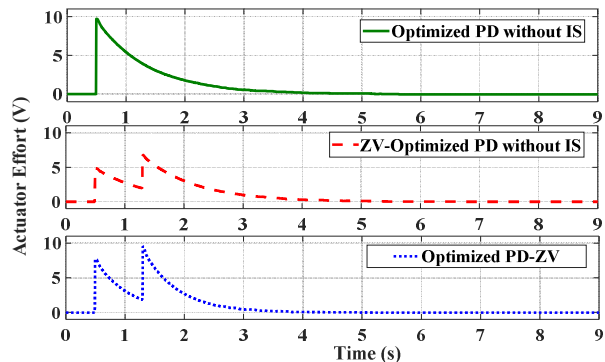


Fig. 6. Actuator effort in three cases: optimized PD without IS, ZV-optimized PD without IS, and optimized PD-ZV.

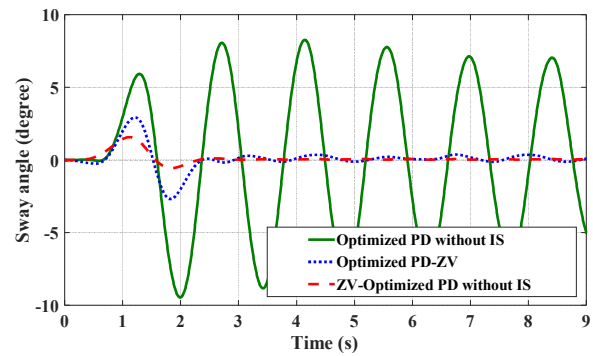


Fig. 7. Sway angle in three cases: optimized PD without IS, ZV-optimized PD without IS, and optimized PD-ZV.

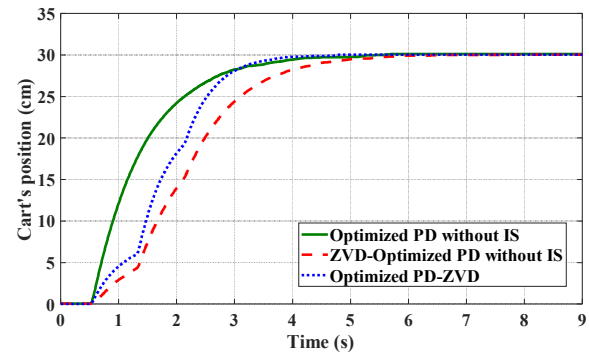


Fig. 8. Cart's position in three cases: optimized PD without IS, ZVD-optimized PD without IS, and optimized PD-ZVD.

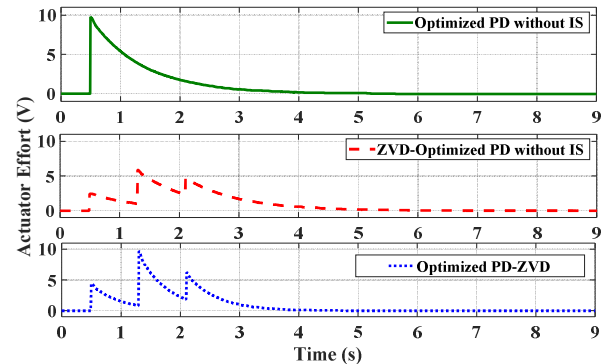


Fig. 9. Actuator effort in three cases: optimized PD without IS, ZVD-optimized PD without IS, and optimized PD-ZVD.

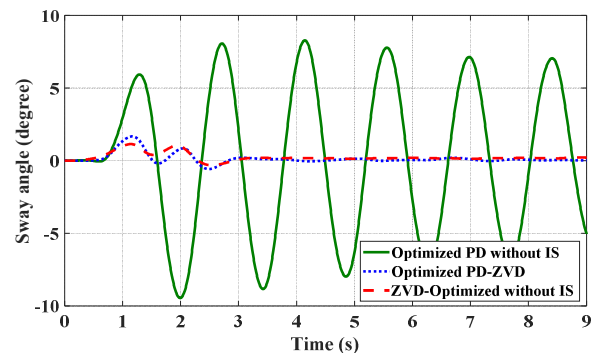


Fig. 10. Sway angle in three cases: optimized PD without IS, ZVD-optimized PD without IS, and optimized PD-ZVD.

TABLE II. CONTROLLER PARAMETERS AND SETTLING TIME

Parameter	Values		
	Optimized PD without IS	Optimized PD-ZV	Optimized PD-ZVD
K_p	0.325	0.52	0.59
K_d	0.01	0.07	0.09
Settling time (s)	2.66 Using ZV: 3.18 Using ZVD: 3.67	2.27	2.64

The experimental results are shown in Figure 5-9. It is clear that ZV and ZVD can suppress the payload vibration significantly. In the case of optimized PD without IS, the settling time is 2.66s. But when the IS is applied to the vibration suppression control, the settling time increases to 3.18s for ZV shaper and 3.67s for ZVD shaper. In addition, the actuator effort also reduces from 10V in the case of optimized PD without IS to 6.80V and 5.90V when applying ZV and ZVD shapers respectively. Therefore, we should design the PD controller in consideration of using IS at the system input. At a result, the actuator effort is larger but still in the required limit, and the system moves faster with settling time only 2.27s for ZV and 2.64s for ZVD shapers.

It is also found that in the case of optimized PD-ZV the settling time is smaller than the one in the case of ZV-optimized PD without IS, but the residual vibration magnitude is larger. The reason for this is the difference between the actual vibration frequency and the designed vibration frequency and the effect of the feedback system to the response of the IS shaper. This can be improved by using ZVD shaper. It is clear that in the case of optimized PD-ZVD the settling time is smaller than the one in the case of ZVD-optimized PD without IS, and the residual vibration magnitude is almost the same.

V. CONCLUSIONS

The current paper proposes a design process for the PD controller of the actuator in a flexible system that uses input shaper for vibration suppression control. The controller gains are chosen such that the feedback system is of the critically damped type and system's settling time is minimized while keeping the actuator effort constraint. The experiments with overhead crane model show the effectiveness of the proposed designing process. The settling time is reduced, in comparison to the case of the optimizing PD controller without considering the use of the input shaper. In the future, a designing tool will be developed to apply the proposed designing process for a real flexible system. In addition, the designing process for the system with time varying vibration frequency is also considered.

ACKNOWLEDGMENT

The paper is supported by the Hanoi University of Science and Technology project T2021-PC-002.

REFERENCES

[1] I. Esen and M. A. Koç, "Dynamic response of a 120 mm smoothbore tank barrel during horizontal and inclined firing positions," *Latin American Journal of Solids and Structures*, vol. 12, pp. 1462–1486, Aug. 2015, <https://doi.org/10.1590/1679-78251576>.

[2] I. Esen, "Dynamic response of a functionally graded Timoshenko beam on two-parameter elastic foundations due to a variable velocity moving mass," *International Journal of Mechanical Sciences*, vol. 153–154, pp. 21–35, Apr. 2019, <https://doi.org/10.1016/j.ijmecsci.2019.01.033>.

[3] I. Esen, "Dynamic response of functional graded Timoshenko beams in a thermal environment subjected to an accelerating load," *European Journal of Mechanics - A/Solids*, vol. 78, Nov. 2019, Art. no. 103841, <https://doi.org/10.1016/j.euromechsol.2019.103841>.

[4] M. Balas, "Feedback control of flexible systems," *IEEE Transactions on Automatic Control*, vol. 23, no. 4, pp. 673–679, Aug. 1978, <https://doi.org/10.1109/TAC.1978.1101798>.

[5] D. Antic, Z. Jovanovic, S. Peric, S. Nikolic, M. Milojkovic, and M. Milosevic, "Anti-Swing Fuzzy Controller Applied in a 3D Crane System," *Engineering, Technology & Applied Science Research*, vol. 2, no. 2, pp. 196–200, Apr. 2012, <https://doi.org/10.48084/etasr.146>.

[6] C. T. Kiang, A. Spowage, and C. K. Yoong, "Review of Control and Sensor System of Flexible Manipulator," *Journal of Intelligent & Robotic Systems*, vol. 77, no. 1, pp. 187–213, Jan. 2015, <https://doi.org/10.1007/s10846-014-0071-4>.

[7] K. G. Aktas and I. Esen, "State-Space Modeling and Active Vibration Control of Smart Flexible Cantilever Beam with the Use of Finite Element Method," *Engineering, Technology & Applied Science Research*, vol. 10, no. 6, pp. 6549–6556, Dec. 2020, <https://doi.org/10.48084/etasr.3949>.

[8] L. Cui, H. Wang, and W. Chen, "Trajectory planning of a spatial flexible manipulator for vibration suppression," *Robotics and Autonomous Systems*, vol. 123, Jan. 2020, Art. no. 103316, <https://doi.org/10.1016/j.robot.2019.103316>.

[9] D. Lee and C.-W. Ha, "Optimization Process for Polynomial Motion Profiles to Achieve Fast Movement With Low Vibration," *IEEE Transactions on Control Systems Technology*, vol. 28, no. 5, pp. 1892–1901, Sep. 2020, <https://doi.org/10.1109/TCST.2020.2998094>.

[10] H. Karagülle, L. Malgaca, M. Dirilmiş, M. Akdağ, and Ş. Yavuz, "Vibration control of a two-link flexible manipulator," *Journal of Vibration and Control*, vol. 23, no. 12, pp. 2023–2034, Jul. 2017, <https://doi.org/10.1177/1077546315607694>.

[11] H. J. Yoon, S. Y. Chung, H. S. Kang, and M. J. Hwang, "Trapezoidal Motion Profile to Suppress Residual Vibration of Flexible Object Moved by Robot," *Electronics*, vol. 8, no. 1, Jan. 2019, Art. no. 30, <https://doi.org/10.3390/electronics8010030>.

[12] B. Spruogis, A. Jakstas, V. Gican, V. Turla, and V. Moksins, "Further Research on an Anti-Swing Control System for Overhead Cranes," *Engineering, Technology & Applied Science Research*, vol. 8, no. 1, pp. 2598–2603, Feb. 2018, <https://doi.org/10.48084/etasr.1774>.

[13] N. C. Singer and W. P. Seering, "Preshaping Command Inputs to Reduce System Vibration," *Journal of Dynamic Systems, Measurement, and Control*, vol. 112, no. 1, pp. 76–82, Mar. 1990, <https://doi.org/10.1115/1.2894142>.

[14] W. Singhose, "Command shaping for flexible systems: A review of the first 50 years," *International Journal of Precision Engineering and Manufacturing*, vol. 10, no. 4, pp. 153–168, Oct. 2009, <https://doi.org/10.1007/s12541-009-0084-2>.

[15] C.-G. Kang, "Impulse Vectors for Input-Shaping Control: A Mathematical Tool to Design and Analyze Input Shapers," *IEEE Control Systems Magazine*, vol. 39, no. 4, pp. 40–55, Dec. 2019, <https://doi.org/10.1109/MCS.2019.2913610>.

[16] M. Kenison and W. Singhose, "Concurrent Design of Input Shaping and Proportional Plus Derivative Feedback Control," *Journal of Dynamic Systems, Measurement, and Control*, vol. 124, no. 3, pp. 398–405, Jul. 2002, <https://doi.org/10.1115/1.1486009>.

[17] J. R. Huey, "The Intelligent Combination of Input Shaping and PID Feedback Control," Ph.D. dissertation, Georgia Institute of Technology, Atlanta, GA, USA, 2006.

[18] J. R. Huey and W. Singhose, "Design of proportional-derivative feedback and input shaping for control of inertia plants," *IET Control Theory & Applications*, vol. 6, no. 3, pp. 357–364, Feb. 2012, <https://doi.org/10.1049/iet-cta.2010.0456>.

- [19] M. Muenchhof and T. Singh, "Concurrent Feed-forward/Feed-back Design for Flexible Structures," in *AIAA Guidance, Navigation, and Control Conference and Exhibit*, Monterey, CA, USA, Aug. 2002, <https://doi.org/10.2514/6.2002-4941>.
- [20] R. Mar, A. Goyal, V. Nguyen, T. Yang, and W. Singhose, "Combined input shaping and feedback control for double-pendulum systems," *Mechanical Systems and Signal Processing*, vol. 85, pp. 267–277, Feb. 2017, <https://doi.org/10.1016/j.ymssp.2016.08.012>.
- [21] D. Newman and J. Vaughan, "Concurrent Design of Linear Control with Input Shaping for a Two-Link Flexible Manipulator Arm," *IFAC-PapersOnLine*, vol. 51, no. 14, pp. 66–71, Jan. 2018, <https://doi.org/10.1016/j.ifacol.2018.07.200>.
- [22] M.-C. Pai, "Closed-loop input shaping control of vibration in flexible structures using discrete-time sliding mode," *International Journal of Robust and Nonlinear Control*, vol. 21, no. 7, pp. 725–737, 2011, <https://doi.org/10.1002/rnc.1618>.
- [23] M.-C. Pai, "Closed-Loop Input Shaping Control of Vibration in Flexible Structures via Adaptive Sliding Mode Control," *Shock and Vibration*, vol. 19, no. 2, pp. 221–233, 2012, <https://doi.org/10.3233/SAV-2011-0625>.
- [24] J. Oliveira, P. M. Oliveira, T. M. Pinho, and J. B. Cunha, "PID Posicast Control for Uncertain Oscillatory Systems: A Practical Experiment," *IFAC-PapersOnLine*, vol. 51, no. 4, pp. 416–421, Jan. 2018, <https://doi.org/10.1016/j.ifacol.2018.06.130>.
- [25] R. M. Corless, G. H. Gonnet, D. E. G. Hare, D. J. Jeffrey, and D. E. Knuth, "On the LambertW function," *Advances in Computational Mathematics*, vol. 5, no. 1, pp. 329–359, Dec. 1996, <https://doi.org/10.1007/BF02124750>.
- [26] D. Qian and J. Yi, *Hierarchical Sliding Mode Control for Under-actuated Cranes*. Berlin, Heidelberg: Springer, 2015.

Prediction of the Stress Wave Amplification Factor of a Spherical Blast Source Using Numerical Simulations

Jawad Ur Rehman

Department of Civil and Environmental Engineering
Hanyang University
Seoul, South Korea
jawad640@hanyang.ac.kr

Can-Ngon Nguyen

Department of Civil Engineering
Vinh University
Vinh, Vietnam
ngon_nguyencan@yahoo.com

Tuan-Anh Nguyen

Department of Civil Engineering
Vinh University
Vinh, Vietnam
anhhandico52@gmail.com

Trong-Cuong Vo

Department of Civil Engineering
Vinh University
Vinh, Vietnam
cuongvqc@gmail.com

Trong-Kien Nguyen

Department of Civil Engineering
Vinh University
Vinh, Vietnam
nguyentrongkien82@gmail.com

Van-Quang Nguyen

Department of Civil Engineering
Vinh University
Vinh, Vietnam
nguyenvanquang240484@gmail.com

Received: 2 August 2022 | Revised: 25 August 2022 | Accepted: 27 August 2022

Abstract—A typical blast wave attenuation curve presents a relationship between Peak Particle Velocity (PPV) at the surface of a geologic profile and distance. As the stress wave is amplified at the free-field boundary, the attenuation curve at the surface is always larger than the within media profile curve. Measurements are made at the rock's surface and test blasts are always conducted to ensure the safety of underground existing structures. In order to design underground blasting, the recorded PPVs are then reduced by a factor of 2. In this paper, particle velocity amplification was studied by using numerical simulation, and the difference between PPV at the surface and within media profiles is quantified. The amplification factor depends upon source depth, incidence angle, and Poisson's ratio of the media. It is calculated as the ratio of the magnitude of PPV at the surface of the media to the within media profile. According to the parametric study, the amplification factor for a uniform medium increases with increasing source depth, while the amplification factor decreases with increasing Poisson's ratio. Considering a three-layer model with a source depth of 30m, the amplification factor is high for low incident angles and low for higher incident angles. The range varies between 1.5 to 2.1.

Keywords—free surface; numerical simulation; underground blasting; wave amplification; wave attenuation

I. INTRODUCTION

Blasting is one of the most extensively utilized methods for extracting rock in mining and construction operations and the most cost-effective excavation method [1]. The appropriate design of blasts and the management and prediction of blast consequences importance is increasing as the magnitude of these operations grows [2, 3]. The majority of the explosive energy is utilized in the crushing and fracturing of the rock mass. When blasting energy is transferred to the rock mass, it might cause damage to the surrounding rock in the form of undesired fractures. Many researchers have contributed to the development of the blast vibration safety criterion, and several criteria or prediction models have been proposed to assess the structural stability of diverse constructions [4, 5]. Peak Particle Velocity (PPV) is the most extensively used indicator for evaluating blast-induced damage. PPVs are widely assumed to be determinable in empirical models based on the maximum charge per delay, distance from the blasting source, and site coefficients. The scaled distance concept proposed by the United States Bureau of Mines (USBM) [6] is the most acceptable vibration prediction equation. It takes into account the quantity of explosive energy in shock and seismic waves, as well as distance effects. Test blasts are usually conducted to record surface PPVs, and an attenuation curve is then

developed by conducting regression analysis. The Scaled Distance (SD) is calculated by taking the distance between the source and measurement locations and dividing it by the maximum charge per delay:

$$SD = \frac{R}{\sqrt{W}} \quad (1)$$

where R is the distance between the charge and monitoring station and W is the maximum charge weight per delay.

The USBM predictor equation for the estimation of the peak particle velocity is:

$$PPV = K(SD)^n \quad (2)$$

where K and n are the site and geological constant factors respectively.

The ground transmission factor, or constant K , is influenced by the confinement of the charge, and the local geology. Higher values of K denote either well-coupled explosives or a mass of rock that is relatively large and fracture-free. The quality of the rock mass affects the constant n , which indicates the impact of attenuation with distance. Lower values of n indicate more competent rock mass with less fracturing, whereas higher values of n indicate poorer quality rock mass that attenuates vibration energy more quickly and within a shorter distance from the charge.

Test blasts are usually conducted to record surface PPVs, and an attenuation curve is then developed by regression analysis. Artificial Intelligence (AI) techniques like Artificial Neural Networks (ANNs) and Particle Swarm Optimization (PSO) have been utilized in mining and civil engineering during the last few years to forecast the PPV based on total charge, distance, maximum charge per delay, frequency, and blasting parameters [7, 8]. Previously, the wave amplification effect studies mainly focused on earthquakes [9-14] and the amplification effect for the blast source has not been studied extensively. This paper uses numerical simulations to study the amplification factors using a spherical blast source.

II. NUMERICAL MODELING

In the present study, numerical analysis is carried out using FLAC 2D version 7.0 [15]. An axisymmetric model with a spherical blast source and a quad mesh with a mesh size of 0.05m is used. The blast-induced fracture zone is described as a spherical cavity with a radius of 0.5m. The half-space was modeled as an elastic material. The computational model and boundary conditions are shown in Figure 1. The reflected wave created at the upper boundary travels to the side wall and the lower end as it propagates in the radial direction with vertical and horizontal velocity components. Therefore, viscous dampers are installed in two directions, at the side wall and at the bottom to absorb the impact of vibrations, as suggested in [16]. The modelling strategy used in this paper is as follows: first, a geometric model of the rock mass is created and a behavioural model and material properties are applied. Then, a mesh is generated, boundary conditions and viscous boundaries are applied, and finally, a blast load is applied.

The explosion depths employed were 10, 20, and 30m. The computational domain has a 70m lateral dimension. The blast

load was applied to the cavity surface in the normal direction as a pressure-time history.

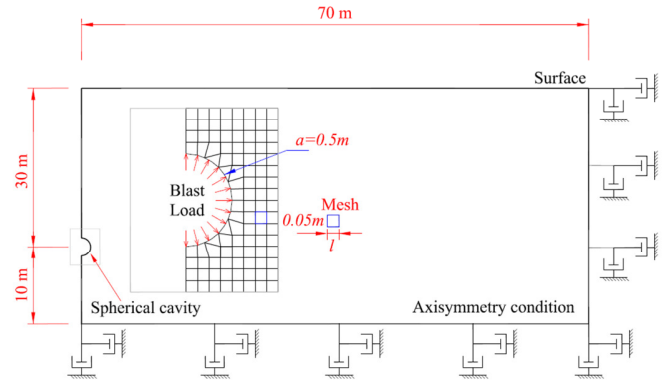


Fig. 1. The computational model.

To verify the numerical model, the results of the dynamic analysis for the undamped case are compared to the closed-form solution in [17]. To solve the spherical charge blasting vibration problem, the authors in [17] simplified the cavity-blasting pressure. The solution showed that the spherical blasting generates only P waves, and an elastic velocity equation for the spherical blasting vibration was later obtained as follows:

$$V(R, \bar{\tau}) = -\frac{a}{R} f(\bar{\tau}) - \left(\frac{a}{R}\right)^2 q(\bar{\tau}) \quad (3)$$

where V is the velocity induced by the blast source, a is the source cavity, R is the distance from the measured point to the charge centre, $f(\tau)$, $q(\tau)$ are time history functions of the wave at R , and τ is the dimensionless time.

$$f(\bar{\tau}) = c \frac{\partial^2 \phi_1}{\partial \bar{\tau}^2}, q(\bar{\tau}) = c \frac{\partial \phi_1}{\partial \bar{\tau}} \quad (4)$$

where c is the wave velocity and ϕ_1 is the displacement potential function:

$$\phi_1 = \frac{-p_c}{\rho_d b_{2d}} \left\{ \left(\bar{\tau} - 2 \frac{b_{1d}}{b_{2d}} \right) e^{-\alpha_c \bar{\tau}} + e^{-\alpha_d \bar{\tau}} \left[\frac{b_{1d}}{\sqrt{b_{2d} \omega_d}} \cos(\omega_d \bar{\tau} - \theta) - \frac{1}{\sqrt{b_{2d}}} \sin(\omega_d \bar{\tau} - \theta) \right] \right\}$$

where:

$$p_c = \frac{P_0}{E} \left(\frac{a}{c} \right)^n, \bar{\tau} = \left(t - \frac{R-a}{c} \right) \frac{c}{a}, \omega_d = \frac{(1-2\nu)^{1/2}}{(1-\nu)}, \alpha_d = \frac{(1-2\nu)}{(1-\nu)}, \alpha_c = \frac{a}{c}, b_{1d} = \frac{a}{c} (\alpha_0 - \alpha), b_{2d} = \left(\frac{a}{c} \right)^2 (\omega_0^2 + (\alpha_0 - \alpha)^2), \theta = \frac{b_{1d}}{\omega_d}.$$

Time-varying blast pressure is applied to the wall of an equivalent cavity using the following formulation [17]:

$$P(t) = P_0 t^n e^{-\beta t} \quad (4)$$

where $P(t)$ and P_0 denote time-varying blast pressure and initial detonation pressure respectively, t represents time, n is an integer, and β denotes decay of the pressure pulse. Figure 2

shows a blast pressure profile calculated using ($P(t) = P_0 t^n e^{-\beta t}$).

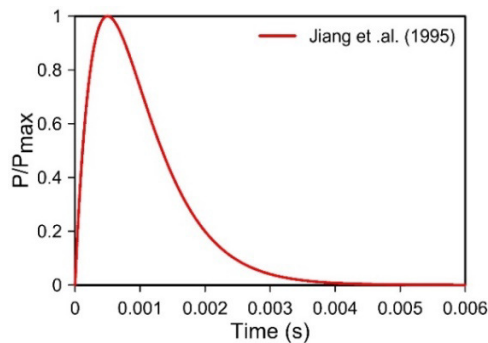


Fig. 2. Pressure time history applied to the wall of an equivalent cavity.

The velocity-time history estimated from the numerical simulation and the equation from [17] for the undamped medium is shown in Figure 3. The shear wave was fixed to 2309m/s, with a Poisson ratio of 0.25, whereas unit weight was set at 24.5kN/m³. The selected loading pressure was 1GPa. n and β were set to 1 and 2000 respectively. The blast equivalent cavity was assumed as 0.5m. It is shown that the numerical model correctly predicts the wave attenuation, providing results that are almost identical to the analytical solution. A parametric study is conducted to study the influence of effective parameters on wave amplification at the surface. These parameters include source depth, angle of incidence, and Poisson's ratio. First, a homogeneous rock mass is modeled and then layered model with weathered rock at the surface, followed by soft rock, and then hard rock mass is considered.

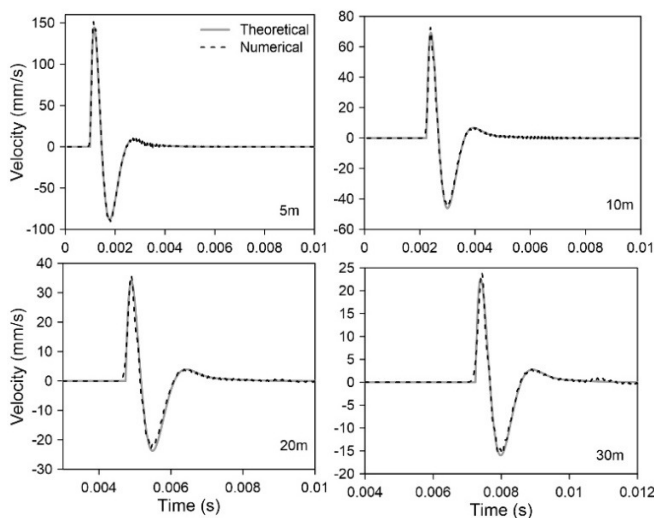


Fig. 3. Comparison of the numerical simulation with a closed-form solution.

III. RESULTS AND DISCUSSION

Blast-induced vibrations are usually recorded in the form of PPV at the surfaces. Surface vibrations are always higher than within profiles [18]. Table I shows the mechanical properties of the rock mass [19]. The attenuation of PPV for surface and

within profiles for the depth of 30m with Poisson's ratio of 0.25 is shown in Figure 4. The calculated PPV at the surface is almost two times the one within profiles.

TABLE I. MECHANICAL PROPERTIES OF THE ROCK MASS [19]

Rock type	Shear velocity (m/s)	Unit weight (kN/m ³)	Poisson ratio
Hard Rock	2500	25	0.25
	2000		
	1500		
Soft Rock	1200	23	0.27
	1000		
	800		
Weathered Rock	650	21	0.3
	500		
	150		

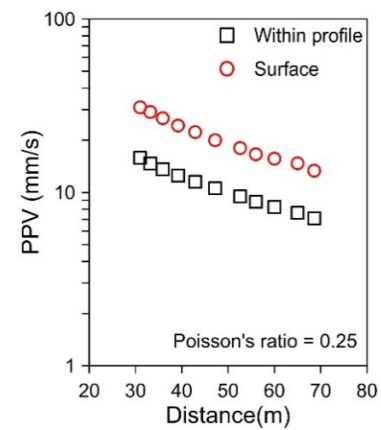


Fig. 4. Comparison of PPV within profile and surface for homogenous media.

To study the amplification factor in detail, three source depths of 10, 20, and 30m from the surface are considered. Three Poisson's ratios of 0.20, 0.25, and 0.30 are selected. For uniform homogeneous rock mass, Figure 5(a) shows the results of Poisson's ratio of 0.20, for the three depths. The amplification factor at high angles is 1.8, whereas at lower angles it increases up to 2. A source at greater depth shows an amplification factor near to 2 at 10° to 50°. For Poisson's ratio of 0.25, at high angles the amplification factor in Figure 5(b) is 1.7 and at lower angles it is 2. The amplification factor for Poisson's ratio of 0.30 in Figure 5(c) is 1.5 at higher angles and 1.9 at lower angles. Low Poisson's ratio has amplification from near 1.8 to 2.1, whereas higher Poisson's ratio shows less amplification factor and gradually increases for lower angles up to 1.9.

Until now, the rock mass was considered homogenous, however, in the real field, it is inhomogeneous. For this purpose, a three-layer model is developed: near the surface the rock mass consists of soft rock, followed by weathered rock, and the lower most part consists of hard rock. Figure 6 shows the computational model for inhomogeneous rock mass. The attenuated PPV at 30m depth is shown in Figure 7. The amplification factor at smaller distances, i.e. at lower incident angles, is more than 2, whereas at greater distances, i.e. at higher incident angles, the amplification factor is 1.5. To further get a clear view, Figure 8 shows the amplification factor

at 30m depth, which shows high amplification factor for low incident angles. The amplification factor decreases for higher angles.

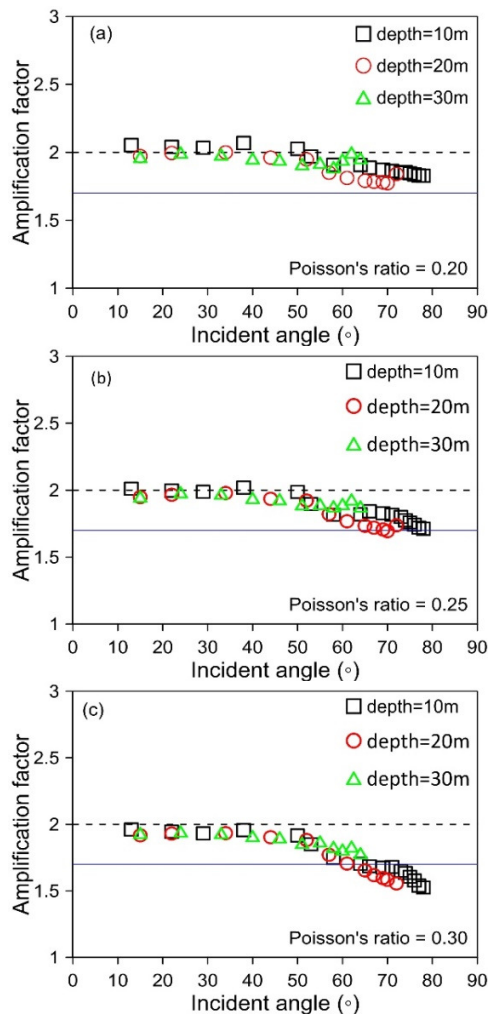


Fig. 5. Amplification factor for homogeneous rock: (a) $\nu = 0.20$, (b) $\nu = 0.25$, (c) $\nu = 0.30$.

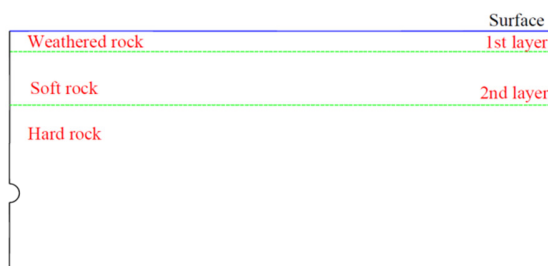


Fig. 6. A computational model for inhomogeneous rock mass.

The results show that the inhomogeneity of rock mass plays a vital role in wave amplification. Amplification factors for different sites will be different based upon rock mass strata. Many studies [20] assume an amplification factor of 2 for homogenous rock mass using a spherical blast source. A numerical simulation is suggested for finding amplification

factors for the specific site. This study is limited to spherical blast sources. In the field, cylindrical blast sources are utilized. Future research will include a complete parametric investigation employing a cylindrical blast source.

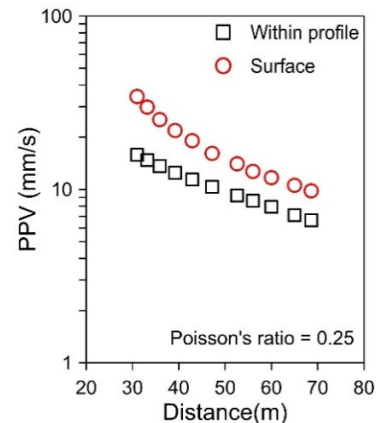


Fig. 7. Comparison of PPV of within profile and surface for inhomogeneous rock mass.

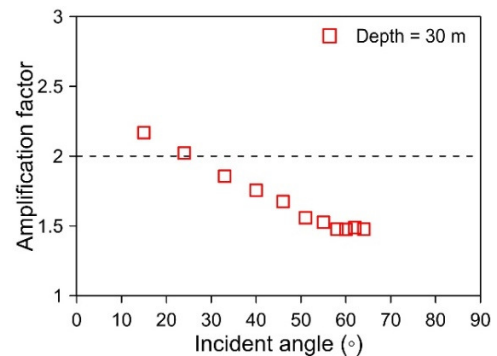


Fig. 8. Amplification factor for inhomogeneous rock mass

IV. CONCLUSIONS

This paper presented a numerical analysis-based amplification factor for a spherical blast source. The velocity amplification factor is defined as the ratio of wave amplitude at the free field boundary to the incident wave amplitude. Poisson's ratio, source depth, angle of incidence, and geological characteristic of a specific site are the main factors that affected the velocity amplification. The results show that the amplification factor varies between 1.5 to 2.1.

As a consequence, velocity amplification phenomena should be taken into account while assessing underground damage. It is recommended to utilize numerical analysis to predict site-specific amplification factor, which can improve design procedures and help engineers predict the inner profile attenuation curves for controlling damage to the surrounding rock mass.

REFERENCES

- [1] I. A. Onederra, J. K. Furtney, E. Sellers, and S. Iverson, "Modelling blast induced damage from a fully coupled explosive charge," *International Journal of Rock Mechanics and Mining Sciences*, vol. 58, pp. 73–84, Feb. 2013, <https://doi.org/10.1016/j.ijrmms.2012.10.004>.

- [2] L. Malmgren, D. Saiang, J. Töyrä, and A. Bodare, "The excavation disturbed zone (EDZ) at Kiirunavaara mine, Sweden—by seismic measurements," *Journal of Applied Geophysics*, vol. 61, no. 1, pp. 1–15, Jan. 2007, <https://doi.org/10.1016/j.jappgeo.2006.04.004>.
- [3] D. Saiang and E. Nordlund, "Numerical Analyses of the Influence of Blast-Induced Damaged Rock Around Shallow Tunnels in Brittle Rock," *Rock Mechanics and Rock Engineering*, vol. 42, no. 3, pp. 421–448, Jun. 2009, <https://doi.org/10.1007/s00603-008-0013-1>.
- [4] J.-H. Shin, H.-G. Moon, and S.-E. Chae, "Effect of blast-induced vibration on existing tunnels in soft rocks," *Tunnelling and Underground Space Technology*, vol. 26, no. 1, pp. 51–61, Jan. 2011, <https://doi.org/10.1016/j.tust.2010.05.004>.
- [5] P. Pal Roy, "Vibration control in an opencast mine based on improved blast vibration predictors," *Mining Science and Technology*, vol. 12, no. 2, pp. 157–165, Mar. 1991, [https://doi.org/10.1016/0167-9031\(91\)91642-U](https://doi.org/10.1016/0167-9031(91)91642-U).
- [6] W. I. Duvall and D. E. Fogelson, *RI 5968 Review of Criteria for Estimating Damage to Residences from Blasting Vibrations ? Summary and Conclusions*. Washington DC, USA: United States Department of the Interior, 1962.
- [7] D. J. Armaghani, M. Hajihassani, E. T. Mohamad, A. Marto, and S. A. Noorani, "Blasting-induced flyrock and ground vibration prediction through an expert artificial neural network based on particle swarm optimization," *Arabian Journal of Geosciences*, vol. 7, no. 12, pp. 5383–5396, Dec. 2014, <https://doi.org/10.1007/s12517-013-1174-0>.
- [8] D. J. Armaghani, E. Momeni, S. V. A. N. K. Abad, and M. Khandelwal, "Feasibility of ANFIS model for prediction of ground vibrations resulting from quarry blasting," *Environmental Earth Sciences*, vol. 74, no. 4, pp. 2845–2860, Aug. 2015, <https://doi.org/10.1007/s12665-015-4305-y>.
- [9] M. Aaqib, D. Park, M. B. Adeel, Y. M. A. Hashash, and O. Ilhan, "Simulation-based site amplification model for shallow bedrock sites in Korea," *Earthquake Spectra*, vol. 37, no. 3, pp. 1900–1930, Aug. 2021, <https://doi.org/10.1177/8755293020981984>.
- [10] M. Aaqib, D. Park, Y.-G. Lee, and U. Pervaiz, "Development of Site Classification System and Seismic Site Coefficients for Korea," *Journal of Earthquake Engineering*, Oct. 2021, <https://doi.org/10.1080/13632469.2021.1990164>.
- [11] Y. Lee, H.-S. Kim, M. I. Khalid, Y. Lee, and D. Park, "Effect of Nonlinear Soil Model on Seismic Response of Slopes Composed of Granular Soil," *Advances in Civil Engineering*, vol. 2020, Nov. 2020, Art. no. e8890247, <https://doi.org/10.1155/2020/8890247>.
- [12] T. Nagao, "Seismic Amplification by Deep Subsurface and Proposal of a New Proxy," *Engineering, Technology & Applied Science Research*, vol. 10, no. 1, pp. 5157–5163, Feb. 2020, <https://doi.org/10.48084/etasr.3276>.
- [13] T. Nagao, "Maximum Credible Earthquake Ground Motions with Focus on Site Amplification due to Deep Subsurface," *Engineering, Technology & Applied Science Research*, vol. 11, no. 2, pp. 6873–6881, Apr. 2021, <https://doi.org/10.48084/etasr.3991>.
- [14] T. Nagao, "Variation Evaluation of Path Characteristic and Site Amplification Factor of Earthquake Ground Motion at Four Sites in Central Japan," *Engineering, Technology & Applied Science Research*, vol. 11, no. 5, pp. 7658–7664, Oct. 2021, <https://doi.org/10.48084/etasr.4405>.
- [15] "FLAC (Fast Lagrangian Analysis of Continua) Version 220," Itasca Consulting Group, Inc., Minneapolis, MN (USA)) Nuclear Regulatory Commission, Washington, DC (USA), Report NUREG/CR--5430-VOL.3, 1989.
- [16] J. Lysmer and R. L. Kuhlemeyer, "Finite Dynamic Model for Infinite Media," *Journal of the Engineering Mechanics Division*, vol. 95, no. 4, pp. 859–877, Aug. 1969, <https://doi.org/10.1061/JMCEA3.0001144>.
- [17] J. Jiang, D. P. Blair, and G. R. Baird, "Dynamic response of an elastic and viscoelastic full-space to a spherical source," *International Journal for Numerical and Analytical Methods in Geomechanics*, vol. 19, no. 3, pp. 181–193, 1995, <https://doi.org/10.1002/nag.1610190303>.
- [18] J.-K. Ahn and D. Park, "Prediction of Near-Field Wave Attenuation Due to a Spherical Blast Source," *Rock Mechanics and Rock Engineering*, vol. 50, no. 11, pp. 3085–3099, Nov. 2017, <https://doi.org/10.1007/s00603-017-1274-3>.
- [19] J.-K. Ahn, D. Park, and J.-K. Yoo, "Estimation of damping ratio of rock mass for numerical simulation of blast induced vibration propagation," *Japanese Geotechnical Society Special Publication*, vol. 2, no. 45, pp. 1589–1592, 2016, <https://doi.org/10.3208/jgssp.KOR-34>.
- [20] P. Zhang, E. Nordlund, G. Swan, and C. Yi, "Velocity Amplification of Seismic Waves Through Parallel Fractures Near a Free Surface in Fractured Rock: A Theoretical Study," *Rock Mechanics and Rock Engineering*, vol. 52, no. 1, pp. 199–213, Jan. 2019, <https://doi.org/10.1007/s00603-018-1589-8>.

Analysis of Particulate Matter Emissions and Performance of the Compression Ignition Engine Using Biodiesel Blended Fuel

Sajjad Bhangwar

Mechanical Engineering Department,
Quaid-e-Awam University of
Engineering Science and Technology,
Nawabshah Pakistan
sajjadbhangwar@quest.edu.pk

Sher Muhammad Ghoto

Mechanical Engineering Department,
Quaid-e-Awam University of
Engineering Science and Technology,
Nawabshah Pakistan
ghotosher@yahoo.com

Aijaz Abbasi

Mechanical Engineering Department,
Quaid-e-Awam University of
Engineering Science and Technology,
Nawabshah Pakistan
aijaz-abbasi@quest.edu.pk

Muhammad Kashif Abbasi

Mechanical Engineering Department,
Quaid-e-Awam University of
Engineering Science and Technology,
Nawabshah Pakistan
muhammadkashif@quest.edu.pk

Arif Ali Rind

Mechanical Engineering Department,
Quaid-e-Awam University of
Engineering Science and Technology,
Nawabshah Pakistan
engineerarif344@yahoo.com

Muhammad Ramzan Luhur

Mechanical Engineering Department,
Quaid-e-Awam University of
Engineering Science and Technology,
Nawabshah Pakistan
luhur@quest.edu.pk

Zohaib Khan

Faculty of Mechanical and
Manufacturing Engineering, Universiti
Tun Hussein Onn Malaysia, Malaysia
and Department of Mechanical
Engineering, QUEST, Pakistan
aghazohaib03@gmail.com

Umair Ahmed Rajput

Department of Mechanical Engineering,
Quaid-e-Awam University of
Engineering, Science and Technology,
Nawabshah, Pakistan
enr.umair@quest.edu.pk

Sanaullah Mastoi

Department of Mathematics, Quaid-e-
Awam University of Engineering
Science and Technology, Campus
Larkana, Sindh, Pakistan
sanaullah.mastoi@quest.edu.pk

Received: 19 July 2022 | Revised: 16 August 2022 | Accepted: 24 August 2022

Abstract—As the world becomes more urbanized, the market for petroleum products increases. The supply of crude oil-based products such as diesel, gasoline, and natural gas is limited. Furthermore, natural resources are finite and their reservoirs are located in certain parts of the globe. Countries with low to no fossil fuel resources are experiencing a scarcity of petroleum products, necessitating the exploration of alternative energy resources. In this research, tests regarding the exhaust particulate emission, sound pressure level, and performance have been carried out using samples from diesel and biodiesel (waste cooking oil) blended fuel. Two fuel samples have been used, B25 (biodiesel 25% and 75% diesel) and 100% diesel as a baseline in a CI engine at constant RPM of 1350 and variable loads of 0.0 to 1.6 at an interval of 0.2Kg-m. The results show that particulate emissions are reduced by about 7.29% when using biodiesel blended fuel, whereas brake-specific fuel consumption of biodiesel blended fuel has decreased as brake power increased, and brake thermal efficiency increased as brake power increased. The sound pressure level was measured from different locations of the engine (back, front, left) and for varying load. The results show that B25 produces less noise than D100 in each case.

Keywords—biodiesel (waste cooking oil); pollution; Diesel engine; particulate emissions; noise

I. INTRODUCTION

Greenhouse gas (GHG) emissions contribute to global warming and harm the environment [1, 2]. A higher quantity of pollutant emissions come as a result of fossil fuels [3]. The Compression Ignition (CI) engine was developed soon after the Spark Ignition (SI) engine and has become quite popular. To reduce environmental pollutant emissions, bio-ethanol has been used in the CI engine, fulfilling the demand of diesel fuel, increasing job opportunities, and conserving natural energy resources [4]. Biodiesel blend NBD25 is a mixture of neem oil methyl ester (25% vol.) and mineral diesel (75% vol.) and can be used as fuel. Nickel oxide nanoparticles were dosed in NBD25 blend at four levels in [5]. JBD100 biodiesel produces a lower level of carbon monoxide (CO), hydrocarbons (HC), and smoke emissions with notable increase in NO_x and carbon dioxide (CO₂) emissions [6]. Methane gas can be produced from wastewater, animal waste, and city garbage landfills. This gas can be produced by the gasification process of wood.

Biofuels [7] are generally considered environment-friendly because they emit fewer GHG emissions than conventional fuels. Fatty Acid Methyl Ester (FAME) is also referred to as pure biodiesel (B100). The lower concentration of biodiesel is known as "biodiesel blend", with B25 representing a mix of 25% of biodiesel in diesel fuel [8, 9]. Biodiesel is the most emerging and green fuel due to its similar properties to the ordinary diesel fuel. It is capable to blend in any proportion with diesel fuel [10, 11]. It is also defined by the time it takes to pass out the liquid from some specified size orifice so it is known as thick oil [12]. The physicochemical properties of gasoline, can affect engine the efficiency and emission characteristics. Biodiesel does not have the same property values with diesel fuel, so researchers blend biodiesels in various proportional ratios to diesel fuel [13, 14]. The use of biodiesel increases agricultural value and income, allowing for greater freedom of energy use and reduces the need for imported petroleum goods [15, 16]. Examples of greenhouse gasses are Methane (CH_4), carbon dioxide (CO_2), and nitrous oxide (N_2O). These gases are responsible for global warming [17].

Due to the increased smoke associated with high fuel-air ratios, the brake specific fuel consumption of the CI engine increases at high loads, the mechanical efficiency decreases at lower loads, and the Brake Specific Fuel Consumption (BSFC) increases [18, 19] due to its higher oxygen contents, higher cetane number and proper spray timing. The emission of CO_2 (2.3%), CO (22%), NO_x (0.97%), and smoke (6.54%) decreased comparatively at 50% load in [20]. A few properties of biodiesel fuel significantly affect brake power, e.g. kinematic viscosity, calorific value, and lubricity [21]. An increase in the temperature of the combustion chamber improves thermal efficiency with a limited quantity of methanol and ethanol. It has been observed that vegetable oil blends give lower thermal efficiency than diesel fuel [21, 22]. Meanwhile, smoke opacity, brake specific particulate emissions, and particle geometric mean diameter drop as the quantity of soluble organic components increases, and biodiesel blends showed more variance [23].

II. RESEARCH METHODOLOGY

In this study, two fuel samples have been tested in a CI engine and parameters like engine performance, exhaust gas emissions, and noise emissions were analyzed. Initially, fuel properties have been tested on ASTM standards. Engine performance, exhaust gases, and sound pressure level tests have been analyzed on variable loading conditions and constant speed. The used engine specifications are shown in Table I.

A. Engine Exhaust Particulate Matter Emission

The results of PM (Particulate Matter) emissions from a diesel engine have been taken while running diesel fuel and biodiesel (waste cooking oil) blended fuel. The engine emissions depend on speed, load, fuel properties and injection timings. The load on the engine can be controlled by using a dynamometer coupled with the engine shaft directly. The instrumentations installed in the test bed were manually controlled. In this work, 3 particle sizes (PM 1.0, PM 2.5, and PM 7.0) were considered.

TABLE I. USED ENGINE SPECIFICATIONS

Stroke	80mm
Output (12hr rating)	4.4kw/2600r/min
Displacement	0.353L
Compression ratio	21-23
Mean effective pressure	576kpa
Piston mean speed	6.93m/s
Specific fuel consumption	278.8g/kwh
Specific oil consumption	4.08g/kwh
Cooling water	1360g/kwh
Injection pressure	14.2+0.5Mpa
Valves clearance	Inlet valve 0.15-0.25mm
Maximum engine power	7.7kw
Maximum engine torque	80Nm

B. Engine Performance Analysis

During the experiments, two fuel tanks were connected to the diesel engine test bed. Fuel was delivered to the engine through a single pipeline. Both fuel tanks were linked by a common line, and flow could be regulated by two separate valves. Based on fuel selection, one tank was filled with diesel fuel (D100) and the other with biodiesel blended fuel. Engine torque, brake strength, brake thermal efficiency, and brake specific fuel consumption were measured in the engine output. Variable loads were applied to calculate separate rpm on each load.

C. Engine Noise Emissions

The noise level (sound pressure level) of the CI engine was calculated when using diesel and biodiesel blended fuels at different loading conditions and constant speed.

III. RESULTS AND DISCUSSION

A. Particulate Matter Emissions

A CI engine is known as being high fuel-efficient and robust, but unfortunately, it is responsible for high PM emissions. Biodiesel (waste cooking oil) on the other hand, generates less PM emissions. However, there are different reasons of PM production from a diesel engine. Incomplete combustion of diesel fuel due to temperature variation of fuel is one of these reasons. It is observed that, overall, diesel fuel is mainly responsible for PM generation in PM 1.0, which is a higher particulate matter on idling condition of diesel fuel D100. Biodiesel blend B25 produces less PM emissions as compared to diesel fuel.

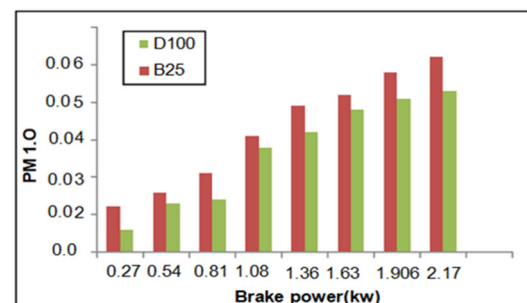


Fig. 1. Comparative results of exhaust PM1.0 emissions.

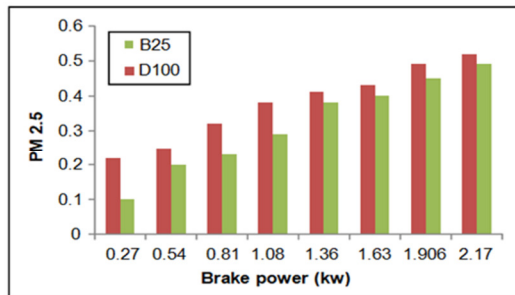


Fig. 2. Comparative results of exhaust PM 2.5 emissions.

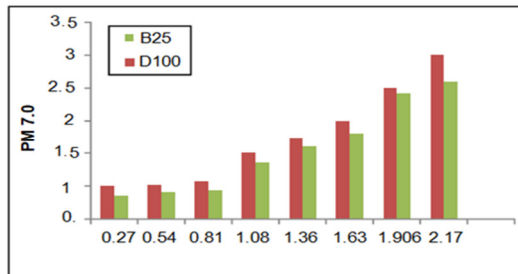


Fig. 3. Comparative results of exhaust PM 7.0 emissions.

B. Brake Thermal Efficiency

The thermal efficiency of the brake was studied next. As the calorific value of the biodiesel decreased, the fuel consumption increased for the same power output as shown in Figure 4.

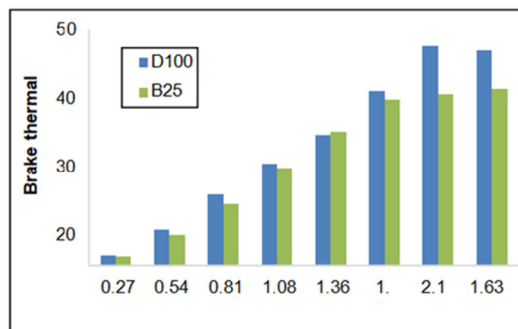


Fig. 4. Comparative results of brake thermal efficiency.

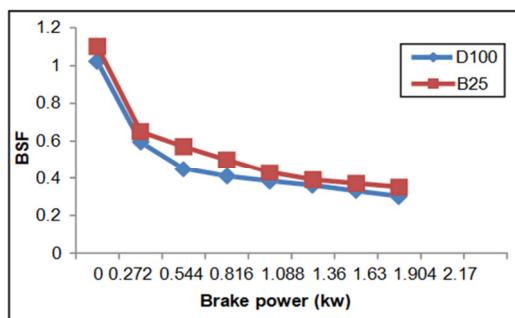


Fig. 5. Comparative results of brake specific fuel consumption.

In comparison to B25, the thermal brake performance of D100 has been increasing with increased load of the engine

from 0.2KW to 1.6KW as shown in Figure 5. BSFC varies depending on engine load, rpm, and biodiesel blending ratio. It was discovered that brake B25 has higher BSFC than D100 because B25 has high oxygen content, which results in a lower heating value. The lower density and lower heating values of the fuels need higher mass of fuel for the same energy output from the engine. It was observed that density and calorific value have a high impact on the degree of UN saturation.

C. Sound Pressure Level

At a constant 1350 rpm, the sound pressure level results were calculated with variable brake loads such as 0.27212, 0.54424, 0.81636, 1.08848, 1.3606, 1.63272, 1.90484, and 2.17696 as shown in Figure 6. In comparison to the back and left sides of the engine, the front side has a higher sound pressure level. The results show that when using D100 in the engine, the sound pressure level is higher than when using the biodiesel blend B25. As a result of the higher oxygen content in gasoline, the cetane number is a key parameter to understand when it comes to ignition delay. During compression ignition, the cetane number plays an important role, as the higher cetane number gives a shorter ignitions delay. B25 has a lower sound pressure because there is more oxygen available.

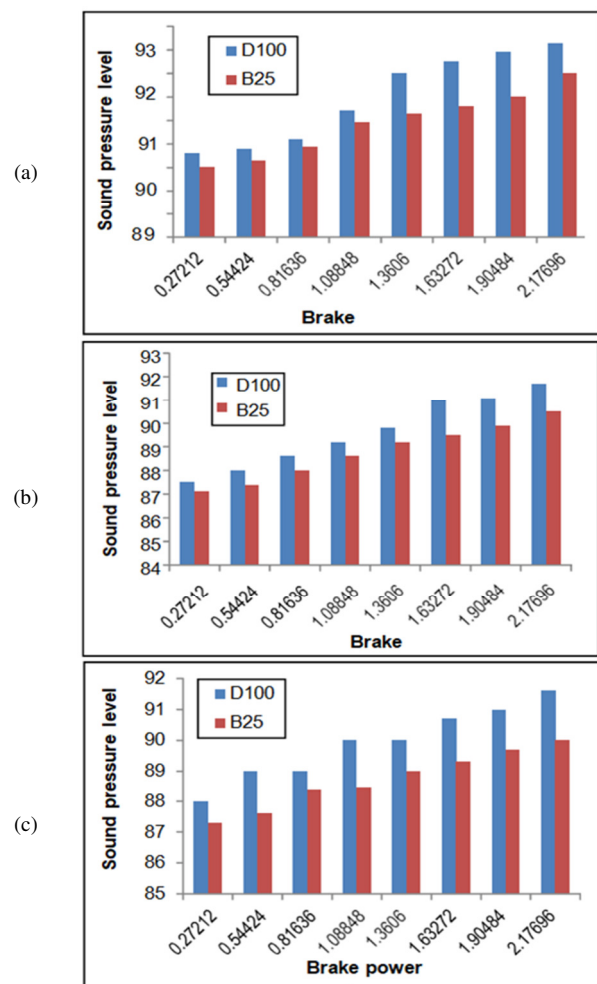


Fig. 6. Comparative results of sound pressure level at (a) the front side of the engine, (b) the left side of the engine, the back side of the engine.

IV. CONCLUSION

In this research, two fuel samples have been used, B25 (biodiesel 25% and diesel 75%) and D100 (100% diesel), which was the baseline in the CI engine, at constant 1350 rpm with variable loads from 0.0 to 1.6 at an interval of 0.2Kg-m. Exhaust particulate emissions, sound pressure level, and performance tests have been carried out. The results of the current study are:

- D100 has lower brake specific fuel consumption than the B25 and higher BTE.
- The results show that the use of biodiesel (waste cooking oil) causes a decrease in sound pressure level.
- The use of B25 reduces exhaust particulate emissions of the compression ignition engine by 7.29%.

Regarding future work, nanoparticles (aluminum oxide and silica oxide) can be added in biodiesel blends to analyze further their performance in the compression ignition engine.

ACKNOWLEDGMENT

The authors are grateful to the Mechanical Engineering Department, Quaid-e-Awam University of Engineering Science and Technology Nawabshah, Pakistan, for their assistance in this research work.

REFERENCES

- [1] G. Paul, A. Datta, and B. K. Mandal, "An Experimental and Numerical Investigation of the Performance, Combustion and Emission Characteristics of a Diesel Engine Fueled with Jatropha Biodiesel," *Energy Procedia*, vol. 54, pp. 455–467, Jan. 2014, <https://doi.org/10.1016/j.egypro.2014.07.288>.
- [2] *Directive 2009/28/EC of the European Parliament and of the Council of 23 April 2009 on the promotion of the use of energy from renewable sources and amending and subsequently repealing Directives 2001/77/EC and 2003/30/EC*, vol. 140, 2009.
- [3] S. Kim and B. E. Dale, "Environmental aspects of ethanol derived from no-tilled corn grain: nonrenewable energy consumption and greenhouse gas emissions," *Biomass and Bioenergy*, vol. 28, no. 5, pp. 475–489, May 2005, <https://doi.org/10.1016/j.biombioe.2004.11.005>.
- [4] A. B. Taylor, D. P. Moran, A. J. Bell, N. G. Hodgson, I. S. Myburgh, and J. J. Botha, "Gasoline/Alcohol Blends: Exhaust Emissions, Performance and Burn-Rate in a Multi-Valve Production Engine," SAE International, Warrendale, PA, USA, SAE Technical Paper 961988, Oct. 1996. <https://doi.org/10.4271/961988>.
- [5] C. Srinidhi, A. Madhusudhan, and S. V. Channappattana, "Parametric studies of CI engine at various injection strategies using biodiesel blended nanoparticles as fuel," *International Journal of Ambient Energy*, vol. 43, no. 1, pp. 117–127, Dec. 2022, <https://doi.org/10.1080/01430750.2019.1630303>.
- [6] K. N. Balan, U. Yashvanth, P. Booma Devi, T. Arvind, H. Nelson, and Y. Devarajan, "Investigation on emission characteristics of alcohol biodiesel blended diesel engine," *Energy Sources, Part A: Recovery, Utilization, and Environmental Effects*, vol. 41, no. 15, pp. 1879–1889, Aug. 2019, <https://doi.org/10.1080/15567036.2018.1549166>.
- [7] M. Christopher and S. Rajagopalan, "Emission analysis of a single cylinder di engine running on biodiesel blend as fuel," vol. 20, no. 6, pp. 681–684, Jan. 2014.
- [8] S. K. Hoekman, A. Broch, C. Robbins, E. Cenicerros, and M. Natarajan, "Review of biodiesel composition, properties, and specifications," *Renewable and Sustainable Energy Reviews*, vol. 16, no. 1, pp. 143–169, Jan. 2012, <https://doi.org/10.1016/j.rser.2011.07.143>.
- [9] A. A. Khaskheli, G. D. Walasai, A. S. Jamali, Q. B. Jamali, Z. A. Siyal, and A. Mengal, "Performance Evaluation of Locally-Produced Waste Cooking Oil Biodiesel with Conventional Diesel Fuel," *Engineering, Technology & Applied Science Research*, vol. 8, no. 6, pp. 3521–3524, Dec. 2018, <https://doi.org/10.48084/etasr.2333>.
- [10] A. K. Agarwal, "Biofuels (alcohols and biodiesel) applications as fuels for internal combustion engines," *Progress in Energy and Combustion Science*, vol. 33, no. 3, pp. 233–271, Jun. 2007, <https://doi.org/10.1016/j.peccs.2006.08.003>.
- [11] M. M. Tunio, M. R. Luhur, Z. M. Ali, and U. Daher, "Performance and Emission Analysis of a Diesel Engine Using Linseed Biodiesel Blends," *Engineering, Technology & Applied Science Research*, vol. 8, no. 3, pp. 2958–2962, Jun. 2018, <https://doi.org/10.48084/etasr.2028>.
- [12] F. Regan Maria Sundar Raj and J. Wilson Sahayaraj, "A comparative study over alternative fuel (biodiesel) for environmental friendly emission," in *Recent Advances in Space Technology Services and Climate Change 2010 (RSTS & CC-2010)*, Aug. 2010, pp. 80–86, <https://doi.org/10.1109/RSTSCC.2010.5712805>.
- [13] K. J. Harrington, "Chemical and physical properties of vegetable oil esters and their effect on diesel fuel performance," *Biomass*, vol. 9, no. 1, pp. 1–17, Jan. 1986, [https://doi.org/10.1016/0144-4565\(86\)90008-9](https://doi.org/10.1016/0144-4565(86)90008-9).
- [14] B. Karpanai Selvan *et al.*, "Utilization of biodiesel blended fuel in a diesel engine – Combustion engine performance and emission characteristics study," *Fuel*, vol. 311, Mar. 2022, Art. no. 122621, <https://doi.org/10.1016/j.fuel.2021.122621>.
- [15] G. Knothe, R. O. Dunn, and M. O. Bagby, "Biodiesel: The Use of Vegetable Oils and Their Derivatives as Alternative Diesel Fuels," in *Fuels and Chemicals from Biomass*, vol. 666, American Chemical Society, 1997, pp. 172–208.
- [16] A. A. Khaskheli, H. J. Arain, I. A. Memon, U. A. Rajput, and M. J. Ahsan, "Emission and Noise Characteristics of a Diesel Engine Fuelled with Diesel-Chicken Oil Biodiesel Blends," *Engineering, Technology & Applied Science Research*, vol. 10, no. 2, pp. 5387–5391, Apr. 2020, <https://doi.org/10.48084/etasr.3348>.
- [17] R. A. Bradley, E. C. Watts, and E. R. Williams, "Limiting net greenhouse gas emissions in the United States," USDOE Office of Policy, Planning and Analysis, Office of Environmental Analysis, Washington DC, USA, Technical Report DOE/PE-0101-Vol.2, Sep. 1991. <https://doi.org/10.2172/5775128>.
- [18] V. Ganesan, *Internal Combustion Engines*, 2nd ed. Singapore, 2004.
- [19] M. Karabektas, G. Ergen, and M. Hosoz, "Effects of the blends containing low ratios of alternative fuels on the performance and emission characteristics of a diesel engine," *Fuel*, vol. 112, pp. 537–541, Oct. 2013, <https://doi.org/10.1016/j.fuel.2011.04.036>.
- [20] B. Karpanai Selvan *et al.*, "Utilization of biodiesel blended fuel in a diesel engine – Combustion engine performance and emission characteristics study," *Fuel*, vol. 311, Mar. 2022, Art. no. 122621, <https://doi.org/10.1016/j.fuel.2021.122621>.
- [21] J. Xue, T. E. Grift, and A. C. Hansen, "Effect of biodiesel on engine performances and emissions," *Renewable and Sustainable Energy Reviews*, vol. 15, no. 2, pp. 1098–1116, Feb. 2011, <https://doi.org/10.1016/j.rser.2010.11.016>.
- [22] "Deposition Formation Effect of Biodiesel in a Diesel Engine Fuel Injector," *International Journal of Emerging Trends in Engineering Research*, vol. 9, no. 8, pp. 1057–1060, Aug. 2021, <https://doi.org/10.30534/ijeter/2021/03982021>.
- [23] D. Yage *et al.*, "Comparative study on combustion and particulate emissions for diesel-biodiesel and diesel-diglyme blends," *Fuel*, vol. 313, Apr. 2022, Art. no. 122710, <https://doi.org/10.1016/j.fuel.2021.122710>.

Visitors' Knowledge, Awareness, and Perception (KAP) of Climate Change in Mashar National Park, Hail-Saudi Arabia

Mohamed Ahmed Said

Architectural Engineering Department, College of Engineering, University of Hail,
Hail, Saudi Arabia and

Department of Architecture and Planning, College of Architecture and Planning,
Sudan University of Science and Technology, Khartoum, Sudan
mo.said@uoh.edu.sa

Received: 3 August 2022 | Revised: 22 August 2022 | Accepted: 28 August 2022

Abstract-This paper assesses the Knowledge, Awareness, and Perception (KAP) of Climate Change among the visitors of Mashar National Park, Hail, Saudi Arabia. Empirically, it has been established that climate change has an impact not only on the cultural and natural heritage but also on the visitor traffic patterns in national parks. The objectives guiding the study center on the identification of the level of knowledge and the investigation of the perception of park visitors regarding climate change. In the Hail Region, which is in the Kingdom of Saudi Arabia's north central region, the average temperature ranges from 39°F to 103°F and is infrequently lower than 31°F or higher than 108°F. This KAP research adopted quantitative methods using a questionnaire survey for data collection. A total of 120 park visitors were purposively sampled for the study. It was concluded that the visitors in Al-Mashar Park are not fully prepared to mitigate the impact of climate change even though Hail is undoubtedly experiencing climate variability. According to the study's findings, recommendations were made to maintain the park and provide opportunities for managing the park in a way that would allow it to better adapt to the effects of climate change, maintain effective resource management, and improve tourist satisfaction.

Keywords-climate change; knowledge; park visitors; perception

I. INTRODUCTION

Climate change is a phenomenon that has been identified by numerous academic fields and authorities. The Intergovernmental Panel on Climate Change, defined climate change as a shift in the condition of the climate that may be identified and measured by changes in the mean and/or variation of its parameters [1]. Extreme weather conditions, including those related to temperature, wind, rainfall, and humidity, may come from climate change, which has been ongoing for decades [2]. Variable consequences of climate change affect the environment, human health, agriculture, and transport. Climate change has resulted, among others, in heat waves and wildfires. According to [3], climate change refers to changes in the typical meteorological occurrences as well as their extremes, timing, and spatial distribution that express as

hot or chilly, dry or moist, snowfall or winds, floods, or thunderstorm tracks, and increasing temperatures, as well as water currents or upwelling. Climate change is a proven tendency toward extremes in the global climate, independent of underlying reason [3]. As a result, in order to discuss climate crisis, the indicators in issue must be quantifiable and show extreme behavior, i.e. a trend that deviates from the usual.

Extreme Temperatures (ETs) have a negative influence on socioeconomic events and human health in Middle Eastern countries [4]. With regard to local climate change, Saudi Arabia, the largest nation in the Middle East, has seen a number of ET occurrences and their aftereffects. For instance, on June 22, 2010, Jeddah city experienced summertime high of 52°C [5]. Several communities lost power as a result of the country's 8 power stations being forced to shut down due to the high temperature. Due to the tremendous negative effects of ETs, it is crucial for every region and nation to conduct thorough investigations of temperature extremes utilizing current records. This is crucial for Saudi Arabia, in which the semiarid and arid environment is dominant [6]. The two basic factors that trigger climate change are aspects related to biogeography, such as natural forces and factors that are caused by human activity, or anthropogenic influences.

Climate changes may result from human actions that lessen the amount of carbon that is absorbed from the atmosphere [7]. Deforestation, farming methods, and other detrimental changes in land use are a few examples of these actions. Growing population, rapid urbanization, and the lack of land use planning, in addition to the effects of changing temperatures, precipitation, wind, and solar radiation, continue to contribute to the degradation of the environment and water supplies [8]. In addition, industrialization, gas flaring, and forest burning contribute to the release of significant quantities of greenhouse gases into the atmosphere, which contributes to climate change. Researchers have cautioned that changes in climatic factors could affect the ability of mountain tributaries to store snow and ice. The shift in seasonality could impede agricultural

Corresponding author: Mohamed Ahmed Said

development, including future hydrological installation planning and operation [9].

Parks and protected areas are a germane context to investigate the perceptions of climate change because some visitors interact with climate-influenced resources and often notice climate-related biophysical impacts [9, 10]. Conversely, many impacts (e.g. increased temperatures, decreased water in the soil, species migration) from a changing climate remain relatively unnoticeable in heavily developed metropolitan areas where the 80% of U.S. citizens reside [11]. Therefore, parks and other nature-based areas provide unique opportunities to experience, notice, and respond to climate change impacts, which are perhaps much less apparent in the metropolitan built environment. National parks' ecological and cultural resources, as well as visitor patterns, will surely be impacted by climate change. With further global warming, it's conceivable that the places, times, and the number of people who visit parks will change. For instance, visitors may avoid the hottest months in low-latitude parks, whereas the season for visiting northern parks may last for several extra weeks or months. Several environmental and social elements will determine whether park visitors monitor climate change and alter their behavior. However, a crucial first step for park management and surrounding communities to predict, plan for, and actively influence future attendance is recognizing likely change in visits based on past records and anticipated trends of change in temperature [12].

According to a UN Habitat report, cities cover 2% of the earth's surface — yet, as hubs of social and economic activity, they consume about 78% of the world's energy. And cities produce, on average, more than 60% of the CO₂ emissions and greenhouse gases that give rise to global warming and climate change. Clearly however, the impact of climate change affects urban and rural dwellers alike — and Saudi Arabia has been experiencing it for at least during the last decade. With dry climatic conditions, its ecosystems are sensitive, water resources are limited, and agricultural fields are vulnerable to environmental transitions. The 2007 Intergovernmental Panel on Climate Change report showed that climate change has caused worldwide changes in precipitation levels, and that these have manifested in Saudi Arabia as increased levels of rainfall. In the major cities of the country, this increased rainfall, coupled with the presence of unplanned settlements, has led to increased hazards such as flash floods [13]. The physical infrastructure, natural ecosystem, cultural resources, visitor experience, and other intrinsic values of parks are at risk from the effects of climate change [14]. Impacts from localized changes in climate may influence the quality of visitors' experience and, therefore, visitors' perceptions of climate change are a concern for resource professionals who manage nature-based leisure services [15, 16].

Several studies show that climate related factors are important considerations for visitors making travel related decisions [17-21]. For example, it was found that certain climate variables, such as rain, storms, and higher humidity are likely to negatively influence travel decisions, in addition to higher temperatures alone, which are not always perceived as negative. Similar researches [20, 21] all found that seasonality,

extreme weather events, and annual climate variability impact visitor decisions. Further, increased temperatures and changes in precipitation impact recreation opportunities and particularly the activities highly reliant on weather conditions [22, 23].

Further, visitor experiences can also be impacted by climatic condition changes that result in loss or relocation of native species, introduction of invasive species, alteration of vegetation patterns, reduced availability of water, and increase in the frequency, severity, and size of wildfires [24]. According to [25], climate change is modifying species distribution, which makes conservation efforts more challenging. According to [16], measurable plant and animal responses to recent climate change within national parks have already been documented. As such, the management may need to alter practices and policies regarding allowable activities to accommodate changing species distributions and invasive species. In addition, the frequency and intensity of extreme weather events can impact the park resources and animal habitats [26-28].

The public's knowledge, understanding, and perception of climate change must be assessed in order to successfully implement sustainable environmental practices. The KAP strategy of this study is therefore very helpful. KAP research techniques are used to discover what people understand, believe, and act regarding a specific topic [29]. In light of this, research was conducted to determine the KAP of park visitors in Mashar National Park regarding climate change.

II. AIMS AND OBJECTIVES

The dominant rationale behind this KAP survey is to address the gaps in climate change knowledge, awareness and perception among park visitors in Al-Mashar National Park. This would be achieved through the objectives guiding the current study, which are:

- To identify the level of knowledge of visitors regarding climate change in Al-Mashar National Park.
- To determine the awareness of visitors on Climate Change in Al-Mashar National Park.
- To investigate the perception of visitors regarding climate change in Al-Mashar National Park.

III. MATERIALS AND METHODS

A. Study Area

The Hail Region is situated in the northernmost region of Saudi Arabia. The area is 118,232km² in size. The only important city in the area is Ha'il (Hael), which is situated in the region's center. It is roughly 600km from Riyadh, 450km from Madinah, and 650km from Tabuk, and has good connectivity to other regional centers. Due to its elevation of 915m above sea level, Ha'il experiences a mild climate. Ha'il's geographic location offers a number of benefits, including a moderate climate and picturesque mountain and desert landscapes [12]. In Ha'il, the winters are chilly, dry, windy, and mainly clear while the summers are lengthy, scorching, desert, and clear. The average annual temperature ranges from 39 to 103°F, rarely falling below 31 or rising over 108 [22]. Early May through early July and early September through mid-

October are the ideal seasons to visit Ha'il for hot-weather activities, according to the beach/pool score [13].



Fig. 1. Mashar National Park.

B. Methodology

This research uses a social constructionist approach to examine subjective meanings, experiences, and behaviors of visitors related to global standards of climate change. This KAP research adopted the quantitative method using a questionnaire survey for data collection. There were 4 sections in the questionnaire. Information on the sociodemographic characteristics of park visitors was presented in Section A and Sections B, C, and D consisted of questions regarding the knowledge, attitudes, and perceptions relating to climate change respectively. The content was validated to make sure that the items measured the things they were meant to measure. Quantitative data analysis was done using SPSS software and was further presented and interpreted using frequency distribution tables and narratives were scripted to discuss the findings.

IV. RESULTS AND DISCUSSION

A. Visitors Knowledge on Climate Change

Table I presents whether the visitors are informed of climate change as a concept. We see that the majority of 108 (90%) visitors claim to know what climate change is while 12 (10%) were not informed about climate change. Table II presents the sources of knowledge on climate change. Table III presents the visitors' perception on the types of change in climate change. It should be noted that the majority of the respondents is aware of at least one major change in weather patterns due to climate change, but a significant minority (22.8%) claims to be unaware or uninformed.

TABLE I. BEING INFORMED ABOUT CLIMATE CHANGE

Informd	Frequency	Percentage
Yes	108	90%
No	12	10%

TABLE II. SOURCES OF KNOWLEDGE ON CLIMATE CHANGE

Sources	Frequency	Percentage
Newspapers	25	15.4%
Radio	19	11.7%
Television	32	19.7%
Health workers	9	5.5%
Teachers	51	31.4%
Family members	13	8.3%
Religious leaders	10	6.2%
Others	3	1.8%

TABLE III. CLIMATE CHANGE ACKNOWLEDGED TYPES

Change	Frequency	Percentage
Excessive temperature	41	26.7%
Excessive cold	19	9.8%
Alteration in the rainfall pattern	42	27.4%
Recurring cyclones or tides	3	1.9%
Periodic floods	10	6.5%
Logging in water	7	4.5%
Unaware or uninformed	35	22.8%

TABLE IV. CAUSES OF CLIMATE CHANGE

Causes	Frequency	Percentage
Deforestation	45	29.4%
Industrial effluents	21	13.7%
Population growth	19	12.4%
Automobiles' dark exhaust smoke	15	9.8%
High carbon emissions from developed nations	17	12.5%
Rapid urbanization and lifestyle changes	7	4.5%
Astrophysical event (polar wander)	3	1.9%
Unaware or uninformed	26	16.9%

Table IV presents visitors' perception of the causes of climate change.

B. Visitors Awareness on Climate Change

Table V presents how often visitors are getting informed on climate change. We can see that the majority is informed either frequently or very frequently. Table VI presents the sources of information on climate change. It should be noted that the majority does not mention mass media as the source of information.

TABLE V. FREQUENCY OF AWARENESS OF CLIMATE CHANGE

Frequency level	Frequency	Percentage
Very frequently	41	34.1%
Frequently	35	29.1%
Occasionally	16	13.3%
Rarely	11	9.1%
Very rarely	7	5.8%
Never	10	8.3%

TABLE VI. SOURCE OF INFORMATION ON CLIMATE CHANGE

Source	Frequency	Percentage
Scientist	44	36.6%
Teacher	40	33.4%
Neighbour/friend	6	5%
Mass media	30	25%

C. Visitors Perception on Climate Change

Table VII presents visitor's perception of climate change while Table VIII presents the component of climate change felt the most by the respondents the majority of which reported temperature change as the most vivid climate change indicator.

TABLE VII. PERCEPTIONS ON CLIMATE CHANGE

Perception	Agree		Undecided		Disagree	
	Frequency	%	Frequency	%	Frequency	%
Rainfall pattern is changing	90	78	10	10.3	20	16.6
Timing of the rainfall is changing	70	58.8	8	6.6	42	33
The amount of rainfall is changing	80	66.6	4	3.3	36	30
The intensity of rainfall is changing	66	55	23	19.1	31	25.8
Summer temperature is changing	60	50	15	12.5	45	37.5
Hot waves are changing	90	75.1	8	6.6	22	18.3
Cold waves are changing	70	58.3	20	16.6	30	25.1
Winter temperature is changing	77	64.1	19	15.8	24	20.1
The overall annual temperature is changing	88	73.3	12	10	20	16.6
Hail-storm event frequency is changing	100	83.3	0	0	20	16.6
Thunderstorm and lightening event frequency is changing	60	50	40	33.3	20	16.6
Wind velocity is changing	85	70.8	17	14.1	18	15

TABLE VIII. COMPONENTS OF CLIMATE CHANGE FELT THE MOST

Component	Frequency	Percentage
Temperature	71	59.1%
Rainfall	32	26.6%
Wind	10	8.3%
Hail-storm	3	2.5%
Lightening	4	3.3%

TABLE IX. BEHAVIORS EXHIBITED TO REDUCE THE IMPACT OF CLIMATE CHANGE FELT THE MOST

Behaviour	Frequency	Percentage
Reducing energy consumption	15	11.8%
Reducing water consumption	16	12.5%
Waste recycling	19	14.9%
Reducing consumption of disposable items	17	13.3%
Buying environmentally friendly products	12	10%
Installing renewable energy equipment, e.g. solar panels	8	6.2%
None	17	13.3%
Don't know/don't understand	23	18.1%

Table IX presents the behaviors reported by the visitors on what they do to reduce the impact of climate change. It should be noticed that the majority already does something regarding climate change in their everyday life, but a significant minority of 23 (18.1%) visitors don't know/understand the habits to be exhibited in order to reduce the impact of climate change.

V. DISCUSSION

This research has made it clear that visitors to Al-Mashar national park feel responsible for the protection of the park but are not fully equipped with the necessary technical know-how in terms of capacity on issues surrounding climate change in their region. It is also evident that the research subjects, i.e the Al-Mashar National Park visitors, want to learn more about climate change and the actions they can take to mitigate its effects on these treasured landscapes. Furthermore, with proper education and access to varying information sources about climate change, visitors can become important advocates in the need to respond to climate change, within the parks and their communities.

VI. CONCLUSION AND RECOMMENDATIONS

Since climate change is a complicated topic that is frequently met with skepticism, there is a need for convincing evidence to prove its truth. The findings of this study prove that, despite the fact that Saudi Arabia is clearly experiencing climate variability, visitors to Al-Mashar Park are not adequately equipped to lessen the effects of climate change. The administration of protected areas, visitor traffic, and regional economics are all expected to be impacted in a complicated and cascading manner by a changing climate. Recognizing the strong correlation between visitation and climate allows for future planning and has two main effects on the management of protected areas and municipal services: travel patterns will change [14] and services and facilities will need to adapt to changing needs. To adjust to the changing conditions, which are a result of climate change, involves minimizing harm and seizing advantageous chances [15]. In the future, it might be necessary for the administration of Al-Mashar National Park to balance the benefits of shifting

visiting patterns with the negative effects of both too few and too many people attend (either not enough tourists to support local businesses and far too many tourists that interfere with recreational fun), e.g. by increased recreation and education opportunities and visitation during shoulder seasons. Changes in the environment as well as modifications in visitor usage and preference patterns are predicted to occur in the ensuing decades. Protected places and their surrounding communities, like Al-Mashar National Park, will need to adapt to the opportunities provided by changing visitors, and they may be able to take use of them. Globally comparable historical weather data and future estimates are available, however the availability and methodology of visitation data in different protected areas varies greatly. Al-Mashar National Park management can increase tourist satisfaction and combine it with increased efforts to measure human visitation trends. The current analysis can be followed by additional studies into relatively brief visitation patterns and other drivers of visitation in order to help the management adapt to the effects of climate change.

REFERENCES

- [1] IPCC, "AR4 Climate Change 2007: Synthesis Report — IPCC," IPCC, Geneva, Switzerland, 2007.
- [2] O. C. Korie *et al.*, "An Overview of Benefits of Organic Agriculture as a Climate Change Adaptation and Mitigation Strategy for Nigeria," *International Journal of Agriculture and Rural Development*, vol. 14, no. 2, pp. 638–643, 2011, <https://doi.org/10.4314/ijard.v14i2>.
- [3] C. Rynkiewicz, "Meeting the Climate Change Challenge," in *Innovation in Life Cycle Engineering and Sustainable Development*, Dordrecht, Netherlands, 2006, pp. 33–48, https://doi.org/10.1007/1-4020-4617-0_3.
- [4] F. Abdulla, "21st Century Climate Change Projections of Precipitation and Temperature in Jordan," *Procedia Manufacturing*, vol. 44, pp. 197–204, Jan. 2020, <https://doi.org/10.1016/j.promfg.2020.02.222>.
- [5] M. Salimi and S. G. Al-Ghamdi, "Climate change impacts on critical urban infrastructure and urban resiliency strategies for the Middle East," *Sustainable Cities and Society*, vol. 54, Mar. 2020, Art. no. 101948, <https://doi.org/10.1016/j.scs.2019.101948>.
- [6] M. Almazroui, M. Nazrul Islam, H. Athar, P. D. Jones, and M. A. Rahman, "Recent climate change in the Arabian Peninsula: annual rainfall and temperature analysis of Saudi Arabia for 1978–2009," *International Journal of Climatology*, vol. 32, no. 6, pp. 953–966, 2012, <https://doi.org/10.1002/joc.3446>.
- [7] K. E. Trenberth, "Attribution of climate variations and trends to human influences and natural variability," *WIREs Climate Change*, vol. 2, no. 6, pp. 925–930, 2011, <https://doi.org/10.1002/wcc.142>.
- [8] M. N. Sharabian, S. Ahmad, and M. Karakouzian, "Climate Change and Eutrophication: A Short Review," *Engineering, Technology & Applied Science Research*, vol. 8, no. 6, pp. 3668–3672, Dec. 2018, <https://doi.org/10.48084/etasr.2392>.
- [9] A. N. Laghari, W. Rauch, and M. A. Soomro, "A Hydrological Response Analysis Considering Climatic Variability: Case Study of Hunza Catchment," *Engineering, Technology & Applied Science Research*, vol. 8, no. 3, pp. 2981–2984, Jun. 2018, <https://doi.org/10.48084/etasr.2056>.
- [10] J. Thompson, S. Davis, and K. Mullen, "Climate Change Communication Campaign Planning: Using Audience Research to Inform Design," *The George Wright Forum*, vol. 30, no. 2, pp. 182–189, 2013.
- [11] M. T. J. Brownlee, J. C. Hallo, and B. D. Krohn, "Botanical garden visitors' perceptions of local climate impacts: awareness, concern, and behavioral responses," *Managing Leisure*, vol. 18, no. 2, pp. 97–117, Apr. 2013, <https://doi.org/10.1080/13606719.2013.752209>.
- [12] "Demographic and Housing Estimates: 2009–2013 5-Year American Community Survey." U.S. Census Bureau, 2013.
- [13] M. T. J. Brownlee and R. I. Verbos, "Measuring outdoor recreationists' beliefs in climate change: Testing the Occurrence and Anthropogenic Causation Scale (OC-AN)," *Journal of Outdoor Recreation and Tourism*, vol. 11, pp. 1–12, Oct. 2015, <https://doi.org/10.1016/j.jort.2015.06.003>.
- [14] M. T. J. Brownlee, J. C. Hallo, and B. D. Krohn, "Botanical garden visitors' perceptions of local climate impacts: awareness, concern, and behavioral responses," *Managing Leisure*, vol. 18, no. 2, pp. 97–117, Apr. 2013, <https://doi.org/10.1080/13606719.2013.752209>.
- [15] S. M. De Urioste-Stone, M. D. Scaccia, and D. Howe-Poteet, "Exploring visitor perceptions of the influence of climate change on tourism at Acadia National Park, Maine," *Journal of Outdoor Recreation and Tourism*, vol. 11, pp. 34–43, Oct. 2015, <https://doi.org/10.1016/j.jort.2015.07.001>.
- [16] W. B. Monahan and N. A. Fisichelli, "Climate Exposure of US National Parks in a New Era of Change," *PLOS ONE*, vol. 9, no. 7, 2014, Art. no. e101302, <https://doi.org/10.1371/journal.pone.0101302>.
- [17] J. B. Elsner, S. C. Elsner, and T. H. Jagger, "The increasing efficiency of tornado days in the United States," *Climate Dynamics*, vol. 45, no. 3, pp. 651–659, Aug. 2015, <https://doi.org/10.1007/s00382-014-2277-3>.
- [18] B. Saghir, "Climate Change in Saudi Arabia: Rethinking the Role of Local Government," *King Salman Center for Local Governance*, 2022. <http://www.kscglg.org/en/publication-project/climate-change-in-saudi-arabia-rethinking-the-role-of-local-government/>.
- [19] N. A. Fisichelli, G. W. Schuurman, W. B. Monahan, and P. S. Ziesler, "Protected Area Tourism in a Changing Climate: Will Visitation at US National Parks Warm Up or Overheat?," *PLOS ONE*, vol. 10, no. 6, 2015, Art. no. e0128226, <https://doi.org/10.1371/journal.pone.0128226>.
- [20] Stop TB Partnership, *Advocacy, Communication and Social Mobilization for TB Control: A Guide to Developing Knowledge, Attitude and Practice Surveys*. Switzerland: World Health Organization, 2008.
- [21] *Hael City Profile*. UN-Habitat, 2019.
- [22] "Ha'il Climate, Weather By Month, Average Temperature (Saudi Arabia)," *Weather Spark*. <https://weatherspark.com/y/101927/Average-Weather-in-Ha'il-Saudi-Arabia-Year-Round>.
- [23] A. Bigano, J. M. Hamilton, D. J. Maddison, and R. S. J. Tol, "Predicting tourism flows under climate change," *Climatic Change*, vol. 79, no. 3, pp. 175–180, Dec. 2006, <https://doi.org/10.1007/s10584-006-9190-7>.
- [24] IPCC, "Summary for policymakers," in *Climate Change 2014: Impacts, Adaptation, and Vulnerability - Contribution of Working Group II to the Fifth Assessment Report of the Intergovernmental Panel on Climate Change*, C. B. Field, V. R. Barros, D. J. Dokken, K. J. Mach, M. D. Mastrandrea, T. E. Bilir, M. Chatterjee, K. L. Ebi, Y. O. Estrada, R. C. Genova, B. Girma, E. S. Kissel, A. N. Levy, S. MacCracken, P. R. Mastrandrea, and L. L. White, Eds. Cambridge, United Kingdom and New York, NY, USA: Cambridge University Press, 2014.
- [25] A. R. Gitlin *et al.*, "Mortality Gradients within and among Dominant Plant Populations as Barometers of Ecosystem Change During Extreme Drought," *Conservation Biology*, vol. 20, no. 5, pp. 1477–1486, 2006, <https://doi.org/10.1111/j.1523-1739.2006.00424.x>.
- [26] C. A. Monz, K. J. Gutzwiller, V. H. Hausner, M. W. Brunson, R. Buckley, and C. M. Pickering, "Understanding and managing the interactions of impacts from nature-based recreation and climate change," *Ambio*, vol. 50, no. 3, pp. 631–643, Mar. 2021, <https://doi.org/10.1007/s13280-020-01403-y>.
- [27] M. A. Said and M. Touahmia, "Evaluation of Allocated Areas for Parks and their Attributes: Hail City," *Engineering, Technology & Applied Science Research*, vol. 10, no. 1, pp. 5117–5125, Feb. 2020, <https://doi.org/10.48084/etasr.3253>.
- [28] O. L. Kupika, E. Gandiwa, S. Kativu, and G. Nhamo, "Impacts of Climate Change and Climate Variability on Wildlife Resources in Southern Africa: Experience from Selected Protected Areas in Zimbabwe," in *Selected Studies in Biodiversity*, B. Sen and O. Grillo, Eds. IntechOpen, 2017, <https://doi.org/10.5772/intechopen.70470>.
- [29] "The KAP Survey Model (Knowledge, Attitudes, and Practices)," *SPRING*. <https://www.spring-nutrition.org/publications/tool-summaries/kap-survey-model-knowledge-attitudes-and-practices>.